mod-Inf.

NATURAL GAS ENGINEERING

Production and Storage

25765 ACC 19E

McGraw-Hill Chemical Engineering Series

Building the Literature of a Profession

Fifteen prominent chemical engineers first met in New York more than 60 years ago to plan a continuing literature for their rapidly growing profession. From Industry came such pioneer practitioners as Leo H. Baekeland, Arthur D. Little, Charles L. Reese, John V. N. Dorr, M. C. Whitaker, and R. S. McBride. From the universities came such eminent educators as William H. Walker, Alfred H. White, D. D. Jackson, J. H. James, Warren K. Lewis, and Harry A. Curtis. H. C. Parmelee, then editor of *Chemical and Metallurgical Engineering*, served as chairman and was joined subsequently by S. D. Kirkpatrick as consulting editor.

After several meetings, this committee submitted its report to the McGraw-Hill Book Company in September 1925. In the report were detailed specifications for a correlated series of more than a dozen texts and reference books which have since become the McGraw-Hill Series in Chemical Engineering and which became the cornerstone of the chemical engineering curriculum.

From this beginning there has evolved a series of texts surpassing by far the scope and longevity envisioned by the founding Editorial Board. The McGraw-Hill Series in Chemical Engineering stands as a unique historical record of the development of chemical engineering education and practice. In the series one finds the milestones of the subject's evolution: industrial chemistry, stoichiometry, unit operations and processes, thermodynamics, kinetics, and transfer operations.

Chemical engineering is a dynamic profession, and its literature continues to evolve. McGraw-Hill and its consulting editors remain committed to a publishing policy that will serve, and indeed lead, the needs of the chemical engineering profession during the years to come.

The Series

Bailey and Ollis: *Biochemical Engineering Fundamentals*
Bennett and Myers: *Momentum, Heat, and Mass Transfer*
Beveridge and Schechter: *Optimization: Theory and Practice*
Brodkey and Hershey: *Transport Phenomena: A Unified Approach*
Carberry: *Chemical and Catalytic Reaction Engineering*
Constantinides: *Applied Numerical Methods with Personal Computers*
Coughanowr and Koppel: *Process Systems Analysis and Control*
Douglas: *Conceptual Design of Chemical Processes*
Edgar and Himmelblau: *Optimization of Chemical Processes*
Fahien: *Fundamentals of Transport Phenomena*
Finlayson: *Nonlinear Analysis in Chemical Engineering*
Gates, Katzer, and Schuit: *Chemistry of Catalytic Processes*
Holland: *Fundamentals of Multicomponent Distillation*
Holland and Liapis: *Computer Methods for Solving Dynamic Separation Problems*
Katz, Cornell, Kobayashi, Poettmann, Vary, Elenbaas, and Weinaug: *Handbook of Natural Gas Engineering*
Katz and Lee: *Natural Gas Engineering: Production and Storage*
King: *Separation Processes*
Luyben: *Process Modeling, Simulation, and Control for Chemical Engineers*
McCabe, Smith, J. C., and Harriott: *Unit Operations of Chemical Engineering*
Mickley, Sherwood, and Reed: *Applied Mathematics in Chemical Engineering*
Nelson: *Petroleum Refinery Engineering*
Perry and Chilton (Editors): *Chemical Engineers' Handbook*
Peters: *Elementary Chemical Engineering*
Peters and Timmerhaus: *Plant Design and Economics for Chemical Engineers*
Probstein and Hicks: *Synthetic Fuels*
Reid, Prausnitz, and Rolling: *The Properties of Gases and Liquids*
Resnick: *Process Analysis and Design for Chemical Engineers*
Satterfield: *Heterogeneous Catalysis in Practice*
Sherwood, Pigford, and Wilke: *Mass Transfer*
Smith, B. D.: *Design of Equilibrium Stage Processes*
Smith, J. M.: *Chemical Engineering Kinetics*
Smith, J. M., and Van Ness: *Introduction to Chemical Engineering Thermodynamics*
Treybal: *Mass Transfer Operations*
Valle-Riestra: *Project Evolution in the Chemical Process Industries*
Van Ness and Abbott: *Classical Thermodynamics of Nonelectrolyte Solutions: With Applications to Phase Equilibria*
Van Winkle: *Distillation*
Walas: *Reaction Kinetics for Chemical Engineers*
Wei, Russell, and Swartzlander: *The Structure of the Chemical Processing Industries*
Wentz: *Hazardous Waste Management*

NATURAL GAS ENGINEERING

Production and Storage

Donald L. Katz

Late Professor of Chemical Engineering
The University of Michigan, Ann Arbor

Robert L. Lee

Assistant Professor
of Petroleum Engineering
The New Mexico Institute of
Mining and Technology, Socorro

McGraw-Hill Publishing Company

New York St. Louis San Francisco Auckland Bogotá Caracas Hamburg
Lisbon London Madrid Mexico Milan Montreal New Delhi Oklahoma City
Paris San Juan São Paulo Singapore Sydney Tokyo Toronto

NATURAL GAS ENGINEERING Production and storage
INTERNATIONAL EDITION 1990

3 4 5 6 7 8 9 0 CMO F C P 9 4 3 2

This book was set in Times Roman by Publication Services.
The editors were B. J. Clarke and John M. Morriss;
the production supervisor was Denise L. Puryear.
The cover was designed by Karen Quigley.
Project Supervision was done by Publication Services.

Library of Congress Cataloging-in-Publication Data

Katz, Donald La Verne, (date).
Natural gas engineering: production and storage/Donald L. Katz, Robert L. Lee

p. cm. — (McGraw-Hill chemical engineering series)
includes bibliographies and index.
ISBN 0-07-033352-1
1. Gas, Natural. 2. Gas, Natural—Storage. I. Lee, Robert L. II. Title. III. Series.
TN880.K38 1990
665.7'3—dc19 89-2322

When ordering this title use ISBN 0-07-100777-6

Printed in Singapore

ABOUT THE AUTHORS

Donald L. Katz, who died May 29, 1989, was Emeritus Professor of Chemical Engineering at the University of Michigan and a retired Consulting Engineer. He earned his doctorate in chemical engineering at the University of Michigan in 1933 and then worked for Phillips Petroleum Company, initiating a research program in oil and gas production. Returning to the University of Michigan in 1936, he developed a research program in phase behavior of light hydrocarbons, served as chairman of the Department of Chemical and Metallurgical Engineering, and was elected by the AIChE as its 1959 President. In 1959 he directed a national educational project to introduce the methods of using computers in instruction to engineering teachers.

He was coauthor of some 250 papers and several books, including the *Handbook of Natural Gas Engineering*. Recent papers have concentrated on the underground storage of natural gas, an area where he served many gas companies as consulting engineer. In the Public Service Sector, he chaired or served as panel member on 14 committees, such as NAS-NRC Advisory Committee to the U.S. Coast Guard on Hazardous Materials and the Committee on Air Quality and Power Plant Emissions requested by the Senate Public Works Committee.

Dr. Katz was declared one of the 30 "eminent Chemical Engineers" by the AIChE and "a Distinguished Member" of the Society of Petroleum Engineers. He received 17 national honors and awards, was elected by the National Academy of Engineering (1968), and received the National Medal of Science from President Reagan in 1983.

Robert L. Lee is an assistant professor in the Petroleum Engineering Department of the New Mexico Institute of Mining and Technology. He holds both a B.S. and M.S. degree from Oregon State University and a Ph.D. from the University of Michigan, Ann Arbor. All three degrees are in Chemical Engineering.

CONTENTS

PREFACE

This book has been prepared for engineering students, graduate engineers, and geologists who desire to practice in the natural gas industry. It treats natural gas in its various stages, from occurrence in the earthen reservoir through production with or without condensate and/or crude oil. Treatment of natural gas on the way to the fuel market and the warehousing of gas in underground storage reservoirs are considered as part of the delivery system.

Background for this endeavor consists of the **Handbook of Natural Gas Engineering**, published in 1959 with coauthors David Cornell, Riki Kobayashi, Fred Poettmann, John Vary, Jack Elenbaas, and Charles Weinaug. This was followed by the **Underground Storage of Fluids** in 1968, with Keith H. Coats as coauthor. A series of monographs and papers was published via American Gas Association (AGA) in cooperation with its Underground Storage Committee and consulting clients. From 1955 to 1987, intensive courses on Underground Storage of Natural Gas were given by the senior author with associates, first at the University of Michigan and then privately (1982–1987). Robert McDonald and Jack Elenbaas gave lectures and prepared material for notes in this latter period. We wish to acknowledge and thank the above-named persons and others involved for their input.

Our goal in this volume was to update, downsize, and consolidate the background gleaned in the senior author's more than 50 years of research and engineering practice in reservoir engineering applied to gas production and underground storage. Much material was extracted from the previous two books. The work of others was also incorporated, especially when it interfaced with the writers' activities. We acknowledge that minimum attention was given to work of others when we were unfamiliar with the subject at hand or bowed to the need

for downsizing. The senior author included the results of certain studies such as "Superheat Limit Explosions with LNG and Water," "Why Oil Lines Heat and Gas Lines Cool" and "Gas Transfer Between Reservoirs."

The senior author appreciates the freedom to investigate and write papers on many items during his consultations. In gas storage, there were continuous associations with Michigan Consolidated Gas Co. and successors (38 years), Northern Illinois Gas Co. (30 years), and Natural Gas Pipeline Co. of America (22 years). Research support from the AGA Pipeline Research Committee was helpful.

The University of Michigan's Department of Chemical Engineering has been very cooperative in this endeavor. H. Scott Fogler as chairman gave encouragement and assistance. The University of Michigan Computing Center provided valuable services in computation and manuscript preparation.

We have received help from the many authors credited in the text. Special efforts were made to assist us to be up to date. The group of Gerald Holder of University of Pittsburgh, Donald Robinson of Robinson Associates, Dendy Sloan and Fred Poettmann of Colorado School of Mines as well as K. Glowacki of New Mexico Tech. on gas hydrates is one example. Another is Mark Mallett of Conoco Inc. with his article in the Oil and Gas Journal on the use of expanders to recover high yields of natural gas liquids. Kenneth Ancell of Dowdle Fairchild & Ancell, Inc. and John McElhiney of Scientific Software—Intercomp provided assistance on Coal Seam Gas, and John Istvan of PB-KBB Inc., on Strategic Petroleum Reserve and Pittsfield Pilot Unit. Abbas Firoozabadi of Stanford University has carried on joint work with the senior author. W.R. Clark and S.F. Nowaczeroski of ANR Pipeline Co. prepared material on logging of wells. Assistance from David Dowhan, E. Grabowski, and Yusuf Hekim of ANR Pipeline Co. should also be acknowledged. Guy Fasanino and Eric Molinard of Gaz de France prepared the material on mixing project, Dennis Coleman of Isotech Lab., Inc. on gas identification, and Roger Logan of Los Alamos National Lab on simulation. Material from ARCO of Dallas and Mike Whims and Robert Lang of ANR Storage Co. was used here. We consulted with Chia-Shun Yih on high velocity flow in porous media.

With the assistance of the Michigan Gas Association, a manuscript was in preparation for a book over several years; it was used as notes for the intensive courses. In 1986 it became clear to the senior author that much more effort was required to improve and complete the manuscript. On August 1, 1986, the junior author, having completed his Ph.D. on "Flow in Porous Media at High Velocity Around Wellbores," agreed to assist the senior author in completion of the project. Appointed as a research engineer, he put the unfinished text on the computer word processor TEX, and then the two of us reconstructed the whole book. It should be noted that in October 1986, the senior author became ill and functioned only part time. The junior author assumed much responsibility for the manuscript. A draft was completed in November 1987. Meanwhile, the junior author became Assistant Professor at New Mexico Institute of Mining and Technology. Reviews obtained by the publisher were very valuable to us and for them we would like

to thank the following people: R. T. Ellington, University of Oklahoma; James Fair, University of Texas at Austin; and Charles Guffey, Texas Tech University. Refinements in manuscript have been addressed, and permission from copyright owner was obtained by May 1988. The final draft was completed in July 1988.

Special thanks for preparing the final manuscript go to Althea Cherry, Cynthia Miller, Joseph Yao, Fang Luo, Jay Keasling, and Naishing Chi.

Donald L. Katz
Robert L. Lee

NATURAL GAS ENGINEERING

Production and Storage

CHAPTER 1

NATURAL GAS TECHNOLOGY AND EARTH SCIENCES

This chapter describes various branches of the oil and gas industry and sets forth an overall view of natural gas engineering in production and underground storage of natural gas. The subjects of geology, geochemistry, and geophysics are given limited treatment here to prepare for the basic engineering topics of later chapters. In particular, earth temperatures and pressures, which are basic information for engineering calculations, are discussed. Miscellaneous topics include (*a*) what petroleum is, (*b*) the use of SI metric and English units, and (*c*) sources of information for natural gas engineering, including underground storage.

The current production of oil and gas worldwide is given in Table 1.1. It should be appreciated that the United States is importing crude oil from diverse sources. Figure 1-1 shows recent U.S. oil and gas production; the United States in 1987 imported some 5 million barrels of oil per day—down from 7 million in 1979.

TABLE 1.1
World oil and gas production [*Oil and Gas Journal*]

1,000 bd*	May 1986	Apr. 1986	5-month average: Production 1986	Production 1985	Chg. vs prev. year: Volume	Chg. vs prev. year: %	Gas (billion cu ft): May 1986	Gas: Apr. 1986	Gas: Cum. 1986
United States	8,800	8,815	8,943	8,872	71	0.8	1,394.0	1,375.0	7,203.0
Canada	1,408	1,365	1,404	1,457	– 53	– 3.6	247.2	267.8	1,464.3
Argentina	430	436	441	448	– 7	– 1.6	58.0	56.2	259.8
Bolivia	20	20	20	20	—	—	7.6	7.4	37.1
Brazil	580	579	579	525	54	10.3	16.6	16.3	82.4
Chile	33	33	33	34	– 1	– 2.9	22.5	18.8	83.4
Colombia	309	297	263	171	92	53.8	15.4	15.0	75.4
Ecuador†	300	300	302	273	29	10.6	0.2	0.2	1.0
Guatemala	6	5	5	3	2	66.7	0.1	0.1	0.5
Mexico	2,527	2,358	2,352	2,750	–398	–14.5	107.8	105.5	521.5
Peru	179	182	180	190	– 10	– 5.3	3.8	3.7	18.5
Trinidad	164	164	165	178	– 13	– 7.3	9.8	9.8	50.1
Venezuela†	1,555	1,555	1,557	1,558	– 1	– 0.1	50.9	49.3	248.0
Latin America	6,103	5,929	5,897	6,150	–253	– 4.1	292.7	282.3	1,377.7
Western hemisphere	16,303	16,109	16,244	16,479	–235	– 1.4	1,933.9	1,925.1	10,045.0
Austria	22	22	22	22	—	—	3.3	3.2	18.8
Denmark	72	76	73	57	16	28.1	3.4	5.2	31.1
France	62	62	60	44	16	36.4	11.4	10.0	63.7
Germany (West)	82	83	83	81	2	2.5	34.5	43.3	260.5
Greece	24	24	26	27	– 1	– 3.7	0.1	0.1	0.7
Italy	50	50	48	45	3	6.7	40.7	39.0	195.4
Netherlands	81	81	76	69	7	10.1	126.5	230.0	1,340.0
Norway	826	319	743	737	6	0.8	75.6	38.2	376.8
Spain	40	40	40	50	– 10	–20.0	0.7	0.7	3.5
Turkey	47	46	43	40	3	7.5	1.5	1.4	6.0
United Kingdom	2,538	2,554	2,644	2,639	5	0.2	117.7	152.0	856.8
Western Europe	3,844	3,357	3,858	3,811	47	1.2	415.4	523.1	3,153.3
Algeria†	600	550	581	656	– 75	–11.4	103.1	100.0	502.4
Angola/Cabinda	280	270	277	224	53	23.7	0.6	0.6	2.8
Cameroon	180	180	180	185	5	– 2.7	—	—	—
Congo	115	115	115	115	—	—	0.1	0.1	0.5
Egypt	845	760	809	874	– 65	– 7.4	12.0	12.0	60.0
Gabon†	160	160	160	150	10	6.7	0.2	0.2	1.0
Ghana	1	1	1	1	—	—	—	—	—
Ivory Coast	20	20	20	20	—	—	—	—	—
Libya†	985	978	997	1,071	– 74	– 6.9	13.5	13.5	67.5
Morocco	1	1	1	1	—	—	0.2	0.2	1.0
Nigeria†	1,600	1,700	1,501	1,553	– 52	– 3.3	5.4	5.4	27.0
Tunisia	100	100	108	105	3	2.9	1.3	1.3	6.5
Zaire	20	21	22	25	– 3	–12.0	—	—	—
Africa	4,907	4,856	4,772	4,980	–208	– 4.2	136.4	133.3	668.7
Bahrain	40	40	40	42	– 2	– 4.8	19.2	18.6	93.5
Iran†	2,100	2,100	2,016	2,233	–217	– 9.7	39.7	38.4	193.4
Iraq†	1,910	1,550	1,741	1,285	456	35.5	1.7	1.7	8.5
Israel	1	1	1	1	—	—	0.2	0.2	1.0
Kuwait†	1,500	1,400	1,283	876	407	46.5	12.1	12.1	60.5
Neutral Zone†	300	200	241	431	–190	–44.1	—	—	—
Oman	550	530	520	466	54	11.6	3.9	3.9	19.5
Qatar†	400	200	321	293	28	9.6	17.5	17.5	87.5
Saudi Arabia†	4,300	4,500	4,297	3,411	886	26.0	21.0	21.0	105.0
Syria	185	185	185	175	10	5.7	0.4	0.4	2.0
United Arab Emirates†	1,300	1,300	1,339	1,100	239	21.7	28.7	27.8	139.8
Middle East	12,586	12,006	11,984	10,313	1,671	16.2	144.4	141.6	710.7
Afghanistan	—	—	—	—	—	—	8.5	8.5	42.5
Australia	400	484	514	552	– 38	– 6.9	45.4	42.7	199.9
Brunei	170	170	170	148	22	14.9	23.0	22.3	112.1
Burma	30	30	30	30	—	—	1.9	1.9	9.5
India	630	637	631	615	16	2.6	19.7	16.2	79.7
Indonesia†	1,300	1,400	1,281	1,256	25	2.0	97.0	93.9	472.5
Japan	13	13	13	10	3	30.0	5.5	6.2	33.7

TABLE 1.1
World oil and gas production [*Oil and Gas Journal*](*continued*)

1,000 bd*	May 1986	Apr. 1986	5-month average Production 1986	5-month average Production 1985	Chg. vs prev. year Volume	Chg. vs prev. year %	Gas (billion cu ft) May 1986	Gas (billion cu ft) Apr. 1986	Gas (billion cu ft) Cum. 1986
Malaysia	500	510	503	447	56	12.5	14.6	14.6	73.0
New Zealand	34	31	30	17	13	76.5	19.2	16.8	77.4
Pakistan	39	41	41	30	11	36.7	34.3	34.1	170.4
Philippines	6	7	7	10	– 3	–30.0	—	—	—
Taiwan	2	2	2	3	– 1	–33.3	2.9	2.8	14.9
Thailand	35	31	36	32	4	12.5	10.7	9.7	49.6
Asia-Pacific	3,159	3,356	3,258	3,150	108	3.4	282.7	269.7	1,335.2
Eastern hemisphere	24,496	23,575	23,872	22,254	1,618	7.3	978.9	1,067.7	5,867.9
Total noncommunist	40,799	39,684	40,116	38,733	1,383	3.6	2,912.8	2,992.8	15,912.9
China	2,496	2,496	2,496	2,390	106	4.4	53.0	53.0	265.0
Romania	226	226	226	226	—	—	100.0	100.0	500.0
U.S.S.R.	12,292	12,215	12,134	11,941	193	1.6	2,005.0	1,983.9	10,060.5
Other communist	207	207	207	227	– 20	– 8.8	83.8	83.8	419.0
Communist	15,221	15,144	15,063	14,784	279	1.9	2,241.8	2,220.7	11,244.5
Total world	56,020	54,828	55,179	53,517	1,662	3.1	5,154.6	5,213.5	27,157.4
† OPEC	18,310	17,893	17,617	16,146	1,471	9.1	391.0	381.0	1,914.1
North Sea	3,484	2,997	3,502	3,469	33	1.0	—	—	—

* Totals may not add due to rounding † OPEC member

World gas-production trends (billion cu ft)

	1978	1979	1980	1981	1982	1983	1984	1985	% change 1985 vs. 1984
United States	19,922.4	19,999.4	20,267.0	19,596.0	18,731.0	16,581.0	18,068.0	17,304.0	– 4.2
Western Europe	4,793.7	6,866.6	6,668.7	6,906.6	6,142.1	6,383.5	6,795.4	6,647.2	– 2.2
Canada	3,133.1	3,646.5	2,668.3	2,623.0	2,546.1	2,414.1	2,651.8	3,350.6	+ 2.6
Latin America	2,533.5	2,610.0	3,297.5	3,227.0	3,071.5	3,340.5	3,451.8	3,443.2	– 0.2
Middle East	2,604.4	1,624.7	1,221.3	1,542.0	1,799.7	1,633.0	1,533.5	1,723.7	+12.4
Asia-Pacific	1,640.1	1,827.9	1,558.4	2,765.0	2,176.6	2,187.7	2,530.7	3,030.8	+19.8
Africa	1,558.1	1,027.9	884.7	1,947.0	1,168.9	1,143.8	1,629.1	1,764.0	+ 8.3
Communist bloc and China	17,683.3	19,591.4	21,069.9	19,210.0	20,258.0	21,383.0	23,272.2	25,457.9	+ 9.4
World total	53,868.6	57,194.4	57,635.8	57,816.6	55,893.9	55,066.5	59,932.3	62,721.4	+ 4.8

* *Source:* International Petroleum Encyclopedia, 1986, PennWell Publishing Co.

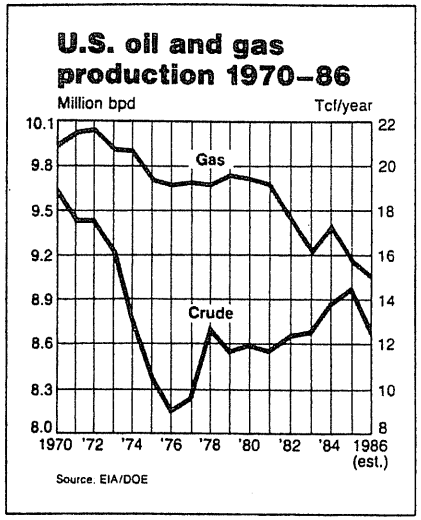

FIGURE 1-1
U.S. oil and gas production 1970–86 [courtesy *Oil and Gas Journal*, 1987].

1.1 BRANCHES OF PETROLEUM INDUSTRY

Several branches or divisions of the oil and gas industry are identified in this section as a way of giving a bird's eye view of the scope of activities encompassed.

The exploration for and finding of oil and gas deposits is where the industry starts. This area encompasses the fields of geology and geophysics, which deal with the layers of the earth wherein oil and gas may have been trapped under pressure in the earth. Exploration rights for the minerals in the earth are leased from the mineral right owner, government or private. Land departments handle the legal work of acquisitions of leases. Once geophysical and geological studies identify a prospective site and an expected horizon to contain the oil and gas, a drilling permit is obtained. Drilling proceeds on the wildcat or exploratory well site, frequently with the employment of a drilling contractor. When the potential horizon is reached, drill stem tests, cores, and logs are obtained to assess the prospects for commercial production. After oil and gas are found, the wellbore is cased, followed by installation of flow and separation equipment at the wellhead. Figure 1-2 illustrates the oil and gas separation facilities for a low-pressure crude oil reservoir and a gas condensate reservoir.

Development and production follow the finding of a commercially valuable deposit of oil and gas; development wells are drilled and tested. Arrangements are made for separating and gathering the oil and gas produced from the wells; such a production system is shown in Fig. 1-3. Crude oil or condensate is readied for the market by assuring that the water content is low (0.2 percent) and the volatile hydrocarbons are removed. The gas is sent to processing plants or possibly compressed and returned to the producing reservoir. Geological and engineering studies are made of the deposit or reservoir.

Molecular percentages

Constituent	Well stream	Separator gas	Separator liquid	Vent gas
Methane	74.4	84.8	18.9	33.4
Ethane	8.3	7.9	11.0	18.2
Propane	4.7	4.2	8.0	22.4
Iso-butane	0.9	0.5	3.0	5.6
Normal butane	1.9	1.1	6.9	10.5
Pentanes	1.4	0.3	7.3	5.7
Hexanes and heavier	7.7	0.3	44.9	3.0
Carbon dioxide	0.7	0.8	—	1.2
Totals	100.0	100.0	100.0	100.0

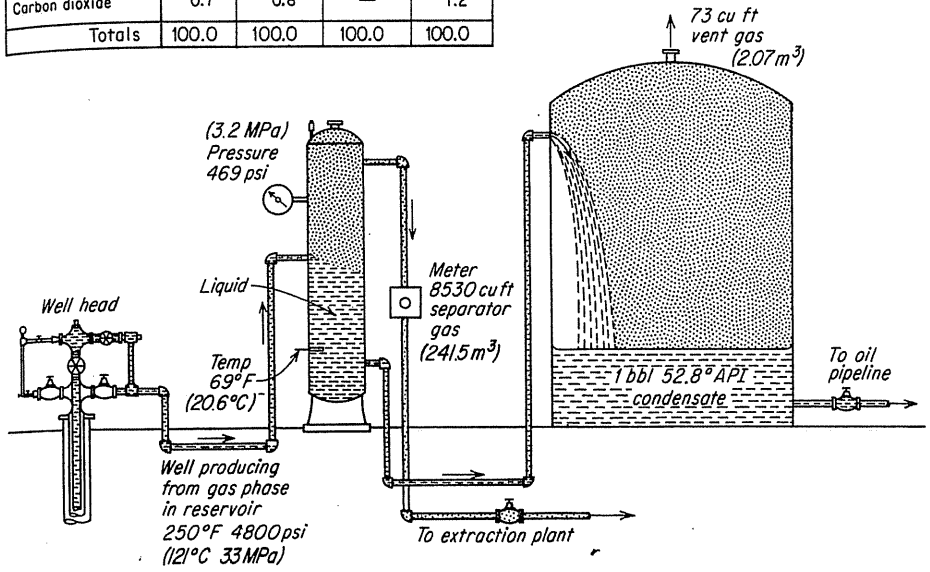

FIGURE 1-2
Well production from crude oil and gas condensate wells [Katz & Williams, 1-92, courtesy AAPG].

Reservoir engineering is the term adopted in the 1930s for detailed consideration of the quantity of oil and gas in a reservoir, and for finding the best ways to recover oil and gas, i.e., the location of wells, rates of production, and monitoring of reservoir pressure. The capillary retention of oil by the porous rock prevents a direct recovery of a high fraction of the liquid. Water influx at the edges or underneath the oil, called *water drive*, may be a factor in oil recovery. Understanding the physical behavior of the oil with dissolved gas is especially important for condensate-producing reservoirs, and also in CO_2 flooding projects. Oil and gas reservoirs normally have a pressure gradient of 0.46 psi/ft (10.4 kPa/m) of depth; pressures of 3000 to 8000 psia (20.7 to 55.2 MPa) are common for oil and gas reservoirs from 6000 to 15,000 feet (1829 to 4572 m).

Processing of gas for liquids recovery, dehydration, and sweetening takes place on the streams gathered from a central or leased separation facility. This technology is quite different from reservoir or production engineering in that its

Composition of streams - molecular percentages

Component	Well effluent	Separator gas	Vented gas	Stock tank oil
Methane	30.3	75.69	15.31	0.05
Ethane	13.1	17.76	35.54	1.35
Propane	9.4	5.19	30.67	5.03
Iso-butane	1.8	0.27	4.15	2.15
Normal butane	4.9	0.82	8.75	6.72
Pentanes	4.5	0.27	3.81	8.07
Hexanes plus	36.0	0.00	1.77	76.63
Totals	100.0	100.0	100.0	100.0

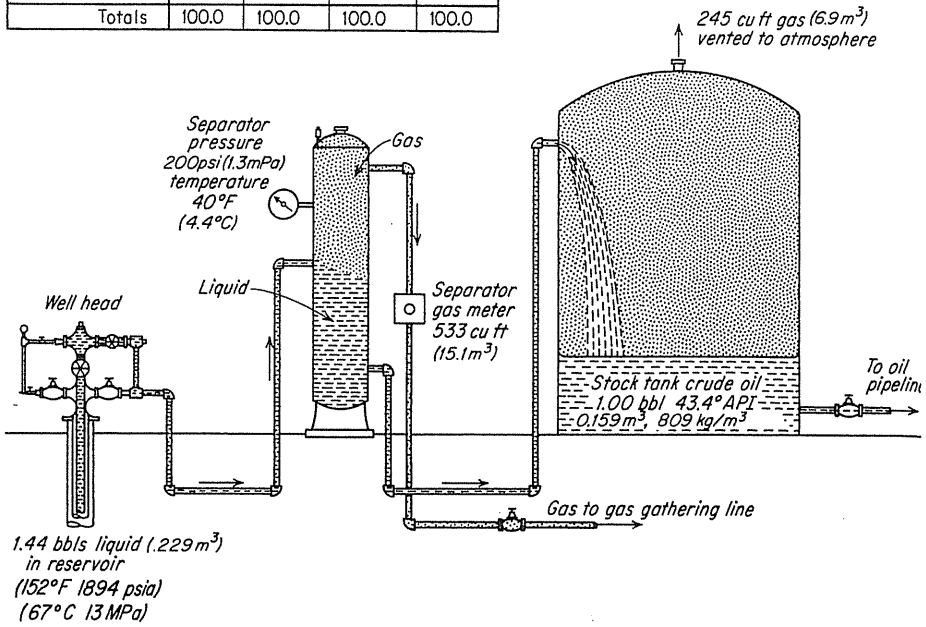

FIGURE 1-2
(*continued*)

processes are carried out in surface vessels. These processes extract the liquefiable constituents and produce propane-butane and LP (liquefied petroleum) products—natural gasoline or a composite NGL (natural gas liquid). The Gas Processors Association, through meetings and annual reports, provides advances in these technologies. Before gas is sent to pipelines, it needs to have a low water vapor content (2–4 lb/MMcf or 3.2–6.4 $\times$ 10^{-5} kg/m^3) so it will not form liquid water in the transcontinental pipelines taking it to market. Natural gas and liquid water can form solid gas hydrates that impede flow. Table 1.2 lists the products of commerce that come from oil reservoirs.

Natural gas pipelines carry the fuel gas to northern and eastern markets as shown by Fig. 1-4 at the rate of some 14 trillion cubic feet per year (396 $\times$ 10^9 m^3/year) with much of the gas going to space heating of homes, schools, hospitals, and commercial buildings. The market load in good part is tied to

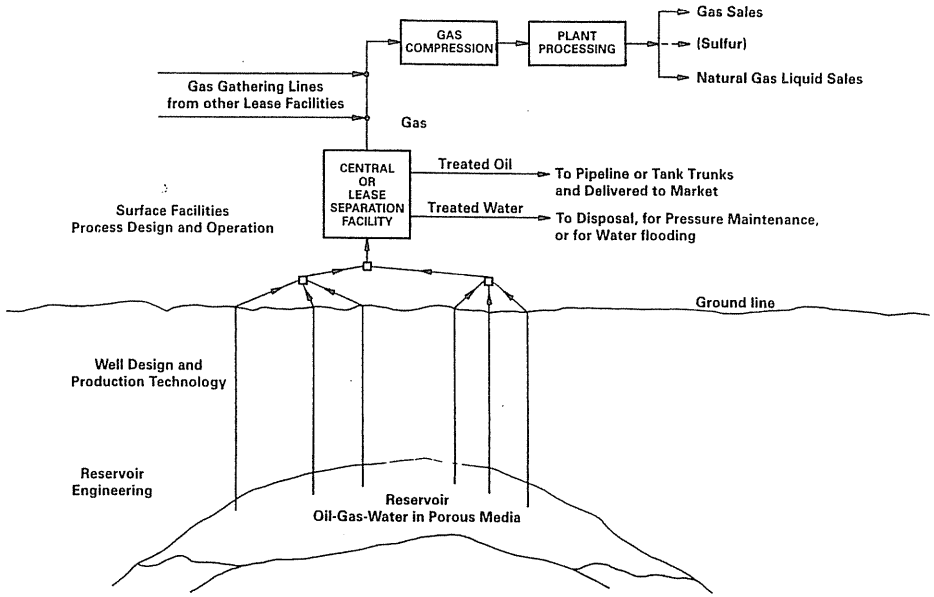

FIGURE 1-3
Diagram of oil and gas production system [courtesy ARCO].

the outside ambient temperature. Liquid products also are carried by pipeline in common carrier systems serving refineries and petrochemical plants.

Underground storage of gases and liquids. Gas storage fields (Fig. 1-5) were developed near the market to reduce the need for large-diameter pipelines to service winter gas demands in cold weather (Fig. 1-6). Figure 1-7 diagrams a pipeline system with underground storage. When depleted gas fields were available as in Michigan, Ohio, West Virginia, New York, California, etc., they were repressured. By drilling many wells and installing a gathering system, compressors, and gas dehydration facilities, large volumes of gas are withdrawn each winter and new gas is injected the following summer, giving rise to the cycle shown in Fig. 1-8. Figure 1-9 shows the growth of gas storage capacity. Figure 1-10 shows the location of gas storage projects. Table 1.3 contains American Gas Association (AGA) statistics on underground gas storage.

Aquifer storage was developed and grew most rapidly in Illinois since it lacked natural gas reservoirs near the market area. Gas companies devised storage in structures on water sands at 1000 feet (305 m) or more in depth. The term *aquifer storage* refers to the water zone in which the gas resides.

Salt occurs in layers in the earth or in salt domes. Solution mining of salt by dissolving it with injected water creates a salt cavity. Techniques were developed in the 1950s for creating and using salt cavities for liquid propane, LP gas, and other liquid storage underground. The gas industry began to use such cavities for

TABLE 1.2
Constituents of petroleum

Name	Formula	Normal boiling point °F	°C
Methane	CH_4	–259	–162
Ethane	C_2H_6	–128	– 89
Propane	C_3H_6	– 44	– 42
Isobutane	i-C_4H_{10}	+ 11	– 12
n-Butane	n-C_4H_{10}	31	– 1
Pentanes	C_5H_{12}	90	+ 32
Hexanes	C_6H_{14}	145	63
Heptanes	C_7H_{16}	195	91
Octanes	C_8H_8	245	118
Decanes	$C_{10}H_{22}$	345	174
Tetradecane	$C_{14}H_{30}$	490	254
Hexadecane	$C_{16}H_{34}$	549	287
Triacontane	$C_{30}H_{62}$	855	457
Tetracontane	$C_{40}H_{92}$	1012	544
Asphaltene	$C_{80}H_{162}{}^+$	1200+	649+

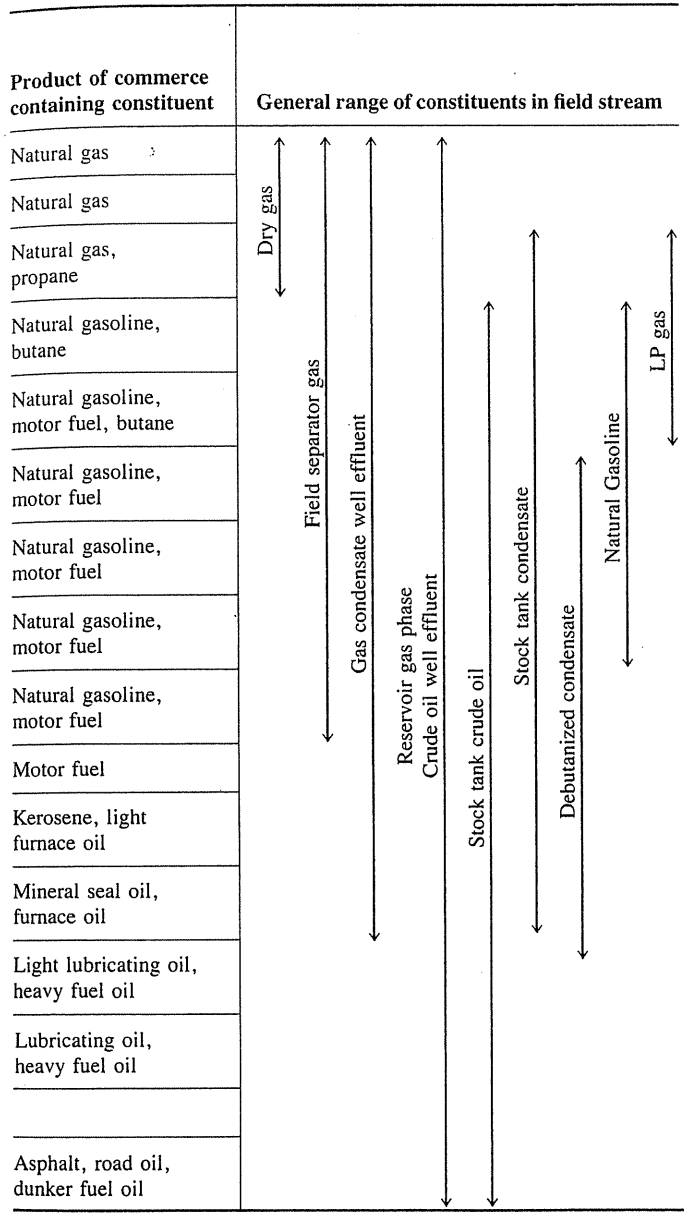

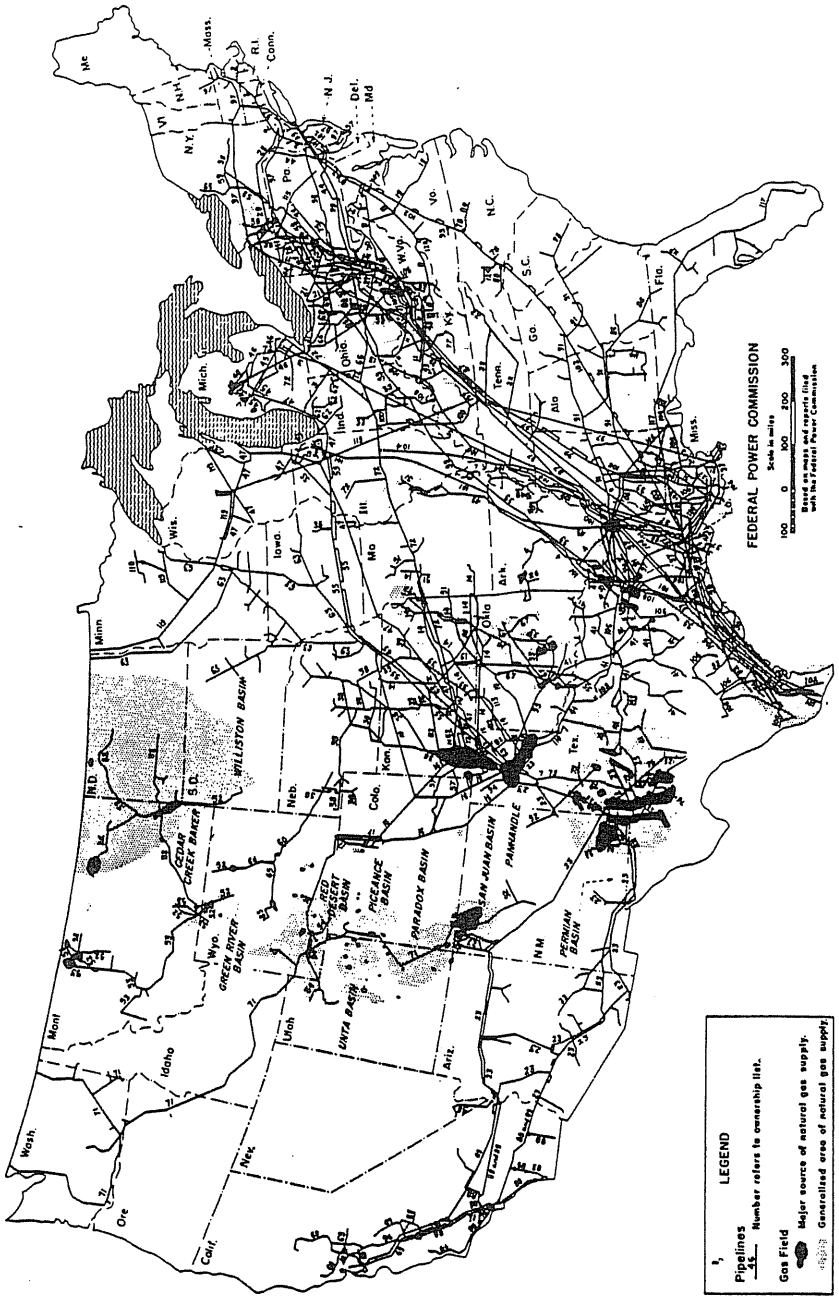

FIGURE 1-4
Gas pipeline systems [courtesy Federal Energy Regulatory Commission, 1987].

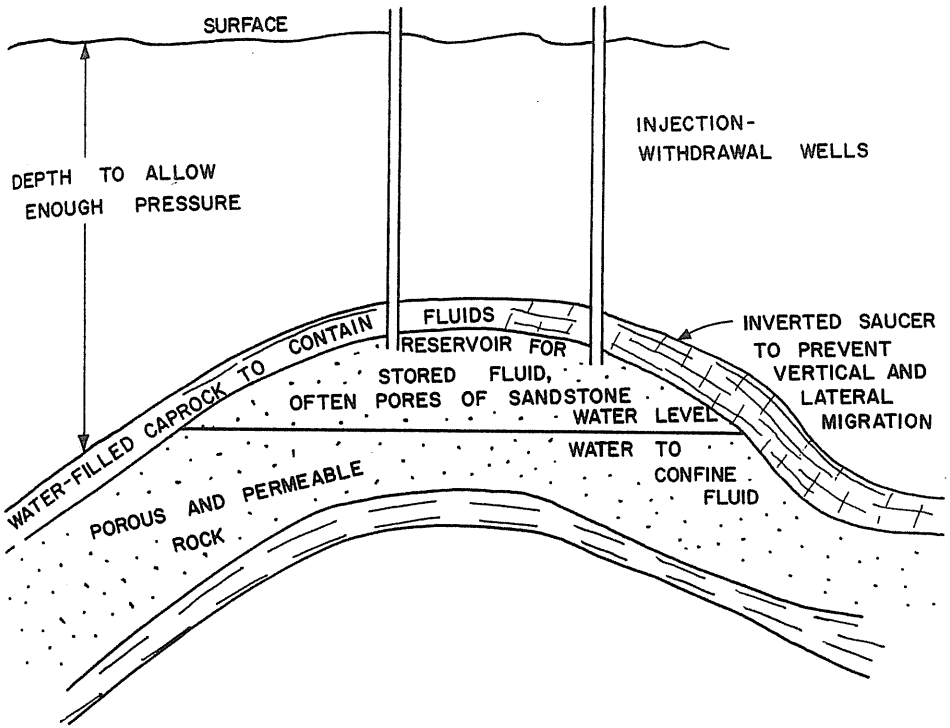

FIGURE 1-5
Basic elements of underground gas storage reservoir [Katz & Coats, 1-2].

storing natural gas in the 1960s [1-2]. Where there is no salt, mined cavities in granite, shale, or limestone are used for LP storage.

Other divisions of the petroleum (oil and gas) industry include *secondary oil recovery* and *enhanced oil recovery*. Secondary oil recovery generally refers to gas injection or water flooding after primary recovery, and enhanced oil recovery refers to more recent procedures such as thermal steam injections, polymer flooding, and CO_2 flooding. Since natural gas and carbon dioxide injection are used for extra oil recovery, this segment of oil production is a part of gas processing.

Offshore technology is the new discipline of drilling for and producing oil from reservoirs below bodies of water. Some 40 years ago, hundreds of wells were drilled in 80 feet (24 m) of water in Lake Maracaibo, Venezuela, and compression plants for separating oil and processing gas were built on platforms over the water. In intervening years, such drilling below Gulf Coast waters offshore has grown in volume of oil and gas produced and in depths of water for drilling. In the last 25 years, the North Sea has been seismically investigated for structures, and many reservoirs have been found. The British sector is producing about 2 million barrels a day (0.32 m^3/s) of crude oil, using platforms in waters at depths such

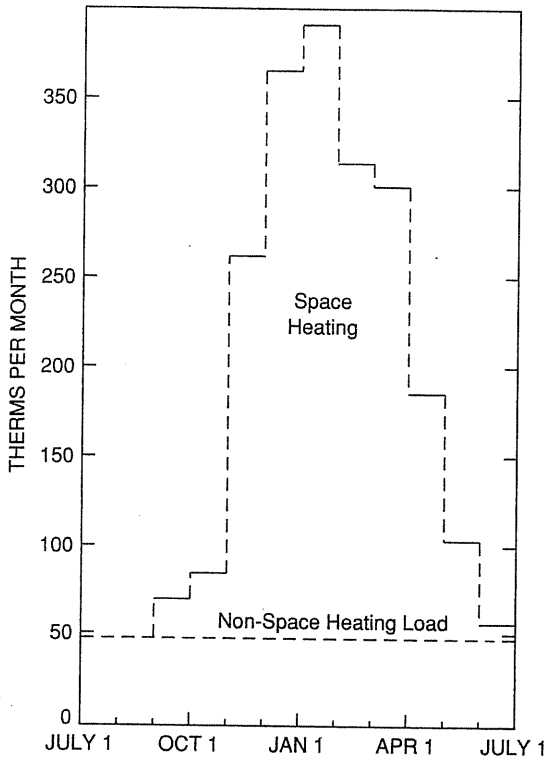

FIGURE 1-6
Use of natural gas in therms (100,000 BTU) per month in average home, Chicago area.

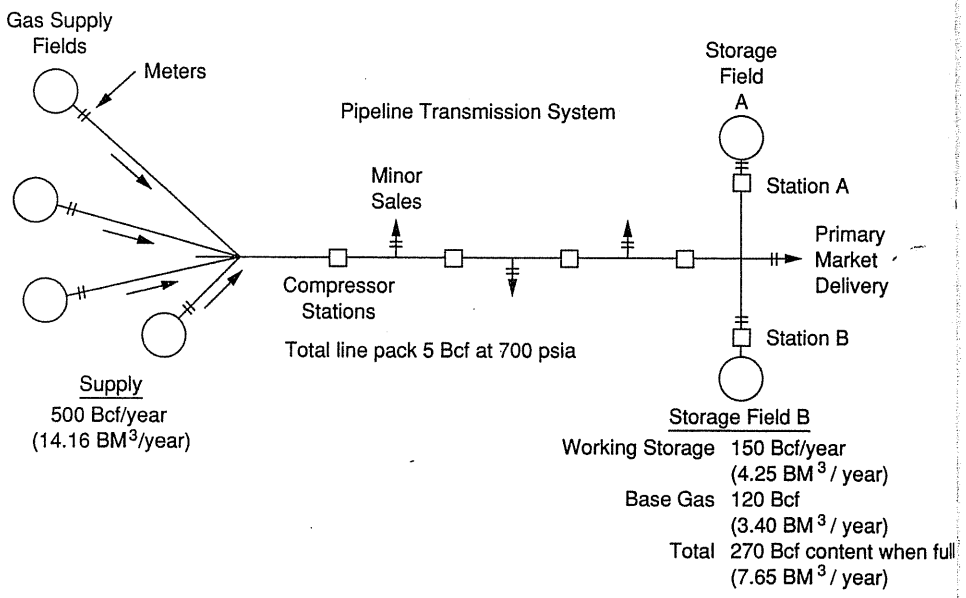

FIGURE 1-7
Schematic diagram for pipeline system with underground storage.

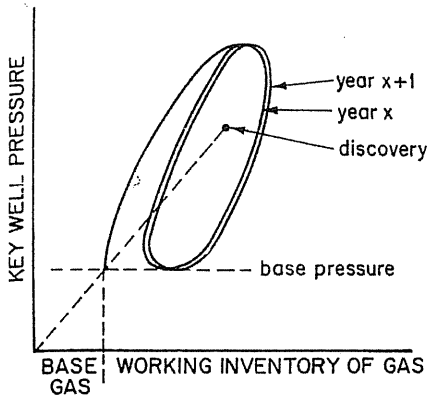

FIGURE 1-8
Pressure cycles on tight gas storage reservoirs [Katz & Tek, 10-13, courtesy SPE-AIME].

as 600 feet (183 m). Offshore drilling is a primary source of new oil found in as many as 20 areas of the planet.

Reservoir simulation is the process of inferring the behavior of a real reservoir from the performance of a mathematical model of that reservoir. This process has been widely accepted by the petroleum industry in the past two decades for monitoring the performance of reservoirs. The process of modifying the existing model according to the injection/production history of a reservoir until it agrees well with the observed field pressure data is called *history matching*. For a gas

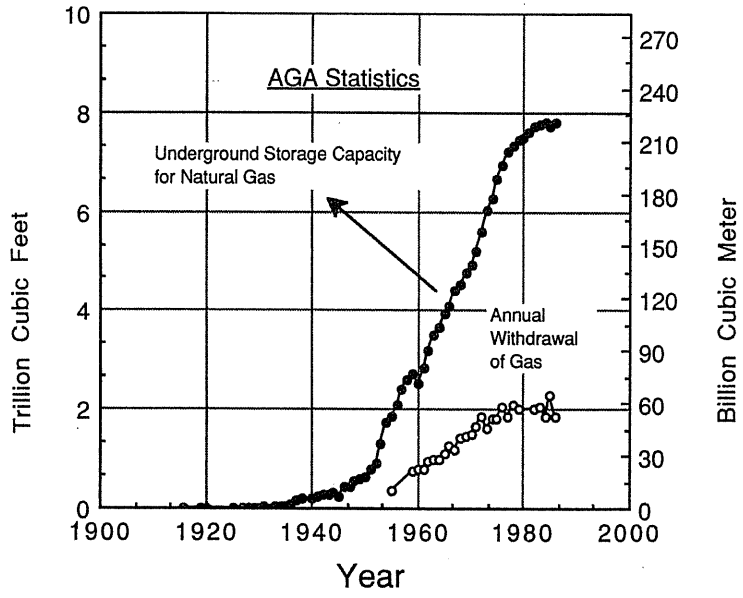

FIGURE 1-9
Growth in annual gas storage capacity and gas usage—AGA Data [Katz & Witherspoon, 1-93].

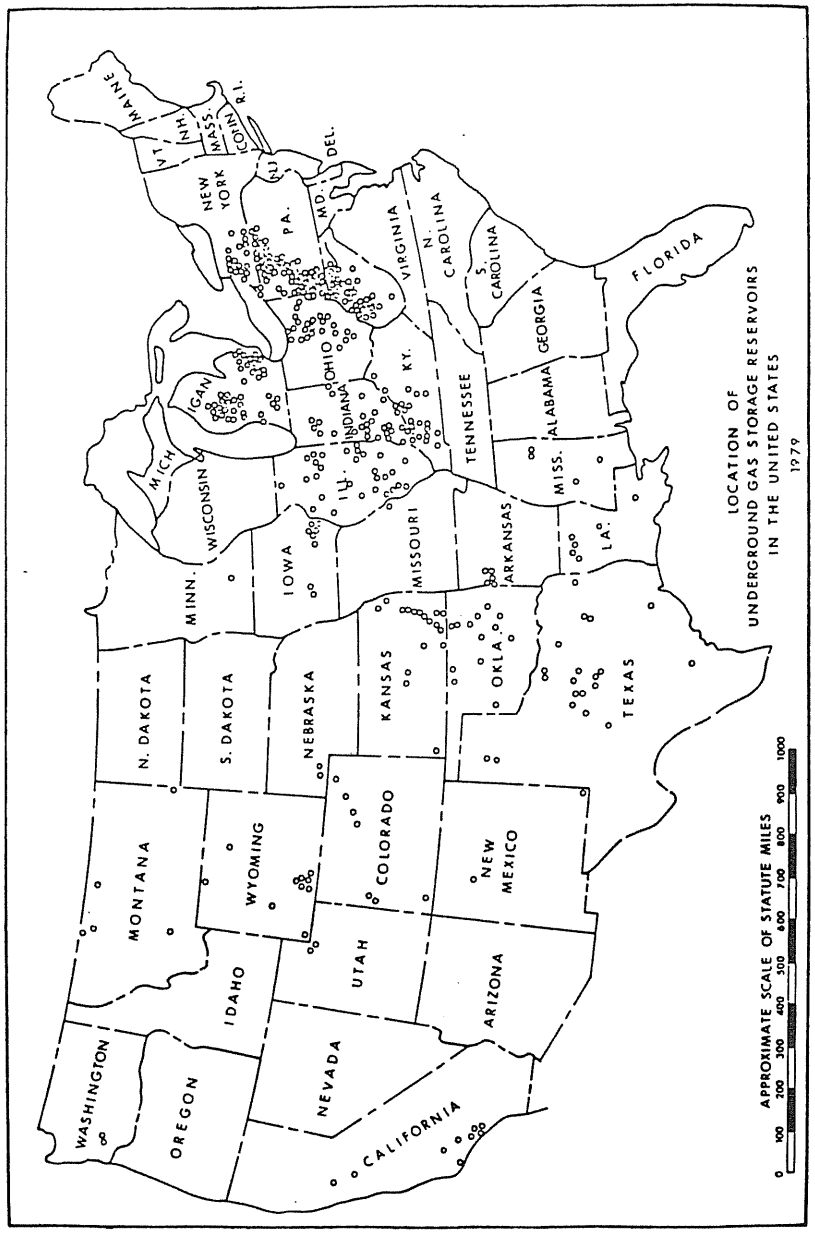

FIGURE 1-10
Map locating underground gas storage projects [courtesy American Gas Association].

TABLE 1.3
AGA statistics on underground gas storage [courtesy American Gas Association, 1987]

Total capacity, Tcf (m^3)	7 .792 (221 × 10^9)
Maximum day output, Bcf (m^3)	38.5 (1.07 × 10^9)
Seasonal gas withdrawn, Tcf (m^3)	1.868 (52.7 × 10^9)
Recoverable gas in storage, Tcf (m^3)	4.965 (140.1 × 10^9)
Number of storage reservoirs, 26 states	396
Number of companies	90
Storage compressor stations, hp	1,676,000
Range of storage reservoir pressure, psi (MPa)	300 to 4000 (2.07 to 27.6)
Aquifers account for more than 18% of storage capacity.	
Aquifers account for 12.1% of maximum day output.	

storage mixing project involving the replacement of valuable gas with injected low-price gases, the transmissibility distribution must be determined by history matching.

1.2 SOURCES OF INFORMATION FOR NATURAL GAS ENGINEERING AND ITS APPLICATIONS

Books on gas engineering can present the subject concisely and give a coherent treatment to the various portions of gas technology as of the time of their writing. *Handbook of Natural Gas Engineering*, written more than 25 years ago, included much of the accumulated information of that period [1-1]. Ongoing studies bring new concepts and extensions of earlier ideas. New books are added at intervals to give information on reservoir engineering [1-2] through [1-20].

Journals and proceedings generate papers, many of which are presented at meetings—often with preprints. Several journals that are important sources of information are listed in the references [1-44] through [1-61]. Monographs and reprints of articles on specific subjects are published by the Society of Petroleum Engineers [1-21] through [1-27]. Studies carried out for the American Gas Association on gas storage are published as monographs or committee reports [1-31] through [1-43]. Geological information of particular interest is represented by the American Association of Petroleum Geologists' monthly bulletin (*Bull. AAPG*) and in the references [1-62] through [1-84].

1.3 GEOLOGY AND EARTH SCIENCES

Geology is an extensive and growing body of knowledge; elements of its language should be acquired by all workers dealing with the layers of the earth and their contained fluids. Important topics include the history of the earth; the sedimentary processes forming shale, sandstones, and carbonate rocks; and earth surface movements creating present rock forms. The nature of the structural traps in

which oil and gas deposits occur deserves study, as do possible methods of oil and gas accumulation. Knowledge of the various modes by which buoyant liquids and gases are trapped in pools helps in their location and in the confinement of fluids in artificially developed earthen storage reservoirs.

Companion earth sciences such as geophysics and geochemistry deserve the attention of engineers. The nature of temperature and pressure increases with depth within the rocks of the earth is basic information in reservoir engineering. Oil and gas science is developing through the integration of earth sciences and engineering.

Earth Sciences

Study of the nature of the earth's crust and of its ability to accumulate petroleum under pressure is important background for the engineer in the producing branch of the natural gas industry. Geology treats all phases of the earth's history, including the processes by which reservoirs were created. It is fortunate that many of the processes that produced the earth's crust are still in evidence, permitting a reconstruction of the processes by which most reservoirs were formed.

There are several branches of geology and related earth sciences. Their nomenclature makes frequent use of such terms as *geo*, earth; *petro*, rock; and *lithos*, stone; and suffixes like *-logy*, science or discourse, and *-graphy*, description. Physical geology is a study of the processes affecting the earth's surface, such as action of wind, water, ice, and atmosphere. Historical geology endeavors to trace the events in the history of the earth, including the formation of the earth's crust. The origin of life and the evolution of plant and animal forms are included. Structural geology treats the processes by which the position and shape of the various members of the earth's crust are determined, and the forces that have brought about both surface and subsurface structures. Stratigraphy covers the character, sequence relationship, distribution, and origin of sedimentary rocks.

Several branches of geology deal with the recognition of rock according to type and age. The study of rocks to determine their character and constitution is termed *lithology*. *Paleontology* and *micropaleontology* classify information about life in past geologic ages by studies of fossils and microfossils. *Mineralogy, petrography,* and *petrology* deal with the physical properties, chemical properties, classification, and identification of minerals or rocks and with their genesis.

Sedimentation is the process of depositing solids at the bottom of a fluid, and the term is frequently used to describe the deposition of particles of rock from bodies of water. Sedimentary rocks are rocks that have been deposited by this process. Essentially all petroleum is contained in sedimentary rock. *Geohydrology*, or ground water geology, combines the principles governing water movement through porous media and the geology of the earth's crust with respect to the ability of the various strata to conduct water.

Geophysics is the application of the principles of physics to problems of the earth. The study of the transmission of shock waves generated either by natural causes, such as earthquakes, by explosions, or by machines is an example. These

principles are utilized in the seismic method of searching for structures. The reflection of elastic waves at the interface between layers of rock with different physical properties permits the mapping of the interface. Other methods of making physical measurements at the earth's surface to find the nature of its subsurface employ the magnetic field, the gravitational field, and the electrical properties of the earth, principally its electric resistivity. These methods usually depend upon anomalies or irregularities in the earth's crust.

Geochemistry is the application of the principles of chemistry to the study of the earth. The search for petroleum by analyzing soils for hydrocarbons is considered a geochemical method. The physical chemistry of molten rock and the chemistry of its disintegration and recrystallization are included.

Diagenesis processes are those by which chemical reactions take place in the earth. Magnesium brine reacts with $CaCO_3$ (limestone) to form $CaMg(CO_3)_2$ (dolomite). Another example is the disintegration of shales at temperatures of 200 to 220°F (93–105°C) at the interface between normal pressure rocks and geopressured rocks. Geochemists study the steps during the conversion of organic material to oil and gas—a maturation process. The recent observation that Michigan reefs have no connate water exemplifies the need for more knowledge of the inorganic chemistry of earthen materials and for the integration of engineering and geological knowledge [1-91].

Historical Geology

Historical geology reconstructs the successive events in the history of the earth since it was in the molten condition. Geologic time scales have been devised to indicate the periods of time during which various layers of the earth's surface were formed. The point at which cooling of the earth's surface led to water precipitation is the zero point on a geologic time scale with respect to sedimentary processes. The erosion by rain and wind of the surface that protruded and the covering of the bottom of adjacent shallow water with the eroded material is believed to be the most active process in the creating of porous rock. The uplifting of areas of the continents to permit erosion while an adjacent area was submerged required movements of the earth's crust now observed only slightly during earthquakes. The geologic time scale has received considerable attention using isotopic dating methods with accuracies of the order of ±5 percent for sedimentary rock [1-66]. Carbon-14, (C^{14}) dating is used for relatively recent times as in archeology. The absolutes of time scale are not important to engineers; the time scale given in Table 1.4 relates to well-known oil and gas fields.

Sedimentation Processes

In the Paleozoic era, Cambrian period, various areas of earth were high, above sea level, and they eroded with rain and the weather. Figure 1-11 shows the inland Pennsylvanian seas into which sedimentary material or carbonates were

TABLE 1.4
The geologic time scale [Katz, et al., 1-1, courtesy McGraw-Hill Publishing Co.]

Era	Period	Epoch	Formations producing oil and gas (field or area)
Cenozoic 71*	Quaternary	Recent Pleistocene 1	
	Tertiary 70	Pliocene 10	Repetto (Ventura, Calif.)
		Miocene 15	(Krotz Springs, Deep Lake, Erath) (Louisiana) (Kettleman Hills, Coalinga) (California)
		Oligocene 10	
		Eocene 20	Cockfield (Conroe, Texas) Yegua (Katy, Texas)
		Paleocene 13	
Mesozoic 130	Upper Cretaceous 35	Lance Montana Colorado	Woodbine (East Texas) Mesa Verde (San Juan, New Mexico, California) Monroe Chalk (Louisiana)
	Lower Cretaceous 20	Dakota Comanche	
	Jurassic 40	Upper Middle Lower	(Fort St. John, British Columbia)
	Triassic 35	Upper Middle Lower	
Paleozoic 300	Permian 30	Upper Lower	Hugoton Dolomite (Kansas, Oklahoma, Texas) Yates (West Texas, New Mexico) Panhandle Dolomites (Texas)
	Pennsylvanian 30	Virgil Missouri Des Moines Morrow	Reef (Scurry County, Texas) Burbank (Oklahoma)
	Mississippian 30	Chester Valmeyer Kinderhook	Michigan Stray Sands
	Devonian 40	Chautauquan Senecan Erian Ulsterian Oriskanian Helderbergian	Dundee, Traverse (Michigan) Leduc (Alberta) Bradford (Pennsylvania)
	Silurian 30	Cayugan Niagaran Medinan	
	Ordovician 60	Cincinnatian Mohawkian Chazyan Canadian	Simpson (Oklahoma) Viola City Wilcox Bromide Trenton (Michigan)
	Cambrian 80	Ozarkian St. Croixian Acadian Waucoban	Arbuckle Lime (Oklahoma City), (Kansas) Galesville aquifer (Herscher, Illinois)
Proterosoic			Pre-Cambrian 4000
Archeozoic			

* Approximate duration in millions of years.

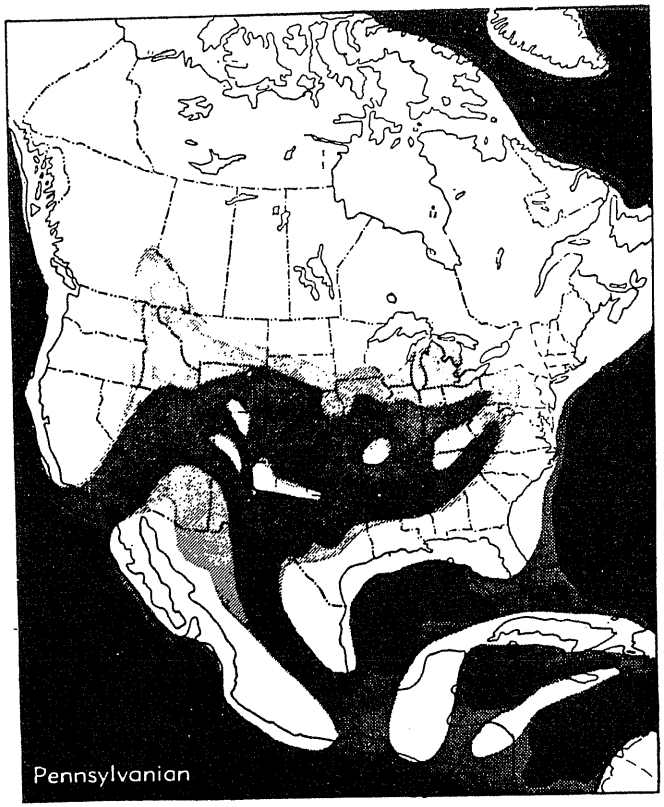

FIGURE 1-11
Distribution of Pennsylvanian Seas [Moore, 1-77, courtesy McGraw-Hill Publishing Co.].

deposited. Figure 1-12 is a section of the East Texas basin showing its various layers and the East Texas field in the Woodbine Sand. The thickness of the sedimentary rocks varies from zero in certain areas like the eastern Canada shield or the northeastern corner of Oklahoma to great depths as in the Gulf coast or the Anadarko basin in southwestern Oklahoma. There are many areas not yet pierced by drills down to the granite or basement rock.

Petroleum Reservoirs

The pores of the rocks below the surface water table are generally filled with water or brine, unless there is an accumulation of oil and gas. The conditions for a trap or reservoir are an impervious caprock above a porous permeable layer, permitting oil and gas to accumulate by buoyant movement. Figure 1-13 shows sections of major types of reservoirs.

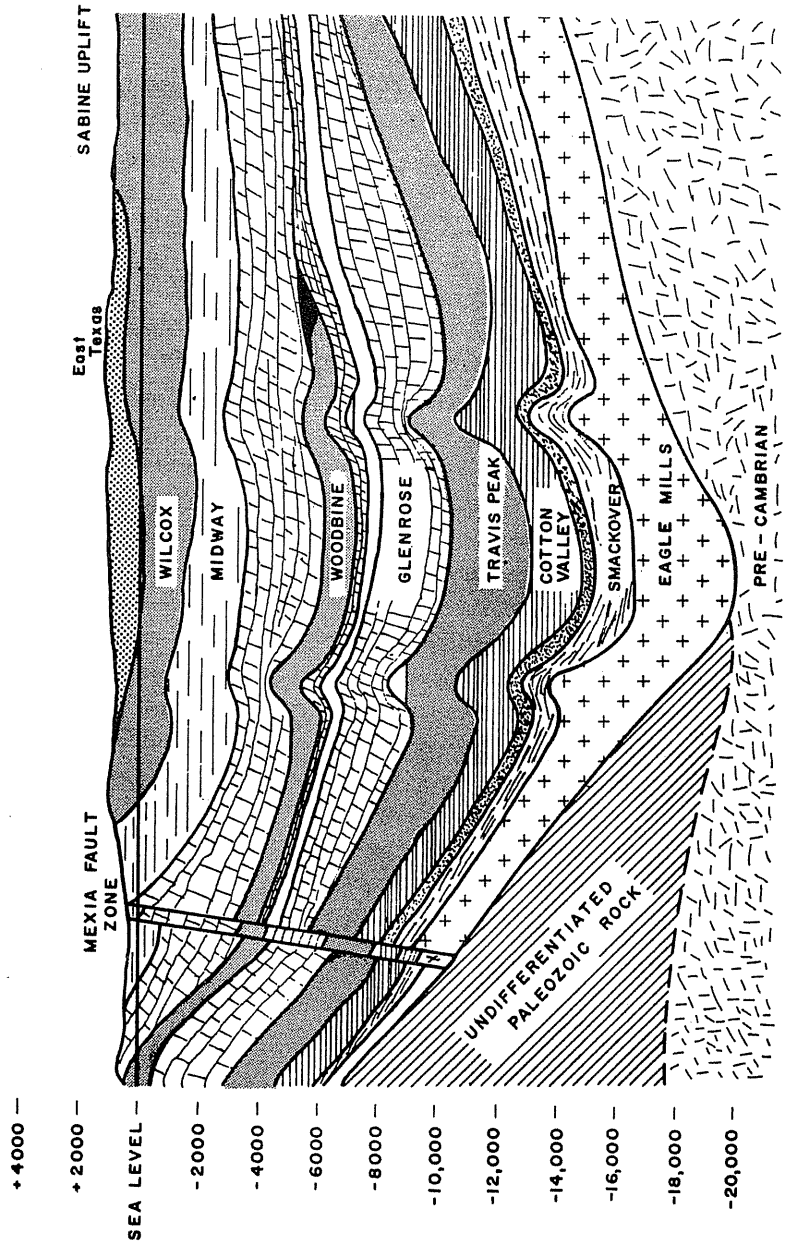

FIGURE 1-12
Cross section East Texas Basin [Bell & Shepherd, 1-85, courtesy SPE-AIME].

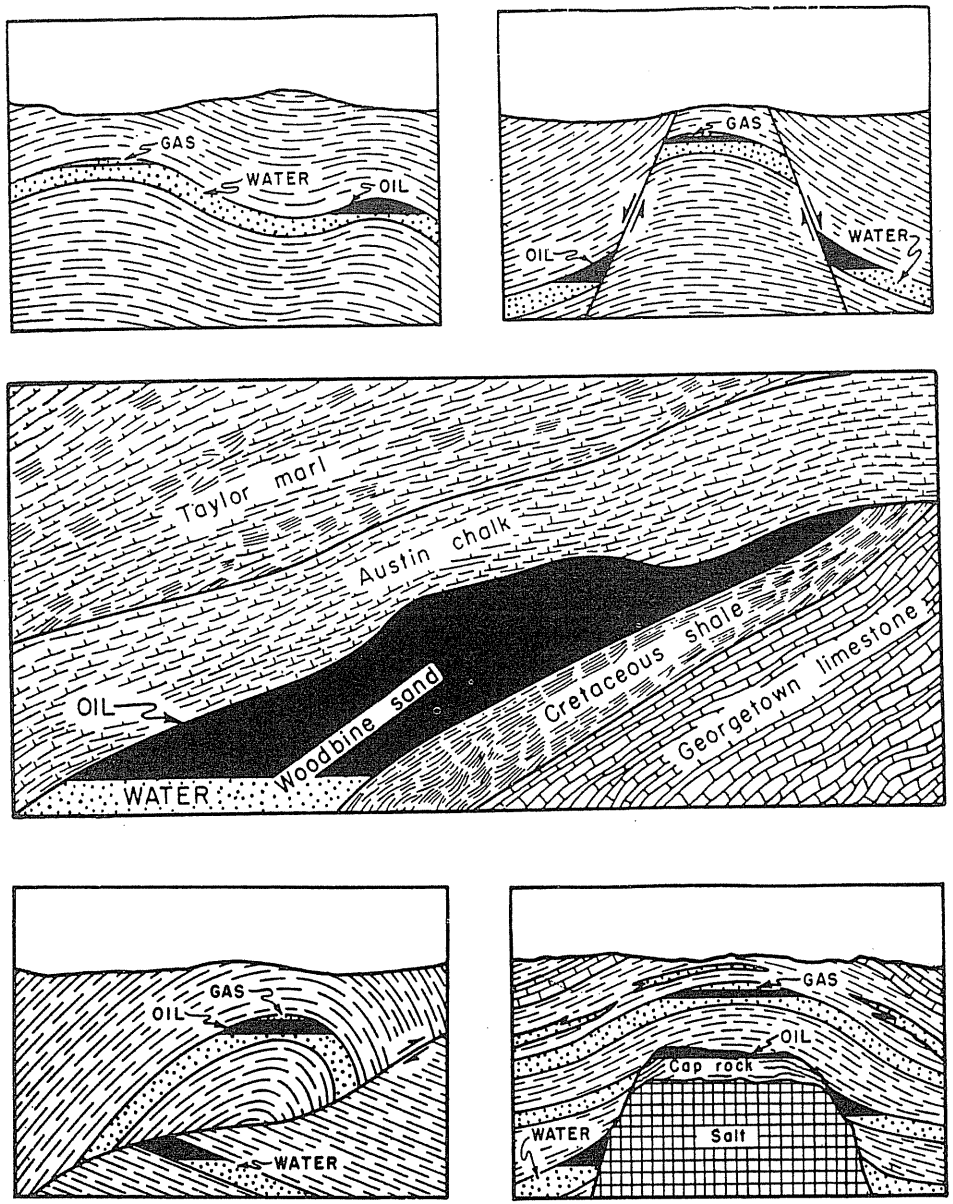

FIGURE 1-13
Major types of reservoir traps [LeRoy, 1-75, courtesy Colorado School of Mines, 1-1].

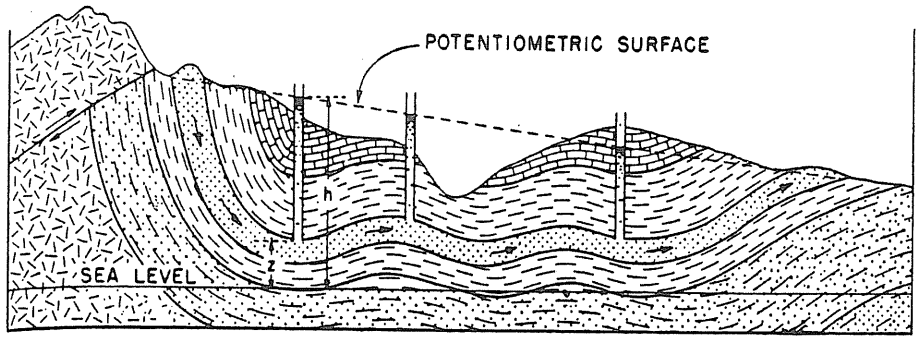

FIGURE 1-14
Regional flow of water through sand from higher to lower outcrops [Hubbert, 1-70, courtesy AAPG].

Origin of Petroleum

The origin of petroleum from organic matter in sedimentary rock is set forth by Tissot and Welte [1-82]. As early as 2500×10^6 years ago, remains of bacteria and primitive algae were deposited in pre-Cambrian rocks. Photosynthesis of plants from CO_2 and H_2O by sunlight, forming glucose and oxygen, started some 2 billion years ago and reached a high yield at the time of coal deposits such as those in the Carboniferous age.

When the organic matter was buried, but still shallow, a process of diagenesis took place, often including consolidation of sediments. Temperature increased with depth of burial, forming kerogen with generation of methane gas. The word *catagenesis* is used for the process by which oil and gas were generated at high pressure due to great depths. At great depths metagenesis of organic matter (kerogen) to anthracite coal and metamorphism of mineral phases also occurred.

Oil and gaseous constituents formed in source beds migrated and were trapped in structures covered by impervious caprocks. Buoyancy of the lower-density oil and gas in water causes upward migration, preventing water movement from carrying the finely divided oil globules along. Figure 1-14 [1-70] shows how water may be moving from a higher to a lower elevation, trapping oil and gas en route, assisted by decreasing pressures.

1.4 EARTH TEMPERATURES AND PRESSURE

The near surface ground temperature is approximately the same as the mean annual atmospheric temperature at the surface. It varies from below 32°F (0°C) in northern permafrost regions to some 80°F (27°C) in the tropics. Earth temperatures increase from 6 to 30°F per 1000 feet depth (10–55°C/1000 m), depending upon the rock's thermal conductivity and its proximity to hot layers. The normal geothermal gradient in a wellbore is disturbed by drilling, oil or gas production,

and liquid or gas injection. There are ways of estimating the differential from geothermal temperature gradients based on rates of flow, fluid density, heat capacities, and time of flow.

Undisturbed fluid pressures in the porous rocks of the earth generally increase by 0.43 to 0.46 psia per foot (9.5–10.4 kPa/m) of depth. There are numerous deviations from this rule, some much lower and many much higher. Deeper zones approach the lithostatic value of 1.0 psia per foot (22.6 kPa/m).

Earth Temperatures

The earth temperature at 100 feet (30 m) approximates the mean annual atmospheric temperature (Figure 1-15). Table 1.5 gives representative earth-depth temperatures that are believed to be geothermal equilibrium values. The gradient in the earth is quite variable. Table 1.6 gives specific gradients. One of the highest gradients, 35°F per 1000 feet (67°C/1000 m), at N. Sumatra, occurs in a general volcanic region and reflects the proximity of hot rock. Figure 1-16, representative of the Gulf Coast, permits reading the temperature when the gradient for an area (*a–f*) is known. Temperature measurements should be made for new reservoirs; preferably some three months or more after drilling and casing has been completed to allow thermal equilibrium.

Natural gas production is unlikely to change the reservoir temperature by more than 2 to 4°F (1–2°C). Gas cycling for years at Katy, Texas, was said to have cooled the rock 30°F (17°C). It is known that gas injection in gas storage can cool the wellbore area of the reservoir, and sustained water injection can change reservoir temperatures, at least in the wellbore area [1-89].

The circulation of drilling mud during drilling or the flow of oil and gas up the wellbore will upset the temperature equilibrium. Figure 1-17 shows the variation of temperature gradients between the static or equilibrium curve, the temperature in the wellbore during drilling, and the temperature while flowing. Eilerts and Schellhardt [1-86] reported temperature data on a gas well in northeast Texas producing from the Trinity formation. The well apparently had been flowing prior to the test period, and was closed in 26 hours before the first static gradient was measured. Figure 1-18 shows the measured temperatures along with an estimated equilibrium earth temperature for the region. The wellbore temperatures near the surface, and hence the well effluent temperatures, rise with increasing flow rates and with time at a given flow rate. At the highest flow rate, the temperature at the bottom of the well dropped, apparently because of the high pressure drop at the sandface causing Joule-Thomson cooling.

It should be clear that calculation of temperature changes during flow needs to include as variables the mass flow rate, the time sequence of flow rates, and the temperature differences. The senior author worked with a gas well producing

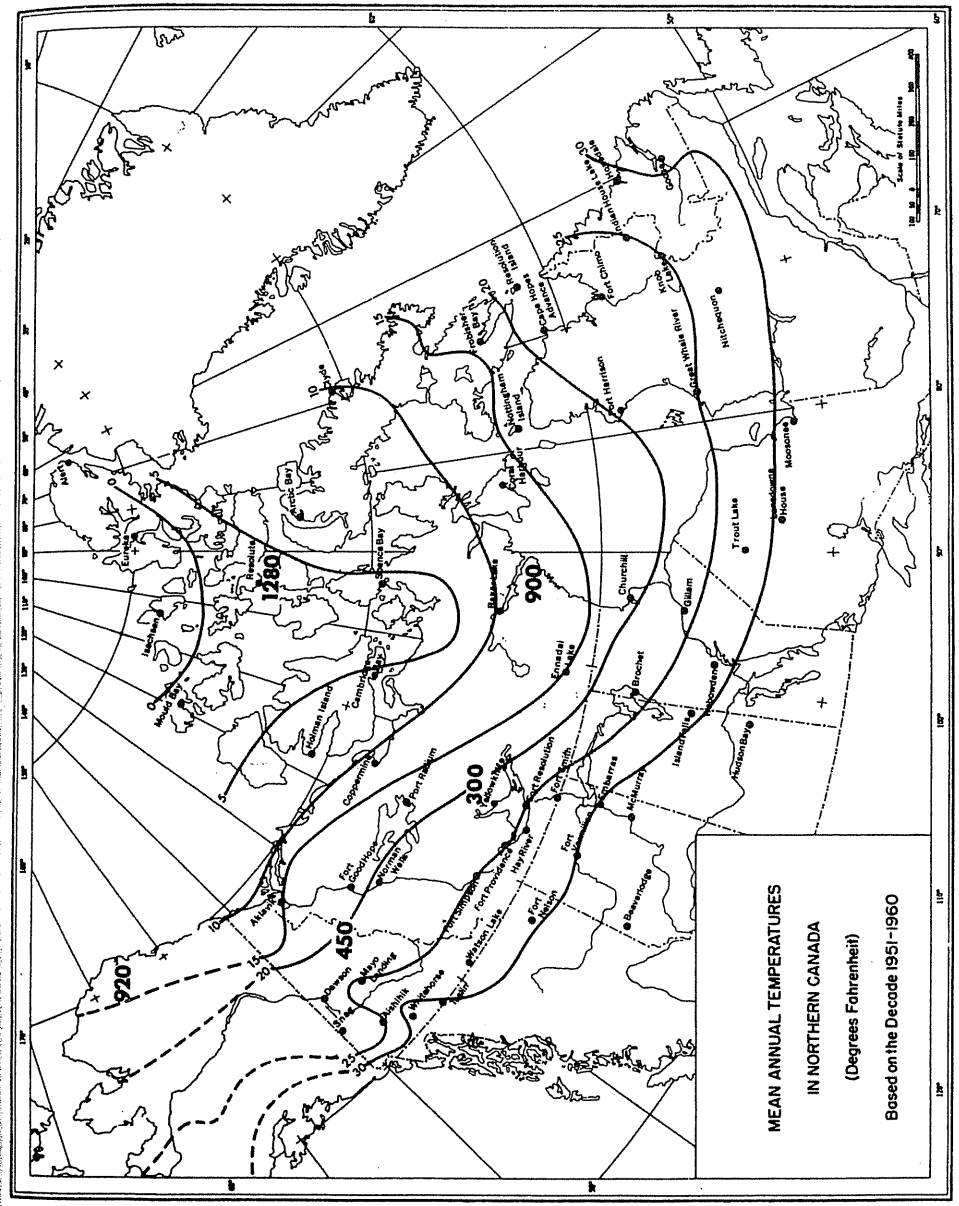

FIGURE 1-15
Mean atmospheric temperatures in arctic regions. Large numbers, such as 450, indicate earth permafrost [after Thomson, 1-88, courtesy SPE-AIME].

TABLE 1.5
Representative earth temperatures at 100 feet [Katz, et al., 1-1, courtesy McGraw-Hill Publishing Co.]

Fields	°F	°C
Norman Wells, Northwest Territories	32	0
Fort St. John, British Columbia	40	4
Austin Field, central Michigan	47	8
Kankakee, Illinois	52	11
Oklahoma City, Oklahoma	60	16
Lea County, New Mexico	66.7	19
New Orleans, Louisiana	69.6	21
Texas:		
Navarro County	67.8	20
Reagon County	67.2	20
Van Zandt County	69.2	21
Brownsville	73.1	23
Houston	69.2	21
Los Angeles, California	72.3	22
Maricaibo, Venezuela	80.0	27

TABLE 1.6
Reservoir temperatures and earth geothermal gradients [1-1]

		Depth		Temperature		Gradient	
Field	State or province	ft	m	°F	°C	°F/1000 ft	°C/100
East Texas, Woodbine	Texas	3,600	1,097	146	63	22	40
Burbank	Oklahoma	2,800	853	122	50	22	40
Panhandle	Texas	3,000	914	81	27	7	13
Monument, Lea County	New Mexico	3,900	1,189	90	32	6	11
Ledue	Alberta	5,300	1,615	153	67	21	38
Paloma–San Joaquin	California	10,600	3,230	256	124	17.3	32
Deep Lake	Louisiana	12,060	3,676	211	99	11.5	21
Oklahoma City	Oklahoma	6,300	1,920	132	56	11.4	21
Carthage	Texas-Louisiana	5,920	1,804	206	97	23.6	43
Hugoton	Oklahoma	3,325	1,013	90	32	8.4	15
North Pettur, Bee	Texas	6,950	2,118	221	105	21.7	39
South Jennings	Louisiana	10,100	3,078	211	99	14	25
Fort St. John	British Columbia	6,400	1,950	156	69	18.1	33
Arun	N. Sumatra	10,000	3,048	350	177	35	64

$$\frac{1°F}{1000\ ft} = \frac{1°F \cdot 1°C/1.8°F}{1000\ ft \cdot 0.3048\ m/ft} = \frac{1.82°C}{1000\ m}$$

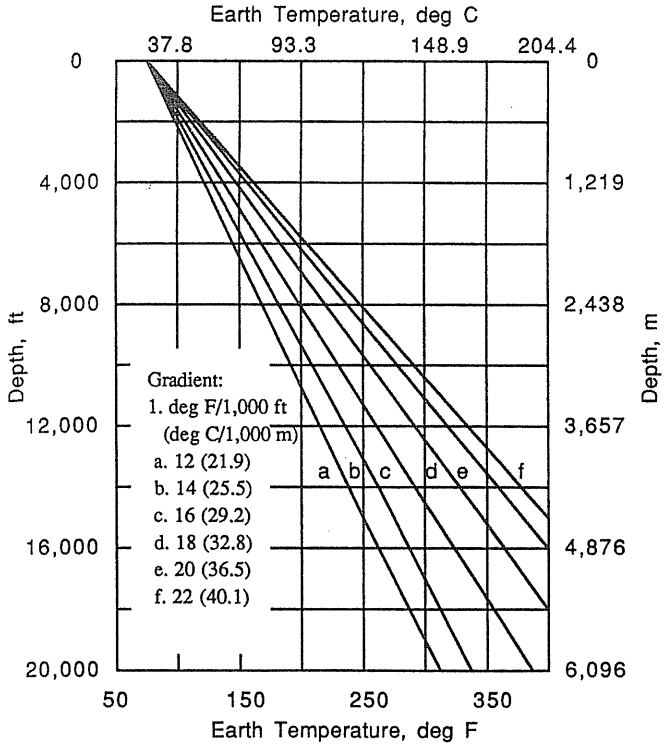

FIGURE 1-16
Earth temperature gradients on the Gulf Coast [Nichols, 1-95, courtesy SPE-AIME].

some 6 million cubic feet per day ($170 \times 10^3 m^3$/day) for three months and found the wellhead temperature increased from 135 to 160°F (57° to 71°C) during the period, while the reservoir was at some 210°F (99°C).

Earth Pressures

There are two kinds of pressure to consider in the underground strata: fluid pressure in the pores of the rock and the overburden pressure exhibited by the solids. The first of these, fluid pressure, is of primary concern in reservoir engineering, while the second, overburden pressure, has much to do with hydraulic fracturing.

Figure 1-19 illustrates the concept of hydraulic head or pressure gradient in water. If one has a column of 10 cubic feet of water, or 3 cubic meters, as shown, what is the increase in pressure as one proceeds down the column? In English units, at the bottom of 1 cubic foot, there are 62.4 pounds mass, which press on 1 square foot or 144 square inches. The pressure increase is 62.4 lb/ft^2 per foot or 62.4/144 = 0.433 psi (lb/in^2) per foot. This calculation assumes a pound mass is the equivalent of a pound force, which is true by the definition of

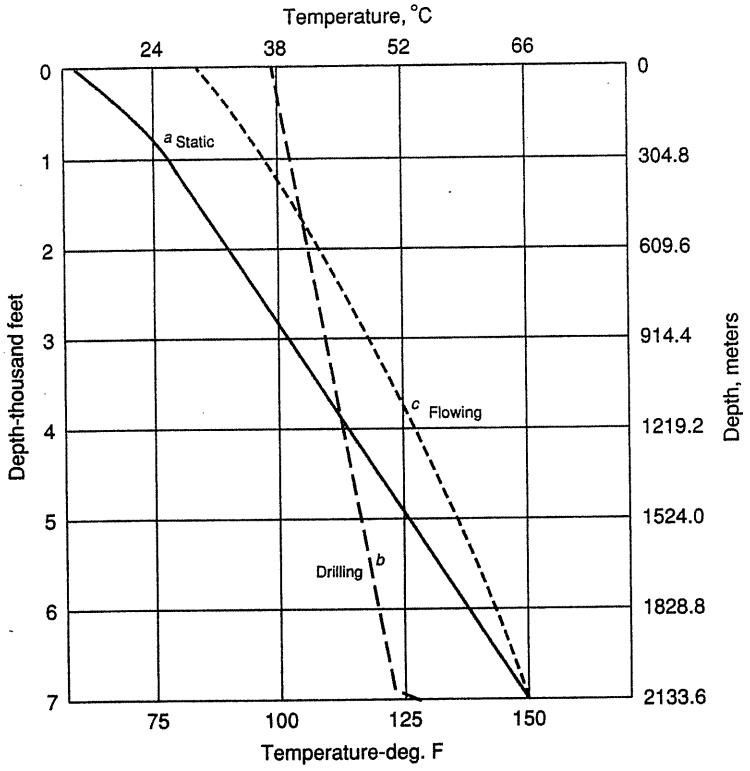

FIGURE 1-17
Temperature gradient distortion by drilling or flowing well [French, 1-87, courtesy API, 1-1].

g_c as explained in Chapter 3. For 10 feet of height, the pressure increase is 4.33 psi.

In *SI metric* units, the pressure gradient is 0.433 psi/ft × 3.28 ft/m × 6.895 kPa/psi = 9.80 kPa/m. For fluids other than water the gradient is $\rho \cdot 9.80$ kPa/m, where ρ is density in g/ml. As described in Chapter 3, when the pressure is expressed in pascals, Pa, a factor of 9.80 is involved when converting density to pressure gradient.

The pores of the sedimentary and near surface rocks are full of water, unless containing oil or gas. So the fluid pressure is related to depth from surface or outcrops. Fluid pressures are plotted against depth in Fig. 1-20. Some typical densities, along with the equivalent fluid pressure gradients, are shown in Table 1.7.

Most undisturbed reservoirs are found to lie on a pressure gradient equal to that for water or a brine, but there are both high and low deviations. The Hugoton gas field between Kansas and Oklahoma is an underpressured reservoir, with a pressure of 485 psia at 3326 feet (0.146 psi/ft), or 3.34 MPa at 1013 m (3.29 kPa/m). The field occurs on a slope at an elevation a considerable distance above a

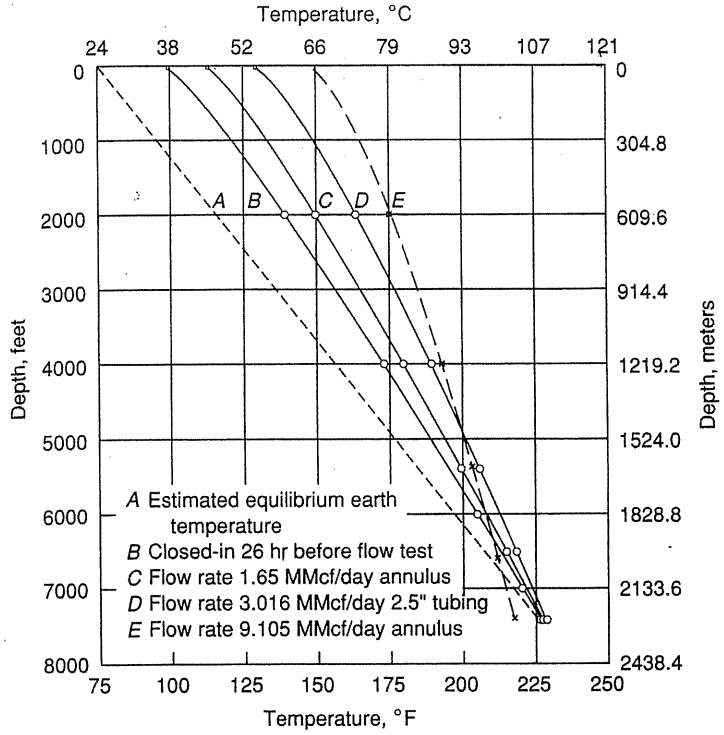

FIGURE 1-18
Temperature gradients in gas well [Eilerts & Schellhardt, 1-86, U.S. Bureau of Mines].

lower outcrop, and could be of the type of Fig. 1-13*e*. Along a belt paralleling the Gulf coastline, strata some 10,000 feet (3048 m) or more in depth at temperatures above some 200°F (93°C) may have abnormal or geopressured values as shown on Fig. 1-20. Some values approach the equivalent to the overburden.

Example 1.1. The wellhead pressure of a gas well is 914.7 psia, and the gas density is 2.83 lb/ft^3. The well is 3000 feet deep. An Echometer reading indicates the gas/water interface is at 2200 feet. With fresh water in the well, what is the bottom hole pressure?

Solution. Bottom hole pressure is the sum of gas column, water column, and wellhead pressure:

$$P(bottom\ hole) = P(wellhead) + \Delta P(gas\ column) + \Delta P(water\ column)$$

$$= 914.7 \text{ psia} + (2200 \text{ ft})(2.83 \text{ lb/ft}^3)/(144 \text{ in}^2/\text{ft}^2)$$

$$+ (0.433 \text{ psi/ft})(3000 \text{ ft} - 2200 \text{ ft})$$

$$= 1304.3 \text{ psia}$$

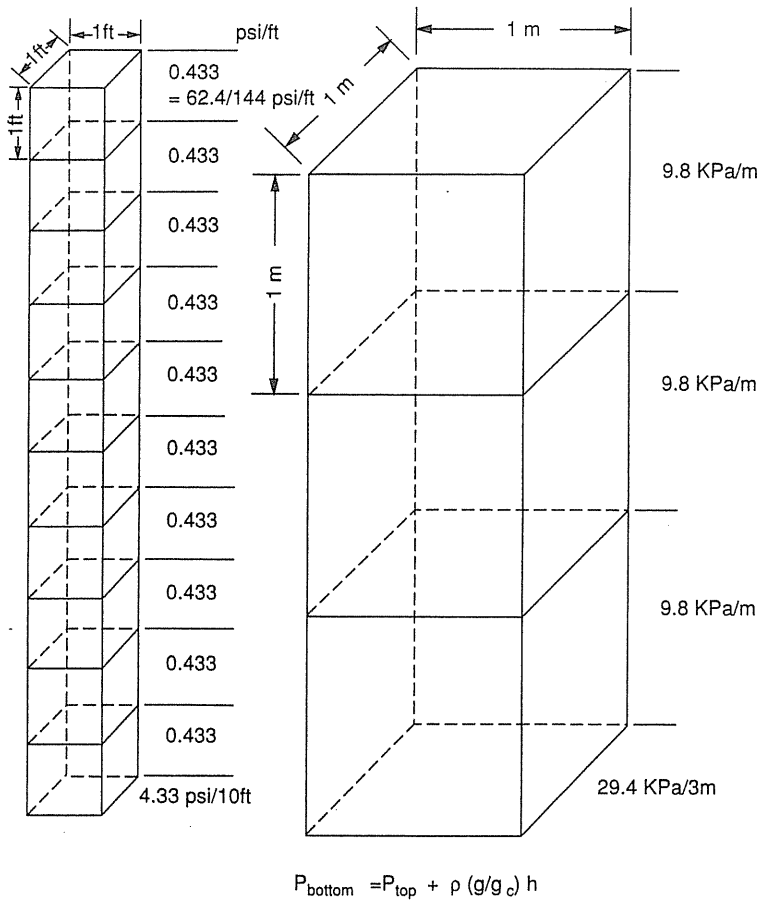

FIGURE 1-19
Hydraulic head in columns of water.

1.5 WHAT IS PETROLEUM: NATURAL GAS, LP GAS, CONDENSATE, AND CRUDE OIL?

The hydrocarbons comprising natural gas range from the most volatile paraffin or alkane compounds (such as methane, CH_4, which boils at −258°F, or −161.5°C) all the way to nonvolatile asphaltic compounds, which are present in road oils. The more volatile constituents are mostly from the alkane family, but naphthenic and aromatic hydrocarbons occur in natural gas liquids and crude oils (see Table 1.8). There are also nonhydrocarbons present in natural gas, including nitrogen (N_2), carbon dioxide (CO_2), hydrogen sulfide (H_2S), helium (He), and water

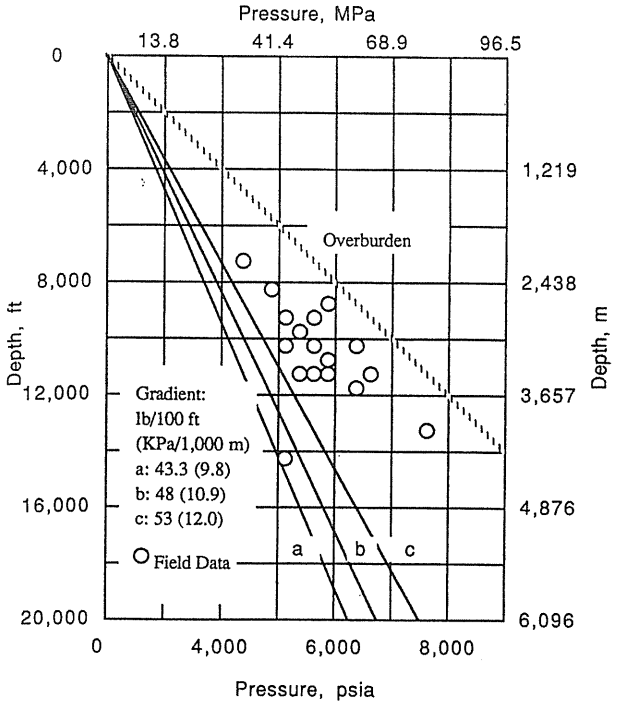

FIGURE 1-20
Pressures in earth [Katz et al., 1-1, courtesy McGraw-Hill Publishing Co.].

vapor. When H_2S exceeds 0.25 grains (1 grain = 0.06479 g; 1 lb = 7000 grains) per 100 cubic feet, the gas is considered to be *sour*; otherwise, it is *sweet* gas.

The constituents in petroleum and their boiling points, formulas, and products of commerce were shown in Table 1.2. Volatility at low or atmospheric pressure defines natural gas constituents. Compounds that are liquids under mod-

TABLE 1.7
Equivalent densities and fluid pressure gradients

Mean density	kg/m³	lb_m/ft^3	psi/ft	kPa/m
Water	1000	62.4	0.433	9.8
Salt brine	1225	76.4	0.530	12.0
	1385	86.4	0.60	13.6
	1617	101.0	0.70	15.8
Overburden	2310	144.0	1.00	22.6

Multiply kg/m³ by 10^{-3} to get g/ml.

TABLE 1.8
Petroleum hydrocarbons

Compound	Formula	Molecular weight	Normal boiling point		Critical temperature	
			°F	°C	°F	°K
Methane	CH_4	16.043	–258.69	–161.52	–116.63	190.6
Ethane	C_2H_5	30.07	–127.48	– 88.58	–90.09	305.4
Propane	C_3H_8	44.097	– 43.67	– 42.07	206.01	369.8
n-Butane	*n*-C_4H_{10}	58.124	31.10	– 0.49	305.65	425.2
Isobutane (2-methylpropane)	*i*-C_4H_{10}	58.124	10.90	–11.81	274.98	408.1
n-Pentane	*n*-C_5H_{12}	72.151	96.92	36.06	385.70	469.6
Isopentane (2-methylbutane)	*i*-C_5H_{12}	72.151	82.12	27.84	369.10	460.4

General formula C_nH_{2n+2}

Compound	Formula	Molecular weight	Normal boiling point		Critical temperature	
			°F	°C	°F	°K
Benzene	C_6H_6 Kekulé structure of benzene	78.11	176.17	80.09	552.2	562.16
Toluene	C_7H_8	92.14	231.13	110.63	605.6	591.8
Ethyl benzene	C_8H_{10}	106.18	277.16	136.20	651.2	617.2
o-Xylene (1,2-dimethyl benzene)	C_8H_{10}		291.97	144.43	675.0	630.3

TABLE 1.8
Petroleum hydrocarbons (*continued*)

Compound	Formula	Molecular weight	Normal boiling point		Critical temperature	
			°F	°C	°F	°K
Cyclopentane	C_5H_{10}	70.14	120.65	49.25	653.8	461.6
Cyclohexane	C_6H_{12}	84.16	161.25	71.81	548.9	499.35
Methyl cyclopentane	C_6H_{12}	84.16	177.29	86.73	591.0	536.7
Methyl cyclohexane	C_7H_{14}	98.19	213.68	100.93	503.5	570.27

erate pressures are separated from the more volatile constituents and marketed as liquefied petroleum gas (usually called LP gas). LP gas is composed of propane, butane, or mixtures thereof. Field streams contain all of the constituents indicated on Table 1.2.

Three families of hydrocarbons are portrayed in Table 1.8. Natural gas contains only a few primary alkanes (paraffins), so they are easily identified by name. In an analysis, however, many more paraffin hydrocarbons appear on the boiling point scale between pentane (96.92°F, 36.02°C) and benzene (176.17°F, 80.09°C) or cyclopentane (120.65°F, 49.25°C). For convenience in reporting analyses, all the compounds present within the boiling range of, for example, C_6 (*n*-hexane) are labeled C_6. Table A.1 in Appendix A gives paraffin isomers up to C_{10} (decane).

It should be emphasized that the hydrocarbon mixtures are families; that is, there is a relationship between the concentrations of successive compounds—propane to ethane, hexane to pentane, etc. This family quality makes it possible to correlate data for naturally occurring hydrocarbon systems using family properties, as in the use of gas gravity [(molecular weight)/(29, the molecular weight of air)] for correlating volumetric properties of natural gases.

Figure 1-2 gave the composition of well streams using analyses giving the hexanes and heavier compounds in a single group, as was customary until recently. Now compositional analyses by chromatograph are carried out to higher-boiling compounds, as in Table 1.9. The C_7 group represents all hydrocarbons boiling between 1°C above the normal boiling point of *n*-hexane to 1°C above the normal boiling point of *n*-heptane. In the analytical discussion, the properties of these C_n groups are presented [1-35].

A table of physical constants of hydrocarbons prepared by the Gas Processors Association is given as Table A.1 in Appendix A.

1.6 DUAL UNITS FOR NATURAL GAS ENGINEERING: ENGLISH AND METRIC

The nation is in a state of slow transition from the English system to SI (System International) units. The metric or CGS (centimeter-gram-second) system has been used in all the sciences and in engineering in many countries. A distinction should be made between metric and SI systems. In gas engineering, a principal difference is the use of pascal for pressure (in SI) rather than atmosphere or bar. Frequently, new names and units are given with conversion factors of 1. Surface tension in dyne/cm is expressed in m · N/m (meter times newton per meter) with the same numerical value.

Already, many engineering journals of technical articles require SI units exclusively, or as alternate values to English units. Initially, it was a major effort to acquaint practicing engineers with the derivation and use of SI units. Now, it appears that engineering and science students entering industry need equal consideration in learning the English units, since their education may have been

TABLE 1.9
Composition using extended analyses for native reservoir fluids [Katz, et al., 1-92, SPE-AIME]

	Cold Springs 12	Rapid River 35
Reservoir temperature, °F (°C)	114 (45)	116 (46)
Calculated dewpoint pressure, psia (MPa)	3526 (24.5)	3263 (22.5)
Measured dewpoint pressure, psia (MPa)	3620 (250)	3309 (22.8)
Molecular weight	23.73	22.35
Last component in analysis	C_{13}	C_{16}
Specific gravity of residue	0.815 C_{14}^+	0.77 C_7^+
Molecular weight	212	125
Component	**Mole percent**	
CO_2	0.001	1.1500
N_2	0.790	0.1400
C_1	80.099	84.1459
C_2	7.460	4.7900
C_3	3.700	2.5600
iC_4	1.750	2.0500
nC_4	1.300	1.4700
iC_5	0.840	0.8800
nC_5	0.390	0.3700
C_6	0.840	0.6100
C_7	0.660	0.4340
C_8	0.580	0.4210
C_9	0.480	0.3320
C_{10}	0.350	0.2354
C_{11}	0.200	0.1455
C_{12}	0.150	0.1007
C_{13}	0.120	0.0786
C_{14}	0.097	0.0475
C_{15}	0.070	0.0257
C_{16}	0.130	0.0101

primarily in SI. It is the writers' judgment that it is better to have both units present during the transition years. Accordingly, dual units will be used in this book, so that it can be used by engineers already accustomed to either English or SI units.

SPE Standards

Most technical societies have committees studying the conversion to SI units. The Society of Petroleum Engineers has given recommended units for various

TABLE 1.10
Frequently used conversion factors: SI and English

Quantity	English unit	To SI	To English	SI unit
Length	feet (ft)	0.3048	3.2808	meter (m)
	e.g., 1 ft = 0.3048 m; 1 m = 3.2808 ft			
	mile	1.609	0.6214	kilometer (km)
	inch (in)	25.4	0.03937	millimeter (mm)
Mass	pound (lb)	0.4536	2.205	kilogram (kg)
	ounce (oz)	28.3495	0.03527	gram (g)
Volume	cu. ft. (ft^3)	0.028317	35.3147	$meter^3$ (m^3)
	gallon (gal)	0.003785	264.172	$meter^3$ (m^3)
	barrel (bbl)	0.15899	6.2898	$meter^3$ (m^3)
	Mcf (1,000 ft^3 gas, 60°F, 14.7 psia) = 28.317 Nm^3 (15°C, 101.325 kPa)			
Area	sq. ft (ft^2)	9.29×10^{-2}	10.764	$meter^2$ (m^2)
	acre	4.0469×10^3	2.471×10^{-4}	$meter^2$ (m^2)
	sq. mile	2.590	0.386	$(km)^2$
Pressure	lb/in^2 (psia)	6.8948	0.1450	kPa (1000 Pa)
	(1 atm = 14.696 psia = 101,325 Pa; 1 psia/ft = 22.62 kPa/m)			
	inch Hg	3.3864×10^3	0.2953×10^{-3}	Pa
Temperature	Rankine (°R) (°R = 460 + °F)	0.5556	1.8	Kelvin (K) (K = 273.15 + °C)
Energy (work)	Btu	1.0551	0.9478	kilojoule (kJ)
	Btu	252.16	3.966×10^{-3}	cal
	ft · lb_f	1.3558	0.73766	joule (J)
	hp · hr	0.7457	1.341	kW · hr

TABLE 1.10
Frequently used conversion factors: SI and English (*continued*)

Quantity	English unit	To SI	To English	SI unit
Viscosity (μ)	(lb/ft · sec)	1.4882	0.672	kg/(m · sec) or (Pa · s)
	cp	10^{-3}	10^{3}	Pa · s
Thermal conductivity (k)	$\frac{\text{Btu} \cdot \text{ft}}{\text{hr} \cdot \text{ft}^2 \cdot {}^\circ\text{F}}$	1.7307	0.578	W/(m · K)
Sp. Heat (C_P)	Btu/(lb_m · °F)	4.184×10^{3}	2.39×10^{-4}	J/(kg · K)
	Btu/lb_m · °F)	1	1	cal/(g · °C)
Density (ρ)	lbm/ft^3	16.02	0.0624	kg/m^3
Permeability (k)	md(= 10^{-3} darcy)	9.8692×10^{-16}	1.0133×10^{15}	m^2
	md	0.9862	1.0133	mD (= 10^{-15} m^2)

Basic definitions:
N (newton) = kg · m/s^2
Pa (pascal) = N/m^2 = kg/m · s^2
J (joule) = N · m = Kg · m^2/s^2
W (watt) = J/s

SI prefixes:

T (tera)	10^{12}
G (giga)	10^{9}
M (mega)	10^{6}*
k (kilo)	10^{3}
m (milli)	10^{-3}
μ (micro)	10^{-6}
n (nano)	10^{-9}
p (pico)	10^{-12}

* In gas industry, M = 10^3, MM = 10^6, and B = 10^9; e.g., 1,000,000,000 ft^3 = 1,000,000 Mcf = 1000 MMcf = 1 Bcf

quantities along with conversion factors [1-96], and it has had lists of standard symbols [1-97] for several years. The AGA also has a committee on conversion, but with minor emphasis on gas engineering calculations [1-32]; the API has also issued a report [1-94]. Here, the SPE system of SI units is adopted. Table 1.10 is a quick reference table of conversion factors for common terms. Table A.2 (Appendix A) is a master list expected to be complete for most terms used in gas engineering.

REFERENCES

Major references

1-1. Katz, D. L., D. Cornell, R. Kobayashi, F. H. Poettmann, J. A. Vary, J. R. Elenbaas, and C. F. Weinaug, *Handbook of Natural Gas Engineering*, McGraw-Hill Publishing Company, New York (1959).

1-2. Katz, D. L. and K. H. Coats, *Underground Storage of Fluids*, Ulrich's Book Store, Ann Arbor, Michigan (1968).

Books, monographs

1-3. Aziz, K., and A. Settari, *Petroleum Reservoir Simulation*, Applied Science Publishers, New York (1979).

1-4. Bradley, H. B., (Editor), *Petroleum Production Handbook*, Society of Petroleum Engineers, Richardson, Texas (1987).

1-5. Brown, Kermit E., *Gas Lift Theory and Practice*, Prentice-Hall, Englewood Cliffs, New Jersey (1967).

1-6. Brown, K. E. and H. D. Beggs, *The Technology of Artificial Lift Methods*, PennWell Publishing Company, Tulsa, Oklahoma (1977).

1-7. Campbell, John M., *Gas Conditioning and Processing*, Vol. I and II, The Campbell Group, Norman, Oklahoma, 5th Edition (SI metric) (1979), 4th Edition (English units) (1976).

1-8. Chilingarian, G. V., and P. Vorabatr, *Drilling and Drilling Fluids*, Elsevier Scientific Publishing Co., Amsterdam and New York (1981).

1-9. Craft, B. C., and M. F. Hawkins, *Applied Petroleum Reservoir Engineering*, Prentice-Hall, Englewood Cliffs, New Jersey (1959).

1-10. Crichlow, H. B., *Modern Reservoir Engineering—A Simulation Approach*, Prentice-Hall, Englewood Cliffs, New Jersey (1978).

1-11. Dake, L. P., *Fundamentals of Reservoir Engineering*, Elsevier Scientific Publishing Co., Amsterdam and New York (1978).

1-12. Frick, T. L. (Editor), *Petroleum Production Handbook*, Society of Petroleum Engineers, Dallas, Texas (1962).

1-13. Ikoku, C. U., *Natural Gas Reservoir Engineering*, John Wiley & Sons, New York (1984).

1-14. Katz, D. L., and E. R. Lady, *Compressed Air Storage*, Ulrich's Books, Ann Arbor, Michigan (1976).

1-15. Katz, D. L., and M. J. Rzasa, *Bibliography for Physical Behavior of Hydrocarbons under Pressure*, J. E. Edward, Inc., University Microfilms, Ann Arbor, Michigan (1946).

1-16. Muskat, Morris, *Physical Principles of Oil Production*, McGraw-Hill Publishing Company, New York (1949).

1-17. Nind, T. E. W., *Principles of Oil Well Production*, McGraw-Hill Publishing Co., New York, 2nd Ed. (1981).

1-18. Peaceman, D. W., *Fundamentals of Numerical Reservoir Simulation*, Elsevier Scientific Publishing Company, Amsterdam and New York (1977).

1-19. Slider, H. C., *Practical Petroleum Reservoir Engineering Methods,* Petroleum Publishing Co., Tulsa, Oklahoma (1976).
1-20. Standing, M. B., *Volumetric and Phase Behavior of Oil Field Hydrocarbon Systems,* Society of Petroleum Engineers, Dallas, Texas (1977).

Society of Petroleum Engineers (SPE), Richardson, Texas, reprint series, monographs

1-21. Earlougher, R. C., Jr., *Advances in Well-Test Analysis* (1978).
1-22. Matthews, C. S., and D. G. Russell, *Pressure Build-up and Flow Tests in Wells* (1967).
1-23. Smith, D. K., *Cementing,* 2nd printing (1976).
1-24. SPE Reprint Series, *Gas Technology,* No. 13, Vols. 1–2 (1977).
1-25. SPE Reprint Series, *Phase Behavior* (1981).
1-26. Stalkup, F. I., Jr., *Miscible Displacement* (1984).
1-27. Williams, B. B., J. L. Gidley, and R. S. Schechter, *Acidizing Fundamentals* (1979).

Gas Processors Association (GPA), Tulsa, Oklahoma

1-28. *Engineering Data Book,* 10th Edition (English units), Volumes I & II (1987); 9th Edition (SI metric units), (1980).
1-29. *Gas Processors Association—Plant Operations Test Manual,* 2nd Edition (1984).
1-30. *Gas Processors Association Technical Standards* (1981).

American Gas Association (AGA), Arlington, Virginia

1-31. *AGA Gas Measurement Manual,* Parts 1, 2, 5, 6, 7, 12, 14 (1981, with revision).
1-32. *Metric Unit (SI) Application Guide* (1980).
1-33. *Survey of Underground Gas Storage Facilities in U.S. and Canada, 1983,* Catalog No. XU0783 (1983).
1-34. *Underground Storage of Gas in the U.S. and Canada* (1977–1982).

AGA monographs

1-35. Bergman, D. F., M. R. Tek, and D. L. Katz, *Retrograde Condensation in Natural Gas Pipelines* (1975); University Microfilms, 300 N. Zeeb Rd., Ann Arbor, Michigan 48106.
1-36. Hardy, H. R. et al., *Feasibility of Utilizing Microseimic Techniques for the Evaluation of Underground Gas Storage Reservoir Stability* (1975).
1-37. Hardy, H. R., et al., *A Study to Evaluate the Stability of Underground Gas Storage Reservoirs* (1972).
1-38. Ibrahim, M. A., M. R. Tek, and D. L. Katz, *Threshold Pressure in Gas Storage* (1970).
1-39. Katz, D. L., M. R. Tek, K. H. Coats, M. L. Katz, S. C. Jones, and M. C. Miller, *Movement of Underground Water in Contact with Natural Gas,* AGA Monograph on Project No. 31 (1963); University Microfilms, 300 N. Zeeb Rd., Ann Arbor, Michigan 48106.
1-40. Ramey, H. J., A. Kumar, and M. S. Gulati, *Gas Well Test Analysis under Water Drive Conditions* (1973).
1-41. Tek, M. R., *Underground Storage; Theory and Practice,* Gulf Publishing Co., Houston, Texas (1987).
1-42. Tek, M. R., and J. O. Wilkes, *New Concepts in Underground Storage of Natural Gas* (1966).
1-43. Witherspoon, P. A., I. Javandel, S. P. Neuman, and R. A. Freeze, *Interpretation of Aquifer Gas Storage Conditions from Water Pumping Tests* (1967).

Journals, periodicals

1-44. *AAPG Bulletin,* American Association of Petroleum Geologists, Tulsa, Oklahoma.
1-45. *Chemical Engineering Progress,* American Institute of Chemical Engineers, New York, N.Y.
1-46. *Earth Sciences, Petroleum Geology, Pipeline Industry,* Gulf Publishing Co., Houston, Texas.

1-47. *Hydrocarbon Processing,* Gulf Publishing Co., Houston, Texas.
1-48. *Oil and Gas Journal,* PennWell Publishing Co., Tulsa, Oklahoma.
1-49. *Operating Section Proceedings,* American Gas Association, Arlington, Virginia.
1-50. *Petroleum Engineer International,* Energy Publications, Dallas, Texas.
1-51. *Pipeline Industry,* Gulf Publishing Co., Houston, Texas.
1-52. *Proceedings,* Gas Processors Association, Tulsa, Oklahoma.
1-53. *Proceedings World Petroleum Congress* (4-year intervals).
1-54. Society of Petroleum Engineers of AIME (SPE) Journal—*Journal of Petroleum Technology (JPT),* Richardson, Texas.
1-55. SPE Journal—*Society of Petroleum Engineers (SPEJ),* Richardson, Texas (2/1972–12/1985).
1-56. SPE Journal—*SPE Drilling Engineering (SPEDE),* Richardson, Texas.
1-57. SPE Journal—*SPE Formation Evaluation (SPEFE),* Richardson, Texas.
1-58. SPE Journal—*SPE Production Engineering (SPEPE),* Richardson, Texas.
1-59. SPE Journal—*SPE Reservoir Engineering (SPERE),* Richardson, Texas.
1-60. *Symposia on Salt,* The Northern Ohio Geological Society (intervals).
1-61. *World Oil,* Gulf Publishing Co., Houston, Texas.

Geology

1-62. Carson, W. H., et al., *Interstate Oil Compace Commission, Oil and Gas Production,* University of Oklahoma Press (1951).
1-63. Cohee, G. V., M. F. Glaessner, and H. D. Hedberg, *The Geologic Time Scale,* AAPG Studies in Geology No. 6, AAPG, Tulsa, Oklahoma (1978).
1-64. Dickey, P. A., *Petroleum Development Geology,* Petroleum Publishing Co., Tulsa, Oklahoma (1979).
1-65. Dobrin, Milton, *Introduction to Geophysics Prospecting,* McGraw-Hill Publishing Co., New York (1976).
1-66. Dott, R. H., Jr., and R. L. Batten, *Evolution of the Earth,* McGraw-Hill Publishing Co., New York (1981).
1-67. Halbouty, M. T. (editor), *Giant Oil Gas Fields of the Decade 1968–1978,* AAPG Memoir 30, Tulsa, Oklahoma (1980).
1-68. Halbouty, M. T., *Salt Domes,* 2nd Ed., Gulf Publishing Co., Houston, Texas (1979).
1-69. Hobson, G. D., *Introduction to Petroleum Geology,* Gulf Publishing Co., Houston, Texas (1984).
1-70. Hubbert, M. K., "Entrapment of Petroleum under Hydrodynamic Conditions," *Bull. AAPG, 37,* (1954).
1-71. King, R. E. (Editor), *Stratigraphic Oil and Gas Fields,* AAPG Memoir 16, Society Exploration Geophysicists, Special Publication No. 10 (1972).
1-72. Klemme H. D., *Short Course on Petroleum Geology,* University of Tulsa, Oklahoma (1979).
1-73. Landes, K. K., *Petroleum Geology,* 2nd Edition, John Wiley & Sons, New York (1959).
1-74. Landes, K. K., *Petroleum Geology of the United States,* Wiley Interscience, New York (1970).
1-75. LeRoy, L. W., *Subsurface Geologic Methods,* 2nd Ed., Colorado School of Mines, Golden, Colorado (1950).
1-76. Miall, A. D. (Editor), *Factors and Principles of World Petroleum Occurrence,* Canadian Society of Petroleum Geologists, Calgary, Alberta, Canada (1980).
1-77. Moore, R. C., *Introduction to Historical Geology,* McGraw-Hill Publishing Co., New York (1949).
1-78. Nettleton, L. L., *Gravity and Magnetics in Oil Prospecting,* McGraw-Hill Publishing Co., New York (1976).
1-79. Payton, C. E., *Seismic Stratigraphy—Applications to Hydrocarbon Exploration,* AAPG, Tulsa, Oklahoma (1977).
1-80. Russell, W. L., *Principles of Petroleum Geology,* McGraw-Hill Publishing Co., 2nd Edition, New York (1960).

1-81. Telford, W. N., L. P. Geldart, R. C. Sheriff and D. A. Keys, *Applied Geophysics,* Cambridge University Press (1976).
1-82. Tissot, B. P. and D. H. Welte, *Petroleum Formation and Occurrence,* Springer-Verlag, Berlin and New York (1978).
1-83. Weeks, L. G. (Editor), *Habitat of Oil,* AAPG, Tulsa, Oklahoma (1958).
1-84. Young, Addison, and J. E. Galley (Editors), *Fluids in Subsurface Environment,* AAPG Memoir No. 4 (to Paul Weaver), Tulsa, Oklahoma (1965).

Other references

1-85. Bell, J. S., and J. M. Shepherd, "Pressure Behavior in the Woodbine Sands," *Trans. AIME,* Vol. 192, p. 19 (1964).
1-86. Eilerts, C. K., and M. A. Shellhardt, "Flow Characteristics, Composition, and Properties of Fluids from a Combination Well," *U.S. Bureau of Mines,* R.O. 3402 (1938).
1-87. French, R. W., "Geothermal Gradients in California Oil Wells," *API Drilling and Production Practice,* p. 653 (1939).
1-88. Katz, D. L., "Depths to Which One May Expect Frozen Gas Fields," *J. Pet. Tech., 28,* 419–423 (1971).
1-89. Katz, D. L., "A Look Ahead in Gas Storage Technology," *AGA Trans. Conference,* T283–T290 (1981).
1-90. Katz D. L., R. A. Herzog, and Yusuf Hekim, "Predicting Yield of Revaporized Condensate in Gas Storage," *SPE preprint 10166* (1981); *J. Pet. Tech.,* Vol. 35, No. 6, 1173–1175, June (1983).
1-91. Katz, D. L., and C. L. Lundy, "Absence of Connate Water in Michigan Reef Gas Reservoir—An Analysis," *AAPG Bull., 66,* No.1, PH-98 (1982).
1-92. Katz, D. L., and B. Williams, "Reservoir Fluids and Their Behavior," *Bull. AAPG,* Vol. 36, 342 (1952).
1-93. Katz, D. L., and P. A. Witherspoon, "Storage of Gas and Oil to Meet Seasonal Demands," *Proceedings of 8th World Petroleum Congress,* Moscow, U.S.S.R. (1971).
1-94. "Manual of Petroleum Measurement Standards," Chapter 15: "Guidelines for the Use of the International System of Units in the Petroleum and Allied Industries," *API Publication 2564,* 2nd Ed., Washington, D.C. (1980).
1-95. Nichols, E. A., "Geothermal Gradients in Midcontinent and Gulf Coast Fields," *Trans. AIME,* Vol. 170, 44 (1947).
1-96. SPE Metrication Subcommittee, "The SI Metric System of Units and SPE's Tentative Metric Standard," *J. Pet. Tech.,* 2019–2056, Sept. (1982).
1-97. SPE Symbols Committee, "Supplements to Letter Symbols and Computer Symbols for Petroleum Reservoir Engineering, Natural Gas Engineering, and Well Logging Quantities," *Trans. SPE,* Vol. 234, 1463–1496 (1965); Vol. 253, 556–574 (1972).

CHAPTER 2

PROPERTIES OF ROCKS

A number of properties of the rocks of the earth are important in producing and storing natural gas. *Porosity* determines the container capacity, *permeability* describes the ability of fluids to flow through the rock, *capillary pressures* indicate the water retention in hydrocarbon-bearing zones, and *threshold pressures* measure the ability of gas to displace water from aquifer caprocks. The properties of rocks containing hydrocarbons and water are needed by the geologists and reservoir engineers who determine the oil and gas content of reservoirs. They are used in developing methods for efficient recovery of oil and gas.

The data-gathering process starts while wells are being drilled; for example, drilling time and penetration rates indicate the nature of the rock being cut. Examination of the drill bit cuttings carried to the surface by circulating mud gives important information. Cores are taken of potentially productive horizons for measurements on site or in laboratories. Logs are taken on wells both before and after casing to obtain properties of rocks as seen at the wellbore. Later production-pressure change tests may yield data used to calculate the quality of the pores within the rocks.

Interest centers around the porosity and permeability of potential productive formations for oil and natural gas. In gas storage, especially aquifers, the properties of the caprock layer are of concern as well as those of the storage container. In deep high-pressure formations, especially those with low porosity and permeability, the effects of the overburden pressure with lowered fluid pres-

sure are crucial to commercial operation. Permeabilities measured with gases at low pressures may be higher than those measured at high pressure, due to Knudsen diffusion or Klinkenberg effects. The permeability and porosity of rock under in-situ conditions of confining pressure and temperature are lower than laboratory values obtained near atmospheric pressure. This character of the rock needs measurement. The alternating-size cross sections for the interstices of rocks are responsible for a quadratic equation relating flow rate and pressure drop that requires the use of a β factor for high-velocity flow, such as around wellbores.

Capillary effects created by the internal shape of a porous bed are responsible for nonrecovery of crude oil, the presence of interstitial water, and residual gas when water displaces a gas phase. Laboratory measurements simulate the reservoir behavior. Interfacial surface properties prevent nonwetting fluids from displacing wetting fluids from tight rock. Threshold pressure measurements show how water can hold hydrocarbons in the earth against a pressure gradient and how to evaluate caprocks for potential aquifer storage reservoirs.

The nature of the interstices of porous rock is hard to visualize. The capillary glass tube in which a liquid rises by surface tension is a model for capillarity, but it is quite misleading if the fluid is flowing. The passages in rock occur in a network of three dimensions with enlarging and contracting cross sections. A section might be represented by a city street map with diagonal as well as rectangular streets and alleys of variable width.

The engineer's interest revolves around the volumetric capacity of the rock for hydrocarbons and the flow rate–pressure drop relationship for a given geometry. Both of these concepts involve capillarity in that the presence of connate or interstitial water reduces the hydrocarbon capacity to some fraction of the pore space depending on the water saturation. Water of different mineral contents may change clay swelling or make fine particles mobile in rock, thus altering the permeability at wellbores. Likewise, flow may be not of a single phase but of two or three phases, in which case the method of *relative permeability* applies. Earlier presentations of these topics are given in [1-1], [1-2], many petroleum books, and a review by Keelan [2-38].

2.1 TYPES OF ROCKS

There are many kinds of rocks; sandstone, shales, and carbonates (limestone or dolomites) are the prime types. Figure 2-1 shows a sandstone similar to rocks used in building garden walls; grains of sand are bound together in various degrees in a matrix. A limestone has a matrix portion but also solution cavities, known as *vugs*, caused by percolating underground waters. Shales are fine-grained matrices, with a tendency to occur in layers.

In earlier days it was assumed that there was disconnected pore space, but data on measured pore space, grain density, and bulk density leave little room for disconnected space (Fig. 2-2). When the concept of threshold pressure is presented, it will be shown that few rocks will not admit liquid under high pressure differentials.

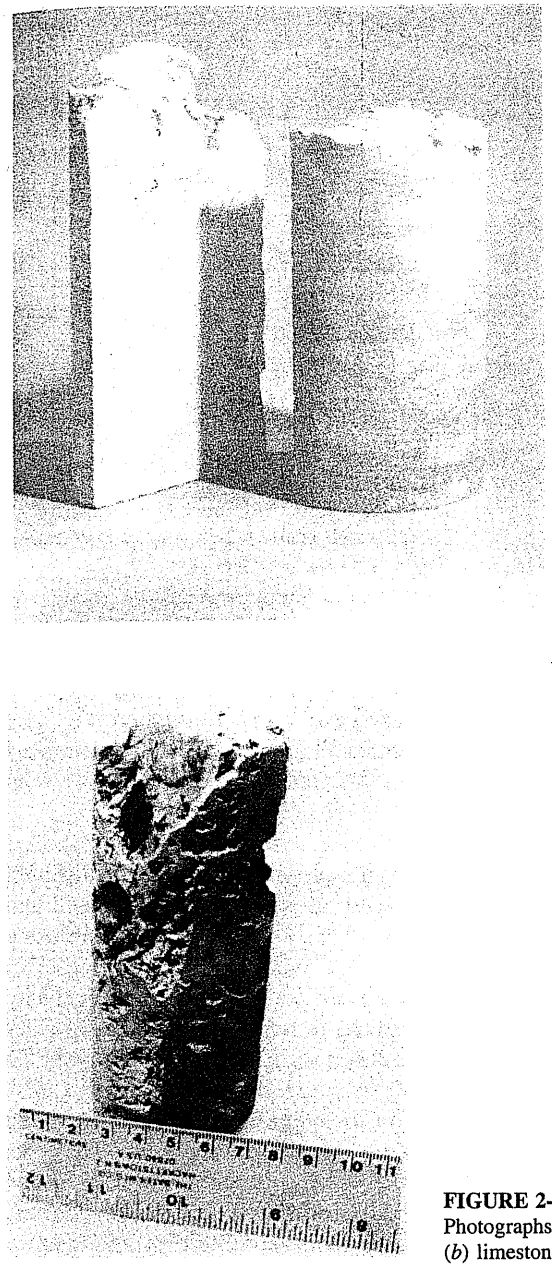

FIGURE 2-1
Photographs of core specimens: (*a*) sandstone, (*b*) limestone core with large vugs.

FIGURE 2-1
(*c*) Siltstone core interlayered with shale. (By J. McLemore, courtesy New Mexico Petroleum Recovery Research Center.)

Flow in porous media is governed by the shape of the interconnected pores. Figure 2-3*a* shows the capillary tube model of rock, with a uniform cross section. Figure 2-3*b* represents a single pore with varying cross section where the fluid presumably leaves one node and enters another. Figure 2-3*c* shows idealized viscous or streamline flow at low velocity and at high velocity, where the fluid separates from the wall surface.

Much can be learned by studying the displacement of one fluid by another from porous media. The concept of a dead end pore space by Coats and Smith [2-12] revealed that some fluid was not displaced directly and only diffused into the stream of flow. Studies of threshold pressure and other factors convince the authors that an apparent dead end may well flow under other conditions. No three-dimensional experiments have been conducted to test whether the velocity in one dimension is affected by the flow gradient in other dimensions. In other words, is the velocity in the x direction, u_x, a function of the flow gradient in the y direction, du_x/dy? Raimondi and Torcaso [2-56] and Salter and Mohanty [2-61, 2-62] conducted similar studies to evaluate the flow mobility of the nonwetting substance during single-dimension flow. More details were presented on this subject in later work on varying threshold pressure as an interface is displaced through a core [2-60].

One school of thought stresses pore sizes and uses mercury injection to determine pore diameter as a function of volume of pores entered by mercury (Fig. 2-4). The pressure required for mercury to enter a pore throat at a node gives the size of the pore at that point.

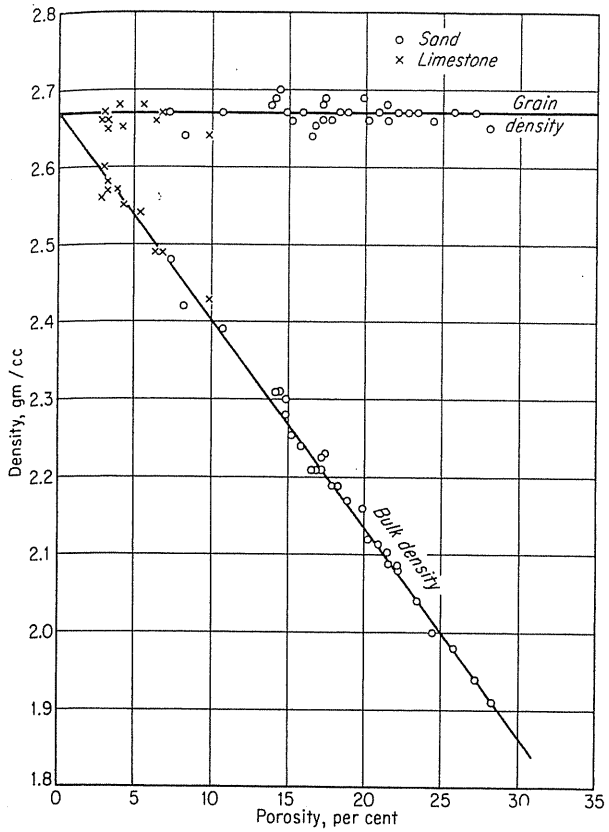

FIGURE 2-2
Bulk and solids density of cores [Katz, et al., 1-1, courtesy McGraw-Hill Publishing Co.].

2.2 POROSITY

Porosity is determined by measuring the volume of a cleaned core specimen and the volume of the pores themselves. One method uses gas under pressure to fill the pores followed by measurement of the gas upon pressure release, permitting calculation of ϕ, the percentage pore space, or porosity. A wet method is to saturate a core with a heavy wetting nonvolatile liquid, weighing the core before and after saturation [1-1]. A method currently used for routine measurements is to measure the volume of air or helium that can be injected into a clean core at a given pressure. A cell holds a cut core plug with blanks to minimize gas space; the container needs to be in a flexible sleeve when overburden pressures confine it.

Mercury impregnation of cores or drill cuttings is used as shown in Fig. 2-4. A specimen is placed in a chamber, and mercury is injected to fill the chamber

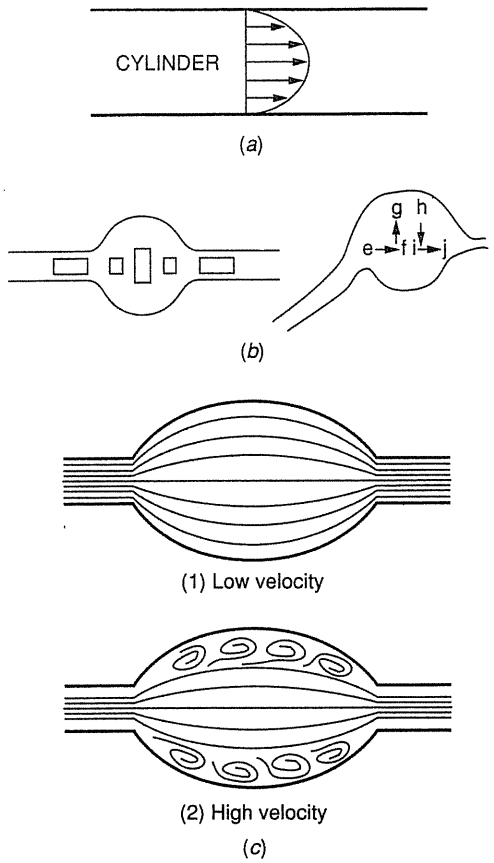

FIGURE 2-3
Idealized flow patterns [Firoozabadi & Katz, 2-19, courtesy SPE-AIME].

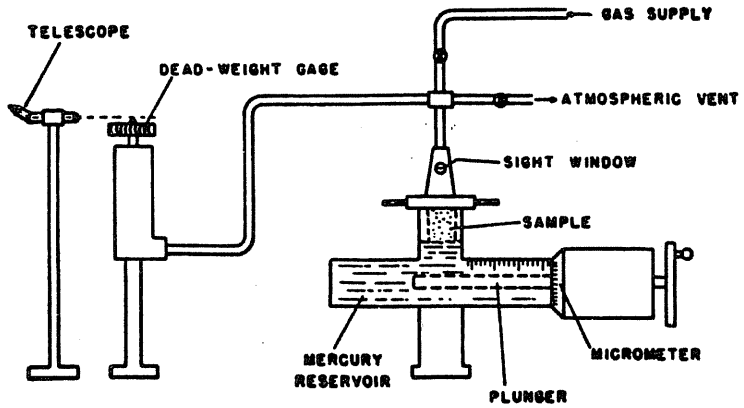

FIGURE 2-4
Kobe porosimeter, mercury injection [Pollard & Reichertz, 2-54, courtesy AAPG].

to a point marked on a sight gauge; this gives the volume of the specimen. With added gas pressure the nonwetting mercury will enter the pores, and the volume of this penetration may be measured by bringing the mercury surface back to the same level. The fractional volume of injected mercury over the bulk volume gives the porosity. Nonwetting mercury injection yields increasing porosity with increased injection pressure.

2.3 PERMEABILITY

Permeability was defined by the American Petroleum Institute in 1935 as shown in Fig. 2-5. A permeability of 1 darcy allows a flow rate of 1 cm^3/s for a fluid of 1 centipoise viscosity through a cross section of 1 cm^2 with a pressure drop of 1 atm per centimeter of length. A more commonly used unit is the millidarcy, or 0.001 darcy.

The SI metric unit of permeability is μm^2 (10^{-12} m^2). One darcy is 0.9869 μm^2. One millidarcy is 0.9869×10^{-3} μm^2 or 0.9869×10^3 nm^2.

The SI definition of permeability is "A permeability of 1 m^2 will permit a flow of 1 m^3/s of fluid of 1 Pa · s viscosity through an area of 1 m^2 under a pressure gradient of 1 Pa/m" [1-96].

Several effects should be noted in measuring permeability and using the data for an in-situ property of a reservoir, including the following:

1. The net confining pressure affects a core (confining pressure on rock minus the pore pressure).
2. Permeability may change between a dry state to a wet state because of mobility of fine particles and/or clay swelling by water foreign to the reservoir system.
3. Measurements by gas flow at close to 1 atm pressure in the laboratory can give higher permeability due to slip (or molecular diffusion effects) than at higher gas pressure in the reservoir—Klinkenberg's description of Knudsen diffusion.

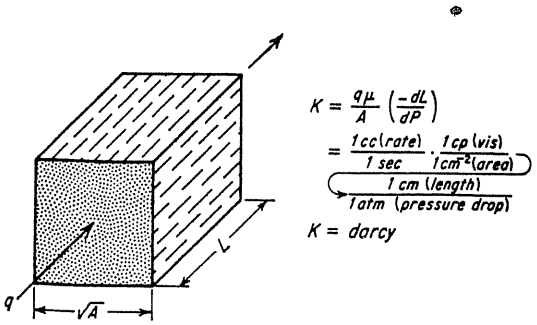

FIGURE 2-5
The unit of permeability, darcy [Katz, et al., 1-1, courtesy McGraw-Hill Publishing Co.].

4. Darcy's law, used in permeability measurements, applies strictly only at low (zero) flow rates; the overriding pressure drop mechanism includes a velocity squared term that becomes numerically significant as the velocity increases, such as near wellbores.

Measurements normally are made on core plugs or on full cores with equipment to be described later. Using well flow tests and draw-down and buildup pressures, the in-situ permeability may be calculated for the physical system around the wellbore. Usually, the measured in-situ value is much higher than data on cores.

Measurement of Permeability

Permeability k is defined by Eq. (2.1):

$$\frac{q}{A} = \frac{k}{\mu}\left(-\frac{dP}{dL}\right) \tag{2.1}$$

where q is the volume flow rate (cm^3/s), A is the cross-sectional area (cm^2), μ is the fluid viscosity (centipoises, cp), k is the permeability (darcies), and $-(dP/dL)$ is the pressure drop per unit length (atm/cm). A cube of a porous medium 1 cm on edge ($\sqrt{A}$ in Fig. 2-5) has a permeability of 1 darcy if water flows between the front and back faces at a rate q of 1 cm^3/s under a pressure drop of 1 atm at a temperature of 68°F (20°C), where the viscosity is 1 centipoise.

Permeability is measured by passing a fluid of known viscosity through a core plug of measured dimensions and then measuring flow rate and pressure drop. The pressure drop is measured by a manometer, and the flow rate either by a calibrated orifice or, with very slow rates, by the rate of movement of a soap bubble in a calibrated glass tube.

Equation (2.1) is written in differential form, and must be integrated to find a suitable equation to use in computing permeability. The volumetric flow rate q is a constant for liquids, because the density does not change significantly during flow through the core plug. Accordingly, Eq. (2.1) becomes Eq. (2.2):

$$q = \frac{kA}{\mu}\frac{(P_1 - P_2)}{L} \tag{2.2}$$

for liquids flowing through porous media when q, A, μ, and k are constant.

The measurement of permeability should be restricted to the low flow rate region, where the pressure drop remains proportional to flow rate within the experimental error. For high flow rates, Eq. (2.2), the *viscous Darcy equation*, is inappropriate to describe the relationship of flow rate and pressure drop (for details see Section 2-5). The gas volumetric flow rate q varies with pressure, and either the value for q at the average pressure in the core must be used in Eq. (2.2) or Eq. (2.1) must be integrated over a finite length L. Both methods give the same final equation when gases follow ideal-gas behavior and viscosity μ is constant.

To convert gas volumes at the mean pressures to gas volumes at a given base pressure P_b, the term Q is introduced for gas flow rate in cubic centimeters per second at pressure P_b, with $Q/q = (P_1 + P_2)/(2P_b)$. Substituting this in Eq. (2.2) yields

$$Q = \frac{kA}{2L\mu P_b}(P_1^2 - P_2^2) \tag{2.3}$$

Eq. (2.3) can be rearranged as

$$k = \frac{2QL\mu P_b}{A(P_1^2 - P_2^2)} \text{ darcies} \quad \text{or} \quad k = \frac{2000QL\mu P_b}{A(P_1^2 - P_2^2)} \text{ millidarcies} \tag{2.4}$$

where Q is in cm^3/s, L, the length of core, is in cm; P is in atm; A is in cm^2; and subscripts 1, 2, and b represent upstream core, downstream core, and base pressure of gas measurement, respectively.

Equation (2.4) is valid only for low pressure, at which gases behave ideally. For a real gas, one can convert pressure P to pseudopressure $m(P)$ (in units of atm^2/cp; usually called *real gas potential* [2-1]) which can be calculated and tabulated for a given specific gravity G at temperature T:

$$m(P)|_{G,T} = 2\int_0^P \frac{P'}{\mu Z}dP' \tag{2.5}$$

This $m(P)$ is a potential form of pressure squared P^2 including the variations of viscosity μ and compressibility factor Z. In terms of $m(P)$, Eq. (2.4) becomes

$$k = \frac{2000QLP_b}{A[(m(P_1) - m(P_2)]} \tag{2.6}$$

for all ranges of measuring pressures. Details of applications of $m(P)$ will be discussed in Chapter 8.

Table 2.1 gives data taken on a sand core of 18.2 percent porosity. The permeability values for the four measurements should be the same. Using Darcy's law, normally no more than one or two values are taken, but in preliminary work it is advisable to take several points to show that the values give a constant permeability within the possible error of measurement. Should the flow rates be too high, the permeability will decrease, for the flow process can no longer be approximated by Darcy's law.

Several commercial devices are available for measuring permeability with a minimum of readings and calculations. In measuring permeability, core plugs are cut both horizontally and vertically, since there may be a distinct difference in the two values. The apparatus in Fig. 2-6 is useful for full core analyses both horizontal and vertical on the same core [2-41].

TABLE 2.1
Calculation of permeability [Katz, et al., 1-1, courtesy McGraw-Hill Publishing Co.]
Core plug, 2.36 cm long, 1.81 cm diameter, 2.58 cm^2 area; barometer, 763 mm Hg; temperature, 68°F; μ (air), 0.181 centipoise

Trial no.	P_1, mm Hg	Orifice used	Orifice differential, mm H_2O	Air Flow Rate Q,cm^3/s	Pressure drop: P_2, mm Hg	P_2, mm Hg abs	P_1, mm Hg abs	$(P_1^2 - P_2^2) \times 10^{-3}$	k, md
1	782	A	17	0.88	1.20	764	1545	1805	9.36
2	729	A	15	0.80	1.10	764	1492	1642	9.35
3	276	B	87	0.24	6.25	769	1039	488	9.44
4	180	B	54	0.15	3.95	767	943	301	9.57

$$C = \frac{Q}{P_1^2 - P_2^2} \quad \text{where} \quad C = \frac{2000 \times 2.36 \times 0.0181 \times 760^2}{2.58} \times \frac{736}{760} = 19.2 \times 10^6$$

P_1 and P_2 in mm Hg abs

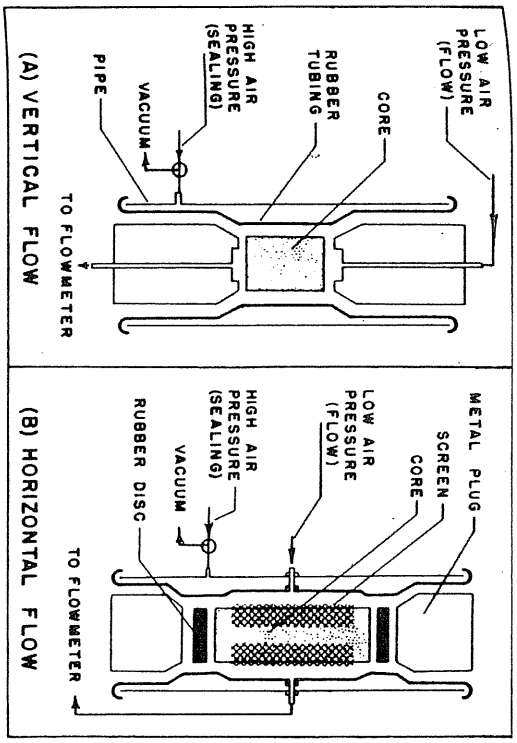

FIGURE 2-6
Hassler-type permeameter [Kelton, 2-41, courtesy SPE-AIME].

Effects of Water on Permeability

Most rocks in reservoirs have connate water in them, and the clays and other minerals are adjusted to the presence of water or brine. Cleaning and drying the core prior to porosity and permeability measurements can alter the permeability results when air is used for measurement. The use of waters foreign to the native water likewise can alter the results, fresh water usually giving the lowest permeability. The ionic content and pH of the water are believed to be prime variables [2-25, 2-42].

The effects of water are much more severe in rocks from recent and tertiary geological periods, like those in California and on the Gulf Coast, while for Ordovician-Cambrian rocks such as Illinois or Iowa aquifers these effects can be minimal. Table 2.2 shows the drastic effect of water on measured permeability [2-31].

The choice of drilling fluids and the use of air drilling or cable tool completions are influenced by the need to keep foreign waters away from some reservoir rocks. However, it may be ascertained that the chemistry of a given reservoir system permits contact with aqueous solutions without reduction of the permeability. Formation clays may be stabilized with hydroxy-aluminum solutions [2-58].

Recent literature has proved that particle movement is a prime mechanism for permeability reduction [2-27]. The aqueous phase apparently makes clay particles mobile, and when they flow, they bridge at small cross sections causing flow stoppage; by reversing flow, permeability can be renewed temporarily [2-42].

TABLE 2.2
Effect of water on core permeability [Johnston & Beeson, 2-31, courtesy SPE-AIME]

Well A, Consolidated				Well B, Loose				Well C, Consolidated			
Permeability, millidarcies,			Fresh-water index,* %	Permeability, millidarcies,			Fresh-water index,* %	Permeability, millidarcies,			Fresh-water index,* %
Air	Salt water	Fresh water		Air	Salt water	Fresh water		Air	Salt water	Fresh water	
285	62	2.2	3.6	660	354	17	4.8	368	41	27	66
481	228	11	4.8	655	340	26	7.6	445	70	62	89
123	82	5.9	7.2	680	342	38	11	221	28	8.3	29
113	43	1.9	4.4	296	198	40	20	302	58	54	93
61	6.8	1.2	18	374	279	63	23	73	2.5	0.8	32
38	0.4	0.1	25	1030	485	22	4.5	33	4.5	5.0	111
159	1.6	0.4	25	192	98	21	22	266	69	50	72
72	2.3	0.7	30	211†	65	48	74	616	230	168	73
310	5.0	1.5	30	625†	242	170	70	262	25	35	140
328	57	31	90	420	216	22	10	191	57	50	88

* Ratio of fresh-water to salt-water permeability, percent.

† Consolidated samples.

Slip Phenomenon: Knudsen-Klinkenberg Effect

Klinkenberg [2-43] called attention to Knudsen diffusion by measurements such as those in Fig. 2-7, which shows permeability versus reciprocal mean pressure of a gas flowing in the core. It should be recognized that most of the measurements of Fig. 2-7 were taken below atmospheric pressure, an unusual condition. The mean free path for ideal gas molecules is inversely proportional to pressure. When the interstices of the rock have spaces of size equal to or less than the mean free path, some gas movement forward is due to molecular diffusion and not pressure drop; this is sometimes called *slip*. This diffusional effect decreases as the mean free path decreases, and at high pressure the gas permeability equals the liquid permeability. For the 23.66-md core of Fig. 2-7, the data shows that a pressure of 9 atm or 132 psia (912 kPa), was sufficient to bring the gas permeability to within 1 percent of the liquid value.

Calhoun and Yuster [2-6] studied Knudsen diffusion effects using Eq. (2.7):

$$k_g = k_l\left(1 + \frac{b}{P_m}\right) \tag{2.7}$$

where k_g is the measured gas permeability, k_l is the known liquid or high-(infinite-) pressure gas permeability, b is a constant for the given porous solid, and P_m is the mean pressure of gas flowing through the core. Their correlation of b with the liquid permeability is b (psi) $= 0.77k_l^{-0.39}$ with k_l in millidarcies. Figure 2-8 shows their results for various gases.

Since air permeability is normally measured at low mean air pressures, a chart, Fig. 2-9 [1-1], was prepared to correct such air permeabilities to high gas pressure permeabilities or liquid permeabilities when the effect of water is negligible.

FIGURE 2-7
Permeability of core sample A to air at various pressures [Klinkenberg, 2-43, courtesy API Drill. Prod. Practice].

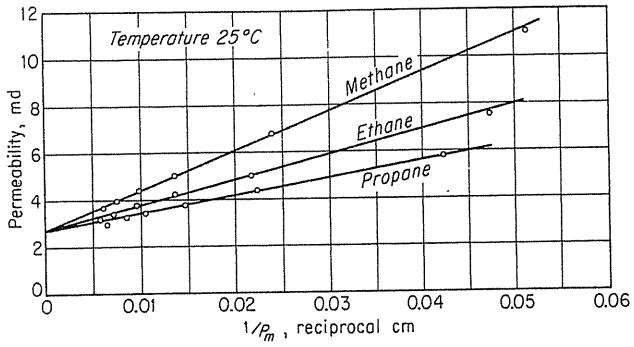

FIGURE 2-8
Effect of gas pressure on measured permeability for various gases [Calhoun & Yuster, 2-6, courtesy API Drill. Prod. Practice].

McMahon [2-48] reported the correlations between permeability k and b in Eq. (2.7) by measuring 162 cores in 1949. Later Jones [2-32] describes a rapid unsteady state method for finding the effect of slip or diffusion on permeability. He obtains for b the following equation for 100 cores:

$$b\,(\text{psi}) = 6.9k^{-0.36}(\text{md}) \qquad \text{or} \qquad b\,(\text{kPa}) = k^{-0.36}(\text{md}) \tag{2.8}$$

Estes and Fulton [2-15] reported that liquid saturation such as connate water has little effect on slip. Sampath and Keighin [2-63] studied gas slip on low-permeability cores from Uinta Basin including the effects of overburden pressure and water saturation. Figures 2-10 and 2-11 give the results of their measurements on a core with $k_g = 0.056$ md, porosity $\phi = 0.077$. Keelan, in a state-of-the-art paper [2-38], included similar effects of overburden, water saturation, and mean gas pressure.

2.4 OVERBURDEN PRESSURE—STRESS ON ROCK

Rocks change their porosity and permeability slowly with increased confining pressure or difference in confining pressure and internal pore pressure. Several investigators studied these effects, including Fatt et al. [2-18], Hall [2-28], and Thomas and Ward [2-68].

The permeability ratio of rocks was determined by Vairogs et al. [2-72]. The results in Fig. 2-12 show that severe reductions in permeability occur for rocks with permeabilities below 1 millidarcy. With permeabilities over 10 md at pressures below 4000 psi (27.58 MPa), this effect is normally ignored, but for deep gas wells with low permeability the reduction in permeability is so costly that without successful fracturing gas reserves may become uneconomical.

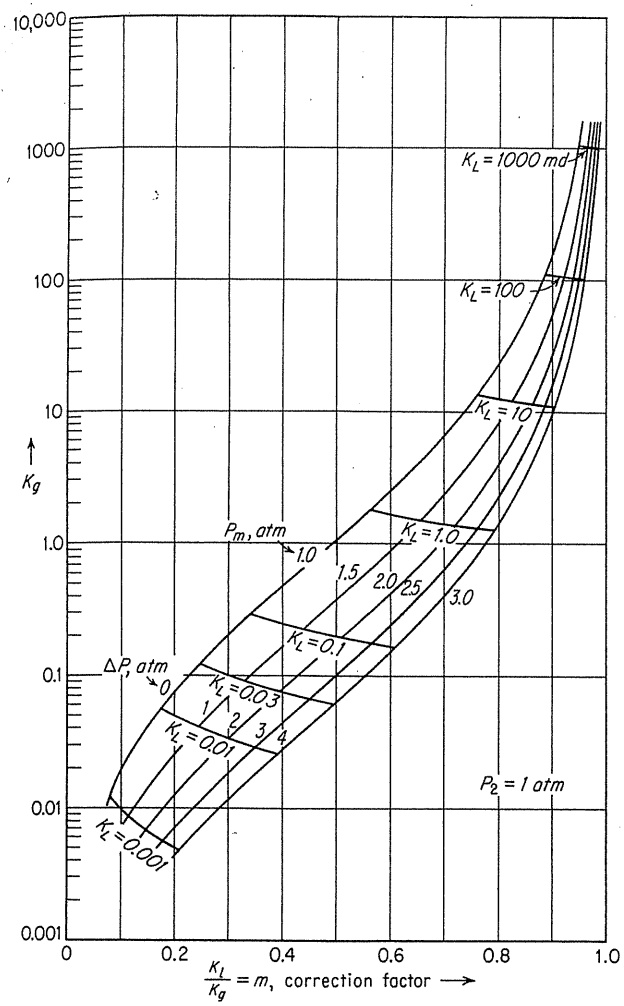

FIGURE 2-9
Correction of air permeability for slip [Katz, et al., 1-1, courtesy McGraw-Hill Publishing Co.].

2.5 HIGH-VELOCITY FLOW

For fluids flowing through porous media, increased flow rate causes more than the linear increase in pressure drop predicted by Darcy's law (Fig. 2-13). Fancher, Lewis, and Barnes [2-17] took measurements and plotted the results as a friction factor versus Reynolds number as in a pipe friction chart; they found the curves leaving a 45° straight line with increased flow rate. Cornell and Katz [2-13] reported a high-velocity flow study using the following equation and evaluating

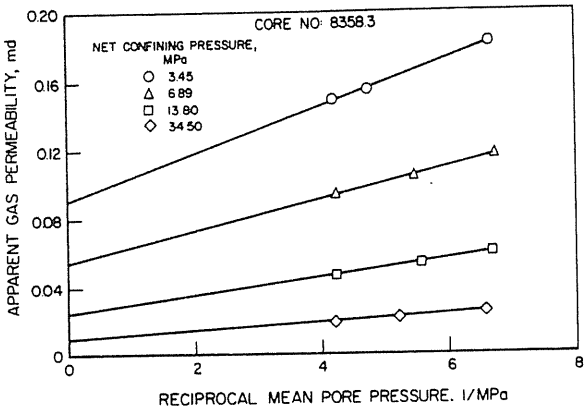

FIGURE 2-10
Effect of confining pressure on gas slip [Sampath and Keighin, 2-63, courtesy SPE-AIME].

β, the high-velocity coefficient:

$$-\frac{dP}{dL} = \frac{\mu}{k}v + \beta\rho v^2, \qquad \text{or in vector form:} \qquad -\nabla P = \frac{\mu}{k}\bar{v} + \beta\rho\bar{v}|\bar{v}| \quad (2.9)$$

Figure 2-14 illustrates the determination of β.

Equation (2.9) is usually referred to as a *Forchheimer-type* equation. Forchheimer noted the nonlinearity of high-velocity flow of water in a sand bed. Bureau of Mines investigators found a v^2 term is needed to fit their air-rock experimental data [2-8, 2-30]. Green and Duwez [2-26] correlated experimental data by using Eq. (2.9) for both liquids and gases flowing through porous metals and mentioned Forchheimer in their references. It is the authors' opinion that the Bureau of Mines laboratory (Chalmers, Johnson, Taliaferro, and Rawlins) should

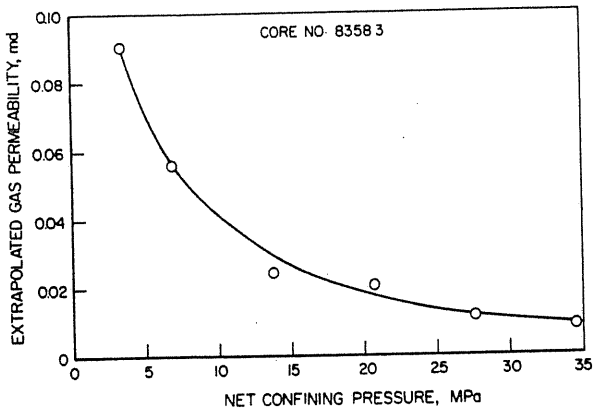

FIGURE 2-11
Effect of confining pressure on extrapolated gas permeability [Sampath and Keighin, 2-63, courtesy SPE-AIME].

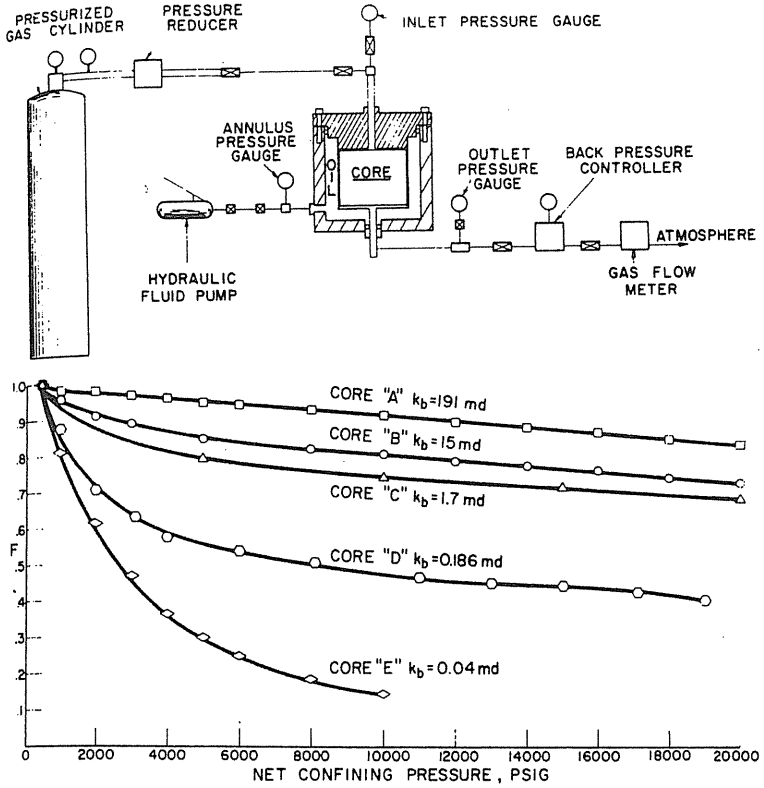

FIGURE 2-12
Permeability ratio versus confining pressure [Vairogs, et al., 2-72, courtesy SPE-AIME].

receive credit rather than Forchheimer for use of v^2 for gases since they used gas flow in consolidated rocks as the basis.

Firoozabadi and Katz [2-19] made a more recent study of high-velocity flow with modified correlations of β with permeability and with a porosity-permeability product (Figs. 2-15 and 2-16). The correlations may have significant differences of predicted and measured values that are attributed to the heterogeneity of the interstices of earthen rocks.

At the time Cornell's work was reported, there was controversy over the use of the word *turbulence* for gas flow. Firoozabadi and Katz [2-19] showed that the extra friction represented by the v^2 or $\bar{v}|\bar{v}|$ term is the result of shear resistance in directions perpendicular to the direction of flow as the cross section of the passage changes size. Some investigators call such resistance an inertial effect. The writers' view is that this extra shear resistance is one of two ongoing mechanisms that consume pressure drop energy: longitudinal and transverse. It

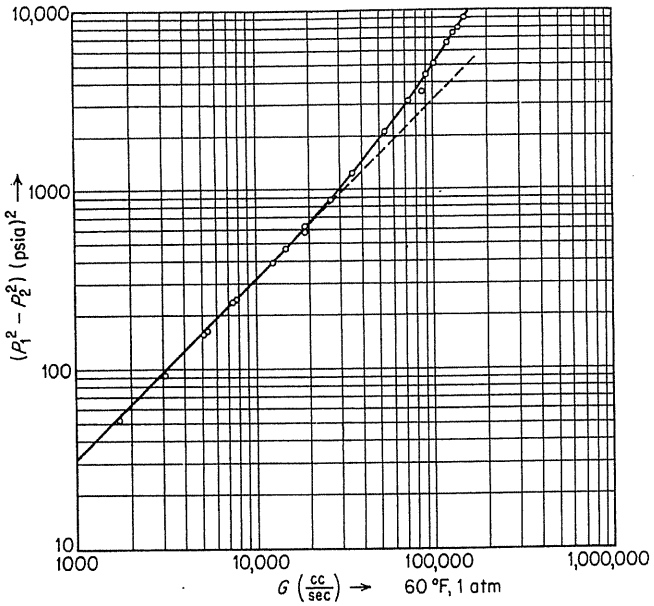

FIGURE 2-13
Pressure drop data for air flowing through a Wilcox sand [Cornell, 2-13, courtesy Ind. Eng. Chem.].

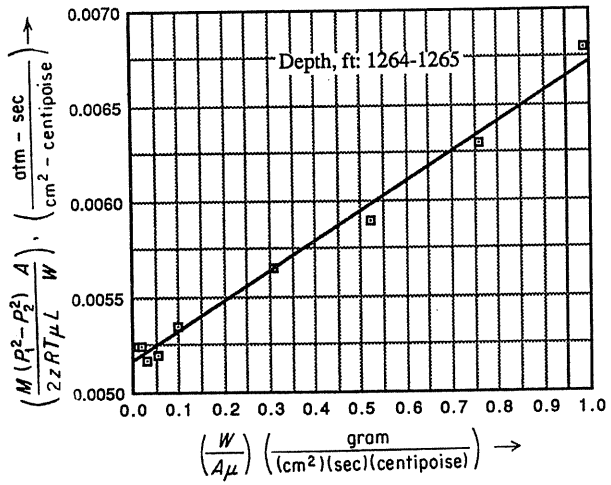

FIGURE 2-14
Determination of velocity coefficient β for St. Peter sandstone ($\phi = 20.1$, $k = 178$ md, $\beta = 4.9 \times 10^7$ ft^{-1}) [Cornell, 2-13, courtesy Ind. Eng. Chem.].

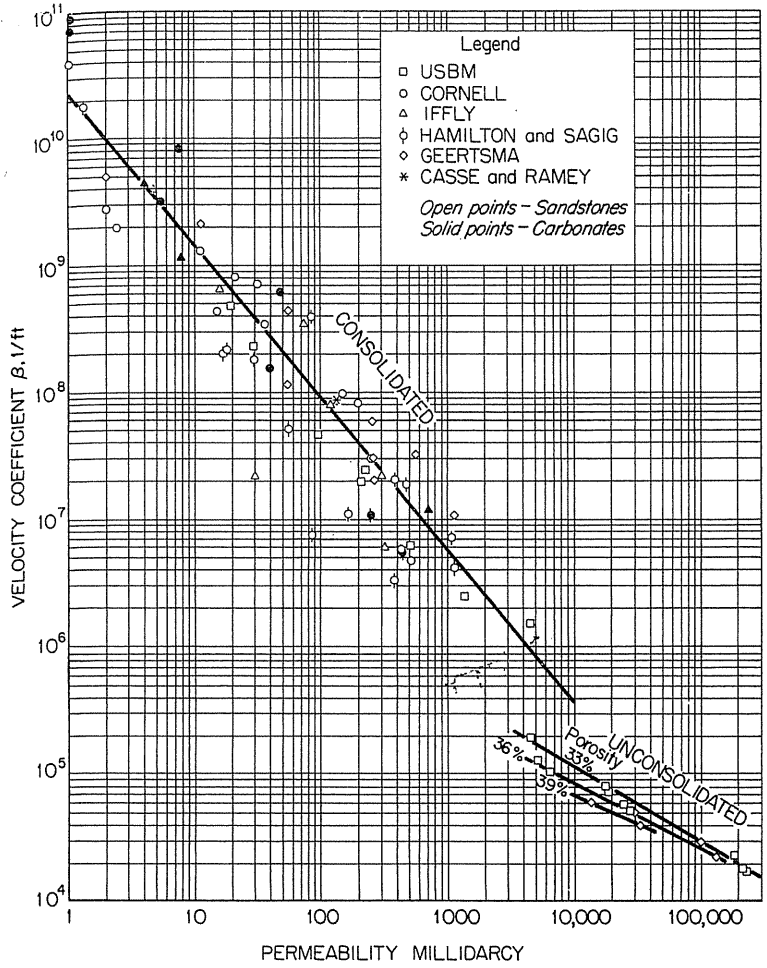

FIGURE 2-15
Correlation of β with permeability [Firoozabadi & Katz, 2-19, courtesy SPE-AIME].

is the transverse shear that varies with the flow velocity as represented by $\beta\rho v^2$, the result of alternating cross-sectional area. One view of what is happening is that there is a separation of the fluid flowing adjacent to the wall, which induces secondary flow (as shown in Fig. 2-3*c*), but not to such an extent that it should be called *turbulence*.

Is There Turbulence at High Velocity?

In the interstices of a normal sandstone or matrix carbonate porous rock, the spaces are too small to visualize turbulence. To obtain a quadratic velocity

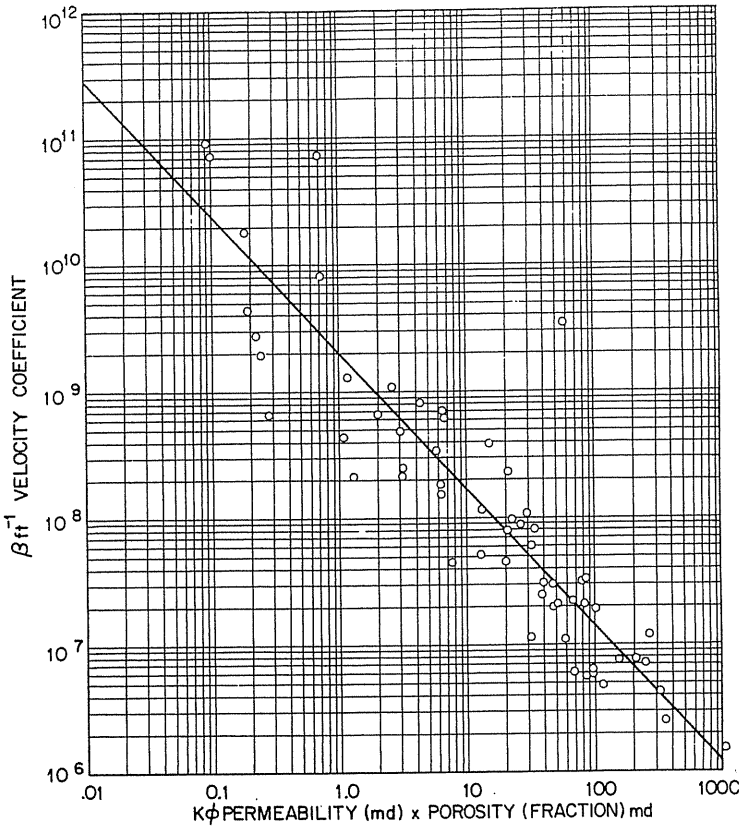

FIGURE 2-16
Correlation of β with the product of porosity and permeability, ϕk [Firoozabadi & Katz, 2-19, courtesy SPE-AIME].

pressure drop, it is not necessary to have turbulence, only the increased transverse movement and separation could cause extra fluid motion and thus added pressure drop.

The concept of "turbulence" adopted was in good part due to the friction factor–Reynolds number curves of Fancher and Lewis [2-17]. Some 25 years ago, the senior author with assistants prepared a column of 15/64-inch glass beads and a liquid permitting vision of flow in the column. Flow rates versus pressure drop were observed and a filament of ink was injected. The filament remained as such through a porous bed at low velocities and plumed at a flow rate corresponding to the Fancher et al. [2-17] friction factor chart. Thus large interstices like carbonate vugs may have physical turbulence causing pressure drop beyond the alternating-sized cross section of the matrix carbonate. The size

of channel for physical turbulence to occur is not known. It is believed that the turbulence may be possible for ordinary sandstone or matrices with permeabilities of 5000 md or above. No record of turbulence has been found for normal cores.

Time to Abandon Concept of Darcy and Non-Darcy Flow

Is there a change in flow mechanism as implied by such terms as "Darcy" and "non-Darcy" flows? Critical examination of the data indicates that there is only one mode of flow in porous media: *the flow through a system of alternating size of the cross section* [2-19]; hence, there is no transition (see Fig. 2-17) from Darcy flow to so-called non-Darcy flow as frequently stated. The friction factor f in Fig. 2-17 is proportional to the ratio of total pressure drop to the pressure drop caused by the v^2 term of Eq. (2.9). The Reynolds number Re is proportional to the ratio of pressure drop caused by the v^2 term to that caused by the v term.

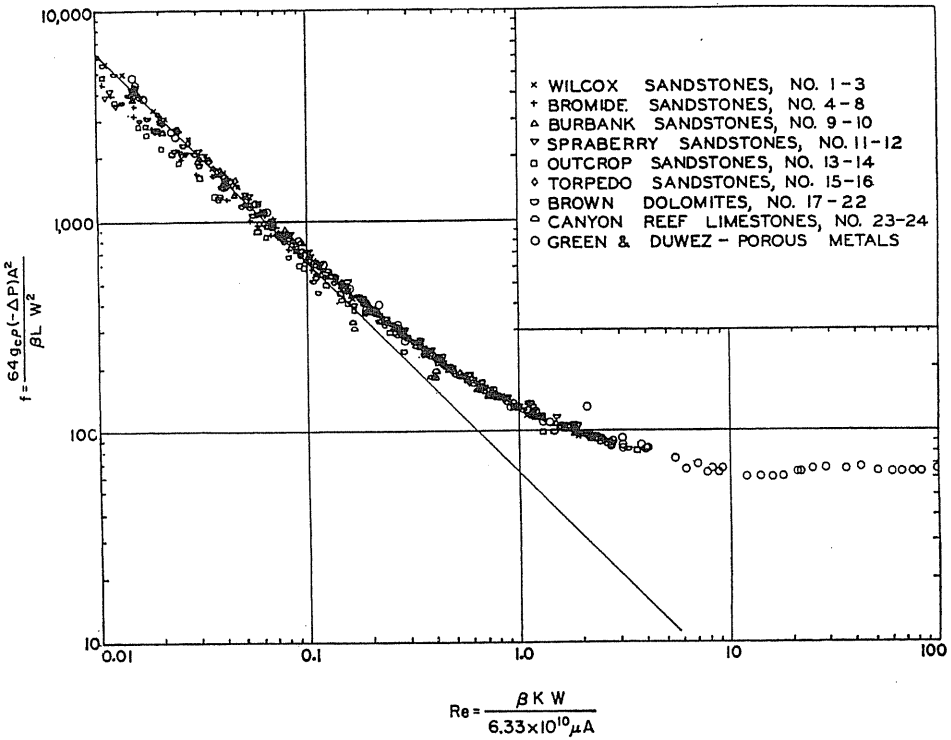

FIGURE 2-17
Friction factor plot for consolidated porous media [Cornell & Katz, 2-13, courtesy Ind. Eng. Chem.].

When Re is small, the magnitude of second terms $\beta\rho v^2$ will be too small to be detected by experimental data. On the friction factor plot, Fig. 2-17, the experimental data points in the lower flow rate region (Re $>$ 0.1) successively cross the selected 45° line; in other words, the relation between f and Re is not a straight line—as the 45° line shown for pipes—but is quadratic in form (i.e., characteristic of porous media or alternate cross section flow).

Johnson and Taliaferro [2-30] presented an extensive study of pressure versus flow rate for natural gas and air flow through pores. Run no. 137 went from 0.426 to 1544.8 cubic feet per 24 hours and from a pressure drop (ΔP^2) of 5.04 to 46,226 psia^2. Over this broad range of flow through a core of 214 md, the plotted data are on a single quadratic curve—no transition point can be identified.

Darcy's law has been useful because the accuracy of measurements cannot detect the nonlinear behavior of gas flow with velocity near zero. Thus, Darcy's law is a convenient and reasonable way to handle low-velocity movement within reservoirs. However, near the wellbore, where radial flow concentration gives higher velocities, a quadratic equation is needed to represent gas flow. It is suggested that proper terminology would be *viscous Darcy flow* (or Darcy flow) for low flow rate and *quadratic Darcy flow* for high-velocity flow. Thus, Eq. (2.9) is the *quad-Darcy flow* equation. The transition from viscous to quad-Darcy flow is a matter of velocity and the numerical effect of the v^2 term as compared to the size of the experimental error in flow measurements. If one insists on complete accuracy in measurements, there is no viscous Darcy flow until the rate reduces to zero [2-19].

For some porous solids, an equation including a velocity cubed term is needed as shown by Forchheimer:

$$-\frac{dP}{dL} = \frac{\mu}{k}v + \beta\rho v^2 + \gamma\rho^2 v^3 \qquad (2.10)$$

This fits data better than Eq. (2.9) [2-19]. Ezeudembah and Dranchuk have discussed the issue and presented an article on combining high-velocity and Klinkenberg effects [2-16]. However, by examining the basic fluid flow equation, the Navier-Stokes equation, and the use of such equations in industry, it is hard to relate the v^3 term to the pressure drop.

2.6 ROCK ELECTRICAL RESISTIVITY FACTOR

The *formation resistivity factor* (F) is defined as the ratio of the resistivity of a rock 100 percent saturated with formation waters to the resistivity of the saturating formation waters [1-1,1-38]. For the laboratory, cleaned cores are saturated with a brine (0.1% KCl is frequently used) and aged for some time. Then they are placed between two silver or platinum electrodes and the resistivity measured by an ac electrical bridge. A parallel resistivity measurement is made on the solution used to saturate the cores.

One may reason that the interference of ion flow by the interstices is akin to the resistance to flow of fluids by the interstices; thus, the electrical resistivity is inversely proportional to permeability. Frequently, F is used in correlating data, but the more available value of permeability generally gives an equally good correlation. Rock resistivity is an important variable in interpreting the logs measured on wells.

2.7 CAPILLARY EFFECTS

Many capillary effects involve interfacial or surface tension between fluids and the solid wall of the interstices of porous media. The concept of the wetting of a surface by a liquid is basic. The following topics are at issue:

1. Imbibition of wetting liquid into porous solids
2. Drainage of liquids from porous beds
3. Connate water as residue of drainage
4. Water-oil displacement and water-gas displacement—capillary pressure
5. Threshold pressure for nonwetting fluid to displace wetting fluid from porous media

These phenomena are controlled by surface forces at phase interfaces. The presence of alternating cross sections with a need for surface change as two phases pass from chamber to chamber via restricted areas creates much of the observed behavior (see Fig. 2-3*b*).

Imbibition is observed when a lump of sugar is held to just touch the surface of coffee in a cup (Fig. 2-18). Coffee fills the pore space as surface forces pull the liquid upward into the porous medium of the sugar.

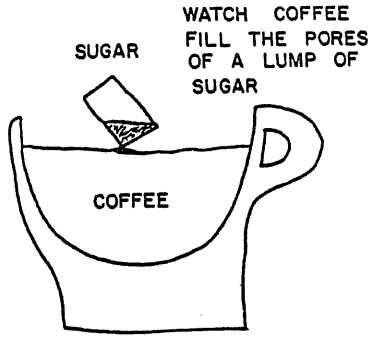

FIGURE 2-18
Surface forces pull coffee into a lump of sugar, (imbibition) [Katz & Coats, 1-2].

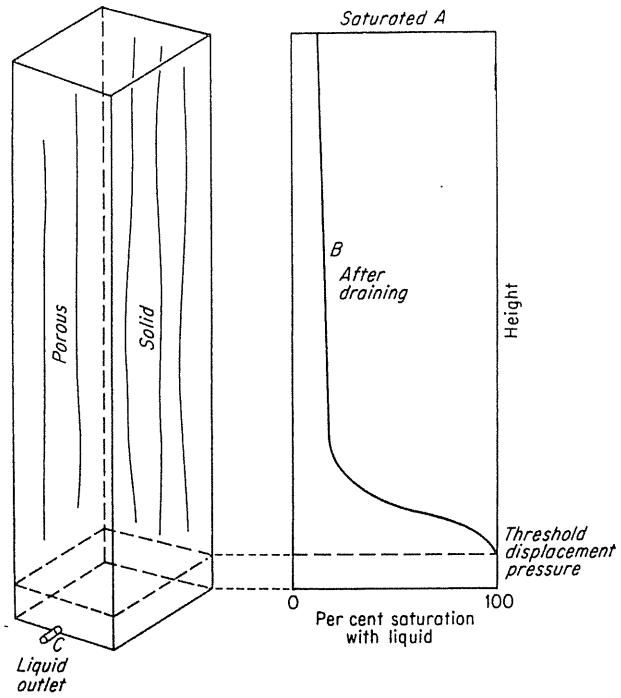

FIGURE 2-19
Saturation after draining liquid from a porous medium [Katz, et al., 1-1, courtesy McGraw-Hill Publishing Co.].

Drainage is illustrated by Fig. 2-19, in which a liquid-filled column of sandstone with sealed walls is subjected to drainage by removing plug C and allowing air to enter the top. Some of the water in the pores is retained as shown by liquid saturation curve B.

Wettability of Solids

A person driving a car in the rain is conscious of the wettability of the windshield by water and of the influence of oil or other substances on the spreading of a smooth film of water over the glass. Water placed on a hot metal surface will form spherical drops, which roll and bounce on the surface without covering or wetting it. Complete wetting or complete absence of wetting is relatively easy to describe; it is the intermediate values that require more refinement. The contact angle between two fluids in contact with a surface is an accepted measure of the degree of wettability as shown in Fig. 2-20. The interfacial tensions are in balance when

$$S_{g,s} = S_{l,s} + S_{g,l} \cos \theta \tag{2.11}$$

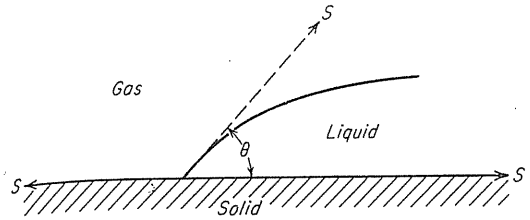

FIGURE 2-20
Contact angle between two fluids in contact with a solid as a measure of wetting [Katz, et al., 1-1, courtesy McGraw-Hill Publishing Co.].

where S is interfacial tension, θ is the contact angle, and subscripts g, s, and l represent gas, solid, and liquid. The contact angle expresses the degree of wetting, with a contact angle of 0° through the wetting fluid for a high degree of wetting and a contact angle of 180° through the wetting fluid for no wetting. Benner and Bartell [2-2] show that it is physically possible to observe various degrees of wetting with intermediate contact angles from 0° to 180°. Surfaces wet by water are called hydrophilic and those not wet, hydrophobic.

Surface Tension Measurement—Capillary Pressure

To understand liquid retention by porous solids, the interfacial tensions between liquids or between a liquid and a gas must be considered. The surface tension of a liquid in the presence of gas is measured by the capillary rise in fine-bored glass tubes (Fig. 2-21). When the liquid wets the surface of the glass capillary, it is drawn up the tube. The surface tension around the periphery of the tube is balanced by the downward force due to the column of liquid that has risen above the free surface. The equation expressing this balance is

$$\cos(\theta)\, \sigma(2\pi r) = \pi r^2 h(\rho_L - \rho_V)g \tag{2.12}$$

where r (cm) is the radius of tube, σ (dyne/cm) is the surface tension, h (cm) is the capillary rise, ρ_L (g/cm^3) is the density of liquid, ρ_V (g/cm^3) is the density of vapor, g is 980.6 cm/s^2, the acceleration due to gravity, and θ is the contact angle between liquid and solid; $\cos\theta = -1$ when $\theta = 180°$ for complete wetting.

It is possible to apply sufficient pressure above the liquid in the capillary to lower the meniscus to the level of the bulk liquid. This pressure is computed from Eq. (2.13):

$$2\pi r\sigma = \pi r^2 hg(\rho_L - \rho_V) = \pi r^2(P_2 - P_1)g_c \tag{2.13}$$

where P is the pressure (gram force/cm^2) and g_c is the conversion factor 980.6 (grams mass/gram force) (cm/s^2).

Solving for pressure difference,

$$P_c = P_2 - P_1 = \frac{2\sigma}{rg_c} \tag{2.14}$$

The pressure difference $P_2 - P_1$ is called the *capillary pressure* P_c. When the

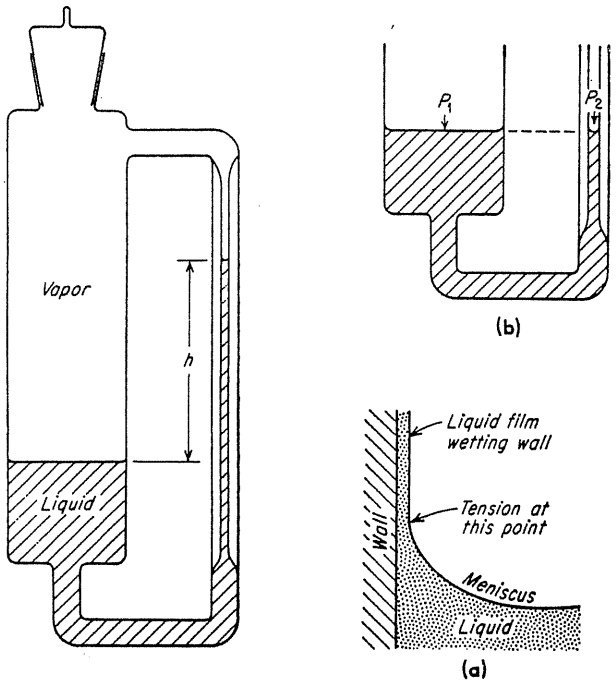

FIGURE 2-21
Surface tension by capillary rise [Katz, et al., 1-1, courtesy McGraw-Hill Publishing Co.].

contact angle of liquid is not 0°,

$$P_c = \frac{2\sigma \cos \theta}{rg_c} \tag{2.15}$$

A pressure difference of P_c must be applied across the meniscus to depress the capillary rise completely.

For a capillary or a space between particles that has a shape other than cylindrical, the capillary pressure is related to the curvature of the menisci by Eq. (2.16):

$$P_c = \frac{\sigma}{g_c}\left(\frac{1}{R_1} + \frac{1}{R_2}\right) \tag{2.16}$$

where R_1 and R_2 are principal radii of curvature of the menisci.

Liquid-Liquid Displacement: Wettability

Garrison looked at rock wettability in 1935 [2-22]. Generally it was taken for granted that water would wet sand rocks. Bartell and coworkers developed the

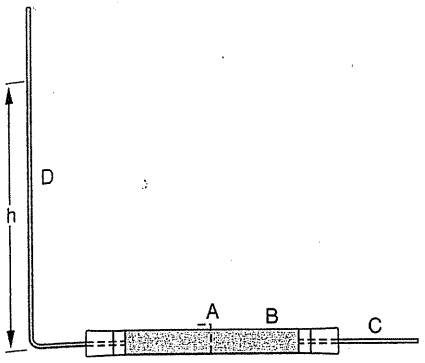

FIGURE 2-22
Bartell displacement cell [Benner & Bartell, 2-2, courtesy API Drill. Prod. Practice].

displacement cell of Fig. 2-22 [2-2]. Section A of the sand-filled tube was saturated with kerosene, and section B was saturated with water. The water wetting the sand pushed oil towards tube D, creating a back pressure of 12.7 in. (0.32 m) of oil. However, when Oklahoma Wilcox crude was used in the displacement tube, there was no buildup or rise in displacement pressure. An experiment showed that when outcrop sand was dropped into Wilcox crude oil and then washed to be free of crude by a solvent, water would no longer displace kerosene from the sand. Adsorption of asphaltic substances is believed to have changed the wettability of the sand in the laboratory test and in situ in the natural reservoir. The Oklahoma Wilcox sand was not water-wet, as shown by tests in 1940 [2-35]. Since that time much has been done on the subject [2-71].

2.8 CONNATE OR INTERSTITIAL WATER

Connate water is the natural water retained in a reservoir after gas or oil have entered the closure by water displacement [2-65]. The water in Fig. 2-19 is the "connate water" retained after drainage. Since the original water may have been displaced over time, some prefer the use of the term *interstitial water* to eliminate questions of whether it was present at the time of rock deposition.

Many studies have been done to determine the connate water content of cores by capillary pressure measurements [1-1]. Since the process of displacing the water is akin to that which occurred in the reservoir during gas accumulation, this is sometimes described as the restored-state method. A typical device for obtaining the effect of drainage of water from cores is the capillary pressure cell (Fig. 2-23). Core plugs saturated with water are placed in contact with a wet, fine, porous plate. Air or gas pressure is admitted over the cores, and water drains out of the plugs. At a given gas pressure, the water content is allowed to come to equilibrium and then measured by weighing; the plug is returned to the cell, and the gas pressure is increased. Gas pressure forces water out of the pores in the core down to the level of the porous plate, just as gas pressure reduced the capillary rise in Fig. 2-21*b*. The porous plate must have such fine pores that gas

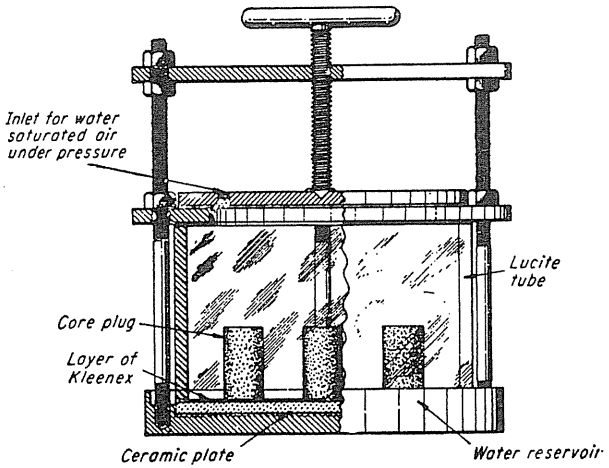

FIGURE 2-23
Apparatus for determining connate water by capillary pressure [Katz, et al., 1-1, courtesy McGraw-Hill Publishing Co.].

will not displace the liquid from it at the highest gas pressure used. Figure 2-24 shows typical miscellaneous curves of saturation versus air pressure.

Raising the air pressure on the cell or the capillary pressure on the core reduces the water content in much the same way as elevating of the core above the gas-water interface in the reservoir does. The asymptote of the rising pressure line in Fig. 2-24 is normally used as the connate water value; for thin zones the whole curve needs averaging.

Use of Centrifuge

An alternate drainage mechanism is to place the saturated core in a centrifuge. By spinning the core for a matter of minutes, the saturation corresponding to a sizable capillary pressure is obtained [2-66]. Figure 2-25 shows a single centrifuge point in relation to capillary pressure measurements [2-37]. Use of higher-speed centrifuges lowers the time of measurement.

Use of Mercury Injection for Capillary Pressure

Purcell [2-55] presented a method of measuring capillary pressure by mercury injection, using apparatus similar to that of Fig. 2-4. The relationship between mercury-air and water-air capillary pressures is given by Eq. (2.17):

$$\frac{\text{Mercury-air capillary pressure}}{\text{Water-air capillary pressure}} = \frac{-480 \cos 140^\circ}{70 \cos 0^\circ} \qquad (2.17)$$

Thus, the saturations can be compared when the mercury pressure is five times

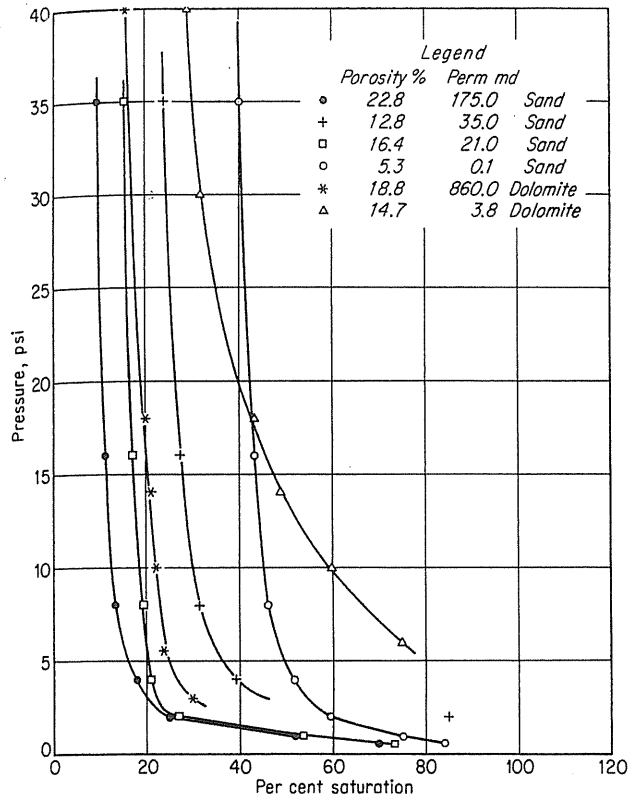

FIGURE 2-24
Miscellaneous capillary pressure–water saturation curves [Katz, et al., 1-1, courtesy McGraw-Hill Publishing Co.].

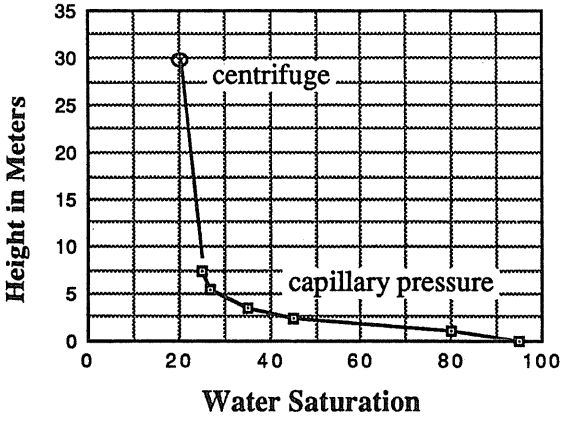

FIGURE 2-25
Interstitial water by capillary pressure and centrifuge on Michigan reef core [Katz and Lundy, 2-37, courtesy AAPG].

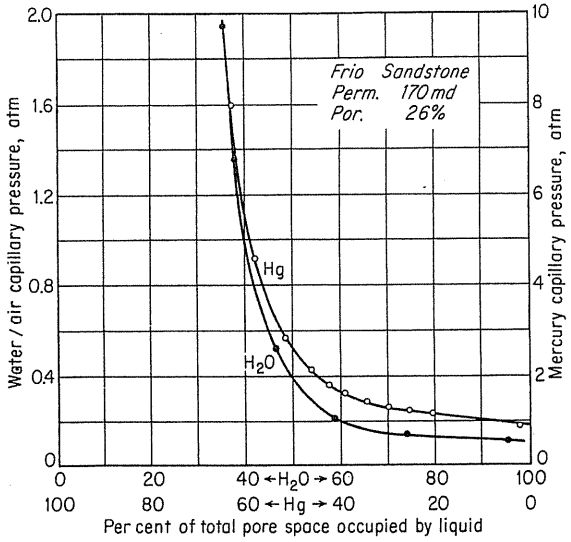

FIGURE 2-26
Comparison of capillary-pressure results with mercury and air-water [Purcell, 2-55, courtesy SPE-AIME].

the air pressure in the air-water measurement (Fig. 2-26). The method has the advantages of speed and the use of high pressures. Also, it can be used on chips or small pieces of core.

Purcell also developed a method for determining permeability from the mercury injection capillary pressure curve. Thomeer [2-69,2-70] introduced a pore geometrical factor from mercury capillary pressure data to characterize rocks and predict permeability.

2.9 WHAT IS CAPROCK?

Caprock prevents upward migration or movement of hydrocarbons in the earth. Most caprocks are shales or carbonates with moderate or low porosities and very low permeabilities. They are water saturated. A few caprocks are believed to be homogeneous solids without pores, including anhydrites and an occasional limestone [1-38].

Figure 2-27 shows water saturation versus hydrocarbon saturation in a caprock. The gas or oil is pressed into the caprock by buoyancy and/or hydraulic pressure, but with decreasing permeability and pore size, less hydrocarbon can be forced into the caprock, and the water saturation ultimately becomes 100 percent.

Natural Capillary Retention Pressure

In a hydraulic system where the water pressures in the layers above the caprock and the hydrocarbon bearing zone are on a hydraulic gradient, one may calculate the *natural capillary retention pressure* for a given reservoir when the height of

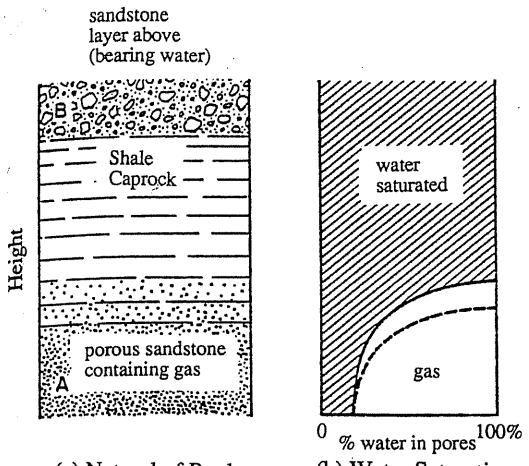

FIGURE 2-27
Nature of the gas water contact in the caprock [Katz, et al., 1-39, courtesy AGA].

the hydrocarbon column and fluid densities are known. Figure 2-28 illustrates the situation for a gas reservoir with a gas column pressure gradient of CB, a hydraulic gradient of AB, and a gas zone height of h.

The pressure drop from the gas phase at D in the base of the porous caprock to the water phase is following the BC line from the depth of point D to the depth

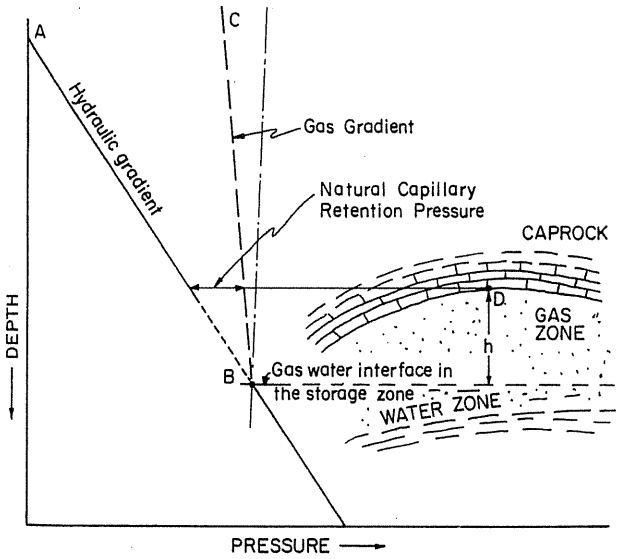

FIGURE 2-28
Illustration of natural capillary retention pressure [Ibrahim, Tek, and Katz, 1-38, courtesy AGA].

of point B. For water density ρ_w and gas density ρ_g, the retention pressure of the surface forces in the caprock is

$$P(\text{retention})\ (\text{psi}) = \frac{h\,(\text{ft}) \times (\rho_w - \rho_g)(\text{lb/ft}^3)}{144}$$

$$P(\text{retention})\ (\text{kPa}) = \frac{h\,(\text{m}) \times (\rho_w - \rho_g)(\text{kg/m}^3)}{1000} \times 9.8 \qquad (2.18)$$

For example, if h = 100 ft (30.48 m), ρ_w = 62.42 lb_m/ft^3 (1000 kg/m^3), and ρ_G = 6.3 lb_m/ft^3 (101 kg/m^3), the natural retention pressure is, in English units, 100 × (62 − 6.3)/144 = 38.9 psi, or in SI units, (1000−101) × 9.81/1000 = 268.8 kPa.

With the exception of the few caprocks of homogeneous solids, the oil and gas is retained in the earth by surface forces within the caprock. In the case of geopressured reservoirs, this natural capillary retention pressure may be as high as 2000 psi (13.79 MPa).

A qualitative representation of water saturation and capillary pressure is given in Fig. 2-29. The high-permeability zones represent the gas- or oil-bearing reservoirs, while the permeabilities of 10^{-6} md represent caprocks.

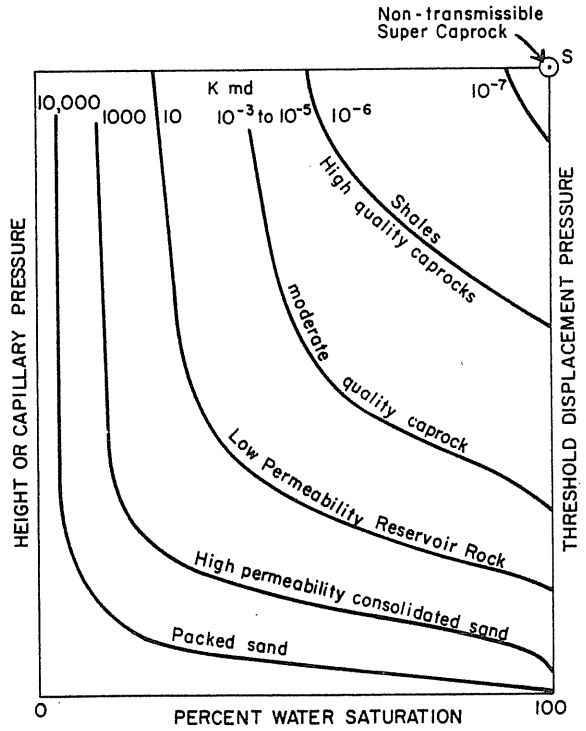

FIGURE 2-29
Variations in capillary pressure behavior for various rocks [Ibrahim, Tek, and Katz, 1-38, courtesy AGA].

Threshold Pressure—The Retention Mechanism for Oil and Gas

It had been known for many years that gas is not free to move in a porous medium saturated with liquid to the extent that throats of passages are liquid-filled. The *Jamin effect* [1-16] is that gas bubbles must reach a threshold pressure to pass through a liquid-saturated medium.

Then, in liquid drainage, 100-percent liquid saturation persists at a greater than zero capillary pressure (Fig. 2-30). The difference is the threshold pressure for gas to enter a liquid-saturated pore. Leverett [2-46], Rose, and Bruce [2-59] were among those measuring such threshold pressures.

In addressing the possible reasons for the leakage of gas from the first large aquifer storage reservoir at Herscher, Illinois [1-2], the threshold pressure test was developed for caprocks of lower permeability by the senior author and co-workers. Thomas carried out a study [2-67], and the AGA underground storage committee sponsored projects resulting in the monograph *Threshold Pressure in Gas Storage* [1-38]. A paper by Pandey et al. was presented on the pressure-leveling technique. Rudd and Pandey submitted data on a scanning technique for investigating the change in pore structure as an interface moves through a core [2-67].

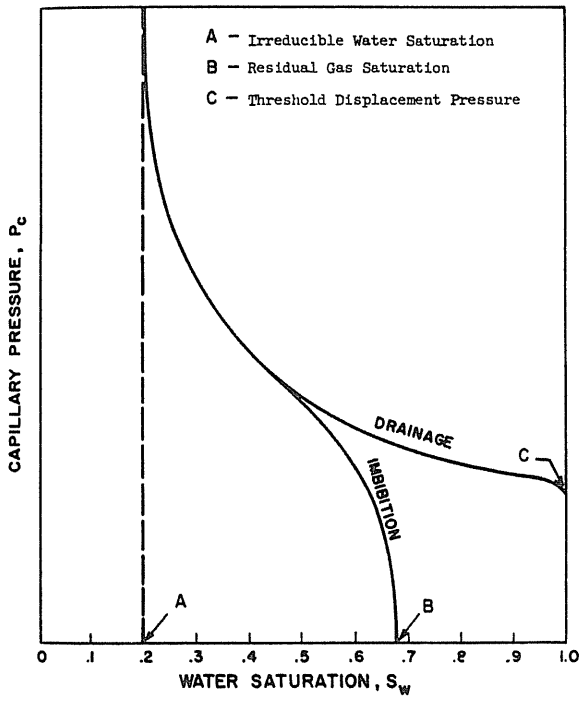

FIGURE 2-30
Imbibition and drainage capillary pressure curves [Leverett, 2-46, courtesy SPE-AIME].

Measurements of Threshold Pressure for Caprocks

In aquifer development, it is customary to core the potential caprock to measure its porosity, water permeability, and threshold pressure for air displacing water. In a core holder that applies overburden pressure on the core, air replaces the water at the entrance to the core following the permeability measurement. By increments, the air pressure is raised until water moves significantly in the capillary tube (Fig. 2-31). Figure 2-32 is a photograph of air breakthrough when the air penetrated the full core.

The data are correlated as threshold pressure versus core permeability (water) (Fig. 2-33) [1-38]. The scatter in the points represents rock heterogeneity.

Pandey et al. employed a new technique labeled the pressure-leveling technique [2-53]. Air was injected into the apparatus of Fig. 2-31 at what was likely to be above the threshold pressure. However, the supply of air was limited and hence its pressure dropped as the air-water interface entered the core, stopping

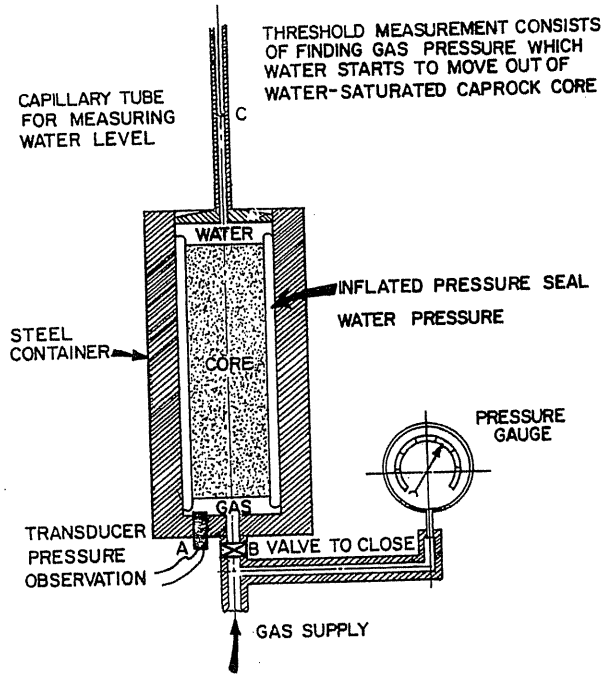

FIGURE 2-31
High pressure core holder for front end threshold displacement pressure tests [Pandey, et.al., 2-53, courtesy AGA].

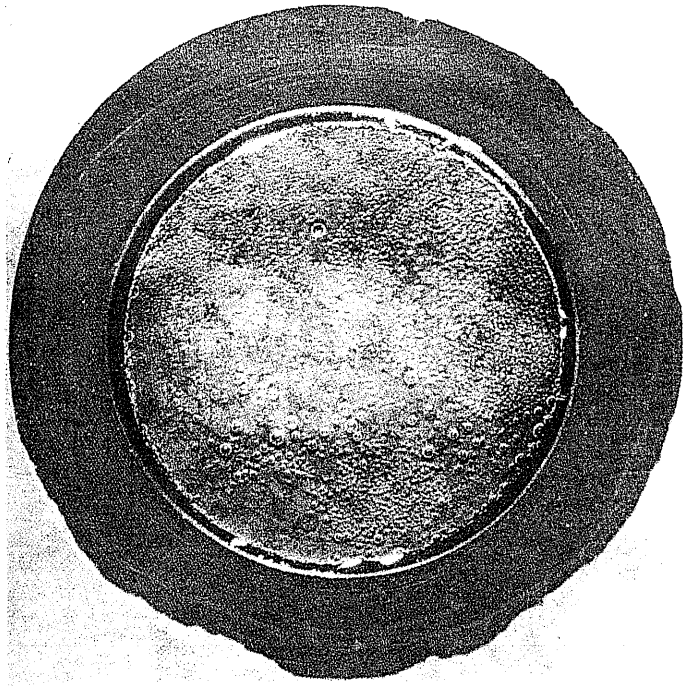

FIGURE 2-32
Photograph of air breaking through a core [Thomas, et. al., 2-67, courtesy SPE-AIME].

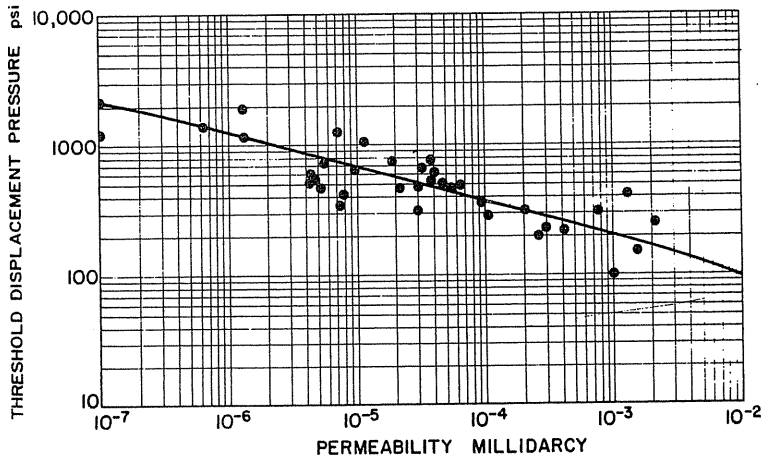

FIGURE 2-33
Threshold pressure versus permeability [Ibrahim, Tek & Katz, 1-38, courtesy AGA].

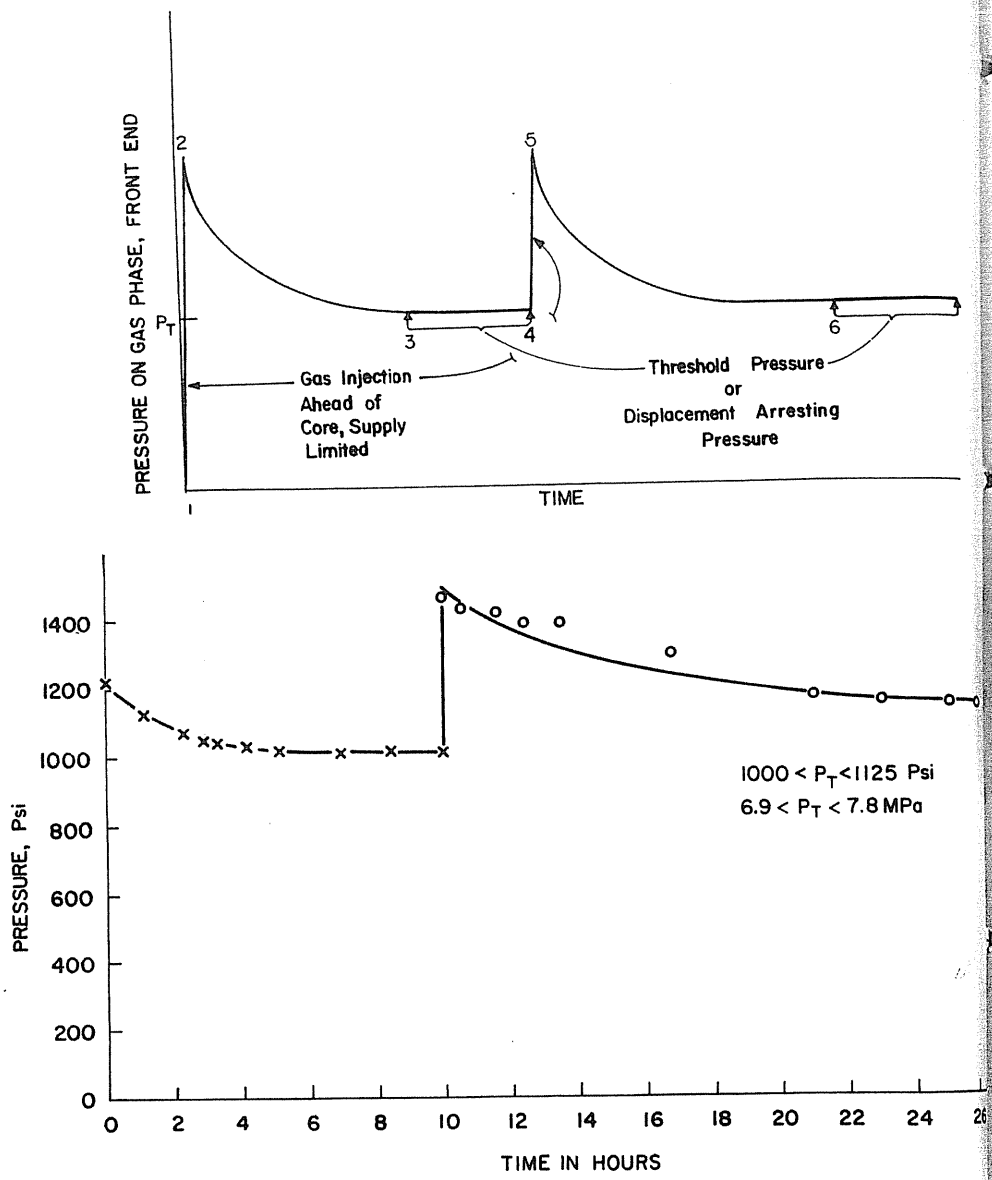

FIGURE 2-34
(*a*) Pressure leveling technique for threshold pressure; (*b*) Pressure versus time for pressure leveling technique [Pandey, et al., 2-53, courtesy AGA].

at the threshold pressure (Fig. 2-34*a*). A repeated injection would give data as shown in Fig. 2-34*b* [2-53].

A scan of the variation of pore throat sizes in a core can be made by slowly forcing air through a core and observing the variation in threshold air pressure, as graphed in Fig. 2-35 by Pandey and Rudd [2-60]. This profile shows the variability of pores within a short core length.

One may compute the maximum pore diameter at the nodes as in the following example:

Example 2.1. With $\sigma = 72.4$ dynes/cm, $P_c = 1000$ psi displacement pressure [the conversion factor to use is 1.45×10^{-5} psi/(dynes/cm^2)], and $\cos\theta = 1$ when water wets the core, what is the maximum pore radius?

Solution. Equation (2.15) relating pore radius, displacement pressure, and interfacial tensions can be rearranged as

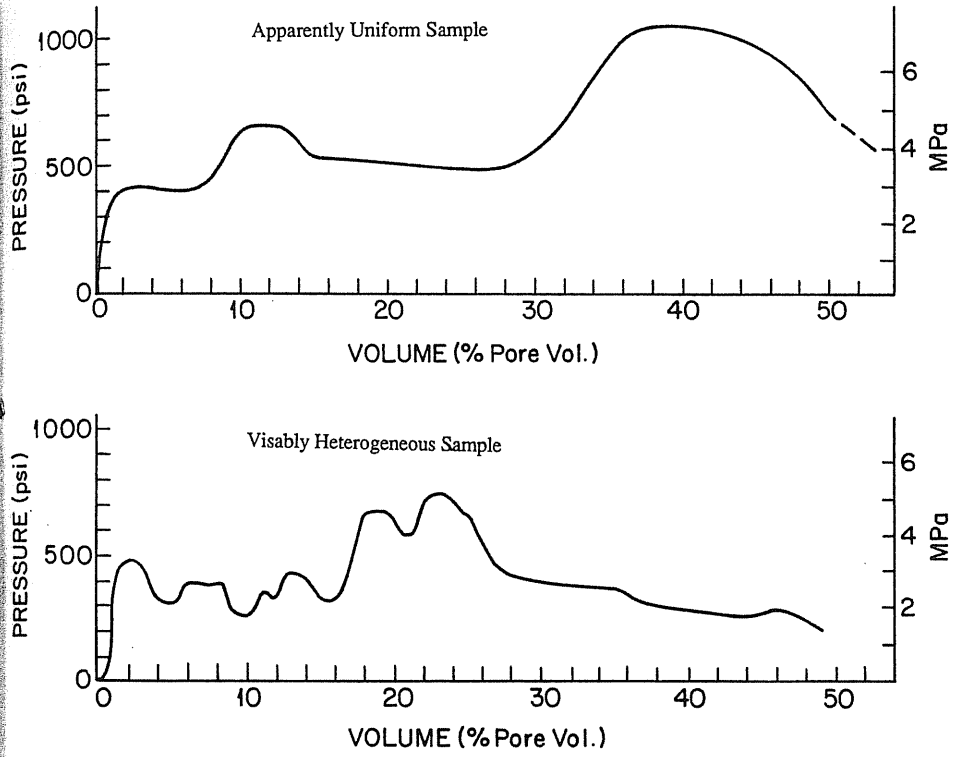

FIGURE 2-35
Profiling threshold pressures of caprocks [Rudd & Pandey, 2-60, courtesy SPE-AIME].

$$r = \frac{2\sigma \cos \theta}{g_c P_c} \tag{2.19}$$

Thus,

$$r = 2 \times 72.4 \times \left(\frac{1.45 \times 10^{-5}}{1000} \right) = 2.10 \times 10^{-6} \text{ cm } (2.10 \times 10^{-8} \text{ m}).$$

2.10 RELATIVE PERMEABILITY

When two or more phases are passing through a rock, each may be measured and the permeability calculated for the rate and pressure drop. By dividing the permeability so obtained by the single-phase permeability, a relative (or fractional) permeability is obtained. Figure 2-36 is the classical curve of Botset [2-3] plotting the relative permeability against the percent liquid saturation.

Measurements are made on cores by injecting the two fluids under consideration at a steady rate until each flows out at the input rate. From Fig. 2-36, it can be seen that a water-saturated core needs to have some 10 percent gas saturation before any gas flows through the sand. Likewise, a gas-filled core will not pass the liquid until some 10 percent or more of the sand has been filled with liquid.

The relative permeability drops precipitously for one phase as the saturation of the other phase increases at intermediate saturations. In gas flow through sands, water invasion beyond the interstitial water content lowers the gas permeability significantly.

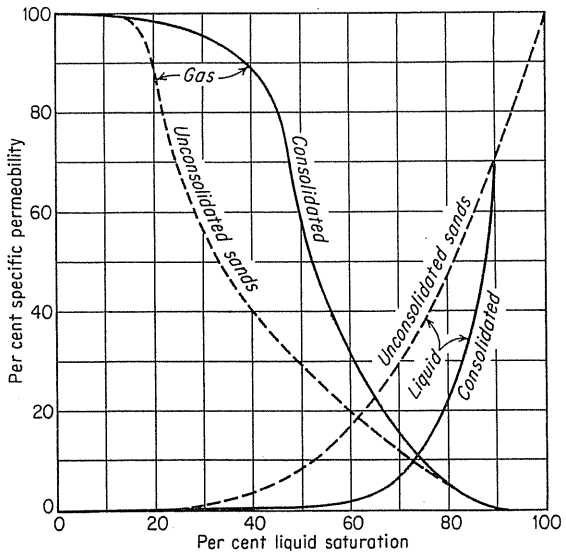

FIGURE 2-36
Relative permeability for consolidated and unconsolidated sands [Botset, 2-3, courtesy SPE-AIME].

This subject becomes very important for oil recovery where one fluid is used to displace another (water displacing oil). A wealth of data is available in the SPE literature; relative permeabilities of oil, water, and gas control oil recovery processes.

In gas production and storage, water present in the producing zones near wellbores reduces the permeability of the rock to gas as water saturation increases. In water drive interfaces, water influx encounters a reduced relative permeability as water enters a zone of high gas saturation.

2.11 RESIDUAL OR TRAPPED GAS AFTER WATER DISPLACEMENT

In water drive reservoirs or aquifer storage, water passes through rock containing gas and interstitial water. A certain fraction of the gas is retained or trapped as residual gas after only water flows through the rock.

Geffen et al. [2-23] presented data showing the amount of residual or trapped gas behind a moving water influx. Gorring et al. [2-36] presented a chart of residual saturation of nonwetting phase related to porosity from published and in-house experiments. To this plot, data by Chierici [2-10] have been added to give a scatter of points within the rectangle of Fig. 2-37. The scatter of the data no doubt reflects the heterogeneity of the rock and differences in ability to retain gas. Keelan and Pugh measured trapped gas in carbonate formations [2-39]. Their data, placed in groupings, are in Fig. 2-38, with the line from Fig. 2-37 imposed. Good relative permeability data down to zero gas flow with continued water flow are needed for specific rocks, accepting Figs. 2-37 and 2-38 (data on typical oil field cores) as general guides. In Gorring's studies, he noted a capillary jump as water advanced by imbibition into a gas-bearing zone. Figure 2-39 illustrates how gas may be entrapped in such an advancing water front.

Firoozabadi et al. [2-20] presented the concept of "mobilized gas saturation" with data on loosely consolidated reservoir sands reporting 30 percent trapped gas for porosities of 30–50 percent. When water was drained from the specimen, the gas saturation increased to 46–50 percent. In aquifer gas storage, early gas withdrawals are accompanied by water influx into the gas zone, entrapping gas within the water-flooded rock. However, continuing development by injection of gas eventually reduces the water content to connate water and eliminates entrapment.

Countercurrent Drainage of Water into a Gas Zone

Briggs [2-4] studied the rate of water drainage into a gas zone. Liquids and air were placed in a glass bead–packed tube to give an average saturation of 50 to 80 percent. After establishing the equilibrium saturation in one vertical

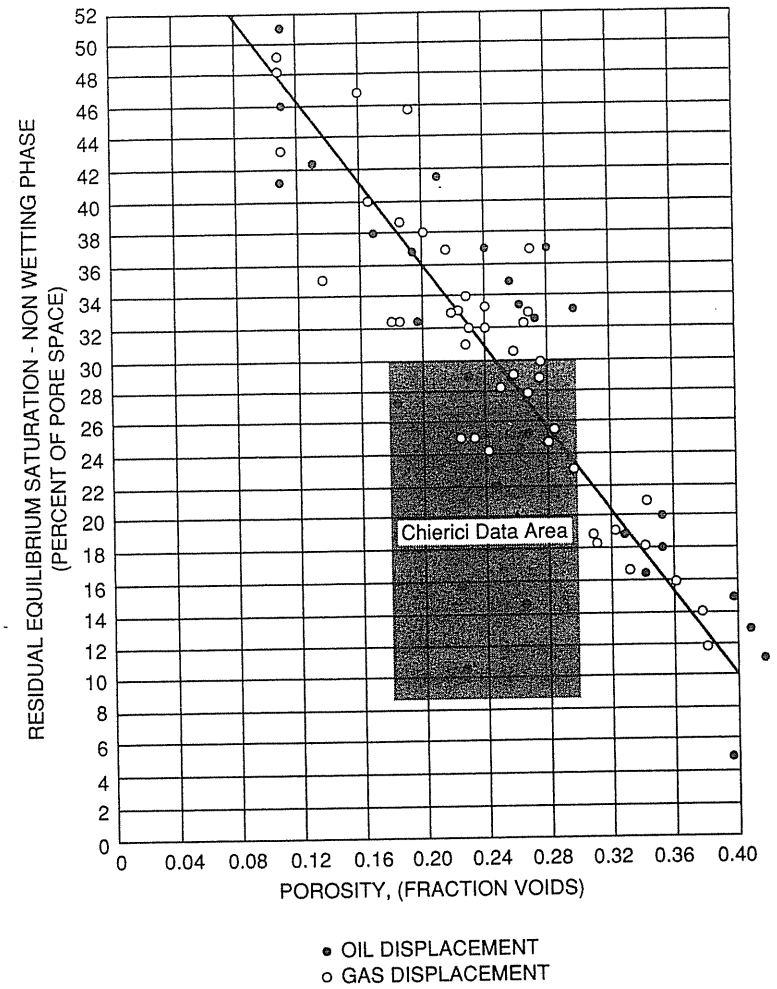

FIGURE 2-37
Trapped gas behind water invaded gas or oil zone in sandstone [Gorring, 2-36, courtesy Oil & Gas J.].

position, the tube was upended and the saturation distribution determined by measuring radioactivity of I^{131} tracer in the liquid. Figure 2-40 [2-4] gives the results of experimental runs. The various curves on Fig. 2-41 [2-36] show that the residue gas left behind the moving water front remains constant and equal to that obtained during the measurement of the capillary pressure by the imbibition process in Fig. 2-30. Figure 2-41 also shows the water-air distribution at two rates of flooding.

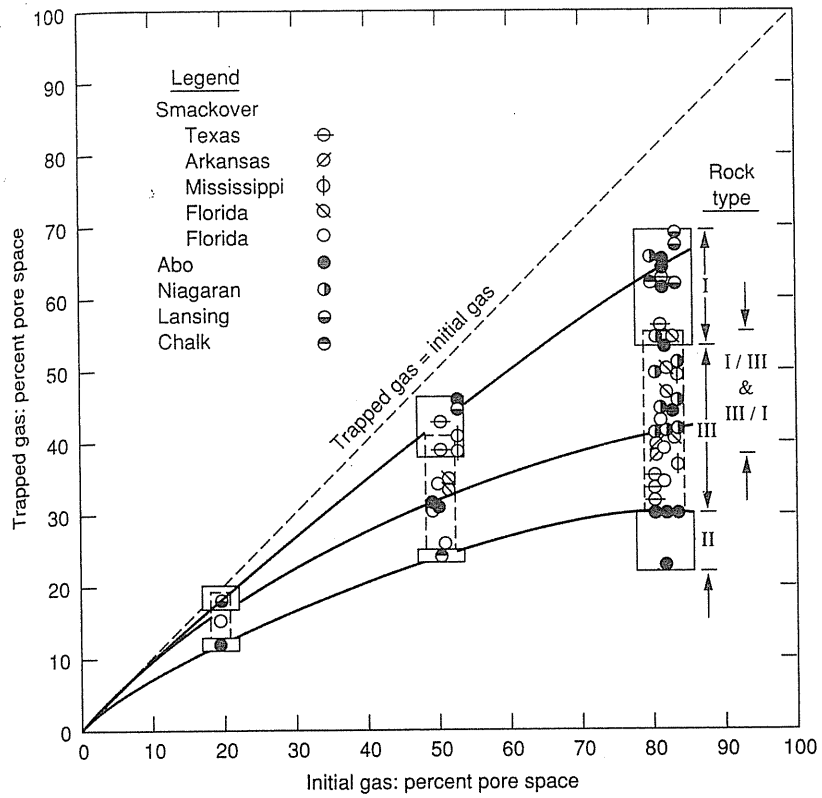

FIGURE 2-38
(*a*) Trapped gas correlation with porosity and rock type (carbonates) [Keelan & Pugh, 2-39].

2.12 DIFFUSION OF GASES THROUGH ROCKS

Gases diffuse by molecular motion at rates inversely proportional to pressure as discussed in Chapter 1. Collisions of one molecule with another stop or divert a moving molecule. When a gas is present within the interstices of a rock, its diffusion is slowed by the striking of the walls of the solid as well as other molecules. The reduction of the diffusion rate within solids is a property of the rock and so is appropriately treated here.

Chen [2-11] studied the diffusion of the methane-nitrogen system in porous solids, mostly cores. She made the measurements in dry rocks and in rocks saturated with water. The ratio of the diffusion coefficient in the rock to diffusion in open space was correlated against the dry permeability-porosity product as

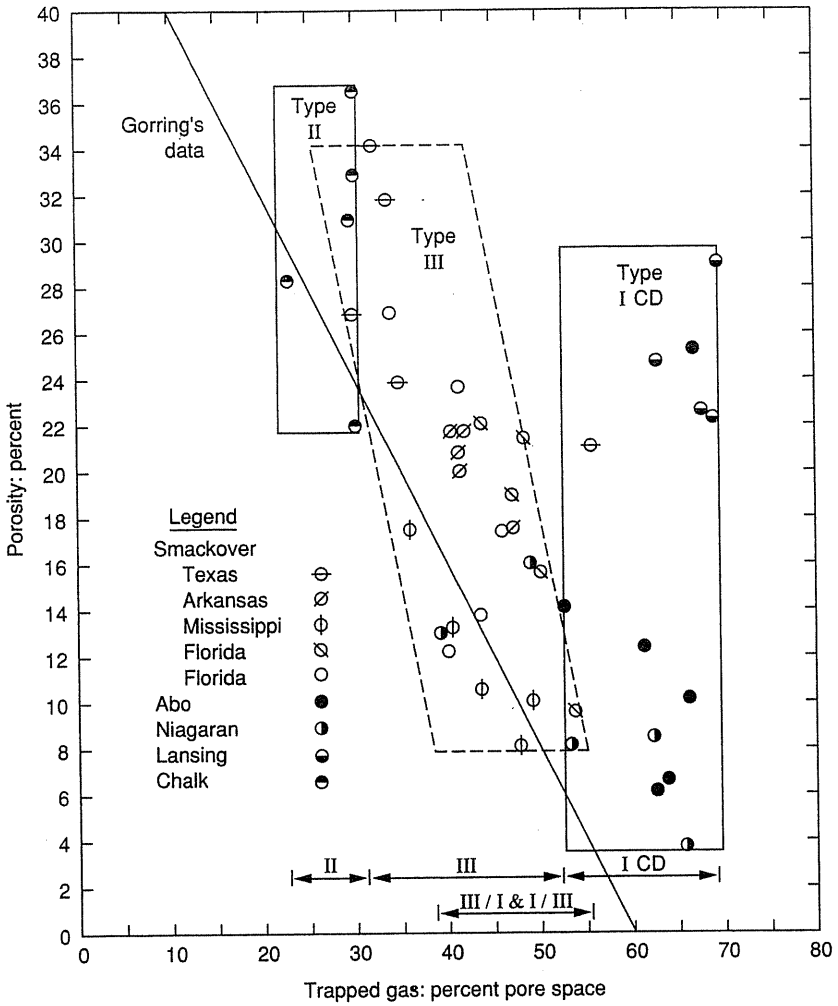

FIGURE 2-38
(*b*) Comparing the correlation (sandstone) [Gorring, et al., 2-36 After Data of Keelan & Pugh, 2-39].

shown in Fig. 2-42. Pandey did similar work [2-52] with helium-nitrogen, and his results were correlated with Chen's. The data on diffusion through water-saturated rocks showed a slowing of the rate as the gases diffused through a water phase. Figure 2-43 gives the scattered data plotted as diffusion coefficients. Figure 2-44 shows data on gas diffusion into a 100-foot layer of one acre of water-saturated sand [2-34].

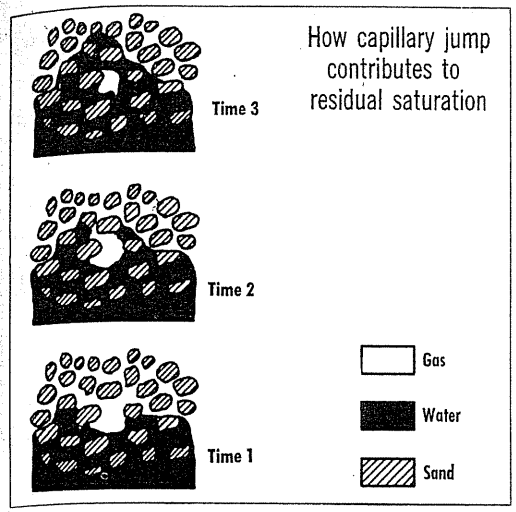

FIGURE 2-39
How capillary jump contributes to residual gas saturation [Katz, et.al., 2-36, courtesy Oil & Gas J.].

2.13 DISPERSION OF GASES DURING FLOW THROUGH ROCKS

Dispersion refers to mixing of fluids as one fluid displaces another. If one fluid follows another in flow through a given rock at a known flow rate and at specified conditions, what will be the composition of the interface gases with flow time or distance? Legatski [2-45] studied this effect, measuring the changing composition of gas interfaces as they leave a core. The correlation followed Eq. (2.20):

$$\frac{D_l}{D_o} = \frac{1}{F\phi} + 0.5\left(\frac{ud_p\sigma}{D_o}\right)^m \tag{2.20}$$

where u is the interstitial velocity, d_p is the particle diameter, and σ is the packing or inhomogeneity factor. It relates the effective longitudinal dispersion coefficient D_l to the molecular diffusion coefficient D_o, the electrical resistivity factor F, the porosity ϕ, and a Peclet number $(ud_p\sigma/D_o)$.

The exponent m varied between 1.0 and 1.5. The "characteristic length," $d_p\phi$ was found to vary between 0.25 cm (0.1 in.) and 1.9 cm (0.75 in.), with an average value of 0.4 cm (0.16 in.). Table 2.3 gives the results of the study.

It should be noted that, in reservoir scale, the $1/F\phi$ in Eq. (2.20) is small. Thus, the dispersion coefficient, D_l, is essentially a function of the characteristic length $d_p\sigma$ and velocity u, and is not related to the molecular diffusion coefficient, D_o. Scheidegger [2-64] showed that for an isotropic medium, the longitudinal and transverse dispersion coeffients (D_L and D_T, respectively) are related to the

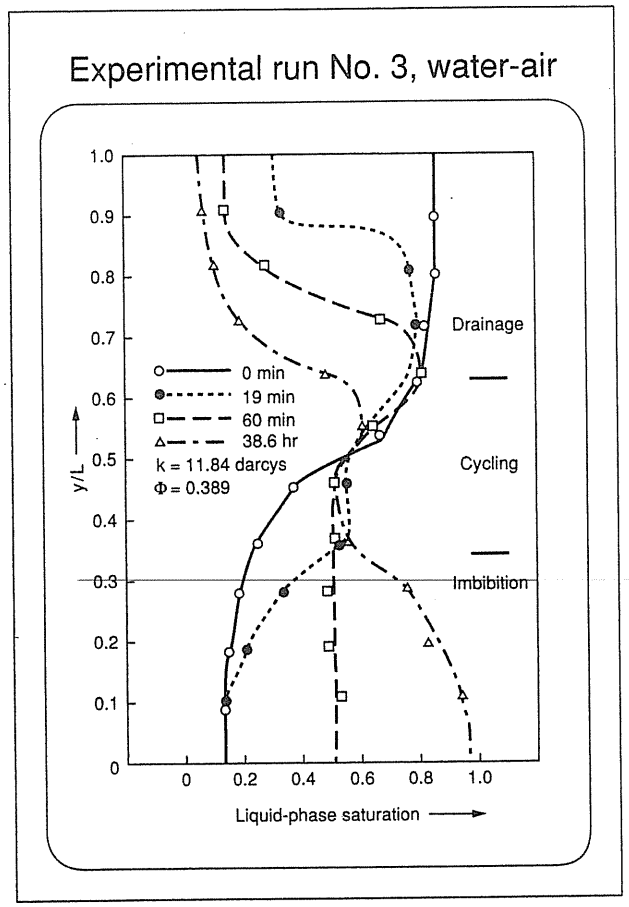

FIGURE 2-40
Experimental run showing the reverse of water saturation [Briggs & Katz, 2-4, courtesy Oil & Gas J.].

dispersivities by

$$D_L = \alpha_L|\bar{u}| \qquad \text{and} \qquad D_T = \alpha_T|\bar{u}| \tag{2.21}$$

where α is the dispersivity coefficient with the dimension of a length. Some discussions of the tensorial forms of the dispersion coefficient for two-dimensional flow in an isotropic field can be found in reference [2-44]. The practical consideration in gas mixing will be discussed in Section 17-6.

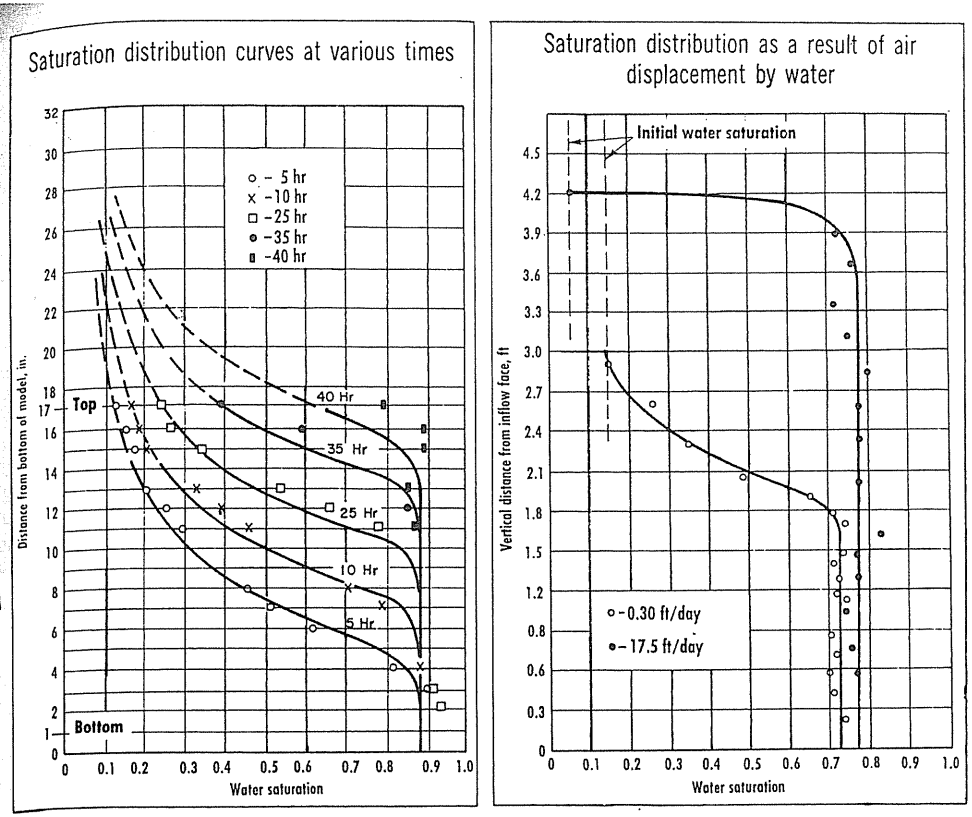

FIGURE 2-41
Saturation distributions of air-water with time after change of vertical positions in column [Katz, et al., 2-36, courtesy Oil & Gas J.].

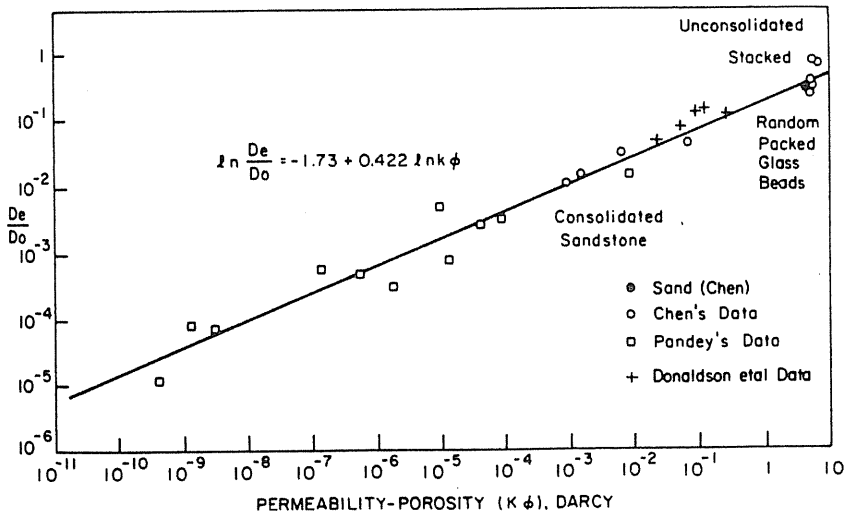

FIGURE 2-42
Diffusion factor versus permeability porosity product for dry porous solids [Chen, Katz, and Tek, 2-11, courtesy AIChE].

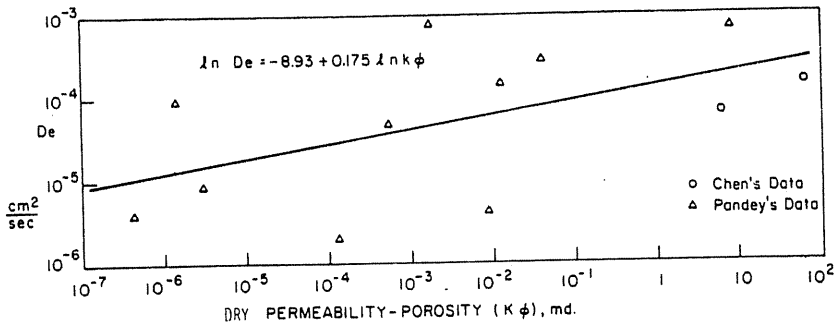

FIGURE 2-43
Effective diffusion coefficient versus dry permeability and porosity product for water saturated porous solids [Chen, Katz, and Tek, 2-11, courtesy AIChE].

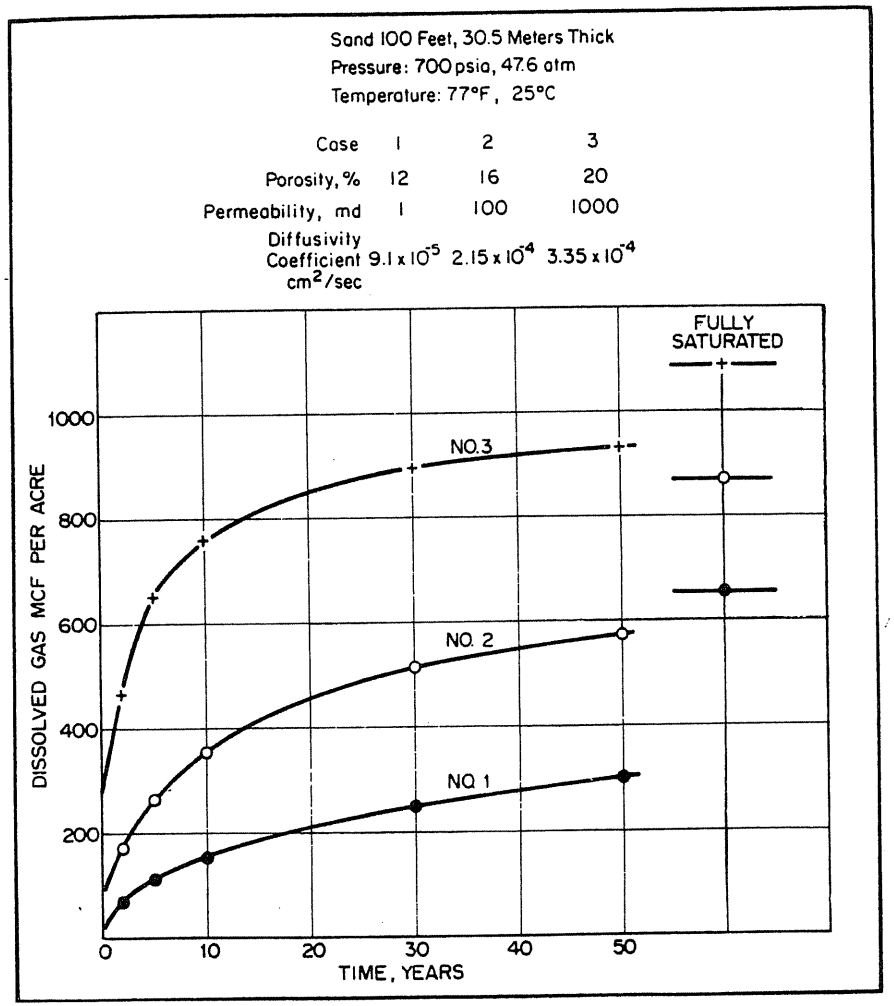

FIGURE 2-44
Gas diffusion into 100 foot layer of one acre of water saturated sand [Katz, 2-34, courtesy AGA].

TABLE 2.3
Properties of rock used in dispersion studies [Legatski & Katz, 2-45, courtesy SPE-AIME]

Core label	Porosity, %	Permeability, md	High-velocity factor β, ft^{-1}	Res. factor F	$d_p\sigma$, cm	Exponent m, Eq. (2-20)
1	23.4	40.0	1.25×10^9	13.3	0.475	1.13
2	21.8	41.6	6.40×10^8	14.2	0.750	1.20
3	31.0	1030	4.60×10^6	13.9	0.670	1.27
4	32.0	258	1.40×10^7	9.5	0.346	—
5	32.0	1430	1.72×10^8	8.3	0.250	—
6	21.8	1008	not determined	13.6	0.410	1.36
7	25.2	227	not determined	13.3	0.366	1.20
8	19.0	300	not determined	15.2	0.316	1.24
9	12.5	61.4	5.20×10^8	27.6	1.870	1.28
10	12.1	4.45	4.45×10^{10}	41.6	1.440	1.40

HOME PROBLEMS

2.1. A core has a permeability k of 63 md and porosity ϕ of 0.217. What is the high-velocity coefficient β for the core?

2.2. If the permeability k of Problem 2.1 were run with air at 1.5 atm mean pressure and 1 atm downstream, what is the corrected k, accounting for the Knudsen diffusion?

2.3. Data were taken on a 175-md core as shown in Fig. 2-24. There is 50 feet of gas sand of the type represented by the core. What is the average connate water saturation?

RECOMMENDED READINGS

Books

1-1. Katz, D. L., D. Cornell, R. Kobayashi, F. H. Poettmann, J. A. Vary, J. R. Elenbaas, and C. F. Weinaug, *Handbook of Natural Gas Engineering,* McGraw-Hill Publishing Company, New York (1959).

1-2. Katz, D. L., and K. H. Coats, *Underground Storage of Fluids,* Ulrich's Book Store, Ann Arbor, Michigan (1968).

Willhite, G. P., *Waterflooding*, Society of Petroleum Engineers, Textbook Series, Richardson, Texas (1986).

REFERENCES

2-1. Al-Hussainy R., and H. J. Ramey, Jr., "Application of Real Gas Flow Theory to Well Testing and Deliverability Forecasting," *J. Pet. Tech.*, Vol. 18, No. 5, 637–642, May (1966).

2-2. Benner, F. C. and F. E. Bartell, "The Effect of Polar Impurities upon Capillary and Surface Phenomena in Petroleum Production," *API Drill. Prod. Prac.*, p. 341 (1941).

2-3. Botset, H. G., "Flow of Gas Liquid Mixtures through Consolidated Sand," *Trans. AIME, Vol. 136*, 91 (1940).

2-4. Briggs, J. E. and D. L. Katz, "Drainage of Water from Sand in Developing Aquifer Storage," *Oil & Gas J., Vol. 66 No. 49*, 61–64 (1968).

2-5. Buckley, S. E. and M. C. Leverett, "Mechanism of Fluid Displacement in Sands," *Trans. AIME, Vol. 146*, 107 (1942).

2-6. Calhoun, J. C., Jr. and S. T. Yuster, "A Study of the Flow of Homogeneous Fluids through Ideal Porous Media," *API Drill. Prod. Prac.*, p. 335 (1946).
2-7. Cannon, J. R. and A. H. Dogru, "Estimation of Permeability and Porosity from Well Test Data," *J. Pet. Tech.*, Vol. 32, No. 8, 1323–1324, Aug. (1980).
2-8. Chalmers, J., D. B. Tailiaferro, and E. L. Rawlins, "Flow of Air and Gas through Porous Media," *Trans. AIME*, pp. 375–400 (1932).
2-9. Chavent, G., G. Cohen, and M. Espy, "Determination of Relative Permeabilities and Capillary Pressures by an Automatic Adjustment Method," *SPE Reprint 9237* (1980).
2-10. Cheierici, G. L., G. Cincci, and G. Long, "Experimental Research on Gas Saturation behind the Water Front in Gas Reservoirs Subjected to Water Drive," *World Petroleum Cong. (Tokyo), Sect. II, Paper 17, PD-6* (1976).
2-11. Chen, L., D. L. Katz, and M. R. Tek, "Binary Gas Diffusion of Methane-Nitrogen through Porous Solids," *AIChE J., Vol. 23*, 336 (1977).
2-12. Coats, K. H. and B. D. Smith, "Dead End Pore Volume and Dispersion in Porous Media," *Trans. AIME*, Vol. 231, 73–84 (1964).
2-13. Cornell, D. and D. L. Katz, "Flow of Gases through Consolidated Porous Media," *Ind. Eng. Chem., Vol. 43*, 2145 (1953).
2-14. Dranchuk, P. M. and L. J. Kolada, "Interpretation of Steady Linear Visco-Inertial Gas Flow Data," *J. Can. Pet. Tech.* Vol. 36, Jan.–March (1968).
2-15. Estes, R. K. and P. F. Fulton, "Gas Slippage and Permeability Measurements," *Trans. AIME, Vol. 207*, 338 (1956).
2-16. Ezeudembah, A. S. and P. M. Dranchuk, "Flow Mechanism of Forchheimer's Cubic Equation in High Velocity Radial Gas Flow through Porous Media," *SPE Preprint 10979* (1982).
2-17. Fancher, G. H., J. A. Lewis, and K. Barnes, "Some Physical Characteristics of Oil Sands," *Ind. Eng. Chem., Vol. 25*, 1139 (1933).
2-18. Fatt, I. and D. H. Davis, "Reduction in Permeability with Overburden Pressure," *Trans. AIME, Vol. 195*, 329 (1952).
2-19. Firoozabadi, A. and D. L. Katz, "An Analysis of High Velocity Flow through Porous Media," *J. Pet. Tech.*, Vol. 31, No. 2, 211–216, Feb. (1979).
2-20. Firoozabadi, A., G. Olsen, and T. van Golf-Racht, "Residual Gas Saturation in Water-Drive Gas Reservoirs," *SPE Preprint 16355* (1987).
2-21. Freeman, D. L. and D. C. Bush, "Low Permeability Laboratory Measurements by Non–steady State and Conventional Methods," *SPE Preprint 10075* (1981).
2-22. Garrison, A. D., "Selective Wetting of Reservoir Rock and Its Relation to Oil Production," *API Drill. Prod. Practice*, p. 130 (1935).
2-23. Geffen, T. M., D. R. Parrish, G. W. Haynes, and R. A. Morse, "Efficiency of Gas Displacement from Porous Media by Liquid Flooding," *Trans. AIME, Vol. 195*, 29 (1952).
2-24. Gewers, C. W. W. and L. R. Nichol, "Gas Turbulence Factor in a Microvugular Carbonate," *J. Can. Pet. Tech.*, Vol. 51, April–June (1969).
2-25. Gray, D. H. and R. W. Rex, "Formation Damage in Sandstone Caused by Clay Dispersion and Migration," *Proc. 14th Conf. on Clay and Clay Minerals*, Pergamon Press, London (1966).
2-26. Green, L. and P. Duwez, "Fluid Flow through Porous Metals," *J. App. Mech., Vol 18*, 39 (1953).
2-27. Gruesbeck, C. and R. E. Collins, "Entrainment and Deposition of Fine Particles in Porous Media," *Soc. Pet. Eng. J.*, Vol. 22, No. 6, 847–856, Dec. (1982).
2-28. Hall, H. N., "Compressibility of Reservoir Rock," *Trans. AIME, Vol. 198*, 309 (1953).
2-29. Hensel, W. H., "Summation of Fluids Porosity Technique," *SPE Reprint 9376* (1980).
2-30. Johnson, T. W. and D. B. Taliaferro, "Flow of Air and Natural Gas through Porous Media," Technical Paper 592, Bureau of Mines (1938).
2-31. Johnston, N. and C. M. Beeson, "Water Permeability of Reservoir Sands," *Trans. AIME, Vol. 160*, 43 (1945).
2-32. Jones, S. C., "A Rapid Accurate Unsteady State Klinkenberg Permeameter," *Soc. Pet. Eng. J.*, Vol. 12, No. 5, 383–397 (1972).

2-33. Kadi, K. S., "Non-Darcy Flow in Dissolved Gas-Drive Reservoirs," *SPE Reprint 9301* (1980).
2-34. Katz, D. L., "Containment of Gas in Storage Fields," *AGA Trans. Conference*, T436–T441 (1978).
2-35. Katz, D. L., "Possibility of Secondary Recovery for Oklahoma City Wilcox Sand," *Trans. AIME, Vol. 146*, 28 (1942).
2-36. Katz, D. L., M. W. Legatski, M. R. Tek, L. Gorring, and R. L. Nielson, "How Water Displaces Gas from Porous Media," *Oil & Gas J., Vol. 64*, 55 (1966).
2-37. Katz, D. L. and C. L. Lundy, "Absence of Connate Water in Michigan Reef Gas Reservoirs—An Analysis," *Bull. AAPG, Vol. 66*, 91–98 (1982).
2-38. Keelan, D., "Core Analysis for Aid in Reservoir Description," *J. Pet. Tech.*, 2483–2491, November (1982).
2-39. Keelan, D. K., V. J. Pugh, "Trapped Gas Saturations in Carbonate Formations," *Soc. Pet. Eng. J.*, Vol. 15, No. 2, 149–160, April (1975).
2-40. Keighin, C. W. and K. Sampath, "Evaluation of Pore Geometry of Some Low-Permeability Sandstones," *SPE Reprint 9251* (1980).
2-41. Kelton, F. C., "Analysis of Fractured Limestone Cores," *Trans. AIME, Vol. 189*, 225 (1950).
2-42. Khiler, K. C. and H. S. Fogler, *SPE Preprint 10103* (1983).
2-43. Klinkenberg, L. J., "The Permeability of Porous Media to Liquids and Gases," *API Drill and Prod. Prac.*, p. 200 (1941).
2-44. Konikow, L. F., and J. D. Bredehoeft, "Computer Model of Two-dimensional Solute Transport and Dispersion in Ground Water," USGS Techniques of Water Resource Investigations, Chapter C2, Book 7 (1978).
2-45. Legatski, M. L. and D. L. Katz, "Dispersion Coefficients for Gases Flowing in Consolidated Porous Media," *Soc. Pet. Eng. J.*, Vol. 7, No. 1, 43–53, Feb. (1967).
2-46. Leverett, M. C., "Capillary Behavior in Porous Solids," *Trans. AIME, Vol. 142*, 152–169 (1942).
2-47. Leverett, M. C., W. B. Lewis, and M. E. True, "Dimensional Model Studies of Oil Field Behavior," *Trans. AIME, Vol. 146*, 175 (1942).
2-48. McMahon, J. J., *An Investigation of Air Permeabilities of Porous Media*, M.S. Thesis, Penn. State University (1949).
2-49. Moran, J. H. and C. M. Papaconstantinou, "A Novel Dynamic Measurement of Permeability," *Trans. AIME, Vol. 271*, 670 (1981).
2-50. Morita, N. and K. E. Gray, "Three Dimensional Permeability Measurements," *SPE Reprint 9377* (1980).
2-51. Narr, W. and J. B. Currie, "Origin of Fracture Porosity Example from Altamont Field, Utah," *Bull. AAPG. Vol. 66*, No. 9 1231–1247 (1982).
2-52. Pandey, G. N., M. R. Tek, and D. L. Katz, "Diffusion of Fluids through Porous Media with Implications in Petroleum Geology," *Bull. AAPG, Vol. 58 No. 2*, 291–303 (1974).
2-53. Pandey, G. N., M. R. Tek, and D. L. Katz, "Studies of Front-End Threshold Pressure Measurements," *Operating Section Proceedings, AGA*, T112–T116 (1973).
2-54. Pollard, T. A. and P. P. Reichertz, "Core Analysis Practices," *Bull. AAPG*, Vol. 36, 230 (1952).
2-55. Purcell, W. R., "Capillary Pressures: Their Measurement Using Mercury and the Calculation of Permeability Therefrom," *Trans. AIME, Vol. 186*, 39 (1949).
2-56. Raimondi, P. and M. A. Torcass, "Distribution of Oil Phase Obtained upon Imbibition of Water," *Trans. AIME, Vol. 231*, 49–55 (1964).
2-57. Ramey, H. J., "Rapid Method for Estimating Reservoir Compressibilities," *J. Pet. Tech.*, Vol. 16, No. 4, 447–454, April (1964).
2-58. Reed, M. G., "Stabilization of Formation Clays with Hydroxy-Aluminum Solutions," *J. Pet. Tech.*, Vol. 24, No. 7, 860–864, July (1972).
2-59. Rose, W. and W. A. Bruce, "Evaluation of Capillary Character in Petroleum Reservoir Rock," *Trans. AIME, Vol. 186*, 127 (1949).
2-60. Rudd, N. and S. N. Pandey, "Threshold Pressure Profiling by Continuous Injection," *SPE Preprint 4597* (1973).

2-61. Salter, S. J. and K. K. Mohanty, "Multiphase Flow in Porous Media. I. Macroscopic Observations," *SPE Preprint 11017* (1982).
2-62. Salter, S. J. and K. K. Mohanty, "Multiphase Flow in Porous Media. II. Pore-Level Modeling," *SPE Preprint 11018* (1982).
2-63. Sampath, K. and C. W. Keighin, "Factors Affecting Gas Slippage in Tight Sandstones of Cretaceous Age in Uinta Basin," *J. Pet. Tech.*, Vol. 34, No. 11, 2715–2720, Nov. (1982).
2-64. Scheidegger, A. E., "General Theory of Dispersion in Porous Media," *J. of Geophysical Res.*, Vol. 66, No. 10, 3273–3278 (1961).
2-65. Schilthuis, R. J., "Connate Water in Oil and Gas Sands," *Trans. AIME, Vol. 127*, 199 (1938).
2-66. Slobod, R. L., A. Chambers, and S. L. Prehn, "Use of Centrifuge for Determining Connate Water, Residual Oil, and Capillary Pressure Curves of Small Core Samples," *Trans. AIME, Vol. 192*, 1927 (1951).
2-67. Thomas, L. K., D. L. Katz, and M. R. Tek, "Threshold Pressure Phenomena in Porous Media," *Soc. Pet. Eng. J.*, Vol. 8, No. 2, 174–184 (1968).
2-68. Thomas, R. D. and D. C. Ward, "Effect of Overburden Pressure and Water Saturation on Gas Permeability of Tight Sandstone Cores," *J. Pet. Tech.*, Vol. 24, No. 2, 120, Feb. (1972).
2-69. Thomeer, J. H. M., "Introduction of a Pore Geometrical Factor Defined by a Capillary Pressure Curve," *Trans. AIME., Vol. 219*, 354–358 (1960).
2-70. Thomeer, J. H. M., *SPE Preprint 10922* (1981).
2-71. Treiber, L. E., D. L. Archer, and W. W. Owens, "A Laboratory Evaluation of the Wettability of Fifty Oil Producing Reservoirs," *Soc. Pet. Eng. J.*, Vol. 12, No. 4, 531–540, Dec. (1972).
2-72. Vairogs, J., C. L. Hearn, and V. W. Rhoades, "Effect of Rock Stress on Gas Production from Low Permeability Reservoirs," *Trans. AIME, Vol. 251*, 1161 (1971).

CHAPTER 3

THERMODYNAMICS: FLOW EQUATION, FLUID PROPERTIES, COMBUSTION

The science of thermodynamics pervades engineering and science. It is a system of thought created for handling the transformation of one form of energy to another. The subject is too voluminous for all of it to be included here; instead, only three items are treated: (*a*) flow equations, including metering, (*b*) relations of thermal properties to volumetric behavior, and (*c*) combustion. Materials are taken from the senior author's earlier works [1-1,3-2] and others [1-28,3-4,3-5].

The system under consideration and its surroundings need to be identified. For example, natural gas flowing in a pipeline interfaces the surroundings at the pipe wall. Thermodynamics considers all forms of energy transfer between the system and the surroundings, usually as heat through a pipe wall or work energy at a compressor or expander. Most engineering is concerned with flow processes, which are described as *open systems*. *Closed systems*, such as a tank or salt cavity, usually require different treatment.

The forms of energy generally used in gas engineering are internal energy, heat energy, work energy, and flow energy. Each form has an intensive factor, such as pressure (P) for expansion energy, and an extensive factor, such as volume

(V). In preparing equations, one must select the forms of energy under consideration. A starting point is defining the internal energy (U) of the fluid in the system, or more properly, the changes in internal energy between state 1 and state 2:

$$\Delta U = \int_1^2 TdS(\text{heat, friction lost work}), + \int_1^2 P(-dV)(\text{expansion energy}),$$
$$+ \int_1^2 \sigma dA(\text{surface energy}), + \int_1^2 \mu_i dm_i, i = 1, 2, \ldots (\text{chemical energy})$$
$$+ \text{magnetic} + \text{electrical, etc.} \tag{3.1}$$

where T is the temperature, S is the entropy, P is the pressure, V is the volume, σ is the surface tension, A is the area, μ is the chemical potential, m is the mass, and subscript i denotes chemical species.

3.1 DERIVATION OF FLOW EQUATION

A continuous-flow system is represented by Fig. 3-1*a*. Fluid enters the pipe system at point 1. While in flow, the fluid may receive heat (q) from the surroundings, or it may expand and deliver work (w) to the surroundings. Point 2 is the exit point

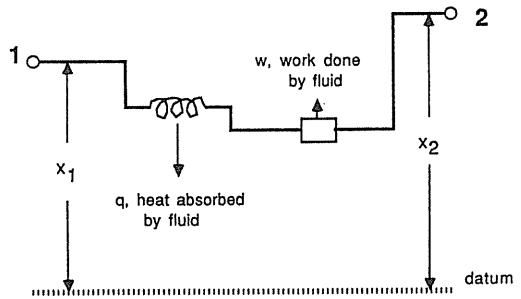

a.

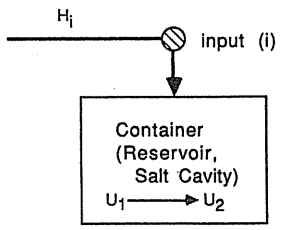

b.

FIGURE 3-1
(*a*) Continuous flow system (steady-state, steady flow) (*b*) closed system (unsteady-state).

for the system. There may be interchanges between the forms of internal energy within the flowing system, such as expansion energy converting to heat through internal friction.

In deriving the flow equation, two forms of energy not included in internal energy are required, the potential energy of position (elevation) and the kinetic energy of flow velocity. By assuming no accumulation or loss of material within the system (steady state), an energy balance may be written around the flowing fluid. The energy coming in at point 1, less the energy lost to the surroundings in transit, plus the energy received during flow, equals the energy at exit point 2. The kinds of energy normally considered in a flow system are given by Table 3.1.

The following equation is written for mass m with internal energy U, kinetic energy $v^2/2g_c$, where v is the velocity of fluid, potential energy gX/g_c, where X is the elevation, and work energy PV for flow from point 1 to point 2. The heat transfer at the interface between the system and surroundings is represented by Q, heat absorbed by system, and W_s is the shaft work done by the system. Work done on the system by compressors is represented by $-W_s$.

$$U_2 + m\frac{v_2^2}{2g_c} + P_2V_2 + m\frac{g}{g_c}X_2 - (U_1 + m\frac{v_1^2}{2g_c} + P_1V_1 + m\frac{g}{g_c}X_1) = Q + (-W_s) \tag{3.2a}$$

or in unit mass:

$$u_2 + \frac{v_2^2}{2g_c} + P_2\bar{v}_2 + \frac{g}{g_c}X_2 - (u_1 + \frac{v_1^2}{2g_c} + P_1\bar{v}_1 + \frac{g}{g_c}X_1) = q + (-w_s) \tag{3.2b}$$

where the lower-case symbols u, $\bar{v}$, q, and w_s are the specific quantities (per unit mass) corresponding to U, V, Q, and W_s respectively. For example, $U = mu$.

By definition,

$$\Delta U = U_2 - U_1$$
$$\Delta(PV) = P_2V_2 - P_1V_1 = \int PdV + \int VdP$$
$$\Delta H = \Delta U + \Delta PV \text{ (enthalpy)} \tag{3.3}$$

TABLE 3.1
Forms of energy in flow system

Internal energy in flowing fluid	Expansion, heat, surface, and chemical
Heat energy at pipe wall	Heat transfer to/from ($+q/-q$) surroundings
Work energy by compressors/pumps	Shaft work energy: output/input ($+w_s/-w_s$)
Flow energy entering/leaving system with fluid	*Potential energy* of position (X) relative to datum *Kinetic energy* due to fluid velocity (v) *PV work energy:* added/lost (entering/leaving)

Equation (3.2*b*), combined with Eq. (3.3), becomes the energy flow equation:

$$\Delta H + \Delta\left(\frac{mv^2}{2g_c}\right) + \Delta\left(\frac{mgX}{g_c}\right) = Q - W_s \tag{3.4}$$

This equation represents thermal energy relationships in flow, but it cannot handle friction, where there is an exchange in forms of internal energy. To relate friction to pressure drop, one inserts the components of U from Eq. (3.1) into Eq. (3.2). When neglecting surface, magnetic, and chemical energy, one finds

$$\int_1^2 TdS + \Delta\left(\frac{mv^2}{2g_c}\right) + \Delta\left(\frac{mgX}{g_c}\right) + \int_1^2 VdP = Q - W_s \tag{3.5}$$

In any process the increase in internal energy due to heat effects, TdS, is equal to the sum of the heat absorbed from the surroundings and all other energy dissipated into heat due to irreversibilities such as overcoming friction (l_w) occurring in the process:

$$\int_1^2 TdS = Q + L_w \tag{3.6}$$

where L_w is the *"lost work"* energy that was available to do work but was dissipated in irreversibilities within the flowing material.

If Eqs. (3.5) and (3.6) are combined and rearranged, one obtains the pressure drop equation:

$$\int_1^2 VdP + \Delta\left(\frac{mv^2}{2g_c}\right) + \Delta\left(\frac{mgX}{g_c}\right) = -W_s - L_w \tag{3.7a}$$

This is the equation (mechanical energy balance) needed in evaluating frictional effects in pipe flow. Since it is a steady state (properties inside the system do not change with time) steady flow (mass into system is equal to mass out of system), the mass m can be canceled out, and Eq. (3.7*a*) becomes

$$\int_1^2 \bar{v}dP + \Delta\left(\frac{v^2}{2g_c}\right) + \Delta\left(\frac{gX}{g_c}\right) = -w_s - l_w \tag{3.7b}$$

Unsteady State—Flow into a Container

For an unsteady state system (Fig. 3-1*b*), mass flowing into the system does not equal the mass out of the system, as in the injection of gas into a reservoir or salt cavity. Therefore, Eq. (3.4) should be modified as follows [3-5]:

Heat + energy flow in = energy flow out

+ energy accumulated inside system + work

$$Q + \sum m_i\left(h_i + \frac{v_i^2}{2g_c} + \frac{gX_i}{g_c}\right) = \sum m_e\left(h_e + \frac{v_e^2}{2g_c} + \frac{gX_e}{g_c}\right) + \left[m_2\left(u_2 + \frac{v_2^2}{2g_c} + \frac{gX_2}{g_c}\right) - m_1\left(u_1 + \frac{v_1^2}{2g_c} + \frac{gX_1}{g_c}\right)\right] + W_s \tag{3.8}$$

where subscripts i and e denote inlet and exit conditions (for the flow into containers, the exit condition terms can be ignored), and subscripts 1 and 2 denote state 1 (initial) and state 2 (final).

Example 3.1. A 5-ft^3 tank initially contains steam vapor at 100 psia. The tank is then injected by 300 psia, 600°F steam until the pressure reaches 300 psia. What is the final temperature?

Solution. The tank is treated as a whole system. Equation (3.8) (with $Q = 0, W = 0, m_e = 0$) reduces to

$$m_i h_i = m_2 u_2 - m_1 u_1$$

and we have

$$m_i = m_2 - m_1$$

$$m_1 \bar{v}_1 = m_2 \bar{v}_2 = V = 5\,\text{ft}^3$$

where $\bar{v}$ is the specific volume (ft^3/lb$_m$).

From steam tables (100 psia, 327.86°F), $\bar{v}_1 = 4.434$ ft^3/lb$_m$, $u_1 = 1105.8$ Btu/lb$_m$, $h_i = 1314.5$ Btu/lb$_m$, and $m_1 = V/\bar{v}_1 = 5/4.434 = 1.1277$. Therefore, Eq. (3.8) can further be rearranged to

$$\left(\frac{5}{\bar{v}_2} - 1.1277\right)(1314.5) = \left(\frac{5}{\bar{v}_2}\right)u_2 - 1.1277(1105.8)$$

There are two unknowns in this equation; it can be solved by trial and error using steam tables. The final temperature $T = 632.5$°F ($\bar{v}_2 = 2.07745, u_2 = 1216.8$, at 300 psia) will satisfy the above equation.

In general, the temperature rises when gases are injected into a reservoir or cavity and falls when gases are released from a reservoir or cavity.

3.2 WORK AND POWER

Power is the time rate of doing work or the rate of expending work energy. A horsepower is defined as expending energy at the rate of 33,000 ft · lb$_f$/min (= 746 J/s = 0.746 kW). In electrical energy, power is defined in terms of watts or kilowatts, while work energy is in terms of kilowatt-hours, watt-hours, or joules. Energy or power can be expressed in equivalent terms for the several forms of energy. Table A.2 (in Appendix A) lists conversion factors from one form to another.

3.3 FLUID PROPERTIES; *P, V, T, H, S* RELATIONSHIPS

Thermodynamic functions relate volumetric properties to enthalpy, entropy, Joule-Thomson coefficient, etc. Since the compressibility factor Z is a volumetric parameter, the relationships extend to using Z to find the effects of pressure on H and S. Time and space do not permit a full development. Table 3.2 is given here to set forth some of these functions, known as Maxwell's equations. Later a Joule-Thomson cooling chart for natural gas will be given (Fig. 4-49). Also, differences in fluid properties will explain why oil lines heat and gas lines cool. For further information on thermodynamics see references [3-4,3-5].

TABLE 3.2
Relating thermal and volumetric properties *P, T, S, H,* and *V*

Gas law	$PV = ZnRT$	(3.9)
Change of enthalpy H with T and P	$dH = \left(\frac{\partial H}{\partial T}\right)_P dT + \left(\frac{\partial H}{\partial P}\right)_T dP$	(3.10)
	$dH = C_P dT + \left[V - T\left(\frac{\partial V}{\partial T}\right)_P\right] dP$	(3.11)
	$dH = C_P dT + \left[\frac{-RT^2}{P}\left(\frac{\partial Z}{\partial T}\right)_P\right] dP$	(3.12)
Change in entropy S with T and P	$dS = \left(\frac{\partial S}{\partial T}\right)_P dT + \left(\frac{\partial S}{\partial P}\right)_T dP$	(3.13)
	$dS = \frac{C_P}{T} dT - \left(\frac{\partial V}{\partial T}\right)_P dP$	(3.14)
	$dS = \frac{C_P}{T} dT - \frac{R}{P}\left[Z + T\left(\frac{\partial Z}{\partial T}\right)_P\right] dP$	(3.15)
The Eucken coefficient Φ and the Joule-Thomson coefficient μ'	$\Phi = \left(\frac{\partial H}{\partial P}\right)_T = V - T\left(\frac{\partial V}{\partial T}\right)_P$	(3.16)
	$\Phi = -\mu' C_P$	(3.17)
	$\mu' = \left(\frac{\partial T}{\partial P}\right)_H$	(3.18)
Other expressions with $PV = ZnRT$	$\Phi = -\mu' C_P = \frac{ZRT}{P} - \frac{RT}{P}\left[Z + T\left(\frac{\partial Z}{\partial T}\right)_P\right]$	
	$= -\frac{RT}{P}\left[T\left(\frac{\partial Z}{\partial T}\right)_P\right]$	(3.19)
	$\mu' = \left(\frac{\partial T}{\partial P}\right)_H = \frac{RT^2}{C_P P}\left(\frac{\partial Z}{\partial T}\right)_P$	(3.20)
	$dT = \left(\frac{1}{C_P}\right)\left(\frac{RT^2}{P}\right)\left(\frac{\partial Z}{\partial T}\right)_P dP$	(3.21)

3.4 ELEMENTS OF COMBUSTION

The heating or calorific value of combustion is a prime characteristic of natural gas, often a factor in the price received in the sale. Combustion is used to provide heat in the field or plant as well as the power for gas engines, and engineers need to understand it. Unwanted combustion or explosion of fugitive gas mixed with air is a prime safety matter; an engineer should know the limits of composition at which various gases explode when mixed with air and ignited. Composition limits of flammability represent a safety problem that should be familiar to engineers. Gross heating values assume the water generated in the combustion is condensed and returned to 60°F (15°C), whereas net heating values are for water leaving the system in vapor form.

Heat Energy

The common forms of heat energy are represented by *heat capacity* C_p, *latent heat* ΔH_v, and *heat of combustion* ΔH_c. Heat capacity is that heat required to raise a given mass of a substance a unit of temperature. The British thermal unit (Btu) is the heat required to raise 1 lb of water 1°F; the calorie is the heat required to raise 1 gm of water 1°C over a prescribed range of temperature. *Specific heat* is another term for heat capacity. A latent heat is the heat needed to cause a phase transformation, such as evaporation of a liquid or liquefaction of a solid. It is added to a pure substance at constant temperature and pressure. The heat of combustion is the chemical energy released when a substance burns, that is, when its constituents react with oxygen to form CO_2 and H_2O.

Thermodynamically, specific heat at constant pressure and at constant volume are defined as

$$C_P = \left(\frac{\partial H}{\partial T}\right)_P \qquad C_V = \left(\frac{\partial U}{\partial T}\right)_V \tag{3.22}$$

For a given heat release in combustion, the temperature rise is governed by the specific heat of the combustion products or flue gases. The specific heats of constituents of flue gases are given in Table 3.3. The values given are mean values between 60°F (15°C) and the temperature indicated.

In SI units, the joule (J = N· m) or kilojoule is used for energy; 1 Btu = 1.055 kJ, and 1 kilocalorie = 4.184 kJ. The SI unit for specific heat is kJ/(kmol · K) and is obtained from Btu/(lb mol · °F) by multiplying by a factor of 4.1868.

Heating Value

The *heating value* of natural gas is the heat (chemical energy) liberated when a unit of fuel is burned with oxygen under specified conditions. Methane has a heating value of 1009.7 Btu per actual cubic foot (37,613 kJ/m^3) of gas at 60°F (15°C) and 14.7 psia (101.3 kPa), when burned with air. This heating value is obtained

TABLE 3.3
Mean modal heat capacities of gases between 60° F (15° C) and temperature
Btu/(lb mol · °F)[× 4.1868 = kJ/(kmol · °C)]

T, °F	T, °C	H_2	N_2	O_2	Air	H_2O	CO	CO_2	CH_4
60	15	6.86	6.96	7.00	6.94	7.99	6.96	8.70	8.3
100	38	6.87	6.96	7.01	6.94	8.00	6.96	8.83	8.4
200	93	6.92	6.97	7.06	6.96	8.04	6.97	9.21	8.7
400	204	6.95	7.00	7.16	7.01	8.13	7.00	9.73	9.48
600	316	6.97	7.05	7.30	7.07	8.25	7.07	10.19	10.30
800	427	6.98	7.11	7.43	7.16	8.39	7.14	10.57	11.06
1000	538	7.00	7.17	7.55	7.24	8.54	7.23	10.93	11.76
1500	816	7.08	7.37	7.80	7.44	8.93	7.44	11.59	13.30
2000	1093	7.16	7.57	8.00	7.63	9.33	7.65	12.10	14.69
2500	1371	7.28	7.72	8.16	7.77	9.70	7.80	12.45	
3000	1649	7.39	7.85	8.26	7.91	10.04	7.93	12.75	
3500	1926	7.51	7.96	8.40	8.01	10.35	8.03	12.98	
4000	2204	7.63	8.06	8.49	8.09	10.63	8.13	13.17	

by cooling the products of combustion to 60°F (15°C). When water remains as a vapor, the energy recovered is the *net heating value*. When the moisture is condensed, the recovered energy is known as the total or *gross heating value*. Hydrocarbon constituents of natural gas have gross heating values as indicated in Table 3.4 and in Table A.1 (Appendix A).

ASTM procedure D2382 [1-30,3-1] outlines a test procedure and describes equipment for measuring the heating value of natural gas. Continuous-recording

TABLE 3.4
Computation of heating value from gas analysis
Data for 14.7 psia, 60°F (101.3 kPa, 15°C)

		Heating value		Total heating value	
Component	Mole fraction	Btu/ft³	MJ/m³	Btu/ft³	MJ/m³
Nitrogen	0.023	0.0	0.0	0.0	0.0
Methane	0.887	1009.7	37.694	895.60	33.435
Ethane	0.056	1768.8	66.032	99.05	3.698
Propane	0.021	2517.4	93.972	52.87	1.973
i-Butane	0.003	3252.7	121.426	9.76	0.364
n-Butane	0.006	3262.1	121.779	19.57	0.731
Pentanes*	0.004	4380.4	163.521	17.52	0.654
	1.000			1094.37	40.855

* Assume 0.001 n-C_5, 0.001 i-C_5, 0.002 n-C_6.
The values above are from an early version of *GPA Engineering Data Book* [1-28]. These values are practically the same as the values shown in the latest *GPA Test Manual* (2172–86) [1-30]. For example, the heating value of CH_4 in the later reference is 1010.0 compared to 1009.7 Btu/ft³ in this table. Also, *GPA Test Manual* shows the sample calculations of water-saturated ideal gross heating value and lists computer code for evaluating the heating values of mixtures.

oxygen bomb calorimeters, either isothermal or adiabatic, are used for measuring the heating value of pipeline gases; such instruments are calibrated by the ASTM procedure.

Since the ASTM method does not determine heating values of natural gas likely to be used in calibrations, it determines only the gross heating values. There is no standard method for determining the net heating value of natural gas. It may be computed from the gas analysis and the heating values of constituents, assuming either the ideal-gas law or additive volumes. Table 3.4 presents such a calculation, assuming additive volumes for the constituents. Heating values are related to gas analysis and hence in turn to gravity. Figure 3-2 shows such a relationship with correction lines for percentage of non–heating value inerts, as N_2 (not H_2S).

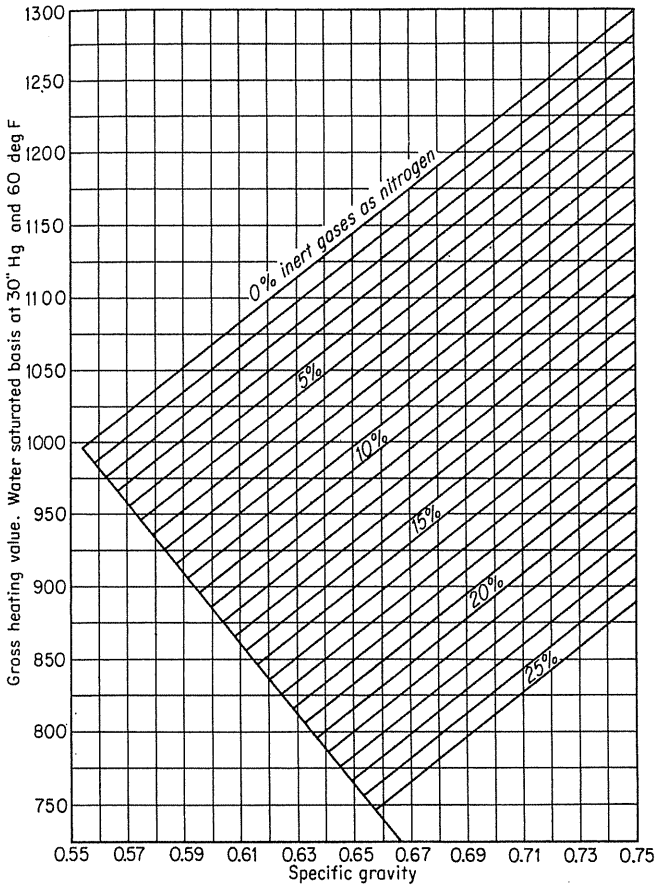

FIGURE 3-2
Conversion between heating value, gravity, and percentage of inerts [Zapffe, 3-3, courtesy Petro. Refin.].

Combustion Calculations

Engineers should be familiar with combustion calculations to estimate fuel requirements and evaluate the effects of excess air on flue gas temperatures. The following example illustrates one method of making the calculations.

The chemical reaction for combustion of 1 pound-mole of methane is as follows:

$$CH_4(g) + 2O_2 \rightarrow CO_2(g) + 2H_2O(l) + 383,171 \text{ Btu} \qquad (3.23)$$

The latent heat of water at 60°F and 1 atm is 1060 Btu/lb, or $18 \times 2 \times 1060 = 38,160$ Btu for 2 lb mol of water:

$$2H_2O(l) \rightarrow 2H_2O(g) + (-38,160 \text{ Btu}) \qquad (3.24)$$

Adding Eqs. (3.23) and (3.24) gives the net heat of combustion when water leaves as a vapor.

$$CH_4(g) + 2O_2(g) \rightarrow CO_2(g) + 2H_2O(g) + 345,011 \text{ Btu} \qquad (3.25)$$

Since 1 lb mol is 379 ft^3, this is 910 Btu/ft^3 ideal (net).

The gross heating value per cubic foot of methane at 60°F (15°C) and 14.7 psia (101.3 kPa) is found for ideal-gas-law conditions by dividing 383,171 Btu by 379.49 ft^3/lb mol for ideal gases to get 1009.7 Btu/ft^3 of ideal volume. Methane has a compressibility factor of 0.998 at 60°F (15°C) and 14.7 psia (101.3 kPa), and so the gross heating value per actual cubic foot is 1009.7/0.998 = 1011.7 Btu/ft^3.

Example 3.2. Combustion. In a gas-treating plant, the glycol-water solution goes to a heater where the temperature of the solution is raised from 27°C (80°F) to 199°C (390°F) by delivering 670,000 watts (2,300,000 Btu/hr) to the solution. Gas of the composition given in the following is used to fuel the heater. Air at 15°C (60°) and 40 percent relative humidity is used in excess by 15 percent over theoretical. Complete combustion may be assumed.

Calculate the amount of this gas needed to deliver the desired heat, using 305°C (580°F) as the stack gas temperature.

(*a*) What is the composition of the stack gas?
(*b*) How much natural gas is required per hour?
(*c*) What is the efficiency of combustion?

Gas Composition:

Constituent	Mole %
C_1	96.0883
C_2	2.2361
C_3	0.0020
i-C_4	0.0024
n-C_4	0.0024
i-C_5	0.0029
n-C_5	0.0026
C_6	0.0202
CO_2	1.2928
N_2	0.3503

Solution (in SI units). First a schematic diagram setting forth a material and heat balance is prepared. The heating value of the fuel gas, the composition of the stack gas, and the heat capacity of the stack gas are calculated. This information makes it possible to solve the heat and material balance for the quantity of fuel gas required per hour.

Material and heat balance:

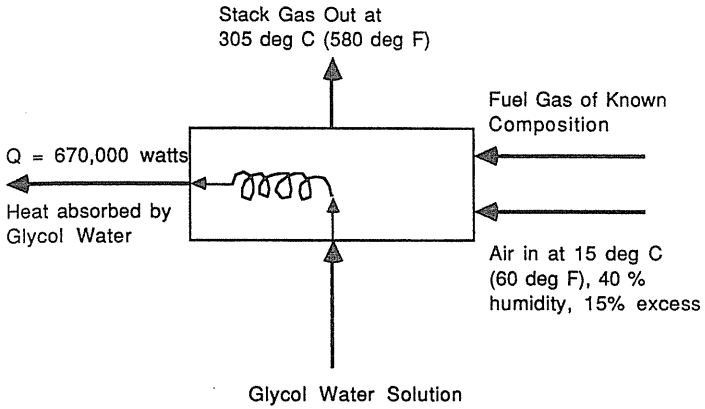

To compute the heating value, oxygen required, and water formed, Table 3.5 is constructed. Here the gross heating value per standard cubic meter is found to be 37.749 MJ, which for 23.63 m^3/kmol becomes 892,008.9 kJ/kmol.

From the moles of water and CO_2 formed and the oxygen requirement, the stack gas composition is obtained, using the 15 percent excess air for complete combustion. From the analysis and specific heats of the stack gas, one computes the heat capacity of the stack gas at 15–305°C as in Table 3.6.

Balance on 100 kmol fuel gas:

$$\text{Heat in} = 100 \text{ kmol} \times 23.63\frac{\text{m}^3}{\text{kmol}} \times 37.749\frac{\text{MJ}}{\text{m}^3} = 89,200.9 \times 10^3 \text{ kJ}$$

$$\text{Heat out} = \text{latent heat of water} + \text{sensible heat stack gas}$$

$$= 199.08 \text{ kmol water} \times 18\frac{\text{kg}}{\text{kmol}} \times 2462.5\frac{\text{kJ}}{\text{kg}}$$

$$+ 37,952.15 \text{ kJ/°C} \times (305 - 15)\text{°C}$$

$$= 8,824,221.0 \text{ kJ} + 11,006,123.5 \text{ kJ} = 19,830,344.5 \text{ kJ}$$

$$\text{Efficiency} = \frac{89,200,900 - 19,830,344.5}{89,200,900} = 0.778 \text{ or } 77.8\%$$

$$\text{Volume of fuel gas} = 670,000\frac{\text{J}}{\text{s}} \cdot \frac{60 \times 60 \text{ s}}{1 \text{ hr}} \cdot \frac{1}{0.778} \cdot \frac{1}{37.749 \times 10^6 \text{J/m}^3}$$

$$= 82.13 \text{ m}^3\text{/hr}$$

TABLE 3.5
Calculation of heating value and products of combustion

				Combustion of constituents					
	Mole %	Gross heating value (MJ/m^3)	Total heating value (MJ/m^3)	Mole H_2O formed per mole	Moles H_2O per 100 moles gas	Moles O_2 per mole	Moles O_2 per 100 moles gas	Moles N_2 per 100 moles gas	Moles CO_2 in stack
CO_2	1.2928	0	0	0	0	0	0	0	1.293
N_2	0.3503	0	0	0	0	0	0	0.35	0
C_1	96.0883	37.694	36.220	2	192.176	2	192.176	722.95	96.088
C_2	2.2361	66.032	1.477	3	6.708	3.5	7.826	29.44	4.472
C_3	0.0020	93.972	0.002	4	0.008	5.0	0.010	0.37	0.006
i-C_4	0.0024	121.43	0.003	5	0.011	6.5	0.016	0.06	0.010
n-C_4	0.0024	121.78	0.003	5	0.011	6.5	0.016	0.06	0.010
i-C_5	0.0029	149.32	0.004	6	0.017	8	0.023	0.07	0.015
n-C_5	0.0026	149.65	0.004	6	0.016	8	0.021	0.08	0.013
C_6	0.0202	177.56	0.036	7	0.141	9.5	0.192	0.72	0.121
Total	100.0		37.749		199.08		200.28	763.43	102.028
Column (1)	(2)	(3)	(4)	(5)	(6)	(7)	(8)	(9)	(10)

For each constituent the equation is written to determine water and CO_2 formed and O_2 required for complete combustion, such as

$$C_2H_6 + 7/2\ O_2 \rightarrow 2\ CO_2 + 3\ H_2O$$

Column (4) = Column (2) × Column (3)
Column (6) = Column (2) × Column (5)
Column (5) = moles water formed = no. of H atoms/2
Column (7) = moles O_2 required = no. of C atoms + no. of H atoms/4
Column (9) = moles N_2 in = moles O_2 × 79/21
Column (10) = moles CO_2 formed = no. of C atoms × moles of constituent in gas

TABLE 3.6
Calculations of composition and heat capacity of stack gas
100 moles fuel gas (15–305°C)

	Moles in stack gas	Mole %	C_{pm}, kJ/kg-mole °C	Heat capacity, kJ/°C
CO_2	102.027	8.46	42.4709	4,333.18
H_2O	206.878	17.2	34.4909	7,135.41
O_2	30.042	2.49	30.5050	916.43
N_2	866.800	71.85	29.4960	25,567.13
	1205.747	100.0		37,952.15

The CO_2 is taken directly from Table 3.5.
The O_2 is the excess, or $0.15 \times 206.878 = 30.042$.
The N_2 is $200.280 \times 1.15 \times 79/21 = 866.449$, plus the small amount in the fuel gas (0.35).
The H_2O is $199.08 + (866.449 + 229.122) \times (0.0071) = 206.878$: the second term is the water content of the supplied air.
Air at 15° (60°F) and 40% relative humidity contains 0.0071 lb · mole H_2O vapor per lb · mole dry air.

3.5 LIMITS OF FLAMMABILITY—SAFETY

Air and natural gas in the proper proportions will ignite, liberating heat, which is absorbed primarily by the products of combustion. The temperature rise of the gases causes an increase in pressure and, under confinement, can result in an explosion. It is important that everyone connected with the natural gas industry understand flammability limits and the nature of combustion.

Equation (3.23) for the combustion of methane does not reveal the mechanism of the chemical reaction. Methane and air in the proper proportions do not react until some ignition source initiates the process. Possible steps in the chemical reaction are given by Lewis and Von Elbe [3-3]. A large number of oxygenated intermediate compounds are formed along with free radicals like OH en route to CO_2 and H_2O formation.

To start the combustion process, the ignition source converts some methane (CH_4) into free radicals, which in turn are converted to oxygenated compounds and OH. The OH radical reacts with methane and is regenerated. Combustion is impeded by processes that destroy the OH radicals before they can react with the hydrocarbon. Solid surfaces often destroy the OH radical; this effect is involved when a gas flows through a porous bed flame arrester. Combustion reaction rates are rapid but measurable. Under certain conditions, time scales expanded to microseconds (1/1,000,000 s) are required. The rates rise rapidly with increasing temperature. A rule of thumb is that reaction rates double for each 27°F (15°C) of temperature rise.

There are two composition limits of flammability for air and a gaseous fuel under specified conditions. The lower limit corresponds to the minimum concentration of combustible gas that will support combustion, the higher limit

TABLE 3.7
Limits of flammability of gases with air at one atmosphere pressure [3-5]

	Volume or mole % gas in mixture	
Constituent	Lower	Higher
Methane	5.0	15.0
Ethane	2.9	13.0
Propane	2.1	9.5
n-Butane	1.8	8.4
Isobutane	1.8	8.4
n-Pentane	1.4	8.3
Isopentane	1.4	8.3
Hexane	1.2	7.7
H_2S	4.3	45.5

the maximum concentration. Table 3.7 lists lower and higher limits for pure hydrocarbons in air at atmospheric pressure and room temperature. For methane in air, the flammable range is from 5 to 15 mole or volume percent; for propane, the range is 2.12 to 9.35 mole or volume percent.

The lower limits of gaseous mixtures can be predicted from the limits of the pure constituents by a simple formula:

$$\frac{n_1}{N_1} + \frac{n_2}{N_2} + \frac{n_3}{N_3} = 1 \tag{3.26}$$

where subscripts 1, 2, and 3 refer to constituents 1, 2, and 3; n (mole or volume percent) is the proportion of each constituent in the total mixture at lower limit; and N (mole or volume percent) is the lower limit for each constituent as a pure hydrocarbon.

Example 3.3. Compute the lower flammability limit for a natural gas composed of 92 vol % CH_4, 5.5 vol % C_2H_6, and 2.5 vol % C_3H_8.

Solution. Let Y = volume percent of gas in mixture of air and gas.

$$\frac{92.0\,Y}{5.0} + \frac{5.5\,Y}{2.9} + \frac{2.5\,Y}{2.1} = 100\%$$

$$18\,Y + 190\,Y + 1.19\,Y = 100\%$$

$$Y = \frac{100}{21.59} = 4.63 \text{ vol. \% of gas in mixture}$$

Pressure influences the flammability limits. At low pressures, say 50 mm Hg, natural gas–air mixtures are not combustible. At high pressures, the upper limit rises rapidly. The diluting of a fuel-air mixture with inert constituents such as nitrogen and carbon dioxide also changes the limits of flammability. Both the lower and higher limits are raised by addition of the diluent, an effect due in part to the lower oxygen content. Natural gas or any fuel is *very combustible* when mixed with oxygen-enriched air or pure oxygen. Usually, odorant is added into natural gas to alert operators when the natural gas concentration in air reaches 20 percent of the lower flammability limit (see Section 14.4).

HOME PROBLEMS

3.1. Repeat Example 3.2 in English units.

REFERENCES

3-1. American Society for Testing Materials, *Annual Book of ASTM Standards*, Section 5, Vols. 5.01–5.03, *Petroleum Products and Lubricants*, Vol. 5.04, *Test Methods for Rating Motor, Diesel, and Aviation Fuels*, American Society for Testing Materials, Philadelphia (1986).

3-2. Brown, G. G., et al., *Unit Operations*, John Wiley & Sons (1950).

3-3. Lewis, B., and G. von Elbe, *Combustion, Flames, and Explosions of Gases*, Academic Press, New York (1951).

3-4. Smith, J. M., and H. C. Van Ness, *Introduction to Chemical Engineering Thermodynamics*, 3rd Edition, McGraw-Hill Publishing Company (1975).

3-5. Van Wylen, G. J., and R. E. Sonntag, *Fundamentals of Classical Thermodynamics*, John Wiley & Sons (1965).

3-6. Zapffe, F., "Natural Gas Correlations," *Petro. Refiner, Vol. 33, No. 4*, 142 (1954).

CHAPTER 4

PHYSICAL BEHAVIOR OF NATURAL GAS SYSTEMS: PHYSICAL AND THERMAL PROPERTIES, PHASE BEHAVIOR, ANALYSES

The language and basic concepts of phase behavior are derived from simple systems: pure substances and binary and ternary mixtures. The study of phase behavior has had a century of progress [1-15,4-35]. Phase equilibria, vapor pressures, critical points, and phase densities are known for various pure constituents of natural gas. The study of mixtures involves added dimensions such as bubble points, dew points, and retrograde condensation. The phase rule gives the relationship between the number of phases, the number of components, and the number of degrees of freedom in specifying or fixing a system.

The volumetric behavior of gases, that is, the deviation from the ideal gas law in the form of compressibility factor, is used in metering gases and in many engineering calculations where density is a factor. Knowledge of volumetric

behavior permits the calculation of thermodynamic properties such as the amount of cooling upon expansion and the effect of pressure on specific heat. Charts and tables for compressibility factors with gas gravity as a parameter are now largely replaced by information calculated directly from equations of state.

The computation of conditions for phase boundaries or of the percentage of phases present at stated temperatures and pressures for a given mixture is of prime concern in natural gas engineering. It too has passed from a chart stage to computerized solutions using equations of state.

The physical and thermal properties of natural gas treated here are viscosity, surface tension, specific heat, effects of pressure on enthalpy, Joule-Thomson cooling and *H-S* relationships. The analysis of gases is presented as well.

Surface metering, processing, transporting, and underground storage are discussed. Reservoir behavior at elevated pressures and temperatures is included. A distinction is sometimes made between natural gas, liquefied natural gas (LNG), and the dense phase in the single-phase region at high pressure near the critical temperature.

The early work on phase behavior for hydrocarbons is reviewed in the *Handbook* [1-1]. The early literature is abstracted and partially copied in [1-15]. An SPE monograph on phase behavior is in preparation (1988).

4.1 PURE SUBSTANCES—VAPOR PRESSURE

Pure substances may occur in vapor, liquid, and solid phases depending upon the temperature and pressure. When a substance is in a single phase, its temperature T and pressure P define the volume V of the component. Figure 4-1 [4-68] is a plot of these three variables (P, V, T) in three dimensions for a pure substance. The phase behavior is represented by the surfaces exposed in the cutaway view.

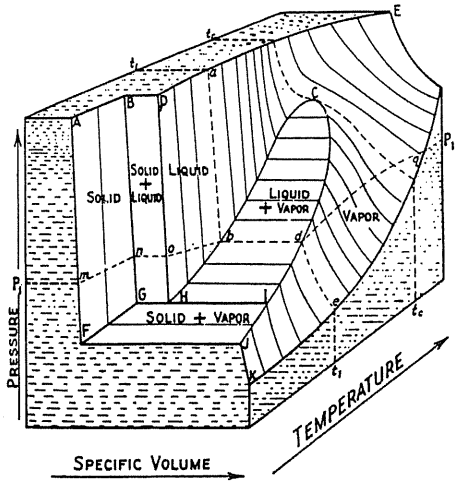

FIGURE 4-1
P-V-T diagram for pure substance [Sherborne, 4-68, courtesy SPE-AIME].

Since three-dimensional figures are more difficult to use than two-dimensional ones, pressure-temperature projections of the intersections of the surfaces (Fig. 4-2 [1-1]) and pressure-volume sections at constant temperature (Fig. 4-3 [4-52]) are more commonly employed. Diagrams such as these are used to portray the phase behavior of natural gas constituents.

The conditions at which vapor and liquid may coexist are represented in Fig. 4-1 by the area H-b-C-d-I. The surface is *ruled*; that is, the lines generating the surface are projections of parallel lines in the base of the figure. The projection of C-b-H and C-d-I on a pressure-temperature plane is a single curve (H-C of Fig. 4-2) known as the vapor pressure curve. The two-phase surface B-D-H-G for solid and liquid is ruled likewise, and projects as curve H-D in Fig. 4-2. The solid-vapor surface projects as H-F. Consider methane in the solid state at m, and increase its temperature at constant pressure P_1. At n, liquid begins to form, and upon continued addition of heat at constant temperature and pressure the methane will become all liquid at o. Further temperature rise occurs before the formation of a less dense fluid phase at b, called vapor. Vaporization takes place at constant temperature until at d it is completed. Temperature rise beyond d to q simply causes the volume to increase without any phase change.

At the triple point H all three phases coexist; only at this single temperature and pressure can one have three phases together at equilibrium for a pure compound.

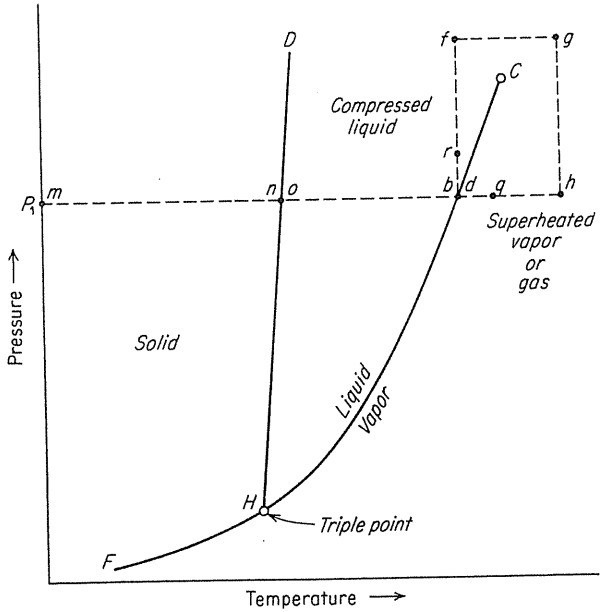

FIGURE 4-2
P-T diagram with vapor pressure curve [Katz et al., 1-1, courtesy McGraw-Hill Publishing Co.].

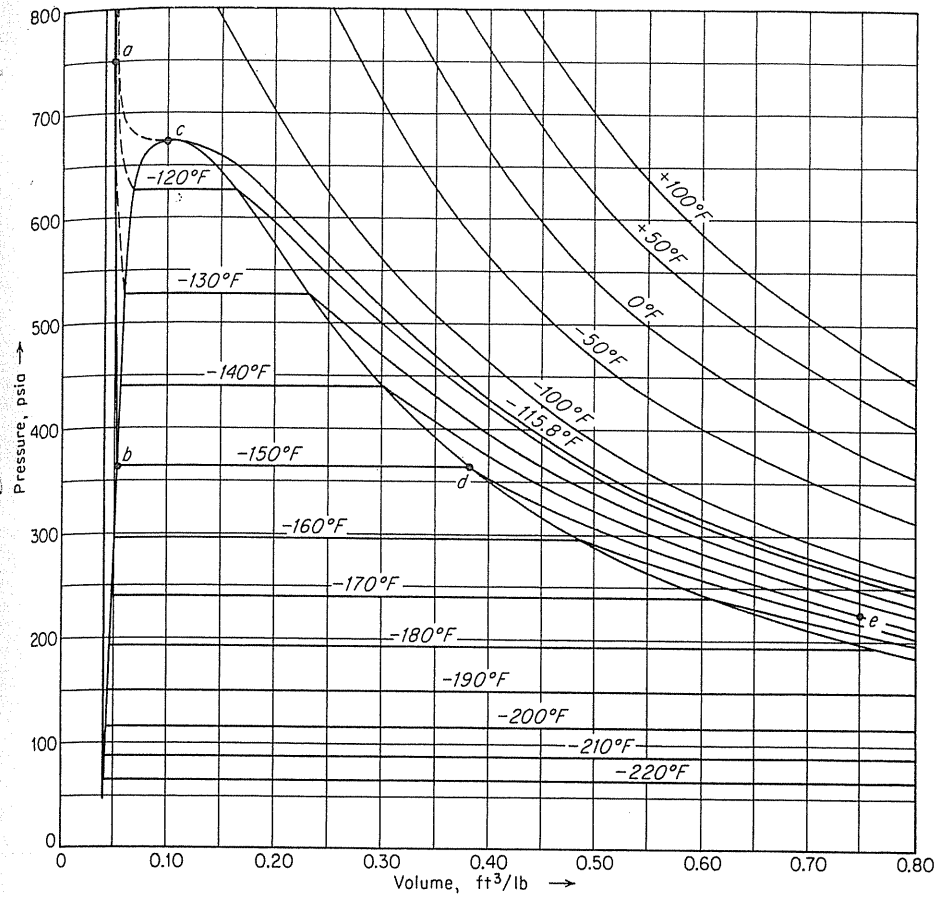

FIGURE 4-3
P-V diagram for methane [data from Matthews & Hurd, 4-52, courtesy AIChE].

The specific-volume sections at constant temperature (such as a-b-d-e of Fig. 4-1) may be plotted as isotherms, as in Fig. 4-3. The densities, reciprocal to the specific volumes, of the saturated phases are plotted in Fig. 4-4 [4-44]. It should be noted that, for increasing temperature, the specific volume of the liquid is rising (density lowering) while the volume of the vapor is decreasing (density rising). At the critical point C, the specific volumes and all other properties of the phases merge. A line drawn through the mean values of the vapor and liquid densities intersects the density curve at the critical density. This principle is known as the law of rectilinear diameters. A procedure to find the critical density was proposed by Cailletet and Mathias (see [1-1]).

The vapor pressure curve giving the boiling point at various pressures is a most important property of pure substances. Pure hydrocarbons are encountered

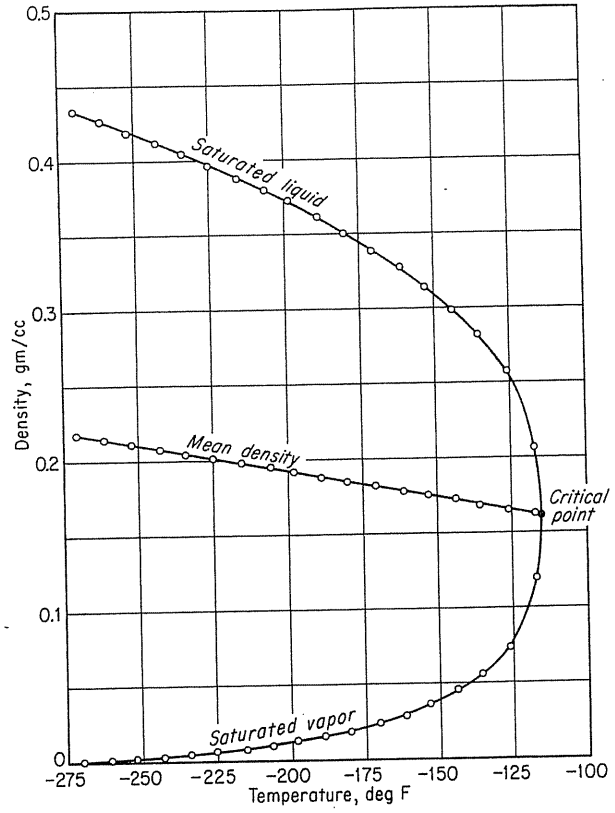

FIGURE 4-4
Orthobaric (saturated) densities of methane [after Keyes, Taylor & Smith, 4-44].

in processing operations or in the laboratory, and vapor pressure curves are very useful in handling them. Figure 4-5 gives the vapor pressures of the volatile hydrocarbons encountered in the gas industry [1-1].

4.2 THE PHASE RULE

The Gibbs phase rule is a most important tool in studying phase behavior. The rule applies to systems at *equilibrium*. Equilibrium between phases can be reached by isolating a system at constant temperature and pressure for long periods of time or by intimate mixing of the parts of a system. At equilibrium, the composition of each phase is uniform throughout, and no net transfer of components occurs between phases when they are permitted to remain in contact over long periods of time. Many natural gas/liquid systems in industry approach equilibrium, but, even for systems that are not in a state of equilibrium, the laws governing equilibrium

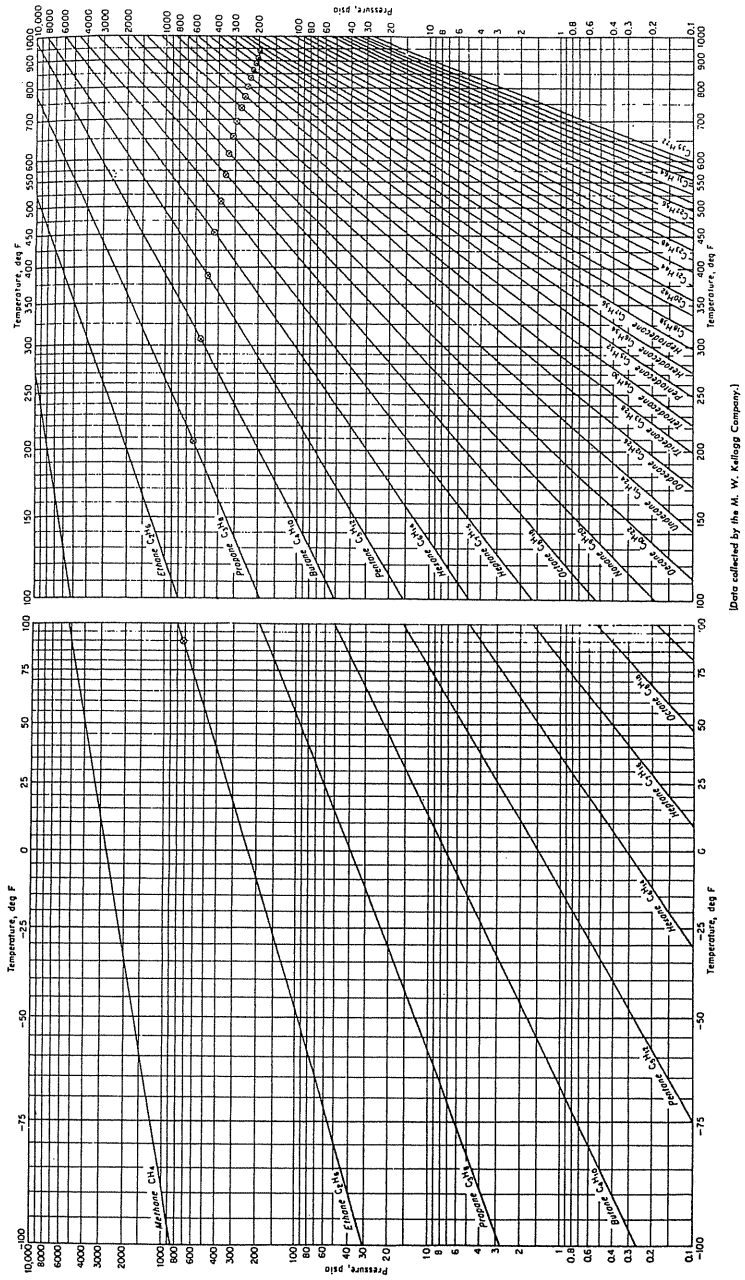

FIGURE 4-5
Vapor pressure of paraffin hydrocarbons, M. W. Kellogg data [Katz et al., 1-1, courtesy McGraw-Hill Publishing Co.].

impose limiting conditions. When phases are in equilibrium with each other, they are said to be *saturated*.

The phase rule is commonly expressed by Eq. (4.1):

$$C_n + 2 - P_n = F_n \tag{4.1}$$

where C_n is the number of independent components, P_n is the number of phases, and F_n is the number of variables required to determine the state of the system at equilibrium, or the number of *degrees of freedom*.

Case [4-13] states that "the phase rule represents simply the application to certain chemical and physical problems of the familiar rule of algebra that the number of independent equations in a set of simultaneous equations must be equal to the number of variables involved in order that the values of the variables shall be fixed." The variables for a system include the temperature, the pressure, and the composition of phases. The overall concentration of a component in a system of two or more phases is not a phase rule variable, although the concentration in a given phase is.

A pure substance in three phases has zero degrees of freedom; this is represented by the invariant triple point. A pure substance in two phases, such as vapor and liquid, has one degree of freedom. Along the vapor pressure curve (Fig. 4-2) specifying either pressure or temperature completely defines the state of the system. For example, at 100°F (38°C) propane in two equilibrium phases is at 189 psia (1.3 MPa), the density of liquid is 0.477 g/cm^3, and the density of the vapor is 0.027 g/cm^3 (27 kg/m^3). The surface tension is 5.5 dyn/cm (5.5×10^{-3} N/m). All properties of the phases are fixed by specifying the temperature and the condition that the system is in two phases. It should be noted that the phase rule is concerned only with the nature of the phases, not their extent.

A two-component system in two phases has two degrees of freedom. Temperature and pressure will define the state of such a system. For a three-component system in two phases, temperature, pressure, and a composition variable will specify the state. The latter can be the concentration of one constituent in a phase but more often is the ratio of the concentration of one constituent in a phase to that of another constituent in that phase. For a natural gas with seven constituents in two phases, seven variables are required to fix the system, such as temperature, pressure, and five concentrations. The prediction from temperature and pressure of phase relationships for such complex mixtures usually depends upon the assumption that the mixtures obey ideal laws for solutions.

Example 4.1 Phase rule. A system is composed of methane, propane, and water. The phases possible are gas hydrate (S), hydrocarbon-rich liquid (L_2), water-rich liquid (L_1), and a vapor phase (V). How many variables are required to fix the system?

Solution. Possible phases $P_n = 4$ (S, L_1, L_2, V). Components $C_n = 3$ (C_1, C_2, H_2O). Therefore, $F_n = C_n + 2 - P_n = 3 + 2 - 4 = 1$ degree of freedom. The locus of the quadruple point for the methane-propane-water system (Fig. 5-35 in [1-1]) is a P-T curve with either P or T fixing the system. The hydrate solid (S) is a single phase.

4.3 BEHAVIOR OF MIXTURES: BINARY, TERNARY, AND COMPLEX

Mixtures bring an added dimension to phase behavior, as demonstrated by the methane-ethane system (Fig. 4-6 [4-7]). The two-phase region for all possible mixtures of methane and ethane is bounded by the vapor pressure curve for methane, curve 1, the vapor pressure curve for ethane, curve 10, and the critical locus connecting the critical points of the pure substances. At pressures above the critical locus all mixtures of methane and ethane remain in single phase. Mixtures 2 to 9 each have a phase boundary curve as shown.

Retrograde condensation is a term coined by Kuenen [4-46] and discussed by Katz and Kurata [1-1,4-38] to describe unusual phase behavior in the critical region for mixtures. The language for mixtures is illustrated by Fig. 4-7. A fluid in single phase at K will exhibit bubbles of vapor when the pressure is lowered to B. Point B is called a *bubble point*. Likewise, when pressure is raised from J to E, liquid forms. This point is called a *dew point*, since the liquid appears as tiny droplets in glass equipment. When the pressure is lowered from L to D, liquid forms by a drop in pressure. This is an example of retrograde condensation.

Retrograde condensation is the formation of a liquid by a pressure or temperature change opposite to that which causes condensation in pure substances or

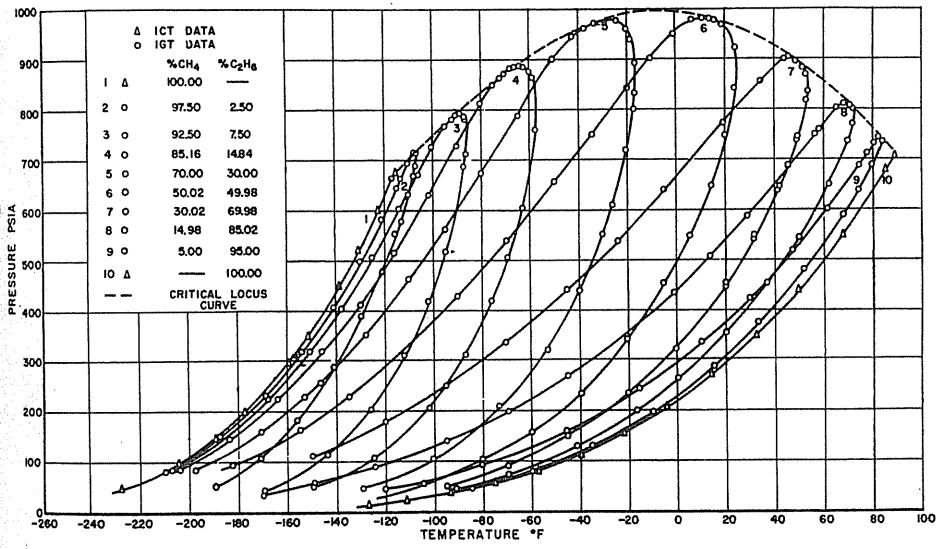

FIGURE 4-6
Phase diagram for methane-ethane mixture, IGT data [Bloomer et al., 4-7; Katz et al., 1-1, 4-38 courtesy IGT].

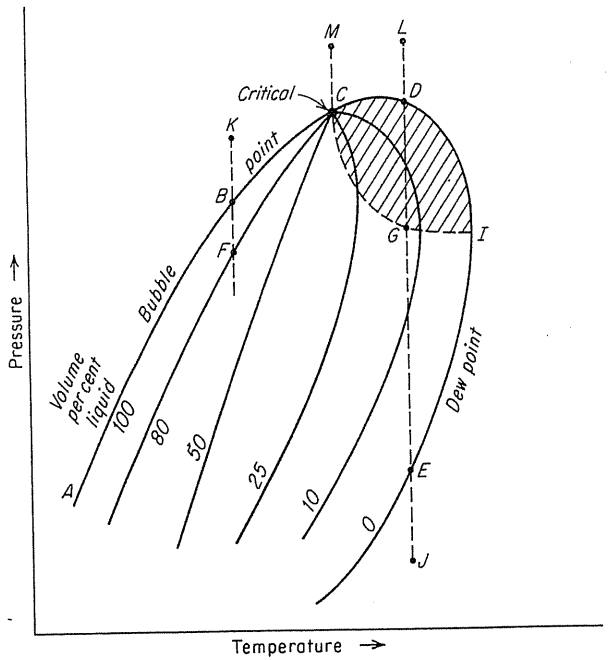

FIGURE 4-7
Phase diagram of methane-ethane mixture [Katz et al., 1-1, courtesy McGraw-Hill Publishing Co.].

at low pressures. Retrograde condensation can occur anywhere within the cross-hatched area of Fig. 4-7. The opposite of retrograde condensation is *retrograde vaporization* by gas pressure rise, as from G to D. The critical point is at the juncture of the bubble and the dew point curves. When the pressure drops from the single-phase region M to the critical point C, rapid changes in density and other properties occur, and at C the system divides into two phases with close to 50 volume percent of each. The lines between the bubble and dew point curves in Fig. 4-7 represent constant volume percent liquid, and they converge at the critical point.

The shape of curves near the critical point depends upon the relative concentrations of volatile and nonvolatile components. Figure 4-7 is for a higher concentration of the more volatile components, like mixture 3 of Fig. 4-6. Diagrams like that of mixture 7, with the bubble point line going through a maximum before reaching the critical point, are very suitable for illustrating isobaric retrograde condensation by temperature rise.

Ternary diagrams from the work of Sage, Lacey, and co-workers illustrating critical loci for methane-propane-pentane and methane–*n*-butane–*n*-decane mixtures are shown in Figs. 4-8 [4-12,4-17] and 4-9 [4-56,4-65]. A triangular diagram of phase compositions and pressures for C_1–*n*-C_4–*n*-C_{10} mixtures at 280°F is shown in Fig. 4-10 [4-56].

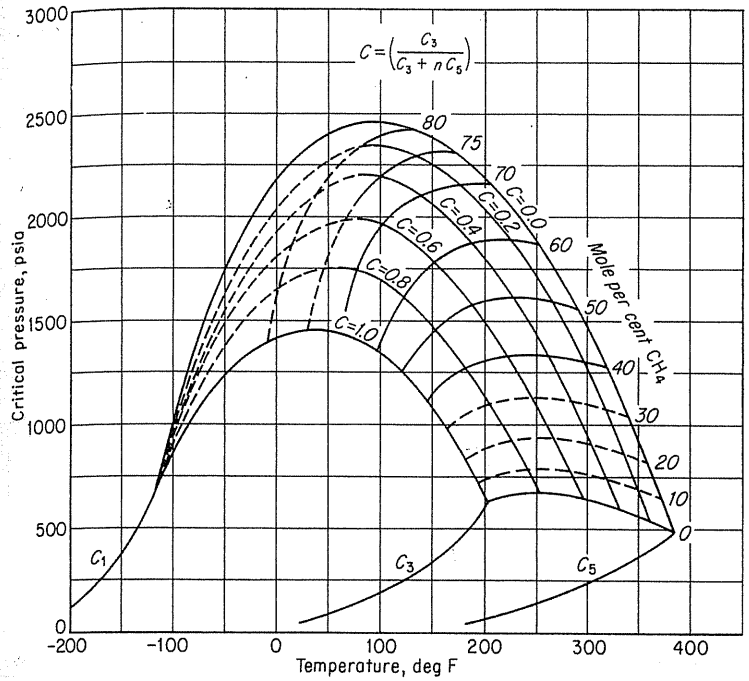

FIGURE 4-8
Critical loci for methane-propane-pentane mixture [data of Sage & Lacey, 4-12, 4-17; Katz et al., 1-1, courtesy McGraw-Hill Publishing Co.].

Complex Mixtures

In the 1930s glass-windowed gauges that could withstand high pressures were used to determine phase behavior (Fig. 4-11). The first known phase diagram of a natural gas containing heavier hydrocarbons (with the composition given in Table 4.1) is given in Fig. 4-12*a* [4-42]. The data were taken by isotherms with a constant temperature bath. The hydrocarbons were brought to a single phase by compression using mercury. The phase changes were observed during a pressure reduction brought about by mercury removal.

TABLE 4.1
Compositions of gas used in Fig. 4-12

C_1	59.7%
C_2	8.9
C_3	5.0
C_4	4.0
C_5	9.3
C_{6+}	12.2

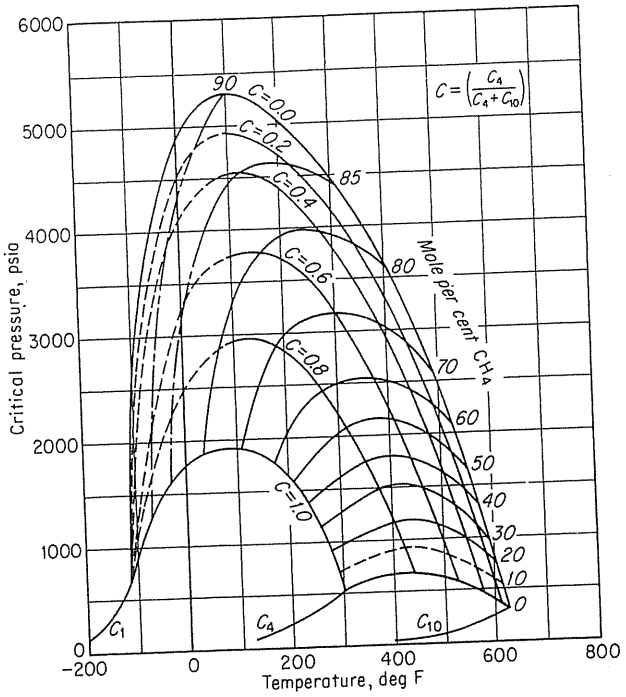

FIGURE 4-9
Critical conditions for C_1-C_4-C_{10} system [data of Sage & Lacey, 4-56, 4-65; Katz et al., 1-1, courtesy McGraw-Hill Publishing Co.].

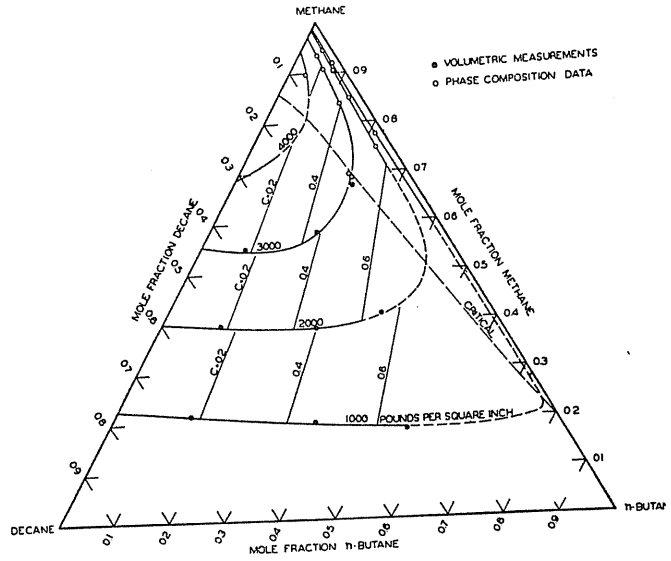

FIGURE 4-10
Compositions of coexisting phases for the C_1–n-C_4–n-C_{10} system at 280°F [Reamer, Sage & Lacey, 4-56, courtesy Ind. Eng. Chem.].

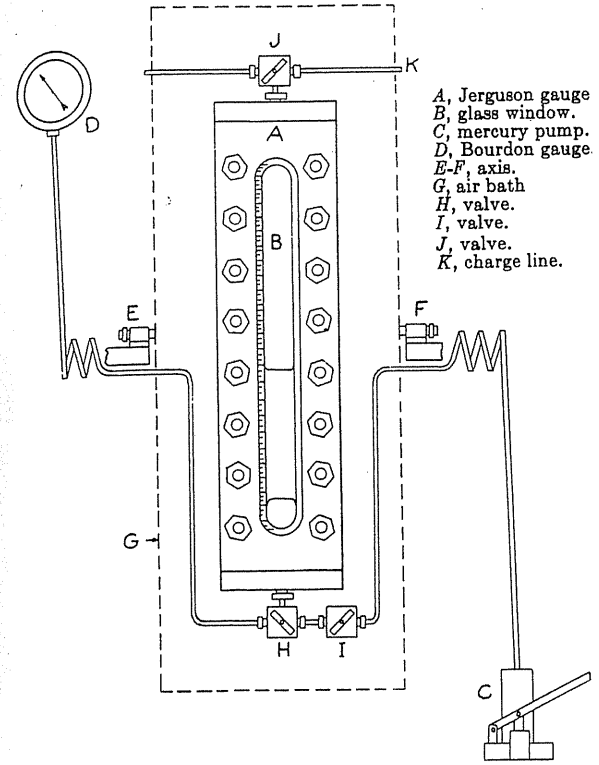

FIGURE 4-11
Apparatus for observing behavior [Katz, Vink & David, 4-42, courtesy SPE-AIME].

The glass-covered chamber appeared clear in single phase, but turned reddish brown by transmitted light near the two-phase boundary in the neighborh of the critical temperature. If the second phase appeared by boiling, a curve like the 85°F isotherm was plotted. If the appearance of a second phase during pressure reduction on the single-phase system resulted in mist or dew formation, a curve like the 212°F isotherm was plotted. Should the temperature be at or close to the critical temperature, the fluid could foam and settle into two phases of roughly equal volume, like the 169°F isotherm. The cross plot of the isotherms gives the more usual *P-T* phase diagram, Fig. 4-12b. The above-mentioned reddish brown persists with time and is called *critical opalescence* [4-38]. The color is attributed to light-absorbing molecular aggregations that occur at the test conditions.

4.4 VAPORIZATION BY GAS PRESSURE

In chemical laboratories, temperature rise (boiling) is used to vaporize liquids. But in the 1890s, Villard, a French investigator, found that he could vaporize paraffin wax, iodine crystals, and camphor by gas pressure (at room temperature) to 4000 psia (276 MPa) [1-1]. In 1948, Rzasa [4-61] vaporized a fuel oil compound

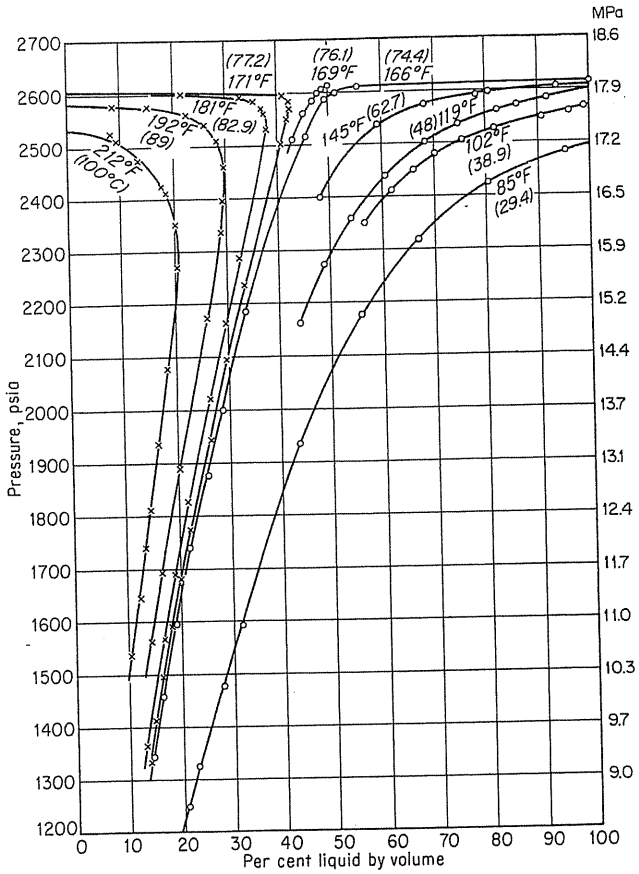

FIGURE 4-12
(*a*) Phase diagram for a mixture of natural gas and natural gasoline [Katz, Vink & David, 4-42, courtesy SPE-AIME].

(molecular weight 248, boiling point 580°F, 304°C) by methane pressure to 14,000 psia (96.5 MPa). The liquid constituents in the gas mixture of Fig. 4-12 were vaporized at 2600 psia (17.9 MPa). Gas condensate reservoirs that exhibit this property will be discussed later.

4.5 MOLECULAR THEORY OF GASES AND LIQUIDS

Gases and liquids are made up of molecules and may be treated on a molecular basis. The nature of the molecules and the forces existing between them control the properties of the fluid. The kinetic theory of gases, developed in the 19th century by such people as Joule, Clausius, Boltzmann, and Maxwell, treats a

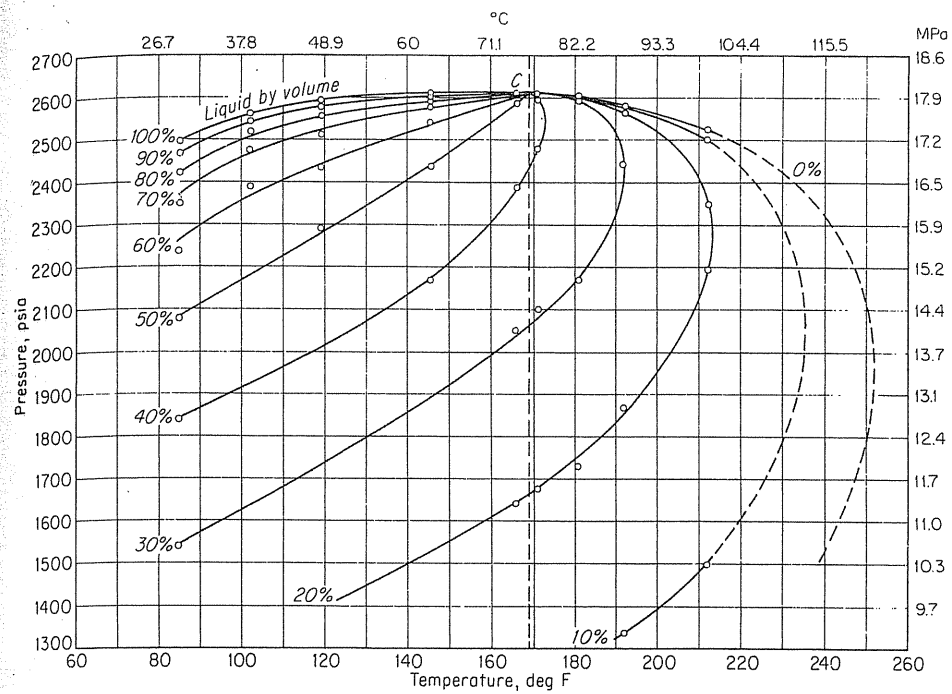

FIGURE 4-12
(*b*) P-T diagram of (*a*).

gas as a crowd of molecules, each moving on its own independent path, entirely uncontrolled by forces from the other molecules, although its path may be abruptly altered in both speed and direction whenever it collides with another molecule or strikes the boundary of the containing vessel. In its simplest state, a gas may be considered as composed of particles that have no volume and between which there are no forces.

Use of Moles

When considering phase behavior and fluid properties, one generally works with *moles* rather than units of mass as such. In the theory of matter, the concept of a mole has been used to relate the quantity of one substance to that of another. A mole is defined as an amount of substance containing as many entities as there are atoms in 12 grams of Carbon-12. For example, a mole (or *gram mole*) of oxygen atoms has a mass of 16 g (compare to 12 of carbon); a mole of O_2 is 32 g, and the mass of moles of other elements or molecules corresponds similarly to their atomic or molecular weights. Avogadro's rule states that at any given temperature and pressure, equal volumes of gas contain an equal number of molecules. The number is 6.02×10^{23} molecules, or 1 gram mole, for 22,415 cm^3 of a gas at 0°C

and 1 atm. A *pound mole* (lb mol) of oxygen gas is 32 lb; it has $453 \times 6.02 \times 10^{23} = 2.7 \times 10^{26}$ molecules. A pound mole occupies 359 ft^3 at 32°F and 1 atm, or 379 ft^3 at 60°F and 14.7 psia.

Equation of State—The Gas Law

The gas law relating pressure, temperature, and volume for a gas with molecules of zero size and without intermolecular forces is known as the *ideal*, or *perfect, gas law*:

$$PV = nRT \tag{4.2}$$

where P is the pressure, V is the volume, n is the number of moles, R is the gas constant and T is the absolute temperature. The values of R for various units of temperature, pressure, and volume are given in Table 4.2. For gases near atmospheric pressure, the ideal gas law is accurate within 5 percent or better. If more precise prediction is necessary or if gases at high pressure are to be treated, the ideal gas equation becomes inadequate. Voluminous data are available of *P-V-T* relations of pure substances and of mixtures of natural gases, from which the deviations from ideal gas laws may be noted. Bibliographies are given in references [1-1,1-15].

The *real gas law* recognizes that gases are not ideal and utilizes a *compressibility factor* Z to represent the deviation from ideality:

$$PV = ZnRT \tag{4.3}$$

TABLE 4.2
Gas law constant R

Unit of pressure	Unit of temp	Unit of volume	R
atm	K (°C + 273.15)	liter	0.082055 (for n in gram moles)
psia	°R (°F + 460)	ft^3	10.73 (lb mol)
lb/ft^2	°R (°F + 460)	ft^3	1545 (lb mol)
kPa	K	m^3	8.314 (kmol)
	R for air when n is given in units of mass		
lb/ft^2	°R	ft^3	53.2 (lb)
kPa	K	m^3	0.287 (kg)
Pressure	**Temperature**	**Volume per mole**	
1 atm	°C	22.414 liters/mol	
14.7 psia	32°F	359 ft^3/lb mol	
14.7 psia	60°F	379 ft^3/lb mol	
101.325 kPa	288 K	23.644 m^3/kmol	
101.325 kPa	273.15 K	22.414 m^3/kmol	

Z varies with pressure and temperature, and it can be measured and tabulated for various gases or derived theoretically. Van der Waals wrote an equation of state a century ago that improved upon the ideal gas law, and a long series of equations have been written since then (e.g., Redlich-Kwong, Soave, and Peng-Robinson) in efforts to improve the accuracy furthur. Equations of state have advantages over graphical information and, based on binary interaction coefficients derived from experimental data, can be extended to systems of any known composition. The derivation of the Peng-Robinson equation is in Appendix D.

Compressibility of Natural Gases

P-V-T measurements for gases under pressure started in the latter part of the 19th century; an upsurge in measurements occurred for natural gases, led by the work of Sage and Lacey on their API project [4-62,4-63]. Out of this study came the compressibility factor chart made by Standing and Katz (Fig. 4-13 [4-72]) with the advice and assistance of G. G. Brown and D. Holcomb. The basis for the correlations of data used with this chart is Van der Waals's *theorem of corresponding states*: Substances should have similar properties at corresponding conditions normalized to some basic properties like the critical temperature and pressure. The use of *reduced pressure*, actual pressure divided by critical pressure, and *reduced temperature*, actual temperature divided by critical temperature (absolute), to determine compressibility factors brought reasonable but not exact correlations [1-1]. For example, at a temperature equal to twice the critical temperature ($T_r = 2$) and a pressure equal to four times the critical pressure ($P_r = 4$), methane and ethane should have the same deviations Z from ideal gas laws; however, they are 0.959 and 0.962 respectively. Reference [1-1] gives other comparisons.

4.6 NATURAL GASES

Natural gases are composed primarily of methane with varying amounts of ethane, propane, and butanes (see Table 1.2). The work of Kay [4-43] made possible the use of the theorem of corresponding states for mixtures. He suggested the use of molal-average critical pressures and temperatures for mixtures in place of the critical pressures and temperatures used for pure compounds. These molal-average properties are called the *pseudocritical temperatures* and *pseudocritical pressures* for mixtures, and they may be used like true criticals for purposes of comparing corresponding states. The pseudocritical point has no physical significance, but it approximates the point of convergence of constant-volume lines (isochors) on a pressure-temperature diagram. Figure 4-14 [4-62,4-63] illustrates this property for the pseudocritical point for a 70 mole % methane–30 mole % butane mixture. It also shows the relationship to the true critical point for the mixture.

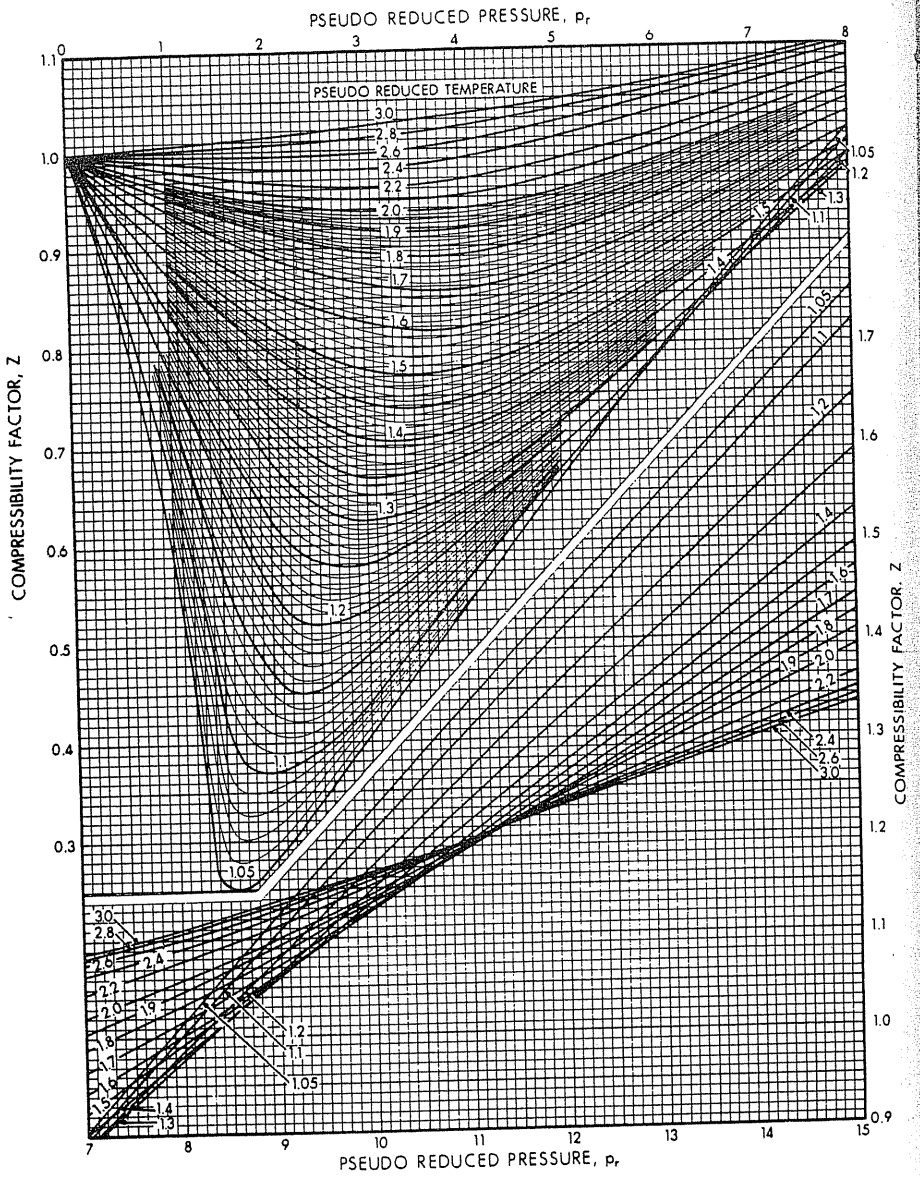

FIGURE 4-13
Compressibility factors for natural gas [Standing & Katz, 4-72, courtesy SPE-AIME].

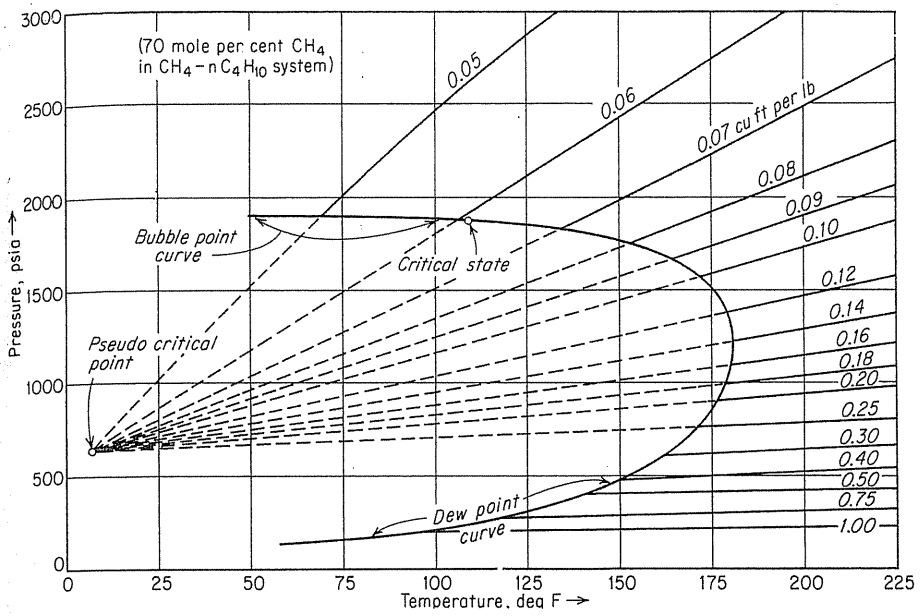

FIGURE 4-14
Pressure-temperature diagram illustrating pseudocritical point of 0.7 mole fraction CH_4 in CH_4-C_4H_{10} system [Sage & Lacey data, 4-62, 4-63; Katz et al.a, 1-1, courtesy McGraw-Hill Publishing Co.].

In using the chart for compressibility factors, Fig. 4-13, for natural gases, other items should be addressed. First, the pseudocritical properties of the heavy constituents in a gas, C_6 or C_7^+, should be determined. A chart has been constructed to give the pseudocritical values when the liquid density and molecular weight of the C_7^+ fraction are known (Fig. 4-15 [4-53]).

It is also useful to correlate pseudocritical properties as a function of gas gravity (mol. wt./29, the mol. wt. of air) for natural gases with no more than 2–3 percent nonhydrocarbons present. To correlate a large number of gases, it seems necessary to give a curve for high pressure gas/condensate reservoir fluids [4-9] (Fig. 4-16).

Table 4.3 illustrates the computation of compressibility factors and gas densities for a gas of known composition at a given temperature and pressure. Table 4.4 gives the critical temperatures and pressures of various constituents.

The original Standing and Katz chart covered pressures to $P_r = 15$ or about 10,000 psia (68.9 MPa). The chart was extended to $P_r = 30$ for the *Handbook* [1-1] (Fig. 4-17). Hall and Yarborough [4-79] used high-pressure data and an equation of state to extend the original Z chart to $P_r = 24$. At temperatures above 1.15 T_r, the agreement of their equation with chart values was within 0.3 percent.

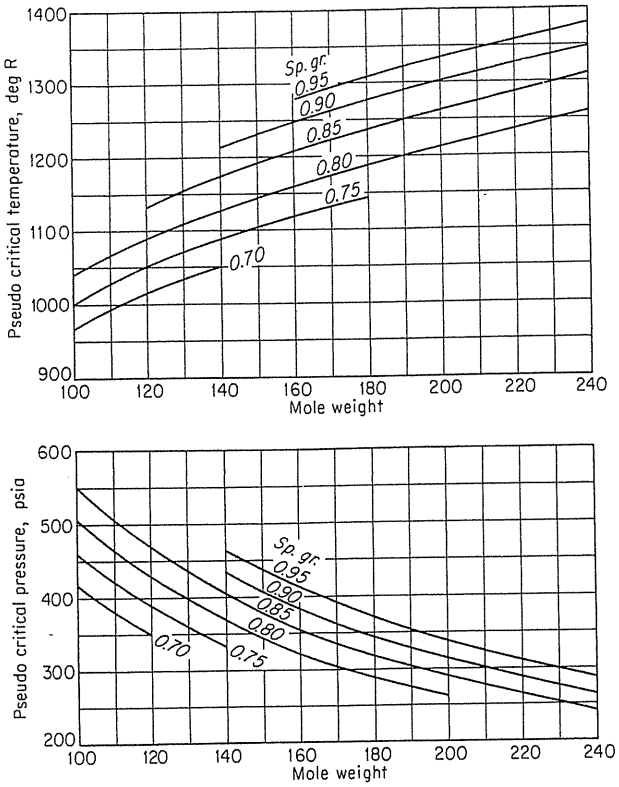

FIGURE 4-15
Pseudocritical temperatures and pressures for C_7^+ fractions [Matthews, Roland & Katz, 4-53, courtesy NGAA (now GPA)].

For natural gases with nominal CO_2 and N_2 present, Z is a function of P, T, and G. For such gases of known gravity, charts such as those in Fig. 4-18 are convenient.

Effects of Nitrogen, Carbon Dioxide, and Hydrogen Sulfide

The general agreement in the theorem of corresponding states for natural gases depends, in part, on the family characteristics of the paraffins (methane, ethane, etc.) and their decreasing amounts in natural gases; in particular, the use of gas gravity depends on these characteristics. Accordingly, the presence of N_2, CO_2, and H_2S in natural gases requires special attention. *P-V-T* data have been taken on gases containing these components, providing the basic information for testing computation procedures and the validity of the Z chart. Table 4.5 [4-66]

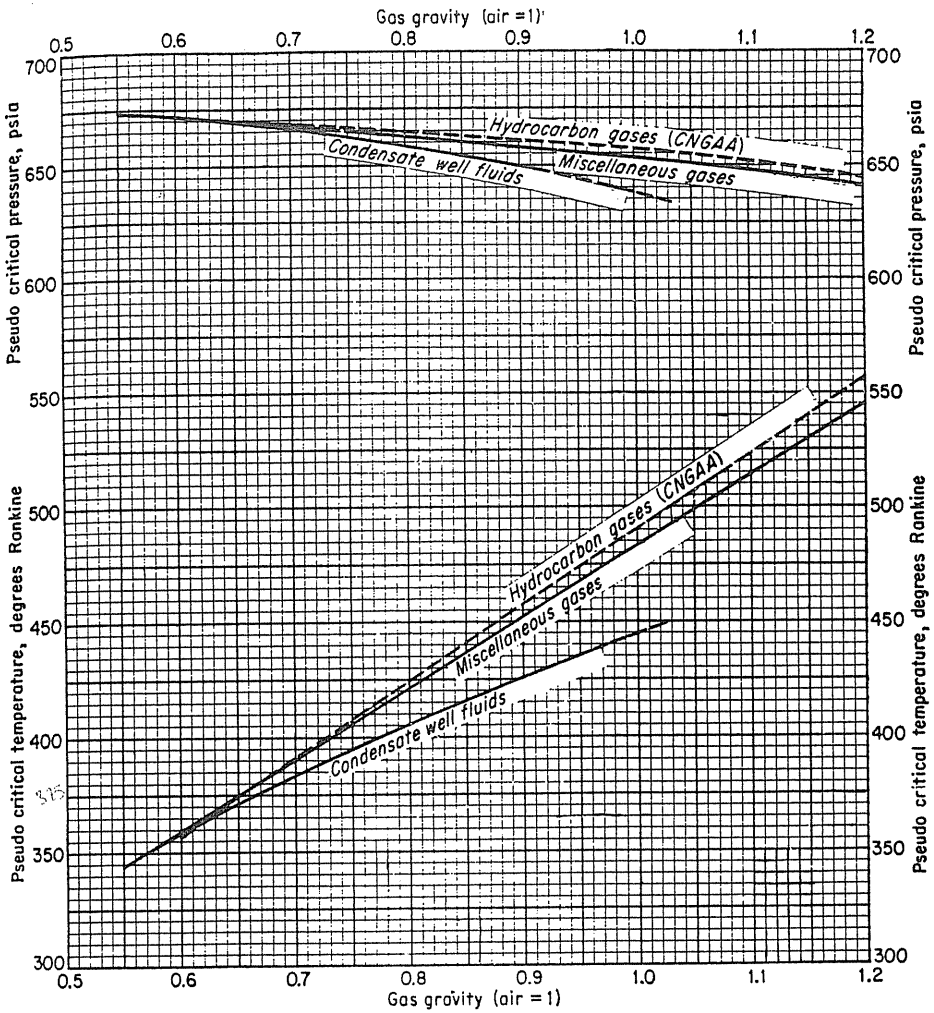

FIGURE 4-16
Pseudocriticals of natural gases including gas condensates [Brown et al., 4-9, courtesy NGAA (now GPA)].

reproduces example data for checking any procedure employed for obtaining Z's [4-10,4-79]. Various ways have been devised for handling compressibility factors for gases with N_2, CO_2, and H_2S [4-10,4-41,4-58,4-66,4-76,4-77].

The Wichert and Aziz [4-76] method of handling the effects of CO_2 and H_2S on Z involves a correction to the pseudocritical temperature and pressure. Figure 4-19 provides the adjustment factor for the pseudocritical temperature based on mole percents of CO_2 and H_2S. Here is an outline of the method:

TABLE 4.3
Computation of the density of a natural gas from the gas composition and the compressibility factor chart

With the composition shown, at 1000 psia and 90°F (6.895 MPa and 32.2°C)

	Computation of pseudocritical point						
Constituent	Mole fraction y	Molecular weight	Pounds per 16 mol gas	Critical temp. T_c, °R	yT_c	Critical pressure P_c, psia	yP_c
CO_2	0.0040	44	0.17	548	2.1	1073	4.3
C_1	0.9432	16	15.09	343	323.5	673	634.7
C_2	0.0390	30	1.17	550	21.4	708	27.6
C_3	0.0117	44	0.51	666	7.8	617	7.2
i-C_4	0.0080	58	0.04	735	0.6	528	0.4
n-C_4	0.0013	58	0.07	766	1.0	551	0.7
	1.0000		17.05		356.4		674.9

Reduced temperature $T_r = T/T_c = (90+460)/356.4 = 1.54$
Reduced pressure $P_r = P/P_c = 1000/674.9 = 1.48$
Gas gravity $G = 17.05/29.0 = 0.588$
From Fig. 4-13, compressibility factor $Z = 0.872$

$$\text{Density } \rho = \frac{PM}{ZRT} = \frac{(1000)(17.05)}{(0.872)(10.73)(550)} = 3.31 \text{ lb/ft}^3$$

$$= \frac{(6.895 \times 10^3)(17.05)}{(0.872)(8.314)(305)} = 53.16 \text{ kg/m}^3$$

It should be noted that CO_2 does not belong to the C-H family; hence, corrections should be made to the above estimates of T_c and P_c. In this case, the corrections are assumed to be negligible.

1. A = sum of the mole fractions of CO_2 and H_2S in the gas.
2. B = mole fraction of H_2S in the gas.
3. The adjustment factor ϵ_3 to the pseudocritical temperature may be read directly from Fig. 4-19 or obtained from the following equation:

$$\epsilon_3 = 120(A^{0.9} - A^{1.6}) + 15(B^{0.5} - B^{4.0}) \tag{4.4}$$

4. The adjusted pseudocritical temperature and pressure of the gas, in terms of °F and psia, can be calculated as follows:

$$T'_c = T_c - \epsilon_3 \text{ and } P'_c = \frac{P_c T'_c}{T_c + B(1-B)\epsilon_3} \tag{4.5}$$

5. With these adjusted P'_c and T'_c, one proceeds to find Z from Fig. 4-13 in the usual manner.

Example 4.2. Given the composition of mixture 18 shown on Table 4.6, find the compressibility factor at 1623 psia (11.2MPa) and 100°F (37.8°C). The measured

TABLE 4.4
Critical properties of constituents of natural gas [courtesy GPA]

Constituent	Molecular weight	Critical temperature °R	Critical temperature °K	Critical pressure psia	Critical pressure MPa
C_1	16.04	343.3	196.7	673.1	4.641
C_2	30.07	549.8	305.4	708.3	4.883
C_3	44.09	666.0	370.0	617.4	4.257
i-C_4	58.12	734.7	408.2	529.1	3.648
n-C_4	58.12	765.3	525.2	550.7	3.797
i-C_5	72.15	829.8	461.0	483.0	3.330
n-C_5	72.15	845.6	469.8	489.5	3.375
C_6	84.0	905.4	503.0	431.6	2.976
C_7	96.0	975.8	542.1	437.1	3.014
C_8	107.0	1032.5	573.6	419.7	2.894
C_9	121.0	1086.1	603.4	391.0	2.696
C_{10}	134.0	1131.9	628.8	361.3	2.491
C_{11}	147.0	1171.0	651.0	335.1	2.318
C_{12}	161.0	1207.0	671.0	311.0	2.144
C_{13}	175.0	1239.0	688.0	292.1	2.014
C_{14}	190.0	1268.0	704.0	277.8	1.915
C_{15}	206.0	1301.0	723.0	268.2	1.849
H_e	4.0	9.4	5.2	33.2	0.228
Air	29.0	238.4	132.4	547.0	3.771
N_2	28.02	226.9	126.0	492.0	3.392
O_2	32.0	277.9	154.3	730.0	5.033
CO_2	44.01	547.7	304.3	1073.0	7.398
H_2S	34.08	672.4	1210.3	1306.0	9.005

Z is 0.8211. Use the Weichert and Aziz adjustment factor method [4-76] and the Standing and Katz chart.

Solution. Find the usual critical temperature and pressure data in Table 4.4. Then, calculate the pseudocritical properties for the mixture as shown in Table 4.6.

From Fig. 4-19, read the critical temperature adjustment factor, using CO_2 and H_2S percentages. In this case, $\epsilon_3 = 20$. The adjusted pseudocritical temperature and pressure are

$$T'_c = T_c - \epsilon_3 = 384.5 - 20 = 364.5°\text{R}$$

$$P'_c = \frac{P_c T'_c}{T_c + B(1-B)\epsilon_3} = \frac{748.3 \times 364.5}{384.5 + 0.0735(1-0.0735) \times 20} = 678.7 \text{ psia}$$

Thus, the reduced temperature T_r and pressure P_r are

$$T_r = \frac{T}{T'_c} = \frac{560}{364.5} = 1.54 \qquad P_r = \frac{P}{P'_c} = \frac{1623}{678.7} = 2.39$$

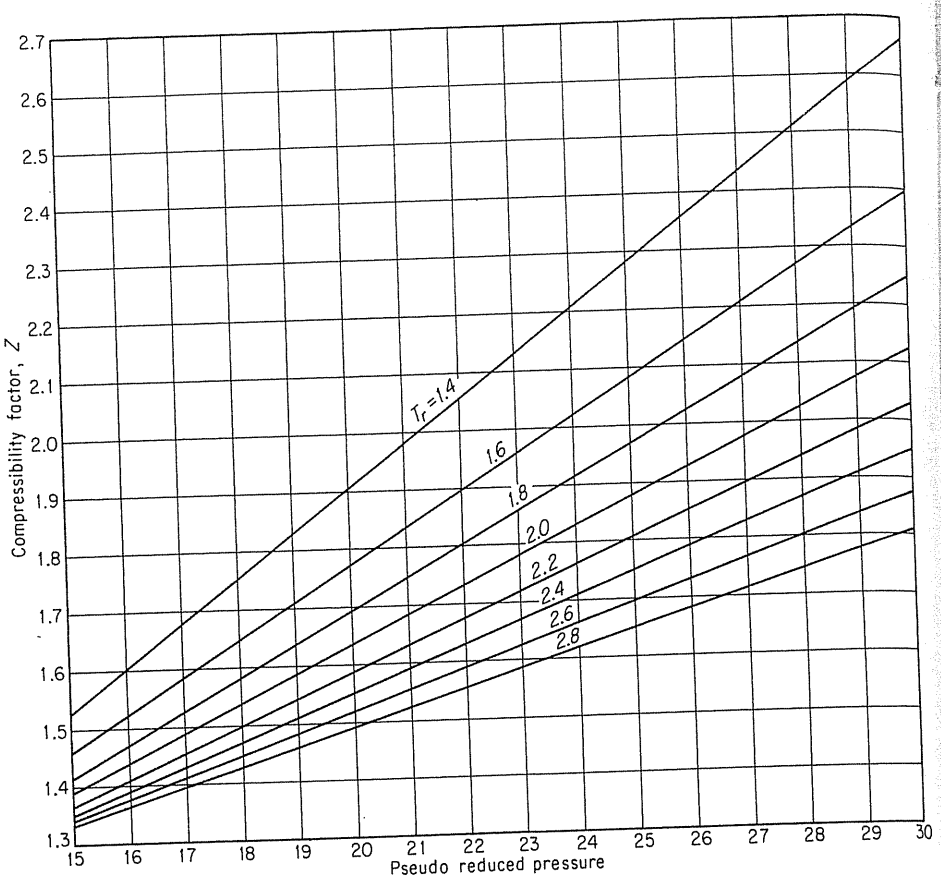

FIGURE 4-17
Compressibility factors for natural gases at 10,000–20,000 psia (68.9–137.9 MPa) [Katz et al., 1-1, courtesy McGraw-Hill Publishing Co.].

From Fig. 4-13 at $P_r = 2.39$ and $T_r = 1.54$, Z is 0.82, which is in good agreement with the measured Z of 0.8211.

Choice of Methods for Obtaining Compressibility Factors (Z)

There are many computer programs for calculating Z at designated temperature and pressure for a given gas composition. Some programs may accept gas gravity instead of composition, but these may require percentages of N_2, CO_2, and H_2S. One may want to calibrate such computations by using data from Table 4.5.

The American Gas Association (AGA) meter committee has a system for finding the ϵ_3 factor or $1/Z$ from gas gravity, temperature, pressure, and composition of constituents CO_2, H_2S, and N_2. AGA Report No. 8, edited by Starling

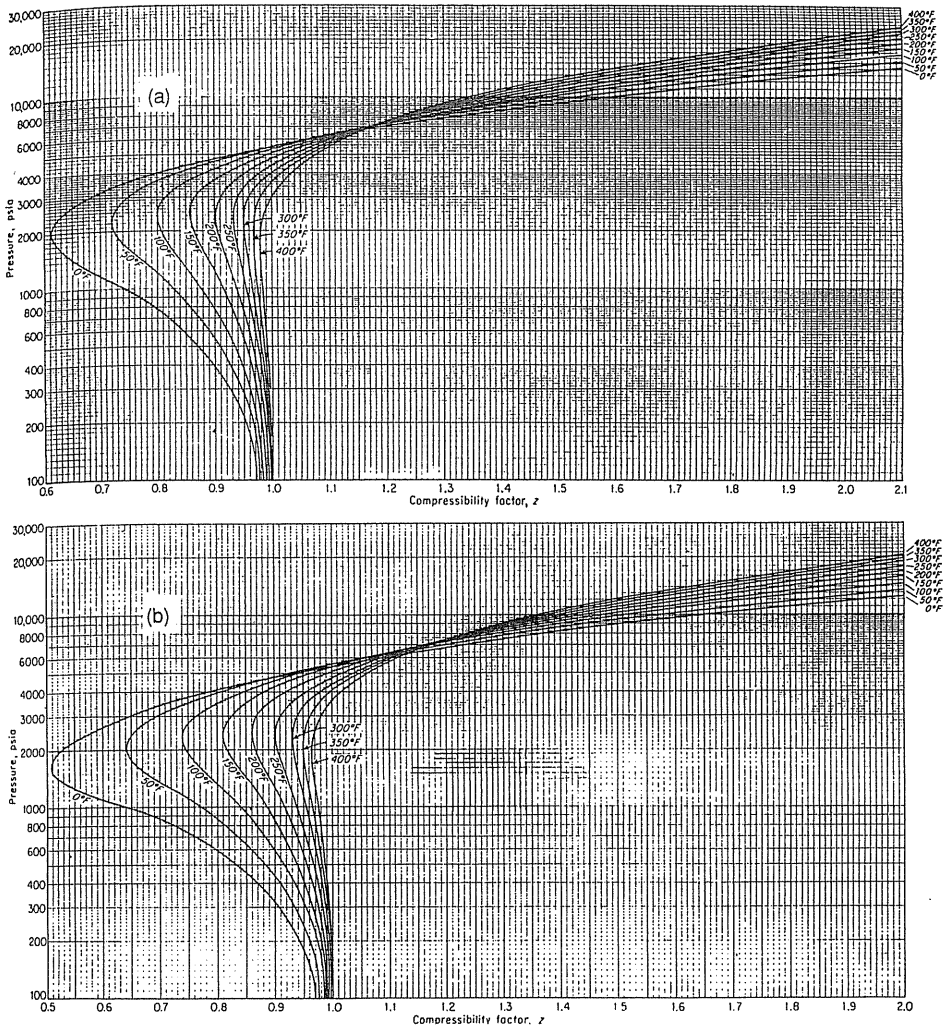

FIGURE 4-18
Compressibility factor for (*a*) 0.6-gravity and (*b*) 0.7-gravity natural gas [Katz et al., 1-1, courtesy McGraw-Hill Publishing Co.].

[6-53], presented a program that is used by AGA as a standard (this will be discussed in Section 6.5). Report No. 8 includes accurate data on Z's to 20,000 psia (1379 MPa).

The chart of Fig. 4-13 may be used for hand calculations or a hand-held computer may have a program (like the one listed in Appendix B) for using Yarborough and Hall's equation [4-79]. Table 4.3 showed a calculation of the density of a natural gas using compressibility factors from the chart. Even

TABLE 4.5
Experimental compressibility factor Z data [4-10,4-66]

Chromatographic analysis of experimental mixtures—
Mixture A (CH_4: 0.8360, C_2H_6: 0.1170, H_2S: 0.0470):
Mixture B (CH_4: 0.7458, C_2H_6: 0.0474, CO_2: 0.2016, N_2: 0.0052)

Pressure, psia	Mixture A			Mixture B		
	101.1°F	129.7°F	160.2°F	100°F	130°F	160°F
1026	0.865	0.887	0.911	0.865	0.889	0.910
2026	0.785	0.825	0.861	0.778	0.825	0.860
3026	0.789	0.825	0.859	0.778	0.820	0.855
4026	0.853	0.876	0.900	0.838	0.867	0.893
5026	0.942	0.954	0.967	0.923	0.941	0.956
6026	1.039	1.042	1.047	1.018	1.026	1.034
7026	1.141	1.134	1.131	1.116	1.116	1.115

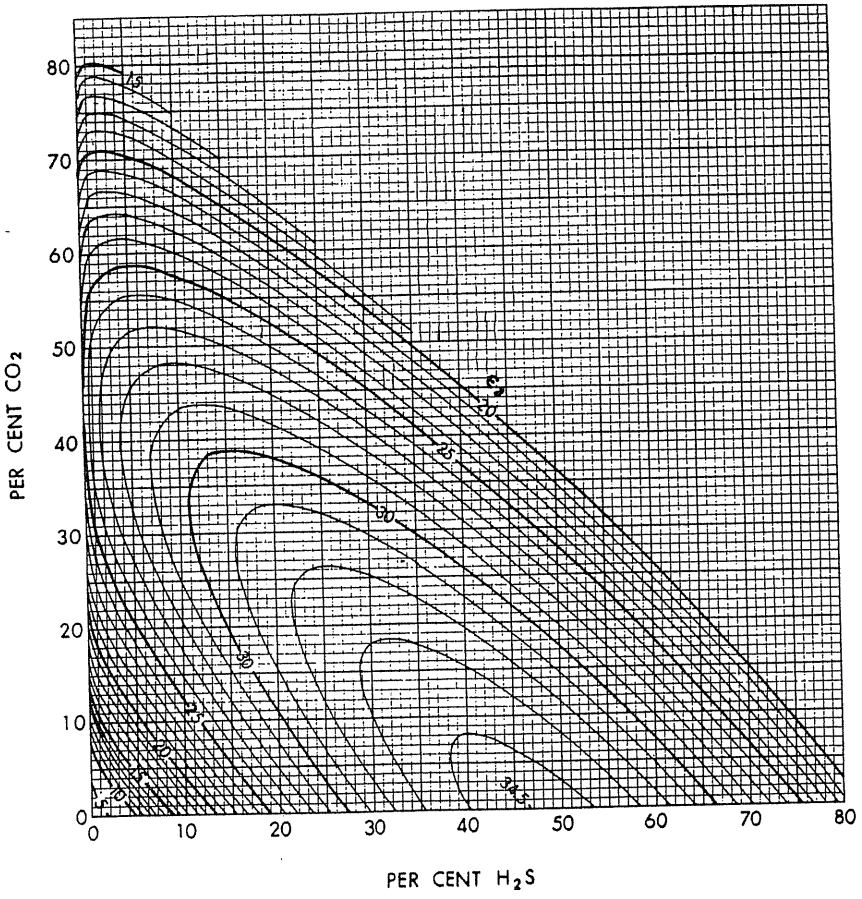

FIGURE 4-19
Correction factor for pseudocritical temperature for gases with CO_2 and H_2S present [Wichert & Aziz, 4-76, courtesy Hydrocarbon Processing].

TABLE 4.6
Mole fractions and critical properties for mixture 18

Component	y	T_c, °R	yT_c	P_c, psia	yP_c
N_2	.0081	226.9	1.8	492	4.0
C_1	.8303	343.3	285.0	673.1	558.9
CO_2	.0744	547.7	40.7	1073	79.8
C_2	.0130	549.8	7.1	708.3	9.2
H_2S	.0735	672.4	49.4	1306	96.0
C_3	.0007	666.0	0.5	617.4	0.4
			384.5°R		748.3 psia

for careful volumetric work with hydrocarbon gases at atmospheric pressure, compressibility factors are needed. McKetta et al. plotted Z data versus reduced temperature and pressure near 1 atmosphere (see [1-1]).

4.7 HANDLING TWO-PHASE SYSTEMS: CONDENSATES MAY HAVE NEGATIVE APPARENT VOLUMES

Natural gases enter the two-phase region during some P-V-T measurements, but the ability to compute the density of the two-phase system diminishes only nominally [1-1]. In computing the material balance on a gas-condensate reservoir the two-phase Z should be used.

Negative apparent volumes for liquids dissolved in a high-pressure gas phase can be determined from compressibility factor data [4-41]. The senior author once observed this unusual behavior in the course of preparing a cylinder of natural gas for use in the laboratory. The cylinder of gas, free from liquid at 75°F (24°C) and 2005 psi (13.8 MPa) was cooled to 32°F (0°C); about a pint of liquid was drained from the cylinder; and its temperature was brought back to 75°F (24°C). The pressure in the cylinder rose to 2060 psi (14.2 MPa). It would follow that if the liquid that was removed were reinjected into the cylinder, the pressure would drop.

Figure 4-20 [4-41] was constructed from data by Sage, Hicks, and Lacey [4-62, 4-63] on the methane-butane system.

4.8 DENSITY OF NATURAL GAS

Since the pseudocriticals of natural gases are a function of gas gravity (G), it follows that the density is a function of T, P, and G. From the pseudocriticals of Fig. 4-16 and the compressibility factors of Fig. 4-13, the density may be computed for a given gas gravity. This has been done for several gas gravities; the density of 0.6-gravity gas is plotted in Fig. 4-21 [4-72].

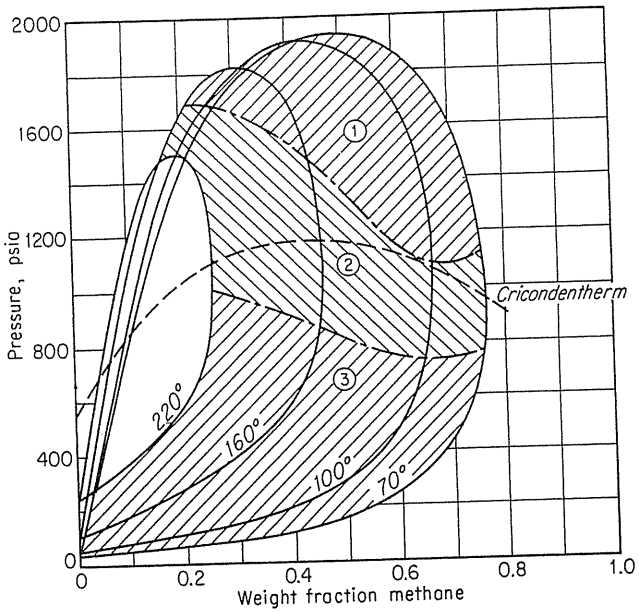

FIGURE 4-20
Apparent volumes of liquid butane in methane-butane system [Katz & Sliepcevich, 4-41, courtesy Oil Weekly].

4.9 DENSITY OF LIQUIDS

The density of liquids for pure substances decreases with increasing temperature and reaches the density of the vapor at the critical temperature (Fig. 4-22). Liquid mixtures have a similar change in density with temperature, as given by tables of corrections [4-2]. The density of a pure constituent is illustrated for propane in Fig. 4-23.

The density of a liquid at atmospheric pressure can be determined in the laboratory by the use of a hydrometer or pycnometer. Corrections of density for temperature to some standard temperature such as 60°F (15°C) are made by using standard measurement tables [4-2]. Pure hydrocarbon liquids such as pentane and hexane have nearly additive volumes at room temperature and pressure.

The densities of hydrocarbon liquids can be computed from the compositions of the liquids and the densities of their components [4-71]. Constituents, propane and the heavier, at 60°F (15°C) are assumed to have additive volumes. Given the densities of liquid mixtures of methane and heavier hydrocarbons at 60°F (15°C) and 1 atm, it is possible to compute the apparent density of the dissolved methane. Figure 4-24 gives the apparent density of methane and ethane in hydrocarbon liquids with weight percent of concentration and density of the

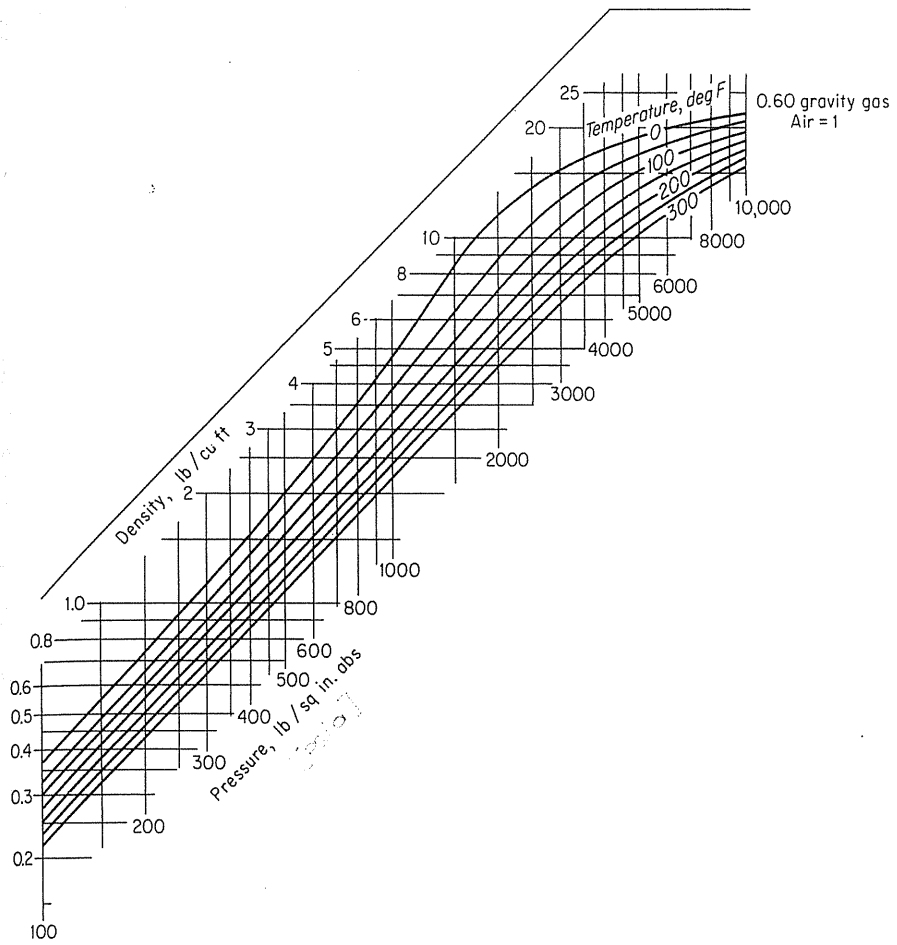

FIGURE 4-21
Density of 0.6-gravity gas [Standing & Katz, 4-72, courtesy SPE-AIME].

solvent as variables. Table 4.7 [1-1] gives an example of computation of a liquid's density from its composition. The apparent density of dissolved nitrogen is 0.48 g/cm^3 for a solvent having a density of 0.68 g/cm^3.

The effect of pressure on the density of a liquid varies with the liquid density, the higher compressibilities occurring for low-density liquids or those approaching the critical temperature. Figure 4-25 gives a correction for pressure at 60°F based on the density of the liquid. Computerized equations of state normally compute the density of the liquid from its composition just as they do for gases.

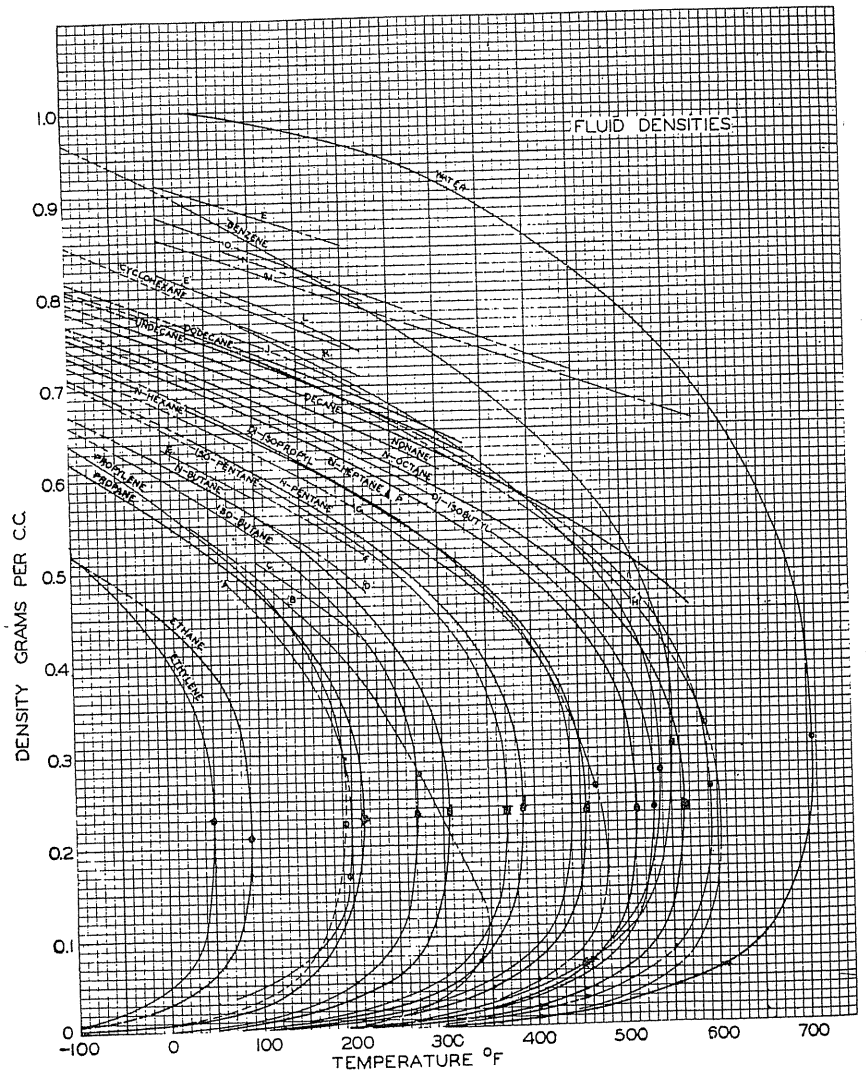

FIGURE 4-22
Orthobaric density of liquids and vapors [Brown, Katz, Oberfell & Alden, 4-9, courtesy NGAA (now GPA)].

4.10 DENSE PHASE

The terms *gas* or *vapor* and *liquid* have been used to distinguish the less dense and the more dense phases when two phases are present as along curve H-C in Fig. 4-2. At high pressures and especially above the critical pressures for a group of mixtures, one searches for a name—is it a gas or a liquid? The term *dense*

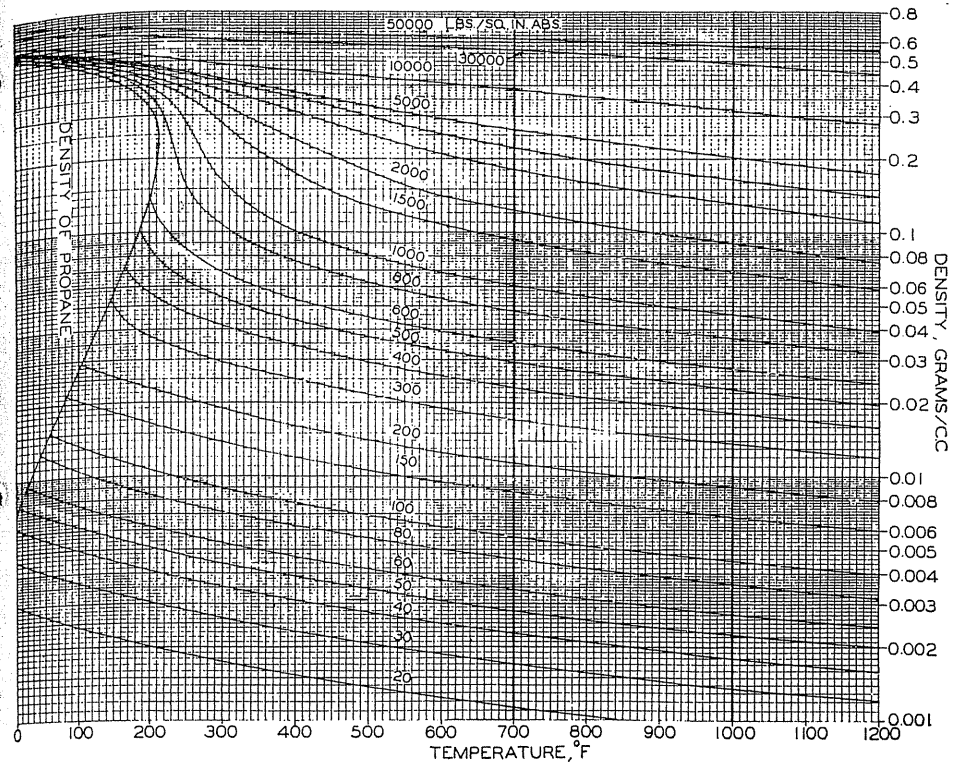

FIGURE 4-23
Density of propane [Brown, Katz, Oberfell & Alden, 4-9, Courtesy NGAA (now GPA)].

phase was coined to describe this condition, as in the area represented by f-g on Fig. 4-2, or at pressures of 2700 psia (18.6 MPa) on Fig. 4-12. A dense phase gas line was designed for bringing natural gas from Alaska to the lower 48 states at temperatures of 15°F (264 K) and top pressures of 1680 psia (11.6 MPa). The density was of the order of 12 lb/ft^3 (300 kg/m^3) [4-45].

4.11 SURFACE TENSION

Surface tension of liquid-vapor systems or interfacial tension in liquid-liquid systems is important in process separations and in flow or displacement from porous media. A system for computing surface tension is based on phase densities and molecular weights, composition, and a parachor for each component.

The measurement of surface tension was discussed in Chapter 2. Here the calculation of vapor-liquid interfacial tension from the composition and properties of the phases is presented. Surface tension is important in the reservoir, particularly for gas-liquid displacement and liquid retention in porous media. In surface

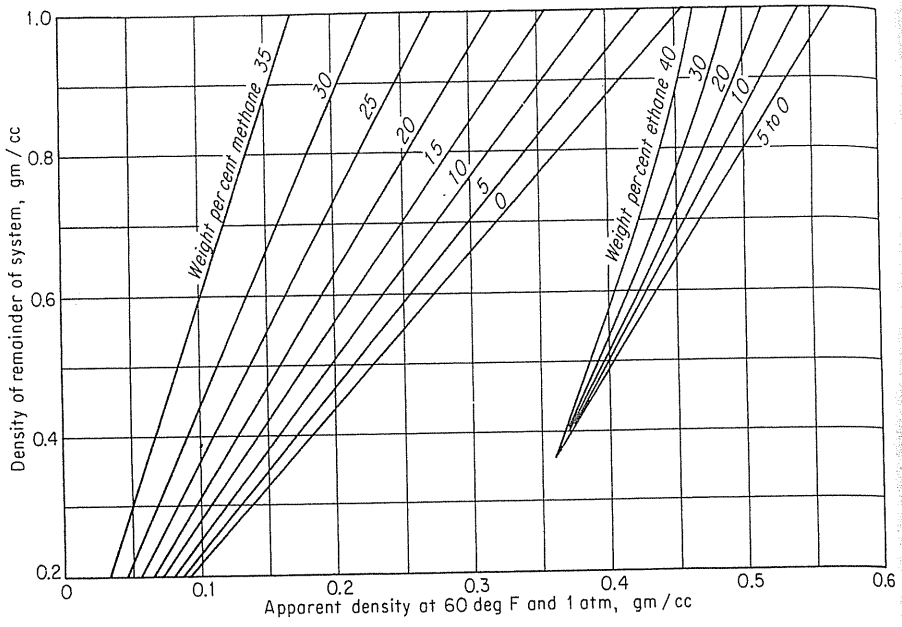

FIGURE 4-24
Apparent density of methane and ethane in liquids [Standing & Katz, 4-71, courtesy SPE-AIME].

processing, surface tension has to do with foams and droplet formation in flowing two-phase streams in process equipment.

Methods other than capillary rise for measuring surface tension include the ring method, wherein the force required to lift a ring out of a liquid is measured [1-1]. A method more easily adapted to pressurized equipment is the pendant-drop method [1-1]. The surface tension for pure substances is shown in Fig. 4-26 [4-40]. The surface tension reduces to zero as the vapor and liquid phase merge at the critical point. Near-critical vapor-liquid mixtures show extreme effects of the low interfacial tension by the persistence of foams. The theorem of corresponding states applies for surface tensions; a single curve represents the paraffin family with moderate deviations [1-1,4-40]. Early work on crude oils and gases showed that dissolved gas reduced the surface tension of the gas-liquid interface.

Weinaug and Katz [4-78] reported the surface tension of methane-propane mixtures under pressure (Fig. 4-27). In Fig. 4-28, surface tension curves are superimposed on a pressure-temperature diagram, starting with zero surface tension at the critical locus. Methane-propane mixtures have surface tensions less than 0.5 dyn/cm over the last 200 psi of pressure below the critical locus.. The surface tensions of methane-propane mixtures were correlated by Weinaug and Katz [4-78] by the use of parachors for the pure constituents and Eq. (4.6):

TABLE 4.7
Computation of liquid density at 1600 psia (11.0 MPa) and 120°F (49°C) from composition [Katz et al., 1-1, courtesy McGraw-Hill Publishing Co.]

Constituent	Liquid mole fraction	Mol. wt	Grams/ mole	Liquid density, grams/cm³	Cm³/ mole
Carbon dioxide	0.0029	44	0.13	(0.420)	0.31
Methane	0.2943	16	4.73	(0.320)	(14.77)
Ethane	0.0510	30	1.53	(0.485)	(3.16)
Propane	0.0356	44	1.57	0.5077	3.09
Isobutane	0.0167	58	0.97	0.5631	1.72
n-Butane	0.0275	58	1.60	0.5844	2.75
Pentanes	0.1463	72	10.55	0.6270	16.80
Hexanes	0.1283	86	11.05	0.6630	16.70
Heptanes +	0.2974	196	58.30	0.8500	68.50
C_1 +			90.43		127.80
C_2 +			85.70		113.03
C_3 +			84.17		109.87

Density $C_1+ = 90.43/127.8 = 0.708$ g/cm³.
Density $C_3+ = 84.17/109.87 = 0.768$ g/cm³.
Density $C_2+ = 85.7/113.03 = 0.757$ g/cm³.
Density at 60°F and 1 atm = 0.708 g/cm³.
By density correction for pressure of 1600 psia (Fig. 4-25), g/cm³, +0.010, density 0.708 goes to 0.718.
By density correction for temperature of 120°F (line B on Fig. 4-22), density 0.718 goes to 0.691.
Density at 120°F and 1,600 psia = 0.691 g/cm³.

$$\sigma^{1/4} = \sum_i \text{Pac}_i \left(x_i \frac{\rho_L}{M_L} - y_i \frac{\rho_V}{M_V} \right) \tag{4.6}$$

where Pac is the parachor for any constituent or mixture, x and y are the mole fractions in liquid and vapor phases respectively, ρ_L and ρ_V are the densities of liquid and vapor phases in g/cm³, M_L and M_V are the molecular weights of liquid and vapor phases, and σ is the surface tension in dyn/cm. Subscript i refers to individual constituents in the mixture.

It should be noted that the densities and molecular weights are for the entire liquid and vapor phases. Parachors are predicted from the structure of the molecules or can be computed for pure substances and mixtures from a surface tension measurement taken under atmospheric conditions. The parachors for pure substances are given in Table 4.8. Measurements were made on the heptane and heavier fractions of crude oils from Standing [4-71] to obtain parachors.

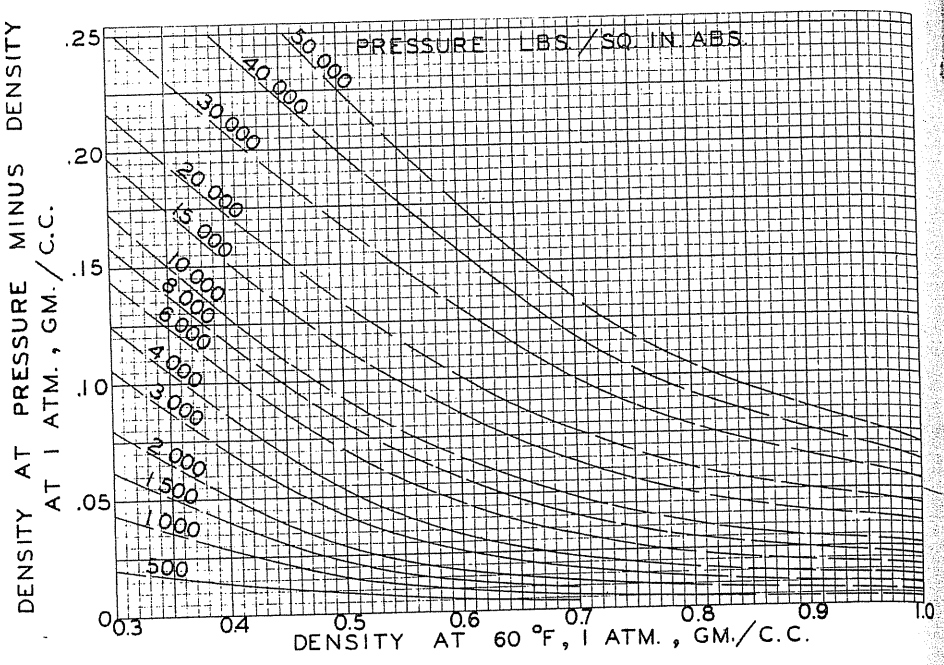

FIGURE 4-25
Effect of pressure on the density of liquids at 60°F [Standing & Katz, 4-71, SPE-AIME].

These values, with those for pure substances, are plotted in Fig. 4-29 [Katz et al., 4-78]. Firoozabadi et al. [4-21] reported parachors and measured surface tensions for crude oil distillation cuts at 1000 to 2000 psia (6.9–13.8 MPa). These parachors are also plotted on Fig 4-29. The study showed that the use of distilled cuts for obtaining parachor measurements gives values that do not lie on the parachor–molecular weight curve found for the last fraction of a crude oil containing asphalts. This work indicated that the calculated results of Katz, Monroe, and Trainer (Fig. 4-30) for high pressure were too low.

Equation (4.6) for computing surface tension was applied to equilibrium mixtures of crude oil and natural gas. The results, along with data from Schwartz [4-67] and Jones [4-30], are given in Fig. 4-30 [4-39]. The surface tension of a crude oil at 115°F (46.0°C) and 2700 psia (18.6 MPa) was later measured at 1.1 dyn/cm; the computed value was 0.85 dyn/cm (0.85 mN/m) [1-1]. In general, one can be fairly sure that a hydrocarbon liquid, condensate, or crude oil, saturated with natural gas in the reservoir at pressures of 3000 psia (20.7 MPa) or more, will have a surface tension of 2.2 dyn/cm (2.2 mN/m) or less. Table 4.9 gives an example computation of surface tension with parachors.

Hough and his associates studied surface tension of hydrocarbon mixtures and concluded that 3/11 would be a better exponent of σ than 1/4. The results

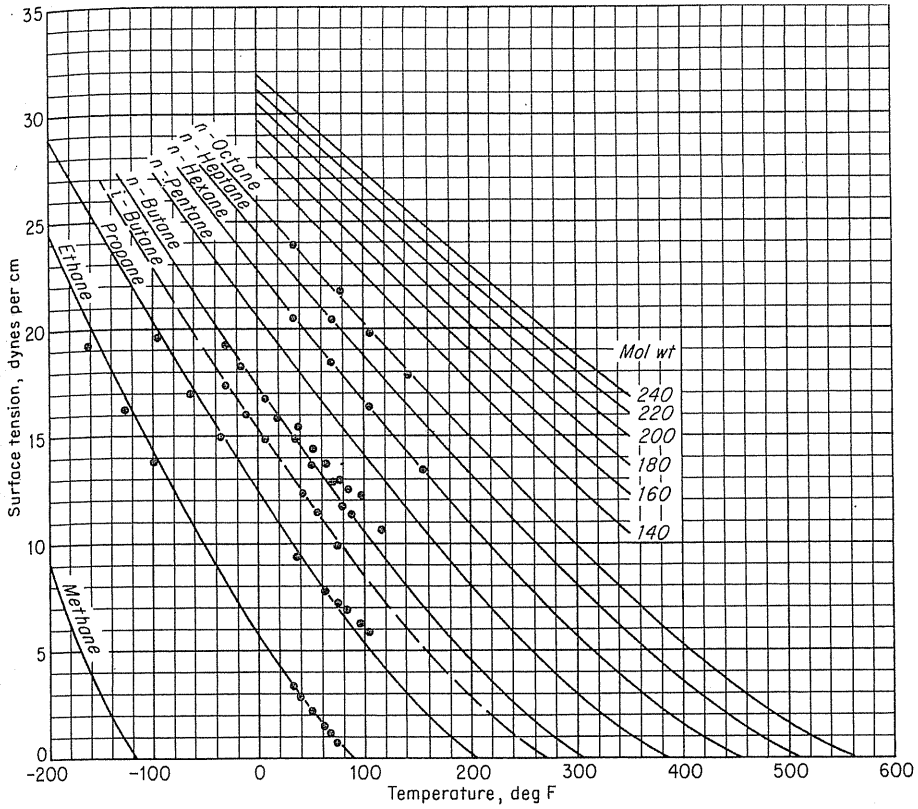

FIGURE 4-26
Surface tension of pure hydrocarbons [Katz et al., 4-40, courtesy SPE-AIME].

of Hough's work are summarized in the paper by Hough and Warren [4-27]. Surface tension between CO_2-rich oils and gases is of interest, as indicated by Simon et al. [4-69], who made a measurement of 0.02 dyn/cm (0.02 mN/m). The prediction method discussed here may give too low a surface tension for reservoir oil at high pressures.

4.12 VISCOSITY

A knowledge of the viscosity of hydrocarbon fluids is essential for a study of the dynamic or flow behavior of these fluids through pipes, porous media, or, more generally, wherever transport of momentum occurs in fluid motion. The influence of fluid viscosity on flow is especially important in petroleum reservoirs, since the flow is predominantly in the laminar region, where the pressure drop

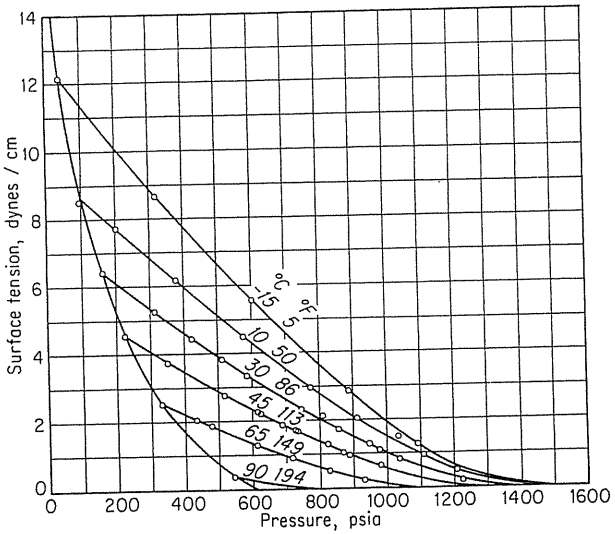

FIGURE 4-27
Surface tension of methane-propane system [Weinaug & Katz, 4-78, courtesy Ind. Eng. Chem.].

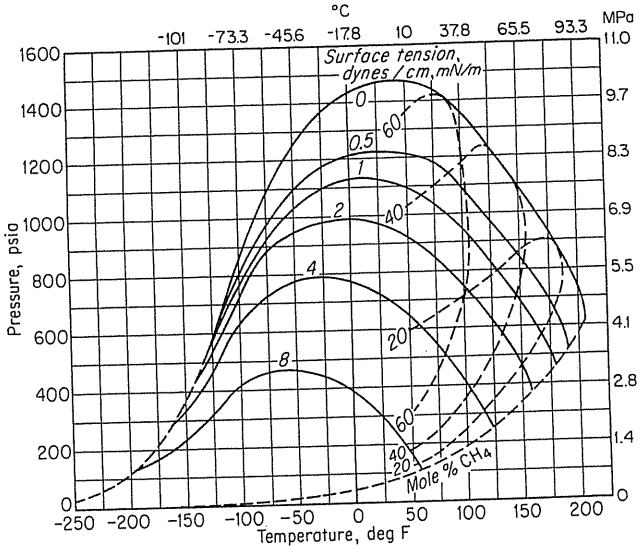

FIGURE 4-28
Surface tension of methane-propane system [Weinaug & Katz, 4-78, courtesy Ind. Eng. Chem.].

TABLE 4.8
Properties of C_6^+ fractions including parachors for computing surface tension

Component	Parachor	Normal boiling point, °F	Normal boiling point, °C	Density, g/ml	Mol. wt.	$C_1 = C_i$ interaction parameter
N_2	(41)					
CO_2	(78)					
C_1	77.9					
C_2	118					
C_3	154					
i-C_4	183					
n-C_4	194					
i-C_5	225					
n-C_5	232					
n-C_6	271					
C_6 (group)	250	147	63.9	0.685	84	0.030
C_7	280	197.5	91.9	0.722	96	0.034
C_8	305	242	116.7	0.745	107	0.037
C_9	340	288	142.2	0.764	121	0.040
C_{10}	375	330.5	165.8	0.778	134	0.042
C_{11}	405	369	187.2	0.789	147	0.043
C_{12}	440	407	208.3	0.806	161	0.044
C_{13}	475	441	227.2	0.811	175	0.046
C_{14}	510	476	246.4	0.822	190	0.047
C_{15}	540	511	266	0.832	206	0.048
C_{16}	580	542	283	0.839	222	0.049
C_{17}	615	572	300	0.847	237	0.050
C_{18}	645	595	313	0.852	251	0.051
C_{19}	675	617	325	0.857	263	0.052
C_{20}	700	641	338	0.862	275	0.052
C_{25}	855	747	397	0.885	345	0.055
C_{30}	975	834	446	0.902	416	0.058
C_{35}	1085	908	486	0.917	486	0.059
C_{40}	—	972	522	0.928	556	0.061

is proportional to the viscosity. In the laminar or viscous region for a Newtonian fluid, viscosity is defined by the relationship

$$\tau = \frac{\mu}{g_c}\frac{du}{dy} \tag{4.7}$$

where μ is the viscosity, in grams mass/cm · s; τ is the shear stress per unit area in the shear plane parallel to the direction of flow, in grams force/cm^2; du/dy is the velocity gradient perpendicular to the plane of shear, in cm/s · cm; and g_c is the conversion factor, in (grams mass/grams force) (cm/s^2).

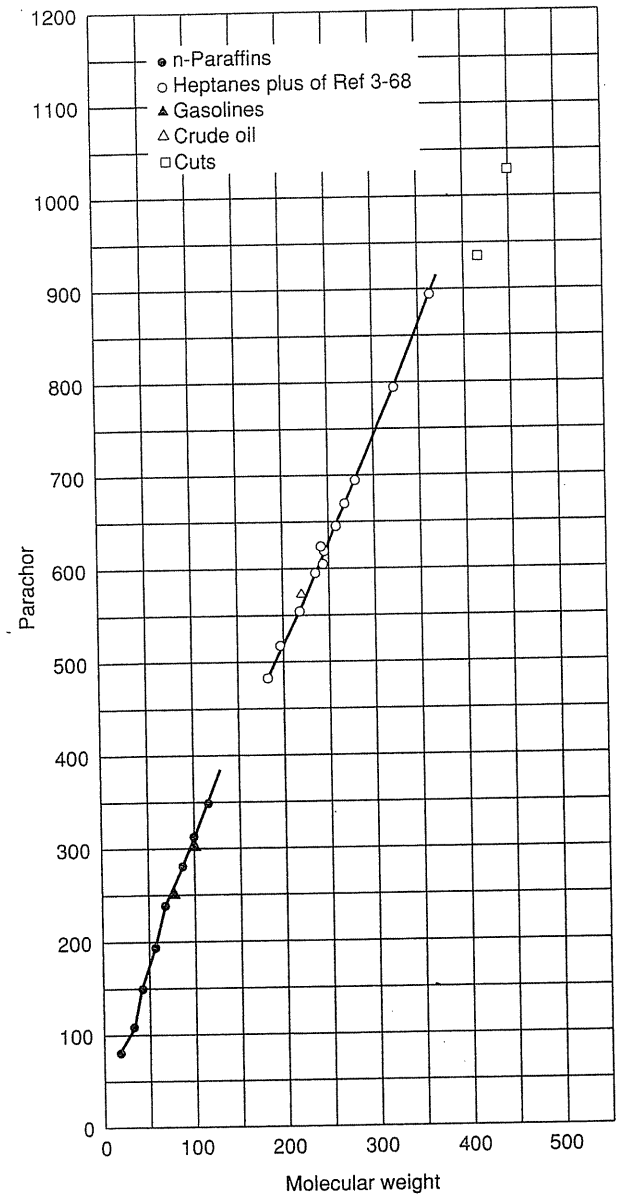

FIGURE 4-29
Parachors for hydrocarbons [after Katz et al., 4-78, courtesy Ind. Eng. Chem.].

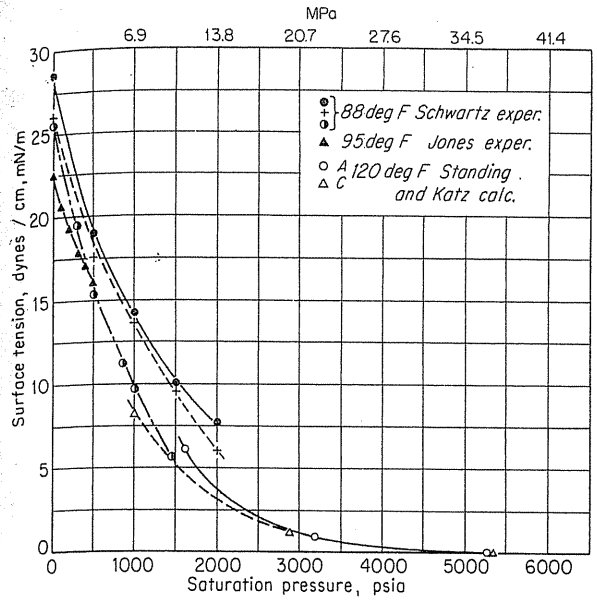

FIGURE 4-30
Surface tension of crude oil [Katz, Monroe & Trainer, 4-39, courtesy SPE-AIME].

TABLE 4.9
Calculation of surface tension [Katz et al., 1-1, courtesy McGraw-Hill Publishing Co.]

For a methane-propane mixture at 808 psia and 86°F

Property	Liquid	Vapor
Mole fraction methane	0.255	0.672
Mole fraction propane	0.745	0.328
Molecular weight	36.9	25.2
Denisty, g/cm^3	0.4200	0.0807

The parachor for methane is 77 and that for propane is 150.3. Compute the surface tension at 808 psia and 86°F.

$$\sigma^{1/4} = 77\left(\frac{0.42}{36.9} \times 0.255 - \frac{0.0807}{25.2} \times 0.672\right)$$

$$+ 150.3\left(\frac{0.42}{36.9} \times 0.745 - \frac{0.0807}{25.2} \times 0.328\right)$$

$$= 1.176$$

$$\sigma = 1.91 \text{ dyn/cm}$$

The experimental value was 2.14 dyn/cm.

The relationship of Eq. (4.7) was first postulated by Sir Isaac Newton and later verified experimentally for the flow of fluids through capillaries by Poiseuille. The unit of viscosity is g/cm · s, or the *poise*. Other units are the centipoise (cp), or 0.01 poise; the millipoise, or 0.001 poise; and the micropoise, (μp), or 0.000001 poise. Water at 68.4°F (20.2°C) has a viscosity of 1.0 centipoise. The SPE-preferred unit is Pa · s; 1 Pa · s = 10 poise = 10^3 cp = 10^7 μp = 10 g/cm · s.

The kinematic viscosity is the ratio of the absolute viscosity to the density:

$$\frac{\mu}{\rho} = \frac{\text{centipoise}}{\text{g/cm}^3} = \textit{centistokes} \tag{4.8}$$

Viscosity measurements on liquids flowing through capillaries [4-18] under the driving force of the head of liquid yield kinematic viscosities.

Viscosities of Gases and Pure Substances

Bicher and Katz [4-6] presented a plot of the viscosity of paraffin gases at 1 atm as a function of molecular weight. This plot was revised slightly by Carr, Kobayashi, and Burrows (Fig. 4-31) [4-11] at low pressure. Gas viscosities increase with increased temperature and decrease with increased molecular weight.

Early gas viscosities under pressure taken in rolling ball viscosimeters gave erroneous results in the low-density region and were not always reliable [4-6, 4-11]. Apparently turbulence effects could not be corrected by calibrations. The Rankine viscometer is the preferred device for measuring gas viscosity [1-1].

The viscosity of methane is given in Fig. 4-32 [4-28,4-35,4-47], showing how the viscosity changes with pressure and temperature. The viscosity of propane is given in Fig. 4-33 [1-1]. High-pressure fluids at temperatures above the critical behave like liquids, having decreasing viscosity with pressure increase.

As early as 1894, Onnes and deHaas recognized that the viscosities of homologues under corresponding states could be correlated. The theorem of corresponding states has been further developed and applied to nonpolar gases by several authors [1-1]. Only two of these correlations will be presented here. Figures 4-34 and 4-35 present the gas viscosity correlation of Carr based on the original correlation of Comings, Maryland, and Egly [4-15] for pure, nonpolar gases. Carr et al. extended the correlation of Comings et al. to higher pressures and to complex mixtures of nonpolar gases [4-11]. The ratio μ/μ_1 of the viscosity at high pressure to the viscosity at 1 atm is shown as a function of the reduced pressure P_r (P/P_c, both in absolute scale) and of the reduced temperature T_r (T/T_c). When mixtures are involved, the pseudocritical pressures and temperatures of typical natural gases may be estimated from gas gravity alone from Fig. 4-16, which is based on typical natural gases. The viscosities of natural gases have been calculated using Figs. 4-34, 4-35, and 4-16 and plotted on Figs. 4-36 and 4-37. Considerable viscosity data are available including work of Sage

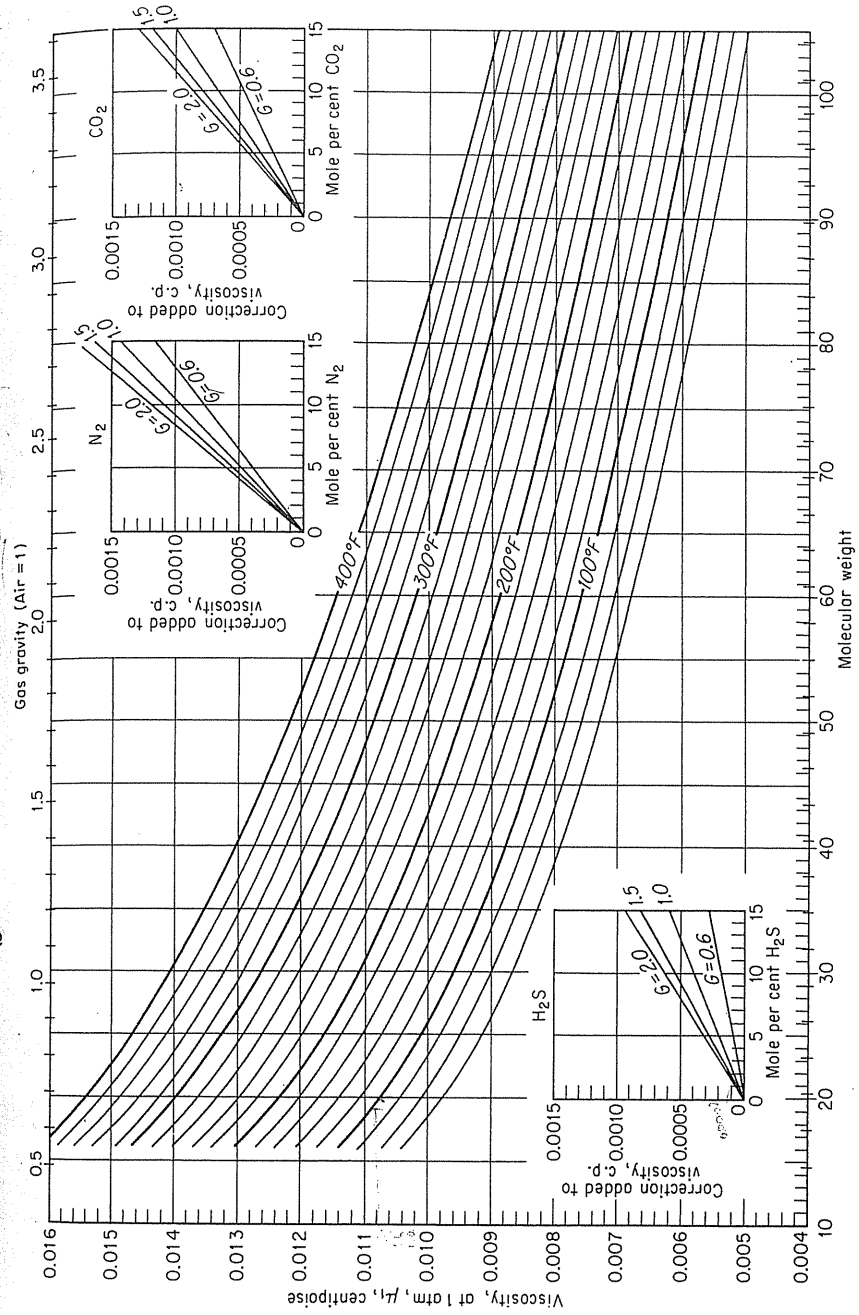

FIGURE 4-31
Viscosity of gases at 1 atm pressure [Carr, Kobayashi & Burrows, 4-11, 1-1, courtesy SPE-AIME].

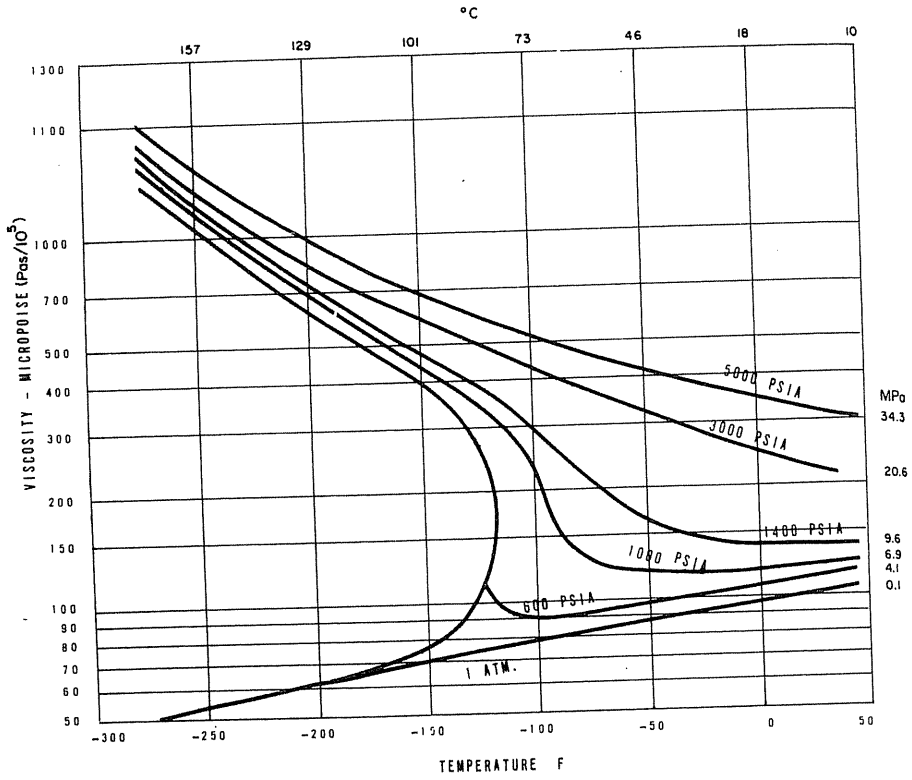

FIGURE 4-32
Viscosity of methane at low temperature [data of Kurata et al., 4-28; Katz, 4-35, courtesy SPE-AIME].

and Lacey, Lee, Eakin, Gonzales, and Starling et al. [4-47]. For high-pressure gases, methane data may be a guide; these are plotted on Fig. 4-38 [1-1].

Like many subjects, the accumulated work on viscosity would fill a book. This abstract only makes it possible for a gas engineer to understand and find gas viscosities for engineering problems. The method using constant-gravity charts to obtain viscosities is illustrated in Table 4.10. The use of the constant-gravity charts (Figs. 4-36 and 4-37) of viscosity gives the poorest agreement with data. When using Figs. 4-34 and 4-35, the effects of CO_2, H_2S, and N_2 can be accounted for by using the pseudocriticals corrections of Fig. 4-39.

For those searching for ways to represent viscosity data in simulation or design programs, the work of Lohrenz, Bray, and Clark [4-50] will be helpful as well as that of Giddings and Kobayashi [4-23]. Since considerable gas containing carbon dioxide is being used in enhanced oil recovery, work by Dewitt and Thodos [4-16] on CH_4-CO_2 mixtures is of interest; some of their results are

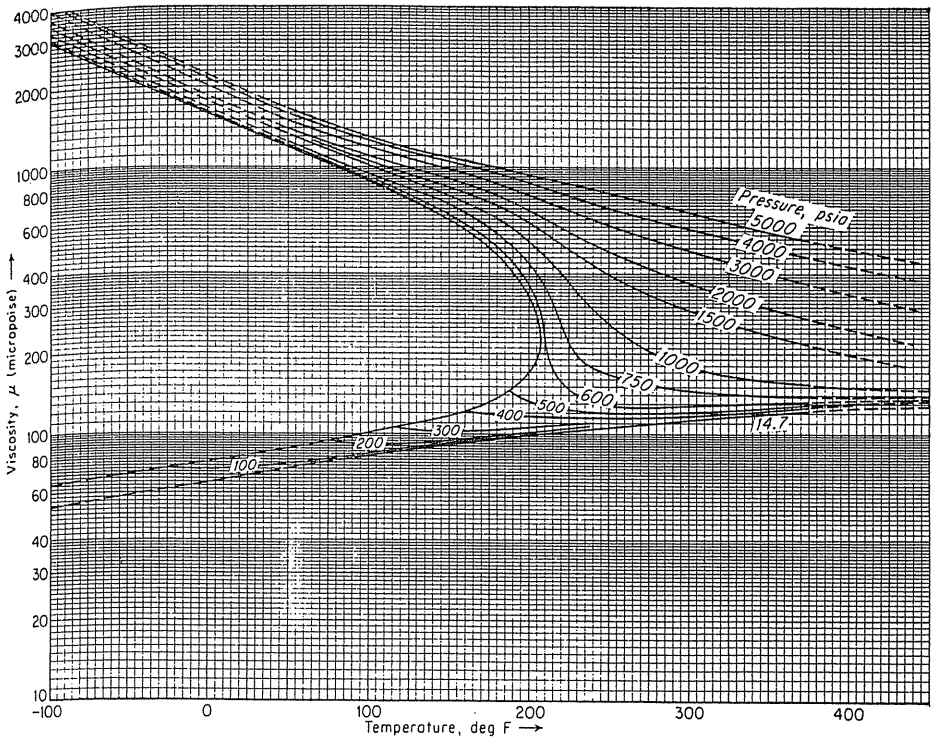

FIGURE 4-33
Viscosity of propane [Katz et al., 1-1, courtesy McGraw-Hill Publishing Co.].

plotted in Fig. 4-40. Michels et al. [4-54] measured the viscosity of CO_2 to 2000 atmospheres. Eakin and Ellington [4-19], Starling and Ellington [4-74], and Lee, Starling, Dolan, and Ellington [4-48] presented a formula to predict viscosity of light hydrocarbons.

Reservoir Liquids

The viscosity of stock tank crude oils may be taken as a routine. On occasion viscosities of reservoir oils may be taken on bottom-hole or separator samples of liquid and gas. Hocott and Buckley report the viscosities on reservoir oils shown in Fig. 4-41 [4-25].

Beal's paper on viscosity included the behavior of "dead" crude oils (stock tank or gas-free oil) with Figs. 4-42 and 4-43 [4-3]. To adjust for saturated oil, Chew and Conally [4-14] and Beggs and Robinson [4-4] presented correlations. An undersaturated oil correlation was proposed by Vasquez and Beggs [4-75].

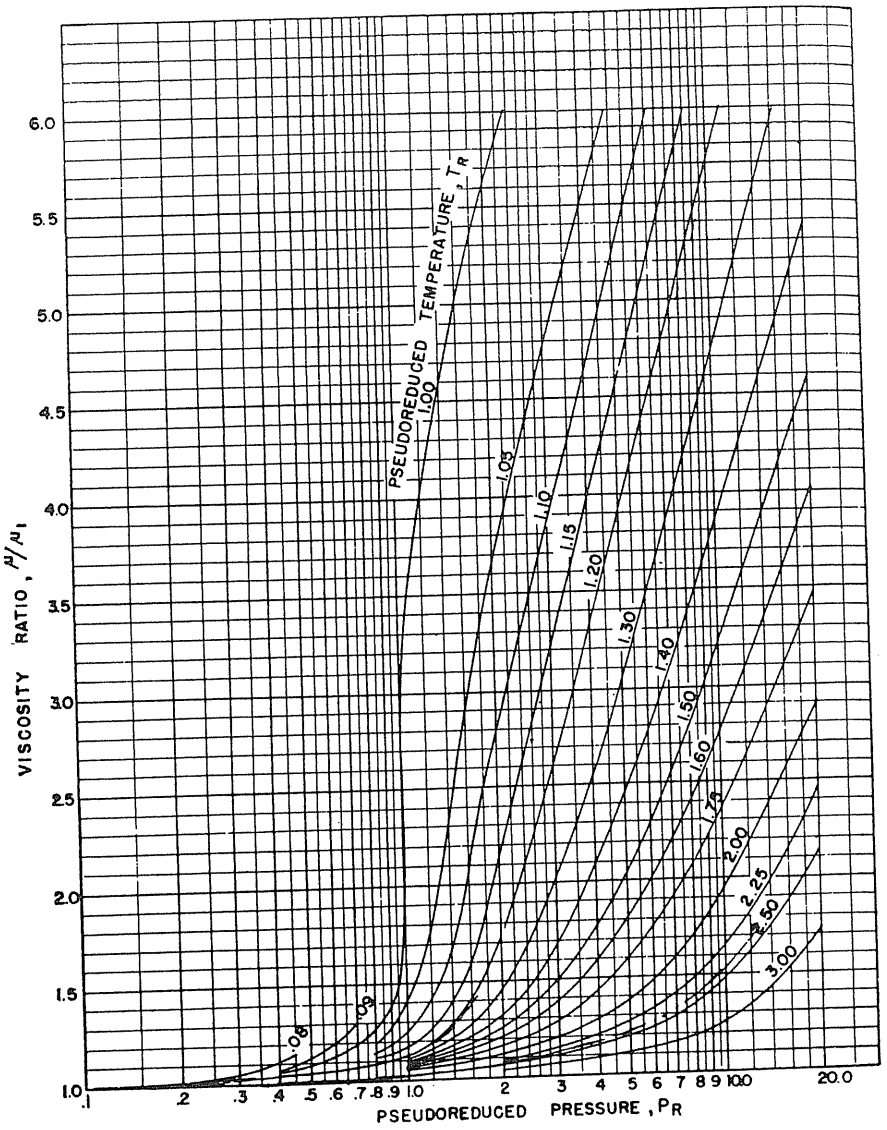

FIGURE 4-34
Correlation of viscosity ratio with reduced pressure [Carr, Kobayashi & Burrows, 4-11, courtesy SPE-AIME].

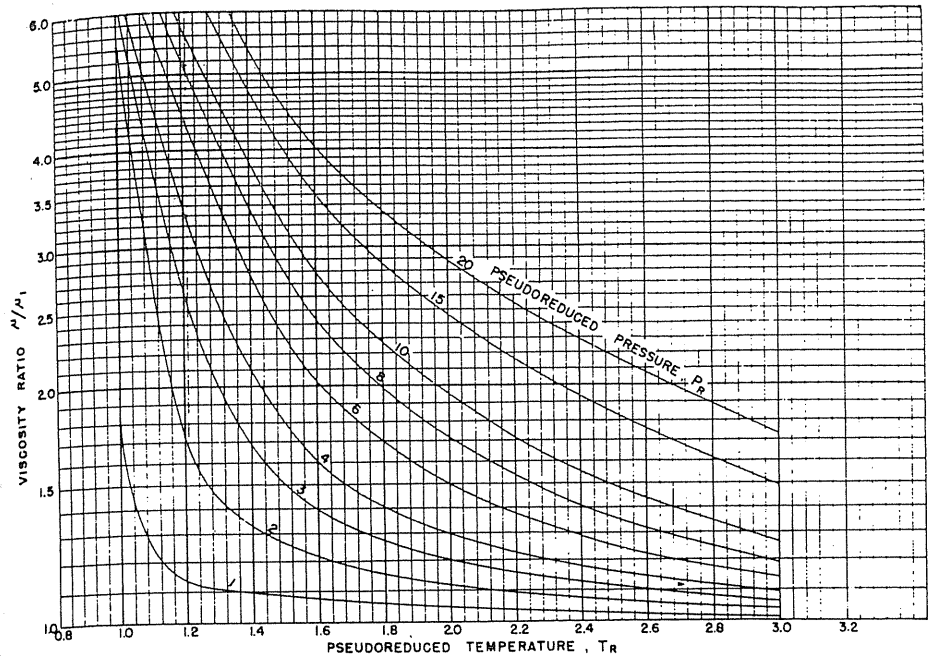

FIGURE 4-35
Correlation of viscosity ratio with reduced temperature [Carr et al., 4-11, courtesy SPE-AIME].

4.13 THERMAL CONDUCTIVITY OF GASES

Thermal conductivity is the fundamental property of substances that governs the rate of transfer of heat by conduction. Thermal conductivity is defined by Fourier's relation, which was first formulated for solids:

$$\frac{dQ}{dt} = -kA\frac{dT}{dx} \tag{4.9}$$

where k is the thermal conductivity of the substance, in Btu/hr · ft^2 · (°F/ft); A is the area at right angles to the direction of heat flow, in ft^2; x is the distance, in ft; dQ/dt is the rate of heat transfer by the mechanism of conduction alone, in Btu/hr; and T is the temperature, in °F.

This section presents correlations for the prediction of the effect of pressure and temperature on the thermal conductivity of pure gases. Tentative correlations are recommended for the thermal conductivity of mixtures, although no experimental data on natural gas mixtures are available to substantiate them. Only limited experimental thermal conductivity data for pure components commonly found in natural gases are available.

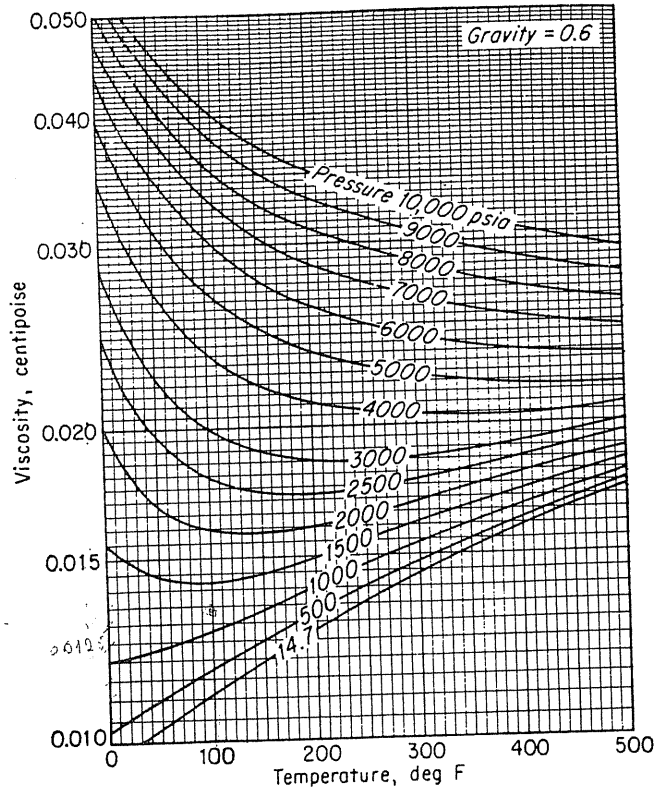

FIGURE 4-36
Viscosity of 0.6-gravity gas [Katz et al., 1-1, courtesy McGraw-Hill Publishing Co.].

The thermal conductivities of some gases at atmospheric pressure are given in Fig. 4-44 [1-1]. The effects of pressure may be estimated from Fig. 4-45 [4-32]. The thermal conductivities of some liquids are given in Table 4.11. Thermal conductivity ratio in Fig. 4-45 is defined as the ratio of the thermal conductivity for a given temperature at high pressure to the thermal conductivity for the same temperature at 1 atm.

4.14 THERMODYNAMIC PROPERTIES

The principles of thermodynamics find wide application in correlating and predicting the properties of hydrocarbons. For example, the effect of pressure on the enthalpy of a gas can be computed from pressure-volume-temperature data. Latent heats can be computed from the slopes of vapor pressure curves. The properties of greatest interest are specific heats of gases and liquids, heats of vaporization, and the effects of pressure on the enthalpies of compressible fluids. Enthalpy-entropy charts for natural gases permit prediction of temperature change when gases are expanding or when reversible work is done by compression.

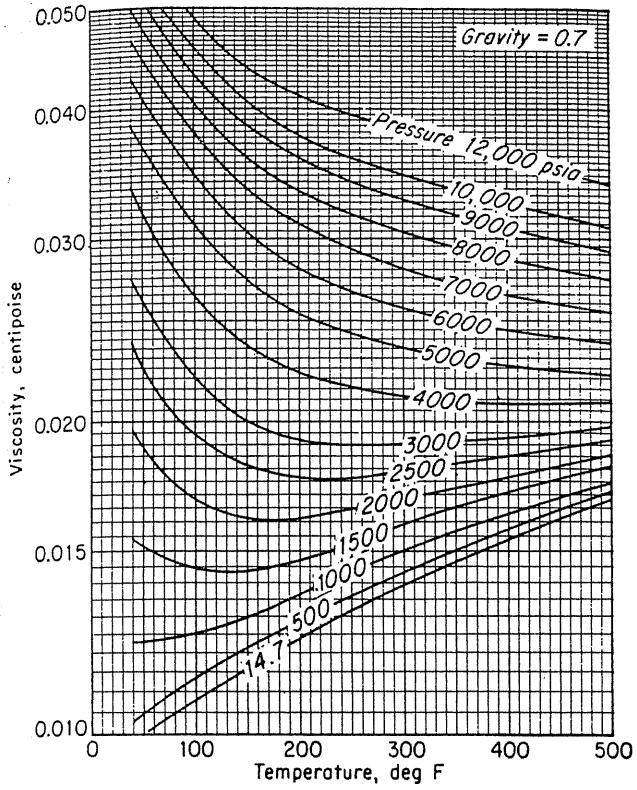

FIGURE 4-37
Viscosity of 0.7-gravity gas [Katz et al., 1-1, courtesy McGraw-Hill Publishing Co.].

Heat Capacity

Changes in enthalpy with changes in temperature T and pressure P for a single-phase fluid are given by Eq. (3.10). The effect of temperature alone on enthalpy is measured by the specific heat C_p at constant pressure [Eq. (3.22)]. The effects of pressure alone are also given by Eq. (3.22). For ideal gases, $(\partial H/\partial P)_T = 0$. An alternative equation, in which changes in enthalpy with pressure are related to

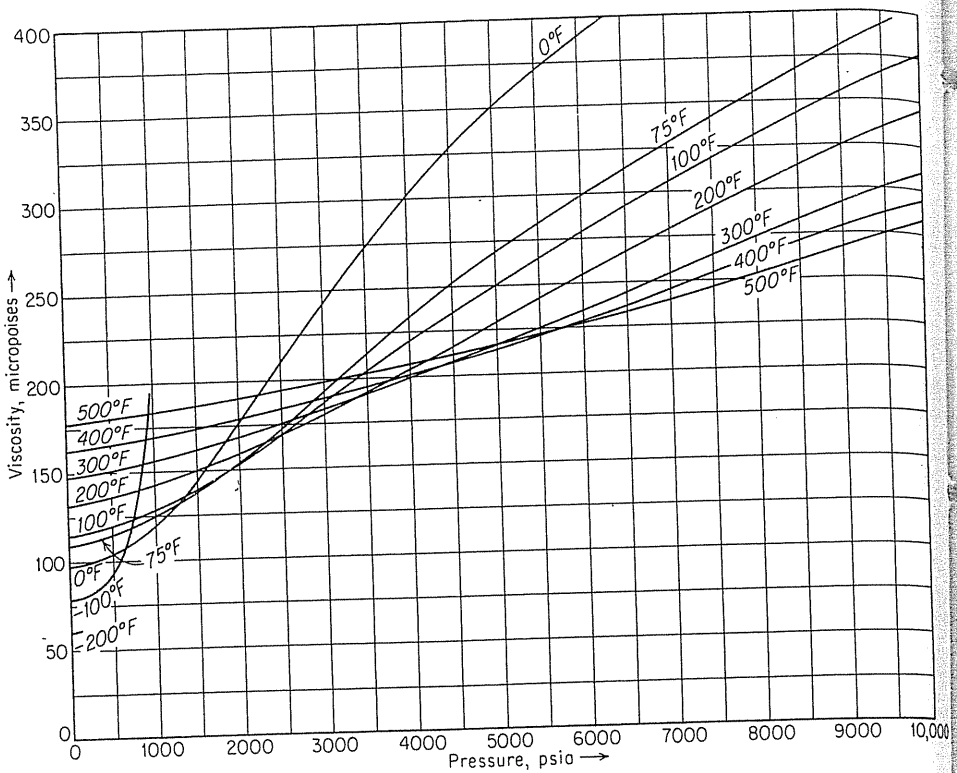

FIGURE 4-38
Viscosity of methane at reservoir conditions [Katz et al., 1-1, courtesy McGraw-Hill Publishing Co.].

the compressibility factor Z, is Eq. (4.10):

$$\left(\frac{\partial H}{\partial P}\right)_T = \frac{-RT^2}{P}\left(\frac{\partial Z}{\partial T}\right)_P \tag{4.10}$$

The specific heats of gases and liquids are determined experimentally in a calorimeter, usually at 1 atm. The specific heat of simple molecules can be predicted from spectroscopic data. For natural gases, the specific heat at 1 atm pressure is a function of temperature and of gas gravity or molecular weight. Figures 4-46 [4-8] and 4-47 [4-26] are plots of specific heats of gases and liquids by Brown and Holcomb. The gravity of a natural gas is used to identify the specific heat line for vapors. For high-boiling liquids, only the characterization factor is required to obtain the vapor specific heat. For liquids, the compound name or the specific gravity of the liquid identifies the hydrocarbon in finding the specific heat from Fig. 4-47.

TABLE 4.10
Determination of gas viscosities by alternate means

Composition of natural gas No. 7 [Lee, Gonzalez & Eakin, 4-47]

Constituent	Mole %	Mol. wt.	Mole % × mol. wt./100%
N_2	4.80	28	1.344
CO_2	0.90	44	0.396
He	0.03	4	0.001
C_1	80.70	16	12.912
C_2	8.70	30	2.610
C_3	2.90	44	1.276
C_4	1.70	58	0.986
C_5	0.13	72	0.094
C_6	0.06	86	0.052
C_7^+	0.03	100	0.030
			19.70

Gas gravity, G = 19.70/29 = 0.679
From Fig. 4-16 T_c = 385°R, P_c = 668 psia

Pressure		Temperature		Viscosity measured,	From Fig. 4-36, 4-37,			
psia	MPa	°F	°C	μp	μp	Pa · s × 10	T_r	P_r
600	4.14	100	37.8	121	113	0.0108	1.45	0.90
2500	17.23	100	37.8	196	191			3.74
6000	41.37	100	37.8	341	336			8.98
600	4.14	160	71.1	131-136	126	0.0117	1.51	0.90
2500	17.23	160	71.1	185	178			3.74
6000	41.37	160	71.1	302	295			8.98
1000	6.89	250	121.1	152	143	0.0132	1.84	1.50
3000	20.69	250	121.1	196	189			4.49
800	55.16	250	121.1	316	313			12.0

μ at 1 atm at 100°F is 0.0108, at 160°F is 0.0117, at 250°F is 0.0132 cp.

Effect of Pressure on Enthalpy and Specific-Heat

The law of corresponding states has been applied to the effects of pressure on enthalpy. It has been convenient to work with the quantity $-\Delta H/T$, since the effects of pressure at constant temperature are being considered. Figure 4-48 by Brown [4-8] is a plot of $-\Delta H/T$ versus reduced pressure, with lines of constant temperature. The chart is for natural gases and is based on the compressibility factors of Fig. 4-13. The enthalpy of a gas decreases upon compression or increases upon expansion when $(\partial Z/\partial T)_P$ is positive, that is, for pressures up to about 5000 psia [P_r = 8 to 10, Eq. (4.10)]. Positive values of $\Delta H/T$ are enthalpies absorbed when expanding a gas, since $\Delta H = H_2 - H_1$. The pseudocritical pressure and temperature are used for gaseous mixtures when obtaining the reduced conditions.

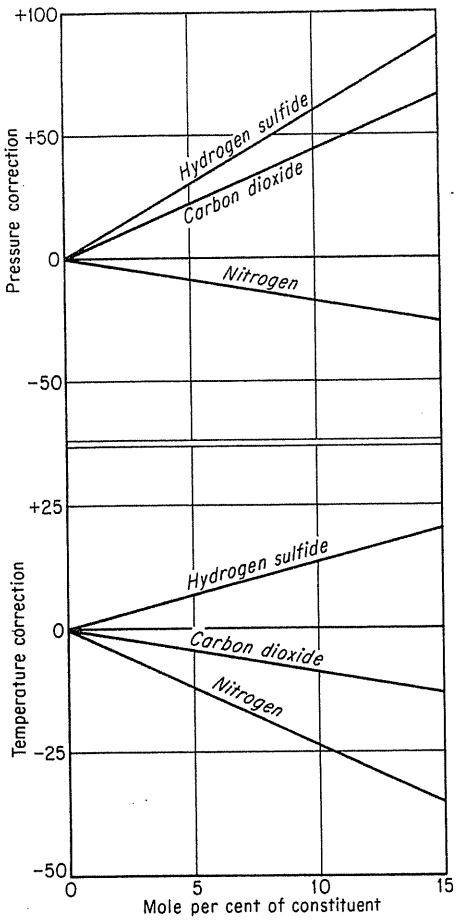

FIGURE 4-39
Correction for CO_2, H_2S and N_2 in using Figs. 4-34 and 4-35 [Katz et al., 1-1, courtesy McGraw-Hill Publishing Co.].

When the $\partial Z/\partial T$ is negative, as for gases at high pressure (Fig. 4-13), heat is released upon expansion.

The Joule-Thomson coefficient is defined in Eq. (3.20). The change in temperature upon expansion, which occurs without heat transfer or work, is determined by the effect of pressure on the enthalpy and the specific heat of the fluid. Figure 4-49 [4-33] is a Joule-Thomson cooling (constant H) chart for natural gases. The 0.6-gravity hydrate curve shows, above the line, hydrates will form if water is present. For a Joule-Thomson cooling process, if a cooling curve passes downward through the curve, hydrates will form.

The isobaric heat capacity or specific heat is a function of pressure for real gases. The increase in specific heat ΔC_p over the atmospheric-pressure value can be used, where ΔC_p equals C_p at reference pressure minus C_p at atmospheric

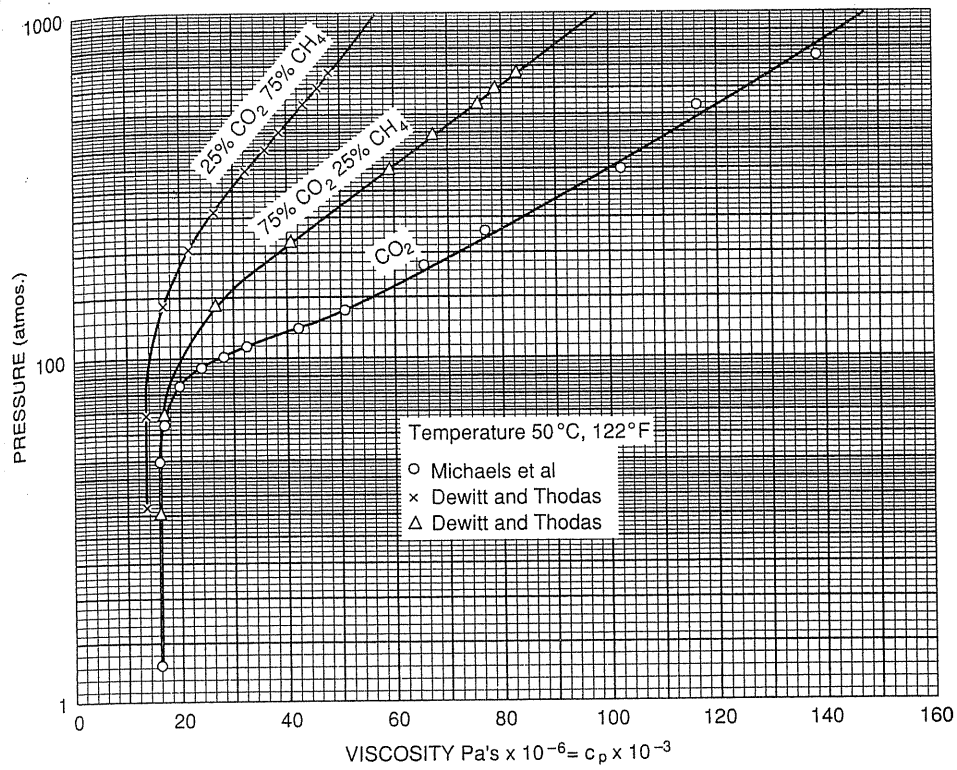

FIGURE 4-40
Viscosity of CO_2 and CO_2-CH_4 mixtures at 50°C (122°F).

pressure. Figure 4-50 [4-20] is such a plot, prepared by Edmister, on a reduced temperature, reduced pressure basis.

The specific heat at constant volume, C_v, is related to specific heat at constant pressure for ideal gases as follows: $C_p = C_v + R = C_v + 1.99$ Btu/(lb mol) (°F). The ratio $\kappa = C_p/C_v$ of the specific heats is useful in computing the adiabatic compression of gases, for which ideal gases follow the relationship PV^κ = constant. Specific-heat ratios for hydrocarbon vapors are given in Fig. 4-51 [1-1].

The latent heat of vaporization of pure substances at their normal boiling point is given in Table A.1 in the appendix, and is plotted in [1-1]. The measurement and prediction of the heats of vaporization of mixtures is a complex matter. A pressure-enthalpy diagram for methane is given in Fig. 4-52 [1-2] to illustrate its behavior under pressure. Powers [4-51,4-80,4-81,4-82] generated much data on light hydrocarbon gases and their mixtures. Such data have been used to test the computerized calculations of enthalpy now generally available.

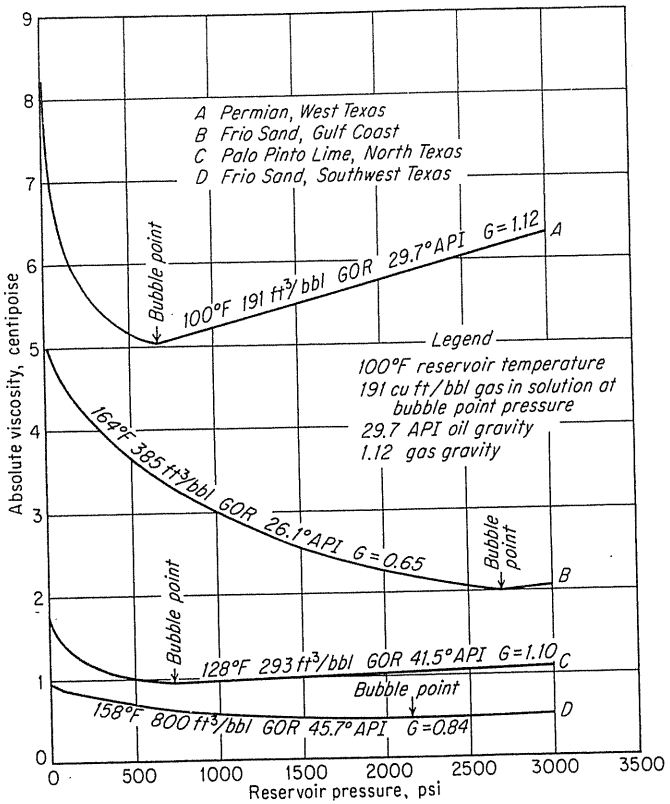

FIGURE 4-41
Viscosity of subsurface sample of crude oil [Hocott & Buckley, 4-25; after Beal, 4-3, courtesy SPE-AIME].

Entropy-Enthalpy (*H-S*) Diagrams

When energy effects are involved, it is helpful to have *P-V-T-H-S* relationships for a system. The Mollier diagram for steam gives the work for adiabatic and reversible expansion, $-\Delta H$ at constant S. Enthalpy-entropy diagrams of natural gases were prepared by Brown and associates for gases of various gravities using 32°F as datum. Figure 4-53 [4-8] is for 0.6-gravity natural gas. The chart is useful for finding theoretical work of compression, or of expansion and cooling at constant enthalpy. The pressure-enthalpy diagram with lines of constant S in vapor phase is very helpful for understanding and solving refrigeration problems; Fig. 4-54 is such a diagram for propane, a common refrigerant.

Vaporization Equilibrium Constants

Natural gas is in contact with condensates and crude oil in the reservoir, wells, surface separators, and processing equipment. Calculation of the distribution

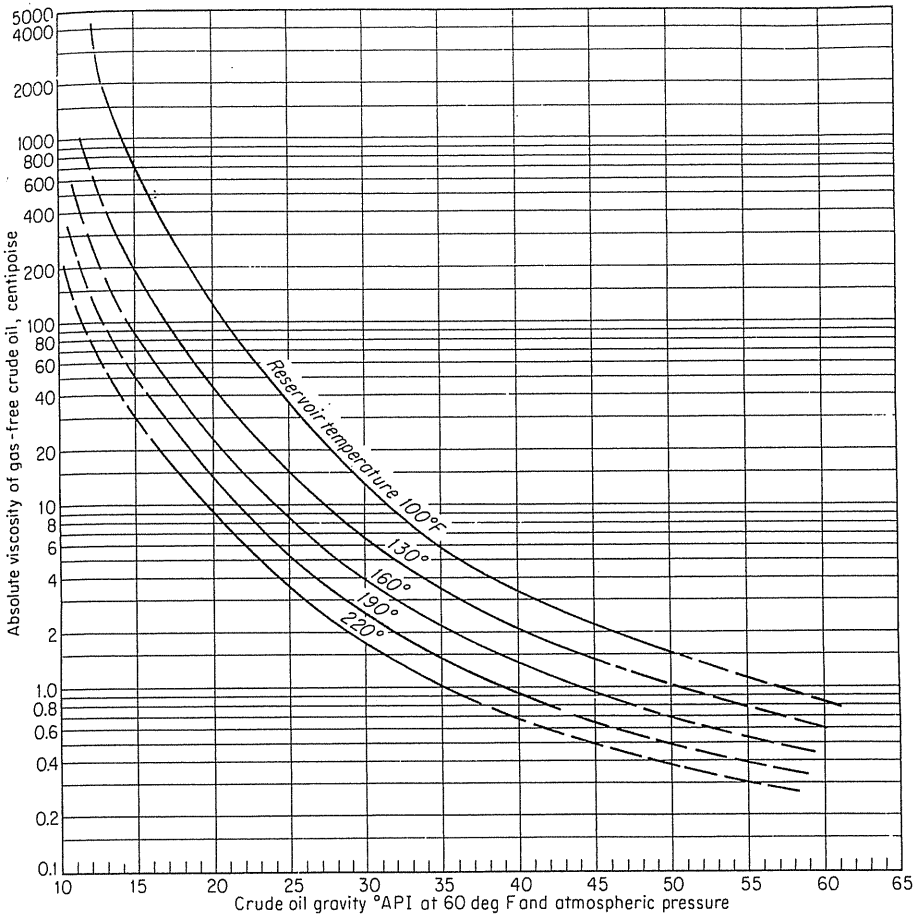

FIGURE 4-42
Viscosity of gas-free crude oil [Beal, 4-3, courtesy SPE-AIME].

of the gaseous constituents between the two hydrocarbon phases began in the 1930s with experimental measurements [1-1]. There have been two approaches to the calculations. Lewis and Luke presented a method of using fugacities of the constituents [4-49]. Brown, Souders, and their associates developed vapor-liquid equilibrium constant charts, based on data and fugacities [4-70]. Katz and Hackmuth [4-37] provided experimental data on a natural gas and crude oil system showing the reversal in volatility change with increasing pressure.

The equilibrium constant is defined as

$$K = \frac{y}{x} \tag{4.11}$$

where y is the mole fraction of a constituent in the equilibrium vapor phase, x

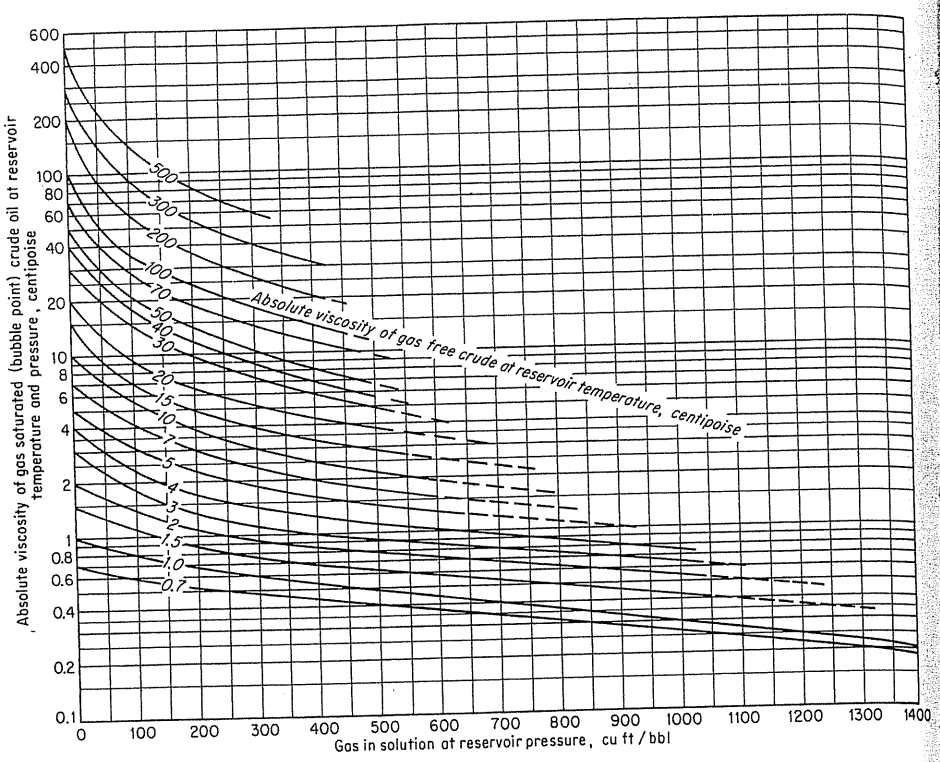

FIGURE 4-43
Effect of dissolved gas on reservoir oil viscosity [Beal, 4-3, courtesy SPE-AIME].

the mole fraction of the constituent in the equilibrium liquid phase, and K the equilibrium constant at given temperature and pressure.

Instead of Raoult's law, the use of fugacities for ideal solution yields

$$x_i f_L = y_i f_V \tag{4.12}$$

where f_L is the fugacity of constituent in liquid and f_V is the fugacity of constituent in vapor. At equilibrium the partial fugacity of a constituent liquid equals the partial fugacity of the constituent in vapor. Also the sum of the fugacities in the vapor equals that in the liquid.

Equilibrium constants K are defined as

$$K = \frac{y_i}{x_i} = \frac{f_L}{f_V} \tag{4.13}$$

with fugacity defined as

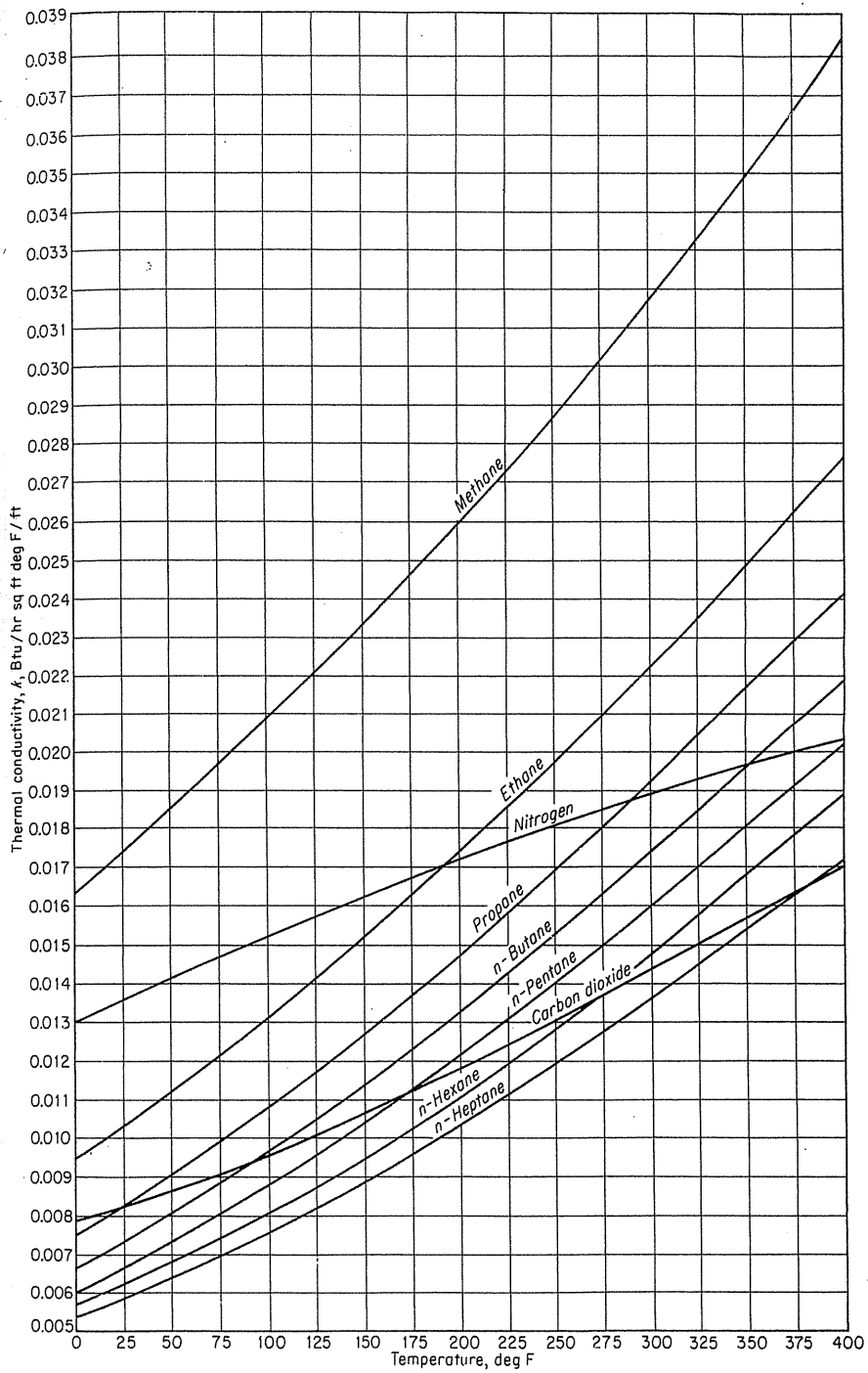

FIGURE 4-44
Thermal conductivity of gases at atmospheric pressure [Katz et al., 1-1, courtesy McGraw-Hill Publishing Co.].

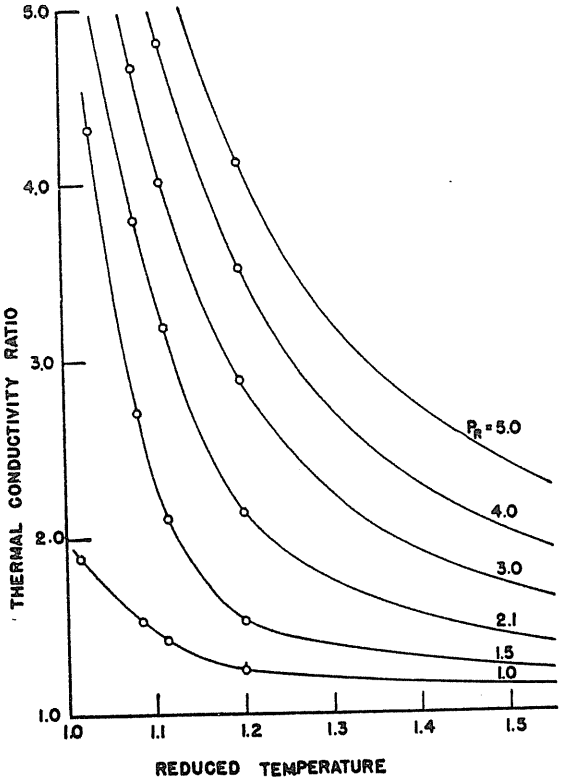

FIGURE 4-45
Thermal conductivity ratio versus reduced temperature [Lenoir, Junk & Comings, 4-32, courtesy AIChE].

TABLE 4.11
Thermal conductivity of liquids

Liquid	Temperature, °F	Thermal conductivity, Btu/(hr)(ft²)(°F/ft)
Water	32	0.343
	100	0.363
	200	0.393
	300	0.395
n-Pentane	86	0.078
	167	0.074
n-Heptane	86	0.081
	140	0.079
Nonane	86	0.084
	140	0.082
Gasoline	86	0.078
Kerosene	68	0.086
	167	0.081
Ethylene glycol	32	0.153

[Katz, et al., 1-1, Courtesy McGraw-Hill Publishing Co.]

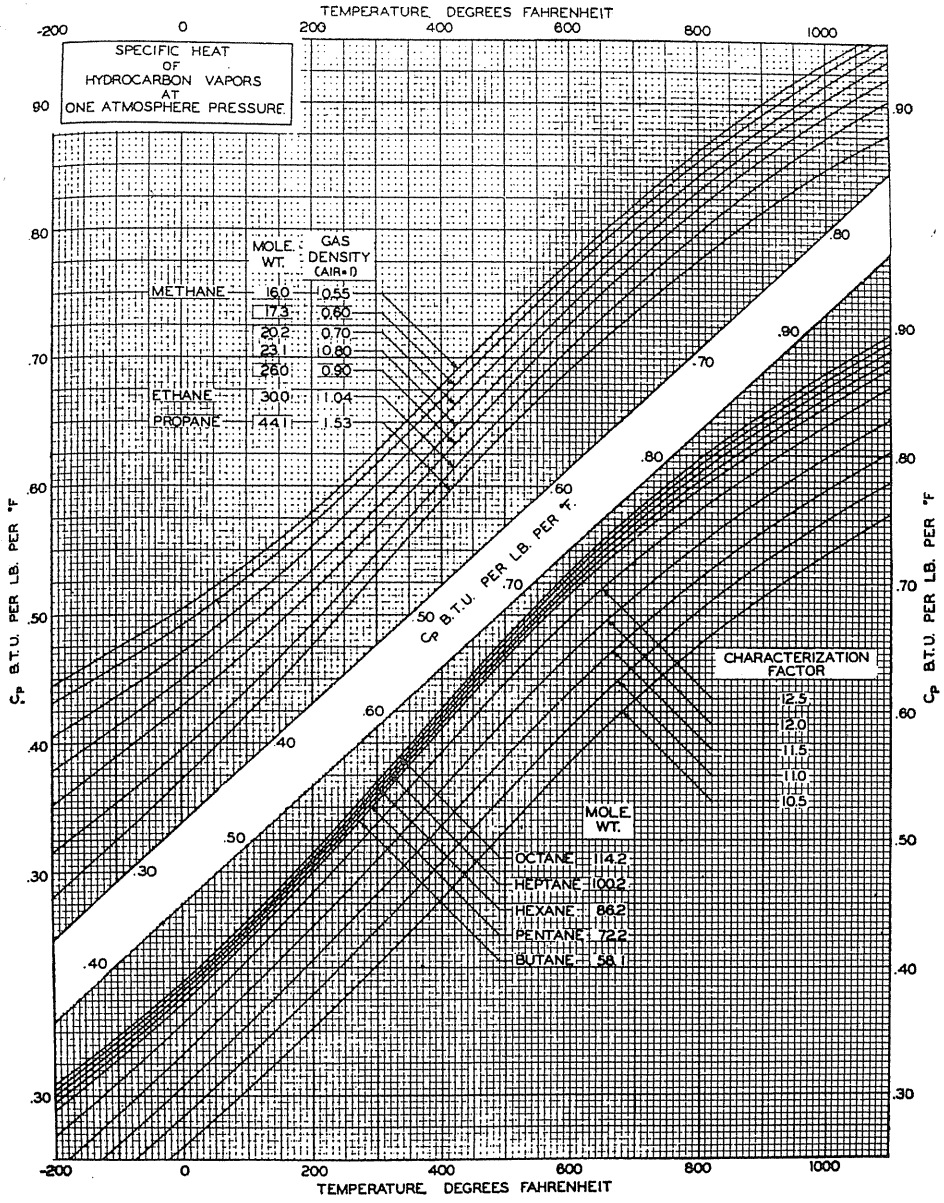

FIGURE 4-46
Specific heat of hydrocarbon gases [Brown, 4-8, courtesy SPE-AIME].

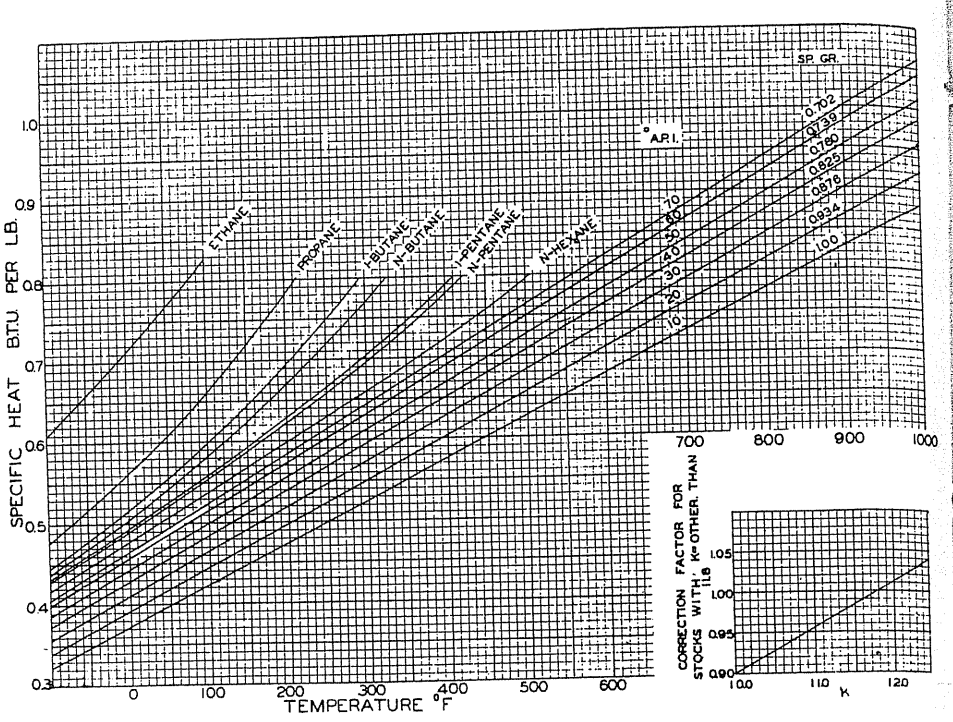

FIGURE 4-47
Specific heat of hydrocarbon liquids [Holcomb & Brown, 4-26, courtesy Ind. Eng. Chem.].

$$\ln f = \ln P - \frac{1}{RT}\int_0^P \left(\frac{RT}{P} - \bar{v}\right) dP \tag{4.14}$$

where R is the gas constant, T is the absolute temperature, and $\bar{v}$ is the specific volume. It may be seen that fugacity is related to volumetric behavior of constituents in vapors or liquids.

Equation (4.14) is equivalent to

$$RTd(\ln f) = \bar{v}dP \tag{4.15}$$

At constant temperature, when energy other than heat and compression is negligible, the fugacity is related to the free energy term F_G:

$$dF_G = \bar{v}dp = RTd(\ln f) \tag{4.16}$$

Equations (4.14) and (4.15) are converted to the following convenient form for computing the fugacity of a liquid or gaseous fluid by graphical means:

$$\ln f = \ln P - \int_0^P \frac{1 - Z}{P} dP \tag{4.17}$$

where Z is the compressibility factor.

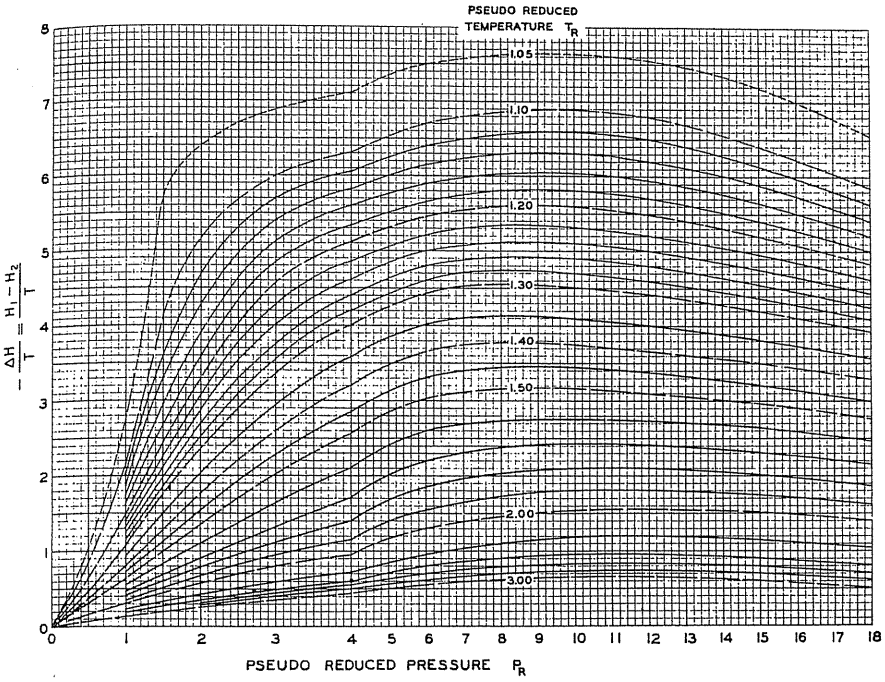

FIGURE 4-48
Effect of pressure on the enthalpy of natural gases [Brown, 4-8, courtesy SPE-AIME].

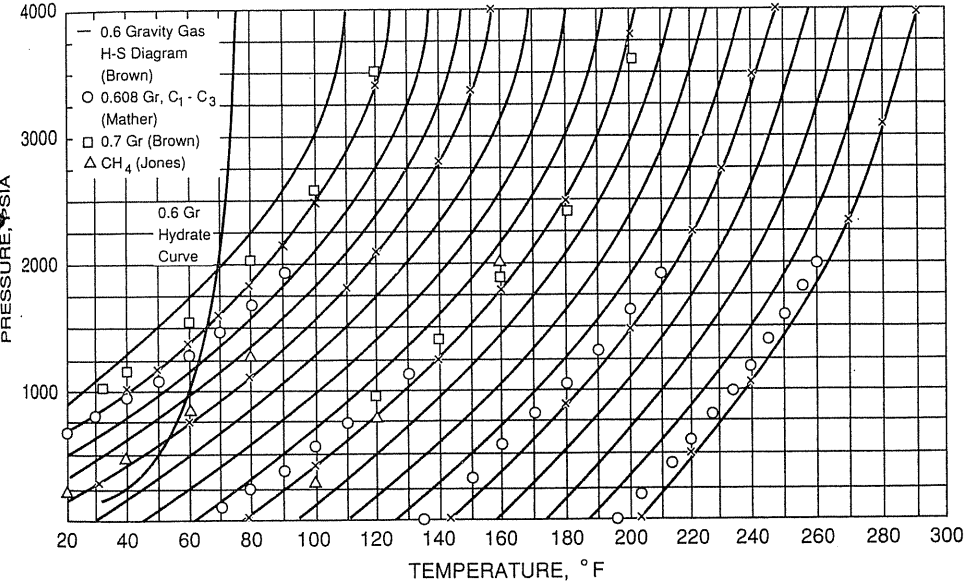

FIGURE 4-49
Joule-Thomson cooling chart for natural gases [Katz, 4-33, courtesy AGA].

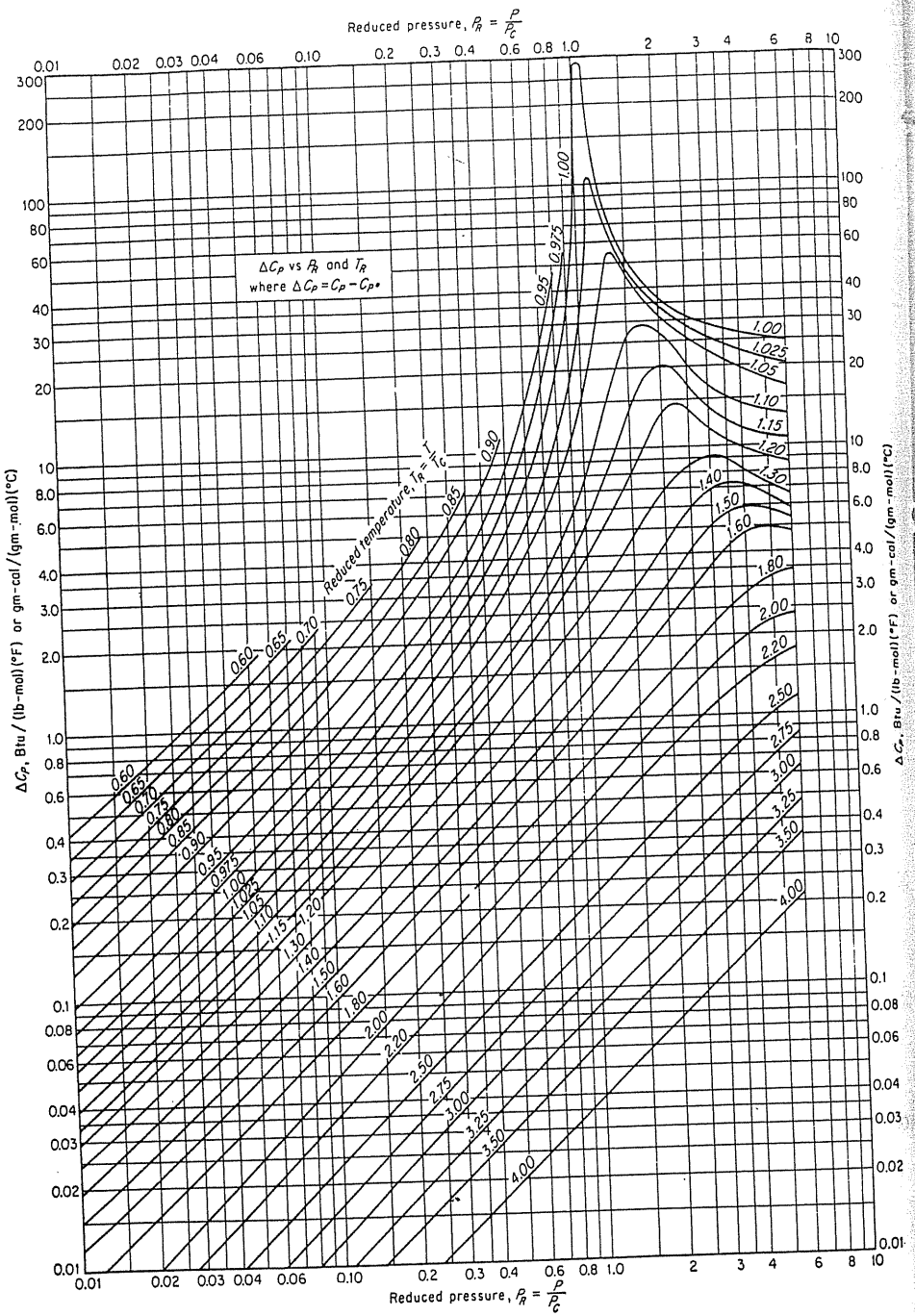

FIGURE 4-50
Isothermal pressure correction to heat capacity of vapors [Edmister, 4-20, courtesy Petro. Engr.].

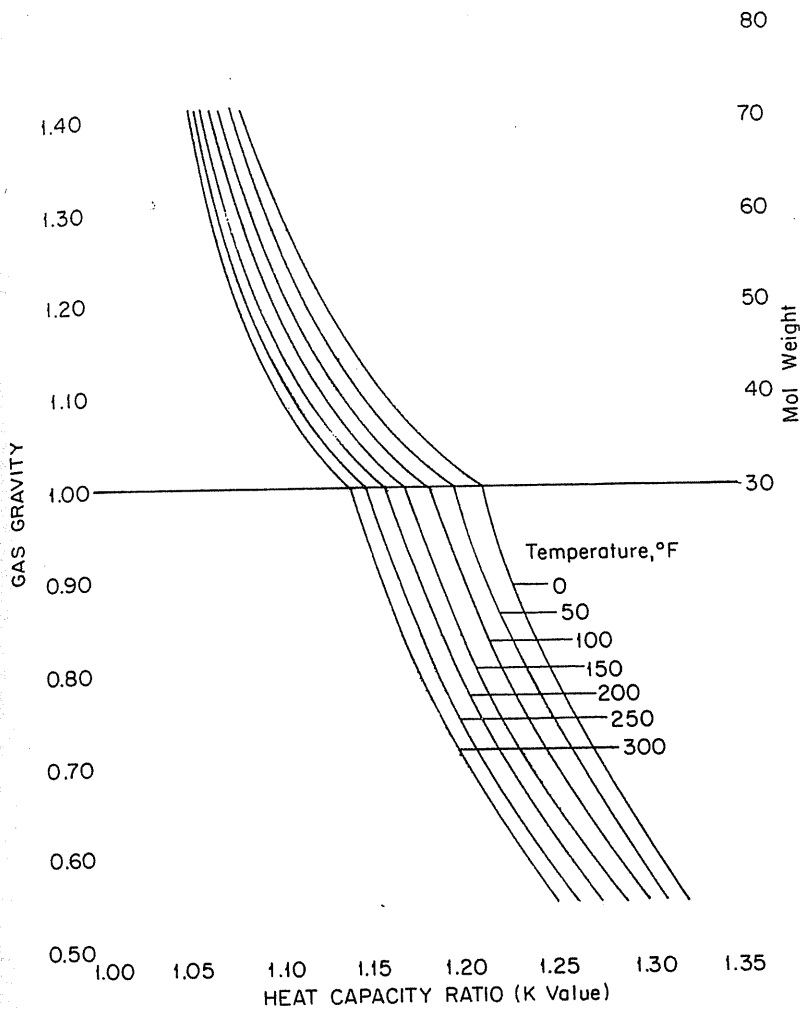

FIGURE 4-51
Specific heat ratio for natural gases at atmospheric pressure.

A generalized fugacity chart for natural gases based on reduced temperatures and pressures is given in Fig. 4-55 [4-8,4-26] in terms of f/P, or the activity coefficient γ_i. These fugacities served to provide ideal equilibrium constants. Equilibrium constants based on experimental determination of vapor and liquid compositions superseded these ideal constants once the data became available.

The reports on constants published in 1937 by Katz and Hackmuth for

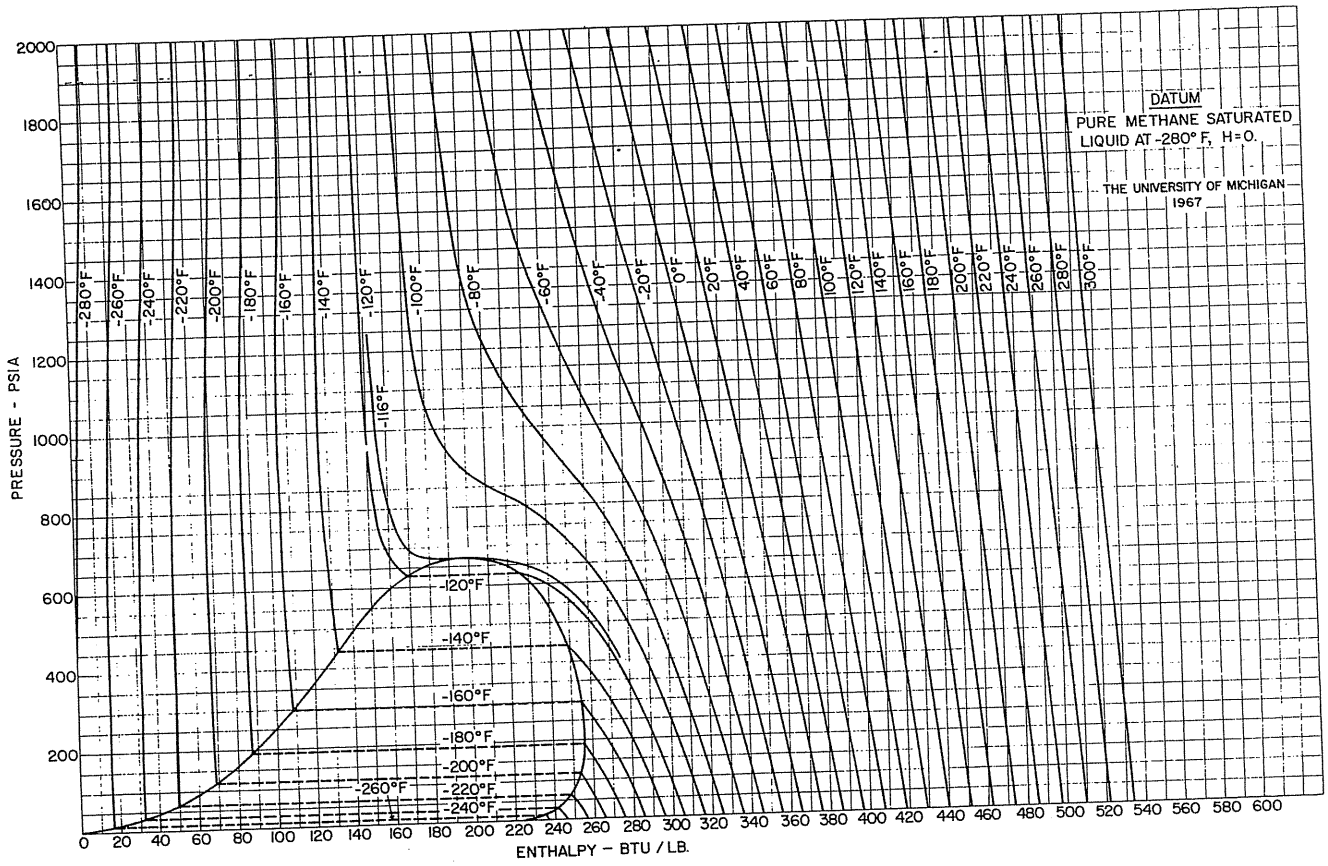

FIGURE 4-52
Pressure-enthalpy diagram for methane [Jone, Mage, Faulkner & Katz, University of Michigan, 1-2].

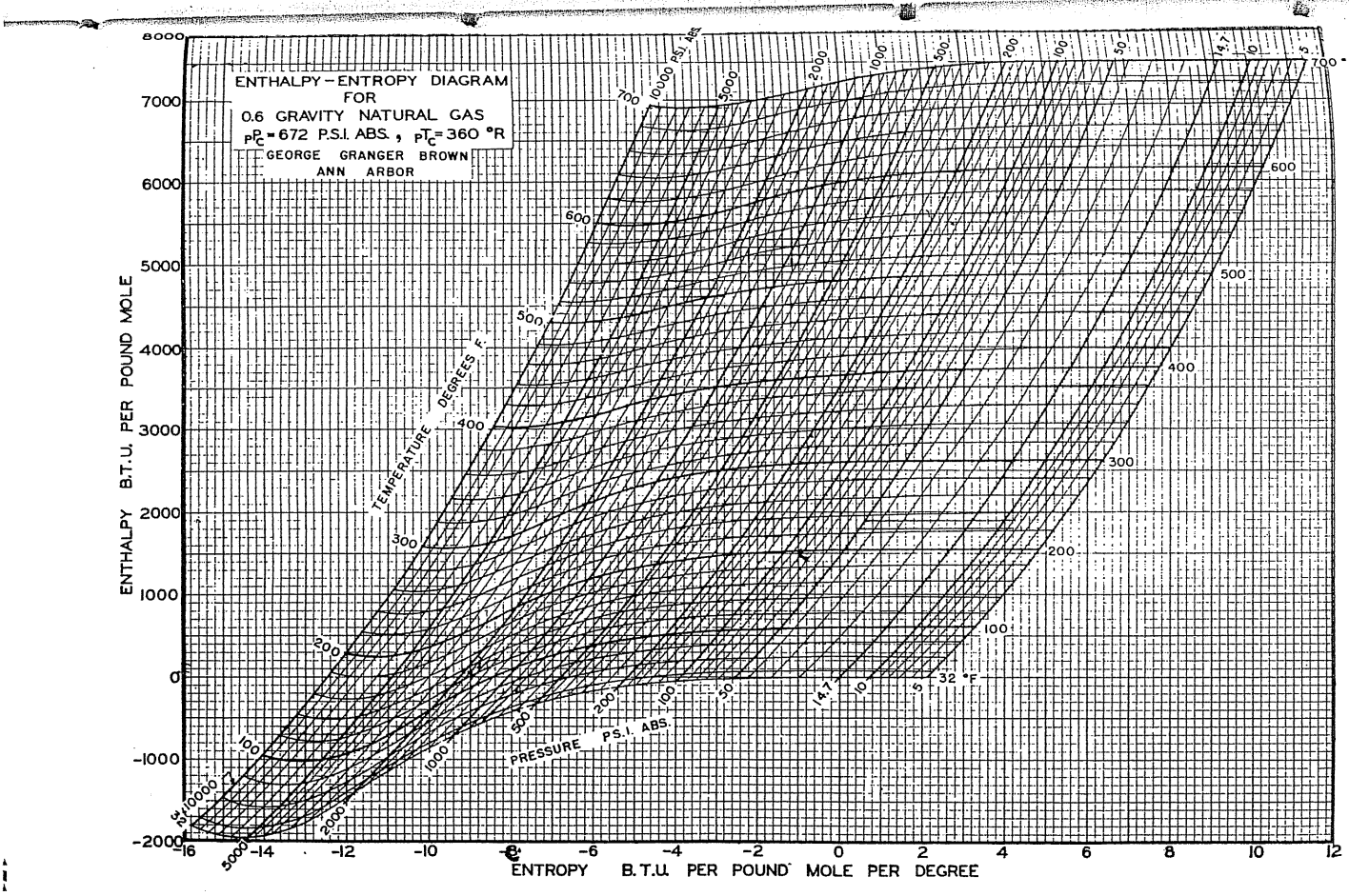

FIGURE 4-53
Enthalpy-entropy diagram for 0.6-gravity natural gas [Brown, 4-8, courtesy SPE-AIME].

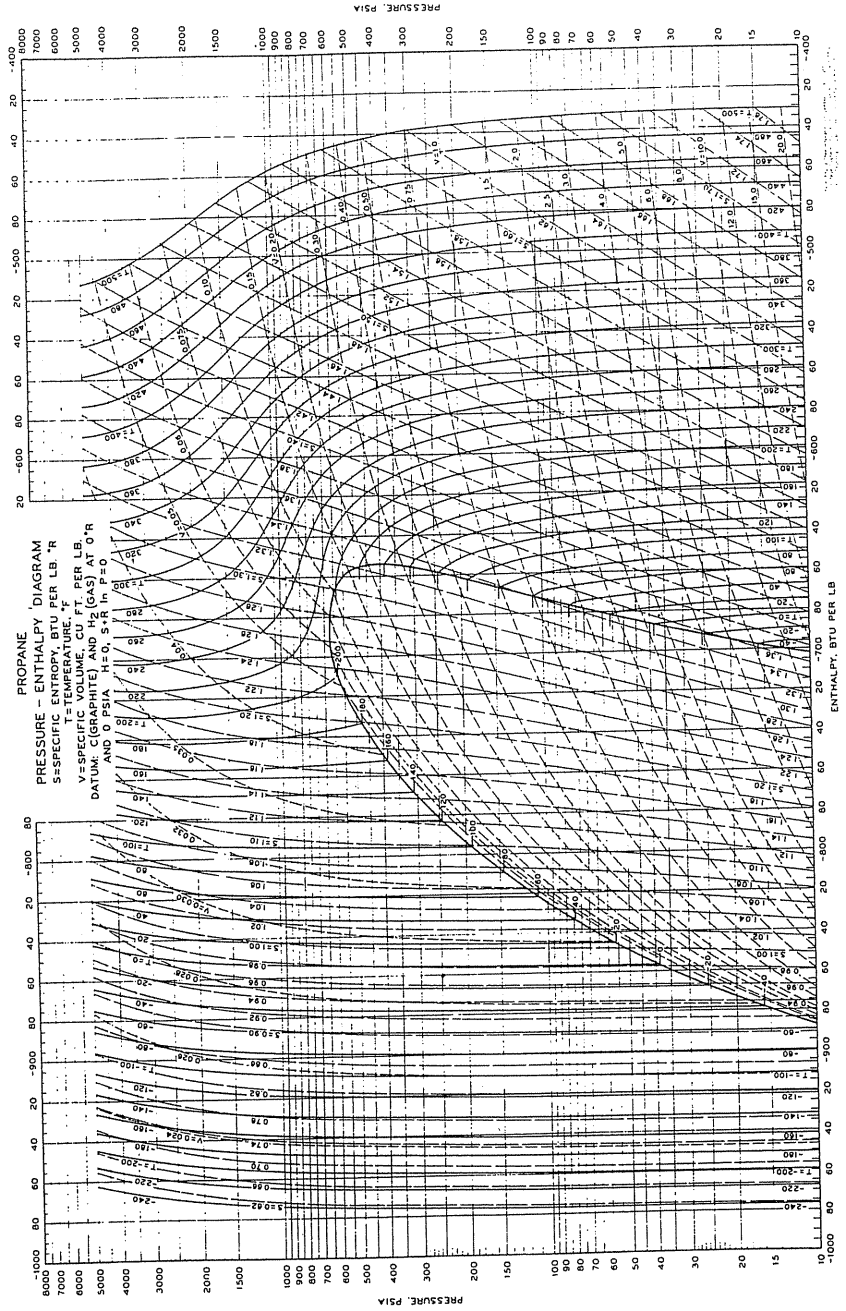

FIGURE 4-54
Pressure-enthalpy diagram for propane [Shell Development Co.].

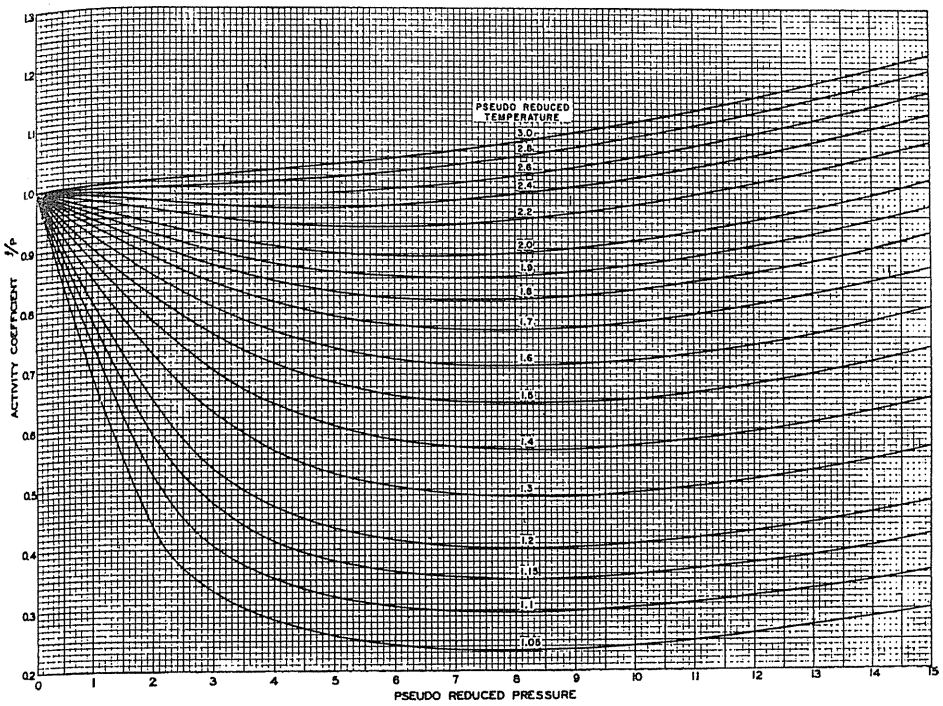

FIGURE 4-55
Fugacity of natural gases [Brown, 4-26, 4-8, courtesy SPE-AIME].

natural gas/crude oil systems [4-37] have been followed by several investigations on complex systems involving natural gases. A comparison of Raoult's law with experimental equilibrium constants is shown in Fig. 4-56. The natural gas/crude oil data at 120°F (49°C) are plotted; the methane-propane binary system from Sage and Lacey and the ethane-heptane system of Kay are traced. On log-log paper, Raoult's law gives a straight line of slope −1. At pressures below the vapor pressure, the experimental constants differ from Raoult's law for propane and the butanes. At higher pressures than the vapor pressures, the experimental constants converge to unity. Thus, propane in methane at 1000 psia (6.9 MPa) and 120°F (49°C) has an actual constant of 0.6 although Raoult's law gives 0.24. This effect of pressure is the reason that the constants vary with composition of the phase and deviate markedly from Raoult's law. Methane and ethane are above their critical temperatures at 120°F (49°C). The extrapolated vapor pressures used to give the lines labeled "Raoult's law" are rather unreliable at any pressure. A binary system may be used to understand critical phenomena and phase behavior; one issue of interest is the reason for a convergence pressure.

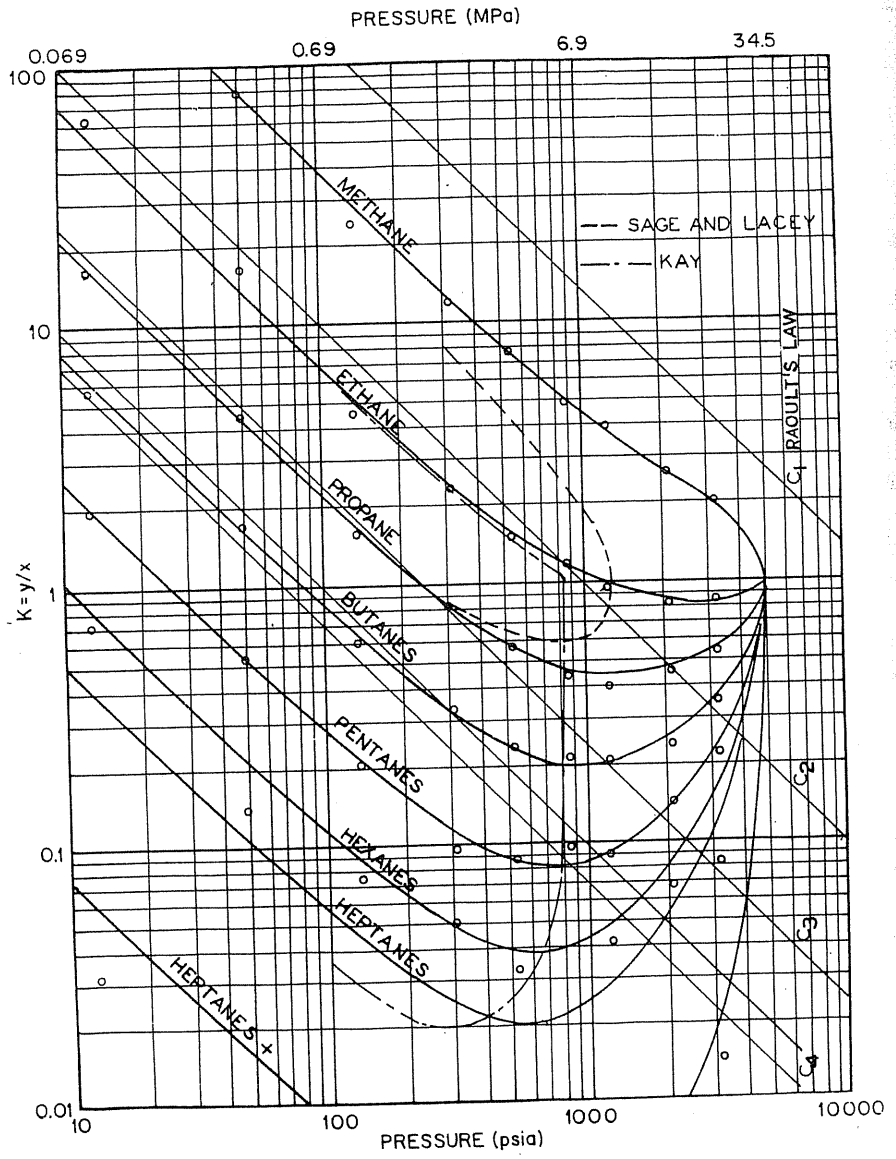

FIGURE 4-56
Comparison of Raoult's law with measured equilibrium constants at 120°F [Katz, 4-34, courtesy SPE-AIME].

Convergence Pressures

According to the phase rule $C_n + 2 - P_n = F_n$, a binary system in two phases has two degrees of freedom. Fixing temperature and pressure fixes the compositions of the phases. Thus the equilibrium constants are fixed by the temperature and pressure for a given binary system.

Figure 4-57, the C_1-C_3 phase diagram, and Fig. 4-58, the C_1-C_3 equilibrium constants at 100°F (38°C), show that the convergence pressure occurs at point E. One may plot the equilibrium constants for the mixture of Fig. 4-57 [4-57,4-64] at 100°F (38°C) on Fig. 4-58. When one starts with the 20% CH_4 mixture, the two-phase region covers pressures A to C and stops at the bubble point. Changing mixtures to 40% CH_4, one can reach bubble point pressure D before the K's are no longer available. To gather equilibrium data up to the convergence pressure one must select the mixture that has a critical temperature at 100°F, namely the 60% CH_4 composition. For ternary mixtures, the critical loci are defined by P, T, and some parameter like $C_3/(C_3 + C_5)$ in Fig. 4-8 for the C_1–C_3–n-C_5 system.

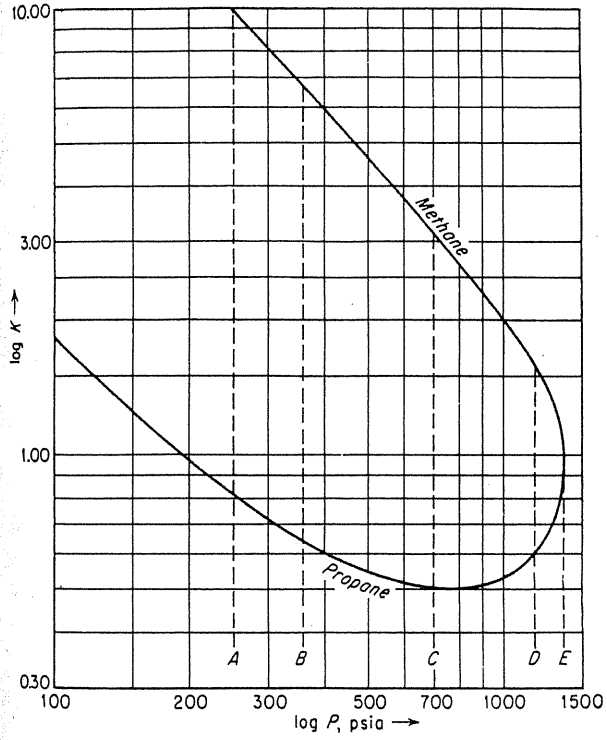

FIGURE 4-57
Phase behavior of methane propane system [data of Sage & Lacey, 4-57, 4-64; Katz et al., 1-1, courtesy McGraw-Hill Publishing Co.].

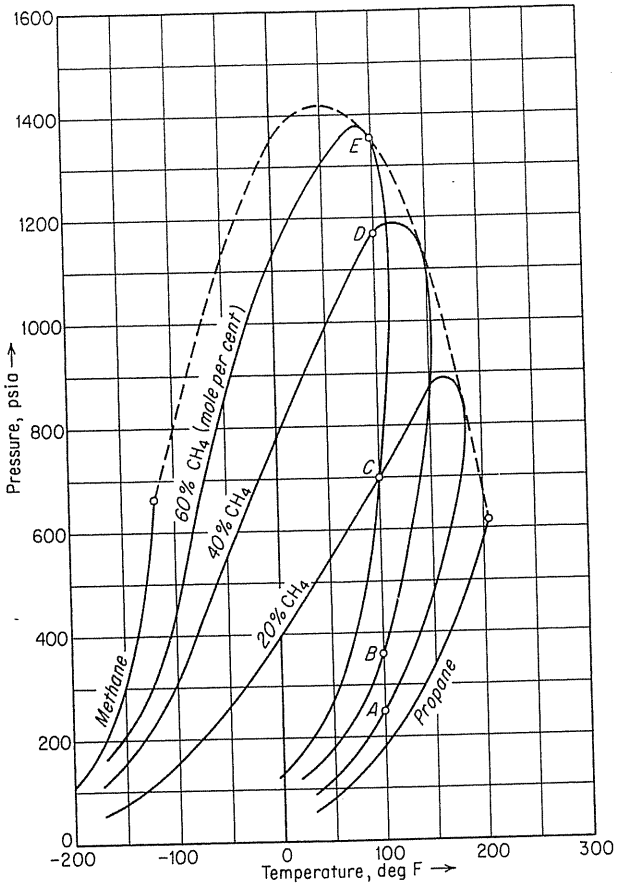

FIGURE 4-58
Equilibrium constants for the methane-propane system [Sage, Lacey & Schaafsma, 4-64, courtesy Ind. Eng. Chem.].

K's in Fig. 4-56 appear to converge, but would do so only if the total mixture had a critical temperature at 120°F (49°C). Roland's data [4-59] illustrate that when one is approaching a dew point at higher pressures, and asphaltic constituents are present, the equilibrium constants do not converge (Fig. 4-59). Standing's data [4-73] showed similar behavior.

Two facts were shown by such data: (1) the equilibrium constants are dependent upon phase composition, especially at high pressure, and (2) asphalt does not have continuous vapor-liquid behavior as might be expected from extrapolation by molecular weights. The authors believe that asphalt does not vaporize, and that the last fraction of a molal analysis like C_{25}^{+} has abnormal vaporiza-

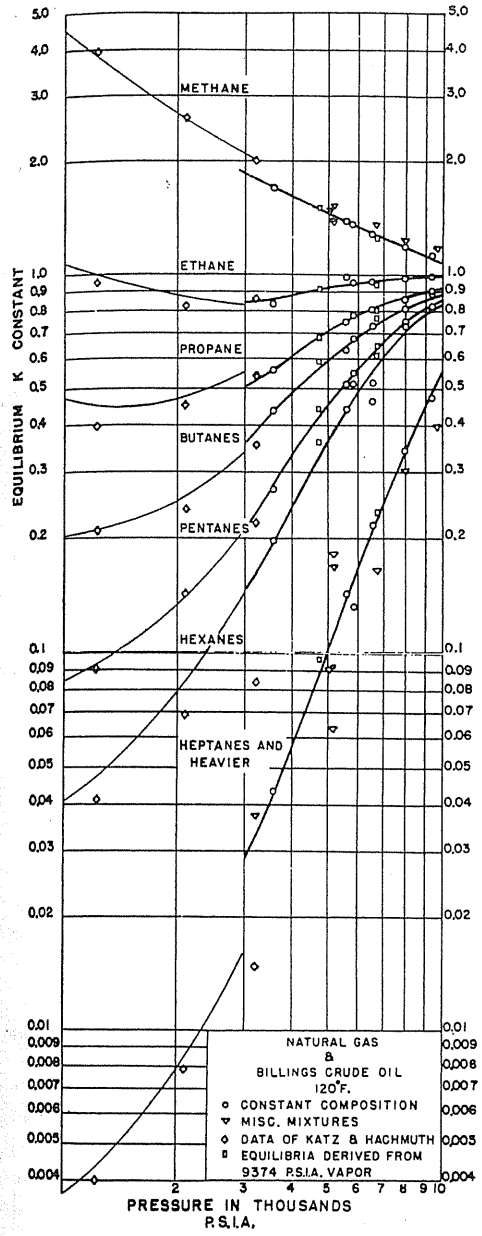

FIGURE 4-59
Vapor-liquid equilibrium constants for natural gas and Billings crude oil at 120°F [Roland, 4-59, courtesy Ind. Eng. Chem.].

tion properties for crude oils due to the asphalt therein, but not for condensates [4-36].

The Gas Processing Association has a series of K charts with designated convergence pressures. They can be very useful but should not be expected to be valid for pressures near the convergence. K's are obtained by using equations of state to obtain the fugacity of each constituent in each phase depending on P, T, and compositions. To permit hand calculations, K charts are given in reference [1-1]. K charts are given in Appendix E of this book for natural gas and natural gas liquids, based on data by Roland, Smith, and Kaveler [4-60].

Calculation of Vapor-Liquid Equilibria

For a mixture of known composition, it is possible to compute from equilibrium constants the temperature and pressure of bubble points and of dew points as well as the distribution of the mixture into two phases at given conditions. The quantity and composition of each phase are found by a trial-and-error calculation [4-34].

The bubble point is the point at which the liquid is just ready to evolve a vapor phase or boil, and occurs at any temperature and pressure at which the sum of the $K_i x_i$ terms equals unity:

$$\sum_i K_i x_i = \sum_i y_i = 1 \text{ at bubble point} \qquad (4.18)$$

where K_i is the equilibrium constant, x_i is the mole fraction of component i in liquid, and y_i is the mole fraction in vapor. Table 4.12 is a bubble point calculation for a natural gasoline. The $K_i x_i$ values are the mole fractions for the first bubble of vapor that forms at equilibrium before its formation changes the composition of the liquid.

The dew point is the point at which the first droplet of liquid or dew is about to form, and it occurs at any temperature and pressure at which the sum of the y_i/K_i terms equals unity:

$$\sum_i \frac{y_i}{K_i} = \sum_i x_i = 1 \text{ at dew point} \qquad (4.19)$$

A dew point calculation is shown in Table 4.13. The y_i/K_i terms are the mole fractions of the initial liquid droplet.

Equilibrium or flash vaporization calculations may be made for a mixture that divides into two phases at a certain temperature and pressure (Fig. 4-60). At that temperature and pressure, all the vapor is in equilibrium with all the liquid. This may be a batch or continuous-flow process. Equations will be derived for trial-and-error computation of the quantity of vapor and liquid formed and of the resultant compositions of the vapor and liquid.

TABLE 4.12
Example of computation of bubble point [Katz et al., 1-1, courtesy McGraw-Hill Publishing Co.]

Compute the bubble point pressure of the following mixture at 120°F (measured value 1225 psia).

Constituent	Mole fraction x	At 120°F and 1400 psi		At 120°F and 1200 psia	
		K	Kx	K	Kx
Methane	0.2208	3.4	0.7507	3.9	0.8611
Ethane	0.0739	0.97	0.0716	1.02	0.0755
Propane	0.0775	0.44	0.0341	0.44	0.0341
Isobutane	0.0203	0.255	0.0052	0.245	0.0050
n-Butane	0.0420	0.212	0.0089	0.208	0.0087
Isopentane	0.0170	0.126	0.0021	0.115	0.0020
n-Pentane	0.0270	0.108	0.0029	0.10	0.0027
Hexane	0.0477	0.056	0.0027	0.048	0.0023
Heptanes plus	0.4738	0.0051	0.0024	0.0042	0.0020
			0.8806		0.9934

By extrapolation, bubble point at 120°F $= 1200 - \frac{0.0066}{0.1194} \times 200 = 1188$ psia.

Let

F = moles of feed
V = moles of vapor
L = moles of equilibrium liquid
z = mole fraction of a constituent in the feed

TABLE 4.13
Example of computation of dew point [Katz et al., 1-1, courtesy McGraw-Hill Publishing Co.]

Compute the dew-point temperature of fractionator overhead at 130 psia.

Constituent	Mole fraction y	At 130 psia and 130°F		At 130 psia and 150°F	
		K	y/K	K	y/K
Propane	0.025	1.85	0.0135	2.2	0.0114
Isobutane	0.904	0.88	1.2730	1.1	0.8218
n-Butane	0.071	0.65	0.109	0.83	0.0085
			1.3955		0.8417

By interpolation, dew point at 130 psia is 144°F.

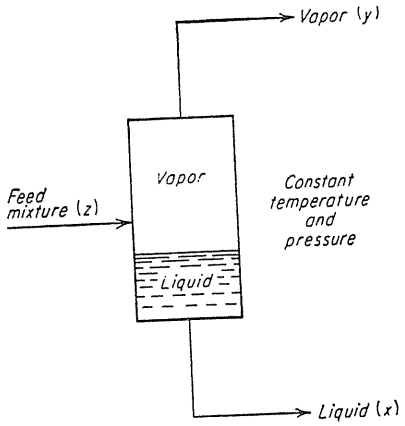

FIGURE 4-60
Equilibrium vaporization [Katz et al., 1-1, courtesy McGraw-Hill Publishing Co.].

x = mole fraction of a constituent in liquid
y = mole fraction of a constituent in vapor
i = any constituent

By equilibrium,

$$\frac{y_i}{x_i} = K_i \tag{4.20}$$

By overall material balance,

$$F = L + V \tag{4.21}$$

By material balance on a constituent,

$$z_i F = x_i L + y_i V \tag{4.22}$$

Substituting for x_i from Eq. (4.20),

$$z_i F = \frac{y_i}{K_i} L + y_i V \tag{4.23}$$

Rearranging,

$$y_i = \frac{z_i F}{L/K_i + V} = \frac{F}{V}\frac{K_i z_i}{K_i + L/V} \tag{4.24}$$

or, letting $F = 1.0$,

$$y_i = \frac{K_i z_i}{(K_i - 1)V + 1} \tag{4.25}$$

Summing over all constituents,

$$\sum_i y_i = 1 = \sum_i \frac{F}{V}\frac{K_i z_i}{K_i + L/V} \tag{4.26}$$

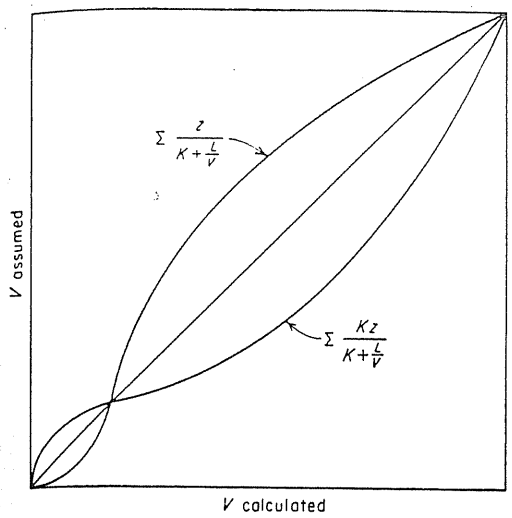

FIGURE 4-61
Solution to equilibrium vaporization equation [Katz et al., 1-1, courtesy McGraw-Hill Publishing Co.].

Similarly, substituting for y_i in Eq. (4.22),

$$x_i = \frac{F}{V}\frac{z_i}{K_i + L/V} = \frac{z_i}{(K_i - 1)V + 1} \tag{4.27}$$

$$\sum_i x_i = 1 = \sum_i \frac{F}{V}\frac{z_i}{K_i + L/V} \tag{4.28}$$

Letting $F = 1$ mole, by Eqs. (4.26) and (4.28),

$$V = \sum_i \frac{K_i z_i}{K_i + L/V} = \sum \frac{z_i}{K_i + L/V} \tag{4.29}$$

Given a composition of feed and equilibrium constants for a selected temperature and pressure, a value of V is assumed and either the $\sum_i K_i z_i/(K_i + L/V)$ or the $\sum_i z_i/(K_i + L/V)$ terms are calculated to find whether the correct value was assumed. A plot of V assumed versus V calculated is given in Fig. 6-61 [1-1,4-71]. It should be noted that the curves approach the origin even though the correct solution is somewhere away from the origin along the 45° line. Table 4.14 gives an example calculation. When handling compositions, methods of analysis should be familiar to the engineer.

4.15 SAMPLING AND ANALYSES

There are several manuals and instruction books available for sampling and analyses, such as those of the ASTM [3-1] and the Gas Processing Association [1-30], and company procedures. Service laboratories are frequently used for analyses.

TABLE 4.14
Example of equilibrium vaporization problem solution [Katz et al., 1-1, courtesy McGraw-Hill Publishing Co.]

Compute the quantity and composition of liquid and vapor when the following mixture is flashed at 1600 psia and 120°F.

Constituent	Mole fraction of mixture z	K at 1600 psia and 120°F	Assume $V = 0.9009$		Assume $V = 0.885$		Mole fraction	
			$K + L/V$	$z/(K + L/V)$	$K + L/V$	$z/(K + L/V)$	Liquid	Vapor
Carbon dioxide	0.0046	1.65	1.76	0.0026	1.78	0.0026	0.0029	0.0048
Methane	0.8345	3.09	3.20	0.2603	3.22	0.2595	0.2943	0.9050
Ethane	0.0381	0.72	0.83	0.0450	0.85	0.0449	0.0510	0.0360
Propane	0.0163	0.39	0.50	0.0326	0.52	0.0314	0.0356	0.0137
Isobutane	0.0050	0.21	0.32	0.0156	0.34	0.0147	0.0167	0.0035
n-Butane	0.0074	0.175	0.285	0.0422	0.305	0.0242	0.0275	0.0048
Pentanes	0.0287	0.093	0.203	0.1413	0.223	0.1288	0.1463	0.0134
Hexanes	0.0220	0.065	0.175	0.1258	0.195	0.1130	0.1283	0.0083
Heptanes plus	0.0434	0.036	0.146	0.2970	0.166	0.2620	0.2974	0.0105
Total	1.0000	. . . . .	. . . . .	0.9633	. . . . .	0.8811	1.0000	1.0000

By extrapolation. $V = 0.887$ mole vapor, $L = 0.113$ mole liquid.
Molecular weight, $C_7^+ = 196$; specific gravity $C_7^+ = 0.850$.

Acquaintance with local laboratories and their quality of work is absolutely essential.

Sampling

Engineers conducting or supervising sample acquisition should concentrate on three items: (*a*) the sample container, (*b*) sampling procedure, and (*c*) the labeling of samples. GPA technical standards include recommendations for containers. For gases at atmospheric pressure, glass pipettes may be employed, while many samples are gathered in steel pressure cylinders. Figure 4-62 [4-22] shows the GPA technical standard steel container for gases and the two-valve cylinder satisfactory for liquids. Preparation of the container may be by evacuating, or filling with a known gas which does not interfere with the analysis. If left filled with air, a purge procedure may be used. The sampling procedure should be such that contamination of the sample is avoided.

Sampling under pressure may utilize a displacement procedure starting with a liquid-filled (two valves) container. Care that heavy hydrocarbons do not condense or adsorb on the container wall may be necessary. Shipping of pressure containers usually requires ICC approval and even testing of the device.

Special devices often are available, such as the Jacoby valve (Fig. 4-63), which permits obtaining the small sample required for hydrocarbon gases or liquids when they are analyzed on a chromatograph [4-29].

It is important to have a labeled tag on a container. Items included are date, exact location, well or sampling point identification, pressure, temperature, contents, and name of sampler. When analyses are found in files, they have to have such information to be useful.

Analyses of Gases and Liquid Hydrocarbons

Early gas and liquid analyses were made by low-temperature distillation in a fractionator, which separated the hydrocarbons by boiling point. Columns were devised by W. L. Podbielniak to be efficient and semiautomatic in their operation [1-1]. Such devices, which were prominent until the 1950s, were often referred to as *pods* [1-1].

A successor analytical device was a mass spectrometer. In this device, the numbers of molecular fragments occurring at various masses were counted [1-1]. By about 1960, the chromatographic device became the normal analytical tool for both hydrocarbon gases and liquids. On occasion distillation analyses are still made, especially for high-boiling liquids. On the AGA project [1-35], distillations were made on pipeline condensates and absorption plant absorber oils (Fig. 4-64).

Chromatographic Analyses

Chromatographic analysis is much better than earlier methods. It can have a more complete separation of the constituents, a smaller sample size, and a shorter test

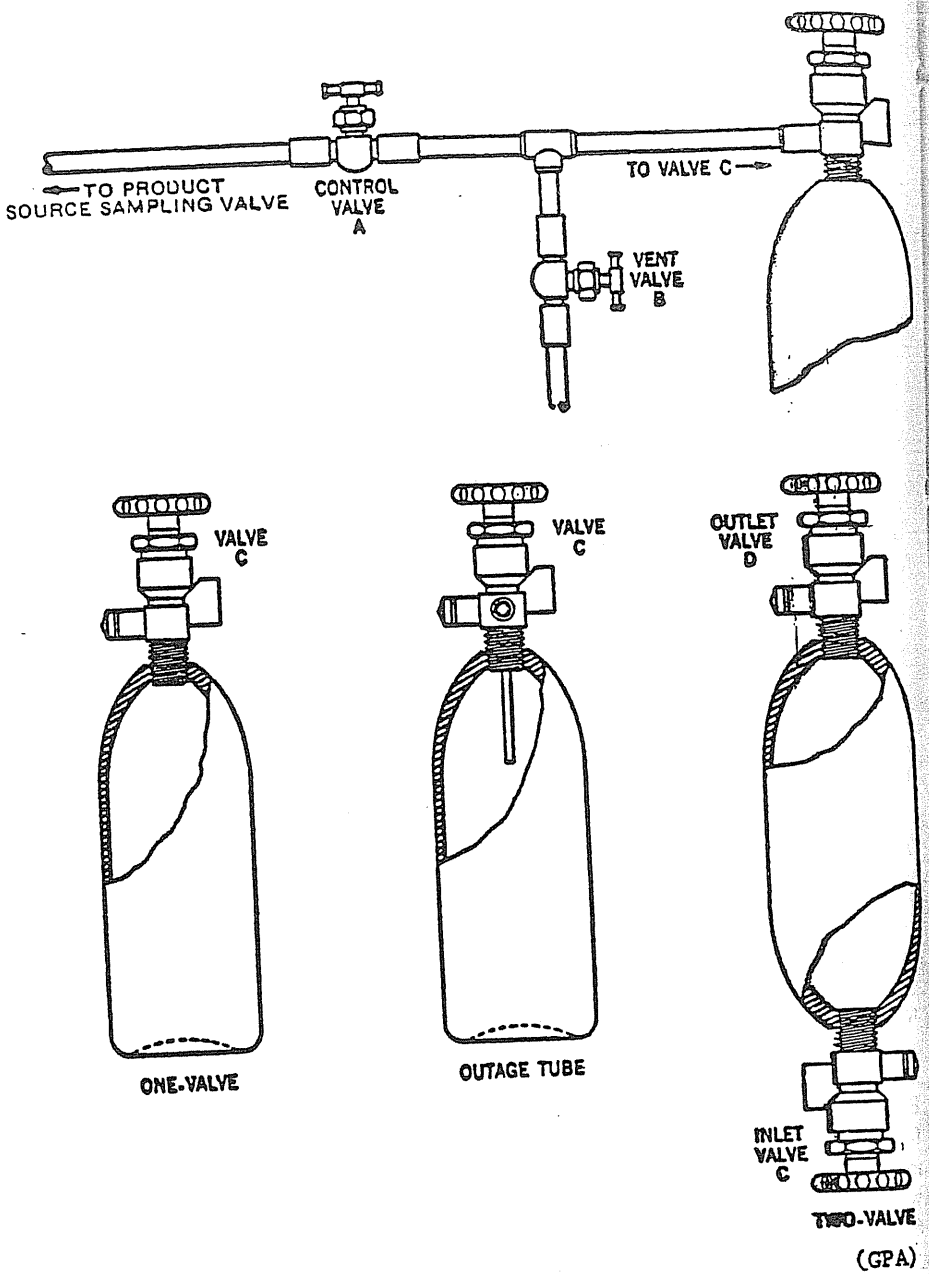

FIGURE 4-62
Sample containers and transfer line [4-22, courtesy GPA].

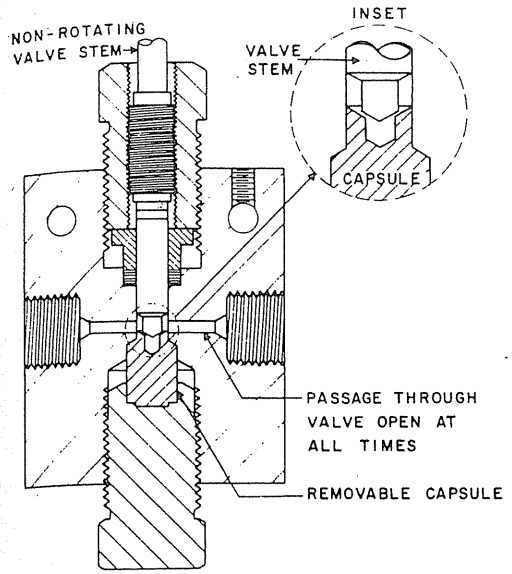

FIGURE 4-63
Jacoby sampling valve [Jacoby & Tracht, 4-29, courtesy *J. Chroma. Sci.*].

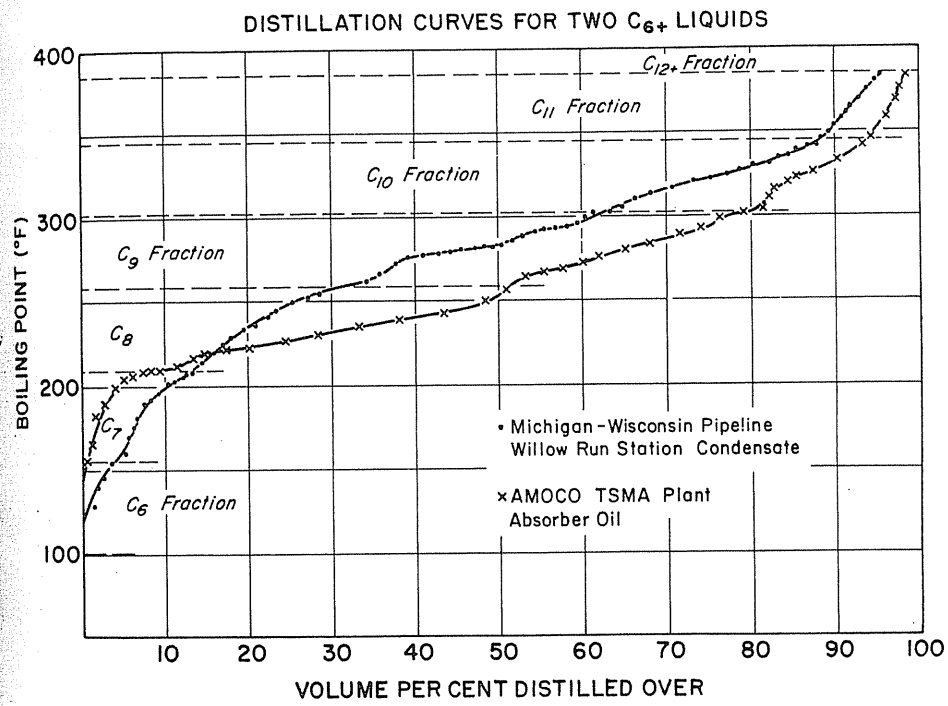

FIGURE 4-64
Distillation curves for two C_6^+ liquids [Bergman et al., 1-35, courtesy AGA].

time. In the AGA project extended chromatographic analyses were made on heavy hydrocarbons out to parts per million (molal basis) [1-35]. ASTM has published standards [4-1] for gas, liquid, thin-layer, and steric exclusion chromatograpy.

A flow diagram for the gas chromatograph is given in Fig. 4-65. The central feature is a packed flow tube in which a separation of the constituents takes place based on boiling points. A carrier gas, often helium, flows through the tube continuously and exits to detector devices based on thermal conductivity or flame ionization. The tube frequently is as long as 20 feet (6.1 m), and it is in an oven for temperature control. Programmed temperature rises may be used in the oven.

Small samples are introduced by a syringe with the needle piercing a septum. A 1-cc gas sample is typical. The carrier gas distributes the sample on the substrate covering the solid packing by both adsorption and absorption. The more volatile components advance through the column faster and arrive at the detector. The arrival sequence and amounts of signal generated provide the analysis.

Two types of detectors are used. One is the *thermal conductivity detector* (TCD), which indicates the change in thermal conductivity of the gas stream. The other is the *flame ionization detector* (FID), in which the separated gas stream is burned in an air-hydrogen flame, creating positive ions and electrons, which are measured to provide the output signal. The amplified output from the detectors is fed to a recorder. Figure 4-66 is an example of recorded output, identifying the constituents by name for C_2, C_3, C_4, etc.

The number of isomers becomes large for higher molecular weights (there are 18 isomeric octanes); one can handle them two ways. One is to identify compounds as such; the other is to group all C_6^+ constituents into groups boiling between normal boiling points of *n*-paraffins plus 1°C. Such grouping is done in Fig. 4-66. The properties of these groups are listed in Table 4.8. Table 4.15 gives gas and liquid analyses taken from a small-scale pilot unit with the flow rates shown. The calculated recombined mixture is also given.

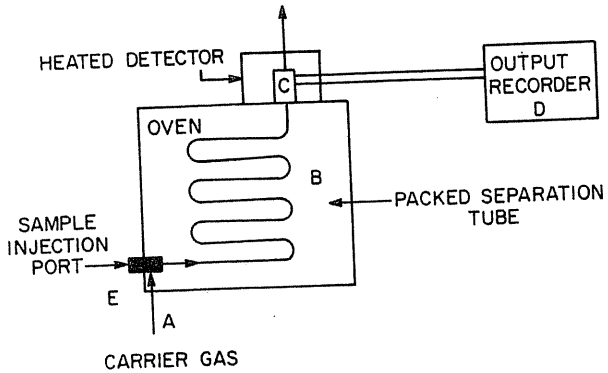

FIGURE 4-65
Flow diagram for gas chromatographic analysis (AGA) [Bergman et al., 1-35, courtesy AGA].

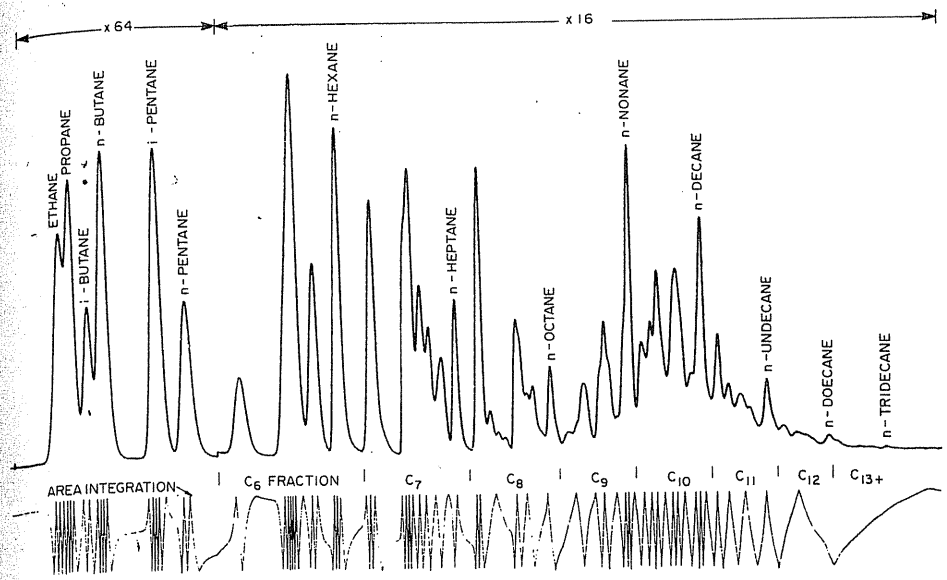

FIGURE 4-66
Chromatographs of Phillips plant outlet gas using C_6^+ concentrator [Bergman et al., 1-35, courtesy AGA].

Molecular Weights and Liquid Densities

Molecular weights and liquid densities were taken on the cuts of some 29 condensates in the AGA project [1-35]. These values were plotted versus the boiling points of the cuts in Figs. 4-67 and 4-68. The average values are listed in Table 4.8.

Gas Gravity

Gas gravity refers to a gas's density or molecular weight relative to air at atmospheric pressure. Gas gravity is an essential measurement in gas metering and is used in calculation of gas flow as well as in determination of physical properties. It may be calculated based on an analysis, as in Table 4.16, or physical measurements may be made. Early measurements were made by gravity balances—finding the air pressure that just balances the gas weight and calculating the gravity. Now there are special instruments for measuring gas gravity; there are recording gravitometers as well. For oils the density is found by floating a gravity spindle in the oil to read the API gravity, which is converted to G, or density in g/cm^3 by the following formula:

$$\text{API gravity at } 60°\text{F} = \frac{141.5}{G, 60°F} - 131.5 \qquad (4.30)$$

TABLE 4.15
Pilot unit gas and liquid analyses, recombined [Bergman et al., 1-35, courtesy AGA]

Wedron meter, NGPL 9 11/8/73
Separator Conditions: −8°F, 350 psia
Liquid data: $cm^3/hr = 57.5$, $\rho(g/cm^3) = 0.6854$, mol. wt. = 73.74, gallon/MMcf = 15.18
Vapor data: Scf/hr = 1000.0, $G = 0.6173$, mol. wt. = 17.88

	Measured compositions, mole %		
Component	Liquid	Vapor	Recombined inlet
CO_2	0.184	0.43999	0.43988
N_2	0.079	3.57992	3.57836
C_1	11.447	89.53803	89.50321
C_2	6.573	4.49990	4.50083
C_3	9.115	1.35997	1.36343
i-C_4	2.639	0.14000	0.14111
n-C_4	8.337	0.27999	0.28359
i-C_5	4.814	0.06000	0.06212
n-C_5	6.981	0.06000	0.06309
C_6	10.205	0.02298	0.02752
C_7	14.554	0.01430	0.02079
C_8	14.474	0.00426	0.01071
C_9	6.408	0.00055	0.00341
C_{10}	2.852	0.00009	0.00136
C_{11}	0.971	0.00001	0.00044
C_{12}	0.364	0.00000	0.00016

To obtain the water content, oils are centrifuged to measure the BS and W (bottom settlings and water).

Analyses for H_2S and CO_2

Since CO_2 and H_2S are soluble in water, great care is needed to bring samples into the laboratory without losing some. Field tests are quite common. H_2S (hydrogen sulfide) is very poisonous and reactive. Its unit of content in gas is grains per 100 standard cubic feet of gas; less than $\frac{1}{4}$ grain is a normal specification. One pound is equal to 7000 grains, and the molecular weight of H_2S is 34.076. Hence, 100 ft^3 of H_2S gas contains $(100/379) \times 34.076 \times 7000 = 62,900$ grains. It follows that 1/4 grain of H_2S per 100 ft^3 is, in parts per million, $(1/4)(10^6)/(62,900) = 3.97$ ppm. Analytical methods include the use of an ecolyzer for field tests and length-of-stain tests, in which gases pass through a tube containing a material sensitive to H_2S. A chromatographic analysis may be made, but special arrangements may be necessary (see GPA *Technical Standards* [4-22]).

CO_2 (carbon dioxide) is included in chromatographic analyses and may also be measured by absorption in caustic solution in an *Orsat pipette*. A concern is to avoid absorption in water in transit or transfer.

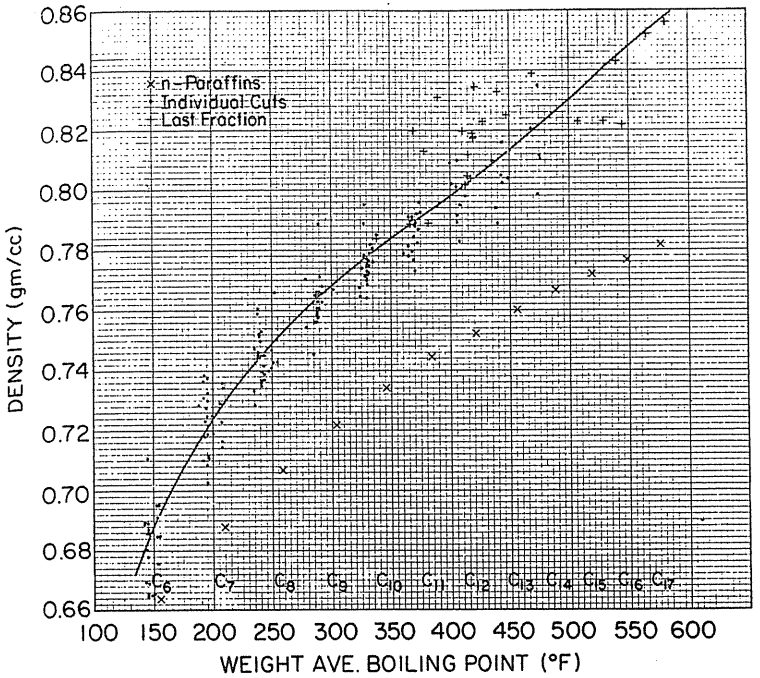

FIGURE 4-67
Density versus boiling point of all cuts obtained by distillation [Bergman et al., 1-35, courtesy AGA].

Liquid Analyses

Distillation has been used for analyzing liquids. The boiling points are recorded for the quantity distilled. Cuts are taken corresponding to boiling ranges for the C_6^+ group. Liquid density and molecular weight can be measured for each cut. The latter measurement involves the measurement of the lowering of the freezing point of benzene by the addition of a known amount of liquid. Table 4.16 gives the results for a particular pipeline condensate. The results of a chromatographic analysis of the condensate are also listed in the table. In checking the effectiveness of the distillation, the chromatography was run on each cut [1-35].

Hexane Plus Concentrator

Chromatographic analyses may do a poor job of giving the concentrations of the higher-boiling constituents, which are present in small amounts. A C_6^+ concentra-

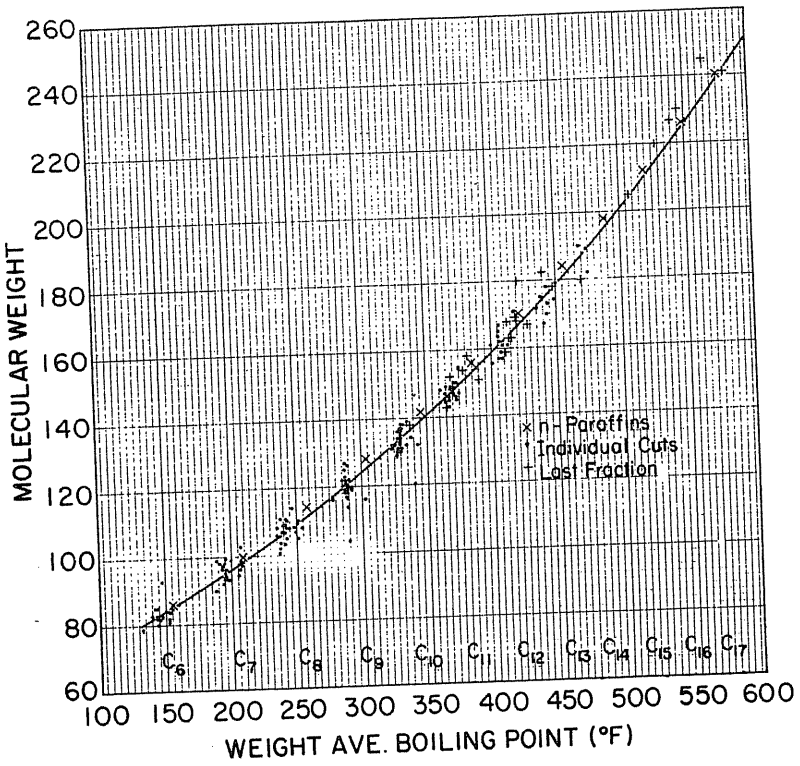

FIGURE 4-68
Molecular weight versus boiling point of all cuts obtained by distillation [Bergman et al., 1-35, courtesy AGA].

TABLE 4.16
Liquid analysis by distillation and chromatograph [Bergman, 1-35, courtesy AGA]
Cuts obtained by distillation of two C_6^+ liquids; Michigan-Wisconsin Pipeline Company: Willow Run, Michigan.
Type of liquid: pilot unit condensate (ANGS)

	Distillation results				Chromatograph	
Fraction	Weight %	Weight average boiling point, °F	Density @ 60°F, g/cm³	Molecular weight	Weight %	Weight average boiling point, °F
C_6	2.18	152.0	0.6954	84.0	3.59	146.0
C_7	9.46	194.0	0.7276	93.0	9.57	194.0
C_8	18.24	242.5	0.7453	105.0	20.16	243.0
C_9	32.97	288.0	0.7630	119.0	31.27	286.0
C_{10}	25.87	330.0	0.7728	133.0	24.13	327.0
C_{11}	7.56	364.0	0.7816	147.0	7.86	362.0
C_{12+}	3.72	419.0	0.8190	169.0	3.42	419.0

TABLE 4.17
Comparison of methods of obtaining extended gas analyses [Bergman & Katz, 4-5, courtesy AGA]

	Normal analysis	Concentrator analysis	Extended analysis using concentrator	Pilot unit combined analysis
	Mole %			
CO_2	.48		.48	.36
N_2	.26		.26	.24
C_1	96.97		96.96	97.23
C_2	2.22		2.22	2.10
C_3	.028		.028	.029
i-C_4	.0059		.0059	.0046
n-C_4	.0085		.0085	.0068
i-C_5	.0077		.0077	.0066
n-C_5	.0043		.0043	.0038
C_6	.0052	32.8	.0052	.0033
C_7	.0027	24.5	.0039	.0029
C_8	.0021	13.2	.0021	.0018
C_9	.0005	10.7	.0017	.0017
C_{10}		13.2	.0021	.0023
C_{11}		4.4	.0007	.0008
C_{12}		.8	.00013	.00014
C_{13}		.4	.00007	.00002
	99.9949	100.0	99.9903	99.99376
C_6^+	.0105		.0159	.01296
C_8^+	.0026		.0068	.00676
C_{10}^+			.0030	.00326

tor was devised and shown to match the use of the pilot separator used to construct Table 4.15. An analysis is made of the usual 0.5 cm³ or so of gas, and then a larger sample (100 cm³) is passed through a short (10 in., 25 mm) packed tube. This short tube section is reversed, put in a heating block, and flushed by carrier gas. The two analyses are combined based on some intermediate constituents. Table 4.17 is a comparison of the results from using a C_6^+ concentrator and those from using a pilot liquid separator followed by recombination [4-5].

HOME PROBLEMS

4.1. A natural gas liquid (NGL) is composed of propane, *i*-butane, *n*-butane, *i*-pentane, *n*-pentane, *n*-hexane, three isomer hexanes, and six heptanes. How many variables must be fixed to determine the boiling point at atmospheric pressure?

4.2. Given the composition of Mixture 18 by Robinson and Jacoby (Table 4.6), find the compressibility factor at 2000 psia and 100°F.

4.3. Compare the calculated Z value of Mixture B (Table 4.5) with the experimental data at 130°F and 3026 psia.

4.4. Compute the compressibility factors for the natural gas of the composition shown at a temperature of 75°F and pressures to 1600 psia.

He	0.007	C_3H_8	0.040
N_2	0.166	i-C_4H_{10}	0.004
CH_4	0.718	H_2S	0.008
C_2H_6	0.057		

4.5. Find the temperature drop when a flowing stream of methane expands from 100°F and 1000 psia down to 200 psia.

4.6. Compute the bubble point pressure of the following mixture at 0°F: C_1 (0.288), C_2 (0.343), and C_3 (0.369). The equilibrium charts are in Appendix E.

4.7. Compute the dew point temperature of the following mixture at 600 psia: C_1 (0.781), C_2 (0.1377), and C_3 (0.0813).

4.8. Compute the quantity of gas in ft^3/bbl condensate formed and the gravity of liquid in separator when the following composition of well fluid is flashed at 1000 psia and 77°F. Also compute the gas gravity.

	Mole fraction	K, at 1000 psia and 77°F
C_1	0.6017	3.8300
C_2	0.0329	0.6700
C_3	0.0223	0.2360
i-C_4	0.0091	0.1600
n-C_4	0.0150	0.1120
i-C_5	0.0135	0.0580
n-C_5	0.0083	0.0366
C_6	0.0336	0.0225
C_7	0.0373	0.0102
C_8	0.0352	0.0051
C_9	0.0314	0.0026
C_{10}^+ (M.W. 184) sp. gr. = 0.8119	0.1597	0.0005

4.9. What is the viscosity of 0.6-gravity natural gas at 2000 psia and 80°F? What is the viscosity of propane vapor at 14.7 psia and 60°F? 200°F? What is the viscosity of propane liquid at 600 psia and 60°F? 200°F?

4.10. The equilibrium compositions of vapor and liquid in a fractionating column are given below for 50°F and 600 psia. (*a*) Compute the surface tension of the liquid. (*b*) Compute the viscosity of each phase.

	Liquid	Vapor
C_1	0.204	0.654
C_2	0.178	0.150
C_3	0.618	0.196

REFERENCES

4-1. American Society for Testing and Materials, *ASTM Standards on Chromatography*, 1st Ed., Philadelphia, Pa. (1981).

4-2. American Society for Testing and Materials, *ASTM-IP Petroleum Measurement Table*, ASTM, Philadelphia (1986).

4-3. Beal, C., "The Viscosity of Air, Water, Natural Gas, Crude Oil, and Its Associated Gases at Oil Field Temperatures and Pressures," *Trans. AIME*, Vol. 165, 94–115 (1946).

4-4. Beggs, H. D., and J. R. Robinson, "Estimating the Viscosity of Crude Oil System," *J. Pet. Tech.*, Vol. 27, No. 9, 1140–1141 (1975).

4-5. Bergman, D. J., and D. L. Katz, "Condensate Formation in Natural Gas Pipelines," *Proc. AGA Trans. Conference*, T146–T156 (1975).

4-6. Bicher, L. B., and D. L. Katz, "Viscosity of Natural Gases," *Trans. AIME*, Vol. 155, 246 (1944).

4-7. Bloomer, O. T., D. C. Gami, and J. D. Parent, *Physical Chemical Properties of Methane-Ethane Mixtures*, Inst. Gas Tech. Research Bull. 22 (1935).

4-8. Brown, G. G., "A Series of Enthalpy-Entropy Charts for Natural Gases," *Trans. AIME*, Vol. 160, 65 (1945).

4-9. Brown, G. G., D. L. Katz, G. G. Oberfell, and R. C. Alden, *Natural Gasoline and Volatile Hydrocarbons*, Natural Gas Association of America, Tulsa, Oklahoma (1948).

4-10. Buxton, T. S., and J. M. Campbell, "Compressibility Factors for Lean Natural Gas–Carbon Dioxide Mixtures at High Pressures," *Trans. AIME*, Vol. 240, 80–86 (1967).

4-11. Carr, N. L., R. Kobayashi, and D. B. Burrows, "Viscosity of Hydrocarbon Gases under Pressure," *Trans. AIME*, Vol. 201, 264–272 (1954).

4-12. Carter, R. T., B. H. Sage, and W. N. Lacey, "Phase Behavior in the Methane-Propane-Pentane System," *Trans. AIME*, Vol. 142, 170 (1941); Vol. 151, 206 (1943).

4-13. Case, L. O., *Elements of the Phase Rule*, Edwards Letter Shop, Ann Arbor, Mich. (1939).

4-14. Chew, J. N., and C. A. Connally, Jr., "A Viscosity Correlation for Gas-Saturated Crude Oils," *Trans. AIME*, Vol. 216, 23–25 (1956).

4-15. Comings, E. W., B. J. Mayland, and R. S. Egly, "Viscosity of Gases at High Pressure," *Ind. and Eng. Chem.*, Vol. 32, 714 (1940).

4-16. Dewitt, K. J., and G. Thodos, "Viscosities of Binary Mixtures in the Dense Gaseous Region C_1-CO_2 System," *Can. J. Chem. Engr.*, Vol. 44, 148–150 (1960).

4-17. Dourson, R. H., B. H. Sage, and W. N. Lacey, "Phase Behavior in the Methane-Propane-Pentane System," *Trans. AIME*, Vol. 151, 206 (1943).

4-18. Eakin, B. E., and R. T. Ellington, "Improved High Pressure Capillary Tube Viscometer," *Trans. AIME*, Vol. 216, 85–91 (1959).

4-19. Eakin, B. E., and R. T. Ellington, "Predicting the Viscosity of Pure Light Hydrocarbons," *J. Pet. Tech.*, Vol. 15, No. 2, 210–214, February (1963).

4-20. Edmister, W. C., "Applications of Thermodynamics to Hydrocarbon Processing," *Petrol. Engr.*, series of articles, 1948–1949: (*a*) Vol. 27, No. 11, 129 (1948); (*b*) Vol. 27, No. 12, 116 (1943); (*c*) Vol. 28, No. 1, 128 (1949); (*d*) Vol. 28, No. 2, 137 (1949).

4-21. Firoozabadi, A., D. L. Katz, H. Soroosh, and V. A. Sajjadian, "Surface Tension of Reservoir Crude-Oil/Gas Systems Recognizing the Asphalt in the Heavy Fraction," *SPE Reservoir Engineering*, 265–272, February (1988).

4-22. Gas Processing Association, (*a*) *Technical Standards*, (*b*) *Plant Operations Test Manual*, Tulsa, Oklahoma (1982).

4-23. Giddings, J. G., and R. Kobayashi, "Correlation of the Viscosity of Light Paraffin Hydrocarbons and Their Mixtures in Liquid and Gaseous Regions," *Trans. AIME*, Vol. 231, 679–682 (1964).

4-24. Hall, K. R., and L. Yarborough, "A New Equation of State for Z Factor Calculations," *Oil & Gas J.*, Vol. 71, No. 25, 82, (June 18, 1973); SPE Reprint Series, No. 13, Vol. 1, 227–232 (1977).

4-25. Hocott, C. R., and S. W. Buckley, "Measurements of the Viscosity of Oils under Reservoir Conditions," *Trans. AIME*, Vol. 142, 131 (1941).

4-26. Holcomb, D., and G. G. Brown, "Thermodynamic Properties of Light Hydrocarbons," *Ind. Eng. Chem.*, Vol. 34, 590 (1942); Vol. 36, 384 (1944).
4-27. Hough, E. W., and H. G. Warren, "Correlation of Interfacial Tension of Hydrocarbons," *Soc. Pet. Eng. J.*, Vol. 6, No. 4, 345–349, Dec. (1966).
4-28. Hwang, E. T. S., G. W. Swift, and F. Kurata, "Viscosities and Densities of Methane-Propane Mixtures at Low Temperatures and High Pressures," *AIChE J.*, Vol. 12, 932 (1966); Vol. 13, 846 (1967).
4-29. Jacoby, R. H., and J. H. Tracht, "Collection of Samples under Pressure," *J. Chromagraphic Sci.*, Vol. 13, 44, Jan. (1975).
4-30. Jones, D. T., "Determination of the Surface Tension and Specific Gravity of Crude Oil under Reservoir Conditions," *Trans. AIME*, Vol. 118, 81 (1936).
4-31. Jones, M. L., et al., "Measurement of the Thermodynamic Properties of Gases—Methane," *Chem. Engr. Progress Sym. Series*, Vol. 59, No. 44, 52 (1963).
4-32. Junk, W. A., and E. W. Comings, "Thermal Conductivity of Gas Mixtures at High Pressure," *Chem. Engr. Prog.*, Vol. 49, 263 (1953).
4-33. Katz, D. L., "A Look Ahead in Gas Storage Technology," *Proc. AGA Trans. Conference*, T283–T289 (1981).
4-34. Katz, D. L., "Application of Vaporization Equilibrium Constants to Production Engineering Problems," *Trans. AIME*, Vol. 127, 159 (1938).
4-35. Katz, D. L., "Overview of Phase Behavior in Oil and Gas Production," *Trans. AIME*, Vol. 275, 1205–1214 (1983).
4-36. Katz, D. L., and A. Firoozabadi, "Predicting Phase Behavior of Condensate–Crude Oil Systems Using Methane Interaction Coefficients," *J. Pet. Tech.*, Vol. 30, No. 11, 1649–1655, Nov. (1978).
4-37. Katz, D. L., and K. H. Hackmuth, "Vaporization Equilibrium Constants in a Crude Oil–Natural Gas System," *Ind. and Eng. Chem.*, Vol. 29, 1076 (1937).
4-38. Katz, D. L., and F. Kurata, "Retrograde Condensation," *Ind. Eng. Chem.*, Vol. 32, 817 (1940).
4-39. Katz, D. L., R. R. Monroe, and R. R. Trainer, "Surface Tension of Crude Oils Containing Dissolved Gases," *Petroleum Technology*, Sept. (1943).
4-40. Katz, D. L., and W. Saltman, "Surface Tension of Hydrocarbons," *Ind. Eng. Chem.*, Vol. 31, 91 (1939).
4-41. Katz, D. L., and C. M. Sliepcevich, "Condensates May Occupy Apparent Negative Volume in a Gas Reservoir," *Oil Weekly*, Vol. 116, No. 13, 30 (1945).
4-42. Katz, D. L., D. J. Vink, and R. A. David, "Phase Diagram of a Mixture of Natural Gas and Natural Gasoline Near the Critical Conditions," *Trans. AIME*, Vol. 136, 106 (1940).
4-43. Kay, W. B., "Density of Hydrocarbon Gases and Vapors," *Ind. Eng. Chem.*, Vol. 28, 1014 (1936).
4-44. Keyes, F. G., R. S. Taylor, and L. B. Smith, "The Thermodynamic Properties of Methane," *J. Math. and Phys.*, Vol. 1, 211 (1922).
4-45. King, G., and D. L. Katz, "Dense Phase Transmission of Natural Gas, Energy Processing," *Canada*, 36–47, Nov-Dec (1973).
4-46. Kuenen, J. P., "On Retrograde Condensation and the Critical Phenomena of Mixtures of Two Substances," *Communs. Phys. Lab.*, Univ. Leiden, No. 4B (1892).
4-47. Lee, A. L., M. H. Gonzalez, and B. E. Eakin, "The Viscosity of Natural Gases," *Trans. AIME*, Vol. 237, 997–1000 (1966).
4-48. Lee, A. L., K. E. Starling, J. P. Dolan, and R. T. Ellington, "Viscosity Correlation for Light Hydrocarbon Systems," *AIChE J.*, Vol. 10, No. 5, 694–697 (1964).
4-49. Lewis, W. K., and C. D. Luke, "Properties of Hydrocarbon Mixtures at High Pressure," *Trans. ASME*, Vol. 54, No. 17, 55 (1932).
4-50. Lohrenz, J., B. G. Bray, and C. R. Clark, "Calculating Viscosities of Reservoir Fluids from Their Compositions," *Trans. SPE*, Vol. 231, 1171–1176 (1964).
4-51. Mather, A., J. Powers, and D. L. Katz, "Direct Determination of the Effect of Pressure on Enthalpy of a Mixture of Methane and Propane," *AIChE J.*, Vol. 15, No. 1, 111–116 (1969).

4-52. Matthews, C. S., and C. O. Hurd, "Thermodynamic Properties of Methane," *Trans. AIChE*, Vol. 42, 55 (1946).
4-53. Matthews, T. A., C. H. Roland, and D. L. Katz, "High Pressure Gas Measurement," *Proc. NGAA*, Vol. 41 (1942); *Petrol. Refiner*, Vol. 21, No. 6, 53 (1942).
4-54. Michels, A., A. Botzen, and W. Schwirman, "The Viscosity of CO_2 Between 0°C and 75°C at Pressures to 2000 Atm," *Physica*, Vol. 23, 95–102 (1957).
4-55. Pfenning, H. W., and J. J. McKetta, "Generalized Z Chart for Low Pressures," *Petrol. Refiner*, Vol. 36, No. 12, 153 (1957).
4-56. Reamer, H. H., B. H. Sage, and W. N. Lacey, "Volumetric and Phase Behavior of the Methane-Butane-Decane System," *Ind. Eng. Chem.*, Vol. 39, 77 (1947); Vol. 43, 1436 (1951); Vol. 44, 1671 (1952).
4-57. Reamer, H. H., B. H. Sage, and W. N. Lacey, "Volumetric and Phase Behavior of the Methane-Propane System," *Ind. Eng. Chem.*, Vol. 42, 534 (1950).
4-58. Robinson, D. B., C. A. Macrygeorgos, and G. W. Govier, "The Volumetric Behavior of Natural Gases Containing H_2S and CO_2," *Trans. AIME*, Vol. 219, 54 (1960).
4-59. Roland, C. H., "Vapor-Liquid Equilibria for Natural Gas-Crude Oil Mixtures," *Ind. Eng. Chem.*, Vol. 37, 930–936 (1945).
4-60. Roland, C. H., D. E. Smith, and H.H. Kaveler, "Equilibrium Constants for a Gas Distillate System," *Oil & Gas J.*, Vol. 39, No. 46, 128 (1941).
4-61. Rzasa, M. J., and D. L. Katz, "The Coexistence of Liquid and Vapor Phases at Pressures Above 10,000 Psi," *Trans. AIME*, Vol. 189, 119 (1950).
4-62. Sage, B. H., R. A. Budenholzer, and W. N. Lacey, "Phase Equilibria in Hydrocarbon Systems—Methane–*n*-Butane System in Gaseous and Liquid Regions," *Ind. Eng. Chem.*, Vol. 32, 1262 (1940).
4-63. Sage, B. H., B. L. Hicks, and W. N. Lacey, "Phase Equilibria in Hydrocarbon Systems Methane–*n*-Butane in Two Phase Region," *Ind. Eng. Chem.*, Vol. 32, 1085 (1940).
4-64. Sage, B. H., W. N. Lacey, and J. G. Schaafsma, "Phase Equilibria in Hydrocarbon Systems—Methane-Propane System," *Ind. Eng. Chem.*, Vol. 26, 214 (1934).
4-65. Sage, B. H., H. M. Lauender, and W. N. Lacey, "Methane-Decane Systems," *Ind. Eng. Chem.*, Vol. 32, 743 (1940).
4-66. Satter, A., and J. M. Campbell, "Non-Ideal Behavior of Gases and Their Mixtures," *Trans. AIME*, Vol. 228, 333–347 (1963).
4-67. Schwartz, C. A., "The Variation in the Surface Tension of Gas Saturated Petroleum with Pressure," *J. Appl. Phys.*, Vol. 1, 245 (1931).
4-68. Sherborne, J. E., "Fundamental Phase Behavior of Hydrocarbons," *Trans. AIME*, Vol. 136, 119 (1940).
4-69. Simon, R., A. Rosman, and E. Zana, "Phase Behavior Properties of CO_2—Reservoir Oil System," *Soc. Pet. Eng. J.*, Vol. 1, No. 1, 20–26, Feb. (1978).
4-70. Souders, M., C. Selheimer, and G. G. Brown, "Equilibria between Liquid and Vapor Solutions of Paraffin Hydrocarbons," *Ind. Eng. Chem.*, Vol. 24, 517 (1932).
4-71. Standing, M. B., and D. L. Katz, "Density of Crude Oils Saturated with Natural Gas," *Trans. AIME*, Vol. 146, 159 (1942).
4-72. Standing, M. B., and D. L. Katz, "Density of Natural Gases," *Trans. AIME*, Vol. 146, 140 (1942).
4-73. Standing, M. B., and D. L. Katz, "Vapor-Liquid Equilibria of Natural Gas-Crude Oil Systems," *Trans. AIME*, Vol. 155, 232–245 (1944).
4-74. Starling, K. E., and R. T. Ellington, "Viscosity Correlations for Nonpolar Dense Fluids," *AIChE J.*, Vol. 10, No. 1, 11–15 (1964).
4-75. Vasquez, M., and H. D. Beggs, "Correlations for Fluids Physical Property Prediction," *J. Pet. Tech.*, Vol. 32, No. 6, 968–970, June (1980).
4-76. Wichert, E., and K. Aziz, "Calculate Z's for Sour Gases," *Hydrocarbon Proc.*, Vol. 51, 119, May (1972).
4-77. Wichert, E., and K. Aziz, "Compressibility Factor of Sour Natural Gases," *Can. J. of ChE.*, Vol. 49, 267–273 (1971).

4-78. Weinaug, C. F., and D. L. Katz, "Surface Tension of Methane-Propane Mixtures," *Ind. Eng. Chem.*, Vol. 35, 239–246 (1943).
4-79. Yarborough, L., and K. R. Hall, "How to Solve Equations of State for Z Factors," *Oil & Gas J.*, Vol. 72, No. 7, 86–88, Feb. 18 (1974).
4-80. Yesavage, V., J. Powers, and D. L. Katz, "Experimental Determinations of Several Thermal Properties of a Mixture Containing 51 Mole Percent Propane in Methane," *AIChE J.*, Vol. 16, No. 5, 867 (1969).
4-81. Yesavage, V., J. Powers, and D. L. Katz, "Experimental Determinations of Several Thermal Properties of a Mixture Containing 77 Mole Percent Propane in Methane," *J. Che. Eng. Data*, Vol. 14, 137 (1969).
4-82. Yesavage, V., J. Powers, and D.L. Katz, "Thermal Properties of Propane," *J. Che. Eng. Data*, Vol. 14, 197 (1969).

CHAPTER 5

GAS HYDRATES AND THEIR PREVENTION

Natural gas and crude oil normally reside in reservoirs in contact with connate water. Water can combine with low–molecular weight natural gases to form a solid *hydrate*, even if the temperature is above the water freezing point. This solid hydrate causes difficulties in many operations in the oil and gas industry. Recently, harvesting natural gas from hydrates in the earth (north Alaska, ocean sediments, and Siberia) became important, and the DOE (Department of Energy) has sponsored several research projects on hydrate occurrence.

The early physicists Faraday, Villard, De Forcrand, and Schroeder conducted research in gas hydrates, including the measurement of hydrate-forming pressures up to 4000 psia (27.58 MPa) [1-15]. Hammerschmidt followed in 1934 with the first report of a natural gas hydrate in transmission pipelines [5-8]. Katz et al. [1-1] in 1942 introduced the *K*-charts method based upon binary system experimental data for predicting hydrate-forming conditions. Since then, numerous research efforts, both theoretical and experimental, have been carried on.

This chapter is intended to provide the basic information needed for engineering operations and not to serve as a base for further scientific research of hydrates. Since, in engineering practice, plain water ice can also plug a pipeline, studies of hydrate-forming conditions below 32°F (0°C) are not included.

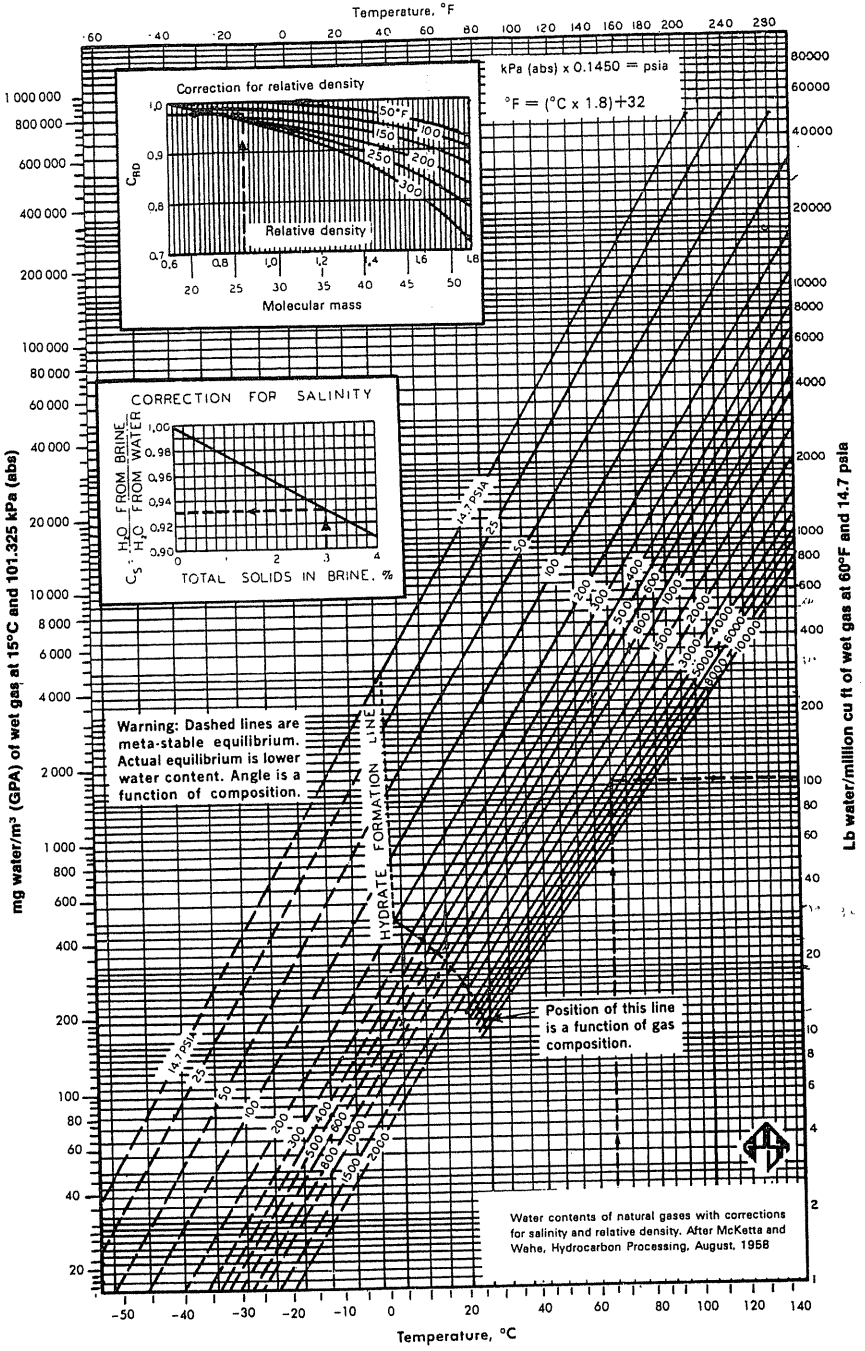

FIGURE 5-1
Water content of natural gas in equilibrium with water [Mcketta's data, GPA, 1-28].

5.1 WATER CONTENT OF NATURAL GAS

When natural gas leaves the reservoir, it flows up the wellbore, which has lower temperatures than the reservoir, and hence the gas saturated with water will tend to yield a liquid water condensate. Pressure drop also affects the water content, but this effect during flow up a wellbore is smaller than that of temperature.

Figure 5-1 [1-28] shows a chart giving the water content of natural gases in pound water per MMcf of gas at equilibrium temperatures and pressures for pure water. Kobayashi's chart is in reference [1-1]. The hydrate-forming line should be a function of gas composition. When dissolved solids (salts) are in the water, they lower the vapor pressure of the water in proportion to the concentration of the salts (Fig. 5-2 [5-18]). It is necessary to discount the water content in a gas reservoir by the effect of the dissolved solids. When only the gravity of the brine is known, it may be used to approximate the concentration. For example, brine of density 1.110 g/mL would have approximately $1.11 - 1.00 \times 10^6$ or 110,000 ppm dissolved solids.

Example 5.1. A natural gas reservoir, A, at 6500 feet has a temperature of 146°F, a pressure of 3005 psia, and a connate water density of 1.100 g/mL. What is the water content of the gas in the reservoir?

Solution. Figure 5-1 reads, at 146°F and 3005 psia, 100 lb/MMcf for pure water. For 110,000 ppm dissolved solids, Fig. 5-2 gives a water content of 92.5 percent. So, there are $0.925 \times 100 = 92.5$ lb-water/MMcf for the above reservoir gas.

Example 5.2. When the gas from the reservoir A reaches the wellhead separator, it is at a pressure of 1000 psia and a temperature of 65°F. Fresh water will have condensed out.

What is the yield of liquid water in the separator?

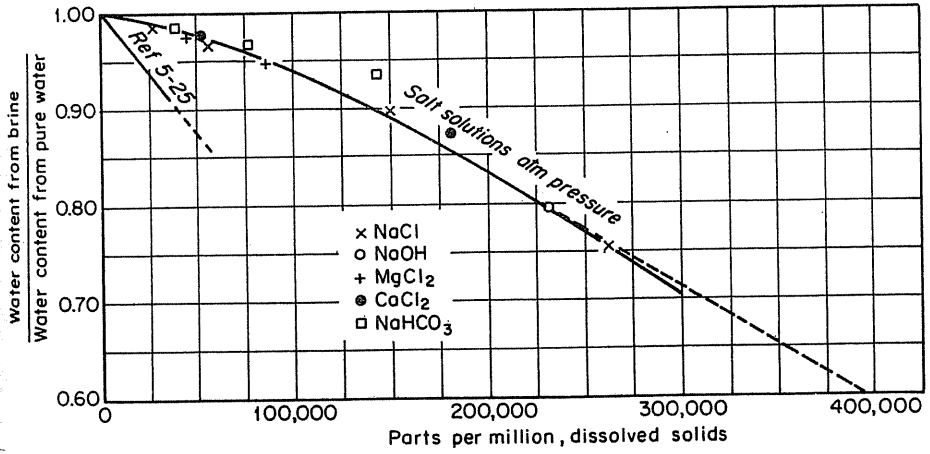

FIGURE 5-2
Effect of dissolved solids on vapor pressure of water [Katz, 5-18, courtesy AAPG].

Solution. Figure 5-1 gives the water content as 23 lb/MMcf. It follows that 92.5 − 23 = 69.5 lb water condensed, or 69.5/8.33 = 8.3 gallons; 69.5/42 = 1.65 bbl. Gas gravity has no noticeable effect on the water content of a natural gas with minor impurities.

5.2 WATER-HYDROCARBON SYSTEMS: GAS HYDRATES

Gas hydrates are solids resembling ice in appearance and form under pressure at temperatures as high as 85°F (29.4°C) and higher. The reaction is between liquid water and gas; in the laboratory a rocking glass-windowed cell is used to observe their formation (Fig. 5-3 [1-1]). Figure 5-4 [5-36] shows the growth of hydrate crystal for a water-CO_2-H_2S system at 800 psia (5.5 MPa) and 70°F (21°C). In the field, hydrates are most likely to form after expansion accompanied by Joule-Thomson cooling, such as in a choke or pinched valve.

A loose association by molecular forces forms a solid structure of water and gas constituents, a clathrate. Unlike solid crystals, liquid water has a mobile lattice structure with two different vacant lattice positions. Gas molecules fit into these vacant lattice positions and cause the water-gas system to solidify (Fig. 5-5 [5-14]). The formation of this solid solution of water and methane can be expressed as

$$CH_4 + n\,H_2O \rightarrow CH_4 \cdot n\,H_2O(s) \qquad (5.1)$$

Each unit cell of hydrate structure I has 2 small and 6 large voids. For structure II, there are 16 small and 8 large voids. In general, CH_4, C_2H_6, CO_2, and H_2S are the *guests* of the *host* to form hydrate water structure I; C_3H_8, i-C_4H_{10}, CH_2Cl_2, and $CHCl_3$ form hydrate structure II. Certainly, the smaller molecules could freely enter structure II also. Pentane and heavier hydrocarbons

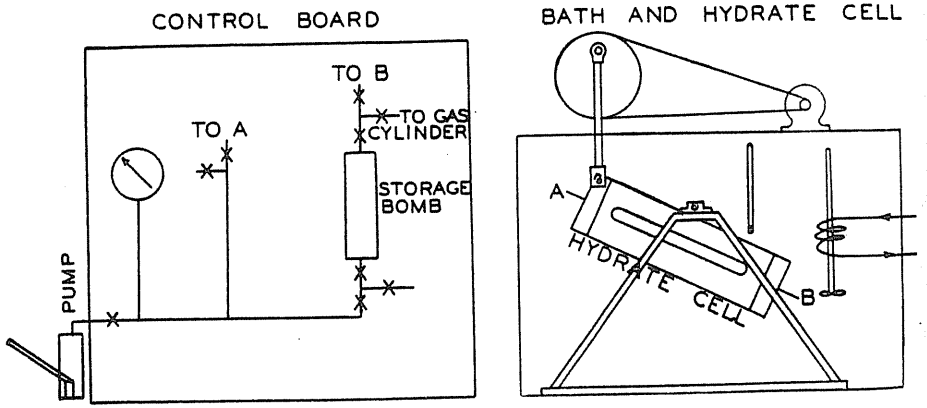

FIGURE 5-3
Early apparatus for forming hydrate [Katz et al., 1-1, courtesy McGraw-Hill Publishing Co.].

FIGURE 5-4
Hydrate of an H_2O-CO_2-H_2S system [Robinson, 5-36].

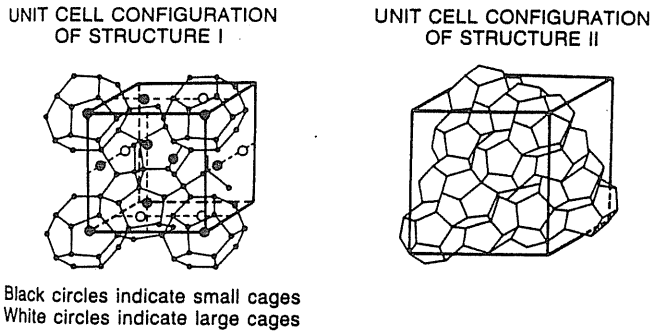

FIGURE 5-5
Structures I and II of hydrate lattice [Holder et al., 5-14, courtesy *Reviews in ChE*].

TABLE 5.1
Hydrate structure and formation conditions for various gases [Holder, et al. 5-14]

Gas	Hydrate lattice structure	$P(VL_1H)$, at 273.15°K, kPa	$(T, K)/(P, kPa)$ at quadruple point* $Q_2(VL_1L_2H)$	Cavities entered
Ar	II	8,820	None	All
Kr	II	1,450	None	All
Xe	I	152	None	All
N_2	I	14,300	None	All
O_2	I	11,100	None	All
CO_2	I	1,260	283.1/4450	All
H_2S	I	93	302.7/2240	All
CH_4	I	2,560	None	All
C_2H_4	I	551	None	All
C_2H_6	I	530	287.8/3390	Large
C_3H_6	II	466	274.1/601	Large
C_3H_8	II	176	278.9/552	Large
Cyclo-C_3H_6	I, II	69	289.4/566	Large
i-C_4H_{10}†	II	113	275.0/167	Large
n-C_4H_{10}†	II	None	None	Large
cis-2-butene‡	II	None	None	Large
trans-2-butane	None	None	None	None

* Q_2 is the quadruple point where the VL_1H curve intersects the VL_1L_2 curve. V is gas, L_1 is water-rich liquid, L_2 is liquid rich in hydrate former, and H is hydrate.

† Will not fit into the large cavity of structure I.

‡ Will only form hydrates for a vapor if a small molecule such as CH_4 is also present. No pure hydrates form from this gas alone.

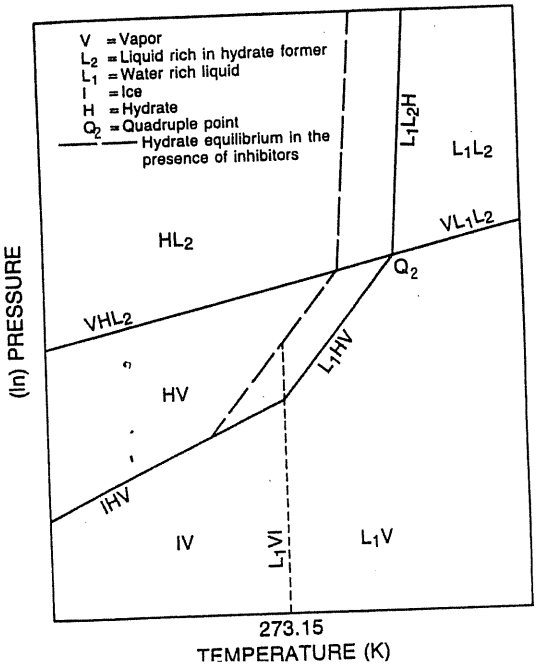

FIGURE 5-6
Schematic representation of hydrate-forming conditions for a subcritical forming gas [Holder et al., 5-14, courtesy *Reviews in ChE*].

are too large to fit into the larger cavities to form hydrates [5-14]. *N*-butane was believed to form hydrates as a pure substance [5-5], but actually, *n*-butane only exists in hydrates when other smaller hydrate-forming molecules (methane) are present [5-31]. Table 5.1 [5-14] gives the hydrate structure for various gases. Figure 5-6 [5-14] is a schematic representation of hydrate-forming conditions for a subcritical hydrate-forming gas.

Conditions for hydrate formation are given in Figs. 5-7, 5-8, 5-9, and 5-10, with the last of these representing a general correlation based on several real storage gases [5-22]. It can be observed that pure hydrate-forming substances form hydrate in the area above the three-phase, liquid water/liquid/gas line (Fig. 5-7). Also, CO_2 and H_2S form hydrates as shown in Fig. 5-9. Subcritical gases reach a quadruple point and have L_1-L_2 equilibria. Carson and Katz [5-5] ran the first L_1-L_2-hydrate point shown on Fig. 5-7.

Deaton and Frost measured the effect of propane on hydrate formation for methane (Fig. 5-11 [5-6]). Similar results have been found for the ethane-methane system [5-11]. It was reported that one percent propane lowers the pressure by 400 psi (2.76 MPa) at 50°F (10°C). At the time, the mole percent was determined by gas gravity or mass spectrum [1-1] instead of chromatographic analyses.

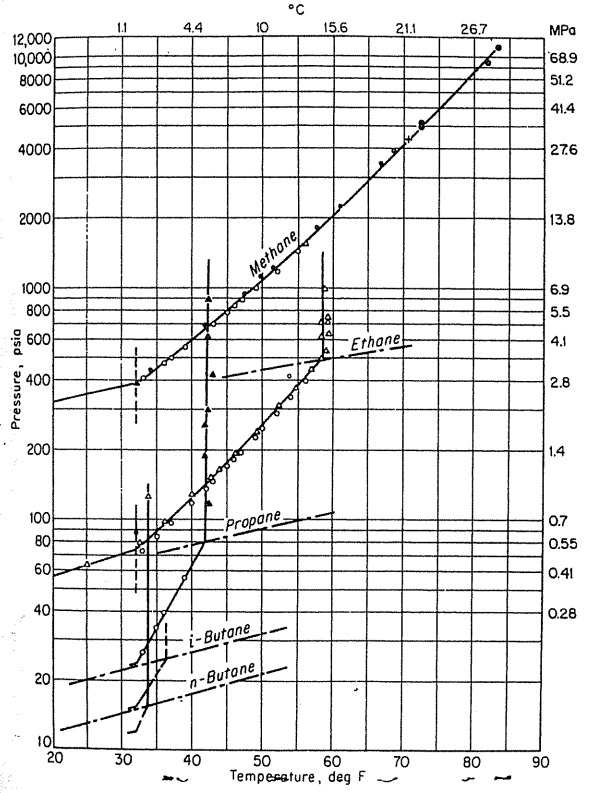

FIGURE 5-7
Hydrate-forming conditions for paraffin hydrocarbons [Katz et al., 1-1, courtesy McGraw-Hill Publishing Co.].

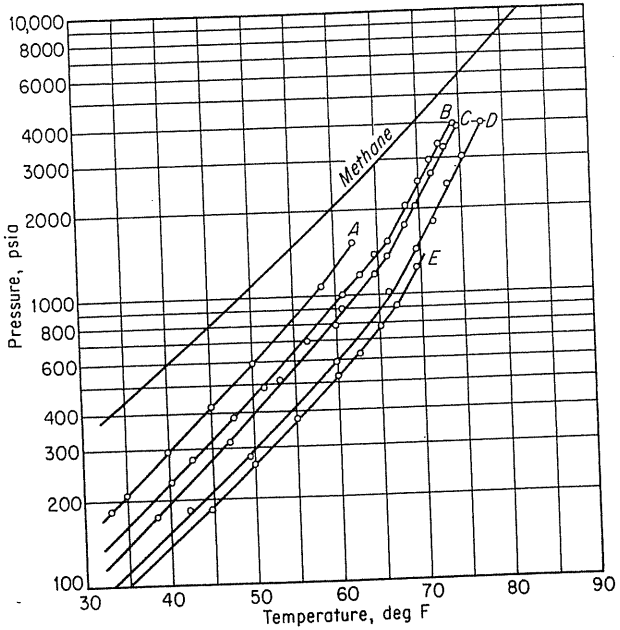

FIGURE 5-8
Hydrate-forming conditions for natural gases [Katz et al., 1-1, courtesy McGraw-Hill Publishing Co.].

The measured dew point of gases that have been brought into equilibrium with gas hydrates, for example in low-temperature separators, will be lower than the equilibrium temperature. This is explained by the fact that measured dew points are metastable equilibria. For details see references [5-21,5-35].

5.3 PREDICTION OF CONDITIONS FOR HYDRATE FORMATION

The *K-value method* was an early method for calculating hydrate-forming conditions using vapor-solid equilibrium constants [1-1,1-2]. Katz et al. reasoned that hydrates were the equivalent of solid solutions and not mixed crystals (see Example 4.1). They postulated that hydrate-forming conditions could be calculated from empirically determined vapor-solid equilibrium constants $K_{vs} = y/x_s$, where y is the mole fraction of a hydrocarbon in the gas on a water-free basis and x_s is the mole fraction of the hydrocarbon in the solid on a water-free basis. The hydrate-forming conditions should satisfy $\sum y/K_{vs} = 1$. This procedure is like the dew point calculation for complex gaseous mixtures (Eq. 4.26). K-charts (Figs. 5-12 to 5-18) for methane, ethane, propane, isobutane, n-butane, H_2S and CO_2 are available for predicting the hydrate-forming points from gas composition.

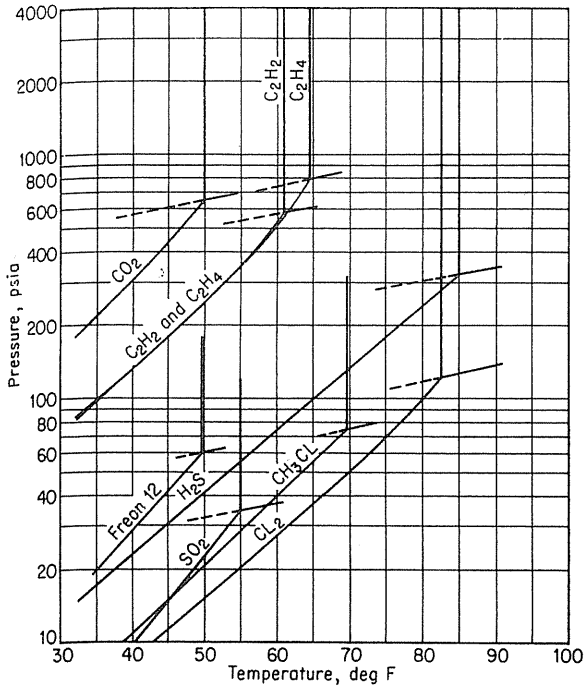

FIGURE 5-9
Hydrate-forming conditions for miscellaneous substances [Katz et al., 1-1, courtesy McGraw-Hill Publishing Co.].

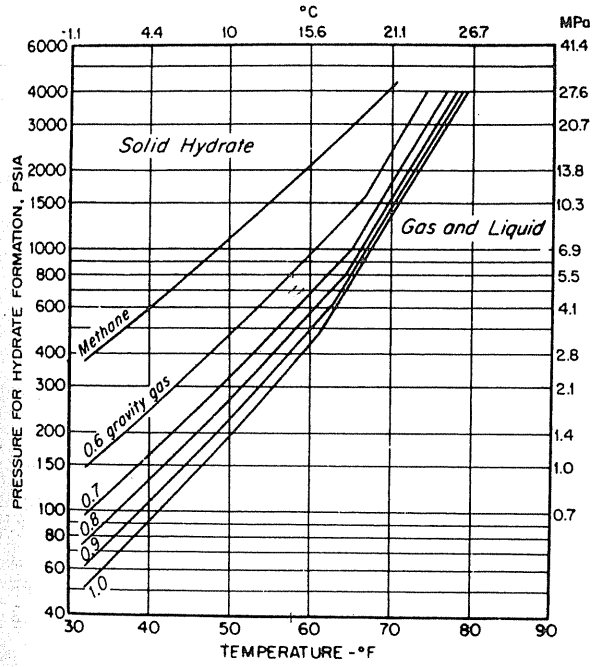

FIGURE 5-10
Hydrate-forming conditions for natural gases with various gravities [Katz, 5-5, courtesy SPE-AIME].

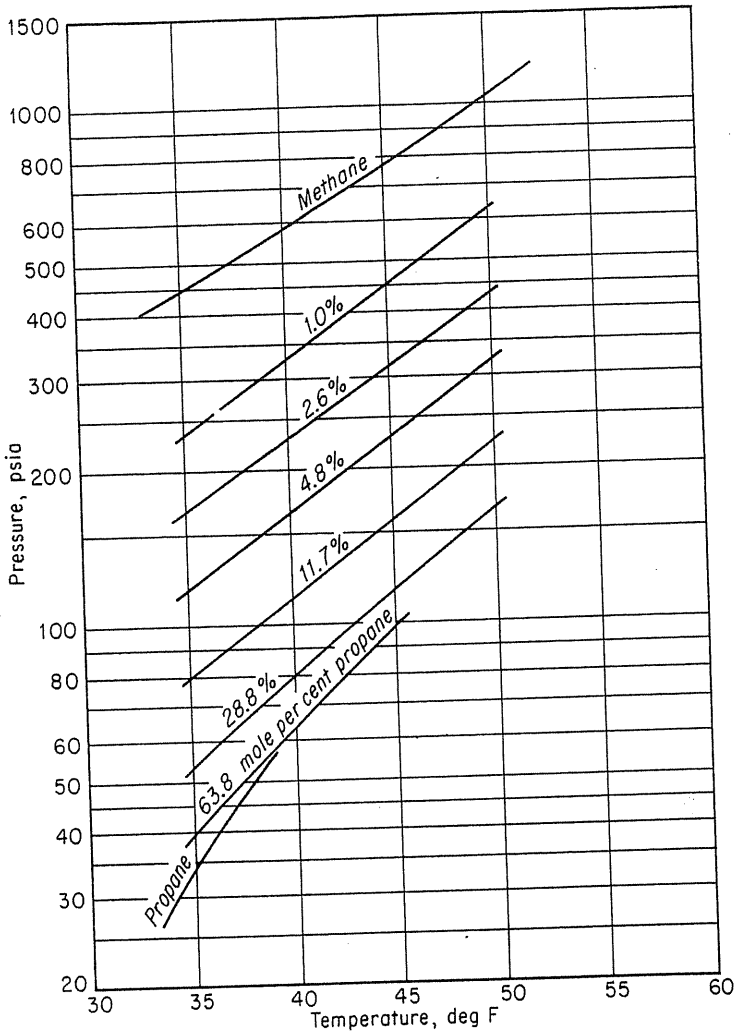

FIGURE 5-11
Hydrate formation conditions of methane-propane mixtures [Deaton & Frost, 5-6].

It should be noted that the H_2S and CO_2 *K*-charts were obtained by analyzing experimental data of a binary system of methane and H_2S or CO_2. Since H_2S and CO_2 are not members of the hydrocarbons family, application of the *K*-charts to conditions other than those used to prepare them may produce erroneous results. Table 5.2 gives the hydrate formation calculation for a natural gas at 50°F (10°C). The calculated pressure of 319 psia (2.2 MPa) agrees satisfactorily with

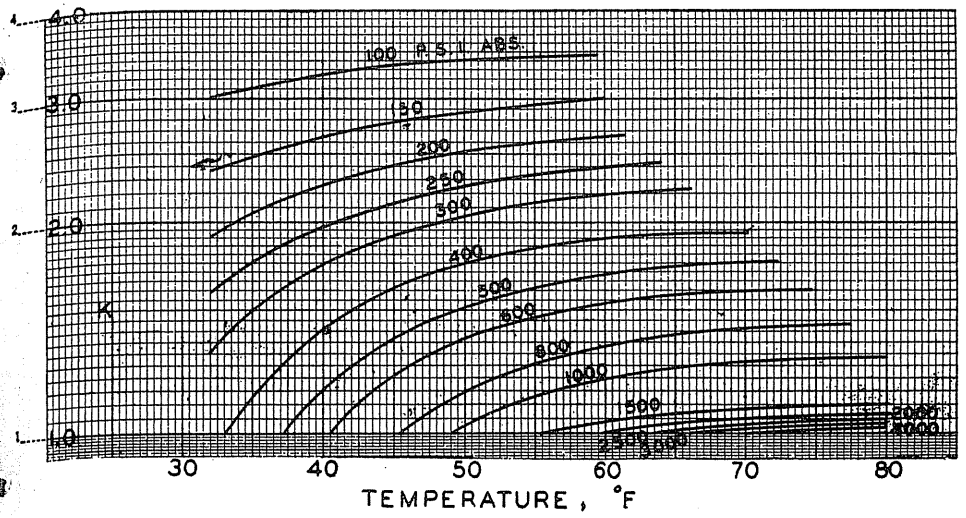

FIGURE 5-12
Vapor-solid equilibrium constant for methane [Carson & Katz, 5-5, courtesy SPE-AIME].

the observed pressure of 325 psia (2.24 MPa). The y/K_{vs} terms each equal the corresponding x_s of the hydrate composition on an anhydrous basis.

The simplified *gravity graphic method* [1-1,1-2] provides quick estimates of the hydrate-forming temperatures and pressures for various gas gravities, as shown in Figs. 5-10 and 5-19. Note that, for a 0.6-gravity gas, the actual hydrate pressure depends upon the propane content of gas mixture; low (0%) and high (5%) extremes are marked in Fig. 5-19. The same phenomena were reported by Sloan [5-43]. However, for a real storage gas the hydrate-forming pressures usually follow the solid curve of Fig. 5-19. When gas gravity approaches 1, the solid curve of Fig. 5-19 appropriately represents the hydrate-forming conditions regardless of the different propane concentrations. Nevertheless, Fig. 5-19 may be inappropriate for predicting the hydrate-forming conditions when gas mixtures contain substantial amounts of nonhydrocarbons N_2, CO_2, and especially H_2S.

The correlated equations for the curves of Fig. 5-20 are listed in Table 5.3 [5-14,5-31], following a general equation based on the gas gravity developed by Makogon [5-23].

5.4 VAN DER WAALS–PLATTEEUW MODEL

During the more than 30 years since Katz and co-workers [1-1,5-5,5-22,5-32, 5-45] proposed both the *K*-value and the gravity graphic methods, several new methods have been proposed to calculate the conditions of hydrate formation. A

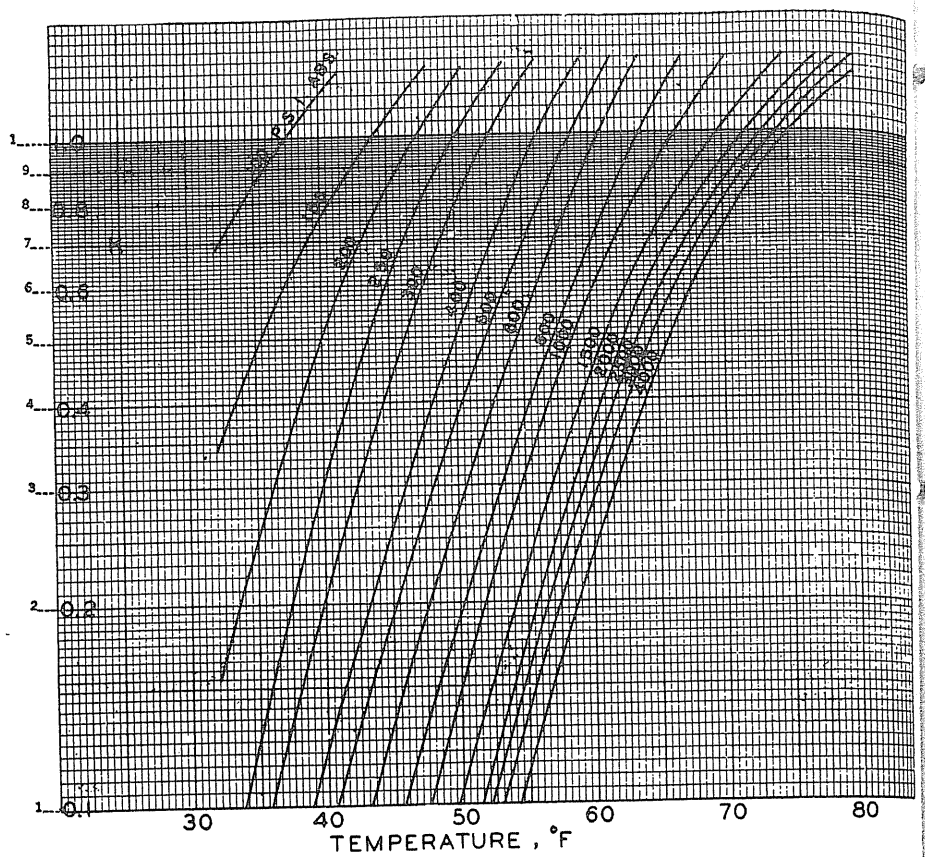

FIGURE 5-13
Vapor-solid equilibrium constant for ethane [Carson & Katz, 5-5, courtesy SPE-AIME].

series of theoretical and experimental work on hydrates has been done by Kobayashi, by Sloan et al. [5-2,5-3,5-7,5-25,5-43,5-44] and by Holder [5-11,5-13,5-14]. Saito et al. [5-39] developed a model based on the van der Waals–Platteeuw model, later generalized by Parrish and Prausnitz [5-33] to predict hydrate-forming conditions for multicomponent gases using a numerical procedure. Later, Ng and Robinson [5-29] introduced a binary interaction parameter, α, and incorporated it into the chemical potential equation (in terms of fugacity) to improve the accuracy of the Parrish-Prausnitz procedure. The Ng-Robinson method, combined with the Peng-Robinson equation of state, was investigated and found accurate for predicting the conditions of hydrate formation [5-28,5-30,5-38]. Byk and Fomina also reported a gas hydrate prediction method [5-4, 5-23].

The method for predicting hydrate equilibrium is based on the criterion that at equilibrium $\mu_H = \mu_W$, where μ_H is the chemical potential of water in the

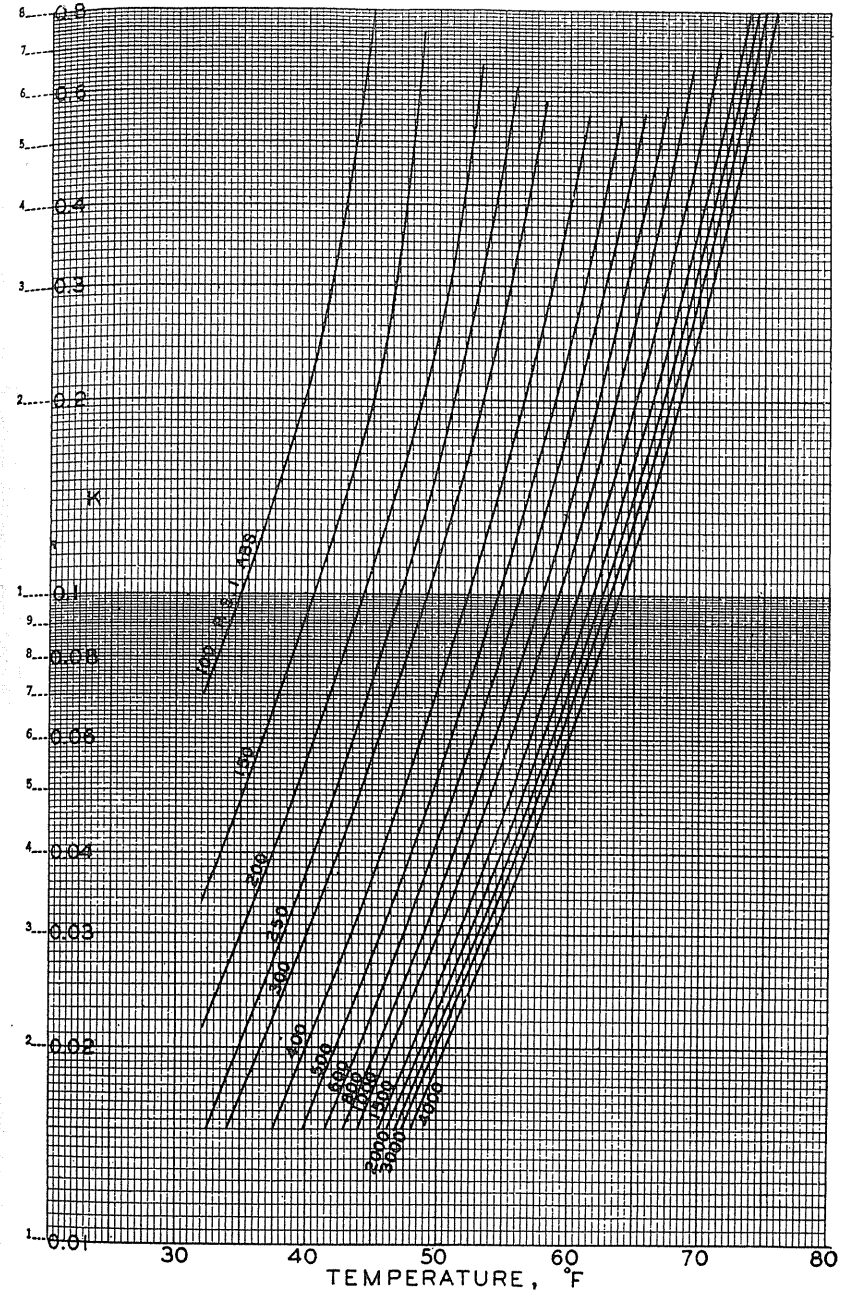

FIGURE 5-14
Vapor-solid equilibrium constant for propane [Carson & Katz, 5-5, courtesy SPE-AIME].

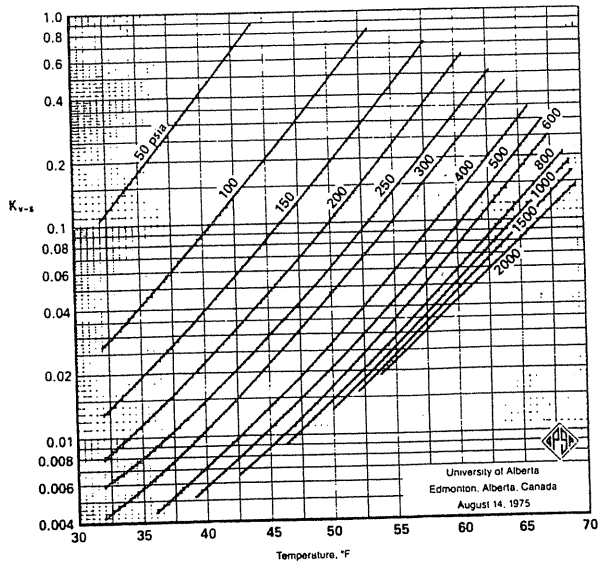

FIGURE 5-15
Vapor-solid equilibrium constants for *i*-butane [Carson & Katz, 5-5, courtesy SPE-AIME].

hydrate phase, and μ_W is the chemical potential of water in the water-rich or ice phase. Using μ_β, the chemical potential of an unoccupied hydrate lattice, as the reference state, the condition for equilibrium can be rewritten as

$$\Delta\mu_W = \Delta\mu_H \tag{5.2}$$

where $\Delta\mu_W = \mu_\beta - \mu_W$ and $\Delta\mu_W = \mu_\beta - \mu_W$.

Since both sides of Eq. (5.2) are functions of temperature and pressure, Parrish and Prausnitz [5-33] introduced an iterative procedure to obtain the hydrate-forming temperature at a given pressure or vice versa. The validity of the Parrish-Prausnitz method and the modified version by Ng-Robinson are verified by comparison with the experimental results for a methane-isobutane mixture in Table 5.4 [5-29]. A thorough review of the derivation of the theory can be seen in Holder et al. [5-14].

Commercial hydrate-forming programs based on the van der Waals-Platteeuw model are available. Figure 5-21 [5-29] shows lines computed by the Ng-Robinson program, along with experimental results[1] (similar plots were reported by Anderson and Prausnitz [5-1] as well as by Wagner, Erbar, and Majeed [5-46]). Sloan also developed a hydrate calculation program at the Colorado School of Mines [5-42].

[1] The program is available through the Gas Processors Association at Tulsa, Oklahoma.

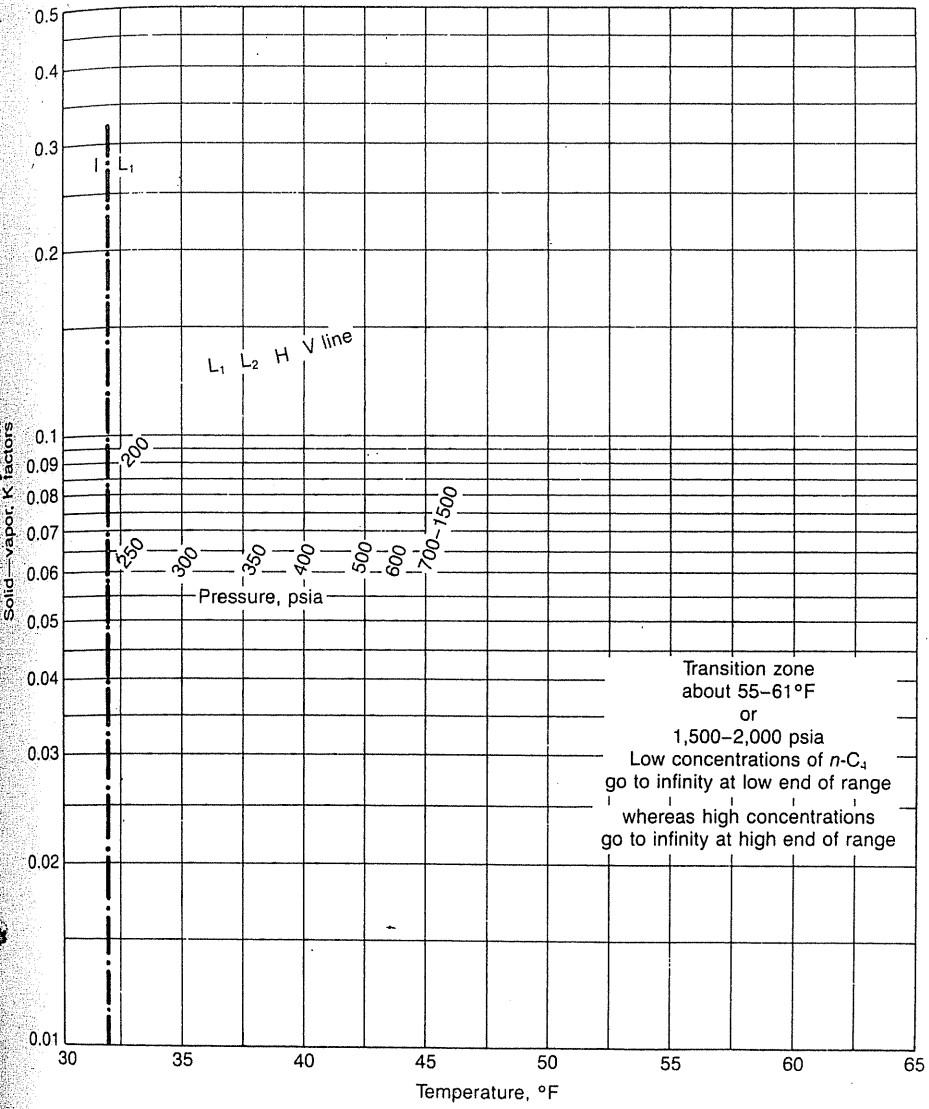

FIGURE 5-16
Vapor-solid equilibrium constant for *n*-butane [Poettmann, 5-34, courtesy *Hydrocarbon Processing*].

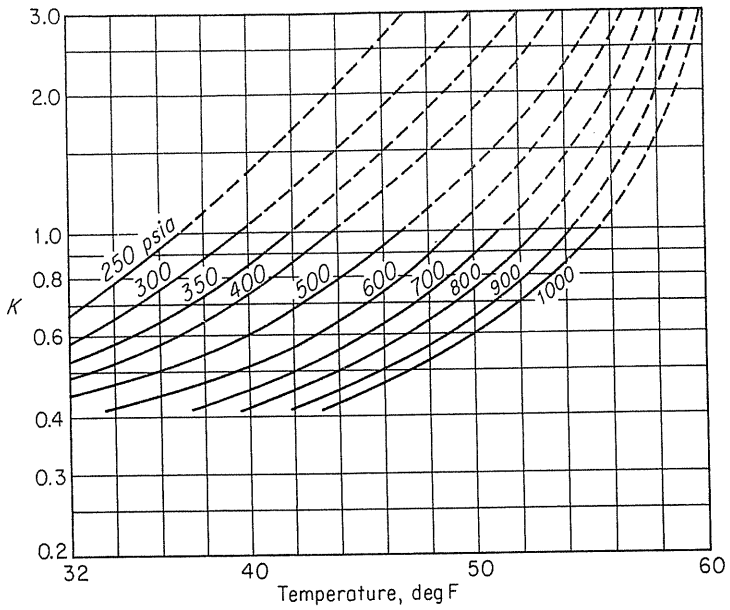

FIGURE 5-17
Vapor-solid equilibrium constant for CO_2 [Unruh & Katz, 5-45, courtesy SPE-AIME].

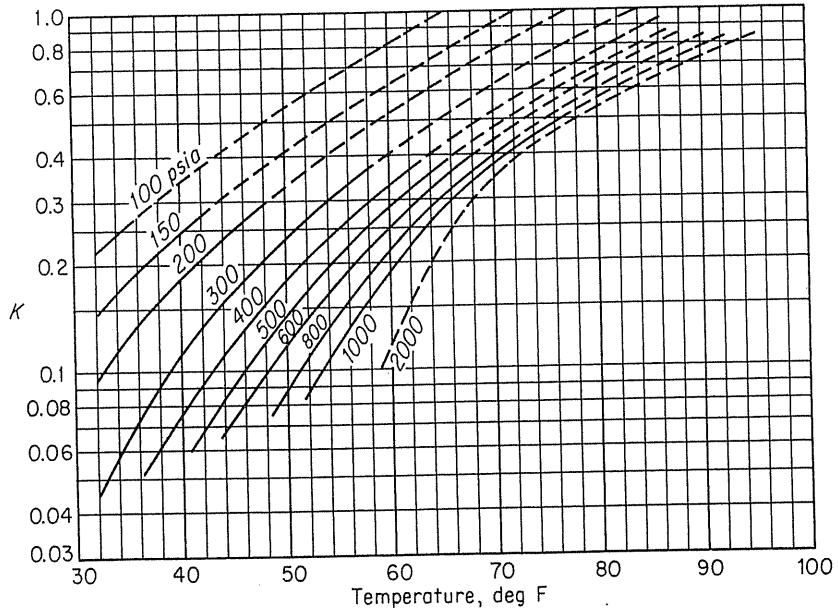

FIGURE 5-18
Vapor-solid equilibrium constant for H_2S [Noaker & Katz, 5-32, courtesy SPE-AIME].

TABLE 5.2
Calculation of pressure for hydrate formation at 50°F [Katz et al., 1-1, courtesy McGraw-Hill Publishing Co.]

Component	Mole % in gas	At 300 psia		At 350 psia	
		K_{vs}	y/K_{vs}	K_{vs}	y/K_{vs}
C_1	0.784	2.04	0.3841	1.9	0.4126
C_2	0.060	0.79	0.0759	0.63	0.0952
C_3	0.036	0.113	0.3185	0.086	0.4186
i-C_4	0.005	0.0725	0.0689	0.058	0.0862
n-C_4	0.019	0.21	0.0900	0.21	0.0900
N_2	0.094	Infinite	0.0000	Infinite	0.0000
CO_2	0.002	3.0	0.0007	2.3	0.0008
Total	1.000	—	0.9381	—	1.1035

Interpolating linearly, $y/K_{vs} = 1.0$ at 319 psia. The experimentally observed hydrate formation pressure at 50°F was 325 psia.

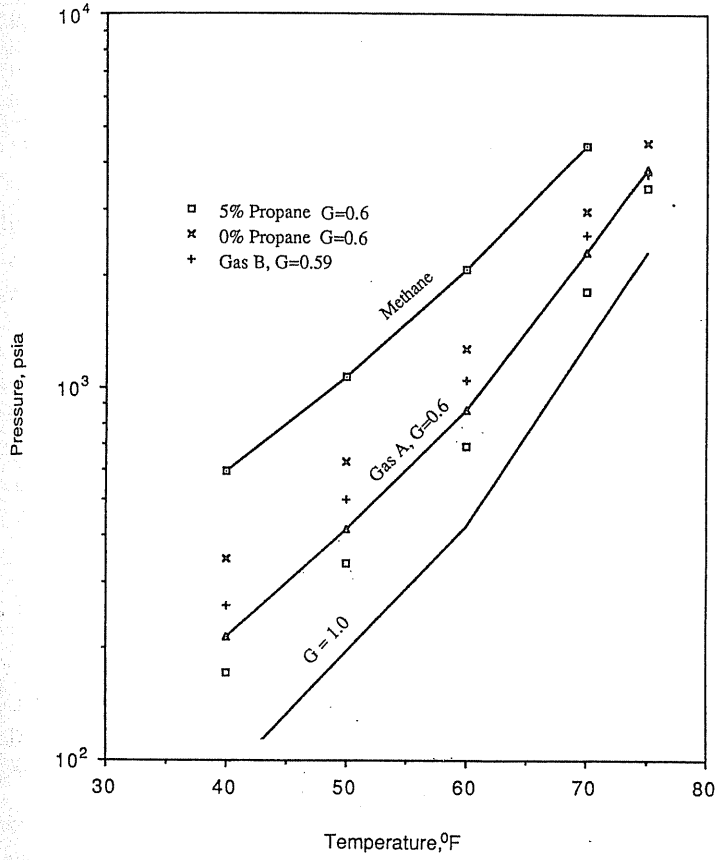

FIGURE 5-19
Compositional effects on hydrate-forming line (constructed by using Robinson's hydrate program [Robinson, 5-36]).

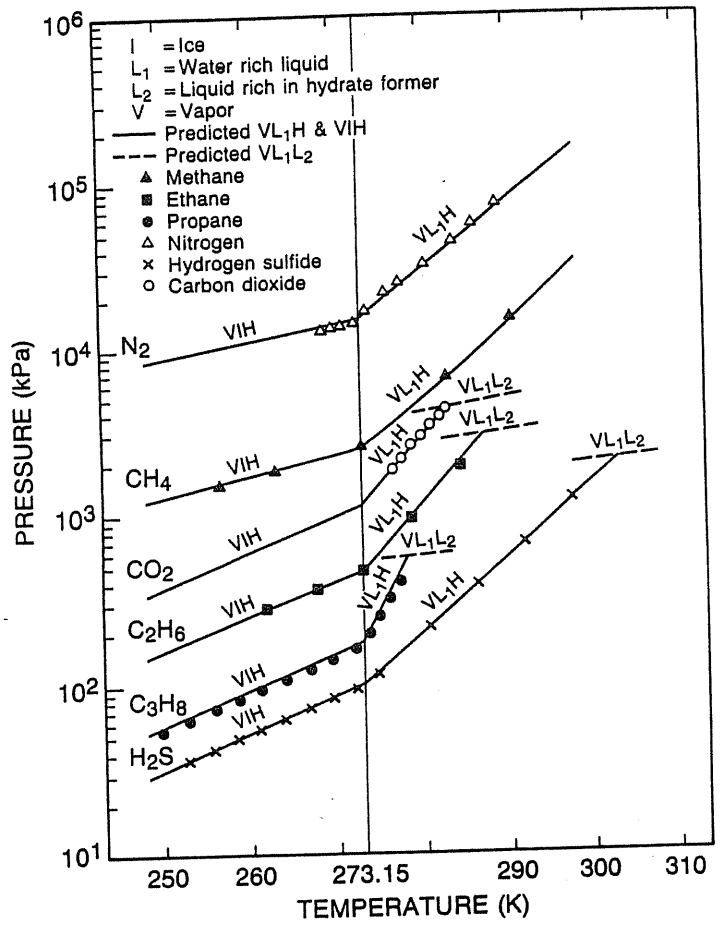

FIGURE 5-20
Hydrate-forming conditions for several gases [Holder, 5-14, courtesy *Reviews in ChE*].

5.5 GAS EXPANSION–JOULE THOMSON COOLING

When gases expand into separators or at wellheads, the temperature drops. Frequently, such a drop in temperature brings a gas (with accompanying water) into the hydrate region. Figure 4-49 gives the cooling curves for a 0.6-gravity gas [1-2].

Given a gas at an initial temperature and pressure that is to be expanded to a lower pressure, one often needs to know if the expansion can cause hydrates to form. A hydrate formation temperature-pressure curve can be plotted on a diagram like Fig. 4-49 to determine where it meets the Joule-Thomson cooling curve for the initial conditions. The point of intersection gives the maximum expansion the

TABLE 5.3
Correlated equations for various gas gravities and selected pure gases [Holder et al., 5-14]

$$P = \exp\left(a + \frac{b}{T}\right) \quad T \text{ in K, } P \text{ in kPa}$$

Gases	Structure	a	b	T range
CH_4	I	14.7170	−1886.79	248–273
CH_4	I	38.9803	−8533.80	273–298
C_2H_6	I	17.5110	−3104.535	248–273
C_2H_6	I	44.2728	−10424.248	273–287
C_3H_8	II	17.1560	−3269.6455	248–273
C_3H_8	II	67.1301	−16921.84	273–278
CO_2	I	18.5939	−3161.41	248–273
CO_2	I	44.5776	−10245.01	273–284
N_2	I	15.1289	−1504.276	248–273
N_2	I	37.8079	−7688.6255	273–298
H_2S	I	16.5597	−3270.409	248–273
H_2S	I	34.8278	−8266.1023	273–298

Natural gases [5-24]: (0–15°C)
$\ln P = 2.3026\beta + 0.1144(T + \kappa T^2)$ P in kg$_f$/cm^2*, T in °C
$(\beta = 2.681 - 3.811G + 1.679G^2;\ \kappa = -0.006 + 0.011G + 0.011G^2)$

* 1 kg$_f$/cm^2 = 0.968 atm = 14.223 psia. G: gas gravity.

TABLE 5.4
Predicted hydrate-forming conditions for methane-isobutane mixtures in L_1-H-G equilibrium [Ng & Robinson, 5-29, courtesy *Ind. Eng. Chem. Fundam.*]

Mole % i-C_4H_{10}	Temp, °F	Experimental results, psia	Predicted results, psia [5-33]	Predicted results, psia [5-29]
0.4	37.5	262	325	301
0.43	53.8	811	982	882
0.46	46.0	457	548	502
0.82	36.0	184	231	213
	50.6	485	622	563
	63.9	1456	1932	1645
1.2	34.2	138	177	163
	50.0	391	514	466
	62.3	1008	1405	1204
2.5	34.3	102	131	120
	53.7	398	492	443
	68.8	1460	1968	1587
6.0	34.9	73.3	91.5	83.7
	59.8	409	525	467
15.2	33.6	44.1	52.9	48.0
	60.3	295	374	334
28.6	33.4	29.7	37.6	34.1
	49.2	114	133	121
63.6	36.2	32.0	32.9	30.8

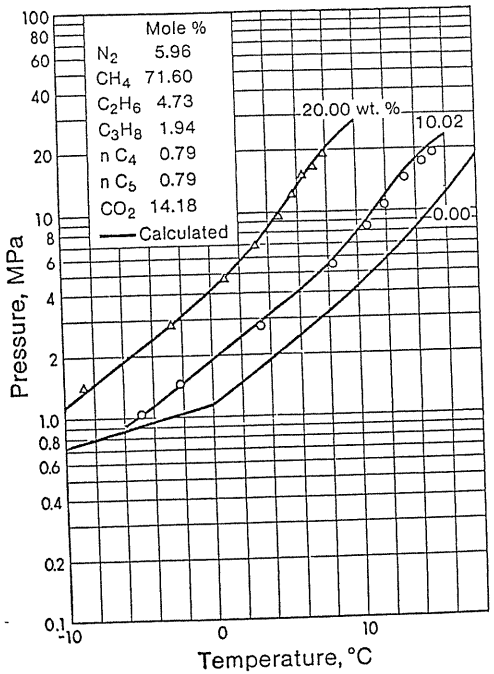

FIGURE 5-21
Experimental and calculated hydrate-forming conditions with methanol solution [Ng and Robinson, 5-29, courtesy *Ind. Eng. Chem. Fundam.*].

gas can undergo without risking hydrate formation. Figure 5-22 [5-19] is a plot of this information.

Example 5.3. If a 0.6-gravity gas at a wellhead at 2100 psia and 110°F is expanded into a separator at 700 psia, will hydrates form?

Solution. From Fig. 5-22, the maximum expansion is to some 850 psia, and thus hydrates could form. Note that this expansion chart neglects any heat effect of liquids present or phase change. There are charts for 0.7 and 0.8 as well as for 0.6-gravity gases.

5.6 USE OF METHANOL TO PREVENT HYDRATES

The freezing points of hydrates may be lowered by inhibitors—alcohol or brines to dilute the water. Basically, inhibitors have the same effect on hydrate formation as they have on ice formation; they make it more difficult. Figure 5-23 [5-26] gives the solubility of methane in water, natural gas in water, and natural gas in brine showing brine's decreased capacity to absorb natural gas compared to fresh

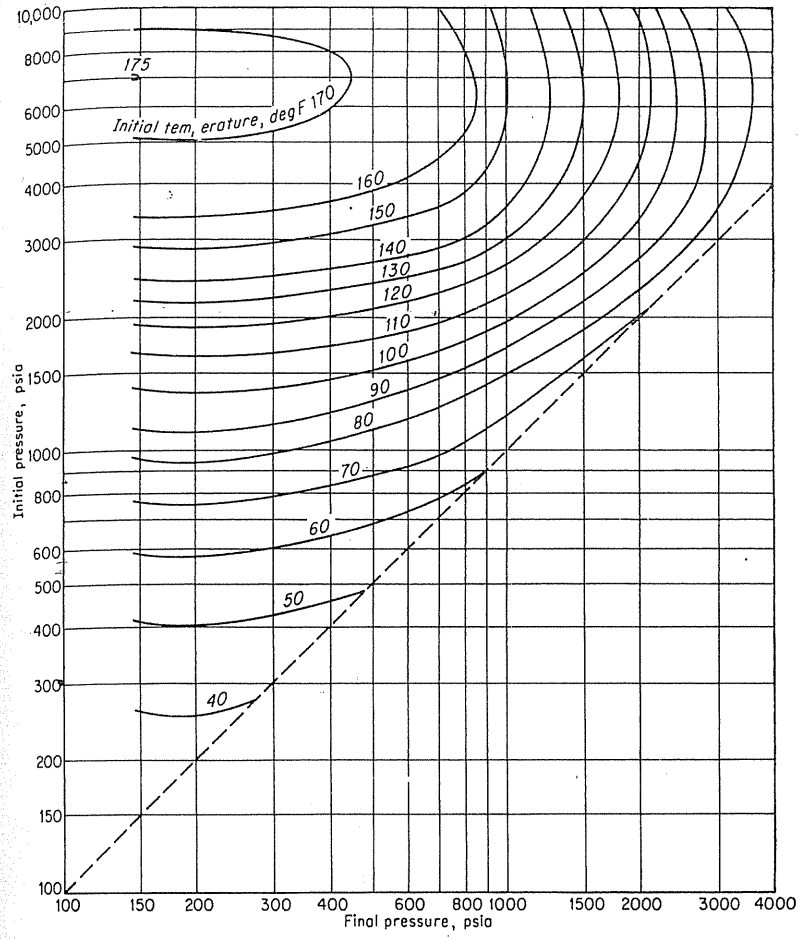

FIGURE 5-22
Permissible expansion of 0.6-gravity gas without hydrate formation [Katz, 5-19, courtesy SPE-AIME].

water. In the gas phase, on the other hand, the presence of non-hydrate-forming molecules (C_{5+}) dilutes the concentration of the hydrate-forming molecules; this also makes it more difficult to form hydrates. Figure 5-21 shows the effect of methanol on hydrate formation for a natural gas [5-29], and Fig. 5-24 [5-37] shows the same effect for methanol in propane. Figure 5-25 [5-37] shows the effect of glycol for CO_2.

Many operators use methanol at wellheads or field lines to prevent hydrate formation. Gas-driven minipumps often inject the methanol. Jacoby [5-15], using

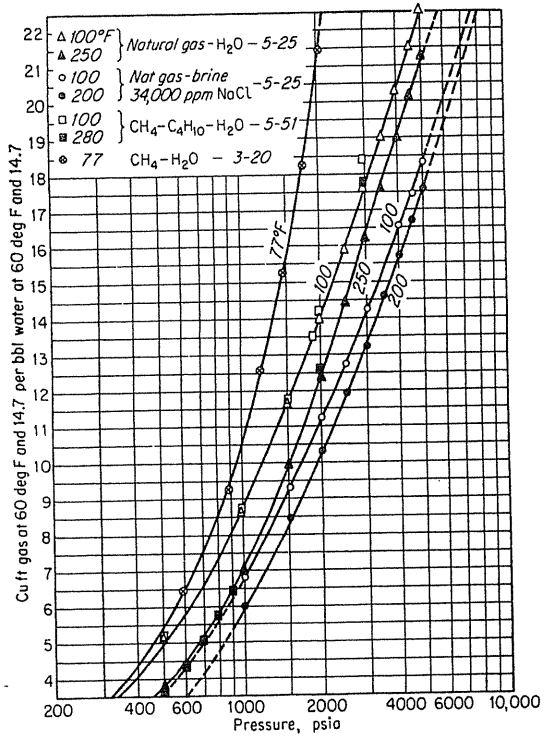

FIGURE 5-23
Solubility of natural gas in water [Mcketta & Katz, 5-26, courtesy SPE-AIME].

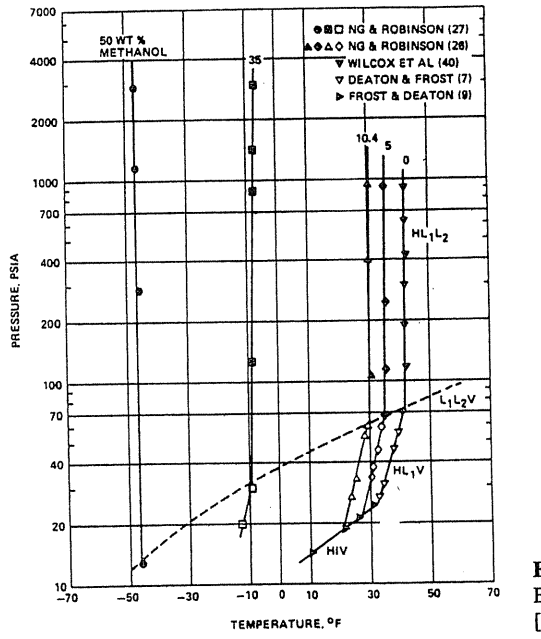

FIGURE 5-24
Effect of methanol on pure propane [Robinson et al., 5-37, courtesy GPA].

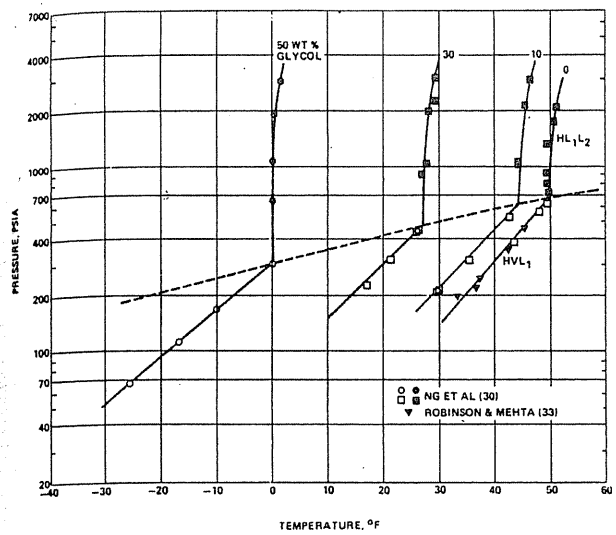

FIGURE 5-25
Hydrate formation in the presence of carbon dioxide and ethylene glycol [Robinson et al., 5-37, courtesy GPA].

Hammerschmidt's data and his own, developed a procedure for computing the amount of methanol needed to prevent hydrate formation. Figure 5-26 [5-15] gives the freezing point lowering of hydrates by methanol solutions; Fig. 5-27 gives the ratio of methanol in vapor to that in liquid water. Table 5.5 [1-2] gives an example of the calculation of the methanol requirement for a 0.67-gravity gas in equilibrium with water at 70°F (21°C) and 700 psia (4.83 MPa) cooled to 40°F (4.4°C). The example shows how to obtain the freezing point lowering and the methanol needed for the aqueous liquid. Then, the ratio of methanol in vapor to that in liquid gives the methanol required for the gas phase. The answer is 4 gallons methanol per million cubic feet. Gas transmission pipelines require dehydrated gas at 4–6 lb/MMcf to prevent the problems of gas hydrates in operations.

The procedures for preventing hydrate formation and the required equipment are outlined as follows:

1. Use of dew-point tester to obtain water content of natural gas:
   a. Bureau of Mines,
   b. Panometric.
2. Water production with natural gas, condensate, or entrained water.
3. Use of minipumps, points of entry in flow system for methanol injection.
4. Design of heaters prior to expansion of high-pressure gases.

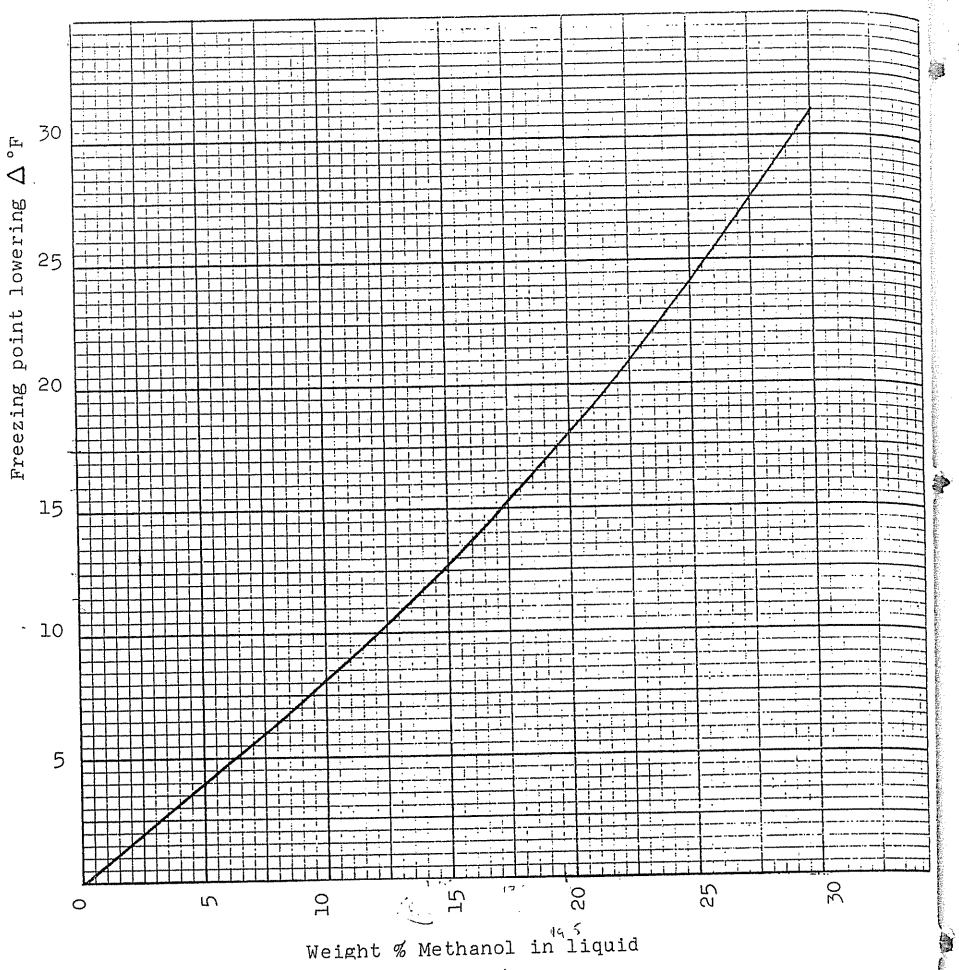

FIGURE 5-26
Effect of methanol on lowering of temperature for hydrate formation [after Hammerschmidt's data, 5-8].

5.7 HYDRATES IN THE EARTH

In addition to handling gas hydrates in surface processing, engineers should be aware that hydrates can form in wellbores and in the rocks of the earth.

Makogon's work in Siberia [5-23] and the conditions in Alaska have indicated depths at which one might expect hydrates to occur due to reduced temperatures in the arctic. Various methods have been put forth for harvesting the gas in hydrate form, as reviewed by Holder et al. [5-12]. The approach requiring heat to melt the hydrate to recover the gas seems futile. On the other hand, lowering the pressure on the hydrate below the equilibrium temperature can cause gas release

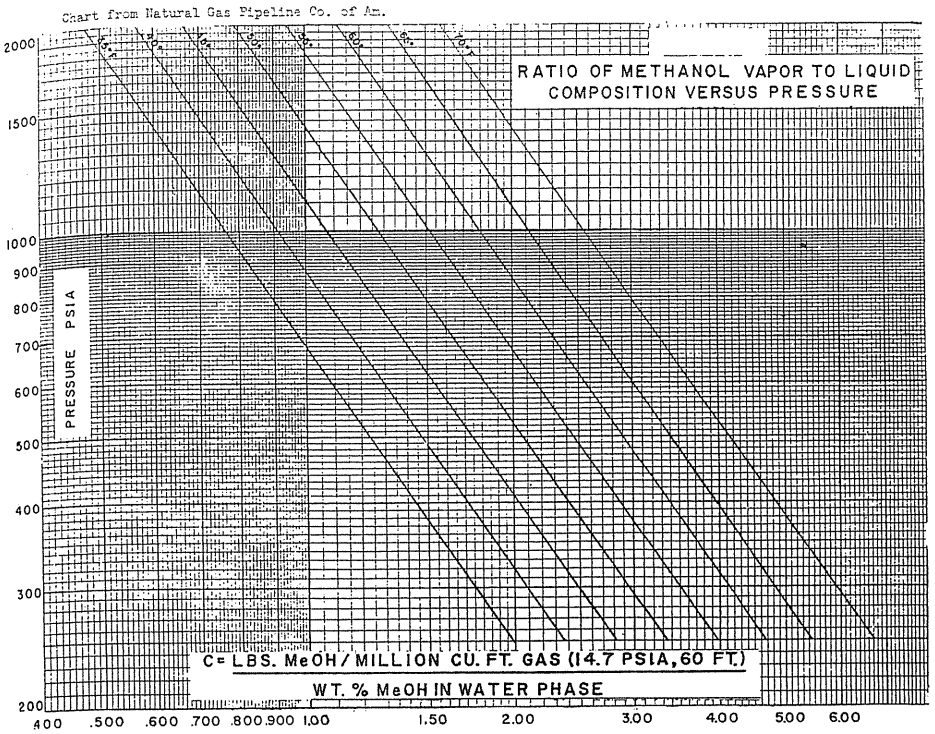

FIGURE 5-27
Ratio of methanol vapor composition to liquid composition versus pressure [Jacoby, 5-15, courtesy *Gas Magazine*].

in a nonequilibrium mode. Figure 5-28 shows conditions for hydrate formation with the North Slope temperature gradient.

A second phenomenon is that water and crude oil with dissolved gas may form hydrates at room temperature. Figure 5-29 shows that a bubble point oil is denuded of its gas phase by hydrate formation when the oil is agitated with water [5-13]. Further study is needed for application of this concept to arctic petroleum reservoirs.

The MOHOLE deep-sea drilling project brought cores to the ship deck that gave off gases over a period of time. This triggered the rediscovery of gas hydrates and initiated the studies of hydrates in ocean sediments. Kaplan conducted a symposium on "Natural Gases in Marine Sediment" [5-9,5-17]. It should be noted that at 4°C (39.2°F) methane requires 1300+feet (396+m) of sea water column to meet hydrate-forming pressure conditions. If methane is present in the deeper ocean sediments, it should be in hydrate form.

The DOE initiated an unconventional gas recovery project for gas hydrates. As part of the studies, a 40-foot (12.2-m) pure methane hydrate core was taken in the Pacific Ocean off Guatemala at 5637 ft (1718 m) (Fig. 5-30 [5-41]).

TABLE 5.5
Worksheet for calculating methanol requirements to prevent hydrate formation for a 0.67-gravity gas [Katz & Coats, 1-2]

Step no.	Quantity	Units	Use:	Calculated values
(1)	Line pressure	psia	Field data	700
(2)	Gas saturated temperature*	°F	Field data	60
(3)	Minimum gas temp.	°F	Field data	40
(4)	Saturated gas water content	lb/MMcf	Fig. 5-1	23
(5)	Gas water content at minimum temperature	lb/MMcf	Fig. 5-1	11
(6)	Change in water content	lb/MMcf	(4) − (5)	12
(7)	Hydrate temp. of gas	°F	Fig. 5-10	58
(8)	Freezing point lowering required	°F	(7) − (3)	18
(9)	Wt. % methanol in liquid	%	Fig. 5-26	20
(10)	Vapor to liquid composition ratio	lb/MMcf / wt. %	(1) & (3) Fig. 5-27	1.17
(11)	Methanol concentration in gas	lb/MMcf	(9) × (10)	23.4
(12)	Methanol to saturate liquid	lb/MMcf	(6) × (9) / 100 − (9)	3.0
(13)	Methanol inject rate	lb/MMcf	(11) + (12)	26.4
(14)	Methanol inject rate (pure Methanol at 68°F)	gal/MMcf	(13)/6.56 lb/gal	4.0

* If gas is unsaturated, use dew point temperature at pressure (1).

Makogon [5-27] related his Siberia experiences to the senior author when he described his tests on a gas well in a hydrate-containing formation. After a treatment of the well by methanol, the gas flow rate increased significantly. When asked about the propane content, he said it rose as expected. The Russian hydrate gas fields have average formation pressures of 78 atm (7.9 MPa or 1145.8 psi) and the temperatures vary from 8°C (46.3°F) to 12°C (53.6°F).

Hydrate Decomposition Rate

A rough estimate of the natural gas hydrate reserve ascribes it one third of the total natural gas on earth. Studies of hydrate will eventually shift their direction toward production from hydrate reservoirs if the process is economical. Only a few papers [5-10,5-40] presently cover the engineering calculations. Sparse information on hydrate decomposition rates may limit the applicability of research.

Recently (1987), Kim et al. [5-20] reported the first decomposition rate data on hydrate methane. The methane is formed above the H-L-V line and the

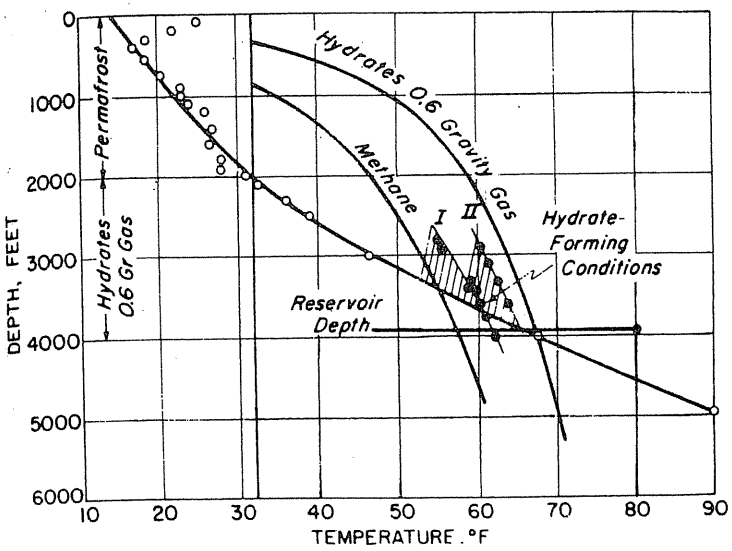

FIGURE 5-28
Earth temperature profile with overlapped quadruple locus [Holder et al., 5-13, courtesy AAPG].

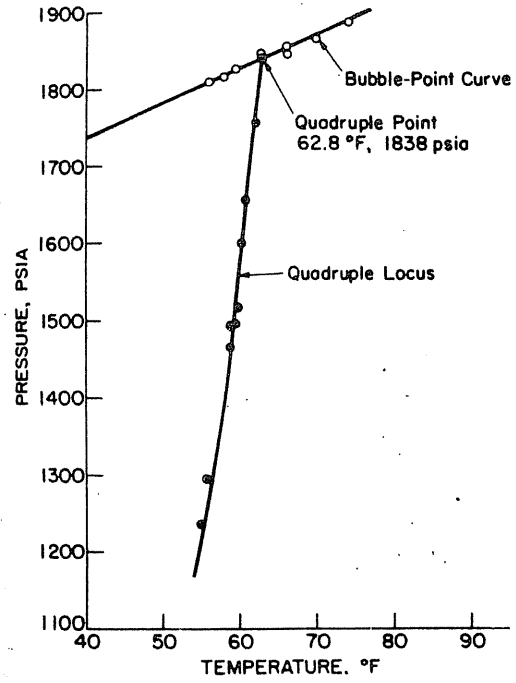

FIGURE 5-29
Quadruple locus and bubble point curve for crude oil–natural gas mixture [Holder et al., 5-13, courtesy AAPG].

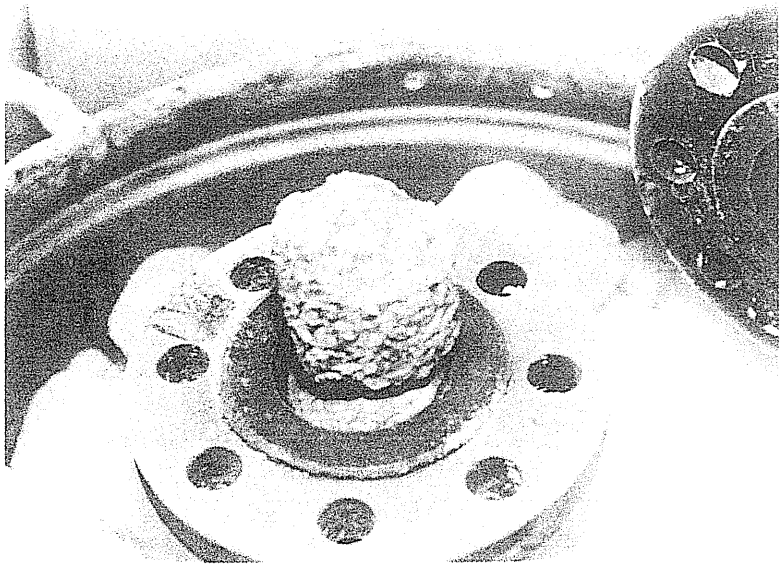

FIGURE 5-30
Methane hydrate core from deep sea drilling [Sloan, 5-41].

pressure is then graduately lowered to just above the decomposition point, to point e′ in Fig. 5-31. After the condition is stabilized, the pressure drops from e to d and the methane coming out of the reactor is then recorded. The whole process is isothermal, and a stirring reactor is used to eliminate the diffusion effect. The data are shown in Fig. 5-32, where n_H and n_0 denote the moles of methane hydrate and its initial moles. The proposed decomposition rate equation is

$$-\frac{dn_H}{dt} = kn_0^{1/3}n_H^{2/3} \tag{5.3}$$

where

$$k = k'\Delta f \tag{5.4}$$

where reaction coefficient k has the dimension of $1/T$ and Δf is the fugacity difference corresponding to the pressure difference imposed on the hydrate. The linear relationship between the decomposition rate and Δf is shown in Fig. 5-33. The scatter of the data at low temperatures is due to the experimental difficulty of maintaining constant temperature. A thorough understanding of the gas releasing rate during depressurization of hydrates could well increase the potential for harvesting natural gas from in-situ hydrate deposits in the earth, including ocean sediments.

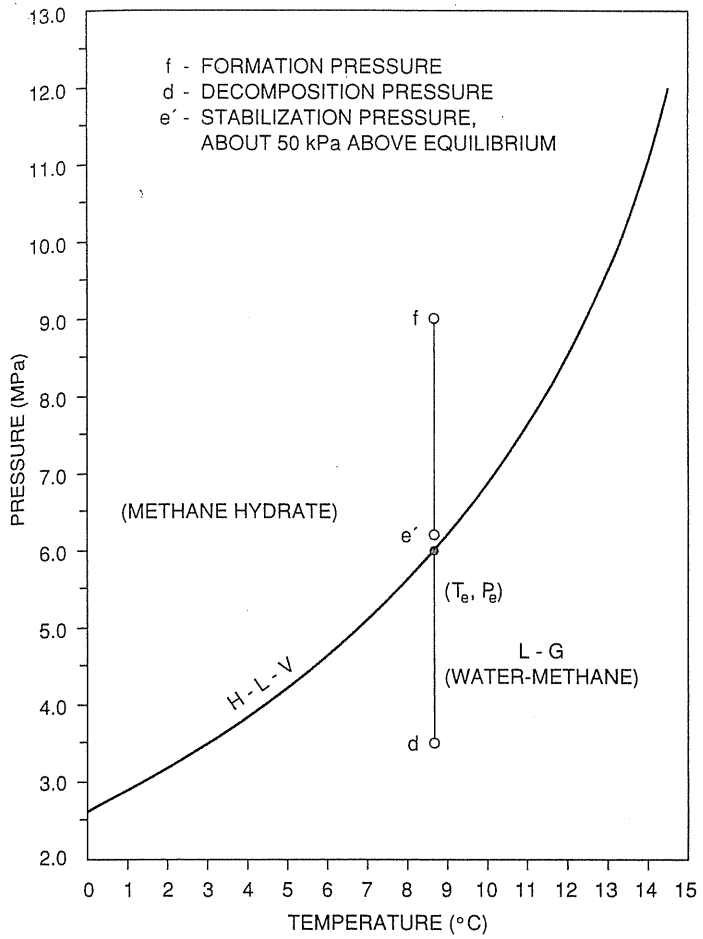

FIGURE 5-31
Experimental path of hydrate decomposition [Kim et al., 5-20, courtesy *Chem. Eng. Sci.*].

A recent informal paper by Makogon [5-24] indicates that pressure reduction is being used to harvest gas from in-situ hydrates. He estimates that some 70 × 10^6 Mcf (2 × 10^9 m^3) of gas has been produced from hydrate decomposition in the Messoyakh gas field.

HOME PROBLEMS

5.1. A 0.6-*G* gas is separated from water having 140,000 ppm of dissolved solid at 101°F and 2050 psia. The gas travels down a pipeline network reaching a pressure of 800

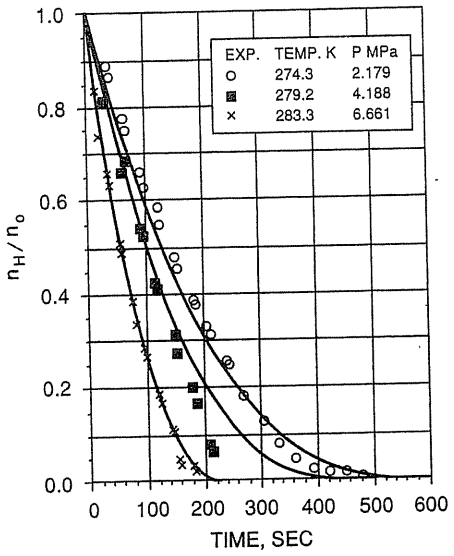

FIGURE 5-32
Normalized moles of methane in the hydrate during decomposition [Kim et al., 5-20, courtesy *Chem. Eng. Sci.*].

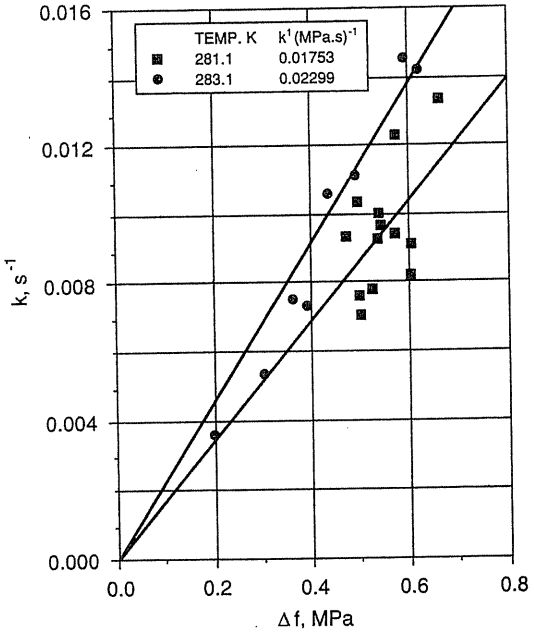

FIGURE 5-33
Effect of fugacity driving force on the constant K [Kim et al., 5-20, courtesy *Chem. Eng. Sci.*].

psia and 40°F. Will hydrate form? How much methanol would be required to prevent hydrate formation?

5.2. Calculate the gas gravity of the gas of Table 5.2, and read the gas gravity curve for hydrate-forming pressure at 50°F.

5.3. The natural gas pipeline serving your storage field is about to take on a new supply of gas. The gas is gathered from high-pressure separators and processed to recover 80 percent of the propane, 96 percent of butanes, and all of the heavier constituents. Before processing, the gas has the following composition as it comes off the field separators operating at 2200 psia and 100°F:

Separator gas analysis

Constituent	Mole fraction
CO_2	0.0041
C_1	0.9276
C_2	0.0303
C_3	0.0136
i-C_4	0.0042
n-C_4	0.0038
C_5	0.0039
C_6	0.0026
C_{7+}, M. W. = 100	0.0099

(a) What is the gravity of the separator gas?
(b) The separator gas at 2200 psia is transported to the processing plant in a gathering line. It is saturated with water in the separator. At what temperature would you expect hydrates to form at 2200 psia?
(c) What is the water content of the separator gas?
(d) If the separator gas were expanded, at what pressure would you expect hydrates to form?
(e) Compute the composition of the gas after processing. What is its gravity?
(f) What is the viscosity of the pipeline gas at 1000 psia and 50°F?
(g) The pipeline gas is stored in a reservoir at 1200 psia and 80°F. It is produced to a gathering system at 45°F and 700 psia. How much methanol is required to prevent hydrate formation?

REFERENCES

5-1. Anderson, F. E., and J. M. Prausnitz, "Inhibition of Gas Hydrates by Methanol," *AIChE J.*, Vol. 32, No. 8, 1321–1333 (1986).
5-2. Aoyagi, K., and R. Kobayashi, "Report on the Water Content Measurement of High Carbon Dioxide Content Simulated Prudhoe Bay Gas in Equilibrium with Hydrates," *Proceedings of 57th Annual GPA Convention*, 3–6 (1978).
5-3. Aoyagi, K., K. Y. Song, E. D. Sloan, P. B. Dhmawardhana, and R. Kobayashi, "Improved Measurements and Correction of the Water Content of Methane Gas in Equilibrium with Hydrates," *Proceedings of 58th Annual GPA Convention*, 25–28 (1979).
5-4. Byk, S., and V. I. Fomina, *Gazovye Gidraty*, Nedra, Moscow (1970).

5-5. Carson, D. B., and D.L. Katz, "Natural Gas Hydrates," *Trans. AIME*, Vol. 146, 150 (1942).
5-6. Deaton, W. M., and E. M. Frost, Jr., *Gas Hydrates and Their Relation to the Operation of Natural Gas Pipelines,* U. S. Bur. of Mines Monograph 8 (1946).
5-7. Galloway, T. J., W. Ruska, P. S. Chappelear, and R. Kobayashi, "Experimental Measurement of Hydrate Numbers for Methane and Ethane and Comparison with Theoretical Values," *Ind. Eng. Chem. Fundam.*, Vol. 9, No. 2, 237–242 (1970).
5-8. Hammerschmidt, E. G., "Formation of Gas Hydrate in Natural Gas Transmission Lines," *Ind. and Eng. Chem.* Vol. 26, 851 (1934).
5-9. Hand, J. H., D. L. Katz and V. K. Verma, "Review of Gas Hydrates with Implications for Ocean Sediments," *Natural Gas in Ocean Sediments*, I. R. Kaplan, Editor, Plenum Press, 179–194 (1974).
5-10. Holder, G. D., and P. F. Angert, "Simulation of Gas Production from a Reservoir Containing Both Gas Hydrates and Free Natural Gas," SPE preprint 11105 (1982).
5-11. Holder, G. D., and G. C. Grigoriou, "Hydrate Dissociation Pressures of (Methane + Ethane + Water) Existence of a Locus of Minimum Pressures," *J. Chem. Thermo.*, Vol. 12, 1093 (1980).
5-12. Holder, G. D., V. A. Kamath, and S. P. Godbole, "The Potential of Natural Gas Hydrates as an Energy Resource," *Ann. Rev. Energy*, 427–445 (1984).
5-13. Holder, G. D., D. L. Katz, and J. H. Hand, "Hydrate Formation in Subsurface Environments," *AAPG Bull.*, Vol. 60, No. 6, 981–988 (1976).
5-14. Holder, G. D., S.P. Zetts, and N. Pradhan, "Phase Behavior in Systems Containing Clathrate Hydrates," *Reviews in Chemical Engineering* (to be published, 1988).
5-15. Jacoby, R. H. "Vapor Liquid Equilibrium Data for Use of Methanol in Preventing Gas Hydrates," *Gas Hydrate Control Conference*, University of Oklahoma, Norman (1953). (Also *Gas Magazine,* Feb. 1955.)
5-16. John, V. T., and G. D. Holder, "Hydrates of Methane + *n*-Butane Below the Ice Point," *J. of Chem. Eng. Data,* Vol. 27, 18 (1982).
5-17. Kaplan, I. R., editor, *Natural Gases in Marine Sediments*, Plenum Press, New York (1974).
5-18. Katz, D. L., "An Analysis of the Absence of Connate Water in Michigan Reef Reservoirs," *AAPG Bull.* Vol. 66, 91–98, Jan. (1982).
5-19. Katz, D. L.,"Prediction of Conditions for Hydrate Formation in Natural Gas," *Trans. AIME*, Vol. 160, 140 (1945).
5-20. Kim, H. C., P. R. Bishnoi, R. A. Heidemann, and S. S. H. Rizvi, "Kinetics of Methane Hydrate Decomposition," *Chem. Eng. Sci.*, Vol. 42, No. 7, 1645–1653 (1987).
5-21. Kobayashi, R., and D. L. Katz, "Metastable Equilibrium in the Dew Point Determination of Natural Gases in the Hydrate Region, " *Trans. AIME,* Vol. 204, 262 (1955).
5-22. Kobayashi, R., H. J. Withrow, G. B. Williams, and D. L. Katz, "Gas Hydrate Formation with Brine and Ethanol Solution," *Proceedings of 13th Natural Gas Association Annual Convention*, 27–31 (1942).
5-23. Makogon, Y. F., *Hydrates of Natural Gas,* Pennwell Publishing, Inc., Tulsa, Oklahoma, (1981).
5-24. Makogon, Y. F., "Natural Gas Hydrates—The State of Study in the USSR and Perspectives for Its Using," paper distributed at *Third Chemical Congress of North America,* June 5–10, Toronto, Canada (1988).
5-25. Marshall, D. R., S. Saito, and R. Kobayashi, "Hydrate at High Pressures Part I: Methane-Water, Argon-Water, and Nitrogen-Water System," *AIChE J.*, Vol. 10, No. 2, 202–205 (1964).
5-26. Mcketta, J. J., Jr., and D. L. Katz, "Phase Relationships on Hydrocarbon-Water Systems," *Trans. AIME,* Vol. 170, 34 (1947).
5-27. Makogon, Y. F., private communication (1971).
5-28. Ng, H. J., and D. B. Robinson, "A Method for Predicting the Equilibrium Gas Phase Water Content in Gas-Hydrate Equilibrium," *Ind. Chem. Fundam.*, Vol. 19, No. 1, 33–38 (1980).

5-29. Ng, H. J., and D. B. Robinson, "The Measurement and Prediction of Hydrate Formation in Liquid Hydrocarbon-Water System," *Ind. Eng. Chem. Fundam.*, Vol. 15, No. 4., 293–298 (1976).
5-30. Ng, H. J., and D. B. Robinson, "The Prediction of Hydrate Formation in Condensed Systems," *AIChE J.*, Vol. 23, No. 4, 477–482 (1977).
5-31. Ng, H. J., and D. B. Robinson, "The Role of *n*-Butane in Hydrate Formation," *AIChE Journal,* Vol. 22, No. 4, 656 (1976).
5-32. Noaker L. J., and D. L. Katz, "Gas Hydrates of Hydrogen Sulfide-Methane Mixtures," *Trans. AIME,* Vol. 201, 237–239 (1954).
5-33. Parrish, W. R., and J. M. Prausnitz, "Dissociation Pressures of Gas Hydrates Formed by Gas Mixtures," *Ind. Eng. Chem. Process Des. Develop.*, Vol. 11, No. 1, 26–34 (1972).
5-34. Poettmann, F. H., "Here's Butane Hydrates Equilibria," *Hydrocarbon Processing,* 111, June (1984).
5-35. Records, J. R., and D. H. Seely, Jr., "Low Temperature Dehydration of Natural Gas," *Trans. AIME,* Vol. 192, 61 (1951).
5-36. Robinson, D. B., private communication (1981).
5-37. Robinson, D. B., H. J. Ng., and C. J. Chen, "The Measurement and Prediction of the Formation and Inhibition of Hydrates in Hydrocarbon Systems," *Proceeding of 66th GPA Annual Convention*, 154–164 (1987).
5-38. Robinson, D. B., D. Y. Peng, and H. J. Ng, "Some Applications of the Peng Robinson Equation of State to Fluid Property Calculations," *Proceeding of 56th Annual GPA Convention,* 11–17 (1977).
5-39. Saito, S., D. R. Marshall, and R. Kobayashi, "Hydrates at High Pressures: Part II. Application of Statistical Mechanics to the Study of the Hydrates of Methane, Argon, and Nitrogen," *AIChE Journal,* Vol. 10, No. 5, 734–740 (1964).
5-40. Selim, M. S., and E. D. Sloan, "Hydrate Dissociation in Sediment," SPE preprint 16859 (1987).
5-41. Sloan, D., private communication (1984).
5-42. Sloan, D., "The Colorado School of Mines Hydrate Program," *Proceeding of 64th GPA Annual Convention*, 125–128 (1985).
5-43. Sloan, E. D., "Phase Equilibrium of Natural Gas Hydrates," *Proceedings of 63rd Annual GPA Convention*, 163–169 (1984).
5-44. Sloan, E. D., F. M. Khoury, and R. Kobayashi, "Water Contents of Methane Gas in Equilibrium with Hydrates," *Ind. Eng. Chem. Fundam.*, Vol. 15, No. 4, 318 (1976).
5-45. Unruh, C. H., and D. L. Katz, "Gas Hydrates of Carbon Dioxide-Methane Mixtures," *Trans. AIME,* Vol. 186, 83–86 (1949).
5-46. Wagner, J., R. C. Erbar, and A. L. Majeed, "AQUASIM—Phase Equilibria and Hydrate Inhibition Using the PFGC Equation of State," *Proceedings of 64th GPA Annual Meeting,* 129–136 (1985).

RECOMMENDED READING

Major resources

Katz, D. L., et. al., *Handbook of Natural Gas Engineering,* McGraw-Hill Publishing Co., New York (1959).
Gas Processors Association, *Proceedings of Annual Meeting*, Tulsa, Oklahoma.
Holder, G. D., S. P. Zetts, and N. Pradhan, "Phase Behavior in Systems Containing Clathrate Hydrates," *Reviews in Chemical Engineering* (to be published, 1987).
Kuustraa, V. A., and E. G. Hammerschmidt, *Handbook of Gas Hydrate Properties and Occurrence*, DOE/MC/19239-1546 (1983).
Makogon, Y. F., *Hydrates of Natural Gas,* Pennwell Publishing, Inc., Tulsa, Oklahoma (1981).

Sloan, D., and R. Kobayashi, *Petroleum Engineering Handbook,* Chapter 25: "Phase Behavior of Water/Hydrocarbon Systems," Society of Petroleum Engineers, Richardson, Texas (1987).

Related literature

Bily, C., and J. W. L. Dick, "Naturally Occuring Gas Hydrates in the MacKenzie Delta, N.W.T." *Bull. of Can. Petro. Geol.*, Vol. 22, No. 3, 340–352, Sept. (1974).

Kamath, V. A., S. P. Godbole, and C. J. Baena, "Effect of Dissociation of Hydrates during Thermal Recovery of Heavy Oils on the North Slope, Alaska," SPE preprint 14224, (1985).

Kamath, V. A., and G. D. Holder, "Dissociation Heat Transfer Characteristics of Methane Hydrates," *AICE J.* Vol. 33, No. 2, 347–350 (1987).

Schroeter, J. P., R. Kobayashi, and M. A. Hildebrand, "Hydrate Decomposition Conditions in the System Hydrogen Sulfide–Methane–Propane," *Ind. Eng. Chem. Fundam.*, Vol. 22, 363–364 (1983).

van der Waals, J. H. and J. C. Platteeuw, "Clathrate Solutions," *Adv. Chem. Phys.*, Vol. 2, No. 1, 1–57 (1959).

Verma, V. K., J. H. Hand, D. L. Katz, and G. D. Holder, "Denuding Hydrocarbon Liquids of Natural Gas Constituents by Hydrate Formation," *J. Pet. Tech.*, Vol. 27, No. 2, 223–226, Feb. (1975).

Vysniauskas, A., and P. R. Bishnoi, "A Kinetic Study of Methane Hydrate Formation," *Chem. Eng. Sci.*, Vol. 38, No. 7, 1061–1072 (1983).

Vysniauskas, A., and P. R. Bishnoi, "Kinetic of Ethane Hydrate Formation," *Chem. Eng. Sci.*, Vol. 40, No. 2, 299–303 (1985).

Wu, B. J., D. B. Robinson, and H. J. Ng, "Three or Four Phase Hydrate Forming Conditions in Methane-Isobutane-Water System," *J. Chem. Thermo.*, Vol. 8, 461, (1976).

CHAPTER 6

APPLICATIONS OF FLOW EQUATIONS: PRESSURE DROP, COMPRESSION, METERING

Flow of natural gas and accompanying liquids through gathering systems, process equipment, and transmission pipelines requires pressure drop as the driving force. Pressure drop during flow is evaluated by use of the flow equation. Vertical flow pressure drops in wellbores are evaluated frequently; the conversion of wellhead pressure to bottom hole pressure in static single-phase conditions is also common. The measurement of flow rates also requires an understanding of the flow equation and fluid properties. The flow equation is also used in relating the power needs for compression of natural gas to thermodynamic properties and the equipment being used. The attendant temperature rise during compression must be evaluated to size the inter or after coolers at compression stations.

6.1 APPLICATION OF FLOW EQUATION

The performance of expanders in gas stream cooling, liquid recovery, and partial recompression can be evaluated using the *flow equation*. The flow equation was derived in Chapter 3; Eq. (3.4) presented the thermal energy balance, work, and heat. It is noted that energy of position (X) and kinetic energy ($mv^2/2g_c$) are not included in the enthalpy (ΔH) of the fluid flowing. When considering friction as a mechanism of changing work energy into heat energy, Eq. (3.7) is used. These equations are the starting point for the derivation of formulas for static pressure gradients in vertical columns, flow in wells and surface pipes, metering, compression, and expansion.

6.2 CALCULATION OF STATIC BOTTOM HOLE PRESSURES IN WELLS

A knowledge of the static bottom hole pressures in wells is of prime importance in predicting reserves and deliverability of oil and gas reservoirs. With single-phase fluids in the wellbore, one may compute the bottom hole pressure from wellhead pressure and fluid density. When two phases are present in the wellbore, measurement of bottom hole pressures or fluid level becomes necessary. In gas storage operations with a large number of wells, surface measurements of gas pressure by a dead weight or accurate pressure gauge followed by calculation of static column pressure differential is an economical and satisfactory method. The following development starts with Eq. (3.7) and assumes: (1) zero gas velocity, (2) no work done, and (3) that a mean fluid specific volume,[1] $\bar{v}$, or density, $\rho = 1/\bar{v}$, may be applied to the fluid column as shown on Fig. 6-1. This gives

$$\int_1^2 \bar{v}dP + (h_2 - h_1)\frac{g}{g_c} = 0 \quad \text{or} \quad \int_1^2 VdP + m(h_2 - h_1)\frac{g}{g_c} = 0 \tag{6.1}$$

where $\bar{v}$ and V are the specific volume and total volume of well fluid, m is the mass, P is the pressure in the wellbore, h is the height above or below a given datum, g is acceleration due to gravity, and g_c is the conversion factor from mass to force units, $lb_m ft/lb_f s^2$.

For gases, it is convenient to evaluate V using the gas law, $PV = ZnRT$:

$$\int_{P_1}^{P_2} \frac{ZnRT}{P}dP = -m\Delta h\frac{g}{g_c} \tag{6.2}$$

Assuming that Z and T may be evaluated at average values (Z_a, T_a) then moved out of the integral, and taking the number of moles $n = (1/29G)$ for unit mass (1 lb_m, kg, . . .) with G the gas gravity (molecular weight divided by 29, the molecular weight of air), Eq. (6.2) becomes

$$\frac{Z_a T_a R}{29G}\int_{P_1}^{P_2}\frac{dP}{P} = -\Delta h\frac{g}{g_c} \tag{6.3}$$

Integrating and rearranging, one finds the usual equation for English units:

$$\Delta P = P_2 - P_1 = P_1\left[\exp\left(\frac{0.01877Gh}{T_a Z_a}\right) - 1\right] \tag{6.4}$$

where 0.01877 is the molecular weight of air divided by R, 29.0/1545.3.

The solution of this equation requires, in addition to wellhead pressure, a knowledge of h, depth of well; G, gas gravity; T_a, the average wellbore temperature; and Z_a, the compressibility factor taken at the mean temperature and pressure in the wellbore. Also, one needs assurance that there is a single gas phase in the wellbore.

The primary problem in solving the Eq. (6.4) is to find a way to obtain Z_a quickly and easily. One should know the basic method of using a Z chart or an equation of state. In practice, a computer program usually will provide the bottom hole pressures from P_1, h, G, and T_a. Such a program may integrate Eq. (6.2) directly, or use depth increments, given temperature as a function of depth.

[1] Specific volume is volume per unit mass, $m = 1$, and mean specfic volume is taken at average T and P.

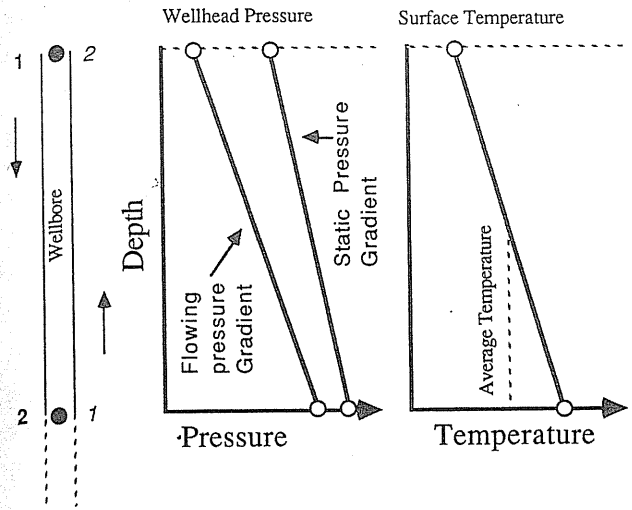

FIGURE 6-1
Pressure and temperature gradients in natural gas wells.

Example 6.1. Find the bottom hole pressure for a gas well with wellhead pressure of 1145 psia (7.895 MPa), a depth of 2450 ft (746.8 m), a gas of gravity 0.6, and mean wellbore temperature of 60°F (288.5 K).

Solution. Using Eq. (6.4), $P_2 = P_1 \exp(0.01877Gh/T_aZ_a)$. *In English units:*

$$P_2 = 1145 \times \exp\left(\frac{0.01877 \times 0.6 \times 2450}{520 \times 0.813}\right) = 1145 \times 1.0674 = 1222 \text{ psia}$$

Z was read from Fig. 4-18 at an estimated P_a of 1175 psia; the result shows that this was a fair estimate, and no second try is needed.

In SI units: P in MPa, h in meters, T in K, and $R = 8.314$:

$$P_2 = P_1 \times \exp\left(\frac{0.03417 \times 0.6 \times 746.8}{288.5 \times 0.813}\right) = 7.895 \times 1.0674$$

$$= 8.427 \text{ MPa (1222 psia)}$$

For a liquid phase such as water, the vertical pressure gradient discussed in Chapter 1 is found simply by rearranging Eq. (6.1) and assuming the specific volume $\bar{v}$ is an average constant value $\bar{v}_a$:

$$\bar{v}_a(P_2 - P_1) = (h_2 - h_1)\frac{g}{g_c} = \frac{P_2 - P_1}{\rho_a} \tag{6.5}$$

Remembering that the equation was written for a unit mass, and that $g = g_c$ numerically in English units or $(g/g_c) = 9.8$ in metric units,

English:
$$P_2 = P_1 + \frac{h\rho_a}{144} \tag{6.6a}$$

SI:
$$P_2 = P_1 + (h\rho_a) \times 9.80 \tag{6.6b}$$

In Eq. (6.6*a*), h is the depth of well in feet, ρ_a is density in lb_m/ft^3, and 144 is the conversion factor of ft^2 to in^2. Thus an oil column of average density 815 kg/m^3 (50.85 lb_m/ft^3) standing in a well of 1310.6 m (4300 ft) would have a pressure increase from top (P_1) of $4300 \times 50.85/144 = 1518.6$ psi or $1310.6 \times 815 \times 9.80 = 10.47 \times 10^6$ Pa = 10.47 MPa at the bottom of the well.

Alternate Ways to Compute Static Column Pressures

Direct solution of Eq (6.4) with trial and error for Z is easily done by hand. When a programmed computer is easily available, the program should be used with attention to input quantities. Should there be liquids in the well column, a combined use of gas and liquid gradients is required.

Since the pressure increase from the top to the bottom of a well is an integral of the fluid density times height [6-51], more accurate results can be obtained by accounting for the changing values of Z and T. Sukkar and Cornell [6-55] developed tables of $\int (Z/P_r)/(1 + B(Z/P_r)^2)dP_r$ to eliminate the effect of averaging the compressibility factor variation with pressure. Cullender and Smith also have

an averaging procedure [6-14]. These methods are not useful to those having computers.

The Energy Resources Board of Alberta, Canada, treats the static and flow formulas in a detailed manner in reference [6-19] (see the third edition, 1975, for English units, and the fourth edition, 1979, for SI units).

Before going on to the flowing pressure change in vertical wellbores, this chapter presents the calculation for friction in pipe flow.

6.3 EVALUATING FRICTION IN PIPELINE FLOW

Before considering frictional energy losses at pipe walls, this section is concerned with the nature of steady state velocity profiles in pipes.

Velocity Profiles in Flow

In reviewing flow in pipes, it is worthwhile to recall the velocity flow profiles for single-phase flow in a cylindrical tube shown in Fig. 6-2 [6-34]. Fluid mechanics describes fluid flow at low velocities as *laminar* or *viscous* in nature. The velocity distribution in undisturbed laminar flow is parabolic, as shown. Reynolds established that at high flow rates, the laminar flow lines are disrupted by turbulence, and a flatter profile develops, as shown in Fig. 6-2.

Let us recall the flow equation, which permits evaluation of frictional pressure drop:

$$\int \bar{v}dP + \Delta\left(\frac{v^2}{2g_c}\right) + \Delta\left(\frac{gX}{g_c}\right) = -w_s - l_w \tag{6.7}$$

For pipe flow, the lost work term is defined in terms of a *friction factor* and a *Reynolds number*.

Friction in Pipe

The term l_w of Eq. (6.7) represents all energy losses resulting from irreversibilities of the flowing stream. In the case of single-phase flow, such as flow of gas in pipe, these irreversibilities consist primarily of friction losses, both internal losses due to viscosity effects and losses due to the roughness of the wall of the pipe.

With the exception of completely laminar flow, the energy losses l_w of actual systems cannot be predicted theoretically, but must be determined by actual experiment and then correlated as some function of the flow variables. Such a relationship is given by the well-known equation

$$l_w = \int_1^2 \frac{fv^2}{2g_c d}dL = \frac{fv^2L}{2g_c d} \tag{6.8}$$

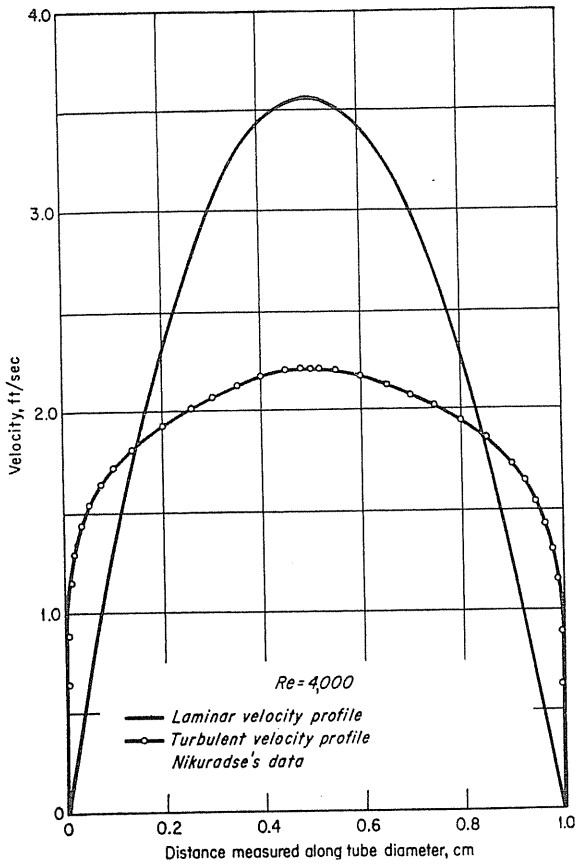

FIGURE 6-2
Comparison of laminar and turbulent velocity profiles at the same average velocity [Knudsen & Katz, 6-34, courtesy McGraw-Hill Publishing Co.].

where the factor f is a dimensionless correlating function, the *friction factor*. By means of dimensional analysis it can be shown that the friction factor is a function of the *Reynolds number*, $dv\rho/\mu$, and the relative roughness, e/d, which is the ratio of absolute roughness e to pipe diameter d. Roughness is defined as the distance from peaks to valleys in pipe-wall irregularities. Figure 6-3 is a plot of f as a function of Reynolds number Re and relative roughness as presented by Moody [6-38]. Quite often the Fanning friction factor f' is used: $f' = f/4$. The Reynolds number is dimensionless[2] and may be converted to field units in this way:

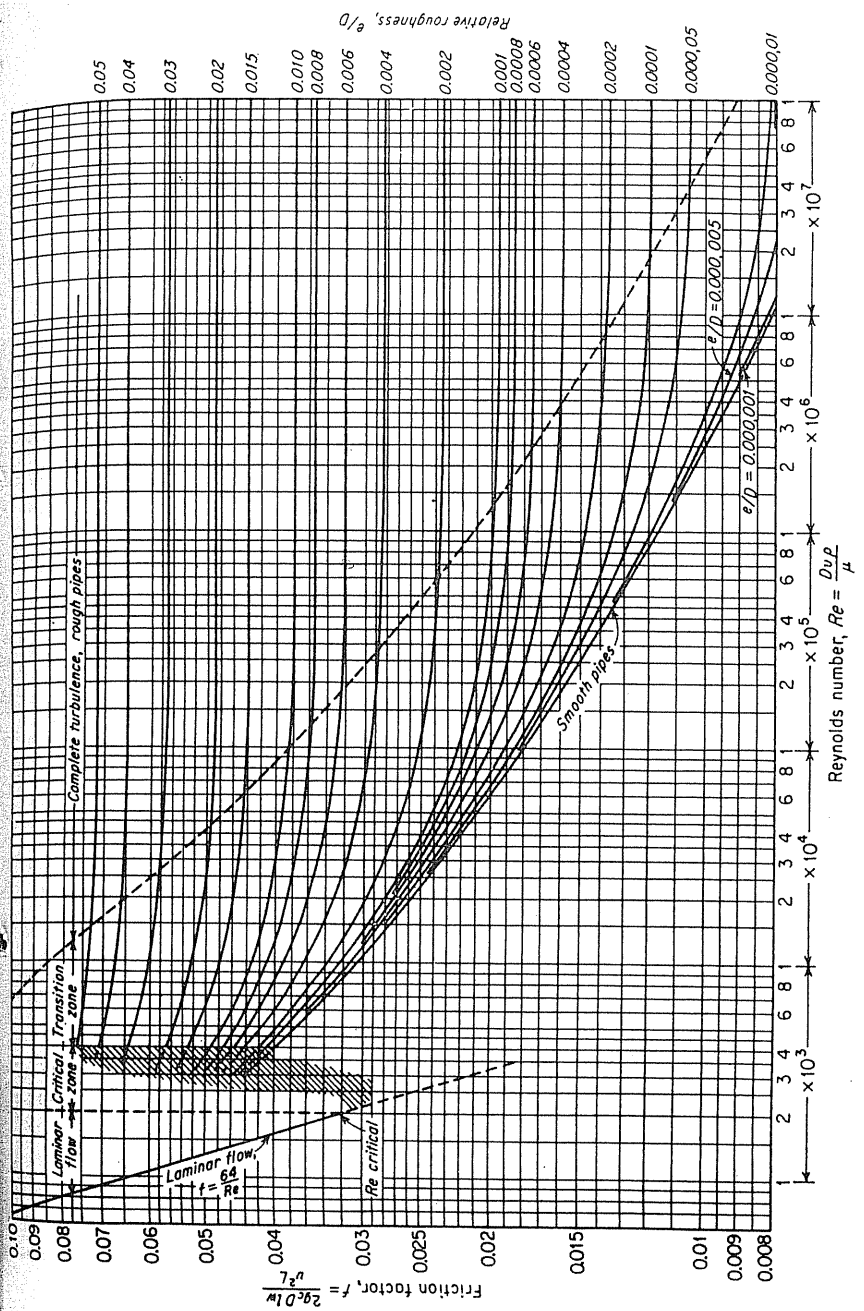

FIGURE 6-3
Friction factor for flow of fluids in pipe [Moody, 6-38, courtesy ASME].

[2] $\mathrm{Re} = \dfrac{d[\mathrm{ft}]v[\mathrm{ft/s}]\rho[\mathrm{lb/ft^3}]}{\mu[\mathrm{lb/(ft \cdot s)}]}$; μ in pounds per foot per second $= \mu$ in centipoises $\times$ 0.000672.

$$\text{Re} = \frac{dv\rho}{\mu} = \frac{dW}{\mu A} = \frac{4dQ \times 12 \times 29G \times 1000}{\mu \times 24\pi d^2 \times 379 \times 2.42} = 20.0\frac{QG}{\mu d} \tag{6.9}$$

where Q (Mcf/day) is gas flow at 60°F (15.6 °C) and 14.7 psia (101.4 kPa), G is the gas gravity, W (lb_m/hr) is the mass flow, d (in.) is the diameter of pipe, μ (cp) is viscosity, and A (ft^2) is flow area.

Fluid flow ranges in nature between two extremes, laminar or streamline flow and turbulent flow (Fig. 6-2). For Reynolds number up to 2100, flow is in the laminar region and $f = 64/\text{Re}$. For higher Reynolds numbers, flow passes through a transition zone and then becomes completely turbulent. For completely turbulent flow, f is virtually a function of relative roughness alone (Fig. 6-3). Gas flows are usually at such high Reynolds numbers that they can be considered completely turbulent. Typical roughnesses (e) for gas lines and well tubing range from 0.00055 to 0.0007 inches (0.0014–0.0018 cm) [1-1].

For turbulent flow in smooth pipe (that is, pipe of zero roughness) the f factor (Fig. 6-3) over the entire range of Reynolds numbers can be expressed by the following relationship, developed by Nikuradse [6-40]:

$$\frac{1}{\sqrt{f}} = 2\log(\text{Re}\sqrt{f}) - 0.80 \tag{6.10}$$

Frictional Pressure Drop in Pipeline Flow

Equation (6.7) is rearranged and combined with the gas law (Eq. 3.9) to develop the pipe flow equation known as Weymouth's equation [6-57]. The use of a standard volume flow rate Q (measuring volume in terms of a standard condition of T_0 and P_0) changes the apparent driving force into a difference of squares of the pressure. Note the P_1 or P_2 is for the driving force and the P_0 is to convert the mass flowing from the higher pressure to atmospheric or measurement pressure as represented by Q of Mcf (thousands of standard or measured volumes). Weymouth's equation is

$$Q = 3.22\frac{T_0}{P_0}\left[\frac{(P_1^2 - P_2^2)d^5}{GTLfZ_a}\right]^{1/2} \tag{6.11}$$

where Q (Scf/hr) is the gas flow measured at T_0 and P_0, L (miles) is the length of line, d (in.) is the internal diameter (ID), P_1 and P_2 (psia) are the upstream and downstream pressures, G is the gas gravity (air = 1), T (°R) is the average line temperature, Z_a is the average compressibility factor (in Weymouth's original equation $Z = 1$), f is the friction factor from Fig. 6-3, T_0 (°R) is the measurement temperature, and P_0 (psia) is the measurement pressure.

Weymouth assumed that f varied as a function of the diameter in inches as follows:

$$f = \frac{0.032}{d^{1/3}} \tag{6.12}$$

With this assumption, Eq. (6.11) becomes

$$Q = 18.062\frac{T_0}{P_0}\left[\frac{(P_1^2 - P_2^2)d^{5.333}}{GTLZ_a}\right]^{1/2} \tag{6.13}$$

The American Gas Association (AGA) has a pipeline flow formula generally used in large pipelines for natural gas [6-2]. The GPA [1-28] has a series of graphs for different gravities of gas and various sizes of tubing. One of these plots for $G = 0.9$ gas is shown in Fig. 6-4, from which flow rate can be calculated for various gas gravity values. The practical transcontinent pipeline equations used by various gas companies will be discussed in Chapter 17.

6.4 FLOWING PRESSURE GRADIENT IN SINGLE-PHASE GAS WELLS

The flowing pressure gradients in gas wells are a combination of the contribution from the density of the column and the frictional pressure drop between the gas stream and the pipe wall. Figure 6-1 illustrates the static and flowing pressures, showing combined effects. Solving Eq. (3.7) for the flowing gas column gives

$$\int VdP + mh\frac{g}{g_c} = -m\frac{fLv^2}{2g_cd} \tag{6.14}$$

The derivation of the final equation from Eq. (6.14) involves (1) converting V to a function of P, T, and Z as for Eq. (6.4), (2) converting velocity of flow into Q, the standard volume flowing, using the diameter of the pipe d, as well as T, P, and Z, and (3) equating h, the depth of the well, to L, the length of pipe, in the friction term of Eq. (6.14). The form frequently used defines the exponent of exp(s) as $s = 2 \times 0.01877Gh/T_aZ_a$ or twice the value for Eq. 6.4 with ΔP at first power, since the above combinations will give the pressure differences as P^2 terms.

By neglecting kinetic energy losses and assuming that mean properties of the flowing stream may be used, the following equation results [1-1,1-2]:

$$P_s^2 - e^sP_w^2 = \pm 6.67 \times 10^{-4}\frac{(QT_aZ_a)^2(e^s - 1)f}{d^5} = b \tag{6.15a}$$

$$s = 0.0375\frac{Gh}{T_aZ_a} \tag{6.15b}$$

where P_s (psia) is the flowing sand face pressure, P_w (psia) is the flowing wellhead pressure, + is for gas production and − for injection, Q (Mcf/day) is the flow rate in, d (in.) is the inside pipe diameter, T_a (°R) is the average temperature, f is the Moody friction factor, Z_a is the average compressibility factor at mean temperature and pressure, b is an abbreviation for the expression, G is the gas

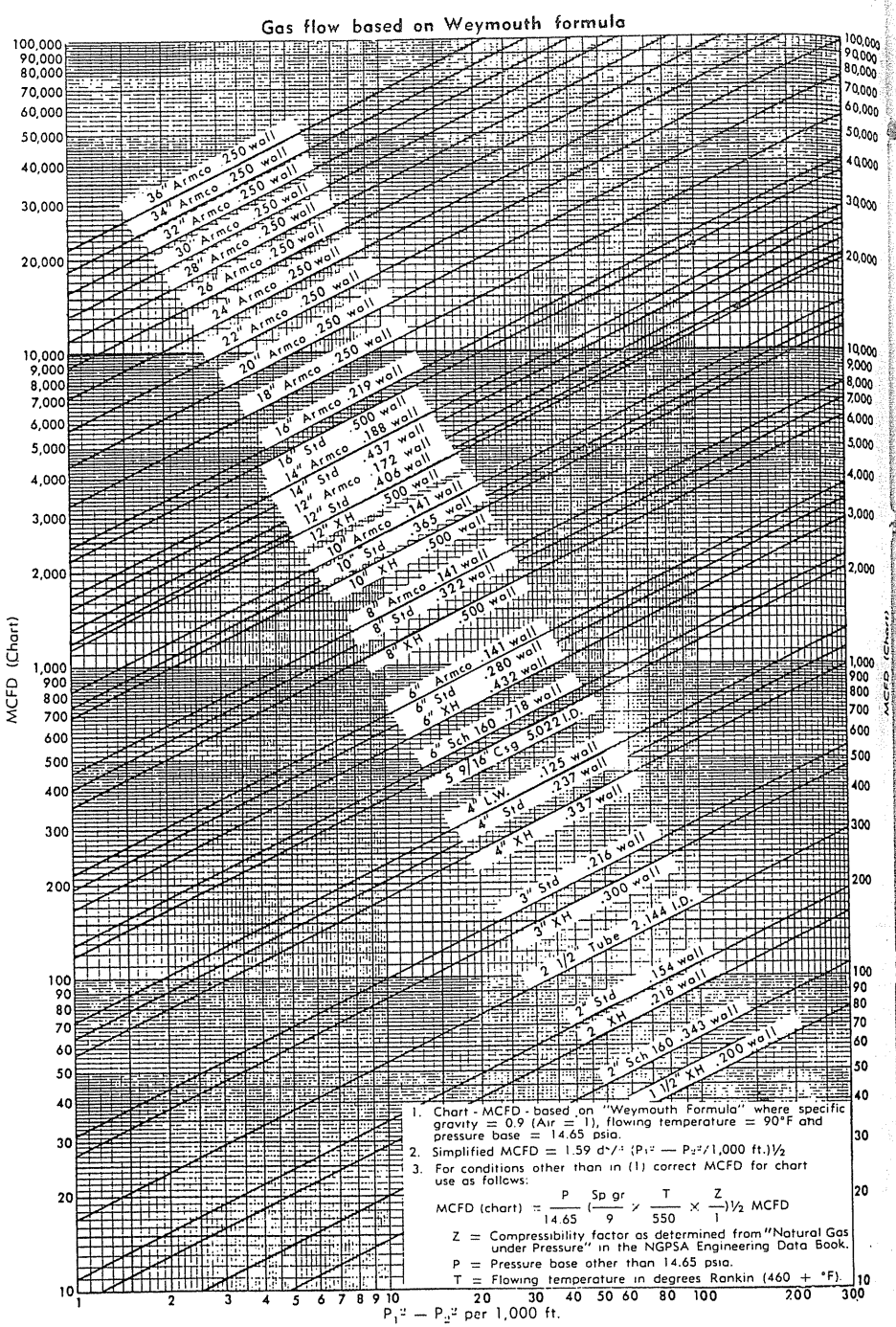

FIGURE 6-4
Gas flow based on Weymouth formula [1-28, courtesy GPA].

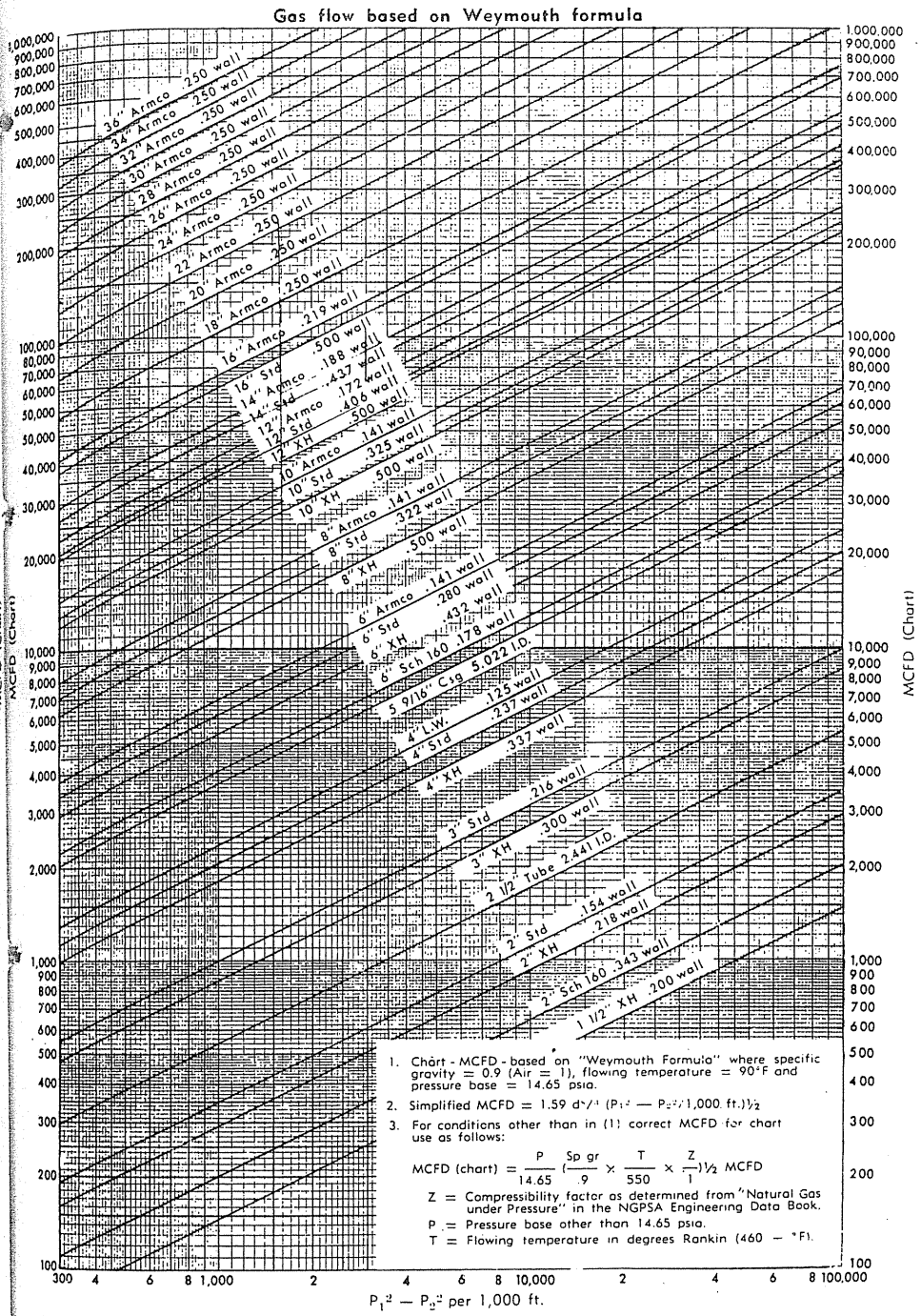

FIGURE 6-4
(continued)

gravity, and h (ft) is the depth of well. The quantity s is two times the exponent in Eq. (6.4); the doubling arises because this equation involves P to the second power.

To solve the equation, one must find f, the Moody friction factor. This may be done in the conventional manner for a given pipe roughness and diameter, or by the tables provided in reference [1-1]. If one assumes that the Reynolds number is so high that the friction factor no longer depends on it, then a simple empirical relation may be used as follows:

$$f = \frac{0.01750}{d^{0.224}} \qquad d \leq 4.277 \text{ in.} \tag{6.16a}$$

$$f = \frac{0.01603}{d^{0.164}} \qquad d > 4.277 \text{ in.} \tag{6.16b}$$

Alternatively, the Colebrook equation [6-13] can be used for various values of relative roughness:

$$\frac{1}{\sqrt{f}} = 2\log\left(\frac{d}{e}\right) + 1.14 - 2\log\left(1 + 9.34\frac{d/e}{\text{Re}\sqrt{f}}\right) \tag{6.16c}$$

which gives conservative values of friction factor.

A procedure for computing both the static gradient and flowing bottom hole pressure is illustrated in Table 6.1. Equation (6.15) with Q equal to zero is equivalent to Eq. (6.4). Once one understands the procedure used in Table 6.1, one can use the computer program in Appendix B for making multiple calculations.

Example 6.2. A well has the static conditions of Example 6.1. The well is flowing at a rate of 3.42 million cubic feet per day through tubing of 2.441 in. ID at a wellhead pressure of 1072 psig. What is the flowing bottom hole pressure?

Solution. Table 6.1 shows the pressure gradient calculations, both the static case and the flowing case. When $b = 0$ in Eq. (6.15) for no flow, one has the static case with the pressure terms squared. The solution for the static case is given along with a start on a second trial.

The flow calculation on Table 6.1 starts with the measured flow rate at standard conditions (60°F, 14.7 psia) and the wellhead flowing pressure. The flowing bottom hole pressure is desired. The compressibility factor Z is needed at the mean temperature and pressure, as in the static case. The average temperature may not be the same as in the static case, and could well be taken as the mean of the flowing wellhead and the reservoir temperatures. In this case, the compressibility factor is read directly from Fig. 4-13 based on the empirically determined P_a. In finding the friction factor, it is recalled that Eqs. (6.16a) and (6.16b) depend on size of pipe; for tubing sizes, Eq. (6.16a) is used, while for casings or annuli, Eq. (6.16b) is used. The remainder of the calculations are straightforward from Eq. (6.15).

TABLE 6.1
Calculation of flowing and static pressure gradients in gas well

	Static case		
	1st trial	2nd trial	Flowing case
Q, flow rate, Mcf/day	0	0	3420
P_w, wellhead pressure, psia	1145.	1145.	1087
T_a, average temperature, °R	520.	520.	520.
P_a, assumed pressure, psia	1175.	1184	1117.
$P_a/P_c = P_r$	1.75	1.76	1.66
$T_a/T_c = T_r$	1.45	1.45	1.45
Z_a, average compressibility	0.818	0.816	0.825
$d^{0.224}$ (tubing) or $d^{0.164}$			1.22
$f = 0.01750/d^{0.224}$ or $0.01603/d^{0.164}$			0.0143
$s = 0.0375\ GL/T_aZ_a$	0.1296		0.1285
$e^s - 1$	0.1384		0.1371
$QT_aZ_a \times 10^{-2}$	0	0	14670.
$(QT_aZ_a)^2 \times 10^{-4}$	0	0	2.153×10^8
$6.67 \times 10^{-4}(QT_aZ_a)^2(e^s - 1)f/d^5 = b$	0	0	3.249×10^4
P_w^2	1.311×10^6		1.182×10^6
$e^sP_w^2$	1.492×10^6		1.344×10^6
$P_s^2 = b + e^sP_w^2$	149×10^6		1.376×10^6
P_s, psia	1222.		1173.

$P_c = 672$ psia, $T_c = 358$°R, $L = 2450$ ft, $G = 0.6$, $d = 2.441$ in., $d^5 = 86.6$

Charts of Pressure Gradients

For a given field with fixed well size, well depth, well temperature, and gas gravity, it is possible to make a chart of the static pressure gradient and flowing gradients for a series of flow rates. In this way it is not necessary to go through the calculation of either static or flowing pressure gradient each time the value is desired. Figure 6-5 is such a chart for the Herscher–Mt. Simon reservoir [6-52] based on wellhead conditions.

To give rough estimates of pressure gradients in static gas wells, a generalized set of curves for 0.7-gravity gas is presented in Fig. 6-6. It is based on typical temperature and pressure gradients with depth.

Computer Programs for Well Static and Flowing Pressure Gradients

A computer program has been written for solving Eq. (6.15) with a subroutine to obtain the appropriate compressibility factor; the program is listed in Appendix B. The subroutine is that of Yarborough and Hall, given in Chapter 4 and Appendix B. To obtain Z, it requires input of gas composition or gas gravity for hydrocarbon gases, wellbore temperature, and pressure.

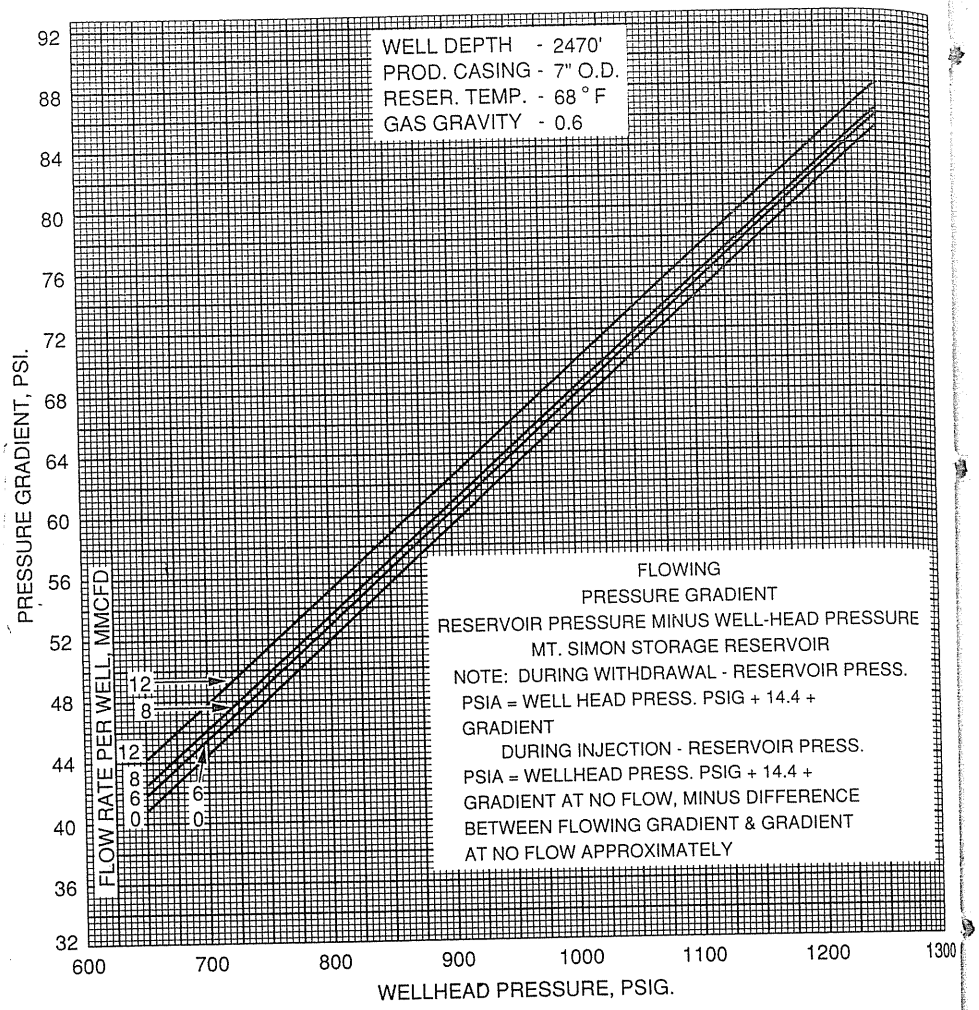

FIGURE 6-5
Pressure gradients calculated for Mt. Simon reservoir [Rzepczynski, 6-52, courtesy *Oil and Gas J.*].

Since the average density in the vertical section may be at issue, the program is set to handle various depth increments. Users can specify any desired increment number.

Example 6.3. A gas-condensate well 15,300 ft deep in Louisiana had a closed pressure at the wellhead of 10,165 psig. A bottom hole survey measured a temperature of 237°F at 12,000 ft and a reservoir temperature of 302°F at 15,300 ft. The closed wellhead temperature is believed to be 100°F because the well had a three-week flow test that ended a week before the well measurements. The well fluid had a G of 1.088.

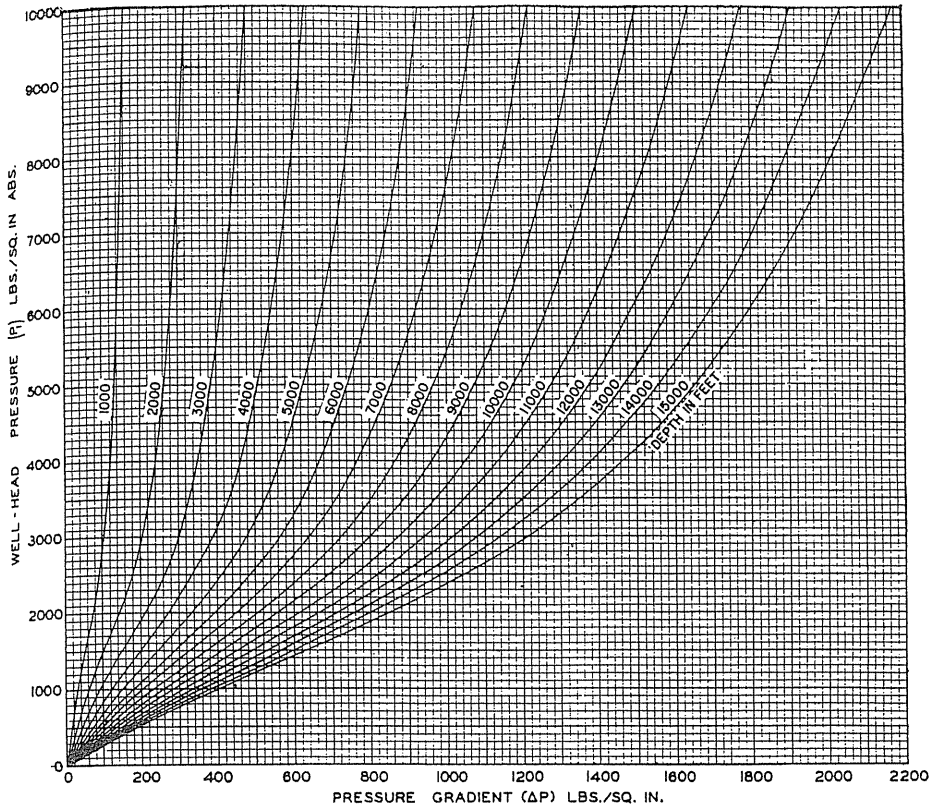

FIGURE 6-6
Pressure gradients in gas wells for $G = 0.7$ gas [Katz & Rzasa, 6-51, courtesy SPE-AIME].

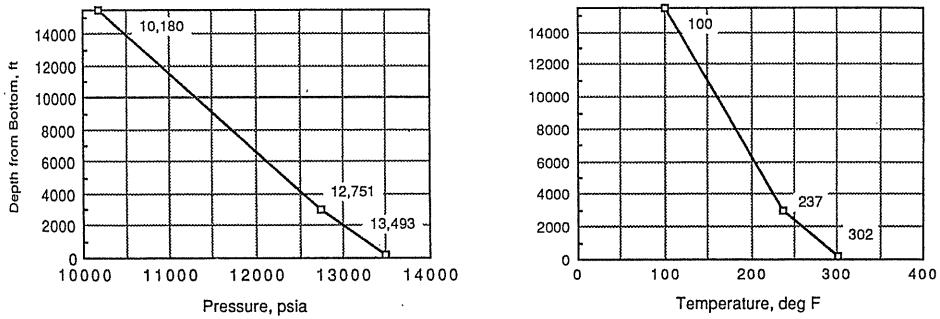

FIGURE 6-7
Well temperature and pressure gradients for Example 6.3.

Compute the static bottom hole pressure in the well to compare with the measured values of 13,493 psia at 15,300 ft and 12,751 psia at 12,000 ft. Try a hand-calculated solution using Fig. 4-16 for pseudocritical conditions and condensate well fluids and using Fig. 4-17 for Z-factor. Figure 6-7 illustrates the well temperature and pressure gradients.

Hand Solution

	12,000 ft	15,300 ft
T_a	$\frac{100 + 237}{2} + 460 = 629°R$	$\frac{237 + 302}{2} + 460 = 730°R$
$T_r = \frac{T_a}{T_c}$	$\frac{629}{445} = 1.41$	$\frac{730}{445} = 1.64$
$P_r = \frac{P_a}{P_c}$	$\frac{11,500}{637} = 18.05$	$\frac{13,138}{637} = 20.62$
Z_a (from Fig. 4-17)	1.75	1.78
$P_2 = P_1 \times \exp\left(\frac{0.01877\,Gh}{T_a Z_a}\right)$	$10,180 \times \exp\left(\frac{0.01877 \times 1.088 \times 12,000}{629 \times 1.75}\right)$	$12,751 \times \exp\left(\frac{0.01877 \times 1.088 \times 3,300}{730 \times 1.78}\right)$
	= 12,718 psia	= 13,430 psia
Measured values	12,751 psia	13,493 psia

6.5 GAS FLOW MEASUREMENTS

Natural gas is in continuous flow from the time it leaves the reservoir until it reaches its ultimate use, usually in a burner. Unlike other products, it is not packaged or put in warehouses where inventory can be taken. Measurement of gas purchases and deliveries is made on a flowing stream of gas; hence accurate flow measurement is of paramount importance to the gas industry. For example, an error of only 1.0 percent in the measurement of natural gas in a pipeline delivering 300 MMcf per day of gas at around $1.50 per Mcf will amount to a loss to either the seller or the purchaser of $1.5 million a year.

Because of the importance of accurate measurement of the quantity of gas delivered, various technical societies have combined their efforts to arrive at standards and procedures for quantitative measurement of gas that are mutually acceptable to both purchasers and sellers of gas products. Also, there is interest in the orifice meter in many industries [6-9,6-48,6-54]. The American Gas Association's [6-1] Gas Committee Report 3 has been widely adopted by industry, along with NX-19, which updates compressibility factors.

Two general classes of metering devices are available for measuring gas rates: dynamic and volumetric meters (Table 6.2). For measuring large volumes, the orifice flow meter is the primary type of dynamic meter. In orifice meters, the

TABLE 6.2
Principal types of meters

Dynamic measurement	Volumetric measurement
Orifice meter	Diaphragm meter
Turbine meter	Laboratory wet-test meter
Centrifugal meter	
Vortex meter	
Sonic meter	
Flow nozzle	
Venturi meter	
Annubar	
Critical-flow prover	
Pitot tube	
Laboratory rotameter	
Choke	

pressure drop occurring at a restriction indicates the flow rate. With the exception of domestic or space heating sales, essentially all gas transactions are based on orifice-meter measurements. The second class of meter, which is used for domestic sales, is the volumetric meter; this meter mechanically receives a definite volume of gas from an upstream source, counts the volume, and discharges it downstream. A large variety of meters are used in special applications or in research activities. While most of the devices are still read manually, electronic digital automation equipment is rapidly entering the gas industry.

Measurement by Orifice Meters

The advantages of the orifice meter—accuracy, ruggedness, simplicity, ease of installation and maintenance, range of capacity, and low cost—readily account for its widespread use. Other factors of importance are the acceptance of the orifice meter for gas measurement by the joint AGA-ASME-API committee, the availability of standard tables of meter factors for orifice meters of standard design, and specifications for meter installations. The two types of orifice meters, flange taps and pipe taps, are illustrated in Fig. 6-8*a*.

The restriction in the flow path causes a velocity increase and a corresponding pressure drop. With a liquid flowing, the pressure profile can be observed by a manometer, as indicated in Fig 6-8*a*. In general, the conversion of pressure energy into velocity head is virtually complete, but the regeneration of pressure when the gas is slowed down beyond the restriction is rather inefficient.

The recording of pressure and of pressure differential for gas was accomplished mostly by meters employing mercury U tubes (Fig. 6-8*b*) until recently, and many meters still use mercury U tubes. A clock turns a chart under recording pens, providing a continuous record of the pressure and the pressure differential. Mercury chart meters are rapidly being replaced by transducers for both pressure level and pressure differential.

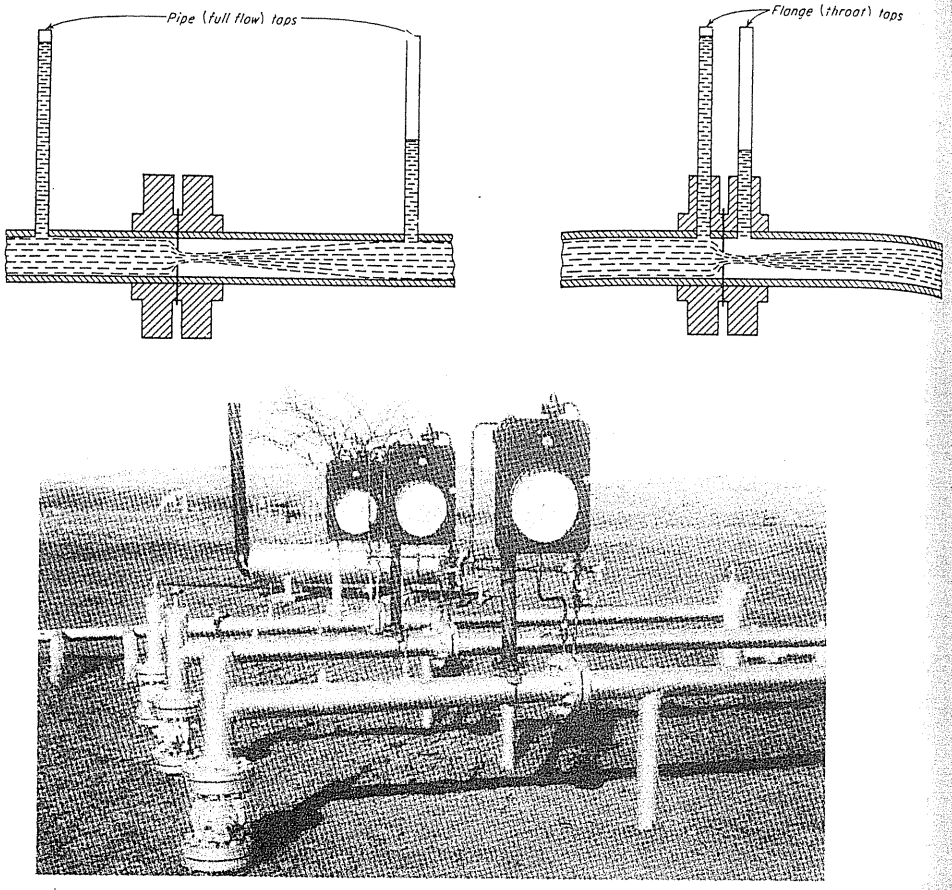

FIGURE 6-8
(*a*) Orifice meters: flange taps, pipe taps [Katz et al., 1-1, courtesy McGraw-Hill Publishing Co.]. (*b*) Recording orifice meter [courtesy Foxboro Company].

Orifice meter formulas. For a horizontal pipe with no work done and neglecting friction, Eq. (3.7) becomes $\int_1^2 V dp = -\Delta m v^2/2g_c$, where flow velocity v is proportional to $\sqrt{P}$. Solution of the equation involves finding V as an average value and relating velocities to equipment dimensions and flow rates. Finally, the working equation adopted by AGA in Report No. 3 [6-1], augmented by NX-19, is as follows:

$$Q_h = C'\sqrt{h_w P} \tag{6.17}$$

where Q_h is the rate of flow at base conditions in ft^3/hr, h_w is the orifice differential in inches of water, P is the (static) pressure at orifice in psia, $\sqrt{h_w P}$ is *pressure extension*, and the *orifice flow constant* C' is

$$C' = F_b \cdot F_r \cdot Y \cdot F_{pb} \cdot F_{tb} \cdot F_{tf} \cdot F_{gr} \cdot F_{pv} \cdot F_m \cdot F_a \cdot F_l \tag{6.18a}$$

or, in many cases, simply

$$C' = F_b \cdot F_r \cdot Y \cdot F_{pb} \cdot F_{tb} \cdot F_{tf} \cdot F_{gr} \cdot F_{pv} \tag{6.18b}$$

F_b is the *basic orifice factor* based on pipe diameter, orifice diameter, and type of meter, F_r is the *Reynolds Number Factor* ($=1 + b/\sqrt{h_w P}$; b is a constant), Y is the *expansion factor*, F_{pb} is the *pressure base factor* ($14.73/P_b$), F_{tb} is the *temperature base factor* ($T_b/519.67°R$), F_{tf} is the *flowing temperature factor* ($\sqrt{519.67/T_f °R}$, T_f is the *fluid flowing temperature*), F_{gr} is the *gas gravity factor* ($\sqrt{1/G}$), F_{pv} is the *supercompressibility factor* ($\sqrt{Z_b/Z} \approx \sqrt{1/Z}$), F_m is the *manometer factor* for mercury type meters only, ($\sqrt{(\rho(\text{Hg}) - \rho_f)/\rho(\text{Hg})}$ where ρ_f is the density of the fluid opposite mercury in the meter, F_a is the *thermal expansion factor*, used when flowing temperatures are outside the limits of 0 to 120°F, and F_l is the *gauge location factor*, specially applicable to the manometer, to adjust for gauges being operated under gravity forces that depart from the standard gravity of 32.174 ft/s. For example, in Mexico City (5000 ft above sea level, latitude 25°), F_l is 0.9988. In most of the metropolitan areas of the United States, F_l is 1.

The factors above, except F_m, F_a, and F_l, are listed in AGA Report No. 3 [6-1] and partially tabulated in reference [1-1]. To obtain the quantity of gas flowing through an orifice meter from the above equation and the AGA tables, the following data are required: (1) diameter of pipe, (2) diameter of orifice, (3) differential across meter, (4) pressure on meter, (5) flowing temperature, (6) gas gravity, (7) CO_2 and N_2 contents of gas, and (8) type of meter, pipe or flange taps.

Example 6.4. Compute the daily flow rate of natural gas through an orifice for the following conditions:

Barometer	14.3 psia
Diameter of pipe	11.938 in. (12-in. schedule 40)
Orifice diameter	4.0 in.
Differential across meter	27.0 in. of water
Static pressure on meter	678 psig
Flowing temperature	73°F
Gas gravity	0.63
Mole fraction CO_2	0.013
Mole fraction N_2	0.031
Type of meter	Flange taps
Temperature base	60°F
Pressure base	14.65 psia

Solution. Daily flow rate $= 24 \cdot F_b \cdot F_r \cdot Y \cdot F_{pb} \cdot F_{tb} \cdot F_{tf} \cdot F_{gr} \cdot F_{pv} \cdot F_m \cdot F_a \cdot F_l \sqrt{h_w P}$

$$\sqrt{h_w P} = \sqrt{27(678 + 14.65)} = 136.7$$

$$F_b \text{ (from AGA tables)} = 3260$$

$$F_r = 1 + b/\sqrt{h_w P} = 1 + 0.0206/136.7 \ (b \text{ from AGA tables}) = 1.00015$$

$$Y(d/D = 4.0/11.938 = 0.335,\ h_w/P_f = 27.0/692.5) \text{ (from AGA tables)} = 0.9996$$

$$F_{pb} = 14.73/14.65 = 1.0055$$

$$F_{tb} \text{ (since 60°F is used)} = 1.0$$

$$F_{tf} \text{ (from AGA tables)} = 0.9859$$

$$F_{gr} \text{ (from AGA tables)} = 1.2599$$

The F_{pv} can be determined by pressure and temperature. If CO_2 and N_2 are present in gas stream, the adjusted temperature and pressure must be calculated by the following equations:

$$\text{adjusted pressure} = \text{flowing pressure } (P_f) \times \text{pressure adjustment factor } (F_P)$$

$$= P_f \frac{156.47}{160.8 - 7.22G + 100x(CO_2) - 39.2x(N_2)}$$

$$= (678)\frac{156.47}{160.8 - 7.22(0.63) + 100(0.013) - 39.2(0.031)}$$

$$= 678.58 \text{ psia}$$

$$\text{adjusted temperature} = \text{flowing temperature } (T_f) \times \text{temperature adjustment factor } (F_T)$$

$$= T_f \frac{226.29}{99.15 + 211.9G - 100x(CO_2) - 168.1x(N_2)}$$

$$= (75 + 460)\frac{226.29}{99.15 + 211.9(0.63) - 100(0.013) - 168.1(0.031)}$$

$$= 535.36°R$$

$$F_{pv} = \text{(from AGA tables)} = 1.0504$$

$$F_m = 0.9985$$

$$F_a = \text{(temperature is within 0°F and 120°F)} = 1.0$$

$$F_l = \text{(North American city)} = 1.0$$

$$Q = 24 \times 3260 \times 1.0 \times 0.9996 \times 1.0055 \times 0.9859 \times 1.2599 \times 1.0504 \times 0.9985 \times 1.0 \times 1.0 \times 136.7$$

$$= 14,007,000 \text{ ft}^3/\text{day} = 14,007 \text{ Mcf/day}$$

Turbine meters (see Fig. 6-9) [6-20,6-41] have been introduced for measuring liquid as well as gas flow. The turning of the turbine is measured by pulses

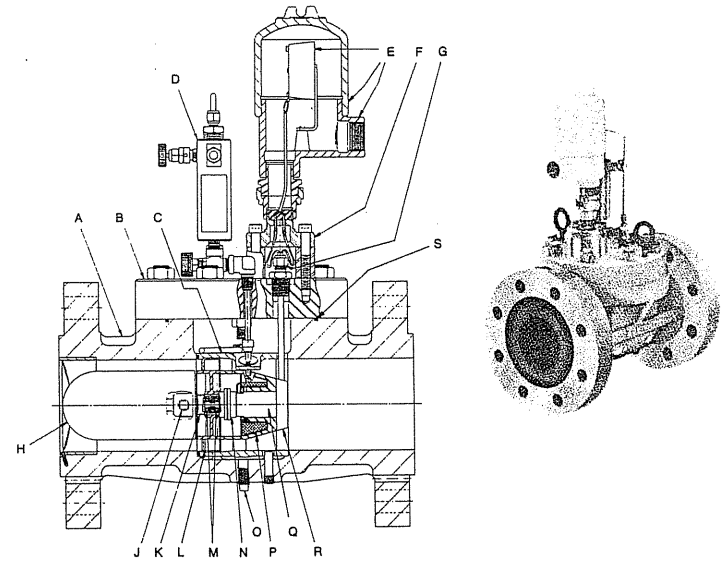

FIGURE 6-9
Turbine meter [courtesy Daniel Industries, Inc.].

generated at each revolution. Calibration gives the flow rates. The *vortex* meter [6-39] utilizes the eddy generated by fluids flowing around a blunt or nonstream object. If the vortex-generating object is correctly shaped and placed in a pipeline with the appropriate relative dimensions, it forms a primary flow element that generates pulse signals at a frequency proportional to the volumetric flow rate over a wide flow range. The *centrifugal* meter is primarily used for large pipe sizes [1-4]. The *sonic* meter has two transducers located in different positions; therefore, the difference in transit times reflects fluid flow rate [1-4].

Effect of condensate in orifice-metered gas streams. Gas in transit to market seldom contains condensate, but gas flowing from high-pressure wells may contain substantial amounts of hydrocarbon condensate as well as some water. Tests were made [6-8] on a horizontal and on a vertical meter run 4 in. in diameter to determine the effect of the presence of condensate at 1400 psi (9.65 MPa), with subsequent separation and measurement of the two phases. Figure 6-10 gives the correction factors determined when the quantity of gas calculated from the meter data was compared with that calculated from a composite of the single-phase gas meters; in other words, the figure converts the condensate to gas volumes.

Studies of *P-V-T* data on gases that enter the two-phase region [6-31] showed that the compressibility factor gave an adequate representation of the composite density of a two-phase stream even though liquid was present. For meters at 1000 psi (6.9 MPa) or more, one or two gallons of hydrocarbon condensate per Mcf can be appropriately accounted for as gas with a factor f based on the gravity of

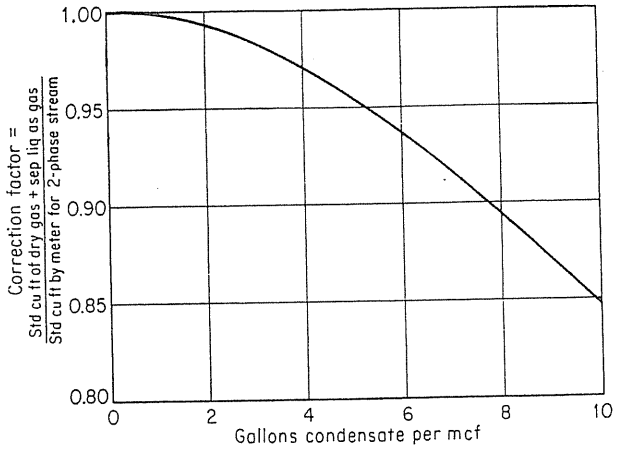

FIGURE 6-10
Correction for condensate in metered gas stream [Brown & Katz, 6-8, courtesy NGAA (now GPA)].

the total stream. This behavior of hydrocarbon systems explains the small corrections at low liquid content in Fig. 6-10.

Meter installations. The nature of the flow of gas through an orifice and the resultant pressure drop depends somewhat upon the type of flow pattern occurring in the stream approaching the orifice. An asymmetrical velocity profile will give different pressure differentials than a symmetrical velocity profile. Accordingly, meter formulas must be based on flow conditions that can be adequately described and duplicated. The AGA has specifications for the minimum lengths of straight pipe upstream and downstream of an orifice, depending on the disturbance ahead of the installation, on whether straightening vanes are used (Fig. 6-11), and on the maximum size orifice to be used. Figure 6-12 shows the lengths A and B for various β values when only a single ell is upstream of the meter. Installations

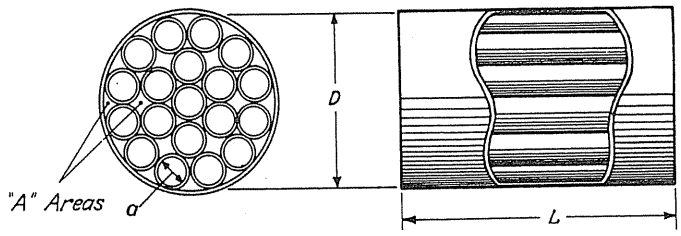

FIGURE 6-11
Straightening vanes for orifice installation [AGA Gas Measurement Committee Report No. 3, 6-1, courtesy AGA].

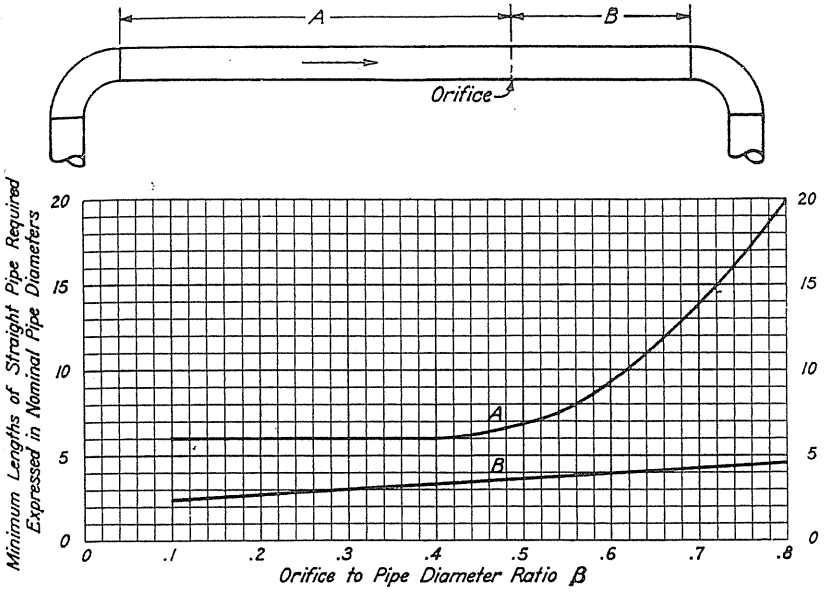

FIGURE 6-12
Installation with one ell preceding meter tube [AGA Gas Measurement Committee Report No. 3, 6-1, courtesy AGA].

often have demands for handling increased flow rates and should provide for orifice sizes up to at least $\beta = 0.6$.

Meter plates. Meter plates are changed when flow rates go beyond the current plate's range of accurate readings. The range of flow rate for a single plate is about 2 to 1 from 20 to 100 in. of differential. Figure 6-13 shows typical orifice installations and plates. The size, measured to ±0.0005 in., is normally stamped on the ear for identification. Special types of installation permit quick changing of orifice plates when the meter is under pressure (Fig. 6-13*b*). The influence of hydrate or foreign material accumulation adjacent to orifice plates is discussed by Kehoe [6-33].

Recording Devices for Pressure and Differential

Recording devices may be installed for individual meters, as shown in Fig. 6-8*b*, or they may be placed in a meter house for a group of meter runs. Differential elements are normally designed for up to 50 or 100 in. of water differential. Pressure elements are available in various ranges such as 0 to 500 psi (0–3.45 MPa), 0 to 1000 psi (0–6.9 MPa), 0 to 2000 psi (0–13.8 MPa), etc. There are two principal types of meter charts, shown in Fig. 6-14. The first is the direct-

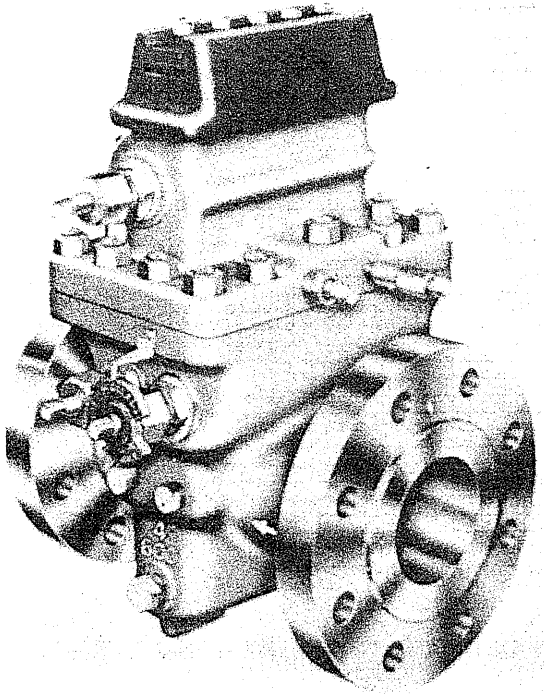

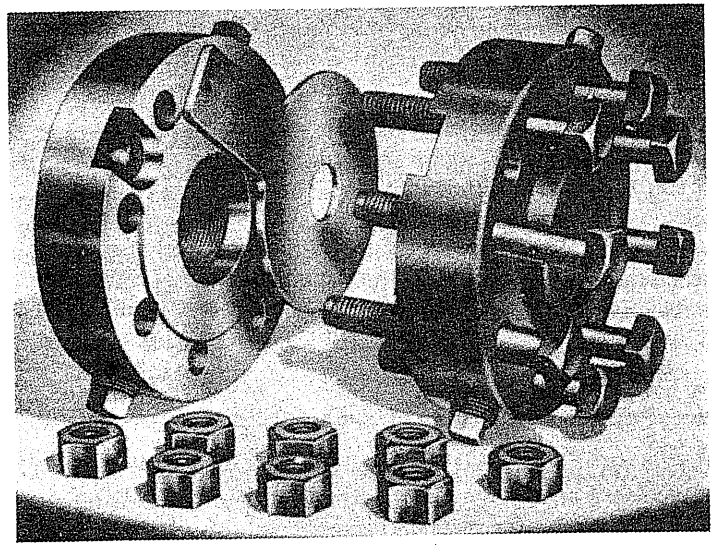

FIGURE 6-13
Orifice plates: (*a*) standard plates [courtesy Foxboro Company], (*b*) orifice assembly permitting changing of orifice under pressure [courtesy Daniel Orifice Fitting Company].

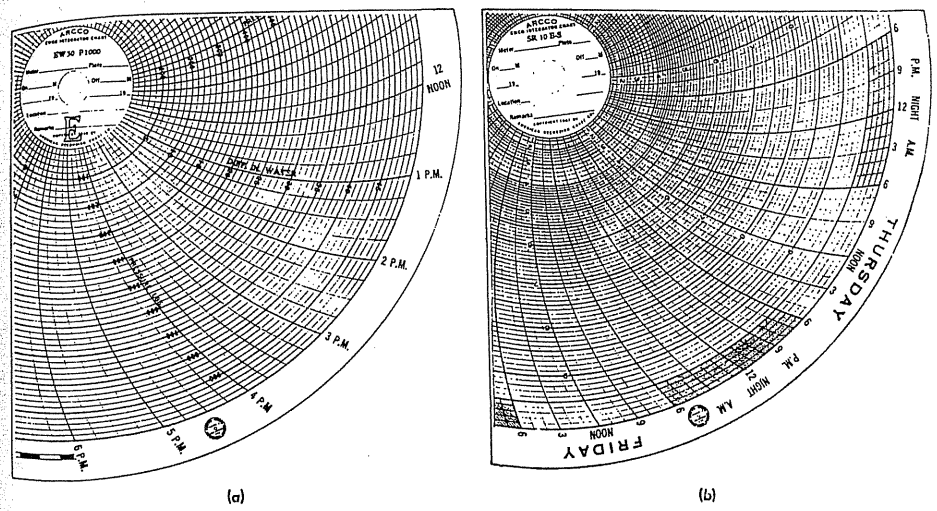

(*a*) (*b*)

FIGURE 6-14
Orifice meter charts: (*a*) direct-reading chart, (*b*) square-root chart [courtesy Rockwell Mfg. Co.].

reading chart for the differential in inches of water and the pressure in pounds per square inch. The second is a chart that reads the square root. Clocks turn the charts at desired speed, one turn each day or other time period.

Critical-Flow Provers

Critical-flow provers are used for metering when gas can be blown to the air or when a large pressure drop is available. Such a device is very simple (Fig. 6-15 [6-47]); it involves only the upstream pressure, upstream temperature, gas gravity, and flow nozzle size. Critical flow occurs when the critical pressure ratio is exceeded and acoustical velocities are attained in the throat of the nozzle. For ideal gases, the critical pressure ratio is found from Eq. (6-19):

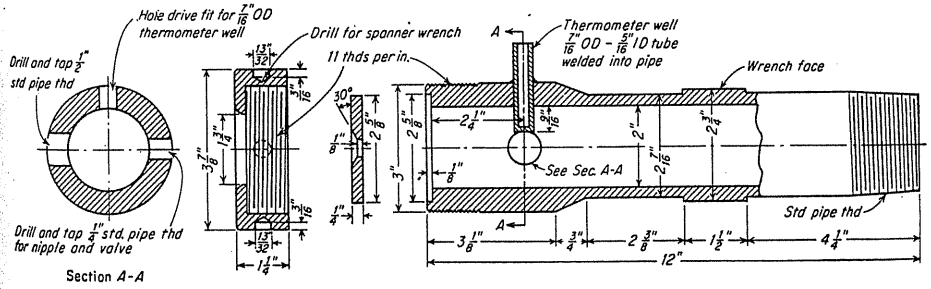

FIGURE 6-15
Design of 2-in. critical flow prover [Rawlins & Schellhardt, 6-47].

$$\frac{P}{P_1} = \left(\frac{2}{k+1}\right)^{k/(k-1)} \tag{6.19}$$

where P is the pressure in the throat of the prover nozzle, P_1 is the upstream pressure, and $k = C_P/C_V$, the ratio of heat capacity at constant pressure to that at constant volume. For air $P = 0.528 \cdot P_1$; for 0.6-gravity gas and $k = 1.299$, $P = 0.546 \cdot P_1$.

The real gas critical flow equation may be written simply:

$$Q = \frac{CP_1}{\sqrt{GT_1}} \tag{6.20}$$

where Q is the gas flow at 14.65 psia and 60°F, in ft^3/hr, G is the gas gravity, P_1 is upstream pressure in psia, and T_1 is upstream temperature in °R. The C of Eq. (6.20) is the coefficient for the given-sized orifice:

$$C = \frac{3600 \times 520 \times \sqrt{778}\sqrt{64.4}A_2\sqrt{C_P}}{14.65\sqrt{29}Z_2}\left(\frac{2}{k+1}\right)^{1/(k-1)}\sqrt{\frac{k+1-2Z_2/Z_1}{k+1}} \tag{6.21}$$

where A_2 is the nozzle area and Z_1 and Z_2 are compressibility factors upstream and downstream.

Eq. (6.20) is the critical flow equation used with provers; it applies only when the value of P_1 is greater than the downstream pressure by an amount sufficient to give critical flow. Upstream pressure must be at least twice atmospheric pressure when exhausting to the atmosphere. McKetta et al. [6-36] evaluated the formula and concluded that at least 40 psia (276 kPa) is needed to obtain accurate calculations for a sharp-edge orifice. Rawlins and Schellhardt [6-47] presented calibrations (Table 6.3) for orifices in 2-in. pipe and 4-in. pipe for plates $\frac{1}{8}$ in. thick. Commercial devices come with tables of constants for various plates. The value of C can be computed from Eq. (6.21). Rawlins and Schellhardt did not make corrections in the meter volumes or in the critical flow prover for deviation from ideal gases; that is they assumed $Z_1 = Z_2 = 1.0$. Their measurements were made on a gas well with closed-in wellhead pressure of 480 psi. Critical expansion ratios and acoustical velocities are given for natural gas constituents in Table 6.4.

Pitot Tubes

The Pitot tube measures flow rate from the impact pressure of a flowing stream. Figure 6-16 shows a differential pitot tube with manometer. The differential between the impact and static pressures is measured, since the static pressure is observed adjacent to the point where the impact pressure is taken. For high flow rates, mercury may be used in the manometer instead of water. For flow rates giving less than 0.5 in. of water on a vertical manometer, an inclined manometer or draft gauge will improve the accuracy of the reading.

The formula for computing flow in a pipe by pitot tube is

$$Q = 7.0 \cdot d^2\sqrt{\frac{h_v P}{G}} \cdot \frac{520}{T_f} \tag{6.22}$$

TABLE 6.3
Coefficient for critical-flow prover and choke nipple [Rawlins & Schellhardt, 6-47]

$Q = \frac{CP}{\sqrt{GT}}$ P = upstream pressure, G = gas gravity, T = upstream temperature, °R, C = coefficient, Q = flow rate measured at 14.4 psia and 60°F, Mcf/day

Orifice size		Value of C		
		Critical flow prover		
No.	in.	2-in. pipe	4-in. pipe	Choke nipple
1/16	0.063	1.524		
1/8	0.125	6.301		5.25
1/4	0.250	25.86	24.92	26.51
3/8	0.375	56.58	56.01	61.21
1/2	0.500	101.8	100.2	112.72
5/8	0.625	154.0	156.1	179.74
3/4	0.75	224.9	223.7	260.99
1	1.00	406.7	396.3	
2	2.00		1.596	

where Q (Mcf/day) is the flow rate at 14.7 psia and 60°F, d (in.) is the diameter of pipe, T_f (°R) is the flowing temperature, G is the gas gravity, P (psia) is the static pressure, and h_v (in.) is the velocity or impact head of water. For a 0.6-gravity gas, T of 60°F, and P at 14.7 psia,

$$Q = 34.7 \cdot d^2\sqrt{h_v} \tag{6.23}$$

This formula is derived below on the basis of the known ratio of the velocity at

TABLE 6.4
Critical expansion ratio

Gas	C_P at 1 atm, 60°F, Btu/(lb mol)(°F)	$k = C_P/C_V$	P_c/P_1	Acoustical velocity at 60°F, ft/s
Air	7.00	1.410	0.528	1031
Helium	4.968	1.66	0.486	2840
Methane	8.44	1.308	0.545	1350
Ethane	12.30	1.193	0.565	967
Propane	17.10	1.133	0.577	793
Isobutane	22.4	1.097	0.585	681
n-butane	23.0	1.094	0.585	680
$G = 0.6$	8.84	1.299	0.546	1309
$G = 0.7$	9.77	1.279	0.550	1035

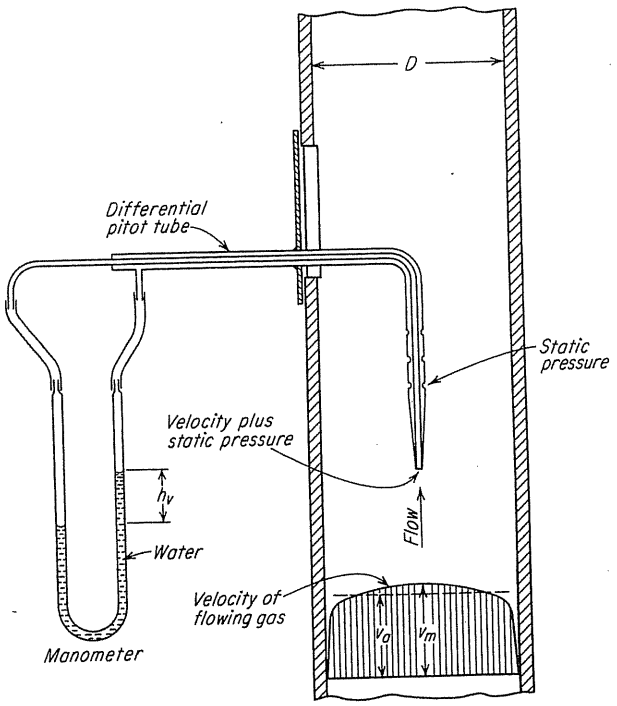

FIGURE 6-16
Pitot tube [Katz et al., 1-1, courtesy McGraw-Hill Publishing Co.].

the center to the average velocity for flow in pipes. This formula was published in the early thirties [6-45,6-47].

When a mercury manometer is used to indicate the impact head h_v in Eq. (6.22), the constant factor becomes $7.0\sqrt{13.55} = 25.8$; when h_v is in psi, the constant becomes $7.0\sqrt{27.75} = 36.9$.

When a pitot tube is held at the outlet of a vent pipe and the static pressure is taken at the side of the vent pipe 4 diameters from the end, the same formula applies [6-47], provided that the static pressure has not reached the point (about 15 psi) where critical flow is reached at the end of the pipe.

The annubar flow meter [6-16] applies the same principle as the pitot tube, with a multi-intake at various positions to account for the flow profiles.

Choke Nipples

Choke nipples (Fig. 6-17) are often used in controlling the flow of oil or gas from wells. Table 6.3 gives values of C for gas flowing through a choke nipple under critical flow.

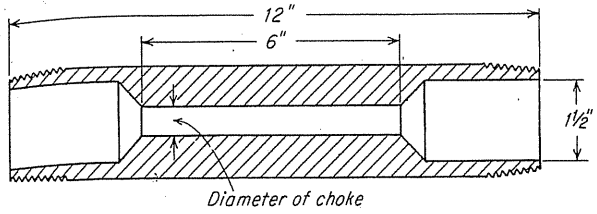

FIGURE 6-17
Choke nipple [Katz et al., 1-1, courtesy McGraw-Hill Publishing Co.].

Automation, Computerization, Digitalization of Metering

Much reconstruction of metering facilities has taken place on transmission lines and more is in progress. Metering systems composed of transducers for pressure, pressure differential, and temperature sensing may well include a chromatograph for determining gas composition. The gas gravity, caloric or gross heating value, and compressibility factor are determined by automatic computation. The total result is a digital readout of cumulative gas flow. Such automation of meter readings has been installed for orifice and other metering devices.

Along with the update of facilities, more attention is being given to more accurate compressibility factors. AGA measurement Report No. 8, edited by Starling [6-53], set forth an elaborate equation of state to provide the very best calculation of compressibility factors from gas composition. Data from Gasunie in Groningen, Netherlands, were used as a standard for verifying the validity of the proposed computer calculation at pressures up to 20,000 psia (138 MPa) and at temperatures from 50 to 400°F (10–204°C).

6.6 COMPRESSION AND EXPANSION OF NATURAL GAS; PUMPING

Natural gas, crude oil, natural gas liquids, and water are normally transported in pipelines. When an increase in pressure is required, gas compressors or liquid pumps are installed. The prime questions that arise have to do with suitable equipment available for the task and the work or power requirements for the assignment. Those working in design and operation will be interested in the details of the units and problems of maintenance in operations. For feasibility studies, the horsepower requirement for the equipment to be installed, costs of facilities, and the fuel or power requirements with attendant costs are needed.

Evaluation of Work Required in Compression

Two basic approaches may be used to evaluate work or horsepower theoretically required to compress gas of a given gravity from pressure 1 to pressure 2. The

more traditional approach has been to utilize Eq. (3.7), and evaluate $\int \bar{v}\,dP$ using the ideal gas law for either adiabatic and reversible compression or isothermal compression. The second method utilizes Eq. (3.4), and obtains the enthalpy increase for an adiabatic and reversible path ($\Delta s = 0$).

By the traditional approach, Eq. (3.7) is reduced to

$$\int_1^2 \bar{v}\,dP = -w_s - l_w \tag{6.24}$$

for a horizontal flow neglecting the differences in kinetic energy between entering and exiting states. The l_w also may be omitted to find the theoretical work; friction losses within the unit can be accounted for later in an efficiency term.

For the adiabatic compression or expansion of ideal gas, the change of state obeys

$$P\bar{v}^k = \text{constant} \tag{6.25}$$

where k is the ideal gas specific heat ratio C_P/C_V, as given in Fig. 4-51. Substituting into Eq. (6.24) and integrating, one obtains the theoretical adiabatic work of compression in ft · lb per lb gas:

$$-w_s = \frac{k}{k-1}\frac{53.241T_1}{G}\left[\left(\frac{P_2}{P_1}\right)^{(k-1)/k} - 1\right] \tag{6.26}$$

where P_1 and P_2 are the suction and discharge pressures, compressibility factor Z_1 and k are evaluated at suction conditions, and T_1 is the temperature of suction gas.

Where deviation from ideal gas behavior is appreciable, Eq. (6.26) is empirically modified [6-18,6-21,6-30]. One such modification presented by Joffe [6-30] is as follows:

$$-w_s = \frac{k}{k-1}\frac{53.241T_1}{G}\left[\left(\frac{P_2}{P_1}\right)^{Z_1(k-1)/k} - 1\right] \tag{6.27a}$$

and the GPA [1-28] formula is

$$-w_s = \frac{k}{k-1}\frac{53.241Z_aT_1}{G}\left[\left(\frac{P_2}{P_1}\right)^{1(k-1)/k} - 1\right] \tag{6.27b}$$

where Z_a is the average compressibilty factor.

For the adiabatic theoretical horsepower required to compress 1 MMcf/day at 60°F and 14.65 psia, Eq. (6.27*a*) gives

$$-W_s = 0.08531\frac{k}{k-1}T_1\left[\left(\frac{P_2}{P_1}\right)^{Z_1(k-1)/k} - 1\right] \tag{6.28}$$

Note that W_s shows total work and w_s the work per unit mass.

The second method for computing the work of compression is using Eq. (3.4) with the increase in enthalpy under adiabatic and reversible conditions. Eq. (3.4) is simplified for the compression step by neglecting elevation and kinetic energy changes, and assuming adiabatic conditions, where $q = 0$. Then, $-w_s = \Delta h$.

Since enthalpies are frequently given on a mole basis and the work for a given compression is desired in terms of theoretical horsepower, a conversion step is needed for a practical equation. A chart or equation-of-state program usually gives the enthalpy increase at constant entropy s in terms of Btu/lb mol.

Since 1 MMcf/day = $10^6/379$ = 2638.5 lb mol/day,

$$H_p \text{ (horsepower)} = 2638.5\,\frac{\text{lb mol}}{\text{day}} \times \Delta h\left(\frac{\text{Btu}}{\text{lb mol}}\right) \times \frac{1 \text{ hp} \cdot \text{hr}}{2545 \text{ Btu}} \times \frac{1 \text{ day}}{24 \text{ hr}}$$

$$= 0.0432 \times \Delta h \tag{6.29}$$

gives the horsepower required for a flow of 1 MMcf/day.

Temperature Rise during Compression

Following the concepts used in developing Eq. (3.7), one finds the temperature after compression for an ideal gas to be

$$T_2 = T_1\left(\frac{P_2}{P_1}\right)^{(k-1)/k} \tag{6.30}$$

Corrections to this ideal case are needed for deviation of gases from ideal and for inefficiency of the compressor. The inefficiency energy loss results in added temperature rise. The final temperature of compression and the heat removed in the intercoolers can be rigorously obtained from enthalpy-entropy diagrams.

In the case of multistage compression for a given number of stages, the compression ratio per stage should be the same for each stage to minimize total work; so the relationship of the compression ratio (CR) per stage to the overall compression ratio is

$$\text{CR} = \left(\frac{P_2}{P_1}\right)^{1/n} \tag{6.31}$$

where n is the number of stages and P_1 and P_2 are the suction and discharge pressures. It is very seldom that a CR greater than 6 is used.

The procedure for calculating horsepower from an enthalpy-entropy diagram can best be shown diagramatically and then demonstrated by means of an example. Figure 6-18 is a qualitative sketch of an enthalpy-entropy diagram. Point 1 is the initial state of the gas as it enters the compressor. Path 1-2 shows the first stage of compression (constant entropy). The gas is then cooled in the intercooler at constant pressure (path 2-3); the difference in enthalpy along this path is equal to the heat removed in the intercooler. Path 3-4 shows the second

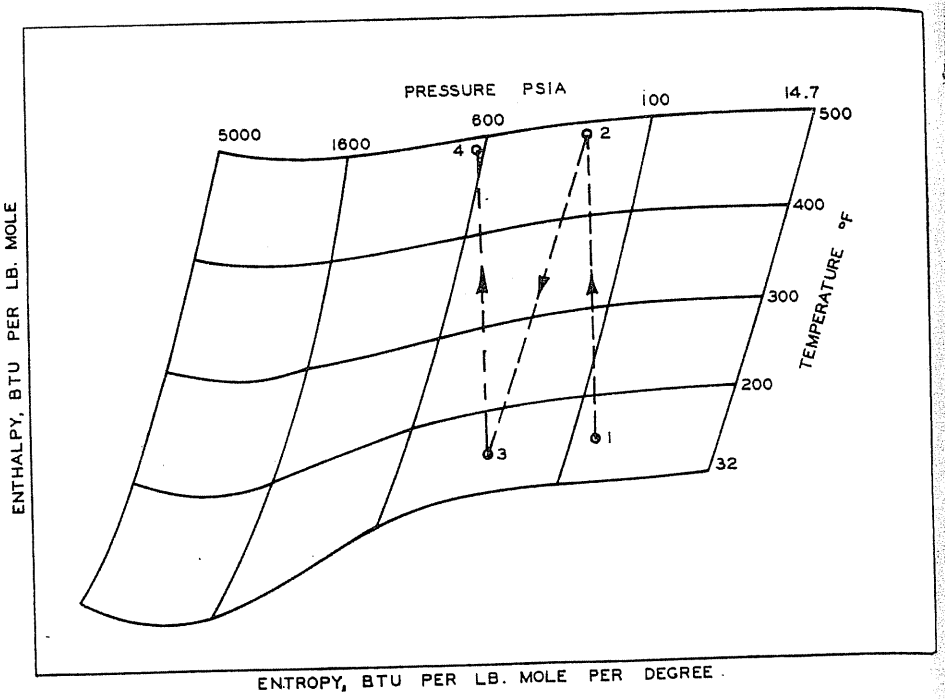

FIGURE 6-15
Use of enthalpy-entropy diagram to find adiabatic work of compression [Katz et al., 1-1, courtesy McGraw-Hill Publishing Co.].

stage of compression. The temperatures at points 2 and 4 are the temperatures of the gas at the end of the first and second stages of compression. The temperature at point 3 is the temperature to which the gas is cooled in the intercooler.

The following example demonstrates the use of *H-S* charts in calculating both the adiabatic and the isothermal horsepower theoretically necessary to compress a gas.

Example 6.5. Calculate the adiabatic and the isothermal theoretical horsepower required to compress 1 MMcf/day of a 0.6-gravity natural gas at 100 psia and 80°F to 1600 psia. Intercoolers cool the gas to 80°F. In the case of the adiabatic compression, what is the heat load on the intercoolers and what is the final gas temperature? Use the *H-S* diagram to solve this problem.

Solution. *Adiabatic compression using enthalpy-entropy charts:* Since the overall CR is 16, two-stage compression, each stage with a CR of 4, should be used:

$$\text{CR} = \sqrt{\frac{1600}{100}} = 4$$

The first stage of compression will be from 100 to 400 psia. Determine the difference

in enthalpy by following a vertical line (constant entropy) between 100 and 400 psia, using the 0.6-gravity *H-S* chart (Fig. 4-53):

$$\Delta h_{1\text{-}2} = h_2 - h_1 = 1990 - 380 = +1610 \text{ Btu/lb mol}$$

The gas is then cooled to 80°F. Follow the 400 psia line down to 80°F and determine the difference in enthalpy. This is the amount of heat removed from the gas in the intercoolers.

$$\Delta h_{2\text{-}3} = h_3 - h_2 = 220 - 1990 = -1770 \text{ Btu/lb mol}$$

The second stage of compression is from 400 to 1600 psia. Repeat the procedure of the first stage:

$$\Delta h_{3\text{-}4} = h_4 - h_3 = 1920 - 220 = +1700 \text{ Btu/lb mol}$$

The adiabatic theoretical horsepower necessary to compress the gas is thus

$$-W_s = 0.0432(\Delta h_{1\text{-}2} + \Delta h_{3\text{-}4}) = 0.0432 \times (1610 + 1700) = 143 \text{ hp/(MMcf/day)}$$

The heat load on the intercoolers is

$$\Delta h_{2\text{-}3} = -1700 \text{ Btu/lb mol}$$

or in terms of 1 MMcf/day,

$$\Delta H_{2\text{-}3} = \frac{-1700 \times 10^6}{379} = -4.67 \times 10^6 \text{ Btu/(MMcf/day)}$$

The final gas temperature is read from the chart at point 4:

$$T = 278°\text{F}$$

Isothermal compression using enthalpy-entropy chart: By following the 80°F constant temperature line on the 0.6-gravity *H-S* diagram (Fig. 4-53), enthalpy H and entropy S can be determined. The enthalpy and entropy at 80°F and 100 psia are

$$h_1 = 380 \text{ Btu/lb mol}$$

$$s_1 = -3.2 \text{ Btu/(lb mol} \cdot °\text{R)}$$

At 80°F and 1600 psia

$$h_2 = -480 \text{ Btu/lb mol}$$

$$s_2 = -9.75 \text{ Btu/(lb mol} \cdot °\text{R)}$$

Thus,

$$\Delta h = h_2 - h_1 = -480 - 380 = -860$$

$$\Delta s = s_2 - s_1 = -9.75 + 3.2 = -6.55$$

The isothermal theoretical horsepower then is

$$-W_s = 0.0432(-860 + 540 \times 6.55) = 115.7 \text{ hp}$$

This is the absolutely minimum horsepower necessary to compress the gas. An actual compressor with an infinite number of intercoolers and stages of compression

would approach isothermal conditions if the gas were cooled to the initial temperature in the intercoolers. Qualitatively, Fig. 6-19 shows horsepower requirements versus number of compression stages. The horsepower approaches the isothermal value as the number of stages increases.

An alternative method using different equations is illustrated in reference [1-1]. For the above specific example, the agreement between values for horsepower calculated by means of the equations and those calculated by means of the enthalpy-entropy diagram is good. However, use of the *H-S* charts is preferred.

Theoretical horsepower can be converted to brake horsepower (horsepower input into the compressor) by the application of the proper factors. The factors involved include the compression efficiency (compressor-valve losses) and the mechanical efficiency of the compressor. The losses vary with equipment, design speed, compression ratio, and other factors. The combined efficiencies have been shown to vary with compression ratio, as shown in Fig. 6-20, and can be used [6-49] for determining brake horsepower from theoretical horsepower as obtained from the enthalpy-entropy diagrams or from the analytical equations.

$$\text{Efficiency} = \frac{\text{adiabatic theoretical horsepower}}{\text{brake horsepower}} \tag{6.32}$$

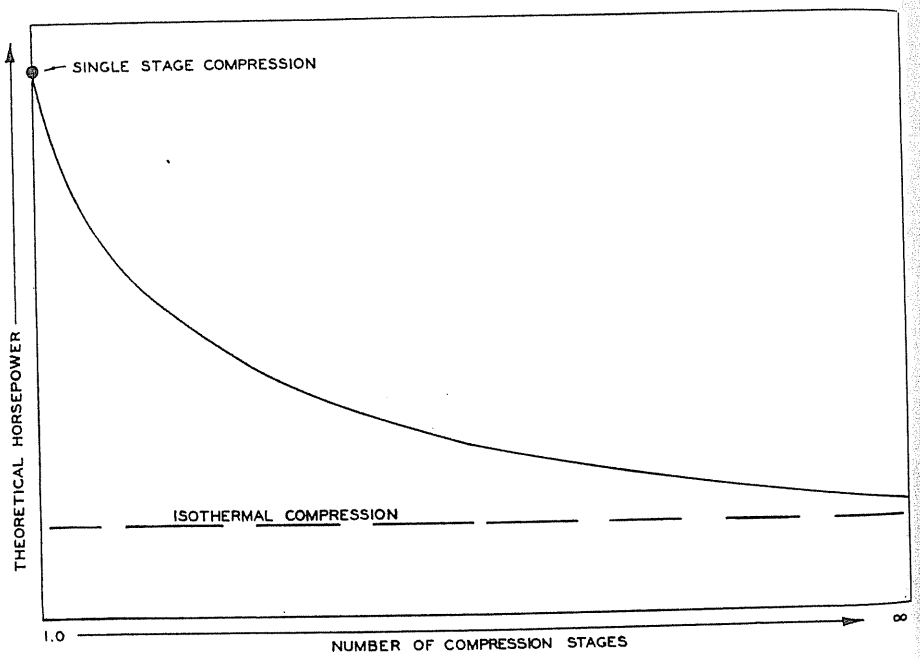

FIGURE 6-19
Variation of compression horsepower with number of stages [Katz et al., 1-1, courtesy McGraw-Hill Publishing Co.].

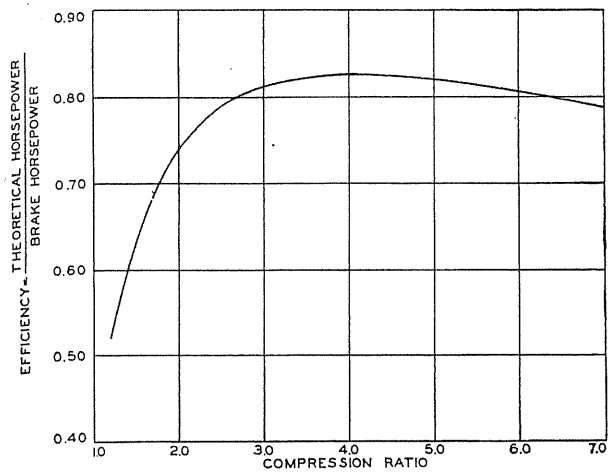

FIGURE 6-20
Compressor efficiency [Ridgeway, 6-49, Katz et al., 1-1, courtesy McGraw-Hill Publishing Co.].

The 143 hp found in Example 6.5 for theoretical adiabatic compression at a CR of 4 converts to 143/0.827 = 172.9 brake horsepower.

Comparison of Efficiency for Different Numbers of Stages

The following example illustrates the different energy requirements for the use of two compression stages and the use of one stage. A computer solution is also given.

Example 6.6. A plant receives 20 MMcf/day of 0.6-gravity natural gas at 70°F and 205 psig. It is to be compressed to 910 psig for processing. After- and intercoolers are to lower the gas to 90 °F.

(*a*) What is the theoretical horsepower required for compression if one stage is used? What if two stages are used?
(*b*) What are the theoretical temperature rises during compression?
(*c*) What is the corresponding heat duty of inter- and/or aftercoolers for the gas?
(*d*) What is reasonable efficiency to use for reciprocating compressors?
(*e*) What effect do inefficiencies have on the temperature rise and heat duty of the coolers?

This problem has been solved by three methods:

1. Determining $\Delta h|_s$ isentropically (s constant) by computer using the Soave-Redlich-Kwong equation of state. This method was used by Arco personnel.

2. Finding $\Delta h|_s$ by H-S chart with temperature rises and enthalpy h.
3. Using an equation dependent upon $k = C_P/C_V$ for the gas, including Z to correct for nonideality.

Solution (hand calculations). The overall compression ratio is (910 + 15)/(205 + 15) = 4.20.

The minimum work for equal-sized compressors is obtained from Eq. (6.31):

$$\text{CR} = \left(\frac{P_2}{P_1}\right)^{1/n}$$

For two stages, CR = $(4.20)^{1/2}$ = 2.05 per stage. Thus, for a suction pressure of 220 psia, the pressure between stages is 220 × 2.05 = 451 psia.

Single-stage case: From Fig. 4-53, read the enthalpy at 225 psia and 70°F: 230 Btu/lb mol ($s = -4.9$). At this entropy, read the h at 925 psia: 1860 Btu/lb mol. Then Δh = 1860 − 230 = 1630 Btu/lb mol. The temperature rises from 70°F to 255°F. $H_p = 0.432 \times 1630 \times 20$ (MMcf/d) = 1408 hp (theoretical).

Read h at 90°F and 925 psia: 50 Btu/lb mol. The energy removed in the aftercooler is 1860 − 50 = 1810 Btu/lb mol or $1810 \times 20,000,000/379 = 95.5 \times 10^6$ Btu/day or 3.98×10^6 Btu/hr.

For the single stage, the temperature rises from 70 to 255°F, a 185°F rise.

Two stage case: The intermediate pressure is 2.05 × 220 = 451 psia. The intercooler gives a second-stage suction temperature of 90°F. For the first stage, 225 psia, 70 °F to 451 psia (h = 1010):

$$\Delta h = 1010 - 230 = 780 \text{ Btu/lb mol}$$

$$H_p = 0.0432 \times 780 \times 20 = 674 \text{ (theoretical)}$$

For the second stage, 451 psia, 90°F (h = 290) to 925 psia (h = 1050):

$$\Delta h = 1050 - 290 = 760 \text{ Btu/lb mol}$$

$$H_p = 0.0432 \times 760 \times 20 = 657$$

Total H_p = 674 + 657 = 1330 hp. Note this is less than the 1408 hp for 1 stage.

The theoretical temperature rise comes directly from the chart. For the first stage temperature rise is from 70 to 160°F, a 90°F rise. For the second stage, temperature rises from 90 to 190°F, a 100°F rise.

Intercooler of first stage: The heat removed is $-\Delta h$ = 1010 − 290 = 720 Btu/lb mol. Heat duty = $720 \times 20 \times 10^6/379 = 38.0 \times 10^6$ Btu/day.

Aftercooler of second stage: Duty = $(1050 - 50) \times 20 \times 10^6/379 = 52.77 \times 10^6$ Btu/day.

The total heat duty for two stages is $(38.0 + 52.77) \times 10^6 = 90.77 \times 10^6$ Btu/day.

The results of various methods are given in Tables 6.5, 6.6, and 6.7, including GPA results using Figs. 6-21, 6-22, 6-23, and 6-24. The Arco program calculated enthalpy by the Soave-Redlich-Kwong equation of state.

There is a difference in computed horsepower between the computer solution here and the hand solutions. The GPA result for horsepower is 1704 while the

TABLE 6.5
Hand calculations using standard calculation enthalpy chart

	1st stage	2nd stage	Single stage
P_1, psia	220	451	220
P_2, psia	451	925	925
T_1, °F	70	90	70
T_2, °F	160	190	255
ΔT	90	100	185
h_2, Btu/lb mol	1010	1050	1860
h_1, Btu/lb mol	230	290	230
Δh, Btu/lb mol	780	760	1630
s, Btu/lb mol/°F	−4.9	−6.03	−4.9
H_p	674	657	1408

	Comparison	
	2 stages	1 stage
H_p	1331	1408
Heat transfer, Btu/day:		
Intercooler	38,000,000	
Aftercooler	52,770,000	95,500,000
Sum	90,770,000	95,500,000

TABLE 6.6
Summary of computer solution

	1st stage	2nd stage	Single stage
P_1, psia	220	451	220
P_2, psia	451	925	925
T_1, °F	70	90	70
T_2, °F	163	188	266.2
ΔT	93	98	196
$k = C_P/C_V$	1.333	1.333	1.278
H_p	685.6	697.9	1493.2
	(Total = 685.6 + 697.9 = 1383.5)		

	Comparison	
	2 stages	1 stage
Intercooler, 10^6 Btu/day	42.6	
Aftercooler	38.6	91.19
Sum	81.6	91.19

TABLE 6.7
Results obtained by various methods

	Computer solution	Hand solution	Eq. (6.26) $k = C_P/C_V$	GPA chart
H_p (1st of 2-stage)	686	674	649	
H_p (2nd of 2-stage)	698	657	673	
H_p (sum of stages 1 & 2)	1384	1331	1322	
H_p (single stage)	1493	1408	1406	1704
ΔT (1st of 2-stage)	93	90		
ΔT (2nd of 2-stage)	98	100		
ΔT (single stage)	196	185	185	188
Total heat transfer, 10^6 Btu/day				
2 stages	81.6	90.77		
1 stage	91.9	95.5		

theoretical hand calculation gives 1406, indicating they may have used an 82.5 percent efficiency value for the compression ratio of 4.2.

The GPA chart of $k = C_P/C_V$, Fig. 4-3 in reference [1-28], was found very difficult to read. Figure 4-51 in the present book is a new version of the chart. It uses pure constituent data and calculated values from Table 4.1 in reference [1-28].

6.7 WHY OIL LINES HEAT AND GAS LINES COOL

Why do oil lines heat and gas lines cool? The senior author had occasion to study this subject in connection with a proposed gas line from Prudhoe Bay to the United States. The Alaska oil line has no heaters; only the work input at pump stations is added for temperature maintenance from Prudhoe to Valdez.

Reference [6-32] is reproduced here in part to promote understanding of internal energy and the properties of fluids. The effect of pressure on entropy (s) for oils is very little, while for gases it is large. As a gas drops in pressure, the need for heat energy to supply the added entropy for the gas to maintain its temperature at the lower pressure is greater than the entropy supplied by frictional energy and so it self-cools. On the other hand, the effect of pressure on the entropy of crude oil is small and so most of the frictional energy consumed in a given pressure drop contributes to a temperature rise.

Analysis of this effect is relatively simple, starting with Eq. (3.4). By assuming horizontal flow, adiabatic conditions, and no work done, and neglecting kinetic energy changes, $\Delta h = 0$ and $\int_1^2 \bar{v}\,dP = \int_1^2 T\,dS$. Thus, the decrease in expansion energy equals the increase in heat energy. However, the effect of pressure on entropy (s) is quite different for gases and liquids. The effect of pressure on s for liquids is small and hence there is a temperature increase, neglecting heat transfer from the flowing field. For gases, the effect of pressure on entropy is large and hence not enough work energy of expansion is expended

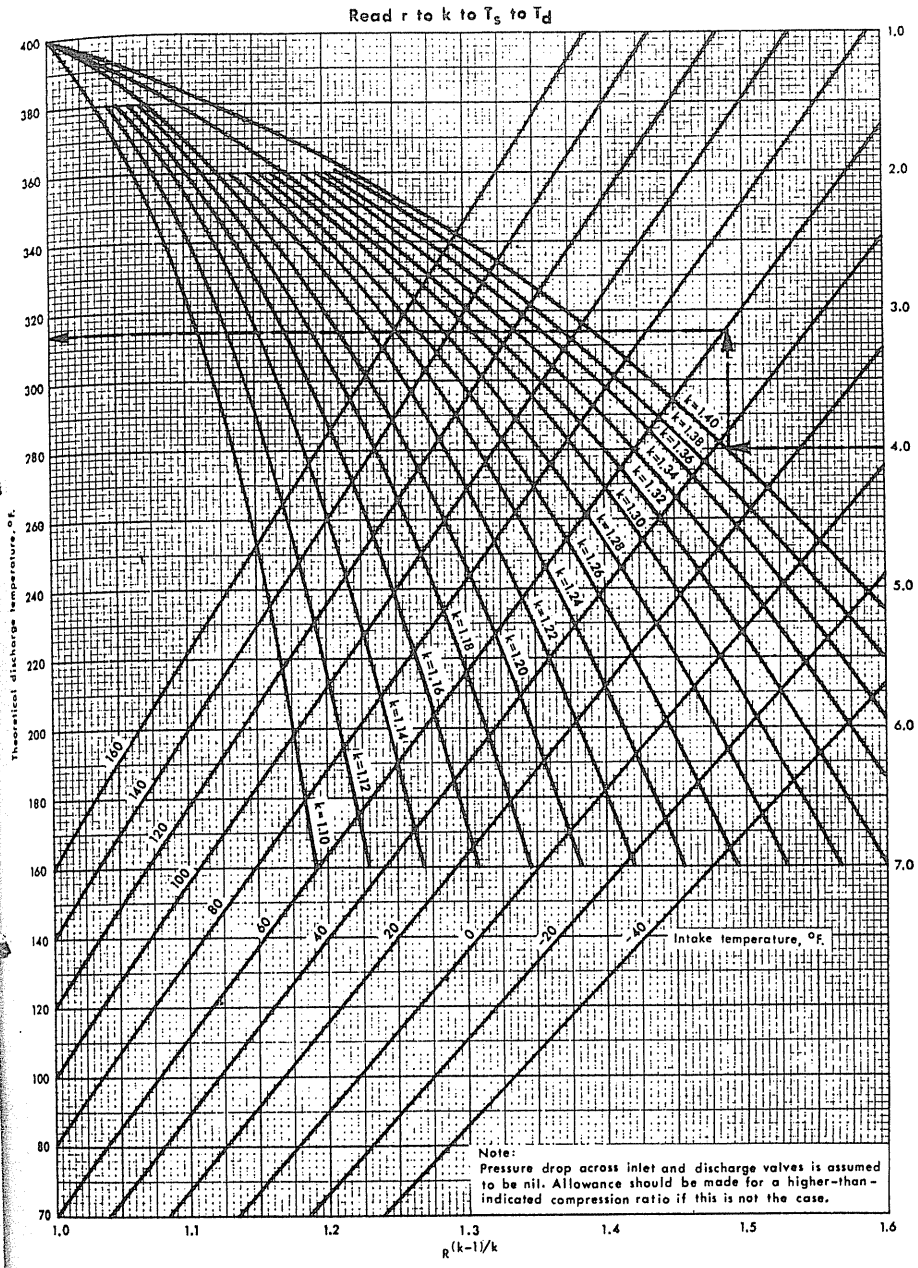

FIGURE 6-21
Theoretical discharge temperatures for single-stage compression [1-28, courtesy GPA].

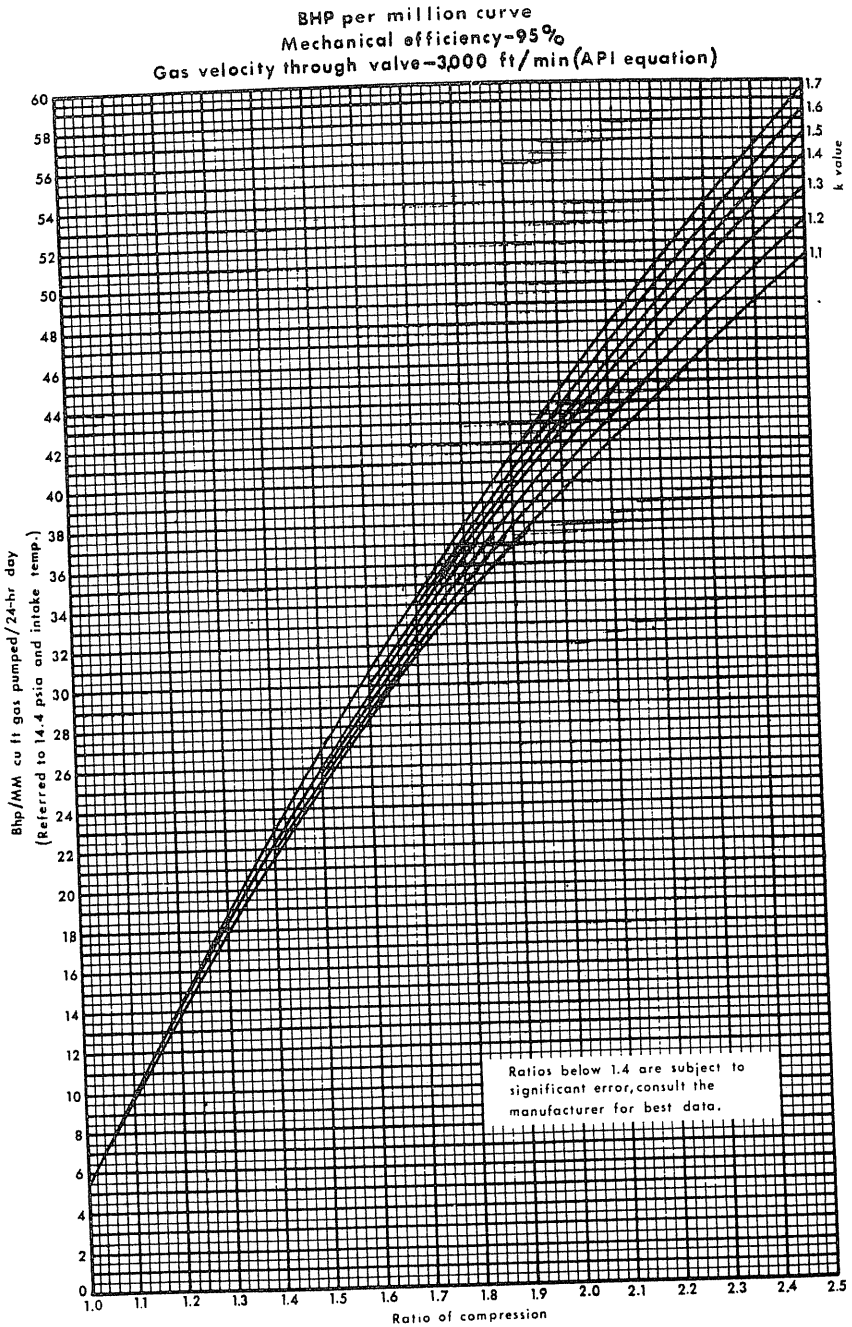

FIGURE 6-22
Power requirements for compressor with mechanical efficiency 95 percent and gas velocity through valve 3000 ft/min (API equation), for $1 < CR < 2.5$ [1-28, courtesy GPA].

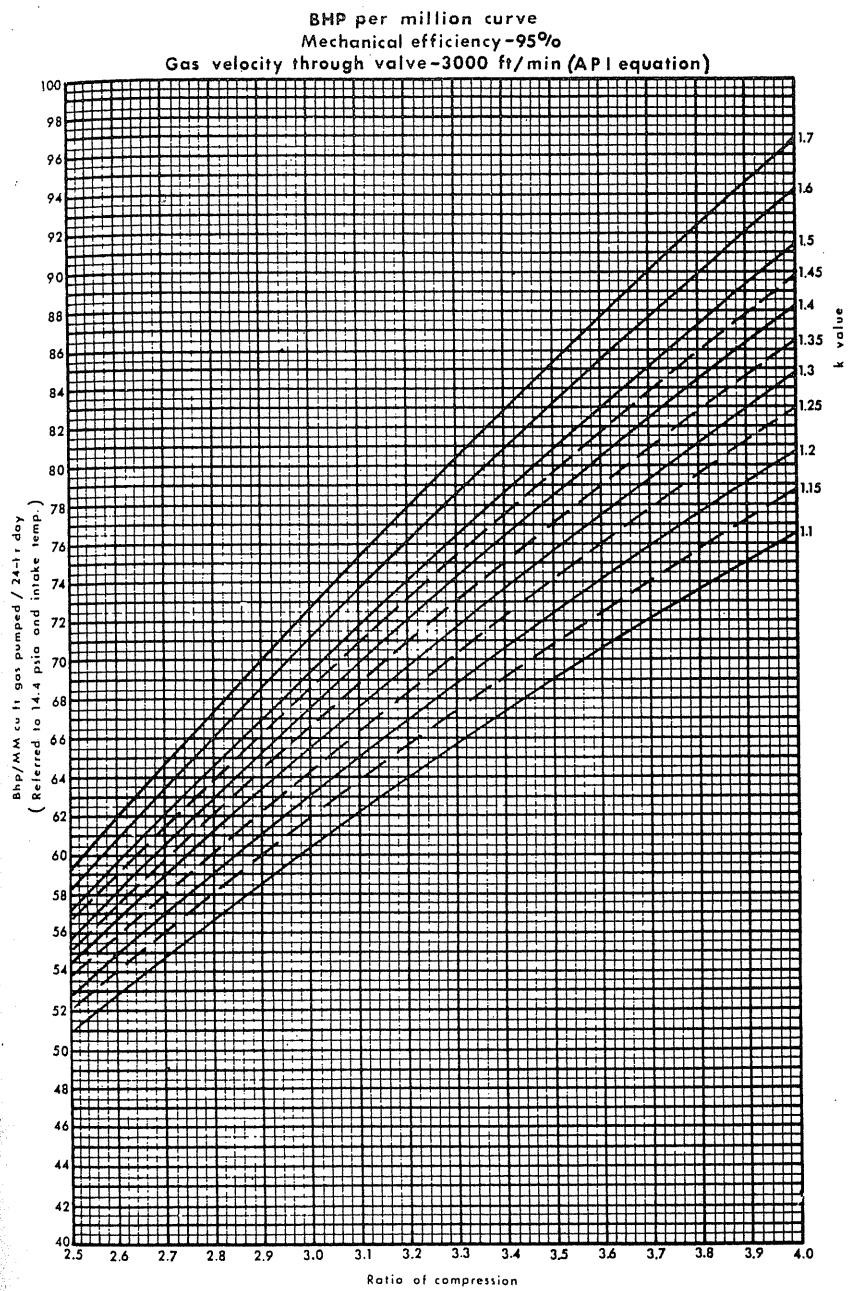

FIGURE 6-23
Power requirements for compressor with mechanical efficiency 95 percent and gas velocity through valve 3000 ft/min (API equation), for $2.5 < CR < 4$ [1-28, courtesy GPA].

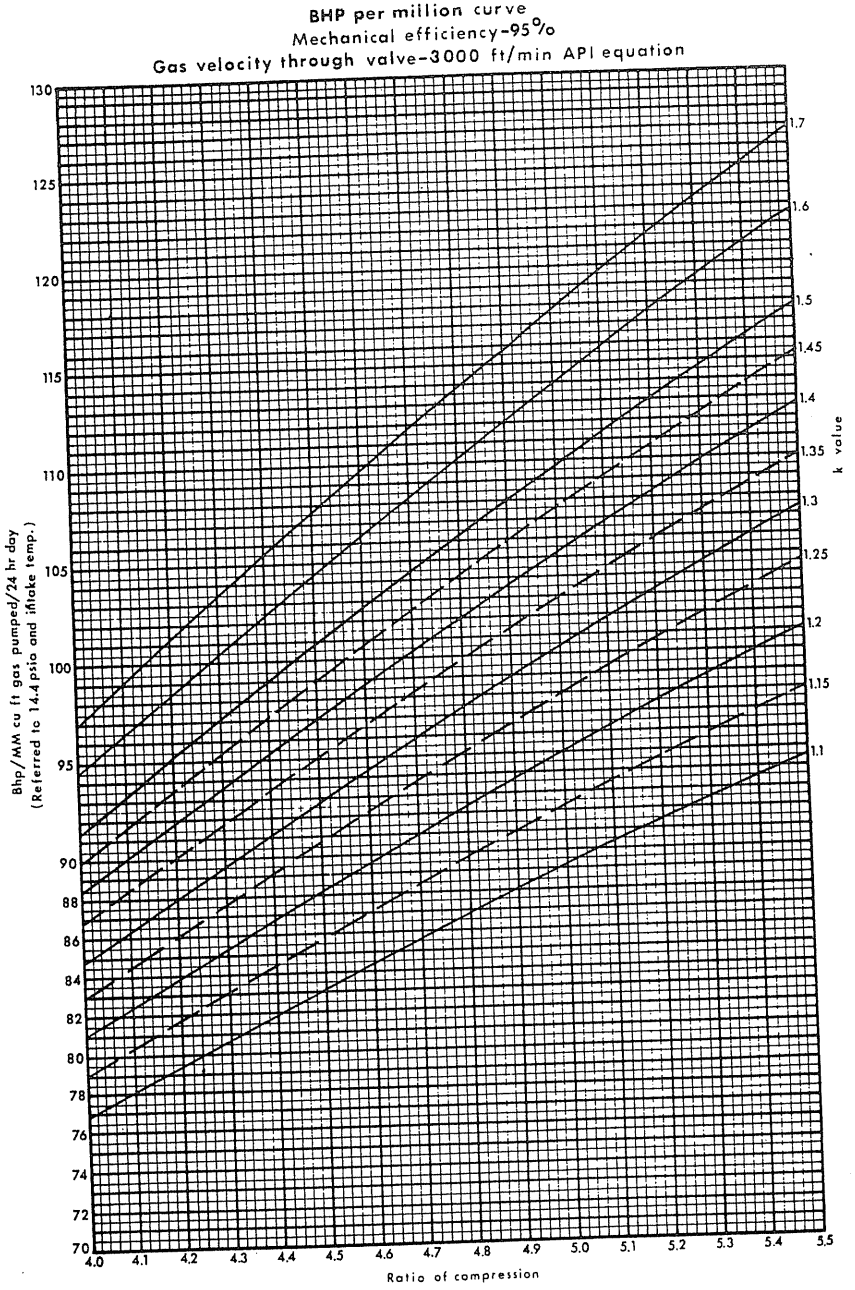

FIGURE 6-24
Power requirements for compressor with mechanical efficiency 95 percent and gas velocity through valve 3000 ft/min (API equation), for $4 < CR < 5.5$ [1-28, courtesy GPA].

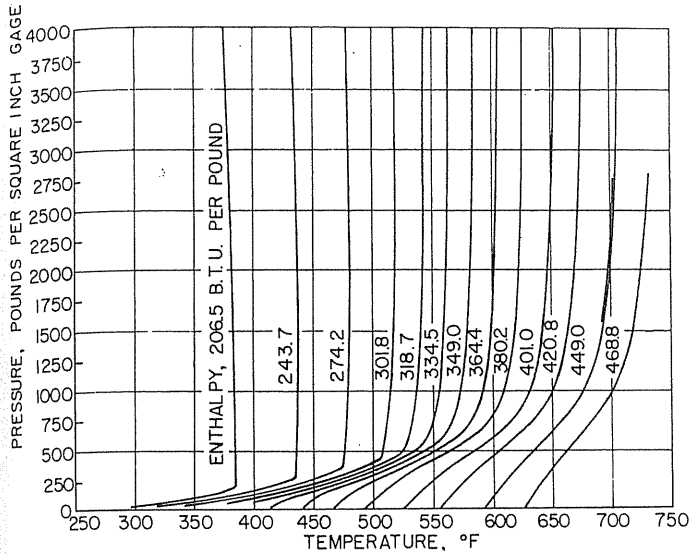

FIGURE 6-25
Temperature change with expansion of gasoline-kerosene mixture based on G. G. Brown unpublished data [Katz, 6-32, courtesy *Oil and Gas J.*].

to maintain the current temperature and so the fluid subcools (Joule-Thomson effect).

Since plots or tables of data showing the effect of pressure on entropy are not generally available, pressure-temperature charts with lines of constant h may be helpful, as may pressure-enthalpy plots with lines of constant temperature. Figure 6-25 shows the effect of pressure on gasoline-kerosene mixtures, and Fig. 6-26 a pressure-enthalpy plot for a methane-propane mixture. A generalized Joule-Thomson inversion chart shows the change from frictional heating to frictional cooling of fluids, as in Fig. 6-27. The transition from heating to cooling is generally in the dense phase region at 0.84 to 0.9 reduced temperature. Figure 6-28 shows the transition region on a pressure-temperature diagram for hydrocarbon fluids.

6.8 TWO-PHASE FLOW IN PIPES AND WELLS

Pressure drop calculations for multiphase flow are more complex than single phase because of the unsteady state nature of the flowing mechanisms. The goal of two-phase research is to find a method to calculate the pressure drop profile along a pipe or a well if the pressure and flow rate of each phase are known at the exit or entrance. Most wells have small amounts of liquid (condensate) present. The usual remedy is to approximate the gas gravity by the following equation [1-1]:

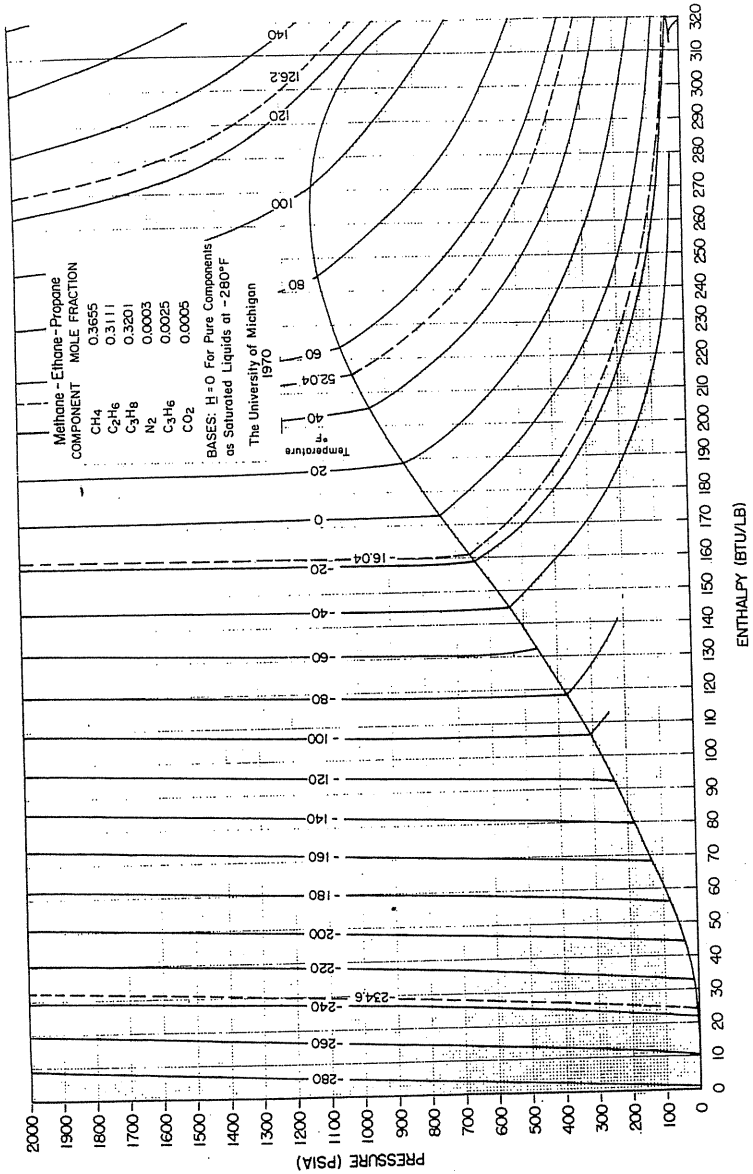

FIGURE 6-26
Pressure-enthalpy plot for a mixture, mainly methane-propane [University of Michigan, 6-32, courtesy *Oil and Gas J.*].

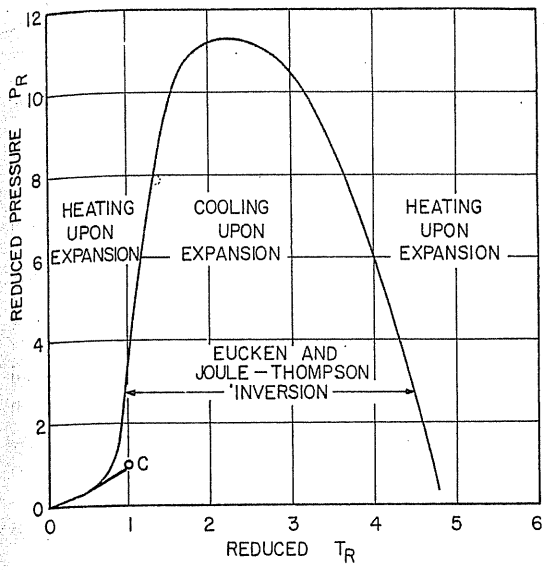

FIGURE 6-27
Generalized Joule-Thomson inversion curve [Katz, 6-32, courtesy *Oil and Gas J.*].

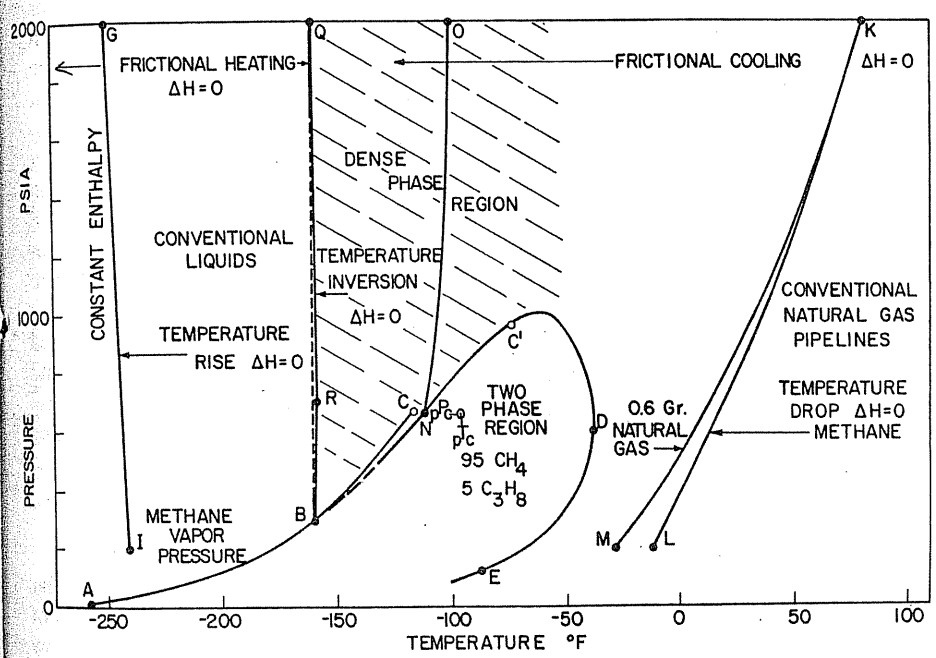

FIGURE 6-28
Pressure-temperature diagram for hydrocarbon fluids showing frictional heating or cooling [Katz, 6-32, courtesy *Oil and Gas J.*].

$$G = \frac{G_g + 4591(\rho/R)}{1 + (1123/R)} \tag{6.34}$$

where G is the well fluid gravity, G_g is the separator gas gravity, ρ is the specific gravity of condensate in g/cm^3, and R is the gas-liquid ratio in ft^3/bbl.

In this section, liquid-gas flow in vertical or inclined wells and the route selection (only for low liquid rates) in natural gas pipelines are discussed. For gas wells carrying water or gas condensate, a method of calculation is described based on work of Ros [6-50] and Gould et al. [6-25].

Poettmann and Carpenter [6-44] presented a friction factor–Reynolds number correlation for well flow at substantial flow rates, high pressure, and low gas-liquid ratios. This friction factor was not appropriate for wells of different flow regimes, especially for low pressure–low production and viscous crude oil wells. Fancher and Brown [6-22] extended Poettmann and Carpenter's correlation to cover the lower-density ranges. Gaither et al. [6-23] and Hagedorn and Brown [6-28] published data for small pipe sizes (1 and $1\frac{1}{4}$ in.). The research mentioned above has not considered changes of flow pattern within a single system. As a result, discrepancies will be found when this research is applied to those cases where the flow regimes change from bottom to top of the well.

Duns and Ros [6-17] measured the liquid slippage and pressure gradients. Several dimensionless groups were recognized to be the key parameters for predicting flow regimes, and different correlations formulas were suggested in various regimes. Orkiszewski [6-43] tested the field data, concluded that the Duns and Ros method works well for mist flow, and presented his formula of correlations. Later, his slug flow correlation was modified by Chierici et al. [6-12]. For bubble and slug flow regimes, improved correlations were proposed by Aziz, Govier, and Fogarasi [6-3]. Beggs and Brill [6-5] collected new data and presented correlations for inclined flow (for any angle, including vertical and horizontal). All the proposed methods were evaluated by Lawson and Brill [6-35], Vohra [6-56], and Browne [6-11]. Recently, various new methods [6-4] were tested against field data by Baker et al.

The group at University of Tulsa, Brown, Beggs, and Brill, have compiled volumes of data on flowing and artificial lift well performance [6-7]. Govier and Aziz in Alberta organized their studies and procedures for handling two-phase flow problems in a book [6-26]. Many important publications and papers related to horizontal flow are referred to in the books mentioned here.

Need to Know Flow Regime at Each Increment

In problems of two-phase flow, the flow regime usually relates to the particular geometric distribution of phases as the two fluids share the cross-sectional area of the pipe. In natural gas pipeline operation, two flow regimes, (1) wave mist flow and (2) annular mist flow, are often found in nearly horizontal or inclined pipline systems with relatively low volume percent liquids. For a high-volume liquid two-phase flow, there are two regimes, (1) bubble flow and (2) slug flow [1-1], which are not of interest in gas operation. The flow regimes for horizontal pipe are sketched in Fig. 6-29.

For vertical columns, (1) slug flow and (2) annular mist flow are commonly encountered in gas operation. As vapor flow rate increases, the flow will start as slug flow and go to annular mist flow (see Fig. 6-30). Again, the bubble flow represents oil well behavior not covered here.

In the wave-mist regime, particularly in horizontal flow (Fig. 6-29), the liquid-gas interface becomes wavy due to the perturbation of the passing gas phase. Some of the waves become unstable and break in white caps, and tiny droplets form. The liquid drops become intermingled in the overflowing gas. The upper part of the pipe wall becomes wetted as well as the lower part.

The annular mist regime shown in Figs. 6-29 and 6-30 is where an annular liquid film wets the entire wall and flows slowly, surrounding the gas stream. The mist is in the form of tiny droplets distributed throughout the cross section of the pipe. Some droplets coalesce on the wall, but the population of the droplets is maintained by reforming of droplets from the waves along the wall.

Different flow regimes represent different flow mechanisms. As a result, it is clear that to predict pressure drop one needs to know the flow regime. Ros

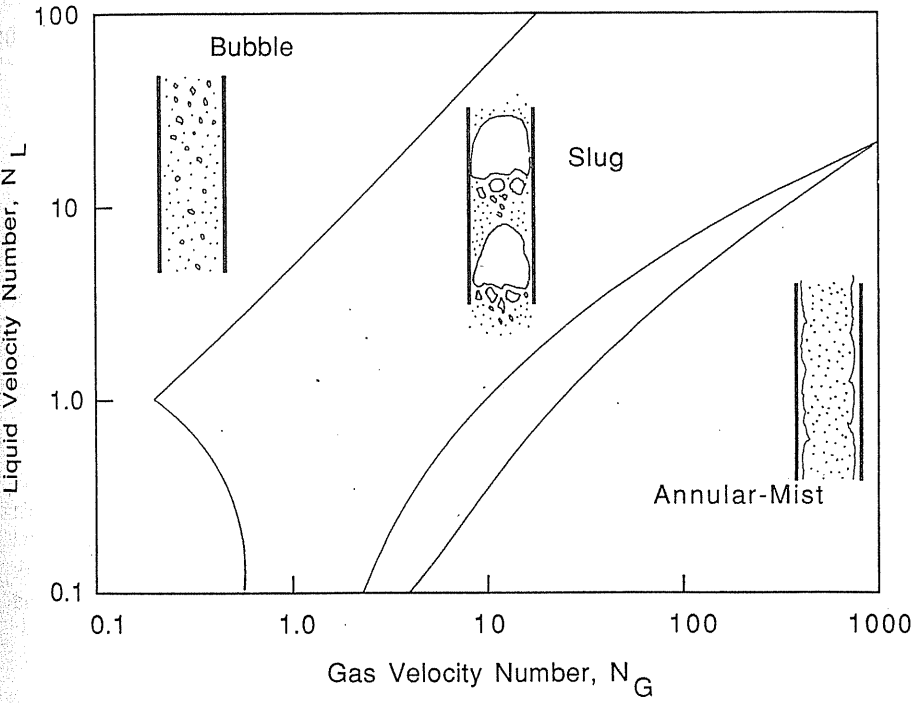

FIGURE 6-29
Flow regimes of horizontal two-phase flow.

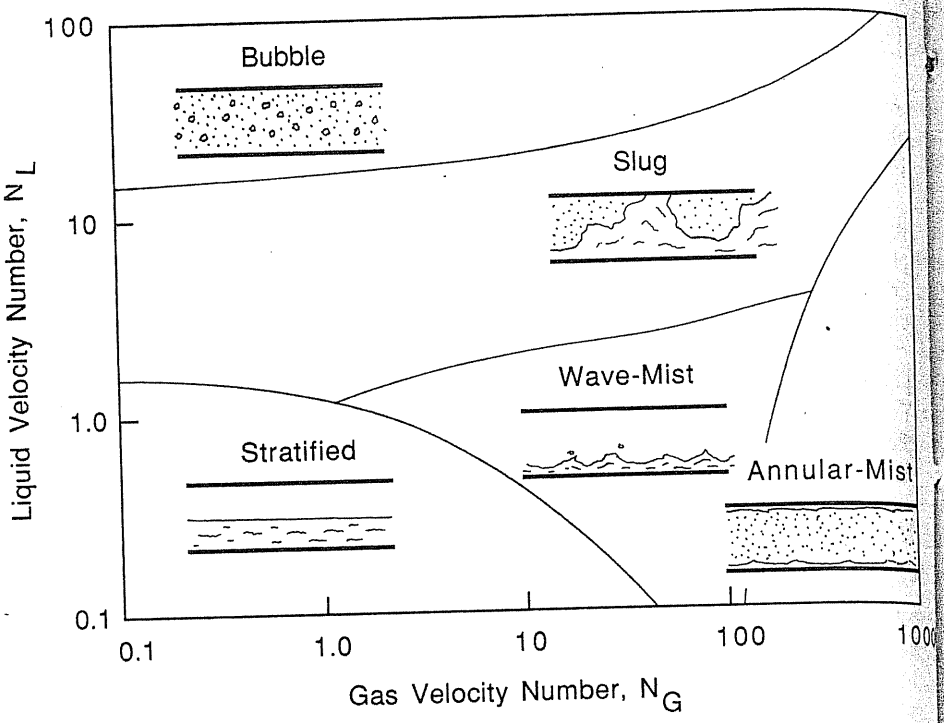

FIGURE 6-30
Flow regimes of vertical two-phase flow.

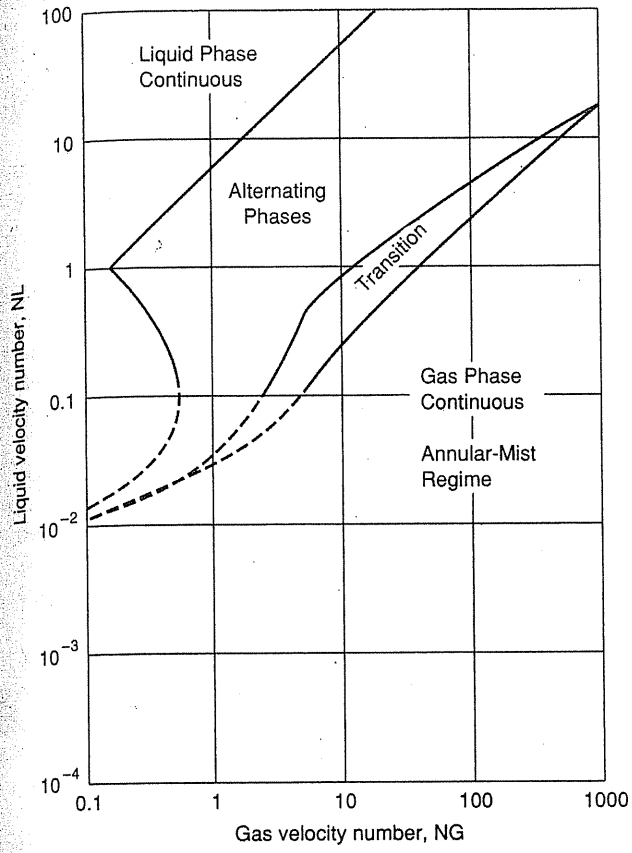

FIGURE 6-31
Flow regime map for vertical two-phase flow [Bergman et al., 1-35, courtesy AGA].

[6-50] presented a study in which flow mechanisms were identified for various conditions. From this study, dimensionless numbers were developed to predict the flow regime. Gould's study [6-25] built upon accumulated experiences; it utilized Ros's dimensionless liquid velocity number and gas velocity number, and their identification of regimes for which different pressure drop correlations are needed. Figure 6-31 is after Ros's chart for vertical flow, which was derived from his measurements.

With a procedure available to predict the flow regime, methods of predicting the pressure drop for specific flow regimes give the desired answers. With knowledge of P, T, flow rate, and gas-to-liquid ratio at the wellhead, one can calculate the pressure drop in increments of depth as the stream approaches the wellhead. Selecting depth increments like 100 feet (30.48 m), one may work down the well to the bottom, evaluating the flow regime, pressure drop, and hence the flowing pressure at each increment.

Flow Equations for Two-Phase Pipe Flow

A thermodynamic fluid energy balance written in differential form between point 1 and point 2 in Fig. 6-32 is

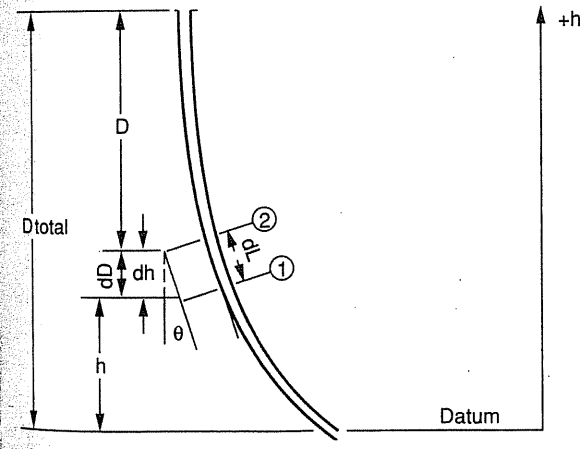

FIGURE 6-32
Well geometry for generalized pressure drop model [Gould et al., 6-25, courtesy SPE-AIME].

$$\int \bar{v}\,dP + d\left(\frac{v^2}{2g_c}\right) + d\left(\frac{gX}{g_c}\right) = -l_w \tag{3.7b}$$

The lost work term in this equation, l_w, is usually written for pipe flow in terms of a friction factor, as in Eq. (6.8). However, in gas-water two-phase flow, the lost work may include terms for wall friction, slippage, frictional effect between phases, viscosity effects, surface tension effects, etc. [1-5].

Slippage occurs in cases of flow in which the gas phase is predominant as the gas will tend to leave liquid behind. Slippage is defined as the net percent of the liquid in the flowing column that does not accompany the gas at its average velocity. Efficiency is the percent of the particles present in a section of pipe that leave with gas. Slipping particles may go up and down or stay stationary, but the net effect is to increase the density of the column of fluid.

The interface phenomena (forces between the two fluids) have not been fully understood, and the flow patterns are different for various gas/liquid properties and velocities. As a result, numerous correlation equations have been developed according to experimental results. References [1-5] and [6-27] are good reviews of those equations and their applicable ranges. Fortran codes for various flow conditions are listed in references [6-7], and [6-46].

The pressure drop gradient along the wellbore can be separated into three categories: (1) holdup, (2) friction, and (3) acceleration:

$$\frac{dP}{dZ}(\text{total}) = \frac{dP}{dZ}(\text{holdup}) + \frac{dP}{dZ}(\text{friction}) + \frac{dP}{dZ}(\text{acceleration})$$

$$= \frac{g}{g_c}\rho_m \cos\theta + \frac{f_m \rho_m v_m^2}{2g_c D} + \frac{\rho_m v_m}{g_c}\frac{dv_m}{dZ} \tag{6.35}$$

where the subscript m denotes the mixture, θ is the angle of inclined pipe, as in Fig. 6-32, and

$$\rho_m = (H_L)\rho_l + (1 - H_L)\rho_g \tag{6.36}$$

H_L is refered to as *holdup*; this is the volume fraction occupied by liquid, and $1 - H_L$ is the volume fraction of gas. H_L depends on the slippage. The mixture friction factor f_m is a function of the two-phase Reynolds number, which involves the diameter of pipe, d, the roughness of pipe, e/d, the mass flow rate of the mixture, and the viscosities of both gas and liquid. Friction correlation charts similar to the Moody chart (Fig. 6-3) for a two-phase flow were proposed by various investigators; a summary can be found in reference [6-7]. More detailed explorations of two-phase flow should always go to the original papers by various authors.

Prediction of the Flow Regime

Vertical two-phase flow rarely is encountered in gas operation; however, it is frequently of interest in wells, pipelines leaving river crossings, and gathering systems offshore.

Figures 6-31 and 6-33 [1-35] show the flow regimes for vertical and horizontal two-phase flow. The two dimensionless groups, *liquid velocity number* N_L and *gas velocity number* N_G, were first developed by Ros [6-50] to represent the relevant physical parameters, i.e., temperature, pressure, rates, and pipe geometry. These dimensionless groups are calculated as follows:

$$N_L = V_{SL}\left(\frac{\rho_l}{g_c g \sigma}\right)^{(1/4)} \tag{6.37a}$$

$$N_G = V_{SG}\left(\frac{\rho_l}{g_c g \sigma}\right)^{(1/4)} \tag{6.37b}$$

where V_{SG} and V_{SL} are the superficial gas and liquid velocities (ft/s, m/s), ρ_l is the liquid density (lb_m/ft^3, kg/m^3), g is the acceleration of gravity (32.17 ft/s^2, 9.8 m/s^2), g_c is a conversion factor (32.17 $lb_m \cdot ft/lb_f \cdot s^2$, 1), and σ is the surface tension (lb_f/ft, dyn/cm). For low gas velocity number N_G, one should include a region of stratified flow. However, in actual pipelines operating under normal conditions, one may not encounter purely stratified flow. To relate gallons of liquid to MMcf of gas-liquid mixture flowing, lines of constant liquid content have been added to Fig. 6-33 based on 0.6-gravity gas flowing at 770 psia (5.31 MPa) and 40°F (4.4°C).

Beside N_L and N_G, Ros [6-50] defined the dimensionless diameter number N_d, from which the holdup H_L is determined:

$$N_d = d\left(\frac{\rho_l g}{g_c \sigma}\right)^{1/2} \tag{6.38a}$$

$$H_L = \frac{20}{N_d^2} \tag{6.38b}$$

Equations (6.38) are only valid when liquid flow rate is low ($N_G > 50 + 36N_L$).

Stepwise Iterative Approach: Gould-Tek-Katz Model

In spite of the overwhelming amount of literature on the subject, there exists no perfectly general model capable of representing vertical, horizontal, and inclined flow. However, there are a number of reliable analytical relations or empirical correlations, usually limited to particular flow regimes or certain ranges of geometry, pressure level, and physical properties. Gould [6-24] developed a stepwise iterative finite difference algorithm to calculate length or depth increments corresponding to selected values of pressure drop ΔP, provided that the holdup and friction gradients can be evaluated at the pressure, temperature, and flow conditions in the increment.

In a gas operation, the gas flow rate Q_G is usually much greater than the liquid flow rate Q_L. Then,

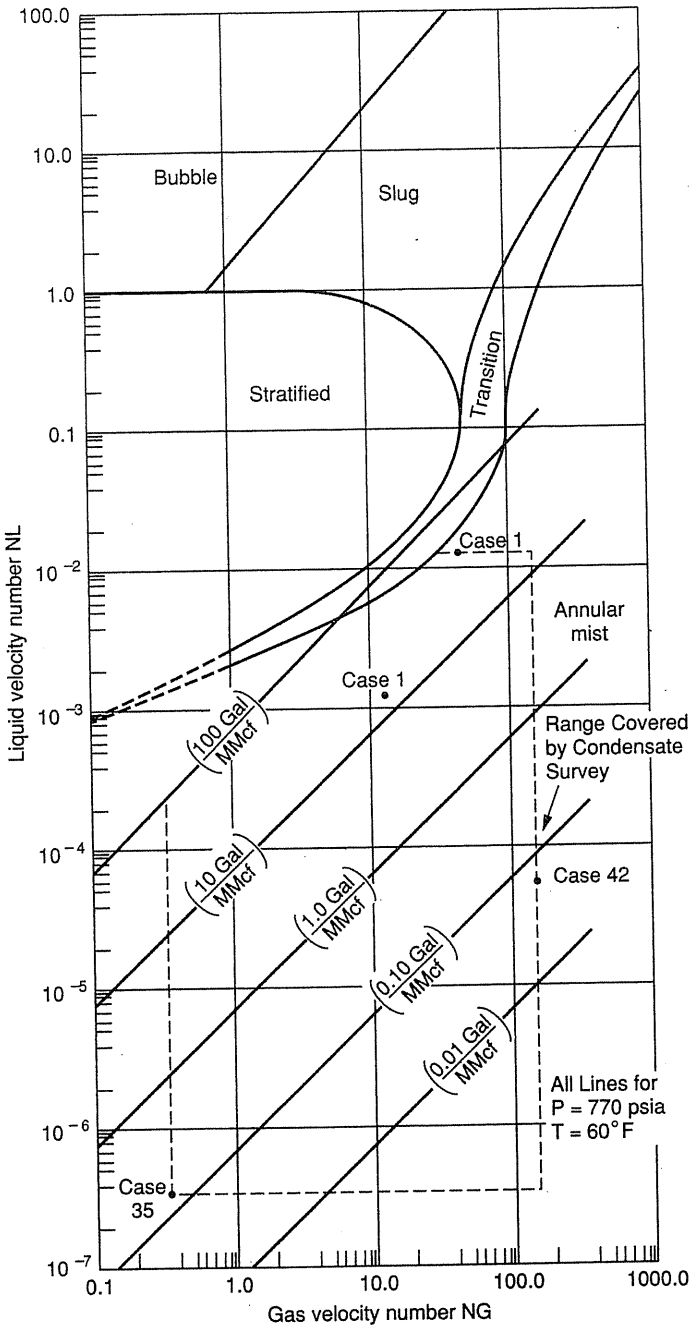

FIGURE 6-33
Flow regime map for horizontal two-phase flow showing range covered by condensate survey [Bergman et al., 1-35, courtesy AGA].

$$\frac{dv_m}{dL} = \frac{d[(Q_G + Q_L)/A]}{dL} \approx \frac{1}{A}\frac{dQ_G}{dL} \tag{6.39}$$

By applying the gas law $PQ_G = ZnRT$,

$$\frac{dQ_G}{dL} = -\frac{Q_G}{P}\frac{dP}{dL} \tag{6.40}$$

Combining Eqs. (6.39) and (6.40), the acceleration gradient of Eq. (6.35) becomes

$$\left(\frac{dP}{dL}\right)_{\text{acceleration}} = \frac{\rho_m v_m}{g_c}\frac{dv_m}{dL} = -\frac{\rho_m}{g_c}\frac{Q_L + Q_G}{A}\frac{Q_G}{AP}\frac{dP}{dL} = -\frac{W_T Q_G}{g_c A^2 P}\left(\frac{dP}{dL}\right)_{\text{total}} \tag{6.41}$$

where P is the average pressure in the section $dL = dh\cos\theta$ of Fig. 6-32 and total mass flow rate is defined as

$$W_T = \rho_m(Q_G + Q_L) \tag{6.42}$$

As a result, the total pressure gradient on the section dL in Fig. 6-32 is

$$-\frac{dP}{dh} \approx -\frac{\Delta P}{\Delta h} = \frac{\rho_m g/g_c + f_m \rho_m v_m^2/2g_c \Delta L\cos\theta}{1 + W_T Q_G/g_c A^2 P} \tag{6.43}$$

The Gould-Tek-Katz approach using the interative finite difference calculation of Eq. (6.43) permits the evaluation of the flow regime in the next segment. Once the flow regime is known, the best correlations available for ρ_m and f_m can then be used. This procedure allows for the presence of several different flow regimes at various depths in the same pipe. The computer simulation codes can be found in reference [6-24]. Figure 6-34 [6-25] shows the flow regimes affected by various angles of inclination, as generated by the simulation.

Studies of two-phase flow show that as the flow rate decreases on a two-phase stream in vertical flow, liquid accumulates in the wellbore. For those desiring a quick order-of-magnitude estimate of the ability of gas to carry water in wells, the work of Dugan is submitted. A rough approximation is that water is carried overhead at a flow velocity of 5 feet per second (1.52 m/s), and accumulates at lower rates. Dugan presented a graph, Fig. 6-35, that shows the flow rate required to keep water from accumulating in a wellbore.

Example 6.7 [1-35]. Determine the flow regime for a two-phase horizontal pipe flow with diameter $d = 0.67$ ft at 133 psia and 60°F. The data are as follows:

Q_G, gas flow rate = 1.5 MMcf/day
Q_L, liquid rate = 120 gal/day, (80 gal/MMcf)
ρ_l, liquid density = 0.7 g/m^3 (43.7 lb/ft^3)
ρ_g, gas density = 0.694 lb/ft^3
σ, surface tension = 12.5 dyn/cm (856×10^{-6} lb/ft)

What are the acceleration and holdup gradients if the pipe inclination angle is 20°?

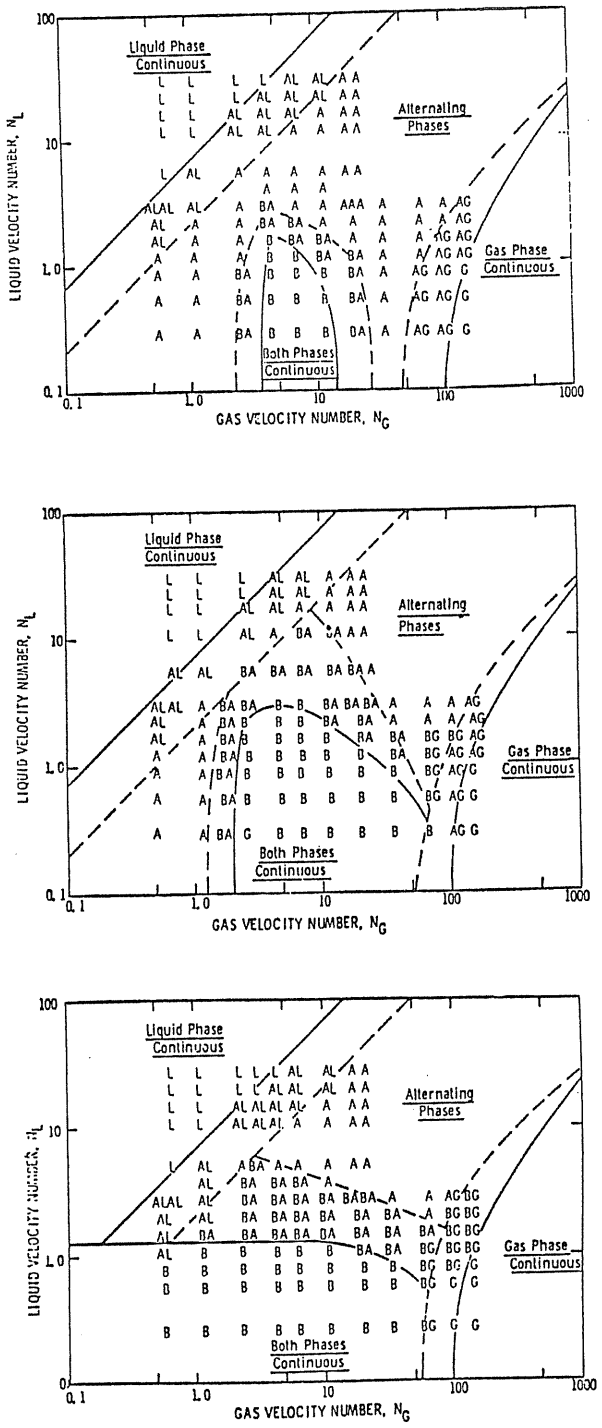

FIGURE 6-34
Flow regime for various inclination angles: (*a*) 0° (vertical), (*b*) 45°, and (*c*) 90° (horizontal) [Gould et al., 6-25, courtesy SPE-AIME].

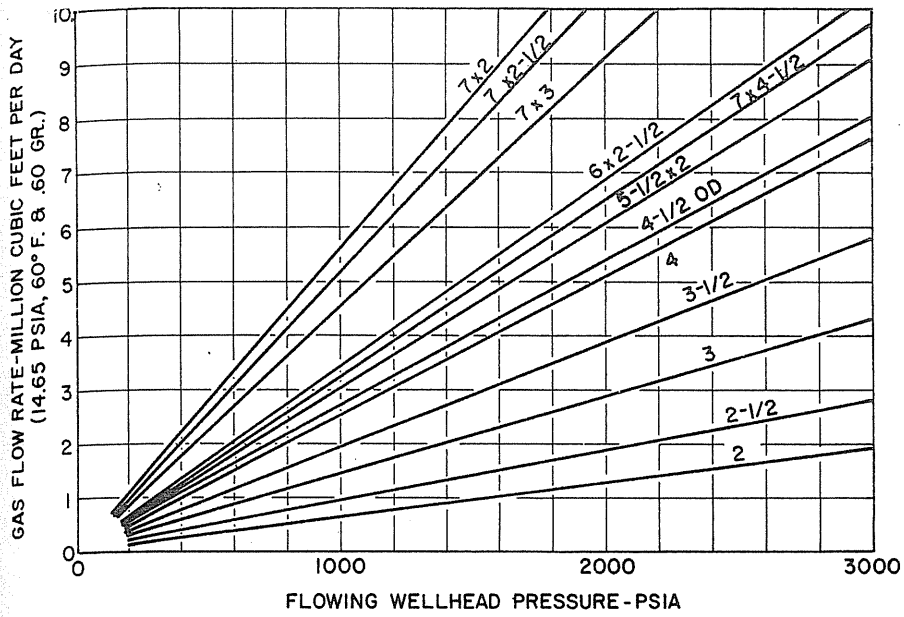

FIGURE 6-35
Minimum flow rate required to keep gas wells unloaded from water [after Dugan; Katz & Coats, 1-2].

Solution. Calculate the gas velocity number, N_G:

$$V_{SG} = \frac{Q_G}{\text{area}} = \frac{Q_G}{\pi d^2/4} = \frac{1.5 \times 10^6 \times 14.7 \times 520 \times 4}{24 \times 3600 \times 133 \times 520 \times 3.14 \times 0.67^2} = 5.44 \text{ ft/s}$$

$$N_G = V_{SG}\left(\frac{\rho_l}{g_c g \sigma}\right)^{1/4} = 5.44 \times \left(\frac{43.7}{32.17 \times 32.17 \times 856 \times 10^{-6}}\right)^{1/4}$$

$$= 5.44 \times 2.64 = 14.37$$

Calculate the liquid velocity number N_L:

$$V_{SL} = \frac{Q_L}{\text{area}} = \frac{Q_L}{\pi d^2/4} = \frac{120 \times 4}{7.48 \times 24 \times 3600 \times 3.14 \times 0.67^2} = 5.3 \times 10^{-4} \text{ ft/s}$$

$$N_L = V_{SL}\left(\frac{\rho_l}{g_c g \sigma}\right)^{1/4} = 5.3 \times 10^{-4} \times 2.64 = 1.4 \times 10^{-3}$$

The two-phase flow, plotted as Case 3 on Fig. 6-33, is in the annular mist regime. Calculate the diameter number N_d, liquid holdup H_L, and average density ρ_m:

$$N_d = d\left(\frac{\rho_l g}{g_c \sigma}\right)^{1/2} = 0.67\left(\frac{43.7 \times 32.17}{32.17 \times 856 \times 10^{-6}}\right)^{1/2} = 225.95$$

$$H_L = \frac{20}{N_d^2} = \frac{20}{(225.95)^2} = 3.91 \times 10^{-4}$$

$$\rho_m = \rho_l H_L + \rho_g(1 - H_L) = (43.7)(3.91 \times 10^{-4}) + (0.694)(1 - 3.91 \times 10^{-4})$$
$$= 0.71 \text{ lb}_m/\text{ft}^3$$

Calculate the holdup gradient:

$$\left(\frac{dP}{dL}\right)_{\text{holdup}} = \frac{\rho_m g \cos\theta}{g_c} = \frac{(0.71)(32.17)(\cos 20^\circ)}{32.17} = 0.667 \text{ (lb}_f/\text{ft}^2)/\text{ft}$$

Calculate the gas flow rate Q_G, liquid flow rate Q_L, and total mass flow rate W_T:

$$Q_G = V_{SG} \cdot A = (5.44)\left(\frac{\pi 0.67^2}{4}\right) = 1.91 \text{ ft}^3/\text{s}$$

$$Q_L = V_{SL} \cdot A = (5.3 \times 10^{-4})\left(\frac{\pi 0.67^2}{4}\right) = 1.87 \times 10^{-4} \text{ ft}^3/\text{s}$$

$$W_T = \rho_m(Q_G + Q_L) = (0.71)(1.91 + 1.87 \times 10^{-4}) = 1.356 \text{ lb}_m/\text{s}$$

Calculate the acceleration gradient $(dP/dL)_{\text{acceleration}}$:

$$\left(\frac{dP}{dL}\right)_{\text{acceleration}} = \frac{W_T Q_G}{g_c A^2 P}\left(\frac{dP}{dL}\right)_{\text{total}} = \frac{(1.356)(1.91)}{(32.17)(\pi 0.67^2/4)^2(133)(144)}\left(\frac{dP}{dL}\right)_{\text{total}}$$

$$= 3.38 \times 10^{-5}\left(\frac{dP}{dL}\right)_{\text{total}}$$

The acceleration gradient is usually small relative to the holdup gradient.

An experiment conducted in 1935 for an oil/gas well flowing in Oklahoma City as the Wilcox sand was in delayed development. The original calculation used the viscosity of the continuous phase (gas) and the density of the total flowing system (gas + oil) to predict the friction and gravitational pressure drop components. Generally, satisfactory results were found.

Route Selectivity by Liquid in Gas Pipelines

In the late 1960s, liquids within U.S. natural gas delivery systems occasionally caused interruption of gas delivery. European gas lines had experienced similar problems of liquid accumulation at control or pressure reduction facilities. A study of the problem was done at the University of Michigan, sponsored by the Michigan Gas Association and the Pipeline Research Committee of the AGA [1-35]. It was not a matter of measuring pressure drop in pipeline in two-phase flow but of determining why large accumulations of liquid occured on occasion. It was fortunate that the work of Oranje in the Netherlands was published in 1973 [6-42], followed by his visit to the United States. He showed that when small amounts of liquid, such as 5 gal/MMcf (6.68×10^{-7} m^3/m^3) and higher, accompanied gas

flow, the liquid may or may not follow side streams of gas taken from the main stream at tees.

This behavior observed by Oranje is described here, including one example that was set forth in the monograph on retrograde condensation in natural gas pipelines [1-35]. It was verified that retrograde condensation did occur below 500 psia (3.45 MPa) in pipeline gases and was a partial cause for the low concentrations of liquid accompanying natural gas. However, the route selection phenomenon is believed to be the main mechanism by which large liquid volumes (1000s of gallons, or several m^3) accumulate and shut down control systems and/or prevent gas delivery.

In Oranje's work, a gas stream with accompanying liquids was circulated in a central system that contained branches through tees. Various amounts of the circulating stream were removed through the branches, and data on flow rates of gas and liquid were recorded. Figure 6-36 is one of several graphs presented in the paper. Oranje states in his conclusions:

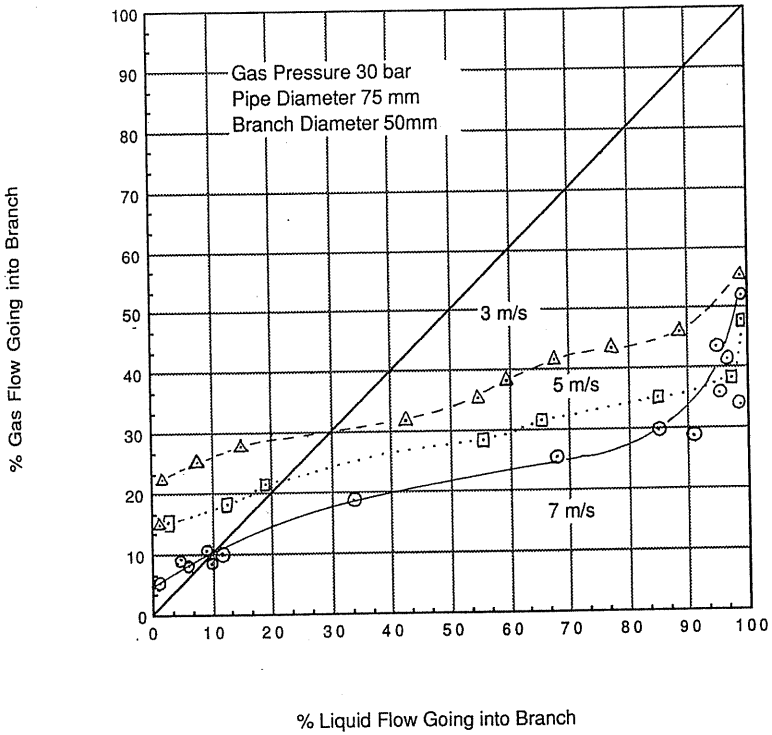

FIGURE 6-36
Part of liquid flowing into branch related to gas velocity upstream [Oranje, 6-42, courtesy *Oil and Gas J.*].

On the basis of Fig. 6-36, it is possible to formulate this rule of thumb for the route of condensate through a regional grid system:

(1) In case less than 20% of the gas stream enters into a branch line, the liquid condensate will follow the straight line and not enter into the branch line.

(2) In case more than 35% of the gas stream enters into a branch line, all of the liquid condensate will enter into the branch.

The applicability of this rule of thumb is tied closely, of course, to the circumstances under which the statistical investigation has been carried out: (a) for gas velocities up to 7 m/sec, (b) for gas pressure between 23 and 39 bar, (c) for pipe diameters of 6 to 12 inch, and (d) for branches in the pipeline with reduced tees.

When the stream flowing through a main pipe is split into two streams by a tee, with one branch continuing forward and the other going off to one side, the part taken off into the lateral may be viewed as a curved stream near the branch connection. This is illustrated in Fig. 6-37*a*. If one is willing to accept the geometry that logically extends the lateral into a curved stream, then one must understand the mechanics of two-phase flow that would describe the events near the tee. It is well known that when a fluid flows in a curved pipe a *secondary flow* occurs [6-11,6-56].

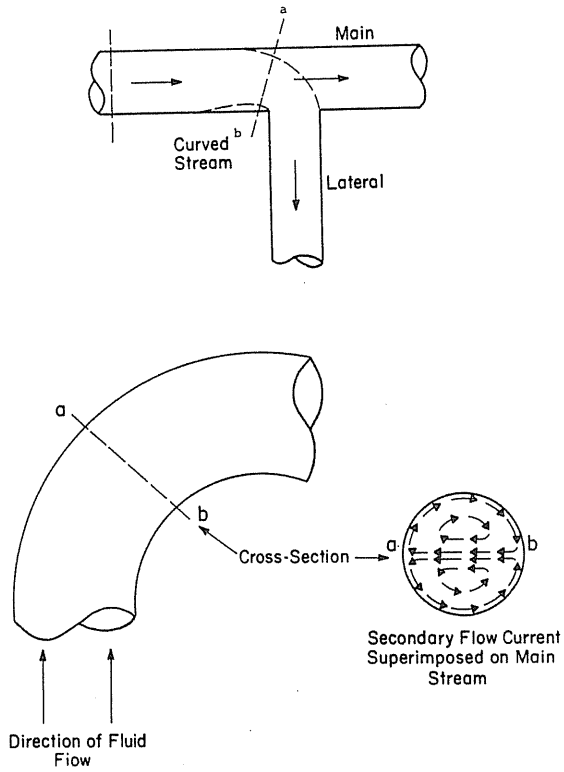

FIGURE 6-37
(*a*) Curved stream representation of a lateral branch, (*b*) secondary flow in a pipe [Bergman et al., 1-35, courtesy AGA].

Without getting into highly theoretical considerations of complex fluid mechanics, it should suffice to observe that along the direction of the radius of curvature, a pressure gradient is set up when the fluid flows along the curved path. This outward pressure distribution causes the fluid to acquire a circulation pattern superimposed on the main flow pattern as shown in Fig. 6-37*b*.

The effect of lateral branch orientation with stratified flow is illustrated in Fig. 6-38 [1-35]. For instance, if the main pipe is carrying stratified flow and if the lateral is vertically downward, gravity will obviously cause the lateral to trap all the segregated liquid approaching the tee, as in Fig. 6-38*a*. The opposite situation is shown in Fig. 6-38*b* where the lateral is assumed to have an inclined upward

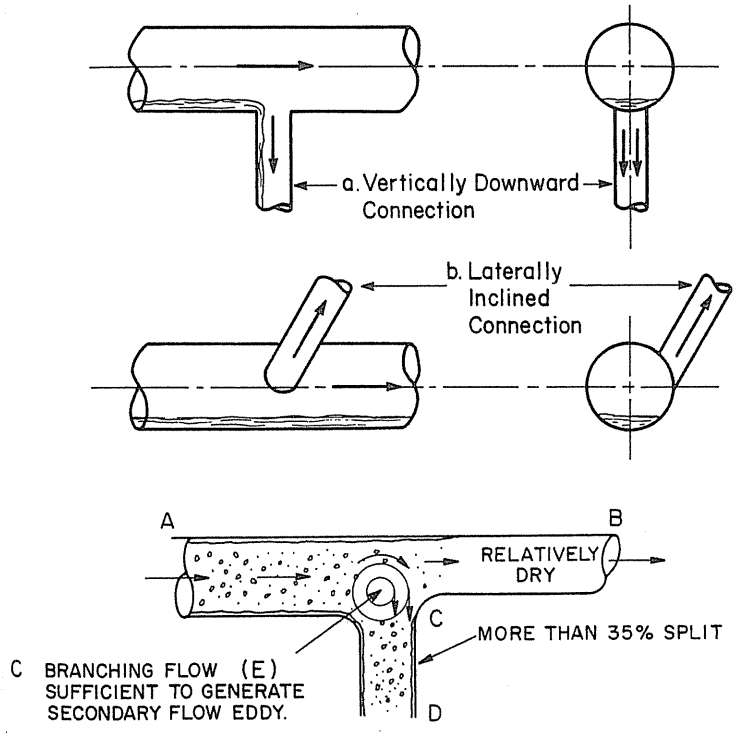

FIGURE 6-38
Lateral branch orientations: (*a*) vertical-downward connection, (*b*) laterally inclined connection, and (*c*) vertical tee for annular mist flow [Bergman et al., 1-35, courtesy AGA].

orientation. In this case, if the approach stream is stratified, it is easy to see how, regardless of how much the lateral takes off, the gravity segregated liquid would remain at the bottom. By contrast, if the the main flow in the foregoing two examples were annular mist, then one would expect some of the liquid to divert along with the gas to the connecting branch. Figure 6-38*c* (in the horizontal plane) depicts flow in the annular mist regime.

On February 4–7, 1975, some 2800 gallons (10.6 m^3) of condensate were removed from a pipeline at the Chalmers Station of Michigan Consolidated Gas Company. Figure 6-39 shows flow rates, pipe sizes, pressures, mileage, etc. for this system. It is highly probable that the liquid collected at Chalmers Station at the valve on the bypass line (Fig. 6-40) after having flowed along with the gas from Lynch Station. The expected yield from retrograde and temperature condensation is some factor like 100 times lower than the yield of 319 gallons per MMcf (4.26×10^{-5} m^3/m^3) found in the side stream to the Chalmers Station. It was reasoned that the condensate came from the Belle River Mills storage field gas, which had a liquid content like 3–5 gallons/MMcf ($4.01–6.68 \times 10^{-7}$ m^3/m^3) as a result of the cooling and the pressure reduction when reaching Lynch station. This liquid would pass through Lynch regulator station into the network shown.

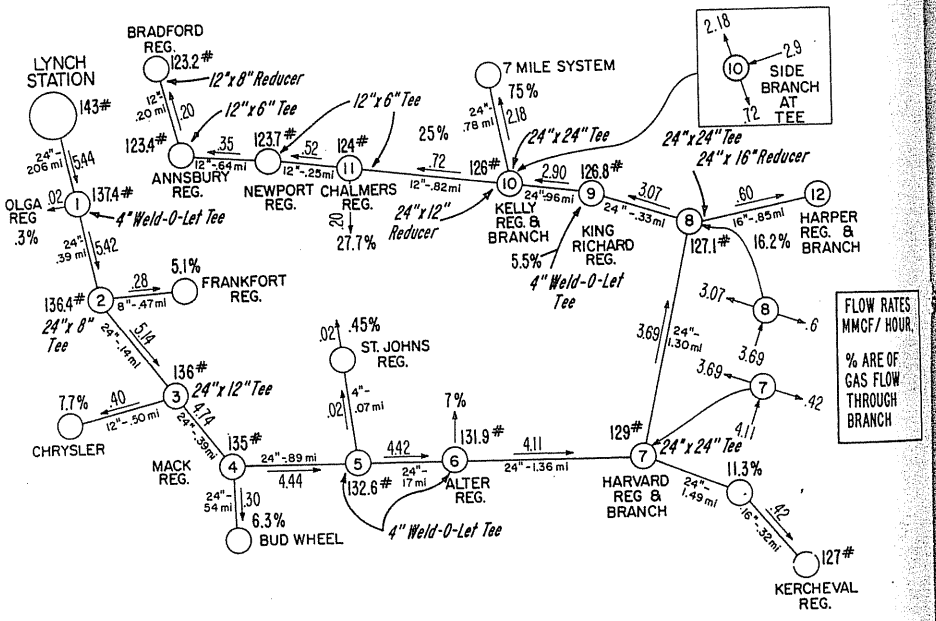

FIGURE 6-39
Representation of distribution from Lynch Station to Chalmers Station [Bergman, 1-35, courtesy Michigan Consolidated Gas Company].

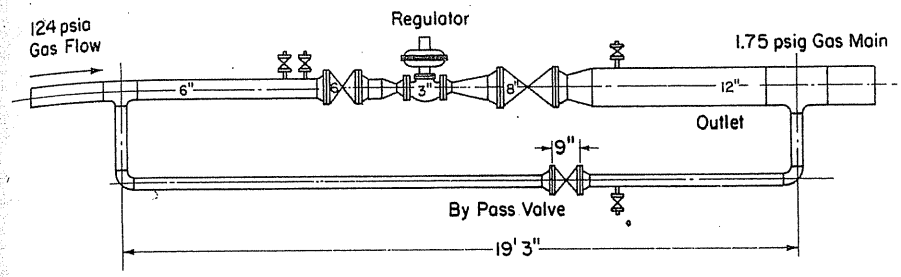

FIGURE 6-40
Drawing of Chalmers regulator with bypass from which condensate was removed [Bergman, 1-35, courtesy Michigan Consolidated Gas Company].

Analyzing the flows through each node of Fig. 6-39, one finds that all but nodes 7, 8, 10, and 11 had less than 10 percent side flow of gas and hence should have removed little if any of the liquid. At nodes 7, 8, and 10 the flow was as indicated in the insets. At these nodes the stream entered from the side branch of the tee and split into two diverging branches, and apparently the liquid followed the 84 percent and 89 percent parts of the gas at nodes 8 and 7. At node 10 the liquid followed the 25 percent part of the gas.

At node 11, there was a conventional tee, with a flow of 27.7 percent through the outlet to the regulator where the liquid accumulated. Thus, substantially all the liquid coming out of Lynch Station could have selected the route to Chalmers Station. The yield of liquid, 1534 gallons (5.81 m^3) per day, is 11.7 gallons per MMcf (9.385×10^{-7} m^3/m^3) on the basis of 5.44 MMcf (0.154×10^6 m^3) per hour leaving Lynch Station. The stream reaching Lynch Station may have already split off from some other stream and accumulated liquid in this split. It is quite easy to understand why certain stations receive liquid in unusual quantities while others receive little or none.

In other occurrences of liquid appearing at unexpected points late in a network, it was concluded that the system should have a liquid removal device (drip, V/L separator) after each pressure drop at control stations, in order to avoid liquid accumulation due to route selection later in the flow network.

Gas Lift

Gas lift is a method of artificially lifting liquid [6-10]. Gas engineers are involved in the design and operation of gas lift systems for recovering crude oil. Crude oils with low gas in solution and/or at low pressures need added gas in the flowing column to lift the oil at a desired rate against a given well pressure.

Many systems are available to allow the gas in the annulus between casing and tubing set on a packer to enter the tubing and lower the density of the flowing oil column, as shown in Fig. 6-41. The gas used for gas lift may strip some

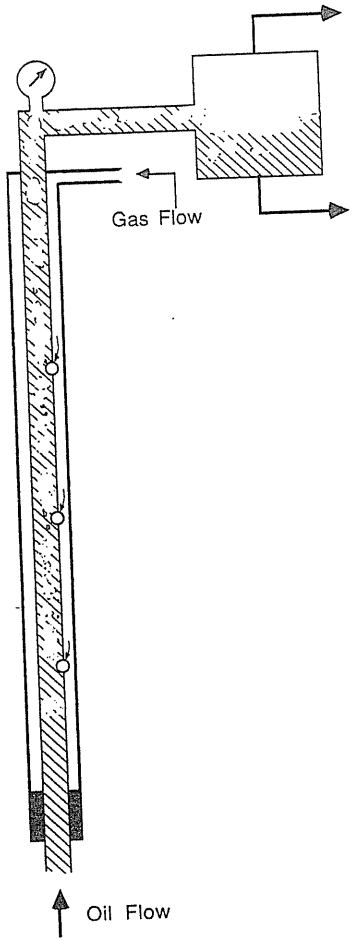

FIGURE 6-41
Elements of gas lift system.

volatile components from the oil in the separator, but it can be recompressed to return to the supply system. Use of the gas with the stripped volatile components can avoid the further stripping.

In gas lift, various two-phase regimes along the wellbore may be encountered. The proper treatments for specific cases will not be covered in this book. Material related to gas lift methods can be found in the book by Brown and Beggs [1-6] exclusively covering this particular subject, both theory and practice. In Brown and Begg's book, multiphase flow theory and various correlations are reviewed; also, gas lift equipment and design are discussed. The numerous figures in Brown and Begg's book illustrating pressure gradients along the wellbore with various flowing conditions (such as oil/water ratio, size of tubing, etc.) are very helpful for engineering use.

HOME PROBLEMS

6.1. A well is 8200 ft deep, the wellhead temperature is 68°F, and the bottom hole temperature is 182°F for a $G = 0.6$ gas. The pressure in the well and bottom hole pressure are 2350 psia and 3300 psia measured at 7700 ft. and 8200 ft. respectively. Is there any water in the column, and at what depth is the gas-liquid interface?

6.2. During a close-in pressure period for the Mt. Simon reservoir (Fig. 6-5), a group of wells showed a wellhead pressure of 950 psig, except for one well in the group that showed 835 psig. How much water was standing in the well?

6.3. An aquifer reservoir is in operation with a production well and an observation well as shown on Fig. 6-42. The water level in the production well was stabilized at 74 ft from the surface prior to gas injection, and the water in the observation well was at 57 ft. After gas injection, with the reservoir closed in, the production well has a wellhead pressure of 1185 psig, and the observation level is at 58 ft.

(*a*) What is the pressure drop across the gas-water interface (threshold pressure) in the bottom of the caprock? Use Fig. 6-5 for gas well pressure gradient. The waters from both zones were under 6000 ppm total solids.

(*b*) How would you characterize the degree of overpressure?

6.4. During development of the Oklahoma Wilcox oil field, in-city drilling was not permitted. When the material balance on the reservoir indicated that there were one billion barrels of oil initially compared with 700 million barrels based on geologic information, the city was opened to drilling. A town lot well, the Freeburg lease, was flow tested on Sept. 4, 1935, with accompanying pressure and temperature measurements. Two tests were made with flow through $9\frac{5}{8}$-in. (9.384 in. ID) API casing set at 6285 ft:

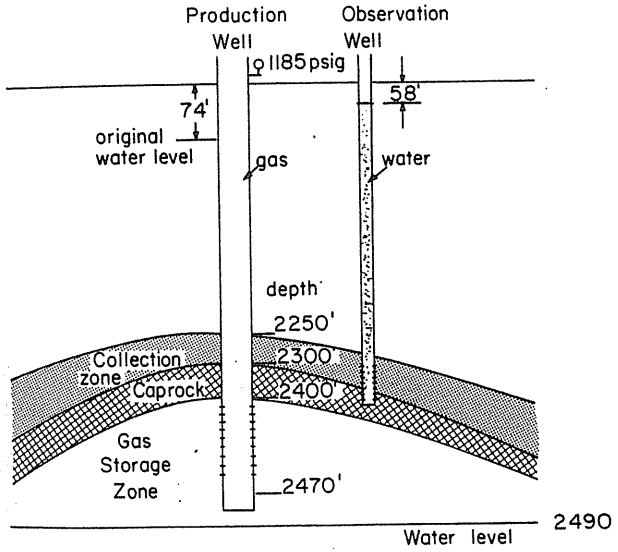

FIGURE 6-42
Diagram for Problem 6.3 [Katz & Coats, 1-2].

	Test I	Test II
Oil rate, bbl/hr	300.	185.
Gas/oil ratio, ft^3/bbl	2380	3220
Separator pressure, psig	12.5	12.5
Wellhead pressure, psig	32.	49.
Pressure (psia) at		
1000 ft	52.	—
1500 ft	—	74.
2000 ft	68.	—
3000 ft	84.	100.
4000 ft	108.	—
4500 ft	—	131.
5000 ft	134.	—
6000 ft	160.	168.
6300 ft	168.	172.
Temperature at 6300 ft, °F	128.	128.
Wellhead temperature, °F	84.	84.
Gravity of atm. crude oil, g/cm^3	0.8368	0.8368
Gas gravity	0.86	0.86
Kinematic viscosity of oil at 100°F, centistokes	5.344	5.344
Surface tension of oil at 100°F, dyn/cm	23.3	23.3

(*a*) Determine the flow regime.
(*b*) Assuming annular flow, what was the approximate thickness of the liquid layer flowing along the well?
(*c*) Plot the pressure profile along the well.

REFERENCES

6-1. American Gas Association, AGA Report No. 3 (1985); American Petroleum Institute, *Manual of Petroleum Measurement Standards,* Chapter 14, API 2530; American National Standards Institute, ANSI/API 2530-1985; Gas Processors Association, GPA 8185-85 (1985).
6-2. American Gas Association, *Steady-State Computation Manual for Natural Gas Transmission Lines,* New York (1964).
6-3. Aziz, K., G. W. Govier, and M. Fogarasi, "Pressure Drop in Wells Producing Oil and Gas," *J. Can. Pet. Tech.*, 38–48, July–September (1972).
6-4. Baker, A., K. Nielsen, and A. Gabb, "Field Data Test New Holdup, Pressure-Loss Calculations for Gas, Condensate Pipelines," *Oil and Gas J.*, Vol. 86, No. 12, 78–86, March 21 (1988).
6-5. Beggs, H. D., and J. P. Brill, "A Study of Two-Phase Flow in Inclined Pipes," *J. Pet. Tech.*, Vol. 25, No. 5, 607–617, May (1973).
6-6. Bertuzzi, A. F., M. R. Tek, and F. H. Poettmann, "Simultaneous Flow of Liquid and Gas through Horizontal Pipes," *Trans. AIME,* Vol. 207, 17–24 (1956).
6-7. Brill, J. P., and H. D. Beggs, "Two-Phase Flow in Pipe," class notes, University of Tulsa, Oklahoma (1984).
6-8. Brown, G. G., and D. L. Katz, "The Sampling and Metering of Wet Gas from High Pressure Condensate Wells," *Proc. NGAA,* Vol. 46 (1946).
6-9. Brown, G. G., et al., *Unit Operations,* John Wiley & Sons, New York (1950).
6-10. Brown, K. E., "Overview of Artificial Lift Systems," *J. Pet. Tech.*, Vol. 32, No. 10, 2384–2396, Oct. (1982).

6-11. Browne, E. J. P., "Practical Aspects for Predicting Errors in Two-Phase Pressure Loss Calculations," SPE Preprint 5000, (1974).
6-12. Chierici, G. L., G. M. Giucci, and G. Sclocchi, "Two-Phase Flow in Oil Wells: Prediction of Pressure Drop," *Annual European Meeting*, April 2–3 (1973).
6-13. Colebrook, C. F., *J. Inst. Civil Engrs.* (London), Vol. 11, 133 (1938–1939).
6-14. Cullender, M. H., and R. V. Smith, "Practical Solution of the Gas Flow Equations for Wells and Pipelines with Large Temperature Gradients," *Trans. AIME,* Vol. 207, 281–287 (1956).
6-15. Dean, W. R., "Motion of Fluid in a Curved Pipe," *Philosophical Magazine,* Vol. 4, 208 (1927); Vol. 5, 37 (1928).
6-16. Dieterich Standard Co., *ANNUBAR and Eagle Eye; Flow Measurement,* Technical Manual, Boulder, Colorado (1980).
6-17. Duns, H., Jr., and N. C. J. Ros, "Vertical Flow of Gas and Liquid Mixtures in Well," *Proceedings, 6th World Petroleum Congress*, 451 (1963).
6-18. Edmister, W. C., and R. J. McJerry, "Gas Compressor Design," *Chem. Eng. Prog.*, Vol. 45, 421 (1949).
6-19. Energy Resources Conservation Board, *Theory and Practice of the Testing of Gas Wells*, Energy Resources Conservation Board 640, 5th Avenue S.W., Calgary, Alberta, T2P 3G4, 3rd Ed., English units (1975); 4th Ed., SI metric units (1979).
6-20. Evans, H. J., "Turbine Meters Gain in Gas Measurement," *Oil and Gas J.*, 67, Aug. 20 (1973).
6-21. Ewing, G. W., *Instrumental Methods of Chemical Analysis,* McGraw-Hill Publishing Co. New York (1954).
6-22. Fancher, G. H., and K. E. Brown, "Prediction of Pressure Gradients for Multiphase Flow in Tubing," *Soc. Petro. Engrs. J.*, Vol. 3, 59, March (1963).
6-23. Gaither, O. D., H. W. Winkler, and C. V. Kirkpatrick, "Single and Two-Phase Fluid Flow in Small Vertical Conduits including Annular Configuration," *J. Pet. Tech.*, Vol. 15, No. 3, 309, March (1963).
6-24. Gould, T. L., "Vertical Two-Phase Flow in Oil and Gas Wells," Ph.D. dissertation, University of Michigan, Ann Arbor, Mich., (1972).
6-25. Gould T. L., M. R. Tek, and D. L. Katz, "Two-Phase Flow through Vertical, Inclined, or Curved Pipe," *J. Pet. Tech.*, Vol. 26, No. 8, 915–926, Aug. (1974).
6-26. Govier, G. W., and K. Aziz, *The Flow of Complex Mixtures in Pipes,* Van Nostrand Reinhold Co. (1972).
6-27. Hagedorn, A. R., and K. E. Brown, "The effect of Liquid Viscosity in Vertical Two-Phase Flow," *J. Pet. Tech.*, Vol. 16, No. 2, 203–210, Feb. (1964).
6-28. Hagedorn, A. R. and K. E. Brown, "Experimental Study of Pressure Gradients Occurring during Continuous Two-Phase Flow in Small Diameter Vertical Conduits," *Trans. AIME*, Vol. 17, 475 (1965).
6-29. Interstate Oil Compact Commission, *Manual of Back Pressure Testing of Gas Wells*, Interstate Oil Compact Commission, Box 3127, Oklahoma City (1962).
6-30. Joffe, J., "Gas Compressors," *Chem. Eng. Progr.*, Vol. 47, 80 (1951).
6-31. Katz, D. L., "High Pressure Gas Measurement," NGAA, Tentative Standards (1942).
6-32. Katz, D. L., "Thermodynamic Analysis of Frictional Heat Effects in Pipeline Flow," *Oil and Gas J.*, Vol. 70, 87–90 (1972).
6-33. Kehoe, W. R., "Orifice Meter Accuracy," *Petro. Refiner,* Vol. 33, No. 4, 118 (1954).
6-34. Knudsen, J. G., and D. L. Katz, *Fluid Dynamics and Heat Transfer*, McGraw-Hill Publishing Co. (1958).
6-35. Lawson, J. D., and J. P. Brill, "A Statistical Evaluation of Methods Used to Predict Pressure Losses for Multiphase Flow in Vertical Oil Well Tubing," SPE Preprint 4267 (1973).
6-36. Lesem, L. B., J. J. McKetta, Jr., and G. H., Fancher, "A Study of the Orifice Well Tester and Critical Flow Prover," *Trans AIME,* Vol. 210, 393–396 (1957).
6-37. McConalogue et al., "Motion of Fluid in a Curved Tube," *Proceedings of Royal Society Series A,* Vol. 37, No. 1088, 37 (1963).
6-38. Moody, L. F., "Friction Factors for Pipe Flow," *Trans ASME,* Vol. 66, 671 (1944).

6-39. Neptune Eastech, "New Design Flowmeters Boost Accuracy, Help Conserve Energy at Process Plant," *Power*, 55–57, December (1976).
6-40. Nikuradse, J., *VDI—Forschungsheft*, No. 356 (1932); *Petro. Engr.*, Vol. 11 (1940).
6-41. November, M.H., "How to Use High-Capacity Axial-Flow Turbine Meters for Gas Measurement," *Oil and Gas J.*, Vol. 70, 69, April 3 (1972).
6-42. Oranje, L., "Condensate Behavior in Gas Pipelines is Predictable," *Oil and Gas J.*, Vol. 77, No. 27, July 2 (1973).
6-43. Orkiszewski, J., "Predicting Two-Phase Pressure Drops in Vertical Pipes," *J. Pet. Tech.*, Vol. 19, No. 6, 829–838 (1967).
6-44. Pottmann, F. H., and P. G. Carpenter, "The Multiphase Flow of Gas, Oil, and Water through Vertical Flow Strings," *API Drill. Prod. Practice*, Vol. 257, 257–317 (1952).
6-45. Radar, C. M., and R. A. Feemster, "A New Method of Measuring Vented Gas," *Trans. AIME*, Vol. 107, 98 (1934).
6-46. Raman Raghu, *Chemical Process Computations*, Elsevier Applied Science Publishers (1985).
6-47. Rawlins, E. L. and M. A. Schellhardt, *Back-pressure Data on Natural Gas Wells and Their Application to Production Practices*, U.S. Bureau of Mines Monograph 7 (1936).
6-48. Redding, T. H., *A Bibliographical Survey of Flow through Orifice*, Chapman & Hall, Ltd., London (1952).
6-49. Ridgeway, R. S., paper presented before CNGA in Los Angeles (1945).
6-50. Ros, N. C. J., "Simultaneous Flow of Gas and Liquid in Well Tubing," *Trans. AIME* Vol. 22, and *J. Pet. Tech.*, Vol. 13, No. 11, 1037–1049, October (1961).
6-51. Rzasa, M. J., and D. L. Katz, "Calculation of Static Pressure Gradients in Gas Well," *Trans. AIME*, Vol. 160, 100–113 (1945).
6-52. Rzepczynski, W. M., M. R. Tek, K. H. Coats, and D. L. Katz, "The Mt. Simon Gas Storage Reservoir in the Herscher Field," *Oil and Gas J.*, Vol. 59, No. 25, 86 (1961).
6-53. Starling, K. E., editor, *Compressibility and Supercompressibility for Natural Gas and Other Hydrocarbon Gases*, Transmission Measurement Committee Report No. 8, American Gas Association, Catalog No. XQ 1285, Arlington, Va. (1985)
6-54. Sterns, R. F., R. R. Johnson, R. M. Jackson, and C. A. Larson, *Fluid Measurement with Orifice Meters*, D. Van Nostrand Company, Princeton, N.J. (1951).
6-55. Sukkar, Y. K., and D. Cornell, "Direct Calculation of Bottom-Hole Pressure in Natural Gas Wells," *Trans. AIME*, Vol. 204, 43–48 (1955).
6-56. Vohra, I. R., J. R. Robinson, and J. P. Brill, "Evaluation of Three New Methods for Predicting Pressure Losses in Vertical Oil Well Tubing," SPE Preprint 4689, (1973).
6-57. Weymouth, T. R., "Problems in Natural Gas Engineering," *Trans ASME*, Vol. 34, 185 (1912).
6-58. Yocum, B. T., "Offshore Riser Slug Flow Avoidance: Mathematical Models for Design and Optimization," SPE Preprint 4312, (1973).

CHAPTER 7

DRILLING AND COMPLETION OF WELLS

Engineers and geologists should be conversant with the terminology and normal procedures of drilling wells. The following topics are defined and described to give background on field practices.

Site selection is the beginning effort in well drilling. It involves both subsurface and surface considerations. The geologist in charge is also guided by lease ownership and well spacing rules in choosing a specific location. A projected depth is part of the geological analysis; it could be uncertain for a wildcat, a well in a new area. For developmental wells or infill drilling, the depth can be predicted closely.

Surface considerations include the topography and the closeness of buildings and roads; generally there are restrictions on distances from property lines. In many cases, a drilling area is designated, and directional drilling is used to reach the final location. The exact surface location is determined by surveys of elevation and coordinate distances from latitude and longitude markers. Surface preparation may include a road into the location from a highway, an area for equipment storage, and a road for service trucks to approach the well.

The *mineral lease* is the legal ownership to the right to drill for oil and gas. The title to normal farm or woodlands includes the surface rights and the right to harvest minerals underlying the surface. When there are prospects for oil, gas, coal, or other minerals in the area, the mineral rights may become

separated from the surface rights. A mineral lease conveys the right to produce the minerals. Right of ingress and egress, and access to roads, well sites, and pipelines are granted to carry out the recovery of oil and gas. In return, the lessee pays a bonus at the time of purchase, an annual fee, and a fraction of the minerals (oil and gas) produced. The standard royalty going to the lessor was $\frac{1}{8}$ of the production. Both state and federal lands are leased, usually by some bidding system. The operating owners frequently then are surface owners, mineral right owners, the operator, driller, or producer of the well under the lease. A well permit is obtained at the state office, giving the above-determined location along with environmental data.

The *equipment used* is a drilling rig with auxiliaries. Drilling rigs are of two general kinds, cable tool and rotary rigs, the latter used in most cases. The cable tool rig is used for well completions, clean-outs, and general servicing of wells, and occasionally for drilling new shallow wells.

Figure 7-1 depicts the key components of a rotary rig, and Fig. 7-2 is a photograph of such a rig in operation. The component parts of a modern rig, as indicated in Fig. 7-1, are as follows: The engines *A* drive the drawworks *C*. The drawworks consist of a hoisting drum around which is spooled steel cable. The steel cable is strung around the sheaves of the crown block *N* and the traveling block *D*, which raises and lowers the drill string. The drill string is made up of the swivel and kelly *E*, drill pipe, drill collars, and the bit *H*. The drill collars have a heavier wall than the drill pipe to give additional weight on the bit. The kelly is square-shaped so that, as it moves downward through the rotary table *F*, the entire drill string is rotated. The rotary table is driven by the drawworks *C*.

The engines *A* also power the slush pump *I*, which pumps mud out of the mud tank *M*. The path taken by the mud is shown by the arrows; it leaves the pump, flows up the standpipe, through the flexible rotary hose and into the swivel connection, down the kelly, drill pipe, drill collars, and out the holes in the bit. It then flows up the annular space and is vented out the casing *G* into a trough *K* and then to the shale shaker *L*. From the shale shaker the mud flows back to the mud pit, and the cycle is repeated. The purpose of the shale shaker is to remove the cuttings brought up by the mud.

A casing program is part of the plan for drilling a well. Figure 7-3 shows a well with three casings and set into producing formation. A second smaller casing may be set to protect drilling from mud loss in a vugular zone or a shallow production zone. The production casing is set on top of the producing zone or, as in Fig. 7-3, is bottomed in or below the producing zone. Production casings are frequently 5.50-in. (0.14-m) or 7-in. (0.18-m) casings.

Mud technology is of increasing importance with added depth of the well because of the increased pressure and temperature, and the high costs for interruption of drilling. Reference [1-8] on drilling and drilling fluids gives a thorough treatment of the use of mud to maintain pressure on zones pierced by the drill, while avoiding undue penetration of the porous zones by building a mud sheath at the drill hole wall. In early, shallow drilling, natural clays gave reasonable quality muds. Formulations are made to give satisfactory viscosity, filtration loss

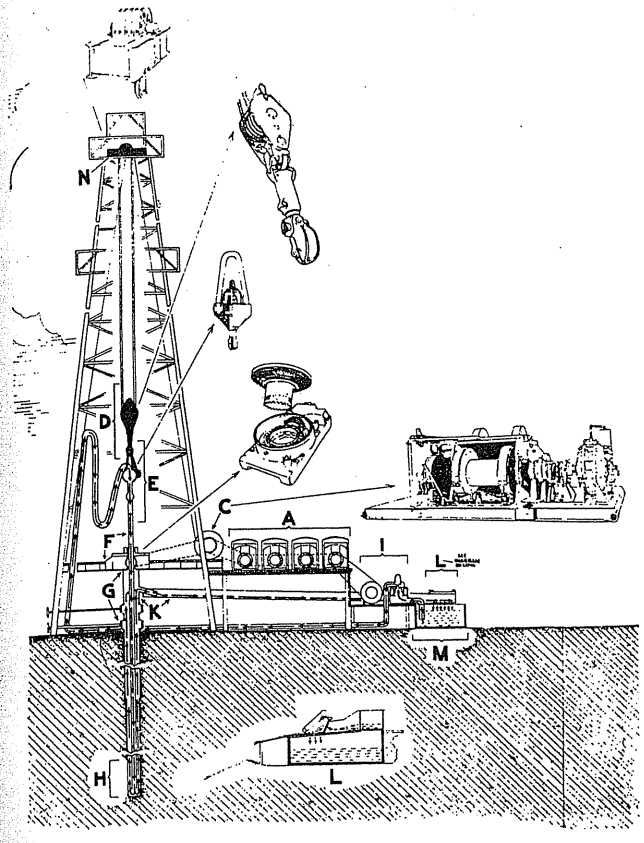

FIGURE 7-1
Sketch of rotary rig [1-5].

of liquid through the mud sheath, and weight. Compared to water at 8.34 lb/gal (1000 kg/m^3), mud density is often raised to as much as 12 lb/gal (1440 kg/m^3) for deeper wells and in extreme cases reaches 20 lb/gal (2400 kg/m^3).

There are water-based muds and oil-based muds, the latter used when water is harmful to potential producing formations. It is necessary to isolate the surface mud circulation system from the environment. When there is some potential for mud loss into irregular zones, a reserve supply of mud and plugging agents may be kept at hand.

The gas content of the mud is logged to identify natural gas in the rocks being drilled. Blowout prevention is an important concern during drilling, and monitoring of the mud characteristics is important to assure that gas does not aerate the mud and lower the density of the column. There are blowout preventers to hold the pipe in the case of an emergency. When the hole has been drilled to its completion depth, production casing is set.

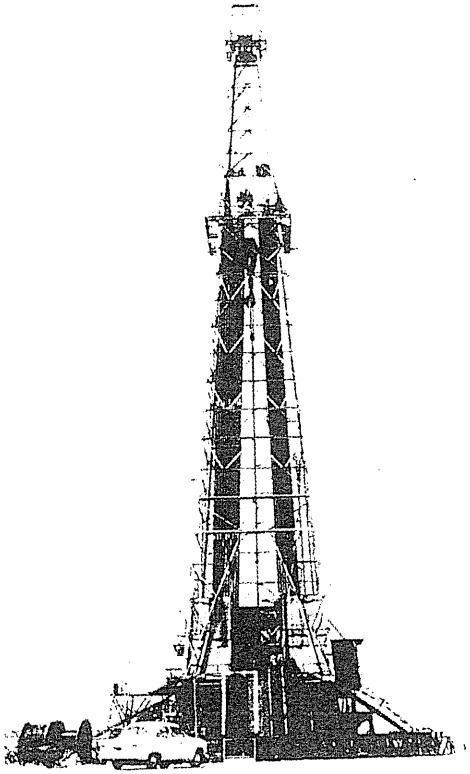

FIGURE 7-2
Photograph of rotary rig [1-1].

Cementing the casing seals the pipe to the rock and prevents oil or gas from flowing up the annulus. After the drilling mud has been circulated to clean the wellbore, the casing is placed in the well joint by joint. The casing head is piped to cement truck pumps, which are prepared to mix dry cement with water in a jet mixer and pump the slurry down the inside of the casing. A calculated volume of cement slurry is used to bring the annulus level to as high as desired, into an intermediate casing or to surface. When this amount of cement has been pumped into the casing, a movable plug is placed on top of the cement and pumped to near the bottom of the casing with mud or water.

Problems arise when the cement slurry breaks into formations instead of coming up the annulus. Also, mixing of cement with mud provides channels where oil and gas may displace the fluids and move up the annulus. The top of the cement outside the casing may be located by temperature measurements after a short set period or by cement bond logs.

The monograph by Smith on cementing [1-23] gives a view of the technology. Work in gas storage on threshold pressure indicates that fully turbulent mixing is required to give high threshold pressures for gas to displace water from the set neat cement [1-38].

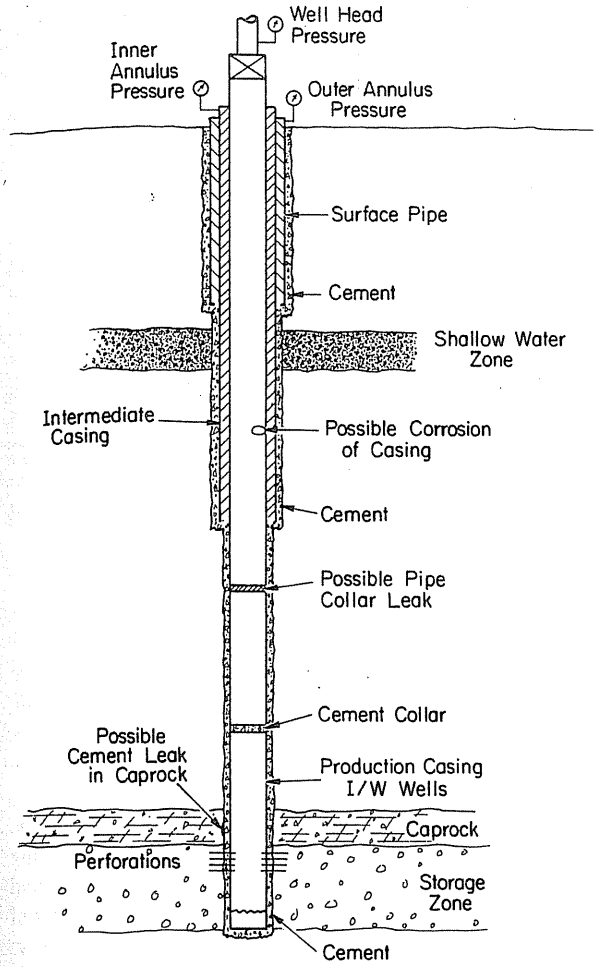

FIGURE 7-3
Well completion with identification of potential leak.

Perforating casing has become a routine tool in completing or recompleting wells. When the cement has set on a well drilled through the producing horizon, a perforating gun is lowered into the casing, normally full of water or mud, and bullets are shot through the casing. This method of completion protects the formation face and facilitates plug backs or recompletion.

Logging of wells was once done by drillers, who maintained a record, known as driller's logs, of activities, events, depths, drill rates, etc., when drilling wells. Then in the 1930s, Schlumberger introduced the electric log by running electrodes on insulated conducting cables into wellbores after drilling and before casing was set. Electric logs receive signals from sonds and transmit them to recorders at the

surface to give the electrical resistivity and the self potential of the formations. Wells with casing in place use neutron and gamma ray logs, in which neutron and gamma ray beams penetrate the steel; these may be repeated over a period of years to detect gas accumulations and movement. A large number of logs are taken especially on wildcat wells, deep wells, and offshore wells. Essentially all logging is done by service companies, and much of the analytical expertise resides with their personnel. Several kinds of logs are described in this chapter.

Drill stem testing [1-21,1-22] is a technique for testing the productivity of a formation before setting the production casing. The drill pipe is removed, the bit is replaced by the drill stem testing equipment, including pressure gauges, and this is floated back into the mud-filled wellbore. The tool is placed opposite the productive horizon at the bottom of the well, and packers seal off the annulus from the formation. The pipe is rotated to open the formation to the low pressure inside the drill pipe. A strong productive formation will flow through the drill pipe, which is equipped to flare gas. The pipe is then rotated back to close off the formation, and buildup pressures are recorded. The results include time for gas to surface, and the amount of liquid, oil, and/or water in the withdrawn drill pipe. See reference [7-5] for a description and a sketch.

7.1 PROGRESS IN DRILLING

Kelly reviews advances in drilling technology [7-9] including measurements while drilling (MWD), new bit developments, advances in drilling fluid technology with oil-based muds, drilling high-angle holes, and the automatic drilling rig. The potential for reducing drilling costs by research on various aspects of drilling is high and has generated many advances.

The MWD concept is to send messages from a sensor at the bit to the derrick floor by electrical signals or by hydraulic pulses in drilling fluid during a brief pause in drilling rotation. It is useful in directional drilling, pressure and temperature measurements, and formation evaluation. The Stratapax™ drill bit of synthetic diamonds and cemented carbide increases penetration rates dramatically. By using such bits with a turbo drill, penetration rates are increased 4 times. The use of oil-based muds, the availability of new drilling fluid additives, and attention to control of solids content have made for wellbore stabilization and improved operation. Improvements of this type have permitted more rapid drilling of high-angle holes at great horizontal distances, such as from platforms.

7.2 STIMULATION OF WELL PRODUCTIVITY

Frequently a reservoir's permeability is too low to permit the desired flow rate of gas or oil for economic operation. Stimulation may not be needed until reservoir pressure declines, but often the practice of fracturing or acidizing wells is included in the well completion.

Fracturing is a way to stimulate production rates. Wellbores connected to potential productive horizons in the earth may be pressurized by water, another liquid, or foam to the extent that the rock fractures, admitting large volumes of fluid. Sand or other solids are mixed into the injected water so that the fractures remain propped open after the injection stops. The pressure required to cause fracturing is normally in the range of 0.8 to 1.1 psi per foot of depth (18 to 25 kPa/m).

Yuster and Calhoun [7-15] observed that water injection rates on water-flooding wells would rise to any limit once pressure at the wellbore reached a level slightly over 1 psi per foot of depth (22.6 kPa/m). They called the phenomenon *pressure parting* of the formation, because the fluid pressure opened a crack or fracture to admit the water. Early acidizing practices used high injection pressures, and fractures were known to take place. The commercial process reported in 1949 by Clark et al. [7-1] involved the placing of sand or other propping agents in the injected fluid so that when pumping stopped, the fracture did not close. Fractures may be vertically or horizontally oriented, depending upon depth and stress status of the in-situ rocks.

Consider the pumping of water into a well with the bottom perforated to a rock formation. As the pump rate rises, so does the required injection pressure. At fracturing pressure, however, the rate will increase even while the pressure drops back to a lesser value. Figure 7-4 shows this type of pressure curve and Fig. 7-5 a developing fracture. The interpretation of the opening is that the formation parted or fractured at the peak pressure and allowed water to flow into the fracture slit.

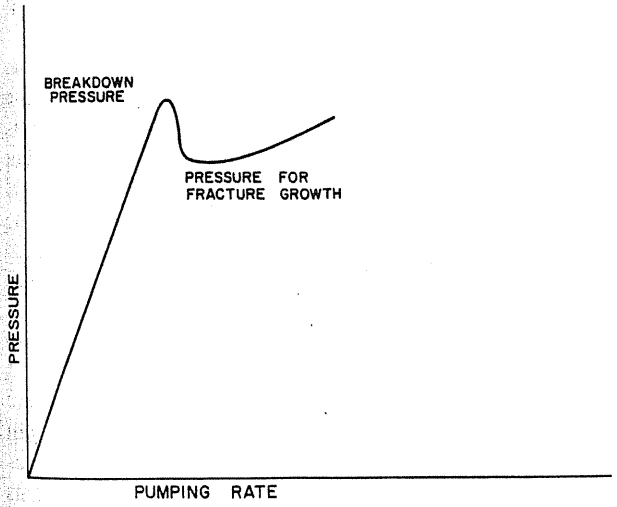

FIGURE 7-4
Pressure-pumping rate while producing a fracture.

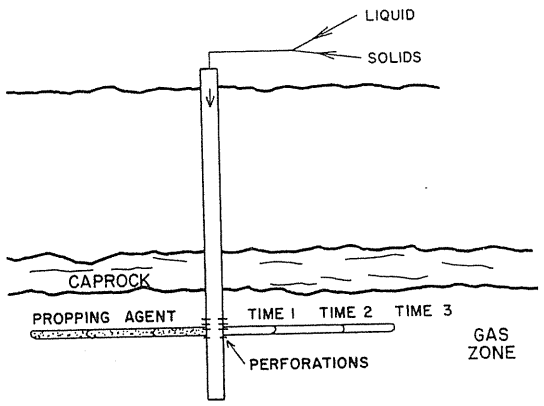

FIGURE 7-5
Schematic diagram of horizontal fracturing.

For horizontal fractures, it is sometimes said that the rock above is lifted, but this is not believed to happen except for very shallow zones. What actually occurs is that the fluid pressure compresses the rock layers above and below the fracture enough to create the disc opening. A fracture may be only 0.01 to 0.1 in. wide, and several hundred feet of rock thickness can be compressed this amount by the pressures used. By analysis, Perkins and Kern [7-11] showed that only when the fracture radius is greater than $\frac{4}{3}$ of the depth does the overburden flex and rise a bit with a horizontal fracture. For practical purposes, no surface movement should be contemplated during fracturing. In waste disposal studies of placing cement slurries of waste into horizontal fractures, elevation rises of 0.06 ft (18×10^{-3}m) were observed with horizontal fractures at depths of 850–950 ft (260–290 m) [7-2].

The fracture initiation pressure depends upon the in-situ stresses in the rock—see Figs. 7-6, 7-7, and 7-8 [7-7]. The vertical stress is caused by the overburden and increases with depth. The minimum horizontal stress depends upon geological history. Generally shallow wells are fractured horizontally, but deeper wells, 2000–3000 ft (610–914 m), are more likely to fracture vertically. Any manmade interference with the stresses at the wellbore can change the fracture pressure. For example, a plastic zone that has flowed into a wellbore during drilling will cause a low fracture pressure for an underlying sand, since the plastic has become more compressible. Also, multiple squeeze jobs on wells will compress the rock, and breakdown pressures will rise as shown on Fig. 7-9 [7-7].

Fracturing fluids may be water, oil, gels, emulsions, or foams [7-6]. There is a constant search for a fluid that does not drain off to the surroundings, will carry and deposit the propping agent securely, and will not interfere with gas or oil flow from matrix into fractures for conveyance to the wellbore. Foams are found to be excellent stimulating fluids with low leak-off, good proppant transport, longer fractures with less fluid, and minimum formation damage [7-6].

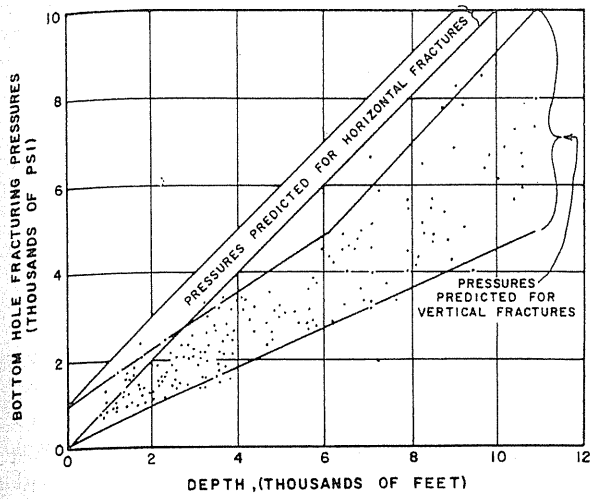

FIGURE 7-6
Theoretically predicted bottom hole fracturing pressures and field data [Perkins & Kern, 7-11].

Propping agents that give the greatest lasting increase in permeability are sought. Higher strengths and resistance to imbedding in fracture wall are needed for deeper wells. For example, zirconium oxide beads are an improvement over sand and glass beads at depths greater than 10,000 ft (3048 m) [7-12]. The benefits from fracturing are variable, becoming an economic matter for a given field.

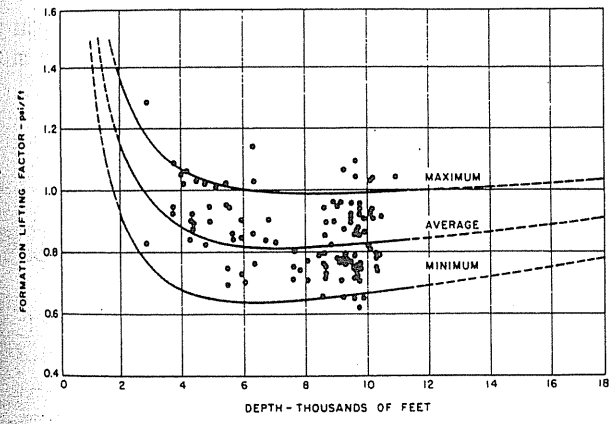

FIGURE 7-7
Formation lifting factors based on break down pressure [Howard & Fast, 7-7].

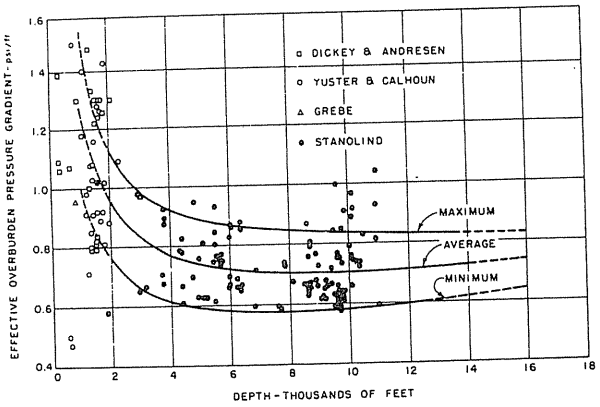

FIGURE 7-8
Comparison of various estimates of effective overburden pressure gradients [Howard & Fast, 7-7].

Frequently, flow rates are increased by factors of 4 to 6, but industry knows that field tests are the way to learn what may be expected in a given field by a given treatment.

7.3 GAS FRACTURING

Can gas under pressure cause formations to fracture? The senior author has been asking this question for some 20 years or more and has not found any occasion on which gas pressure initiated a fracture at pressures at or below 1 psi/ft (22.6 kPa/m). This question is raised in connection with the degree of delta pressure used, like above 0.7 psi/ft (15.8 kPa/m). It is believed that gas can cause fractures at some pressure, possibly at levels as high as 1.5 psi/ft (34 kPa/m), and that gas may open fractures already present at the usual pressure of 1.0 to 1.1 psi/ft (22.6–24.8 kPa/m).

The idea of storing gas in thick shale beds by fracturing the beds at depths of 800–1000 ft (244–305 m) has been tried, and the results teach a lesson in

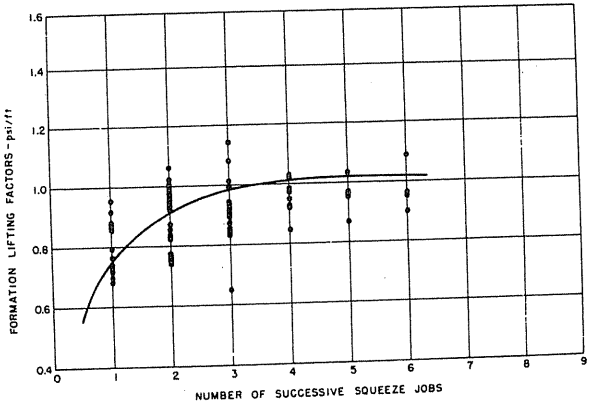

FIGURE 7-9
Trend of formation lifting factors with number of squeeze jobs [Howard & Fast, 7-7].

fracturing. Water was required to initiate the fractures, but then gas could be injected at 1.1 to 1.2 psi per foot (24.8–27.1 kPa/m) of depth. In other words, with an initiated fracture, one can pump fluids into the earth continuously through a dynamic fracture at some pressure in this range. Some of the fractures into which gas was injected had been propped.

When the injection of gas ceased, the well pressure returned to about 1.05 psi/ft (23.7 kPa/m) in a matter of minutes. At this point, the fractures were not propagating, just maintained in an open position by the gas pressure. Since shale has a very low permeability and high threshold displacement pressure, gas could be confined in such a fracture.

Consider what would happen when gas was withdrawn from an injection well. Lowering the gas pressure in the casing by production would lower the pressure in the fracture near the wellbore. Since the fracture gap results from compression of the rock above and below and is maintained by the gas pressure, lowering the pressure will allow the fracture gap to close unless it is propped. Experience showed that gas withdrawal was accompanied by a drop in the well pressure that indicated that the injected gas was not in communication with the well. Production–pressure drop relations were predictable on the basis of the casing volume and the propped fracture gap volume. Duplicate withdrawal experiences occurred for three different injection amounts, telling that the physical phenomenon of closing off the well from injected gas was not related to the volume of gas in the fracture gap. Figure 7-10 shows how a dynamic fracture will accept the gas and how a pressure reduction will allow the fracture gap to

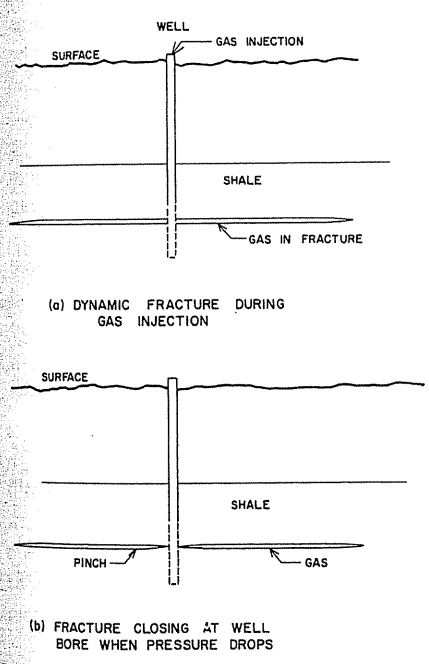

FIGURE 7-10
Diagrams showing gas storage in fractures and seal off as gas pressure at wellbore lowered.

close near the wellbore when propping is not provided. When propping is used, the gap closes at the outer perimeter of the propped area. The closed gap in a ring around the well is not a perfect seal, and well pressure may build up slowly after blowing down quickly by production. Since high withdrawal rates are desired for stored gas, the almost complete closure for the fracture gap near the well renders this method impractical.

7.4 ACIDIZING OPERATIONS

There are three general types of acidization operations [1-16,1-27]. One is a mud acid or cleanup treatment used on either sand or limestone reservoirs right after perforation. Such mud acid contains addition agents that permit the fluid to enter the producing formation and, when flushed out, to remove drilling mud and any debris that has entered the pore space. The second acidization method is acid fracturing, the third matrix acidization.

The usual acidization [1-27] employs hydrochloric acid, 15–28 percent by weight. Often tests are done on cores or cuttings to determine the best acid formula for dissolving the rock for a particular well or area. Methyl alcohol may be used along with acid to lighten the weight of the column and lower surface tension as the acid stream is pushed into the producing formation. In acid fracturing, the acid is pumped under pressure into the tubing and down the well. The acid is controlled and the pressures carefully observed as the fluid is pumped into the formation. The acidization is expected to cause a fracture in the formation in order to break it down and permit the acid to enter at a reasonable rate. Usually, the pumping rate for a given injection pressure will increase markedly as soon as the acid reaches the formation, causing the permeability to increase. Acid may be allowed to return by producing the well after the acid has stayed in the formation for an hour or so. After acidization, liquids in the hole may prevent a gas well from producing; then, it is common practice to use a swab on the tubing to remove the liquid column and allow gas to enter the wellbore. As soon as gas does come into the wellbore in large enough quantities, it will blow the liquids out and clean itself.

Matrix acidization is described in the monograph [1-27] as a series of three treatments: a preflush, acidization of matrix with a hydrochloric-hydrofluoric acid mix, and an afterflush. The preflush by an inhibited 5–15% HCl solution is to remove water and eliminate problems when the HCl-HF is used. The injection of acids is done at pressures low enough to avoid fracturing. A 3% HF, 12% HCl solution will react with clays and nonquartz materials.

Success with the use of HF-HCl acids and designed conditions elsewhere were the basis for the development of such techniques for Stray sand storage wells by Fogler and Crain [7-4]. The work includes a knowledge of the constituents of the formation and a design procedure. Use of acid strengths, rates of injection, and pretreatments assure gradual entrance of the acids into the pores to increase the permeability.

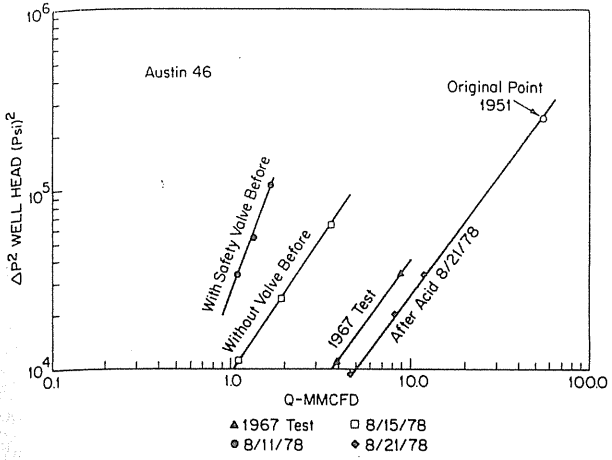

FIGURE 7-11
Results of acidization of Austin 46 well [Fogler & Crain, 7-4].

The removal of accumulated compressor oil and fine particles by organic solvents helps production. Figure 7-11 shows the results of acid treatment of well 46 at Austin on isochronal back pressure tests. With study and careful designs a high fraction of the wells can be restored to near their early deliverability. This is one of the areas in which work on gas and oil technology is and will be extended to gas storage operations.

7.5 WELL LOGGING

Wire line well logging has developed into a scientific and engineering discipline since the initial work by Conrad and Marcel Schlumberger in France in 1927. The senior author witnessed the first log taken by Phillips Petroleum at the Fitts Pool in 1935. These logs are designed to give geologic correlations of strata depth and thickness along with in-situ properties of the rock and degree of saturation by water, oil, and gas phases. The drilling operation can change the fluid saturation by mud filtrate invasion. Since logs are influenced by the near wall rocks and their fluid content, log interpretation may require information on the conductivity or salinity of the drilling fluid.

Since the porosity, permeability, and fluid saturation reported from logs are all indirect measurements and are based on interpretations, every effort should be made to calibrate the interpretations by all possible means. Data on cores, well fluids produced, etc., for given geologic provinces or areas can be helpful and refine the interpretations made. The service company carrying out the logging operation gives their interpretation, but geologists and reservoir engineers often develop their own interpretations based on experience. This treatment can do little more than give background and nomenclature used in logging.

When the casing has been set, logs taken, and stimulation operations completed, the well is put on production. Gas wells are connected to gathering systems and as shown in Fig. 1-3, are likely to have liquid separators and meters. Oil wells are illustrated on Fig. 1-2. As the well is put on stream, a flow test is normally performed to learn the productivity of the well for oil, gas, and/or condensate.

With the well equipped to flow to the separator, the mud, if still present, is circulated and changed to water. For full hydraulic reservoir pressures, gas may aerate the liquid column to lower the pressure of the formation face and initiate flow. The mud and water are separated out and gas sent to the gathering system. Oil wells or low permeability gas formations may require swabbing or gas injection to lower the liquid column at the reservoir face to permit a "kickoff" of well flow. A flow period is required to clean the well piping and sand face.

A gas well test, often called a back pressure or performance test, uses some four flow rates of 30 min to 1 hr in duration, with measurement of gas and liquid flow for each. Since it is the formation that is being tested, the pressure drop measured is that between the initial closed pressure out in the reservoir and the wellbore pressure at the bottom of the well. Wells with considerable liquid flow need a bottom hole recording pressure gauge in place; gas well bottom hole pressures may be computed as discussed in Chapter 6, using only wellhead flow and static measurements.

Open Hole Logging

Some logs are taken before casing the well and depend upon having the drill hole full of mud. Typical among these are electric logs with their resistivity, conductivity, and self potential measurements, and porosity logs of acoustic, density, and neutron measurements.

W. R. Clark and S. F. Nowaczewski of Michigan Wisconsin Pipe Line Co. prepared the following material on open hole logs with examples, and the following section on cased hole logs.

The following examples of open hole logs will be of the following types:

Resistivity
Spontaneous potential
Acoustic
Gamma ray
Density
Neutron

These common open hole logs measure rock properties, which can be used to determine type and amount of porosity and type and amount of fluid in the pore space. It is important to keep in mind that the interpretation of logs is facilitated by a knowledge of the local geology. Log interpretation is best when log data is combined with data from cuttings, cores, and drill stem tests.

The first suite of logs is from a gas well completed in the Michigan Stray sandstone in Mecosta County, Michigan, and includes a resistivity log and gamma ray, density, neutron, and acoustic logs.

Compensated neutron log. The compensated neutron log, Fig. 7-12, displays gamma radiation on the left in API units. Gamma ray logs are used for formation correlation because they measure the natural radiation of sediments, which generally indicates shaliness. The compensated neutron log, displayed on the right, compensates for borehole conditions, and readings are recorded directly in porosity units for a given matrix material (limestone in the example). The logs are for the top of the Stray sandstone at approximately 1355 ft (413 m). The Stray appears to be of nearly uniform shaliness to 1430 ft (436 m). Above the Stray are alternating beds of shale and anhydrite. The compensated neutron log reads low porosity in the anhydrite beds and higher porosity in the shale beds. In the Stray sandstone section, the neutron log shows lower porosity in the upper 50 ft (15 m). If it is true that the Stray is relatively uniform throughout the logged section, then the lower neutron response in the upper part of the Stray could mean the presence of gas, which can be verified by obtaining a porosity log such as an acoustic or density log.

Sonic and density logs. An acoustic log measures the compressional wave travel time through the rock. If lithology is known, then travel time can be related to porosity. The sonic curve of Fig. 7-13 shows large attenuation through the interval 1355–1431 ft (413–436 m), suggesting the presence of gas. Figure 7-14, a density log in the same wellbore, shows a lower density between 1355 to 1413 ft than from below 1413 ft. Gas-filled porosity rather than brine-filled porosity in the same rock type could account for the density difference.

Dual lateralog. Figure 7-15 is a resistivity log from the same well as the above examples. This is a *dual lateralog*, a log recorded by a focusing electrode device run in conductive muds and having two depths of investigation. (*Induction logs* are resistivity-measuring tools run in nonconductive muds.) The deep curve can read beyond the invaded zone and hence its reading can be taken as the true resistivity of the rock. Below 1406 ft (428.6 m), both deep and shallow curves record uniform low readings, which might be expected in a uniform rock with saltwater-filled pores. Above 1406 feet, the curves show a marked increase in resistivity, particularly the deep curve which, along with the neutron, density, and acoustic logs, indicates gas-filled porosity. The example well is a gas well, originally completed open hole (the logs were run after deepening) for over 25 MMcf per day.

Gamma ray neutron log. Two other log examples come from a well in a gas field in the Michigan Stray sandstone in Newaygo County, Michigan. The gamma

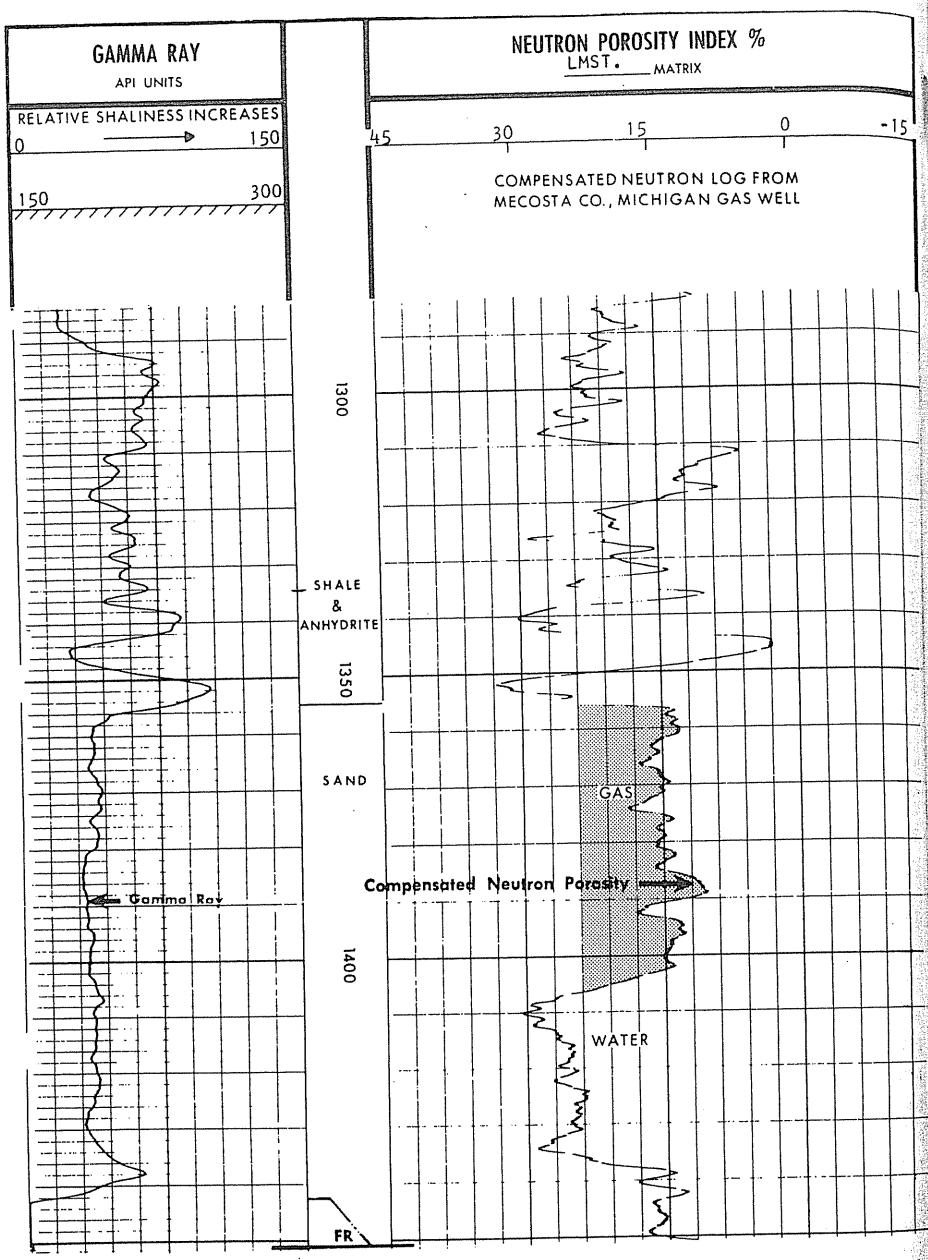

FIGURE 7-12
Compensated neutron log from Mecosta Co., Michigan gas well.

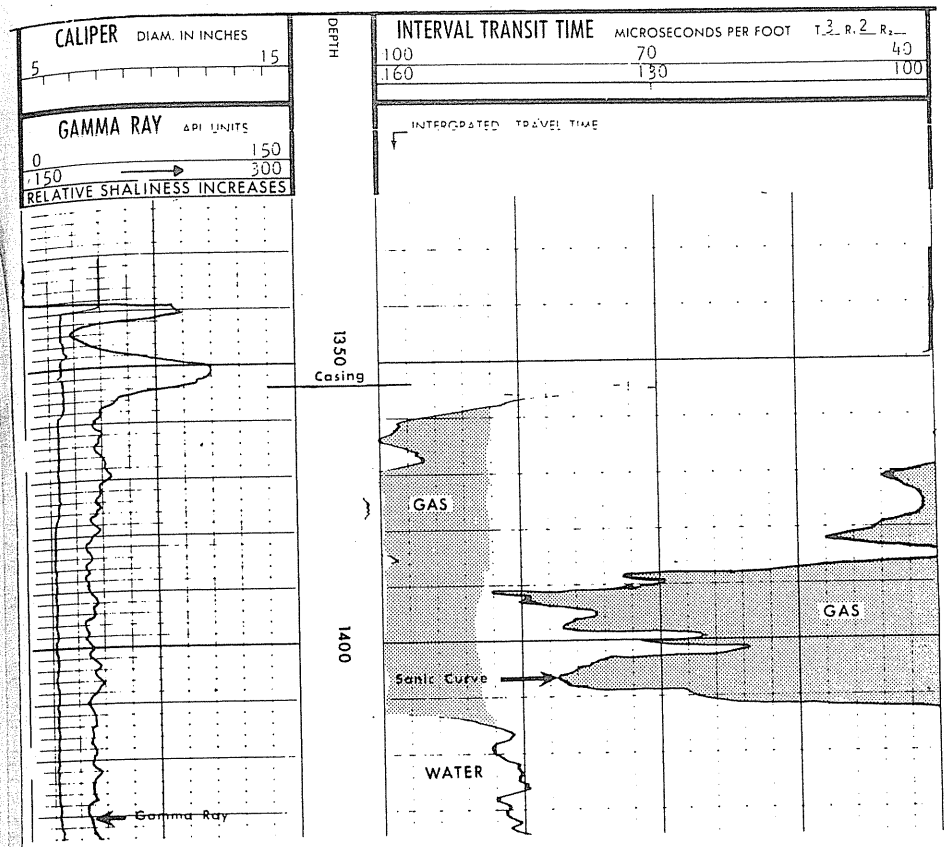

FIGURE 7-15
Sonic log from Mecosta Co., Michigan gas well.

ray neutron log, Fig. 7-16 (run in a cased hole), is similar to the compensated neutron log except that neutron readings are not presented in porosity units. Again, the response of the neutron curve in a gas zone (1085–1150 ft) is evident. Note also that the neutron curve response in shale is opposite to the curve response in a gas zone. As the rock becomes shalier with depth, the neutron curve reading, in calibrator units, decreases.

Electrical log. Figure 7-17 is an old electrical log from the same well as the above example. It displays the spontaneous potential log on the left and the induction log on the right. The spontaneous potential occurs as a result of an electrical current between the borehole mud, sands, and shales. The spontaneous potential (SP) log is used for formation correlation, identification of permeable beds, and shale volume determination, and it can be used to determine formation

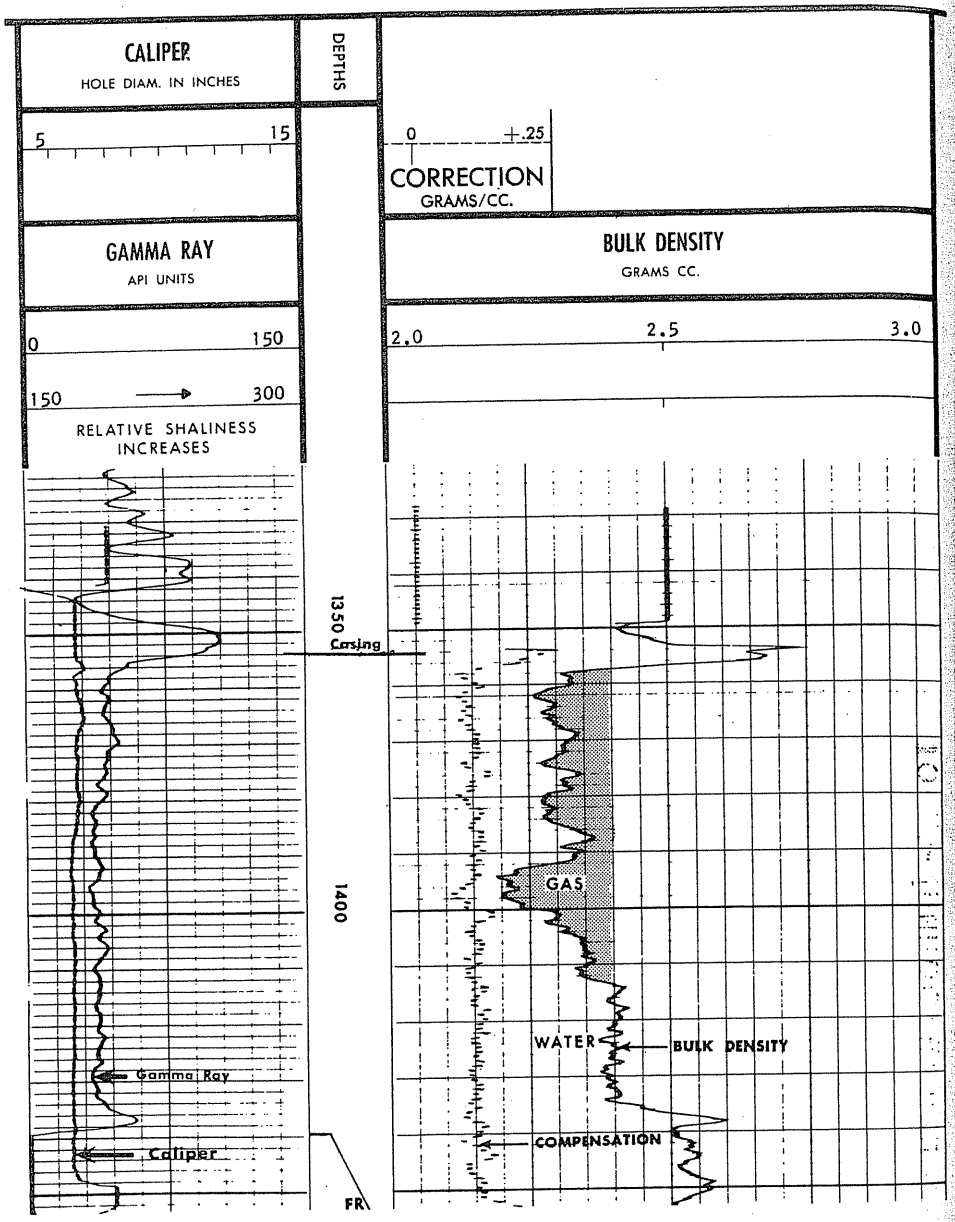

FIGURE 7-14
Density log from Mecosta Co., Michigan gas well.

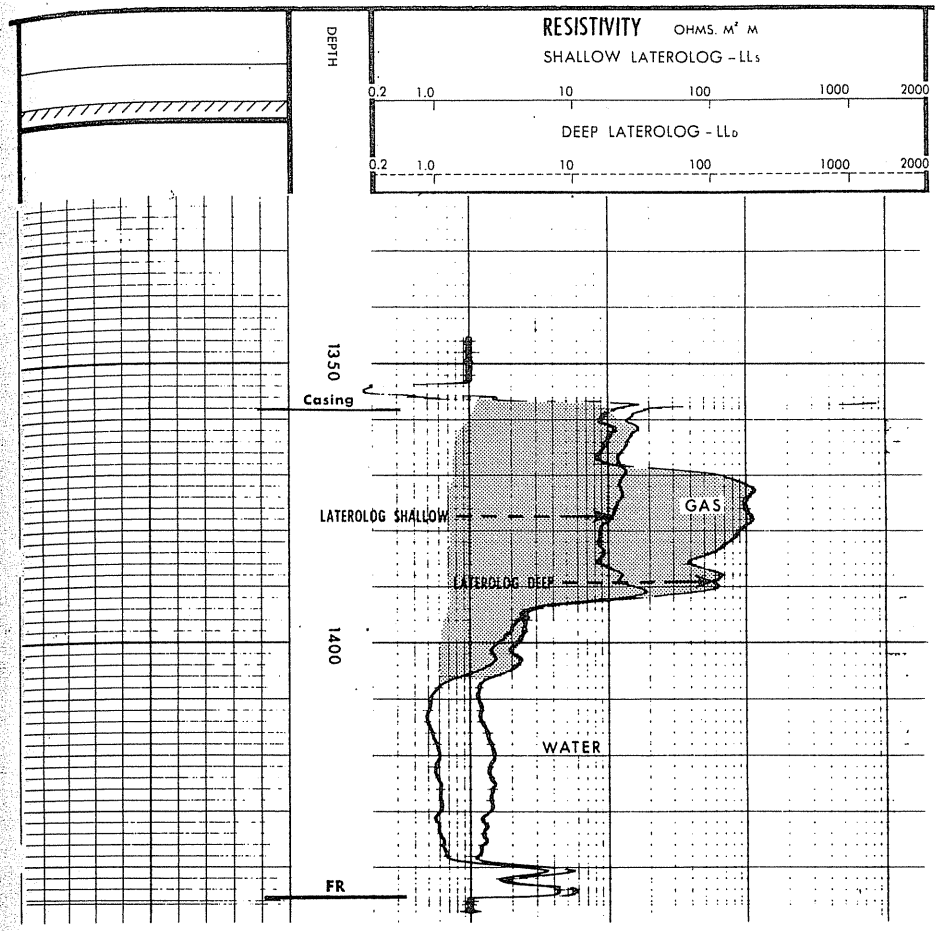

FIGURE 7-15
Dual lateralog from Mecosta Co., Michigan gas well.

water resistivity. Note that the SP log shows some hydrocarbon suppression in the example. Resistivity increases significantly in the gas zone.

Induction electric log. Figure 7-18 is another example of an induction log, from St. Mary Parish, Louisiana. The SP log on the left clearly shows shales, sands, and shaly sands. The induction log, with shallow, deep, and amplified resistivity curves and a conductivity curve, indicates a high resistivity through some of the sands, suggesting nonconductive fluid in the pore spaces. Porosity and water saturation estimates can be obtained using log data along with drilling

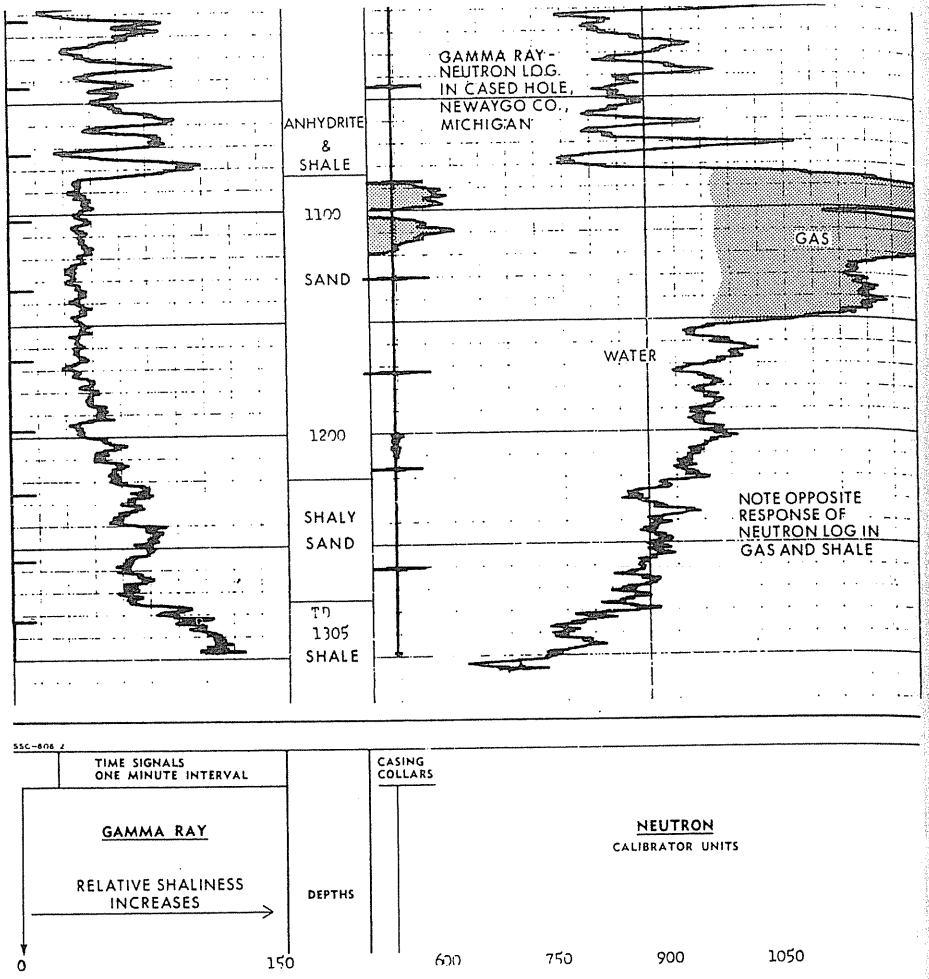

FIGURE 7-16
Gamma ray neutron log.

fluid information. The zone from 14,595 to 14,640 ft had an initial production of 69 BOPD (bbl/day, oil) and 3015 MCFGD (Mcf/day, gas).

Cased Hole Logs

The logs taken after the casing is set and cemented use gamma rays, neutrons, or sound waves to communicate from inside the pipe to cement and/or formation beyond the drilled hole. Some of the logs may be run on uncased hole as well.

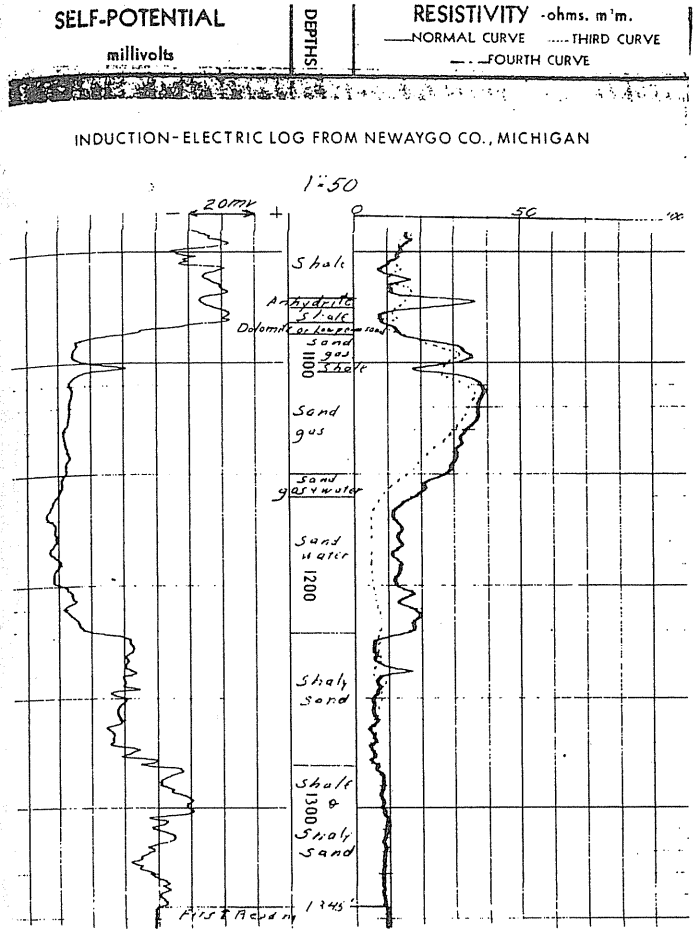

FIGURE 7-17
Electrical log, self potential and resistivity.

The presentation here includes:

Gamma ray neutron logs
Noise logs
Cement bond logs
Temperature logs
Casing inspection logs

Temperature log. Temperature logs are run commonly for several purposes. A sensitive thermocouple is attached to an insulated cable, and the fluid temperature

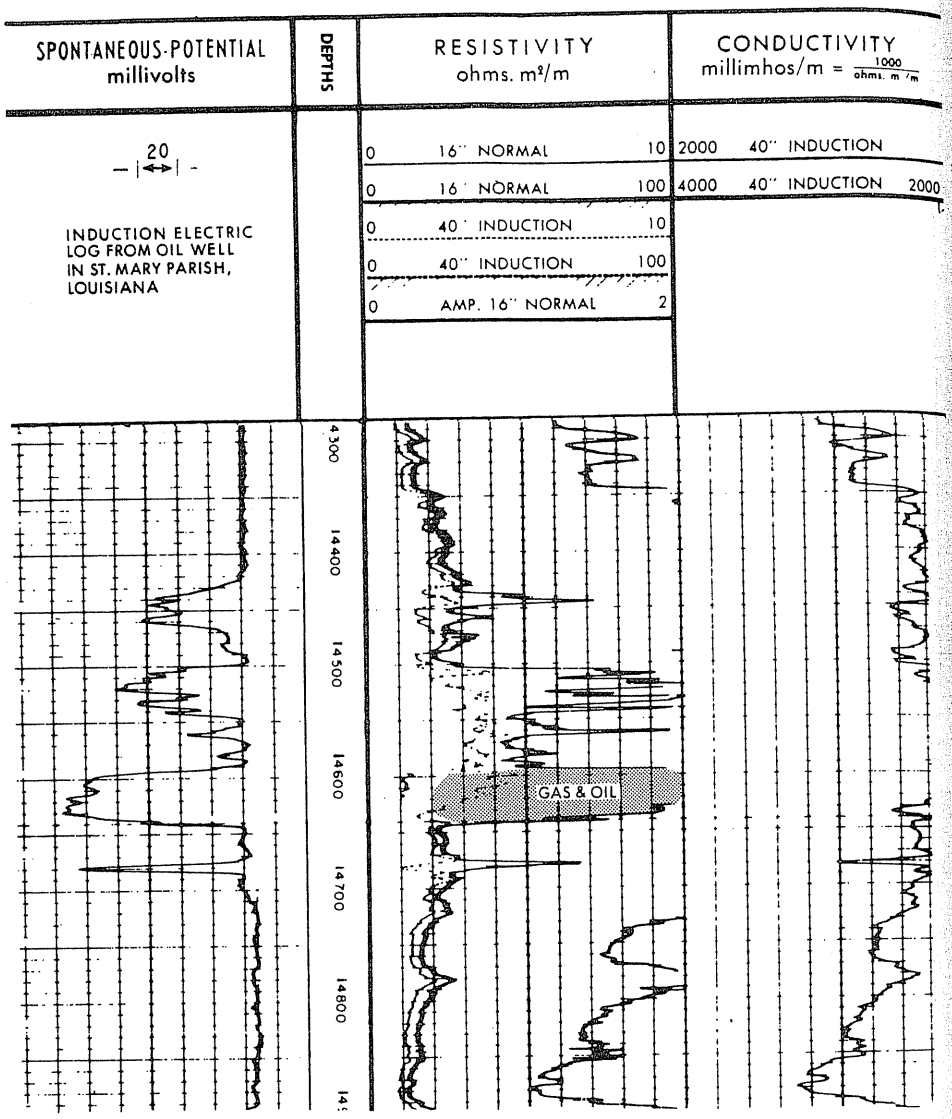

FIGURE 7-18
Induction log.

in the wellbore is traced. Anomalies are found in the temperature curve when fluid in the wellbore is passing through imperfections in the pipe. Joule-Thomson cooling by gas expansion can locate gas leaks, as illustrated later.

Gamma ray neutron log. The gamma ray neutron log, in combination with a cement bond log, is the most frequently run log in the gas storage industry. The

primary application of the gamma ray log is the identification and correlation of the various rock formations penetrated by the well. The neutron log, on the other hand, affords a means of locating porous intervals in the formations. In gas storage wells, for example, the neutron curve can be used to detect vagrant gas accumulations behind the casing and the gas bubble thickness in the storage reservoir.

All rock units exhibit a certain level of radioactivity. The gamma ray log is a measurement of the natural, or primary, gamma rays emitted from the various rock units. The companion log, the neutron log, measures induced radiation from a self-contained source of high-energy neutrons that bombard the formations.

Four basic types of detectors have been used; ionization chambers, Geiger-Mueller detectors, scintillation detectors, and proportional counters, although the latter are used only in neutron logging.

With the exception of the scintillation detectors, the detectors operate by the ionization of an inert gas by gamma rays intercepted by the chamber. Scintillation detectors are relatively large crystals (sodium or cesium iodide) that produce flashes of light when struck by gamma radiation.

Both logs can be run in either open holes or cased holes, regardless of the type of fluid in the wellbore or casing (i.e., air, gas, and/or water). Figure 7-19 is a gamma ray neutron log from a well in the Lincoln gas storage field in Clare County, Michigan. The well was selected primarily because of the two gas accumulations that are evident behind the production casing at 500 ft (152 m) and 1100 ft (335 m).

Noise log. The noise log can identify both single- and two-phase fluid movement inside and outside well casings. The log is particularly useful in interpreting or locating well problems such as cement channels, annular gas pressure, increasing rate of water production, and casing leaks.

The down-hole instrument contains an extremely sensitive microphone. The surface equipment includes the power supply, amplifiers, filters, and four digital voltmeters. Four prime frequencies are used: 200, 600, 1000, and 2000 Hz. The band pass filter for 200 Hz passes all frequencies above 200; similarly, the 600-Hz filter includes all frequencies above 600, the 1000-Hz filter includes all above 1000, and the 2000 Hz filter includes all above 2000. The log is not continuously recorded. Instead, the instrument is positioned at closely spaced intervals and the data from each of the four voltmeters is recorded when they stabilize. The microphone is so sensitive that noise from the cable and tool movement can mask the sounds that should be recorded.

Generally, when low frequencies predominate, it probably indicates two-phase movement. When midrange frequencies are evident, the flow is probably single-phase. Figure 7-20 shows gas entry into a fluid column at the 1480-ft (451-m) level and possible gas movement above 1200 ft (366 m) behind the casing.

Cement bond log. The specific purpose of the cement bond log is to evaluate the characteristics of the cement sheath around the casing. The various determi-

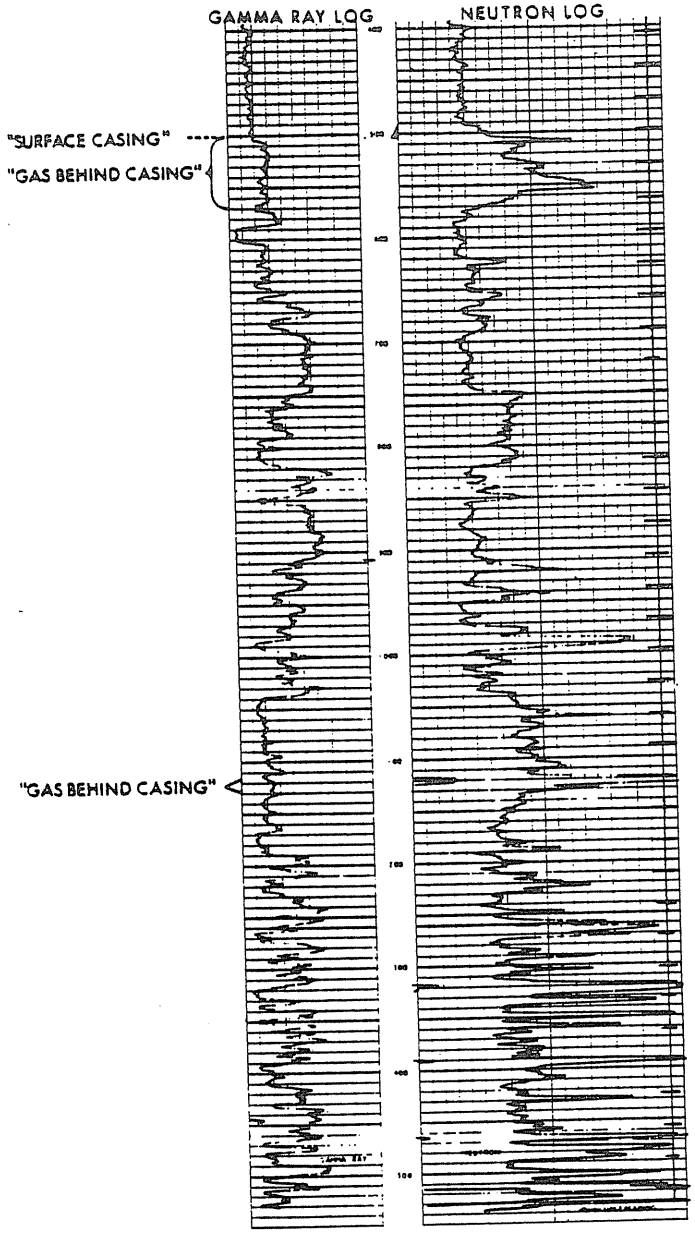

FIGURE 7-19
Gamma ray-neutron log from Lincoln Field, Clare Co., Michigan.

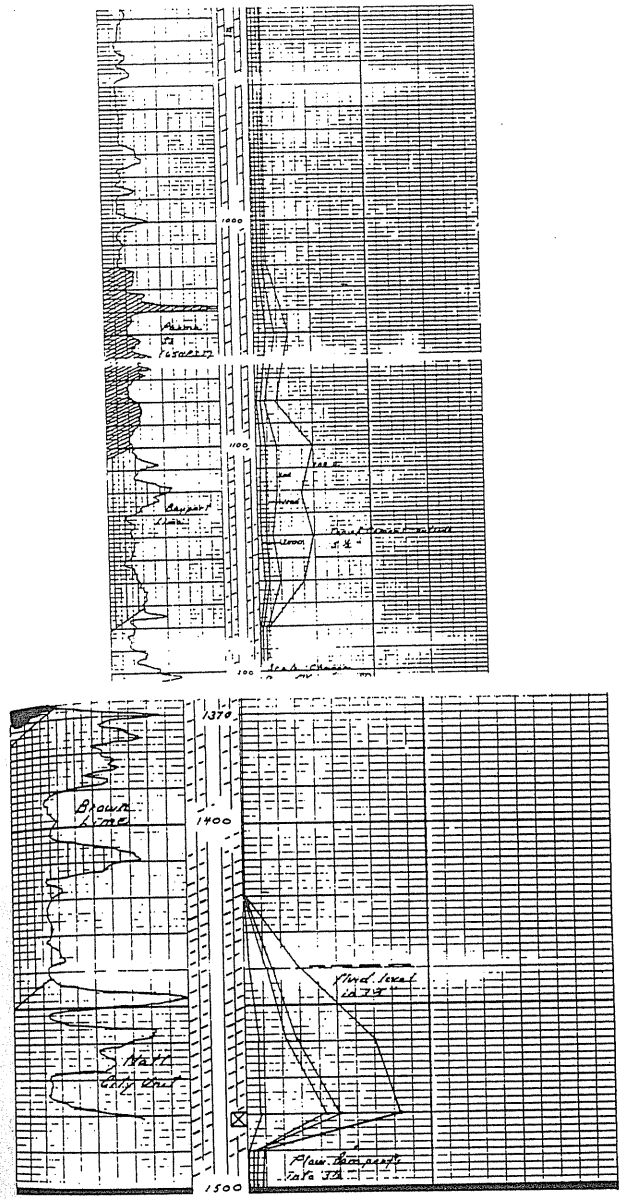

FIGURE 7-20
Noise log from Lincoln Field, Clare Co., Michigan.

nations include the cement top and the degree of casing-to-cement and cement-to-formation bonding.

The cement bond logging instrument consists of an energy transmitter and a receiver. During logging, a 20,000-Hz signal leaves the transmitter at a rate of 60 times per second, travels through the borehole fluid, and hits the casing. If bonding is present between the casing cement and formation, the compressional wave will continue into the formation and generate a shear wave. If bonding is poor or not present, the compressional wave will travel down the casing and back to the receiver. The character of the returning full or half wave train reaching the receiver is displayed on an oscilloscope. The oscilloscope is scaled with time increasing either to the right or left (depending upon the particular service company). The resulting log shows the relative times that each signal in the wave train reaches the receiver.

The amount or type of bonding varies from no bond to partial bonding to good bonding. Frequently, large intervals of partial bonding are evident. This may indicate a cement channel behind the casing or a "micro-annulus." In order to identify the latter, pressure is applied to the fluid column and the log repeated. The slight expansion of the casing will eliminate the micro-annulus, and increased bonding will be shown in intervals that had shown partial bonding.

Figure 7-21 is also from the Lincoln field in Clare County, Michigan. It illustrates a very poor to no-bonding interval below 1400 ft (427 m), a bonded interval above, and the top of cement.

Casing inspection log. It is necessary to evaluate the external and internal condition of well casings for possible defects. The actual depth of penetration is determined by measuring the deflection of the pit and referring to the appropriate charts for the particular weight and grade of the casing.

In a casing inspection log, four channels are recorded. The FL-1 and FL-2 channels are flux leakage circuits, each of which investigate the entire circumferential area of the casing. Defects, usually pitting, are located and recorded by position (measured from the wellhead). The third channel is the discriminator, or eddy current circuit, which is used to differentiate between internal and external defects. The fourth channel is the average; it evaluates the cross-sectional areas of the casing and aids in identifying casing collars, centralizers, scratchers, and other external well completion equipment. The instrument can be run with any type of fluid—water, air, or gas—in the casing.

Figure 7-22*a* shows a Class IV defect near the center of joint 21, with 89 percent penetration. Since both FL curves "saw" the slit, it was in the area of overlap between an FL-1 and a corresponding FL-2 shoe. Note the small average response indicating that probably only one FL-1 shoe identified the penetration. Figure 7-22*b* is a repeat of the same interval. On this run, the FL-2 curve shows the largest deflection, whereas on the first run, the FL-1 was the largest. This is characteristic of a good repeat. Because of the rotation of the instrument in the casing, it would be unusual if an exact repeat occurred.

The prediction and the monitoring of corrosion in gas pipelines is discussed in reference [7-8].

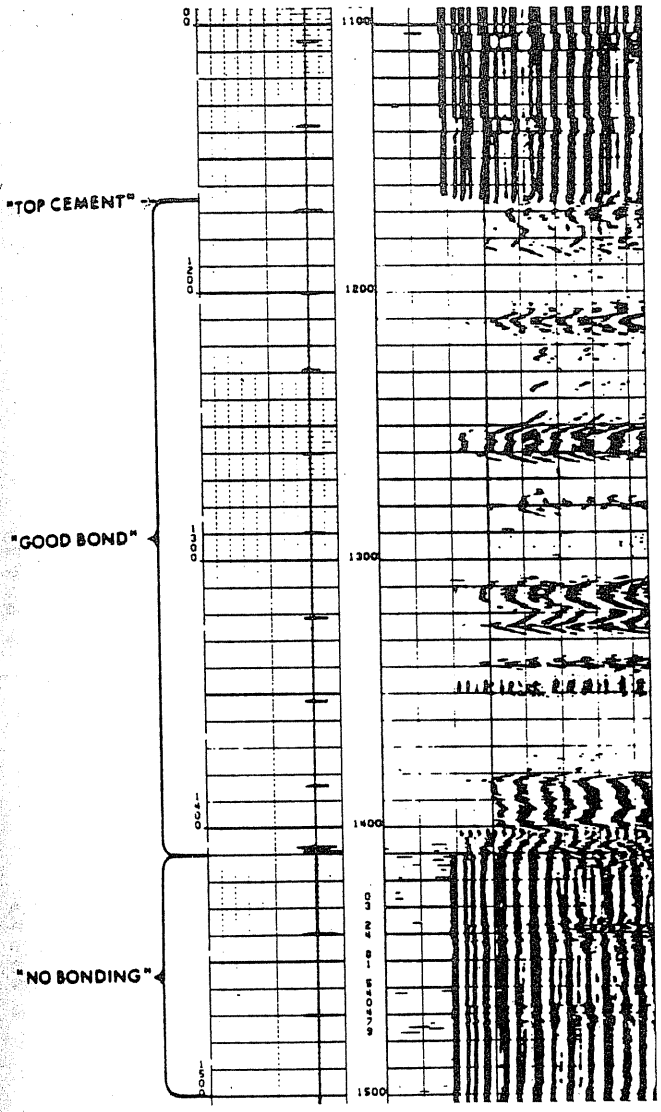

Cement bond log from Lincoln Field, Clare Co., Michigan.

Literature on Logging

Major logging organizations have booklets describing the logs in their repertoire. Frequent articles appear in the literature showing advances being made and experience in the use of logs. Most subjects can be found in [7-1,7-3,7-13,7-14] and the references of SPE monograph [7-8].

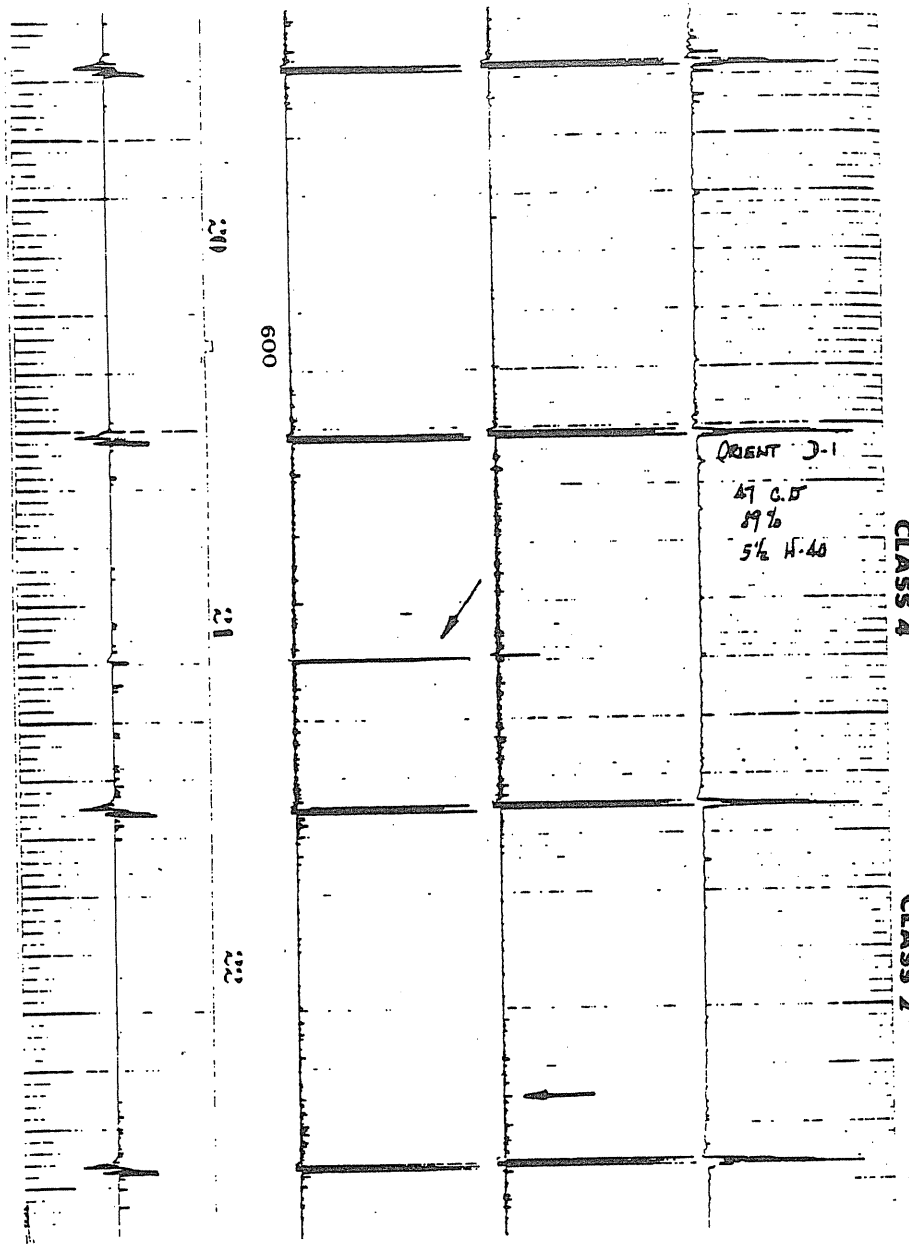

FIGURE 7-22
(*a*) A casing inspection log.

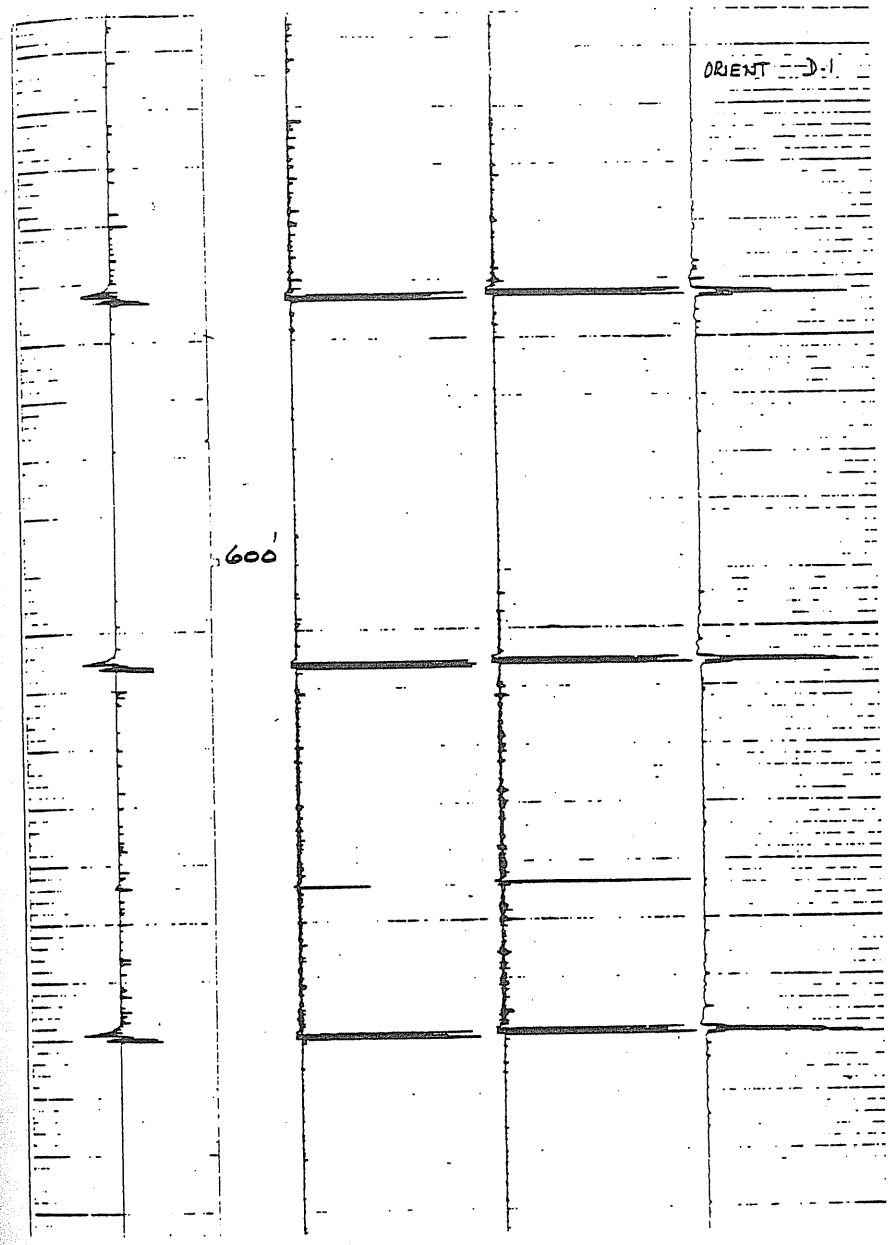

FIGURE 7-22
(*b*) Repeat casing inspection.

REFERENCES

7-1. Clark, J. B., "A Hydraulic Process for Increasing the Productivity of Wells," *Trans. AIME*, Vol. 186, 1 (1949).

7-2. de Laguna, W. H., O. Weeren, F. T. Binford, E. J. Witkowski, and E. G. Struxness, "Safety Analysis of Waste Disposal by Hydraulic Fracturing at Oak Ridge," *ORNL 4665*, Waste Disposal and Processing (1971).

7-3. Fertl, W. H., "Well Logging and Its Application to Cased Holes," *J. Pet. Tech.*, Vol. 36, No. 2, 249–266, Feb. (1984).

7-4. Fogler, H. S. and E. R. Crain, "Stimulation of Gas Storage Fields to Restore Deliverability," *J. Pet. Tech.*, Vol. 32, No. 9, 1612–1620, Sept. (1980).

7-5. Giuliano, F. A., *Introduction to Oil and Gas Technology*, Intercomp-SSI, Houston, Texas (1981).

7-6. Grundmann, S. R., and D. L. Lord, "Foam Stimulation," *J. Pet. Tech.*, Vol. 35, No. 3, 597–602, March (1983).

7-7. Howard, G. C., and C. R. Fast, *Hydraulic Fracturing*, SPE Monograph, Richardson, Texas (1970).

7-8. Jorden, J. R., and F. L. Campbell, *Well Logging I—Rock Properties, Borehole Environment, Mud and Temperature Logging*, SPE Monograph, Richardson, Texas (1984).

7-9. Kelly, John J., "Drilling Now," *Trans. SPE*, Vol. 271, 2293–2296 (1981).

7-10. Mincy, J. E., "A Practical Approach to Predicting and Monitoring Internal Corrosion in Gas Pipelines," *AGA Operating Section Proceedings*, 100–114 (1985).

7-11. Perkins, T. K., and L. R. Kern, "Widths of Hydraulic Fractures," *Trans. SPE*, Vol. 222, 937 (1961).

7-12. Sarda, Jean-Paul, "Use of High Strength Ceramic Beads for Propping Deep Hydraulic Fractures," *Trans. SPE*, Vol. 271, 55–56, (1981).

7-13. Szilas, A. P., *Production and Transport of Oil and Gas*, Elsevier Scientific Publishing Co., New York (1975).

7-14. Wiese, H. C., "TDT™ Log Applications in California," *J. Pet. Tech.*, Vol. 35, No. 2, 429–444, Feb. (1983).

7-15. Yuster, J. T. , and J. C. Calhoun, "Pressure Parting of Formations in Water Flood Operations," *Oil Weekly*, Vol. 117, 34 (1945).

CHAPTER 8

FLOW IN THE RESERVOIR AND ADJACENT AQUIFER

The total flow system for a reservoir is illustrated in Fig. 8-1. The system consists of four steps: (1) pipe flow in surface facilities, which was described in Chapters 3 and 6, (2) vertical flow in the wellbore, as given in Chapter 6, (3) gas flow through porous media toward the wellbore, and (4) water movement on the edge of the gas bubble. This chapter concentrates on the last two elements.

Two-phase flow (such as gas/water or gas/condensate) and three-phase flow (gas/condensate/water) will not be treated here; their complexity may demand full-scale simulation. In the first part of this chapter, the single-phase gas flow equation is derived and its solution at the wellbore obtained; it will be used to analyze gas testing (e.g., drawdown, buildup) data. This is the basis for determining in-situ rock properties around the wellbore. The water movement around the gas bubble is described by the pure liquid (water) equation and its solutions at the edge of the gas bubble, as discussed in the second part of this chapter.

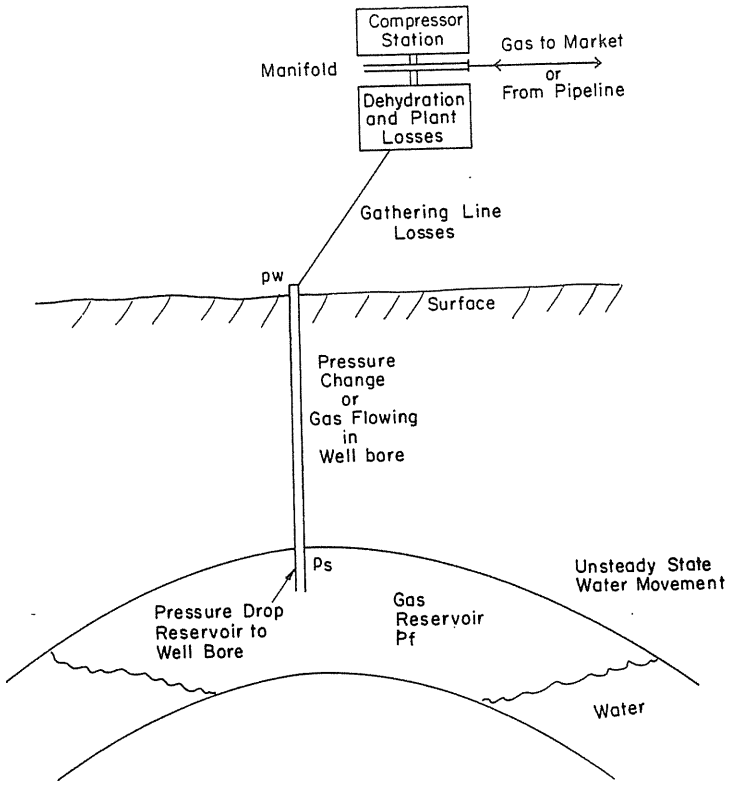

FIGURE 8-1
Components of underground storage flow system [Katz & Coats, 1-2].

8.1 PRESSURE DROP FROM RESERVOIR TO WELLBORE—A SIMPLIFIED STEADY STATE APPROACH

Determinations of the permeability of the rock from core data and of the geometry of the gas reservoir permit calculations of gas flow rates and pressure drops, when a series of assumptions is employed. Production from a gas reservoir almost never operates in steady state; if the flow rate is fixed, the well pressure decreases; see Fig. 8-2. If the well pressure be fixed, the flow rate decreases with production time.

By combining the viscous Darcy equation and radial geometry with fixed well and drainage dimensions, a flow equation assuming a pseudo (or quasi) steady state is derived as follows, in field units (see Table 8.1):

$$\overline{P}_f^2 - P_w^2 = 1.422 \times 10^6 \frac{T\overline{\mu Z} Q}{kh} \ln\left(\frac{r_d}{r_w}\right) \tag{8.1}$$

where temperature T, average viscosity $\overline{\mu}$, average compressibility factor $\overline{Z}$,

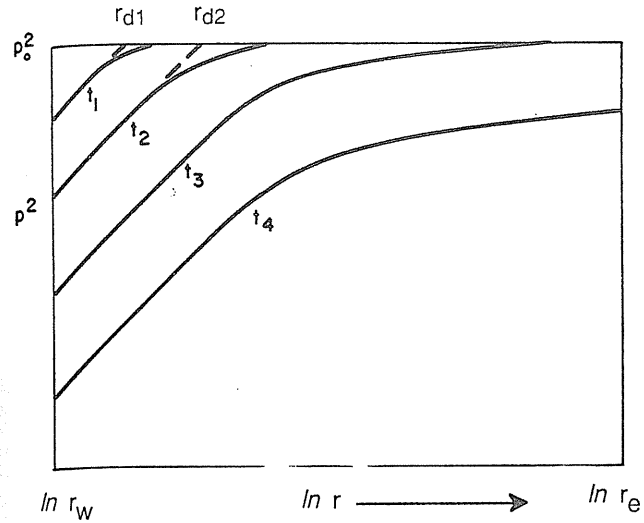

FIGURE 8-2
Typical variation of pressure in a reservoir with time [Katz & Coats, 1-2].

formation thickness h, and permeability k are assumed to be constant. $\overline{P}_f$ and P_w are average formation and wellbore pressures; flow rate Q is at standard conditions (14.7 psia, 60°F, or 101.325 kPa, 288.15K). The variable r_w is the well radius, and r_d is defined as the drainage radius (this will be discussed in Section 8.3). Typical pressure profiles are shown in Fig. 8-3.

If one accepts that all flow in porous media requires the β (quad-Darcy) term, then the equation derived is

$$\overline{P}_f^2 - P_w^2 = 1.422 \times 10^6 \frac{T\mu\overline{Z}}{kh} \ln\left(\frac{r_d}{r_w}\right) Q + 3.161 \times 10^{-6} \frac{\beta G \overline{Z} T}{h^2} \left(\frac{1}{r_w} - \frac{1}{r_d}\right) Q^2 \tag{8.2}$$

where β is in the unit of ft^{-1}. These simplistic equations permit drawing a generalized flow chart, which relates the pressure squared difference (ΔP^2) between reservoir and wellbore terms to Q/kh for a given well.

From this simple model one can derive equations for the unsteady state and for interpreting pressure drop–flow rate data to find

1. permeability reduction at wellbore (skin effect)
2. stimulation effect (negative skin)
3. extra pressure drop caused by the β coefficient (high-velocity effect)
4. duration time for unloading initial wellbore contents (wellbore storage effect)
5. radius of drainage, r_d, at any time

This analysis uses the pseudopressure $m(P)$, which is believed to accommodate the variations of μ and Z due to pressure changes (gas property variation effect). Also, one must know whether the well completion includes the full gas zone

TABLE 8.1
Definition of dimensionless variables for radial-cylindrical system

Variables:	Gas, pressure squared P^2	Gas, pseudopressure $m(P)$	Liquid, pressure P
r_D	$\frac{r}{r_w}$	$\frac{r}{r_w}$	$\frac{r}{r_w}$
t_D	$\frac{\lambda kt}{\phi\overline{\mu c}r_w^2}$	$\frac{\lambda kt}{\phi\mu_i c_i r_w^2}$ *	$\frac{\lambda kt}{\phi\mu c r_w^2}$
P_D	$\frac{P_i^2 - P^2}{P_i^2 Q_D}$	$\frac{m_i - m}{m_i Q_D}$	$\frac{P_i - P}{P_i Q_D}$
Q_D	$\frac{\gamma\overline{Z\mu}TQ_{sc}}{khP_i^2}$	$\frac{\gamma TQ_{sc}}{khm_i}$	$\frac{\gamma B\mu Q_{sc}}{khP_i}$
C_D	$\frac{\eta V_w C_w}{\phi h\bar{c}r_w^2}$	$\frac{\eta V_w C_w}{\phi hcr_w^2}\left(\frac{c\mu}{c_i\mu_i}\right)$	$\frac{\eta V_w C_w}{\phi hcr_w^2}$
N_T	$\frac{\theta k^2\beta G P_i^2}{T\bar{\mu}^2\bar{Z}r_w}$	$\frac{\theta k^2\beta G m_i}{T\mu_i r_w}$	—
	Constants for above definitions		
Darcy units:			
λ	1	1	1
γ	$\frac{1}{\pi}\frac{P_{sc}}{T_{sc}}$	$\frac{1}{\pi}\frac{P_{sc}}{T_{sc}}$	$\frac{1}{2\pi}$
η	$\frac{1}{2\pi}$	$\frac{1}{2\pi}$	$\frac{1}{2\pi}$
θ	1.745×10^{-7}	1.745×10^{-7}	—
Field units:			
λ	2.637×10^{-4}	2.637×10^{-4}	2.637×10^{-4}
γ	1.422×10^{6}	1.422×10^{6}	141.2
η	$\frac{1}{2\pi}$	$\frac{1}{2\pi}$	$\frac{1}{2\pi}$
θ	1.564×10^{-18}	1.564×10^{-18}	—
Metric units:			
λ	3.6×10^{-3}	3.6×10^{-3}	3.6×10^{-3}
γ	1.295	1.295	1.842×10^{3}
η	$\frac{1}{2\pi}$	$\frac{1}{2\pi}$	$\frac{1}{2\pi}$
θ	2.069×10^{-15}	2.069×10^{-15}	—

Units of measurement

Parameters	Darcy	Field	Metric
r	cm	ft	m
k	darcy	md	mD (= 1.01033 md $= 10^{-15}$ m^2)
t	s	hr	hr
T	K	°R	K
μ	cp	cp	μPa · s
P	atm	psia	kPa
V	cm^3	ft^3	m^3
Q	cm^3/s	MMcf/day (gas) bbl/d (oil)	m^3/day
β	cm^{-1}	ft^{-1}	m^{-1}

* $\mu_i c_i$ is written for simplicity; one may use average value, $\overline{\mu c}$.
† μ_i and c_i could be replaced by $\bar{\mu}$ and $\bar{c}$ if $\overline{\mu c}$ is used in t_D.

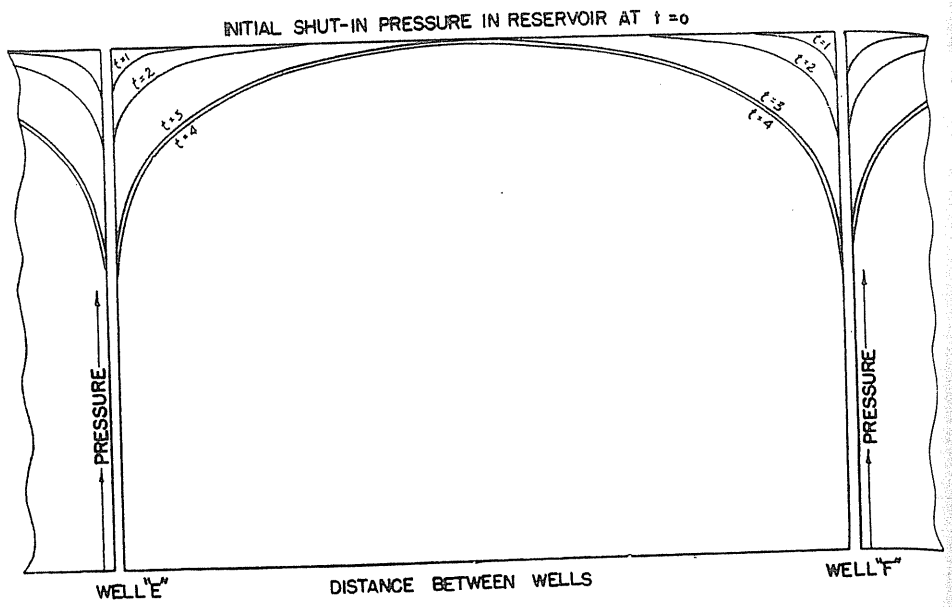

FIGURE 8-3
Pressure profiles [Katz et al., 1-1, courtesy McGraw-Hill Publishing Co.].

thickness or just a partial penetrated well. The computation of in-situ permeability near the wellbore uses unsteady state relationships, which also can be used to determine the reservoir limit.

8.2 BASIC FLUID FLOW EQUATIONS

Several basic equations are needed to derive the flow equation for porous media:

Continuity equation (conservation of mass)
Equation of state ($\rho = PM/ZRT$)
Flow rate equation[1] ($-dP/dr = (\mu/k)u + \beta\rho u^2 + \cdots$)

The continuity equation is a generalization of mass conservation:

Rate of mass flow in − rate of mass flow out
= rate of mass accumulation; divergence of $\rho\bar{u}$

$$-\frac{\partial}{\partial t}(\phi\rho) = \nabla \cdot (\rho\bar{u})$$

$$= \frac{\partial(\rho u_x)}{\partial x} + \frac{\partial(\rho u_y)}{\partial y} + \frac{\partial(\rho u_z)}{\partial z} \quad \text{for Cartesian coordinates } (x, y, z)$$

[1] All derivations of this chapter are in Darcy units unless mentioned otherwise.

$$= \frac{1}{r}\frac{\partial}{\partial r}r(\rho u_r) + \frac{1}{r}\frac{\partial(\rho u_\theta)}{\partial\theta} + \frac{\partial(\rho u_z)}{\partial z} \quad \text{for cylindrical coordinates } (r, \theta, z) \tag{8.3}$$

where ϕ is the porosity, ρ the density, and $\bar{u}$ the superficial velocity vector; the ∇ operator is given in references [8-17,8-22] in terms of rectangular, cylindrical, and spherical coordinates.

Considering the geometry of a gas well and its surroundings, as shown in Fig. 8-4, a cylindrical model is most suitable for describing the flow in reservoirs. Hence, in a one-dimensional case, Eq. (8.3) becomes

$$-\frac{\partial}{\partial t}(\phi\rho) = \frac{1}{r}\frac{\partial}{\partial r}r\rho u \tag{8.4}$$

Usually the gravity force $\rho z(g/g_c)$ in the z direction is negligible for gas. The rate equation derived by truncating the higher-order terms (u^3, u^4, . . .) is

$$-\frac{dP}{dr} = \frac{\mu}{k}u + \beta\rho u^2 \quad \text{or} \quad u = -\frac{k}{\mu}\delta\frac{dP}{dr} \tag{8.5}$$

where μ is the viscosity, β the high-velocity coefficient, and δ the flow correction factor:

$$\delta = \left(1 + \frac{\beta\rho k u}{\mu}\right)^{-1} \tag{8.6}$$

For a real gas,

$$\rho = \frac{PM}{ZRT} \tag{8.7}$$

where M is the gas molecular weight, Z the compressibility factor, R the gas

r_w - WELL RADIUS
r_d - EFFECTIVE DRAINAGE RADIUS
r_e - RESERVOIR RADIUS

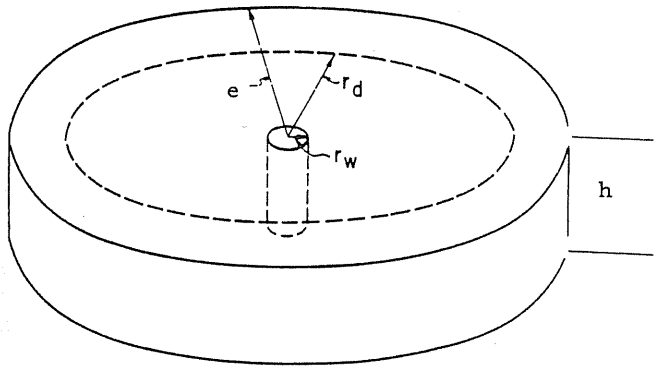

FIGURE 8-4
Model for horizontal radial flow [Katz & Coats, 1-2].

constant, and T the reservoir temperature. Combining Eqs. (8.4), (8.5), and (8.7) results in

$$\frac{\phi}{k}\frac{\partial}{\partial t}\left(\frac{P}{Z}\right) = \frac{1}{r}\frac{\partial}{\partial r}r\left(\frac{P}{\mu Z}\delta\frac{\partial P}{\partial r}\right) \tag{8.8}$$

which assumes that the reservoir is isothermal (no temperature change). Additional assumptions required for Eq. (8.8) are as follows:

Assumption 1: A radial cylindrical model (one-dimensional flow).

Assumption 2: Single-phase flow (only gas flow).

Assumption 3: The reservoir is homogeneous: k is the same despite the position ($k \neq f(r)$) and the Klinkenberg effect is negligible ($k \neq f(P)$); also porosity ϕ is constant.

Assumption 4: The gravity effect is negligible ($\partial P/\partial z + \rho g \approx 0$).

The validity of these assumptions is essential to applications of Eq. (8.8).

The high nonlinearity caused by the presence of the flow correction factor δ renders the equation insolvable. An additional assumption is needed:

Assumption 5: Flow is viscous ($\beta = 0$; $\delta = 1$).

With this assumption, Eq. (8.8) becomes

$$\frac{\phi}{k}\frac{\partial}{\partial t}\left(\frac{P}{Z}\right) = \frac{1}{r}\frac{\partial}{\partial r}r\left(\frac{P}{\mu Z}\frac{\partial P}{\partial r}\right) \tag{8.9}$$

Appendix C gives details of further expansions of Eq. (8.8) in terms of pressure P [8-36], pressure squared P^2 [1-1], or pseudopressure (real gas potential) $m(P)$ [8-6]:

$$m(P) = 2\int_0^P \frac{P'}{\mu Z}dP' \tag{8.10}$$

Figure 8-5 shows $m(P)$ for a particular gas ($G = 0.6$) at a certain temperature ($T =$ 580°R), and the corresponding values of μZ. The following is a brief description of the assumptions involved and the resulting equations:

Flow equation in terms of pressure P (for liquid flow, $\delta = 1$):

$$\frac{1}{r}\frac{\partial}{\partial r}r\delta\frac{\partial P}{\partial r} = \frac{\phi\mu c}{k}\frac{\partial P}{\partial t} \tag{8.11}$$

Assumption 6: Pressure gradients are small, $(\partial P/\partial r)^2 \rightarrow 0$, or $P/(\mu Z)$ is constant.

Flow equation in terms of pressure squared P^2:

$$\frac{1}{r}\frac{\partial}{\partial r}r\delta\frac{\partial P^2}{\partial r} = \frac{\phi\mu c}{k}\frac{\partial P^2}{\partial t} \tag{8.12}$$

Assumption 7: Pressure squared gradients are small, $(\partial P^2/\partial r)^2 \rightarrow 0$, or μZ is constant.

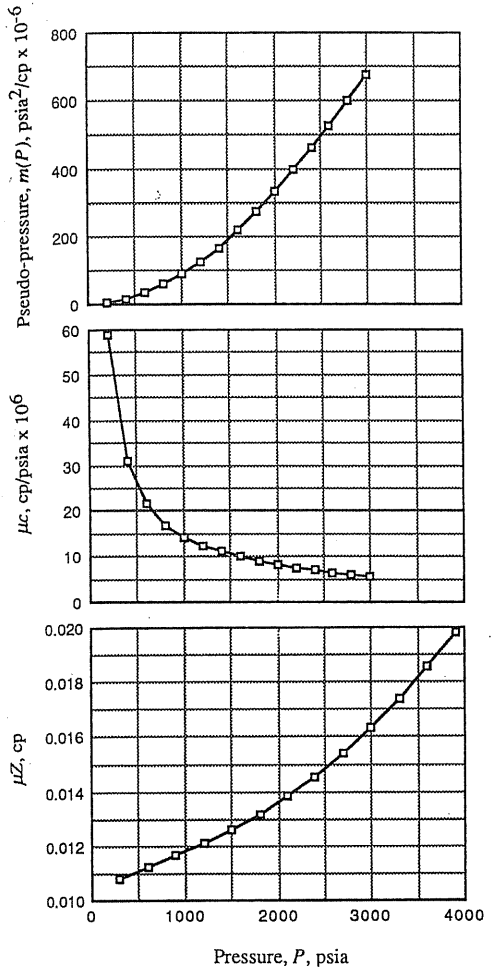

FIGURE 8-5
Plots of $m(P)$, μc, and μZ vs. P($G = 0.6$ and $T = 580$°R).

Flow equation in terms of pseudopressure m(P) (for gas flow):

$$\frac{1}{r}\frac{\partial}{\partial r}r\delta\frac{\partial m(P)}{\partial r} = \frac{\phi\mu c}{k}\frac{\partial m(P)}{\partial t} \tag{8.13}$$

Eq. (8.13) is the most rigorous form of various flow equations. Assumptions 6 and 7 could be fatal to a high–flow rate process or in a tight formation where high pressure gradients are expected. If a pressure drawdown, ΔP, is less than 200 psia, according to Fig. 8-5, the μZ may be approximated by a constant value for low pressure range and the $P/(\mu Z)$ is constant for high pressure range. The cutoff point of these two ranges may be arbitrarily chosen as at $P = 2000$ psia. It may suggest that Eq. (8.11) is valid for $P > 2000$ psia and Eq. (8.12) is for $P < 2000$ based on Assumptions 6 and 7. However, Fig. 8-5 does not

restrict the ranges of applying Eq. (8.11) in terms of P and Eq. (8.12) in terms of P^2; actually, it only represents a single case. For a high-temperature reservoir with reduced temperature $T_r < 1.35$, the choice of P or P^2 for high or low pressure, respectively, may result in serious error, because the product μZ behaves abnormally as indicated in Fig. 8-6 [8-9].

Even assuming $\delta = 1$, the gas flow equation [Eq. (8.11)] is not completely linear, because product μc varies significantly when the pressure is low (Fig. 8-5). In an attempt to achieve total linearity, Agarwal [8-3] introduced the concept of pseudotime:

$$t_a = \int_0^t \frac{1}{\mu c} dt' \tag{8.14}$$

to interpret the buildup data. However, it cannot be tabulated as pseudopressure without knowing the pressure profile of time. It is also mathematically insufficient to achieve total linearity of the flow equation. For details, refer to Lee [8-31], Lee and Holditch [8-30], and Aaronsen [8-2].

General Flow Equation in Dimensionless Forms

Eqs. (8.11), (8.12), and (8.13), in terms of P, P^2, and $m(P)$, respectively, are in similar form and could be generalized as

$$\frac{1}{r}\frac{\partial}{\partial r} r\delta \frac{\partial \psi}{\partial r} = \xi \frac{\partial \psi}{\partial t} \tag{8.15}$$

	ψ	ξ
Pressure	P	$(\phi\overline{\mu c})/k$
Pressure squared	P^2	$(\phi\overline{\mu c})/k$
Pseudopressure	$m(P)$	$(\phi\mu_i c_i)/k$ or $(\phi\overline{\mu c})/k$

The average value $\overline{\mu c}$ product should be used for P, P^2, and $m(P)$ expressions. For simplicity, the use of $\mu_i c_i$ (product of μ and c evaluated at initial conditions) is suggested for the $m(P)$ approach. For modifications by pseudotime ratio, see Lee [8-31].

The general dimensionless form is

$$\frac{1}{r_D}\frac{\partial}{\partial r_D}\left(r_D \delta \frac{\partial P_D}{\partial r_D}\right) = \left(\frac{\partial P_D}{\partial t_D}\right) \tag{8.16}$$

Solutions of Eq. (8.16) ($\delta = 1$) for various relevant boundary conditions have been obtained by Carslaw and Jaeger [8-11]. The dimensionless groups are defined in Table 8.1 [8-17] for the various modes of flow.

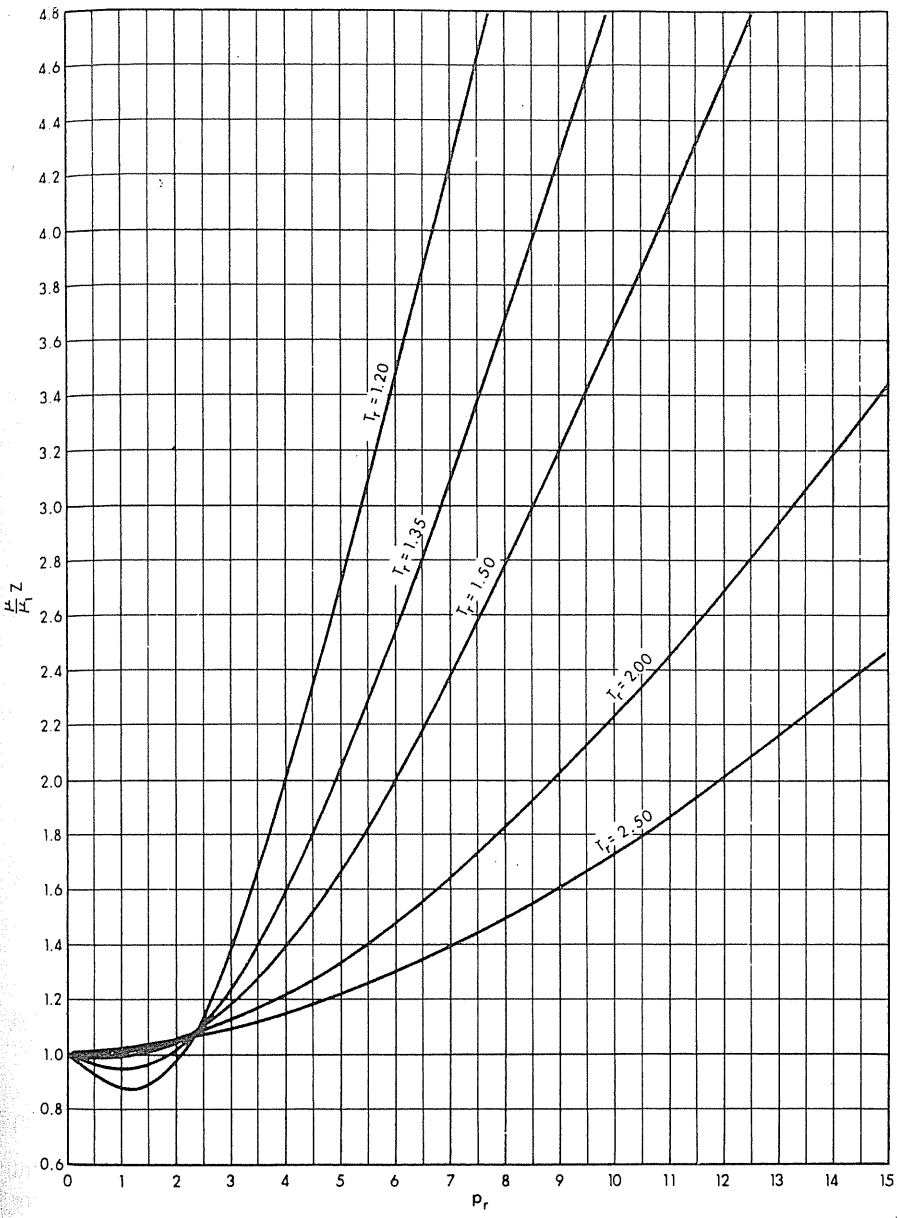

FIGURE 8-6
Variation of $(\mu/\mu_1)Z$ with reduced temperature and pressure [Aziz, et al., 8-9, courtesy *J. Can. Pet. Tech.*].

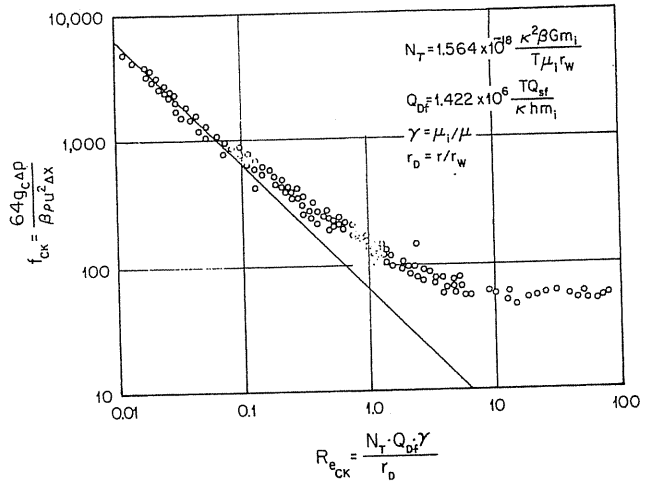

FIGURE 8-7
Friction factor–Reynolds number plot [After Cornell & Katz, 8-15, Lee, 8-29].

The flow correction factor δ also can be generalized in dimensionless form:

$$\delta = \frac{1}{1 + \mathrm{Re}_{CK}}$$

$$\mathrm{Re}_{CK} = \frac{N_T Q_{Df} (\mu_i/\mu)}{r_D} \tag{8.17}$$

where Re_{CK} is the porous-media Reynolds number defined by Cornell and Katz [8-15] and modified into wellbore conditions by Lee, Logan, and Tek [8-30] (Fig. 8-7); and Q_{Df} is the flow rate at sandface in terms of standard conditions (14.7 psia, 60°F; 101.3 kPa, 15°C).

Boundary Conditions

For a withdrawal or injection process, the difference between the amount of gas withdrawn from the wellhead and the gas flow through the sandface should be equal to wellbore accumulation—see Fig. 8-8 [8-37]:

$$Q_{sf} \text{ sandface} - Q_{sc} \text{ wellhead} = \text{accumulation rate of wellbore content} \tag{8.18}$$

where Q_{sc} and Q_{sf} are the flow rates at wellhead and sandface, all in standard conditions (14.7 psia, 520 °R, or 101.3 kPa, 15°C). Q and q denote volumes for standard (SC) and reservoir conditions respectively throughout this chapter, and Q could be regarded as the equivalent to mass flow rate (379.5 ft^3 of gas in SC = 1 lb mol).

Using the rate equation to express the flow rate at sandface:

$$q_{sf} = -2\pi r h u = \frac{2\pi r h k}{\mu} \left(\delta \frac{\partial P}{\partial r} \right)_{\text{sandface}} \tag{8.19}$$

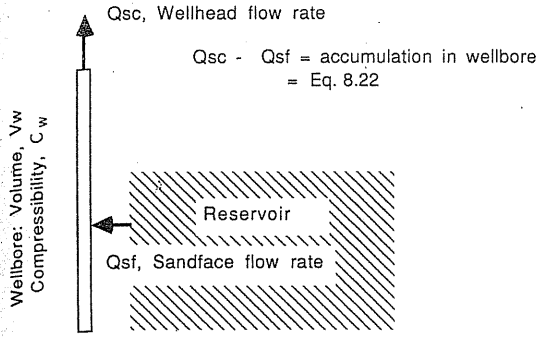

FIGURE 8-8
Sketch of boundary conditio
[Lee, 8-29].

In order to convert sandface flow rate q_{sf} to the standard-conditions flow rate Q_{sf}, the *formation volume factor* is defined:

$$B = \frac{q_{sf}}{Q_{sf}} = \frac{ZRT/P}{(ZRT/P)_{sc}} \approx \frac{P_{sc}}{P} \frac{T}{T_{sc}} \cdot Z \quad (Z_{sc} \approx 1) \tag{8.20}$$

Then Q_{sf} can be expressed as follows:

$$Q_{sf} = 2\pi k h \frac{T_{sc}}{P_{sc} T} r \delta \frac{P}{\mu Z} \frac{\partial P}{\partial r} \tag{8.21}$$

The wellbore accumulation rate depends upon the wellbore size, V_w, the overall pressure drop rate, dP/dt, and the overall compressibility of the gas inside the wellbore, C_w:

$$\text{Accumulation rate} = V_w \frac{T_{sc}}{P_{sc}} \cdot \left(\frac{C_w}{T} \frac{P}{Z} \frac{dP}{dt} \right)_{\text{wellbore}} \tag{8.22}$$

Furthermore, it is assumed that

$$\left(\frac{P}{TZ} \cdot \frac{dP}{dt} \right)_{\text{wellbore}} = \left(\frac{P}{TZ} \cdot \frac{\partial P}{\partial t} \right)_{\text{sandface}} \tag{8.23}$$

Combining Eq. (8.18) through (8.23), the general boundary conditions in dimensionless form are as follows (see Example 8.1).

$$\frac{Q_{sf}}{Q_{sc}} = -r_D \delta \frac{\partial P_D}{\partial r_D} = 1 - C_D \frac{\partial P_D}{\partial t_D}$$

$$C_D = \frac{\eta V_w C_w}{\phi h c r_w^2} \tag{8.24}$$

where C_D is the wellbore storage constant given in Table 8.1. Strictly speaking, C_D is not a constant, but is dependent on the ratio of wellbore overall compressibility C_w to sandface compressibility c. Since the above approach ignores the friction loss and the temperature gradient in the vertical pipe flow, C_D should be considered as an effective value rather than an actual one. Also, Eq. (8.23) is a questionable assumption that may imply that the steady state has been reached.

Example 8.1. Derive Eq. 8.24 in terms of P^2, all units are in Darcy units.

Solution. First calculate

$$\frac{\partial P_D}{\partial P} = -\frac{2Pkh}{\gamma Z \mu Q_{sc} T} \qquad \frac{\partial t_D}{\partial t} = \frac{\lambda k}{\mu \phi c r_w^2}$$

$$\frac{\partial r_D}{\partial r} = \frac{1}{r_w}$$

where P_D and r_D are listed in Table 8.1,

$$\gamma = \frac{1}{\pi}\frac{P_{sc}}{T_{sc}}, \quad \lambda = 1$$

Second, divide Eq. 8.21 with Q_{sc} and by chain rule.

$$\frac{Q_{sf}}{Q_{sc}} = \frac{2\pi kh}{Q_{sc}}\frac{T_{sc}}{P_{sc}T} r\delta \frac{P}{\mu Z}\frac{\partial P}{\partial r}$$

$$= \frac{2\pi kh}{Q_{sc}}\frac{T_{sc}}{P_{sc}T} r\delta \frac{P}{\mu Z}\left(\frac{\partial P}{\partial P_D}\right)\left(\frac{\partial P_D}{\partial r_D}\right)\left(\frac{\partial r_D}{\partial r}\right)$$

Substitute $(\partial P/\partial P_D)$ and $(\partial r_D/\partial r)$, then

$$\frac{Q_{sf}}{Q_{sc}} = -r_D \delta \frac{\partial P_D}{\partial r_D}$$

Combining Eq. 8.18 and 8.22,

$$Q_{sf} - Q_{sc} = V_w \frac{T_{sc}}{P_{sc}}\left(\frac{C_w}{T}\frac{P}{Z}\frac{dP}{dt}\right)$$

Divide by Q_{sc}

$$\frac{Q_{sf}}{Q_{sc}} = 1 + \frac{V_w}{Q_{sc}}\frac{T_{sc}}{P_{sc}}\left(\frac{C_w}{T}\frac{P}{Z}\frac{dP}{dt}\right)$$

Use of chain rule

$$\frac{Q_{sf}}{Q_{sc}} = 1 + \frac{V_w}{Q_{sc}}\frac{T_{sc}}{P_{sc}}\frac{C_w}{T}\frac{P}{Z}\left(\frac{\partial P}{\partial P_D}\right)\left(\frac{\partial P_D}{\partial t_D}\right)\left(\frac{\partial t_D}{\partial t}\right)$$

Substitute $(\partial P/\partial P_D)$ and $(\partial t_D/\partial t)$

$$\frac{Q_{sf}}{Q_{sc}} = 1 - C_D \frac{\partial P_D}{\partial t_D}$$

8.3 UNSTEADY STATE SOLUTION; CONSTANT TERMINAL RATE

Equation (8.16) with boundary condition Eq. (8.24) has not yet been solved analytically. All the previous work assumed viscous flow (no high-velocity effect: $\delta = 1$) [8-18] and went on to include the skin effect [8-3,8-19]. One would start from the assumptions of no high-velocity effect, no skin, and no wellbore storage

to derive the *line-source* solution. Then all effects of skin, wellbore storage, and high velocity would be incorporated into the line-source solution. The final equation would be used as the basis of various gas well–testing data analyses.

Line Source Solutions

First of all, the inner boundary r_w is replaced by a *line sink*[2] for simplicity. Witherspoon [1-43] reported that such approach yielded results practically identical to those derived from Eq. (8.24). This line sink concept modifies Eq. (8.24) to

$$\lim_{r_D \to 0} r_D \frac{\partial P_D}{\partial r_D} = -1 \tag{8.25}$$

At all times outer-boundary ($r \to \infty$) pressure is the same as the initial formation pressure:

$$P_D \to 0 \qquad \text{as} \qquad r_D \to \infty \text{ for all } t_D \tag{8.26}$$

The initial pressure is assumed to be equal throughout the reservoir:

$$P_D = 0 \qquad \text{at} \qquad t_D = 0 \text{ for all } r_D \tag{8.27}$$

Assuming Eqs. (8.25) through (8.27), Eq. (8.16) ($\delta = 1$) can be solved by using a Boltzmann transformation (for details see Appendix C), resulting in:

$$P_D = -\frac{1}{2}\,\mathrm{Ei}\left(-\frac{r_D^2}{4t_D}\right) \tag{8.28}$$

where Ei is the exponential integral, defined by

$$\mathrm{Ei}(X) = \int_{-\infty}^{X} \frac{e^{-\epsilon}}{\epsilon} d\epsilon \tag{8.29}$$

where ϵ is a dummy variable of integration. For X less than 0.01, Eq. (8.28) can be approximated as

$$P_D = \frac{1}{2}\left[\ln\left(\frac{t_D}{r_D^2}\right) + 0.80907\right] \tag{8.30}$$

At the wellbore ($r_D = 1$), Eq. (8.30) becomes

$$P_{DW} = \frac{1}{2}[\ln(t_D) + 0.80907] \qquad t_D > 25 \tag{8.31}$$

where subscript DW denotes dimensionless form at the wellbore condition.

Eq. (8.31) is obtained by assuming that the reservoir behaves as an infinite one (Eq. 8.26). For a finite reservoir, the pressure drop at the wellbore will

[2] Instead of solving the equation at r_w, it is solved at $r \to 0$, center of the well.

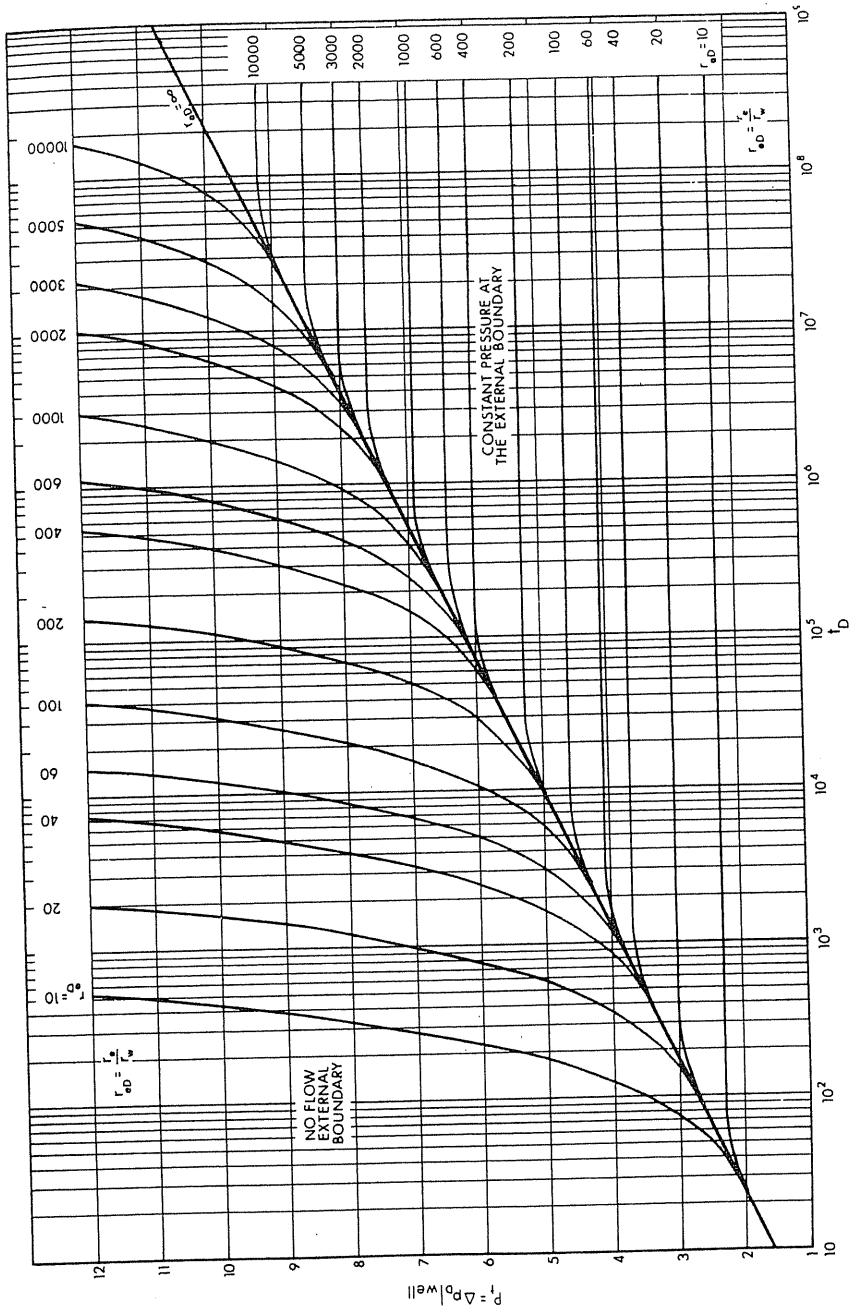

FIGURE 8-9
Values of P_D at wellbore for various finite circular reservoirs with no flow at the external boundary [Aziz & Flock, 8-8, courtesy *J. Can. Pet. Tech.*]

deviate from Eq. (8.31) after some time. Figure 8-9 shows the time at which this deviation occurs for different reservoir sizes. In the figure, r_{eD} (r_e/r_w) is the dimensionless reservoir external radius. To describe the pressure drop for a finite reservoir after the pressure drop profile veers away from the infinitive behavior, one should use [1-22]

$$P_{DW} = \frac{2t_D}{r_{eD}^2} + \ln r_{eD} - \frac{3}{4} \qquad \text{for } t_D > 0.25r_{eD}^2 \tag{8.32}$$

which implies that the transition from infinitive to finite behavior occurs at $t_D \approx 0.25r_{eD}^2$. Katz and Coats [1-2] determined this by equating the rates of pressure drop for infinite-acting and finite-acting reservoirs:

$$\frac{\partial}{\partial t_D} P_{DW} \text{ (Eq. 8.31)} = \frac{\partial}{\partial t_D} P_{DW} \text{ (Eq. 8.32)} \tag{8.33}$$

By carrying out the partial differentiation, one can conclude that the time at which the infinite-acting behavior ends and finite-acting behavior begins is

$$t_D = 0.25r_{eD}^2 \tag{8.34a}$$

$$t_s = 948\frac{\phi\overline{\mu c} r_e^2}{k} \tag{8.34b}$$

Example 8.2. A gas well with a 4-in. diameter in a 20-ft-thick formation is scheduled to produce 0.6-gravity gas at the constant terminal rate of 5 MMcf/day. Permeability is 20 md and porosity is 0.15 around the wellbore. The initial pressure is 2700 psia. What is the responding pressure after 1, 3, and 10 hours? Gas properties are listed in Table 8.2.

TABLE 8.2
Gas property table [8-35]
Temperature: 130°F
Gas gravity: 0.6

Pressure P, psia	Compressibility c, vol/vol/psi	Compressibility factor Z	Viscosity μ, cp	Pseudopressure m, psia²/cp×10⁻⁶*
300.0	3.40×10^{-3}	0.9682	0.01115	7.482
600.0	1.77×10^{-3}	0.9385	0.01196	31.944
900.0	1.12×10^{-3}	0.9116	0.01279	71.223
1200.0	9.23×10^{-4}	0.8881	0.01365	124.165
1500.0	7.35×10^{-4}	0.8688	0.01453	189.606
1800.0	6.01×10^{-4}	0.8545	0.01543	266.309
2100.0	4.98×10^{-4}	0.8457	0.01635	352.937
2400.0	4.12×10^{-4}	0.8425	0.01728	448.056
2700.0	3.46×10^{-4}	0.8447	0.01823	550.193
3000.0	2.92×10^{-4}	0.8520	0.01919	657.910
3300.0	2.48×10^{-4}	0.8636	0.02016	769.881
3600.0	2.12×10^{-4}	0.8787	0.02147	884.943
3900.0	1.83×10^{-4}	0.8968	0.02212	1002.504

* The base pressure is 100 psia, not 0 psia.

Solution. First, calculate the dimensionless flow rate (from Tables 8.1, 8.2):

$$Q_D = \frac{1.422 \times 10^6 \, TQ_{sc}}{khm_i}$$

$$= \frac{1.422 \times 10^6 (130 + 460)(5)}{(20)(20)(550.193 \times 10^6)} = 0.01906$$

Second, calculate corresponding dimensionless times for 1, 3, and 10 hours (from Tables 8.1, 8.2):

$$t_D = \frac{2.637 \times 10^{-4} kt}{\phi \mu_i c_i r_w^2}$$

$$t_D(1\text{hr}) = \frac{2.637 \times 10^{-4}(20)(1)}{(0.15)(0.01823)(3.46 \times 10^{-4})(4/12)^2} = 50.17 \times 10^3$$

$$t_D(3\text{hr}) = 150.5 \times 10^3$$

$$t_D(10\text{hr}) = 501.7 \times 10^3$$

From Eq. (8.31), the responding pseudopressures are

$$P_{DW} = \frac{m_i - m}{m_i Q_D} = \frac{1}{2}[\ln(t_D) + 0.80907]$$

$$m = m_i - m_i Q_D \cdot \frac{1}{2}[\ln(t_D) + 0.80907]$$

$$m(1\text{hr}) = 550.193 \times 10^6 - (550.193 \times 10^6)(0.01906) \cdot \frac{1}{2}[\ln(50.17 \times 10^3) + 0.80907]$$

$$= 489.2 \times 10^6$$

$$m(3\text{hr}) = 483.4 \times 10^6$$

$$m(10\text{hr}) = 477.1 \times 10^6$$

From Table 8.2, the corresponding pressures are 2520.8 psia, 2503.8 psia, and 2485.3 psia for 1, 3, and 10 hours drawdown.

Drainage Radius and Steady State Solution

During a constant terminal rate drawdown process, the pressure drop profile propagates toward the outer boundary over time, as shown in Fig. 8-2 [1-2]. The straight line portion of Fig. 8-2 represents a pseudo–steady state of the reservoir, at which the pressure drops are equal for equal changes in logarithm radius. The pseudo–steady state region could be approximated as steady state by simply integrating Darcy's equation (replacing u by $q_{sf}/(\pi r^2)$ and $q_{sf} = B \cdot Q_{sf}$ of Eq. 8.20) to get, in dimensionless form:

$$\overline{P}_{DW} = \ln\left(\frac{r_d}{r_w}\right) = \ln\left(\frac{r_e}{r_w}\right) - \frac{3}{4} \tag{8.35}$$

where $\overline{P}_{DW}$ uses average pressure $\overline{P}$ (P_{DW} uses P_i). Combining Eqs. (8.31) and (8.35) by assuming $\overline{P}_{DW}$ and P_{DW} are approximately equal yields

$$\overline{P}_{DW} \approx P_{DW}$$

$$\ln\left(\frac{r_d}{r_w}\right) \approx \frac{1}{2}(\ln t_D + 0.80907) \tag{8.36}$$

This defines r_d, the drainage radius describing the area subject to the significant pressure drop. It follows that the drainage radius propagates away from the wellbore as

$$\frac{r_d}{r_w} \approx 1.5\sqrt{t_D} \tag{8.37a}$$

and the *investigation radius* is defined:

$$\frac{r_i}{r_w} \approx 2.0\sqrt{t_D} \tag{8.37b}$$

As shown in Fig. 8-10 by Aronofsky and Jenkins [8-7] as well as Al-Hussainy [8-5], the drainage radius r_d increases as described in Eq. (8.35) until the reservoir ends its infinite-acting behavior. The drainage radius finally settles as a constant value with respect to size of reservoir:

$$\overline{P}_{DW} = \ln\left(\frac{r_d}{r_w}\right) = \ln\left(\frac{r_e}{r_w}\right) - \frac{3}{4} \tag{8.38a}$$

$$r_d = 0.473 r_e \tag{8.38b}$$

For a viscous Darcy flow, Eq. (8.35) implies that *the drainage radius propagating rate is not a function of gas flow rate*. Hence, any terminal withdrawal rate results in the same drainage area at any drawdown time for a particular well.

The pseudo–steady state equation, Eq. (8.35), could be expressed in terms of P_i as $P_{DW} = \ln(r_e/r_w) - \frac{1}{2}$.

Example 8.3. Estimate the flowing time required in a pressure drawdown test to investigate the area of a well drilled on a 640-acre spacing. The permeability of the formation is 100 md, the gas viscosity is 0.013 cp, the system compressibility is approximately 0.001 vol/vol · psi, and the average porosity is 0.15.

Solution. From Eq. (8.38), the radius of drainage for the 640-acre is

$$r_d = 0.473 r_e = 0.473\left(\frac{\text{area}}{\pi}\right)^{1/2}$$

$$= 0.473\left[\frac{(640 \text{ acres})(43,560 \text{ ft}^2/\text{acre})}{\pi}\right]^{1/2} = 1410 \text{ ft}$$

From Eq. (8.37), $r_d/r_w \approx 1.5\sqrt{t_D}$, and from Table 8.1, the time required for r_d to reach 1410 ft is approximately

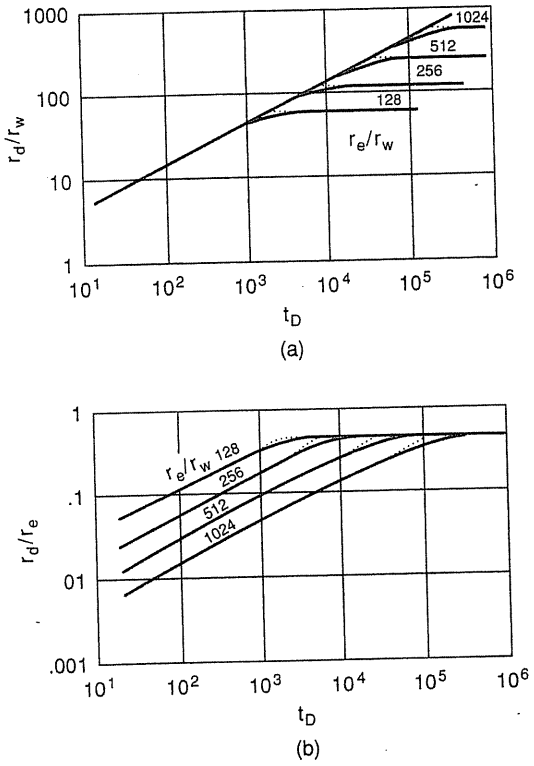

FIGURE 8-10
Effective drainage radius as a function of time [Al-Hussainy, 8-6, Aronofski & Jenkins, 8-7].

$$t_D = \frac{2.637 \times 10^{-4} kt}{\phi \bar{\mu} \bar{c} r_w^2} = \frac{1}{(1.5)^2}\left(\frac{r_d}{r_w}\right)^2$$

$$t = \frac{(0.15)(0.013)(0.001)}{(2.637 \times 10^{-4})(100)} \frac{1}{(1.5)^2}(1410)^2 = 65 \text{ hr}$$

This example illustrates one of the problems associated with pressure transient testing of gas wells. Because the compressibility of the gas is high, it takes a long time for the pressure transient to propagate through the reservoir. Thus, the identification of boundary effects using pressure transient testing techniques is often not practical.

Skin Effect

The near zone of a wellbore is usually blocked by drilling mud or improved in permeability by hydraulic fracture and acidization. Figure 8-11 depicts the phenomenon of an extra dimensionless pressure drop due to the alteration of permeability within a finite zone near the wellbore. Van Everdingen [8-19] defined the dimensionless pressure drop with this effect as

$$P_{DW}(S) = P_{DW} + s \tag{8.39}$$

where S denotes a solution including skin effect.

Hawkins [8-21] assumed that the skin was confined within the skin radius r_s and the altered permeability was k_s, (Fig. 8-11). Since the skin zone is so close to the wellbore, the pressure profile would reach the pseudo–steady state in a short period of time. The steady state approach by Craft and Hawkins [8-16] in the skin zone yields this equation:

$$\Delta P_D(r_s \to r_w) = \frac{m_s - m}{m_i Q_D} \cdot \frac{k_s}{k} = \ln\left(\frac{r_s}{r_w}\right) \tag{8.40}$$

where P_{D,r_s} is the dimensionless pressure drop at radius of skin r_s:

$$P_{D,r_s} = \frac{m_i - m_s}{m_i Q_D} = \frac{1}{2}\left[\ln\left(t_D \cdot \frac{r_w^2}{r_s^2}\right) + 0.80907\right]$$

$$= \frac{1}{2}(\ln t_D + 0.80907) + \ln\left(\frac{r_w}{r_s}\right) \tag{8.41}$$

Combining Eqs. (8.40) and (8.41), the dimensionless pressure drop at wellbore can be expressed as

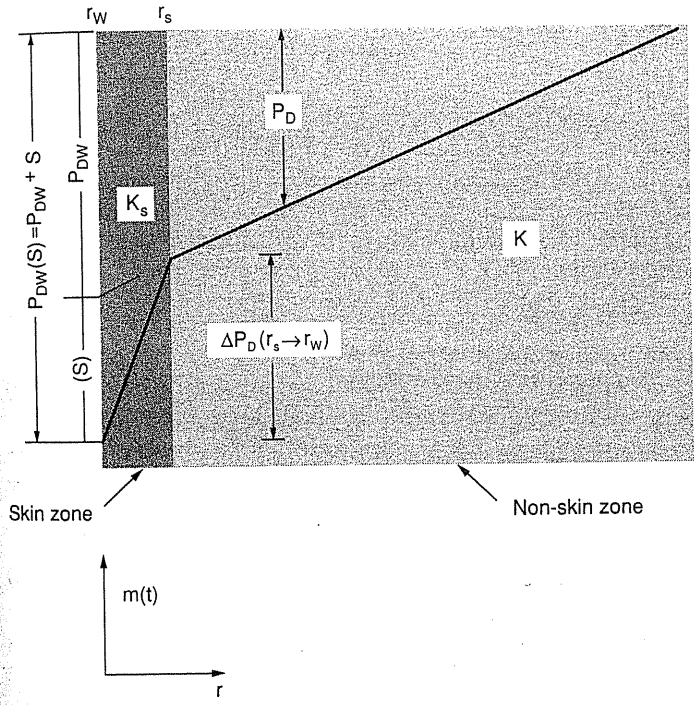

FIGURE 8-11
Sketch of skin effect [Lee, 8-29].

$$P_{DW}(S) = P_{D,r_s} + \frac{\Delta P_D(r_s \rightarrow r_w)}{k_s/k}$$

$$= \frac{1}{2}[\ln t_D + 0.80907] + \left(\frac{k}{k_s} - 1\right) \ln \frac{r_s}{r_w} \tag{8.42}$$

Comparing Eq. (8.42) to the definition of skin, Eq. (8.39), the skin factor is

$$s = \left(\frac{k}{k_s} - 1\right) \ln \frac{r_s}{r_w} \tag{8.43}$$

Although Eq. (8.43) seems rigorous enough to handle both positive and negative skin, there would be more than a single solution. This problem has been discussed by Agarwal, Al-Hussainy, and Ramey [8-4] and by Wattenbarger and Ramey [8-42]. Lee [8-31] pointed out that for a strong negative case ($s < -2$) the pressure profile inside the skin zone took a long time to reach pseudo–steady state; thus, Eq. (8.43), derived from the steady state approach, should be used with caution.

High-Velocity Quad-Darcy Flow

The derivations up to this point are all for viscous (Darcy) flow ($\delta = 1$). However, equations that do not consider the high-velocity effect are inadequate to describe gas flow, especially near the wellbore, where high velocity is expected. Smith [8-39] treated high-velocity quad-Darcy flow by adding an extra rate proportional term to Eq. (8.31):

$$P_{DW}(T) = P_{DW} + DQ_{sc} \tag{8.44}$$

where T denotes a solution including high-velocity effect.

By assuming the existence of the pseudo–steady state, Wattenbarger and Ramey [8-41] integrated the quad-Darcy flow equation inside the drainage area and examined the Q_{sc}^2 term to obtain the high-velocity factor D:

$$D = 2.224 \times 10^{-12} \frac{k^2 \beta G}{kh} \int_{r_w}^{r_d} \frac{1}{\mu r^2} dr \tag{8.45a}$$

$$\approx 2.224 \times 10^{-12} \frac{k^2 \beta G}{kh\overline{\mu}} \left(\frac{1}{r_w} - \frac{1}{r_d}\right) \tag{8.45b}$$

where the variables are in field units. In dimensionless form, the extra high-velocity term in Eq. (8.44) (in terms of pseudopressure $m(P)$ as shown in Table 8.1) can be expressed as

$$DQ_{sc} = \frac{\mu_i}{\overline{\mu}} N_T Q_D \tag{8.46}$$

where r_d is assumed much larger than r_w and N_T is defined by Lee, Logan, and Tek [8-29] as the high-velocity intensity in Table 8.1, and $\overline{\mu}$ is the average value of viscosity throughout the drainage area. Based on numerical simulations, Logan, Lee, and Tek [8-29,8-34] concluded that, for a high flow rate case, a pseudo–steady state profile no longer existed and the use of Eq. (8.44) should

be restricted to the flow range where Reynolds number Re_{CK} (Eq. 8.17) at the wellbore was less than one.

With the skin effect, Eq. (8.44) can be extended to

$$P_{DW}(ST) = \frac{1}{2}(\ln t_D + 0.80907) + s + \frac{\mu_i}{\overline{\mu}} N_T Q_D$$

$$= \frac{1}{2}(\ln t_D + 0.80907) + s + DQ_{sc} \tag{8.47}$$

where ST denotes a solution including both skin and high-velocity effects.

Example 8.4 [MacDonald, 8-35]. What effect in terms of a skin factor should the invasion of drilling mud to a radius of 2 ft have on the steady state performance of a well if the formation permeability is reduced by a factor of 2? The wellbore radius is 4 in. What is the apparent skin, $s' = s + DQ_{sc}$, if the high-velocity coefficient is 10^8 ft^{-1}, the flow rate is 20 MMcf/day, the gas gravity is 0.6, the permeability of the far zone is 100 md, the viscosity is 0.013 cp, and the formation thickness is 40 ft?

Solution. From Eq. (8.43), the skin factor is

$$s = \left(\frac{k}{k_s} - 1\right) \ln \frac{r_s}{r_w} = (2 - 1) \ln \frac{(2)(12)}{(4)} = 1.8$$

From Eqs. (8.45) and (8.47), the apparent skin factor can be obtained by assuming r_d is much larger than r_w; that is, $D = 2.224 \times 10^{-12}(k\beta G)/(h\overline{\mu}r_w)$:

$$s' = s + DQ_{sc} = 1.8 + 2.224 \times 10^{-12} \frac{(100)(10^8)(0.6)}{(40)(0.013)(4/12)}(20) = 3.34$$

In laboratory, the $k\beta$ values for various rocks range from 10^8 to 10^{12}.

Wellbore Storage Effect

Van Everdingen and Hurst [8-18] reported solutions involving skin and wellbore storage effects simultaneously, but without considering high-velocity effect. Agarwal, Al-Hussainy, and Ramey [8-3] gave a similar discussion later. So far there is no analytical solution including all these effects: wellbore storage, skin, and high velocity. Figure 8-12 shows the solution of the viscous Darcy case. Figure 8-13 indicates the viscous case with skin effect. Both cases express the curves as straight lines at the very inception of drawdown processes [8-3]:

$$P_{DW}(STW) = \frac{t_D}{C_D} \tag{8.48}$$

where STW means a solution including all the effects.

The physical meaning is that, near the beginning of a drawdown process, the pressure drop within the wellbore is due only to the unloading of its initial contents, and that the reservoir flow through sandface is insignificant to have any effect on the pressure drop.

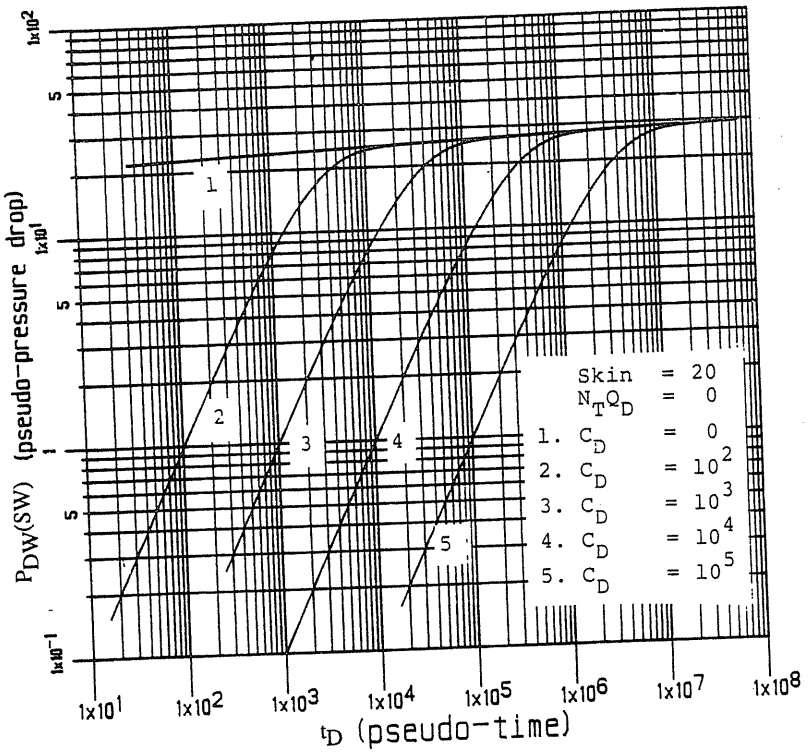

FIGURE 8-12
P_D versus t_D for various C_D's without considering skin and high-velocity effects [Lee, 8-31].

The wellbore storage effect tends to distort the viscous Darcy profile (upper curve) in varying degrees before eventually approaching the Darcy profile asymptotically, as in Fig. 8-12. The presence of skin prolongs the duration of the wellbore storage effect, as indicated by a comparison between Fig. 8-12 and Fig. 8-13. For all practical purposes, Agarwal, Al-Hussainy, and Ramey [8-3] showed that the duration time to ignore the wellbore storage effect could be expressed as

$$t_D = (60 + 3.5s)C_D \tag{8.49}$$

Based on numerical simulations, Lee [8-31] incorporated all the effects (wellbore storage, skin, and turbulence) into the rigorous Eq. (8.47) by introducing a decay factor W_D:

$$P_{DW}(STW) = W_D \cdot P_{DW}(ST) = W_D\left[\frac{1}{2}(\ln t_D + 0.80907) + s + \frac{\mu_i}{\bar{\mu}}N_TQ_D\right] \tag{8.50}$$

where

$$W_D = \{1 - \exp[-2.935C_D^{-0.974}t_D^{-0.097}(s' + 6)^{-1.129}]\} \tag{8.51}$$

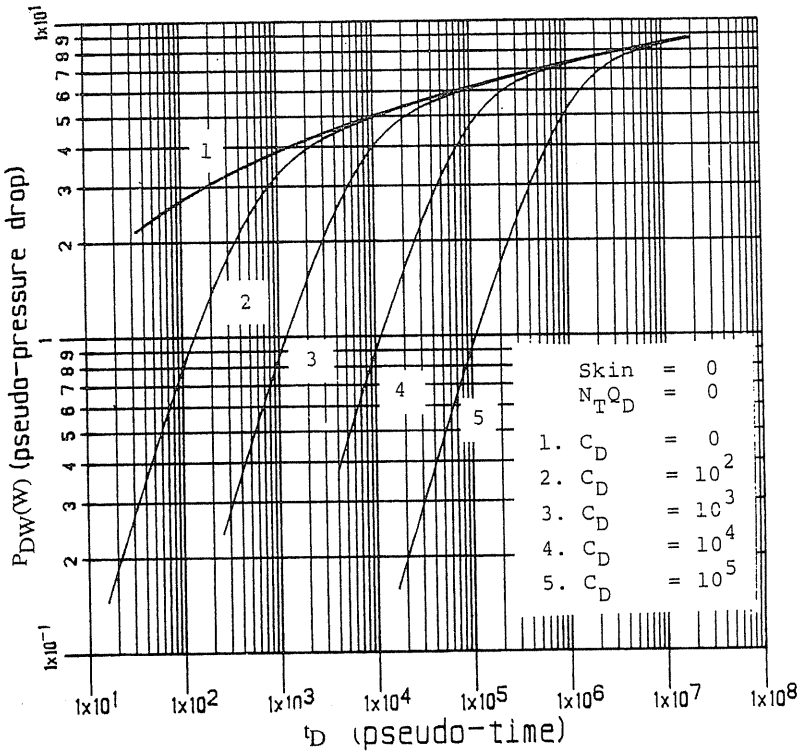

FIGURE 8-13
P_D versus t_D for various C_D's without considering high-velocity effects [Lee, 8-31].

$$s'(\text{apparent skin}) = s + DQ_{sc} = s + \frac{\mu_i}{\bar{\mu}}N_TQ_D \tag{8.52}$$

Since this is a correlated equation, its safe range of application is certainly limited to the range over which the correlation of the simulated results was performed. The suggested applicable ranges of applying Eqs. (8.50), (8.51), and (8.52) are

$$\begin{aligned} Q_D &< 0.2 \\ t_D &< 10^7 \\ s &> -2 \\ 10^2 < C_D &< 10^6 \end{aligned} \tag{8.53}$$

Figure 8-14 shows good agreement between the use of correlated equations and numerical values. More details of derivations and discussion could be found in references [8-31,8-37].

Example 8.5. Assuming there is no wellbore damage, compare the duration of the wellbore storage effect for annulus flow and tubing flow in a 4000-ft well.

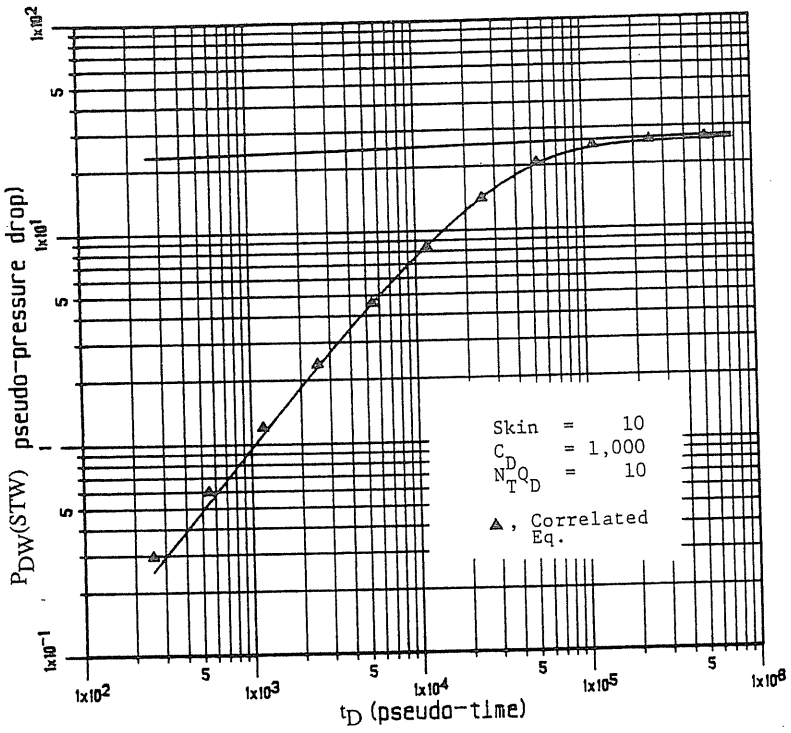

FIGURE 8-14
P_D versus t_D for various C_D's compared to the results of correlated equation [Lee, 8-31].

The casing is $5\frac{1}{2}$ in. (5.012 in. ID) and the tubing is $2\frac{3}{8}$ in. (1.955 in. ID). The product of permeability and thickness is 50 md·ft, the viscosity is 0.018, and the gas compressibility is 0.00043 vol/vol/psi.

Solution. Volumes of the tubing string and the annulus are

$$V_w(\text{tubing}) = \frac{(\pi)(1.995/12)^2}{4}(4000) = 87 \text{ ft}^3$$

$$V_w(\text{annulus}) = \frac{(\pi)[(5.012/12)^2 - (2.375/12)^2]}{4}(4000) = 425 \text{ ft}^3$$

From Eq. (8.49) assuming no skin, and Table 8.1:

$$t_D = \frac{2.637 \times 10^{-4} kt}{\phi\bar{\mu}\bar{c}r_w^2} = 60C_D = 60\frac{(1/2\pi)V_wC_w}{\phi h\bar{c}r_w^2}$$

$$t(\text{hour}) = 36,213\frac{\bar{\mu}C_wV_w}{kh}$$

Hence, the times free of the wellbore storage effect are

$$t(\text{tubing}) = 36,213\frac{(0.018)(0.00043)(87)}{(50)} = 0.49 \text{ hr}$$

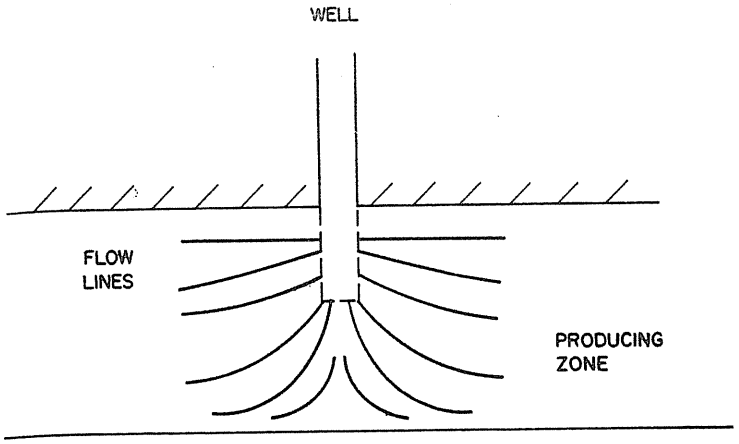

FIGURE 8-15
Flow in a partially penetrated well [Katz & Coats, 1-2].

$$t(\text{annulus}) = 36,213\frac{(0.018)(0.00043)(425)}{(50)} = 2.38 \text{ hr}$$

8.4 PARTIALLY PENETRATED WELLS

Often a well does not fully penetrate the thickness of a gas layer, if any bottom water is evident. Figure 8-15 shows the gas entering a partially penetrated well. Muskat computed the relative flow rates for partially penetrated wells [8-36] and his results have been translated into Fig. 8-16 as an approximate correlation factor for the sand thickness, which should be used in all the equations derived. Figure 8-16 shows that a well penetrating only 10 ft of a 40-ft gas layer would flow like a well completely penetrating a 17-ft sand body, and so the formation thickness h would become 17 instead of 10 in the derived equations.

Brons and Marting [8-10] introduced a pseudo–skin factor S_b, which could be determined by the penetration ratio b and the ratio h/r_w, as shown in Fig. 8-17. These two parameters are defined as

$$b = \frac{\text{total interval open to flow}}{\text{total thickness of the production zone}} \tag{8.54}$$

$$\frac{h}{r_w} = \frac{\text{thickness of the production zone}}{\text{wellbore radius}} \tag{8.55}$$

Various penetrating schemes are shown in Fig. 8-18 [8-10]. The values of b are 0.2(30/150) for schemes (a), (b), and (c) on Fig. 8-18 while the h/r_w are 150/0.25 = 600, 75/0.25 = 300, 15/0.25 = 60, respectively. It should be noted that the h is defined as the thickness of production zone where the fluid will flow toward the open interval of wells. For example, on Fig. 8-18b fluids in the lower 75 ft of the reservoir will flow to the lower 15 ft of the open interval, and

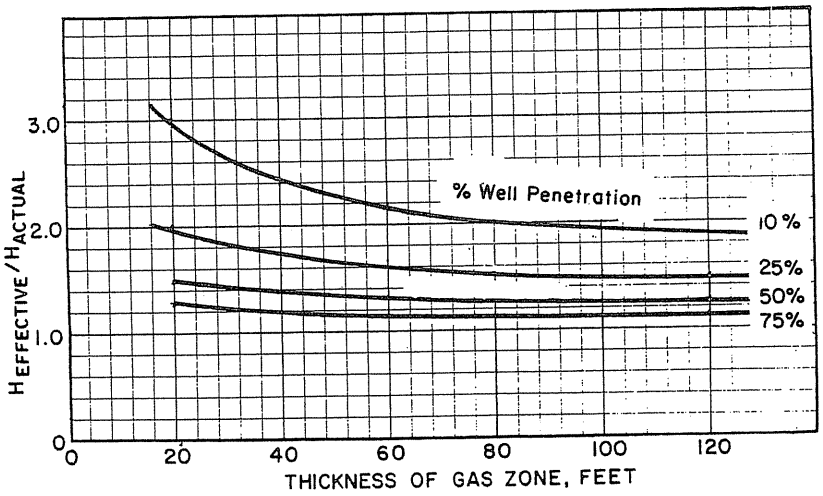

FIGURE 8-16
Effective sand thickness for partially penetrated well [Katz & Coats, 1-2].

on Fig. 8-18*c* the fluid in the 15 ft section will only flow to the lower 3 ft of the 6 ft open interval. The objective of the penetrating scheme of Fig. 8-18*c* is to control the flow rate in each layer of the production zone.

Example 8.6 [MacDonald, 8-35]. A gas well is drilled into the upper 15 ft of a 40-ft formation and completed open hole. The well produces at a stabilized flow

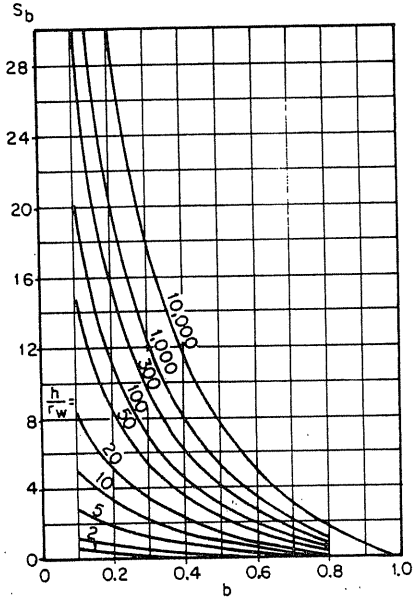

FIGURE 8-17
Pseudo–skin factor S_b as a function of perforation ratio b and ratio of production zone to wellbore, h/r_w [Brons & Marting, 8-10, courtesy SPE-AIME].

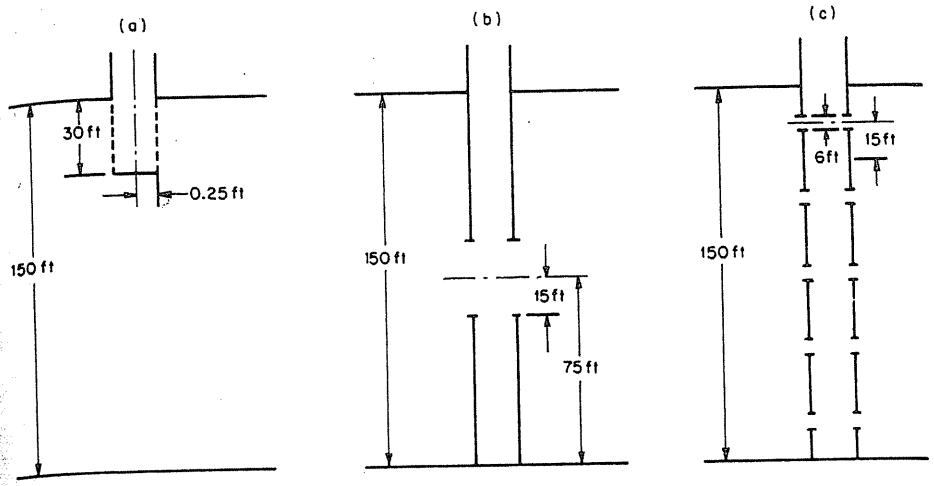

FIGURE 8-18
Determinations of parameters h/r_w and b for different types of completion [Brons & Marting, 8-10, courtesy SPE-AIME].

rate of 1500 Mcf/day. The wellbore radius is $\frac{1}{4}$ ft and the outer reservoir radius for the well is 2800 feet. What flow rate could be expected from the well if it were completed through the entire formation? Assume that there is no completion damage to the well other than the effects of the partial penetration. Compare the Muskat method and the Brons and Marting technique for calculating the effect of partial penetration.

Solution—Muskat's method. The well has penetrated 37.5% of the formation. From Fig. 8-16 the ratio of effective thickness to actual thickness penetrated for a 40-ft gas zone is 1.5. The effective completion interval for the well is therefore 1.5 times the 15-ft actual completion thickness or 22.5 ft.

The flow rate is directly proportional to the effective completion thickness. Thus, the estimated flow from a well completed across the entire 40-ft gas zone is

$$Q(\text{total zone}) = Q(\text{partial zone})\frac{h(\text{total})}{h(\text{effective})}$$

$$= 1500 \text{ Mcf/day}\ \frac{40 \text{ ft}}{22.5 \text{ ft}} = 2667 \text{ Mcf/day}$$

Solution—Brons and Marting's method. The ratio of the completion interval thickness to the gas zone thickness, b, is 0.375. The ratio of the gas zone thickness to the wellbore radius, h/r_w, is 40/0.25 = 160. From Fig. 8-17 a value of 6.5 is read for the pseudo–skin factor, S_b, accounting for the effects of partial penetration. The estimated flow can be calculated as follows:

$$Q(\text{total zone}) = Q(\text{partial zone})\frac{P_{DW}(S),\ \text{Eq. (8.39)}}{P_{DW},\ \text{Eq. (8.35)}}$$

$$= Q(\text{partial zone})\frac{\ln(r_e/r_w) - 3/4 + S_b}{\ln(r_e/r_w) - 3/4}$$

$$= 1500\frac{\ln(2800/0.25) - 0.75 + 6.5}{\ln(2800/0.25) - 0.75} = 2448 \text{ Mcf/day}$$

This example shows that a high skin value obtained from gas testing may be caused by the partial penetration effect; this pseudo-skin cannot be minimized by an acidization or a fracturing process.

8.5 SUPERPOSITION PRINCIPLE

The equations derived so far are all based on a constant terminal withdrawing rate. Actually, in field practice, it is hard to maintain the flow rate as constant. Thus, in order to utilize the constant terminal rate equations, a typical flow rate curve (Fig. 8-19) should be discretized to several constant rate periods, and then the *superposition principle* should be applied to summarize the effects of all the different constant rates.

Superposition may be considered as a problem-solving philosophy. The pressure behavior at any given time represents the sum of the history of all previous effects. Its application to the situation illustrated by Fig. 8-19 proceeds as follows:

For the first time interval, the pressure drop (in terms of $m(P)$) is given by

$$\frac{m_i - m}{m_i} = Q_{D1}|_{Q_1} \cdot P_{DW}|_{Q_1,t}$$

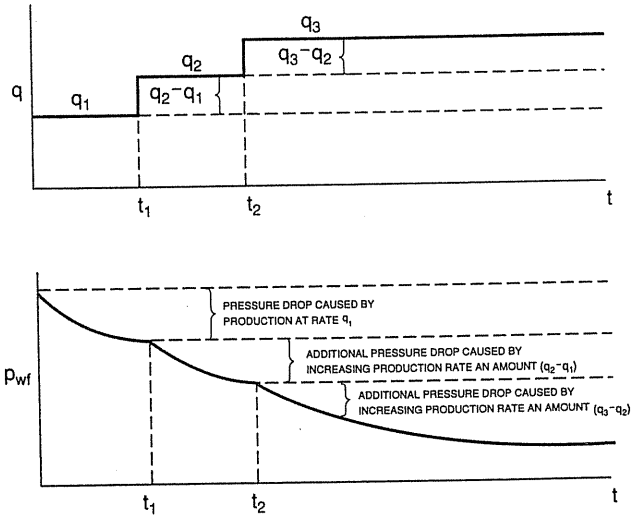

FIGURE 8-19
Superposition. [ERCB, Calgary, 8-17].

$$= \frac{\gamma T Q_1}{khm_i}\left\{\frac{1}{2}\left[\ln\left(\frac{\lambda kt}{\phi\mu_i c_i r_w^2}\right) + 0.80907\right]\right\} \tag{8.56}$$

which is only valid before t_1 is reached. Assuming that the first flow rate's effect lasts forever, it would seem that at time t_1 another flow rate $(Q_2 - Q_1)$ is added, and its effect should be superposed onto the effect of the first rate, that is,

$$\frac{m_i - m}{m_i} = Q_{D1}|_{Q_1} \cdot P_{DW}|_{Q_1,t} + Q_{D2}|_{Q_2-Q_1} \cdot P_{DW}|_{Q_2-Q_1,t-t_1}$$

$$= Q_{D1}|_{Q_1} \cdot P_{DW}|_{Q_1,t} + \frac{\gamma T(Q_2 - Q_1)}{khm_i}\left\{\frac{1}{2}\left[\ln\left(\frac{\lambda k(t - t_1)}{\phi\mu_i c_i r_w^2}\right) + 0.80907\right]\right\} \tag{8.57}$$

Similarly, one could extend to all the succeeding flow rates. This superposition principle and its applications serve as the basis for analyzing the data from buildup or multirate tests, which will be discussed in Chapter 9.

8.6 MISCELLANEOUS AND RELATED REFERENCES OF GAS FLOW

So far, the gas flow equations derived considered only the simplified model: a single-layer reservoir with a single porosity,[3] rock properties independent of pressure, and so on. Further treatments of particular cases with more complicated systems can be found in the SPE monograph, volume 5: *Advances in Well Test Analysis* [1-21] and its summarized references.

Be reminded that the equations derived above are only applicable to the single well inside the gas bubble. The later treatment in this chapter of water movements around the edge of the gas bubble is intended for use with single-phase water equations. Actual physical complications between the gas bubble and adjacent aquifer, such as gas trapping/untrapping due to contraction/expansion of the gas bubble, are assumed to be negligible for storage operations.

For liquids, the equation of state is quite different than for gases, so water and oil flow equations are developed differently. Water drive for gas or oil requires equations for the water movement. In gas storage, the displacement of water by gas injection is a practical example of a case involving a water flow–pressure drop relation.

8.7 WATER INFLUX AT GAS RESERVOIR EDGE

Water drive denotes the mechanism of water flowing into an oil or gas reservoir from the surrounding water-filled formation when the pressure is lowered below

[3] Natural fractured reservoirs are considered to be dual porosity.

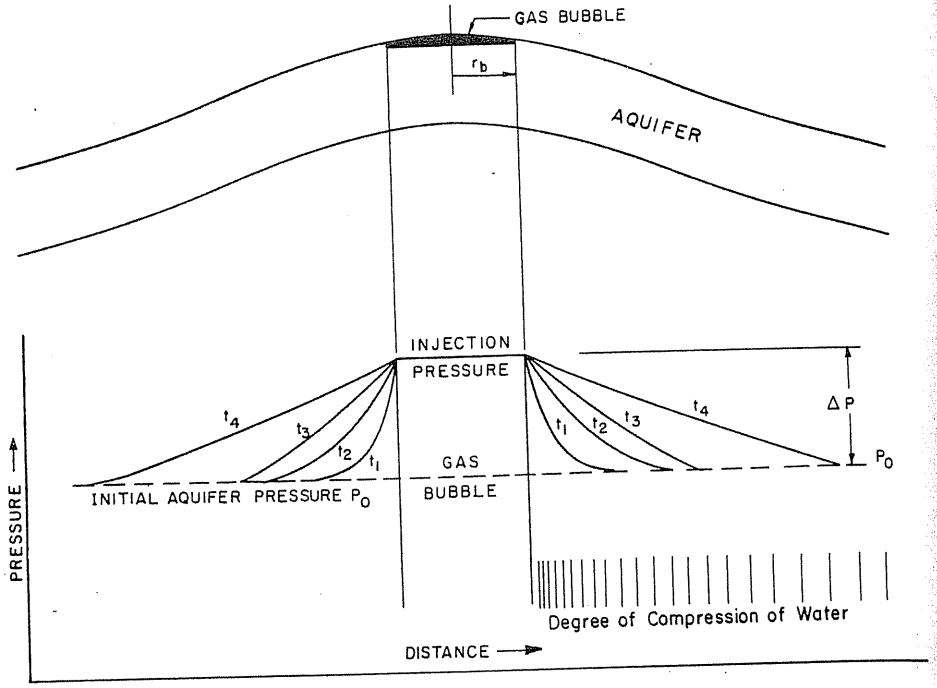

FIGURE 8-20
Effect of time on the pressure distribution in aquifer [Katz & Coats, 1-2].

the discovery pressure. Schilthuis first described the water movement using a steady state approach [8-38].

Considering a growing gas bubble in an aquifer gas storage project (see Fig. 8-20), gas is injected rapidly enough to hold the gas bubble at a pressure ΔP above the initial aquifer pressure. Water flows away from the gas bubble as it expands. The pressure in the surrounding sand is raised as indicated at successive times, t_1, t_2, t_3, etc. When water flows out from the gas bubble, where does it go? It simply compresses the water ahead of it. Since such movement is in a radial direction away from the bubble, there is an increasing quantity of water associated with successive increments of radial distance.

Figure 8-21 [1-2] shows radial and linear models. Here, the radial model is emphasized because it represents most real gas storage reservoirs. The water flow rate equation for the radial model is exactly the same as Eq. (8.11); the diffusivity, $k/(\phi\mu c)$, is near constant for water. Thus, Eq. (8.11) is linear and subject to analytical solution. The boundary is not considered to be at the wellbore r_w, but at the edge of the gas bubble r_b as shown in Fig. 8-21. The *line source* solution, Eq. (8.28), is not suitable because of the requirement of Eq. (8.25) ($r_D \rightarrow 0$). Van Everdingen and Hurst [8-18] solved Eq. (8.11) for the aquifer-reservoir system by applying a Laplace transform for both constant terminal rate and constant pressure cases.

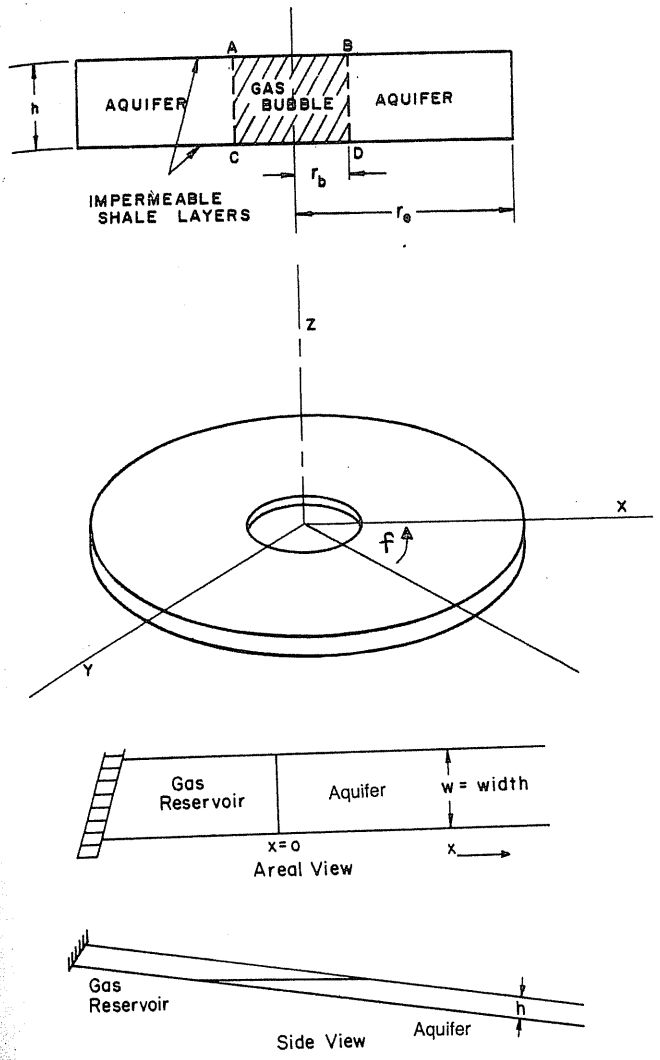

FIGURE 8-21
Radial and linear models [Katz & Coats, 1-2].

1. *In the constant terminal rate case*, pressure drop P_t at the reservoir boundary r_b is computed as a function of time for a constant water influx rate.
2. *In the constant terminal pressure case*, cumulative flow Q_t across the aquifer-reservoir boundary is computed as a function of time for a constant pressure drop at this boundary r_b.

For the constant pressure case shown in Fig. 8-20, it can be seen that the pressure profile propagates toward the edge of aquifer from t_1 until t_4, when the

boundary starts to feel the pressure drop. Thus, during the time period from t_1 to t_4, the aquifer behaves as if it has an infinite boundary. After t_4, it behaves as a finite aquifer. The crossover time t_4 can be calculated using the following formula proposed by Klins, Bouchard, and Cable [8-28] based on the numerical values from the tables of van Everdingen and Hurst [8-18]:

Constant terminal rate:

$$t_{D,\text{cross}} = 0.0980958(R - 1) + 0.10068(R - 1)^{2.03863} \quad (8.58)$$

Constant terminal pressure:

$$t_{D,\text{cross}} = -1.767 + -0.606R + 0.12368R^{2.25} + 3.02(\ln R)^{0.5} \quad (8.59)$$

TABLE 8.3
Dimensionless pressure P_t for finite radial aquifer [1-39, courtesy AGA]

$R = 2$		$R = 3$		$R = 4$		$R = 5$	
t_D	P_t	t_D	P_t	t_D	P_t	t_D	P_t
2.2×10^{-1}	0.443	5.2×10^{-1}	0.627	1.5	0.927	3.0	1.167
2.4×10^{-1}	0.459	5.4×10^{-1}	0.636	1.6	0.948	3.1	1.180
2.6×10^{-1}	0.476	5.6×10^{-1}	0.645	1.7	0.968	3.2	1.192
2.8×10^{-1}	0.492	6.0×10^{-1}	0.662	1.8	0.988	3.3	1.204
3.0×10^{-1}	0.507	6.5×10^{-1}	0.683	1.9	1.007	3.4	1.215
3.2×10^{-1}	0.522	7.0×10^{-1}	0.703	2.0	1.025	3.5	1.227
3.4×10^{-1}	0.536	7.5×10^{-1}	0.721	2.2	1.059	3.6	1.238
3.6×10^{-1}	0.551	8.0×10^{-1}	0.740	2.4	1.092	3.7	1.249
3.8×10^{-1}	0.565	8.5×10^{-1}	0.758	2.6	1.123	3.8	1.259
4.0×10^{-1}	0.579	9.0×10^{-1}	0.776	2.8	1.154	3.9	1.270
4.2×10^{-1}	0.593	9.5×10^{-1}	0.791	3.0	1.184	4.0	1.281
4.4×10^{-1}	0.607	1.0	0.806	3.5	1.255	4.2	1.301
4.6×10^{-1}	0.621	1.2	0.865	4.0	1.324	4.4	1.321
4.8×10^{-1}	0.634	1.4	0.920	4.5	1.392	4.6	1.340
5.0×10^{-1}	0.648	1.6	0.973	5.0	1.460	4.8	1.360
6.0×10^{-1}	0.715	2.0	1.076	5.5	1.527	5.0	1.378
7.0×10^{-1}	0.782	3.0	1.328	6.0	1.594	5.5	1.424
8.0×10^{-1}	0.849	4.0	1.578	6.5	1.660	6.0	1.469
9.0×10^{-1}	0.915	5.0	1.828	7.0	1.727	6.5	1.513
1.0	0.982			8.0	1.861	7.0	1.556
2.0	1.649			9.0	1.994	7.5	1.598
3.0	2.316			10.0	2.127	8.0	1.641
5.0	3.649					9.0	1.725
						10.0	1.808
						11.0	1.892
						12.0	1.975
						13.0	2.059
						14.0	2.142
						15.0	2.225

where R is the ratio of the outer radius of aquifer, r_e, to the gas bubble radius, $r_b (R = r_e/r_b)$, and $t_{D,\text{cross}}$ is the dimensionless crossover time. Tables 8.3 and 8.4 list P_t and Q_t.

Constant Terminal Flow Rate Case

It is assumed that the withdrawing or injection of gas has an immediate effect on the edge of gas bubble. Also:

1. There is no pressure gradient and hence no flow at the exterior boundary of the aquifer, r_e.

TABLE 8.3
(continued)

$R = 6$		$R = 7$		$R = 8$		$R = 9$		$R = 10$	
t_D	P_t	t_D	P_t	t_D	P_t	t_D	P_t	t_D	P_t
4.0	1.275	6.0	1.436	8.0	1.556	10.0	1.651	12.0	1.732
4.5	1.322	6.5	1.470	8.5	1.582	10.5	1.673	12.5	1.750
5.0	1.364	7.0	1.501	9.0	1.607	11.0	1.693	13.0	1.768
5.5	1.404	7.5	1.531	9.5	1.031	11.5	1.713	13.5	1.784
6.0	1.441	8.0	1.559	10.0	1.653	12.0	1.732	14.0	1.801
6.5	1.477	8.5	1.586	10.5	1.675	12.5	1.750	14.5	1.817
7.0	1.511	9.0	1.613	11.0	1.697	13.0	1.768	15.0	1.832
7.5	1.544	9.5	1.638	11.5	1.717	13.5	1.786	15.5	1.847
8.0	1.576	10.0	1.663	12.0	1.737	14.0	1.803	16.0	1.862
8.5	1.607	11.0	1.711	12.5	1.757	14.5	1.819	17.0	1.890
9.0	1.638	12.0	1.757	13.0	1.776	15.0	1.835	18.0	1.917
9.5	1.668	13.0	1.801	13.5	1.795	15.5	1.851	19.0	1.943
10.0	1.698	14.0	1.845	14.0	1.813	16.0	1.867	20.0	1.968
11.0	1.757	15.0	1.888	14.5	1.831	17.0	1.897	22.0	2.017
12.0	1.815	16.0	1.931	15.0	1.849	18.0	1.926	24.0	2.063
13.0	1.873	17.0	1.974	17.0	1.919	19.0	1.955	26.0	2.108
14.0	1.931	18.0	2.016	19.0	1.986	20.0	1.983	28.0	2.151
15.0	1.988	19.0	2.058	21.0	2.051	22.0	2.037	30.0	2.194
16.0	2.045	20.0	2.100	23.0	2.116	24.0	2.090	32.0	2.236
17.0	2.103	22.0	2.184	25.0	2.180	26.0	2.142	34.0	2.278
18.0	2.160	24.0	2.267	30.0	2.340	28.0	2.193	36.0	2.319
19.0	2.217	26.0	2.351	35.0	2.499	30.0	2.244	38.0	2.360
20.0	2.274	28.0	2.434	40.0	2.658	34.0	2.345	40.0	2.401
25.0	2.560	30.0	2.517	45.0	2.817	38.0	2.446	50.0	2.604
30.0	2.846					40.0	2.496	60.0	2.806
						45.0	2.621	70.0	3.008
						50.0	2.746		

TABLE 8.4
Dimensionless flow rate Q_t for finite radial aquifer [1-39, courtesy AGA]

$R = 2$		$R = 3$		$R = 4$		$R = 5$	
t_D	Q_t	t_D	Q_t	t_D	Q_t	t_D	Q_t
5.00×10^{-2}	0.278	3.0×10^{-1}	0.755	2.00	2.442	3.0	3.195
7.50×10^{-2}	0.345	4.0×10^{-1}	0.895	2.20	2.598	3.5	3.542
1.00×10^{-1}	0.404	5.0×10^{-1}	1.023	2.40	2.748	4.0	3.875
1.25×10^{-1}	0.458	6.0×10^{-1}	1.143	2.60	2.893	4.5	4.193
1.50×10^{-1}	0.507	7.0×10^{-1}	1.256	2.80	3.034	5.0	4.499
1.75×10^{-1}	0.553	8.0×10^{-1}	1.363	3.00	3.170	5.5	4.792
2.00×10^{-1}	0.597	9.0×10^{-1}	1.465	3.25	3.334	6.0	5.074
2.25×10^{-1}	0.638	1.00	1.563	3.50	3.493	6.5	5.345
2.50×10^{-1}	0.678	1.25	1.791	3.75	3.645	7.0	5.605
2.75×10^{-1}	0.715	1.50	1.997	4.00	3.792	7.5	5.854
3.00×10^{-1}	0.751	1.75	2.184	4.25	3.932	8.0	6.094
3.25×10^{-1}	0.785	2.00	2.353	4.50	4.068	8.5	6.325
3.50×10^{-1}	0.817	2.25	2.507	4.75	4.198	9.0	6.547
3.75×10^{-1}	0.848	2.50	2.646	5.00	4.323	9.5	6.760
4.00×10^{-1}	0.877	2.75	2.772	5.50	4.560	10	6.965
4.25×10^{-1}	0.905	3.00	2.886	6.00	4.779	11	7.350
4.50×10^{-1}	0.932	3.25	2.990	6.50	4.982	12	7.706
4.75×10^{-1}	0.958	3.50	3.084	7.00	5.169	13	8.035
5.00×10^{-1}	0.983	3.75	3.170	7.50	5.343	14	8.339
5.50×10^{-1}	1.028	4.00	3.247	8.00	5.504	15	8.620
6.00×10^{-1}	1.070	4.25	3.317	8.50	5.653	16	8.879
6.50×10^{-1}	1.108	4.50	3.381	9.00	5.790	18	9.338
7.00×10^{-1}	1.143	4.75	3.439	9.50	5.917	20	9.731
7.50×10^{-1}	1.174	5.00	3.491	10	6.035	22	10.07
8.00×10^{-1}	1.203	5.50	3.581	11	6.246	24	10.35
9.00×10^{-1}	1.253	6.00	3.656	12	6.425	26	10.59
1.0	1.295	6.50	3.717	13	6.580	28	10.80
1.1	1.330	7.00	3.767	14	6.712	30	10.98
1.2	1.358	7.50	3.809	15	6.825	34	11.26
1.3	1.382	8.00	3.843	16	6.922	38	11.46
1.4	1.402	9.00	3.894	17	7.004	42	11.61
1.6	1.432	10.00	3.928	18	7.076	46	11.71
1.7	1.444	11.00	3.951	20	7.189	50	11.79
1.8	1.453	12.00	3.967	22	7.272	60	11.91
2.0	1.468	14.00	3.985	24	7.332	70	11.96
2.5	1.487	16.00	3.993	26	7.377	80	11.98
3.0	1.495	18.00	3.997	30	7.434	90	11.99
4.0	1.499	20.00	3.999	34	7.464	100	12.00
5.0	1.500	22.00	3.999	38	7.481	120	12.0
		24.00	4.000	42	7.490Q		
				46	7.494		
				50	7.497		

TABLE 8.4
(continued)

$R = 6$		$R = 7$		$R = 8$		$R = 9$		$R = 10$	
t_D	Q_t	t_D	Q_t	t_D	Q_t	t_D	Q_t	t_D	Q_t
6.0	5.148	9.00	6.861	9	6.861	10	7.417	15	9.965
6.5	5.440	9.50	7.127	10	7.398	15	9.945	20	12.32
7.0	5.724	10	7.389	11	7.920	20	12.26	22	13.22
7.5	6.002	11	7.902	12	8.431	22	13.13	24	14.09
8.0	6.273	12	8.397	13	8.930	24	13.98	26	14.95
8.5	6.537	13	8.876	14	9.418	26	14.79	28	15.78
9.0	6.795	14	9.341	15	9.895	28	15.59	30	16.59
9.5	7.047	15	9.791	16	10.361	30	16.35	32	17.38
10.0	7.293	16	10.23	17	10.82	32	17.10	34	18.16
10.5	7.533	17	10.65	18	11.26	34	17.82	36	18.91
11	7.767	18	11.06	19	11.70	36	18.52	38	19.65
12	8.220	19	11.46	20	12.13	38	19.19	40	20.37
13	8.651	20	11.85	22	12.95	40	19.85	42	21.07
14	9.063	22	12.58	24	13.74	42	20.48	44	21.76
15	9.456	24	13.27	26	14.50	44	21.09	46	22.42
16	9.829	26	13.92	28	15.23	46	21.69	48	23.07
17	10.19	28	14.53	30	15.92	48	22.26	50	23.71
18	10.53	30	15.11	34	17.22	50	22.82	52	24.33
19	10.85	35	16.39	38	18.41	52	23.36	54	24.94
20	11.16	40	17.49	40	18.97	54	23.89	56	25.53
22	11.74	45	18.43	45	20.26	56	24.39	58	26.11
24	12.26	50	19.24	50	21.42	58	24.88	60	26.67
25	12.50	60	20.51	55	22.46	60	25.36	65	28.02
31	13.74	70	21.45	60	23.40	65	26.48	70	29.29
35	14.40	80	22.13	70	24.98	70	27.52	75	30.49
39	14.93	90	22.63	80	26.26	75	28.48	80	31.61
51	16.05	100	23.00	90	27.28	80	29.36	85	32.67
60	16.56	120	23.47	100	28.11	85	30.18	90	33.66
70	16.91	140	23.71	120	29.31	90	30.93	95	34.60
80	17.14	160	23.85	140	30.08	95	31.63	100	35.48
90	17.27	180	23.92	160	30.58	100	32.27	120	38.51
100	17.36	200	23.96	180	30.91	120	34.39	140	40.89
110	17.41	500	24.00	200	31.12	140	35.92	160	42.75
120	17.45			240	31.34	160	37.04	180	44.21
130	17.46			280	31.43	180	37.85	200	45.36
140	17.48			320	31.47	200	38.44	240	46.95
150	17.49			360	31.49	240	39.17	280	47.94
160	17.49			400	31.50	280	39.56	320	48.54
180	17.50			500	31.50	320	39.77	360	48.91
200	17.50					360	39.88	400	49.14
220	17.50					400	39.94	440	49.28
						440	39.97	480	49.36
						480	39.98		

2. The pressure gradient in the radial direction at the gas-water contact r_b is constant, implying constant flow.
3. The original pressure P_0 throughout the aquifer is constant.

Then, the pressure drop at the interface could be expressed as

$$P_0 - P = k_r \dot{E}_w P_t$$

$$k_r = \frac{25.15\mu}{khf} \tag{8.60}$$

where $\dot{E}_w$ (+/−, withdrawing/injection) is the constant volume rate at r_b (ft^3/day)[4], P_0 and P are the initial and current pressures (psia), μ is the viscosity of water (cp), k is the permeability (md), h is the formation thickness (ft), and f is the fraction of circle open to flow. In case of full radius f equals unity. P_t is the *influence function* of van Everdingen and Hurst, plotted in Fig. 8-22 as a function of dimensionless time $t_D = (\lambda kt)/(\mu\phi c r_b^2)$.

[4] For bbl/day, 25.15 should be replaced by 141.2.

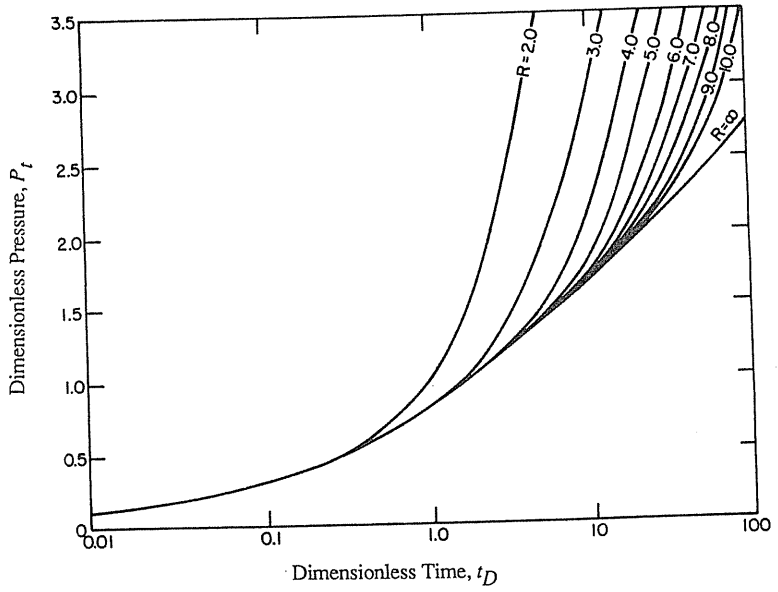

FIGURE 8-22
Van Everdingen and Hurst dimensionless pressure, P_t, as a function of dimensionless time [Chatas, 8-13, courtesy *Petro. Engr.*].

Example 8.7 [Katz et al., 1-39]. Starting with a uniform aquifer pressure of 700 psia, it is desired to grow a storage reservoir at a constant rate of 50,000 ft^3 pore volume per day. Calculate the reservoir pressure at 30, 60, 120, and 300 days after initiation of a gas bubble. Assume the aquifer to be infinite and that its performance can be approximated by the radial model.

The following physical and geometric data for the gas bubble aquifer system are available:

original pressure P_0	700 psia
formation thickness h	80 ft
bubble radius r_b	1000 ft
permeability k	400 md
system compressibility c	7×10^{-6} vol/vol/psi
porosity ϕ	0.17
viscosity μ	1 cp

Solution. Using t as time in days, the dimensionless time value is calculated as shown in Table 8.5:

$$t_D = \frac{6.333 \times 10^{-3} kt}{\mu\phi c r_b^2} = \frac{(0.00633)(400)t}{(1)(0.17)(7 \times 10^{-6})(1000)^2} = 2.13t$$

Dimensionless pressure values, P_t, for the infinite radial model, constant terminal rate case, are obtained from Fig. 8-22. Eq. (8.60) is used to obtain the reservoir pressure.

t in days	$t_D = 2.13t$	P_t	$P = 700 + 39.4P_t$, psia
30	64	2.479	797.7
60	128	2.784	809.7
120	256	3.183	825.4
180	384	3.384	833.3
300	640	3.640	843.4

$$P = P_0 - \frac{25.15\dot{E}_w\mu}{khf}P_t = 700 - \frac{(25.15)(-50{,}000)(1)}{(400)(80)(1)}P_t = 700 + 39.4\,P_t$$

It may be noted that the rate of pressure rise over and above the initial aquifer value decreases with time for a constant rate water efflux (from gas bubble to aquifer).

Actually, for gas storage operations, the constant terminal rate case is of little interest; the constant terminal pressure case is more applicable.

Constant Terminal Pressure Case

Most gas storage reservoirs have high enough permeabilities to equalize bubble pressure in a short time. The assumptions for the constant terminal pressure case

TABLE 8.5
Summary of flow equations for water movement [Katz et al., 1-39, courtesy AGA]

Constant terminal rate case: $P = P_0 - k_r \dot{E}_w P_t$
Constant terminal pressure case: $W_e = k_p(P_0 - P)Q_t$

Parameter	Radial	Linear	Thick sand	Hemispheric
t_D	$\frac{0.00633kt}{\mu\phi c r_b^2}$	$\frac{0.00633kt}{\mu\phi c L^2}$	$\frac{0.00633kt}{\mu\phi c r_b^2}$	$\frac{0.00633kt}{\mu\phi c r_b^2}$
Ω	—	$\frac{0.00633kt}{\mu\phi c}$	—	—
k_r	$\frac{25.15\mu}{kh}$	Infinite: $178\mu/Ak$ Finite: $158\mu L/Ak$	$\frac{25.15\mu}{kh}$	$\frac{50.2\mu}{kr_b}$
k_p	$6.283\phi c r_b^2 h$	Infinite: $1.13\ \phi cAL$ Finite: ϕcAL		$3.14 r_b^3 \phi c$
P_t	Fig. 8-22	Infinite: $\sqrt{\Omega}$ Finite: ref. [1-39]	ref. [1-39]	$1 - e^{t_D}[1 - \text{erf}(\sqrt{t_D})]$
Q_t	Fig. 8-24	Infinite: $\sqrt{\Omega}$ Finite: ref. [1-39]	—	$t_D + 2\sqrt{t_D/3.14}$

A cross sectional area, ft²
c compressibility, vol/vol/psi
k permeability, md
L length of finite aquifer, ft
r_b radius of gas bubble, ft
t time, days
Ω transformed time, ft²
μ viscosity, cp
ϕ porosity

An elliptical model was presented in [1-39] as well.

are similar to those for the constant terminal flow rate case:

1. The initial pressure throughout the aquifer is constant, P_0.[5]
2. There is no pressure gradient and hence no flow at the extension boundary of the aquifer, r_e.
3. The pressure at the gas-water interface is constant.

[5] It may be changed after some cycles of storage [8-25].

Figure 8-23*a* shows a system for observing pressures in a gas injection process. Figure 8-23*b* and *c* shows the variation of influx rate injection pressure with time. Initially, only the first time period ($t_0 \rightarrow t_1$) is considered. The pressure drop is taken as the difference of average pressures:

$$\Delta P_0 = \left(\frac{P_1 - P_0}{2}\right)_{\text{gas bubble}} \tag{8.61}$$

The governing water influx equation[6] for t_0 to t_1 is

$$W_{e,1} = k_p \cdot \Delta P_0 \cdot Q_t(t_0 \rightarrow t_1)$$

$$k_p = 6.283\phi c r_b^2 h \tag{8.62}$$

As in the constant terminal rate case, the ratio of the exterior radius to the gas bubble radius, $R = r_e/r_b$, may be finite or infinite. In the solution for dimensionless cumulative water influx, the influence function Q_t is dependent upon the boundary conditions chosen. The $W_{e,1}$ is the water influx due to ΔP_0 and $Q_t(t_0 \rightarrow t_1)$ is dependent upon the values of $R = r_e/r_w$ as shown in Fig. 8-24.

For the second time period ($t_1 \rightarrow t_2$), the change in pressure is based on the average gas bubble pressure, $(P_0 + P_1)/2$, that is,

$$\Delta P_1 = (P_{\text{avg}})_{t_1 \rightarrow t_2} - (P_{\text{avg}})_{t_0 \rightarrow t_1}$$

$$= \frac{P_1 + P_2}{2} - \frac{P_0 + P_1}{2} = \frac{P_2 - P_0}{2} \tag{8.63}$$

and the cumulative water flow, by applying the superposition principle, is

$$W_{e,2} = k_p \Delta P_0 Q_t(t_0 \rightarrow t_2) + k_p \Delta P_1 Q_t(t_1 \rightarrow t_2) \tag{8.64}$$

The generalized equations for the constant terminal rate case and the constant terminal pressure case are summarized as follows:

Constant terminal pressure case:

$$W_{e,n} = k_p\left[\Delta P_0 Q_t(t_0 \rightarrow t_n) + \Delta P_1 Q_t(t_1 \rightarrow t_n) + \cdots + \Delta P_{n-1} Q_t(t_{n-1} \rightarrow t_n)\right]$$

$$= k_p \sum_{j=0}^{n-1} \Delta P_j Q_t(t_j \rightarrow t_n) \tag{8.65}$$

where

[6] In the constant terminal rate case, $\dot{E}_w$ (ft³/day) denotes water flow rate; on the other hand, W_e (ft³) is used to represent cumulative flow for constant pressure cases.

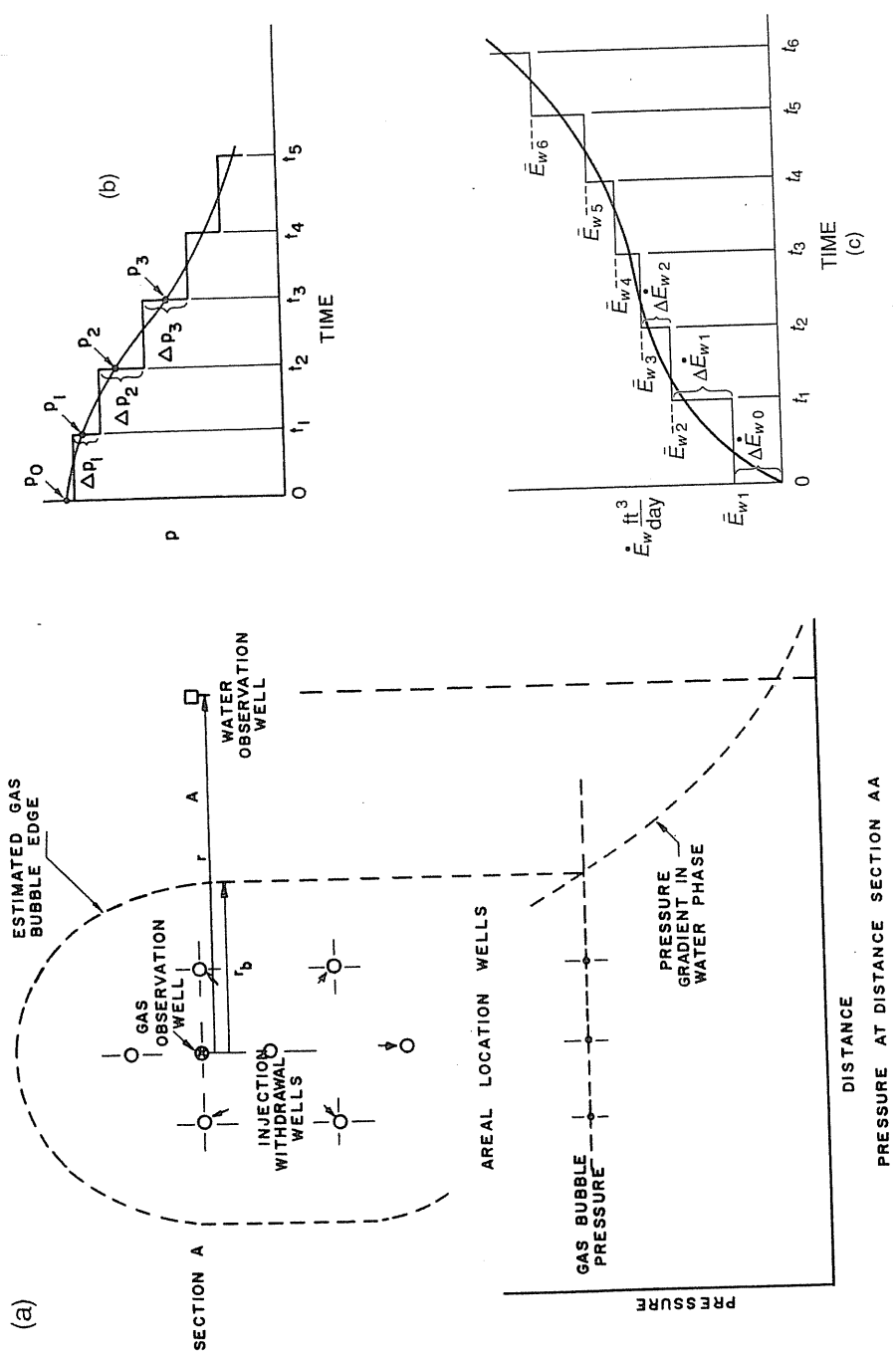

FIGURE 8-23
(a) Observation wells in gas bubble and aquifer; (b) approximation of pressure curve by step function; (c) approximation of influx rate curve by step

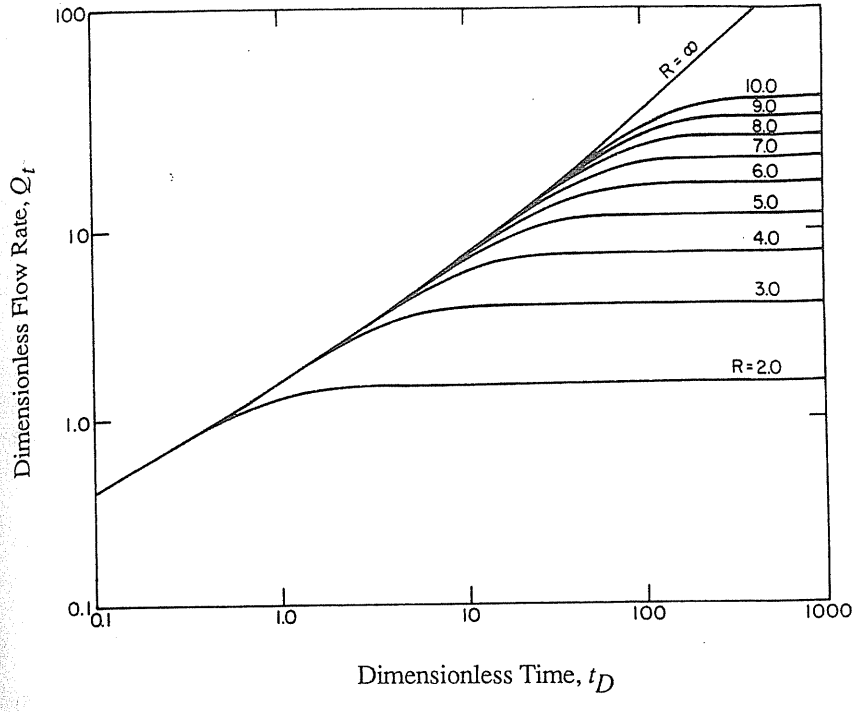

FIGURE 8-24
Van Everdingen and Hurst dimensionless pressure, Q_t, as a function of dimensionless time [Klins et al., 8-28, courtesy SPE-AIME].

$$\Delta P_0 = \frac{P_0 - P_1}{2},\ \Delta P_1 = \frac{P_0 - P_2}{2},\ \Delta P_2 = \frac{P_1 - P_3}{2},\ \ldots,\ \Delta P_{n-1} = \frac{P_{n-2} - P_n}{2} \tag{8.66}$$

Constant terminal rate case:

$$\begin{aligned} P_0 - P_n &= k_r\big[\Delta\dot{E}_{w,0}P_t(t_0 \to t_n) + \Delta\dot{E}_{w,1}P_t(t_1 \to t_n) + \cdots \\ &\quad + \Delta\dot{E}_{w,n-1}P_t(t_{n-1} \to t_n)\big] \\ &= k_r \sum_{j=0}^{n-1} \Delta\dot{E}_{w,j}P_t(t_j \to t_n) \end{aligned} \tag{8.67}$$

where

$$\Delta\dot{E}_{w,0} = \frac{\dot{E}_{w,1} - \dot{E}_{w,0}}{2},\ \Delta\dot{E}_{w,1} = \frac{\dot{E}_{w,2} - \dot{E}_{w,0}}{2},$$

$$\Delta\dot{E}_{w,2} = \frac{\dot{E}_{w,3} - \dot{E}_{w,1}}{2}, \ldots, \Delta\dot{E}_{w,n-1} = \frac{\dot{E}_{w,n} - \dot{E}_{w,n-2}}{2} \tag{8.68}$$

Example 8.8 [Katz et al., 1-39]. A tentative pressure schedule is given below for the first year of depletion of a natural gas reservoir.

Time in months	Reservoir pressure, psia
0	700
3	680
6	645
9	610

It is desired to calculate the water influx. The aquifer may be considered to be of infinite extent. The original reservoir pressure P_0 is 700 psia. The following additional data are available:

formation thickness h	30 ft
compressibility c	7×10^{-6} vol/vol/psi
permeability k	100 md
porosity ϕ	0.15
radius of gas bubble r_b	5000 ft
viscosity μ	1 cp

Solution. Since the reservoir pressure is specified and varies with time, Eq. (8.65) may be used, superposing the effects of three constant pressure steps. For time up to 3 months:

$$k_p = 6.283\phi c r_b^2 h = 6.283(0.15)(7 \times 10^{-6})(5000^2)(30) = 4950$$

$$\Delta P_0 = \frac{P_1 - P_0}{2} = \frac{680 - 700}{2} = -10$$

$$t_D = \frac{0.000264kt(\text{hr})}{\mu\phi c r_b^2} = \frac{(0.000264)(100)(3 \times 30 \times 24)}{(1)(0.15)(7 \times 10^{-6})(5000^2)} = 2.17$$

$$Q_t = 2.575 \text{ (from Fig 8-24, } R = \infty)$$

$$W_{e,1} = k_p \sum_{j=0}^{0} \Delta P_j Q_t(t_0 \rightarrow t_1) = (4950)(-10)(2.575) = -127,500 \text{ ft}^3$$

The results for later time periods are summarized below:

$j\ (t_j \rightarrow t_n)$	t_D	$Q_{t,j}$	ΔP_j	$W_{e,n}$ (formula)	$W_{e,n}$
0 (0 → 3)	2.17	2.575	−10	$k_p\Delta P_0 Q_{t,0}$	−127,500 ft^3
1 (3 → 6)	4.34	4.113	−27.5	$k_p(\Delta P_0 Q_{t,1} + \Delta P_1 Q_{t,0})$	−555,000 ft^3
2 (6 → 9)	6.51	5.448	−35	$k_p(\Delta P_0 Q_{t,2} + \Delta P_1 Q_{t,1} + \Delta P_2 Q_{t,0})$	−1,230,000 ft^3

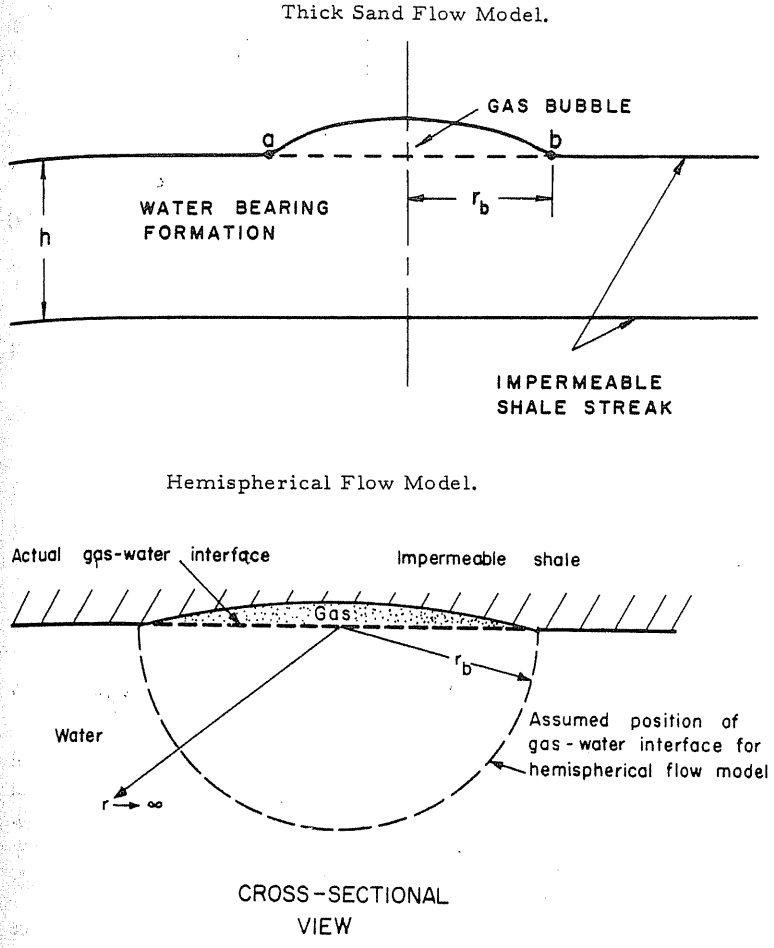

FIGURE 8-25
Storage gas bubble models: thick sand and hemispherical [Katz et al., 1-39, courtesy AGA].

If the aquifer in this example had been limited in extent, then the Q_t values would have been taken from Fig. 8-24 for the appropriate value of R.

Practical Considerations

This chapter has emphasized the radial model. In reality, different geometries exist, as shown in Figs. 8-25 and 8-21: the linear model, the thick sand model, the hemispherical model, and even more complex structures. Table 8.5 lists several ideal cases for both constant terminal rate and constant terminal pressure; the details are discussed in reference [1-39].

The spatial variation of permeability k and reservoir aquifer geometry are

seldom known with sufficient accuracy to justify any solution of the flow equation (Eq. 8.11) for the real storage reservoir. Actually, k_pQ_t should be obtained directly from field data. How to obtain k_pQ_t? It all depends on how engineers interpret the data of key wells and observation wells. For a particular gas bubble (linear model) and aquifer storage system, a graph of empirical base such as Fig. 8-26 should be constructed and k_pQ_t approximated as

$$k_pQ_t = C_1\sqrt{t} \tag{8.69}$$

where C_1 is the characteristic constant for the particular operating reservoir, as determined by field data analysis.

Example 8.9 [1-2]. The influence function k_pQ_t for a linear aquifer is proportional to the square root of time, as shown in Table 8.5:

$$k_pQ_t = 10^5 \cdot \sqrt{t(\text{days})} \quad \text{ft}^3/\text{psi}$$

An aquifer storage reservoir is to be grown in a linear aquifer by gas injection at 200 psi above initial aquifer pressure. Estimate the water influx/efflux 2 years after initiation of gas injection.

Solution. From Table 8.5 for the linear flow case:

$$W_e = k_p\Delta PQ_t = 10^5\sqrt{t(\text{days})}(P_1 - P_0) = 10^5\sqrt{2 \times 365}(200)$$
$$= 5.4 \times 10^8 \text{ ft}^3 \text{ (efflux)} \quad = -5.4 \times 10^8 \text{ ft}^3 \text{ (influx)}$$

For the radial model, k_pQ_t could be, and is preferred to be, obtained by analyzing field data, while Q_t is set to be the ideal values of van Everdingen and Hurst's charts [8-19] as shown in Fig. 8-24. How to obtain the optimal value of k_p from field data was discussed in an AGA monograph on water movement [1-39]. Also, Coat, Rapoport, McCord, and Drews [8-14] reported that, by using linear simplex programming, the influence function P_t could be determined from field data.

The prediction of water movement is straightforward once the influence function $F(t)$ (either k_pQ_t or k_rP_t) is known. If no field data are available, then the $F(t)$ corresponding to some idealized model must be employed in predicting water movement [1-39]. If, however, field pressure production data are available, $F(t)$ may be "backed out" from the data, since the observed field performance

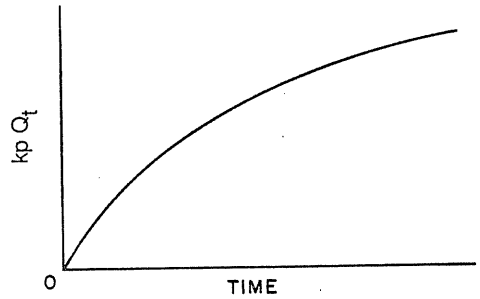

FIGURE 8-26
Empirical influence function k_pQ_t versus time [Katz & Coats, 1-2].

reflects the aquifer characteristics. As noted above, the use of $F(t)$ for an idealized model involves choice of (1) model geometry, (2) exterior boundary conditions (e.g., infinite, closed, or constant pressure), and (3) model parameters (k_p and k_r in Table 8.5). Advantages of "backing out" the influence function from field data are that

1. none of the above choices is required, and
2. the influence function determined reflects actual field performance.

Disadvantages are that

1. the resemblance of the backed-out $F(t)$ to the true function is proportional to the accuracy of field data, and
2. the influence function is obtained only up to the time of the last available field data; extrapolation is required to predict future water movement.

Applications of the influence function to date have met little difficulty from either of these disadvantages. The accuracy of the influence function constructed for the reservoir depends on the accuracy of the initial gas-in-place estimation. The material balance approach described below is essential for obtaining the initial gas in place.

Continuation of Material Balance with Movement Equations

The ability to calculate influx from a known pressure schedule is useful but not sufficient, since in most practical cases, the reservoir pressure itself needs to be determined. That is, the information normally known or estimated beforehand is the injection/withdrawal schedule rather than pressure. A method is therefore required for calculating reservoir pressure from a given production schedule.

As shown in Fig. 8-27, the material balance for a gas field is simply

V_0 (initial pore volume) = V_n (current pore volume)
+ ΔV (pore volume invaded by water)

$$G_0B_{g,0} = (G_0 - G_p)B_g + W_{e,n} \tag{8.70}$$

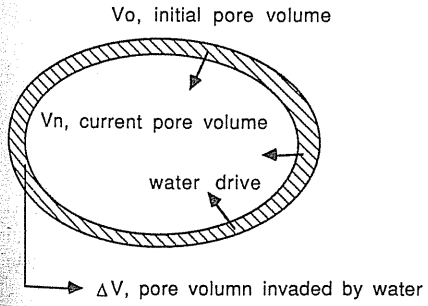

FIGURE 8-27
Material balance of gas bubble with consideration of water movement at the edges [Katz & Coats, 1-2].

where subscripts g and 0 denote gas phase and initial values, and G_0 and G_p are the initial gas in place and accumulative production, both in standard conditions. B is formation factor as in Eq. (8.20) which converts the pore volume at standard conditions to reservoir pore volume. It could be represented by

$$B \approx \frac{a}{P} + b \tag{8.71}$$

since in most cases the compressibility factor Z can be represented as a linear function of pressure over the pressure range encountered. $B_{g,0}$ is the value of B_g at initial pressure P_0.

Combining Eqs. (8.65), (8.70), and (8.71) gives

$$G_0 B_{g,0} = (G_0 - G_{p,n})\left(\frac{a}{P_n} + b\right) + k_p \sum_{j=0}^{n-1} \Delta P_j Q_t(t_j \rightarrow t_n) \tag{8.72}$$

Applications of Eq. (8.72) are illustrated in Example 8.10, which shows how to obtain initial gas in place G_0 as well as the influence function $k_p Q_t$ with known pressures and production history (P_0, P_1, . . . , P_n, and G_p).

Example 8.10 [Katz & Coats, 1-2]. A gas field has a gas formation factor ($B_g = 15/P - 0.0012$ ft^3/Scf) and a "pressure case" influence function $k_p Q_t = C_1\sqrt{t(\text{days})}$ ft^3/psi. P is reservoir pressure in psia; initial pressure P_0 is 1000 psia. Estimate field initial gas in place and the reservoir characteristics constant C_1 for the following production schedule:

t, months	$G_p \times 10^{-9}$ ft^3	P, psia	B_g
0	—	1000	0.0138
6	0.6	987	0.0140
12	1.6	951	0.01457

Solution. Rearranging Eq. (8.72) and using the influence function $C_1\sqrt{t}$

$$(B_{g,0} - B_{g,n})G_0 - C_1 \sum_{j=0}^{n-1} \Delta P_j \sqrt{t}(t_j \rightarrow t_n) = -B_{g,n} G_p$$

For time periods $t = 0$ to $t = 6$ and $t = 0$ to $t = 12$, one obtains two equations:

$$(0.01380 - 0.01400)G_0 - (1000 - 987)(\sqrt{30(6-0)})C_1 = -0.01400(0.6 \times 10^9)$$

$$(0.01380 - 0.01457)G_0 - \left[(1000 - 987)(\sqrt{30(12-0)}) + (987 - 951)(\sqrt{30(12-6)})\right]C_1 = 0.01457(-1.6 \times 10^9)$$

The above two equations with the two unknowns G_0 and C_1 can be solved to get

$$G_0 = 20 \times 10^9 \text{ ft}^3$$

$$C_1 = 15{,}000$$

This method has its limitations. An error analysis shows it is so sensitive to the difference of formation factors, $B_{g,0} - B_{g,n}$, that a high pressure drop $\Delta(P/Z) > 200$ psia is required to estimate the initial gas in place. It implies that withdrawal of a large amount of top gas (usually 20 to 40 percent) is essential for an accurate inventory check.

As long as the initial gas in place G_0 and the influence function $k_p Q_t$ are established, to predict the pressure drop with proposed injection/withdrawn schedule becomes straightforward.

The Moving Boundary Problem

An assumption implicit in the above discussion is the existence of a fixed reservoir-aquifer gas-water interface. That is, all pressures appearing in the water movement equations are pressures at a fixed boundary or surface in space that does not move with time. In reality, of course, this gas-water interface necessarily moves by virtue of the water influx/efflux. The amount of movement in the case of a partial water drive field is generally small in relation to the magnitude of the field radius r_b. However, the assumption of a small relative variation in r_b is not a good assumption in the early growth period of an aquifer storage reservoir.

Equations (8.60) and (8.62) hold only for a fixed boundary. Hence, their application in Eqs. (8.65) and (8.67) is invalid if the gas-water boundary moves with time.

The prediction of early growth of an aquifer storage reservoir can be handled by an analysis that considers water movement across a fixed boundary at $r = r^*$ or (in case of a linear aquifer) $x = x^*$. The unknown pressure at this fixed position is related to the gas bubble pressure through the assumption that steady state water flow exists at any instant between the bubble edge r_b and r^*. Figure 8-28 illustrates the growing bubble with fixed position x^* or r^* greater than the ultimate bubble size.

The first part of the analysis is the relation between bubble or gas-water interface pressure and pressure at the fixed boundary. For steady state flow this relation is derived from Darcy's law, $q = (kA/\mu)(\Delta P/\Delta L)$:

Linear:
$$\Delta P = P_b - P^* = -158\frac{\dot{E}_w \mu}{khw}(x^* - x_b) \tag{8.73}$$

Radial:
$$\Delta P = P_b - P^* = -25.15\frac{\dot{E}_w \mu}{kh}\ln\left(\frac{r^*}{r_b}\right) \tag{8.74}$$

where P_b (psi) is the pressure at the gas-water interface, x_b or r_b (ft) the position of the gas-water interface, x^* or r^* (ft) the position of the fixed boundary, $\dot{E}_w$ (ft^3/day) the rate of water influx/efflux, k (md) the permeability, h (ft) the aquifer thickness, w (ft) the linear aquifer width, μ (cp) water viscosity, and P^* (psi) water pressure at the fixed boundary.

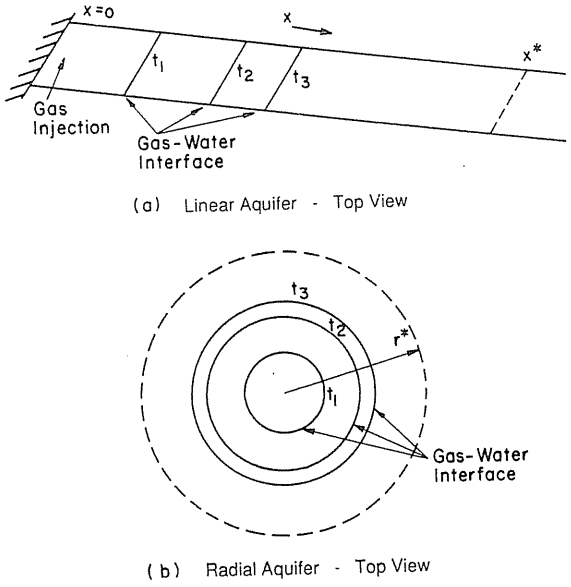

FIGURE 8-28
Expanding gas bubble during initial growth of an aquifer storage reservoir [Katz & Coats, 1-2].

The second element of the analysis is the relation between the interface position x_b or r_b and the reservoir pore volume (gas-occupied space). This relation is

$$r_b \propto V^{\omega} \tag{8.75}$$

where $\omega = \frac{1}{2}$ for a cylinder, $\frac{1}{4}$ for a reservoir with a parabolic-shaped cap rock, $\frac{1}{3}$ for a cone-shaped reservoir, and 1 (with r_b replaced by x_b) for a linear aquifer. The pore volume V is given by

$$V = (G_0 - G_p)B_g = (G_0 - G_p)\left(\frac{a}{p} + b\right) \tag{8.76}$$

where the constants a and b derive from a linearization of the compressibility factor Z versus pressure at constant temperature.

Rearranging Eq. (8.67) at the fixed boundary,

$$P_0 - P_n^* = k_r \sum_{j=0}^{n-1} \Delta\dot{E}_{w,j} P_t(t_j \rightarrow t_n) \tag{8.77}$$

Here, as before, P_n^* is the pressure at the fixed boundary at time $n\Delta t$ and $\Delta\dot{E}_{w,j} = (\dot{E}_{w,j+1} - \dot{E}_{w,j-1})/2$, ft^3/day.

Finally the reservoir pore volume V_n at time $n\Delta t$ is simply

$$V_n = V_{n-1} - \Delta t\overline{E_{w,n}} \tag{8.78a}$$

$$V_n = -\Delta t \sum_{j=0}^{n-1} \frac{\dot{E}_{w,j} + \dot{E}_{w,j+1}}{2} = -\Delta t \sum_{j=1}^{n} \overline{E_{w,j}} \tag{8.78b}$$

Eq. (8.74) is written at time $n\Delta t$ as

$$P_{b,n} - P_n^* = -k_r\overline{E_{w,n}} \ln \frac{r^*}{r_{b,n}} \tag{8.79}$$

Then, subtraction of Eq. (8.79) from Eq. (8.77) yields a single equation allowing calculation of bubble growth rate from specified gas bubble pressure:

$$P_0 - P_{b,n} = k_r \sum_{j=0}^{n-1} \Delta\dot{E}_{w,j} P_t(t_j \rightarrow t_n) + k_r\overline{E_{w,n}} \ln \frac{r^*}{r_{b,n}} \tag{8.80}$$

$$\overline{E_{w,n}} = \frac{P_0 - P_{b,n} - k_r\left(\sum_{j=0}^{n-2} \Delta\dot{E}_{w,j} P_t(t_j \rightarrow t_n) + P_t(t_{n-1} \rightarrow t_n)\overline{E_{w,n-1}}\right)}{k_r\left[P_t(t_{n-1} \rightarrow t_n) + \ln(r^*/r_{b,n})\right]} \tag{8.81}$$

since

$$\Delta\dot{E}_{w,n-1} = \overline{E_{w,n}} - \overline{E_{w,n-1}} \tag{8.82}$$

This equation along with Eq. (8.78) allows calculation of the growth rate of an aquifer storage reservoir. A trial-and-error calculation is necessary since $r_{b,n}$ in Eq. (8.81) is known only if $\overline{E_{w,n}}$ is known.

Example 8.11 [1-2]. An aquifer storage reservoir is to be grown by gas injection at a constant pressure 200 psi above initial aquifer pressure. Structure indicates the radial flow model is reasonable and that the bubble should grow roughly as a cylinder. Estimate bubble pore volume and gas in place after 6 months using two 3-month time increments.

The formation volume factor is $B_g = (15/P - 0.0012)$ ft^3/Scf, and other estimated data are

gas fixed radius r^*	5000 ft
aquifer thickness h	50 ft
permeability k	200 md
viscosity of water μ	1 cp
initial aquifer pressure P_0	1000 psia
compressibility c	7×10^{-6} vol/vol/psi
porosity ϕ	0.15

Solution. For the infinite radial aquifer, Table 8.5 gives

$$k_r = \frac{25.15\mu}{kh} = \frac{25.15(1)}{200(50)} = 0.002515$$

$$t_D = \frac{0.000264kt}{\mu\phi c r^{*2}} = \frac{0.000264(200)(24t)}{(1)(0.15)(7 \times 10^{-6})(5000)^2} = 0.0483t$$

where 5000 ft is selected for the fixed radius r^*. Linear interpolation in Fig. 8-22 yields

j	t, days	t_D	P_t
0	0	0	0
1	90	4.35	1.306
2	180	8.7	1.5907

If the bubble grows roughly as a cylinder, then r_b and pore volume are related by

$$\pi r_b^2 h\phi = V$$

$$r_b = \left(\frac{V}{\pi h\phi}\right)^{1/2} = \left(\frac{V}{\pi(50)(0.15)}\right)^{1/2} = 0.206\sqrt{V} \qquad (8.83)$$

Assuming $r_{b,1} = 280$ ft for the first 90 days, Eqs. (8.81) and (8.78) give

$$\overline{E_{w,1}} = \frac{1000 - 1200 - 0 + 0}{0.002515[1.306 + \ln(5000/280)]} = -19,000 \text{ ft}^3/\text{day}$$

$$V_1 = -90(-19,000) = 1.71 \times 10^6 \text{ ft}^3$$

For time $j = 0$, the last two terms in the numerator of Eq. (8.81) are zero according to true physical meanings.

Equation (8.83) as a check gives

$$r_{b,1} = 0.206\sqrt{1.71 \times 10^6} = 270 \text{ ft}$$

which is sufficiently close to the assumed 280 ft.

For the next 90 days, assuming $r_{b,2}$ is 380 ft, Eqs. (8.81) and (8.78) give

$$\overline{E_{w,2}} = \frac{1000 - 1200 - 0.002515(-19,000)(1.5907) + 0.002515(-19,000)(1.3606)}{0.002515(1.306 + \ln(5000/380))}$$

$$= -19,100 \text{ ft}^3/\text{day}$$

$$V_2 = -90(-19,000 - 19,100) = 3.42 \times 10^6 \text{ ft}^3$$

Equation (8.83) gives a good check:

$$r_{b,2} = 0.206\sqrt{3.42 \times 10^6} = 382 \text{ ft}$$

Thus after six months of gas injection at 1200 psi, reservoir pore volume is 3,420,000 ft^3 and gas in place is

$$G_2 = \frac{V_2}{B_{g,2}} = \frac{3.42 \times 10^6}{15/1200 - 0.0015} = 311 \times 10^6 \text{ Scf}$$

8.8 FURTHER METHODS FOR WATER MOVEMENT CALCULATIONS

An empirical method referred to as *pound-day* was introduced by Katz, Tek, and Coats [8-24] and will be presented in Chapter 12. Since van Everdingen and Hurst's classic paper [8-18], several attempts have been made to extend its applicable ranges or to overcome the difficulties caused by its tedious superposition calculations. The van Everdingen and Hurst charts, Figs. 8-22 and 8-24, were extended by Chatas [8-13]. M. Katz extended several of these tables to give the pressure distribution out into the aquifer [1-2,1-39]. Two methods proposed by Carter and Tracy [8-12] and by Fetkovitch [8-20] (finite aquifer) could yield satisfactory results without the superposition calculations. Recently (1986), Leung applied a convolution method to several previous models to increase their accuracy and efficiency [8-32]; Leung further extended the method to natural fractured reservoirs [8-33].

HOME PROBLEMS

8.1. Determine the time in hours at which Eq. (8.31) becomes valid for a reservoir of $k = 20$ md, $\phi = 0.12$, $r_w = 0.25$ ft, and pressure 1000 psia. Gas properties are in Table 8.2.

8.2. Estimate stabilization time for a well in a reservoir with properties given in Problem 8.1. Use 40-acre spacing ($r_e = 600$ ft).

8.3. Geological evidence indicates the presence of a sealing fault about 100 feet distant from a gas well. Estimate the duration of well test necessary to obtain the second linear portion on the drawdown curve, indicating the presence of the fault. Estimated data are $k = 100$ md, $\mu = 0.13$ cp, $\bar{P} = 1000$ psia, and $\phi = 0.1$.

8.4. A gas well was produced at a constant rate from an initial shut-in condition. A plot of ΔP^2 vs. log of time (hours) showed two linear portions, the later one of about twice the slope of the first one. Average pressure is 1200 psia, porosity is 0.1, formation thickness is 22 ft, and gas properties are in Table 8.2. The slope of the first linear portion of the drawdown curve is 8×10^4 psi^2/cycle. The intersection time for the two linear portions is 83 hr, and the flow rate is 2000 Mcf/day. Estimate distance to the flow barrier.

8.5. If a strong high-velocity effect is present, does the drainage radius propagating rate increase or decrease? Why?

8.6. The influence function k_pQ_t is given for a reservoir aquifer system as

$$k_pQ_t = 8000\sqrt{t(\text{days})} \text{ ft}^3/\text{psi}$$

Estimate water influx at the end of one year for the following pressure schedule:

t, months	*P*, psia
0	500
3	480
6	450
9	410
12	350

8.7. A natural gas–producing reservoir had an original discovery pressure of 700 psia. The shape of the gas bubble is cylindrical. The thickness of the aquifer is 30 ft. For the first three months of gas production, the pressure in the gas bubble is to be maintained at 690 psia.

Calculate the cumulative water influx into the gas sand during the first three months of gas production after discovery. The radius of the gas field or the inner boundary of the aquifer is 5000 ft. The compressibility of the aquifer is 7×10^{-6} vol/vol/psi. The permeability of the aquifer sand is 100 md. The porosity is 0.15. The viscosity of the water in the aquifer is 1 cp.

8.8. It is desired to grow a gas bubble at the rate of 100 ft^3/day in an aquifer extending indefinitely in one direction and located between two parallel faults. Determine the gas reservoir pressures at 30, 60, 90, and 365 days after initiation of the gas bubble. The available data on the physical and geometric properties of the gas bubble/aquifer system are given below:

$$P_0 = 400 \text{ psia}$$

$$c = 7 \times 10^{-6} (1/\text{psi})$$

$$\mu = 1 \text{ cp}$$

$$k = 30 \text{ md}$$

$$\phi = 0.16$$

$$A \text{ (cross section)} = 20{,}000 \text{ ft}^2$$

8.9. A well located in the center of a reservoir with $h = 40$ ft, $k = 20$ md, $\phi = 0.15$, $r_w = 0.4$ ft, $r_e = 1000$ ft, $\beta = 2.8 \times 10^{10}$, and no skin, is produced at a constant terminal rate of $Q_{sc} = 6.55$ MMcf/day. Fluid properties are in Table 8.2.

(*a*) Calculate the high-velocity intensity N_T and the flow rate Q_D.

(*b*) Determine the stabilized time t_s for the pseudo–steady state to be established throughout the reservoir.

(*c*) Calculate the pressure at the wellbore for the producing time of 0.2 hr.

(*d*) Calculate the pressure at the wellbore when pseudo–steady state is attained.

8.10. Prove that if pseudotime (Eq. 8.14) and pseudopressure (Eq. 8.10) are used, Eq. (8.15) becomes

$$\frac{\phi}{0.0002637 k_r}\left(\frac{\partial m}{\partial t_a}\right)_r = \frac{1}{r}\left[\frac{\partial}{\partial r} r \left(\frac{\partial m}{\partial r}\right)_{t_a}\right]_{t_a} + \left(\frac{\partial^2 m}{\partial t_a^2}\right)_r \left(\frac{\partial t_a}{\partial r}\right)_t^2 + 2\left(\frac{\partial^2 m}{\partial r \partial t_a}\right)_{t_a, r}\left(\frac{\partial t_a}{\partial r}\right)_t + \frac{1}{r}\left(\frac{\partial m}{\partial t_a}\right)_r \left(\frac{\partial t_a}{\partial r}\right)_t + \left(\frac{\partial m}{\partial t_a}\right)_r \left(\frac{\partial^2 t_a}{\partial r^2}\right)_t$$

Hint: For $\psi(r, t) = \psi(r, t_a)$,

$$d\psi = \left(\frac{\partial \psi}{\partial t}\right)_r dt + \left(\frac{\partial \psi}{\partial r}\right)_t dr = \left(\frac{\partial \psi}{\partial t_a}\right)_r dt_a + \left(\frac{\partial \psi}{\partial r}\right)_{t_a} dr$$

RECOMMENDED READING

Energy Resources Conservation Board, *Theory and Practice of the Testing of Gas Wells*, 3rd. Ed., Calgary, Canada (1979).

Katz, D. L., and K. H. Coats, *Underground Storage of Fluids*, Ulrich's Book Store, Ann Arbor, Michigan (1968).

8-1. Matthews, C. S., and D. G. Russell, *Pressure Build-up and Flow Tests in Wells*, SPE Monograph (1967).

REFERENCES

8-2. Aaronsen, S., "Application of Pseudo-time to Estimate Average Reservoir Pressure," SPE Preprint 14256 (1986).

8-3. Agarwal, R. G., R. Al-Hussainy, and H. J. Ramey, Jr., "An Investigation of Wellbore Storage and Skin Effect in Unsteady Liquid Flow: I. Analytical Treatment," *Soc. Pet. Eng. J.*, Vol. 10, No. 3, 279–290, Sept. (1970).

8-4. Agarwal, R. G., "Real Gas Pseudo-time: A New Function for Pressure Build-up Analysis of MHF Gas Wells," SPE Preprint 8279 (1979).

8-5. Al-Hussainy, R., H. J. Ramey, Jr., and P. B. Crawford, "The Flow of Real Gases through Porous Media," *J. Pet. Tech.*, Vol. 18, No. 5, 624–636, May (1966).

8-6. Al-Hussainy, R., *Transient Flow of Ideal and Real Gases through Porous Media*, Ph.D. thesis, Texas A & M Univ., College Station, Texas (1967).

8-7. Aronofsky, J. S., and R. Jenkins, "A Simplified Analysis of Unsteady Radial Gas Flow," *Trans. AIME*, Vol. 201, 149 (1954).

8-8. Aziz, K., and D. L. Flock, "Unsteady State Gas Flow—Use of Drawdown Data in the Prediction of Gas Well Behavior," *J. Can. Pet. Tech.*, 131–135, Feb. (1963).

8-9. Aziz, K., L. Mattar, S. Ko, and G. S. Brar, "Use of Pressure, Pressure Squared, or Pseudo-pressure in the Analysis of Gas Well Data," *J. Can. Pet. Tech.*, No. 2, 58–65, April–June (1976).

8-10. Brons, F., and V. E. Marting, "The Effect of Restricted Fluid Entry on Well Productivity," *J. Pet. Tech.*, Vol. 13, No. 2, 172–174, Feb. (1961).

8-11. Carslaw, H. S., and J. C. Jaeger, *Conduction of Heat in Solids*, Oxford University Press, London (1959).

8-12. Carter, R. D., and G. W. Tracy, "An Improved Method for Calculating Water Influx," *J. Pet. Tech.*, Vol. 12, No. 12, 58–60, Dec. (1960).

8-13. Chatas, A. T., "A Practical Treatment of Nonsteady-state Flow Problems in Reservoir Systems," *Petroleum Engineer*, Vol. 25, No. 5, B42; No. 6, B38; No. 9, B44 (1953).

8-14. Coats, K. H., L. A. Rapoport, J. R. McCord, and W. P. Drews, "Determination of Aquifer Influence Functions from Field Data," *J. Pet. Tech.*, Vol. 16, No. 12, 1417-1424, Dec. (1964).

8-15. Cornell, D., and D. L. Katz, "Flow of Gases through Consolidated Porous Media," *Ind. Eng. Chem.*, 45, 2145 (1953).

8-16. Craft, B. C., and M. F. Hawkins, Jr., *Applied Petroleum Reservoir Engineering*, Prentice-Hall, Englewood Cliffs, N.J. (1959).

8-17. Energy Resources Conservation Board, *Theory and Practice of the Testing of Gas Wells*, 3rd. Ed., Calgary, Canada (1979).

8-18. van Everdingen, A. F., and W. Hurst, "The Application of the Laplace Transformation to Flow Problems in Reservoir," *Trans. AIME*, Vol. 186, 305–326 (1949).

8-19. van Everdingen, A. F., "The Skin Effect and Its Influence on the Productive Capacity of a Well," *Trans. AIME*, Vol. 198, 171 (1953).

8-20. Fetkovitch, M. J., "A Simplified Approach to Water Influx Calculations—Finite Aquifer Systems," *J. Pet. Tech.*, Vol. 23, No. 7, 814–828, July (1971).

8-21. Hawkins, M. F., Jr., "A Note on the Skin Effect," *Trans. AIME*, Vol. 207, 65 (1956).

8-22. Hughes, W. F., and E. W. Gaylord, *Basic Equations of Engineering Science*, Shaum's Outline Series, McGraw-Hill Publishing Co., New York (1964).

8-23. Hutchinson, T. S. and V. J. Sikora, "A Generalized Water-Drive Analysis," *Trans. AIME*, Vol. 216, 169 (1959).

8-24. Katz, D. L., M. R. Tek, and K. H. Coats, "Effect of Unsteady State Aquifer Motion on the Size of an Adjacent Gas Storage Reservoir," *Trans. AIME*, Vol. 216, 18 (1959).

8-25. Katz, M. L., *Fluid Flow and Heat Transfer in Stratified Systems*, Ph.D. dissertation, University of Michigan, Ann Arbor (1960).

8-26. Katz, D. L., M. R. Tek, and S. C. Jones, "A Generalized Model for Predicting the Performance of Gas Reservoirs Subject to Water Drive," SPE Preprint 428 (1962).

8-27. Katz, D. L., "Handling Variations in Aquifer Pressure in Gas Storage," *AGA Operating Section Proceedings*, 675–682 (1985).

8-28. Klins, M. A., A. J. Bouchard, and C. L. Cable, "A Polynomial Approach to Determine the van Everdingen-Hurst Dimensionless Variables P(td) and Q(td) for Water Encroachment Modeling," SPE Preprint 15433 (1986).

8-29. Lee, R. L., R. W. Logan, and M. R. Tek, "Effect of Turbulence of Real Gas through Porous Media," SPE Preprint 14205 (1985); *SPE Formation Evaluation*, 108–120, March (1986).
8-30. Lee, W. J., and S. A. Holditch, "Application of Pseudo-time to Buildup Test Analysis of Low Permeability Gas Wells with Long Duration Wellbore Storage Distribution," *J. Pet. Tech.*, Vol. 34, No. 12, 2877–2887, Dec. (1982).
8-31. Lee, R. L., *Deliverability of Natural Gas*, Ph.D. dissertation, University of Michigan, Ann Arbor (1986).
8-32. Leung, W. F., "A Fast Convolution Method for Implementing Single-Porosity Finite/Infinite Aquifer Models for Water-Influx Calculations," *SPE Reservoir Engineering*, Vol. 1, No. 5, 490–510, Sept. (1986).
8-33. Leung, W. F., "A New Pseudosteady-State Model for Dual-Porosity/Dual-Permeability Aquifers and Two Interconnected Single-Porosity Aquifers," *SPE Reservoir Engineering*, Vol. 1, No. 5, 511–520, Sept. (1986).
8-34. Logan, R. W., R. L. Lee, and M. R. Tek, "Microcomputer Gas Reservoir Simulation Using Finite Element Methods," SPE Preprint 14449 (1985).
8-35. MacDonald, R., private communication (1987).
8-36. Muskat, M., *The Flow of Homogeneous Fluids through Porous Media*, McGraw-Hill Publishing Co., (1937).
8-37. Oren, P. E., R. L. Lee, and M. R. Tek, "The Effects of Wellbore Storage, Skin, and Turbulence Intensity on Early Time Transient Flow of Real Gas through Porous Media," SPE Preprint 15525 (1986), accepted for publication (1987).
8-38. Schilthuis, R. J., "Active Oil and Reservoir Energy," *Trans. AIME*, Vol. 118, 33 (1936).
8-39. Smith, R. V. "Unsteady-State Gas Flow into Gas Wells," *J. Pet. Tech.*, Vol. 13, No. 11, 1151–1159, Nov. (1961).
8-40. Theis, C. V., "The Relationship between the Lowering of Piezometic Surface and the Rate and Duration of Discharge Using Groundwater Storage," *Trans. AGU*, Vol. 16, 519 (1935).
8-41. Wattenbarger, R. A., and H. J. Ramey, Jr., "Gas Well Testing with Turbulence, Damage, and Wellbore Storage," *J. Pet. Tech.*, Vol. 20, No. 8, 877–887, Aug. (1968).
8-42. Wattenbarger, R. A., and H. J. Ramey, Jr., "An Investigation of Wellbore Storage and Skin Effect in Unsteady Liquid Flow: II. Finite Difference Treatment," *Soc. Pet. Eng. J.*, Vol. 10, No. 3, 291–297, Sept. (1970).

CHAPTER 9

GAS WELL-TESTING

Generally speaking, there are two types of gas well testing. The first kind, deliverability testing, includes the well-known *back pressure* and *isochronal* tests. The purpose of such tests is to obtain the bottom hole pressure drop (ΔP^2) corresponding to a given constant wellhead flow rate (Q_{sc}) for a particular well. It has been accepted that $\log(\Delta P^2)$ versus $\log(Q_{sc})$ has a nearly linear relationship. Figure 9-1 [1-1] illustrates the relationship between the flow rate Q_{sc} and the driving force ΔP^2 at the sandface. The first low flow rate is usually above the line, suggesting that the curve may be gradually concave upward. Generally, the straight line relationship for a particular well applies throughout the lifetime of the well, as long as the production remains in single phase. By extending the performance curve, $\log \Delta P^2$ versus $\log Q_{sc}$, one can obtain the *absolute open flow*, or AOF[1]. Though this AOF number does not reflect reality, it does approximate the capacity of the well. Usually, a deliverability test does not need any information on fluid/reservoir parameters, and is developed on an empirical basis.

The second kind of well testing includes drawdown, buildup, two-rate, and multi-rate tests, as well as the type-curve method. These tests are designed to determine the near-well reservoir parameters, such as flow capacity defined as the product of permeability and formation thickness (kh), skin factor (s), high-velocity factor (D), and wellbore storage capacity (C_D).[2]

[1] AOF is defined as the flow rate against zero atmospheric back pressure; in other words, AOF is the maximum theoretical flow rate that could be delivered.

[2] k, h, s, D, and C_D are defined in Chapter 8.

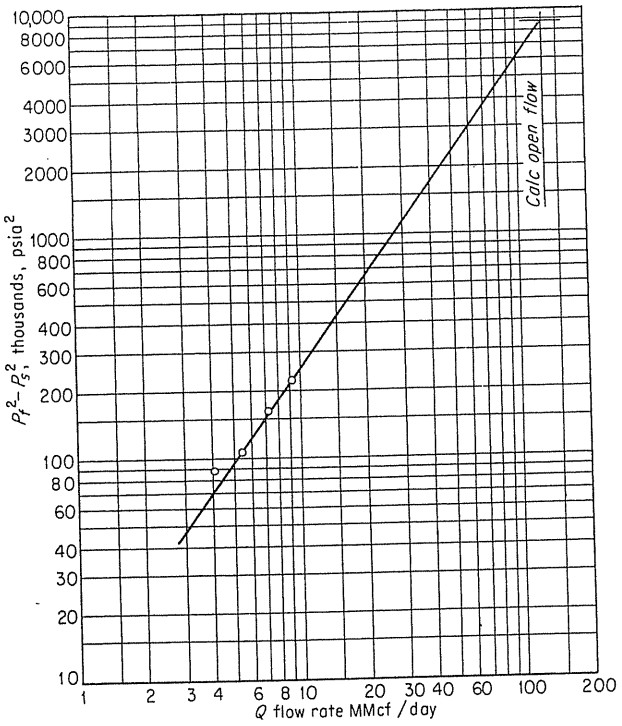

FIGURE 9-1
Typical back pressure plot [Katz et al., 1-1, courtesy McGraw-Hill Publishing Co.].

9.1 DELIVERABILITY TESTS

Deliverability tests are conventionally called *back pressure* tests because they make possible the prediction of well flow rates against any particular pipeline back pressure. Since Rawlins and Schellhart [6-47] of the U.S. Bureau of Mines published the well-known Monograph 7: *Back-pressure Data on Natural Gas Wells and Their Application to Production Practices* introducing the later widely used "back pressure test," many supplemental methods have been suggested. In this chapter, besides the back pressure test, several selected methods will be included and discussed; they are the *isochronal test*, the *modified isochronal test*, the *inverse productivity index* (IPI), and the *modified inverse productivity index*.

Back Pressure Test

Rawlins and Schellhardt [6-47] observed that a plot of $\Delta P^2 = \overline{P}_f^2 - P^2$ ($\overline{P}_f$: closed average formation pressure; P: flowing stabilized sandface pressure) versus Q_{sc} would yield a straight line on a logarithmic plot. The back pressure equation is expressed as

$$Q_{sc} = C(\overline{P}_f^2 - P^2)^n = C(\Delta P^2)^n \tag{9.1}$$

or in another form:[3]

$$\log_{10} \Delta P^2 = -\frac{1}{n} \log_{10} C + \frac{1}{n} \log_{10} Q_{sc} \tag{9.2}$$

where Q_{sc} is the flow rate at standard conditions, C is the performance coefficient, and n is an exponent that describes the inverse of the slope $1/n$ of the plot.

Figure 9-2 shows the typical four-point back pressure test, which is a standard regulatory testing procedure in several states of the United States.

From a theoretical point of view, the stabilized pressure could be obtained by integrating the Darcy equation in the drainage area:[4]

$$P_{DW} = \frac{\Delta P^2}{P_i^2 Q_D} = \ln \frac{r_d}{r_w} \tag{8.35}$$

which can be rearranged in terms of P^2:

$$\log_{10} \Delta P^2 = \log_{10}\left(\frac{\gamma \mu \overline{Z} T}{kh} \ln \frac{r_d}{r_w}\right) + \log_{10} Q_{sc} \tag{9.3}$$

where all the variables are defined as in Chapter 8 for the particular set of units used.

Equation (9.3) shows that, for a viscous Darcy approach, the slope of log ΔP^2 versus log Q_{sc} should be 1 ($1/n = 1$). Slopes greater than 1 ($1/n > 1$) may be due to the high-velocity effect or the variation of gas properties (μ, Z, and c); see Fig. 9-3 [1-1]. Elenbaas and Katz [9-13] calculated a curve that was gradually concave upward to account for the high-velocity effect (Fig. 9-4). Cornell [2-13] measured the high-velocity coefficient β of core samples and correlated it with permeability k to show there is no transient behavior from viscous to quad-Darcy flow [2-19] (discussed in Chapter 2). Indeed, the gradual change of slope of back pressure curves proves their point.

Figure 9-5 is a plot of ΔP^2(psia^2) versus Q/kh(Mcf/day/md/ft) for various discovery pressures and permeabilities; using this chart, the approximate permeability could be obtained by back pressure test. The empirical equation (9.1) could be useful in correlating multiple well data. The constant C at a given ΔP^2 is a deliverability of the well, and the sum of the constant C's represents the total capacity of the field. One immediate drawback of the back pressure test is its need of stabilized pressures, which may only be obtained after a long duration time, especially for some tight sand wells (k is small).

Isochronal Test

Cullender [9-11] proposed a series of flow tests at different rates for the same length of time (Fig. 9-6). The resulting plot of ΔP^2 versus Q_{sc}, would have the

[3] Log_{10} is used for convenience of plotting.
[4] Despite different flow rates, drainage area is the same.

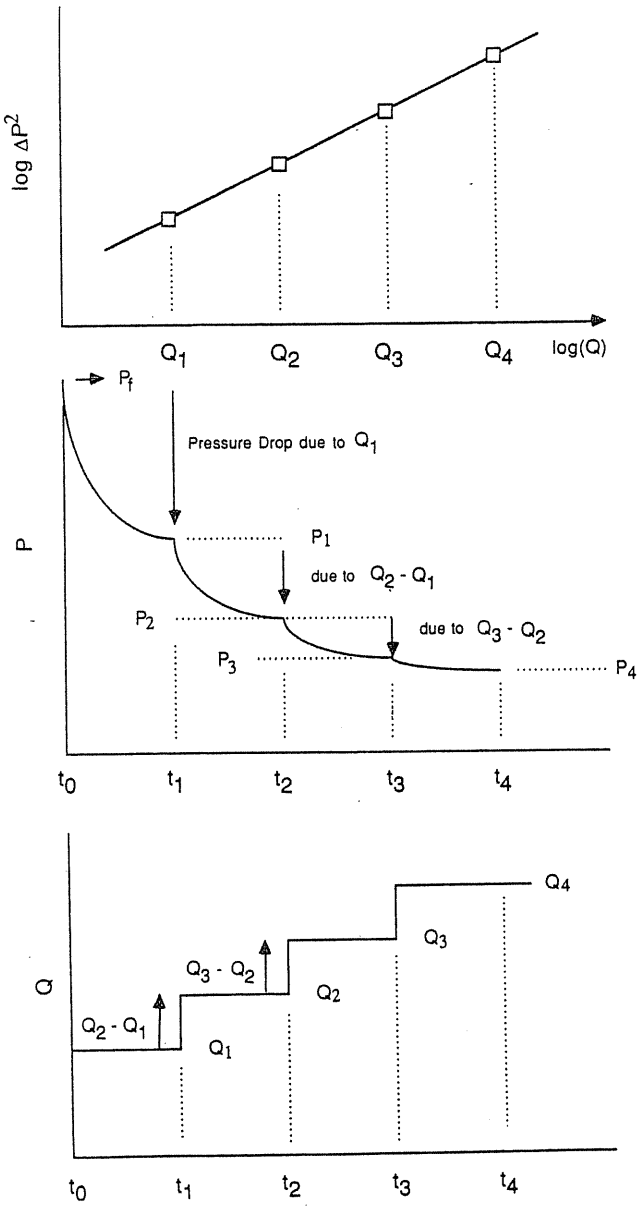

FIGURE 9-2
Typical four-point back pressure test.

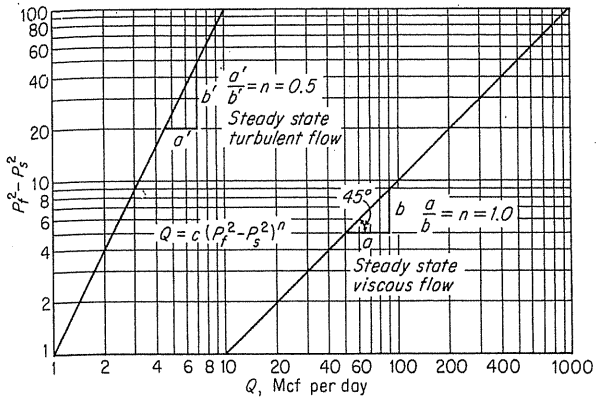

FIGURE 9-3
Variation of slope of back pressure curves for viscous and turbulent flow [Katz et al., 1-1, courtesy McGraw-Hill Publishing Co.].

same slope as the stabilized back pressure performance curve. Then, extending the last flow rate to reach stabilized pressure P and imposing the slope onto the stabilized point $(P_f^2 - P^2)$, one could obtain an approximate performance curve without stabilizing the pressures except for the last flow rate. Figure 9-7 shows the typical isochronal test procedure.

The isochronal test can be justified mathematically. Theoretically, the pressure drop at wellbore for a viscous Darcy case (no high-velocity effect) is

$$P_{DW} = \frac{1}{2}(\ln t_D + 0.80907) + s \tag{9.4}$$

which can be explicitly expressed in logarithmic form as

$$\log_{10} \Delta P^2 = \log_{10} \left\{ \frac{\gamma \overline{\mu Z} T}{kh} \left[\frac{1}{2} \left(\ln \frac{\lambda k t}{\phi \overline{\mu c} r_w^2} + 0.80907 \right) + s \right] \right\} + \log_{10} Q_{sc} \tag{9.5}$$

Eq. (9.5) indicates that as long as one keeps the same duration time, (the first term of the right-hand side has the same magnitude for all flow rates), the slope of the unstabilized performance curve should be one, the same as for the stabilized performance curve. Indeed, Equation (8.37) shows that, assuming wellbore storage and high velocity do not have an effect, the drainage radius r_d moves away from the wellbore with the same speed regardless of the flow rate applied.

It should be noted that too short a duration time in isochronal testing may lead to erroneous interpretation of data because of the wellbore storage effect. The minimum duration time free of wellbore storage effect is

$$t_D = (60 + 3.5s)C_D \tag{8.49}$$

C_D, s, and D could be obtained by the type-curve or the two-rate test, and k (used in t_D) could be determined either by the drawdown test or the buildup test.

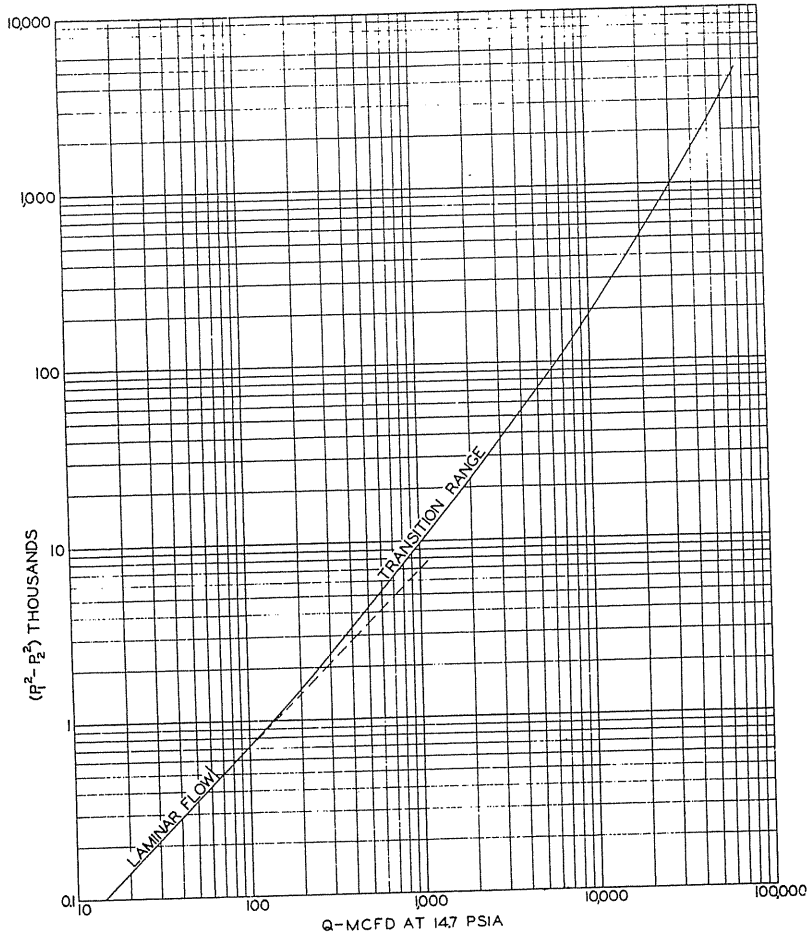

FIGURE 9-4
Calculated back pressure curve showing transition from laminar to turbulent flow [Elenbaas & Katz, 9-13, courtesy SPE-AIME].

For shallow storage fields, the wellbore storage effect may go away in a short time; however, for deep wells, the effect of unloading wellbore contents has to be handled carefully.

Like the back pressure test, the isochronal test requires the shut-in pressure to be returned to the original pressure between measurements. As a result, the isochronal test is impractical for many wells.

Modified Isochronal Test

In order to conserve time and operational cost, Katz et al. [1-1] suggested a modified isochronal test conducted with a shut-in period equal to the flow period,

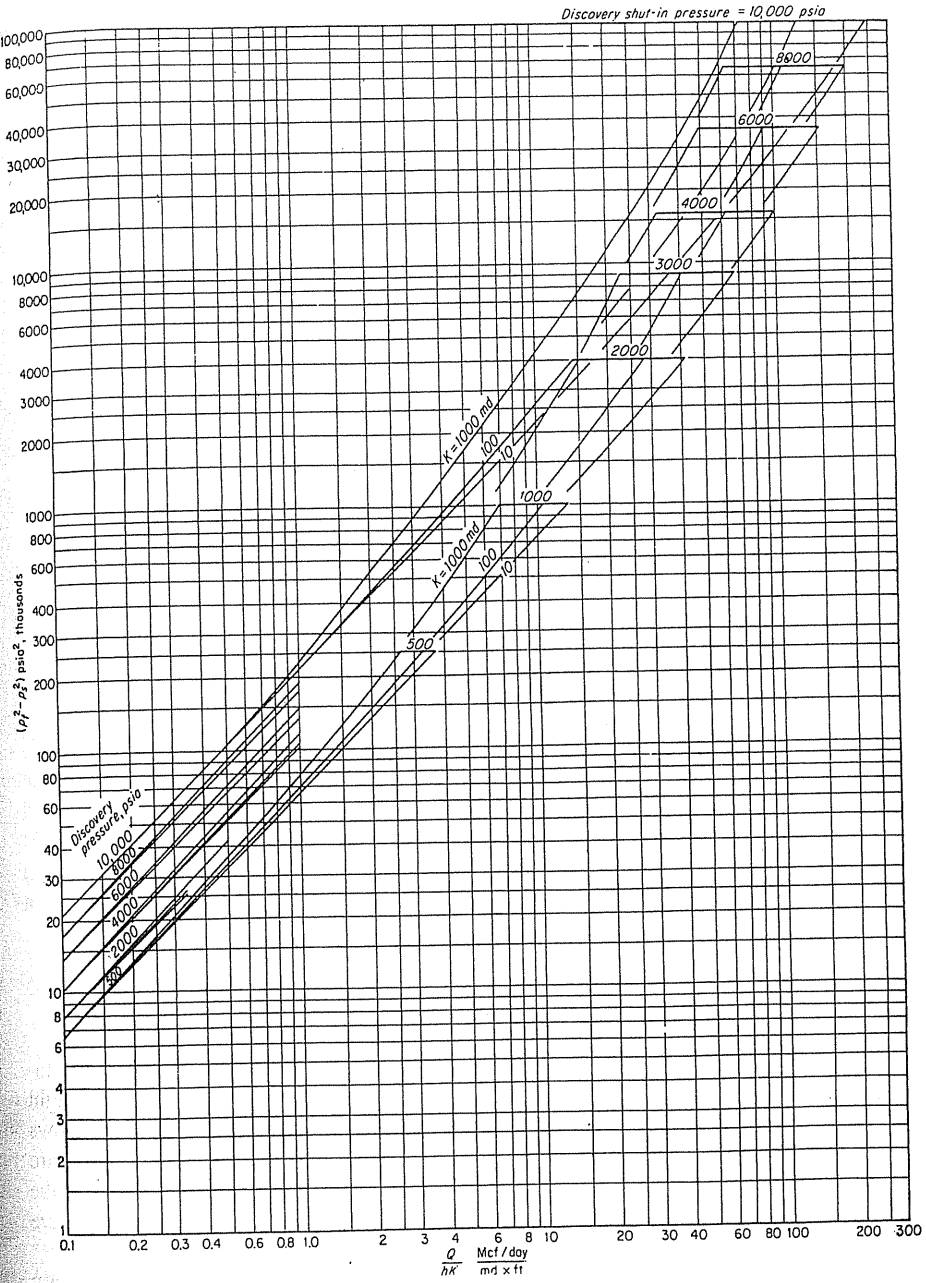

FIGURE 9-5
Performance curves from core data for 0.6-gravity gas [Katz et al., 1-1, courtesy McGraw-Hill Publishing Co.].

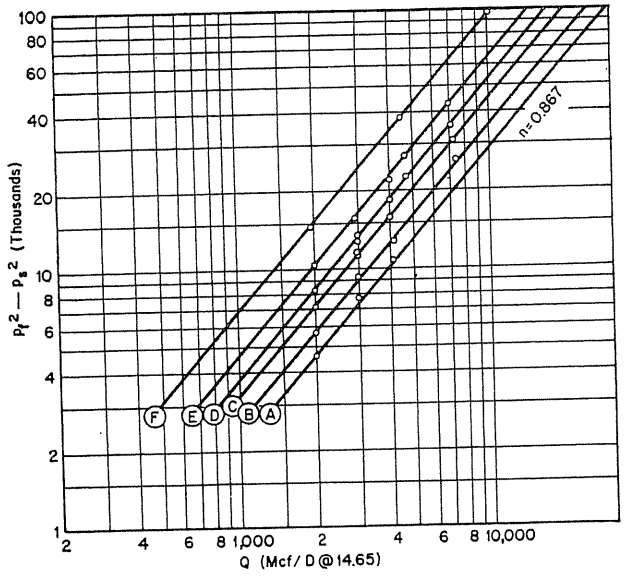

FIGURE 9-6
Isochronal performance curves of gas well No. 1. Duration of flow: (*a*) 0.1 hr, (*b*) 0.2 hr, (*c*) 0.5 hr, (*d*) 1.0 hr, (*e*) 3.0 hr, and (*f*) 24 hr [Cullender, 9-11, courtesy SPE-AIME].

as depicted in Fig. 9-8. Instead of waiting for pressures to be stabilized, the unstabilized shut-in pressures are used. This is a purely empirical approach that does not yield a true isochronal curve but closely approximates one. This method has given satisfactory results for many wells. Hinchman and Poettmann [9-15] performed an error analysis and concluded that the stabilizing time (shut-in) should be as long as possible and about twice as long for the last flow rate of a four-point test as for the other flow rates.

Inverse Productivity Index

Many researchers reported that the back pressure test performance curve is actually concave upward as the flow rate increases, as shown in Fig. 9-9. The straight line concept is just regionally applicable. Extrapolating beyond the test flows region may lead to erroneous results [9-14]. In Fig. 9-9, two test regions are selected; the high flow rate (Test 2) region has a higher slope (smaller n) than the low flow rate (Test 1) region. What causes the performance curve to be concave upward? Is there any theoretical basis?

The flow equation with additional considerations of skin and high-velocity effects is:

$$P_{DW}(ST) = P_{DW} + s + DQ_{sc} \tag{8.47}$$

Combining Eqs. (8.47) and (8.31) in terms of P^2, results in

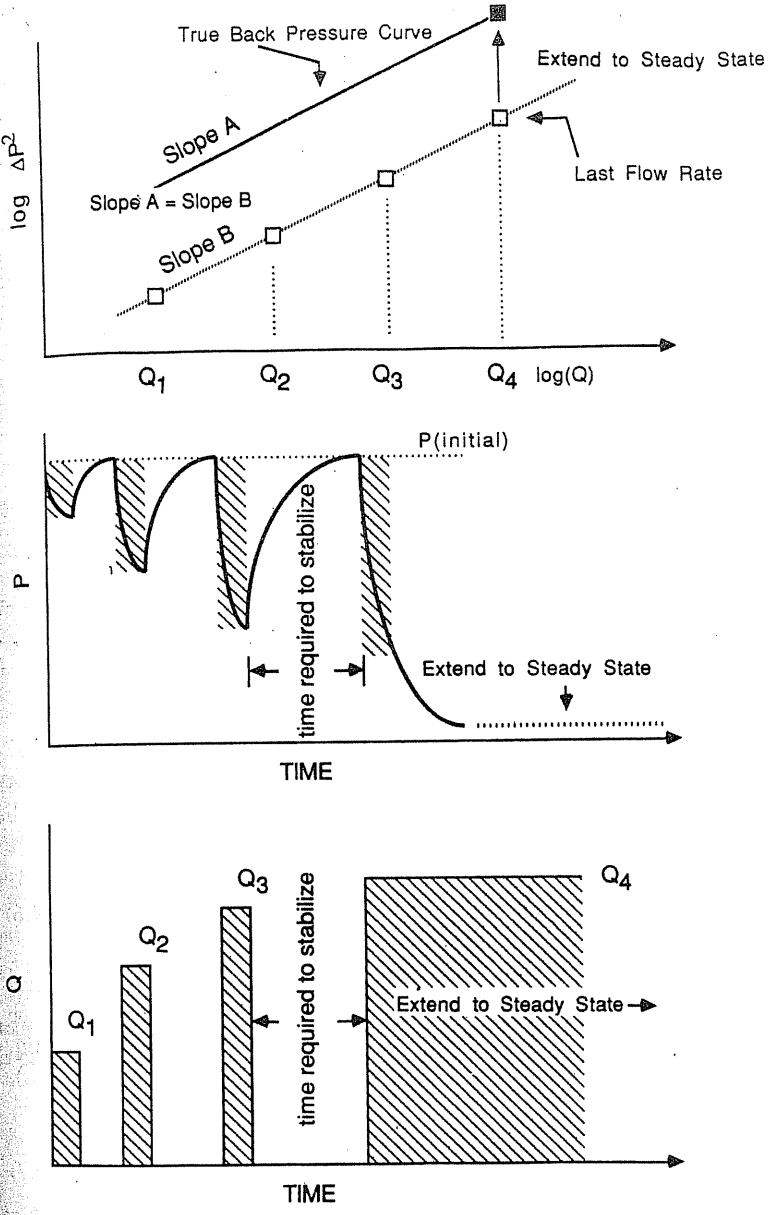

FIGURE 9-7
Typical isochronal test.

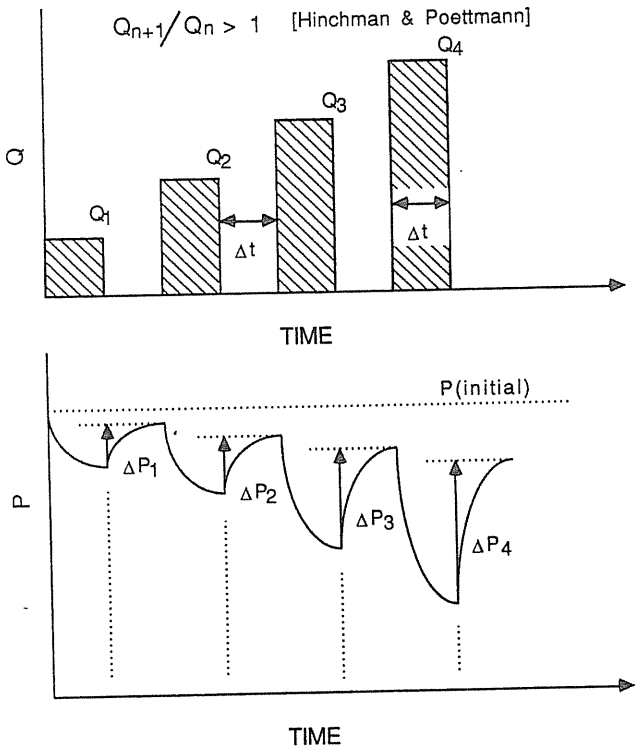

FIGURE 9-8
Modified isochronal test.

$$\Delta P^2 = \left\{ \frac{\gamma\mu\bar{Z}T}{kh}\left[\frac{1}{2}\left(\ln\frac{\lambda kt}{\phi\overline{\mu c}r_w^2} + 0.80907\right) + s\right]\right\} \cdot Q_{sc} + \left(\frac{\gamma\mu\bar{Z}T}{kh} \cdot D\right)Q_{sc}^2 \quad (9.6)$$

Assuming the times for stabilizing pressures are roughly the same for different flow rates, the Q_{sc}^2 term of Eq. (9.6) will cause further deviation from the unique slope line when the flow rate (Q_{sc}) increases. If the magnitude of Q_{sc}^2 term of Eq. (9.6) is much larger than that of the Q_{sc} term (high-velocity effect dominates), the equation can be rearranged as

$$\log_{10}\Delta P^2 = \log_{10}\left(\frac{\gamma\mu\bar{Z}T}{kh} \cdot D\right) + (2)\log_{10} Q_{sc} \quad (9.7)$$

Plotting $\log \Delta P^2$ versus $\log Q_{sc}$ for this case will yield a performance curve with a slope equal to 2 ($n = \frac{1}{2}$). Thus, the back pressure performance curve always has the slope between 1 (viscous Darcy) and 2 (high-velocity effect); that is, $\frac{1}{2} \le n \le 1$.

Jones et. al. [9-17] and Lee [9-18] suggested a plot of $\Delta P^2/Q_{sc}$ versus Q_{sc}. This idea comes from rearranging Eq. (9.6) as

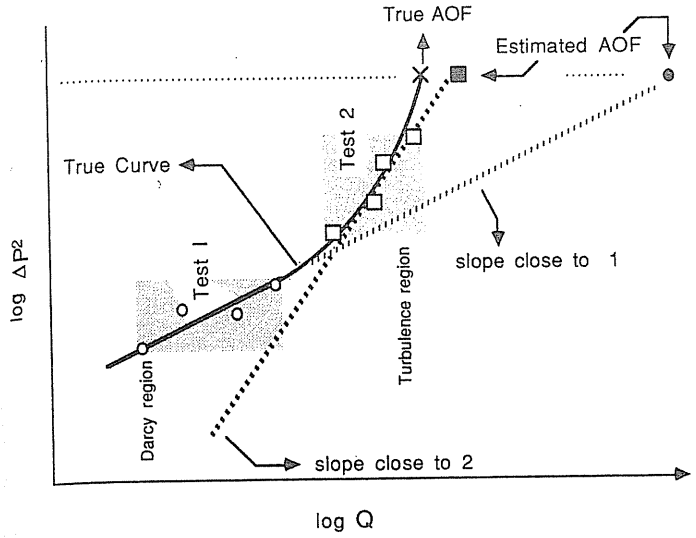

FIGURE 9-9
True deliverability curve and the four-point back pressure test.

$$\frac{\Delta P^2}{Q_{sc}} = \left\{ \frac{\gamma\mu\bar{Z}T}{kh}\left[\frac{1}{2}\left(\ln\frac{\lambda kt}{\phi\overline{\mu c}r_w^2} + 0.80907\right) + s\right]\right\} + \left(\frac{\gamma\mu\bar{Z}T}{kh} \cdot D\right) \cdot Q_{sc} \quad (9.8)$$

The first term in the right-hand side of Eq. (9.8) is of the same magnitude for all flow rates if the stabilization times are long and roughly close. By plotting $\Delta P^2/Q_{sc}$ versus Q_{sc}, one should obtain a straight line whose slope reflects the high-velocity factor D; see Fig. 9-10.

In oil field technology, a useful indicator of deliverability has been the productivity index J, expressed in terms of stock tank barrels per day per psi pressure drop within the drainage matrix: $J = q/(P_{avg} - P)$. Logan et al. [8-34] extended this concept to gas wells by defining $Q_{sc}/\Delta P^2$ as the productivity index, representing the deliverability of gas wells. Hence, a plot of $\Delta P^2/Q_{sc}$ versus Q_{sc} is called *inverse productivity index*, or IPI, plot.

Furthermore, Lee [8-29], normalized IPI by dividing it by P_f^2:

$$\text{IPI}_N = \frac{\Delta P^2}{P_f^2 Q_{sc}} \quad (9.9)$$

A plot of $\Delta P^2/(P_f^2 Q_{sc})$ versus Q_{sc} has

$$\text{Slope} = \frac{\gamma\mu\bar{Z}T}{kh} \cdot \frac{D}{P_f^2} \quad (9.10)$$

as shown in Fig. 9-11. Under the condition of AOF, IPI_N becomes approximately equal to $1/Q_{sc}$; therefore, by extrapolating the operating line (Fig. 9-11) to intercept the AOF line ($1/Q_{sc}$ line), one obtains AOF graphically.

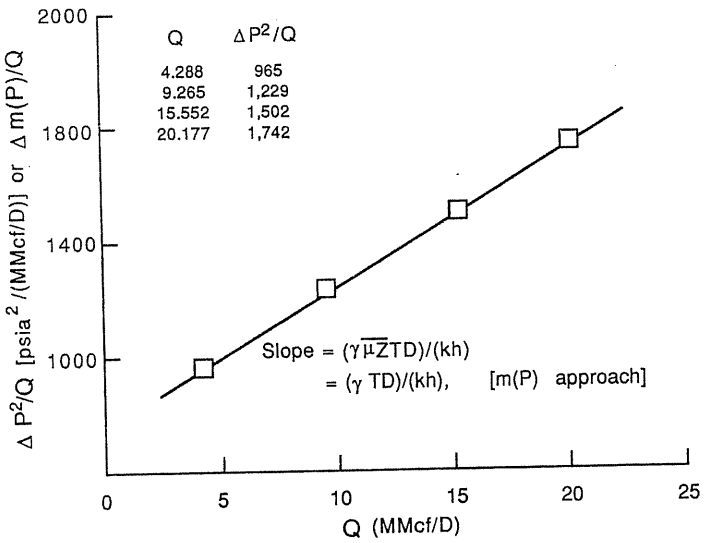

FIGURE 9-10
Inverse productivity index plot.

This normalized IPI concept not only could serve as an alternative to the back pressure plot, but also could be used for isochronal tests, as long as measurements are free of wellbore storage effect.

So far in this chapter, the pressure squared, P^2, has been exclusively used instead of the pseudopressure $m(P)$. However, Corbett and Wattenbarger [9-10] reported that not only does the high-velocity effect cause P^2 performance curves to be concave upward, but also gas property (μ, Z, and c) variations due to pressure drop cause the performance curve to move downward. Thus, if a large pressure drop is expected, the pseudopressure approach is suggested (simply change P^2 to $m(P)$, P_f^2 to $m(P_f)$, and $\gamma\mu Z$ to γ from Eq. (9.1) through Eq. (9.10)).

The last flow rate may not be stabilized in a low-permeability reservoir. Poettmann proposed utilizing the *pseudostabilization time* t_{ps}, to locate the stabilized lines in plots such as those in Figs. 9-7 and 9-11. The pseudostabilization time is obtained by equating Eqs. (8.31) and (8.32):

$$t_{ps} = \frac{376\phi\overline{\mu c}r_e^2}{k} \tag{9.11}$$

All variables are in field units and $\overline{P}$ (not P_i) is used in this calculation.

Poettmann's method is practical. Eq. (9.8) can be simply expressed as $\Delta P^2/Q_{sc} = a(t) + bQ_{sc}$. By conducting at least 3 or 4 isochronal or modified isochronal tests with different flowing times, the relationship between $a(t)$ and time can then be determined (plotting $\Delta P^2/Q_{sc}$ versus Q_{sc}); that is, $a(t) = A + B\log_{10}(t)$. With calculated t_{ps}, the stabilized $a(t_{ps})$ can be calculated. As a result,

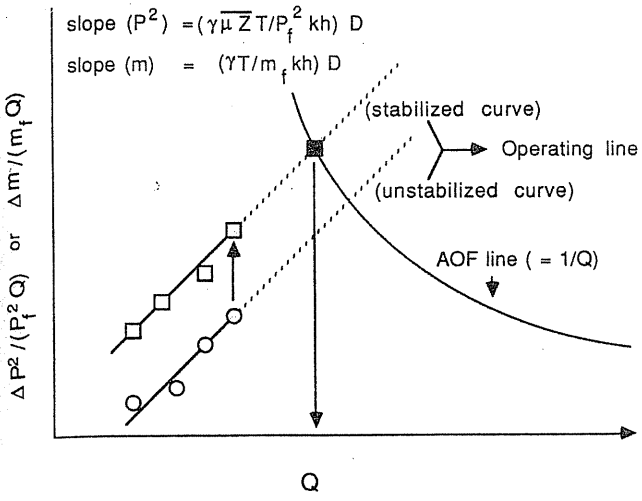

FIGURE 9-11
Normalized inverse productivity index plot.

the stabilized lines in Figs. 9-7 and 9-11 can be located without conducting the extended flow. It should be noted that, theoretically, with strong high-velocity effect, the stabilization time is more than that predicted by Eq. (9-11) [8-34].

Example 9.1. A four-point back pressure procedure was conducted. The pressures were recorded twice during each flow rate; one after $\frac{1}{2}$ hour and the other at the stabilized condition. Well was shut-in between flow rates. The pressures recorded are [9-18]:

P, psia	Q_{sc}, MMcf/day	$P_f^2 - P^2$, psia²	$\Delta P^2/Q_{sc}$	$\Delta P^2/(P_f^2\, Q_{sc})$; IPI_N
408.2 (P_f)	0	—	—	—
406.9 (1/2 hr)	4.288	1,060	247	0.00148
403.1	4.288	4,138	965	0.00580
402.1 (1/2 hr)	9.265	4,943	534	0.00320
394	9.265	11,391	1229	0.00739
393.7 (1/2 hr)	15.552	11,628	748	0.00449
378.5	15.552	23,365	1502	0.00903
383.1 (1/2 hr)	20.177	19,862	984	0.00591
362.6	20.177	35,148	1742	0.01047
14.7	AOF	166,411	—	—

Calculate the AOF by each of the following methods:

1. Back pressure plot, using stabilized data
2. Normalized inverse productivity index, using stabilized data
3. Using only flow data for $\frac{1}{2}$ hour, except for the last flow rate (20.77 MMcf/day), for which you may use the stabilized data.

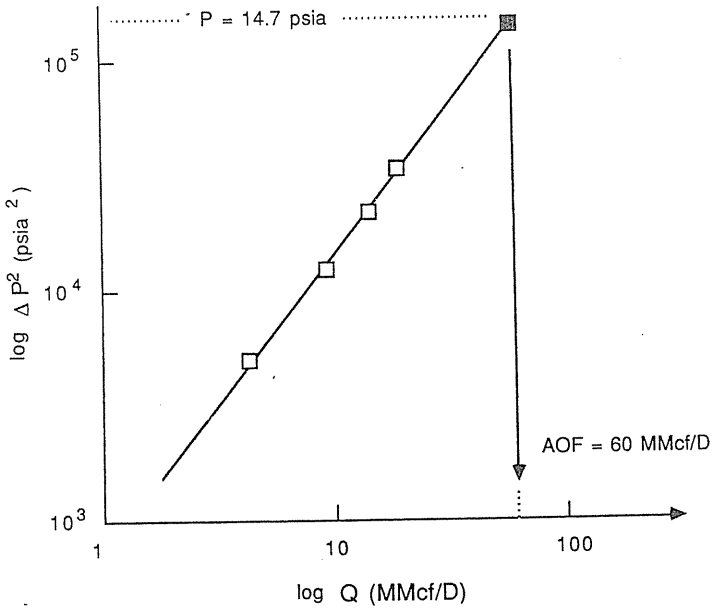

FIGURE 9-12
Stabilized gas well deliverability test.

Solution. Plot ΔP^2 versus Q_{sc} on log-log coordinates (Fig. 9-12) and extend the straight line to $\Delta P^2 = 166{,}411$ psia^2:

$$\text{AOF} = 60 \text{ MMcf/day (back pressure test)}$$

Plot $\Delta P^2/(P_f^2 Q_{sc})$ versus Q_{sc} on arithmetic coordinates (Fig. 9-13) and extend the straight line to the AOF line $(1/Q_{sc})$:

$$\text{AOF} = 51.5 \text{MMcf/day (normalized IPI)}$$

Plot $\Delta P^2/(P_f^2 Q_{sc})$ ($\frac{1}{2}$ hour) versus Q_{sc} (Fig. 9-14) and draw a parallel line through the stabilized point of the last flow rate ($Q_{sc} = 20.177$ MMcf/day, $\Delta P^2/(P_f^2 Q_{sc}) = 0.01047$):

$$\text{AOF} = 53 \text{ MMcf/day (isochronal type IPI}_N\text{)}$$

The use of a straight line approach on log-log coordinates (back pressure plot) results in a 15.8 percent error in the calculation of AOF.

9.2 TEST FOR DETERMINING RESERVOIR PARAMETERS

This section will introduce the gas well tests for obtaining important reservoir parameters such as the flow capacity kh, the skin factor s, and the high-velocity factor D.

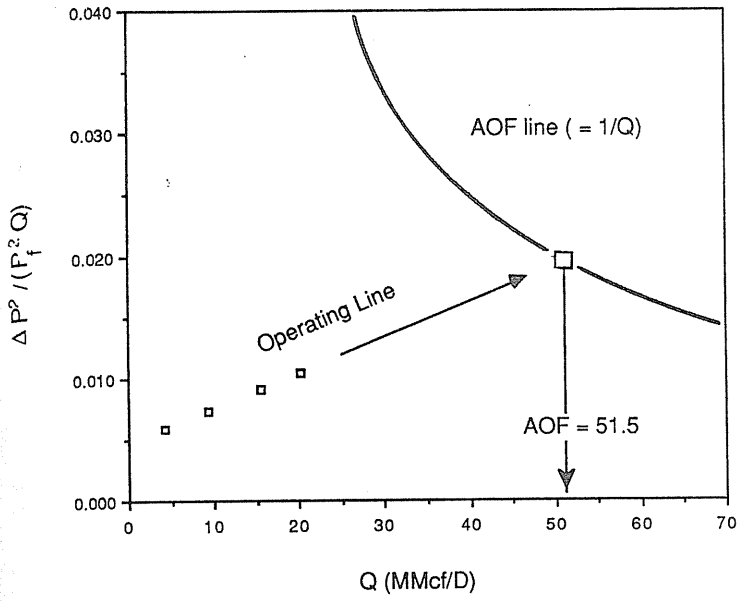

FIGURE 9-13
Normalized inverse productivity index (IPI) plot.

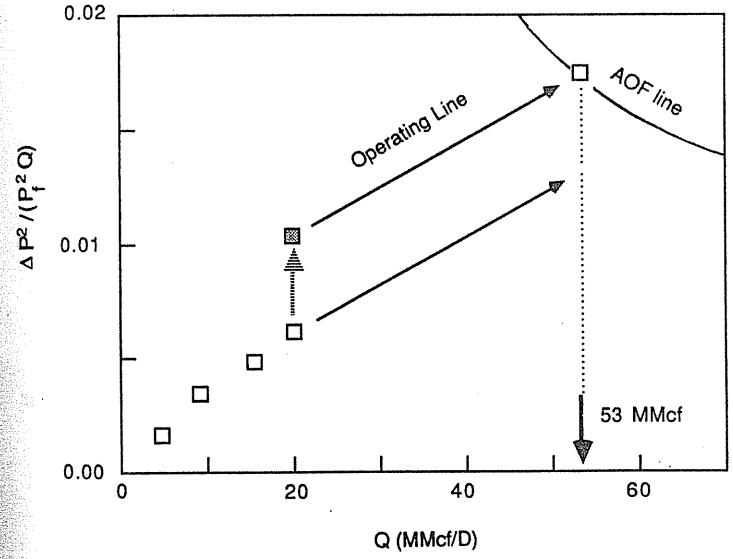

FIGURE 9-14
Isochronal type normalized inverse productivity index (IPI) plot.

By interpreting dynamic responses (pressure drop history at sandface) for a constant wellhead flow rate withdrawing process, the *drawdown test* gives the value of the flow capacity kh. The *multi-rate test*, which uses several different wellhead flow rates, permits the calculation of kh as well as the skin factor s and the high-velocity factor D. The *buildup test*, a special case of multi-rate test with an immediate shut-in after a drawdown process, also allows one to obtain kh by observing the sandface pressure being gradually brought back to its original value.

Unlike most deliverability tests described in the first part of this chapter, these tests are extensions from oil well testing practice and are based on a theoretical rather than an empirical background. The purpose of these tests is to determine the reservoir characteristics that will affect flow performance.

Drawdown Test

Figure 9-15 shows a constant terminal flow rate withdrawing process and its responding pressure history. There are three stages of the pressure response: (1) early time flow, (2) transient flow, and (3) pseudo–steady state flow.

In the early time flow period, data are affected by wellbore storage, flow through fractures, and unstabilized flow rate at the wellhead; thus, it can not

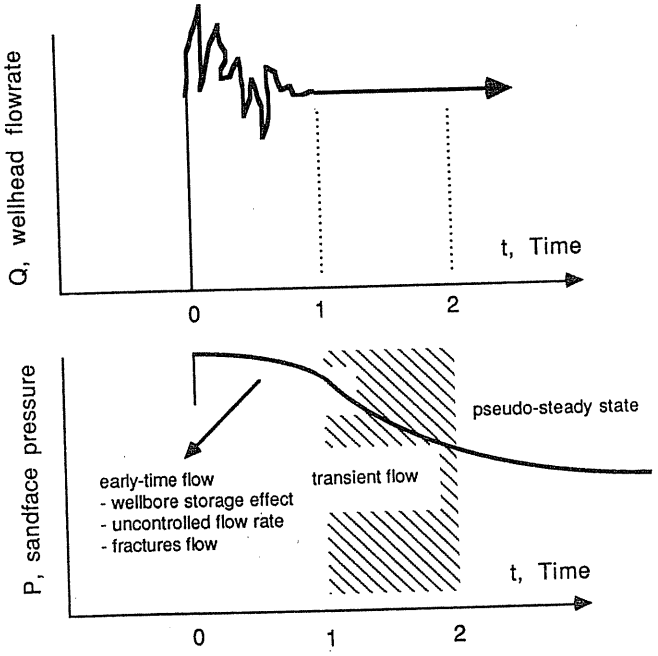

FIGURE 9-15
Wellhead flow rates and responding sandface pressures: A procedure of drawdown test.

really reflect the true reservoir response. The wellhead flow rate is physically difficult to keep constant, especially when the valve has just opened.

The transient flow period begins at time $t_D = 60(C_D + 3.5s')$, after which the pressure response can be described by Eq. (8.47):

$$P_{DW}(ST) = \frac{1}{2}(\ln t_D + 0.80907) + s + DQ_{sc} \tag{8.47}$$

which can be expressed in explicit form as in terms of pseudopressure $m(P)$,

$$\Delta m = (m_i - m)$$
$$= \frac{2.3026\gamma TQ_{sc}}{2kh}\log_{10} t + \frac{\gamma TQ_{sc}}{2kh}\left(\ln\frac{\lambda k}{\phi\overline{\mu c}r_w^2} + 0.80907 + 2s + 2DQ_{sc}\right) \tag{9.12a}$$

and in terms of pressure squared P^2,

$$\Delta P^2 = (P_i^2 - P^2) = \frac{2.3026\gamma\overline{\mu Z}TQ_{sc}}{2kh}\log_{10} t + \frac{\gamma\overline{\mu Z}TQ_{sc}}{2kh}\left(\ln\frac{\lambda k}{\phi\overline{\mu c}r_w^2} + 0.80907 + 2s + 2DQ_{sc}\right) \tag{9.12b}$$

Pseudopressure $m(P)$ will be used in the rest of this chapter instead of pressure squared P^2. When one chooses to use P^2 for simplicity, the coefficient γ should be replaced by $\gamma\overline{\mu Z}$. In using $m(P)$, the average value of $\overline{\mu c}$ will be assumed to be roughly equal to its initial value $\mu_i c_i$; by making this assumption, one can avoid a tedious iteration (trial-and-error) procedure. The subscript i will be used to denote the initial value. Also, except for plotting purposes, $\ln(x)$ will be used instead of $\log_{10}(x)$.

A plot of Δm (or ΔP^2) versus $\log_{10} t$ (versus t on semilogarithmic coordinates) gives a straight line (Fig. 9-16). By examining Eq. (9.12a), the slope should be

$$\text{Slope} = 1.151\frac{\gamma TQ_{sc}}{kh} \tag{9.13}$$

and kh is simply

$$kh = 1.151\frac{\gamma TQ_{sc}}{\text{slope}} \tag{9.14}$$

If Δm_1 is defined as the value at $t = 1$, which can be obtained from the straight line portion (extrapolated, if necessary), the apparent skin factor s' is

$$s' = s + DQ_{sc} = \frac{1}{2}\left(\frac{2.3026\Delta m_1}{\text{slope}} - \ln\frac{\lambda k}{\phi\mu_i c_i r_w^2} - 0.80907\right) \tag{9.15}$$

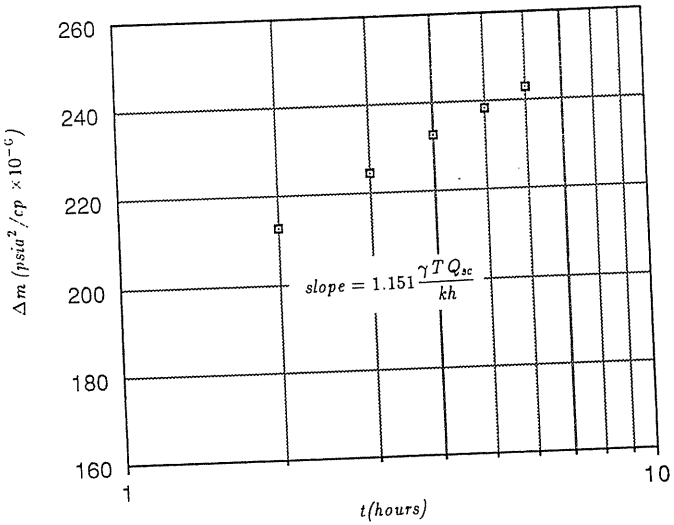

FIGURE 9-16
Typical drawdown test analysis.

The transient flow ends at the time

$$t_D = \frac{\lambda k t}{\phi \mu_i c_i r_w^2} = \frac{4}{9}\left(\frac{r_d}{r_w}\right)^2 = \frac{4}{9}\left(\frac{0.473 r_e}{r_w}\right)^2 \approx 0.1\left(\frac{r_e}{r_w}\right)^2 \qquad (9.16)$$

which is a rearranged form of Eq. (8.37*a*). Data obtained beyond the stabilized time, as shown in Fig. 9-15, should not be included in the analysis.

Example 9.2. A drawdown process was conducted for well A. The pressure-time data for a flow rate of Q_{sc} = 29.14 MMcf/day were as follows:

t, hr	$\log_{10} t$	P, psia	m, psia²/cp, × 10^{-6}	Δm
0	—	4217	1099.8	0
1	0	3792	929.8	170.0
2	0.301	3685	887.0	212.8
3	0.477	3655	875.0	224.8
4	0.602	3635	867.0	232.8
5	0.699	3621	861.4	238.4
6	0.778	3610	857.0	242.8

Well/reservoir/fluid data are as follows:

T = 645°R

h = 35 ft

ϕ = 0.055

r_e = 5000 ft

r_w = 0.4 ft

μ_i = 0.022 cp

c_i = 0.00018 psia^{-1}

m (psia²/cp) = $-587 \times 10^6 + 0.4 \times 10^6 \times P$ (psia) (3500 psia < P < 4500 psia)

Calculate the permeability k near the wellbore and the apparent skin factor $s' = s + DQ_{sc}$.

Solution. Plot Δm versus $\log_{10} t$ (Fig. 9-16):

$$\text{slope} = 63 \times 10^6$$

Obtain kh and k from Eq. (9.14):

$$kh = 1.151\frac{\gamma T Q_{sc}}{\text{slope}} = 1.151\frac{(1.422 \times 10^6)(645)(29.14)}{(63 \times 10^6)} = 488.29$$

$$k = \frac{kh}{h} = \frac{488.29}{35} = 14\text{md}$$

Calculate s' from Eq. (9.15) ($\Delta m_1 = 194.3 \times 10^6$ by extrapolation to t = 1 in Fig. 9-16):

$$s' = \frac{1}{2}\left(\frac{2.3026\Delta m_1}{\text{slope}} - \ln\frac{\lambda k}{\phi \mu_i c_i r_w^2} - 0.80907\right)$$

$$= \frac{1}{2}\left(\frac{(2.3026)(194.3 \times 10^6)}{(63 \times 10^6)} - \ln\frac{(2.637 \times 10^{-4})(14)}{(0.055)(0.022)(0.00018)(0.4)^2} - 0.80907\right)$$

$$= -2.64$$

Check the time at which the transient behavior ends, Eq. (9.16):

$$t_D = \frac{\lambda k t}{\phi \mu_i c_i r_w^2} \approx 0.1\left(\frac{r_e}{r_w}\right)^2$$

$$t = \frac{\phi \mu_i c_i r_w^2}{\lambda k}(0.1)\left(\frac{r_e}{r_w}\right)^2 = \frac{(0.055)(0.022)(0.00018)(0.4)^2}{(2.637 \times 10^{-4})(14)}(0.1)\left(\frac{5000}{0.4}\right)^2$$

= 147.5 hr > 6 hr of testing time

Hence, it is appropriate to apply Eqs. (9.14) and (9.15).

When a drawdown lasts long enough, deviation from the straight line of Fig. 9-16 can be observed. At later stages, a plot of Δm versus t gives a straight line on arithmetic coordinates, and its slope reflects the flow rate and size of the reservoir. This test technique is referred to as the *reservoir limit test*. This is of little use for gas storage but is important for off-shore production operations.

Multi-Rate Test

As discussed in Chapter 8, based on the superposition principle, one can describe pressure transient behavior by summarizing effects of all previous flow histories [9-20]; that is,

$$\frac{\Delta m_n}{m_i} = \frac{m_i - m_n}{m_i} = \sum_{j=1}^{n} (Q_{D,j} - Q_{D,j-1}) P_{DW}\Big|_{Q_j - Q_{j-1}, t_n - t_{j-1}} \tag{9.17}$$

which is simply an extension of Eq. (8.57).

Since a constant wellhead flow rate is hard to maintain, it helps to discretize it to several constant rate regions, and then apply Eq. (9.17) to analyze the data of the pressure transient behavior.

Eq. (9.17) can be expressed in explicit form:

$$\begin{aligned}\Delta m_n &= m_i - m_n \\ &= \frac{\gamma T}{2kh}\left[\sum_{j=1}^{n} (Q_j - Q_{j-1}) \ln (t_n - t_{j-1}) \right. \\ &\qquad \left. + \sum_{j=1}^{n} (Q_j - Q_{j-1}) \left(\ln \frac{\lambda k}{\phi \mu_i c_i r_w^2} + 0.80907 + 2s_j' \right) \right] \end{aligned} \tag{9.18}$$

The last summation term of Eq. (9.18) involving s_j' $(s + DQ_1, s + DQ_2, \ldots, s + DQ_n)$, can be further simplified by ignoring DQ_j terms up to the last flow rate; in other words, by assuming D_1 up to D_{n-1} have no transient effects and vanish immediately after switching the flow rate. Then, Eq. (9.18) can be simplified to

$$\Delta m_n = m_i - m_n = \frac{\gamma T}{2kh} \left\{ \left[\sum_{j=1}^{n} (Q_j - Q_{j-1}) \ln (t_n - t_{j-1}) \right] + C_n \right\}$$

$$C_n = Q_n \left[\ln \frac{\lambda k}{\phi \mu_i c_i r_w^2} + 0.80907 + 2(s + DQ_n) \right] \tag{9.19}$$

As shown in Fig. 9-17, by plotting Δm_n versus the newly defined *flowrate-time* factor, FT:

$$\mathrm{FT}_n = \sum_{j=1}^{n} (Q_j - Q_{j-1}) \ln (t_n - t_{j-1}) \tag{9.20}$$

for flow rates $n = 1, 2, 3, 4$, the slope should be $(\gamma T)/(2kh)$, which reflects the value of kh. In addition, C_n of each flow rate could be obtained by extrapolating to the point at which FT = 0. In practice, the positive values of $\ln (t_n - t_{j-1})$ are preferred; that is, the magnitudes of $t_n - t_{j-1}$ should be made to fall between 1 and 20 by choosing the appropriate units.

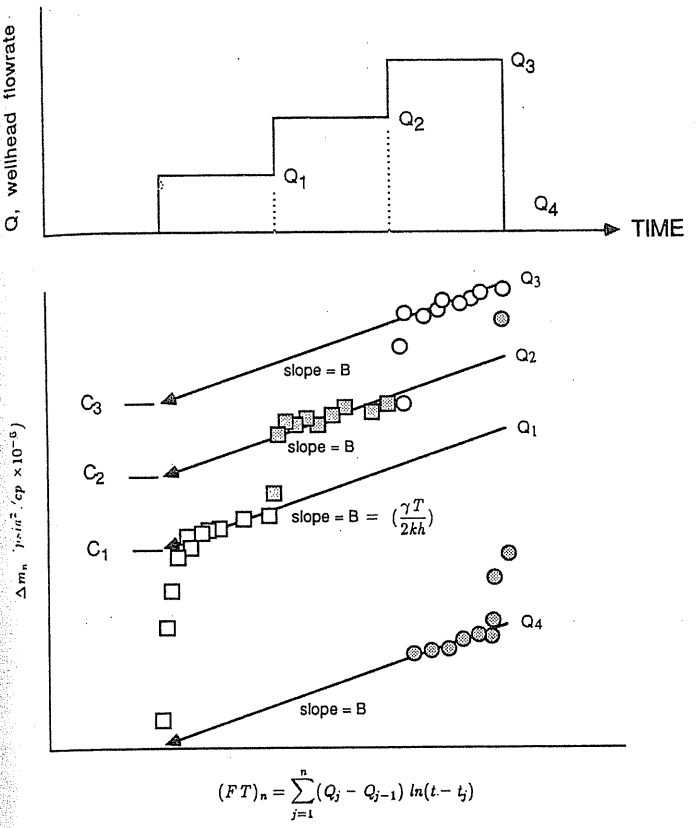

FIGURE 9-17
Multirate test analysis: Δm_n vs. FT_n.

The C_n term can be rearranged as:

$$\frac{C_n}{Q_n} = \left(\ln \frac{\lambda k}{\phi \mu_i c_i r_w^2} + 0.80907 + 2s \right) + (2D) Q_n \tag{9.21}$$

Thus, a plot of C_n/Q_n versus Q_n has a slope of $2D$ (Fig. 9-18). With the k obtained from the slope $(\gamma T)/(2kh)$ of the Δm_n-versus-FT_n plot, one can calculate the skin factor s.

It is believed [9-12] that this method has been used in Europe for some time. More related material can be seen in reference [8-17]. The method can only be applied in the time before the transient behavior of pressure drop ends. Extension of this method for a finite reservoir can be seen in reference [1-11]. Odeh and Jones [9-20] proposed plotting $\Delta P^2/Q$ versus log-time factor FT/Q to retrieve kh and s from the slope and intercept.

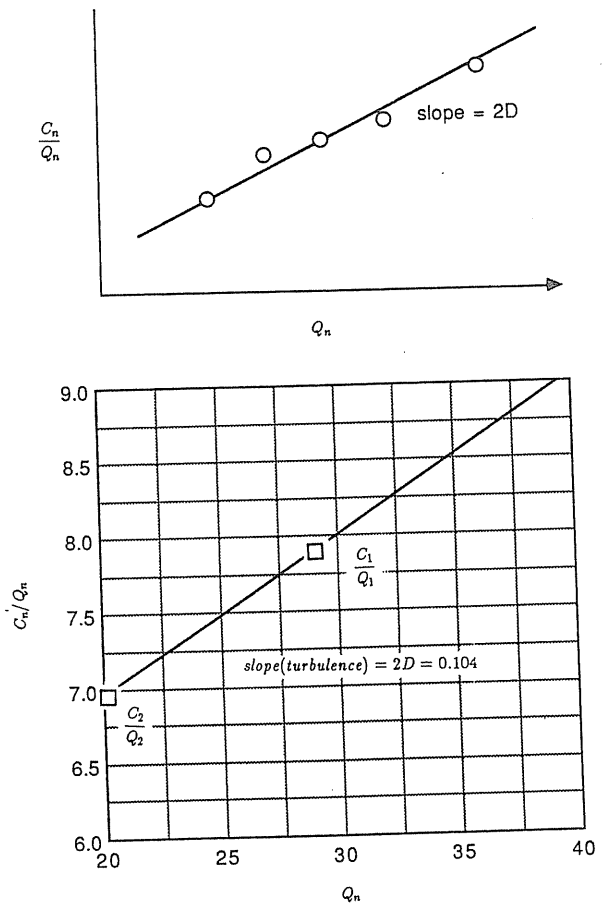

FIGURE 9-18
High-velocity effect plot of multirate test: C_n/Q_n versus Q_n.

Two-Rate Test

The two-rate test, developed by Russell [9-23], is a particular form of multi-rate test applying two rates only (Fig. 9-19). It is a simple gas well test to separate the skin factor s and the high-velocity factor D from apparent skin factor s'.

The first flow rate represents a simple drawdown test. Equation (9.19) for the second flow rate can be simplified to

$$\Delta m_2 = m_i - m_2 = \frac{\gamma T}{2kh}\{[Q_1 \ln (t_2 - t_0) + (Q_2 - Q_1)\ln (t_2 - t_1)] + C_2\}$$

$$C_2 = Q_2\left\{\ln\frac{\lambda k}{\phi\mu_i c_i r_w^2} + 0.80907 + 2s + 2DQ_2\right\} \qquad (9.22)$$

The procedures of conducting a two-rate test are summarized as follows:

1. Apply two different terminate rates—usually the first one doubles the second. Record the sandface pressures continuously after switching the flow rate.
2. Plot Δm_2 versus the FT factor, $Q_1 \ln (t_2 - t_0) + (Q_2 - Q_1)\ln (t_2 - t_1)$, on arithmetic coordinates. Slope is $(\gamma T)/(2kh)$, from which kh can be determined; also, the product (slope $\cdot$ C_2) can be obtained by extrapolating the straight line portion to FT = 0.
3. Draw a line through the endpoint of the first flow rate with slope $(\gamma T)/(2kh)$ from step 2, and extrapolate it to obtain (slope $\cdot$ C_1) at FT = 0.
4. Either plot C_n/Q_n versus Q_n to obtain the slope $2D$, with which s can be calculated, or solve s and D simultaneously from C_1 and C_2 with the kh obtained from step 2.

Example 9.3. As in Example 9.2, the initial pressure in a well was 4217 psia and the first flow rate was 29.14 MMcf/day. The record up to 6 hours was missing, but the final pressure was 3610 psia. After the flow rate was switched to 20.06 MMcf/day, the pressure-time data were as follows:

t, hr	Δt	FT_2	P, psia	m, psia²/cp	Δm, psia²/cp
6	0	52.21	3610	857×10^6	242×10^6
7	1	56.70	3793	930.2×10^6	169.6×10^6
9	3	54.06	3799	932.6	167.2
11	5	55.26	3797	931.8	168.2
13	7	57.08	3791	929.4	170.4
15	9	58.94	3789	928.6	171.2
17	11	60.78	3785	927.0	172.8
19	13	62.26	3781	925.4	174.4
21	15	64.13	3777	923.8	176.0
23	17	65.64	3774	922.6	177.2
25	19	67.06	3771	921.4	178.4
27	21	68.40	3768	920.2	179.6
29	23	69.65	3765	919.0	180.8
31	25	70.84	3763	918.2	181.6

Well/reservoir/fluid data are the same as in Example 9.2.

Calculate the permeability k near the wellbore, the skin factor s, and the high-velocity factor D.

Solution. Plot Δm versus FT factor, $\sum_{j=1}^{2}(Q_j - Q_{j-1}) \ln (t_2 - t_{j-1})$, on arithmetic coordinates (Fig. 9-20).

$$\text{slope} = \frac{\gamma T}{2kh} = 0.858 \times 10^6$$

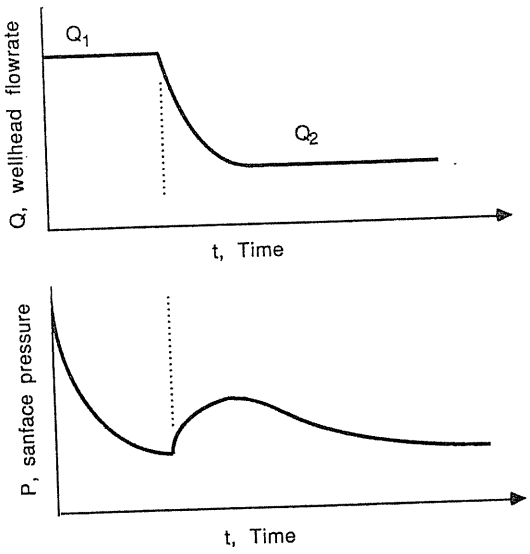

FIGURE 9-19
Typical flow rates and corresponding pressures for a two-rate test.

Obtain kh and k by rearranging this equation:

$$kh = \frac{\gamma T}{2(\text{slope})} = \frac{(1.422 \times 10^6)(645)}{2(0.858 \times 10^6)} = 534.5 \text{ md} \cdot \text{ft}$$

$$k = \frac{kh}{h} = \frac{534.5}{35} = 15.3 \text{ md}$$

Draw a line through the point ($\Delta m = 242.8 \times 10^6$ from Example 9.2, and FT = 52.21) with slope $= 0.858 \times 10^6$. The intercept (FT = 0) should be slope $\cdot C_1$:

$$\Delta m_1(\text{FT} = 0) = \text{slope} \cdot C_1 = 198.0 \times 10^6$$

$$\Delta m_2(\text{FT} = 0) = \text{slope} \cdot C_2 = 120.9 \times 10^6$$

Plot C_n/Q_n versus Q_n, as in Fig. 9-18.

$$\frac{C_1}{Q_1} = \frac{\Delta m_1(\text{FT} = 0)}{\text{slope} \cdot Q_1} = \frac{198.0 \times 10^6}{(0.8585 \times 10^6)(29.14)} = 7.92$$

$$\frac{C_2}{Q_2} = \frac{\Delta m_2(\text{FT} = 0)}{\text{slope} \cdot Q_2} = \frac{120.9 \times 10^6}{(0.8585 \times 10^6)(20.06)} = 6.97$$

$$\text{slope (high-velocity effect)} = 2D = 0.104$$

$$D = 0.0521/\text{MMcf/day}$$

Calculate s by rearranging Eq. (9.22):

$$s = \frac{1}{2}\left\{\frac{C_2}{Q_2} - \ln\frac{\lambda k}{\phi \mu_i c_i r_w^2} - 0.80907 - 2DQ_2\right\}$$

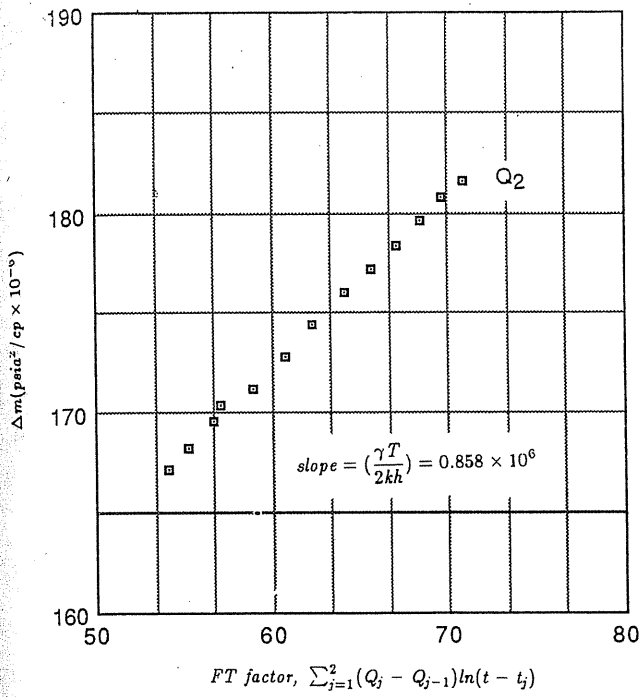

FIGURE 9-20
Two-rate test analysis: Δm versus FT factor, $\sum_{j=1}^{2}(Q_j - Q_{j-1})\ln(t_2 - t_{j-1})$.

$$= \frac{1}{2}\left\{6.972 - \ln\frac{(2.637 \times 10^{-4})(15.3)}{(0.055)(0.022)(0.00018)(0.4)^2} - 0.080907 - 2(0.052)(20.06)\right\}$$

$$= -3.79$$

Total test time is 31 hours during which the pressure drop is still in the transient period.

Buildup Test

The *buildup test* consists of a shut-in immediately after a constant flow rate withdrawing process. Figure 9-21 shows the wellhead flow rate curve and the corresponding sandface pressure responses. The buildup test is the simplest test and is just an extreme form of the two-rate test. Theis [8-40], and later Horner [9-16], showed that a plot of the shut-in pressure P versus $\log((t_1 + \Delta t)/\Delta t)$ would result in a straight line for an infinite-acting reservoir.

For a buildup test, $Q_2 = 0$ in Eq. (9.22), reducing the equation to

$$\Delta m = m_i - m = \frac{\gamma T_1}{2kh}\left\{Q_1 \ln\frac{t}{t - t_1}\right\} = (2.3026)\frac{\gamma T Q_1}{2kh}\log_{10}\frac{t_1 + \Delta t}{\Delta t} \qquad (9.23)$$

As shown in Fig. 9-22, plotting Δm versus $(t_1 + \Delta t)/\Delta t$ on semilogarithmic coordinates should result in a straight line with

$$\text{Slope} = (2.3026)Q_1\frac{\gamma T}{2kh} \tag{9.24}$$

from which kh could be calculated:

$$kh = 1.151\frac{\gamma T Q_1}{\text{slope}} \tag{9.25}$$

Eq. (9.23) does not give any information on the skin factor or the high velocity factor. However, the apparent skin factor, $s' = s + DQ_{sc}$, still could be obtained by utilizing the shut-in pressure at $\Delta t = 0$:

$$s' = s + DQ_{sc} = \frac{1}{2}\left\{\frac{\Delta m_2(\Delta t = 0)}{Q_1}\cdot\frac{2kh}{\gamma T} - \ln\frac{\lambda k t_1}{\phi\mu_i c_i r_w^2} - 0.80907\right\} \tag{9.26}$$

where k and $(\gamma T)/(2kh)$ are obtained from a buildup test plot.

Example 9.4. A well is tested under the same conditions as Example 9.3; however, instead of switching to the second flow rate, an immediate shut-in was conducted; the pressure-time data after the shut-in were as follows:

t, hr	Δt, hr	$(t_1 + \Delta t)/\Delta t$	P, psia	m, psia²/cp, $\times 10^{-6}$	Δm psia²/cp, $\times 10^{-6}$
6	0	—	3610	—	242.6
7	1	7	4086	1047.4	52.4
8	2	4	4123	1062.2	37.6
9	3	3	4143	1070.2	29.6
11	5	2.2	4164	1078.6	21.2
13	7	1.86	4175	1083.0	16.8
15	9	1.67	4183	1086.2	13.6
17	11	1.55	4187	1087.8	12.0
19	13	1.465	4192	1089.8	10.0
21	15	1.4	4194	1090.6	9.2
22	16	1.375	4196	1091.4	8.4
26	20	1.3	4199	1092.6	7.2

Calculate the permeability k near the wellbore and the apparent skin factor $s' = s + DQ_{sc}$.

Solution. Plot Δm_2 versus $\log((t_1 + \Delta t)/\Delta t)$ (Fig. 9-22).

$$\text{Slope} = 2.3026\frac{\gamma T}{2kh}\cdot Q_1 = 62.17 \times 10^6$$

Obtain kh and k from Eq. (9.23):

$$kh = 1.151\frac{\gamma T Q_1}{\text{slope}} = 1.151\frac{(1.422 \times 10^6)(645)}{62.17 \times 10^6}(29.14) = 494.9 \text{ md} \cdot \text{ft}$$

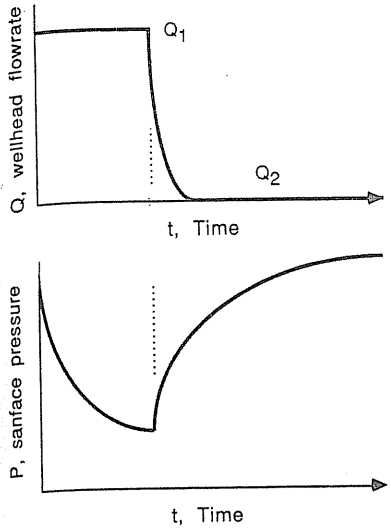

FIGURE 9-21
Wellhead flow rates and corresponding sandface pressures for a buildup test.

$$k = \frac{kh}{h} = \frac{494.9}{35} = 14.2 \text{ md}$$

Calculate $s' = s + DQ_{sc}$ from Eq. (9.26) with $\Delta m(\Delta t = 0) = 242.6 \times 10^6$:

$$s' = s + DQ_{sc} = \frac{1}{2}\left\{\frac{\Delta m_2(\Delta t = 0)}{Q_1}\cdot\frac{2kh}{\gamma T} - \ln\frac{\lambda k t_1}{\phi\mu_i c_i r_w^2} - 0.80907\right\}$$

$$= \frac{1}{2}\left\{\frac{(242.6 \times 10^6)(2.3026)}{62.17 \times 10^6} - \ln\frac{(2.637 \times 10^{-4})(14.2)(6)}{(0.055)(0.022)(0.00018)(0.4)^2} - 0.80907\right\}$$

$$= -2.6$$

Determination of Equalized Reservoir Pressures

Periodic measurements of the shut-in or formation reservoir pressure must be made in order to calculate gas reserves and to correct the back pressure as the field is depleted. In low-permeability formations appreciable pressure differences may exist between various points even after long shut-in times. These differences are due to the low rates at which gas can flow through a low-permeability formation to reach the depleted zones. Such pressure differences should be taken into account by the calculation of an *equalized reservoir pressure*. The equalized pressure is the uniform pressure that would exist in the reservoir after such a long time had passed that flow of gas to the depleted areas had ceased and, for practical purposes, no pressure gradients existed in the reservoir.

The method of Matthews, Brons, and Hazebroek (MBH) [9-19] involves the use of a buildup curve with time. Figure 9-23 shows the plot of pressure squared P^2 versus $\log \Delta t/(t_1 + \Delta t)$. The straight line portion of such a plot, which develops

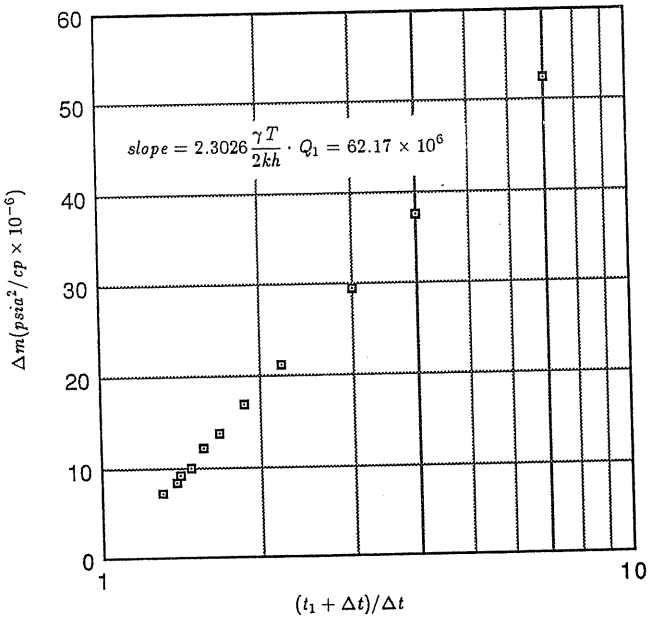

FIGURE 9-22
Typical buildup test plot: Δm versus $(t_1 + \Delta t)/\Delta t$.

after a short time following the shut-in, is extrapolated to $\Delta t/(t_1 + \Delta t) = 1$, or infinite shut-in time. This extrapolated pressure squared, denoted by P^{*2}, is greater than the equalized shut-in pressure squared $\overline{P}^2$ because of the overall decline in the reservoir pressure as a whole that will have taken place when the equalization is complete. The relationship between P^{*2} and $\overline{P}^2$ is

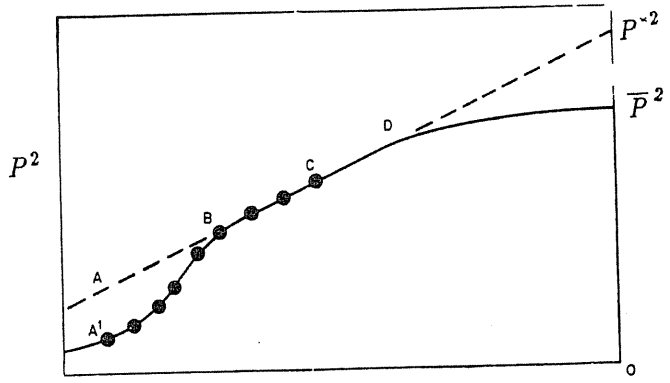

FIGURE 9-23
Sketch of pressure buildup curve, P^2 vs. log $\Delta t/(t_1 + \Delta t)$.

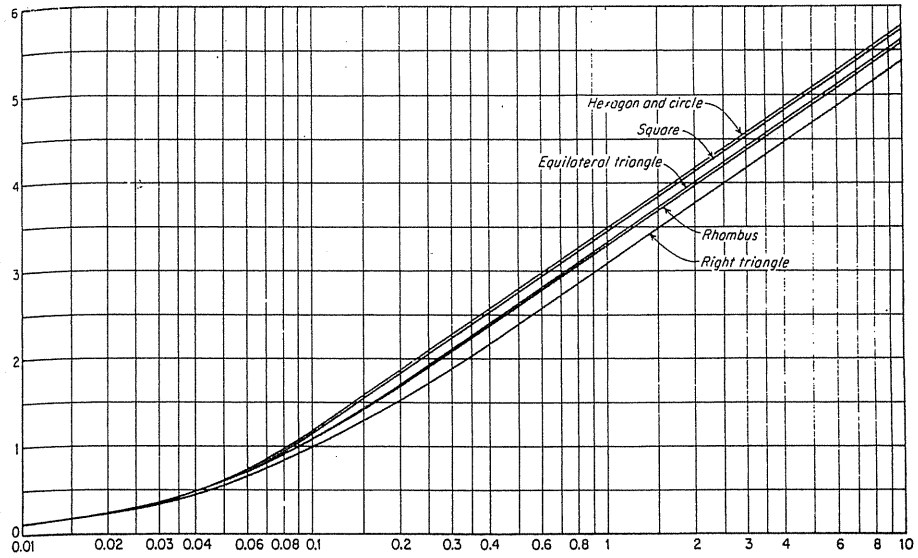

FIGURE 9-24
Pressure function of one well in center of equilateral figures [Matthew, Brons, and Hazebroek, 9-19, courtesy SPE-AIME].

$$\overline{P}^2 = P^{*2} - \frac{\text{slope}}{2.303}F \tag{9.27}$$

where "slope" is the slope of the straight line portion of Fig. 9-23 and F is the MBH factor, showed in Fig. 9-24 for various shapes of finite reservoirs. The dimensionless time t_{DA} used in Fig. 9-24 is defined as

$$t_{DA} = t_D\frac{r_w^2}{A} = \frac{\lambda kt}{\phi\mu_i c_i A} \qquad \text{where} \qquad A = \text{area of finite reservoir} \tag{9.28}$$

Example 9.5 [1-1]. A finite square-shape reservoir was withdrawn for 24 hr; a buildup plot was plotted in terms of P^2, and the slope of the straight line portion was 44.1×10^3. The extrapolated P^{*2} is 3,983,200 psia^2, as shown in Fig. 9-25. Reservoir/well data are as follows:

Initial pressure P_f	2000 psia
Wellbore radius r_w	0.5 ft
Average viscosity μ	0.016 cp
Porosity ϕ	0.15
Reservoir radius r_e	400 ft
Compressibility c	5×10^{-4} 1/psia
Permeability k	20 md

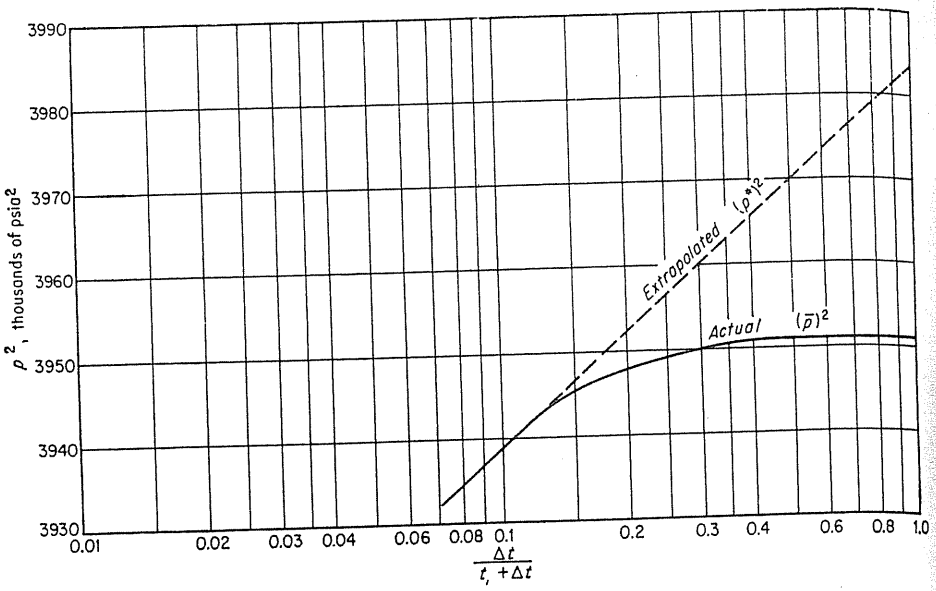

FIGURE 9-25
Calculated buildup pressure plot to determine P^* [Katz et al., 1-1, courtesy McGraw-Hill Publishing Co.].

What is the equalized pressure $\bar{P}$?

Solution. Calculate t_{DA}:

$$t_{DA} = \frac{\lambda k t}{\phi \mu_i c_i A} = \frac{(2.637 \times 10^{-4})(20)(24)}{(0.15)(0.016)(5 \times 10^{-4})(\pi 400^2)} = 0.21$$

and $F = 1.85$ (from Fig. 9-24).
From Eq. (9.27) expressed in terms of P^2, the equalized pressure is

$$\bar{P} = \left(P^{*2} - \frac{\text{slope}}{2.303} F\right)^{1/2} = \left(3,983,200 - \frac{44100}{2.303}(1.85)\right)^{1/2} = 1986.9 \text{ psia}$$

Type-Curve Method

When the skin factor s and the high-velocity contribution DQ_{sc} are lumped together as the apparent skin factor s', Eqs. (8.13) and (8.16) can be solved for $P_{DW}(STW)$ numerically or analytically with r_D and t_D as independent variables for different values of C_D and s'. The results are shown in Fig. 9-26 [9-22]. It is a general purpose chart because all the variables are dimensionless. This chart is used in the *type-curve method*.

The relationships between dimensionless variables and real physical variables on a log-log basis are

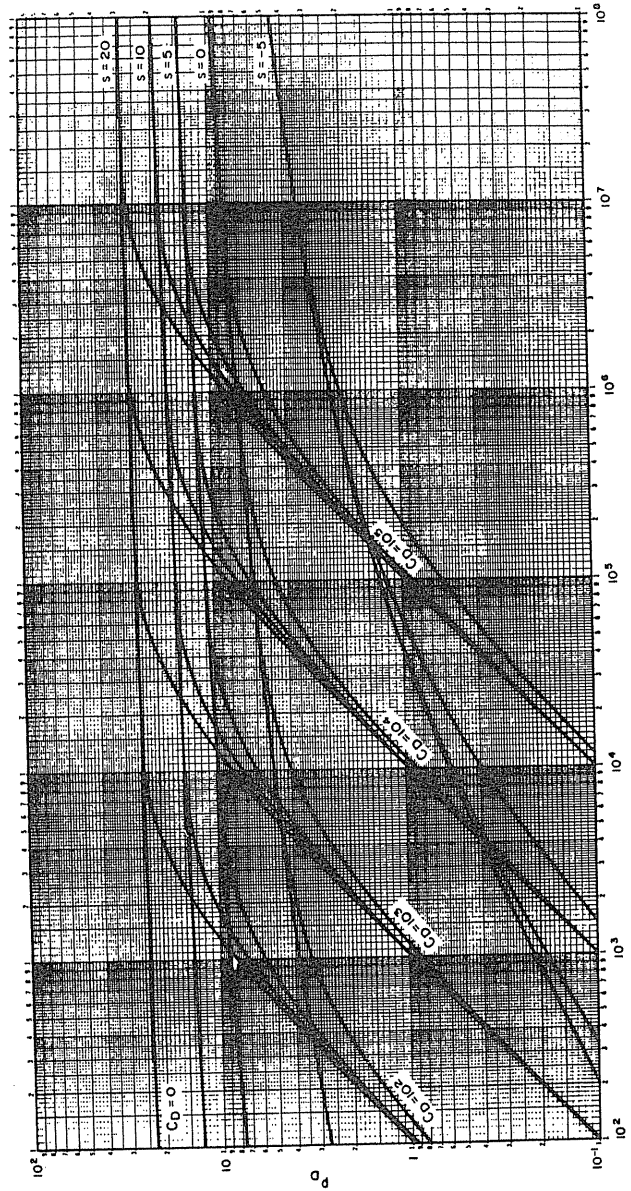

FIGURE 9-26
General type-curve: $P_{DW}(STW)$ versus t_D for various C_D and s' [Ramey, 9-22, courtesy SPE-AIME].

$$\log_{10} P_{DW}(STW) = \log_{10}(\Delta m) - \log_{10}\frac{\gamma TQ}{kh}$$

$$\log_{10} t_D = \log_{10} t + \log_{10}\frac{\lambda k}{\phi\mu_i c_i r_w^2} \tag{9.29}$$

Equation (9.29) and Fig. 9-27 show that a plot of Δm versus t and P_D versus t_D should result in two curves with the same slope in log-log coordinates. Therefore, the generalized chart of P_D versus t_D in Fig. 9-26 serves as a reference chart, and by matching a plot of Δm versus t to that of P_D versus t_D and measuring the difference of positions between the two charts, one can determine kh.

With the two curves matched, it is convenient to take $t = 1$ as the match point.[5] The permeability k can be calculated by

$$t_{D\text{match point corresponding to } t=1} = \frac{\lambda k}{\phi\mu_i c_i r_w^2} \tag{9.30}$$

Alternatively, by choosing $P_D = 1$ as the match point, one could use

$$\Delta m_{\text{match point corresponding to } P_D=1} = \frac{\gamma TQ}{kh} \tag{9.31}$$

to determine the flow capacity kh.

[5] Actually, after matching two curves, all the points on both charts could be used as the match point.

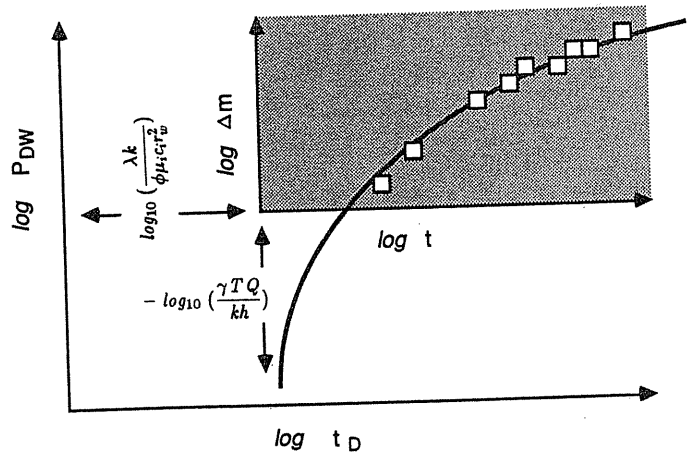

FIGURE 9-27
Relationship between dimensionless plot (P_D vs. t_D) and real physical property plot (Δm vs. t).

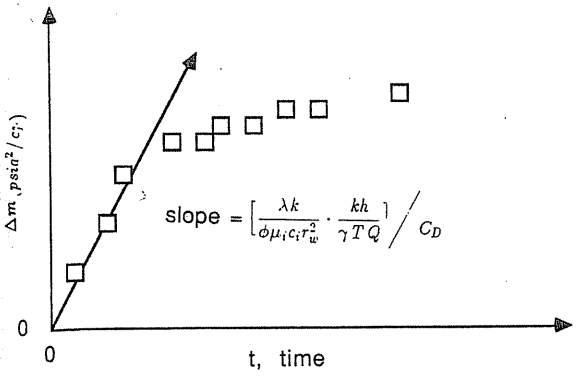

FIGURE 9-28
Utilization of very early time data to determine the wellbore storage constant, C_D.

An immediate drawback of the type-curve method is that all the curves in Fig. 9-26 have similar shapes—the curves could be matched at many possible positions. As a result, it most likely will mislead unless another constraint is included to help the determination of the right position.

After kh and C_D are obtained by this matching technique, one must go back to check the value of C_D by rearranging Eq. (8.48) for the very early time data:

$$C_D = \frac{t_D}{P_{DW}} = \frac{t}{\Delta m}\left(\frac{\lambda k}{\phi\mu_i c_i r_w^2}\cdot\frac{kh}{\gamma TQ}\right) \tag{9.32}$$

where $t/\Delta m$ could be obtained graphically, as shown in Fig. 9-28. The C_D values obtained from the matching technique and from Eq. (9.32) should be close; if not, an iterative (trial-and-error) procedure must be used until satisfactory results are achieved. Since the flow rate at early time could not possibly be kept constant, utilization of such C_D values may be questionable in many cases.

Bourdet et al. [9-8], published a breakthrough paper using another constraint: pressure gradient with respect to time dP/dt on the same graph with pressure P versus time. Figure 9-29 shows this type-curve and the matching procedure. The variables shown in Fig. 9-29 can be found in Table 8.1.

Most type-curves follow the same principle as stated above. More details of using type-curves can be found in references [1-21,8-17]. A selected type-curves package can be ordered directly from SPE [9-24].

9.3 COMMENTS

It is hard to judge which tests are superior to which others. They all serve their own purposes and have been used for years. The decision to conduct any particular test procedure should take into account the production/injection schedule as well as state regulations. A combination of more than one test is recommended and should give better understanding and predictions of a particular well/reservoir's characteristics.

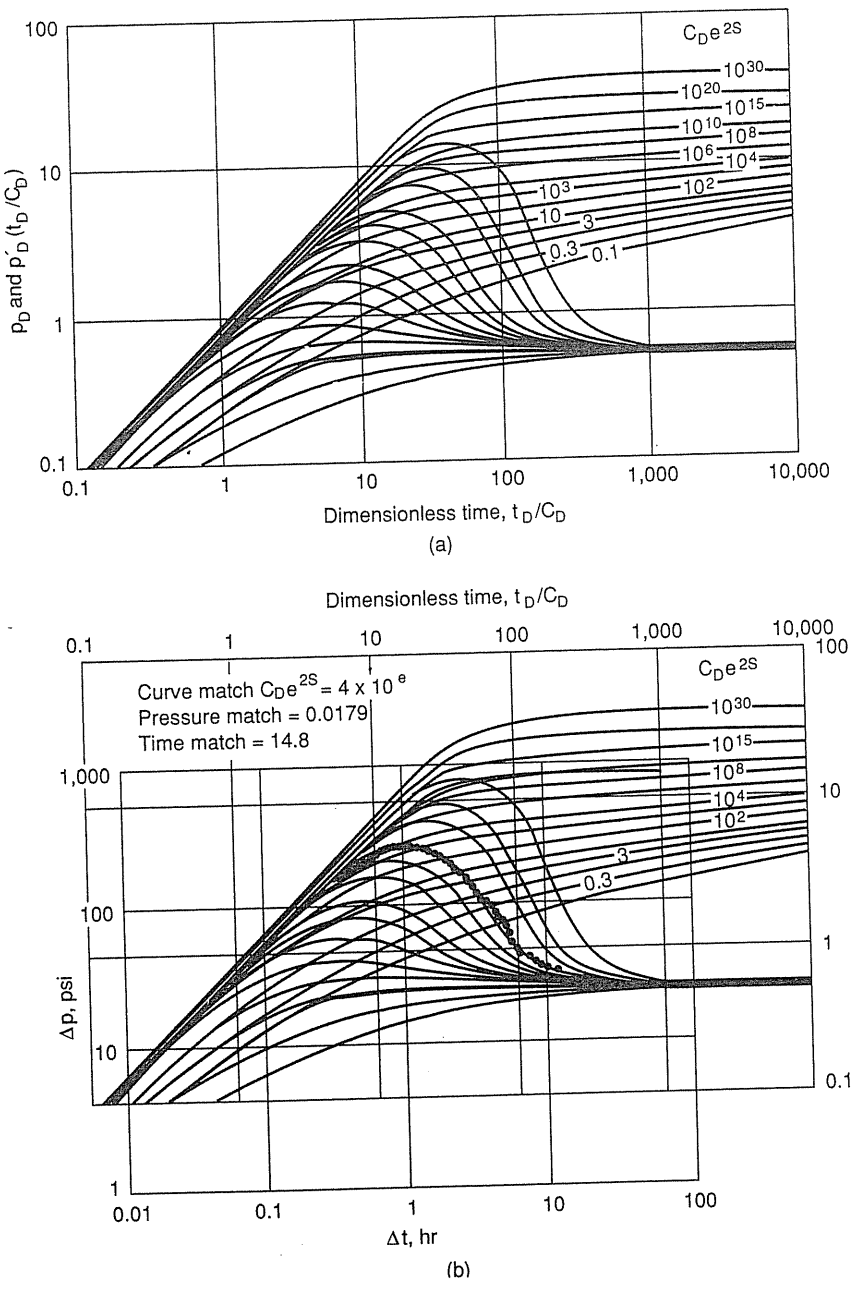

FIGURE 9-29
Type-curve with both pressure and pressure derivative [Bourdet et al., 9-8, courtesy *World Oil*].

This chapter includes only arbitrarily selected testing procedures with which the authors are familiar, and it has omitted others that the authors are not qualified to discuss.

HOME PROBLEMS

9.1. A well is 2500 ft deep and produces 0.6-gravity gas from perforations in the upper 55 feet of a 110-ft section of gas sand. The open flow measured on the well is 15 Mcf/day when the pressure is 1150 psia. The measured permeability of the cores from the well average 50 md. How close is the performance to that predicted from core data?

9.2. Determine the performance coefficient C and exponent coefficient n for the following four-point test:

Q, Mcf/day	ΔP^2, psia^2, $\times 10^3$
1000	310
2300	950
3900	2100
5200	4000

9.3. Consider the following data from two drawdown tests on a single well. Estimate the permeability k, skin factor s, and turbulence factor D for the well [9-7].

Gas properties are shown in Table 8.2, and reservoir data are as follows:

Initial pressure	2300 psia
Formation thickness	10 ft
Wellbore radius	0.5 ft
Porosity	0.1
Gas saturation	0.77

Transient pressure data are as follows:

Time, hr	1.6 MMcf/day	3.2 MMcf/day
0.0	2300	2300
0.0232	1855	1105
0.04	1836	1020
0.06	1814	954
0.08	1806	906
1.00	1797	860
2.00	1758	700
4.00	1723	539
6.00	1703	387

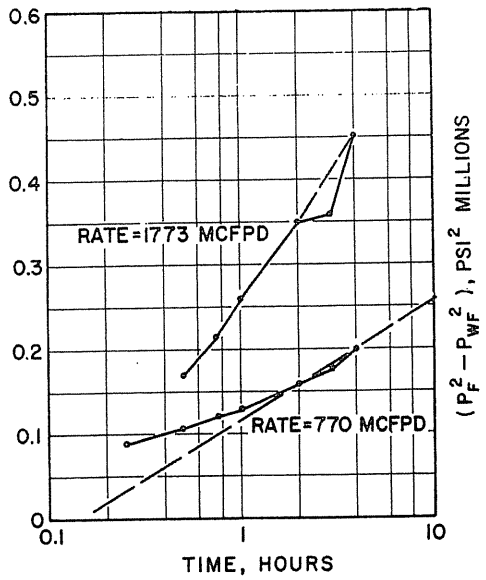

FIGURE 9-30
Drawdown curves for well 4 [Carter, Miller & Riley, 9-9, courtesy SPE-AIME].

9.4. After 100 hours flowing 1.6 MMcf/day of gas, the well in Problem 9.3 was shut in and the pressure buildup observed. Just before the well was closed in, the flowing pressure was measured to be 1584 psia. The buildup pressure response is as follows [8-35]:

Time, after shut-in, hr	Pressure, psia
0.2	1831
0.4	2010
0.6	2048
0.8	2117
1.0	2141
2.0	2173
4.0	2205
6.0	2224

9.5. The drawdown and buildup data for two flow rates on a low-permeability gas well are given below, and the gas properties are given in Table 8.2. Estimate the permeability and skin factor for the well.

Initial pressure	4000 psia
Formation thickness	200 ft
Porosity	0.2
Water saturation	0.2
Wellbore radius	0.5 ft

Transient pressure data are:

Time, hr	10 MMcf/day	5 MMcf/day
0.0	4000	4000
0.2	2253	3311
0.5	2185	3277
1.0	2133	3250
2.0	2078	3224
4.0	2023	3198
7.0	1979	3178
10.0	1952	3166
20.0	1899	3142
40.0	1844	3118
70.0	1798	3099
100.0	1769	3086
	Shut-in	
100.2	2300	3300
100.5	3000	3600
101.0	3668	3838
102.0	3719	3862
104.0	3769	3886
107.0	3808	3905
110.0	3831	3917
120.0	3875	3938
140.0	3913	3957
170.0	3939	3970
200.0	3952	3976

What is the permeability around the wellbore?

9.6. Pressure drawdown curves for a well with production rates of 770 and 1773 Mcf/day are given in Fig. 9-30. Other available data for this well are as follows:

$$T = 590°\text{R}$$
$$\overline{Z} = 0.879$$
$$\phi = 0.114$$
$$\overline{P} = 1200 \text{ psia}$$
$$\mu = 0.0164 \text{ cp}$$
$$h = 8 \text{ ft}$$
$$r_w = 0.5 \text{ ft}$$
$$r_e = 2980 \text{ ft (640-acre spacing)}$$

Determine the equation of the stabilized back pressure curve; i.e., the constants a, b in the equation

$$P_f^2 - P^2 = aQ_{sc} + bQ_{sc}^2$$

where Q_{sc} is Mcf/day production.

9.7. Calculate skin factor s, high-velocity factor D, and permeability k from the following data [F. E. Beck].

Flow 1 2.05 MMcfD		Flow 2 4.835 MMcfD		Flow 3 5.981 MMcfD		Flow 4 8.117 MMcfD		Shut-in —	
t,min	P, psia	t, min	P, psia	t, min	P, psia	t, min	P, psia	t, min	P, psia
201.2	1418.31	409.53	1401.79	471.37	1381.73	530.57	1355.77	582.83	1321.55
202.03	1412.41	411.07	1392.35	472.28	1374.65	531.52	1347.51	583.12	1392.94
202.90	1408.87	412.40	1386.42	473.63	1368.18	532.75	1339.25	584.03	1397.66
204.47	1408.28	413.87	1382.91	474.92	1359.31	534.28	1328.63	585.17	1398.84
209.68	1408.28	416.02	1382.91	477.02	1356.36	535.55	1322.73	586.52	1399.43
215.00	1407.69	418.52	1382.91	482.02	1356.36	537.35	1322.14	587.42	1399.43
220.50	1407.10	420.57	1382.91	487.37	1356.36	542.52	1322.14	588.80	1400.61
225.82	1407.10	422.87	1382.91	492.62	1356.36	547.72	1322.14		
231.50	1407.10	428.40	1382.91	497.75	1355.77	553.03	1322.14		
236.75	1407.10	433.53	1382.91	503.22	1355.77	557.95	1322.14		
241.87	1407.10	438.75	1382.91	508.38	1355.77	563.35	1321.55		
247.02	1407.10	443.95	1382.91	513.77	1355.77	568.60	1321.55		
252.45	1406.51	449.08	1382.91	519.35	1355.77	573.90	1321.55		
257.75	1406.51	454.18	1381.73	524.60	1355.77	579.52	1321.55		
263.12	1406.51	459.80	1381.73	530.57	1355.77	582.83	1321.55		
268.28	1406.51	464.75	1381.73						
273.52	1406.51	471.37	1381.73						
279.52	1406.51								
284.82	1406.51								
290.17	1406.51								
295.23	1406.51								
300.48	1405.92								
306.10	1405.92								
311.12	1405.33								
316.30	1404.74								
322.22	1404.15								
327.87	1404.15								
333.22	1404.15								
338.62	1404.15								
343.68	1404.15								
348.67	1404.15								
354.10	1403.56								
359.92	1403.56								
365.25	1402.97								
370.63	1402.38								
376.25	1402.38								
381.63	1401.79								
409.53	1401.79								

Formation thickness $h = 59$ ft

Gas gravity $G = 0.56$

Porosity $\phi = 0.34$

System compressibility $c = 5.44 \times 10^{-4}\text{psia}^{-1}$

Reservoir temperature $T = 109°\text{F}$

Wellbore Radius $r_w = 0.25$ ft

RECOMMENDED READINGS

9-1. Dake, L. P., *Fundamentals of Reservoir Engineering*, Elsevier Scientific Publishing Company (1978).

9-2. Donohue, D. A. T., and T. Ertekin, *Gaswell Testing: Theory, Practice, and Regulation*, International Human Resources Development Corporation, Boston (1982).

9-3. Earlougher, R. C., Jr., *Advances in Well Test Analysis*, SPE Monograph Vol. 5., SPE, Dallas (1978).

9-4. Energy Resources Conservation Board, *Gas Well Testing, Theory, and Practice*, 3rd Ed. (field units, 1975), 4th Ed. (metric units, 1979).

9-5. Lee, W. J., *Well Testing*, first printing, Society of Petroleum Engineers, Dallas (1982).

9-6. Matthews, C. S. and D. G. Russell, *Pressure Buildup and Flow Tests in Well*, AIME Monograph Vol. 1, SPE-AIME, New York (1967).

REFERENCES

9-7. Al-Hussainy, R., and H. J. Ramey, Jr., "Application of the Real Gas Potential," SPE Preprint 1234B (1965).

9-8. Bourdet, D., T. M. Whittle, A. A. Dougla, and Y. M. Pirard, "A New Set of Type Curves Simplifies Well Test Analysis," *World Oil*, 95–104, May (1983).

9-9. Carter, R. D., S. C. Miller, and H. G. Riley, "Determination of Stabilized Gas Well Performance from Short Flow Test," *J. Pet. Tech.*, Vol. 15, No. 6, 651–658, June (1963).

9-10. Corbett, T. G. , and R. A. Wattenbarger, "An Analysis of and Correction Method for Gas Deliverability Curves," SPE 14208, SPE 60th Annual Meeting, Las Vegas (1985).

9-11. Cullender, M. H., "The Isochronal Performance Method of Determining the Flow Characteristics of Gas Wells," *Trans. AIME*, Vol. 204, 137–142 (1955).

9-12. De Loos, J. M., private communication (1986).

9-13. Elenbaas, J. R., and D. L. Katz, "A Radial Turbulent Flow Formula," *Trans. AIME*, Vol. 204, 25 (1948).

9-14. Govier, G. W., "Interpretation of the Results of Back Pressure Testing of Gas Wells," *Trans. AIME*, 511–514, LXIV, (1961).

9-15. Hinchman, S. B., and F. H. Poettmann, "Error Analysis and Design Considerations for Backpressure Testing of Gas Wells," SPE Preprint 15520 (1986).

9-16. Horner, D. R., "Pressure Build-Up in Wells," *Proceedings, 3rd World Pet. Congress—Set III*, 503–521 (1951).

9-17. Jones, L. G., E. M. Blount, and O. H. Glaze, "Use of Short Term Multi Rate Flow Tests to Predict Performance of Wells Having Turbulence," SPE Preprint 6133, 51st SPE Annual Meeting, New Orleans (1976).

9-18. Lee, W. J., *Well Testing*, first printing, Society of Petroleum Engineers, Dallas (1982).

9-19. Matthews, C. S., F. Brons, and P. Hazebroek, "A Method of Determination of Average Pressure in a Bounded Reservoir," *Trans. AIME*, Vol. 201, 182 (1954).

9-20. Odeh, A. S., and L. G. Jones, "Pressure Drawdown Analysis, Variable-Rate Case," *Trans. AIME*, Vol. 234, 960–964 (1964).

9-21. Poettmann, F. H., "Discussion of Analysis of Modified Isochronal Test to Predict the Stabilized Deliverability Potential of Gas Wells without Using Stabilized Flow Data," *J. Pet. Tech.*, Vol. 38, No. 10, 1122–1124, Oct. (1986); discussion, G. S. Barr, L. Matter, S. B. Hinchman, and H. Kazemi, *J. Pet. Tech.*, Vol. 19, No. 1, 89–96, Jan. (1987).

9-22. Ramey, H. J., Jr., "Short Time Well Test Data Interpretation in the Presence of Skin Effect and Wellbore Storage," *J. Pet. Tech.*, Vol. 22, No. 1, 97–104, Jan. (1970).
9-23. Russell, D. G., "Determination of Formation Characteristics from Two-Rate Flow Tests," *J. Pet. Tech.*, Vol. 15, 1317–1355 (1963).
9-24. Society of Petroleum Engineers, "Type-Curves Package," Richardson, Texas (1985).

CHAPTER 10

RESERVOIR ENGINEERING APPLIED TO GAS, GAS/CONDENSATE, AND GAS/OIL FIELDS

Reservoir engineering starts with the gathering of information about the system being studied. The first information assembled describes the extent and thickness of the rock layers and the character of the porous media, as described in Chapter 2. The knowledge about a reservoir begins to grow with the completion of the first well. The discovery well or drill stem tests give the reservoir liquid and gas compositions and the performance of the rock in carrying flow to the wellbore, as discussed in Chapter 7. Next, the phase behavior at reservoir pressures and temperatures and the material balances on various reservoir types are examined. Rock property and well test data are needed for predicting well flows and establishing an operational plan. The need for secondary and enhanced recovery will become apparent soon after the development drilling has been completed. Production–pressure decline information is required for material balance calculations.

When a well is drilled and completed for production, the effluent, emerging from separators, as illustrated in Fig. 1-2, indicates the nature of the fluids in the reservoir. The logs and completion technique generally make possible the isolation of the phases in the reservoir so that the production is from an oil or a gas phase. Figure 10-1 gives the phase diagrams (conceptual) for the two layers and their percentages of liquid and vapor phases for different temperatures and pressures. The curves A-A' represent the fluid coming up the wellbore, where

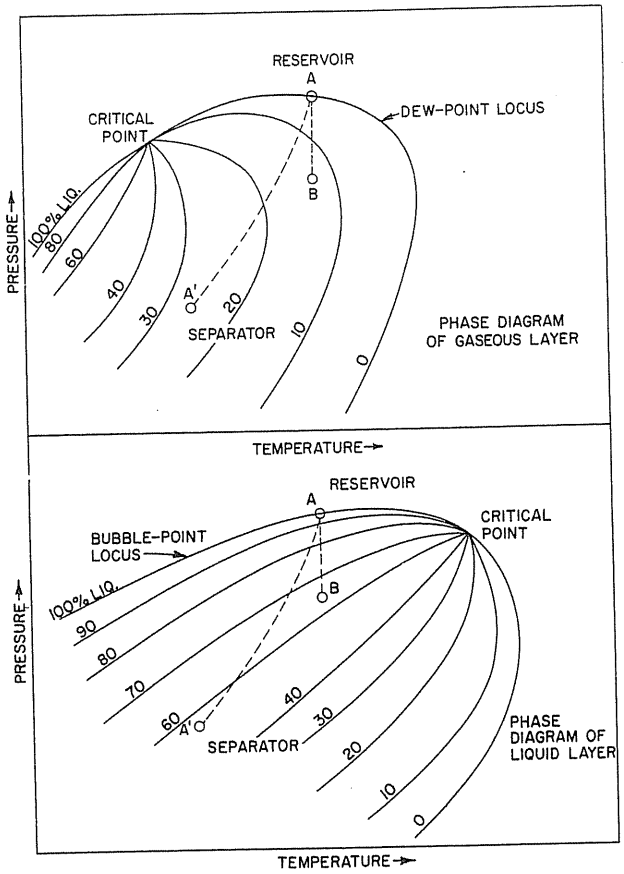

FIGURE 10-1
Relative phase diagrams of liquid and vapor layers [Katz & Williams, 10-14, courtesy AAPG].

both temperature and pressure are lowered. Route *A-B* gives the behavior of the fluid left behind in the reservoir at constant temperature.

By recombining the liquids and gases from the separators, the combined well stream material may be tested in the laboratory, simulating reservoir operation. After bringing the reservoir fluid to a single phase at the reservoir temperature, the pressure is lowered to reach a bubble or dew point. Then removing the single gaseous phase remaining in the reservoir (test cell), the amount of the remaining liquid in the reservoir is observed. For oil reservoirs, the liquid is found to shrink with the vaporization of dissolved gases at decreasing pressures. The results are shown in Fig. 10-2 for crude oil.

For a gas/condensate well sample, Fig. 10-3 shows the formation of liquid by pressure drop and the retrograde liquid amount. At pressures below the point of maximum liquid yield, the retrograde liquid vaporizes at reduced pressures.

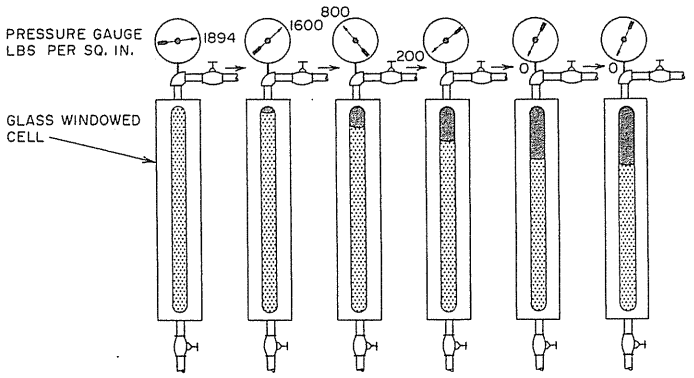

PRESSURE - LBS. PER SQ. IN. GAUGE	1894	1600	800	200	0	0
TEMPERATURE - DEGREES FAHRENHEIT	152	152	152	152	152	60
VOLUME LIQUID PHASE - BBLS.	1.40	1.36	1.26	1.16	1.04	1.00
VOLUME GAS PHASE - BBLS.	0.00	0.04	0.14	0.24	0.36	0.40
GAS EVOLVED - CU. FT. FROM PREVIOUS PRESSURE	0	88	238	212	208	0
GAS EVOLVED - CU. FT. ACCUMULATIVE	0	88	326	538	746	746

FIGURE 10-2
Gas evolution causing the shrinkage of crude oils [Katz & Williams, 10-14, courtesy AAPG].

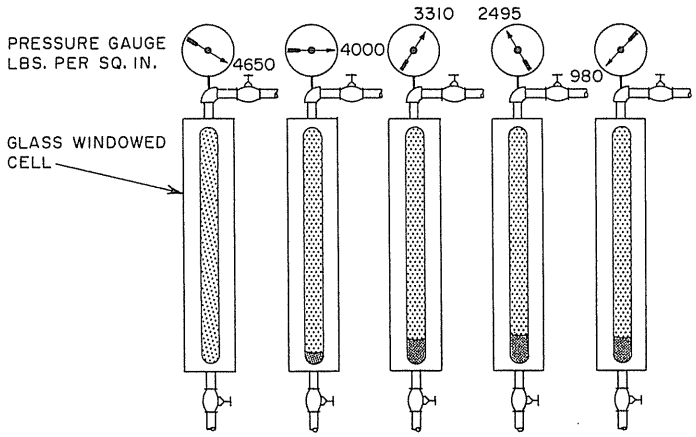

PRESSURE - LBS. PER SQ. IN. GAUGE	4650	4000	3310	2495	980
TEMPERATURE - DEGREES FAHRENHEIT	256	256	256	256	256
VOLUME LIQUID PHASE - C.C.	0	5.1	9.4	10.7	9.4
VOLUME GAS PHASE - C.C.	100	94.9	90.6	89.3	90.6
GAS WITHDRAWN - BETWEEN PRESSURES *	0	1770	2330	3600	6900
GAS WITHDRAWN - ACCUMULATIVE *	0	1770	4100	7700	14,600

* — — — C.C. MEASURED AT 60° F., 14.7 LB. PER SQ. IN.

FIGURE 10-3
Retrograde condensation from gas phase by pressure reduction [Katz & Williams, 10-14, courtesy AAPG].

The gas-oil ratio is a reasonable indicator of whether the reservoir contains gas/condensate or crude oil, as shown in Fig. 10-4. Between gas-oil ratios of 3000 and 5000 ft^3/bbl hydrocarbon liquid, one cannot be certain whether the reservoir temperature is above the critical temperature of the reservoir fluid (crude oil) or below it (gas/condensate). Low gas-oil ratios indicate crude oil and high gas-oil ratios indicate gas/condensate.

The gravity and color of the liquid at atmospheric conditions help decide the type of reservoir. Crude oil is darker, green to black. Condensates vary from clear to straw color to orange brown. Asphalt present in crude oil does not vaporize, so if a well produces at 10,000 ft^3/bbl (1781 m^3/m^3) and the oil is dark in color, it is likely that an oil phase is being produced along with the gas/condensate.

The depth and pressure are to be considered; a gas well at 2000 ft (610 m) and 860 psia (5.93 MPa) would have a water-white condensate, if any formed, and a shallow oil well would have a solubility gas-oil ratio of 200–400 ft^3/bbl (35.62–71.24 m^3/m^3).

Reservoir fluids have been found that have a critical temperature close to the reservoir temperature. If the reservoir pressure surpasses the critical pressure and upper dew point pressures, reservoir fluid production can occur with a drop in reservoir pressure and no liquid or second phase forming in the reservoir.

Shallow gas wells frequently produce little or no hydrocarbon liquid in a separator. For such a case, curve *A-A'* (Fig. 10-1) would reach a low pressure without entering the two-phase region (still above the two-phase loop of the *P-T* diagram).

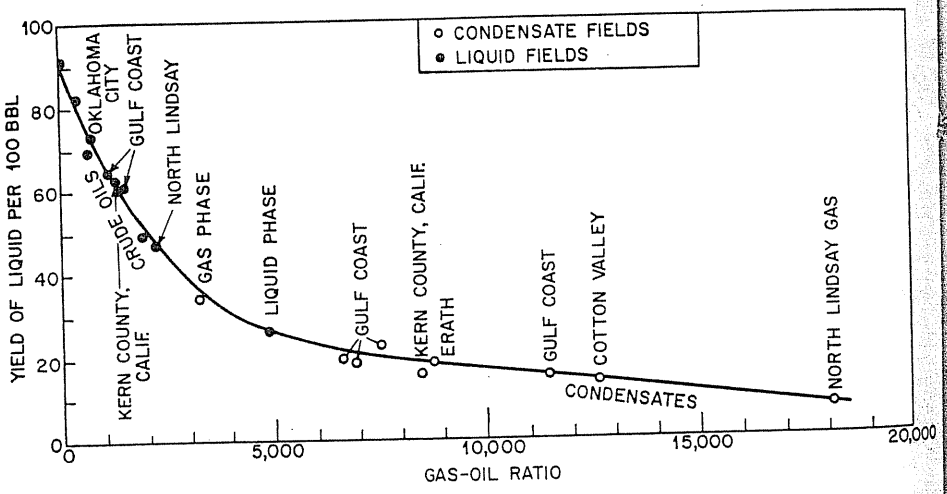

FIGURE 10-4
Gas-oil ratio for condensate and oil fields [Katz & Williams, 10-14, courtesy AAPG].

10.1 Solubility and Shrinkage (*PVT*) Curves

Bottom hole or reservoir samples along with recombined separator samples are used to measure *P-V-T* behavior, including the solubility and shrinkage curves, using methods similar to that of Fig. 10-2. The results of such measurements on several crude oils are given in Figs. 10-5 and 10-6 [1-1]. The solubility curves are measured for a differential depletion process at the reservoir temperature with the gas measured at standard conditions, 60°F, 14.7 psia (15°C, 101 kPa), and the oil at one atmosphere and 60°F (15°C). Shrinkage values are required for converting stock tank (atmospheric pressure) barrels (m^3) to reservoir conditions at the temperature and pressure prevailing. The *formation volume factor* (FVF) is the volume of the oil including dissolved gas in the reservoir per volume of stock tank crude oil measured at 60°F (15°C). The FVF reflects two effects; the major part usually is the vaporization of dissolved gas down to 1 atm pressure, followed by the decrease in volume as the residual oil cools from reservoir temperature to 60°F (15°C).

In contrast to differential vaporization measurements, separator yields of gas are taken in a flash process at the temperature of the separator. For the Leduc crude oil, the combined separator gases' volume of 778 ft^3/bbl (138.6 m^3/m^3) (Fig. 1-2*a*) almost equals the value read from the solubility curve (Fig. 10-5) of 745 ft^3/bbl (133 m^3/m^3) at 1894 psia (13.06 MPa), the discovery reservoir pressure. Often there is a significant difference between these values.

Example 10.1. Calculate the solubility change (ΔS) per ft^3 volume change (ΔV) of reservoir from 1000 to 2000 psia based on 1 barrel of residue oil for Leduc oil.

Solution. The following values are read from Figs. 10-5 and 10-6:

Pressure	FVF, bbl oil and gas/ bbl residue oil	Solubility, ft^3 standard condition/ bbl residue oil
2000	1.41	775
1000	1.20	475

$$\Delta V(ft^3) = (FVF_{1000} - FVF_{2000})\left(\frac{\text{bbl reservoir}}{\text{bbl residue oil}}\right) \times \frac{5.61 ft^3}{\text{bbl}}$$

$$= (1.21 - 1.41)(5.61) = -1.122 \frac{ft^3 \text{reservoir space}}{\text{bbl residue oil}}$$

$$\Delta S = S_{1000} - S_{2000} = 475 - 775 = -300 \frac{ft^3 \text{gas}}{\text{bbl residue gas}}$$

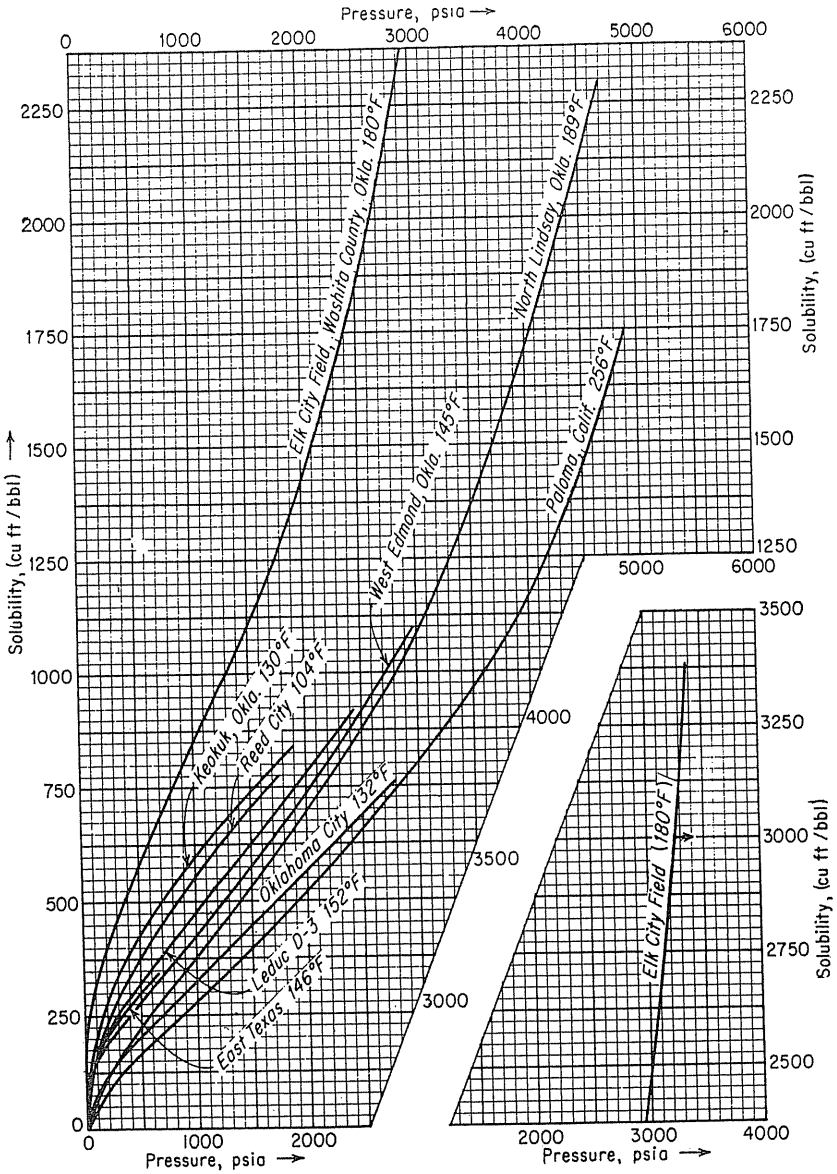

FIGURE 10-5
Solubility curves for natural gas in crude oils [Katz et al., 1-1, courtesy McGraw-Hill Publishing Co.].

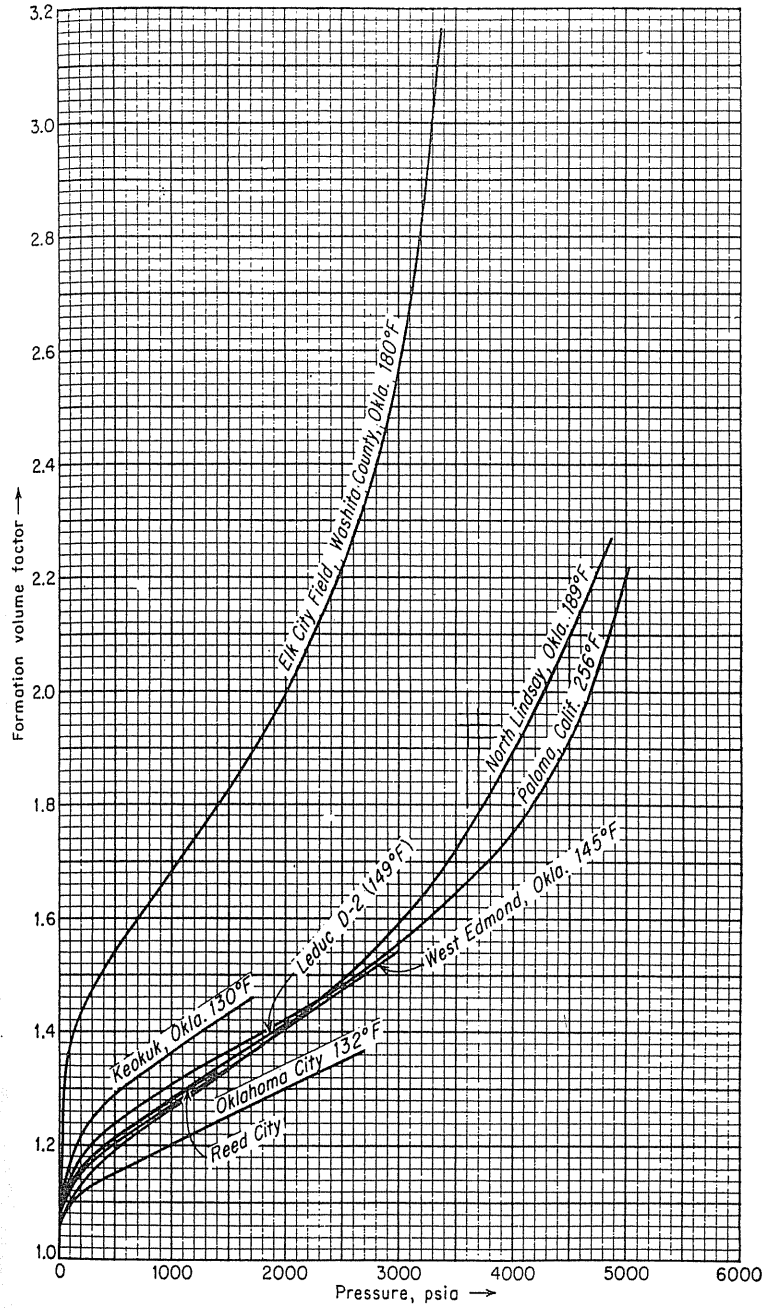

FIGURE 10-6
Shrinkage density of crude oils with gas evolution [Katz et al., 1-1, courtesy McGraw-Hill Publishing Co.].

Hence,

$$\frac{\Delta S}{\Delta V} = \frac{-300}{-1.122} = 267.37 \frac{\text{ft}^3 \text{gas in standard condition}}{\text{ft}^3 \text{reservoir space}}$$

Using the gas gravity 0.7, $\bar{Z} = 0.82$, and 612°R, the reservoir holds (2000/14.7) × (520/612) × (1/0.82) = 141 ft³ gas/ft³ reservoir gas space. Thus, when pressure increases from 1000 to 2000 psia, 267.37 ft³ of gas will swell a liquid volume by 1 ft³ if an oil phase exists, while only 141 ft³ could enter the 1-ft³ space in gas phase, or almost 50 percent less.

10.2 Predicting Solubility and Formation Volume Factors (FVF)

Solubility and shrinkage behavior may be approximated using field data such as separator gas-oil ratio, gas gravity, and stock tank oil gravity. Katz [10-10] examined the behavior of a large group of crude oils with measured solubility and shrinkage to correlate the variables and devise a chart giving the apparent density of dissolved gases based on gas gravity and crude oil gravity, Fig. 10-7. By combining the gas in liquid phase with the oil at the gas-oil ratio, the

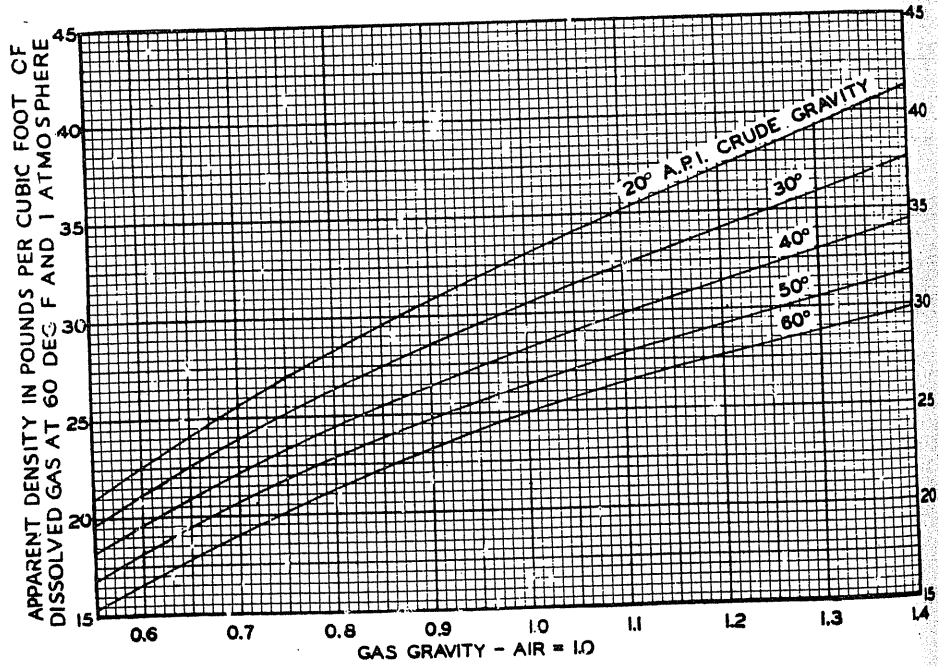

FIGURE 10-7
Apparent density of natural gas dissolved in crude oil [Katz, 10-11, courtesy *API Drilling and Prod. Practice*].

mixture volume and mass at 60°F (15°C) and one atmosphere may be corrected for pressure and then temperature to obtain the reservoir volume as described in Chapter 4 for calculating liquid (gas and oil) densities.

Standing [1-20] has presented detailed methods of predicting *P-V-T*, solubility, and formation volume factors for crude oil/natural gas systems. The change in crude oil gravity with pressure and temperature is given in Figs. 10-8 and

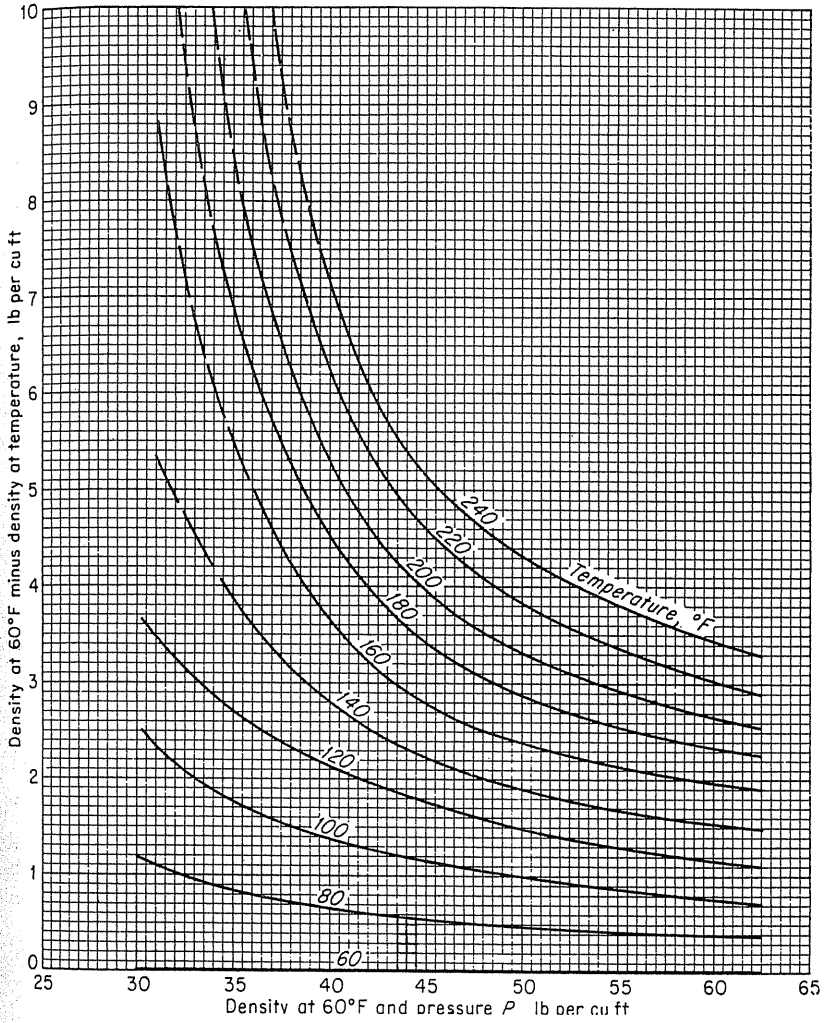

FIGURE 10-8
Change of density of crude oils with pressure [Standing, 1-20, courtesy Reihold Publishing Corporation].

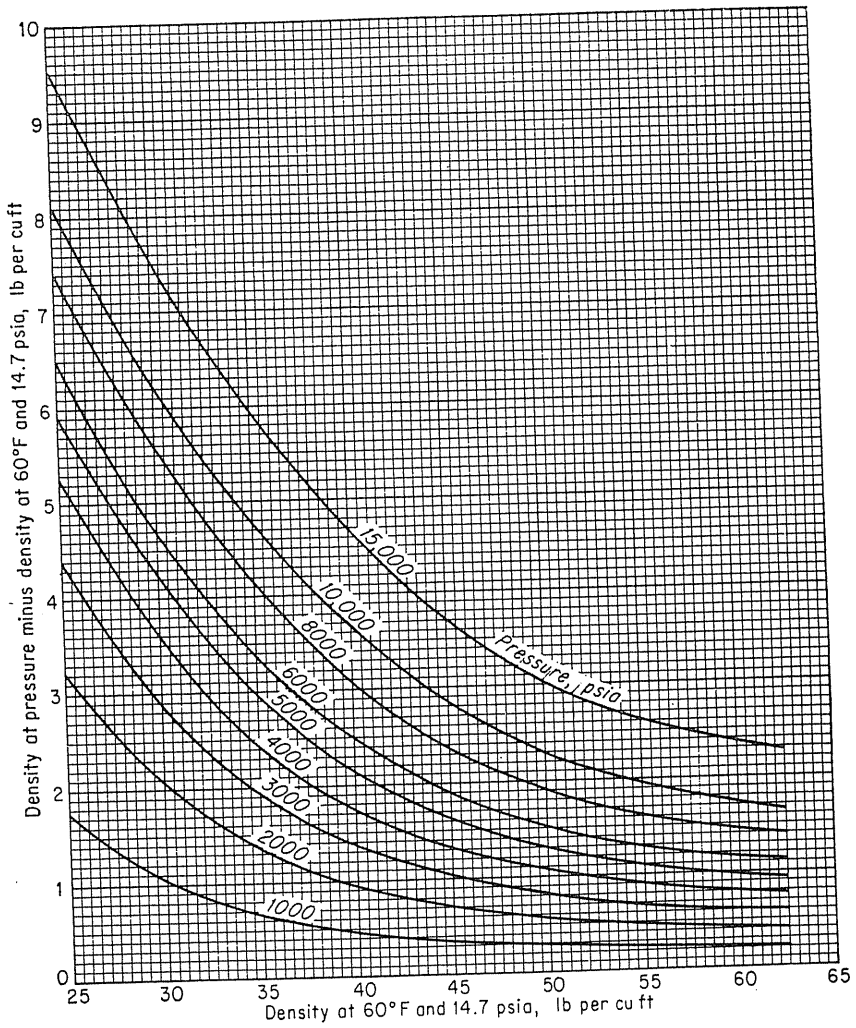

FIGURE 10-9
Change of density of crude oils with temperature [Standing, 1-20, courtesy Reihold Publishing Corporation].

10-9. His correlation of bubble point with separator variables is given by Fig. 10-10 and his correlation of the formation volume factors by Fig. 10-11.

When an oil well is drilled in a new reservoir and the separator gas-oil ratio, oil gravity, and gas gravity are known, Figs. 10-10 and 10-11 give the bubble point pressure and the formation volume factors. Viscosity and surface tension in the reservoir frequently are also desired; typical values are shown in Figs. 10-12 and 10-13.

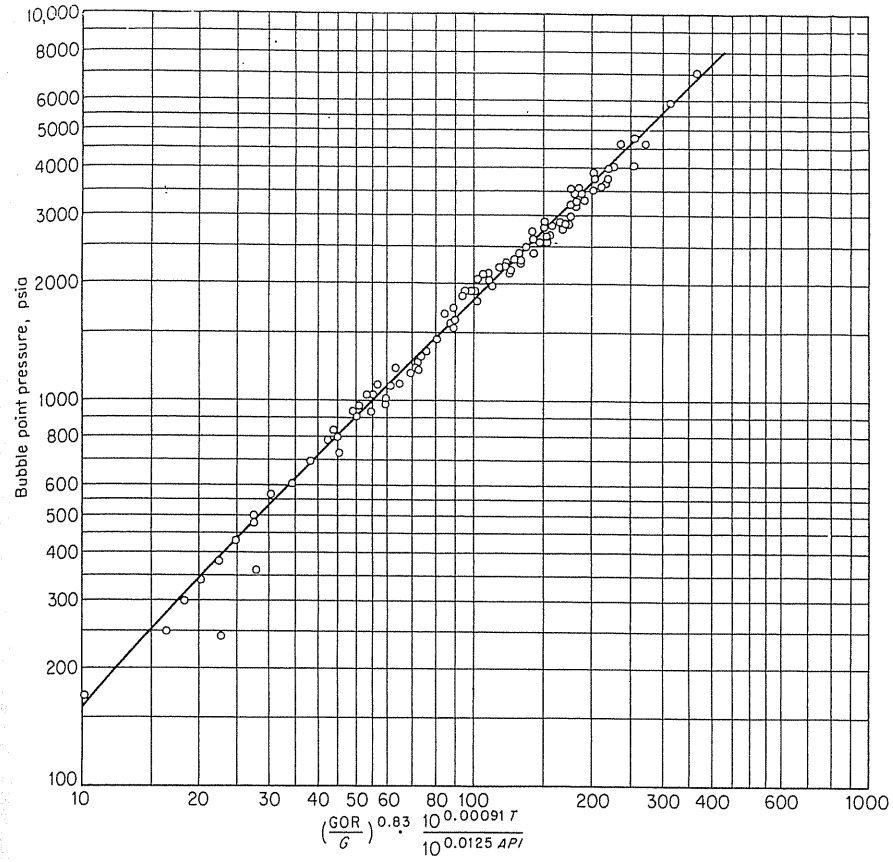

FIGURE 10-10
Prediction of bubble point from separator variables [Standing, 1-20, copyright 1947, courtesy California Research Corp. (now Chevron)].

10.3 Oil and Gas Reserves

The determination of the initial oil and gas in place followed by an estimate of the recoverable amounts of oil and gas is an important part of a reservoir engineer's domain. There are two quite different ways to determine the initial hydrocarbon present: (1) the use of geological knowledge and volumetric calculations for the pore volume and fraction of hydrocarbons present, and (2) the use of early production history of gas and oil recovery along with pressure drop in the reservoir. The second method is sensitive to well fluid analyses, phase behavior calculations, equalized pressure measurements, and possibly water movement into the reservoir. This method is considered to be a material balance in which calculations are made of what the reservoir contents must be to support the production and pressure behavior observed.

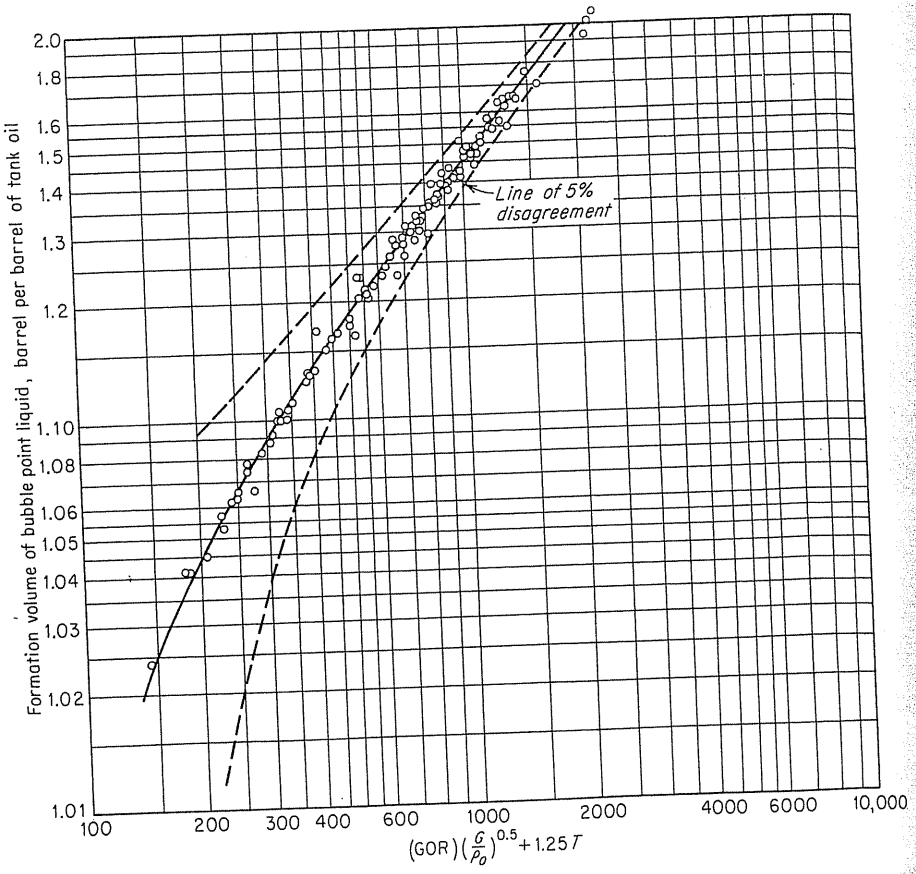

FIGURE 10-11
Prediction of FVF from separator variables [Standing, 1-20, copyright, courtesy California Research Corp. (now Chevron)].

Volumetric Method

The volumetric method of estimating gas reserves is used for new fields before any significant production takes place. The items comprising a volumetric estimate are as follows:

1. Reservoir extent A and thickness h
2. Average porosity ϕ of producing formation
3. Fractional saturations S_w of pore space with connate water
4. Reservoir pressure P and temperature T
5. Compressibility factor Z of gas, based on gas analysis or gas gravity

The volume of gas contained in a reservoir is computed by finding the volume of pore space containing gas and the gas content of a unit space from temperature, pressure, and the compressibility factor. For those desiring an equation, Eq. (10.1) is presented:

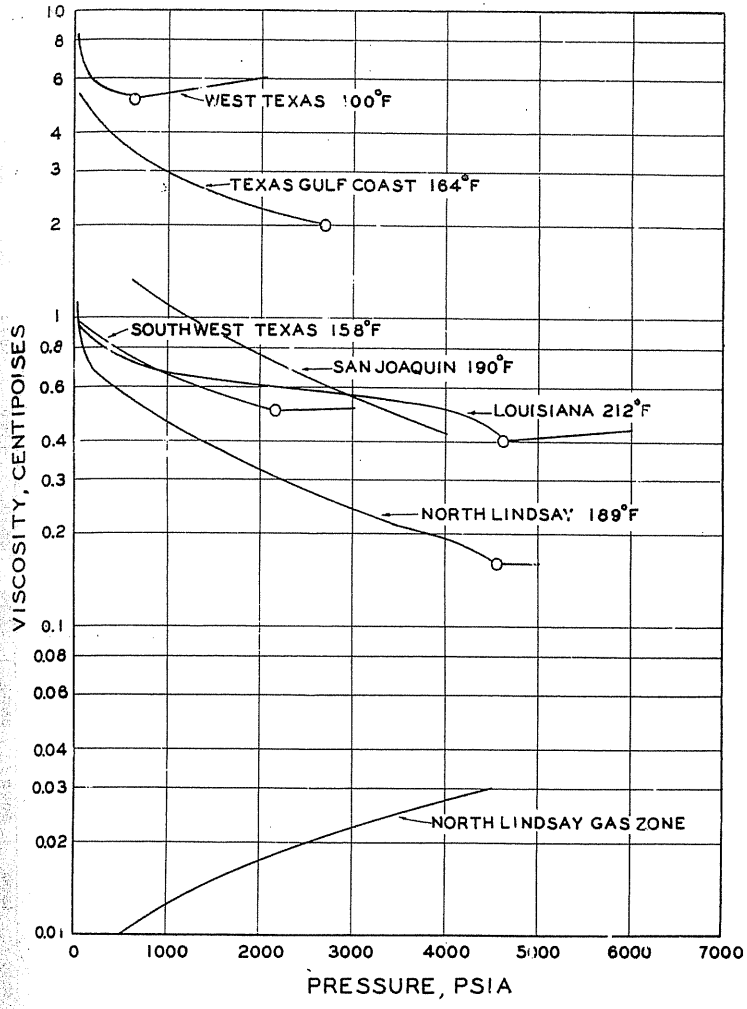

FIGURE 10-12
Viscosity of crude oils with dissolved gas [Katz & Williams, 10-14, courtesy AAPG].

$$Q_{sc}\,(\text{ft}^3) = \frac{q_f}{B_g} = \frac{(4.356 \times 10^4)Ah\phi\,(1 - S_w)}{B_g} \qquad \text{where} \qquad B_g \approx \frac{P_{sc}T}{PT_{sc}} \cdot Z \tag{10.1a}$$

$$Q_{sc}\,(\text{m}^3) = \frac{A(\text{m}^2)h(\text{m})\phi(1 - S_w)}{B_g} \tag{10.1b}$$

In Eq. (10.1a), Q_{sc} is the gas in place (GIP) measured at P_{sc} (14.7 psia, 101.3

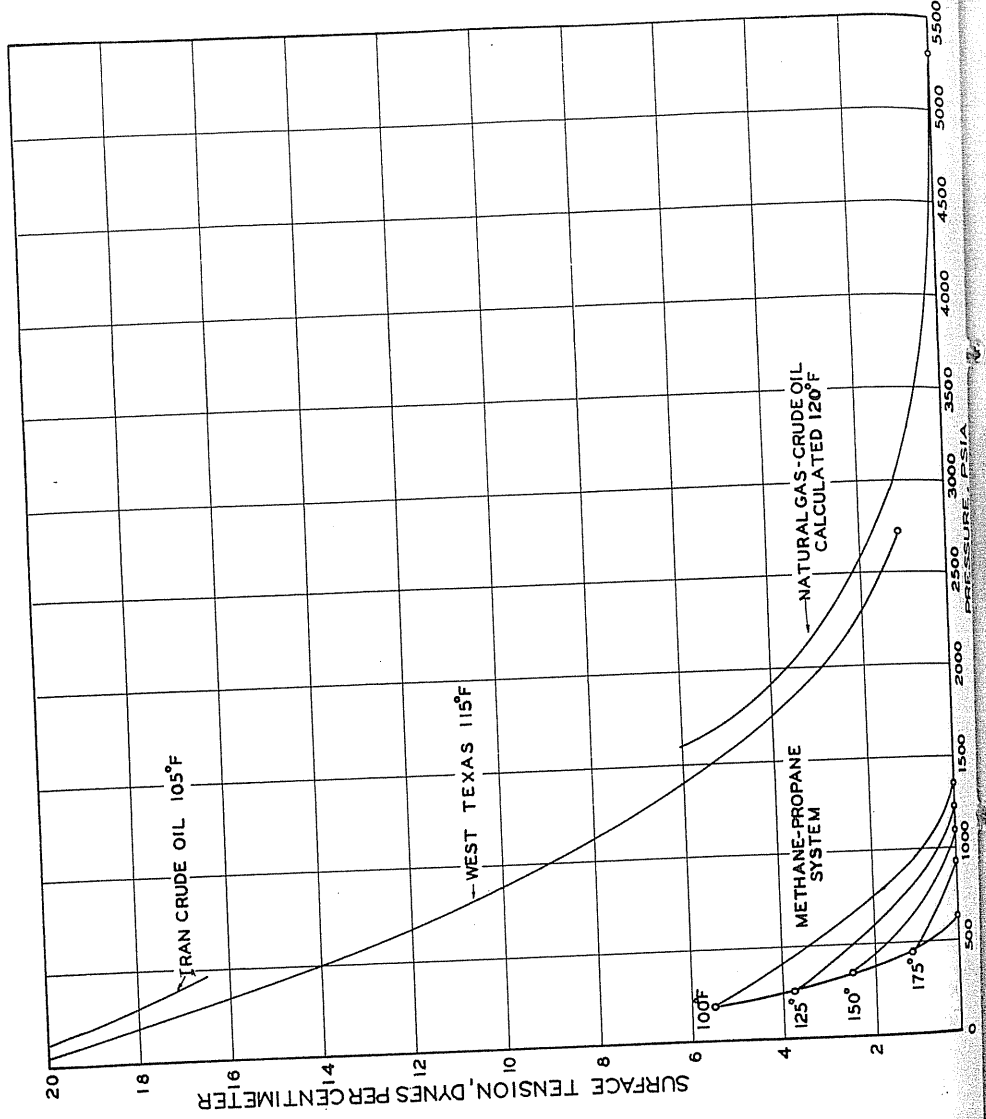

FIGURE 10-13
Surface tension of crude oils with dissolved gas [Katz & Williams, 10-14, courtesy AAPG].

kPa) and T_{sc} (520°R, 15°C), q_f (ft^3) is the volume at reservoir conditions, A (acres) is the areal extent, h (ft) is the thickness of formation, ϕ is the fractional porosity, S_w is the fractional saturation of pore space with water, P (psia) is the reservoir pressure, T (°R) is the reservoir temperature, B_g is the conversion factor from reservoir conditions to wellhead standard conditions, and Z is the compressibility factor for gas.

The areal extent A and formation thickness h are based on geological information and maps drawn to portray the structure. Figure 10-14 [1-1] shows an isopachous map, which is used to determine the pore volume. A planimetering of the isopachous map gives the area of the zones with the indicated thicknesses. The average thickness times the area gives the product Ah in acre · ft (or m^3). The data used in preparing the structural and isopachous maps include all data on the wells such as electric logs, core data, drill stem tests, logs from cuttings, drilling rate, seismic results, etc. To obtain the water level, it is necessary to have one well reach the level. When the porosity occurs intermittently, it is customary to give a total formation thickness and a net pay thickness h to be used in computing the gas reserve.

Example 10.2 [Katz et al., 1-1]. Compute the gas reserve for sand No. 44 at Deep Lake, Louisiana. The isopachous map is given in Fig. 10-14, and reservoir conditions are given in Table 10.1.

Solution. Find the acre-feet of sand by planimetering area between contours and multiplying by average thickness between contours.

Countour interval	Area, acres	Average thickness, ft	Volume, acre · ft
0–5	153.37	2.5	383.4
5–10	142.75	7.5	1,070.6
10–15	136.78	12.5	1,709.8
15–20	128.38	17.5	2,246.7
20–25	183.55	22.5	4,129.6
25–30	506.10	27.5	13,917.6
30–30	23.77	30.0	713.1
30–35	569.79	32.5	18,518.2
35–40	281.41	37.5	10,552.9
40–44	132.69	42.0	5,573.0
44–44	27.77	44.0	1,045.9
Total	2286.36		59,861

Gas reserve:

$$Q_{sc} = 43,560Ah\phi(1 - S_w)\frac{PT_{sc}}{P_{sc}T}\frac{1}{Z}$$

$$= 43,560(59,861)(0.28)(1 - 0.25)\frac{(5164)(520)}{(14.73)(657)}\frac{1}{(0.987)} = 153.9 \times 10^9 \text{ ft}^3$$

$$= 153.9 \text{ Bcf}$$

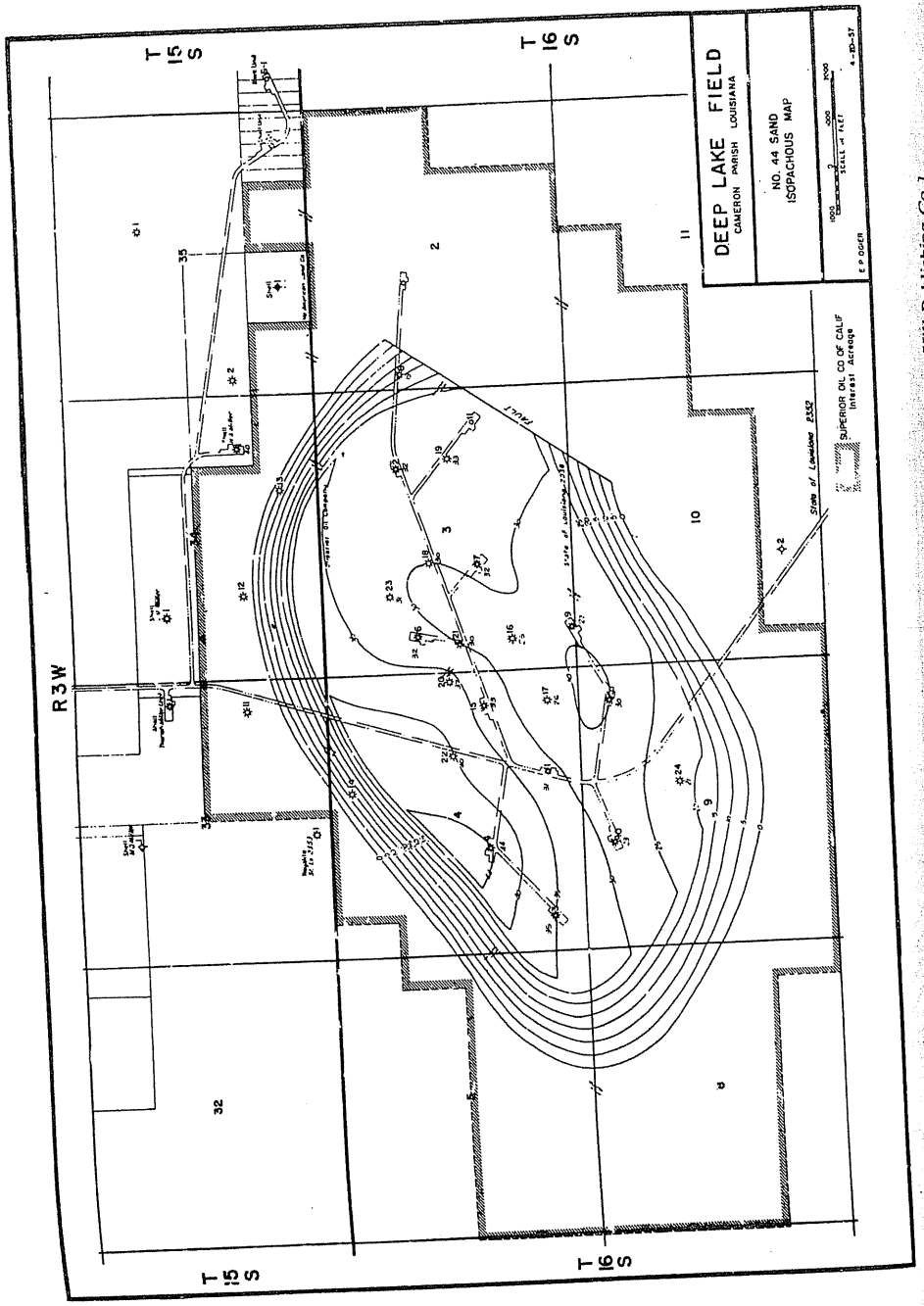

FIGURE 10-14
Isopachous map, Sand 44, Deep Lake field [after Spooner & Ogier; Katz et al., 1-1, courtesy McGraw-Hill Publishing Co.].

TABLE 10.1
Data on sand 44, Deep Lake field [after Spooner & Ogier; Katz et al., 1-1]

Cameron Parish, Louisiana	
Average depth, ft	11,330
Gas-water contact, ft	11,420
Gas gravity	0.653
Heating value, Btu/ft^3	1,050
Reservoir pressure, psia	5,164
Reservoir temperature, °F	197
Compressibility factor of gas	0.987
Average porosity, percent	28
Connate water, percent	25
Gas content, Mcf/(acre · ft)	2,572
Estimated productive area, acres	2,282
Average sand thickness (Miocene), ft	26.23
Reservoir volume, acre · ft	59,861
Gas content, Bcf	153.9

The definition of the water table and the possibility of tilted water tables for dynamic reservoirs should not be overlooked [1-70].

The porosity and connate water content are determined by methods described in Chapter 2. Measurements on cores are desirable when working with unfamiliar formations. These values may be estimated from electrical logs, especially after experience has been gained in an area. The compressibility factor determination requires either the gas analysis or the gas gravity, and the reservoir temperature and pressure, as discussed in Chapter 4. In some low-permeability reservoirs, it may be necessary to select a permeability limit below which the gas, though present, is not counted in the reserve, since it cannot be produced in the usual time limits of depleting the field. The increase of connate water content of low-permeability rock reduces the gas content of such low-permeability formations considerably.

Material Balances

The most successful material balances are made on natural gas reservoirs with enough permeability to permit pressure equalization after producing natural gas and with a minimum of water movement (pore volume occupied by gas stays constant).

The equation or graphical procedure for determining the initial gas in a reservoir from production data is derived by applying the gas law ($PV = ZnRT$) to a constant pore volume reservoir:

$$\frac{n_1}{n_1 - n_2} = \frac{(P_1/Z_1)(V/RT)_1}{(P_1/Z_1)(V/RT)_1 - (P_2/Z_2)(V/RT)_2} \approx \frac{P_1/Z_1}{P_1/Z_1 - P_2/Z_2} \qquad (10.2)$$

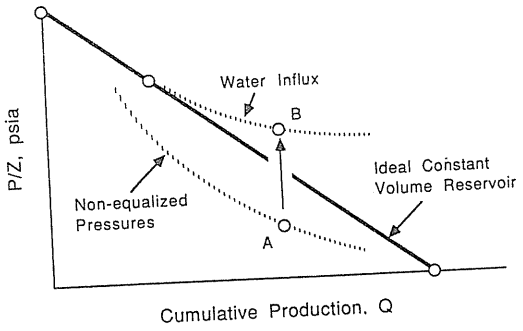

FIGURE 10-15
Schematic of P/Z vs. gas production ($Q_1 - Q_2$).

where subscripts 1 and 2 denote the first and second conditions. The quantity $(n_1 - n_2)$ is the gas production removed from the reservoir in moles, which could be converted to gas at standard conditions: $Q_{sc}/379$ ft^3 $= n$ (lb mol) ($Q_{sc}/24.45$ m^3 $= n$ [kmol]).

$$Q_1 = \frac{(Q_1 - Q_2)(P_1/Z_1)}{P_1/Z_1 - P_2/Z_2} \quad \text{or} \quad \frac{P_2}{Z_2} = \frac{P_1}{Z_1} + \left(-\frac{P_1}{Z_1}\frac{1}{Q_1}\right)(Q_1 - Q_2) \quad (10.3)$$

Plotting this relationship on coordinate scales gives Fig. 10-15, where the slope $(-P_1/Z_1Q_1)$ of the curve should reflect the initial gas in place Q_1; this is, however, decreasing while water influx increases (Q_1 decreases for each time step). The nonequalized pressure line shows that water is still coming in and that the recorded pressure A would eventually reach point B after a long shut-in period.

The discovery pressure at zero production over the compressibility factor is the anchor point at $Q_1 - Q_2 = 0$. To obtain the compressibility factor Z in the reservoir, the gas composition or gravity and the pressure and the reservoir temperature are needed.

After significant production (5 percent of the contents of most reservoirs; usually, $P_1/Z_1 - P_2/Z_2 > 200$ psia, or 1.38 MPa) $Q_1 - Q_2$ is obtained along with the equalized pressure at that time as P_2/Z_2, the second point on the line. To have an accurate check of inventory, it is suggested that all gas storers withdraw a significant part of the total top gas during each yearly cycle.

Recoverable Gas

For reservoirs producing by gas expansion and without water drive, there is no reason that essentially all the gas may not be produced, down to atmospheric pressure. However, the production rates decrease so rapidly when the pressure approaches atmospheric that some abandonment pressure is normally established for commercial production. These abandonment pressures are set as low as 50 psia

for shallow reservoirs and as high as 500 psia or more for deep gas reservoirs (to overcome pressure head lost in wells). The initial gas content minus the content at a selected abandonment pressure is the *recoverable gas*.

For water drive reservoirs, the pressure decline is not the occasion for final depletion of the reservoir. Instead, water production from the wells will drown out gas production when most of the gas has been produced. The exact effectiveness of water in displacing gas is not known for reservoir conditions.

How much gas remains when water passes through a zone containing connate water and a gas phase? Figures 2-37 and 2-38 were prepared to indicate the fraction of trapped gas based on experimental data. There is a wide range of gas saturations for a given porosity, indicating the effect of internal structure for a particular porous solid.

The highest gas recovery will occur if the gas can be produced fast enough to prevent the water influx from flooding much of the pore space. This matter will be addressed when considering the abandoning of a water drive gas storage reservoir. From examining the mobility ratio $M = (k_w/\mu_w)(\mu_g/k_g)$, water displacing gas is recommended because it does not favor viscous fingering (which usually occurs if $M > 1$); on the other hand, the slower the processes while converting aquifers to gas storage, the better the ratio of top gas (recoverable) to base gas (unrecoverable) will be.

If strong water movements are expected, the material balance equation (Eq. 10.3) should include the water influx as shown in Example 8.9, except assuming the water influx rate $\dot{E}_w$ is not a function of time ($\neq C_1\sqrt{t}$) and is proportional to the pressure drop between aquifer and gas bubble. Details will be discussed in Chapter 14.

Example 10.3. Given the gas production and reservoir pressure data of Table 10.2 [10-23], find the total gas content of reservoir S and estimate the gas reserve. The gas is of 0.60 gravity, and the reservoir temperature is 105°F (41°C).

Solution. Read the compressibility factors for the reservoir pressures and reservoir temperature from Fig. 4-18 [1-1], and plot P/Z versus Q (Fig. 10-16). The total gas content was 49.1 Bcf (1.39×10^9 m^3).

Suppose one used the first production point to predict the total gas content. Use Eq. (10.3) to solve:

$$Q_1 = \frac{\Delta Q(P/Z)_1}{(P/Z)_1 - (P/Z)_2} = \frac{(6.9)(2680)}{2680 - 2319} = 51.2 \text{ Bcf } (1.45 \times 10^9 \text{ m}^3)$$

The depth of the reservoir was not given, but assuming 0.44 psi/ft (10 kPa/m), the depth is 4886 ft. The points on Fig. 10-16 indicate there is no significant water influx or nonequalization of pressures, and hence there is a reasonable permeability thickness product kh for the producing formation. The reserve might be taken to a reservoir pressure of 50 psia, which corresponds to 48.4 Bcf in Fig. 10-16. Alternatively, using $Q/(P/Z) = 49, 100/2680 = 18.31$ MMcf/psi, all but 50 psia $\times$ 18.31 MMcf/psi $= 915$ MMcf would be recovered, or $49.1 - 0.915 = 48.185$ Bcf.

TABLE 10.2
Data and material balance calculations on gas reservoir S [Smith, 10-23]

Pressure P		Cumulative production		Z (105°F, 40.6°C)	P/Z	
psia	kPa	Bcf	m^3		psia	kPa
2150	14,824	0	0	0.802	2680	18,484
1885	12,997	6.9	0.195×10^9	0.813	2319	15,986
1620	11,170	14.0	0.396×10^9	0.825	1964	13,539
1205	8,308	23.7	0.671×10^9	0.862	1398	9,638
888	6,123	31.0	0.878×10^9	0.893	994	6,857
645	4,447	36.2	1.025×10^9	0.917	703	4,850
			Calculated values:			
14.7	101.325	48.9	1.385×10^9	1.000	14.7	101.325
0	0	49.1	1.390×10^9	1.000	0	0

10.4 VARIATIONS IN BEHAVIOR

The above example problem shows that successive production points with corresponding P/Z values plot on a straight line. This indicates that there is a constant volume container and the pressure is representative of the total gas body present. Water intrusion from the surrounding aquifer as the reservoir pressure drops will give the kind of behavior shown in Fig. 10-15. Should the pressure on the wells used not have risen to the full equalized pressures, then the lower curve indicated in Fig. 10-15 could occur. Since gas production rates decline in the later years of production, the later pressures generally come closer to the applicable straight line. The water-drive case, when extrapolated from early production

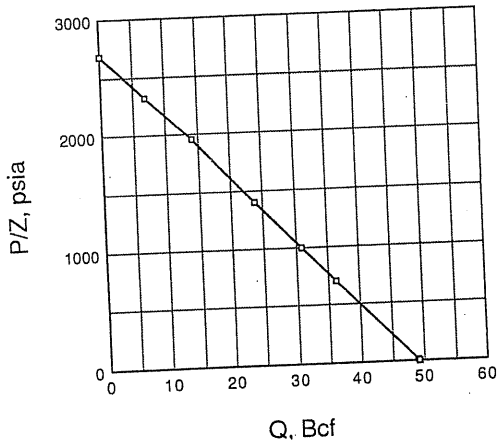

FIGURE 10-16
Example of P/Z plot for Field S [data of Smith, 10-23].

data, gives too high an initial gas in place, while the gas reservoir without full equalization in pressure gives too low a gas content. However, extrapolation of later years' production, when flow rate decreases, can give too high an ultimate reserve.

10.5 MECHANISM OF OIL RECOVERY FROM RESERVOIRS

The following mechanisms recover oil from underground porous rock: (1) water drive, (2) dissolved gas drive, (3) gas cap drive, and (4) gravity drainage. Various combinations of these mechanisms occur in specific reservoirs. The impetus for oil movement may be water pressure forcing oil to the wellbore, the expansion of gas either from the dissolved state or as free gas, or the force of gravity causing oil to run downhill. Figure 10-17 illustrates these mechanisms. Secondary recovery processes include water flooding, gas injection, and combinations thereof. Usually even enhanced oil recovery techniques [10-7] are planned early in the producing life of an oil reservoir. The initial fluid distribution in a reservoir is a basic consideration.

Water drive in contact with the oil expands under pressure reduction and moves into the oil zone in an unsteady process. The water may enter the oil zone so readily that oil production reduces the reservoir pressure very little, as in the Kansas Arbuckle Lime reservoirs. The East Texas oil field maintains an

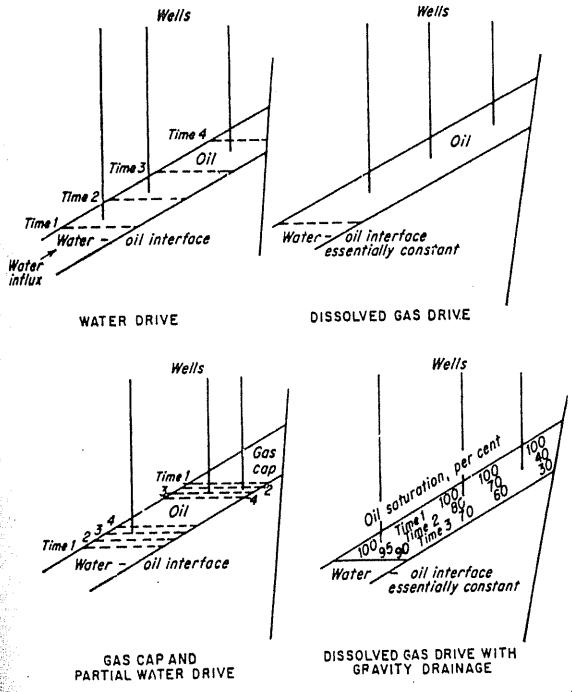

FIGURE 10-17
Primary mechanisms of oil recovery [Katz et al., 1-1, courtesy McGraw-Hill Publishing Co.].

intermediate reservoir pressure of 1000 psi (6.895 MPa), as compared to 1600 psi (11.03 MPa) initially, by control of oil and water production and of water return.

Gas production accompanying crude oil for a complete water drive field will be directly proportional to the oil production rate. Without any pressure reduction in the reservoir, no gas is evolved there and so only dissolved gas accompanies the produced crude oil. The pattern of oil production is that downstructure wells gradually go to water; eventually the oil recovery is so low that expenses are not met by oil production and the well is productive no longer. Criss and McCormick [10-4] have presented a case history for the Coldwater oil field, a water drive reservoir.

The dissolved gas drive reservoir is considered to have a constant pore volume. Oil is forced to the wellbore by gas evolving from solution in the crude oil as the pressure is lowered. The reservoir may or may not have an initial gas cap. The main deterrent to high oil recovery is the fact that because of the high relative permeability of rock to gas, once the liquid saturation is down to 70 or 80 percent, gas bypasses oil on the way to the wells. Reservoirs containing oil with 700 ft^3 per bbl (125 m^3/m^3) of dissolved gas may produce oil with gas-oil ratios of 3500 ft^3/bbl (623 m^3/m^3). In essence this means that four out of five barrels of oil furnishing the gas remain in the reservoir, because the gas from these four barrels helps to produce the single barrel of oil. It should be noted that all the gas dissolved in the oil is produced and that the initial oil content, not the oil production, is of interest when finding gas reserves.

Gravity segregation of oil takes place in varying degrees in gas drive reservoirs and must be considered [10-9]. Likewise, some water may encroach on the reservoir and reduce its volume.

Methods of estimating the original oil and gas content of a constant volume reservoir have been devised, using solubility and shrinkage data. Coleman, Wilde, and Moore [10-3] published a paper in 1930 on the quantitative effect of gas-oil ratio on decline in average rock pressure. In 1936, papers by Schilthuis [10-21] and Katz [10-8] gave alternative procedures for estimating the oil content of a gas drive reservoir. Schilthuis presented the calculations in equation form, now described as the *material balance equation*. Katz gave a tabulative procedure intended to give an understanding of the reservoir production mechanism. The material balance equation has proved advantageous for the utilization of mathematical calculations on reservoirs.

The material balance procedure presented by Katz [10-8] states that the initial crude oil is equal to the oil produced as of a given date, plus the oil that supplied the gas produced in excess of that initially dissolved in the produced crude oil, plus the oil that supplied the gas phase gas to maintain the reservoir pressure. The data required are (1) initial or saturation pressure for reservoir crude oil; (2) reservoir temperature; (3) oil production; (4) gas production; (5) reservoir pressure at end of oil and gas production; (6) solubility and shrinkage data; (7) gas-oil ratio of saturated crude oil at separator conditions; (8) information on any gas cap; and (9) water production from or water influx into the reservoir.

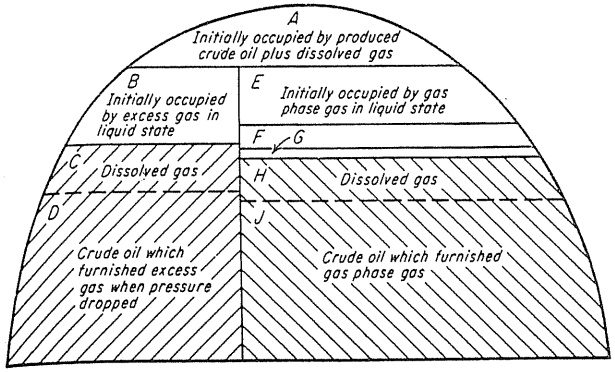

FIGURE 10-18
Graphical allocation of initial reservoir fluid [Katz, 10-8, courtesy SPE-AIME].

Figure 10-18 [1-1] illustrates the allocation of initial space in a reservoir containing saturated crude oil without water production or influx. The production process removes oil and gas from the reservoir. The space occupied by the produced crude oil plus its dissolved gas (space *A*) can be computed from the oil production and the formation volume factor or shrinkage. Gas that was produced in excess of that dissolved in the crude oil came from oil still in the reservoir. With the reservoir pressure known as of a given date in the producing life, the solubility curve gives the cubic feet of gas per barrel that have been evolved by each barrel in the reservoir. The excess gas and the rate of shrinkage per unit of evolved gas permit computation of the space voided (space *B*) when this gas vaporized from the crude oil and the quantity of crude oil (*D* and *C*) required to supply this gas.

Spaces *A* and *B* are filled with the gas phase by vaporization of crude oil still in the reservoir. Space *E* is voided when crude oil is vaporized to fill gas phase *A* and *B*. Space *F* is voided when space *E* is filled with gas from solution in the crude oil; space *G* is voided when *F* is filled, etc. To find the gas cap space without using a trial-and-error procedure, a solution to a converging series is employed. Spaces *H* and *J* contain the crude oil and dissolved gas that furnished the gas to fill the gas phase. The total initial crude oil as stock tank barrels equals the produced crude oil, the oil *D* that provided the excess gas, and the oil *J* that provided the gas phase gas.

An example of a material balance tabulation is given by Table 10.3 [10-9]. The reservoir was calculated to have an initial gas cap with 10.3 Bcf (60°F, 14.65 psia) of gas in it. The gas produced from the cap during a given pressure reduction is removed from the total production of gas to find the gas produced from the oil reservoir. The solubility and shrinkage data were taken from curves of Fig. 10-19. Table 10.3 gives the computations of the initial oil and gas content at seven annual intervals, assuming the reservoir volume is constant.

TABLE 10.3
Computation of initial oil content of Wilcox Pool, Oklahoma City [10-9, 1-1].

Calculations made from reservoir conditions at dates indicated

Item	Unit	1/1/33	1/1/34	1/1/35	1/1/36	1/1/37	1/1/38	1/1/39
1. Crude oil produced	MMbbl	69.8	119	166	212	255	301	333
2. Gas produced	Bcf	177	378	550	630	701	751	780
3. Bottom-hole pressure	psia	1,640	895	430	203	111	58	34.8
4. Gas dissolved in crude at bottom hole pressure	ft^3/bbl	487	308	198	132	94	57.5	32
5. Gas evolved initial condition to bottom hole pressure	ft^3/bbl	248	427	537	603	641	677.5	703
6. Shrinkage crude from bottom hole pressure to atmospheric	Percent	26.0	18.9	14.2	11.3	9.4	7.7	6.2
7. Shrinkage crude from initial pressure to bottom-hole pressure	Percent	10 1	17.2	21.9	24.8	26.7	28.4	29.9
8. Solution gas for produced crude	Bcf	51.3	87.5	122	156	188	222	245
9. Compressibility factor reservoir gas	Ratio	0.82	0.885	0.926	0.955	0.97	0.985	0.99
10. Gas from initial gas cap	Bcf	4.0	7.1	8.8	9.6	9.9	10.1	10.2
11. Excess gas produced	Bcf	121.7	283.4	419.2	464.4	503.1	518.9	524.8
12. Volume 1 Scf gas at reservoir conditions	ft^3	0.0083	0.0165	0.0359	0.0785	0.146	0.283	0.475
13. Volume produced oil and dissolved gas	MMcf	533	910	1,270	1,620	1,950	2,300	2,540
14. Initial volume excess gas in liquid state	ft^3/Scf	0.00228	0.00226	0.00229	0.00231	0.00234	0.00235	0.00238
15. Initial volume excess gas	MMcf	277	640	961	1,072	1,178	1,219	1,249
16. Reservoir volume total production oil and gas	MMcf	810	1,550	2,231	2,692	3,128	3,519	3,789
17. $a = 16/12$	Bcf	97.6	94.0	62.1	34.3	21.4	12.4	8.0
18. $1/b = 14/12$	Ratio	0.275	0.137	0.064	0.029	0.016	0.008	0.005
19. $a/(1 - 1/b)$ = gas cap gas	Bcf	135	109	66	35.4	21.7	12.5	8.0
20. Crude for gas cap gas	MMbbl	544	255	123	59	34	13	11
21. Crude for excess gas	MMbbl	490	664	781	770	785	766	747
22. Total initial crude	MMbbl	1,104	1,038	1,070	1,041	1,074	1,085	1,091
23. Total initial fluid	MMbbl	1,503	1,411	1,457	1,419	1,462	1,478	1,487

Solubility at 2686 psia: 735 ft^3/bbl residual oil. Shrinkage: 36.1 percent. Reservoir temperature: 132°F. Average initial residual oil: 1072 MMbbl. Reservoir fluid: 1460 MMbbl.

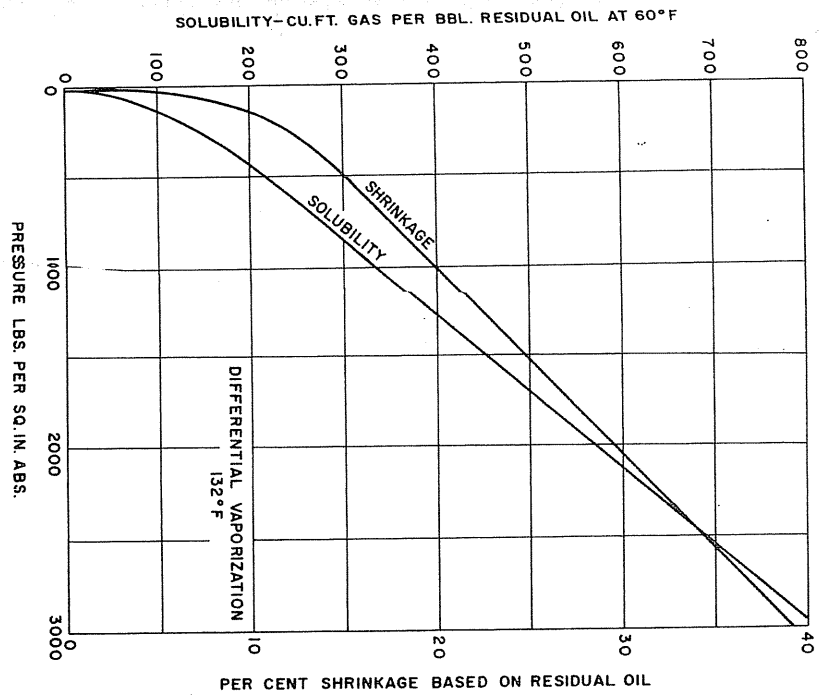

FIGURE 10-19
Solubility and shrinkage curves for Oklahoma City crude oil [Katz, 10-9, courtesy SPE-AIME].

Items 1 to 7 are given or are obvious. Item 8 is the product of crude oil production and 735 ft^3/bbl as solution gas, found either by differential vaporization at 132°F or by flash vaporization in separators. Item 9 is taken from Fig. 10-20, which gives compressibility factors calculated from gas compositions. Item 10 is the initial gas cap gas that left the reservoir as the pressure dropped to the pressure of item 3. Item 11 equals item 2 minus the sum of items 8 and 10. Item 13 equals item 1 times 5.61 and times 1.361. Item 14 equals item 7 divided by item 5 and multiplied by 5.61. Item 15 is item 11 times item 14. Item 16 equals items 13 plus 15. The computation of the quantity of gas in the gas phase or in the developed gas cap where the evolution of gas creates more space uses the expression for a converging series, item 19. The values a and b in the expression for the gas cap gas (A, B, E, F, G, etc., Fig. 10-18) are given by items 17 and 18. Item 20 is item 19 divided by item 5. Item 21 is item 11 divided by item 5. The calculated average quantity of initial residual crude oil is 1072 MMbbl.

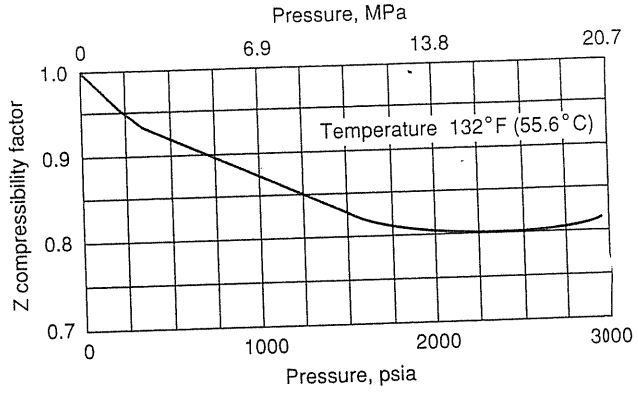

FIGURE 10-20
Compressibility factors for Oklahoma City reservoir gas [Katz, 10-9, courtesy SPE-AIME].

The initial gas reserve is 1072 MMbbl × 735 ft³/bbl or 789 Bcf plus 10 Bcf in the initial gas cap, or 799 Bcf. By 1939, the Oklahoma City Wilcox reservoir had produced 780 Bcf of gas, and the pressure was approaching atmospheric. By January 1, 1957, it had produced 563 MMbbl of crude oil, or 52.4 percent of its initial content, and was still producing at the rate of 6500 bbl/day. The production of water or the intrusion of water into the reservoir accounts for changes in the gas phase volume in the above procedure.

The material balance equation of Schilthuis [10-21] may be derived on the basis of a gas balance as follows [1-1,10-5,10-21], using the nomenclature of Table 10.4.

Original gas = produced gas + gas in solution + gas phase gas

TABLE 10.4
Nomenclature for material balance equation [Katz et al., 1-1]

N	Initial oil content of reservoir, stock tank barrels
ΔN	Accumulative oil production at given time, stock tank barrels
g	Original gas content of reservoir in gas phase, Scf
R	Gas-oil ratio, Scf/bbl
R_s	Gas-oil ratio for saturated crude oil, Scf/bbl
S_0	Solubility of gas at initial pressure and reservoir temperature, Scf/bbl
S	Solubility of gas at any pressure, Scf/bbl
v	Formation volume, ft³/Scf; subscript 0 for initial conditions
B	Formation volume factor for crude oil, bbl liquid in reservoir per bbl stock tank oil; subscript 0 for initial conditions
m	Ratio of initial gas cap pore volume to initial oil phase pore volume
w	Accumulative water production, ft³
W	Accumulative water influx into reservoir, ft³

$$NS_0 = R\Delta N + (N - \Delta N)S + \frac{[NB_0 - (N - \Delta N)B](5.61)}{v} \quad (10.4)$$

Multiplying through by v and regrouping terms,

$$N = \Delta N \frac{5.61B + v(R - S)}{5.61B + v(S_0 - S) - 5.61B_0} \quad (10.5)$$

This equation applies for constant volume reservoirs without water intrusion or water production, and without an initial gas cap. When these two items are included in a consideration of the material balance for natural gas and rearranged as before, the result is

$$N = \frac{\Delta N[5.61B + v(R - S)] - g(v_0 - v) + w - W}{5.61B + v(S_0 - S) - 5.61B_0} \quad (10.6)$$

An alternative equation may be appropriate when the initial gas cap volume is known relative to the oil volume:

$$N = \frac{\Delta N[B + v(R + S)] + w - W}{B + v(S_0 - S) - B_0 + mB_0(v - v_0)/v_0} \quad (10.7)$$

where m = (gas cap volume)/(oil volume).

Table 10.5 gives the solution to Eq. (10.6) for the data of Table 10.3 and the dates 1/1/33 and 1/1/37. The answers found equal those of Table 10.3. The numerical manipulations appear to be equivalent. The procedure of Table 10.3 gives some sense of the physical phenomena occurring in the reservoir and may be preferred in teaching for acquainting students with the concepts of reservoir behavior. The equation has the advantage that it can be combined with other equations for reservoir calculations. The material balance on the gas gives a simpler equation than would result if the material balance on crude oil used in Table 10.3 were reformulated in equation form.

Both of these procedures assume that crude oil and gas are distinct substances, although the method of separation may cause greater or lesser quantities of gas to be evolved. The proportion of gas evolved from saturated crude oil by differential vaporization at the reservoir temperature may not be equal to the gas-oil ratio in a flash separation at the wellhead. Therefore, the solubility S_0 may not equal the gas-oil ratio R_0, and different values may be used in the procedures given.

The initial reservoir pressure may be well above the saturation pressure of the crude oil. In this case, time zero is taken to be the moment at which the saturation pressure is reached. Estimates of oil in place may be made from fluid compressibilities in the period of production before the saturation pressure is reached. Normally reservoir crude oils are rather uniform, but examples of variation in reservoir oils have been noted when the reservoir was extensive or had high relief.

TABLE 10.5
Solution to material balance equation [Katz et al., 1-1]

Item	Symbol	Unit	Data as of Jan. 1, 1933	Data as of Jan. 1, 1937	Initial condition
1. Crude oil produced	ΔN	MMbbl	69.8	255	
2. Gas produced	$R\Delta N$	Std Bcf	177	701	
3. Gas-oil ratio	R	Scf/bbl	2540	2750	735
4. Reservoir pressure	P	psia	1640	111	2686
5. Formation volume factor	B	—	1.26	1.094	1.361
6. Solubility of gas	S	Scf/bbl	487	94	735
7. Compressibility factor of reservoir gas	Z	—	0.82	0.97	0.802
8. Reservoir volume of 1 Scf of gas in gas phase	v	ft^3/Scf	0.0083	0.146	0.00498
9. Gas in initial gas cap	g	Std Bcf	—	—	10.3
10. $R - S$	—	Scf/bbl	2053	2656	
11. $v(R - S)$	—	ft^3/bbl	17.02	387.5	
12. $5.61B + v(R - S)$	—	ft^3/bbl	24.10	393.6	
13. $\Delta N[5.61B + v(R - S)]$	—	MMcf	1682	100,300	
14. $v - v_0$	—	ft^3/Scf	0.00332	0.141	
15. $g(v - v_0)$	—	MMcf	34.2	1450	
16. Item 13 − item 15	—	MMcf	1648	98,850	
17. $S_0 - S$	—	Scf/bbl	248	641	
18. $v(S_0 - S)$	—	ft^3/bbl	2.06	93.6	
19. $5.61B + v(S_0 - S) - 5.61B_0$	—	ft^3/bbl	1.49	92.1	
20. Item 16 ÷ item 19	N	MMbbl	1105	1071	
21. Initial gas content	—	Std Bcf	864	789	

Woods and Muskat [10-25] present an analysis of material balance calculations when water is entering the reservoir in a partial maintenance process in unsteady state. The water influx may be evaluated from unsteady state formulas in conjunction with the material balance equation to give the most reliable estimate of the initial oil in place.

A typical production history for a gas drive field produced by pressure depletion is a gradual rise in the gas-oil ratio for a period, followed by a rapid rise when the gas phase in the reservoir has reached sufficient saturation to give the gas a high relative permeability. By using a relative permeability curve and material balance calculations, the future production history can be projected. Simple calculations in small increments of production will show how the gas-oil ratio rises as the percentage of gas phase in the reservoir increases. Such calculations neglect any effects of gravity on the segregation of oil and gas. Muskat and Taylor [10-17] presented generalized solutions for the depletion of gas-drive reservoirs, giving gas-oil ratio and pressure histories for selected conditions.

Conservation practices and the demands of economics have led to better procedures for producing gas drive reservoirs than allowing them to "blow down" in the fashion described up to this point. Gas repressuring, selective production

of oil from wells of low gas-oil rates, and water injection are some of the methods that were used for increasing recovery before enhanced recovery methods evolved.

Gravity drainage. The segregation of oil and gas systems into an oil layer and a gas cap is evidence that gravity had an important role in the accumulation process. That wells on the top of a structure in oil fields have high gas-oil ratios and that downstructure wells have lower ratios is an indication of the effects of gravity on producing operations. High permeability, high relief, low oil viscosity, and low surface tension of crude oils contribute to the movement of oil by gravity; in thin flat formations with horizontal layers of impervious material, on the other hand, there may be no gravity effects. In such reservoirs as the Oklahoma City Wilcox sand [10-9], gravity reduced the saturation of oil in the upper hundred feet of sand to 7 to 12 percent of the pore space, with sand of 400 to 600 md permeability. One well drilled downstructure after the reservoir was at atmospheric pressure pumped 900 bbl (143 m^3) of oil per day for a period of months. An oil recovery of about 33 percent had occurred by the time the reservoir reached atmospheric pressure (wellhead) and 20 percent more had been recovered by 1956.

10.6 OIL RECOVERY PREDICTIONS

Oil recovery predictions will be discussed as a prelude to the use of simulation for oil. In established oil production fields in a decline mode, without new secondary or tertiary procedures being inaugurated, the recovery may be estimated by plotting log oil production versus time and extrapolating to the economic limit.

In the oil industry, plotting *productivity index*, PI $= Q/(\bar{P} - P$ (well)) versus Q shows a trend of productivity declining. Extrapolating the PI plot, one may predict the oil recovery. Logan extended the PI concept to gas wells by plotting PI (gas) $= Q/(\bar{P}^2 - P^2$ (well)) [8-34].

Gas/Condensate Reservoirs

The phase diagrams of Fig. 10-1 showed that some reservoirs occur at temperatures above the critical temperature of the composite reservoir fluid. Phase behavior studies and early experiences showed that the greatest harvest of the condensate required a displacement process to prevent retrograde condensation in the reservoir. For most fluids the volume percent of hydrocarbon liquid formed by condensation is insufficient for production of the liquid phase. In the 1940s a cycling process (earlier called recycling) was utilized to recover a higher yield of condensate than depletion (Fig. 10-21).

The elements required for a cycling project are unitization of ownership, a pattern of wells to permit effective gas withdrawal, and injection of dry gas to minimize mixing of rich and dry gas. High-permeability layers in the formation can be detrimental to displacement efficiencies, since dry injected gas can reach producing wells ahead of the general interface for most reservoirs. Considerable

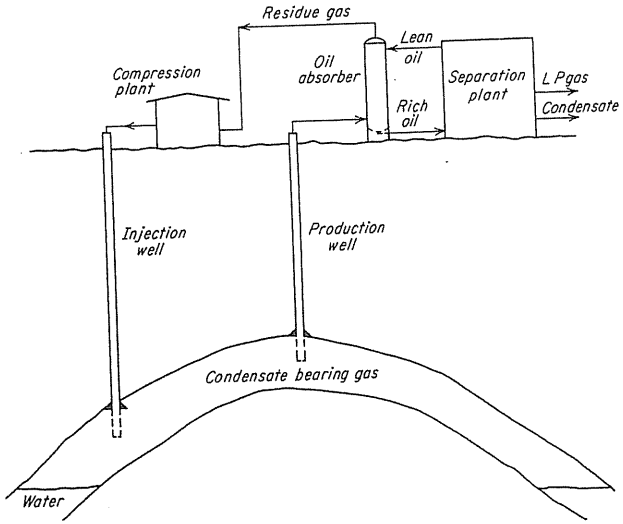

FIGURE 10-21
Flow diagram for cycling operation [Katz et al., 1-1, courtesy McGraw-Hill Publishing Co.].

variation occurs in the permeability of the various layers or strata. Should the producing formation contain several layers of different permeabilities, the more permeable zone would sweep first. It is desirable to isolate into separate zones as far as possible all strata of different permeabilities. Methods have been presented of predicting the overall sweep results for reservoirs with variable permeability. Standing, Lindblad, and Parsons [10-24] have presented a chart showing the effect of permeability variation on the ratio of dry gas to wet gas in the production from wells (Fig. 10-22). Permeability variation is defined as the ratio of (1) the difference between the median permeability and the permeability above which 84.1 percent of the values lie to (2) the median permeability. Permeabilities are plotted on logarithmic probability paper as permeability over maximum permeability versus "percent larger than" (Fig. 10-23). The median permeability is read at the 50 percent line. Muskat has developed charts for predicting sweep for various permeability distributions [10-16].

Processing Condensate Well Fluids

Cycling plants normally operate on fields with reservoirs having pressures enough in excess of 2000 psi (13.8 MPa) that the gas-liquid mixtures may be delivered to the plant at around this pressure. The primary separation normally takes place at pressures from 1000 to 2000 psi (6.89–13.8 MPa), to allow recompression of the residue gas without undue horsepower requirements. Oil absorption is the common recovery process. Since high-boiling hydrocarbons are involved, cycling plants [10-18] often make their absorption oil from the condensate produced. Cycling

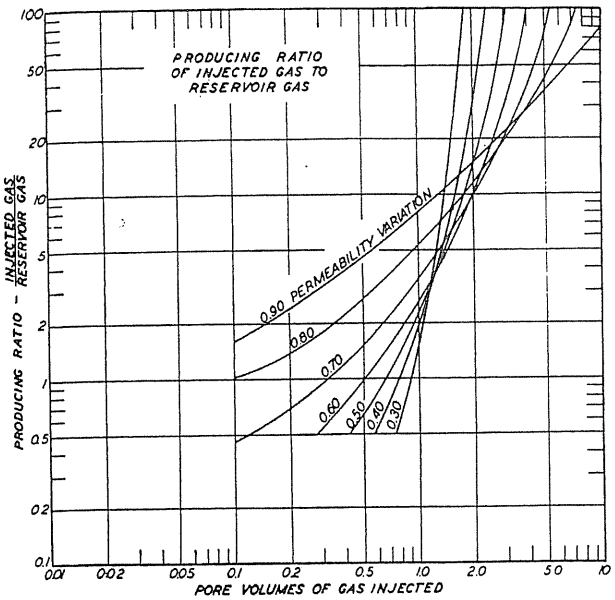

FIGURE 10-22
Effect of permeability variation on producing ratio of injected to reservoir gas [Standing, Lindblad & Parsons, 10-24, courtesy SPE-AIME].

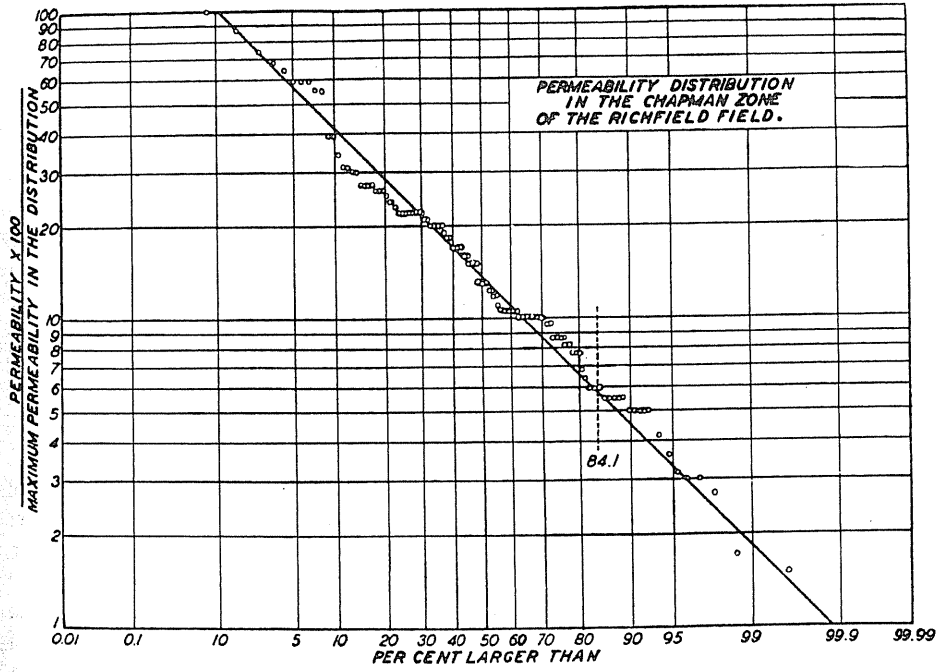

FIGURE 10-23

plants stabilize condensate by blending with butane, propane, and sometimes a natural gasoline.

Vapor-Liquid Equilibria Applied to Reservoirs

When the first set of equilibrium constants for crude oil/natural gas systems was measured in 1934 [4-37], gas cap gas compositions were predicted from reservoir fluid analysis by a bubble point calculation. By a series of flash calculations, the depletion phase compositions could be predicted as an approximation to the differential process. Such calculations by K charts and hand calculators were laborious.

The employment of an equation of state along with fast machine computations made possible more elaborate phase behavior calculations. Reference [1-25] set forth a series of articles representing the progress in this direction, and an overview paper described the status [4-35]. At the time of this writing, SPE is preparing a phase behavior monograph (1988).

For the senior author, a series of works has produced a depletion program appropriate for gas/condensate reservoirs, starting with the study of retrograde condensation in natural gas pipelines [1-35]. The introduction of extended gas analyses, the adoption of the Peng-Robinson equation of state, and the use of interaction parameters between methane and the C_{6+} constituents made possible the prediction of the behavior of the gas/condensate system at reservoir pressures.

For crude oils, the presence of asphalt has made it necessary to calibrate its interaction coefficient [4-36] by one experimental bubble point for a given system.

Laboratory Tests on Condensate Well Fluid

The behavior of a condensate well effluent may be determined in the laboratory [10-20]. Table 10.6 gives analyses of the effluent samples taken in a well test (No.7) set up like Fig. 1-2*b*. The extended analysis method is needed here. A sample of the recombined well stream is subjected to *P-V-T* measurements and to differential depletion of gas at the reservoir temperature, as in Fig. 10-3. Table 10.7 gives the gas compositions. Table 10.8 gives the *P-V-T* data, dew point, and retrograde liquid volumes. Figure 10-24 is a plot of the retrograde liquid volume. Tests like these give the reservoir behavior and serve as a basis for verifying the equation-of-state phase calculation.

The well No. 7 test gives 4697 ft^3/bbl condensate, or 212.9 bbl/MMcf (1195 m^3/MMm^3), and a gravity of 46.5° API. The reservoir fluid is approaching the critical temperature. From Fig. 10-4 and early studies, there are indications that the gas-oil ratio of 3000/5000 ft^3/bbl (543/891 m^3/m^3) was among the richest possible mixtures, giving 200 to 330 bbl/MMcf (1123–1853 m^3/MMm^3). Many reservoirs' fluids yield from 25–100 bbl/MMcf (140–561 m^3/MMm^3) of gas.

TABLE 10.6
Field data and analyses for condensate well No. 7 [courtesy Core Lab. Inc.].
Original reservoir pressure at 11,300 ft, 7000 psig.
Reservoir Temperature 256°F (398 K).
At sampling B. H. pressure 1505 psig (10.4 MPa), tubing rd. 780 psig (5.5 MPa).
Separator liquid 185 bbl/day (46.5° API).
Separator gas primary 869 Mcf/day (gr. 0.699).
Gas-liquid ratio 4697 Scf/bbl, 212.9 bbls/MMcf.

Component	Separator liquid, mol percent	Separator gas		Well stream	
		Mol percent	GPM	Mol percent	GPM
Hydrogen sulfide	0.00	0.00		0.00	
Carbon dioxide	0.00	0.01		0.01	
Nitrogen	0.01	0.13		0.11	
Methane	10.76	83.01		68.93	
Ethane	6.17	9.23	2.454	8.63	2.295
Propane	8.81–	4.50	1.231	5.34	1.461
Isobutane	2.85	0.74	0.241	1.15	0.374
n-Butane	7.02	1.20	0.376	2.33	0.730
Isopentane	3.47	0.31	0.113	0.93	0.338
n-Pentane	3.31	0.25	0.090	0.85	0.306
Hexanes	8.03	0.21	0.085	1.73	0.702
Heptanes plus	49.57	0.41	0.185	9.99	6.006
	100.00	100.00	4.775	100.00	12.212
Properties of heptane plus					
API gravity at 60°F	39.0				
Density, g/cm^3 at 60°F	0.8293			0.827	
Molecular weight	160	103		158	

Calculated separator gas gravity = 0.699
Calculated gross heating value for separator gas = 1230 Btu per cubic foot of dry gas at 14.65 psia and 60°F.

Primary separator gas collected at 440 psig and 87°F.
Primary separator liquid collected at 440 psig and 87°F.

Primary separator gas/separator liquid ratio = 3944 Scf/bbl at 60°F.
Primary separator liquid/stock tank liquid ratio = 1.191 bbls at 60°F/bbl
Primary separator gas/well stream ratio = 805.19 Mcf/MMcf.
Stock tank liquid/well stream ratio = 171.4 bbl/MMcf.

Recovery of Precipitated Gas Condensate

In 1952, Katz [10-10] suggested that high-pressure gas could be used to vaporize crude oil and then be displaced by cycling as a gas phase. The phase behavior and economics were not attractive to industry and no operations resulted. However, when gas/condensate fields that had been produced by depletion were recharged with gas in a storage operation, condensate was revaporized and recovered.

Firoozabadi, Hekim, and Katz [10-6] had devised a depletion program for computing the retrograde condensate deposited in the reservoir in depletion

TABLE 10.7
Depletion study at 256° F (398 K) reservoir temperature, well No. 7 [courtesy Core Lab. Inc.].
Hydrocarbon analyses of produced well stress, mole percent

	Reservoir pressure, psig							
Component	**6010**	**5000**	**4000**	**3000**	**2100**	**1200**	**700**	**700***
Carbon dioxide	0.01	0.01	0.01	0.01	0.01	0.01	0.01	Trace
Nitrogen	0.11	0.12	0.12	0.13	0.13	0.12	0.11	0.01
Methane	68.93	70.69	73.60	76.60	77.77	77.04	75.13	11.95
Ethane	8.63	8.67	8.72	8.82	8.96	9.37	9.82	4.10
Propane	5.34	5.26	5.20	5.16	5.16	5.44	5.90	4.80
Isobutane	1.15	1.10	1.05	1.01	1.01	1.10	1.26	1.57
n-Butane	2.33	2.21	2.09	1.99	1.98	2.15	2.45	3.75
Isopentane	0.93	0.86	0.78	0.73	0.72	0.77	0.87	2.15
n-Pentane	0.85	0.76	0.70	0.65	0.63	0.68	0.78	2.15
Hexanes	1.73	1.48	1.25	1.08	1.01	1.07	1.25	6.50
Heptanes plus	9.99	8.84	6.48	3.82	2.62	2.25	2.42	63.02
	100.00	100.00	100.00	100.00	100.00	100.00	100.00	100.00
Molecular weight of heptanes plus	158	146	134	123	115	110	109	174
Density of heptanes plus	0.827	0.817	0.805	0.794	0.784	0.779	0.778	0.837
Deviation factor *Z*								
Equilibrium gas	1.140	1.015	0.897	0.853	0.865	0.902	0.938	
Two-phase	1.140	1.016	0.921	0.851	0.799	0.722	0.612	
Well stream produced, cumulative percent of initial	0.000	6.624	17.478	32.927	49.901	68.146	77.902	

* Composition of equilibrium liquid phase.

TABLE 10.8
Volumetric and retrograde liquid measurements on condensate well fluid, well No. 7 [courtesy Core Lab. Inc.].

Pressure, psig	Relative volume	Retrograde liquid volume, percent of pore space
7500	0.9341	
7000 (reservoir pressure)	0.9523*	
6500	0.9727	
6300	0.9834	
6200	0.9891	
6100	0.9942	
6010 (dew point pressure)	1.0000†	0.0
5950	1.0034	Trace
5900	1.0076	0.1
5800	1.0138	0.2
5600	1.0267	0.5
5300	1.0481	2.0
5000 (first depletion level)	1.0749	7.8
4500	1.1268	—
4000	1.2024	21.3
3500	1.3096	—
3000	1.4689	25.0
2500	1.7169	—
2100	2.0191	24.4
1860	2.2747	—
1683	2.5150	—
1460	2.9087	—
1290	3.3173	—
1200	—	22.5
1160	3.7153	—
1050	4.1342	—
700	—	21.0
0	—	17.6

* Gas expansion factor = 1.545 Mcf/bbl.
† Gas expansion factor = 1.471 Mcf/bbl.

mode. This program was employed in studying gas storage operations and predicting ensuing yields of condensate. The paper describing the results is reproduced here. The equilibrium constants were those described in reference [4-36]. This program was based on the results of previous research [1-35]. The algorithm is illustrated in [10-6] and the applications of the Peng-Robinson equation are in Appendix D.

The need for good well samples for analysis is very important, including an extended gas analysis. The gas and condensate from a producing gas/condensate well at initial reservoir conditions are normally collected at measured rates. The samples are recombined for reservoir fluid *P-V-T* behavior and the gas and liquid

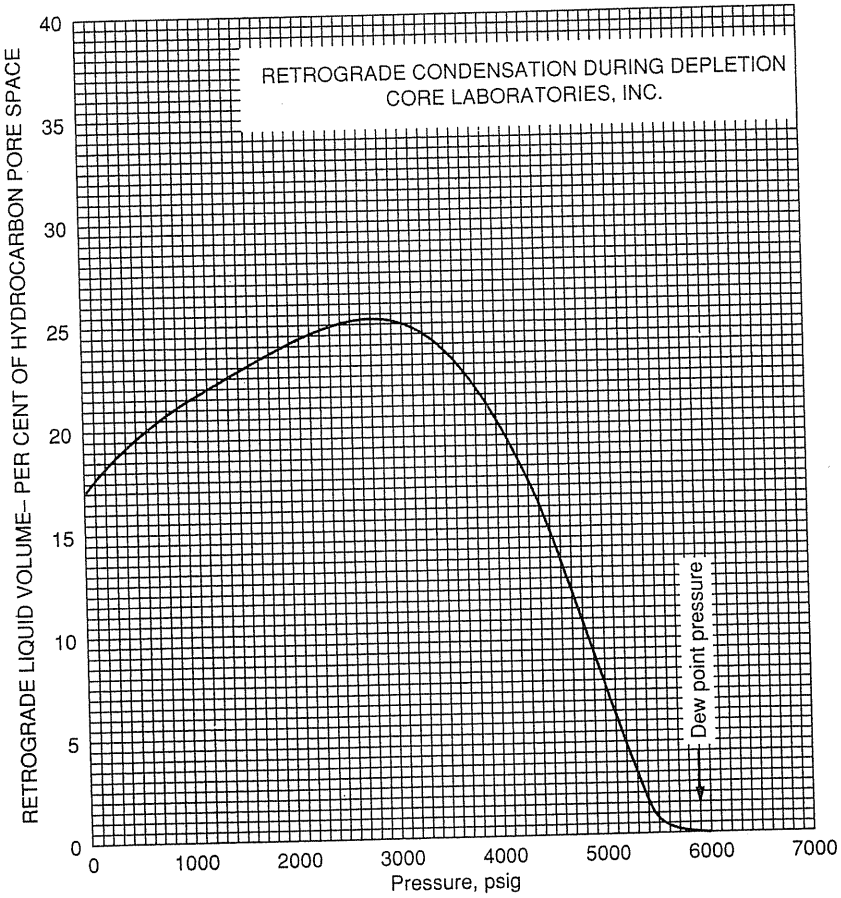

FIGURE 10-24
Retrograde condensation during depletion, reservoir condensate No. 7 [courtesy Core lab. Inc.].

compositions are recombined to give a composite well stream analysis. In case the separator liquid only has a C_{7+} last fraction, as in Fig. 1-2*b*, with molecular weight and specific gravity, it is necessary to expand the C_{7+} fraction into the higher-boiling constituents. Katz [4-35] prepared an empirical chart for this purpose based on six analyses, (Fig. 10-25).

Many samples with analyses have been studied by Eilerts [10-5] and by Allen [10-1] as well as earlier reports [1-1]. Coats [10-2] studied the simulation of condensate reservoirs. Data on a rich condensate well test have been provided with the well stream analysis and phase behavior study [10-20]. They are presented here in our abridged edition.

In making material balances on constant volume gas condensate reservoirs (P/Z versus gas production), the question may arise as to which Z should be used. A study of the above data will reveal that the two-phase Z should be used.

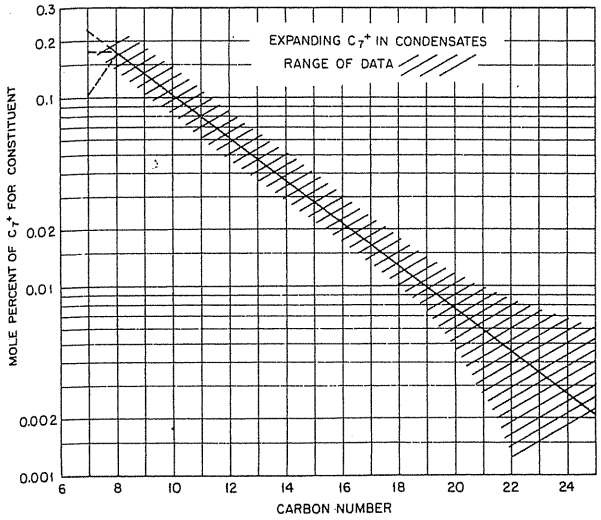

FIGURE 10-25
Method of expanding C_{7+} fraction of condensates [Katz, 4-35, courtesy SPE-AIME].

When rich condensate reservoirs at pressures above the dew point are produced by depletion, a P/Z curve may start off in the normal mode, with well flow capacities like gas wells. However, as the two-phase status is reached rather precipitously, the reduced well flow rates and the high liquid saturations may baffle the operator.

10.7 PREDICTING YIELD OF REVAPORIZED CONDENSATE IN GAS STORAGE

Phase behavior calculations for gas/condensate systems were used to predict depletion yields of condensates. The same procedures may be used for predicting revaporization and depletion yields of condensates in gas storage cycles. Data on two Niagaran reef storage reservoirs in Michigan show yields less than ideal for complete mixing and revaporization in the reservoir.

Phase Calculations for Gas/Condensate Reservoirs

Depletion of gas/condensate reservoirs of fixed volume is accompanied by retrograde condensation of liquid in the reservoir. Calculations of phase behavior during primary production are needed to verify the surface yield of condensate and to obtain the composition and quantity of retrograde liquid in the reservoir. The depletion program used for studying Michigan Silurian reef fields for con-

version to storage is that of Firoozabadi et al. [10-6] based on the Peng-Robinson equation of state [10-19] and interaction parameters for methane and the C_{6+} constituents [10-12].

A first step in these phase behavior calculations is to obtain a recombined separator gas and liquid well stream analysis at an early date in the life of the reservoir along with the reservoir temperature and pressure. The extended analysis basic to these calculations should include constituents with boiling points as high as C_{13} to C_{20} groups [1-35,4-35]. Figure 10-25 [4-35] and Example 10.4 show how to obtain extended analyses for C_{7+} components. Knowledge of gas and condensate production versus reservoir pressures is needed for material balance of yields and determination of reservoir size.

Example 10.4. A condensate well fluid has the composition shown below. The data end at C_{7+}. How does one expand the (C_{7+}) to smaller fractions (C_7–C_{22+})? The extended analysis allows a more accurate prediction of fluid behavior.

CO_2	0.0053
N_2	0.0195
C_1	0.5176
C_2	0.1536
C_3	0.1060
i-C_4	0.0155
n-C_4	0.0444
i-C_5	0.0091
n-C_5	0.0167
C_6	0.0202
C_{7+}	0.0921

First, one could obtain the mole fraction of the heavier constituents in the pseudocomponent C_{7+} from Fig. 10-25 or the following correlated equation:

$$y(C_i) = e^{0.342-0.26i} \tag{10.8}$$

The results are shown in column (2) of Table 10.9. By multiplying these numbers by the mole fraction of C_{7+} (0.092); the mole fractions can be obtained to C_{21}. The residue is lumped into the final pseudocomponent C_{22+} and the total mole percent from C_7 to C_{22+} remains 0.092.

Figure 10-26 for Cold Springs 12 and Fig. 10-27 for the Rapid River 35 reservoir show a comparison of primary yields of condensate with calculated yields. The agreement verifies that the phase relationships, compositions of well fluids, and depletion balances used are reliable for gas storage vaporization and depletion calculations. The calculated compositions of the reservoir gas and retrograde liquid (some 3 to 4 percent by volume of pore space) are needed in gas storage calculations.

With pressures above discovery in gas storage, reservoirs may deliver 80 to 100 percent of the primary content in a 100-day withdrawal period. When condensate is present in the reservoir because of retrograde condensation, it is

TABLE 10.9
Illustration of extended analysis

Component (1)	Fraction in C_{7+} from Eq. (10.8) or Fig. 10-25 (2)	Extended mole fraction (3) = (2) × 0.092	(4) = Σ(3)	Experimental data (5)
C_7	0.2026*	0.01864	0.01864	0.0184
C_8	0.1759	0.01618	0.03482	0.0143
C_9	0.1356	0.01248	0.04730	0.0110
C_{10}	0.1046	0.00962	0.05692	0.00866
C_{11}	0.0810	0.00745	0.06437	0.00690
C_{12}	0.0620	0.00570	0.07007	0.00552
C_{13}	0.0480	0.00442	0.07449	0.00428
C_{14}	0.0370	0.00340	0.07789	0.00340
C_{15}	0.0290	0.00267	0.08056	0.00265
C_{16}	0.0220	0.00202	0.08258	0.00212
C_{17}	0.0170	0.00156	0.08414	0.00166
C_{18}	0.0130	0.00120	0.08534	0.00138
C_{19}	0.0100	0.00092	0.08626	0.00110
C_{20}	0.0078	0.00072	0.08698	0.00065
C_{21}	0.0060	0.00055	0.08753	0.00105
C_{22+}	0.0485	0.00446	0.09200	

* $y(C_7) = \exp[0.342 - 0.26(7)] = 0.2026$

produced by vaporizing it with gas pressure, followed by depletion or displacement.

Modes of Operation

There are several modes of operation for injecting and withdrawing gas, three of which are discussed here. Mode 1 is to inject into all wells and withdraw gas from all wells. One might assume a completely mixed fluid of dry gas, reservoir gas, and reservoir liquid. In the initial withdrawal, the gas will be leaner than calculated because the condensate near the wellbore will have been stripped before full pressurization. Mode 2 uses gas injection on one end of a reservoir to sweep through the reservoir as it pressurizes the space and differentially vaporizes the condensate. Then the first withdrawal of gas would start at the end without gas injection, giving a higher yield of liquid than mode 1. The gas from the injection end when the wells are needed for deliverability would have lower yields. It is possible to reach an equilibrium dew point before reaching the full reservoir pressure by using pressure above discovery. Then the added gas can be introduced where desired to give the option of withdrawing for peaking dry gas that does not require processing to make it of pipeline quality; this is mode 3.

Well positions and completion depths along with geologic variations in permeability thwart attempts for ideal behavior of gas contacting the condensate wetting the rock, reducing yields and preventing ideal recoveries.

Recovery of Condensate

Retrograde condensate and residual crude oil in secondary gas caps of non–water drive oil fields defy recovery except by vaporization. The use of circulating low-pressure gases to recover natural gasoline has been practiced for a long time. The use of high-pressure gas to recover heavier hydrocarbons generally will have insufficient economic incentives until this miscible oil recovery process can be coupled with a gas storage project.

Examination of the data on the Cold Springs 12 and Rapid River 35 reservoirs (Table 10.9 and Figs. 10-26, 10-27) shows considerable condensate recovery, but far short of the yields calculated assuming equalized mixing. The decreases in yield in successive years is in general accord with repetitive retrograde processes. However, the injected gas is contacting only a portion of the reservoir rock. Normally, gas storage wells are drilled to obtain deliverability with minimum interference in flow. For condensate recovery, the spatial relationship could be designed for more effective sweep by using mode 2.

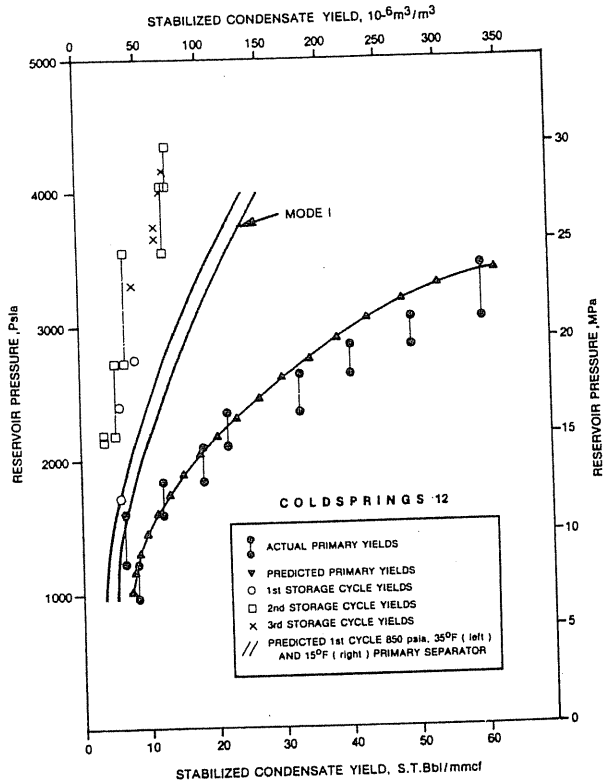

FIGURE 10-26
Yields of condensate in primary and gas storage for Cold Springs 12 [Katz et al., 10-15, courtesy SPE-AIME].

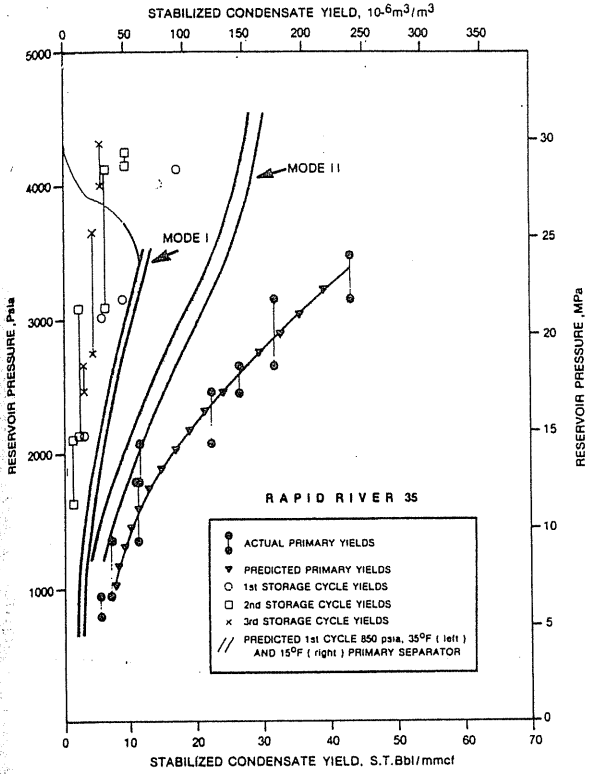

FIGURE 10-27
Yields of condensate in primary and gas storage for Rapid River 35 [Katz et al., 10-15, courtesy SPE-AIME].

The amount of condensate recovered in three years of storage operation is 35 to 57 percent of the amount of primary production. Native compositions of reservoir fluids in the two Michigan Reef reservoirs are given in Table 10.10.

10.8 SUMMARY

After carefully sampling the fluid from the separators (Fig. 1-2), phase behavior analyses have to be performed. A constant volume experimental calculation (Figs. 10-2, 10-3) gives the solubility and shrinkage formation volume factor. Then a computational model based on an equation of state can be set up, which should result in phase behavior similar to experimental data. Finally, an optimal operation model is chosen to keep the gas-oil ratio down—in other words, to minimize fluid volume in the reservoir, with gas dissolved in oil as much as possible.

The mechanisms of oil recovery as well as material balances give a physical feeling of the volumetric behavior of reservoirs. The Schilthuis (oil) and Katz (gas)

TABLE 10.10
Data on Michigan Reef storage reservoirs [Katz et al., 10-15, courtesy SPE-AIME]

	Cold Springs 12		Rapid River 35	
Primary production				
Discovery pressure, psia (MPa)	3,453	(23.8)	3,485	(24.0)
Reservoir temperature, °F(°C)	114	(45.6)	118	(47.8)
Depth, ft (m)	6,675	(2,035)	6,704	(2,043)
Pay thickness, ft (m)	313	(95)	374	(114)
Primary gas content, Bcf (10^9 m ^{3})	26.28	(0.744)	15.58	(0.441)
Pressure at conversion, psia (MPa)	930	(6.4)	370	(2.5)
Gas production (dry), Bcf (10^9 m^3)	18.87	(0.534)	13.50	(0.382)
Condensate production, STB (m^3)	427,000	(87,890)	255,000	(40,540)
Initial condensate yield, bbl/MMcf (10^6 m^3/m^3)	60.0	(337)	44.0	(247)
Gas gravity	0.74		0.87	
Storage operation design				
Maximum pressure, psia (MPa)	4,642	(32.0)	4,649	(32.0)
Base pressure, psia (MPa)	600	(4.1)	600	(4.1)
Working storage, Bcf (10^9 m^3)	23.6	(0.668)	14.7	(0.416)
First storage cycle, 1980–81				
Maximum pressure, psia (MPa)	4,026	(27.7)	4,555	(31.4)
Gas injected, Bcf (10^9 m^3)	19.92	(0.564)	15.70	(0.444)
Gas withdrawn, Bcf (10^9 m^3)	14.22	(0.402)	7.84	(0.222)
Condensate produced, bbl (m^3)*	78,557	(12,493)	38,121	(6060)
Second storage cycle, 1981–82				
Maximum pressure, psia (MPa)	4,345	(30)	4,240	(29.3)
Gas withdrawn, Bcf (10^9 m^3)	12.16	(0.344)	11.21	(0.317)
Condensate produced, bbl (m^3)*	120,799	(19,209)	39,011	(6202)
Third storage cycle, 1982 to Feb. 3, 1983				
Maximum pressure, psia (MPa)	4,200	(29.0)	4,325	(29.8)
Gas withdrawn, Bcf (10^9 m^3)	4.60	(0.130)	6.73	(0.191)
Condensate produced, bbl (m^3)*	45,185	(7184)	11,867	(1886)
Total condensate yield, bbl (m^3)	244,541	(38,882)	88,999	(17,328)
Reservoir temperature, °F (°C)	114	(45)	116	(46)
Calculated dew point pressure, psia (MPa)	3,562	(24.5)	3,265	(22.5)
Measured dew point, psia (MPa)	3,620	(25.0)	3,309	(22.8)
Composition				
CO_2	0.001		1.1500	
N_2	0.790		0.1400	
C_1	80.099		84.1495	
C_2	7.460		4.7900	
C_3	3.700		2.5600	
i-C_4	1.750		2.0500	
n-C_4	1.300		1.4700	
i-C_5	0.840		0.8800	
n-C_5	0.390		0.3700	
C_6	0.840		0.6100	
C_7	0.660		0.4340	
C_8	0.580		0.4210	
C_9	0.480		0.3320	
C_{10}	0.350		0.2354	
C_{11}	0.200		0.1455	
C_{12}	0.150		0.1007	
C_{13}	0.120		0.0786	
C_{14}	0.090		0.0475	
C_{15}	0.070		0.0257	
C_{16}	0.130		0.0101	
Molecular weight	23.73		22.35	
Last component in analysis	C13		C6	
Specific gravity of residue	0.815 (C_{14+})		0.77(C_{7+})	
Molecular weight of residue	212		125	

* Stock-tank yields used as separator yields ÷ 1.5

material balance equations plus equations of state will allow full-scale calculations (simulation mode).

The second part of this chapter described how to deal with condensate reservoirs. A depletion calculation program developed by Firoozabadi et al. [10-6] predicts the liquid yields of a reservoir when pressures go down. The accuracy of this approach depends upon how well the dew point of the fluid is predicted. This requires an extended analysis of C_{7+} components, because the dew point varies significantly with the presence of heavy molecules.

REFERENCES

10-1. Allen, J. C., "Factors Affecting the Classification of Oil and Gas Wells," *API Drill. Prod. Practice*, 118 (1952).

10-2. Coats, H. H., "Simulation of Gas Condensate Performance," *SPE Preprint 10512* (1982).

10-3. Coleman, S., H. D. Wilde, Jr., and T. W. Moore, "Quantitative Effect of Gas-Oil Ratio on Decline of Average Rock Pressure," *Trans. AIME*, Vol. 86, 174 (1930).

10-4. Criss, C. R., and R. L. McCormick, "History and Performance of the Coldwater Oil Fields, Michigan," *Trans. AIME*, Vol. 201, 22 (1954).

10-5. Eilerts, C. K., "Phase Relations of Gas-Condensate Fluids," *Monograph 10, U.S. Bureau of Mines*, Two Volumes (1957).

10-6. Firoozabadi, A., Y. Hekim, and D. L. Katz, "Reservoir Depletion Calculations for Gas Condensates," *Cdn. J. of Chem. Engr.*, Vol. 56, 610 (1978).

10-7. Haynes, H. I., L. W. Thrasher, M. L. Katz, and T. R. Eck, *Enhanced Oil Recovery*, National Petroleum Council (1976).

10-8. Katz, D. L., "A Method of Estimating Oil and Gas Reserves," *Trans. AIME*, Vol. 118, 18 (1936).

10-9. Katz, D. L., "Possibilities of Secondary Recovery for the Oklahoma City Wilcox Sand," *Trans. AIME*, Vol. 146, 28 (1942).

10-10. Katz, D. L., "Possibility of Cycling Deep Depleted Oil Reservoirs after Compression to a Single Phase," *Trans. AIME*, Vol. 195, 175 (1952).

10-11. Katz, D. L., "Prediction of the Shrinkage of Crude Oils," *API Drill. Pod. Practice*, 137 (1942).

10-12. Katz, D. L., and A. Firoozabadi, "Predicting Phase Behavior of Condensate/Crude-Oil System Using Methane Interaction Coefficient," *J. Pet. Tech.*, Vol. 30, No. 11, 1649-55, Nov. (1978).

10-13. Katz, D. L., and M. R. Tek, "Overview on Underground Storage of Natural Gas," *J. Pet. Tech.*, Vol. 33, No. 6, 943–51, June (1981).

10-14. Katz, D. L., and B. Williams, "Reservoir Fluids and Their Behavior," *Bull. AAPG*, Vol. 36, 342 (1952).

10-15. Katz, D. L., R. A. Herzog, and Y. Hekim, "Predicting Yield of Revaporized Condensate in Gas Storage," *J. Pet. Tech.*, Vol. 35, No. 6, 1173–1175, June (1983).

10-16. Muskat, M., "Effect of Permeability Stratification in Cycling Operations," *Trans. AIME*, Vol. 179, 303 (1949).

10-17. Muskat, M., and M. O. Taylor, "Effect of Reservoir Fluid and Rock Characteristics on Production Histories of Gas Drive Reservoirs," *Trans. AIME*, Vol. 165, 78 (1946).

10-18. Noble, F. G., "Operating Features of Katy Gas Cycling Plant," *API Drill. Prod. Practice*, 43 (1943).

10-19. Peng, D. Y., and D. B. Robinson, "A New Two Constant Equation of State," *Ind. Eng. Chem. Fund.*, Vol. 15, 59–64 (1976).

10-20. Private communication, Core Laboratories, Inc. (1982).

10-21. Schilthuis, R. J., "Active Oil and Reservoir Energy," *Trans. AIME*, Vol. 118, 33 (1936).

10-22. Smith, M. R., and J. H. Henderson, "Performance of a Solution Gas Drive Reservoir, Rosenwald Pool, Oklahoma," *J. Pet. Tech.*, Vol. 9, No. 1, 25–29, Jan. (1957).

10-23. Smith, R. V., *Practical Natural Gas Engineering*, Penn Well Books, Tulsa, Oklahoma (1983).

10-24. Standing, M. B., E. N. Lindblad, and R. L. Parsons, "Calculated Recoveries by Cycling from a Retrograde Reservoir of Variable Permeability," *Trans. AIME*, Vol. 174, 165 (1948).

10-25. Woods, R. W., and M. Muskat, "An Analysis of Material Balance Calculations," *Trans. AIME*, Vol. 160, 124 (1945).

CHAPTER 11

SIMULATION: FIELD AND RESERVOIR PERFORMANCE

In the early days of gas storage, it was clearly desirable to be able to predict the gas arrival pressure at a dehydration compression plant as a function of flow rate and reservoir inventory. The chart in Fig. 11-1 [1-1] was developed to predict the pressure at the station, and the match for one season was within ±5 psi accuracy. Today, with the availability of high-speed computers, the complicated prediction process can be computerized. One can predict either the performance of the reservoir as a system or the performance of the system up to the compression station, including wellbore, gathering line and plant pressure losses.

Given a reservoir of variable sand thickness, well locations, and individual deliverabilities, one may obtain the week-to-week or daily deliverability of the reservoir via simulation for a given withdrawal schedule. Usually, the properties of the reservoir rock, such as thickness, permeability, porosity, etc., may be defined separately for various areas, as shown in Fig. 11-2 [1-2]; these properties are the basic information needed for simulations.

Simulation work has been studied and accepted by gas and oil industries for years. Many methods have been developed to solve various engineering problems. This chapter intends to cover only the basic concept of the numerical approach. Starting with the Taylor series expansion, the chapter demonstrates how to convert

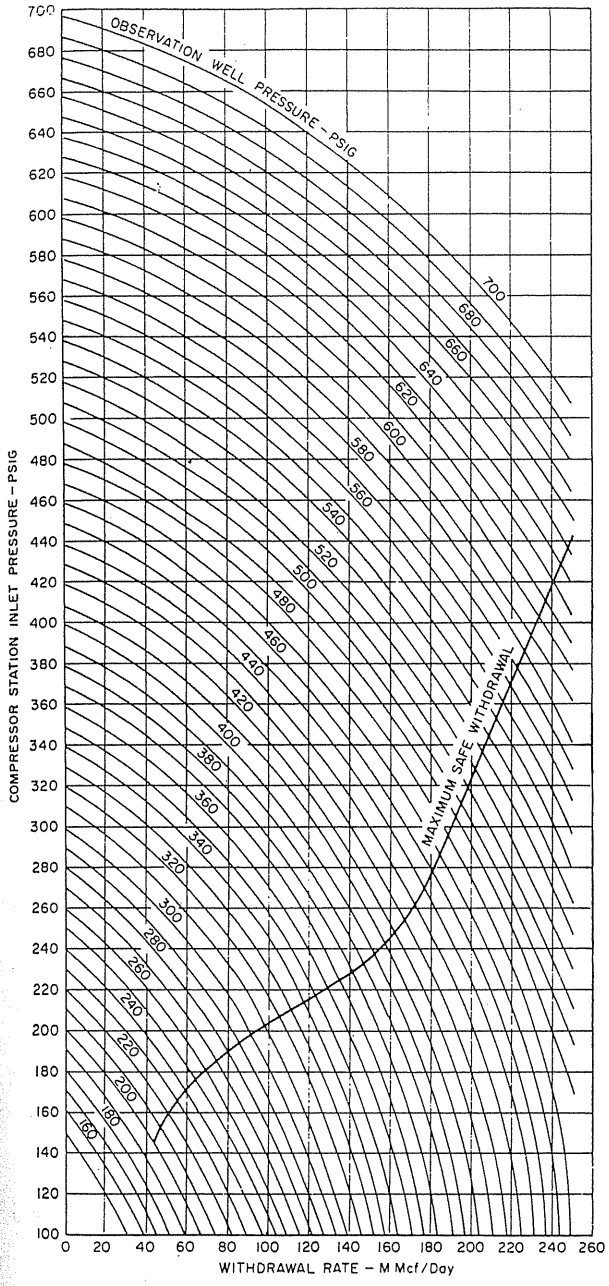

FIGURE 11-1
Rate–terminal pressure relationship chart [Katz et al., 1-1, courtesy McGraw-Hill Publishing Co.].

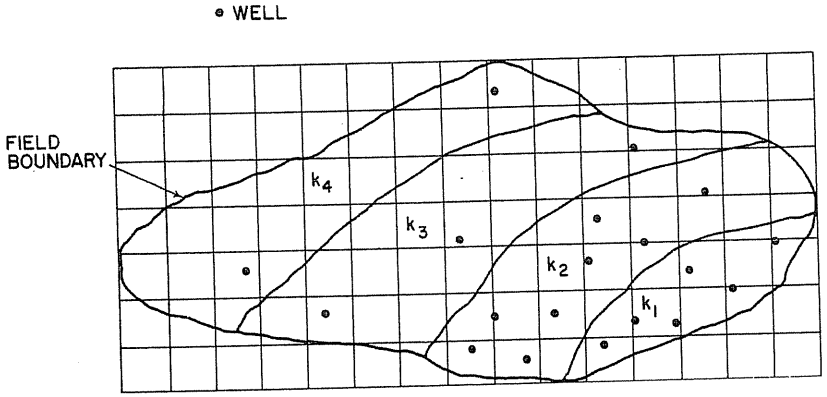

FIGURE 11-2
Area view of gas storage reservoir, with various K's and well locations [Katz & Coats, 1-2].

a partial differential equation (PDE) to a finite difference equation (FDE) plus a truncation error (TE) term. Then, by discretizing the given domain (reservoir) to numerous subdomains (blocks of reservoir; see Fig. 11-2), a FDE can be established for each subdomain. Finally, combining all the FDEs, a set of algebraic equations with pressures P_i as unknowns:

$$[\text{FDE}]_i(P_1, P_2, \ldots, P_n) = 0, i = 1, 2, \ldots, n \ (n = \text{number of blocks}) \tag{11.1}$$

can be solved simultaneously by computer programming.

An example will be given to show the algorithm for a single-phase, one-dimensional simulation with known rock/fluid properties (k, G, T, etc.). In addition, the history match technique, by which one can obtain rock properties if the pressure response and its withdrawal/injection history are known, will be discussed.

Two practical problems are included. One is the deliverability forecast; the other is the "mixing" project (replacing valuable base gas with cheap gas). The field examples of "mixing" were provided.

11.1 FINITE DIFFERENCE APPROXIMATION OF THE GAS FLOW EQUATION

As shown in Appendix C, the governing gas flow equation in PDE form for a one-dimensional case, in terms of pseudopressure $m(P)$, is

$$C_1 \frac{\partial}{\partial x} k \frac{\partial m}{\partial x} = C_2 \frac{\partial m}{\partial t} + C_3 Q_{sc} \tag{11.2}$$

where $C_1 = 1$, $C_2 = \phi\mu c$, $C_3 = P_{sc}(T/T_{sc})/V$, if darcy units are used.

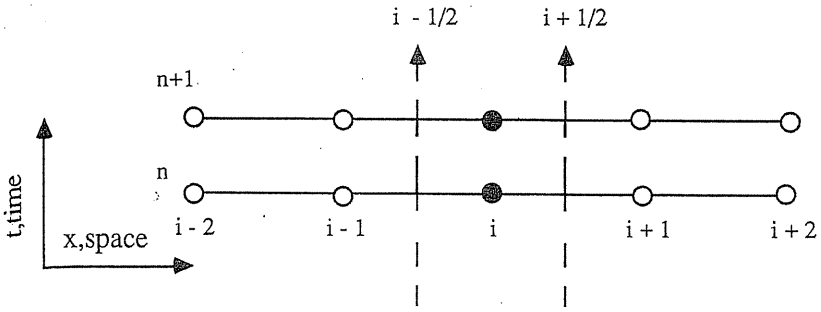

FIGURE 11-3
Grid points distribution in both space and time directions.

Equation (11.2) describes the gas flow at every node of Fig. 11-3, wherein a domain has been discretized to small sections in spatial and time coordinates. Now the task is to approximate Eq. (11.2) by its FDE, which relates each node to its nearby nodes. In order to do so, some mathematical background is necessary, beginning with the Taylor series expansion.

Taylor Series Expansion

The finite difference approximation of a partial differential equation is often derived from a truncated Taylor's series. Considering the grid points shown in Fig. 11-4, three adjacent equidistant points with Δx in between, the Taylor's

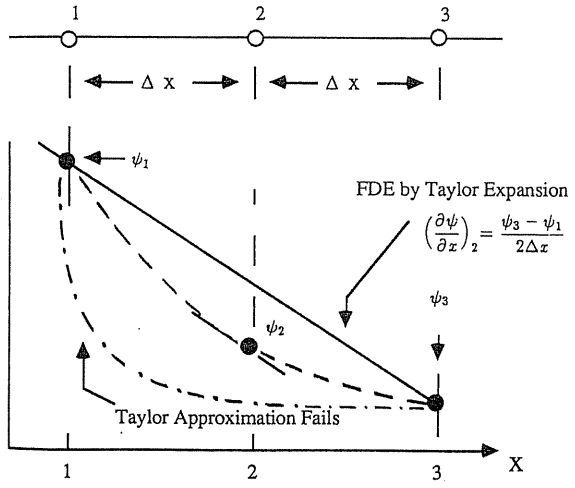

FIGURE 11-4
Three grid points and their corresponding ψ values.

series applied around point 2 gives:

$$\psi_1 = \psi_2 - \Delta x\left(\frac{\partial\psi}{\partial x}\right)_2 + \frac{1}{2}(\Delta x)^2\left(\frac{\partial^2\psi}{\partial x^2}\right)_2 - \frac{1}{6}(\Delta x)^3\left(\frac{\partial^3\psi}{\partial x^3}\right)_2 + \frac{1}{24}(\Delta x)^4\left(\frac{\partial^4\psi}{\partial x^4}\right)_2 + \cdots \tag{11.3}$$

$$\psi_3 = \psi_2 + \Delta x\left(\frac{\partial\psi}{\partial x}\right)_2 + \frac{1}{2}(\Delta x)^2\left(\frac{\partial^2\psi}{\partial x^2}\right)_2 + \frac{1}{6}(\Delta x)^3\left(\frac{\partial^3\psi}{\partial x^3}\right)_2 + \frac{1}{24}(\Delta x)^4\left(\frac{\partial^4\psi}{\partial x^4}\right)_2 + \cdots \tag{11.4}$$

where ψ is an arbitrary function. By arranging Eqs. (11.3) and (11.4), the first and second derivatives are obtained:

$$\overbrace{\left(\frac{\partial\psi}{\partial x}\right)_2}^{\text{PDE}} = \overbrace{\frac{\psi_3 - \psi_1}{2\Delta x}}^{\text{FDE}} + \overbrace{\left[\frac{1}{6}(\Delta x)^2\left(\frac{\partial^3\psi}{\partial x^3}\right)_2 + \cdots\right]}^{\text{TE, } O(\Delta x)^2} \tag{11.5}$$

$$\underbrace{\left(\frac{\partial^2\psi}{\partial x^2}\right)_2}_{\text{PDE}} = \underbrace{\frac{\psi_3 - 2\psi_2 + \psi_1}{(\Delta x)^2}}_{\text{FDE}} + \underbrace{\left[-\frac{1}{12}(\Delta x)^2\left(\frac{\partial^4\psi}{\partial x^4}\right)_2 + \cdots\right]}_{\text{TE, } O(\Delta x)^2} \tag{11.6}$$

The truncation error (TE) terms of Eqs. (11.5) and (11.6) are of the order of $(\Delta x)^2$ (referred to as second-order accuracy, or $O(\Delta x)^2$), and they become exactly zero when ψ behaves like a function of second- or first-order polynomial ($\psi = a + bx + cx^2$). In that case, the finite difference approximation becomes:

$$\left(\frac{\partial\psi}{\partial x}\right)_2 = \frac{\psi_3 - \psi_1}{2\Delta x} \quad \text{and} \quad \left(\frac{\partial^2\psi}{\partial x^2}\right)_2 = \frac{\psi_3 - 2\psi_2 + \psi_1}{(\Delta x)^2} \tag{11.7}$$

The idealized FDE approach of Eq. (11.7) yields good results only when the distance Δx is small enough and ψ behaves well within Δx (that is, behaves like a low-order polynomial type).

Finite Difference Form in Space Coordinate

At time level n and grid point i in Fig. 11-3, the spatial term $C_1\partial/\partial x(k\partial m/\partial x)$ of Eq. (11.2) can be approximated as follows:

$$\left(C_2\frac{\partial m}{\partial t} + C_3 Q_{sc}\right)_i^n = \left[C_1\frac{\partial}{\partial x}\left(k\frac{\partial m}{\partial x}\right)\right]_i^n \tag{11.8a}$$

$$= \left[C_1\frac{(k\partial m/\partial x)_{i+1/2} - (k\partial m/\partial x)_{i-1/2}}{\Delta x}\right]_i^n \tag{11.8b}$$

$$= \left\{\frac{C_1}{\Delta x}\left[k_{i+1/2}\left(\frac{m_{i+1} - m_i}{\Delta x}\right) - k_{i-1/2}\left(\frac{m_i - m_{i-1}}{\Delta x}\right)\right]\right\}_i^n \tag{11.8c}$$

$$= \left[+\frac{C_1 k_{i-1/2}}{(\Delta x)^2}\right]\cdot m_{i-1}^n + \left[-\frac{C_1(k_{i+1/2} + k_{i-1/2})}{(\Delta x)^2}\right]\cdot m_i^n + \left[+\frac{C_1 k_{i+1/2}}{(\Delta x)^2}\right]\cdot m_{i+1}^n \tag{11.8d}$$

$$= A_{i,i-1}\cdot m_{i-1}^n + A_{i,i}\cdot m_i^n + A_{i,i+1}\cdot m_{i+1}^n = B_i^n \tag{11.8e}$$

(The superscripts n here identify time value; they are not exponents.) The derivation from (11.8a) to (11.8b) is a Taylor series expansion of $\partial/\partial x(k\partial m/\partial x)$ at point i between points $i + \frac{1}{2}$ and $i - \frac{1}{2}$. Similarly, from (11.8b) to (11.8c) is the expansion of $(\partial m/\partial x)$ at $i + \frac{1}{2}$ between i and $i + 1$ and at $i - \frac{1}{2}$ between $i - 1$ and i.

By applying the same approach for the time level $n + 1$, one could obtain

$$\left(C_2\frac{\partial m}{\partial t} + C_3 Q_{sc}\right)_i^{n+1} = \left[C_1\frac{\partial}{\partial x}\left(k\frac{\partial m}{\partial x}\right)\right]_i^{n+1}$$
$$= A_{i,i-1}\cdot m_{i-1}^{n+1} + A_{i,i}\cdot m_i^{n+1} + A_{i,i+1}\cdot m_{i+1}^{n+1}$$
$$= B_i^{n+1} \tag{11.9}$$

Finite Difference Form in Time Coordinate

The above conversion of the PDE to the FDE is only for the space coordinate (x); in the time coordinate (t), the derivative $\partial m/\partial t$ at node i is usually approximated as

$$\left(\frac{\partial m}{\partial t}\right)_i = \frac{m_i^{n+1} - m_i^n}{\Delta t}\, xO(\Delta t) \tag{11.10}$$

This approximation has a first order of accuracy, $O(\Delta t)$. The reason for using this expression is that the time coordinate is a *one-way coordinate*: whatever happened before will affect present happenings, but the future coordinates have no influence on what happens now.[1]

To take another approach, the slope of the straight line between time points n and $n + 1$, as shown in Fig. 11-5, could be approximated by the weighted combination of slopes at times n and $n + 1$, that is,

$$\frac{m^{n+1} - m^n}{\Delta t} = \theta\left(\frac{\partial m}{\partial t}\right)^{n+1} + (1 - \theta)\left(\frac{\partial m}{\partial t}\right)^n \tag{11.11}$$

[1] An application of a one-way coordinate in space is called the *upstream method*, e.g., $(\partial m/\partial x)_i = (m_i - m_{i-1})/\Delta x$.

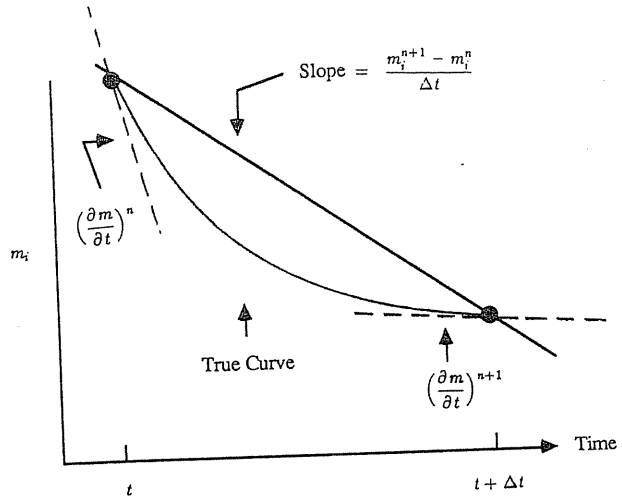

FIGURE 11-5
Finite difference approximation and its weighting scheme in time coordinate.

where θ is the weighting factor, $0 \leq \theta \leq 1$. Using this same principle, the right-hand side of the PDE (11.2) can be expanded to

$$\left(C_2\frac{\partial m}{\partial t} + C_3 Q_{sc}\right)_i = (C_2)_i^{n+\theta}\frac{m^{n+1} - m^n}{\Delta t} + (C_3)_i^{n+\theta} Q_{sc}$$
$$= \theta\left[C_2\frac{\partial m}{\partial t} + C_3 Q_{sc}\right]_i^{n+1}$$
$$+ (1-\theta)\left[C_2\frac{\partial m}{\partial t} + C_3 Q_{sc}\right]_i^{n} \qquad (11.12)$$

where $(C_2)_i^{n+\theta}$ and $(C_3)_i^{n+\theta}$ should be evaluated at a time level $n + \theta$ if they are nonlinear (a function of m).

Substituting Eqs. (11.8) and (11.9) into Eq. (11.12), one obtains[2]

$$\theta\left[A_{i,i-1}m_{i-1}^{n+1} + A_{i,i}m_i^{n+1} + A_{i,i+1}m_{i+1}^{n+1}\right]$$
$$+ (1-\theta)\left[A_{i,i-1}m_{i-1}^{n} + A_{i,i}m_i^{n} + A_{i,i+1}m_{i+1}^{n}\right]$$
$$= (C_2)_i^{n+\theta}\frac{m_i^{n+1} - m_i^n}{\Delta t} + (C_3)_i^{n+\theta} Q_{sc} \text{ and, } O\left[(\Delta x)^2, \Delta t\right] \qquad (11.13)$$

[2] Eq. (11.13) is referred to as the θ method.

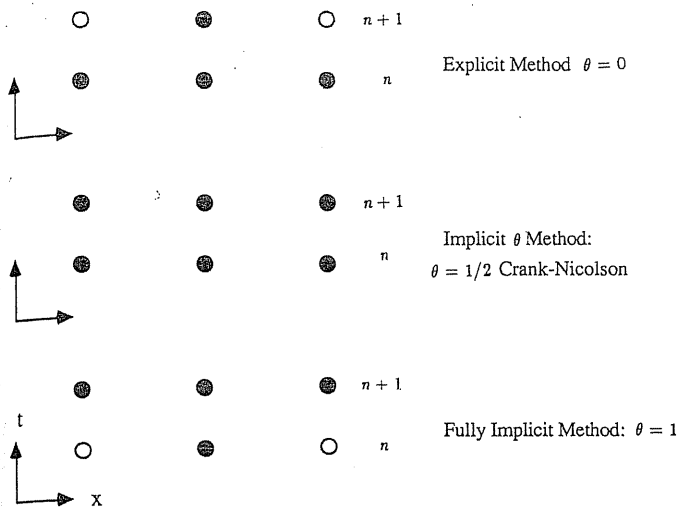

FIGURE 11-6
Finite difference schemes: (*a*) explicit method, (*b*) implicit θ method, (*c*) fully implicit method.

where $\theta = 1$ for the *fully implicit* or *backward difference method*, $\theta = \frac{1}{2}$ for the *Crank-Nicolson method*, and $\theta = 0$ for the *explicit* or *forward difference method* [11-2]. Schematics of these methods are shown in Fig. 11-6.

Boundary Conditions

There are three kinds of boundary conditions (BCs): (1) Dirichlet (essential), (2) specified flux (natural), and (3) mixed. In petroleum terminology, the first kind is referred to as a constant pressure BC. For example, the pseudopressure at the edge point j of the gas bubble is a constant, $m(P_0)$, if 100 percent water drive applies. Thus, the FDE at j can be simply specified as

$$m_j = m(P_0) \qquad (11.14)$$

A special case for the specified flux BC is a no-flow BC, which can be applied to a grid point j at a reservoir fault where no fluids are allowed to penetrate—that is,

$$k\frac{\partial m}{\partial x}\Big|_j = \dot{q}_j = 0 \qquad (11.15)$$

A no-flow situation at point j could be modeled by assuming the permeability $k_{j+1/2} = 0$. As a result, the FDE at j can be approximated by rearranging Eq. (11.13) to

$$\theta\left[A_{j,j}m_j^{n+1} + A_{j,j-1}m_{j-1}^{n+1}\right] + (1-\theta)\left[A_{j,j}m_j^{n} + A_{j,j-1}m_{j-1}^{n}\right]$$

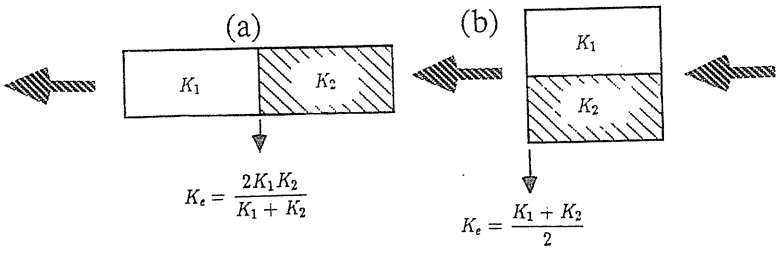

FIGURE 11-7
The equivalent permeability at interface: (*a*) in series, (*b*) in parallel.

$$= (C_2)_j^{n+\theta}\frac{m_j^{n+1} - m_j^n}{\Delta t} + (C_3)_j^{n+\theta}Q_{sc},\ O[(\Delta x),\ \Delta t] \qquad (11.16)$$

Other BCs and their descriptions can be found in reference [1-3].

Interface Permeability

When it is necessary to evaluate the equivalent permeability, k_e, at the interface of two different permeability zones, the *harmonic mean*,

$$k_e = \frac{1}{1/k_1 + 1/k_2} = \frac{2k_1k_2}{k_1 + k_2} \qquad (11.17)$$

is preferred for a block-in-series case (Fig. 11-7); for a block-in-parallel case, one could use the *arithmetic mean*:

$$k_e = \frac{k_1 + k_2}{2} \qquad (11.18)$$

More details of the interface permeability can be found in references [1-3,1-10].

Final Matrix Form of FDE

After converting the PDE at each grid point to its corresponding FDE for an n-node system, the set of n algebraic equations for n unknowns $(m_1, m_2, \ldots, m_n)$ can be solved simultaneously. For a 5-node system as shown in Fig. 11-8, the governing equations in FDE form, from Eqs. (11.13) and (11.16), are

FIGURE 11-8
One-dimensional finite reservoir section with five grid points.

$i = 1$:

$$\left[\theta A_{1,1} - \frac{(C_2)_1^{n+\theta}}{\Delta t}\right]m_1^{n+1} + \left[\theta A_{1,2}\right]m_2^{n+1} = \left[-\frac{(C_2)_1^{n+\theta}}{\Delta t}m_1^n + (C_3)_1^{n+\theta}Q_1 - (1-\theta)B_1^n\right]$$

$i = 2, 3, 4$:

$$\left[\theta A_{i,i-1}\right]m_{i-1}^{n+1} + \left[\theta A_{i,i} - \frac{(C_2)_i^{n+\theta}}{\Delta t}\right]m_i^{n+1} + \left[\theta A_{i,i+1}\right]m_{i+1}^{n+1} = \left[-\frac{(C_2)_i^{n+\theta}}{\Delta t}m_i^n + (C_3)_i^{n+\theta}Q_i - (1-\theta)B_i^n\right]$$

$i = 5$:

$$\left[\theta A_{5,4}\right]m_4^{n+1} + \left[\theta A_{5,5} - \frac{(C_2)_5^{n+\theta}}{\Delta t}\right]m_5^{n+1} = \left[-\frac{(C_2)_5^{n+\theta}}{\Delta t}m_5^n + (C_3)_5^{n+\theta}Q_5 - (1-\theta)B_5^n\right] \qquad (11.19)$$

or in matrix form:

$$a_{ij}m_i = b_i \quad \text{or} \quad [a]\{m\} = \{b\} \qquad (11.20a)$$

$$\downarrow$$

$$\begin{bmatrix} a_{11} & a_{12} & 0 & 0 & 0 \\ a_{21} & a_{22} & a_{23} & 0 & 0 \\ 0 & a_{32} & a_{33} & a_{34} & 0 \\ 0 & 0 & a_{43} & a_{44} & a_{45} \\ 0 & 0 & 0 & a_{54} & a_{55} \end{bmatrix}\begin{bmatrix} m_1 \\ m_2 \\ m_3 \\ m_4 \\ m_5 \end{bmatrix}^{n+1} = \begin{bmatrix} b_1 \\ b_2 \\ b_3 \\ b_4 \\ b_5 \end{bmatrix} \qquad (11.20b)$$

where $a_{ij,i\neq j} = \theta A_{i,j}$, $i = 1, 2, \ldots, 5$; $j = 1, 2, \ldots, 5$

$$a_{ii} = \theta A_{i,i} - \frac{(C_2)_i^{n+\theta}}{\Delta t},\ i = 1, 2, \ldots, 5$$

$$b_i = -\frac{(C_2)_i^{n+\theta}}{\Delta t}m_i^n + (C_3)_i^{n+\theta}Q_i - (1-\theta)B_i^n,\ i = 1, 2, \ldots, 5$$

$(C_2)^{n+\theta}$ and $(C_3)^{n+\theta}$ must be obtained by an iteration procedure. One may use $(C_2)^n$ and $(C_3)^n$ values at the time level n for the first iteration to solve for m_i', an intermediate value, from which $(C_2)^{n+\theta}$ and $(C_3)^{n+\theta}$ can be updated. The calculations should be carried out repeatedly until

$$\left|\frac{(m_i')^{k+1} - (m_i')^k}{(m_i')^k}\right| \leq \text{tol} \tag{11.21}$$

where k is the number of iteration steps and the tolerance tol is set at some arbitrary value, e.g., 10^{-3}. After the m_i' values at all points meet the convergence criterion, these values are used for m_i^{n+1}.

Matrix-solving techniques are mathematical procedures that can be found in references [1-3,1-10,11-2] and many other books on numerical methods. A tridiagonal solver (TRIDAG) [11-2] is often used for the one-dimensional single-phase case discussed here.

11.2 STABILITY ANALYSIS

An FDE [Eq. (11.20)] approximation to a PDE [Eq. (11.2)] may be consistent but the solution will not necessarily converge to the solution of the PDE. When it does converge, the computational scheme is referred to as *stable*; otherwise, it is *unstable*. Stability is usually tested by using a Fourier analysis (von Neumann criterion). Thoughtful analyses for various numerical schemes are discussed in references [11-2,1-18].

The stability criteria of the explicit, fully implicit, and Crank-Nicolson schemes used for Eq. (11.20) are summarized in Table 11.1.

Example 11.1. A one-dimensional reservoir section, Fig. 11-9, is scheduled to produce 10 MMcf/day at node 1. Both ends of this section are impermeable. Calculate the pressure response of each node after one hour using a fully implicit FDE scheme ($\theta = 1$).

The reservoir/fluid data are:

$$\mu_i = 0.02 \text{ cp}$$

$$P_i = 5000 \text{ psia}$$

TABLE 11.1
Stability criteria

Scheme	θ	Stability criterion
Explicit	0	$\Delta t \leq \frac{C_2(\Delta x)^2}{2C_1 k}\left[\frac{\Delta t}{(\Delta x)^2} \leq \frac{1}{2}\left(\frac{C_2}{C_1 k}\right)\right]$ (11.22)
Implicit	1	Unconditionally stable
Crank-Nicolson	$\frac{1}{2}$	Stable, if linear

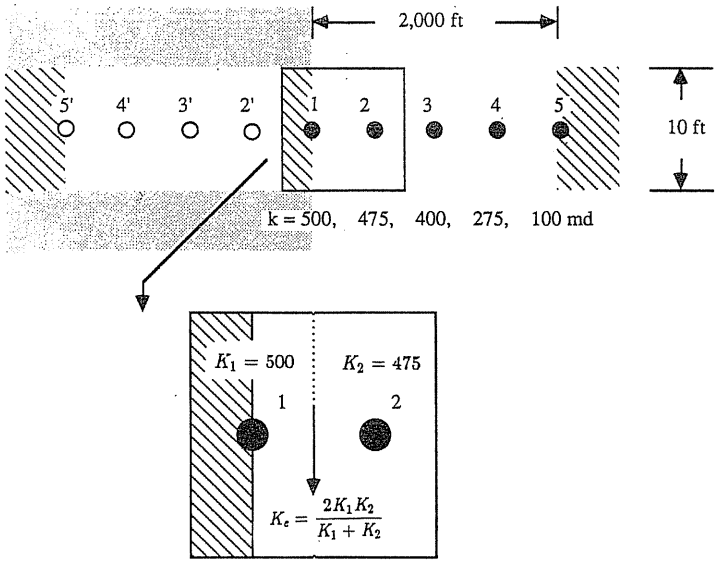

FIGURE 11-9
One-dimensional section of reservoir for Example 11.1.

$$Z = 0.86$$

$$T = 580 \text{ °R}$$

$$h = 40 \text{ ft}$$

$$\phi = 0.15$$

$$\frac{\partial(P/Z)}{\partial m} = 2.020 \times 10^{-6} \text{ psia}^{-1}$$

Solution. Since the section is symmetric, only the nodes for one half (1–5) need be considered, and node 1 can be treated as an impermeable (no-flow) boundary. Blocks of constant permeability are defined to be centered around each node.

Calculate the equivalent permeabilities at the interfaces between blocks. For example, as shown in Fig. 11-9, the interface permeability between nodes 1 and 2 can be calculated by using Eq. (11.17):

$$k_{1+1/2} = \frac{2k_1k_2}{k_1 + k_2} = \frac{2(500)(475)}{500 + 475} = 487.2 \text{ md}$$

Similarly,

$$k_{2+1/2} = 434.3 \text{ md}, \quad k_{3+1/2} = 325.9 \text{ md}, \quad k_{4+1/2} = 146.7 \text{ md}$$

From Appendix C, the coefficients C_1, C_2, C_3, for field units, are

$$C_1 = 1$$

$$C_2 = (3739.5)2\phi\left[\frac{\partial(P/Z)}{\partial m}\right]$$

$$= (3739.5)(2)(0.15)(2.0202 \times 10^{-6}) = 2.299 \times 10^{-3}$$

$$C_3 = 1.5806 \times 10^8(2)\frac{T}{T_{sc}} \cdot P_{sc} \cdot \frac{1}{V}$$

$$= (1.5806 \times 10^8)(2)\frac{(580)}{(460 + 60)} \cdot (14.7) \cdot \frac{1}{(2000/4)(20)(40)} = 1.296 \times 10^4$$

assuming all the properties (μ, Z) stay constant.[3]

Construct the matrix as in Eq. (11.20). For example, a_{11} and b_1 can be calculated as follows:

$$a_{11} = \theta A_{1,1} - \frac{(C_2)_1^{n+\theta}}{\Delta t} = \theta\left(-\frac{C_1(k_{1-1/2} + k_{1+1/2})}{(\Delta x)^2}\right) - \frac{(C_2)_1^{n+\theta}}{\Delta t}$$

$$= (1)\left(-\frac{(1)(0 + 487.2)}{(2000/4)^2}\right) - \frac{2.299 \times 10^{-3}}{1} = -4.2478 \times 10^{-3}$$

$$b_1 = -\frac{(C_2)_1^{n+\theta}}{\Delta t}m_1^n + (C_3)_1^{n+\theta}Q_1 - (1 - \theta)B_1^n$$

$$= -\frac{(2.299 \times 10^{-3})}{1}(1.453 \times 10^9) + (1.296 \times 10^4)(10) - (1 - 1)B_1^n$$

$$= -3.2121 \times 10^6$$

where $k_{1-1/2} = 0$, and m_1^n is the initial pseudopressure:

$$m_1^n = 2\int_0^{P_i}\frac{P}{\mu Z}dP \approx \frac{(5000)^2}{(0.02)(0.86)} = 1.453 \times 10^9 \text{ psia}^2/\text{cp}$$

The final matrix form is

$$\begin{bmatrix} -4.248 \cdot 10^{-3} & 1.949 \cdot 10^{-3} & 0 & 0 & 0 \\ 1.949 \cdot 10^{-3} & -5.985 \cdot 10^{-3} & 1.737 \cdot 10^{-3} & 0 & 0 \\ 0 & 1.737 \cdot 10^{-3} & -5.340 \cdot 10^{-3} & 1.304 \cdot 10^{-3} & 0 \\ 0 & 0 & 1.304 \cdot 10^{-3} & -4.189 \cdot 10^{-3} & 5.867 \cdot 10^{-4} \\ 0 & 0 & 0 & 5.867 \cdot 10^{-4} & -2.886 \cdot 10^{-3} \end{bmatrix}$$

$$\times \begin{bmatrix} m_1 \\ m_2 \\ m_3 \\ m_4 \\ m_5 \end{bmatrix}^{n+1} = \begin{bmatrix} -3.2121 \cdot 10^6 \\ -3.3417 \cdot 10^6 \\ -3.3417 \cdot 10^6 \\ -3.3417 \cdot 10^6 \\ -3.3417 \cdot 10^6 \end{bmatrix}$$

[3] This simplified approach is just for illustrative purposes. In practice, an iteration procedure is necessary.

Solve for the m_i^{n+1} vector using any matrix-solving technique (in this case, the TRIDAG method is preferred [11-2]):

$$\begin{bmatrix} m_1 \\ m_2 \\ m_3 \\ m_4 \\ m_5 \end{bmatrix}^{n+1} = \begin{bmatrix} 1.4169 \cdot 10^9 \\ 1.4402 \cdot 10^9 \\ 1.4488 \cdot 10^9 \\ 1.4520 \cdot 10^9 \\ 1.4532 \cdot 10^9 \end{bmatrix} \text{psia}^2/\text{cp} \rightarrow \begin{bmatrix} P_1 \\ P_2 \\ P_3 \\ P_4 \\ P_5 \end{bmatrix}^{n+1} = \begin{bmatrix} 4936.7 \\ 4977.1 \\ 4991.9 \\ 4997.4 \\ 4999.5 \end{bmatrix} \text{psia}$$

Figure 11-10 shows the results for various θ values; unstability occurs when $\theta = 0$, because

$$\Delta t = 1\text{hr} \not< \frac{C_2(\Delta x)^2}{2C_1 k} = \frac{(2.299 \times 10^{-3})(2000/4)^2}{2(1)(487.2)} = 0.589$$

Finite difference matrices cannot be absolutely accurate in determining the pressure drop at a line source or sink (injection/production). For a particular well, however, a steady state flow calculation between the well and the nearby node may give the well pressure. For example, with the well located at node 1 (Fig. 11-9) and assuming steady state between nodes 2 and 1 with distance r_{12} in between, Eq. (8.35) can be used to obtain the pressure at node 1 (well):

$$\frac{m_2 - m(\text{well})}{m_2 Q_{D1}} = \ln\left(\frac{r_{12}}{r_w}\right) + s + DQ_{sc}$$

using specific well data (r_w, s, D).

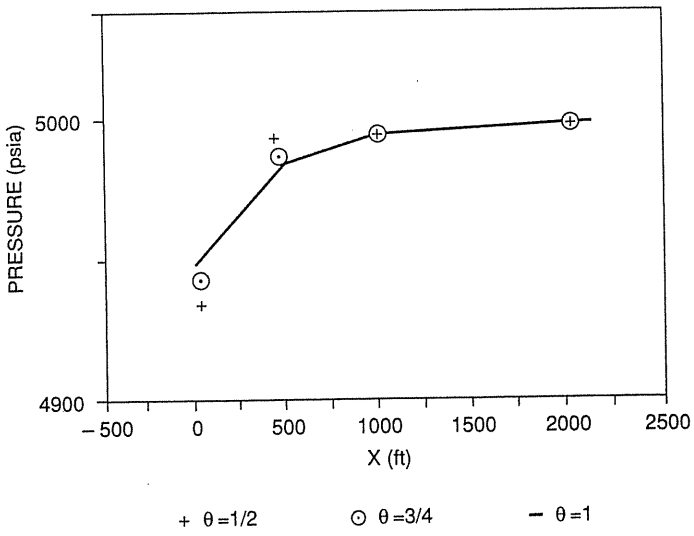

FIGURE 11-10
Pressures response at each node after one hour, Example 11.1.

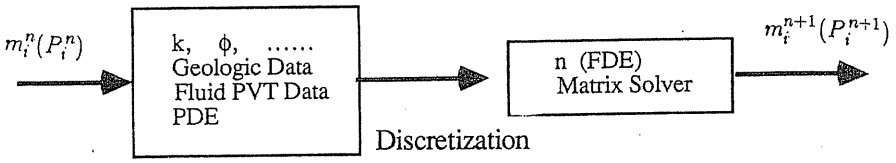

Forward approach: known m_i^n, and parameters$(k\,\phi, \cdots)$ $\Rightarrow$ m_i^{n+1}.

History Matching: known m_i^n, m_i^{n+1} $\Rightarrow$ parameters$(k, \phi, \cdots)$.

FIGURE 11-11
Algorithm of forward simulation procedures and its inverse approach, history matching.

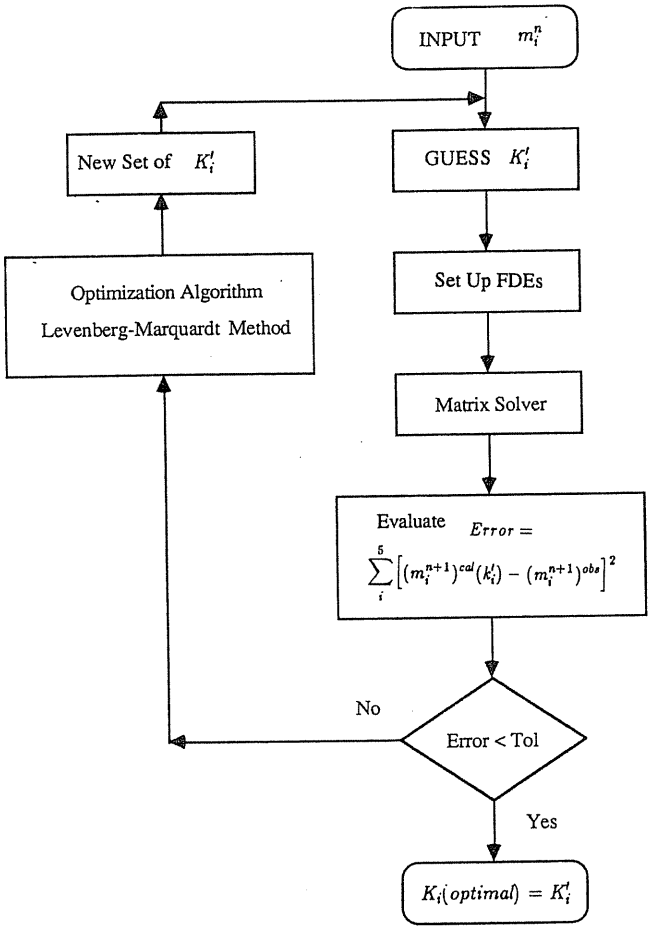

FIGURE 11-12
Permeability history-matching algorithm of Example 11.1.

11.3 HISTORY MATCHING

In reservoir engineering, the available data are usually the pressures at wells, the fluid *PVT* behavior, and the geologic data (if one is lucky). It is desirable to obtain certain rock properties, such as permeability k, without which the future operational prediction of the reservoir is impossible. Well testing is an effort to find rock properties; however, its applications are limited to the near zone of the well and only for the ideal model (cylindrical or other simple shape reservoirs).

Permeability information is needed a priori to obtain m_i^{n+1} in the algorithm used so far in this chapter, as shown in Fig. 11-11. How about the inverse approach? For example, what if pressure history is known (both m_i^n and m_i^{n+1}), and k_i is the unknown to be solved for? This backward approach is referred to as *history matching*, the *inverse model*, or the *identity problem*.

History matching for unknown permeabilities k_i involves minimizing

$$\text{Error} = \sum_i^5 \left[(m_i^{n+1})_{\text{calculated}}(k_i') - (m_i^{n+1})_{\text{observed}}\right]^2$$

The k_i' are altered until the error is smaller than the given tolerance. Figure 11-12 is a flow chart of a history matching algorithm that was applied to the reservoir section of Example 11.1. Figure 11-13 shows the matched k_i values along with the

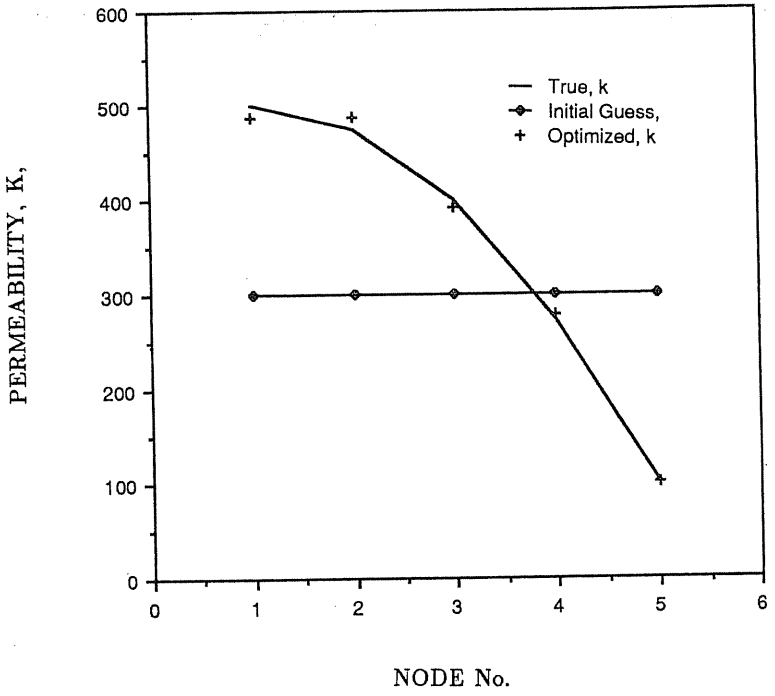

FIGURE 11-13
Permeability history-matching results of Example 11.1.

initial guesses of 300 md all through the five blocks. The optimization procedure used is the Levenberg-Marquardt algorithm [11-11,11-13]; other procedures can be found in reference [11-8].

11.4 PRACTICAL APPLICATIONS

Simulation is a tool for describing reservoir behavior. Many simulations have been proposed and put into practice in the last thirty years. Here, two types of gas storage applications are presented. One is the deliverability forecast, which provides the information for engineers to plan the future operational schedule. The other is the "mixing" project to replace valuable base gas with cheap gases or to sweep one gas with another of different thermal content for economic purposes.

Deliverability Forecast

The procedure involved in simulations consists of discretizing the reservoir into blocks and performing the mass and energy balances on these blocks simultaneously. For example, the isopach map of Fig. 11-14 [11-12], generated by geologic information, was discretized, and accordingly the PDEs at each point were converted to FDEs similar to Eq. (11.19).

Both reservoir rock and fluid properties are essential to satisfactory simulation results. The fluid properties (Fig. 11-15) usually can be correctly determined in service laboratories and stored in a computer data base. On the other hand, accurate rock property values are difficult to determine. The determination requires gas testing or analysis of core samples, and the validity of extrapolating the near zone rock properties throughout the whole reservoir is questionable. The more usual approach is to determine the rock properties via history matching. The rock properties, thickness, porosity, and permeability, for each block, as shown in Fig. 11-16, are stored in the data base. For a two-phase flow system, a relative permeability chart should also be included.

After establishing the final matrix of FDEs and the data base of rock and fluid properties, the simulation can be performed according to the injection/producing schedule. Figure 11-17 shows the initial pressure profile and the field performance prediction for the storage gas field of Fig. 11-14. Many field problems (wellbore leakage, gas migration, etc.) are usually discovered by observing field performance different from the simulation results.

Mixing Project

In the past, 30 to 60 percent of the valuable gas in storage reservoirs, commonly known as *base gas*, was considered unrecoverable. A suggested method of recovery is the mixing project [11-3,11-5], which is the replacement of the base gas by less expensive gas (*town gas*). Actually, the phenomena of one fluid replacing another had been investigated since the late 40s by Standing et al. [10-24] and Marshall and Oliver [11-14] on cycling from retrograde reservoirs. In the early

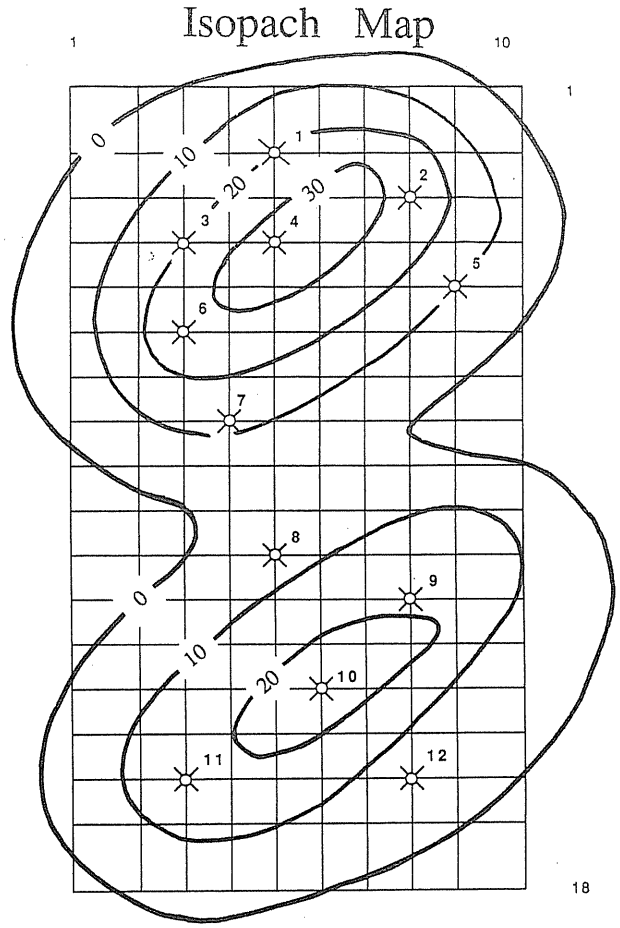

FIGURE 11-14
Discretized isopach map of a reservoir [MacDonald, 11-12].

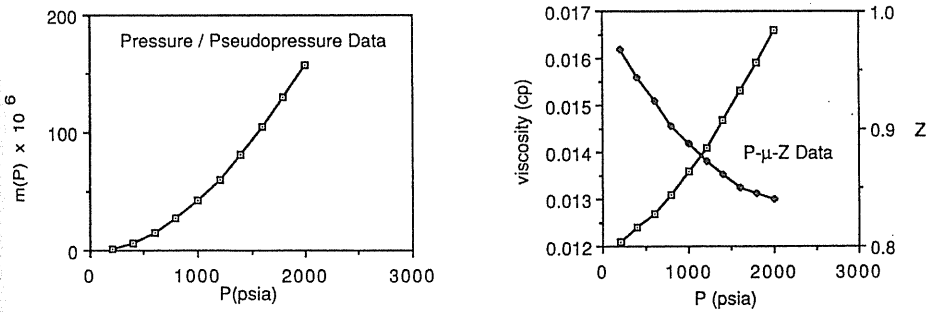

FIGURE 11-15
Reservoir fluids property charts: (*a*) P-$m(P)$, (*b*) P-μ-Z.

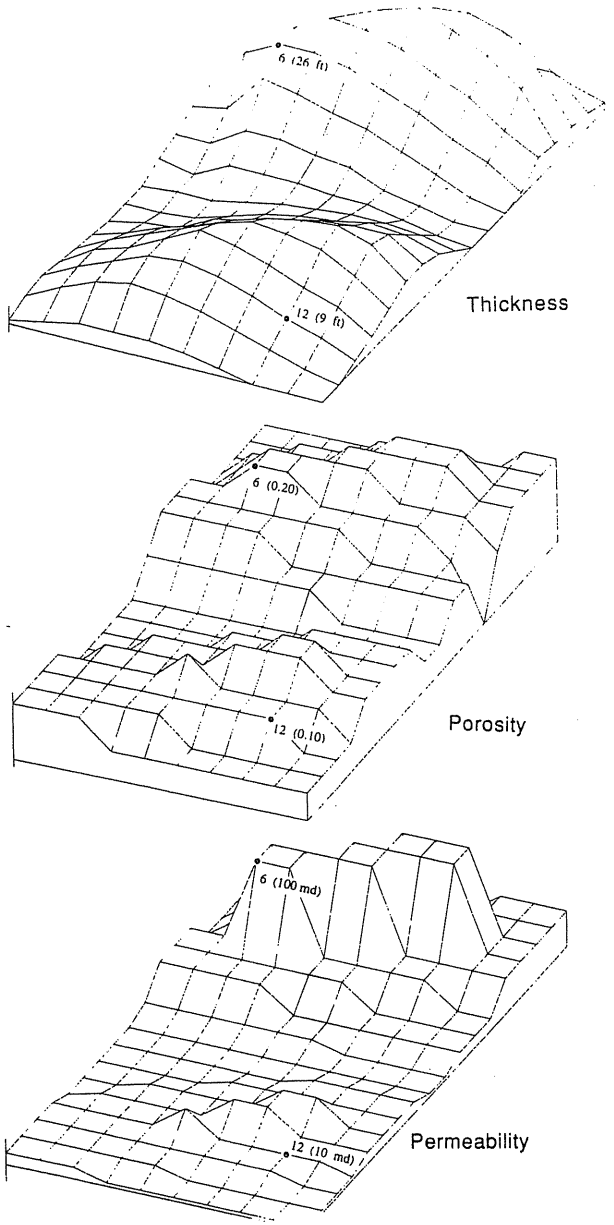

FIGURE 11-16
Reservoir rock property profiles: (*a*) thickness, (*b*) porosity, and (*c*) permeability.

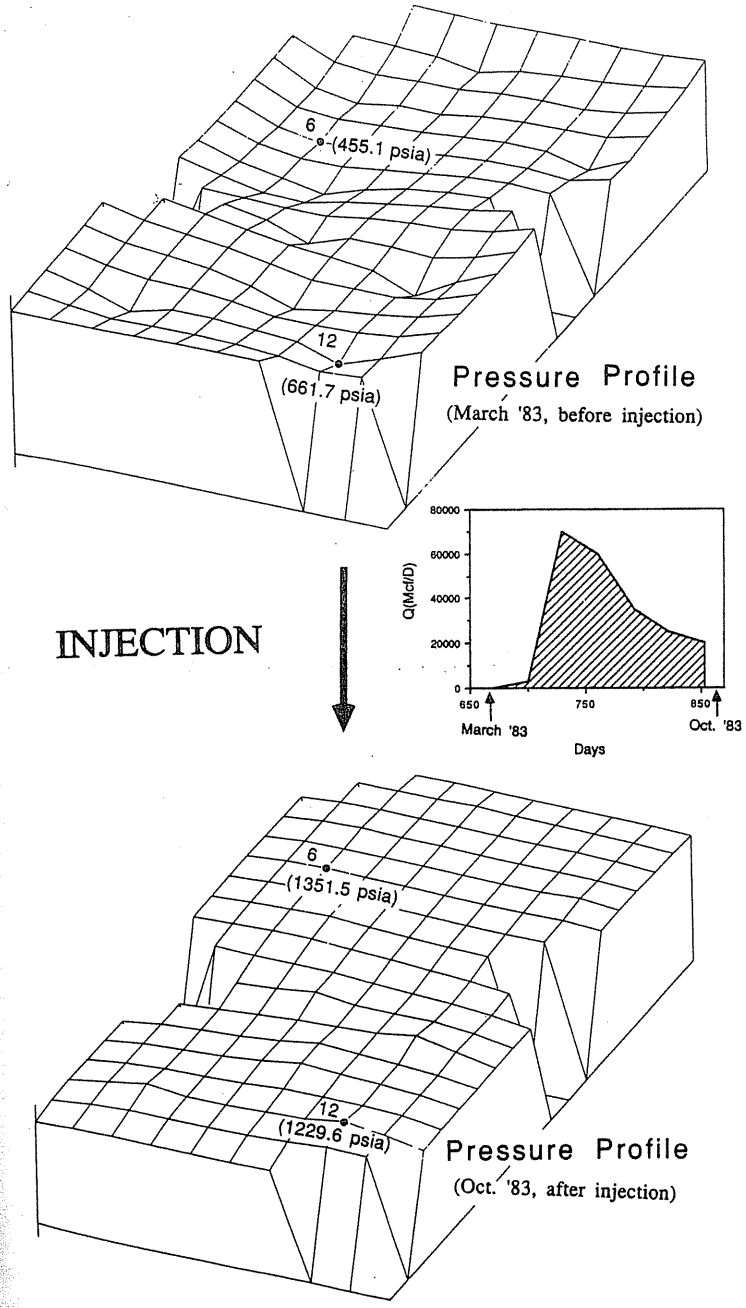

FIGURE 11-17
Pressure profiles before and after the injection period, March '83 to October '83.

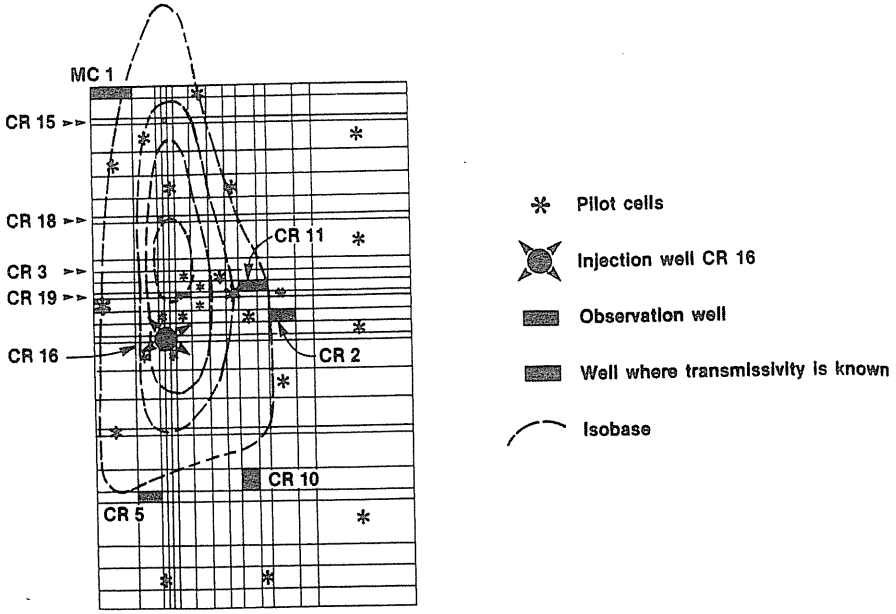

FIGURE 11-18
Discretized storage field [Fasanino et al., 11-6, courtesy SPE-AIME].

60s, the U.S. Bureau of Mines and the American Gas Association supported study of the feasibility of using inert gases to replace base gas [11-19].

Now, numerical procedures are essential to mixing calculations. First, the storage reservoir is discretized to finite blocks, as in Fig. 11-18 [11-6]. The given transmissibility (kh) contours obtained by geologic study and well tests may not reflect the real performance of the storage reservoir. Thus, by history matching based on a limited number of the production/injection data and their responding pressure profiles, a modified contour should be established.

Once the modified reservoir transmissibility contour is established, the possible and optimal mixing schedule (where and how much may be injected without contamination of the working gas) can be determined via simulation. Before the actual injection in practice, a tracer test should be conducted to verify the hypothesis derived from simulation results.

An additional advantage of the mixing process is the resulting high storage pressure, which ensures gas deliverability in the winter. The details of mixing projects are discussed in Chapter 17.

11.5 NUMERICAL DISPERSION AND ORIENTATION

Discretizing from the PDE to the approximate form of FDE results in losses of the information. These losses are usually referred to as *numerical dispersion* and *grid orientation effect*.

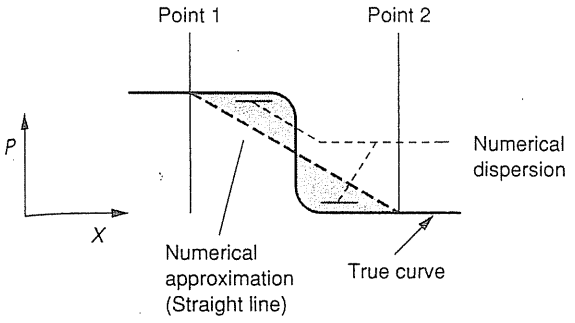

FIGURE 11-19
Numerical dispersion.

Figure 11-19 shows the true curve (PDE) and the approximate straight line (FDE) between two grids. The smoothing effect of the FDE on the PDE curve is like an additional diffusion coefficient in the PDE. This unrealistic effect is called numerical dispersion, and it can be minimized by reducing the grid size (more grids). Related references are [11-1,11-10,11-17].

False diffusion is caused by the grid block structure used. For example, in Fig. 11-20 [11-15], two fluids, one cold (0°C) and one hot (100°C), flow in parallel and quickly over the grid block from the southwest corner; physically, the temperature should maintain 100°C above the diagonal and 0°C below because the two fluids do not have time to transfer energy between them since the flow rate is fast. However, the numbers shown in Fig. 11-20 do not reflect the reality. Actually, at the midpoint, instead of seeing the flow from the southwest corner, one observes flow from south and west because of this particular grid block setup; this discretized grid generates an artificial transfer between two fluids.

De Vahl Davis, and Mallinson [11-18] characterized this unrealistic numerical phenomenon as an additional diffusion coefficient:

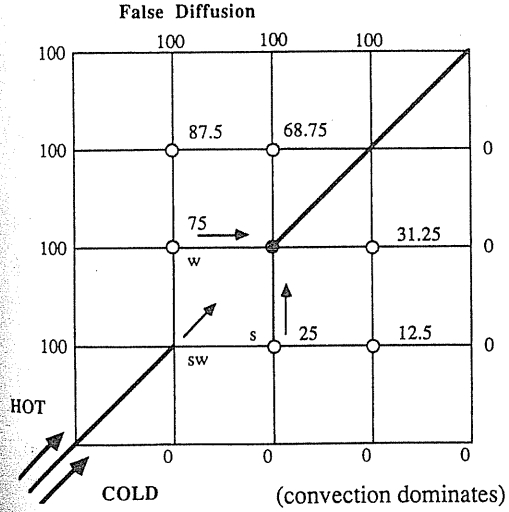

FIGURE 11-20
False diffusion effect [Patankar, 11-15].

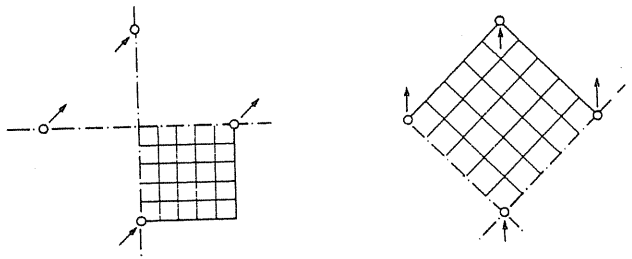

FIGURE 11-21
Parallel and diagonal five-spot patterns [Coats, 11-4, courtesy SPE-AIME].

$$D_{\text{false}} = \frac{\rho U \Delta x \Delta y \sin 2\theta}{4(\Delta y \sin^3 \theta + \Delta x \cos^3 \theta)} \tag{11.23}$$

where U is the resultant velocity and θ is the intercept angle between U and the x direction. From this criterion, the false diffusion effect could be minimized by either reducing the grid sizes (smaller Δx and Δy) or making U parallel with or perpendicular to direction x.

Coats et al., [11-4] found that, for a high mobility ratio case, different answers were obtained for parallel and diagonal grids using the five-spot pattern (see Fig. 11-21). This unrealistic effect is referred to as grid orientation effect, and it cannot be reduced by smaller grid sizes. Yanosik and McCracken [11-20] introduced a nine-point scheme (Fig. 11-22) to minimize the grid-orientation effect, but it is only valid for mobility ratios of 1 to 20. Ziegler [11-21] compared the validities of the five-point and nine-point patterns. Many other schemes [11-7,11-9,11-16] were proposed using a different weighting method to reduce the grid orientation effect and to stabilize the simulator.

HOME PROBLEMS

11.1. Write the finite difference equation at the midpoint of the five-point pattern (Fig. 11-22) for

$$\frac{\partial}{\partial x} k_x \frac{\partial \psi}{\partial x} + \frac{\partial}{\partial y} k_y \frac{\partial \psi}{\partial y} = Q$$

11.2. For a function $\psi = 8x^4 + 2x + 7$, what is the truncation error of the FDE of $\partial^2 \psi / \partial x^2$ for $\Delta x = 1$ and for $\Delta x = 0.01$?

11.3. Write the FDE at $r = 0$ (center of the well) for

$$\frac{1}{r} \frac{\partial}{\partial r} k_r \frac{\partial \psi}{\partial r}$$

11.4. For $\psi = e^{-0.05t}$ at node i, what are the optimal θ values for $\Delta t = 1$, 10, and 100, starting from $t = 0$.

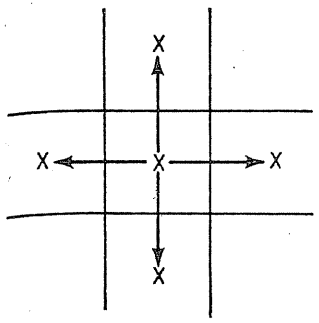

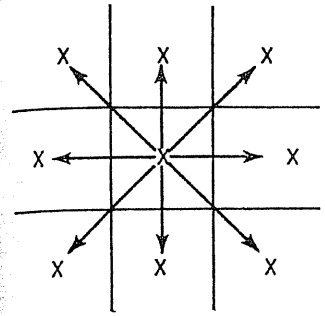

FIGURE 11-22
Five-spot and nine-spot patterns [Yanosik and McCracken, 11-20, courtesy SPE-AIME].

11.5. Starting from the Darcy equation $u = -k/\mu(\partial P/\partial x)$ for a steady state situation, prove that the equivalent permeability k_e, is the harmonic mean at the interface in series shown in Fig. 11-7, if μ stays constant.

RECOMMENDED READINGS

Aziz, K., and A. Settari, *Petroleum Reservoir Simulation,* Applied Science Publishers, New York (1979).

Crichlow, H. B., *Modern Reservoir Engineering—A Simulation Approach,* Prentice-Hall, N.J. (1978).

Peaceman, D. W., *Fundamentals of Numerical Reservoir Simulation,* Elvesier Scientific Publishing Company, New York (1977).

Thomas, G. W., *Principles of Hydrocarbon Reservoir Simulation,* International Human Resources Development Co., Boston (1982).

REFERENCES

11-1. Bell, J. B., and G. R. Shubin, "High-Order Godunov Methods for Reducing Numerical Dispersion in Reservoir Simulation," SPE preprint 13514 (1985).

11-2. Carnahan, B., H. A. Luther, and J. O. Wilkes, *Applied Numerical Methods*, J. Wiley & Sons, New York (1969).

11-3. Carriere, J. F., G. Fasanino, and M. R. Tek, "Mixing in Underground Storage Reservoirs," SPE preprint 14204 (1985).
11-4. Coats, K. H., W. D. George, C. Chu, and B. E. Marcum, "Three-Dimensional Simulation of Steamflooding," *Soc. Pet. Eng. J.*, Vol. 14, No. 6, 573–592, Dec. (1974).
11-5. Fasanino, G. (Gaz de France), private communication (1987).
11-6. Fasanino, G., J. E. Molinard, G. de Marsily, and V. Pelce, "Inverse Modelling in Gas Reservoir," SPE preprint 15592 (1986).
11-7. Frauental, J. C., R. B. di Franco, and B. F. Towler, "Reduction of Grid-Orientation Effects in Reservoir Simulation with Generalized Upstream Weighting," *Soc. Pet. Eng. J.*, Vol. 25, No. 6, 902–908, Dec. (1985).
11-8. Gill, P. E., W. Murray, and M. H. Wright, *Practical Optimization*, Academic Press (1981).
11-9. Ko, S. C. M., and A. D. K. Au, "A Weighted Nine-Point Finite Difference Scheme for Eliminating the Grid Orientation Effect in Numerical Reservoir Simulation," SPE preprint 8248 (1979).
11-10. Lantz, R. B., "Quantitative Evaluation of Numerical Diffusion (Truncation Error)," *Trans. AIME.*, Vol. 251, 315–320 (1971).
11-11. Levenberg, K., "A Method for the Solution of Certain Problems in Least Squares," *Quart. Appl. Math.*, Vol. 2 (1944).
11-12. MacDonald, R. C., private communication (1986).
11-13. Marquardt, D., "An Algorithm for Least Squares Estimation of Nonlinear Parameters," *SIAM, J. Appl. Math.*, Vol. 11 (1963).
11-14. Marshall, D. L. and L. R. Oliver, "Some Uses and Limitations of Model Studies in Cycling," *Trans. AIME,* Vol. 174, 67–87 (1948).
11-15. Patankar, S. V., *Numerical Heat Transfer and Fluid Flow,* Hemisphere, Washington, D.C. (1980).
11-16. Potempa, T. C., "Mobility Weighting in Numerical Reservoir Simulation," *Soc. Pet. Eng. J.*, Vol. 25, No. 4, 565–572, Aug. (1985).
11-17. Todd, G. R., P. M. O'Dell, and G. J. Hirasaki, "Methods for Increased Accuracy in Numerical Simulators," *Soc. Pet. Eng. J.*, Vol. 12, No. 6, 515–530, Dec. (1972).
11-18. de Vahl Davis, G., and Mallinson, G. D., "False Diffusion in Numerical Fluid Mechanics," Univ. of New South Wales, School of Mech. and Ind. Eng. Report 1972/FMT/1 (1972).
11-19. Walker, C. J., and R. V. Huff, "Feasibility of Inert Gas Cushions in Gas Storage," report of investigation 6534, Bureau of Mines, U.S. Department of Interior (1964).
11-20. Yanosik, J. L., and T. A. McCracken, "A Nine-Point, Finite-Difference Reservoir Simulator for Realistic Prediction of Adverse Mobility Ratio Displacements," *Soc. Pet. Eng. J.*, Vol. 19, No. 4, 253–262, Aug. (1979).
11-21. Ziegler, V. M., "A Comparison of Steamflood Strategies: Five-Spot Pattern vs. Inverted Nine-Spot Pattern," SPE preprint 13620 (1985).

CHAPTER 12

CONVERSION OF DEPLETED GAS AND GAS/CONDENSATE FIELDS TO GAS STORAGE RESERVOIRS

PREFACE TO GAS STORAGE: A WORTHY GOAL

Developing a Mental Model for a Gas Storage Reservoir (by Donald L. Katz)

Ways are presented to develop a mental model against which new information can be tested. There are principles of behavior that establish how gas bodies respond to gas production, gas injection, or confining water movement. Even unwanted gas movement responds to engineering principles of pressure difference as a driving force and of gas flow following the route of least resistance.

Starting with geological knowledge, the boundaries of the gas phase need identification as to position and possible movement. Likewise, the status of the wellbores into the storage zone and their ability to confine the gas to the inside of the casing need continued inquiry.

Water movement in the storage zone due to gas pressures should be observed. Likewise, observations of water zones in layers of rock between caprock and surface are an indication of gas movement into such zones.

The concept of potential theory in unsteady state gas or water movements is important. The deviations detected from this theory indicate the anomalies worth noting.

The integration of new information into the conceptual model is a way to verify or modify the model. Such matching of information gives insight into impending changes about to occur.

The knowledge that might be brought to bear on a problem is found in various places. This treatment attempts to identify important sources and presents ways to handle many of the problems that may arise. The attention to a model concept is likely to be most fruitful.

The reservoir engineering of gas and oil fields has been discussed earlier. This chapter deals with the design and operation of gas storage reservoirs [1-2]. Gas storage is the warehouse for the natural gas distribution system. Storage provides for the cold weather needs of the space-heating market by putting a high-deliverability supply nearby. Before treating the conversion of gas reservoirs to underground storage usage, a statement concerning the need is in order. Also, the extent of the industry is set forth.

12.1 THE NEED FOR GAS STORAGE

Gas storage primarily is used to handle the increased fuel need for space heating in cold weather. It levels the load for the pipeline carrying gas from the gas supply—often a distance of over 1000 miles (1600 km) to the market area (see Fig. 1-7). For example, offshore gas fields in Louisiana supply pipelines to the Detroit area in Michigan. Many gas suppliers now could not provide the fluctuation in gas flow rate needed in winter even if the pipelines could carry the varying load.

Variation in space heating needs is measured in degree-days, using 65°F (18.3°C) mean temperature as the base temperature [1-1]. A mean temperature of 45°F (7.2°C) corresponds to 20 degree-days. For space heating, Fig. 12-1 shows the variation in heating loads for the Detroit area, totaling 6404 degree-days in any one heating season, November through March. Table 12.1 gives data for various metropolitan areas.

Gas distribution loads include commercial establishments and industrial plants geared to the work week. Homes have hot water heaters, kitchen stoves, refrigerators, etc. Summer loads may be especially low, such as on the Labor Day weekend, when much of the industrial load usually shuts down.

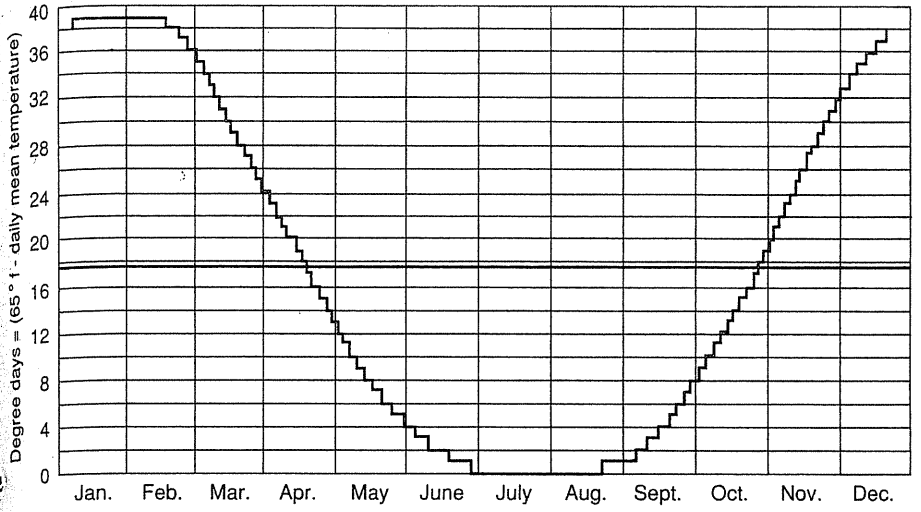

FIGURE 12-1
Normal degree-days for Detroit area [Katz et al., 1-1, courtesy McGraw-Hill Publishing Co.].

The growth in gas storage paralleled the conversion of space heat from coal or oil to natural gas. A large expansion of gas line installations took place in the late 1940s and 1950s, some areas reaching 90 percent gas usage for space heating. The growth in storage gas is shown from AGA statistics in Fig. 1-9. The location of gas storage reservoirs is shown in Fig. 1-10 (AGA), limited to areas with sedimentary rocks. Table 1.3 gives statistics on the gas storage industry.

12.2 BASIC CHARACTER OF A STORAGE RESERVOIR

A section and a plan view of a reservoir equipped for storage are shown in Fig. 12-2. The storage container is a porous solid with a caprock overhead to prevent

TABLE 12.1
Annual degree-days (65°F base) for various locations in North America

Area	°F-days below 65°F	Area	°F-days below 65°F
Albuquerque	4386	Omaha	6100
Atlanta	2826	Portland, Maine	7618
Bismarck	9033	San Francisco	3421
Detroit	6404	Seattle	5275
Houston	1388	St. Louis	4699
Los Angeles	2015	Tampa	674
New York	4965	Winnipeg, Manitoba	10,881

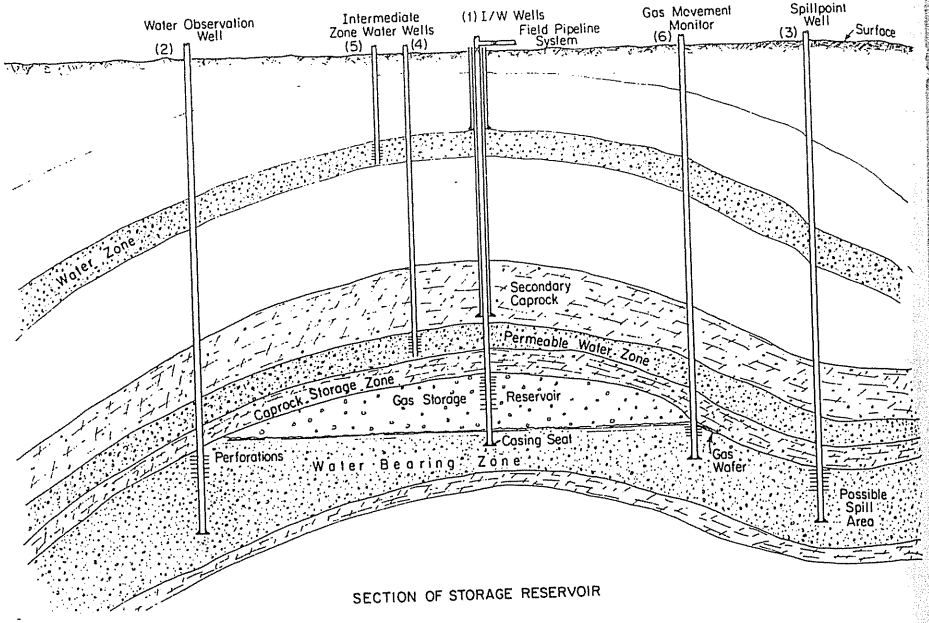

FIGURE 12-2
Schematic section and plan view of gas storage field [Katz, 14-9, courtesy AGA].

vertical migration. Water in the storage zone underlies all or part of the gas-filled sand or carbonate. Wells designated I/W, for "input and withdrawal," are completed in the storage zone. Observation wells are completed in the water-bearing porous media to permit observation of the pressure and any migrating gas.

Depleted gas reservoirs are prime candidates for conversion to storage. The size of the reservoir is determined by calculation from geological data or from the gas production and reservoir pressures. Such calculations are relatively simple for cases with little or no water movement. In considering a depleted gas field, it should be recognized that as much as 80 to 100 percent of the initial gas content in a storage reservoir will be withdrawn within 120 days in a given year. This requires many more wells than are used for production, and an enlarged gathering and injection pipeline system from the wells to a central station.

The typical injection and withdrawal pattern in storage is shown by Fig. 12-3. A delivery system can be installed to cover the market demand for the year, and ideally the unused gas in summer is stored for use in winter. Some flexibility is needed, since variation in weather causes varying demands. Storage fields and pipelines may require some period of reduced load in summer for testing.

The storage gas is considered in two parts. The base gas provides for sufficient gas pressure to produce gas adequately at the end of withdrawal. The gas at pressures above the base pressure is termed *working storage gas* and makes up the annual turnover of gas. Figure 12-4 [1-38] illustrates the pressure–gas quantity relation, showing base gas and working storage. The choice of base pressure is an economic and investment decision gleaned from an engineering analysis of seasonal gas volumes, delivery rate, number of wells drilled, and horsepower to be installed.

The use of pressures above discovery, a *delta pressure*, gives added usage for a given container (larger than the discovery gas quantity). This practice has demonstrated large economic benefits to the storage industry for converted gas

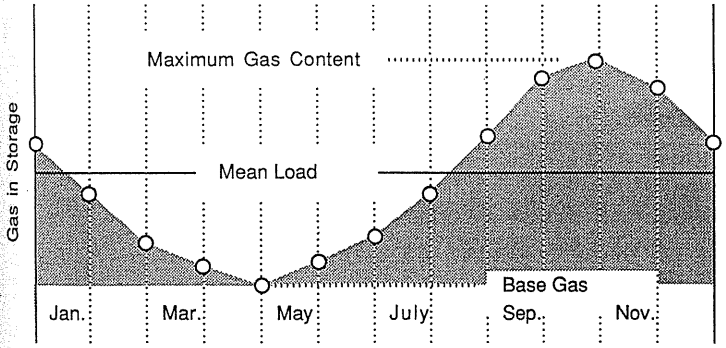

FIGURE 12-3
Typical gas injection and gas withdrawal schedule for storage reservoirs.

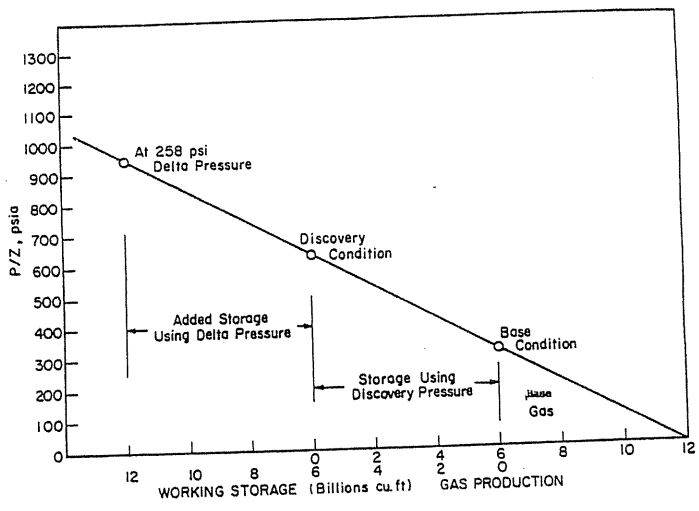

FIGURE 12-4
P/Z versus gas content for hypothetical gas reservoir.

reservoirs and is a built-in mode of operation for water drive and/or aquifer storage reservoirs. An AGA monograph [1-38] discusses the issue in great detail. In gas storage, pressures in the earth may be up to 0.7 psi/ft (15.83 kPa/m). Figure 12-5 is a chart of the hydraulic head of pure water and brines.

Pressures in operating storage reservoirs are noted daily or weekly at key observation wells. Storage cycle curves for field A are relatively close, as shown in Fig. 12-6, while typical curves for lower-permeability reservoirs may show more hysteresis (Fig. 1-8).

12.3 PROCEDURES FOR CONVERSION OF GAS FIELDS TO STORAGE

Many gas storage fields are partially depleted gas fields that have been converted to storage. This section gives a brief review of the design procedures for the conversion. The following steps may be followed in designing the storage facility:

Gathering of geological and engineering information in primary
Assessing the mechanical condition of wells
Determining the working storage content of the reservoir
Determining the wells needed
Considering compression, field lines, and conditioning of gas

In order to find the working storage content of the reservoir, the range of pressures used must be selected. The upper pressure selected is based upon the

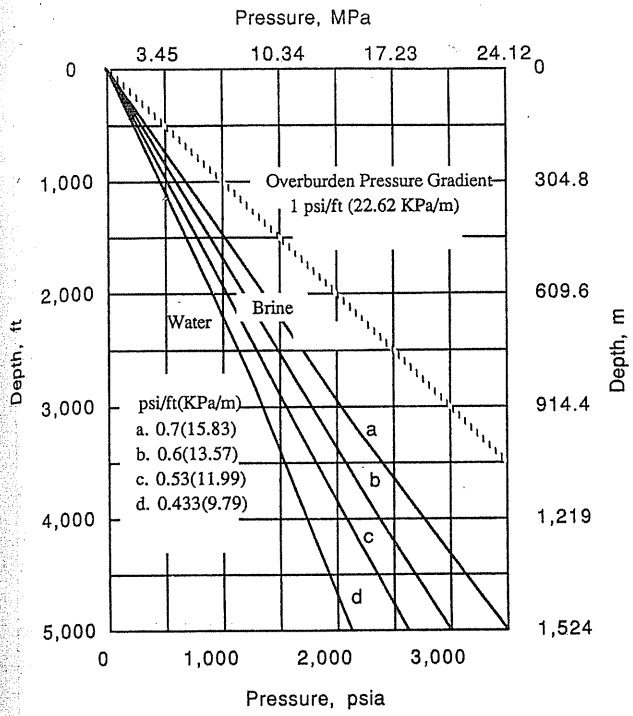

FIGURE 12-5
Fluid pressure gradients in gas storage [Katz et al., 1-1, courtesy McGraw-Hill Publishing Co.].

information available, particularly the mechanical condition of the wells. The pressure range also has much to do with the flow capacity of wells.

Record of Facilities and Operations

The first job is to gather information on the field, such as the following:

Geologic information
Initial reservoir pressure
Gas production versus reservoir pressure
Reservoir temperature
Gas composition or gravity
Wells drilled, locations, depths, and core data
Logs on wells
Reservoir structure, isopach maps
Degree of water drive

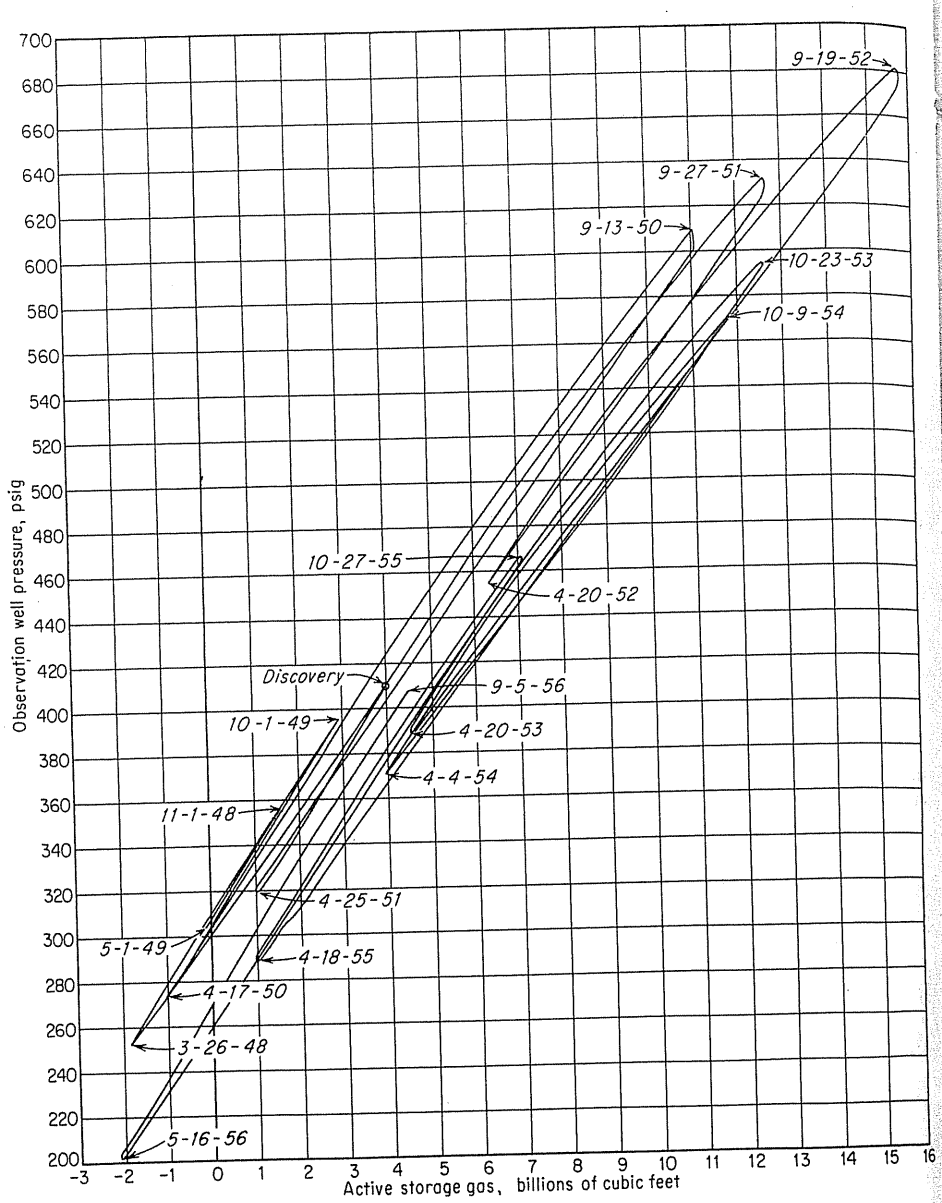

FIGURE 12-6
Pressure-production history of field A [Katz & Coats, 1-2].

Well flow capacity
Mechanical condition of wells
Areal map showing neighboring reservoirs

It must be determined that all wells drilled to the producing horizon can be located, checked by cement bond logs, etc., and made mechanically sound. Where poor bonds exist, squeeze cementing is in order. When the casing is corroded, a liner may be cemented in or set on a packer with a noncorrosive fluid in the annulus. Even wells classed as dry holes should be opened, recemented, or cased as observation wells. When the mechanical condition is known and the character of the caprock is known, the upper operating pressure can be determined. Often new casing tops and heads are installed because of corrosion and new pressure levels of operation.

Selection of Top Reservoir Pressure

Most gas fields are discovered at a pressure level corresponding to a head of water or brine, from 0.43 to 0.52 psi/ft (9.73–11.76 kPa/m) of depth. Experience shows that adding a delta pressure above discovery up to 0.65 psi/ft (14.70 kPa/m) of depth is commonplace with good caprocks, and 0.70 psi/ft (15.83 kPa/m) has been used. Since the use of the field at the highest pressure level possible will normally give the maximum storage capacity and the highest flow capacity for the wells, a pressure cycle to this maximum pressure is normally the goal of the design. In selecting the lower or base pressure, the horsepower requirements for compressing the gas to market, production problems, and economics are considered. Should there be a thin caprock, or no collector zone between the caprock and the surface, or unfavorable environmental situations, etc., the discovery pressure may be used as the upper pressure.

Storage Capacity

When the pressure-production history is available, a plot of reservoir pressure over compressibility factor (P/Z) versus gas production will indicate the total gas initially in the field and permit computation of the gas pore space. The P/Z data versus production plot will show the abnormal behavior (P/Z values are higher than the predicted values) if there is significant water drive. For a low-pressure depleted field, the initial reservoir pressure and the gas production can be converted to a simple volume of gas produced per pound pressure drop.

Wells Required

Field designs are matched to peak load requirements, usually near the end of the severe weather period. For example, when 70 percent of working storage

has been produced, the lower reservoir pressure is predicted and used with well performance curves to obtain well flow. Then, the number of wells required may be ascertained, along with the horsepower requirements if the gas is compressed after withdrawal. Frequently, the delivery pressure on withdrawal is set for free flow out.

Examples are the best way to illustrate design procedures. It should be noted that few if any sets of data on a reservoir are complete and that judgment is needed to fill in the gaps. Earlier studies have given designs and performance data [1-2] for Goodwell, Loreed, Ancona, and Belle River Mills reservoirs.

12.4 THE MUTTONVILLE RESERVOIR: AN EXAMPLE

The Muttonville reservoir is a Niagaran reef reservoir in southeastern Michigan. It was discovered in 1966 and converted to storage in 1975 by the American Natural Resource Companies. Tables 12.2 and 12.3 give pertinent data, including general data and the reservoir pressure-production information. Table 12.4 gives the idealized stratigraphic section, and Table 12.5 the early gas analyses. Figure 12-7 is a structure map of the Niagaran reef. Figure 12-8 is a P/Z–versus–primary production line, indicating a constant volume for the reservoir.

The type of feasibility design studies carried out by students is quite similar to a "first pass" evaluation in industry. In the final design, computerized calculations are more likely to be used than pocket calculators.

Example 12.1. Given the data on Muttonville, design the reservoir for gas storage. The suggested top pressure is 0.65 psi/ft top reef. The supply gas pressure is 740 psig, and the delivery pressure is 850 psig. Storage gas gravity is 0.6.

The deliverability curve, Q vs. ΔP^2, for the seven production wells runs through the points 3700 Mcf/day at 50,000 psia^2 and 15,000 Mcf/day at 300,000 psia^2.

(*a*) Find the annual storage capacity (working), base gas pressure, and gas quantity.

(*b*) Using a maximum day flow of 1/40 of working content and maintaining this daily production until 75 percent of working capacity is produced, how many added I/W and observation wells are required and recommended?

(*c*) Find the horsepower required to inject and/or deliver gas.

Solution: Muttonville design. Since the data were reported at the wellhead, it is necessary to convert them to bottom hole or reservoir conditions for careful work. The static wellhead pressure and subsequent wellhead pressures are calculated using Eq. (6.15). With the ground temperature at 48°F and the reservoir at 74°F, the mean static wellbore is at (48 + 74)/2 = 61°F for a mean wellbore temperature of 61 + 460 = 521°R (289.4 K). Table 12.3 gives the calculated reservoir pressures.

The next step is to obtain the reservoir Z to calculate P/Z. The gas analysis gives a reduced temperature of 1.466 rather than the 0.65-gravity chart's 1.425. The

TABLE 12.2
Data of storage field, Muttonville

Storage field: Muttonville; township: T.4N-R.14E.; county: Macomb.

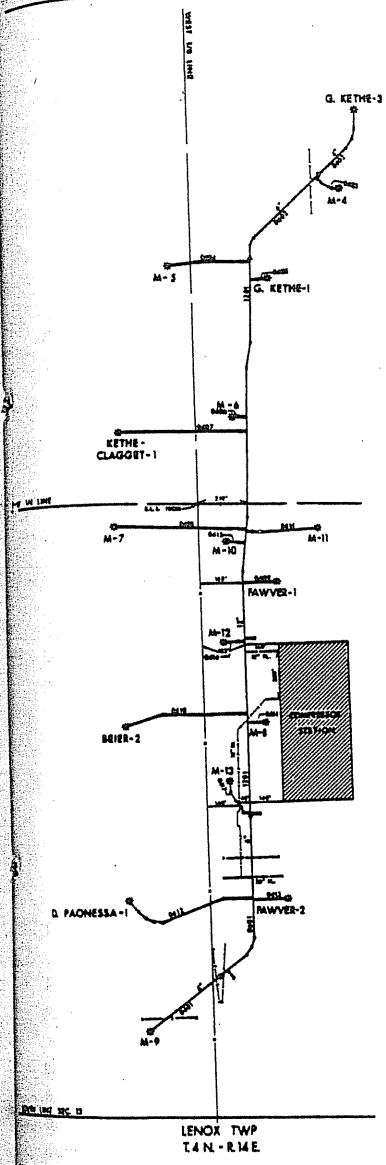

Discovery year	1966
Storage activation year	1975
Wellhead discovery pressure, psig	1217
Surface temperature 100′	48°F
Reservoir temperature	74°F
Reservoir limits, acres	280
Storage formation	Niagaran reef
No. injection/wdrl. wells	17
No. observation wells	1
Max. formation thickness, ft.	276
Max. wellhead operating pressure, psig	1525
Min. wellhead operating pressure, psig	300
Average permeability, md	19.1
Average porosity, %	6.0
Original reserves, Bcf	10.72
Base gas: Native, Bcf	1.64
Injected, Bcf	0.67
Cert. working gas, Bcf	11.1
1982 working capacity, Bcf	10.8
Average depth, ft.	2600
Top of formation (depth/datum), ft.	2562 (−1887)
Original g/w contact, ft.	2861 (−2186)

Common well completions

Perforated completions

8-5/8″ Surface csg.	@ 420′ ±
5-1/2″ Product csg.	@ 2950′ ±
Perforations (avg.)	2695′–2740′
Acre · ft, reservoir	43,200
Original production wells	7
Storage facility wells	10
Total	17

H_p installed 2 × 3200 hp used for injection and withdrawal

Gathering system

15 psi ΔP	@ 300 MMcfd
25 psia ΔP	@ 400 MMcfd

TABLE 12.3
Primary production of gas at Muttonville and corresponding pressures

Date	Wellhead pressure, psig	Cumulative gas production, MMcf	Reservoir pressure, psia	Z	P/Z, psia
1966	1217.0	0	1337.5	0.815	1640
12/20/67	1146.5	697.0	1259.5	0.831	1515
12/10/68	913.0	3031.0	1002.3	0.860	1165
10/29/69	758.6	4533.0	833.3	0.877	950
11/18/70	440.6	7204.0	488.1	0.924	528

reservoir P/Z's give the data plotted on Fig. 12-8, showing an initial gas content of 10.7 Bcf (gas in place, or GIP, in standard conditions).

The pore volume is computed:

$$\text{Pore volume} = \text{GIP} \times \frac{T}{T_{sc}} \frac{P_{sc}}{P/Z}$$

$$= 10.7 \times 10^9 \frac{534}{460 + 60} \frac{14.7}{1640} = 98.5 \times 10^6 \text{ ft}^3$$

The reservoir pressure of working and base storage gases for the 0.65-psi/ft upper pressure level is $0.65 \times 2650 = 1722$ psia. Using the Z chart for 0.6-gravity gas at 1725 psia and 74°F, $Z = 0.783$ and $P/Z = 2203$ psia. Assuming the base gas pressure is 300 psia wellhead, which is equivalent to 333 psia sandface, the base gas $P/Z = 333/0.95 = 350$ psia. Thus,

$$\text{Working storage} = \text{top storage capacity} - \text{base gas}$$

$$= 10.7 \times \frac{2203}{1640} - 10.7 \times \frac{350}{1640}$$

$$= 14.4 - 2.3 = 12.1 \text{ Bcf}$$

This may be determined graphically as shown on Fig. 12-9. The delta pressure is $1725 - 1337 = 388$ psia.

The peak day requirement is $1/40 \times 12,100 = 300$ MMcf/day. For 75 percent working gas withdrawal, there is $14.4 - 12.1 \times 0.75 = 5.3$ Bcf left in the reservoir.

By reading Fig. 12-9 at 5.3 Bcf content, $P/Z = 810$, or by calculating, $P/Z = 5.3 \times (2203/14.4) = 810$. At 720 psia, $Z = 0.89$, so $P = 810 \times 0.89 = 720$ psia where the corresponding wellhead is 720/1.07 = 673 psia. The ratio of sandface pressure to wellhead pressure is approximated by 1.07 (e.g., 10/29/69 data on Table 12.3 shows the ratio = 833.3/[758.6 + 14.7] = 1.077). Thus, the minimum wellhead pressure after withdrawal of 75% working gas is set to be 675 psia.

Wellhead flow rates for various wellhead pressures as plotted on the back pressure plot, Fig. 12-10, are shown in Table 12.6. So, *20 wells* are required

TABLE 12.4
Idealized stratigraphic section of Muttonville gas field, Macomb County, Michigan

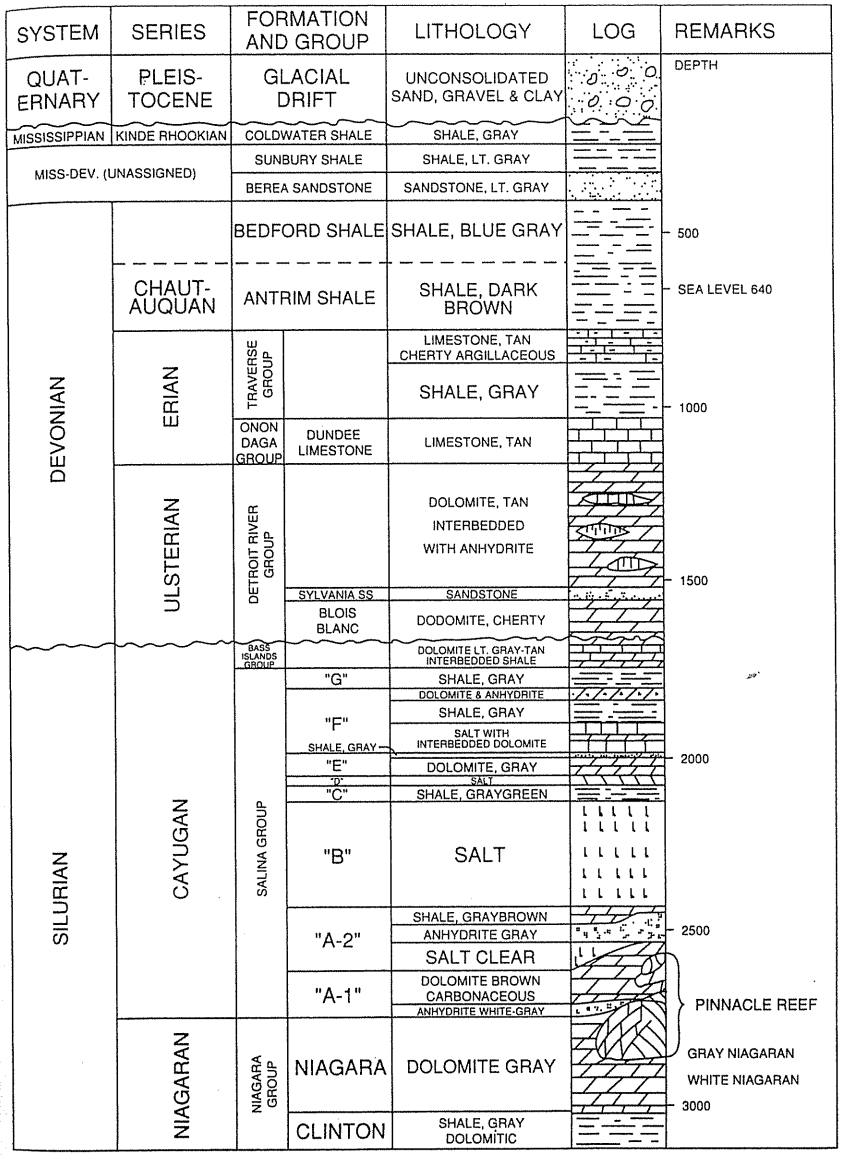

TABLE 12.5
Muttonville gas analyses

	Date	
	10/24/67	**5/1/70**
N_2	2.24	2.37
CO_2	0.61	0.05
He	0.12	0.10
C_1	87.73	87.84
C_2	4.79	5.03
C_3	2.21	2.34
i-C_4	0.91	0.94
n-C_4	0.64	0.57
i-C_5	0.23	0.31
n-C_5	0.18	0.23
C_{6+}	0.32	0.20
Gas gravity	0.654	0.648
Calculated heat value	1092 Btu/ft^3	1099 Btu/ft^3 (sat.)
Calorimeter	—	1098 Btu/ft^3 (sat.)

Primary gas gravity 0.65; storage gas 0.58

if the wellhead flowing pressure is chosen as 395 psia higher than the minimum values of 300 psia shown in Table 12.6. (In practice, 10 facilities were added to 7 primary wells during the conversion; one well is the key well and 16 are functioning I/W wells.)

The power required to lift 300 MMcf/day from 380 to 850 psia on delivery (withdrawal) can be calculated using an enthalpy-entropy (H-S) chart (Fig. 4-53): $S = -6$ (Btu/lb · mol °F), $H = 300$ Btu/lb · mol at 380 psia, 80°F, and $S = -6$, $H = 1030$ at 850 psia, 180°F. Then,

$$\text{Horsepower } H_p = 0.0432 \times (1030 - 300) \times 300 = \underline{9460 \text{ hp}}$$

Actually two 3200 hp's or one 6400 hp was installed since the wells are a little better and the load generally is not that high at such a low reservoir pressure. The field recorded a 10 Bcf delivery in a season.

HOME PROBLEMS

12.1. The primary production data of the Bell River Mills gas field are as follows:

Year	Cumulative production, Mcf	P/Z
1962	0	1400
1963	6,752,900	1200
1964	11,733,642	1080
1965	18,644,574	889

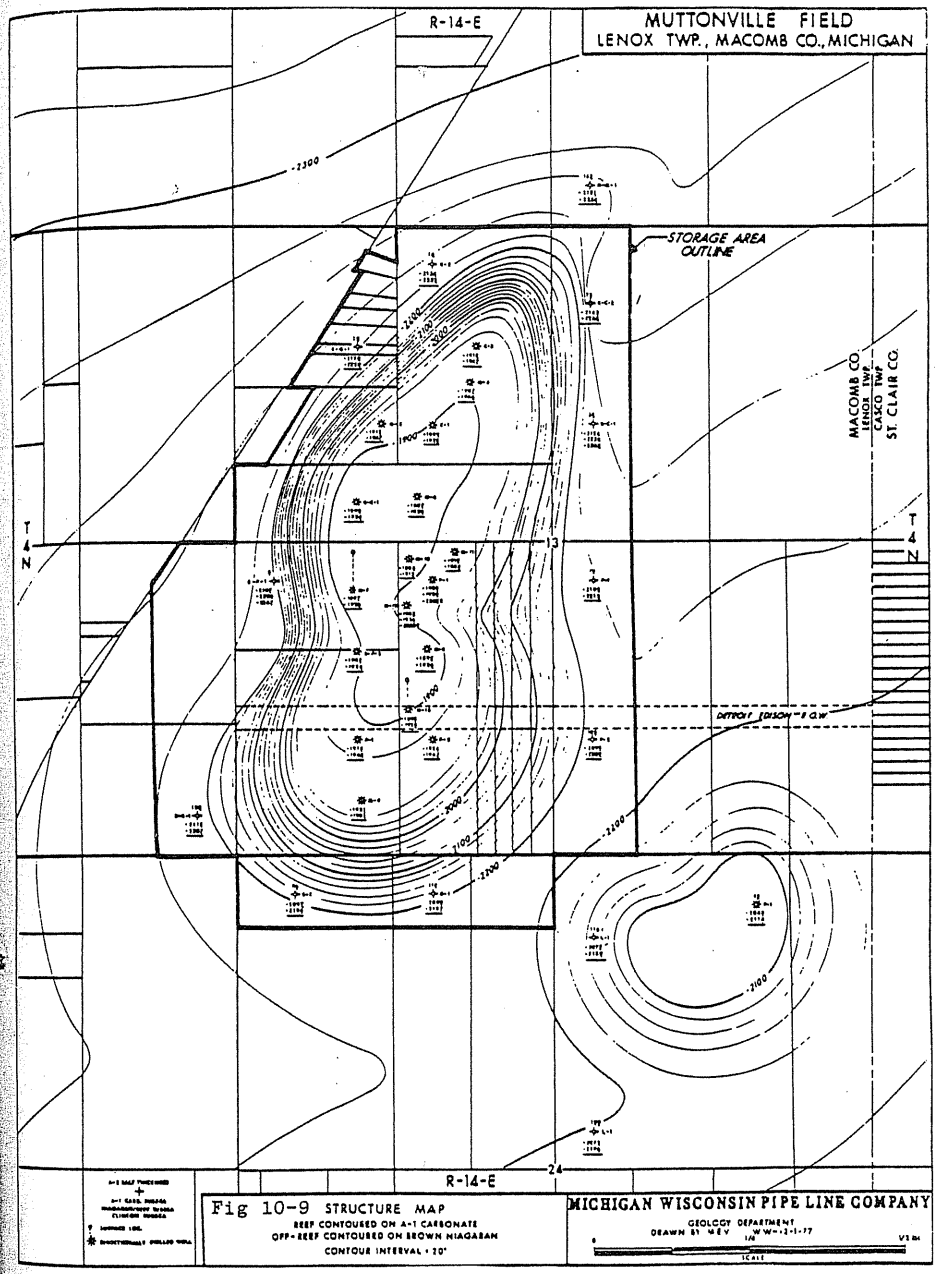

FIGURE 12-7
Structure map of Muttonville gas field.

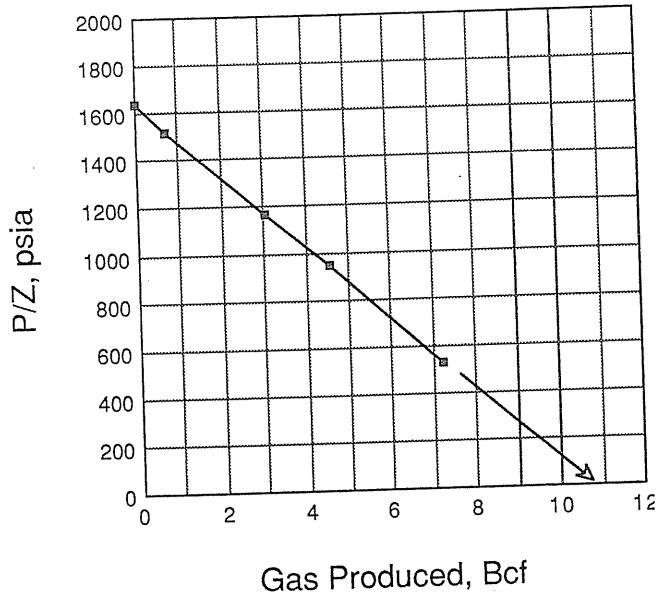

FIGURE 12-8
P/Z versus production in primary for Muttonville.

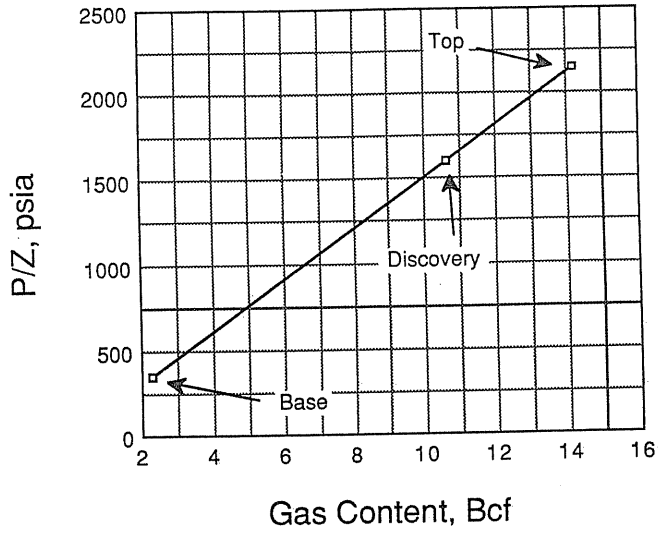

FIGURE 12-9
P/Z versus gas in place for Muttonville development.

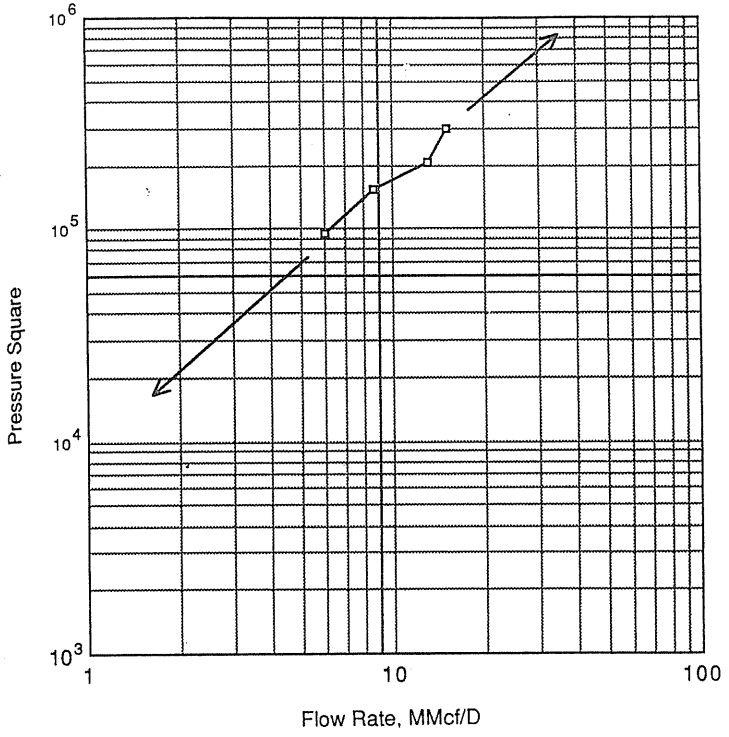

FIGURE 12-10
Back pressure plot based on wellhead pressures for Muttonville development.

TABLE 12.6
Wellhead static, flowing pressures and corresponding flow rates

Wellhead static (P_1)	Flowing (P_2)	$\Delta P^2 \times 10^{-3}$	Flow rate, MMcf/day	Wells for 300 MMcf/day
675	600	95.6	6	50
675	550	153.1	8.7	34
675	500	205.6	13	23
675	395	299.6	15	20
675	300	365.6	17	18

What is the total gas in place of the field? The field was intended to be converted to gas storage at 200 psia above the original discovery pressure. Estimate the minimum capacity of the storage field now.

12.2. The production-pressure history of reservoir C is given by Fig. 12-11. This reservoir is being considered for gas storage. The stored gas would have a gravity of 0.60; the reservoir is at 2000 ft and 74°F. The back pressure curve for a typical well on 40-acre spacing is given by $Q = (\Delta P)^{0.6}$, with Q in Mcf per day and pressure in psia. Figure 12-12 gives a static pressure gradient for the wells of reservoir C.

(*a*) What was the initial gas content of the reservoir?

(*b*) What would the seasonal working storage content (top storage, cyclic) be for a lower reservoir pressure of 300 psia and upper pressures at (1) discovery, (2) 0.58 psi/ft depth, and (3) 0.65 psi/ft depth?

(*c*) How many wells would be needed to deliver 1/35 of the season's storage volume in one day after 60 percent of the season's top storage volume has been produced under case (*b*)(2) above, using a 50 psi drawdown at the sandface?

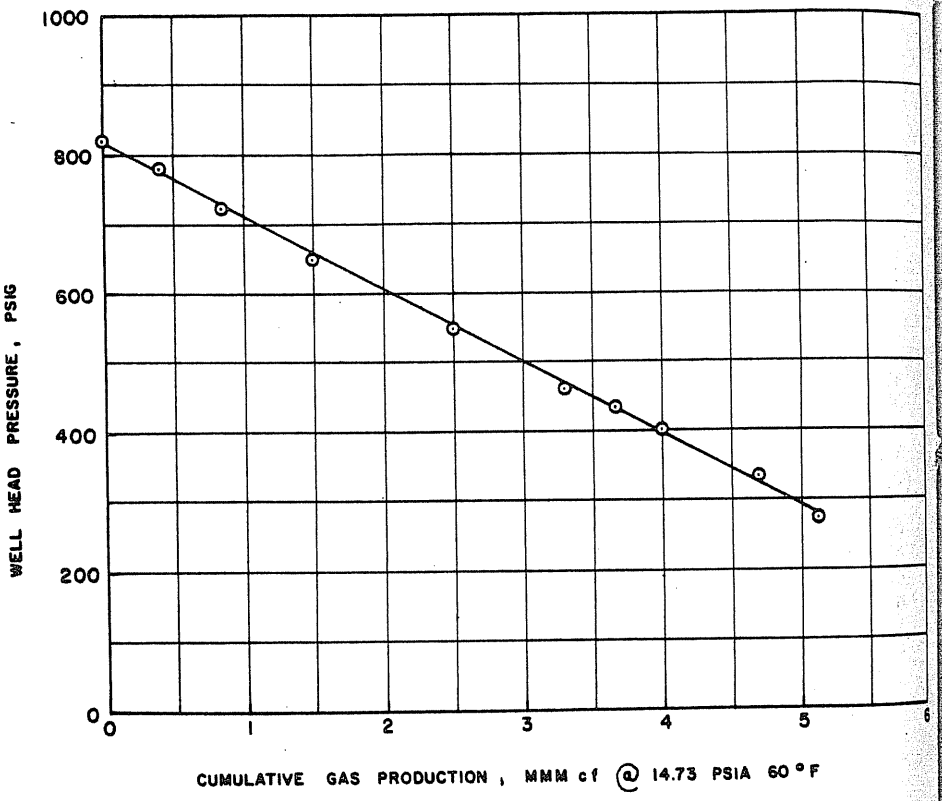

FIGURE 12-11
Wellhead pressure–cumulative production curve of reservoir C, 2000 ft, 74°F [Katz & Coats, 1-2].

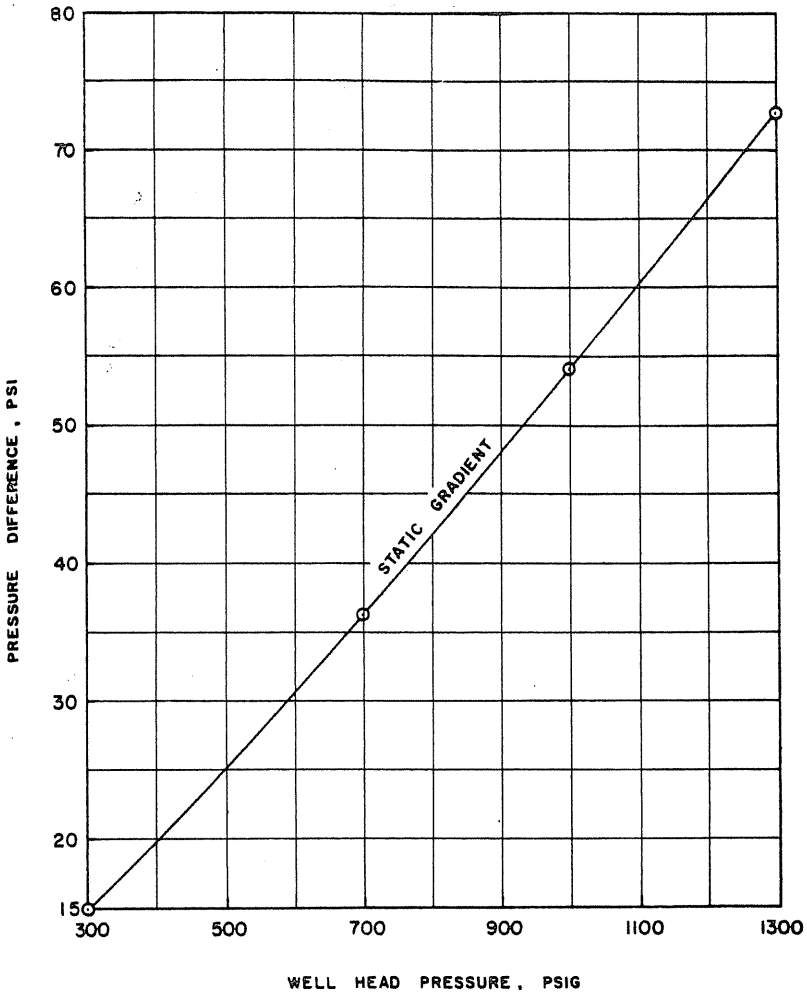

FIGURE 12-12
Pressure gradient in static wells 2000 ft deep for 0.6-gravity gas [Katz & Coats, 1-2].

RECOMMENDED READING

Katz, D. L., and K. Coats, *Underground Storage of Fluids*, Ulrich's Book Co., Ann Arbor (1968).

CHAPTER 13

GAS STORAGE IN AQUIFERS

Aquifer Storage reservoirs are zones that originally bore only water and have been converted to gas reservoirs by gas injection. Gas displaces water as described in Chapter 8. Once the aquifer gas reservoir has been developed through the stage where confinement by the caprock has been affirmed, the operation and engineering considerations are similar to those for water drive primary gas-producing reservoirs that have been converted to gas storage. There are few distinctions between manmade gas storage reservoirs in water-bearing zones and natural water drive storage reservoirs once the early development stages have passed.

The first part of this chapter describes the location and testing of a proposed aquifer storage site, along with the initial steps in gas injection. The second part treats water drive gas reservoirs, including discussion of their performance in primary and the later conversion of an aquifer to storage. A later section covers the operating characteristics of storage reservoirs when pore volume and pressures are affected by water movement in the usual storage cycle.

13.1 LOCATING AND DEVELOPING AN AQUIFER STORAGE RESERVOIR

The character of underground structure and rock layers desired for an underground aquifer site is illustrated by Fig. 1-5. First, there is a structure under which gas may accumulate. Second, there is a container, a porous bed of rock into

and out of which fluids may flow through wells. Third, there is a water-filled caprock, which prevents the stored fluid from rising vertically due to buoyant forces. Fourth, there is enough overburden to allow storage at pressures much above atmospheric. Depth is considered an element of importance. Economic consideration requires a certain amount of depth, generally 1000 ft (305 m) or more, to permit fluid pressures high enough to store satisfactory quantities in a given space and to move gas in and out readily. Fifth, there is water to confine the stored fluid from all directions. Below the stored gas, water moves under a pressure gradient to make room for the stored gas, while in the caprock it seals the tight rock from penetration by the gas phase.

In a free system, oil and gas float to the top of water, and so it is in the underground porous media container. A storage reservoir caprock of low permeability and high threshold pressure is needed to hold these buoyant fluids below it by surface forces. The caprock must not only stop vertical movement, but must also be shaped to prevent lateral movement. The anticline or inverted saucer type of structure is common. The hill in an underground structure may well disappear at the surface of the earth and so may be difficult to locate. A discussion of geological processes will show why few underground structures continue to the surface.

If the gas stored goes beyond the lower rim of the caprock, it will *spill* out of the storage area. The height of the storage zone above the spill depth is called *closure*.

The steps in the procedure for locating and initiating an aquifer storage zone are given in Table 13.1.

TABLE 13.1
Steps in procedure for locating and developing an aquifer storage reservoir

1. Study state geological records, U.S. Geological Survey records, and geological journals for area in question.
2. Look for outcrops in quarries, mines, river banks, etc.
3. Review water well data, especially deeper ones for villages or commercial plants.
4. Seek any records of dry holes in search for oil. Possibly make seismic or gravity studies.
5. Establish a likely geological column, select a shallow marker bed for structure, and take cores to obtain a near-surface structure.
6. Drill a deep well through the contemplated storage zone, and examine cores, water levels, and brines.
7. Do a feasibility study of the storage project.
8. Drill more deep wells to give structure and interval for extending shallow structure maps.
9. Select possible collector zone above caprock, drill wells for monitoring and pump test.
10. Conduct pump test to evaluate reservoir in-situ permeability and evidence of water movement through caprock.
11. Refine feasibility study.
12. Establish closure, possible spill area.
13. Obtain governmental permission to proceed with project.

13.2 SOURCES OF INFORMATION

Potential structures for aquifer storage of natural gas are located (1) by reviewing geological studies already made by state or federal agencies, (2) by gathering well data, (3) by geophysical surveys, and (4) by shallow core drilling. Many potential structures are found to have too small a closure, under 50–75 ft (15.24–22.86 m), forcing a project to be abandoned. This discussion of development assumes that preliminary geological data have been assembled and that sufficient closure for the structure will be proven.

The storage rock should extend over distances of tens of miles. The aquifer must absorb by pressure rise the volume of water displaced. The rock porosity represents the storage capacity and is nominally found in the 12–25 percent bracket. The permeability needs to be high enough to allow sufficient gas flow rates around the wellbore and to permit water displacement by an acceptable pressure differential between the gas phase and the undisturbed water phase. This pressure difference, the *delta pressure*, is limited by the threshold pressure for gas penetrating the caprock. The likelihood of natural fractures in the caprock is a concern, should there be severe folding.

The caprock, frequently a shale, is of low permeability, like 10^{-4} to 10^{-6} md, which corresponds to a threshold displacement pressure of 400–1500 psi (2.8–10.3 MPa). A cored well through the caprock and storage zone is used in the evaluation of a specific site. Tests should show a displacement pressure more than twice the expected delta pressure.

The earlier text [1-2] gave a thorough illustration of the development of the Ancona–Garfield aquifer in Illinois. This is now a single storage reservoir, which reached 160 Bcf (4.53×10^9 m^3) of total injected gas and delivered gas at rates over 700 MMcf/day (19.8 MMm^3/day), with more than 45 Bcf (1.27×10^9 m^3) withdrawal per season. Some of the data procured at the time of development and initial feasibility design are repeated here.

13.3 DATA AND FEASIBILITY DESIGN FOR ANCONA AQUIFER GAS STORAGE PROJECT (1962–1967)

The following development information is from the text *Underground Storage of Fluids* [1-2]:

> The Ancona-Garfield storage field in Livingston and LaSalle Counties, Illinois, is the second storage project developed by Northern Illinois Gas Company. The Mt. Simon sand at 2,150 (−1,510) feet is used to store gas in two closely associated structures which have merged. Gas injection at Ancona started in August 1963 and at Garfield in July 1964. The senior writer was associated with the project since its beginning and with presentations made to the Illinois Commerce Commission. Much of the information here came from the exhibits and testimony, while the remainder was supplied recently by the company.

The Ancona project will be used as a vehicle for discussing the development of aquifer storage reservoirs, and experiences and information on other projects will also be included. The development will start with geology and go on to the pump test, gas injection, and production experiences.

Geology

The presence of the structure at Ancona–Garfield was learned from shallow correlation drilling based on a regional map developed from state records. The structures are located southwest of Chicago between Livingston County and LaSalle County. The basic geological information was obtained by drilling and logging over 100 correlation wells to depths varying from some 300 to 825 ft (91.44–244 m) in depth. Most of these wells reached the St. Peter sand. A total of 8 Mt. Simon wells were drilled at Garfield and 10 at Ancona before gas injection was started. A total of 10 wells were cored, sampling the lower Eau Claire and the top of the Mt. Simon zone, and cores of the Galesville and St. Peter formations were taken. The wells were logged (using gamma ray lateral logs, micro logs, and sonic logs) and cuttings examined.

Referring to Figs 13-1 and 13-2, a columnar section, and starting from the top, the Pleistocene system is glacial drift composed of 20 to 60 ft (6–18 m) of clays, sand, and gravel. The following applies equally well to the Garfield and Ancona areas:

The Pennsylvanian system ranges in thickness from about 110 to about 300 ft (33.5–91.4 m), and is composed of siltstone, micaceous shale, and sandstone, with minor lenses of limestone. Several beds of coal and black carbonaceous shale are also found in the Pennsylvanian system at Garfield.

The Ordovician system, which lies below the Pennsylvanian, is primarily a carbonate section. In descending order, the formations of the Ordovician system are the Maquoketa, which varies from 0 to 120 ft (0–36.6 m) in thickness and is found only on the edges of the Garfield structure; the Galena, Decorah, and Platteville limestones and dolomites, which are, in total, approximately 390 feet (119 m) thick; the St. Peter sandstone, which is about 155 feet (47 m) in thickness; the Shakopee formation, which consists of approximately 200 ft (61 m) of sandy dolomite; the New Richmond sandstone, which is approximately 135 ft (41 m) thick; the Oneota dolomite, which is approximately 220 ft (67 m) thick; and the Gunter formation, which is approximately 15 ft (4.57 m) thick.

Below the Ordovician system are beds of Cambrian age. The upper formations, which are essentially all dolomite and sandstone, are the Eminence, the Potosi, the Franconia, the Ironton, and the Galesville. The combined thickness of these formations is approximately 750 ft (229 m). Below these formations is the Eau Claire formation, which is about 400 ft (122 m) thick and is at least 1775 ft (541 m) below the surface.

The Eau Claire formation can be readily subdivided into an upper and a lower unit. The upper unit, which is about 250 ft (76 m) thick, consists of fine-

COMPOSITE COLUMNAR SECTION
GARFIELD DOME AREA
LA SALLE COUNTY, ILLINOIS

SYSTEM	SERIES	GROUP OR FORMATION	COLUMN	THICKNESS	LITHOLOGY
PLEISTOCENE				20 to 60	Drift and till; clay; gray, interbedded with sand and gravel lenses.
PENNSYLVANIAN	MISSOURIAN	Mc LEANSBORO		110 to 300	Shales; gray, black, brown, green, very micaceous, silty, calcareous, soft. Siltstones; gray, very micaceous, shaly. Sandstones; fine to medium, angular, micaceous, silty. Coal. Few limestones; gray-green, argillaceous. Pennsylvanian uncomformably overlies beds ranging in age from Maquoketa to Platteville.
	DES MOINESIAN	CARBONDALE			
		SPOON			
ORDOVICIAN	CINCINNATIAN	MAQUOKETA		0 to 120	Limestone; white to brownish-gray, medium to coarse crystalline, fossiliferous. (Divine member) Shale; gray-brown, firm, calcareous.
	CHAMPLAINIAN	GALENA		0 to 180	Limestone; buff to tan, slightly to very dolomitic, medium to coarse crystalline, fossiliferous. Dolomite; brown, medium crystalline, vuggy.
		DECORAH		0 - 10	Limestone; tan, very dolomitic, shaly, slightly speckled and cherty.
		PLATTEVILLE		150 to 190	Limestone; some slightly dolomitic, very fine to medium crystalline, slightly cherty, dense.
	CHAZYAN	ST. PETER		145 to 165	Sandstone; white, fine to coarse grained, frosted, friable, subangular to subround. Slightly shaly and dolomitic at top. Basal sand contains shale, dolomite pebbles and chert.
	CANADIAN	SHAKOPEE		195 to 210	Dolomite; gray to brown, very fine to coarse crystalline, slightly to very sandy, argillaceous. Thin bands of light green shale and oolitic chert.
		NEW RICHMOND		125 to 140	Sandstone; white, fine to coarse grained, frosted, some dolomitic. Dolomite; buff to gray, fine to medium crystalline, sandy. Green shale and oolitic chert.
		ONEOTA		215 to 220	Dolomite; light gray to white, medium to very coarse crystalline. Scattered lenses of chert. Slightly glauconitic at base.
		GUNTER		15-25	Sandstone; white, medium to coarse grained, dolomitic, incoherent.

FIGURE 13-1
Upper composite columnar section at Garfield [Katz & Coats, 1-2, courtesy of Northern Illinois Gas Company].

COMPOSITE COLUMNAR SECTION
GARFIELD DOME AREA
LA SALLE COUNTY, ILLINOIS

CAMBRIAN	CROIXAN	EMINENCE		70 to 90	Dolomite; gray to buff, fine to medium crystalline, very finely sandy, slightly glauconitic. Trace geodal quartz.
		POTOSI		170 to 185	Dolomite; buff to tan, fine to medium crystalline, very slightly sandy, slightly glauconitic at base.
		FRANCONIA		200	Dolomite; brown, fine to medium crystalline very finely sandy, argillaceous, slightly glauconitic. Sandstone; gray to green, fine grained, angular, dolomitic, glauconitic.
		IRONTON		125 to 175	Alternating bands of medium to coarse grained, subround to round sandstone and medium to coarse crystalline, sandy, gray and pinkish dolomite.
		GALESVILLE		25 to 75	Sandstone; fine to medium grained, dolomitic, subround. Becomes very dolomitized.
		EAU CLAIRE		390 to 410	Upper 250' consists largely of: Siltstone; reddish-buff, micaceous, argillaceous, glauconitic. Sandstone; fine to medium grained, argillaceous. Shales; green and red, micaceous. Lower 150' is largely: Shale; dark gray-green, firm, blocky, dense, fossiliferous. Dolomite; brown, fine to coarse crystalline, fossiliferous, glauconitic, argillaceous. Zone becomes silty and studded with "sooty" sandstone lenses at base.
		MT. SIMON			Sandstone; pinkish, fine to coarse grained, subround, frosted, glassy, hard and semi-quartzitic. Sandstone; white to reddish-buff, medium to very coarse grained, granules, coherent to friable. Shale; greenish-gray and red, silty, micaceous, firm and platy. Sandstone; white to dark reddish-buff, medium to coarse grained, abundant granules, very hematitic zones. Shale; reddish-brown, hematitic, very micaceous, silty. 600' of penetration. Total Mt. Simon thickness - 2000' (estimated)

FIGURE 13-2
Lower composite columnar section at Garfield [Katz & Coats, 1-2, courtesy of Northern Gas Company].

grained, shaly, dolomitic sandstones and siltstones interlaminated with red and green micaceous shales. The lower unit is about 150 ft (48 m) thick; it consists almost entirely of dense, fossiliferous, grayish-green shale with some argillaceous dolomite lenses. This shale unit becomes silty and interlaminated with bands of "sooty" sandstone at its extreme base. The Eau Claire formation forms the principal caprock for the Garfield gas storage project.

Below the Eau Claire formation is the Mt. Simon sandstone, which was penetrated 600 ft (183 m) at Garfield. It consists of very fine-grained to granular sandstone and scattered red and green micaceous shales. The sorting in the Mt. Simon sand is poor, and the porosity and permeability improve with depth. Lenses of reddish-brown and grayish-green, micaceous, hematitic, and silty shale stringers are found within the Mt. Simon formation.

Figure 13-3 is a partial gamma ray laterolog on the Scheuer No. 1 well at Garfield, covering formations from the Ironton to the top of the Mt. Simon. Electric correlation and drilling time logs indicate how readily the top of the St. Peter sandstone can be distinguished from the overlying Galena-Platteville limestones. This point was used as a marker for structural correlation during the test drilling at Ancona-Garfield. In some test wells the top of the Galena formation was used as a marker when Maquoketa cover was present, and 390 ft (119 m) of Galena-Platteville section was used to estimate the St. Peter top. Figures 13-4, 13-5, and 13-6 show the St. Peter structural map at Ancona-Garfield, the isopachous map of the interval between the St. Peter top and the Mt. Simon top, and the Mt. Simon structural top maps, respectively.

Depth corrections were deemed necessary for wells on the north flank at Ancona-Garfield when determining the St. Peter–Mt. Simon interval. Because of the steepness of the dip, the correction consists of multiplying the measured depths by the cosine of the dip angle, one measurement being as high as 21.5°. In this case the measured interval of 1947 ft (593 m) becomes $1947 \times \cos(21.5°) = 1812$ ft (552 m); see Fig. 13-7.

The corrections were made first to the drilled depths in making the isopach and again in reverse manner to project the estimated drilled depth to the Mt. Simon structure.

The Mt. Simon structure has slightly less closure to the west than the St. Peter because the interval thins in that direction. Along the north there is more closure for the Mt. Simon because of the thickening of the interval. The Ancona-Garfield structure has over 300 ft (119 m) of closure. The relatively steep dip on the north flank was examined closely to find whether there was evidence of faulting. The dipmeter readings, the evidence of dip seen in the cores, and the results on closely spaced test holes all pointed to a smooth change in elevation without any steps that would indicate faulting. The geology clearly indicated a satisfactory overall structure for containing the gas.

Core Information

Cores were taken on 10 wells and routine plug porosities and permeabilities were determined for the Mt. Simon storage zone. Whole core tests were made of the

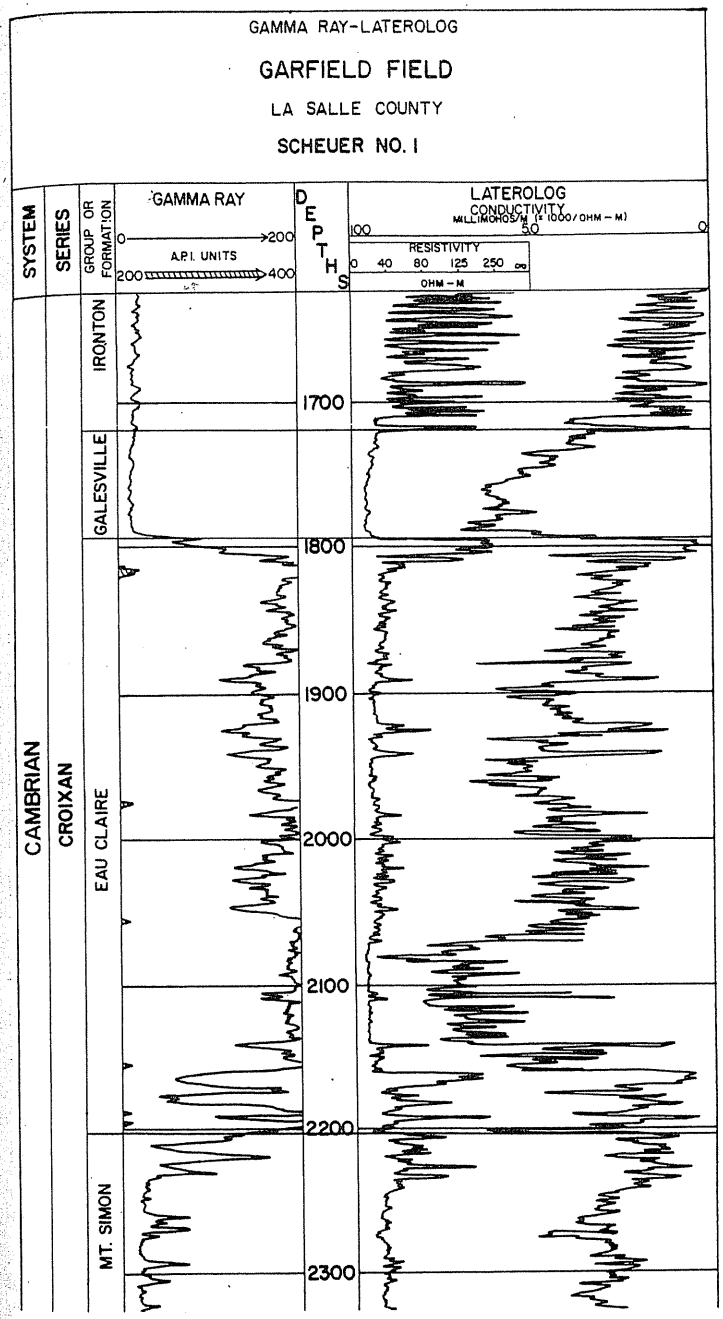

FIGURE 13-3
Gamma-ray laterolog on Scheuer No. 1 well at Garfield [Katz & Coats, 1-2, courtesy Northern Illinois Gas Company].

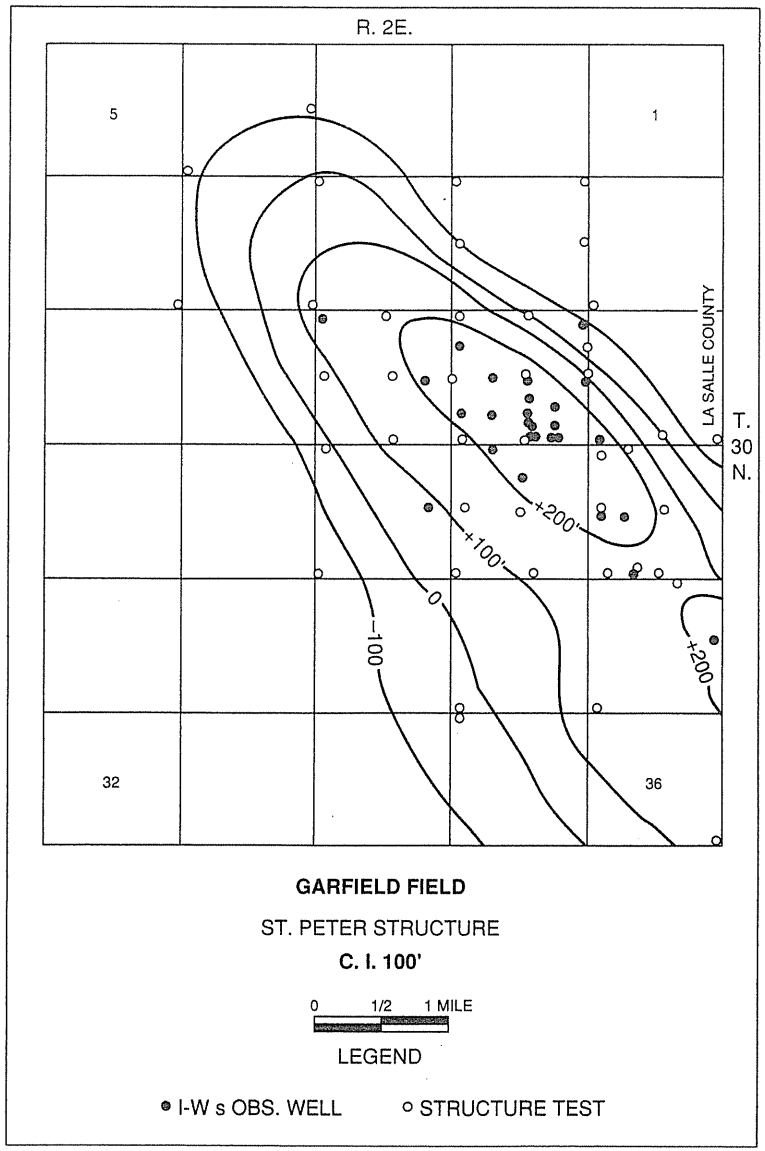

FIGURE 13-4
St. Peter structural map of Ancona-Garfield [Katz & Coats, 1-2, courtesy of Northern Illinois Gas Company].

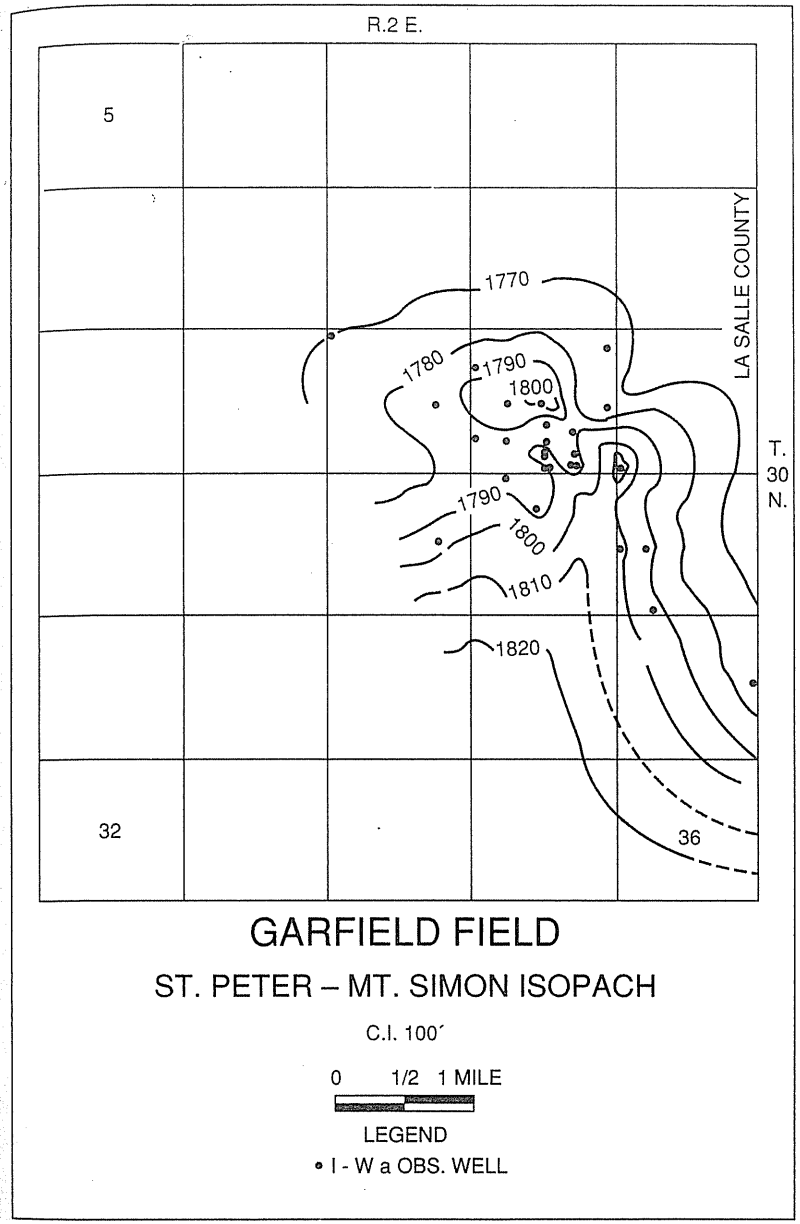

FIGURE 13-5
Isopachous map of interval of St. Peter to Mt. Simon tops [Katz & Coats, 1-2, courtesy of Northern Illinois Gas Company].

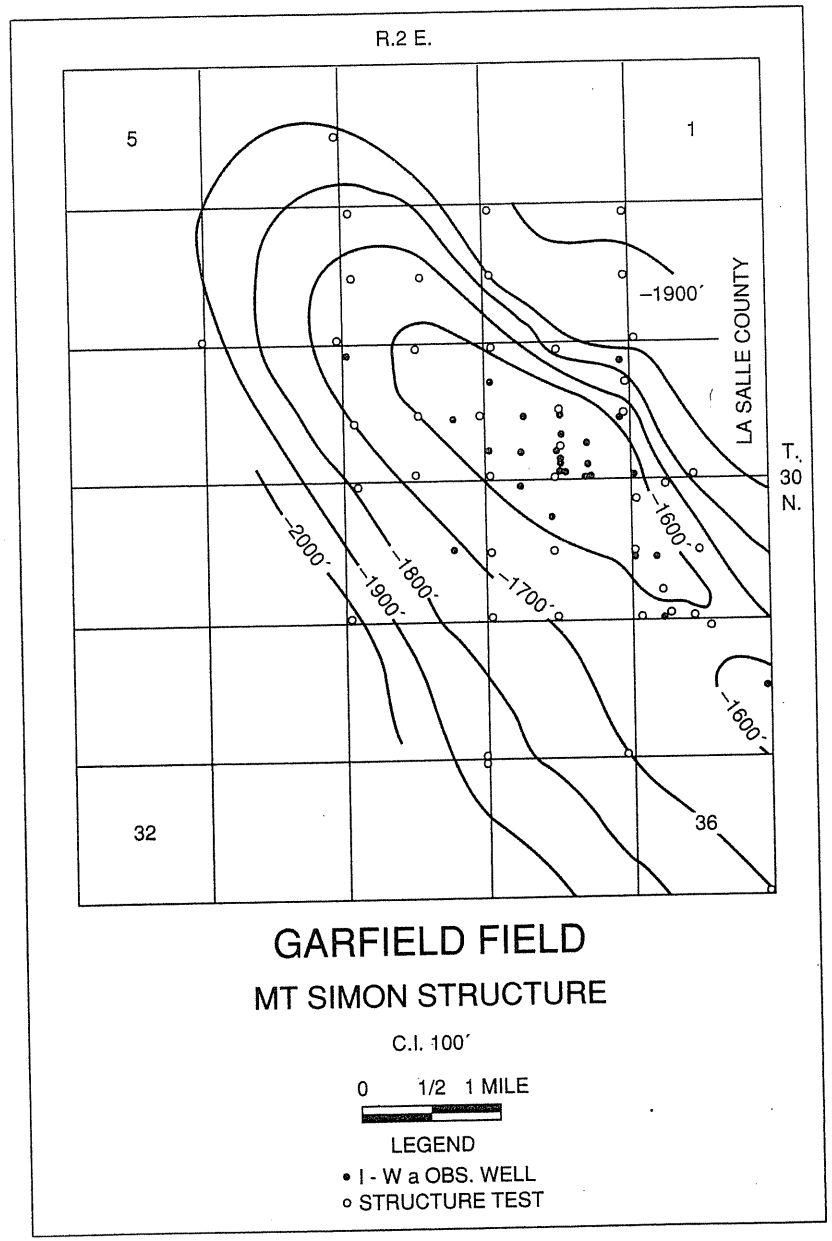

FIGURE 13-6
Garfield structural map on top of Mt. Simon [Katz & Coats, 1-2, courtesy of Northern Illinois Gas Company].

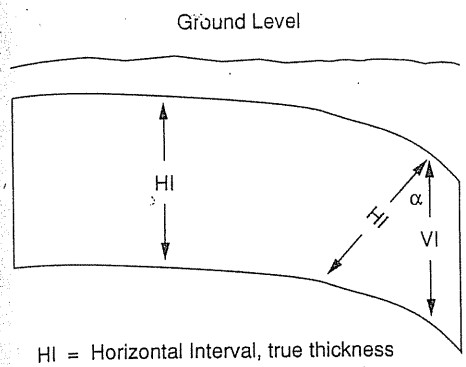

HI = Horizontal Interval, true thickness of strata when beds are flat-lying

VI = Vertical Interval, actual thickness of dipping beds when drilled

α = Angle of dip

Formula: $\frac{HI}{\cos \alpha} = VI$

FIGURE 13-7
Illustration of true and actual thicknesses [Katz & Coats, 1-2, courtesy of Northern Illinois Gas Company].

caprock. Cores coming out of the core barrel were washed, marked, and placed in boxes. Color photographs (Fig. 13-8) were made, and word descriptions foot by foot were recorded. The Eau Claire caprock cores were placed in plastic bags and sent to the laboratory promptly to avoid drying. Whole core tests of vertical permeability to water (down to 10^{-3} md) and of porosity were run. At selected intervals, if conditions permitted, permeability measurements were made down to 10^{-6} md, and threshold displacement pressures were obtained. Table 13.2 gives typical caprock core data.

Plug samples were taken from cores of the storage zone for routine permeability and porosity measurements. Table 13.3 gives typical conventional core plug data on the Galesville and Mt. Simon zones. Table 13.4 gives the average porosity as 12.3 percent and the average horizontal permeability as 102 md for all cores taken.

Capillary pressure measurements were made on a series of Mt. Simon core plugs to determine the residual water that would be retained by the sand after the gas bubble had been developed. Figure 13-9 gives typical data on three cores, Table 13.5 lists the information on several cores, and Fig. 13-10 is a plot of the permeability versus residual or connate water. At the average permeability of 102 md, the connate water was 18.5 percent of the pore space.

Water Levels

Water levels were taken on all deep wells as they were completed. The Ancona data were obtained before any gas injection. The average level was 613.6 ft

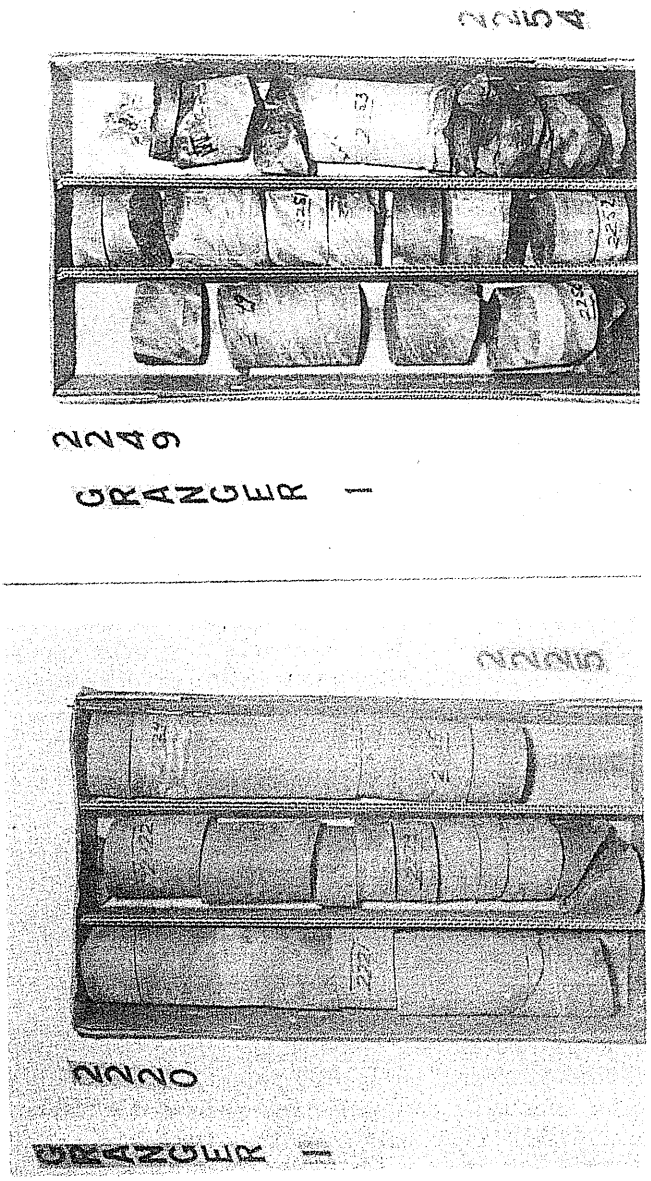

FIGURE 13-8
Photographs of cores from Ancona-Garfield showing slickensides [Katz & Coats, 1-2, courtesy of Northern Illinois Gas Company].

TABLE 13.2
Whole core analyses on caprock of Garfield reservoir [Katz & Coats, 1-2, courtesy Hydrocarbon Engineering, Inc.]

Depth ft	Vert. perm. to water	Porosity %	Low vert. perm. to water, md	Threshold pressure, psi
1791.0–92.0	<0.001	8.2	Top Eau Claire	
1792.0–93.1	<0.001	1.3		
1793.1–94.0		1.5	0.000016	700
1794.0–95.3	<0.001	1.7		
1795.3–95.9	<0.001	1.0		
1795.9–96.9	<0.001	1.6		
1796.9–97.7	<0.001	1.0		
1797.7–99.0	0.001	1.1		
1799.0–00.1	<0.001	1.5		
1800.1–01.1		1.7	0.000013	>800
1801.1–02.1	<0.001	1.0		
1802.1–02.9	0.001	2.7		
1802.9–03.9	0.001	10.9		
1803.9–05.0	<0.001	3.9		
1805.0–06.1	0.001	1.6		
1806.1–07.1	<0.001	1.6		
1807.1–00.1	<0.001	3.9		
1808.1–09.1	0.001	4.4		
1809.1–10.0	<0.001	6.8		
1810.0–11.0	<0.001	6.8	Core No. 11 1810.0–1837.0′	
1811.0–11.8	<0.001	14.4		
1811.8–12.8		5.2	0.000028	800
1812.8–13.9	<0.001	5.9		
2038.0–39.0	0.001	14.0	Core No. 20 2038.0–2066.0′	
2039.0–40.0		13.1	0.000904	25
2040.0–41.2	<0.001	11.4		
2041.2–42.0	<0.001	14.0		
2042.0–43.0	<0.001	16.0		
2043.0–44.1	0.001	13.7		
2044.1–45.2	0.133	11.9		
2045.2–46.1	0.004	10.6		
2046.1–47.0	<0.001	11.7		
2047.0–48.0	<0.001	12.4		
2048.0–49.0	<0.001	12.3		
2049.0–50.2	0.010	14.1		
2050.2–51.0		10.7	0.000023	200
2063.2–63.9	<0.001	2.2		
2063.9–65.2		2.9	0.000020	200
2065.2–66.0	<0.001	3.2		
2066.0–66.9	<0.001	6.2	Core No. 21 2066.0–2093.0′	
2066.9–67.5	0.001	2.0		
2067.8–69.0	<0.001	1.8		
2069.0–70.0		3.9	0.000072	500
2070.0–71.2	<0.001	2.1		
2071.2–72.1	<0.001	2.2		
2072.1–72.9		7.0	0.000024	800

TABLE 13.2
(*continued*)

Depth ft	Vert. perm. to water	Porosity %	Low vert. perm. to water, md	Threshold pressure, psi
2072.9–73.9	0.014	3.0		
2073.9–74.7	<0.001	5.3		
2074.7–75.7	0.006	2.8		
2075.7–76.8	0.003	6.8		
2076.8–77.9	0.006	6.9		
2077.9–78.9	0.005	1.5		
2078.9–79.8	0.009	1.2		
2079.8–81.0		1.5	0.000014	600
2081.0–82.0	<0.001	1.0		

TABLE 13.3
Conventional core analyses on formations at Garfield [Katz & Coats, 1-2, courtesy Hydrocarbon Engineering, Inc.]

Depth, ft	Permeability, md		Porosity %
	Horizontal	Vertical	
Galesville			
1717.5	3040.	1379.	19.9
1718.5	1020.	852.	19.8
1719.5	240.	643.	15.4
1720.5	2842.	385.	19.6
1721.5	1002.	311.	21.4
1722.5	2660.		18.1
1723.5	605.	120.	14.7
1724.5	818.		20.5
1725.5	1970.	131.	18.1
1726.5	1760.	236.	18.1
1727.5	2857.	3790.	21.2
1728.5	2215.	589.	19.4
1729.5	1688.	777.	11.9
1730.5	302.	211.	19.1
1731.5	809.	250.	18.8
LOST CORE 1731.5–1754.0′			
Mt. Simon			
2205.5	10.	1.6	13.9
2206.5	7.7	1.3	10.6
2207.5	0.69	0.47	11.0
2208.5	26.	4.8	12.8
2209.5	6.1	8.4	14.4
2210.5	18.	1.2	9.4
2211.5	43.	5.5	8.2
2212.5	32.	2.3	6.5
2213.5	30.	8.9	9.4
2214.5	1.1	1.1	8.6
2215.5	18.	12.	10.3
2216.5	15.	44.	16.0
2217.5	9.9	0.84	13.1
2218.5	1.7	0.14	13.8
2219.5	22.	6.0	13.7
2220.5	13.	5.8	13.8
2221.5	20.	8.4	14.5
2222.5	32.	0.13	7.2
2223.5	144.	48.	6.5
2224.5	2.8	14.	6.2
2225.5	2.5	1.7	5.6
2236.5	40.	11.	10.5
2237.5	53.	4.9	11.2
2238.5	43.	19.	9.7
2239.5	22.	20.	12.5
2240.5	86.	21.	11.2
2241.5	130.	197.	12.4
2242.5	95.	222.	9.6
2243.5	21.	26.	10.8
2244.5	70.	29.	12.0
2245.5	121.	121.	10.1
2246.5	278.	233.	12.1
2247.5	207.	179.	11.6

TABLE 13.3
(*continued*)

Depth, ft	Permeability, md		Porosity %	Depth, ft	Permeability, md		Porosity %
	Horizontal	Vertical			Horizontal	Vertical	
Mt. Simon							
2248.5	111.	57.	10.2	2277.5	605.	50.	12.4
2249.5	196.	18.	9.2	2278.5	168.	116.	11.3
2250.5	142.	76.	11.6	2279.5	108.	43.	11.3
2251.5	102.	6.7	10.6	2280.5	55.	38.	13.0
2252.5	204.	202.	11.3	2281.5	64.	99.	11.4
2253.5	74.	28.	9.7	2282.5	147.	24.	12.5
2254.5	195.	368.	13.1	2283.5	52.	98.	11.4
2255.5	98.	21.	10.5	2284.5	27.	50.	12.6
2256.5	1.9	2.6	8.7	2285.5	120	60.	11.0
2257.5	40.	11.	8.5	2286.5	23.	59.	10.2
2258.5	63.	49.	12.7	2287.5	101.	53.	12.8
2259.5	70.	50.	11.7	2288.5	144.	192.	12.2
2260.5	110.	68.	11.9	2289.5	101.	15.	11.3
2261.5	63.	29.	12.9	2290.5	18.	30.	11.0
2262.5	0.72	0.15	9.0	2291.5	55.	33.	13.7
2263.5	58.	34.	10.2	2292.5	23.	14.	8.5
2264.5	75.	49.	12.5	2323.5	79.	56.	9.9
2265.5	27.	28.	10.3	2324.5	119.	16.	7.5
2266.5	64.	31.	10.6	2325.5	49.	50.	11.5
2267.5	39.	16.	9.3	2326.5	69.	41.	11.3
2268.5	80.	48.	10.4	2327.5	137.	42.	9.8
2269.5	28.	29.	11.1	2328.5	79.	13.	6.6
2270.5	1.1	0.23	5.3	2329.5	30.	46.	7.5
2271.5	0.91	0.65	8.9	2330.5	23.	14.	9.5
2272.5	90.	90.	14.3	2331.5	8.5	24.	7.0
2273.5	285.	84.	12.7	2332.5	16.	6.9	11.8
2274.5	120.	100.	14.8	2333.5	8.3	2.5	8.2
2275.5	221.	11.	15.3	2334.5	0.35	0.08	2.6
2276.5	448.	64.	13.0	2335.5	2.1	0.02	12.0

TABLE 13.4
Summary of core data at Ancona-Garfield [Katz & Coats, 1-2]

Average porosity and permeability for the Mt. Simon sand.

Well	No. of samples analyzed	Average permeability, md	Average porosity, %
Fordyce No. 1	143	63	12.8
Fehr No. 1	141	100	12.0
Musser No. 1	126	73	12.9
Smith No. 1	142	97	11.8
Krischel No. 2	120	109	12.8
Barr No. 1	85	116	11.5
Granger No. 1	97	108	12.5
Healy No. 1	101	112	11.6
Scheuer No. 1	283	152	12.6
Scheuer No. 4	87	94	12.1
	Average	102	12.3

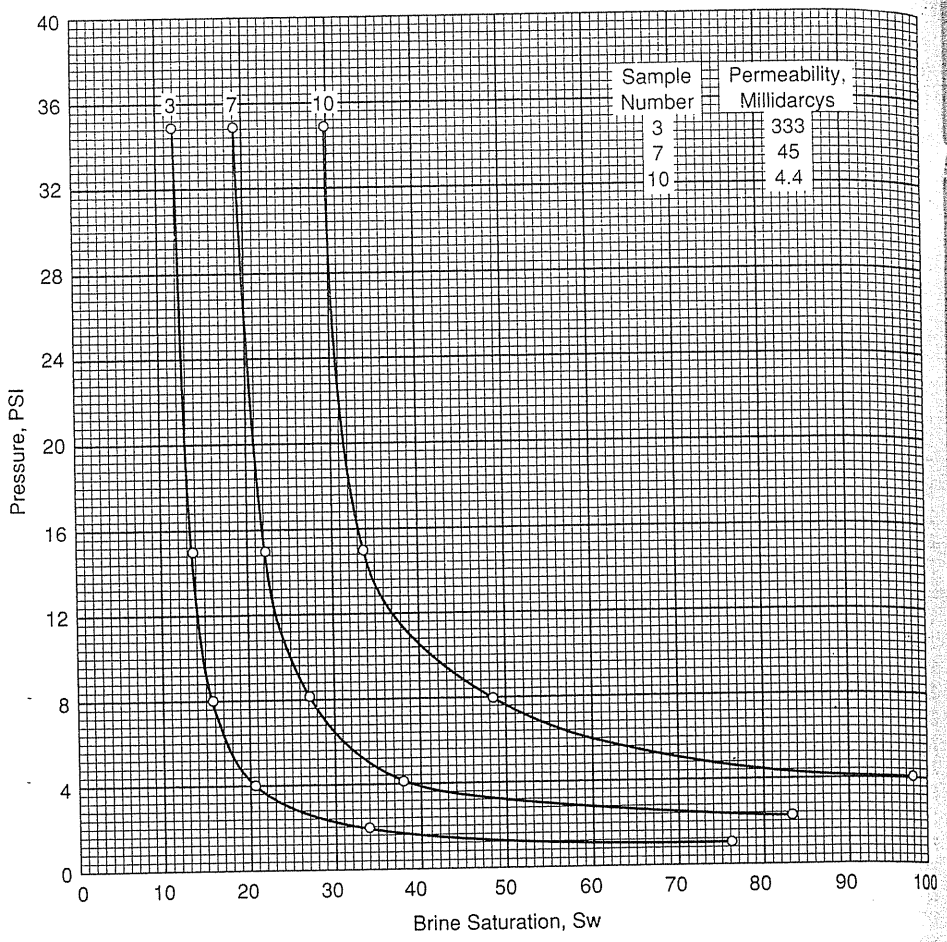

FIGURE 13-9
Capillary pressure measurements to determine residual water on Mt. Simon sand [Katz & Coats, 1-2, courtesy of Northern Illinois Gas Company].

TABLE 13.5
Summary of capillary pressure data on Mt. Simon sandstone

Sample no.	*k*, md	Porosity, %	Brine saturation, % of pore space Pressure, psi 1	2	4	8	15	35
1	783	11.2	63.9	53.1	45.2	41.3	38.3	35.2
2	530	14.1	42.7	29.1	23.5	20.3	17.4	15.2
3	333	18.1	76.9	34.6	21.1	16.6	14.0	12.2
4	277	16.8	60.1	34.9	26.5	21.7	18.6	16.2
5	151	15.0	96.4	48.2	30.6	25.3	22.0	18.8
6	98	12.4	76.2	51.7	39.5	33.1	28.5	24.0
7	45	11.4	100.0	83.6	38.5	26.9	22.4	19.2
8	21	11.7	100.0	92.3	64.3	48.1	41.7	36.4
9	13	11.1	100.0	87.4	62.8	46.7	37.9	31.2

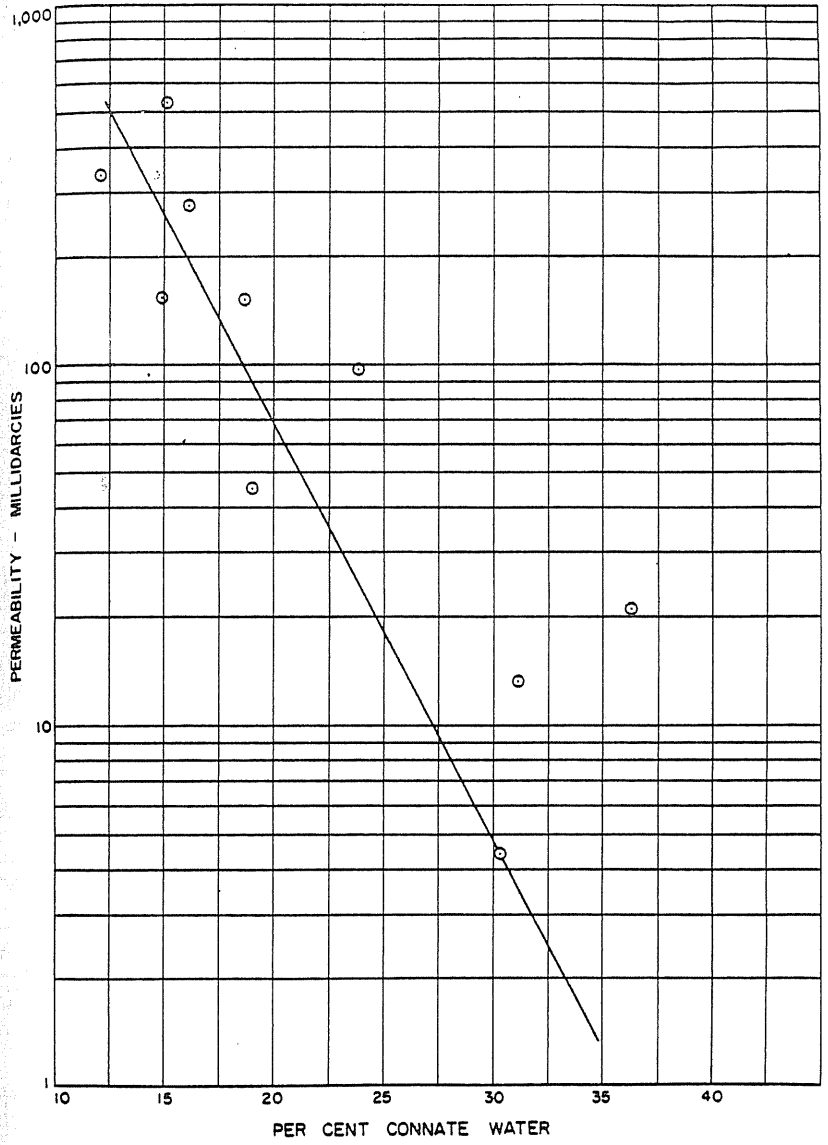

FIGURE 13-10
Connate water versus permeability for Mt. Simon sandstone [Katz & Coats, 1-2, courtesy of Northern Illinois Gas Company].

(187 m), with a low of 606.5 (185 m) and a high of 619.8 (189 m), on Mt. Simon. Other levels were 499 ft (152 m) on St. Peter and 497 (151 m) on Galesville. These data indicated no communication between the Mt. Simon and upper zones. Later data in the Garfield area showed a water level gradient of 2 ft per mile (0.379 m/km), decreasing in the southeast direction.

From these water levels the initial aquifer pressures were accepted as 960 psia (6.62 MPa) at −1545 ft (−471 m) at Garfield and 960 psia (6.62 MPa) at −1535 ft (−468 m) at Ancona.

Water Analyses

Water analyses were done on samples of St. Peter, Galesville, and Mt. Simon waters. Table 13.6 gives typical analyses of these waters. They show that the Mt. Simon water was much higher in dissolved solids than the upper waters, and hence it was believed to be uncontaminated by any water percolating through the caprock. If water transfer through the Eau Claire were taking place, it would be upward from the Mt. Simon to the Galesville (129 ft, or 39 m, water head for 410 ft, or 125 m, of Eau Claire).

Pump Tests

Three series of pump tests were conducted, the first two at Ancona before any gas injection took place and the third at Garfield after gas had been injected at Ancona. Garfield pump test results are given by Figs. 13-11 and 13-12. Figure 13-13 shows the location of the pump test and its cross section.

TABLE 13.6
Water analyses of Ancona-Garfield

	Well				
	Fordyce No. 1	**Scheuer No. 1**	**Musser No. 1**	**Fordyce No. 3**	**Clark No.**
Formation	Mt. Simon	Mt. Simon	Mt. Simon	Galesville	St. Peter
pH	7.5	7.5	7.9	7.3	7.8
	Parts per million				
Carbon dioxide	15	17	6	19	—
Bicarbonate	240	282	250	238	274
Chlorides	10,200	6,995	11,400	1,800	473
Hardness	2,350	1,750	3,040	968	234
Calcium	676	504	880	254	45
Magnesium	150	120	200	80	30
Sulfates	660	500	590	460	145
Iron	14	17	47	4.5	2.5
Total dissolved solids:	17,901	13,174	18,416	3,785	1,243

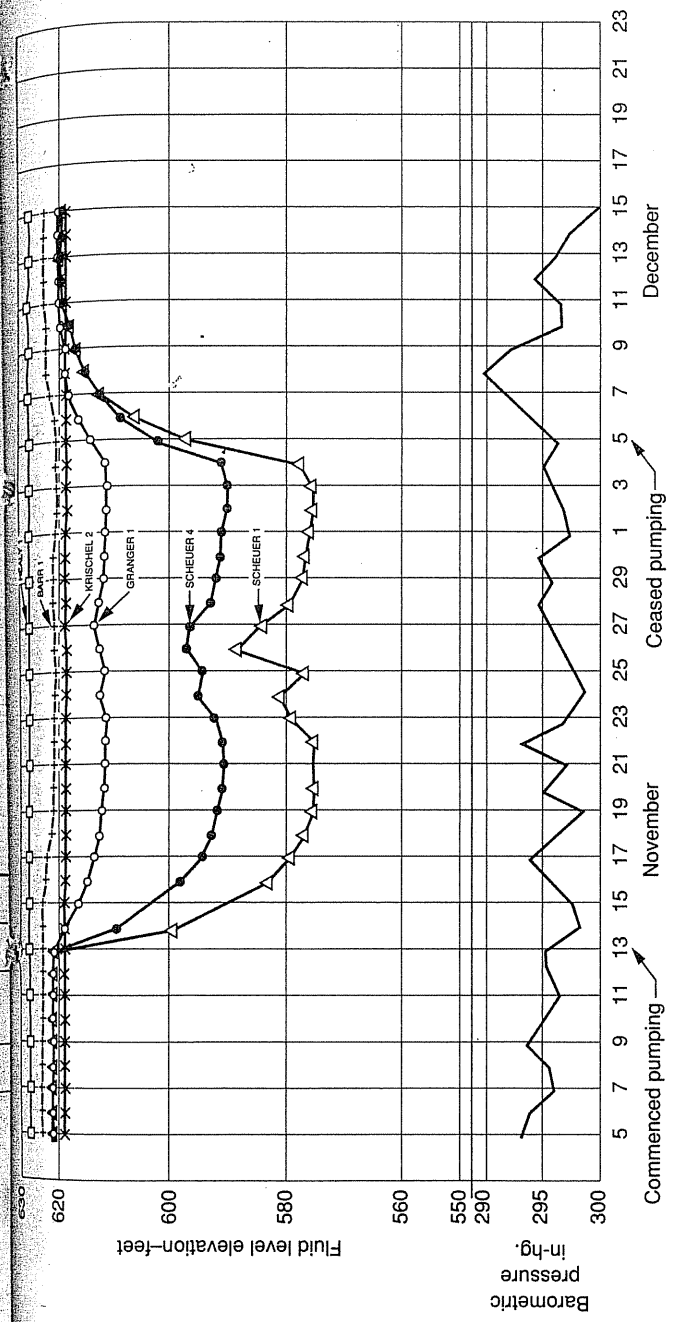

FIGURE 13-11
Water levels on Mt. Simon wells during Garfield pump test [Katz & Coats, 1-2].

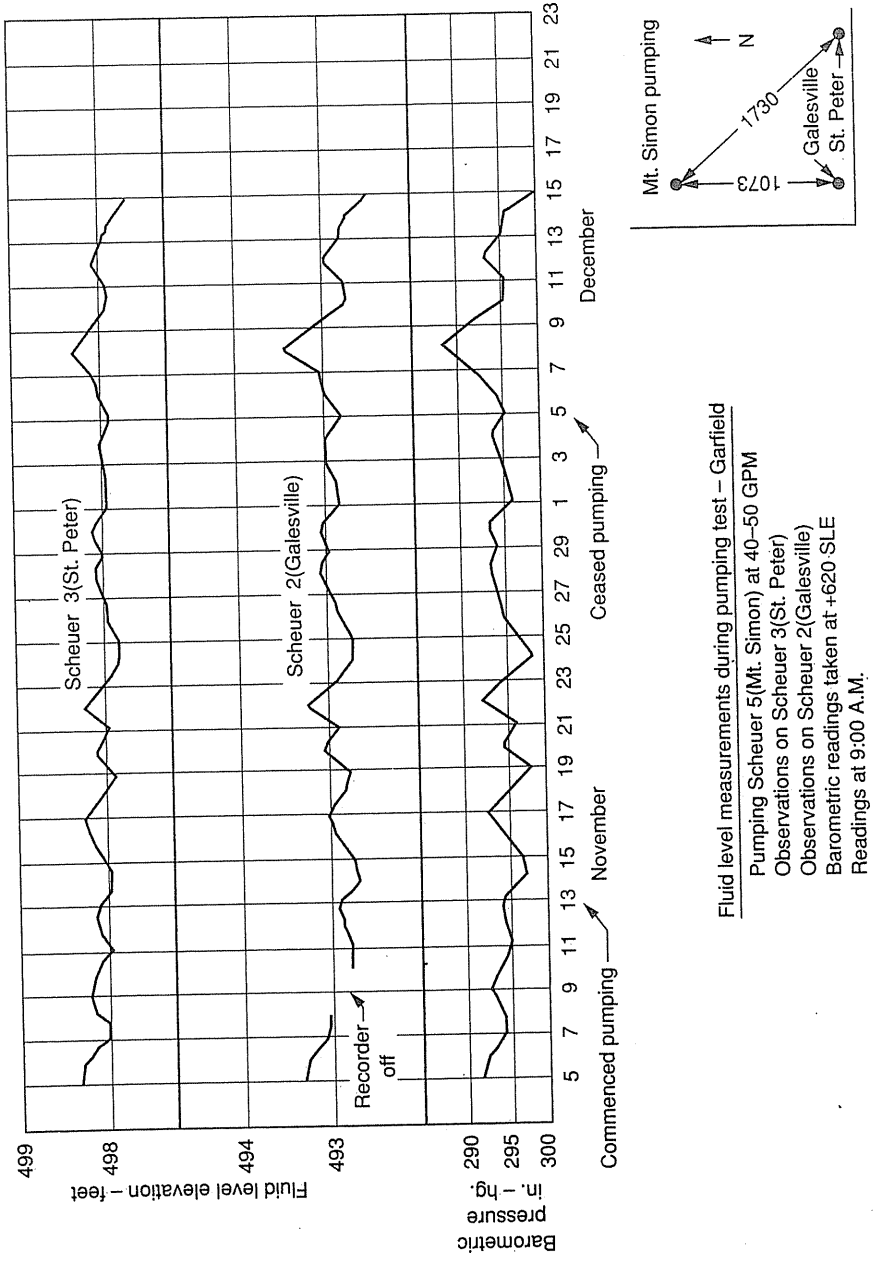

FIGURE 13-12
Water levels on St. Peter and Galesville zones during Garfield pump test [Katz & Coats, 1-2].

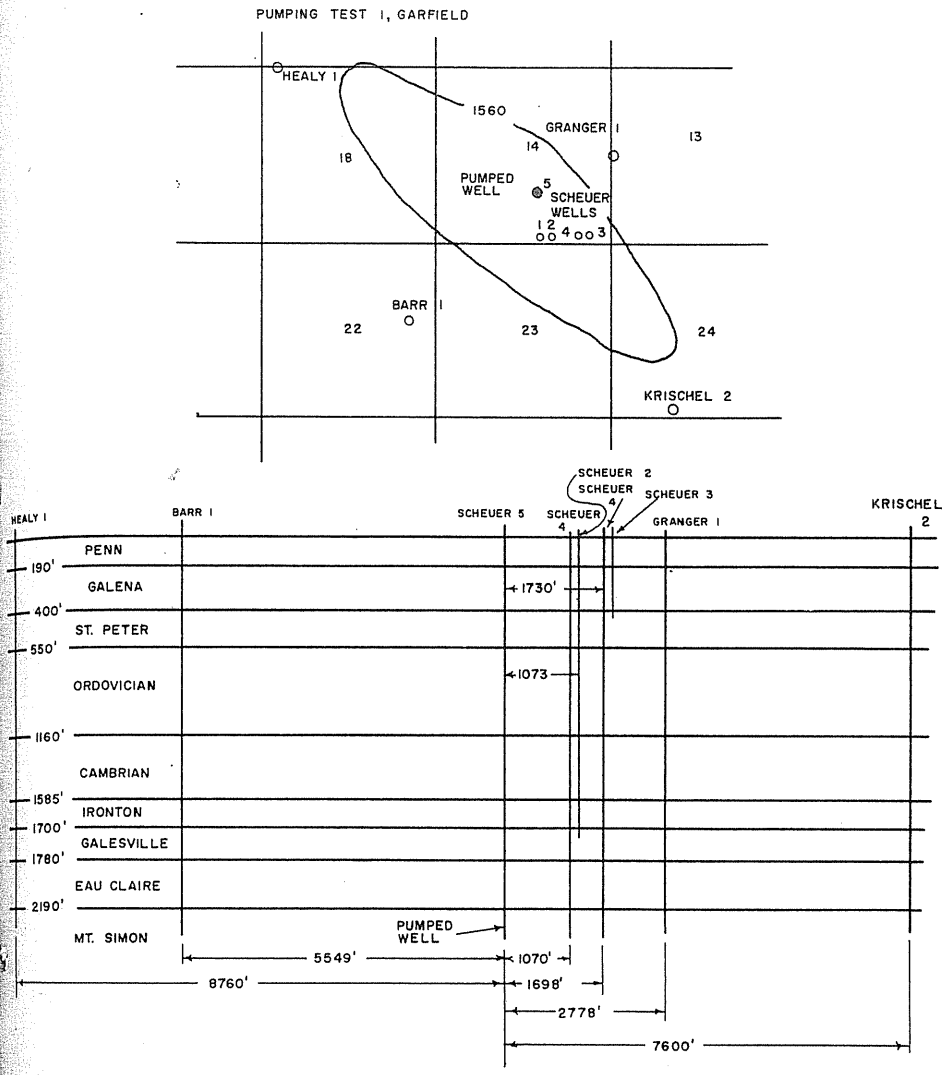

FIGURE 13-13
Pump test location and its cross section [Katz & Coats, 1-2].

On November 13, 1963, the first pumping test was initiated at the Garfield storage aquifer. Pumping the Mt. Simon sand for 22 days, the aquifer yielded 1,352,000 gallons (5117 m^3) of water at an average rate of 42.7 gallons per minute (2.69×10^{-3} m^3/s). A 30-hp Reda motor and an 82 D-33E pump were placed downhole on a string of 2.375, J-55 upset tubing. The pump was placed at approximately 1860 ft (567 m) inside a 7-in (0.18 m) 23 casing. Electricity

was supplied by a 75-kW engine-generator, which supplied power through a switchboard and step-up transformer.

Drawdown in the pumped well was approximately 950 ft (290 m) during the test with 75 ft (23 m) of casing perforated at the top of the Mt. Simon sand. The six Mt. Simon observation wells were all completed into the upper 50 ft (15 m) of the Mt. Simon sand with the exception of Krischel 2, which had 46 ft (14 m) open. Two observation wells above the Eau Claire caprock were completed into the Galesville and St. Peter sands.

This pumping test was used to evaluate both the suitability of the Eau Claire caprock and the characteristics of the Mt. Simon sand. It was concluded that the caprock was not passing water in the vicinity of the pumping well.

Conclusions on Geological Study

The geology and well studies showed that a structure was present to hold the gas. The porosity and permeability of the proposed storage zone seemed satisfactory. Geological study of the caprock, examination of cores, and permeability and threshold displacement tests showed the caprock to be continuous and impermeable to gas. The pump tests verified that no pressure communication took place across the caprock during a reduction in the water head below it.

At this point, the project proceeded to the engineering aspects of volumetric content, capacity of wells for gas injection and withdrawal, and the estimated rate of development.

Volumetric Content of Reservoir

The volumetric content of a reservoir for gas depends upon the structural configuration, the rock porosity, the expected residual or connate water, and the pressures used.

The volume of sand contained between the top of the Mt. Simon sand and each of the levels corresponding to the contours on the map is found by planimetering the scaled map along the contours. For each interval, the mean area multiplied by the sand thickness gives the volume, or the trapezoidal formula may be used. Table 13.7 gives the sand volumes obtained from the contour maps.

Before the gas content of a given space can be computed, the gas gravity must be known and the compressibility factors obtained. The gas gravity is 0.65, and Fig. 13-14 gives the compressibility factors determined by the method of Chapter 4. It is convenient to compute the gas space F occupied by a million standard cubic feet of gas:

$$F = 1{,}000{,}000\frac{14.7}{P}\frac{T}{460 + 60}Z \qquad (13.1)$$

where F is the space occupied by 1000 Mcf (28.3 Mm^3) of gas, pressure P is in psia, temperature T in °R, and Z is the compressibility factor. This has been done for the gas at Ancona-Garfield at the reservoir temperature of 75°F (24°C) as shown in Fig. 13-15.

TABLE 13.7
Sand volumes at Ancona-Garfield

Thickness of gas bubble, ft	Water level contour, SLE	Sand volume down to water level, acre · ft
	Garfield	
19	−1540	1,545
39	−1560	10,885
59	−1580	26,115
79	−1600	47,715
	Ancona	
6	−1520	306
26	−1540	5,446
46	−1560	19,586
66	−1580	45,536
86	−1600	84,716
	Garfield-Ancona combined	
106	−1620	213,151
126	−1640	313,371
146	−1660	443,341
166	−1680	586,871
186	−1700	752,941

For a fully developed storage reservoir, the water level is obtained by assuming that it is receding ideally. The gas content is computed using the sand volume data, the gas content of a given space, and the calculation shown in Table 13.8. The gas contents calculated for a series of pressures are given in Table 13.9. Equalized pressure is assumed throughout the reservoir; that is, it is assumed that the water has drained down to the final saturation and the gas-water contact fits the various contour levels.

Selection of Delta Pressure

In making the above calculations of gas content, pressures are selected to include the top storage pressure used. What amount of delta pressure should be used?

The Eau Claire caprock is continuous, thick, and has a high threshold displacement pressure of greater than 800 psia (5.52 MPa). It has a good record of holding gas in other reservoirs such as Mt. Simon, Herscher, and Troy Grove. The initial pressure in the aquifer at Garfield was 960 psia (6.62 MPa) corresponding to 0.439 psia per foot (9.93 kPa/m) for the 2150 ft (655 m) of depth. A pressure

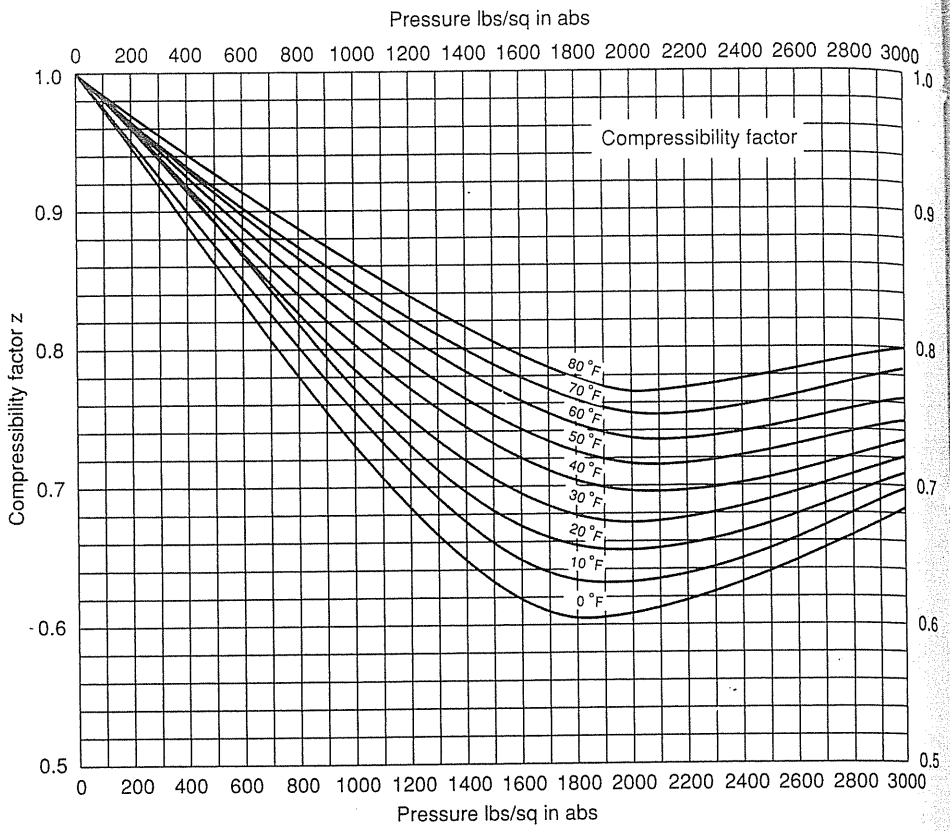

FIGURE 13-14
Compressibility factors for 0.65-gravity gas stored at Ancona-Garfield [Katz & Coats, 1-2].

rise of 100 psia (689 kPa) for the initial gas bubble seemed conservative and was adopted (0.482 psi/ft, 10.9 kPa/m). A delta pressure of 200 psia (1.38 MPa), bringing the pressure to 1160 psia (8.0 MPa) in the reservoir (0.527 psi/ft, 11.9 kPa/m) was judged to be a good operating value once the soundness of the caprock had been verified by field operation.

Not only the soundness of the caprock must be considered, but also the possibility of mechanical leakage at wellbores. The degree of delta pressure used in earlier years also has much to do with gas *wafering*, or pushing far into the more permeable zones before gravity effects can exert their influence.

Well Capacity

Before gas is injected, the well capacity may be predicted from permeability data, depth of penetration, gas properties, and the flow equation. This has been done

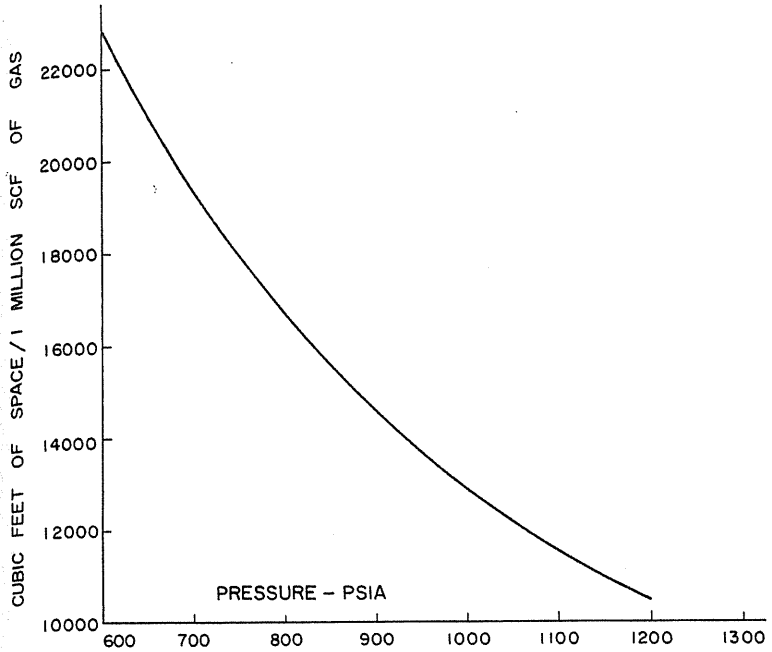

FIGURE 13-15
Pore space occupied by a million cubic feet of 0.65 gravity gas at 75°F [Katz & Coats, 1-2].

in Table 13.10 using a *kh* of 5800 md · ft (1768 md · m). The core permeability averaged 102 md, and on this basis, the contemplated effective penetration is 57 ft (17 m). Table 13.11 lists the computed flow rates for selected drawdowns (or buildups) at three pressure levels. These capacities are for dry sand around the wellbore and would be expected to prevail sometime after the field has been developed.

TABLE 13.8
Method of calculation of volumetric capacity for Mt. Simon sand [Katz & Coats, 1-2]

Basic formula:

where $V = 43{,}560 \times (\text{acre} \cdot \text{ft}) \times \phi \times (1 - S_w)/F$
V = volume, MMcf
ϕ = porosity
S_w = connate water saturation
F = ft³ of space/MMcf of gas (Eq. 13.1)

At 126 ft formation thickness (313,371 acre · ft, Table 13.7) and 900 psia [F = 14,575, from Eq. (13.1) or Fig. 13-15],

$V = 43{,}560 \times 313{,}371 \times 0.123 \times (1 - 0.185) \times (1/14{,}575) =$ 93,885 MMcf capacity

TABLE 13.9
Computed gas contents at contour water levels and selected pressures for Ancona-Garfield [1-2]
V-MMcf

Thickness	Contour	Pressure, psia								
		600	700	800	900	1000	1060	1100	1160	1200
					Ancona					
6	–1520	58.9	70.0	81.5	92.4	103.9	114.0	116.5	124.0	129.0
26	–1540	1,045.0	1,245.0	1,450.0	1,640.0	1,845.0	2,030.0	2,070.0	2,205.0	2,280.5
46	–1560	3,750.0	4,480.0	5,200.0	5,900.0	6,640.0	7,300.0	7,440.0	7,910.0	8,230.0
66	–1580	8,720.0	10,402.0	12,100.0	13,710.0	15,450.0	17,000.0	17,300.0	18,400.0	19,100.0
86	–1600	16,250.0	19,280.0	22,600.0	25,600.0	28,700.0	31,300.0	32,300.0	34,300.0	35,600.0
					Garfield					
19	–1540	295.0	351.0	407.0	463.0	524.0	560.0	584.0	620.0	646.0
39	–1560	2,070.0	2,470.0	2,860.0	3,260.0	3,680.0	3,940.0	4,110.0	4,370.0	4,550.0
59	–1580	4,999.0	5,920.0	6,600.0	7,820.0	8,850.0	9,460.0	9,850.0	10,500.0	10,990.0
79	–1600	9,100.0	10,850.0	12,580.0	14,300.0	16,200.0	17,320.0	18,100.0	19,200.0	20,100.0
					Combined structure					
106	–1620	40,392.0	48,257.0	56,760.0	64,680.0	72,072.0	75,768.0	81,048.0	86,592.0	90,024.0
126	–1640	62,280.0	70,947.0	83,213.0	93,885.0	105,876.0	113,834.0	118,505.0	126,463.0	131,134.0
146	–1660	84,370.0	100,372.0	118,547.0	134,563.0	150,436.0	162,305.0	169,455.0	180,180.0	186,901.0
166	–1680	110,940.0	132,870.0	156,090.0	177,375.0	198,293.0	214,140.0	222,009.0	236,715.0	246,390.0
186	–1700	142,175.0	170,468.0	200,255.0	228,690.0	254,100.0	247,791.0	285,560.0	304,920.0	315,810.0

TABLE 13.10
Calculation of well performance from core data—Mt. Simon sand [Katz & Coats, 1-2]

Basic formula:

$$P_1^2 - P_2^2 = \frac{1424\mu ZT}{kh} \ln\left(\frac{r_1}{r_2}\right) \cdot Q + \frac{3.161 \times 10^{-12}\beta GZT}{h^2}\left(\frac{1}{r_2} - \frac{1}{r_1}\right)Q^2$$

where P_1 = reservoir pressure, psia
T = temperature, °F = 535
r_1 = drainage radius, ft = 330
μ = viscosity, cp = 0.013
β = high-velocity coefficient, $ft^{-1} = 9.0 \times 10^{-7}$
Q = flow rate, Mcf/day
P_2 = flowing bottom hole pressure, psia
Z = compressibility factor = 0.85
r_2 = wellbore radius, ft = 0.406
G = gas gravity = 0.65
k = permeability, md
h = formation thickness, ft

Values calculated for $kh = 5800$ md · ft:

$P_1^2 - P_2^2$, psia²	Q, Mcf/day	$P_1^2 - P_2^2$, psia²	Q, Mcf/day
974	100	9,813	1,000
19,830	2,000	29,942	3,000
50,760	5,000	72,230	7,000
105,550	10,000	164,600	15,000
227,500	20,000		

Rate of Bubble Development

Predictions of the rate of bubble development due to water push-back may be made, although such calculations have not come too close to field experience. It is necessary to set a gas bubble radius, the formation thickness and permeability, and the aquifer compressibility. Table 13.12 shows the calculation made before

TABLE 13.11
Calculated well capacities for various pressures and drawdown [1-2]

Reservoir pressure, psia	Drawdown (ΔP), psia	Flow rate, MMcf/day
1200	50	10.8
1200	100	20.5
1160	50	10.7
1160	100	20.0
1000	50	9.3
1000	100	17.0
700	50	6.5
700	100	12.0

TABLE 13.12
Calculation of water movement while developing gas bubble [Katz & Coats, 1-2].

Basic formulas:

$$t_D = \frac{0.00632kt}{\phi\mu C_t r_b^2}$$

$$q = 6.283\phi C_t r_b^2 h(P_g - P_f)Q_t$$

where
q = accumulative water movement, ft^3
ϕ = porosity = 0.122
μ = water viscosity, cp = 1.1
h = formation thickness, ft = 200
r_b = gas bubble radius, ft = 3000
$P_g - P_f$ = pressure difference of gas bubble and aquifer
C_t = total compressibility, psia^{-1} = 6.8×10^{-6}
k = average permeability, md = 115
t = time, days

$Q_t(t_D)$ can be obtained from Fig. 8-24

Time, days	$q(\times 10^{-3})$ ft^3	V of gas equivalent to q, Mcf	Flow rate, Mcf/day
Calculated values: for $P_g - P_f$ = 100 psia			
0.111	104.23	8,657.3	77,832.7
1.11	375.96	31,227.2	28,074.4
2.22	563.94	46,840.8	21,055.8
5.56	949.21	78,841.4	14,176.2
8.9	1,264.69	105,045.2	11,804.0
11.1	1,460.11	121,276.7	10,930.2
55.6	4,223.99	350,844.6	6,308.4
111.2	6,896.68	572,848.2	5,150.1
222.5	11,464.06	952,204.8	4,280.3
556.2	23,130.06	1,921,182.8	3,454.5
Calculated values: for $P_g - P_f$ = 200 psia			
0.111	208.45	17,313.9	155,658
1.11	751.92	62,484.5	56,470
2.22	1,127.89	93,682.5	42,199
5.56	1,888.92	157,682.8	28,360
8.9	2,529.37	210,089.5	24,106
11.1	2,902.22	241,058.4	21,717
55.6	8,467.99	701,690.1	11,457
111.2	13,793.35	1,145,675.7	10,321
222.5	22,928.12	1,904,409.7	8,578
556.2	46,260.12	3,842,365.6	6,911

gas injection at Ancona-Garfield. The selection of 200 ft (61 m) as the sand thickness is a judgment item, knowing there will be partial pressure penetration into the zones below the gas. The in-situ compressibility of the aquifer also is known to be quite variable. The actual and predicted rates of gas injection are given on Table 13.13.

Plant and Field Lines

When approvals were obtained from the Illinois Commerce Commission, field lines and a compressor station were installed. The initial compressor was a 1000-hp Cooper Bessemer with gas suction at 600 psia (4.14 MPa) and discharge up to 1200 psia (8.27 MPa). In 1965, a 1000-hp White unit was added. In 1966, two 1500-hp White compressors were added. Central glycol dehydration is used with alcohol injection at the wellhead.

Operations at Ancona-Garfield

By November 1, 1966, there was 10.8 Bcf (0.306 Bm^3) in Ancona and 5.0 Bcf (0.142 Bm^3) in Garfield. During the winter, 1.77 and 0.98 Bcf (0.05 and 0.028 Bm^3) were withdrawn at rates up to 44.6 and 32.7 Mcf/day (1.26 and 0.926 Mm^3/day) respectively. It was expected that the combined reservoirs would contain 22 Bcf by November 1967, corresponding to some 40 Mcf/day (1.13 Mm^3/day) injection. The flow capacity of an occasional well had reached the predicted rate, but the average was only about 20 percent of the predicted dry permeability performance. Table 13.14 gives the projected operations.

Several aquifer storage reservoirs have been developed, as illustrated by the Ancona-Garfield reservoir data in the early part of this chapter. The combined

TABLE 13.13
Rates of gas injection experienced at Ancona-Garfield [Katz & Coats, 1-2]

Date	Field	Injection rate pressure: MMcf	Injection rate pressure: psia	Cubic feet space per MMcf of gas	Water movement, ft^3/day/psi
May 1, 1964	Ancona	5.4	1085	11,850	509
Oct. 1, 1964	Ancona	5.9	1050	12,000	787
Dec. 1, 1964	Ancona	11.8	1080	11,800	1160
Mar. 1, 1965	Garfield	3.4	1036	12,500	558
Sept. 1965*	Ancona	22.0	1160	10,850	1200
Sept. 1965*	Garfield	12.0	1135	11,100	800
1966*	Combined	46.0	1160	10,850	2500
1967*	Combined	55.0	1160	10,850	3000

* Estimated figures.

TABLE 13.14
Projected operation of the Ancona-Garfield storage project [Katz & Coats, 1-2]

Year	Maximum inventory, Bcf	Annual withdrawal, Bcf	Peak day withdrawal, MMcf/day	Average injection rate, MMcf/day	
				Summer	Spring
1967	22	5	100	50	100
1968	27	7	125	55	100
1969	32	9	150	60	115
1970	37	11	175	65	150
1971	42	13	200	70	175
Ultimate	120	60	600	50	400

reservoirs have contained as much as 160 Bcf (4.53 Bm^3) of gas and delivered 50 Bcf (1.42 Bm^3) to market in a single season. The water displacement to create the gas bubble was 1.9 billion cu ft. (0.054 Bm^3) of water. Surely the pressure in the aquifer surrounding such a development would not remain constant.

13.4 ECONOMIC CONSIDERATIONS OF BASE GAS IN AQUIFER STORAGE

When many of the aquifer gas storage fields were developed in the 1950s and 1960s, base gas had a commodity value of some 30–40 cents/Mcf. Accordingly, base gas cost, though important, was not an overriding issue. With the commodity value of gas above $3.00 per Mcf, the investment required may make aquifer storage unattractive for natural gas.

There is an interest in storing air for the electric utilities; for air, the cost of base gas would be unimportant. The interaction of base gas cost and reservoir permeability should be noted. High-permeability rocks (> 500 md) in an annual gas storage cycle may reach 55 percent working storage and 45 percent base gas. The relationship between the reservoir permeability and the base gas ratio is summarized as follows:

Bas gas/storage gas	Base gas %	Reservoir permeability, md
1–0.7	50–40%	500–1000
1.9–1.2	65–55%	200–500
3.0	75%	50

It follows that only high-permeability aquifers have the quality sought for new aquifer storage projects.

13.5 CONVERTING A WATER DRIVE OIL RESERVOIR TO GAS STORAGE

The Loreed reservoir (Michigan Reed City oil field) was converted to gas storage in 1963 after producing 38.5 million barrels of oil (6.12 MMm^3) and 32.8 Bcf (0.93 Bm^3) of gas. It was utilized for oil recovery as the initial step in conversion to storage. Prior to conversion, the 168 wells at Loreed were producing 10,000 barrels (1590 m^3) of oil and 250,000 barrels (39,750 m^3) of brine per month by pump.

The reservoir was essentially liquid filled when gas injection began. In the 1978–1980 cycles, the reservoir produced some 27 Bcf (0.76 Bm^3) out of 49 Bcf (1.39 Bm^3) net injected, with a broad hysteresis loop due to water movement, as shown in Fig. 13-16. The initial pressure gas content cycles showed how water was being displaced. The reservoir has been used continuously to date. It was necessary to drill several western edge observation wells as the gas phase moved in that direction (Fig. 13-17). A high delta pressure approaching 800 psia (5.52 MPa) was used; there were no problems with the caprock but the horizontal movement was not completely anticipated.

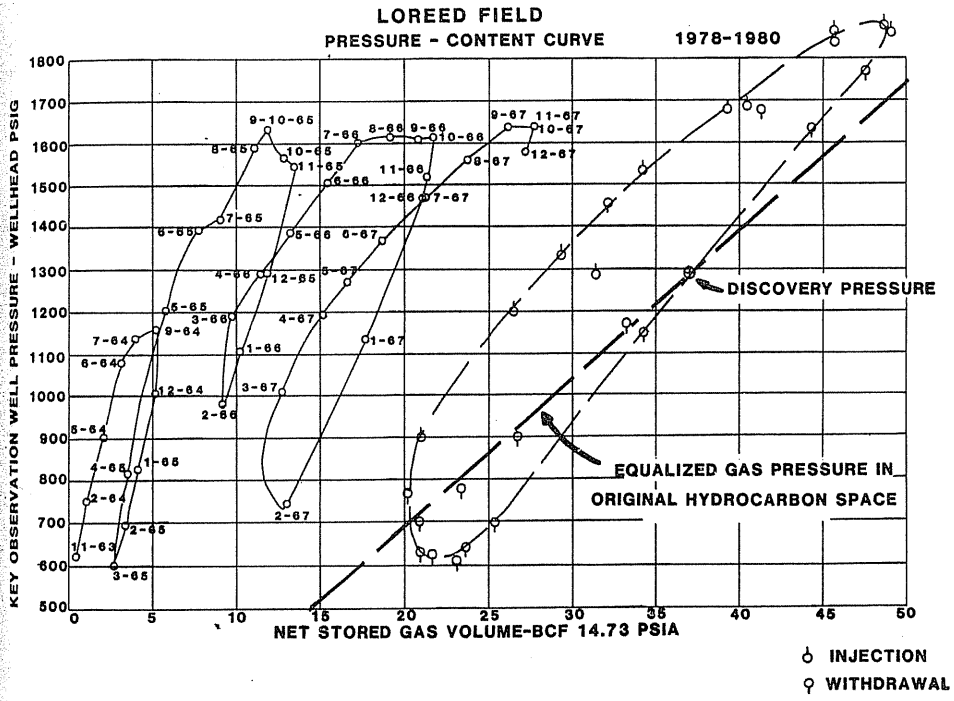

FIGURE 13-16
Pressure–gas content relationship, Loreed Field [Katz & Coats, 1-2].

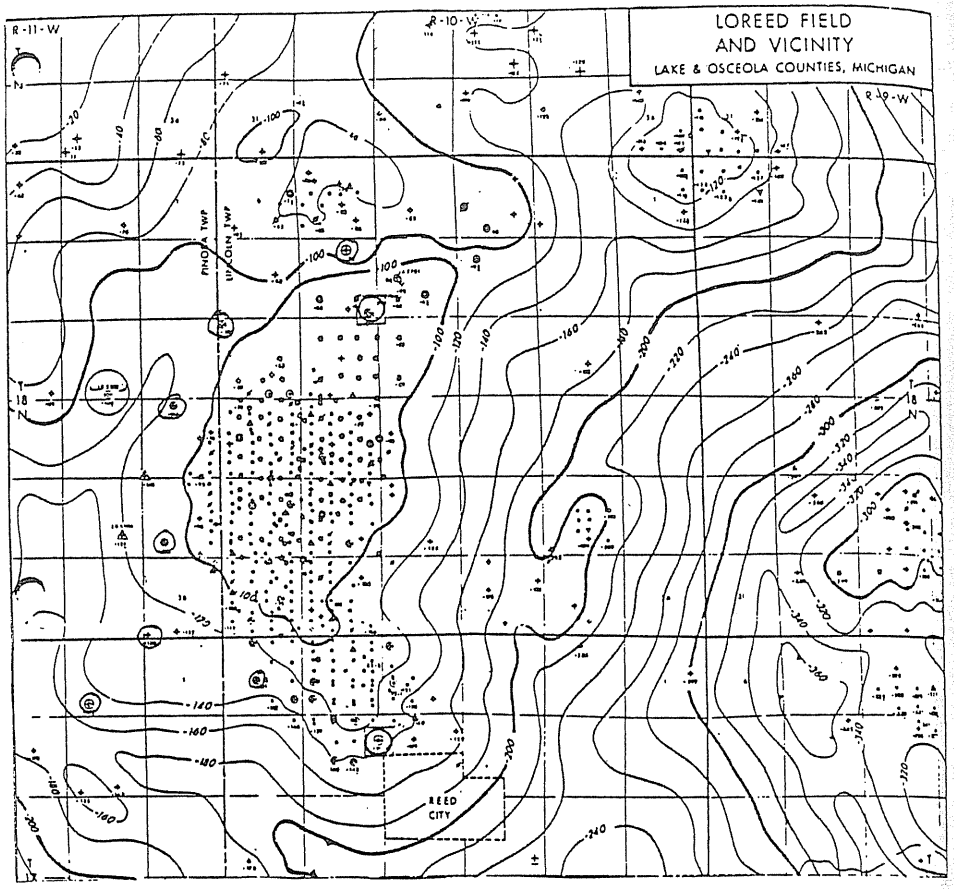

FIGURE 13-17
Added observation well, Loreed Field [Katz & Coats, 1-2].

Another oil reservoir developed for storage is the Louden field in Illinois. It too started with liquid filling the reservoir. Many gas caps underlain by oil layers have been converted to gas storage. Such reservoirs as Aliso Canyon and Montebello in California give excellent service. In such reservoirs, the material balance on the storage gas shows that a fraction of the residual oil in the reservoir becomes resaturated with gas.

13.6 HANDLING AQUIFER PRESSURE VARIATIONS IN GAS STORAGE

Here, a study is given of an Illinois aquifer storage reservoir that has a rim of pressurized water surrounding the aquifer. The effective aquifer pressure for water

movement during the annual storage phase is above the original pressure, because it is within the pressurized rim.

It is concluded that thorough inventory verification studies should include water movement to and from the aquifer. This in turn requires a knowledge of the character of the aquifer. Aquifer observation wells are useful in monitoring water movement.

Empirical Methods—The Pound-Day Concept

Before unsteady state reservoir calculations of water movement (the van Everdingen and Hurst equations mentioned in Chapter 8) were made in gas storage operations, water levels on observation wells adjacent to gas fields were found to rise and fall during a cycle. High gas reservoir pressures caused the water to move away from the bubble and the pressure to rise in the observation well. On the other hand, low gas reservoir pressures caused the water to return, leading to low observation well pressures. It was reasoned that, if the product "days at high pressure" times the "high pressure minus the initial aquifer value" and the product "days at low pressure" times "the difference between the low pressure and initial aquifer value" were equal, there was no net water movement. This is valid only if there is as much flow returning to the gas reservoir per unit of lowered pressure as there is going out per unit of raised pressure. By adding the daily gas bubble pressures expressed as pounds per square inch above initial pressure (positive) or pounds per square inch below initial pressure (negative), the net *pound-days* is obtained for an annual cycle. If the annual sum is negative, the gas bubble would be expected to shrink due to water influx, and, if it were positive, the bubble would grow due to net water expulsion. Katz et al. [13-6] set up a series of calculations to establish the validity of the above rule of thumb for estimating gas storage reservoir behavior.

Quantitative evaluation may be made of the water movement that corresponds to a pound-day. Consider a storage reservoir with an initial aquifer pressure of 1000 psia (6.89 MPa) into which a 0.6-gravity gas is injected at a rate of 30 MMcf/day (0.85 MMm^3/day), while the gas reservoir pressure is essentially constant at 1100 psia (7.58 MPa). At this pressure and a reservoir temperature of 100°F (38°C), the volume of gas at reservoir conditions is 82 standard cubic feet per cubic foot space (82 m^3/m^3). The rate of water movement is $30,000,000/82 = 366,000$ ft^3/day (103,645 m^3/day). As the pressure was 100 psia (689 kPa) above the aquifer, the quantity on a pound-day basis is $366,000/100 = 3660$ ft^3 water efflux/(psi · day), or 150.4 $m^3/(kPa \cdot day)$. Similar evaluations may be made during withdrawal periods. The influx per pound-day may be 10 to 20 percent less than the efflux per pound-day during injection.

Figure 13-18 illustrates reservoir pressure relative to aquifer pressure during growth and subsequent cycling of an aquifer storage reservoir. The pound-day product represented by the area *A* considerably exceeds the pound-days

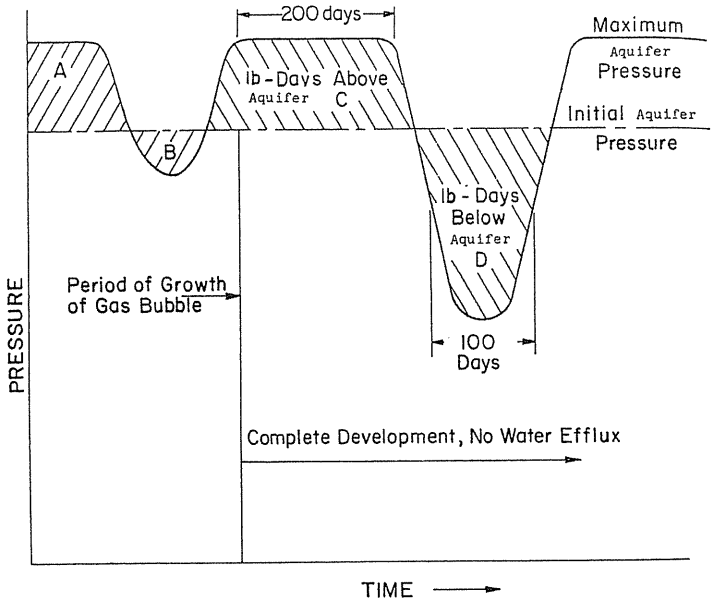

FIGURE 13-18
Pound-days concept [Katz et al., 13-6 courtesy SPE-AIME].

of area *B*, resulting in growth of the bubble. After growth to the desired size, further growth or shrinkage is avoided by a pressure schedule having as many pound-days above initial aquifer pressure (area *C* of Fig. 13-18) as below (area *D*).

Early Studies of Aquifers

An early advance in understanding of aquifers came from the study of the Woodbine aquifer supporting the East Texas water drive oil reservoir [13-1]. With a discovery pressure of 1628 psia (11.22 MPa) at some 3800 ft (1158 m) depth, a bubble point for crude oil averaging some 750–850 psia (5.17–5.86 MPa), and 30,000 oil wells drilled, a crisis arose. When the reservoir withdrawal lowered the reservoir pressure locally to the 800 psia (5.52 MPa) level, gas evolved, and its production threatened to abort the water drive mechanism. Studies revealed a pressure gradient in the Woodbine sand 100 miles (161 km) westward.

The water influx rate by 1935 was sufficient to support only 400,000 bbl (64.4 km^3) oil production at constant reservoir pressure of 1215 psia (838 kPa). The Hawkins field, within the aquifer, was found to have a pressure difference of 280 psia (193 kPa) on opposite sides of a major fault. Figure 1-12 shows a cross section of the aquifer, after Bell and Shepherd [13-1]. Figure 13-19 shows the pressure contours and the location of the Hawkins field [13-1].

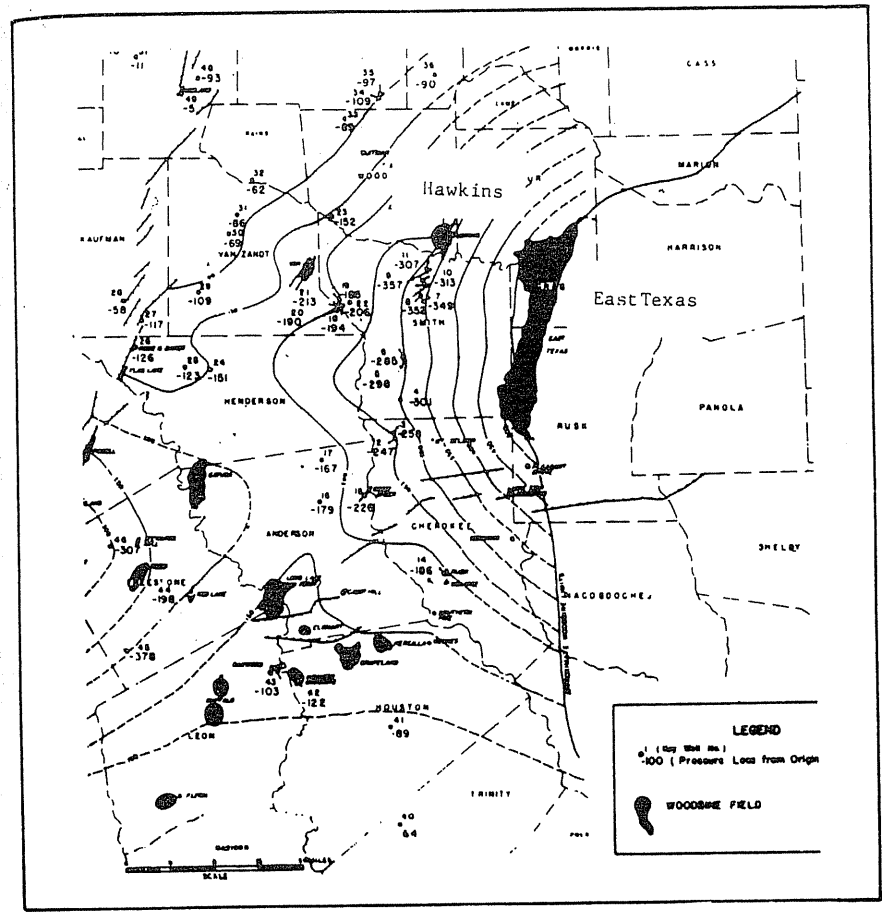

FIGURE 13-19
Pressure contours and location of Hawkins Field on Woodbine Aquifer [after Bell and Shepherd, 13-1, courtesy SPE-AIME].

From this work Schilthuis set forth a pseudo–steady state water movement equation [13-8], and Van Everdingen and Hurst established dimensionless solutions to the unsteady state flow equations [8-18].

New Behavioral Characteristics of Aquifers

Two different areas have been noted where oil and gas withdrawal from water-bearing strata has depleted the ability of the aquifer to maintain the water pressure surrounding storage reservoirs. In developing aquifer storage reservoirs, it was foreseen that the water compression process would build up the pressure in a rim

of aquifer sand when the aquifer became pressurized. In the past it was thought that the pressure rim would dissipate quickly, but now it is clear that this takes considerable time.

The following observations have been made on aquifer behavior in gas storage:

1. The so-called constant volume reservoirs with no observable water movement may well have significant water movement.
2. The accepted water drive mechanism for aquifers hitherto considered infinite may not be valid.
3. Limited aquifers that respond quickly may have limited water supply or extent.
4. Aquifers can be depleted by volumetric removal of adjacent oil and gas.
5. Pressurized water rims develop in aquifer storage and dissipate with time upon shrinkage of a storage reservoir.

An understanding of water movement is essential for accurately verifying gas inventory.

The Nature of Aquifers

Blanket water-bearing zones may have low or high porosities, which are factors in the quantity of water present to expand or contract with pressure changes. The rate at which water moves in or out responding to pressure changes depends upon the permeability and thickness.

Material balances could well be made on water zones when water movement is expected. Generally, it is accepted that water is compressible in the range of 3.0–3.2 $\times 10^{-6}$ vol/vol/psi (0.44–0.46 $\times 10^{-6}$ vol/vol/kPa), with variations due to pressure level and temperature. Likewise, the rock itself as the water container is compressible at a coefficient of 3.2–4.5 $\times 10^{-6}$ vol/vol/psi (0.46–0.65 $\times 10^{-6}$ vol/vol/kPa), [1-39]. The combination gives a round number value of 7 $\times 10^{-6}$ vol/vol/psi (1.02 $\times 10^{-6}$ vol/vol/kPa), i.e., a million ft^3 of water will accept 7 ft^3 of water when its pressure is raised 1 psi.

In practice, at least in oil and gas territory, the apparent compressibility of the system depends upon the quantity of gas and oil bodies in contact with the aquifer. Little has been done to find the effective compressibility of aquifers in contact with gas storage reservoirs.

The time has arrived for aquifer behavior to be included in our evaluation of storage reservoir performance. Water observation wells can be very helpful in measuring pressures. Evaluating the depletion of a gas reservoir with partial water drive in primary when contemplating conversion to storage gives a special opportunity for evaluating the water movement rate. Pressure changes in a gas reservoir may be related to both a withdrawal quantity and an injection quantity. Likewise, the water movement that changes the gas phase volume has two

different components of driving force. These four equations permit evaluation of the water movement rate and other selected variables.

Water Movement Calculations

Consider a gas reservoir some 3000 ft (914 m) in radius surrounded by an aquifer 100 ft (30.5 m) thick with a porosity of 20 percent. From the generalized behavior plot of Fig. 8-20, one knows there is a group of time curves for the pressure distribution in the aquifer. In that figure, the lines give an idea of the degree of compression.

Supposing the gas bubble in the 3000-ft (914 m) radius case is held at 300 psia (2.07 MPa) above the spring pressure for five months, using the constant terminal pressure relationship of reference [1-39], the variation of pressure versus radius may be determined. The result is Fig. 13-20, [1-2]. From calculating the water entering each annular ring out to 15,000 ft (4572 m), it is found that 2.3 million ft^3 (65 km^3) of water have been driven into the aquifer. (A compressibility of 7 $\times 10^{-6}$ vol/vol/psi, or 1.02 $\times 10^{-6}$ vol/vol/kPa, was used.) The gas reservoir will have a volume 2.3 $\times 10^6$ ft^3 (65 km^3) larger in fall than in springtime.

The monograph on water movement [1-39] set forth physical models and computerized solutions for a series of reservoirs, as to the water quantities going into and out of the gas reservoir. The agreement of calculated and measured pressures was used as a check. Superposition of constant terminal pressure functions was handled, always starting with an initial equalized pressure state. The early starting point required in this procedure discouraged its use for handling year-to-year activity. The simpler Schilthuis equation can be helpful in finding changes in reservoir volume.

The pseudo–steady state method of computing water movement put forth by Schilthuis [8-38] (see Section 10-5) applies after the gradient in a given direction

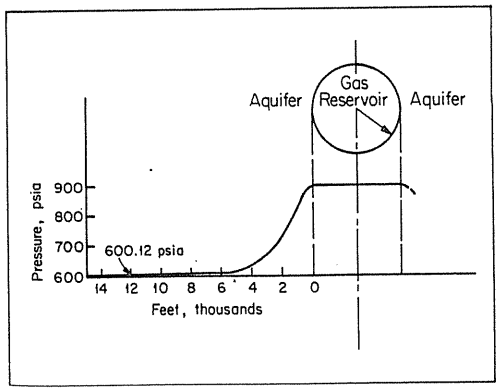

FIGURE 13-20
Pressures for calculating quantity of water moving into an aquifer [Katz & Coats, 1-2].

has been initiated. Each geometry and system will have a water rate coefficient $\dot{E}_w$ giving the flow per unit of pressure difference between gas phase and water phase and per unit of time. For example, the senior writer recalls that the Herscher Galesville reservoir displaced 26,000 ft^3 (736 m^3) per day of water per psia difference in pressure between the gas bubble and the surrounding water pressure. The equation is written

$$W_e = \dot{E}_w(P_0 - P_a)\Delta t \tag{13.2}$$

The cumulative water influx (or efflux) is equal to a water rate coefficient (volume per unit time per unit driving force) times the driving force and time. The driving force is the original or prevailing aquifer pressure minus the hydrocarbon reservoir pressure.

For a storage reservoir, one can adjust the gas injection rates to maintain the gas bubble pressure. The gas rate and pressure permit calculating W_e which in turn gives E_w from Eq. (13.2).

13.7 EXPERIENCES WITH VARIOUS CATEGORIES OF AQUIFERS

Generally, the porous rocks of the earth are full of water. The threshold pressure for hydrocarbon displacing water from tight but porous caprocks is responsible for oil and gas accumulations in the earth [1-38]. Most porous rocks containing oil and gas contain interstitial or connate water, but a few have been identified as being dry [1-91]. Five categories of aquifer behavior in connection with gas storage are discussed here.

Constant volume reservoirs. Reservoirs that have straight line P/Z-versus-production curves and gas injection curves that return along the primary curve are considered constant volume. Reefs in southeastern Michigan as well as some stray sand reservoirs are of this character. Figure 13-21*a* illustrates the behavior. Normally, some movement of the gas-water interface occurs, but the movement may be inconsequential, at least in a single cycle.

Some reservoirs hitherto considered constant volume have been observed to grow as much as 25 percent over 10 years with the use of delta pressures. In such cases, it must be known that the gas bubble will not reach a spill area to assure gas retention. The Goodwell field shown in reference [1-2] has grown more since the behavior shown for 1968.

Moderate water drive. During primary production, water influx raises the pressure above the P/Z curve, and when the observed curve is extrapolated, it gives a high initial content. The type of curve found in gas storage depends upon time/rate phenomena. To push the intruded water out, the gas pressure must exceed the prevailing aquifer pressure; see Fig. 13-21*b*.

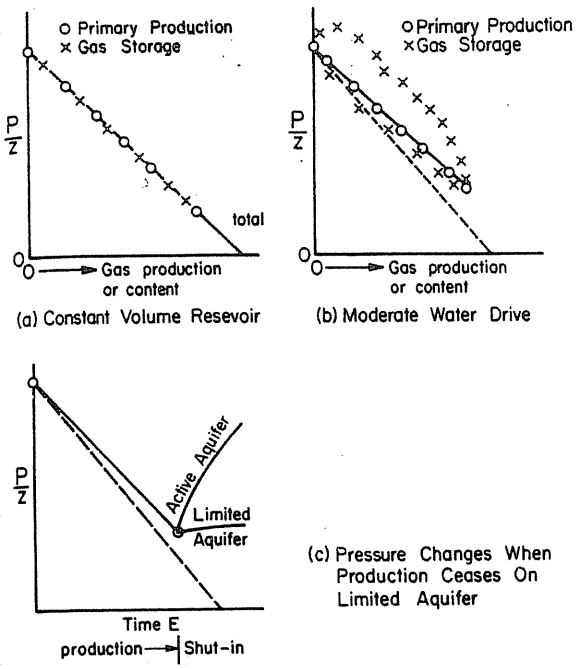

FIGURE 13-21
Types of aquifers surrounding gas storage reservoirs [Katz, 13-4, courtesy AGA].

The pound-day diagram verified by Coats [13-3] using the prevailing aquifer pressure as the base line controlling water movement in or out is shown in Fig. 13-18. It is well to have this behavior in mind for moderate water drive reservoirs.

Limited aquifers. Sometimes the aquifer may pinch out on one edge and be cut off in the other directions by a fault. With high permeabilities it may be difficult to separate gas expansion from water influx. One may be fooled by the behavior when closed in from production; the reservoir pressure does not rise significantly, but levels off within a short time (Fig. 13-21*c*). This behavior reveals the limited character of the aquifer.

Infinite aquifers. Extensive sandstone layers for 10–30 miles (16.1–48.3 km) or more in each direction are considered to behave like infinite aquifers. The Mt. Simon sand layers in Illinois are of this character. This type will be discussed further in the section on the study of the Illinois aquifer storage reservoir, Fig. 13-22 or Table 13.15.

The foregoing types of aquifer behavior are based on the relative effects of gas injection/withdrawal and water movement in controlling the reservoir pressure. A fifth class of aquifer behavior is seen when the removal of oil or gas from other reservoirs in the vicinity of the storage reservoir changes the aquifer

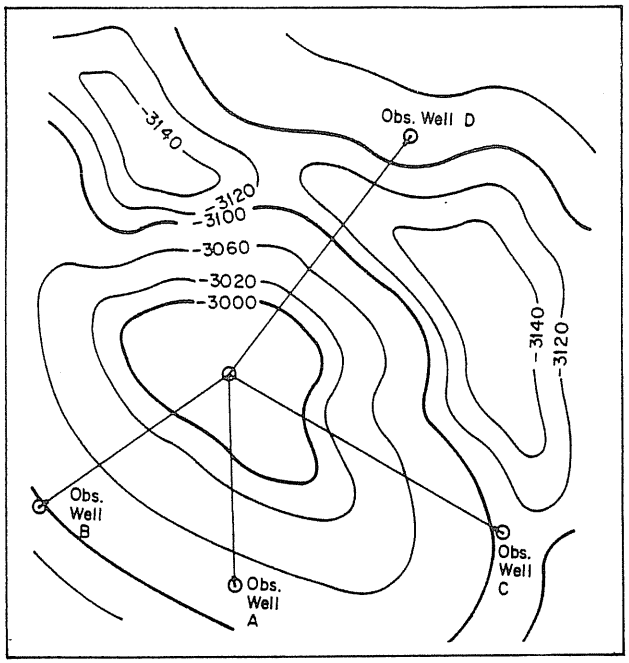

FIGURE 13-22
Structure and area map of aquifer gas storage reservoir A [Katz, 13-4, courtesy AGA].

TABLE 13.15
Data on Illinois aquifer storage reservoir, Mt. Simon [Katz, 13-4, courtesy AGA]

Depth to gas-water contact	3710 ft (1131 m)
Initial aquifer pressure	1625 psia (11.2 MPa)
Reservoir temperature	100°F (38°C)
Reservoir permeability:	
md (reported)	37
md (used in calculations)	50
Porosity	0.11
Water viscosity	1.05 cp (1.05×10^{-3} Pa · s)
Total compressibility	9×10^{-6}(vol/vol/psi)(1.3 vol/vol/kPa)
No. of injection/withdrawal wells	32
No. of observation wells	13
Gas in place, maximum to date	50.7 Bcf (1438×10^6 m^3)
Storage gas gravity	0.60
Radius of observation wells from center of gas reservoir	
Well A	9,896 ft (3016 m)
Well B	12,386 ft (3775 m)
Well C	12,725 ft (3878 m)
Well D	15,571 ft (4746 m)

pressure. All such reservoirs occur within the same strata and are part of the same system.

In Michigan an early discovery gas reservoir initially at 1460 psia (10.07 MPa) was converted to gas storage. Each year the withdrawn gas was returned in like quantity to the storage reservoir to maintain the initial gas inventory at the end of injection. An investigation of reduced performance revealed that the surrounding aquifer no longer was at 1460 psia (10.07 MPa) but had been reduced to some 1100 psia (7.58 MPa), permitting injected gas at pressures above the aquifer to spill. The oil and gas production in many other reservoirs on the same aquifer apparently had absorbed the expansion of the aquifer [13-2].

Concept of Aquifer Movement

In calculating water movement for material balances on Illinois aquifers, it became clear that the effective aquifer pressure rose during periods of high rates of reservoir growth. Likewise, one would expect the aquifer pressure to recede when the storage volumes in the gas reservoirs were reduced. How could such behavior be predicted or handled? One could no longer refer to the discovery pressure as a basis for water movement in a storage cycle.

Within the time limits of a storage cycle, after a rim of pressurized water has accumulated, one would expect the pressure gradients to look like Fig. 13-23. The height of the effective aquifer pressure P_e above the original pressure P_0 as water is pushed out into the aquifer depends upon the water volume displaced per unit time and upon kh, the product of permeability and thickness of the aquifer in the area around the gas reservoir. Another item of interest is the distance r to reach P_e, that is, how far out in the aquifer one needs to go to find the relatively stable reservoir pressure during the storage cycle.

Information on these items was given by reference [13-4], which made available 10 years of development history: gas injection rates, reservoir pressure,

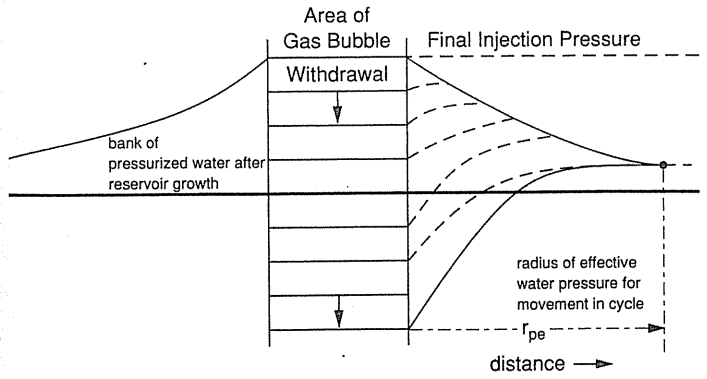

FIGURE 13-23
Illustration of pressures in aquifer after growing bubble and during a storage cycle [Katz, 13-4, courtesy AGA].

initial reservoir conditions, observation well data, and other data. Some basic information is given in Table 13.15. Figure 13-22 gives the structure and location of wells, including four aquifer observation wells, for reservoir A.

Unsteady State Calculations of Water Movement and Radial Pressure Gradients

Background for the procedures to predict reservoir pressures and aquifer pressure gradients is provided in an AGA monograph [1-39]. Therein the procedures in Chapter 8 of Van Everdingen and Hurst [8-18] are set forth for the several models, with illustrations of history matching to obtain reservoir characteristics, followed by prediction of reservoir pressures for postulated gas injection/withdrawal schedules. In references [13-4,13-5], unsteady state calculations were made to obtain the pressure gradients in an aquifer following the general format proposed by references [1-39,13-7].

Comparison of Predicted Performance with Actual Data

Using a time step of 30 days, gas bubble pressures in reservoir A for the last 10 years were used as input, and bottom hole pressures were predicted for the four observation wells using the method of superposition. The closest observation wells A and B are continuously in severe unsteady state. The observed pressure values for observation well B are higher than those for observation well A. The radii of observation wells from the center of the gas bubble are listed in Table 13.15. The closer a water observation well is to the gas bubble, the greater the conformance of the pressure variations to the gas pressure changes. Wells close to the gas bubble should not be considered completely reliable in representing the pseudoequilibrium pressure.

The other two observation wells, C and D, are farther away and in a different direction from the gas bubble. Figure 13-24 shows the behavior of observation well D for five years.

Observed and Calculated

Pressure gradients are plotted in Fig. 13-25 for March 1982, just as the injection operation started. The variation has been lowered to 7 psia (1 kPa). From the calculated aquifer pressure gradients, the radial pressure curves can be plotted. Figure 13-26 shows how these pressures converge at observation wells C and D. The pseudo aquifer pressure at observation well D drops slowly when the gas reservoir no longer is growing in size.

The study indicates there is a stable reservoir pressure during a single cycle that in effect controls water movement during the cycle in this case. This aquifer pressure used to represent the driving force does not match observation well pressures. More accurate calculations can be achieved via full-scale simulation.

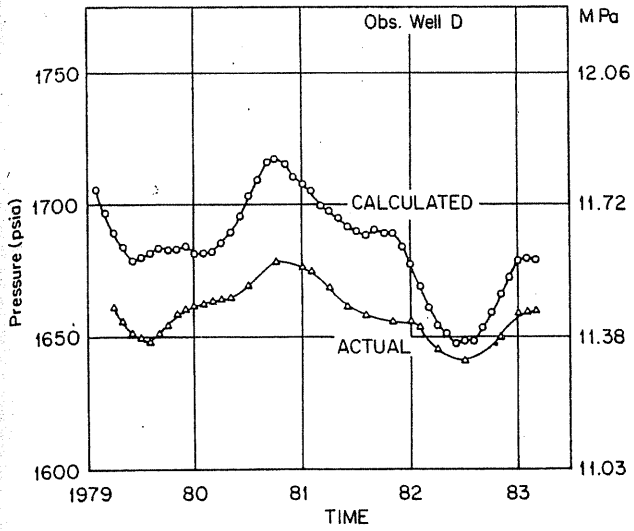

FIGURE 13-24
Comparison of computed and observed pressures at observation well D [Katz, 13-4, courtesy AGA].

The pseudo aquifer pressure for controlling water influx into the gas reservoir over an annual storage cycle was 1655 psia (11.4 MPa) in 1982 as compared to the original of 1625 psia (11.2 MPa).

Such calculations and observation well data will indicate the radius for a stable pressure in an annual cycle.

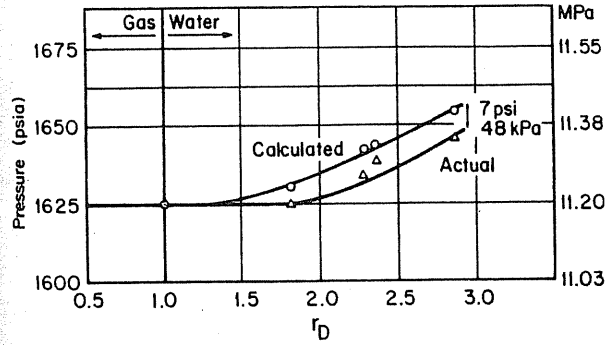

FIGURE 13-25
Calculated and observed pressure gradients in water phase [Katz, 13-4, courtesy AGA].

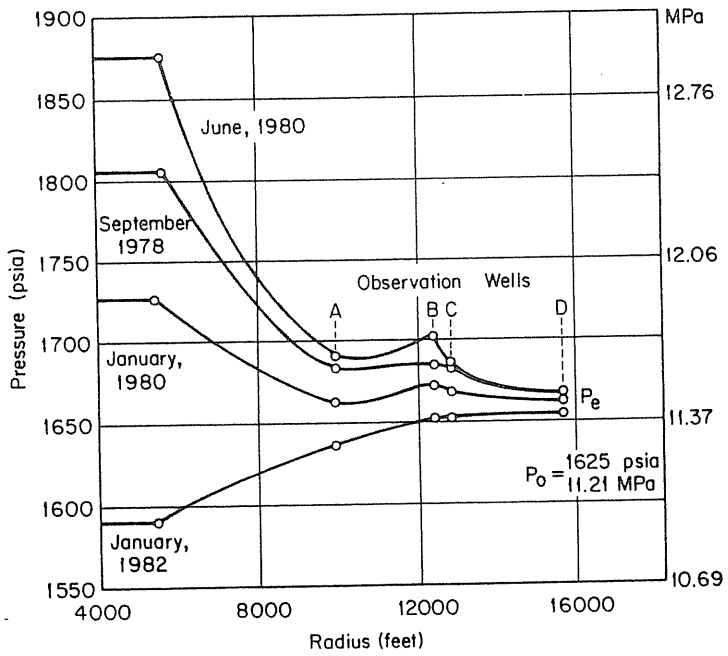

FIGURE 13-26
Illustration of pseudo-equilibrium pressure in aquifer storage reservoir A [Katz, 13-4, courtesy AGA].

Water Rates

At the end of gas injection, an injection rate can be found at which the gas bubble pressure remains constant. The volume of injected gas can be converted to reservoir volume and the water rate per unit time determined. Then, with the pseudoequilibrium pressure of the aquifer and the stable gas bubble pressure, the rate per unit time per unit driving force (pressure difference) can be determined. Alternately, pressure changes during an injection period and a withdrawal period can be used to write material balance equations and evaluate the water rate coefficient.

Adjustment of Material Balance for Water Movement

A single equation that parallels the constant volume reservoir formula is obtained by accounting for changes in the available gas pore volume due to water movements, using the pseudo–steady state model. From Eq. (13.2) and water movement calculations, the following relation is derived:

$$Q_1 = \frac{\Delta Q - (\dot{E}_w/B_g)\cdot \Delta t(P_e - P_a)}{(P/Z)_1 - (P/Z)_2}\left(\frac{P}{Z}\right)_1 \qquad (13.3)$$

Example 13.1. The aquifer storage reservoir A has a metered inventory of 45.048 Bcf (1.23×10^9 m^3) at 1614 psia (11.1 MPa; $Z = 0.833$). During withdrawal of 2.706 Bcf of gas, the pressure dropped to 1545 psia (10.65 MPa; $Z = 0.839$) over a period of 38 days. The water rate coefficient is estimated to be 1400 ft^3/(day · psi). The equilibrium aquifer pressure is 1655 psia (11.4 MPa). The reservoir temperature is 100°F (38°C). Calculate the initial gas present based on its performance during gas withdrawal.

Solution. The use of Eq. (13.3) requires knowing whether $P_e > P_a$ or $P_a > P_e$; that is, whether gas is withdrawn or injected [13-5]. For gas withdrawal, $P_e > P_a$, Eq. (13.3) applies as written.

$$P_a = \frac{1614 + 1545}{2} = 1579 \text{ psia (10.89 MPa)}$$

$$\text{Water influx} = \dot{E}_w \cdot \Delta t(P_e - P_a) = 1400 \times 38(1655 - 1579)$$
$$= 4.04 \times 10^6 \text{ ft}^3$$

$$\frac{1}{B_{g2}} = \frac{(1545)(520)}{(0.839)(560)(14.7)} = 116.32 \text{ Scf/ft}^3 \text{ of space}$$

$$\frac{1}{B_{g1}} = \frac{(1614)(520)}{(0.833)(560)(14.7)} = 122.8 \text{ Scf/ft}^3 \text{ of space}$$

$$\text{Gas displaced by water} = 116.32(4.04 \times 10^6) = 460 \times 10^6 \text{ Scf}$$

Thus,

$$Q_1 = \frac{\Delta Q - (\dot{E}_w/B_g)\cdot \Delta t(P_e - P_a)}{(P/Z)_1 - (P/Z)_2}\left(\frac{P}{Z}\right)_1$$

$$= \frac{2.706 \times 10^9 - 4.04 \times 10^6 \times 116.32}{1614/0.833 - 1545/0.839}\,\frac{1614}{0.833} = \underline{45.09 \text{ Bcf}}\ (1.28 \times 10^9 \text{m}^3)$$

By an alternative method [13-4], examining Fig. 13-27, where the initial gas in pore space $(GPV)_1$, equal to the water influx plus the current gas in pore space $(GPV)_2$:

$$(GPV)_1 - 4.043 \times 10^6 = (GPV)_2$$

Also,

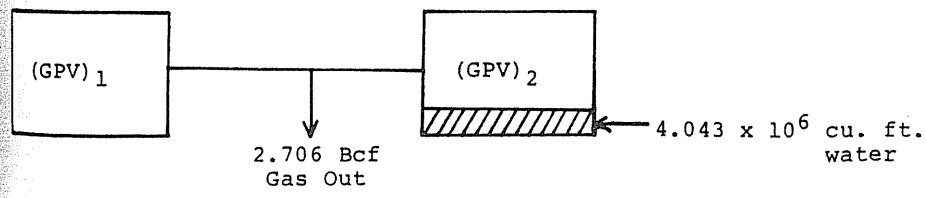

FIGURE 13-27
Sketch of material balance for Illinois Aquifer [Katz, 13-4, courtesy SPE-AIME].

$$(\text{GPV})_1 \cdot \frac{1}{B_{g1}} = 2.706 \times 10^9 + (\text{GPV})_2 \cdot \frac{1}{B_{g2}}$$

$$(\text{GPV})_1(122.8) = 2.706 \times 10^9 + \left[(\text{GPV})_1 - (4.043 \times 10^6)\right](116.72)$$

$$(\text{GPV})_1(122.8 - 116.72) = 2.706 \times 10^9 - (4.04 \times 10^6)(116.72)$$

$$(\text{GPV})_1 = 367.4 \times 10^6 \text{ ft}^3 \text{ pore space}$$

Thus,

$$\text{Initial gas, } Q_1 = (\text{GPV})_1 \frac{1}{B_{g1}} = 367.4 \times 10^6 \times 122.8$$

$$= \underline{4.512 \times 10^{10} \text{ Scf}}$$

It is preferred that the denominator $\Delta(P/Z)$ in Eq. (13.3) be greater than 200. When this closed value to inventory was found, the range of water rate values that might occur was considered. By an alternate calculation the water movement rate coefficient $\dot{E}_w$ was found to be 1659 ft^3/(day · psi). Using this value in Eq. (13.3), the initial gas in place is calculated as 43.25 Bcf, as compared with metered inventory of 45.058 Bcf. The calculated value is 1.81 Bcf (4.0 percent) below the measured inventory. If no water movement were used in this calculation, 54.5 Bcf would be the calculated result, 9.45 Bcf more than metered (21 percent higher).

13.8 CONCLUSIONS

Aquifer pressure should not be taken as the discovery value without verification. Growing of gas reservoirs in aquifer storage builds a ring of pressurized water around the gas bubble. For many years, the effective water pressure controlling water movement into or out of the gas space may be that within this ring. *Prevailing aquifer pressure* is the preferred term.

Some natural gas reservoirs occur within aquifers that become depressurized by water moving into oil and gas space vacated by natural production. Then there are limited aquifers, which can have arrested levels of water movement. Water observation wells can be helpful in monitoring aquifer behavior.

Some day an investigator will find a way to predict the minimum distance from the gas bubble for finding the equilibrium aquifer pressure, as a function of *kh*, delta pressure level, and other pertinent variables.

Inventory verification procedures must include consideration of the behavior and condition of the surrounding aquifer.

HOME PROBLEMS

13.1. A gas field with a moderate degree of water drive is converted to gas storage. The initial or discovery pressure in the reservoir was 1430 psia. The contemplated pressures during a storage cycle are shown. Will the gas space grow, shrink, or remain stable with this pressure schedule?

Average pressures during month, psia			
January	1400	July	1600
February	1070	August	1800
March	700	September	1900
April	650	October	1900
May	870	November	1800
June	1210	December	1700

13.2. *Aquifer design problem*: Figure 13-28 shows the structure of the top of the New Richmond sandstone. The caprock above the New Richmond consists of a dense

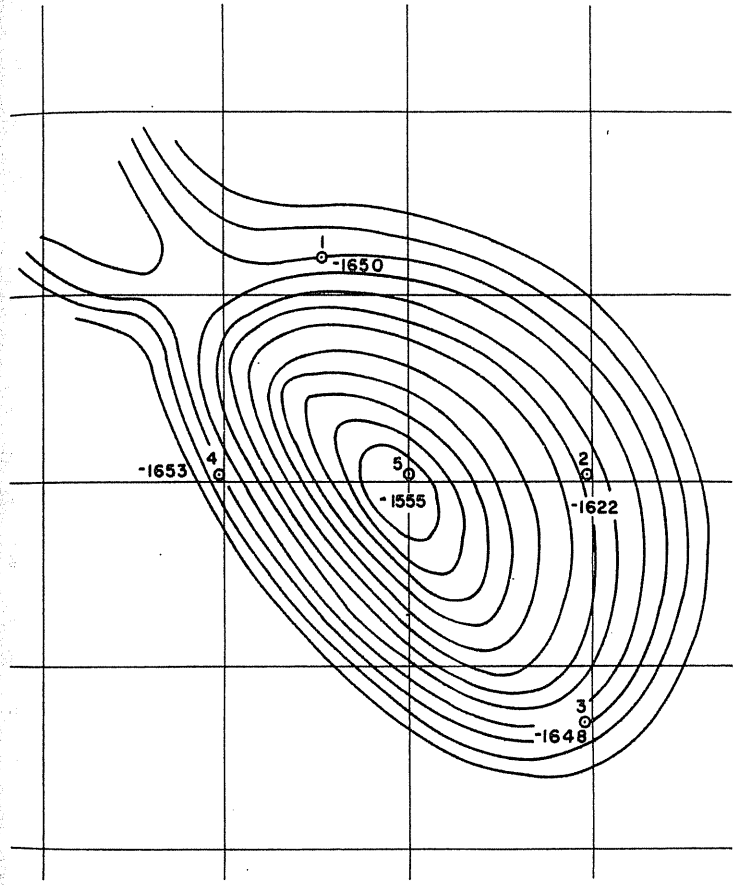

FIGURE 13-28
Contours on top of New Richmond sand, surface elevation 550 ft, one-mile grid [Katz & Coats, 1-2].

rock 40 ft thick with permeability of 10^{-6} md or less and gas displacement pressure of 500 psi and greater. The sand has an average porosity of 0.185 and a permeability of 365 md. Its average thickness is 68 ft on the top of the structure, but four miles away from the structure it thins to 40 feet in one quadrant and 52 feet in another while it thickens to 80 feet in the other two quadrants.

Gas of 0.6 gravity is to be stored. The water in the aquifer has 5000 ppm dissolved solids. The temperatures in well No. 5 were measured as 52°F at 100 ft and 81°F at 2100 ft (elev. 550 feet).

The wells are drilled through the New Richmond sand and $5\frac{1}{2}$ in. casing cemented. The top five feet of the sand are perforated. The original water levels observed in the five wells are $+421 \pm 2$ ft.

Prepare a development plan for this reservoir, including a timetable from date of approval on May 1 by quarters, showing the drilling wells, gas injection quantities, availability of gas for market, etc. The timetable could well be carried on for five years. It should be made after the conditions for complete development have been determined. It may be assumed that gas is available for injection as needed except from December 15 through March 1. During the first winter of development, 10 Mcf/day are available during 50 of these days. Gas is delivered to the field at 500 psia and to market at 400 psia. Include in your development plan a schedule of well completions, gas injection, gas withdrawal to market, reservoir pressures, and installed horsepower at complete development, and then give a timetable for the development process.

REFERENCES

13-1. Bell, J. S., and J. M. Sheperd, "Pressure Behavior of the Woodbine Sand," *Trans. AIME,* Vol. 192, 19 (1951).

13-2. Clark, F. H., and D. L. Katz, "Finders Keepers," *Proc., AGA Distribution/Transmission Conference,* 688–698, Boston (1985).

13-3. Coats, K. H., *Prediction of Gas Storage Reservoir Behavior,* Ph.D. Thesis, U. of Michigan (1959).

13-4. Katz, D. L., "Handling Variations in Aquifer Pressure in Gas Storage," *Proceedings, AGA Trans. Conference,* 675–682 (1985).

13-5. Katz, D. L., and Divyesh Shah, "Establishing the Effective Aquifer Pressure Controlling Water Drive for Gas Storage Cycles," SPE Preprint 13234 (1984).

13-6. Katz, D. L., M. R. Tek, and K. H. Coats, "Effect of Unsteady State Aquifer Motion on the Size of an Adjacent Gas Storage Reservoir," *Trans. AIME,* Vol. 216, 247 (1959).

13-7. Katz, Marvin L., *Fluid Flow and Heat Transfer in Stratified Systems,* Ph.D. Thesis, U. of Michigan, Ann Arbor (1960).

13-8. Schilthuis, J. R., and William Hurst, "Variations in Reservoir Pressure in the East Texas Field," *Trans. AIME,* Vol. 114, 164 (1935).

CHAPTER 14

MONITORING, INVENTORY VERIFICATION, DELIVERABILITY ASSURANCE, AND SAFETY IN STORAGE OPERATIONS

There are four key elements in observing ongoing gas storage operations: (1) monitoring, (2) inventory verification, (3) deliverability assurance, and (4) safety. Based on the senior author's experiences, each of these elements will be discussed briefly in this chapter.

14.1 MONITORING

Monitoring means more than taking data and making records. It is the analysis of the data that usually detects the early signs of unwanted gas movement. The system under consideration, in addition to the reservoir, includes

1. Surface piping
2. Wellbores
3. Layers of rock above and below the storage zone
4. Surrounding area at distances of 1 to 3 miles or more

The reservoir storage engineer should develop a mental model of the reservoir behavior. Only then will deviations due to unwanted behavior become evident. For example, gas losses through corrosion spots or casing collars can be detected by rising annulus gas pressures, temperature, noise, and neutron logs in wells, or even lower than normal closed wellhead pressures in comparison with neighbors.

The challenge is to gather large amounts of data and display them so that the reservoir engineers may see trends and note anomalies that imply that all is not according to the model in mind. It may be difficult to distinguish routine changes of no particular moment from those that have serious consequences. Annual reviews by teams of engineers, geologists, field operators, and management are helpful. The analysis of the data is a key ingredient. Table 14.1 is a guide to monitoring.

Delineation of System

The primary components of the system are the surface lines and meters, the wells, and the storage reservoir container, as shown in Fig. 14-1. The gas is confined by water in the pores of the caprock, on the edges, and below the gas bubble. This water also is part of the system, for it can move significantly in some cases in response to gas pressures.

The system consists of any fluid in rocks within or near the storage area that is or might become subject to pressure changes and/or fluid movement during a series of storage cycles. With this broad definition of the storage system, an areal map is needed.

Reservoir Behavior

The curve of P/Z versus accumulative flow rate Q should be a straight line if water influx/efflux is not significant (Fig. 10-15). With water movement, P/Z would be higher than expected after withdrawing gas and lower for injection, when the pressure exceeds that of the surroundings. Usually, P/Z stabilizes with 48–72 hours shut-in; however, for some storage reservoirs it takes two weeks or more to reach reservoir equilibrium.

The overall compressibility factor Z of combined top and base gases can vary as much as 3–5 percent if gas of different composition is injected. The compositions of injecting and withdrawing gases should be continuously monitored to make possible a determination of the average compressibility factor.

Data Gathering

The gathering and analysis of data are an important part of storage operations. Daily observation of the gas bubble pressure in a static key well and of gas flows to or from the reservoir are needed for inventory and operating purposes.

TABLE 14.1
A guide to monitoring gas storage reservoirs: storage inventory reports, consultants review

- Overview
  - Historical data in files for each reservoir
  - Current field data taken periodically
  - Current reports of data from field in office files
  - Closed pressure data fall and spring
  - Analysis of data for estimating migration and losses
  - Monthly write-off for gas lost and unaccounted for
  - Annual report
  - Consultants review of report and data
- Historical data in files
  - Geology, primary production
  - Conversion to storage, base, and book gas content
  - Reservoir data sheet
- Field data taken
  - Wellhead pressures, bottom hole pressures, gas injection and withdrawal
  - Fuel use, annulus pressures, observation well data, blowdowns
  - Incidents indicating unwanted gas movement, etc.
- Where field data resides
  - For field personnel
  - For office personnel
  - Plans for updating periodically
- Closed pressure data
  - Management arrangements between field and office
  - Guide to field practice—dead weight, periods of measurement, need for bottom hole measurements
  - Office examination of data, review for anomalies, methods of averaging, maps and planimetering
- Analysis of monitoring and shut-in pressure data
  - Office analysis of closed pressure data
  - In P/Z vs. contents plots, assessing changes and degree of verification of gas migration; alternate use of Horner plots
- Review of monitoring data
  - Edge water wells going to gas, pressures at periphery along possible migration routes, pressures, interpretation
  - Field work on wells, casings
  - Upper zone well behavior
  - Logging data, interpretation
  - Changes in nearby reservoirs
  - Recommendations for work, studies in coming year
- Write-off of monthly gas lost and unaccounted for, current and cumulative—as a matter of record
- Annual inventory report
  - Decision as to what goes into report and information retained in files
  - Goal for completion date, management needs
- Consultants review procedure
  - Attendance list—field representatives?
  - Assembly of data for review over and above information in annual report
  - Review of previous year's recommendations
  - Review of data on various topics for each reservoir
  - Minutes of meeting, letters of recommendation, and/or approval
- Supplement: Field performance on gas deliverability
  - Changes in wells, new ones, clean outs
  - Withdrawal experience, field test, agreement between field and individual wells
  - Plans for maintenance and usage in coming year

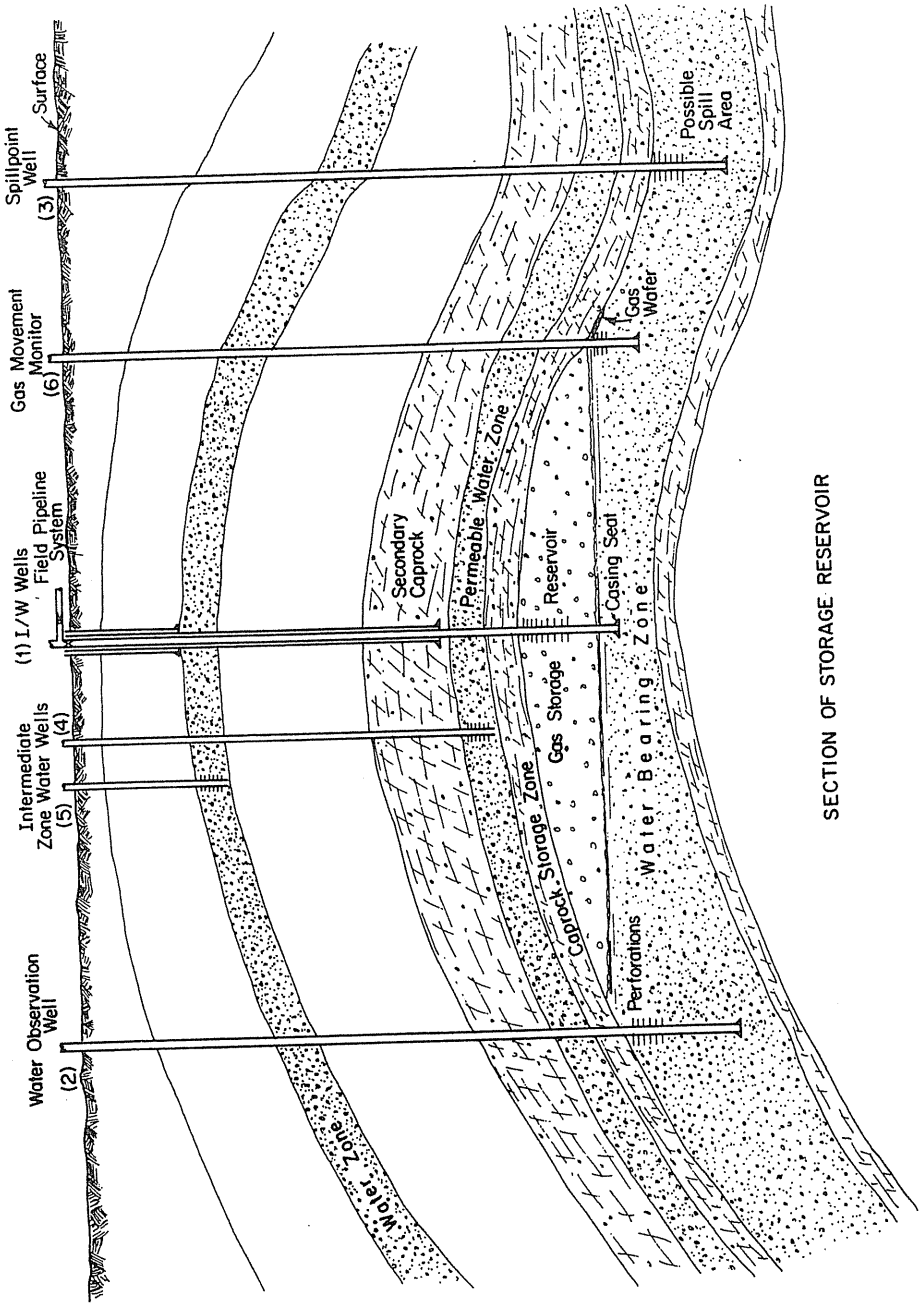

FIGURE 14-1
Definition of storage system [Katz, 14-12, courtesy SPE-AIME].

TABLE 14.2
Measurements employed in monitoring

Gas metering injection, withdrawal
Gas usage, compression, fuel
Gas loss on blowdowns, seepage, and unaccounted for loss estimates
Storage pressures
Key wells in storage zone
Closed pressures on all I/W wells
Flowing pressures on production tests
Annulus pressures on storage wells
Periodic or recording pressures on observation wells
Temperatures
Static reservoir
Flowing at meters, wellhead
Wellbore survey for anomalies
Pressures on water wells
Bottom hole pressures on water seal when column is partially full of gas
Water levels in wellbores on observation wells
Fluid levels and wellhead pressures
Logs
Neutron logs for accumulations of gas
Noise logs for indications of gas movement out of or behind casing
Presence of gas
In edge wells at water seal
In upper zone, water layers
Local water supplies
As evidenced by vegetation damage
Gas samples and analyses
For discriminating between storage gas and other gases
For finding movement of injected gases
Analysis of gases dissolved in water
Routine for gas gravity and Btu value

Observation well data, annuli pressures, and any information that could signal unwanted gas loss or movement are part of monitoring.

Should accumulated data indicate a problem, decisions are needed as to the steps that should be taken for fully understanding and correcting the problem. Table 14.2 lists some of the measurements made.

Not only are data obtained, but an analysis is done by personnel familiar with the particular system. When the data have been analyzed, decisions may be necessary for action. Follow-up of corrective actions should also be considered as part of monitoring.

Possible Gas Loss Mechanisms

There are six mechanisms, as shown in Fig. 14-2, for gas to be lost from the reservoir:

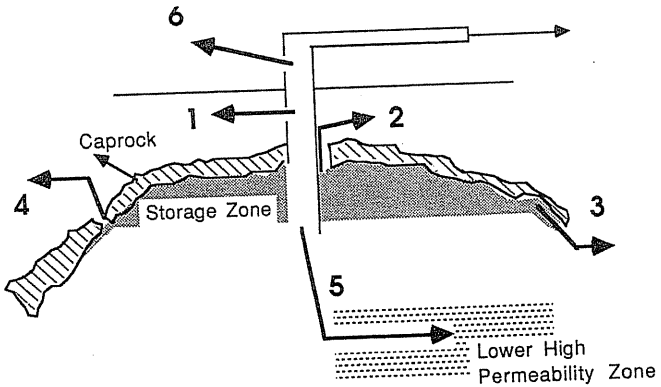

FIGURE 14-2
Possible gas loss mechanisms.

1. Gas leaving casing through collars, corrosion, or tool holes
2. Gas moving through imperfect cement at caprock, casing shoe, or perforated area
3. Gas migrating past spill points in storage zone
4. Gas penetrating caprock on aquifers
5. Gas moving downward along axis of structure or to zone below storage zone
6. Piping and compression station seepage and valve losses

Each of these will be discussed: What route does gas take? What are the driving forces and the resistances? What measurements monitor possible losses by a given mechanism?

CASING LEAKS. Gas leaks along the wellbore (Fig. 7-3) are likely to cause higher annulus pressures, and such incidents are a cause for logging the well. Annual or semiannual temperature logs or neutron logs on key wells should be made with particular attention to the porous and permeable observation zone above the storage zones. The logs would locate the casing leaking spot by giving an abnormal reading at that spot. Sometimes accumulation may occur in the fall after an injection season, but not be there in springtime, presumably because of upward migration of the accumulated gas during winter. Figure 14-3 illustrates upward movement of leaked gas through the annulus cement column with time. Casing patches or setting of a tubing or liner can eliminate the problem when gas loss is verified. Tracers inside the casing can be observed as they move up the annulus. Reduction in the closed pressure of a well below its neighbors may flag a loss.

Many annulus pressures stand at 20, 30, or 50 psia (138, 207, or 345 kPa) only as the result of gas seepage. Blowdown time on such annuli and rate of

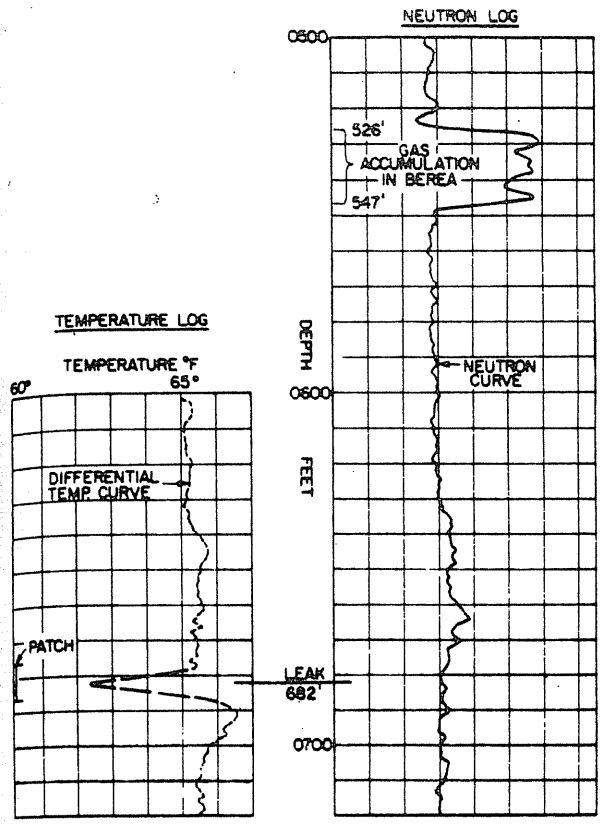

FIGURE 14-3
Temperature and neutron logs on well with casing collar leak [Katz, 14-9, courtesy of East Ohio Gas Co.].

buildup thereafter tell something of the source of the gas. A quick blowdown and slow buildup indicate a small leak.

In one real case, gas percolated to the surface as the first observation. A temperature log located the leak at 700 ft (213 m) depth, and it was sealed by a casing patch. An examination of closed pressure data showed a 29, 17, and 3 psia (200, 117, and 21 kPa) depression compared to neighbor wells in the three prior years. Here is a case where monitoring data were obtained but not examined carefully.

The driving force between gas in the casing and the earth will cause gas to move out of the casing. Figure 14-4 shows pressure versus depth for a storage reservoir. Also, the extra driving force that occurs is shown for several delta pressures. The driving force is the pressure at B, C, or D minus the pressure at A, the hydraulic pressure in the earth. The use of delta pressure raises the pressure gradient significantly only at deeper levels.

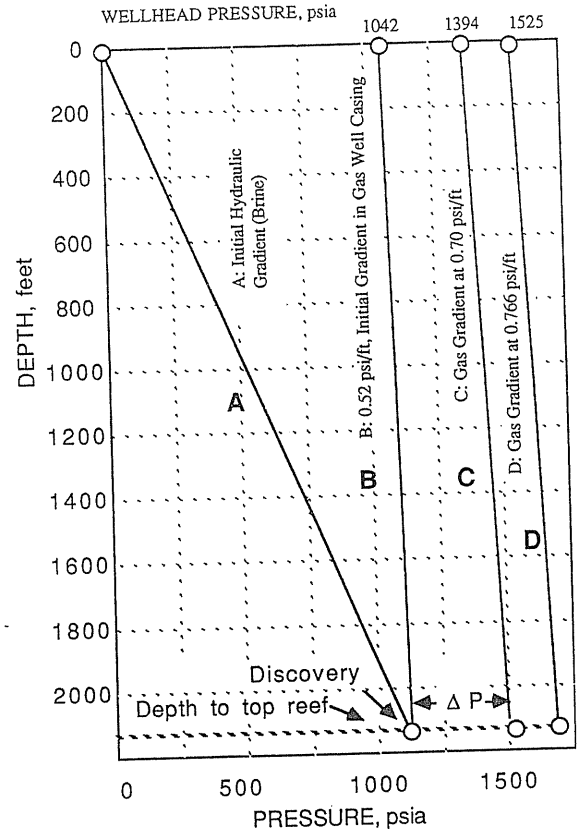

FIGURE 14-4
Pressures in wells at Michigan Reef reservoir.

GAS MOVING BEHIND THE PIPE, CASING SHOE LEAKS. A small proportion of cemented wells may have imperfect cement sheaths at the caprock. The high-pressure gas may penetrate the cement sheath, dehydrate it, and migrate up the annulus as with casing leaks. The observations used to find the leak are quite similar to those for casing leaks, only with special attention to the bottom-of-the-well temperature, neutron logs, and noise logs.

A remedy is to squeeze cement the caprock; there may be some penalty with thin caprocks, which do not provide enough working space to assure a complete seal.

Wells with high bottom hole temperatures (>160°F, or 71°C) may have significant cooling at the entrance to the storage zone resulting from gas injection. This condition masks results of temperature surveys, and in such cases, leaks are best detected by noise logs. High-temperature storage wells seem to have a higher potential for casing shoe leaks than wells at <120°F (49°C); this is possibly due to the alternate cooling and heating in storage cycles.

GAS MIGRATING PAST SPILL POINTS. Reservoirs with moderate or high rock permeability ($k > 25$ md) may have gas pressing toward spill points, Figs. 14-1 and 14-2, as the end of the injection cycle is reached. Observation wells on such a route should detect the presence of migrating gas. This loss mechanism can attain high rates with no surface indications, especially when there are insufficient observation wells.

Gas may go down the axis of a reservoir structure when there is a high permeability for the crestal rock zone. In water drive carbonates, the permeability along the crest may be high, allowing water to move more easily, and gas to go along with water below the general gas-water interface within the bubble. Even sand deposits exhibit this phenomenon [14-15].

It is believed that any gas that passes a well completion will be detected by gas bubbling up through a water column of the observation wells.

GAS PENETRATING THE CAPROCK IN AQUIFERS. Caprocks for depleted gas or oil fields are believed to have proven seals at the discovery pressure level. However, aquifer caprocks need to be tested by gas injection as well as by core tests (Chapter 2).

Fractures or other anomalies are believed to be responsible for the few incidents of caprock leakage that have occurred. Herscher (Illinois, Galesville) has a continuous recycle to gather shallow migrated gas, and other reservoirs recycle gas to lower the upper zone pressure or remove gas from shallow zones. Shale-to-shale faults hold gas, and sand opposite sand at faults provides complete transmissibility as shown at the Troy Grove aquifer.

Water-filled observation wells in the upper zone would display a pressure rise when gas enters the water zone. A few aquifers have been abandoned because of caprock leakage: two examples, Lake of the Woods in Indiana and Brooksville in Illinois, have been documented in an AGA monograph [1-38].

When gas percolates to the surface, it causes vegetation to be stunted or die. It appears to interrupt the capillary moisture-gas system. Figure 14-5 is a photograph of corn fields with gas migration through the soil. Instances are known where a water well point driven into the ground 2–3 ft gives enough gas to ignite a small torch.

GAS MOVING DOWNWARD TO ZONES BELOW. Gas on occasion moves downward to a deeper zone for two possible reasons. In water-confined gas bubbles, water movement from the well takes place more easily in a deeper zone because of its high permeability (Fig. 14-6*a*). The second reason is that a low-pressure reservoir in a deeper horizon may provide a pressure sink to attract gas via incompletely cemented wellbores penetrating both a storage zone and the low-pressure zone below (Fig. 14-6*b*).

In developed aquifers on thick zones like the Mt. Simon in Illinois, there are thin layers of shale that have considerable but not complete continuity. Using delta pressures of 200 or 300 psia (1.38–2.07 MPa), gas may find a route downward

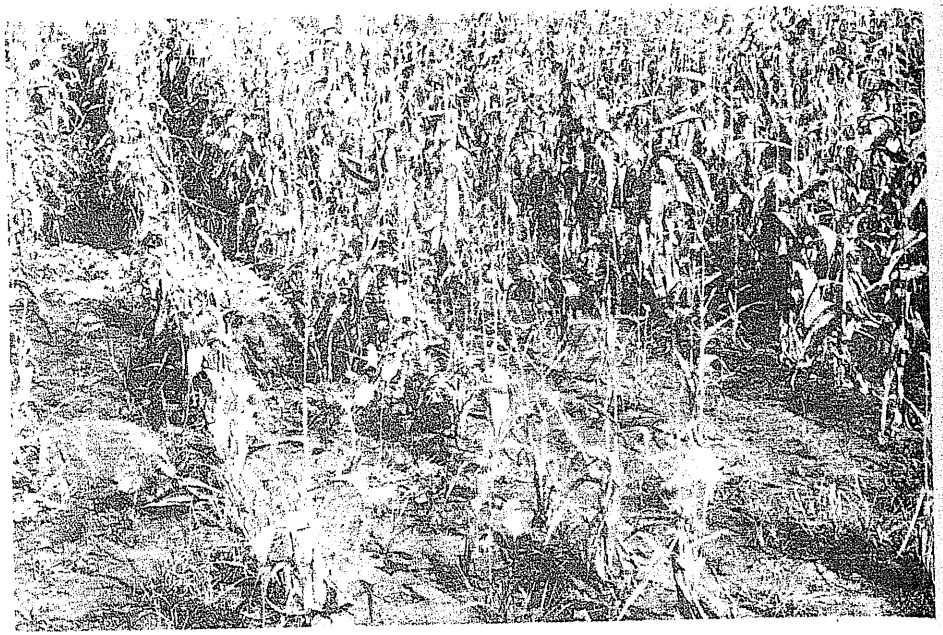

FIGURE 14-5
Gas in soil preventing corn growth in localized area [Katz & Coats, 1-2].

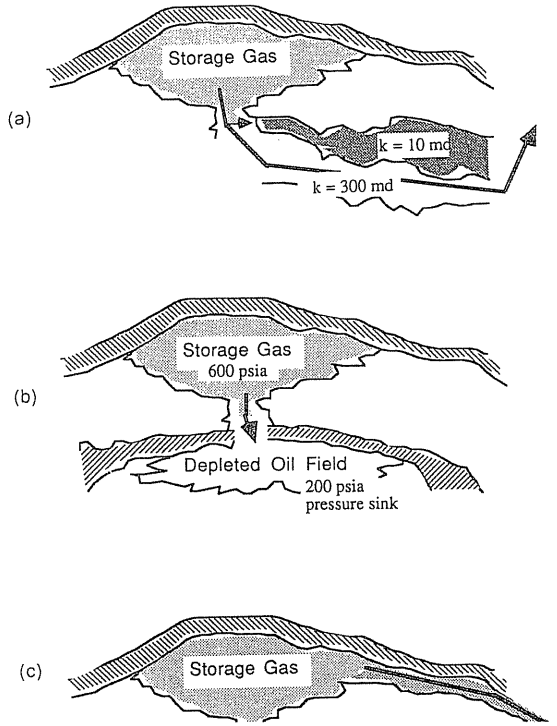

FIGURE 14-6
Gas moving downward

to a deeper permeable zone [14-15] leaving a water-filled zone between. Such gas does not return to the upper zone when its pressure is lowered.

The downward transfer route appears to water out and thereby trap gas below during the withdrawal cycle. On one occasion [14-15], a well completed in the deeper zone produced at 10 MMcf/day (0.283 MMm^3/day) even though no gas had been injected into it.

SURFACE PIPING AND COMPRESSOR LOSSES. Many companies prepare a "gas lost and unaccounted for" plan which results in a monthly "field use" deduction from inventory. The amount of gas loss from the surface equipment depends on the average prevailing pressures.

Usually one uses the average leaking rate per unit pipe surface per pound gas pressure, e.g., 0.0002 Mcf/yr/ft^2/psi [1-1]. For 20 reservoirs that contain 500 Bcf (14.2 Bm^3) gas when full, the annual loss is estimated to have reached one Bcf per year. Over a 25-year period, with storage reservoirs added periodically, the accumulative gas lost calculated by this procedure was some 14 Bcf (0.4 Bm^3).

Transmission pipe walls are believed to represent a small portion (< 10 percent) of unaccounted-for gas losses. Fittings, valves, flanges, meter runs, control systems, and compressors account for most of the escaping gas. Accordingly, it is important to know whether there is a compressor station within the boundaries of a given storage system; that is, metered gas enters the system containing the station, and withdrawal gas goes through the station when it is leaving the system.

At high pressures (> 1500–2000 psia, 10.3–13.8 MPa), equipment is usually constructed and maintained better than at low pressures (500–1000 psia, 3.45–6.89 MPa), since leaks in high-pressure systems are obvious (noise) and cannot be tolerated. Judgment indicates that compressor station losses are some 60 percent of the total unaccounted-for losses, along with 30 percent in lines and wellheads and 10 percent in casing strings of wells. Base lines of gas loss may be found for small pipeline systems that comprise an areal network, with metered gas entering and leaving it. Here an annual gas loss may be calculated by differences of gas in and gas out. Such systems often have compressor stations within them. Losses are expected to be 0.3–1.0 percent of throughput.

A Simple Field Survey

Not long ago, on visits to a storage field, one would not have been surprised to hear a hissing sound of gas leaking. In a compressor station, a strong gas odor shows gas leaking.

A field survey was made using a sensitive flame ionization gas detector, a sound meter, and an ultrasonic indicator. It was found that some 15 out of 20 points checked at a wellhead leaked gas. The presence of leakage gas in the atmosphere was noted by analyses out to 5–10 ppm. A crude measurement with an orifice indicated an audible leak might well represent a loss rate of 1.0

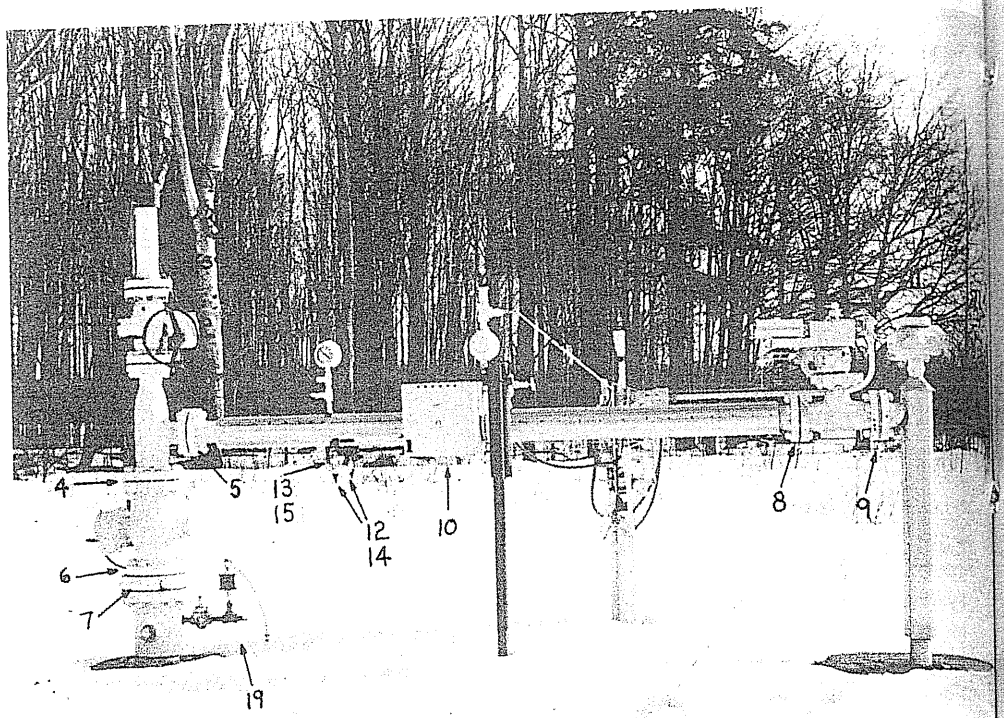

FIGURE 14-7
Storage well installation with identification of sampling points.

MMcf/yr (0.0283 MMm^3/yr). Figure 14-7 shows the possible gas leak points of a wellhead: valves, flanges, and screw joints.

As environmental concern rises, the leaking gas has to be monitored and controlled, especially for refineries in southern California. The American Institute of Chemical Engineers (AIChE) conducted a symposium, "Fugitive Emissions—Measurement and Control Problem," with several papers presented [14-1]. The EPA has made extensive studies of gas losses from plants [14-8], and API made a study of atmosphere emissions of refineries [14-2].

14.2 INVENTORY VERIFICATION

Good monitoring data should lead to accurate inventory verification. Inventory verification tells how well field measurements can be used to ascertain the inventory of base gas to support a lower pressure, and to determine that the top or

working storage gas injected may be withdrawn when needed. In making gas withdrawal measurements, the term *effective gas content* is used to mean the quantity of gas that is there and effective in delivering gas during the withdrawal period. Differences between effective gas content and the metered inventory can be gas within the storage reservoir that is so remote from the producing wells that its full pressure is not utilized at the delivery point within the time frame of a storage cycle. Also, any gas lost from the storage reservoir can become part of the difference.

Pressure-Volume Relationships

Each year those responsible for operations must assure management that the inventory of net stored gas resides in the reservoir in communication with the wellbores. Closed pressure measurements for a period of 3 to 15 days or more are used for all wells, normally when at maximum and minimum storage pressures. For constant pore volume reservoirs, for which the closed pressures are relatively uniform and stabilized, the pressure content data relates the metered production or change in inventory to the initial content.

$$\text{Initial content} = \frac{\text{change in content}}{(P_1/Z_1) - (P_2/Z_2)}\left(\frac{P_1}{Z_1}\right)$$

$$Q_1 = \frac{Q_1 - Q_2}{(P_1/Z_1) - (P_2/Z_2)}\left(\frac{P_1}{Z_1}\right) \tag{9.3}$$

where Z can be obtained from pressure P, temperature T, and gas gravity G. When water movement rates during withdrawal are known, the volume change of the reservoir must be used to modify the relationship accordingly, that is:

$$Q_1 = \frac{(Q_1 - Q_2) - (\dot{E}_w/B_g) \cdot \Delta t \cdot (P_0 - \overline{P})}{P_1/Z_1 - P_2/Z_2}\left(\frac{P_1}{Z_1}\right) \tag{13.3}$$

which has been discussed in Chapter 13. Establishing two independent relations for two time periods in the form of Eq. (13.3), the values $\dot{E}_w$ and Q_1 could be obtained. Aquifer pressure P_0 is recorded in an observation well in the aquifer, and $\overline{P}$ is the average gas bubble pressure.

Observation Wells

Observation wells are the instruments for measuring pressures in the gas storage zone and the water-bearing zones surrounding the stored gas. As shown in Fig. 14-1, there are six classes of observation wells: *Class 1* wells are used for operating the gas storage project. They are attached to a gas pipeline system for carrying the gas to and from a compressor plant. Normally, one of these gas wells, a key well, is closed in and used in static condition for measuring the gas bubble pressure. The second group of wells, *Class 2*, contain water. They are drilled to

determine the structure and used to measure the water level and/or water pressure in the storage zone beyond the gas bubble. Spill point wells, *Class 3*, are used to observe whether any gas reaches the saddle. *Class 4* and *Class 5* wells monitor the water level in the intermediate permeable layer to note pressure changes that might be caused by mechanical gas leaks from the casing or cement at the wellbores. Wells used to follow the downward movement of gas prior to a spill point are identified as *Class 6*.

Gas Transfer between Reservoirs

When gas is stored at pressures equal to or above the discovery pressure, one must examine the nearby presence or absence of oil and gas reservoirs in the same formation. When such reservoirs are at a stage of depletion, there is a driving force between the storage zone and such pressure sinks. A water seal in the productive zone of 100 or 200 ft (30.5–61 m) represents only a 45–90 psi (310–621 kPa) barrier [14-13]. Over a period of time water can be pushed out of the seal, permitting storage gas to transfer to a producing reservoir. One example is the gas migration from West Unionville to Ruston in Louisiana [14-4].

Pressure Gradient

Figure 14-8 is a sketch of West Unionville and Ruston with several key wells. Well depths, gas contents (percent of storage gas), and selected pressure records are included. The figure shows the pressure decrease from Ruston to West Unionville around 1968. After West Unionville was converted to a storage field, the direction of the pressure gradient reversed; then the storage gas migrated from West Unionville to Ruston. Despite gas production, the pressures rose from 1968 to 1977 at Ruston.

Gas Analysis

A possible way of identifying gas transfer is the use of gas analyses of reservoir gases. Table 14.3 gives sample calculations for West Unionville and Ruston based on all the constituents. In Fig. 14-8, a higher percentage of storage gas appeared near the saddle than at far away places, showing gas transfer from West Unionville to Ruston through the saddle. In reference [14-4], a study concluded that 33 Bcf of storage gas was transferred. Staff at FERC agreed with the analysis and, finally, the engineers of IRS accepted the study.

At the time of the leakage of gas at Herscher [1-2], several tracers were considered. Propylene from LP gas at refineries was a convenient and effective tracer. Small pressurized tanks like those used for propane at homes were used, with a mini-pump to inject the C_3H_6-rich LP liquid into a well. The propylene is easily detected in produced gas by a chromatograph, since no natural gas system contains propylene.

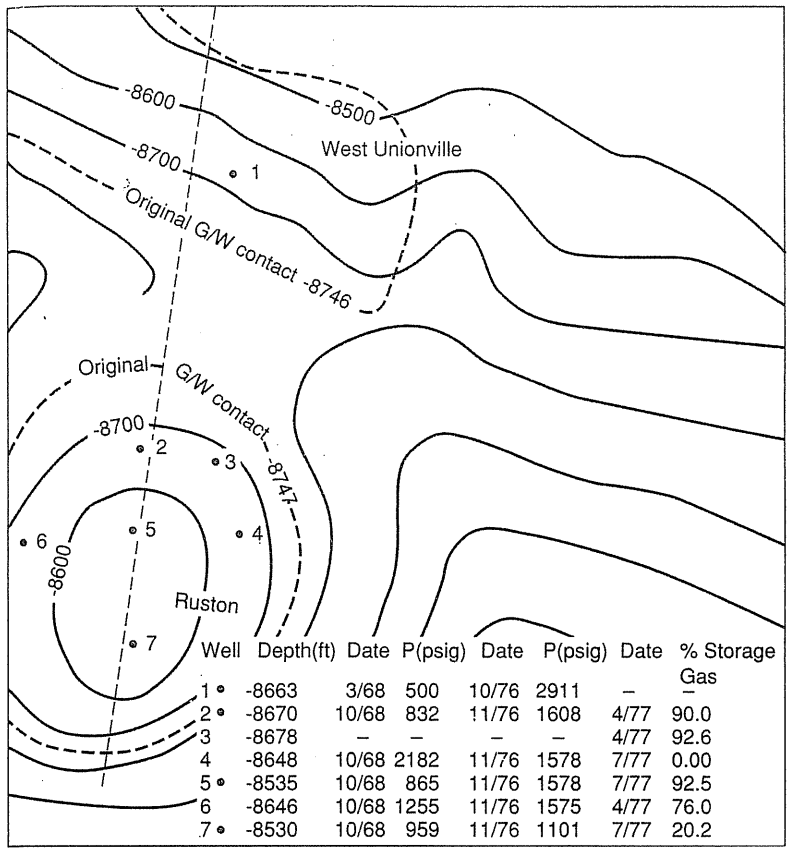

Well	Depth(ft)	Date	P(psig)	Date	P(psig)	Date	% Storage Gas
1	-8663	3/68	500	10/76	2911	–	–
2	-8670	10/68	832	11/76	1608	4/77	90.0
3	-8678	–	–	–	–	4/77	92.6
4	-8648	10/68	2182	11/76	1578	7/77	0.00
5	-8535	10/68	865	11/76	1578	7/77	92.5
6	-8646	10/68	1255	11/76	1575	4/77	76.0
7	-8530	10/68	959	11/76	1101	7/77	20.2

FIGURE 14-8
(*a*) Map of West Unionville, Ruston area—Lincoln and Union Parishes, Louisiana; contours on top of Vaughn sand [after Clark & Katz, 14-4, courtesy AGA].

Frequently, a naturally occurring constituent like N_2, CO_2, or He may be used alone as a tracer when it is absent in one of the gases. At West Unionville and Ruston, the N_2 and CO_2 give the same mixture of storage and native gases; therefore, a material balance on all constituents could be used as tracer.

Native gas in California has less than 10–20 ppm He, and storage gas from Texas contains over 300 ppm He; hence, He is a good tracer for storage gas movement for such a project. As gas transfers, it may contact liquid (oil) and become enriched, especially by the C_{5+} constituents. Therefore, these constituents may not be useful tracers.

Gas analyses of base gas, often native gas, and of storage gases (working top gas) should be obtained early for any project. The isotopic C^{13} method is recommended as an independent analytical route for clear identification. The C^{13}

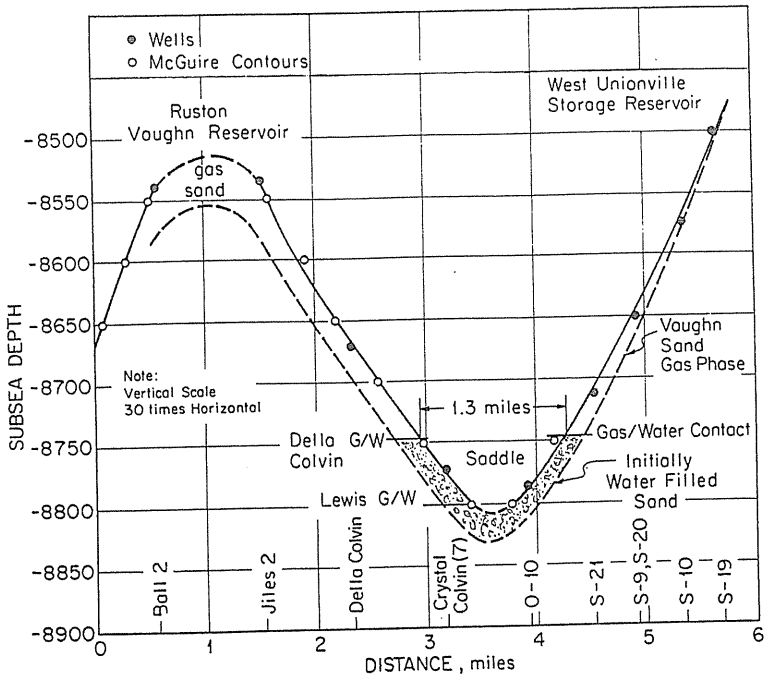

FIGURE 14-8
(*b*) Section from well 1 of West Unionville to well 7 of Ruston [Clark & Katz, 14-4, courtesy AGA].

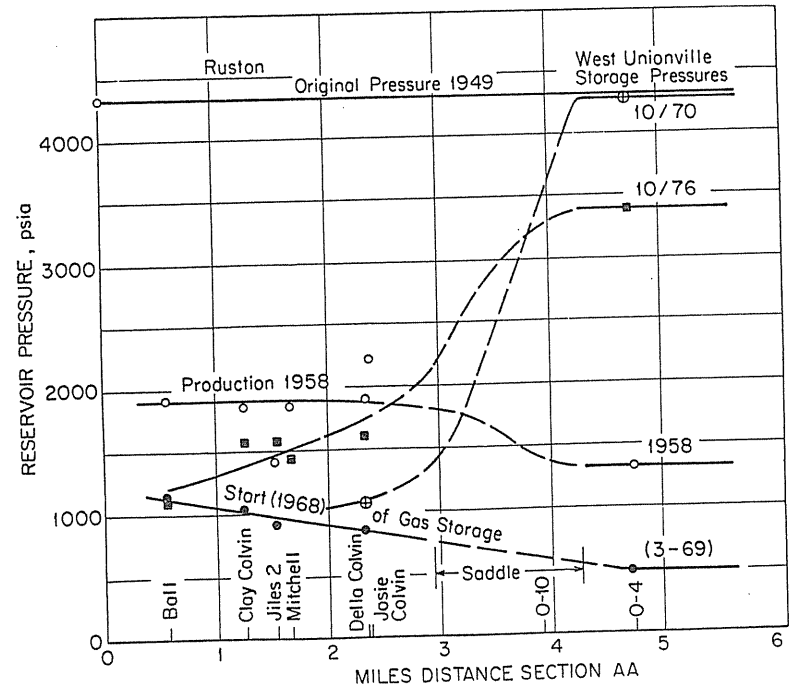

FIGURE 14-8

TABLE 14.3
Method of computing storage gas breakthrough from gas analysis [Katz, 14-9]

Constituent	A Native gas recipient well	B Storage gas in storage reservoir	C Current recipient gas	Percentage storage gas in C
N_2	0.58	0.59	0.50	—
CO_2	3.21	0.98	1.03	97.8
C_1	88.01	94.82	94.31	92.5
C_2	5.13	3.12	3.48	82.1
C_3	1.74	0.31	0.44	96.9
i-C_4	0.30	0.04	0.07	88.5
n-C_4	0.49	0.06	0.09	93.0
C_{5+}	0.54	0.08	0.08	0.08
	100	100	100	

Calculation of percentage of gas B in gas C assuming gas C is the mixture of gas A and gas B:

$$\%\text{ of gas B in gas C} = \frac{100(\%\text{ in gas C} - \%\text{ in gas A})}{(\%\text{ in gas B} - \%\text{ in gas A})}$$

Example using methane:

$$\%\text{ storage gas B in gas C, current recipient} = \frac{100(94.82 - 88.01)}{(94.31 - 88.01)} = 92.5\%$$

content of methane is a distinct characteristic for a given source. Should the gases for a given situation have different $\delta 13/\delta 12$ values in base analyses (see Chapter 17), this tracer is independent proof of the presence of transfer gas [14-5]. This analytical method is given in Chapter 4; several laboratories provide such service.

Gas Flow between Reservoirs

When two adjacent gas reservoirs have a differential pressure, the water seal separating them may become displaced and natural gas may transfer from the high pressure to the lower pressure (Fig. 14-8) [14-4]. This happened from Ruston to West Unionville to the extent of some 15 Bcf (0.425 Bm^3) in primary.

It is necessary to analyze the transfer situation carefully. For example, the first gas transferred may be native gas in the storage reservoir, but in due time the storage gas follows. So the first breakthrough gas may not be a reliable criterion.

How to evaluate the gas flow between reservoirs is shown in Fig. 14-9. Instead of conducting a full-scale simulation, a simple relationship has been derived for computing the approximate time for breaking the water seal between reservoirs when a pressure differential exists. It neglects elevation difference and assumes that gas flows behind the advancing gas-water interface with an estimated constant gas saturation and effective permeability in plug flow fashion, that is,

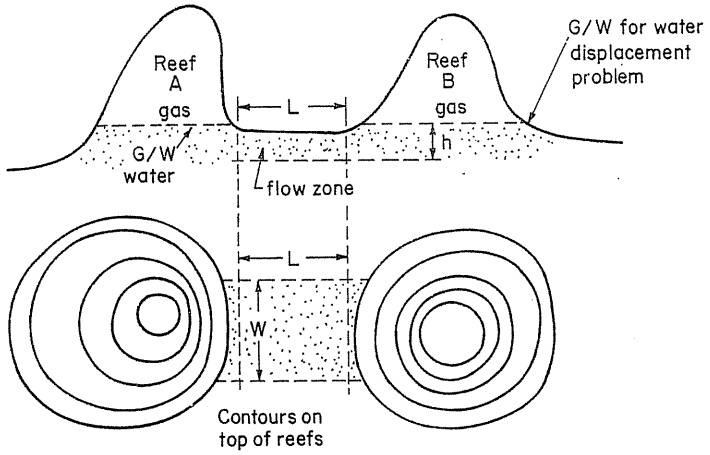

FIGURE 14-9
Adjacent reefs connected by water-filled low-permeability dolomite [Katz & Tek, 14-13, courtesy SPE-AIME].

$$t \text{ (days)} = 79L^2\frac{\mu_w}{k_w}\phi S_g\frac{1}{P_1 - P_2}\left(1 + \frac{k_w\mu_g}{k_g\mu_w}\right) \tag{14.1}$$

where subscripts w and g denote water and gas, L (ft) is the length of water seal as shown in Fig. 14-9, μ (cp) is the viscosity, k (md) is the permeability, ϕ is the porosity, S_g is the gas saturation, and P_1 and P_2 are the pressures of the two adjacent reservoirs. The constant 79 is replaced by 5×10^{11} in SI units.

Once gas has broken through a seal between reservoirs, there is interest in finding the expected range of flow rates. The linear flow formula for the geometry of Fig. 14-9 becomes

$$Q_g \text{ (MMcf/day)} = 1.12 \times 10^{-7}\frac{k_g hW}{L\mu_g ZT}(P_1^2 - P_2^2) \tag{14.2}$$

where Q_g is the gas flow rate, h (ft) is the thickness of the saddle, W (ft) is the width of the saddle, Z is the average compressibility factor, and T (°R) is the average temperature of the reservoirs. In SI units, the constant is 1.42×10^{-15} to give m^3/s.

Example 14.1 [14-4]. Two adjacent reservoirs are separated by 5000 ft (1524 m) as shown in Fig. 14-9. Calculate the time needed for the water seal to break while the reservoirs have a pressure difference of 500 psi (3.45 MPa), and calculate the gas flow rate between two reservoirs after the water seal is broken.
The fluid/reservoir properties are

$$L = 5000 \text{ ft}$$

$$S_g = 0.5$$

$$\mu_g = 0.0135 \text{ cp}$$

$$\mu_w = 0.80 \text{ cp}$$

$$\phi = 0.2$$

$$k_w = 1200 \text{ md}$$

$$k_g = 100 \text{ md}$$

$$G = 0.6$$

$$Z = 0.83$$

$$hW = 1000 \text{ ft}^2$$

$$T = 540°\text{R}$$

$$P_1 = 1500 \text{ psia}$$

$$P_2 = 1000 \text{ psia}$$

Solution. From Eq. (14.1),

$$t \text{ (days)} = 79L^2\frac{\mu_w}{k_w}\phi S_g\frac{1}{P_1 - P_2}\left(1 + \frac{k_w\mu_g}{k_g\mu_w}\right)$$

$$= 79(5000)^2\frac{0.8}{1200}(0.2)(0.5)\frac{1}{1500 - 1000}\left(1 + \frac{1200}{100}\frac{0.0135}{0.8}\right) = \underline{317 \text{ days}}$$

From Eq. (14.2),

$$Q_g \text{ (MMcf/day)} = 1.12 \times 10^{-7}\frac{k_g hW}{L\mu_g ZT}(P_1^2 - P_2^2)$$

$$= 1.12 \times 10^{-7}\frac{(100)(1000)}{(5000)(0.0135)(0.83)(540)}(1500^2 - 1000^2)$$

$$= \underline{0.463 \text{ MMcf/day}}$$

14.3 ASSURANCE OF DELIVERABILITY

Flow tests on individual wells are obtained as in gas production operations. From gas inventory and/or reservoir pressure measurements plus deliverability data, one can predict the field flow at several stages of the storage cycle [14-10]. The performance of storage reservoirs becomes less predictable during periods of prolonged high withdrawal rate due to pressure sinks that may develop as a result of heterogeneities.

Another problem of continuing interest is interference by water reaching the wellbore. The presence of water not only reduces the permeability to gas but also effectively cuts down the bottom hole pressure drawdown available for gas flow due to increased density of well fluid in the flowing column. For aquifers, water interference problems are likely to subside as the gas bubble thickens. Each

reservoir and set of wells must be tested to determine which wells will have water intrusion at a given stage of the withdrawal cycle. Deliverability of storage wells after 20, 30, or 40 years of repetitive use may decrease as a result of sandface contamination.

The deliverability of wells in Michigan Stray sand reservoirs has declined 4.5 percent per year because of fines, salt precipitation, shale sloughing, and oil residues. Early attempts to remove salt gave only a slight increase in deliverability. Recent techniques generally have been successful in increasing deliverability by as much as 426 percent. This was achieved by alternately injecting volumes of (1) xylene, (2) 3% HF/4% HCl, and (3) 2% NH_4Cl [7-4]. Virtually all the wells that were stimulated maintained the increase in deliverability the following year.

Deliverability Tests

There are three components to calculating deliverability from individual well test data: (1) the effective permeability of the rock adjacent to the well, (2) the location of the observation well at which the upstream pressure (P_f) is measured for calculation of the flow, and (3) the position of the stored gas and its ability to travel to the wells.

Initially, four-point back pressure tests should be conducted individually to obtain the absolute open flow (AOF) for each well. Periodically, one- or two-point flow tests are in order. Since the drainage areas of wells may overlap, the overall deliverability of the field should be measured periodically; it may range from unchanged to 20 percent or more less than the sum of all individual wells' deliverability.

Practically the overall deliverability could be obtained by free flowing all the withdrawing wells for 2–3 days during the peak of the market demand (extra cold days).

Applying the superposition principle, the interference of all the effects from each well was calculated and found to agree with field data [14-6]. It was found that the actual deliverability fell far short (39 percent) of predictions from each individual well's back pressure test. It was concluded that an additional well in Heartland (a high-permeability zone) might not significantly increase the total deliverability because of the pressure decline in that area. As a matter of fact, an extra well in Hinderland (a low-permeability zone) might help the total deliverability, because it would raise the pressure at Heartland. An interference study is essential for further planning and design.

Theory of Flow Limitation in Finite Reservoir

The flow limitation among a multitude of flowing wells draining from an oil-producing reservoir has been discussed and the effective flows for a discrete number of wells have been mathematically evaluated by Muskat [8-3]. The same

principles have been utilized to determine the effective flow for gas storage reservoirs during both injection and withdrawal.

The maximum deliverability of a single well depends upon its drainage area. However, the number of wells is not proportional to the total deliverability. In practice, the production wells are usually concentrated in the heartland of the gas reservoir. If one uses the formation pressure, P_f, as the driving upstream pressure for all the wells, the overall deliverability (sum of all individual well deliverabilities obtained by back pressure test) may be overestimated. Actually, for a particular well, the upstream driving pressure should be the drainage radius pressure, which may be declining during full-scale whole reservoir drawdown in the winter. Figure 8-3 illustrates the drainage area between two wells during a simultaneous drawdown. Example 9.5 shows the difference between a drainage pressure (equalized pressure) for a finite reservoir and the initial formation pressure. This finite drainage area concept for reservoir wells is usually referred to as the *well interference*.

In order to calculate the true deliverability for a given storage reservoir, a dimensionless time is defined based on drainage area A:

$$t_{DA} = \frac{\lambda k t}{\phi \overline{\mu c} A} \tag{14.3}$$

where all the variables are as defined in Table 8.1.

For large t_{DA}, when all the boundaries have been affected by the gas withdrawal, that is, at pseudo–steady state, the pressure at wells can be expressed as

$$\Delta P^2 = P_0^2 Q_D \left(\frac{1}{2} \ln \frac{4A}{1.781 r_w^2 C_A} + 2\pi t_{DA} \right) \tag{14.4}$$

where C_A is the shape function defined by Dietz [14-7] as in Table 12.4. Example 14.2 illustrates the deliverability calculation for a multiwell system in a finite reservoir.

Example 14.2. To illustrate the effect of adjacent wells on flow of gas from a given block (640 acre) of reservoir, as in Fig. 14-10, calculate the maximum deliverability for one, two, or four wells at the end of a continuous withdrawing month (720 hours), January. Initial pressure is 2000 psia and the fluid/reservoir properties are

$$k = 40 \text{ md}$$

$$r_w = 0.4 \text{ ft}$$

$$\mu_{avg} = 0.016 \text{ cp}$$

$$\phi = 0.2$$

$$Z_{avg} = 0.86$$

$$h = 40 \text{ ft}$$

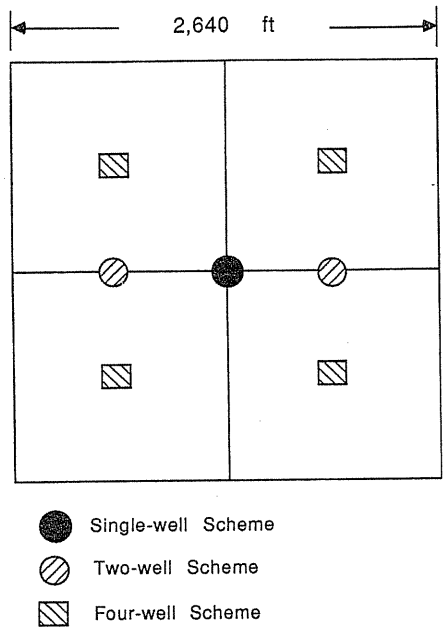

FIGURE 14-10
Wells in a finite area.

$$c_{avg} = 0.0005 \text{ psia}^{-1}$$
$$T = 590°\text{R}$$

Solution. **One-well scheme.** (1 × 1 in Table 14.4.) First, check the time of stabilization by using Eq. (14.3):

$$t_{DA} = \frac{\lambda kt}{\phi\overline{\mu c}A} = \frac{(2.637 \times 10^{-4})(40)(720)}{(0.2)(0.016)(0.0005)(6.9696 \times 10^6)}$$
$$= 0.681$$

which exceeds 0.1; hence, pseudo–steady state has been reached and Eq. (14.4) is valid:

$$\Delta P^2 = P_0^2 Q_D \left(\frac{1}{2} \ln \frac{4A}{1.781 r_w^2 C_A} + 2\pi t_{DA} \right)$$

which can be rearranged as

$$Q_{sc} = \frac{(kh/\gamma\overline{\mu Z}T)\Delta P^2}{1/2 \ln (4A/1.781 r_w^2 C_A) + 2\pi t_{DA}}$$

The maximum Q_{sc} can be obtained when $\Delta P = (P_0^2 - 14.7^2)$, against zero back pressure and $C_A = 30.9$ from Table 14.4:

$$Q_{sc} = \frac{[(40)(40)/(1.417 \times 10^6)(0.016)(0.86)(590)](2000^2 - 14.7^2)}{1/2 \ln[4(6.9696 \times 10^6)/1.781(0.4)^2(30.9)] + 2\pi(0.681)}$$

TABLE 14.4
Pseudo–steady state shape factors for various reservoirs [Dietz, 14-7, courtesy SPE-AIME]

	ln C_A	C_A	Stabilized conditions for $\frac{kt}{\phi\mu cA}$ >
In bounded reservoirs >			
	3.45	31.6	0.1
	3.43	30.9	0.1
	3.45	31.6	0.1
	3.32	27.6	0.2
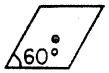	3.30	27.1	0.2
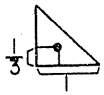	3.09	21.9	0.4
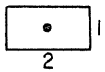	3.12	22.6	0.2
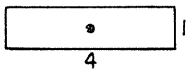	1.68	5.38	0.7
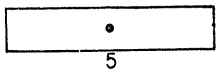	0.86	2.36	0.7
	2.56	12.9	0.6
	1.52	4.57	0.5

	ln C_A	C_A	Stabilized conditions for $\frac{kt}{\phi\mu cA}$ >
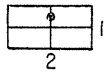	2.38	10.8	0.3
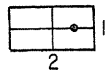	1.58	4.86	1.0
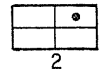	0.73	2.07	0.8
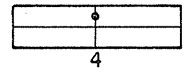	1.00	2.72	0.8
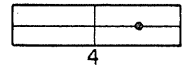	—1.46	0.232	2.5
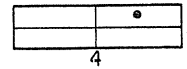	—2.16	0.115	3.0
	1.22	3.39	0.6
	1.14	3.13	0.3
	—0.50	0.607	1.0
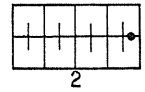	—2.20	0.111	1.2
	—2.32	0.098	0.9
In water-drive reservoirs			
	2.95	19.1	0.1
In reservoirs of unknown production character			
	3.22	25	0.1

$$= \underline{47.3 \text{ MMcf/day}}$$

Two-wells scheme. (Two 2 × 1 in Table 14.4.) The time $t_{DA} = 1.362$ exceeds stabilized time 0.2, and $C_A = 22.6$; hence, following the same calculations as above, the maximum flow rate is

$$Q_{sc} = 2 \cdot Q(\text{single well})$$

$$= 2 \cdot \frac{[(40)(40)/(1.417 \times 10^6)(0.016)(0.86)(590)](2000^2 - 14.7^2)}{1/2 \ln[4(6.9696 \times 10^6/2)/1.781(0.4)^2(22.6)] + 2\pi(1.362)}$$

$$= \underline{70.19 \text{ MMcf/day}}$$

Four-wells scheme. (Four 1 × 1 in Table 14.4.) The time $t_{DA} = 2.724$ exceeds stabilized time 0.1, and $C_A = 30.9$; hence, following the same calculations as above, the maximum flow rate is

$$Q_{sc} = 4 \cdot Q(\text{single well})$$

$$= 4 \cdot \frac{[(40)(40)/(1.417 \times 10^6)(0.016)(0.86)(590)](2000^2 - 14.7^2)}{1/2 \ln[4(6.9696 \times 10^6/4)/1.781(0.4)^2(30.9)] + 2\pi(2.724)}$$

$$= \underline{93.08 \text{ MMcf/day}}$$

This example implies that a well can perform only up to (70.19/2)/47.3 = 74.2 percent of its AOF capacity obtained by gas test if another well is producing nearby.

The increase in deliverability by applying additional wells has to be carefully studied via full-scale simulation and justified according to the total capital invested. When producing a condensate field of low permeability and pressure above the dew point, adding wells and allowing the reservoir to enter the two-phase region—retrograde condensation—can cause all wells to have a much lower gas flow rate since the liquid-gas system has a severely reduced gas relative permeability.

Should the wellbore area have been stimulated to increase the flow adjacent to the well, the effect shown in Example 14.2 would have been greater for added wells. In this case, the extra drawdown of the source gas for the well would reduce the driving force further than in the uniform permeability case.

14.4 SAFETY AND RISK

Risk is the possibility of loss or injury due to an incident in storage operations. Natural gas storage operations have two kinds of risk. The first has to do with the safety of people and property from harm due to explosions or fires resulting from uncontrolled gas losses or movement. The second risk is economic, the possible loss of unretrievable gas underground or into the atmosphere.

Safety

A consideration of safety must always put the total system in perspective. No one expects our highways to be perfectly safe, and although people work hard at reducing accidents, they are also forced to admit that accidents cannot be prevented altogether. All technology carries some degree of hazard, which should be minimized while at the same time making use of the technology. After an incident, investigation of the causes often leads to corrections, preventing it from happening again in the future. Good safety practice includes as thorough an anticipation of such happenings as possible and the making of the necessary corrections prior to the incident contemplated.

In long-range perspective, workmen or the public involved in the technology find that certain social costs are borne by them when appropriate corrective measures have not been taken. Not all hazards are contemplated and there can well be social costs or penalties found after the fact. It behooves each company or organization to do their best in minimizing such unforeseen events.

Odorization of Gases—A Safety Measure

Natural gases serving as domestic fuel in the United States must be odorized so that leaking gas may be detected by its odor. The requirement is that a gas concentration of 20 percent of the lower combustion limit will indicate its presence by smell, a safety factor of 5. This requirement applies to fuel gas in a gas distribution system, but may not apply to high-pressure transcontinental pipelines or distribution lines.

Odorants are organic compounds containing sulfur, usually mercaptans, disulfides, thioethers, or carbon sulfur ring compounds. They are marketed as liquids with densities of 0.8 to 1.0 g/ml, initial boiling points of 120–230°F (49–110°C), Reid vapor pressures from 1 to 8 psia (6.89–55.1 kPa), and molecular weights around 85. The odorization rate is in the range of 0.25 to 0.75 lb/MMcf of gas. Odorants increase the sulfur content by 0.07 grains/100 ft^3 for the 0.25 lb/MMcf of gas.

Odorizing stations often are situated at distribution pipelines' delivery points to towns—usually with pressure controls. Two methods are employed, injection or bypass odorizers. Since the gas flow being odorized is variable with time, the injection pump rate must be connected to the flow rate. The bypass system involves a sidestream of the fuel gas passing over liquid odorant to carry the vaporized odorant to the main fuel supply. The bypass rate is controlled by the fuel gas flow rate.

LP gas (propane) is marketed as a liquid, often in cylinders. Here the odorant is placed in the liquid, which in turn gives off a vapor fuel with the proper odorant concentration. Ethyl mercaptan (C_2H_5SH) is used for this service at 1.5 lb per 10,000 gallons of propane. This concentration is 25 ppm by volume in the liquid and diminishes to 4.5 ppm at 32°F (0°C) and 5.8 ppm at 90°F (35°C) for the gas. A study of the detection of odor in propane vapor was made in the Bartlesville Research Center of DOE in 1977 [14-17].

A 30-to-50-Year Lifetime for an Underground Gas Storage Reservoir

Gas storage reservoirs developed either from original oil and gas reservoirs or aquifers may be expected to have a storage operation lifetime of 30, 40, or 50

or more years. There really is no reason to put a time limit on the life of the reservoir, assuming that gaseous fuel will be used indefinitely and that a given reservoir will not become an uneconomic venture.

From this time perspective, there is a reasonable possibility that over this period, gas from some of the wells will leak through the casing or cement to enter zones above the intended storage zone. A concern is that this gas eventually might reach water supplies and appear in the local user's water. Gas might even permeate the soil at the surface and enter homes or buildings to provide explosive mixtures.

Many precautions are taken to minimize and hopefully eliminate such gas leakage, but it is foolhardy to say that such leakage will not occur in a reservoir being developed with a projected 30-to-50-year lifetime. The question then may be raised as to what policies and activities should be carried on by the gas storage organizations to minimize the hazards to people and property involved, both the public and workers associated with the storage project. The gas storage industry has a good safety record with few serious accidents.

Land Use Plan

A variety of arrangements are made between the land owner and the gas storage operator relative to the land use. Some portion of the land is normally purchased by the gas storage operator to be used for plant sites or, in some cases, the entire surface may be purchased. Storage rights for the underground strata may be purchased along with rights of ingress and egress for pipelines and wells. For agricultural use, the latter procedure seems appropriate, provided attention is paid to water supplies and particularly the basements of the homes in the area of the gas storage reservoir. Would gas entering the water supply of a given residence cause combustible gas mixtures to accumulate in the home and provide a hazard? Double-tank pump systems with intermediate venting may be used. It would be preferable to have the homes on concrete pads without basements, and this type of new construction might be well advised in gas storage areas. Monitors in basements that would detect low concentrations of natural gas could possibly be installed to provide adequate warning before gas reached the explosive limit, should gas ever enter a basement.

On occasions, gas has bubbled through low ditches or ponds and permeated the soil, causing damage to vegetation. However, adequate recompense can be made for such damage and it is not the type of hazard of concern here, since the presence of the gas would be obvious, permitting corrections and the recompense.

Managers of gas storage fields adjacent to villages or cities should be concerned if subdivisions are planned in the storage area, or close enough to wells so that any leak is as likely to cause an incident in a home as to be detected by the monitoring procedures. Would it be possible to include an agreement in the purchase of the storage zone that the land would not be converted from agricultural to residential use? Probably not, but many operators learn to cope with urbanization of storage field areas by monitoring.

Recommended Policies

It is recommended that a policy of storage acquisition and operation be followed to permit the maximum control over hazards should some leak occur in the storage field. A monitoring procedure with annual review of the situation in each field should be followed, with all parties to the storage operation in attendance. Follow-up checks should be made to see that decisions from the review meetings are carried out. Likewise, attention should be given to casing strings, annulus pressures, and corrosion in wells. Review of pressure observations in the monitoring of water zones above the storage level also is important and should continue with a high level of precaution.

Ownership of the land by the storage operator, with subleases for agricultural use or other appropriate land uses, appears to be a good policy when it does not bear an undue economic burden. Acquisition of land in the storage area might be carried out for fields currently in operation. Any land in the storage area that enters the market through the normal course of events might then be procured, especially if there are residences near any facilities. Education programs for the residents of the area, along with monitoring of water streams, is important. Early reporting of any unusual happenings that might be construed as evidence of gas in the soil or water should be encouraged, and appropriate means for this reporting should be provided.

Effect of Earthquakes on Water Level Variations

A surprise observation is that water wells may be good seismographs, in that earthquakes at great distance can cause the water levels to bounce up and down. Following the Alaskan earthquake in 1964, water levels through the United States responded by level fluctuations as much as tens of feet as the earth waves passed the area. The levels of a good number of water zones had a permanent rise, varying from inches to five feet. This permanent rise is believed to be due to the settling of overburden on the aquifer, causing enough compression to reduce the porosity, thus increasing the fluid pressure. Figure 14-11 shows the nature of the water level recorder reading following an earthquake. Experiences of the USGS, assuring that such behavior did not represent storage gas movement, reinforce this theory [14-3].

Flags Indicating Need for Special Attention at This Time

From everyday reading of the papers, it is clear that environmental groups are finding occasions for bringing suits and injunctions for stopping certain operations. Any operator should be prepared that others may have an incident that may raise public interest or cause ardent investigators to review his precautions. Environmental impact statements are needed for storage field approval by the FERC, so there is a need for great detail in understanding the operations.

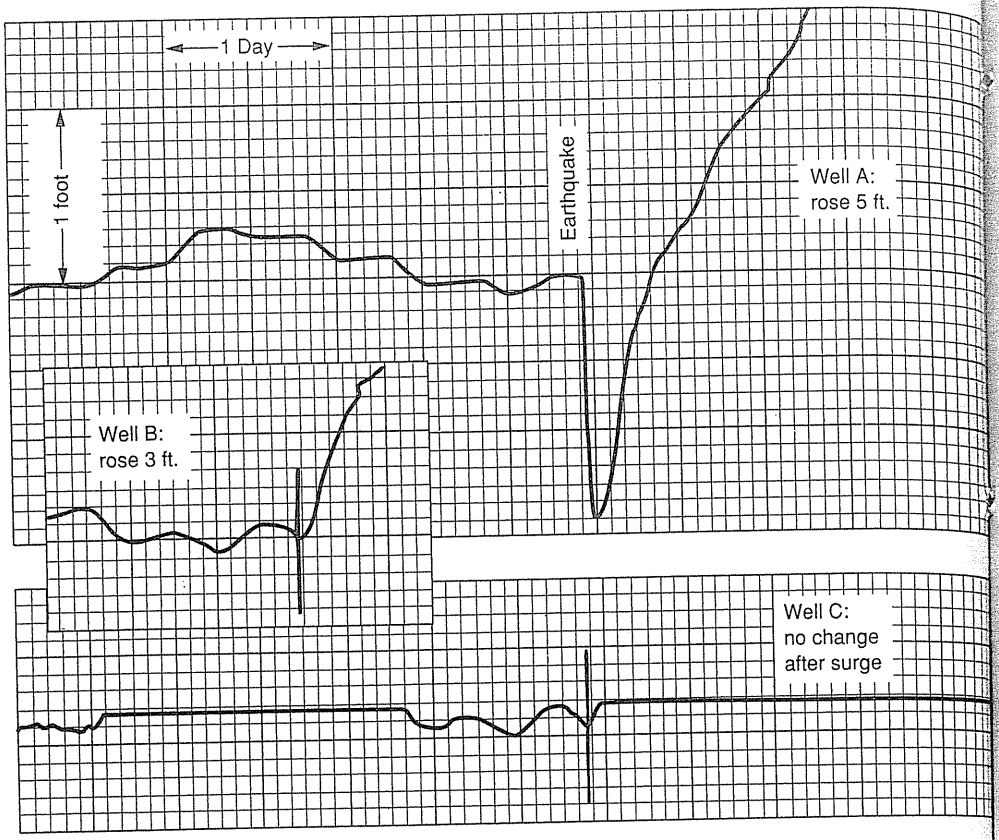

FIGURE 14-11
Nonrecoverable gas in reservoir [Katz & Coats, 1-2].

Caution must be exercised in claiming that no gas will ever be found outside the intended well–gathering line–reservoir system. If any gas is found outside the intended system, it is possible that it can be handled so as to cause little or no harm, and should be no cause for calling a halt to the operations. Therefore, it is necessary in any full description of a 50-year plus life for a storage operation to admit that, on occasions, some gas will enter the waters and even the soil, but to state that mechanical repairs are available so that the leak can be halted.

14.5 DETERMINATION OF NONRECOVERABLE GAS

The amount of nonrecoverable gas is of interest in storage reservoirs since it has to do with the mechanics of storage reservoirs and taxation methods. For non–water drive reservoirs, it is a matter of economics, well flow capacity, and how low a

rate one can use for the utility. Abandonment pressures vary for such gas fields, with pressures like 50–100 psi (345–689 kPa) often used. The nonrecoverable gas content of a field is the gas left at the abandonment pressure.

In water drive gas fields or aquifer storage projects, water will flush a portion of the reservoir while gas is being removed below the original aquifer pressure. Such invading water will trap gas at the prevailing pressure as described in Chapter 2. Consider the abandonment of an aquifer storage reservoir. How much gas will be nonrecoverable?

In abandoning a field, it is assumed that gas will be produced from the wells following a withdrawal period. Water from the aquifer will enter the reservoir, interfering with well operation. At some point, it will become noneconomical to continue production of the remaining gas and the reservoir will be abandoned. This does not mean that no more gas can be produced—only that it is not economical or it is impractical to use the field to serve the utility market.

At abandonment, the reservoir is divided into three portions (Fig. 14-12). The first is the low-pressure gas space at the crest of the reservoir, from which the last gas is withdrawn. This layer must be thick enough to permit gas production from a group of wells without interference by advancing water. The other two parts of the reservoir are the part that has been invaded by water, which has a residual gas saturation, and the bypassed reservoir sand below the level of the advancing water front.

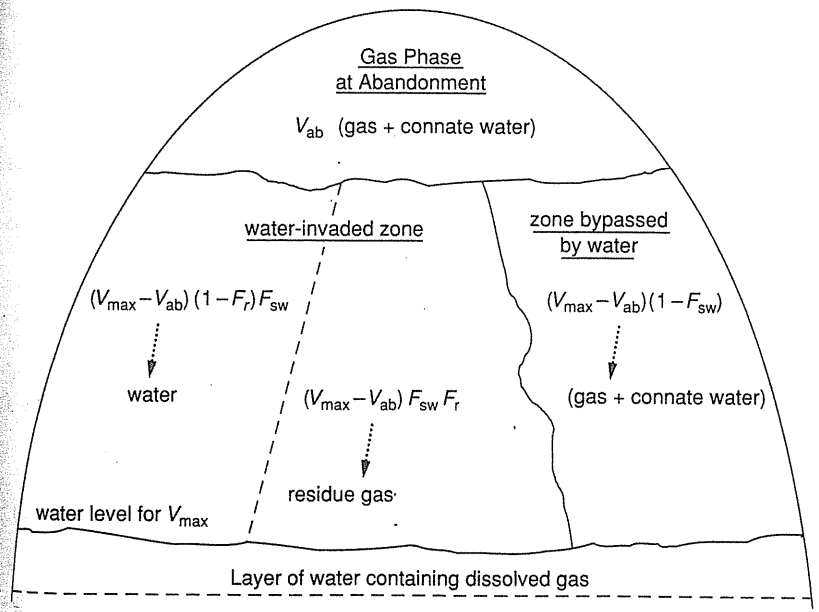

FIGURE 14-12
Illustration of nonrecoverable gas in reservoir.

The calculation of the nonrecoverable gas includes these three portions of the reservoir and the gas that has dissolved in water contacted by the gas at any time during operation.

Formula Developed

The formula used for calculating the nonrecoverable gas is

$$Q_{nr} = V_{ab}(1 - S_w)\frac{1}{B_{g,\,ab}} + (V_{max} - V_{ab})(1 - S_w)(1 - F_{sw})\frac{1}{B_{g,\,m}}$$

$$+ (V_{max} - V_{ab})F_{sw}F_r\frac{1}{B_{g,\,m}} + Q_s \qquad (14.5)$$

where Q_{nr} (scf) is the volume of nonrecoverable gas in standard conditions; V_{ab} (ft^3) is the volume of gas reservoir space not flooded at abandonment (ab) conditions; S_w is the connate water saturation; B (ft^3 at reservoir conditions/ft^3 at standard conditions) is the formation factor; subscript m denotes condition at the mean reservoir pressure ($P_{max} + P_{ab}/2$); V_{max} (ft^3) is the maximum volume of reservoir space ever containing gas at the maximum pressure P_{max}; F_{sw} is the sweep factor, fraction of space below gas-water contact at abandonment flushed with water; F_r is the residue gas saturation for water flooded zone, which can be estimated by Fig. 2-37; and Q_s (ft^3) is the gas dissolved in water.

The first term on the right-hand side of Eq. (14.5), $V_{ab}(1 - S_w)/B_{g,\,ab}$, is the gas contents (scf) for the unflooded zone above the gas-water contact at abandonment shown in Fig. 14-12. The gas content of the nonswept, or bypassed, zone below the gas-water contact line is $(V_{max} - V_{ab})(1 - S_w)(1 - F_{sw})/B_{g,\,ab}$, and the third term, $(V_{max} - V_{ab})F_{sw}F_r/B_{g,\,m}$, represents residue gas contents for the swept portion. The unit of all terms is scf (ft^3 in standard conditions).

The water level rises, or water enters the space once occupied by gas, as the pressure recedes from its maximum value. The gas trapped will be at a range of pressures from the maximum pressure to the abandonment pressure, so the simple mean pressure P_m is used in the equation.

F_r is the fraction of the water-flushed sand containing gas. It is either measured by imbibition tests on reservoir cores or taken from Figs. 2-37 and 2-39, using the porosity of the reservoir rock. The sweep factor F_{sw} is a judgment number based on shape of the reservoir, nature of the porous rock, location of producing wells, and so on. It is clear that a considerable body of sand below a general level where wells have watered out has not been swept by water.

The gas in solution is approximated as follows:

$$Q_s = Q(\text{gas dissolved in connate water}) + Q(\text{gas dissolved at base of bubble})$$

$$Q_s = S_g S_w[V_{ab}P_{ab} + (V_{max} - V_{ab})P_m] + S_g\phi h(A_{max}P_{max}) \qquad (14.6)$$

where S_g is the gas solubility with the unit of (ft^3 gas)/ft^3 water · psi), ϕ is the porosity, A_{max} (ft^2) is the area of water-gas contact at the base of the maximum gas bubble, and h (ft) is the thickness of the water layer below the gas bubble having dissolved gas. It is known that gas will diffuse slowly into the water layer underlying the gas bubble.

Some factors used for the Mt. Simon aquifer are V_{max} and P_{max}, the actual values; V_{ab}, an arbitrarily selected value about the 25-ft thick gas bubble; P_{ab}, 175 psia, the lowest pressure at which gas can be free-flowed to a local market; S_w, 11–16%, determined by core analysis; S_g, 0.002 (ft^3 gas)/(ft^3 water)(psi); F_{sw}, 0.75; F_r, determined by Figs. 2-37 and 2-38 for various porosities; h, 5 ft; and A_{max}, determined by planimeter and neutron log observations to locate the gas-water interface.

HOME PROBLEMS

14.1. Should one reach a smaller spacing than 40 acres, what reduction in flow per well would occur for a 40-acre block with 1, 2, or 4 wells? Fluid/reservoir properties are the same as in Example 14.2.

14.2. Stored gas is being injected at the rate of 4.5 Mcf/day into a well that is adjacent to a suspected leak area. It is decided to trace the leakage with propylene (C_3H_6), using a refinery mixture of 62 mole % C_3H_6 and 38 mole % C_3H_8 with a density of 0.515 g/ml. What rate of liquid at 60°F is recommended? Assume a final concentration of propylene of 5 ppm (by volume) is desired after 20-to-1 dilution has occurred.

14.3. A natural gas supply is odorized by adding 0.25 lb odorant per MMcf of gas. The odorant has a density of 6.73 lb/gallon and a molecular weight of 87. What is the concentration of the odorant in the gas in ppm?

REFERENCES

14-1. AIChE Symposium "Fugitive Emissions: Measurement and Control Problems," Miami, CEP Symposium Series (1978).

14-2. American Petroleum Institute, "Hydrocarbon Emissions," *Manual on Disposal of Refinery Wastes,* Chapter 7, p. 12, Volume on Atmosphere Emissions, American Petroleum Institute Publication 931, Washington, D.C. (1976).

14-3. Bredehoeft, J. D., H. H. Cooper, Jr., I. S. Papadopulos, and R. R. Bennett, *Seismic Fluctuations in an Open Artesian Water Well,* USGS Professional Paper 525C (1965).

14-4. Clark, F. H., and D. L. Katz, "Finders Keepers," *AGA Trans. Conference Proceedings*, 588–698 (1985).

14-5. Coleman, D. D., private communication (1986).

14-6. Dereniewski, E., Y. Hekim, and J. L. Roberts, "Deliverability Interference in Gas Storage Reservoir," *AGA Trans. Conference Proceedings* (1982).

14-7. Dietz, D. N., "Determination of Average Reservoir Reservoir Pressure from Build-up Surveys," *Trans. AIME*, Vol. 234, 955–959 (1965).

14-8. Environmental Protection Agency, *Screening Study for Miscellaneous Sources of Hydrocarbon Emissions in Petroleum Refineries*, No. EPA-45013-36-041 EPA Research Triangle Park, N.C. (1976).

14-9. Katz, D. L., "Containment of Gas in Storage Fields," *Proc. AGA Trans. Conference*, T436 (1978).

14-10. Katz, D. L., "A Look Ahead in Gas Storage Technology," *Proc. AGA Trans. Conference*, T283 (1981).

14-11. Katz, D. L., "Making Good Use of Observation Wells," *Proc. AGA Trans. Conference*, T251 (1977).
14-12. Katz, D. L., "Monitor Gas Storage Reservoir," SPE 3287 (1971). SPE reprint series 13, *Gas Technology* Vol. 2, 31–38 (1977).
14-13. Katz, D. L. and M. R. Tek, "Overview of Underground Storage of Natural Gas," *J. Pet. Tech.*, Vol. 33, No. 6, 943-951, June (1981).
14-14. Morgester, J. J., D. L. Frisk, G. L. Zimmerman, R. C. Vincent, and G. H. Jordan, "Control of Emissions from Refinery," CEP, 40–45 (1979).
14-15. Rzepczynski, W. M., and D. L. Katz, "Gas Penetration into Deeper Strata in Aquifer Storage," SPE Preprint 2561 (1969).
14-16. Udegbunam, E. O., and M. R. Tek, "New Methods of Locating the Moving Gas/Water Boundary in Underground Storage Reservoirs," SPE Preprint 12077 (1983).
14-17. Whisman, M. L., et al., "A New Look at Odorization Levels for Propane Gas," NITS, DOE-BERC/R1—77/1, Sept. (1977).

CHAPTER 15

NATURAL GAS LIQUID RECOVERY AND GAS FOR THE FUEL MARKET

Produced natural gas is generally associated with crude oil or condensate, and a primary separation (Fig. 1-2) is made in the field. Natural gas from the field separators contains the full range of condensible hydrocarbons, such as ethane (C_2) through the C_{6+} heavier hydrocarbons, which are more valuable as liquids than as gaseous fuel. The heavier constituents control the hydrocarbon dew points, and their removal prevents condensate formation in pipelines and fuel delivery systems [1-35].

Natural gases either from natural production or storage reservoirs contain water, which may condense and form solid gas hydrates to block pipeline flow and especially control systems. Natural gas in transit to market should be dehydrated to a controlled water content to avoid hydrate as well as to minimize the corrosion problems.

Often hydrogen sulfide (H_2S) is present in field gases and has to be removed to a specific level (0.1 to 0.25 grain per 100 Scf) because of its toxicity. Treating processes are included in the preparation plant for natural gas sent to the fuel market. Carbon dioxide (CO_2) is a corrosive diluent, but it has value for some enhanced oil recovery processes and is included in acid gas removal processes.

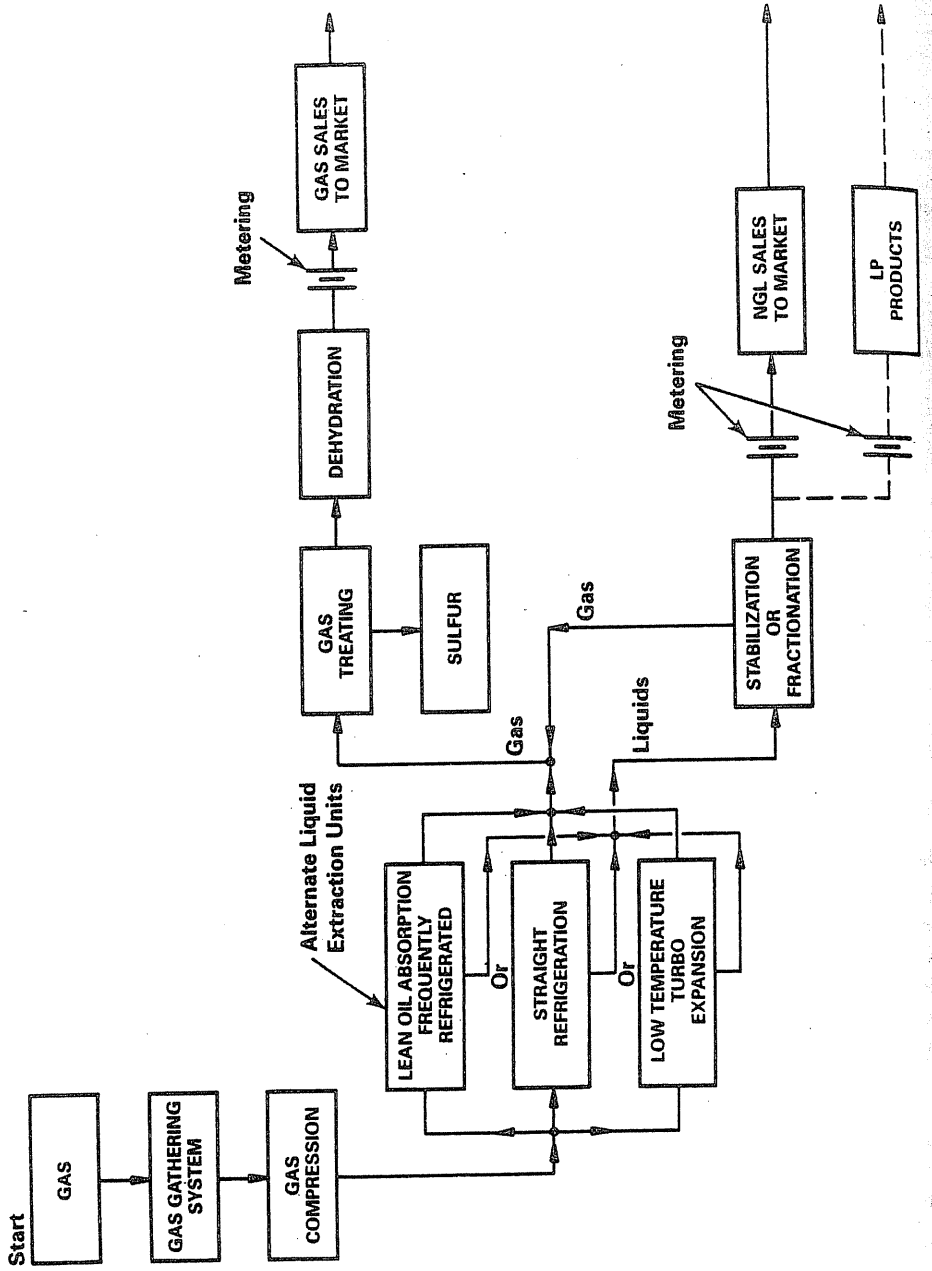

The Gas Processors Association reports and proceedings [1-52] give updated state-of-the-art processes for natural gas liquid (NGL) recovery, dehydration, sweetening, and CO_2 removal. Other journals [1-45, 1-47, 1-48] and books [1-1, 1-7,15-23] cover the subject as well.

Figure 15-1 is a schematic natural gas flow diagram. H_2S removed from the natural gas stream cannot be emitted to the environment and should be converted to elementary sulfur (S), solid or liquid. The residue gas, mainly methane from the gas processing plant, is metered and sampled for calorific value before being sent to the fuel market via pipelines.

15.1 NATURAL GAS LIQUID (NGL) RECOVERY

Natural gas liquid, or NGL, which consists of ethane (C_2H_6), propane (C_3H_8), butanes (C_4H_{10}), pentanes (C_5H_{12}), and condensate, has been recovered by three general processes:

1. Straight refrigeration
2. Oil absorption and stripping
3. Cryogenic expansion/compression

Oil absorption and stripping cannot recover ethane and propane effectively. A large number of oil absorption plants are still in operation. They require circulating large amounts of absorption oil, demand attendant maintenance, and consume too much fuel.

There has been a trend of increasing the ethane and propane recovery from natural gas because the demand for these liquids in chemical plants increases their value as separate products over their value as components in fuel gas. Lower separation temperatures are generally needed to accomplish the increased recovery.

An oil absorption plant can be modified to improve its propane recovery by adding a propane refrigeration cycle for cooling [15-11]. However, at high pressure, like 1000 psia (6.89 MPa), the pentane plus (C_{5+}) yield would decrease because of revaporization of the low molecular weight oil. One advantage of the modified plant is the conservation of energy by using light oil circulating at low rate as the absorbent instead of using high-rate heavy oil.

Cryogenic expander plants obtain even lower temperatures than modified oil absorption plants and are capable of essentially complete ethane recovery using separation pressures in the 250–350 psia (1.72–2.41 MPa) range and temperatures from −80°F (−73°C) to −150°F (−102°C).

Early Natural Gasoline Recovery

The state of the gas processing art up to the late 1950s is included in reference [1-1], where whole chapters are devoted to field separation and oil absorption

TABLE 15.1
Operation units in gas processing plants

1. Compressor, reciprocal or turbo
2. Heat exchangers
3. Cooling water, exchangers, air cooler systems
4. Expansion coolers
5. Refrigeration systems
6. Gas absorbers and strippers
7. Gas adsorption units
8. Fractionation columns (demethanizer, deethanizer, and depropanizer)
9. Heating and stripping stills
10. Condensers
11. Vapor/liquid separators
12. Expander/compressors
13. Circulating pumps

processes, fractional distillation, low-temperature processing, dehydration, and sweetening. Space is not available in this book for such an elaborate presentation, but each of these areas is discussed in this chapter.

A gas processing plant has a group of units, as listed in Table 15.1, which are chosen to suit a given gas stream and desired liquid recovery.

Before NGL recovery plants are discussed, several key components of many plants will be described: absorbers, fractionators, strippers, expander/compressors, propane refrigeration chillers, solid adsorption beds, heat exchangers, etc.

15.2 GAS ABSORPTION VERSUS FRACTIONATION

The two common towers A and B in Fig. 15-2 appear to be performing the same function—countercurrent vapor-liquid contacting. For column A, an *absorber*, absorption of selected constituents from a rising gas by a liquid passing downward is taking place in a vertical cylindrical vessel. The trays or plates are vapor-liquid contactors for bringing the two phases into equilibrium. The liquid is an absorbent "oil" pumped to the top of the vessel. Liquefiable constituents in the entering gas are extracted and leave along with the rich oil containing dissolved gases.

In column B, a *fractionator*, with its series of plates or trays, a similar contacting process takes place but with a different driving force. The differences in the volatility of the constituents cause vapor-liquid exchange of constituents at the trays or plates. The feed to the column may be a liquid/gas mix or all of one phase or the other. Heat is applied at the bottom of the still or reboiler to generate the rising vapor. Some of the top vapor is condensed to provide a

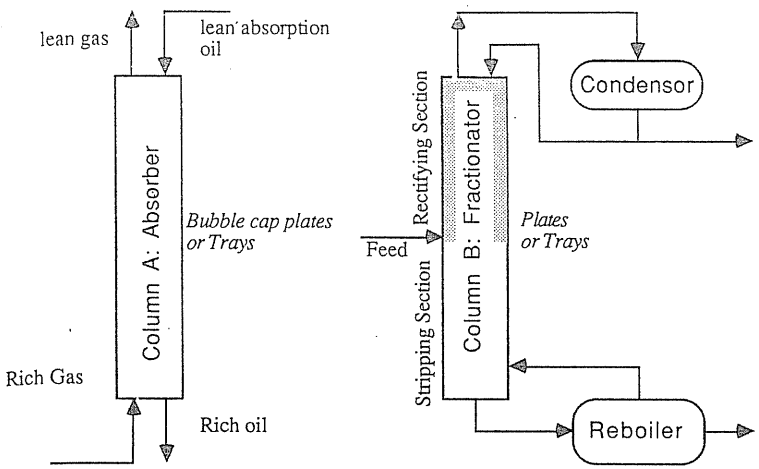

FIGURE 15-2
Absorber versus fractionator.

reflux liquid, which carries constituents of lower volatility downward. Actually, a fractionation column can perform both absorption in the rectifying section (above the feed plate) and stripping in the lower part of the column.

In gas processing, removal of a constituent from a gas phase by a solvent liquid, e.g., propane by absorber oil or water by a glycol solution, is carried out in a gas absorption–type plant. When a natural gas liquid is to be separated as in demethanizers, deethanizers, or splitters, a fractionation process is required with a heat input at the base of the column and cooling at the top to form a reflux.

15.3 COOLING IN GAS PROCESSING

Cooling of gases flowing from wells takes place in chokes, which lower the pressure at constant enthalpy (H)—the Joule-Thomson effect shown in Fig. 4-49. The degree of cooling depends upon the deviation from ideal gases and is influenced by phase change. Cooling water is used to adjust warm streams to the ambient temperature in heat exchangers, or the passage of gases and/or liquids through air-cooled finned tube banks is used to vent heat. Most of the cooling duty below the ambient temperature in a gas-processing plant is supplied by the propane refrigeration cycle.

Propane Refrigeration Cycle

To bring a stream below the ambient temperature, refrigeration is used. Propane is a commonly used refrigerant. As shown in Fig. 15-3, the cycle consists of dropping the pressure on liquid propane at A to pressure B, causing vaporization

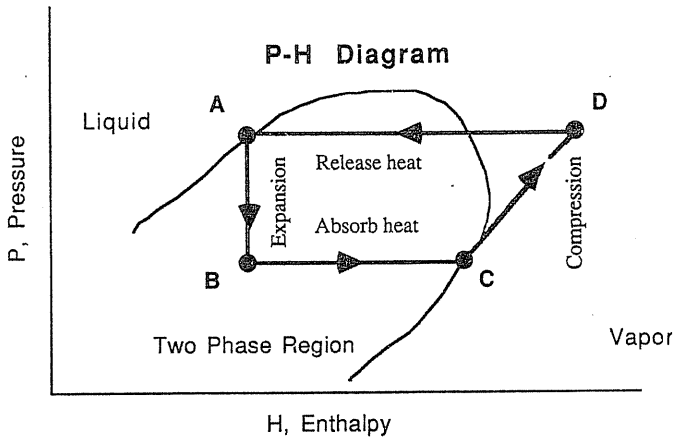

FIGURE 15-3
Schematic of a refrigeration cycle.

and chilling of the lower-pressure mixture, which absorbs heat. The saturated vapor at C is compressed to D, a superheated vapor at the same pressure as A. Energy removal at the higher temperature by cooling water or air returns propane to the liquid state at A to complete the cycle.

Figure 15-4 is a schematic flow chart of a refrigeration cycle. The refrigerant, propane, is condensed at high pressure by cooling water and then passes through the chiller, where the condensed liquid expands and vaporizes to absorb heat from the countercurrent flowing fluid, natural gas. The vaporized refrigerant leaving the chiller will be compressed back to high pressure and be ready to be cooled and condensed again. The economizer, a flash vessel functioning at the interstage pressure between two compression stages, provides an intermediate-pressure vapor for recompression. Thus part of the vapor requires less compression duty than if all the vapor were allowed to drop to the boiling pressure.

These propane refrigeration cycles, with and without the economizer, are shown in the P-H diagrams of Fig. 15-5 [15-10]. The expansion steps are adiabatic.

Example 15.1 [15-10]. A gas stream is to be chilled to 0°F using propane as a refrigerant. Propane is to be vaporized in the gas chiller at a pressure that results in a bath temperature of −10°F. Refrigerant duty has already been determined to be 12,000,000 Btu/hr. Propane vapors are compressed in a two-stage compressor that has an adiabatic efficiency of 80 percent. The compression ratio for each stage is identical. The compressed propane vapors are condensed at a temperature of 120°F. Assume there is a 10 percent pressure drop between the chiller and the first-stage compressor and that the second-stage compressor discharge pressure is 15 psi higher than the condenser pressure.

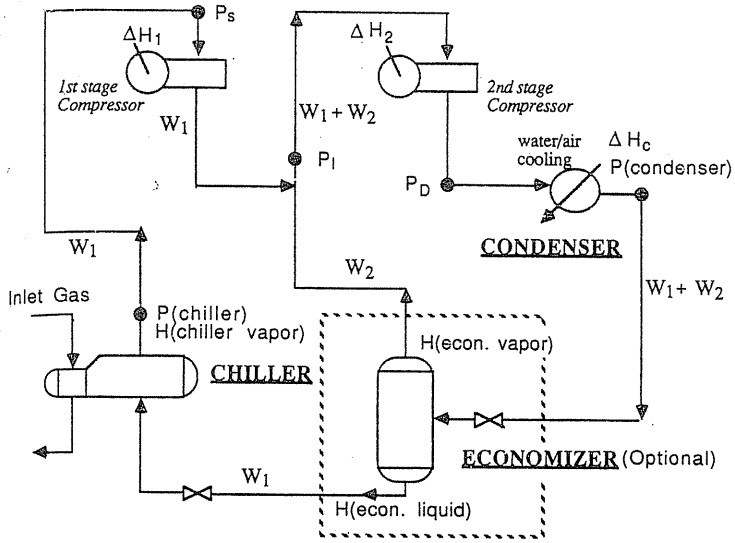

FIGURE 15-4
Flow diagram of refrigeration cycle.

For both uneconomized and economized refrigeration systems, determine the following (refer to Fig. 15-4):

1. Chiller pressure, P(chiller).
2. Condenser pressure, P(condenser).
3. Interstage pressure on compressor, P_I.
4. Refrigerant flow rate in first-stage compressor, W_1.
5. Refrigerant flow rate in second-stage compressor, $W_1 + W_2$.
6. First-stage compressor horsepower, ΔH_1.
7. Second-stage compressor horsepower, ΔH_2.
8. Condenser duty, ΔH_c.

The P-H diagrams are shown in Fig. 15-5.

Solution

Uneconomized system.

1. Chiller pressure: Using a pressure-enthalpy diagram for propane, find that at −10°F propane boils at about 31.5 psia.
2. Condenser pressure: Again using the pressure-enthalpy diagram find that at 120°F propane condenses at 245 psia.
3. Interstage pressure:
   (*a*) First stage suction pressure $P_s = 0.9 \times 31.5 = 28.4$ psia.

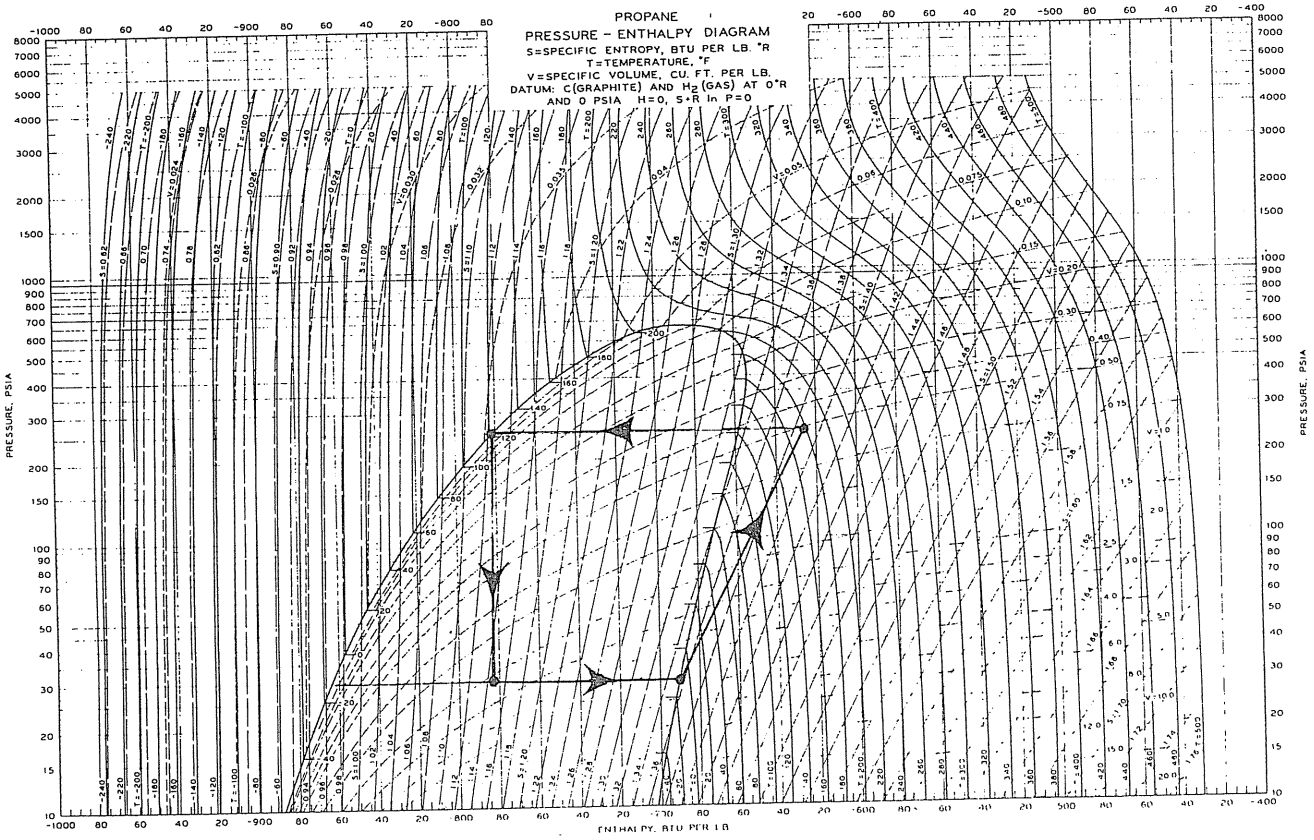

FIGURE 15-5
(*a*) Refrigeration cycle for uneconomized system on propane *P-H* diagram.

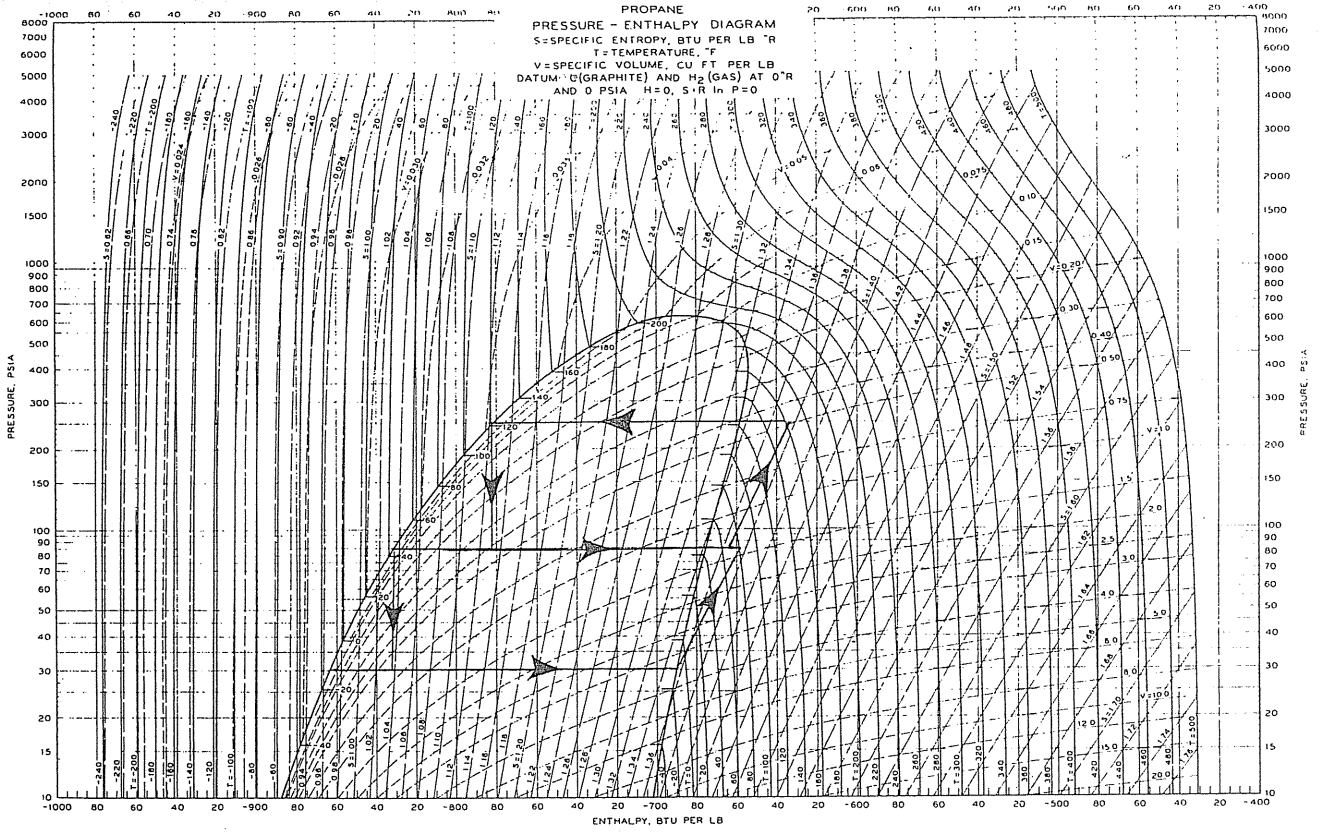

FIGURE 15-5
(*b*) Refrigeration cycle for economized system on propane *P-H* diagram.

(*b*) Second stage discharge pressure $P_d = 15 + 245 = 260$ psia.
(*c*) Since $R_1 = P_I/P_s = R_2 = P_d/P_I$,

$$P_I = \sqrt{P_d P_s} = \sqrt{260 \times 28.4} = \underline{85.9 \text{ psia}}$$

4. First-stage refrigerant flow rate: Determine the following from the *P-H* diagram:
   (*a*) Enthalpy of liquid from condenser: h (245 psia, 120°F) = −783 Btu/lb.
   (*b*) Enthalpy of chiller liquid: h (31.5 psia, −10°F) = −862 Btu/lb.
   (*c*) Enthalpy of chiller vapor: h (31.5 psia, −10°F) = −690 Btu/lb.

$$\text{First stage refrigerant flow rate } W_1 = \frac{\text{chiller duty}}{h(\text{chiller vapor}) - h(\text{condensor liquid})}$$

$$= \frac{(12{,}000{,}000)}{(-690) - (-783)} = \underline{129{,}032 \text{ lb/hr}}$$

5. Second-stage refrigerant flow rate: $W_1 + W_2 = W_1 = \underline{129{,}032 \text{ lb/hr}}$, since there is no economizer.
6. First-stage compressor horsepower: On the *P-H* diagram find the first-stage suction pressure and enthalpy (28.4 psia, −690 Btu/lb). Follow a path of constant entropy ($s = 1.36$) to the interstage pressure of 85.9 psia. Determine the enthalpy at this condition (−667 Btu/lb).

$$\Delta h_1 = \frac{\Delta h(\Delta s = 0)}{\text{efficiency}} = \frac{(-667) - (-690)}{0.80} = 28.8 \text{ Btu/lb}$$

$$H_{p1} = \frac{W_1 \Delta h_1}{2545} = \frac{(129{,}032)(28.8)}{2545} = \underline{1460 \text{ hp}}$$

7. Second-stage compressor horsepower: Second-stage suction enthalpy is −690 + 28.8 = −661.2 Btu/lb. Follow a path of constant entropy to the discharge pressure of 260 psia. Determine the enthalpy at this condition (−633 Btu/lb).

$$\Delta h_2 = \frac{(-633) - (-661.2)}{0.8} = 35.2 \text{ Btu/lb}$$

$$H_{p2} = \frac{(129{,}032)(35.2)}{2545} = \underline{1785 \text{ hp}}$$

Thus, total compression requires $H_{p1} + H_{p2} = 1460 + 1785 = 3245$ hp.

8. Condenser duty: Second-stage discharge enthalpy is −661.2 + 35.2 = −626 Btu/lb; hence,

$$\Delta h_c = (-626) - (-783) = 157 \text{ Btu/lb}$$

$$\text{condenser duty} = (W_1 + W_2)\Delta h_c = (129{,}032)(157) = \underline{2.0258 \times 10^7 \text{ Btu/hr}}$$

Economized system.

1. Chiller pressure (same): 31.5 psia.
2. Condenser pressure (same): 245 psia.
3. Interstage pressure (same): 85.9 psia.

4. First-stage refrigerant flow rate:
   (*a*) h of condenser liquid = −783 Btu/lb.
   (*b*) h of chiller liquid = −862 Btu/lb; vapor = −690 Btu/lb.
   (*c*) h of economizer liquid (85.9 psia) = −831 Btu/lb; vapor = −675 Btu/lb.

$$W_1 = \frac{\text{chiller duty}}{h(\text{chiller vapor}) - h(\text{economizer liquid})}$$

$$= \frac{12{,}000{,}000}{(-690) - (-831)} = \underline{85{,}106 \text{ lb/hr}}$$

5. Second-stage refrigerant rate:

$$W_1 + W_2 = W_1 + \text{economizer vapors}$$

$$\text{duty of economizer} = W_1[h(\text{condenser liquid}) - h(\text{economizer liquid})]$$

$$= (85{,}106)[(-783) - (-831)] = 4{,}085{,}088 \text{ Btu/hr}$$

$$\text{economizer vapors} = \frac{\text{duty}}{h(\text{economizer vapor}) - h(\text{condenser liquid})}$$

$$= \frac{4{,}085{,}088}{(-675) - (-783)} = 37{,}825 \text{ lb/hr}$$

$$W_1 + W_2 = 85{,}106 + 37{,}825 = \underline{122{,}931 \text{ lb/hr}}$$

6. First-stage compressor horsepower:

$$\Delta h_1 = \text{same as uneconomized system} = 28.8 \text{ Btu/lb}$$

$$H_{p1} = \frac{(85,106)(28.8)}{2545} = \underline{963 \text{ hp}}$$

7. Second-stage compressor horsepower: Calculate second-stage suction enthalpy,

$$h_s = \frac{W_1 h_1 + W_2 h_2}{W_1 + W_2} = \frac{(-661.2)(85{,}106) + (-675)(37{,}825)}{85{,}106 + 37{,}825} = -665.5 \text{ Btu/lb}$$

Using this enthalpy and the interstage pressure of 85.9 psia, follow a path of constant entropy to the discharge pressure of 260 psia. Determine the enthalpy at this condition (−638 Btu/lb); then

$$\Delta h_2 = \frac{(-638) - (-665.5)}{0.8} = 34.4 \text{ Btu/lb}$$

$$H_{p2} = \frac{(122{,}931)(35.2)}{2545} = \underline{1662 \text{ hp}}$$

Thus, total compression requires $H_{p1} + H_{p2} = 963 + 1662 = 2635$ hp.

8. Condenser duty: Second-stage discharge enthalpy is −665.5 + 34.4 = −631.1 Btu/lb, so

$$\Delta h_c = (-631.1) - (-783) = 151.9 \text{ Btu/lb}$$

$$\text{condenser duty} = (122{,}931)(151.9) = \underline{18{,}673{,}000 \text{ Btu/hr}}$$

It should be noted that the compressions require 2635 hp and 3245 hp for economizer and noneconomizer systems respectively.

Note that the theoretical minimum energy needed can be approximated by $\int SdT$, the total entropy change from −10°F (450°R) to 120°F (580°R, ambient temperature), which is roughly equal to $\{12{,}000{,}000/[(450 + 580)/2]\} \times 130 = 2{,}971{,}428$ Btu/hr = 1190.2 hp

Expander/Compressor Cryogenic Process

When the natural gas expands in an expander/compressor unit from high pressure to low pressure for an isentropic process ($\Delta S = 0$), the temperature decreases (Fig. 4-54). In the meantime, enthalpy decreases to release energy to spin a turbine which is connected by a shaft to a centrifugal compressor. Should the expander not give the desired outlet temperature, the gas is precooled using the propane refrigeration cycle. A paper by Swearingen [15-32] reviews the development history of turboexpanders and processes that use them.

Example 15.2. Natural gas with average molecular weight of 18.3, leaving the high-pressure separator at 800 psia, is to be expanded to 155 psia. The expander efficiency is 75 percent. The flow rate is 841 lb mol/hr. What are the outlet gas temperature and the work performed by the expander? The *H-S* chart is shown in Fig. 15-6.

Solution. Since the vapor entering the expander is at its dew point, the intersection of the 800-psia constant pressure line and the dew point line gives $T = -43$°F, $h_1 = -55$ Btu/lb, and $s_1 = 1.875$ Btu/(lb · °F). Extend the vertical line (isentropic: $\Delta s = 0$) from point (h_1, s_1) to intersect the 155-psia constant pressure line; the theoretical energy released is

$$\Delta h(\text{theoretical}) = h_2(\text{theoretical}) - h_1 = -104 - (-55) = -49 \text{ Btu/lb}$$

The actual enthalpy decrease should be $\Delta h(\text{actual}) = \Delta h(\text{theoretical}) \times$ efficiency. Thus,

$$h_2 = \Delta h(\text{theoretical}) \times \text{ efficiency} + h_1 = (-49)(0.75) - 55 = -91.75 \text{ Btu/lb}$$

The actual outlet gas point on the *H-S* chart should be at the 155-psia line with $h_2 = -91.75$ Btu/lb; that gives $T = -147$°F and liquid fraction $L = 7.5$ percent.

The work performed is

$$\text{Work} = \Delta h(\text{actual}) \times \text{ mass flow rate}$$

$$= [(-91.75) - (-55)] \text{ Btu/lb} \times (841 \times 18.3) \text{ lb/hr} \times \frac{1}{2545} \text{ hp/(Btu/hr)}$$

$$= 222 \text{ hp}$$

Figure 15-6 is generated by a computer program using thermodynamic and experimental equilibria data. All current designs are using computer programs due to the complicated iterative calculations required.

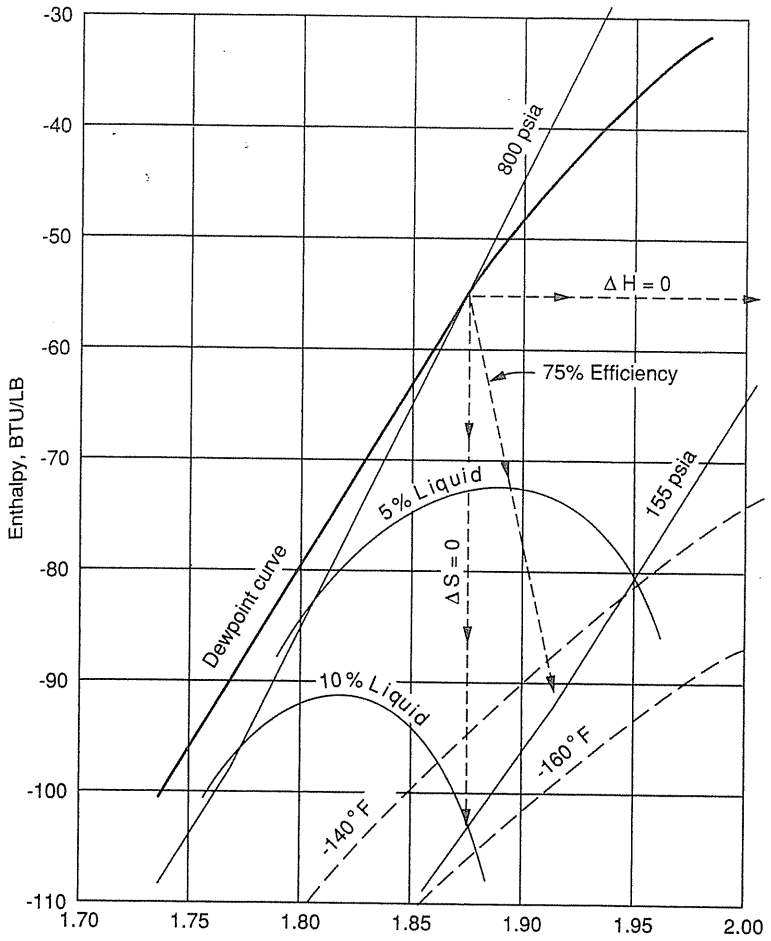

FIGURE 15-6
Expander procedure on *H-S* chart [15-10].

Example 15.3. One hundred pounds of natural gas (mainly methane) at 500 psia and 50°F passing through

1. A choke (a throttling isenthalpic process, $\Delta h = 0$)
2. A turboexpander (an isentropic process, $\Delta s = 0$)

undergoes a pressure drop to 150 psia. What are the outlet temperatures of the two processes? Is any work done by either of the two processes? Both processes are assumed to be ideal and adiabatic ($q = 0$).

Solution. In Fig. 15-7, path A represents the isenthalpic process ($\Delta h = 0$) from 500 psia, 55°F, to 150 psia, $T = 30$°F; path B shows the isentropic process ($\Delta s = 0$), ending at 150 psia and $T = -80$°F.

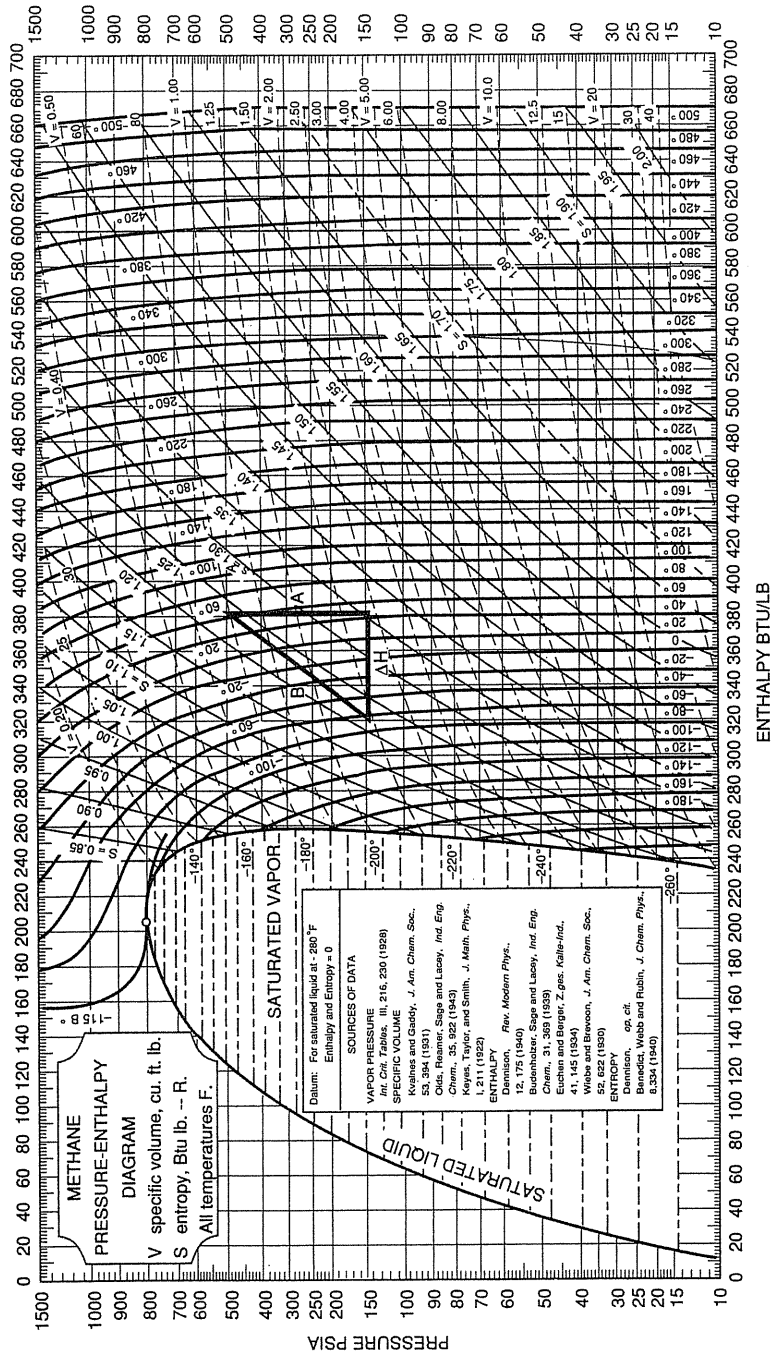

FIGURE 15-7
Isentropic ($\Delta S = 0$) and isenthalpic ($\Delta H = 0$) paths on P-H chart.

Since both processes are adiabatic ($q = 0$), the work (w) is equal to the change in enthalpy H. For the isenthalpic process (Joule-Thomson effect), *no work has been done*; on the other hand, the isentropic process provides

$$\begin{aligned}\text{Work} &= \text{flow rate} \times \text{enthalpy change } (\Delta h)\\ &= (100 \text{ lb})(382 - 320) \text{ Btu/lb}\\ &= 6200 \text{ Btu}/(2544.5 \text{ Btu/hp} \cdot \text{hr})\\ &= \underline{2.437 \text{ hp} \cdot \text{hr}}\end{aligned}$$

which is a by-product of expander cooling and could be utilized to spin the compressor on the side of the expander/compressor units.

Heat Exchanger

Heat exchangers, devices for transferring heat from a hot flowing fluid to a cold one, are necessary for optimizing energy utilization in a gas processing plant. Figure 15-8 [15-4] is a view of a single-pass shell-and-tube exchanger with baffles to control the flow of the fluid outside the tubes. For details of the principles of heat exchangers as well as their varieties, please see references [15-4, 15-22].

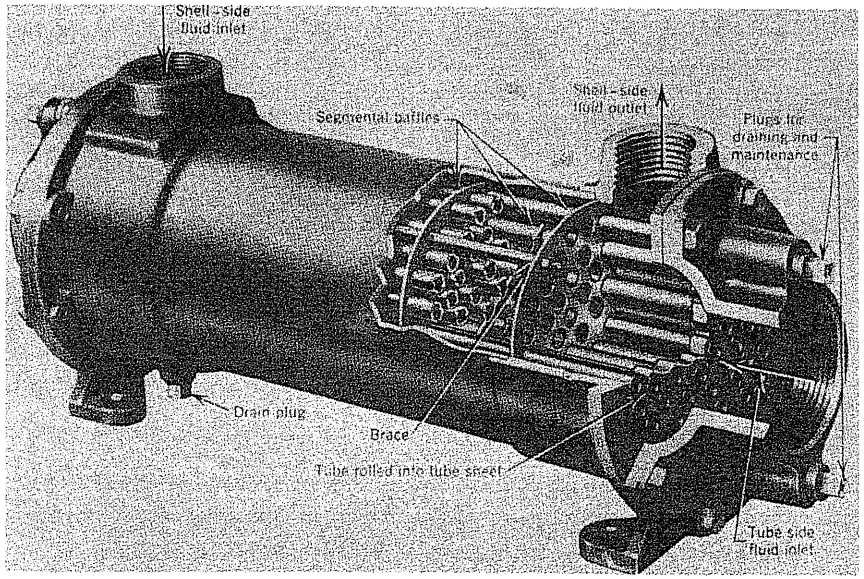

FIGURE 15-8
Cutaway view of a single-pass shell-and-tube exchanger [Brown et al., 15-4, courtesy John Wiley & Sons, Inc.].

15.4 GAS ABSORPTION/STRIPPING CYCLES FOR LIQUID RECOVERY

Fifty years ago, gas absorption was the common method of recovering natural gasoline including LP gases, butane, and a portion of the propane present in field gases. Figure 15-9 [1-1] illustrates the absorption/stripping cycle flow when steam is used to heat the rich oil and lower the partial pressure of the hydrocarbons stripped from the absorption oil. As the desire for more propane recovery arose, this cycle was modified. Pressure reduction vessels were devised for flashing off methane and ethane from the rich oil prior to its stripping. The molecular weight of the absorption oil was from 200 to 230, and lowering of the molecular weight to the 120–140 range would permit lower oil circulation rates. The use of steam for stripping rich oil was abandoned in favor of a stripping fractionating column.

Brown-Souders [15-5,15-31] set forth an absorber design procedure making simplifying assumptions of constant temperature throughout the absorber and a constant L/V (liquid/vapor) ratio, even though absorbed constituents entered the liquid phase.

The purpose of Brown-Souders' derivation is to relate the top and bottom compositions (Y_{n+1}, Y_1, Y_0 in Fig. 15-9) to the absorption factor $A = L/KV$ (K is

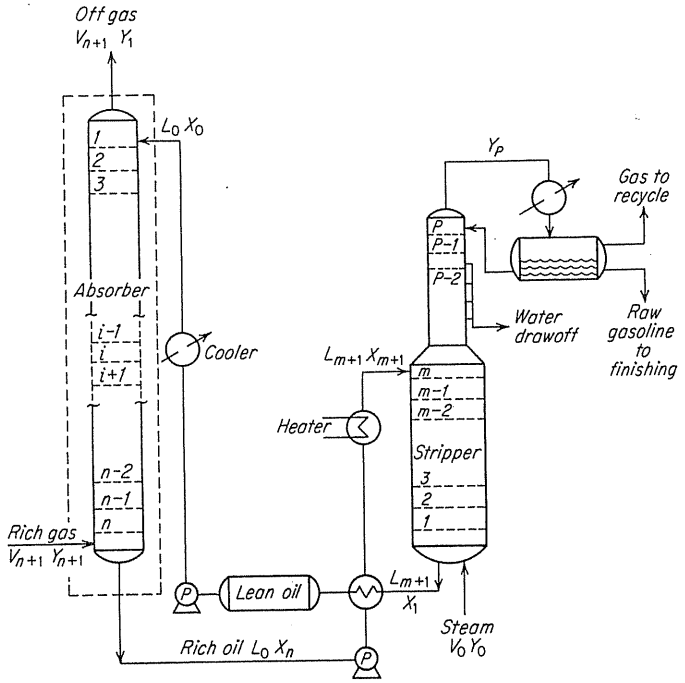

FIGURE 15-9
Flow diagram for absorption and stripping [Katz et al., 1-1, courtesy McGraw-Hill Publishing Co.].

the vaporization equilibrium constant) for various plates or trays used. As shown in Fig. 15-9, Y_{n+1} is the mole fraction of absorption component in the bottom rich gas stream, Y_1 is the mole fraction in the top off gas stream, and Y_0 is the ideal mole fraction in equilibrium with entering lean oil having the absorption component at mole fraction X_0 ($Y_0 = 0$ if $X_0 = 0$). It should be noted that the mole fractions (Y_{n+1}, Y_1, Y_0) are based on one mole of rich gas, and X_0 is based on one mole of lean oil.

By combining the material balance equations for all the trays,[1] the final absorption equation is obtained:

$$\frac{Y_{n+1} - Y_1}{Y_{n+1} - Y_0} = \frac{A^{n+1} - A}{A^{n+1} - 1}; \quad A = \frac{L}{KV} \tag{15.1}$$

Similarly, the corresponding equation with the stripping factor $S = KV/L$ for the stripping section of the column is

$$\frac{X_{m+1} - X_1}{X_{m+1} - X_0} = \frac{S^{m+1} - S}{S^{m+1} - 1}; \quad S = \frac{KV}{L} \tag{15.2}$$

Graphic solutions of Eqs. (15.1) and (15.2) may be shown by a family of curves, as indicated in Fig. 15-10, for a given kind of plate or tray. The advantage of the Brown-Souders procedure is its simplicity.

Usually, the top product of the column is more volatile than the bottom product. It is not always true that propane will be the bottom product for fractionating a water solution containing a small amount of propane. This is an example of the many abnormal phase behaviors.

Example 15.4 [Katz et al., 1-1]. A natural gas of the following composition is to be extracted with a 210 molecular weight 44° API gas oil at 200 psia and 90°F. Find the amount of each constituent extracted for an oil rate of 20 gal/Mcf of gas at 60°F and 14.7 psia when eight equilibrium stages are used. Without changing the L/V ratio, can the propane recovery be improved by adding some more equilibrium stages?

Solution

$$L = \frac{20 \times 8.33 \times 0.8063}{210} = 0.64$$

$$V = \frac{1000}{379} = 2.64$$

$$A = \frac{L}{KV} = \frac{(0.64)}{(2.64)K} = \frac{0.243}{K}$$

[1] Details of the derivation are on pages 514–515 of reference [1-1].

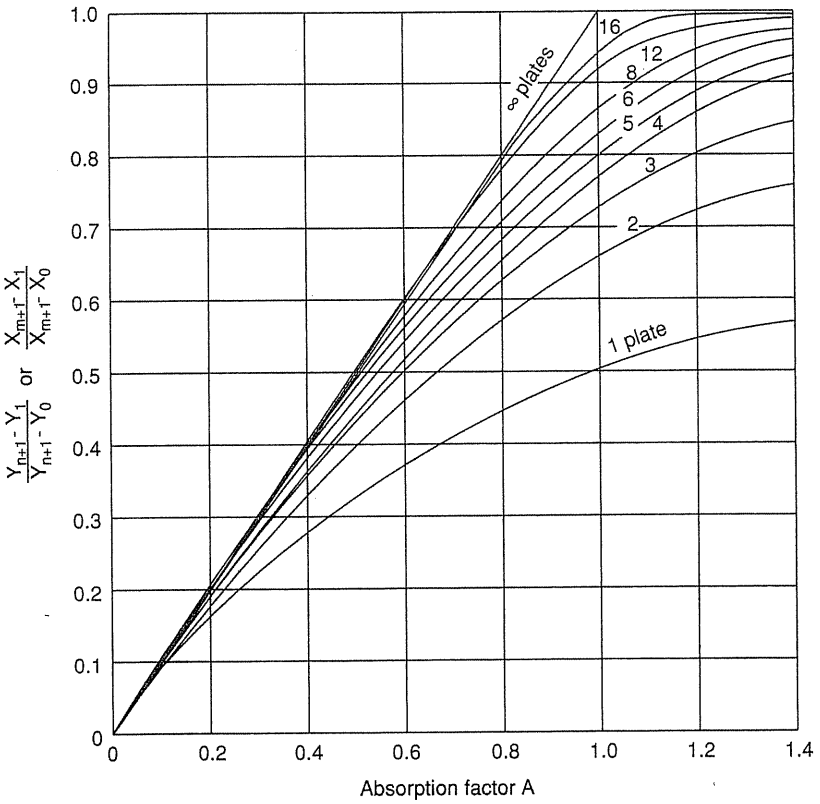

FIGURE 15-10
Solution to absorption factor and stripping factor equations [Souders & Brown, 15-31, courtesy *Ind. Eng. Chem.*].

Component	Mole %	*K* (90°F, 200 psia)	*A* = 0.243/*K* (Fig. 15-10)	% absorbed	Gallons per Mcf	
					Absorbed	Remaining
Methane	0.8319	18.2	0.0133	1.33		
Ethane	0.0848	2.85	0.085	8.5		
Propane	0.0437	0.85	0.286	28.6	0.35	0.87
Isobutane	0.0076	0.375	0.648	64	0.164	0.092
n-Butane	0.0168	0.282	0.861	81	0.441	0.104
Isopentane	0.0057	0.131	1.85	99.6	0.207	0.001
n-Pentane	0.0032	0.105	2.31	99.9	0.115	0.000
Hexanes	0.0063	0.038	6.40	99.9	0.260	0.000

From Fig. 15-10, with $A = 0.286$ for propane, one can hardly increase the absorption ratio by adding trays. Actually, two or three trays already achieve the maximum propane recovery for $A = 0.286$.

15.5 ADSORPTION VERSUS ABSORPTION

Absorption of hydrocarbons in a liquid is a solution process. The absorbate becomes a part of the solution and may be removed from the liquid by distillation or a stripping process.

Adsorption is the adhering of fluids on the surface of a solid— for example, odors of food adsorbing on the metal of a refrigerator. The adsorbed fluids may be *desorbed* by heating the surface. In adsorption processes, solids with porosity are selected for gases to penetrate the interstices of the solid. The adsorbing surface consists of active sites in fine pores, to which sites certain substances will adhere. Mixtures of hydrocarbons attach themselves to dessicants like bauxite alumina, silicon gel, and molecular sieves. In manufacturing the latter, the size of the pores and hence the size of molecules that will be adsorbed or rejected may be controlled. Molecular sieves are able to dehydrate gases to the very low water contents required in cryogenic systems. Practical design of molecular sieves can be found in reference [15-24].

Temperature increase is the usual way of desorbing substances from an adsorption bed. The bed is desorbed by circulating hot gases, and cold gases are used to prepare the bed for another dehydration cycle.

Condensate in Natural Gas Pipeline

A study was made of condensate found in natural gas pipelines to determine which part of the condensate gas processing plants were responsible [1-35]. The study involved the use of extended gas analyses and the operation of high-pressure absorption plants on the Gulf Coast. By the 1970s, the absorber plants used low molecular weight absorber oil and employed low temperatures. New plants are likely to go to low temperature expander plants.

The flowing diagram for heavy oil absorption was of the type shown in [1-35], where the stream was used to regenerate the absorption oil. For more complete C_2 and C_3 recovery, the heavy oil absorption process evolved into the processes of fractionation and low temperatures; see Fig. 15-11 [15-10]. Because of the low temperatures, the feed gas had to be dehydrated. Steam stripping was no longer used; the rich oil can be fractionated by a deethanizer to produce fuel gas (usually ethane) and send the bottom liquid to another fractionator, where the product from the top of the column is a natural gas liquid and the bottom product is the higher-boiling hydrocarbons used as the absorbent. Both the dehydrated gas feed and the stripped oil were refrigerated.

The operating conditions from several plants are shown in Table 15.2 [1-35]. The plants were obtaining the highest recovery known for propane by absorption plants. Table 15.3 gives gas and lean oil compositions.

The concentration of pentanes and butanes in the outlet gas could go under 10 ppm, but the concentration of the oil constituents (C_{7+}) reached nearly 200 ppm. These heavier constituents in the lean oil were revaporizing. The Exxon plant used a sponge oil to recover the vaporized constituents.

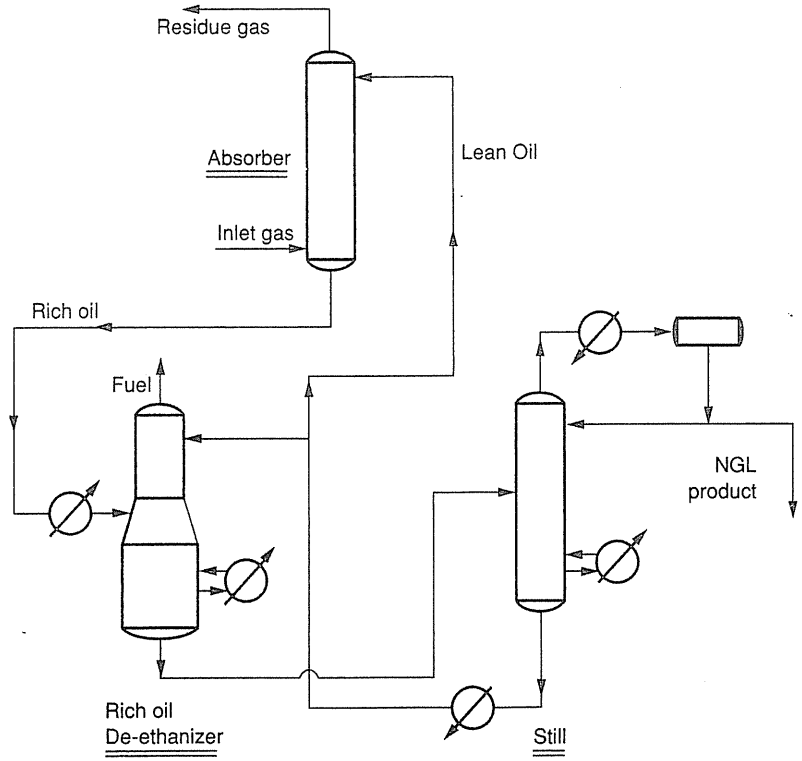

FIGURE 15-11
Low-temperature process for stripping natural gas [15-10, courtesy Arco].

TABLE 15.2
Plants sampled in Louisiana, 1974 [Bergman et al., 1-35, courtesy AGA]

		Arco Bayou Sale	Phillips Rollover Lake Arthur	Amoco TSMA Kaplan	Exxon Centerville Garden City
Absorber P,	psig	1010	975	920	985
Oil	°API	49.1	47.6	57.2	60.0/49.4
	g/cm^3	0.7833	0.7902	0.7497	0.7389/0.7823
Oil mol. wt.		138/140	145/143	119/116	101/132
Oil T, °F:	In	48	−26	−24	−20
	Out			−17	(Sponge oil in) −4
Gas T, °F:	In	−8	−6.5	−27	−36.5
	Out	(Chiller) −18	−4	−4	−14
Oil rate,	gal/min	234	515	800	550/20
	g/Mcf	4.2	7.0	6.2	3.88/0.14
Gas rate,	MMcf/day	82	115	170	204
Plant liq.,	gal/day		76,000	160,000	285,000

TABLE 15.3
Amoco-TSMA plant conditions, gas and oil analyses [Bergman et al., 1-35, courtesy AGA]

	2/13/74	2/14/74
Ambient, °F	55	64
Inlet gas, MMcf/day	170	185
Lean oil rate, gal/min	800	858
Outlet gas, MMcf/day	163	175.2
Stabilizer overhead Mcf/day	6.3	7.1
Gas in, °F	−27	−33
Lean oil in, °F	−24	−23
Gas out, °F	−4	−10
Absorber, psia	935	935
Plant liq. C_{2+}, gal/day	157,000	164,000

	Gas analysis Mole %	Lean oil analysis Mole %	Mol. wt.	Density, g/cm^3 at 60°F	Boiling point, °F
CO_2	0.9415				
N_2	0.3925				
C_1	97.1044	0.26			
C_2	1.5210	0.18			
C_3	0.0086	0.05			
i-C_4	0.0009	0.02			
n-C_4	0.0004	0.02			
i-C_5	0.0003	0.04			
n-C_5	0.0002	0.04			
C_6	0.0016	0.09	86	0.665	148
C_7	0.0076	10.74	95	0.729	206
C_8	0.0167	48.71	108	0.742	242
C_9	0.0035	25.59	121	0.760	288
C_{10}	0.0007	10.30	134	0.770	330
C_{11}	0.0001	2.81	148	0.779	361
C_{12}	0.0000	0.54	171	0.804	417

More complete recovery of ethane was attained by the cryogenic expander plants coming on stream in the 1970s.

15.6 SAN JUAN EXPANDER PLANT [Mallet, 15-19]

The San Juan plant owned by Conoco Inc. and Tenneco Oil Co. is given here as a modern example of an expander plant. It has been operated in northwestern New Mexico since November 1986 to replace an ambient oil absorption plant. It employs the turbo expander/compressor to obtain very low temperatures (−150°F, −101°C) and thus yields high ethane (98 percent) recovery.

The San Juan plant has a design throughput capacity of 500 MMcf/day (14.2×10^6 m^3/day) of natural gases to recover 42,000 bbls/day (6.68 km^3/day)

TABLE 15.4
Gas and product conditions of the San Juan plant [Mallett, 15-19, courtesy Conoco and *Oil and Gas J.*]

Composition, mole %	Inlet	Residue
N_2	0.55	0.64
CO_2	1.13	0.54
C_1	85.57	98.67
C_2	7.60	0.15
C_3	3.03	0.0
i-C_4	0.53	0.0
n-C_4	0.78	0.0
C_{5+}	0.81	0.0
	100.00	100.00
Gal/Mcf	3.59	0.04
Btu/Scf	1,154.9	978.9
Volume, MMcf/day	500.0	420.0

Hydrogen sulfide: less than 0.25 grain/100 Scf
Residue specifications: 120°F at 850 psig; max. water of 7 lb/MMcf

Product composition, mole %	EPBC*	PBC†
N_2	0.0	0.0
CO_2	0.0	0.0
C_1	0.9	0.0
C_2	58.6	0.7
C_3	23.8	54.2
i-C_4	4.2	11.2
n-C_4	6.1	16.6
C_{5+}	6.4	17.3
	100.00	100.00
Max. production, bbl/day	42,000	25,700
Water content	No free water	No free water
Corrosivity	No. 1 Cu strip	No. 1 Cu strip

* Ethane, propane, butane, and condensate.
† Propane, butane, and condensate.

of natural gas liquids (NGL). Table 15.4 [15-19] shows the compositions of the inlet gas, the residue gas, and the recovered liquid. The superiority of the San Juan plant is shown in Table 15.5 [15-19] by comparing the 42,000 bbls/day (6.68 km^3/day) liquid yield to 11,000 bbls/day (1.75 km^3/day) of the previous oil absorption plant.

Step-by-Step Flow through the Plant

Following the flow diagram of Fig. 15-12, the field gases are compressed to 850 psia (5.86 MPa). After cooling to the ambient temperature, this stream is split

TABLE 15.5
Capacities and percent recoveries of two New Mexico plants [Mallett, 15-19]

	Oil absorption plant	Conoco/Tenneco San Juan plant
Processing capacity, MMcf/day	585	500 (at design recovery levels)
Ethane recovery, %	0	98
Propane recovery, %	25	100
Butanes recovery, %	70	100
Natural gasoline recovery, %	95+	100
Total liquid production, bbl/day	11,000	42,000

between two identical 250 MMcf/day (7.08 MMm^3/day) cryogenic trains. In each train, the gas is dehydrated to a minimum dew point of −150°F (−101°C) with three molecular sieve (75,000 lb, 34,050 kg, for each train) adsorption beds; two on 12 hours dehydration and one on regeneration by using 14 MMcf/day (0.4 MMm^3/day) of dehydrated gas in the heating/cooling cycle.

The now dehydrated inlet gas is chilled by a propane refrigeration unit and then flows through the turboexpander to the 350-psi (2.41 MPa) demethanizer tower at −150°F (−101°C).

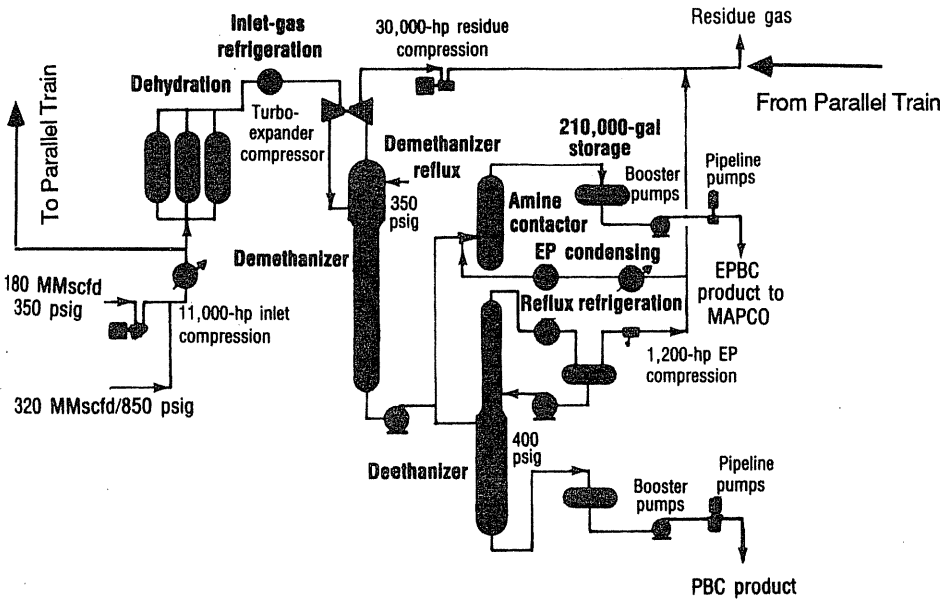

FIGURE 15-12
Flow diagram of San Juan gas processing plant [Mallett, 15-19, copyright 1987, Conoco, reprinted by permission].

The turboexpander in each train operates at 14,000 rpm. It delivers a gas-liquid stream to the demethanizer by removing 36 percent of the total energy (the chiller removes 64 percent). The compressor, connected by a shaft on the other side of the turboexpander, recovers 4800 hp for the gas recompression step.

The demethanizers, fractionating columns, are constructed of 316 stainless steel with 28 valve trays. Each tower has upper side, lower side, bottom, and trim reboilers to provide a tower temperature gradient of −150°F (−101°C) at top to 63°F (17.2°C) at bottom. Reflux is provided by recycling a portion of the overhead residue stream after compression and condensation.

Final compression of the residue gas streams is achieved by two 15,000-hp turbo-driven centrifugal compressors equipped with waste heat recovery on the turbine exhaust to provide 70 MMBtu/hr of process heat.

Separation of Ethane from NGL Product

The liquid EPBC (ethane, propane, butane, and condensate) off the bottom of the two demethanizers is sent either to the amine system for removal of CO_2 or to the deethanizer (another fractionating column). The bottom liquid PBC (propane, butane, and condensate) from the deethanizer is delivered into a NGL pipeline while the overhead EP (ethane/propane: 90/10) and CO_2 can be sent into the residue gas line (from the top of the demethanizer) or condensed and joined with the treater feed stream (from the bottom of the demethanizer).

The deethanizer (Fig. 15-13) is a 35-valve tray tower capable of processing 25,000 bbls/day (3975 m^3/day). The tower operates at 400 psig (2.76 MPa), with a partial condenser taking EP (ethane, propane) and CO_2 overhead at 58°F (14°C). The PBC bottom product is at 220°F (104°C).

The amine system can treat up to 42,000 bbls/day (6678 m^3/day) of EPBC to remove the 5 mole percent CO_2 contained in the stream from the demethanizer. Liquid EPBC containing CO_2 is contacted with 30 weight % diethanolamine in a tower containing four liquid-liquid countercurrent packed sections operating at 655 psig (4.52 MPa) and 85°F (29°C). The amine phase is a continuous phase circulating at a maximum flow rate of 600 gal/min (0.03785 m^3/s) to mix and coalesce the fluid (EPBC and CO_2) going through the packed beds. Rich amine (with CO_2) is regenerated in the amine still, a fractionating column operated at 25 psia (172 kPa) with top and bottom temperatures of 210°F (99°C) and 248°F (120°C). Reboiler heat is provided by recirculating heat transfer fluid at 350°F (177°C).

The feature of being able to recover up to 98 percent of the ethane, when it is more valuable as part of the NGL, recognizes the variability of fuel prices. The lower vapor pressure product stream, PBC, is delivered at 800 psig (5.52 MPa) by pipeline to a local fractionator to be split into propane, isobutane, normal butane, and natural gasoline. The stream containing the ethane is transported by pipeline at pressures of 700–1400 psia (4.83–9.65 MPa) en route to Mt. Belvieu, Texas.

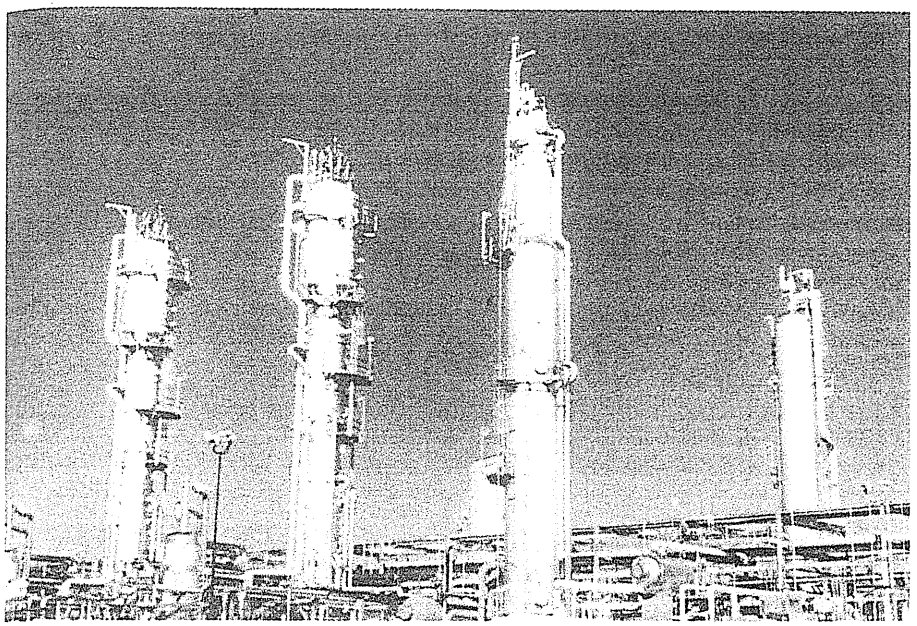

FIGURE 15-13
The demethanizer (left) and the deethanizer (right) in the San Juan plant [Mallett, 15-19, courtesy Conoco].

The article by Mallett [15-19] gives considerably more detail on the total plant's facilities and operation. Table 15.6 is a summary of the necessary supporting facilities of the San Juan plant. Treating of the feed gas is vital to successful operation of all the other stages of cryogenic gas processing [15-21].

15.7 DEHYDRATION

Dehydration of natural gas is the removal of the water that is associated with natural gases in vapor form. The natural gas industry has recognized that dehydration is necessary to ensure smooth operation of gas transmission lines. Dehydration prevents the formation of gas hydrates and reduces corrosion. Unless gases are dehydrated, liquid water may condense in pipelines and accumulate at low points along the line, reducing its flow capacity. Several methods have been developed to dehydrate gases on an industrial scale. Since no single process is unequivocally superior to the others, familiarity with all the methods is necessary in selecting the best method for a given drying problem.

The three major methods of dehydration are (1) direct cooling, (2) adsorption, and (3) absorption. Molecular sieves (zeolites), silica gel, and bauxite are the desiccants used in adsorption processes. In absorption processes, the most fre-

TABLE 15.6
Support facilities of the San Juan plant

Inlet compressors:
The San Juan Plant provides an 11,000-hp inlet gas-fired, turbine-driven centrifugal Dresser Clark compressor. The unit consists of a Rolls Royce 1535 Super-Maxi Avon gas generator, a Dresser Clark DJ200 two-stage power turbine, a Lufkin double-helical speed-increasing gear, and a Dresser Clark vertical split-barrel five-stage centrifugal compressor.

Water cooling:
The cooling tower is a three-cell counterflow design with a maximum water flow rate of 12,000 gal/min for removal of 89 MMBtu/hr from the process.

Self-sufficient power:
The plant has four Solar Centaur T4500 gas turbine–driven generators of 8.8 MW electrical power with a voltage of 4160. A 350-kW diesel engine is used for startup.

Safety pressure relief:
The *flare stack* is 200 ft high with a diameter of 36 in. All plant pressure safety valves and equipment vents or blowdowns are tied into the flare system. All pumps and compressors in hydrocarbon service have tandem seals with any leakage between the seals vented to the flare system.

Fire protection:
A *firewater loop* with more than a mile of 12-in. pipe and 20 monitor stations. A diesel-driven firewater pump provides 2000 gal/min of water from a 7000-bbl storage tank at 150 psig for 2 hours.

Outlet compressors:
The plant has two 15,000-hp gas-fired turbine-driven centrifugal compressors almost identical to the inlet compressor to obtain the required residue gas pipeline pressures.

Process control:
The process is controlled by a Rosemount System 3 distributed electronic process control system.

Staffing:
The plant has a permanent staff of 22 and is attended around the clock with one operator per 12-hr shift.

quently used dessicants are diethylene and triethylene glycols. Detailed descriptions of the desiccants are given in references [15-25,15-28]. Usually, the absorption/stripping cycle is used for removing large amounts of water, and adsorption is used for cryogenic systems to reach low moisture contents—fractions of pounds per MMcf of gas.

Direct Cooling

The saturated water content of natural gas decreases with increased pressure or decreased temperature (Fig. 5-1). Thus, hot gases saturated with water vapor may be partially dehydrated by direct cooling. Gases subjected to compression are normally "after-cooled," and this cooling may well remove water from the gas. The cooling process must reduce the temperature to the lowest value that the gas will encounter at the prevailing pressure to prevent further condensation of water. The required refrigeration duty was discussed in the previous section.

Absorption of Water in Glycols

Water and the glycols show complete mutual solubility in the liquid phase due to the hydrogen-oxygen bonds [1-1], and their water vapor pressures are very low. One frequently used glycol for dehydration is triethylene glycol, or TEG:

$$\begin{array}{l} CH_2 - O - CH_2 - CH_2 - OH \\ | \\ CH_2 - O - CH_2 - CH_2 - OH \end{array}$$

The flow sheet of a TEG dehydration unit is shown in Fig. 15-14 [15-8]. This is mainly an absorption/stripping type process, similar to the oil absorption process. The wet gas is dehydrated in the absorber, and the stripping column regenerates the water-free TEG. The glycol stream should be recharged constantly because some TEG may react and form heavy molecules, which should be removed by the filter shown in Fig. 15-14 or by distillation of a slip stream.

Adsorption of Water by Solid

Solid desiccants or adsorbents are commonly used for dehydrating gases in cryogenic processes. The use of solid adsorbent has been extended to the dehydration of liquid. Solid adsorbents remove water from the hydrocarbon stream and release it to another stream at higher temperatures in a regeneration step. A flow diagram for adsorption is shown in Fig. 15-15 [1-1].

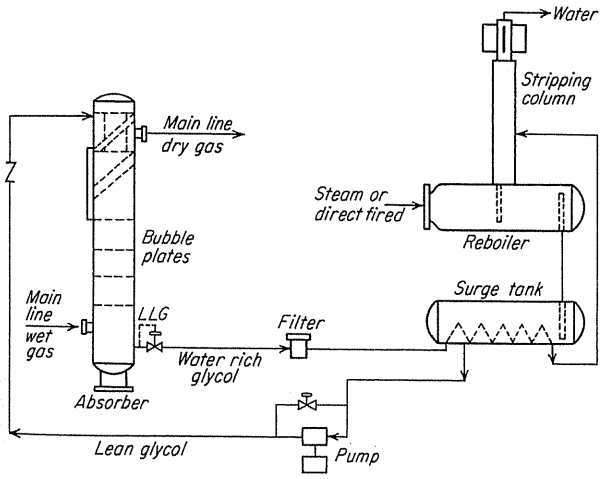

FIGURE 15-14
Flow sheet for triethylene glycol (TEG) dehydration plant [Campbell & Laurence, 15-8, courtesy *Petro. Refin.*].

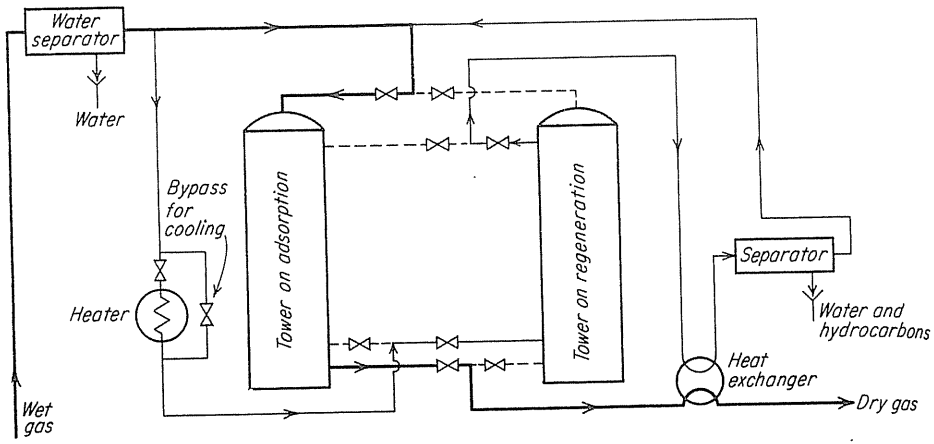

FIGURE 15-15
Flow diagram for solid desiccant dehydration [Katz et al., 1-1, courtesy McGraw-Hill Publishing Co.].

The distribution of water in the bed and in the gas stream is shown in Fig. 15-16 [1-1] for the beginning of a drying period, an intermediate time (30 percent), and the conclusion of the drying period just prior to breakthrough. The regeneration period should start just before breakthrough of the nondehydrated gas to obtain maximum capacity for each regeneration. Calculations of the breakthrough time can be found in reference [15-28,15-34].

At the start of a dehydration cycle, the bed is saturated with methane as the gas flows through the bed. Then ethane replaces methane, and propane is absorbed next. Finally, water will replace all the hydrocarbons. In fact, a "quick cycle," applied before the breakthrough of pentanes, can be utilized as an alternative method of removing heavier components of natural gases, or as a dew point control mechanism [1-1].

For good dehydration, the bed should be switched to regeneration just before the water content of outlet gas reaches an unacceptable level. The regeneration of the bed consists of circulating hot dehydrated gas to strip the adsorbed water, then circulating cold gas to cool the bed down. Clocked quick action valves switch the stream flow.

Adsorption beds deteriorate with repeated cycles. The effects of temperature may place restraints on the temperature rise used in desorbing the bed. Lubricating oil or other foreign liquids must be kept from contacting solid dessicants. The acting life of dessicants varies, with replacements required after 1 to 5 years of operation.

Dehydration of Liquids

As mentioned, liquid hydrocarbons need to be dehydrated; wet propane may form hydrates. Solid adsorbents can be used as for gases.

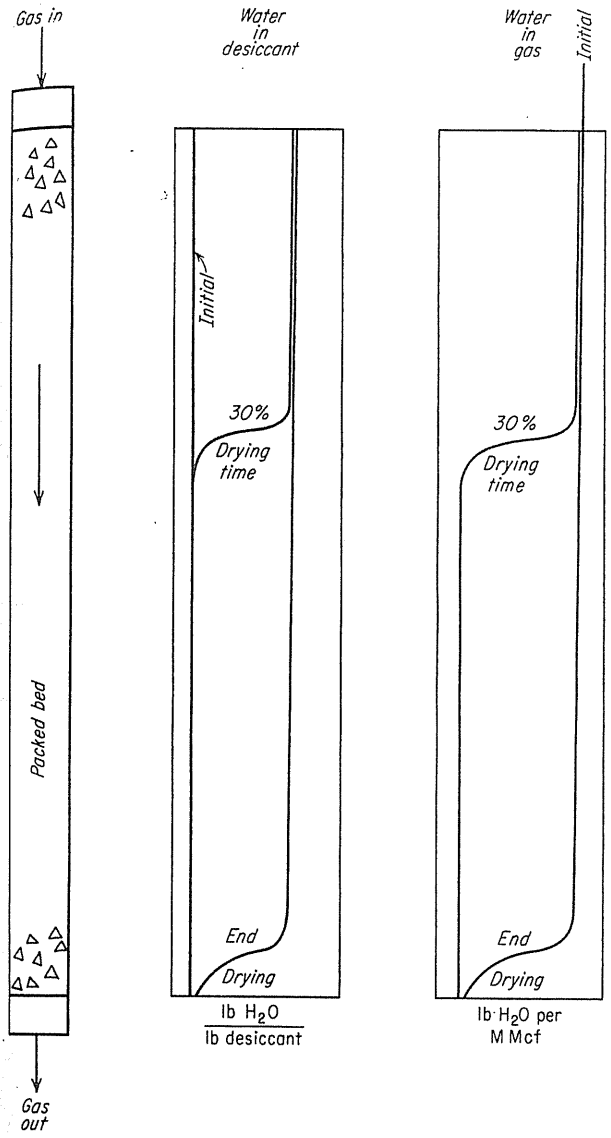

FIGURE 15-16
Typical moisture gradient curves in the desiccant and in the gas phase during absorption periods [Katz et al., 1-1, courtesy McGraw-Hill Publishing Co.].

Systems that exhibit limited miscibility with water in the liquid-liquid-gas region may be dehydrated by distillation, provided the feed concentration is less than or in the neighborhood of the saturation conditions for the light hydrocarbon. For example, the distillation carried out in the near area of line EF between lines EF and AB, the $L_2 - V$ area of Fig. 15-17 [1-1], will concentrate the liquid with respect to hydrocarbon and reject water in the vapor. The reversed volatility of water and hydrocarbon with only a vapor hydrocarbon and liquid hydrocarbon partially saturated with water is a little-known phase behavior.

Figure 15-18 [15-15] is a flow diagram of a distillation dryer in which water is rejected overhead and dehydrated hydrocarbons are the bottoms product. Calculated or experimental equilibrium-vaporization ratios for water in light hydrocarbons may be used to calculate the ideal number of stages to effect the desired dehydration. However, the utility of the equilibrium-stage approach is diminished by the fact [15-15] that the overall plate efficiencies will probably only be of the order of 4 to 8 percent. When the theoretical plates number 1 or 2, the actual trays required may be as high as 30.

It is very unusual to find a fractionator producing an overhead stream boiling at 212°F (100°C) with a bottoms product boiling at −40°F (−40°C). This is due to the abnormal vapor-liquid equilibria for the two-phase water-hydrocarbon system between the two-phase and the one-phase vapor curves (Fig. 15-17). Sheffer learned this unusual phase behavior in his study of the hexane-water system [15-27].

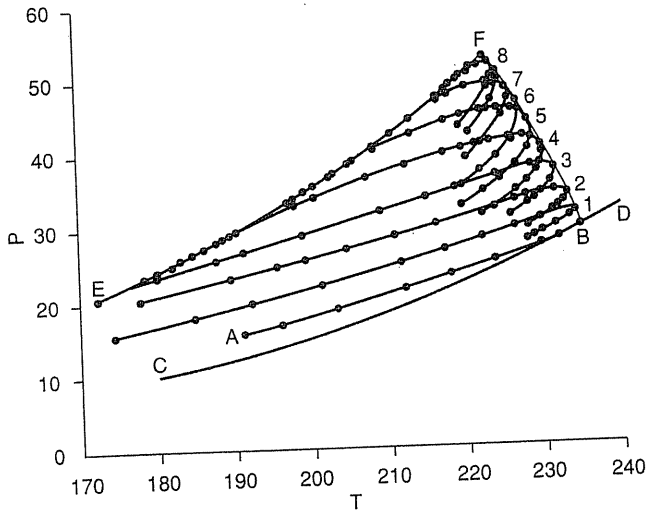

FIGURE 15-17
Phase behavior of hexane-water system [Scheffer, 15-27].

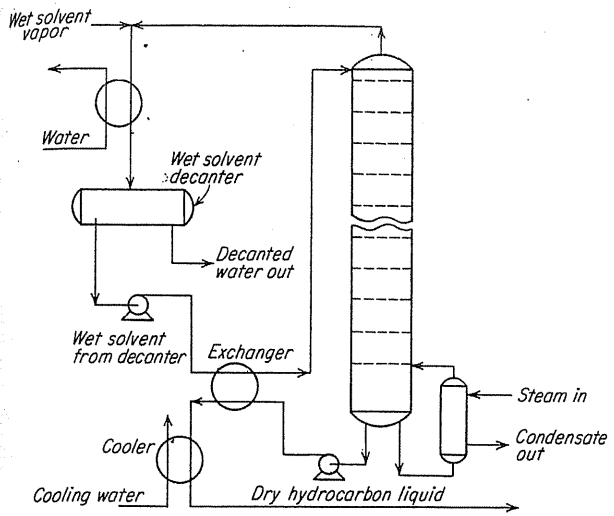

FIGURE 15-18
Process for dehydration of hydrocarbon liquids by distillation [Gester, 15-15, courtesy *Chem. Eng. Prog.*].

15.8 SWEETENING

Many natural gases contain hydrogen sulfide (H_2S) in concentrations ranging from barely detectable quantities to over 30 mole percent. Gases containing H_2S or CO_2 are classified as *sour*, and gases free from H_2S and CO_2 are called *sweet*. Natural gas that is transported to the fuel market must meet legal requirements, which specify a maximum H_2S content in the range of 0.1 to 0.25 grain per 100 Scf (0.229–0.573 g/100 m^3). These requirements are justified, since H_2S is a toxic gas, and its combustion product is sulfur dioxide or trioxide.

The removal of H_2S from natural gas is accompanied by the removal of CO_2 and COS if present, since these have similar acid characteristics.

Sweetening processes are usually of the absorption/stripping type, like the oil absorption process. The solution used should have a high capacity for absorbing the acid gases through chemical reaction while exerting a very low equilibrium vapor pressure on gases. Another requirement is that the phase reaction be reversible at some higher temperature in order to permit regeneration and reuse of the original solution.

The common solutions used are monoethanolamine (MEA), diethanolamine (DEA), and triethanolamine (TEA), as well as the combination of sulfolane disopropanolamine (DIPA) and 3% water for Shell's sulfinol process [15-12, 15-13]. The basic schematic flow chart of a sweetening unit is shown in Fig. 15-19. Shell's higher costing sulfinol process, except for the high absorption of heavy hydrocarbons and aromatics, is believed to be superior to the conventional

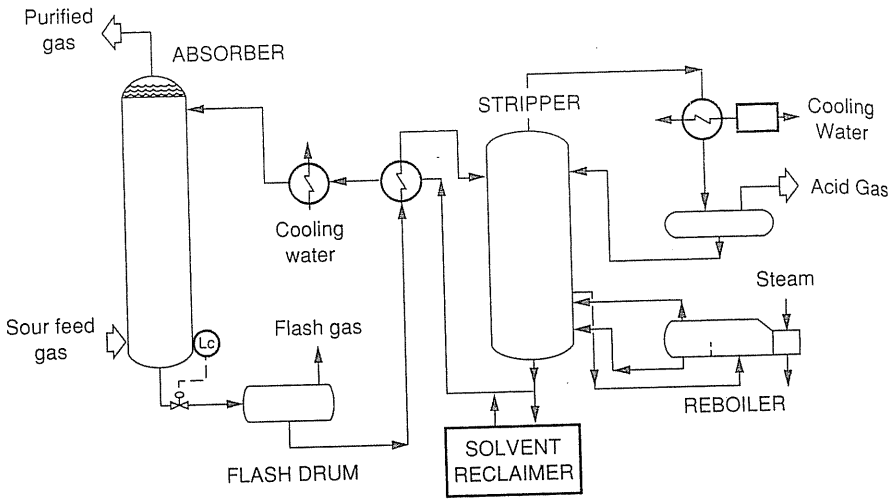

FIGURE 15-19
Gas-sweetening process flow diagram (Shell sulfinol process) [Deal et al., 15-12, courtesy Shell Oil Co.].

amine processes [15-18]. Improved sulfinol processes were also introduced by Shell [15-14,15-35].

It should be noted that a combination of amines and glycols can extract the water vapor, H_2S and CO_2 simultaneously from the natural gas stream. However, the loss of amine and the corrosion problems of this type of process make it impractical. More information on the amine system and the Claus processes (including conversion of H_2S or COS to solid sulfur S), can be found in references [1-1,15-7,15-20,15-23,15-30].

Carbon Dioxide and Nitrogen Used in Tertiary Oil Recovery

New field processes may be required in gas processing for removing nitrogen to increase NGL recovery after a nitrogen injection enhanced recovery process. Nitrogen rejection systems [15-1,15-6,15-9] are needed in gas processing plants for downstream operations. The use of CO_2 in enhanced oil recovery may place a premium on its recovery in gas processing. Separating CO_2 and H_2O may be desirable, and processes may be found to accomplish this. Some references on this subject are [15-3,15-16,15-17,15-26,15-33].

The San Juan plant removes CO_2 from the fuel gas, since it is corrosive in pipelines at the rate related to CO_2 partial pressure. At concentrations under 1 percent, CO_2 is accepted as a diluent in pipeline gases, and assurance that lines are free of liquid water will reduce opportunities for corrosion.

TABLE 15.7
Summary of process capabilities [1-28, courtesy GPA]

	Normally capable of H_2S spec.[e]	Removes mercaptan and COS sulfur	Selective H_2 absorbed	Solution degraded (by)
Monoethanolamine	Yes	Partial	No	Yes (COS, CO_2, CS_2)
Diethanolamine	Yes	Partial	No	Some (COS, CO_2, CS_2)
Sulfinol	Yes	Yes	Yes[c]	Some (CO_2, CS_2)
Diglycolamine	Yes	Partial	No	Yes (COS, CO_2, CS_2)
Selexol	Yes	Slight	Yes[c]	No
Hot Pot-Benfield	Yes[a]	No[b]	No	No
Fluor solvent	No[d]	No	No	No
Stretford	Yes	Partial	Yes	Yes (HCN via thiocyanate)
Iron sponge	Yes	Partial	Yes	—
Molecular sieve	Yes	Yes	Yes[c]	—

[a] Hi-pure version
[b] Hydrolyzes COS only.
[c] Some selectivity is exhibited by these processes.
[d] Can be met with special design features.
[e] $\frac{1}{4}$ grain H_2S/100 Scf = 5.7 mg/m^3 (GPA)

15.9 CONCLUSION

The gas processing industry stands ready to convert natural gas to an acceptable fuel. By using the components or units available to the industry, an economical process scheme is likely to be found. New schemes and liquids used appear in the literature when a new problem arises. Although the equipment used in these plants as well as the whole process could be designed by using a computer simulator such as FLOWTRAN [15-29], only the principles of some basic operations have been discussed here. The capabilities of commercial processes are summarized in Table 15.7.

RECOMMENDED READING

Astarita, G., D. W. Savage, and A. Bisio, *Gas Treating with Chemical Solvents,* John Wiley & Sons, New York (1983).

Campbell J. M., *Gas Conditioning and Processing,* Volume 2, Campbell Petroleum Series, Oklahoma (1976).

Henley, E. J., and J. D. Seader, *Equilibrium-Stage Separation Operations in Chemical Engineering,* John Wiley & Sons (1981).

Katz, D. L., et al., *Handbook of Natural Gas Engineering,* McGraw-Hill Publishing Co. (1959).

King, C. J., *Separation Processes,* 2nd Ed., McGraw-Hill Publishing Co. (1980).

Mallett, M. W., "Largest U.S. Gas Processing Plant Begins Operations," *Oil and Gas J.,* Vol. 85, No. 3, Jan. 19 (1987).

The Petroleum Publishing Company, *Sour Gas Processing and Sulfur Recovery,* Tulsa, Oklahoma (1979).

REFERENCES

15-1. Alvarez, M. R., M. F. Hilton, and H. L. Vines, "Design and Startup of a Nitrogen Rejection Unit for Associated Gas from an EOR Project," *Proceedings, 63rd GPA Annual Meeting,* 131–137 (1984).

15-2. American Gas Association, *Gas Engineering Handbook,* First Ed., 2nd Printing, Arlington, Va. (1966).

15-3. Barnwell, J., and B. K. Marshall, "Tertiary Recovery with CO_2 May Inject New Life Offshore," *Proceedings, 64th GPA Annual Meeting,* 168–171 (1985).

15-4. Brown, G. G. et al., *Unit Operations*, John Wiley & Sons, New York (1950).

15-5. Brown, G. G., and M. Souders, Jr., "Separation of Petroleum Hydrocarbons by Distillation," *Science of Petroleum,* Vol. 2, 1544, Oxford University Press, New York (1938).

15-6. Browne, L. W., and J. L. Aberle, "Flexible, Integrated NGL Recovery/Nitrogen Rejection Systems," *Proceedings, 62nd GPA Annual Meeting,* 167–175 (1983).

15-7. Bullin, J. A., J. C. Polasek, and J. W. Holmes, "Optimization of New and Existing Amine Gas Sweetening Plants by Computer Simulation," *Proceedings, 60th GPA Annual Meeting,* 142–148 (1981).

15-8. Campbell, J. M., and L. L. Laurence, "Dehydration of Natural Gas and Hydrocarbon Liquid, Part IV," *Petro. Refiner, Vol. 31*, 109 (1952).

15-9. Chesney, J. D., R. A. Davis, M. F. Hilton, and H. L. Vines, "Optimizing Hydrocarbon Recoveries in Nitrogen Rejection Units," *Proceedings, 62nd GPA Annual Meeting,* 176–186 (1983).

15-10. Davidson C. D., and K. D. Watson, Arco, (1981).

15-11. Daviet, G. R., and N. C. Hircock, "Improving LP-Gas Recovery on Standard Refrigeration Plants," *Proceedings of 64th GPA Annual Meeting,* 86–91 (1985).

15-12. Deal, C. H., et al., "Sulfinol—A New Process for Gas Purification," Section IV, Paper 32, *6th World Petroleum Congress,* Frankfurt, Germany (1963).

15-13. Fisch, E. J., "Acid Gas Removal by Versatile Shell Processes," *Proceedings, 59th GPA Annual Meeting,* 167–170 (1980).

15-14. Flynn, A. J., C. B. Wallace, R. G. Christensen, and W. T. Knowles, "Shell's Recent Improvements in Gas Treating and Claus Tail Gas Cleanup," *Proceedings, 60th GPA Annual Meeting,* 149–151 (1981).

15-15. Gester, G. C., Jr., "Design and Operation of a Light Hydrocarbon Distillation Drier," *Chem. Eng. Progr.*, Vol. 43, 117 (1947).

15-16. Goar, B. G., "CO_2 Removal from EOR Gases and Attendant Sulfur Handling Problems," *Proceedings, 64th GPA Annual Meeting,* 330–336 (1985).

15-17. Johnson, J. E., and F. B. Walter, "EOR Gas Processing—What Is Special About It?" *Proceedings, 64th GPA Annual Meeting,* 337–345 (1985).

15-18. Klein, J. P., "Developments in Sulfinol and ADIP Processes Increase Uses," *Oil and Gas J.*, Vol. 10, No. 9 (1970).

15-19. Mallett, M. W., "Largest U.S. Gas Processing Plant Begins Operations," *Oil and Gas J.*, Vol. 85, No. 3, Jan. 19 (1987).

15-20. Morrow, D. C., and G. P. McClure, "MALAPROP™—An Amine Process for Removal of COS from Propane," *Proceedings, 58th GPA Annual Meeting,* 135–138 (1979).

15-21. Neumann, W. M., Jr., "Importance of Feed Gas Conditioning," *Proceedings, 56th GPA Annual Meeting,* 88–91 (1977).

15-22. Perry, R. H., and C. H. Chilton, *Chemical Engineering Handbook,* 5th Ed. Sec. 10, McGraw-Hill, New York (1973).

15-23. The Petroleum Publishing Company, *Sour Gas Processing and Sulfur Recovery,* Tulsa, Oklahoma (1979).

15-24. Petty, L. E., "Practical Aspects of Molecular Sieve Unit Design and Operation," *Proceedings, 55th GPA Annual Meeting,* 103–108 (1976).

15-25. Ruthreu, D. M., *Principles of Absorption and Adsorption Processes,* John Wiley & Sons, New York (1984).

15-26. Schaffert, F. W., N. V. Wood, and J. V. O'Brien, "The Seminol San Andres Unit CO_2 Recovery Plant—Meeting the Challenges of EOR Gas Processings," *Proceedings, 65th GPA Annual Meeting,* 86–89 (1986).

15-27. Scheffer, F. E. C., "On the System Hexane-Water," *k. Akad. Wet.*, Pro. Vol. 16, 404–418 (1913).

15-28. Schweitzer, P. A., editor-in-chief, *Handbook of Separation Techniques for Chemical Engineers,* McGraw-Hill (1979).

15-29. Seader, J. D., W. D. Seider, and A.C. Pauls, *Flowtran Simulation—An Introduction*, 2nd Ed., CACHE, Cambridge, Mass. (1977).

15-30. Sigmund, P. W., K. F. Butwell, and A. J. Wussler, "The HS Process: An Advanced Process for Selective H_2S Removal," *Proceedings, 60th GPA Annual Meeting,* 134–141 (1981).

15-31. Souders, M., Jr., and G. G. Brown: "Fundamental Design of Absorbing and Stripping Columns for Complex Vapors," *Ind. Eng. Che.*, Vol. 24, 519 (1932).

15-32. Swearingen J. S., "Turboexpanders and Processes That Use Them," *Chem. Eng. Prog.*, Vol. 68, No. 7, 95–102 (1972).

15-33. Sweny, J. W., "High CO_2–High H_2S Removal with SELEXOL Solvent," *Proceedings, 59th GPA Annual Meeting,* 163–166 (1980).

15-34. Treybal, R. E., *Mass Transfer Operations*, 3rd Ed., McGraw-Hill Publishing Co. (1980).

15-35. Wallace, C. B., and A. J. Flinn, "The Cascade Sulfinol-Scot Process," *Proceedings, 62nd GPA Annual Meeting,* 150–153 (1983).

CHAPTER 16

STORAGE IN SALT CAVITIES AND MINED CAVERNS

In 1950 the use of salt cavities for storing propane and butane underground was introduced [1-2,16-29]. Although there had been a long history of creating salt cavities by solution mining of salt [16-5,16-6], the creation of a salt cavern for the purpose of LP gas storage was an innovation. Underground LP gas storage has since grown, reaching 125 million barrels (19.9×10^6 m^3) in the United States by 1966 [1-2], and 560 million barrels (89×10^6 m^3) by 1983 [16-23].

In 1961 Southeastern Michigan Gas Company first used a salt cavern for gas storage [1-2,16-45]. After many Morton Salt Company salt-mining wells were tested for leakage, one was found to be completely sealed and was converted to gas storage. The well was then equipped for handling gas injection/withdrawal and brine displacement by natural gas.

In earlier LP gas storage, the cavity was maintained full of liquid; therefore, there was no pressure variation. However, in gas storage, a pressure fluctuation on walls of the cavity was expected. The salt cavity at 2050 ft (625 m) held 341 MMcf (9.66×10^6 m^3) of gas at a wellhead pressure of 1100 psi (7.58 MPa) down to 150 psi (1.03 MPa). The early operating pressure range was 1154–479 psig (7.96–3.31 MPa) at the wellhead; in 1966 the well delivered 22,120 Mcf (626×10^3 m^3) of gas per day. This performance showed that a cavity in a salt bed could be stable even though there were frequent pressure changes.

A second gas storage facility was developed in Saskatchewan, Canada, by 1966, in a salt cavity at 3400 ft (1036 m) [16-2,16-14,16-40]. Gaz De France initiated a gas storage project in 1968 near Lyons, France in the evaporite salt at 4593 ft (1400 m).

Unfortunately, salt deposits occur in limited areas of the world. The alternative is to create mined cavities for LP gas and volatile liquids in the absence of salt deposits.

16.1 OCCURRENCE OF SALT BEDS

Salt beds occur in two modes within limited areas of the United States and Europe. These beds may be extensive layers of evaporite such as occur in the Silurian age or extruded domes of salt such as those found in the Gulf Coast area of the United States. Figures 16-1 [16-27] and 16-2 [16-12] are maps showing locations for the salt beds in North America. Figure 16-3 [16-3,16-4] depicts a salt dome, a tall vertical column of salt.

Salt layers in beds are quite different from salt domes. The nature of the beds can be observed in rock-salt mines. Layers of limestone, dolomite, or anhydrite may occur in the salt beds; these do not dissolve in solution mining, but form ledges that fall in as the dissolution progresses. A core hole in the bed is a prerequisite for an LP or natural gas storage project. Generally, the NaCl in salt domes is more homogeneous than that in evaporite beds. A Columbian salt mine has intermingled nodules of asphaltic substance.

What protection do salt layers have from percolating streams of aquifer water? On the top of salt beds or domes, there are a series of evaporites including gypsum ($CaSO_4 \cdot 2H_2O$), dolomite, and anhydrite ($CaSO_4$).

Anhydrite-Gypsum-Water Reactions

Anhydrite was encountered in the study of the threshold pressure of caprock cores [1-38]. It was found to have an unmeasurable permeability and hence was declared a homogeneous rock or super caprock. A study on anhydrite was carried out by Goldman [16-22], who examined a core through the top of a salt dome. Anhydrite reacts with water to form gypsum:

$$CaSO_4\,(s) + 2H_2O\,(l) \rightarrow CaSO_4 \cdot 2H_2O\,(s) \qquad (16.1)$$

In an experiment in the senior author's office, a polished anhydrite core was placed in tap water and found to react, forming a white substance (Fig. 16-4). Examination by x-rays showed the core to be anhydrite and the white layer on the surface of the core to be a mixture of anhydrite and gypsum. It was suggested that anhydrite might not react with the dense brine. A fresh surface did not react with the dense brine found in the basal Niagaran, which had a dissolved solid content of 405,000 g/ml. The vapor pressure of the brine was 59 percent of that of pure water at the same temperature. The latter value fitted the extended curve of vapor pressure versus solid content [1-1] (Fig. 5-2).

FIGURE 16-1
Major salt basins of North America [Landes, 16-27, courtesy Northern Ohio Geological Society].

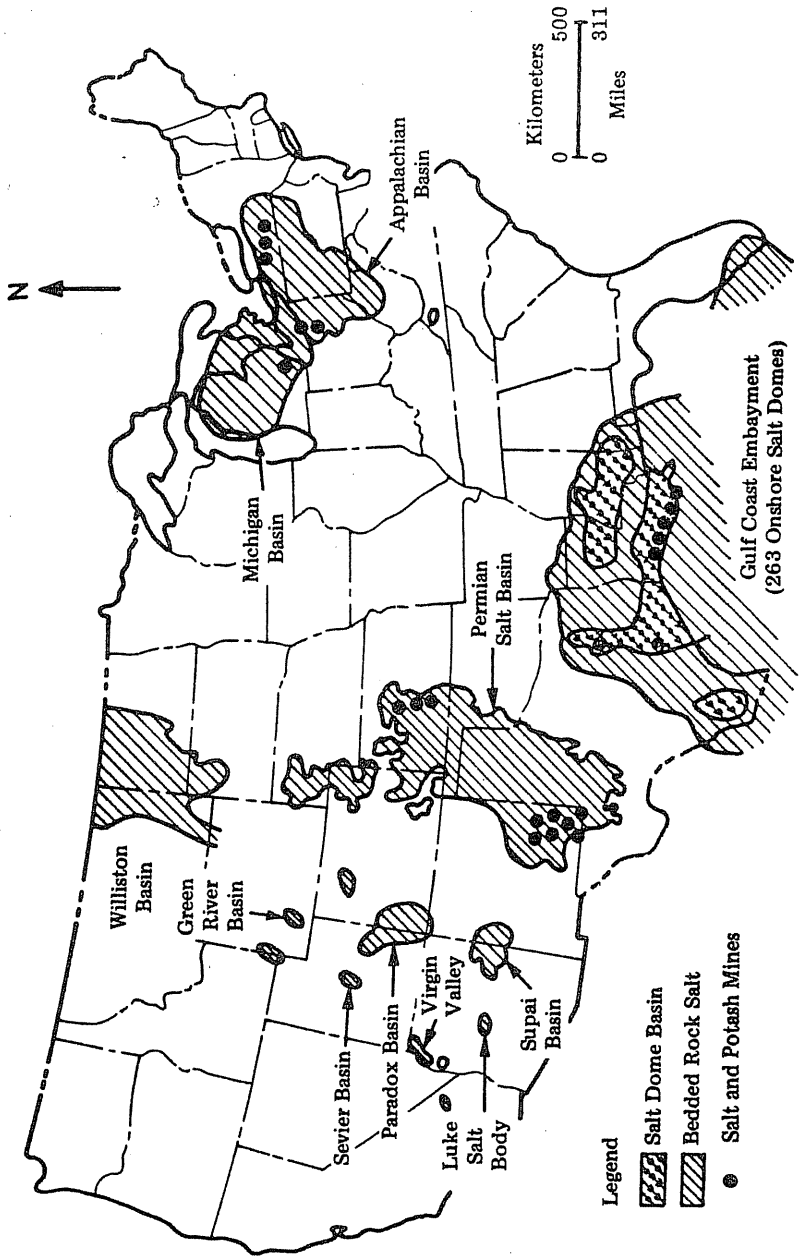

FIGURE 16-2
Known salt deposits in the United States [16-12, courtesy CER Co.].

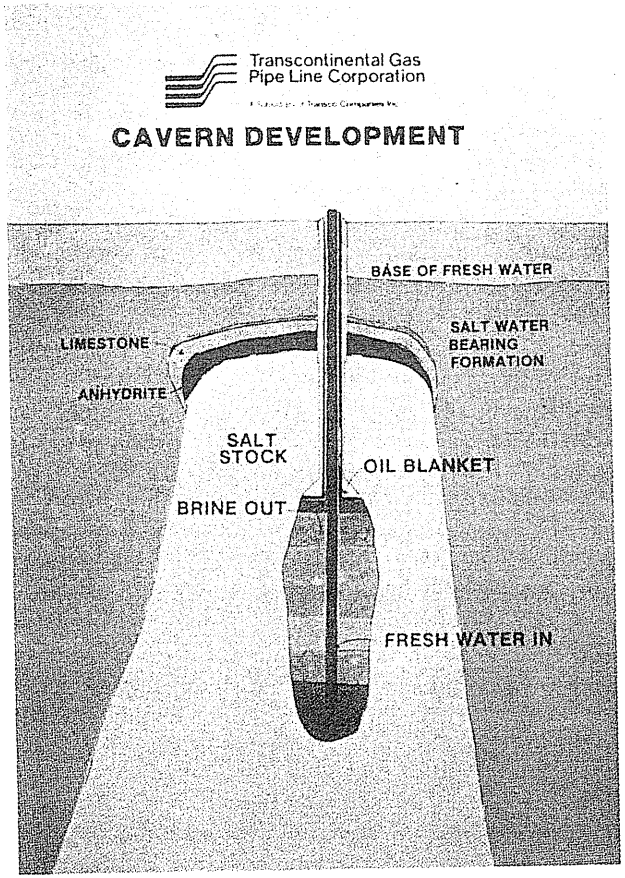

FIGURE 16-3
Salt dome structure and operation, Eminence [16-3, Transcontinental Gas Pipe Line Corporation].

What isolates salt beds in the earth? Salt layers have anhydrite in their caps, and gypsum is present. The latter is believed to protect the salt layer from fresh water dissolution. When the edge of salt beds have no anhydrite covering, salt dissolves over geologic time as found on the edges of the Michigan basin. The conversion of anhydrite to gypsum is an ongoing process that isolates salt from ground waters.

What is the nature of the salt bed? The rock has a very low porosity and permeability even after coring. Anhydrite is more stable and has been shown to be essentially a zero porosity rock with zero permeability. It reacts with pure water but not with indigenous brine. Salt layers may have occlusions of liquid brine but otherwise are generally dry. Some salt mines are dusty because of particles given

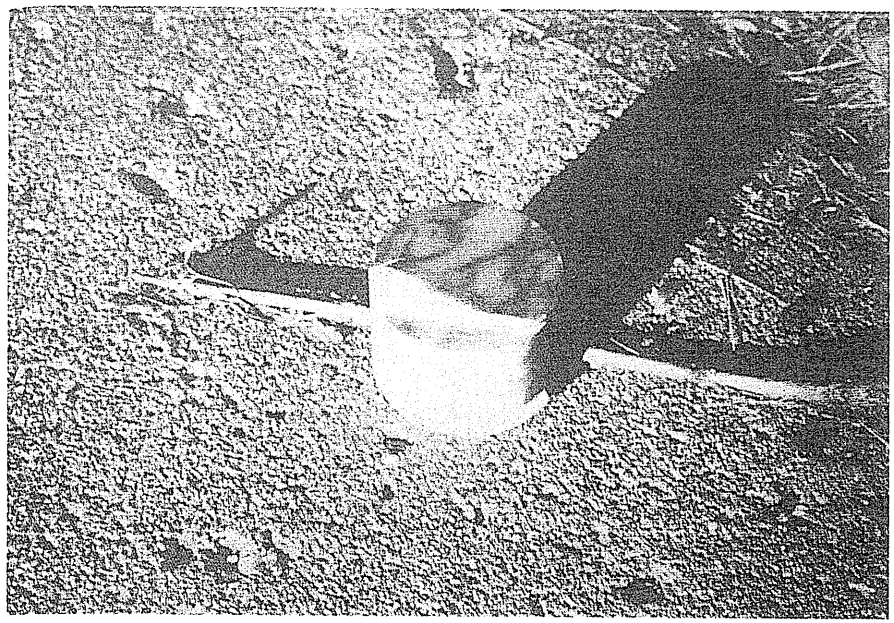

FIGURE 16-4
Anhydrite core reacted with water.

off in the physical handling of salt. The character of salt is given by monograph [16-25] and many articles in the Symposium on Salt series, issued at intervals [16-2,16-5,16-7,16-10,16-14,16-15,16-27,16-32,16-38,16-40,16-45]. Table 16.1 shows the physical and thermal properties of salt [1-14]. Table 16.2 is a brief description of the Huntorf salt cavity for gas storage in Germany.

Effect of Water on Salt

The porosity of rock salt taken from mines is on the order of 0.6 to 2.0 percent. The dry permeability of a specimen with a minimum confining pressure varies considerably from practically zero to over 100 md. The permeability of salt decreases with time when the specimen is subjected to overburden pressures of 100 to 800 psi (689–5520 kPa) or more [16-5]. A specimen confined at a minimum pressure had a permeability of 15 md; when it was confined at 800 psi (5.52 MPa) pressure for 17 hours, the permeability was reduced to 0.33 md, and when confined for 500 hours, to 0.13 md.

There are very significant effects when salt crystals have their surfaces met by water or brine; Barnes's [16-6] study indicated that water enters the salt crystal. Dry brittle rods of crystals may be tied into knots when wet for a period of time.

TABLE 16.1
Physical and thermal properties of salt [Katz & Lady, 1-14]

Temperature °C	Temperature °F	Density, g/cm³	Linear expansion from 20°C, %	Specific heat, cal/(g · °C) or Btu/(lb · °F)	Thermal conductivity, Btu/(hr · ft · °F)	Density sat. solution in water, g/cm³
−200	−328	2.211		0.157	14.	
−100	−148			0.176		
0	32	2.168		0.204	4.	1.209
20	68		0			
50	122	2.155			2.80	1.187
100	212		0.32	0.217	2.43	1.160
200	392		0.74	0.221	1.80	
300	572				1.44	
400	752		1.71	0.229	1.20	
500	932			0.232		
600	1112		2.82	0.237		

Melting point: 800 °C, 1472°F
Poisson ratio ≈ 0.27
Linear coefficient of expansion: 3.9×10^{-5} at 0°C
Cubic coefficient of expansion, 0–50°C: 115×10^{6}

TABLE 16.2
Huntorf salt cavity

Company	Energieversorgung Weser-Ems AG	
Location	Huntorf, Germany	
Completion	1975	
Number of caverns	4	
Purpose of storage	Peak shaving (seasonal)	
Type of formation	Dome	
Geologic age	Permian	
Cavern temperature	95°F	35°C
Total spatial volume	40.61 MMcf	1.32×10^{6} m³
Total storage capacity	6.36 Bcf	180×10^{6} m³
Total working gas	4.59 Bcf	130×10^{6} m³
Total Cushing gas	1.77 Bcf	50×10^{6} m³
Withdrawal rate	191 MMcf	7.2×10^{6} m³
Maximum design pressure	1422 psi	100 bar
Minimum design pressure	356 psi	25 bar
Depth to top of cavern	2133 ft	650 m
Maximum diameter	197 ft	65 m
Height	656 ft	200 m
Percent insolubles	5%	
Depth to salt formation	1640 ft	500 m
Last cemented casing setting depth	2034 ft	650 m

A specimen of salt cut into halves and reassembled had an apparent permeability of 1000 md. However, when it was subjected to 800 psi (5.52 MPa) overburden pressure, its permeability was reduced to 0.1 md. One gets the impression that both overburden pressure and liquid brine pressure cause any permeability channels in the rock salt to heal and reduce permeability to very low values as compared to the dry salt. This appears to be the basis for the high (92–99 percent) recovery of liquid hydrocarbons from storage cavities.

Laboratory measurements on dry salt indicate it extrudes at 125,000 psi (862 MPa). Knowing the effect of water on the crystals, one would expect this pressure to be much less when wet. Underground extrusion is said to be the cause of formation of salt domes, and such salt is no doubt affected by surrounding water.

16.2 CREATION OF SALT CAVITIES—DISSOLUTION

Creation of a salt cavity requires not only a main well for injecting water into the cavity, but also a source of fresh water and a brine disposal system, often rock layers of high permeability containing brackish water. Brine generated in the leaching process has been discharged into the ocean: in the development of several strategic salt cavities, brine was carried by 36-in. (0.91-m) pipelines to a 12-acre (48.6×10^{3} m³) brine distribution area (3-in., or 0.0762 m, plastic pipe distribution network) 12 miles (19.3 km) offshore of federal land [16-24,16-42]. The time of dissolution is predictable; it depends upon the water injection rate.

Cavern development on a site located by core drilling or other data involves drilling the well through which fluids enter and leave the cavity. Using normal surface casing for potable water protection, the main casing size is determined by the size of the cavern. When drilling into salt, mud with saturated brine gives protection from further dissolution of salt while the hole is drilled to the bottom of the proposed cavern. A bottom chamber is used for insolubilities. The casing of a cavity in bedded salt should be set near the top of the salt layer, but an arbitrary depth may suffice in dome salt.

Van Fossan [16-44] set forth safety precautions for designing the well completion and the allowable pressure on the well system. Fracturing of salt is to be avoided for storage projects. The direct leaching flow system involves pumping fresh water down the inner tube of the well to the bottom of the drilled hole. The brine, after dissolution, comes up the annulus between the fresh water tube and the casing (Fig. 16-5 [16-44]).

For reversed leaching (Figure 16-6 [16-18]) the fresh water is introduced in midchamber from an annulus, with brine exiting through the inner tube. A computer program could include the flow rates and pressure drops at each step in the flow. Hydraulic heads become important with brine at 1.22 g/ml density. Experiences show that the brine concentration and the shape of the cavern can be controlled by using various positions of the water supply and exit.

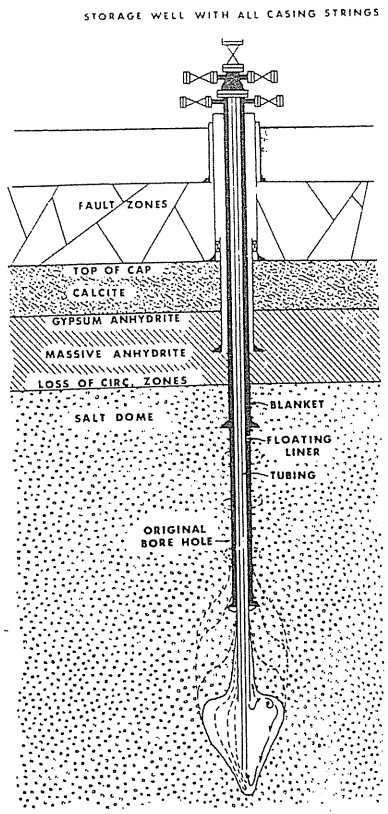

FIGURE 16-5
Leaching to create salt cavities [Van Fossan, 16-44, courtesy GPA].

No attempt is made here to set forth the art of water injection procedures to control the shape of the cavity. Simulation is used to quantitatively choose the shape of the space. Experience has shown that use of lower-strength tubing within the cavity is advisable, so that fallen ledges of anhydrite or dolomite create less interference with the tubes in the upper cased hole.

The casing seat of the primary casing is a critical point in completion of the well. Logs are needed to ensure that the cement not only fills the annulus but also is completed within and above the salt to prevent losses. Hydrocarbon liquid (gas oil) is placed in the cavity to prevent unsaturated brine from leaching salt behind the casing.

16.3 MEASUREMENT OF CAVITY SIZE AND SHAPE

Sonar Caliper tools (Fig. 16-7 [16-32]) are used to obtain the wall distances at various levels. Figure 16-8 [16-32] gives the four quadrants of measurements

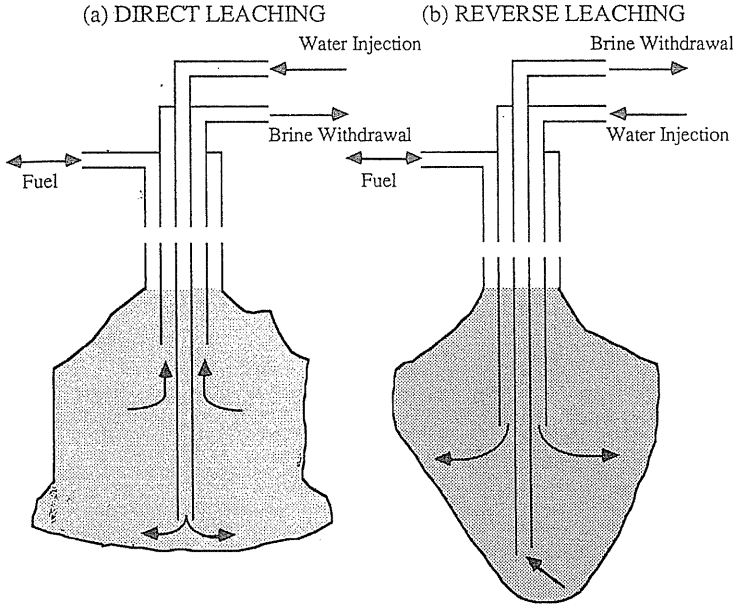

FIGURE 16-6
Leaching mechanisms: (*a*) direct leaching, (*b*) reverse leaching [after M. Duchassin, M. Dussaud, & B. Hugout, 16-18, courtesy Pipeline Industry].

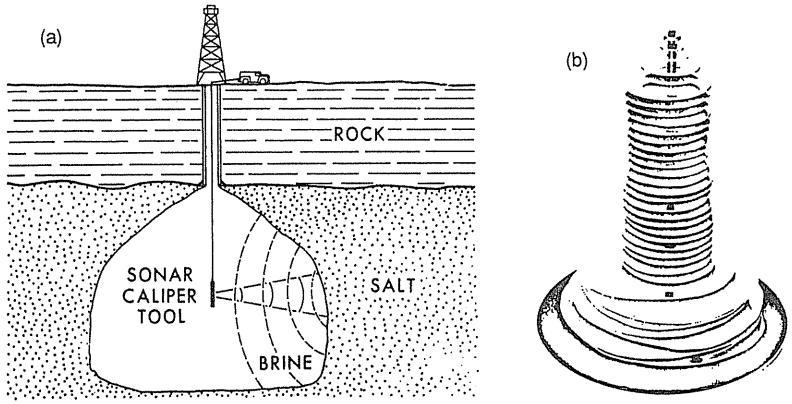

FIGURE 16-7
(*a*) Schematic diagram of sonar caliper survey; (*b*) three-dimensional model of sonar findings in salt cavity [A. J. Myers, 16-32, courtesy Northern Ohio Geological Society].

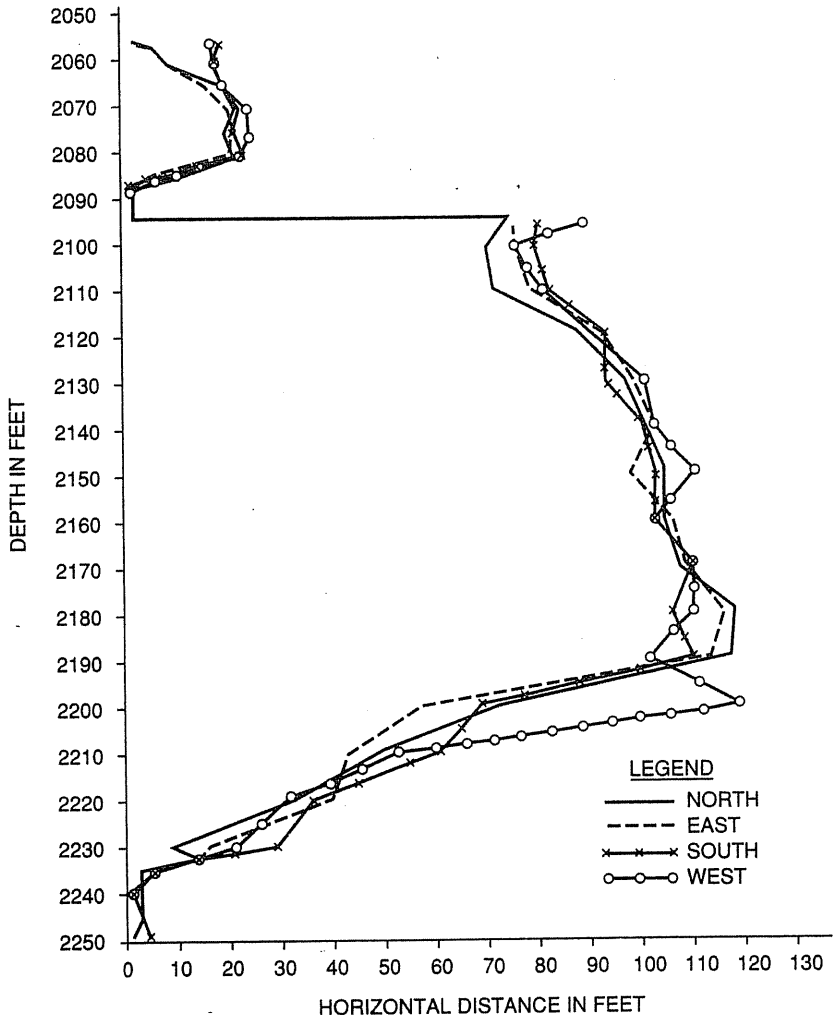

FIGURE 16-8
Sonar measurements on gas storage cavern, Marysville [Vance, 16-45, courtesy Northern Ohio Geological Society].

on the Marysville cavity [16-7]. Three-dimensional plastic models of the cavern shape are made using multiple measurements one below the other. The proportion 6.3 bbl water/bbl salt and values for brine densities and flow are used in writing a material balance for the volumetric capacity. When injecting LP, the level of the hydrocarbon-brine interface and the metered quantity of injected hydrocarbon should verify the volume.

16.4 STABILITY OF CAVITIES

Cavity stability is the extent to which an acceptable amount of cavity storage volume can be utilized and economically maintained over the planned life of a facility. Thoms [16-43] reviewed the long-term stability of compressed air energy storage (CAES) in salt domes and pointed out three possible cavity instability cases: (1) Creeping closure caused by anomalies or by the stress around the cavity may rapidly (several months) reduce cavity volume to a space inadequate for storage purposes. (2) Roof falls, wall slabbing, and floor heaves in the cavity may occur because of an abrupt depressurization of a CAES cavity due to equipment failure or human error. (3) Cyclic loading effects, i.e., fatigue, may cause the rock salt to behave as a brittle material after a certain time period.

Stability and creep can be simulated for various conditions. Serata [16-41] created a creep meter to measure the directional stresses in a freshly drilled hole. These experiments were carried out in mined salt as well as storage cavities to indicate the effect of cavity spacing on creep rate as well as effects of pressure range and time in service. Others have considered this problem [16-1, 16-9,16-16,16-21,16-23,16-26,16-28,16-33,16-35]. It should be noted that brine-compensated liquid (propane, crude oil) storage maintains the pressure in the cavity and contributes to stability.

16.5 CREEP AND CLOSURE OF SALT CAVITY

Salt has a degree of plasticity, and thus it can be extruded. It is more mobile at higher temperatures under a given stress. In salt domes, with almost a full choice of depth, a balance is struck. At greater depths there are higher temperatures, and therefore more creep. However, a certain depth is needed to permit a desired pressure to be no more than 0.8 of overburden pressure. A cavity at Eminence, Alabama, closed 50 percent within two years when a lower pressure (3800 psia to 1200 psia, 26.2 to 8.27 MPa) was employed in gas storage [16-3]. French experience [16-17,16-18] indicates 35–40 percent reduction of cavities (Tersanne, 4600 ft, 1400 m) over 14 years of operation with a pressure range of 3200 psia to 1100 psia (220–80 bar, 221–7.56 MPa) [16-31].

16.6 BRINE-COMPENSATED VERSUS GAS PHASE

There are two possible cavern operating configurations: compensated (Fig. 16-9 [1-2]) and uncompensated (Fig. 16-9 without brine) systems. The cost of developing the compensated system is higher than that for an uncompensated system. On the other hand, in order to prolong the life of a salt cavity, high-pressure operations are desirable and for high pressures, the brine-compensated system has advantages. Uncompensated caverns depend upon gas pressure changes in the cavern as would occur in gas storage, and this depends on the ability of the cavern salt structure to resist salt creep.

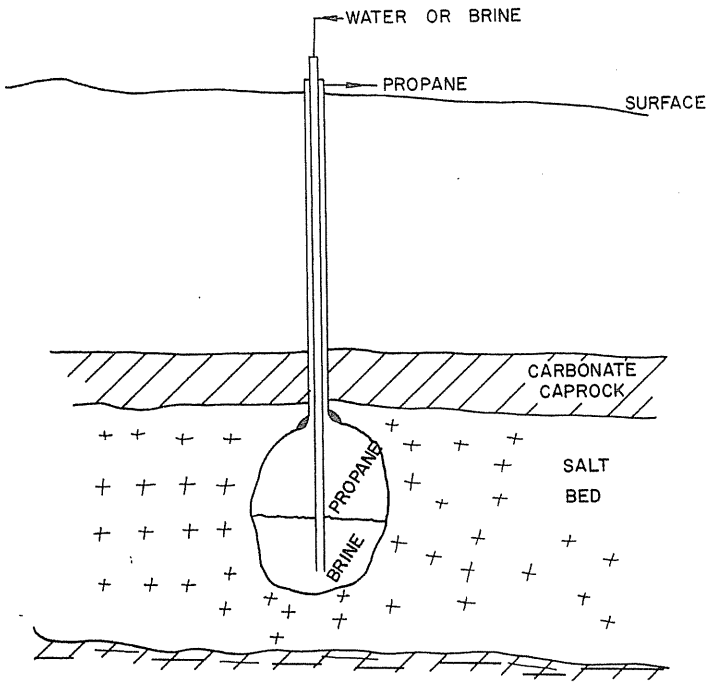

FIGURE 16-9
Sketch of a simple compensated brine/propane system [Katz & Coats, 1-2].

Propane and butane (LPG) are stored in the liquid or dense phase state. In brine compensation, the two liquids, LPG and brine, displace each other; LPG displaces brine on injection, and brine displaces LPG on withdrawal.

Figure 16-9 is a sketch of a brine-compensated storage cavity in which a brine head displaces the hydrocarbon during withdrawal. This mode is used for propane–butane–natural gas liquid storage. Injection of hydrocarbon requires a differential head pump. The static pressure differences for a water- or brine-compensated butane/propane cavern storage system are shown in Figure 16-10 [1-2].

Example 16.1. Consider a brine/propane compensated storage system, as shown in Figure 16-11 [16-30]. The brine level is at the bottom of the cavern at −(2324 + 85) ft. What is the pressure at the wellhead of the propane storage?

Solution. From Fig. 16-10, the pressure difference for a depth of 2399 ft is 840 psi.

16.7 TEMPERATURE CHANGE—CLOSED SYSTEM

When gas is injected into the salt cavity, the temperature of the gas in the cavity will rise before it is cooled by the surroundings. On the other hand, temperature

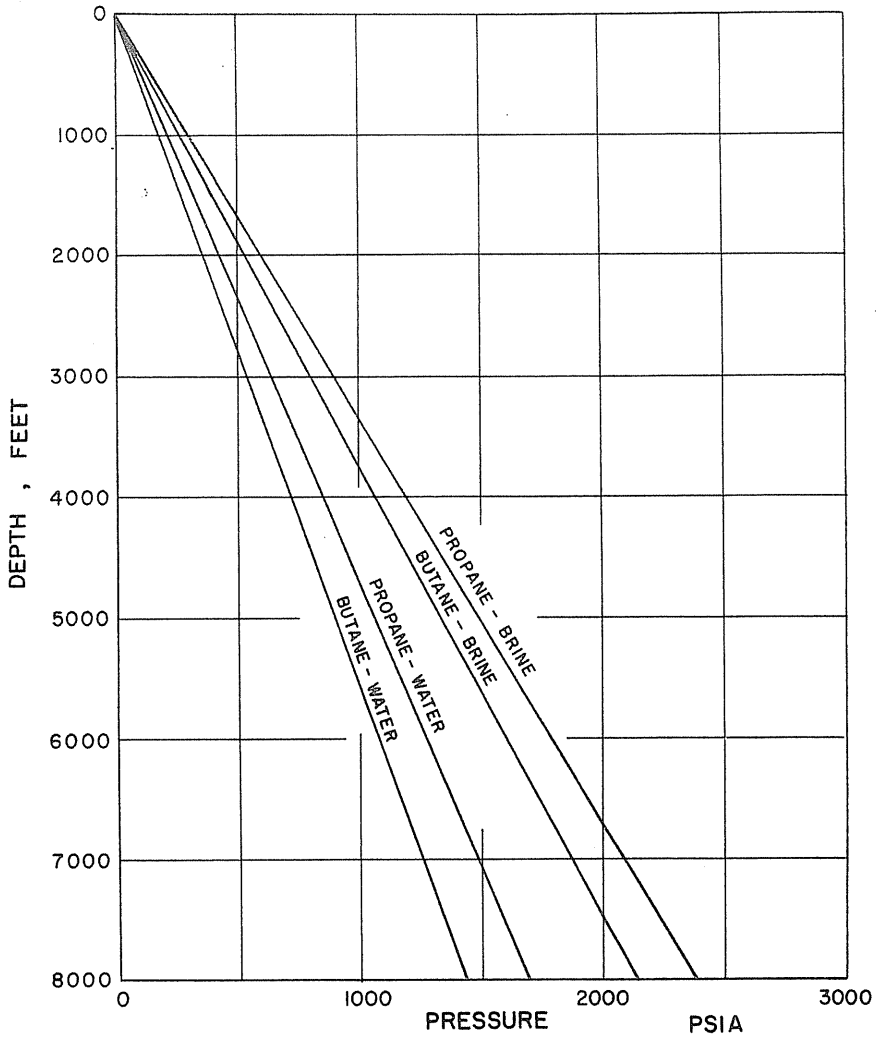

FIGURE 16-10
Static wellhead pressure differences due to column densities [Katz & Coats, 1-2].

decreases during the withdrawal of the gas (Example 3.1 for steam). An inventory estimation based on earth temperature and the responding pressure right after the injection or withdrawal may lead to erroneous conclusions.

Example 16.2. A salt cavity at 2150 ft depth has a volume of 4,050,000 ft^3. It contains 0.6-gravity gas. Geothermal temperature is 65°F; the surface rock is at 48°F.

(*a*) How much gas does it contain at 1100 psig (wellhead) at equalized temperature?
(*b*) With the well and reservoir at equalized temperature 65°F, 4 MMcf gas at 80°F

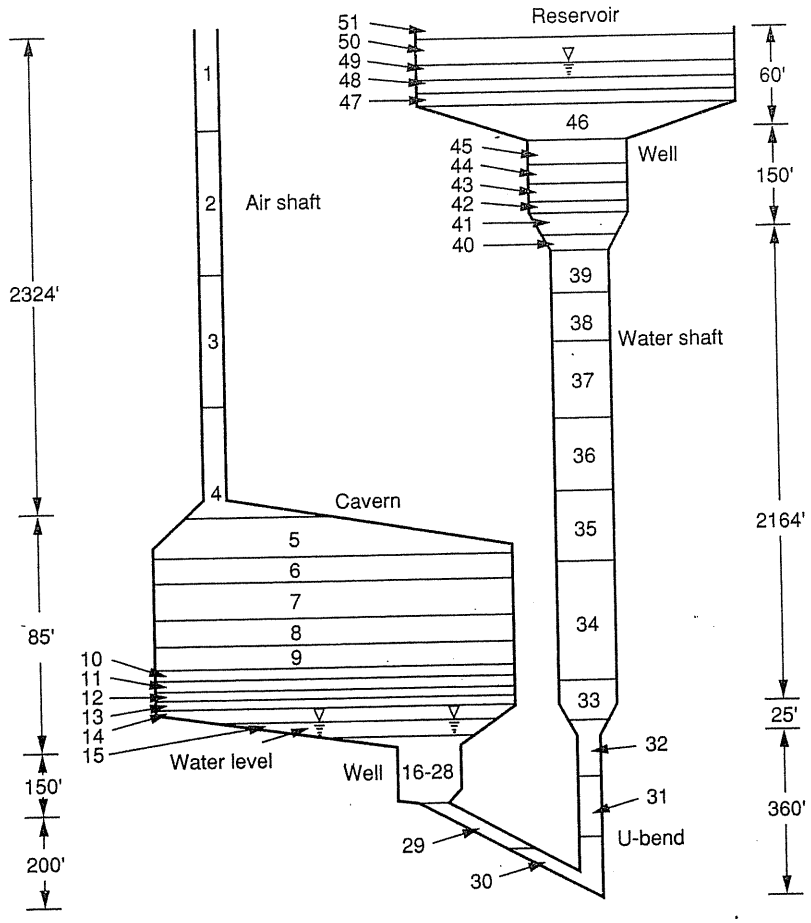

FIGURE 16-11
Model for water compensated storage in mined cavern [McMonagle and Rowe, 16-30].

is injected. What reservoir pressure rise would occur if the system returns to the original temperature?

Solution. (*a*) For $G = 0.6$, $T_c = 360°R$, and $P_c = 673$ psia, a trial-and-error procedure is needed to estimate the cavity pressure, using Eq. (6.4):

$$P(\text{cavity}) = P(\text{wellhead}) \exp\left(\frac{0.01877Gh}{T_a Z_a}\right)$$

The first guess of $Z_a = 0.841$ is the wellhead Z value at $T_r = T_a/T_c = 1.435$, with $T_a = (525 + 508)/2 = 516.5$ and $P_r = (1100 + 14.7)/673 = 1.6563$. The intermediate P(cavity) is 1178.6 psia, for which Z_a can be reevaluated as 0.837. After several iterations, P(cavity) converges to 1178.9 psia. Thus, the cavity gas quantity is

$$n(\text{original}) = \frac{PV}{ZRT} = \frac{(1178.9)(4{,}050{,}000)}{(0.84)(10.73)(525)}$$

$$= \underline{1.01 \times 10^6 \text{ lb mole}} \frac{379 \times 10^{-6} \text{ MMcf}}{\text{lb mol}}$$

$$= \underline{383 \text{ MMcf}}$$

(*b*) 4 MMcf is equivalent to

$$n(\text{injected}) = \frac{4 \times 10^6}{379} = 10.538 \times 10^3 \text{ lb mol}$$

Thus, the total gas in place is

$$n(\text{total}) = n(\text{original}) + n(\text{injected}) = 1.01 \times 10^6 + 10.538 \times 10^3$$

$$= 1.02054 \times 10^6 \text{ lb mol}$$

and the pressure at 65°F is

$$P = \frac{nZRT}{V} = \frac{(1.02054 \times 10^6)(0.84)(10.73)(65 + 460)}{4{,}050{,}000} = \underline{1192.37 \text{ psia}}$$

Example 16.3. The original gas ($G = 0.6$) at 600 psia, 65°F was adiabatically compressed by the injection gas to $\frac{3}{4}$ its original volume. Assuming there is an insulation membrane (no heat or mass transfer) between the injected and original gases, what are the resultant pressure and temperature?

Solution. The first law of thermodynamics:

$$Q = \Delta U + W = U_2 - U_1 + \int_1^2 PdV \tag{16.2}$$

shows that the PV work done on a gas will cause a rise of the internal energy U (temperature rise). U is converted to the measurable enthalpy $H(H = U + PV)$ by the following rearrangement:

$$U_2 - U_1 = (U_2 + P_2V_2) - (U_1 + P_1V_1) - P_2V_2 + P_1V_1$$

$$= H_2 - H_1 - P_2V_2 + P_1V_1 \tag{16.3}$$

Combining Eq. (16.3) and Eq. (16.2) for no heat loss ($Q = 0$):

$$0 = H_2 - H_1 - P_2V_2 + P_1V_1 + \int_1^2 PdV \tag{16.4}$$

The integration term can be approximated by $P_{avg}\Delta V$.

Since there is no mass transfer,

$$n(\text{original}) = \frac{P_1V_1}{Z_1RT_1} = \frac{P_2V_2}{Z_2RT_2}; \quad V_2 = \frac{3}{4}V_1 \tag{16.5}$$

Both Eq. (16.4) and Eq. (16.5) depend on P_2 and T_2, which can be obtained by trial and error. Both equations are satisfied at $\underline{P_2 = 897.6 \text{ psia}}$, $\underline{T_2 = 596°R\ (126°F)}$. Hence, the temperature rise during the compression is $(126 - 65) = 61°F$.

Alternatively, the use of Eqs. (6.27), (6.28), and (6.30) would result in the same answer.

16.8 STRATEGIC PETROLEUM RESERVE

When the embargo was placed on crude oil shipments to the United States and Europe from Middle East countries in the 1970s, the United States government set up the Strategic Petroleum Reserve Project through the Department of Energy (DOE). The objective was to have enough crude oil on hand to offset any future curtailments of crude supply needed for military and industry.

The plan was carried out using salt domes on the Gulf Coast well situated with regard to pipeline systems to carry crude oil to refineries. The project expanded the size of the salt cavities to 10 million bbl (1.59×10^6 m^3) and initiated refined methods of operation. For example, Sandia National Laboratory in New Mexico designed a computer simulation of leaching processes that established contract specifications beyond earlier codes available, such as the one developed by the Solution Mining Research Institute.

The size of the project was related to the economics of crude oil purchasing and to governmental decisions. The original target was one billion bbl (179×10^6 m^3); later it was reduced to 750 million bbl (119×10^6 m^3), and at this writing, it is down to some 500 million bbl (79.5×10^6 m^3).

DOE issued a design standard using the Sandia leaching program. The West Hackberry schedule shown in Fig. 16-12 [16-13] directs the formation of a 10 million bbl (1.59×10^6 m^3) storage cavity over 2000 ft (610 m) tall (5000–2600 ft depth, 1524–792 m) with a 120 to 60 ft (36.6–18.3 m) radius.

16.9 ABSENCE OF CONNATE WATER IN MICHIGAN GAS REEF RESERVOIRS

It was known for more than a decade that natural gas stored in Michigan gas reefs, like Belle River Mills (Fig. 16-13 [16-19,16-20]) and Ray, did not need dehydration upon withdrawal. Analysis of the withdrawn gas showed a water content of no more than 4 lb/MMcf (6.46 kg/10^5m^3). Equilibrium gas content from contact with reef brine would have been 13 to 17 lb/MMcf (21 to 28 kg/10^5m^3) for the five reefs. The reefs pierce the carbonate, salt, and anhydrite strata on the margin of the Silurian Sea.

Explanation for Absence of Connate Water

No definite explanation has been found for the absence of connate water in these reservoirs. Two possibilities are (1) connate water was absorbed by anhydrite; and (2) fresh connate water vaporized and diffused to the dense brine underlying the gas [1-91]. The porous zones of the reef had been flushed by fresh water, removing salt, according to Gill [16-19,16-20]; see Fig. 16-14. Later in geologic time heavy brine came into the basal Niagaran layers in contact with the reef. There was residual anhydrite in the cores of the reef examined by Gill.

STAGE	TIME DAYS	INJECTION DEPTH	PRODUCTION DEPTH	BLANKET DEPTH	OIL FILL RATE
S-C	175.	5000.	2900.	2650.	0.
R1	135.	2900.	4750.	2650.	0.
R21	66.	3750.	4700.	2700.	2000.
R22	113.	3750.	4700.		10000.
R3	95.	4400.	4800.		50000.

TOTAL INJECTION RATE = 150000.BPD

INSOLUBLES CONTENT = 5. PERCENT

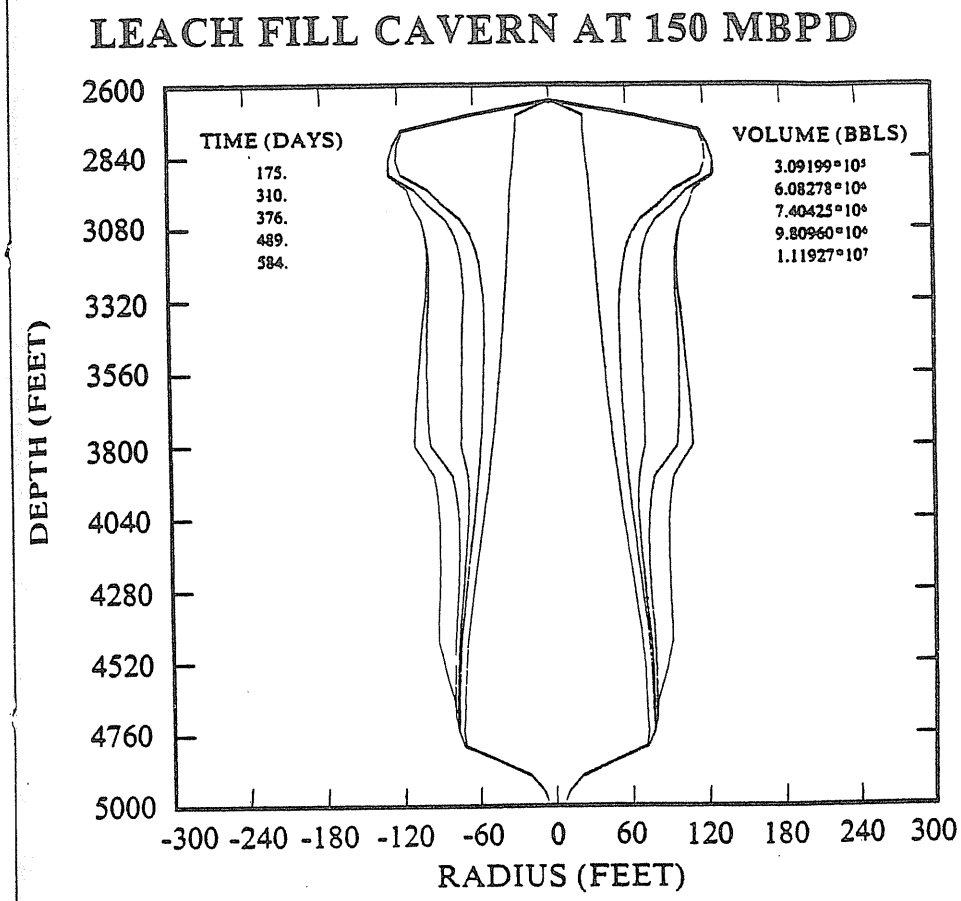

FIGURE 16-12
West Hackberry leaching schedule using Sandia program.

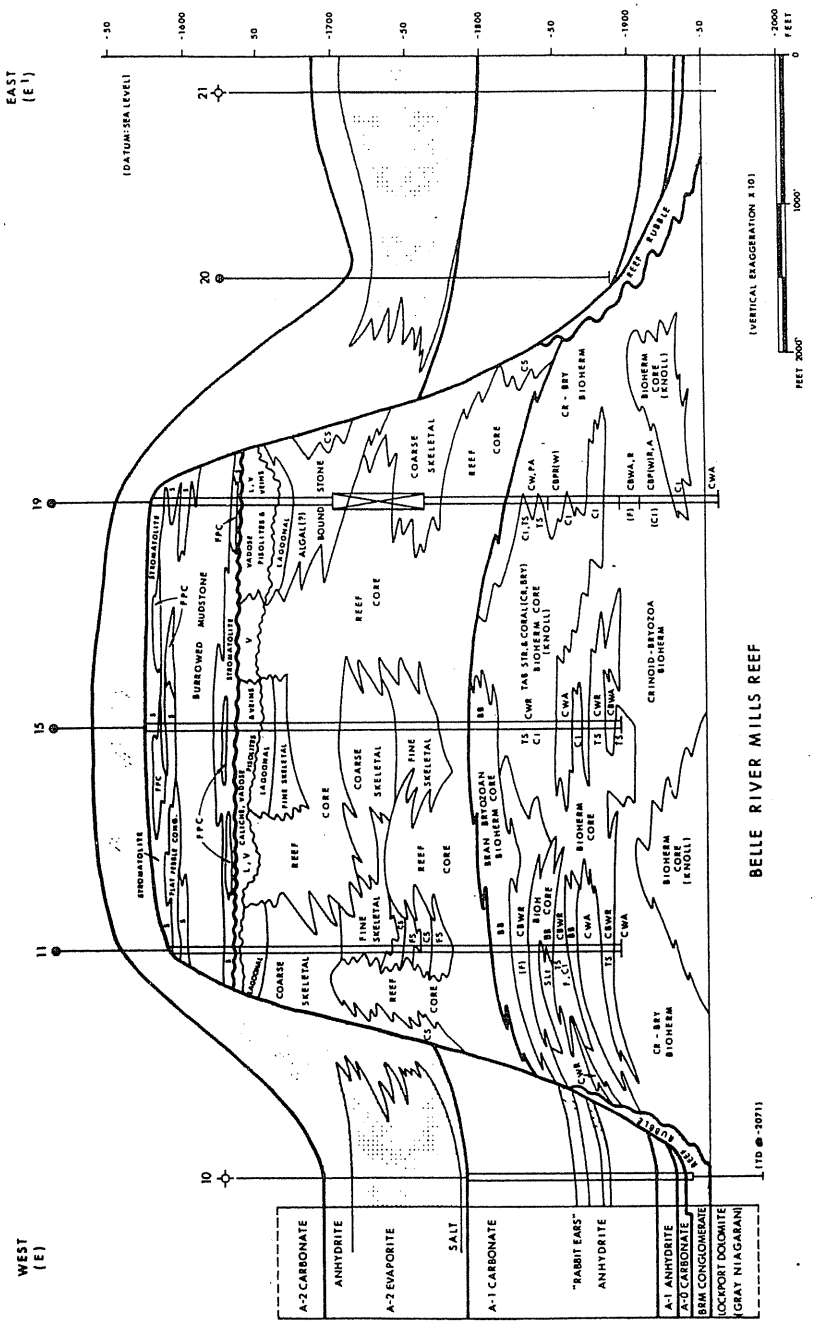

FIGURE 16-13
Section of Michigan reef [after Gill, 16-19, 16-20, courtesy AAPG].

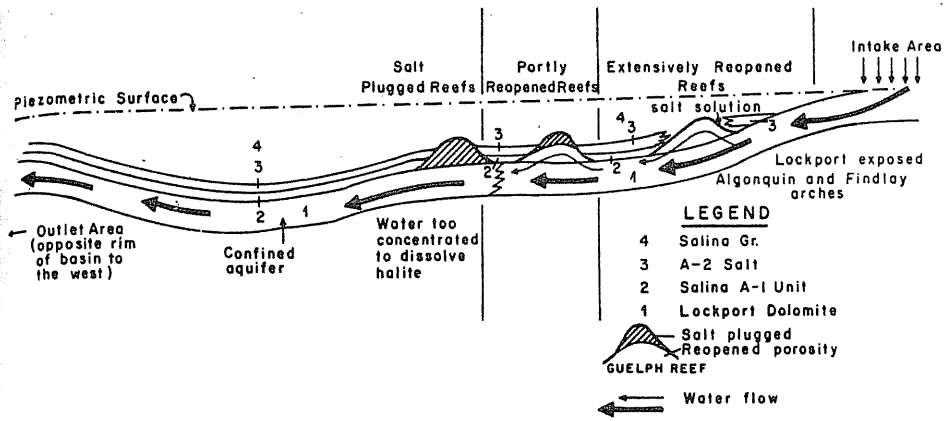

FIGURE 16-14
Schematic hydrodynamic model of fresh water flushing and reef porosity reopening during late Silurian to early and middle Devonian [after Gill, 16-19, 16-20, courtesy AAPG].

The combination of geology, geochemistry, and engineering performance leaves gaps in knowledge but suggests that fresh connate water was absorbed by anhydrite, forming gypsum; or, that connate water was vaporized with the full vapor pressure of pure water, diffused to the base of the reef, and was absorbed in the dense brine that invaded the lower Niagaran layer; see Fig. 16-15 [1-91]. A specific geologic history and sequence of events including the gas accumulation is necessary for either of these scenarios to have happened.

It appears that the northern Michigan reefs as well as southeastern storage reservoirs have little connate water, while midwestern reefs in Calhoun County encounter a water brine situation with full water drive into the pore space [1-91]. This example is presented to emphasize that in the future new concepts

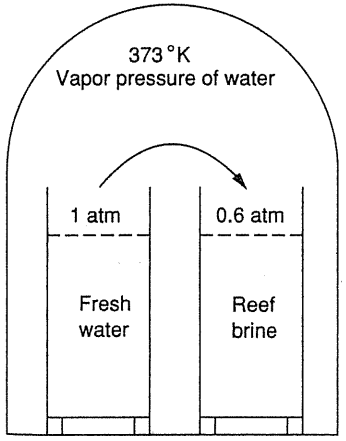

FIGURE 16-15
Water vapor transfer by diffusion due to higher vapor pressure of fresh water relative to reef brine [Katz & Lundy, 1-91, courtesy AAPG].

may be derived from synergistic effects of all the information which may add to our understanding of the earth sciences.

16.10 MINED CAVITIES FOR LPG LIQUIDS

In addition to aquifers, old oil and gas reservoirs, and salt cavities, mined space in rock can be used for storage (Fig. 16-16). New mined space is preferred, although abandoned mined space can also be used [16-8,16-11]. Only a few successful cases have been reported of using abandoned mined spaces, which usually have leaks and need a complete sealing (grouting) procedure.

Allen [16-4] reviewed the existing experiences of underground hydrocarbon storage and discussed mined storage activities. Mined cavities, after a core test, are designed to be drilled with large diameter shafts for access and ventilation to the mining level. The rock is excavated by drilling and blasting and is then hoisted to the surface for disposal or other uses. The walls of a mined cavern should be grouted carefully before it is used for storage. Hard rock caverns with rooms and pillars are often used for liquid storage.

Bedrock or preglacial layers are required for mined caverns. To minimize the cost, the depth should be as shallow as possible. However, there should be sufficient structural strength to avoid subsidence, and hydraulic pressures at the chosen depth must exceed the storage pressure. At 60°F (15.6°C), ethane has a vapor pressure of some 500 psi (3.45 MPa), and propane has a vapor pressure of 100 psi (689 kPa). Assuming the water table is 30 ft (9 m) from the surface and fresh water is in the rocks, the minimum depth for hydraulic balance is 1250 ft (381 m) for ethane and 260 ft (79 m) for propane. Figure 16-17 [16-21] illustrates mined storage for propane.

The use of abandoned mines usually yields small storage space. If one wants a large-capacity storage, a new mined space should be used.

As is the case for salt cavities, there are compensated and uncompensated mined cavern systems (Fig. 16-18 [16-4]). For conventional mined caverns, high construction costs normally dictate the compensated technique. Compensated caverns are usually small hard rock structures (not sensitive to water degradation) and require a surface reservoir for high-density fluid (brine) of the same volume as the cavern. Uncompensated systems are used to eliminate the possible adverse environmental impact of the surface reservoir and are usually used for compressed air or natural gas storage.

Cryogenic Gas Storage

Peak-shaving LNG terminals store liquid methane at 1 atm (101.3 kPa) and −250°F (−157°C) in insulated tanks above ground. Trial usage of frozen earth bottoms as storage tanks was not encouraging for general usage. Witherspoon, Lindholm, and Janelid [16-46] developed the economics for cryogenic gas storage caverns operating at 14.7 psia (101.3 kPa), −259°F (−162°C) and at 600 psia

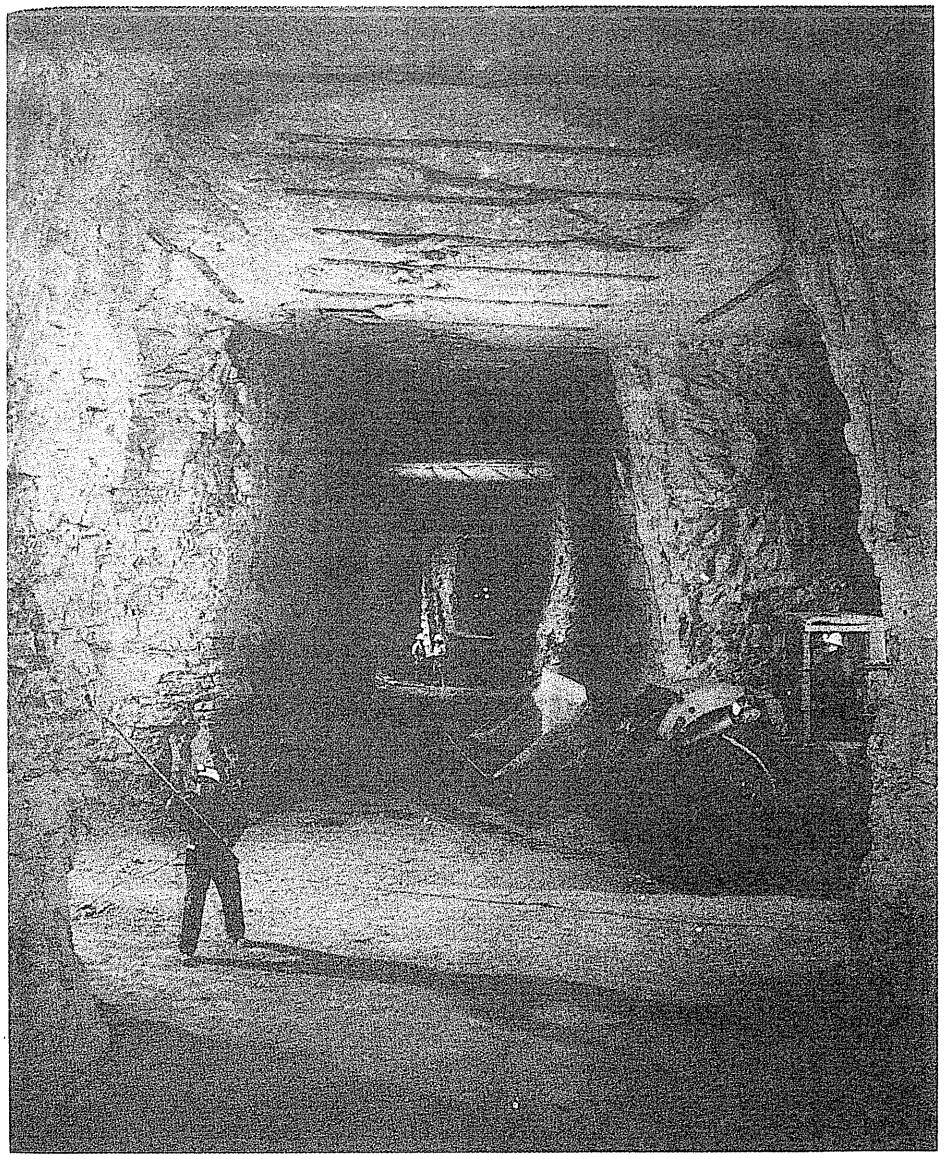

FIGURE 16-16
A granite cavern in Pennsylvania [courtesy Fenix and Scisson Inc.].

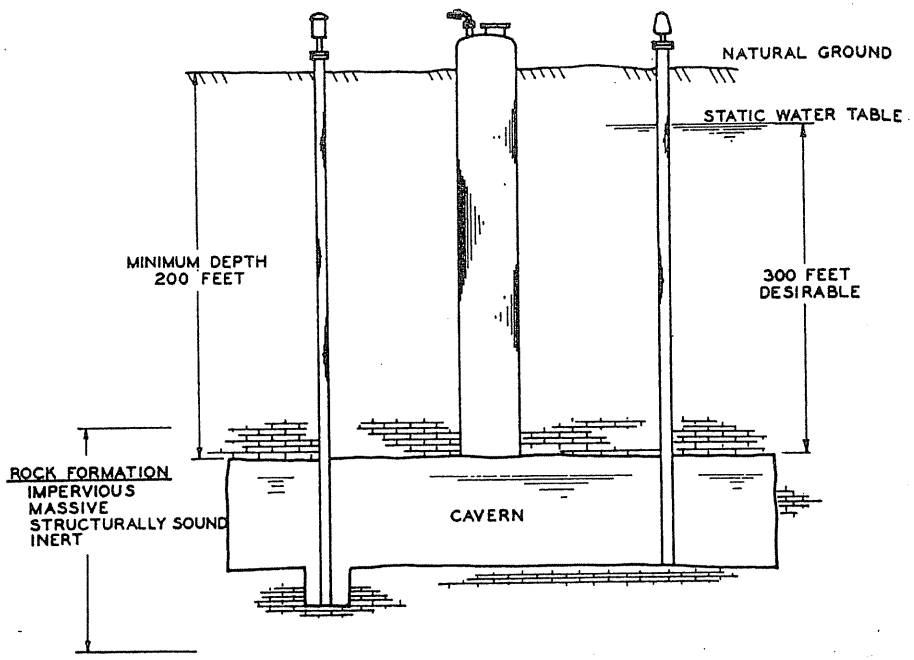

FIGURE 16-17
Illustration of mined cavern storage [Scisson, 16-39, courtesy NGPA (Now GPA)].

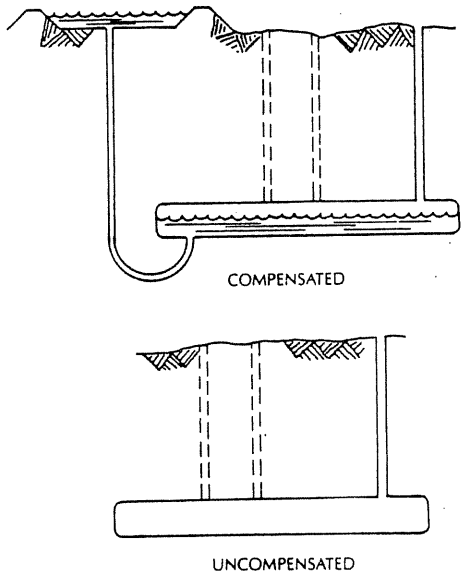

FIGURE 16-18
Compensated and uncompensated mined CAES cavern [Allen, 16-4, courtesy Fenix and Scisson Inc.].

(4.14 MPa), −120°F (−84°C). The volume increase factors are 590 and 320 Scf/cf (590 and 320 m^3/m^3) respectively.

The storage chamber pressure should be 90 percent of the hydrostatic pressure in the surrounding rock. The chamber depth should not be less than 1500 ft (457 m) if the pressure is to be held at 600 psia (4.14 MPa). For low pressures, smaller depths could be utilized, but in view of the technical advantages connected with deeper locations, only cryogenic storage chambers with depths of more than 1500 ft (457 m) were considered [16-46].

HOME PROBLEMS

16-1. A brine cavity is 4000 ft deep in a salt dome. What is the minimum pumping pressure to displace brine when injecting propane?

16-2. It is desired to store 1 Bcf of 0.6-gravity gas in a salt cavity at a depth of 3600 ft (130°F). Knowing that 6.2 ft^3 of water will dissolve 1 ft^3 salt, how long will it take to create the cavity using a 200-gal/min centrifugal pump? It was agreed to use a top pressure of 0.7 psi/ft of depth.

REFERENCES

16-1. Albrecht, H., and M. Langer, "The Theoretical Behavior of Rock Salt and Related Stability Problems of Storage Caverns," *Proc. 3rd Symp. Int. Soc., Rock Mechanics*, Denver, Colo., p. 967 (1974).

16-2. Allan, M. H., "Natural Gas Storage in Caverns in Saskatchewan," Rau, J. L. (Editor), *Second Symposium on Salt,* 2 volumes, Northern Ohio Geological Society, Cleveland, Ohio (1966) p. 412.

16-3. Allen, K., "Eminence-Dome-Natural Gas Storage in Salt Comes of Age," SPE Preprint 3433 (1971).

16-4. Allen, K., "Underground Storage: A Compressed Air Energy Storage (CAES) Prerequisite," Fenix and Scisson Inc., Tulsa, Oklahoma (1984).

16-5. Aufricht, W. R., and K. C. Howard, "Salt Characteristics as They Affect Storage of Hydrocarbons," *J. Pet. Tech.*, Vol. 8, 733, Aug. (1961).

16-6. Barns, R. B., "The Plasticity of Rock Salt and Its Dependence upon Water," *Physical Rev.*, Vol. 44, Dec. (1933).

16-7. Bays, C. A., "Use of Salt Solution Cavities for Underground Storage," Bersticker, A. C. (Editor), *Symposium on Salt,* Northern Ohio Geological Society, Inc., Cleveland, Ohio (1963) p. 564.

16-8. Bleakley, W. B., "Leyden Storage Project Passes Severe Winter Test," *Oil and Gas J.*, Vol. 61, 38, Sept. 23 (1963).

16-9. Bradshaw, R. L., T. F. Lomenick, W. C. McClain, and F. M. Empson, "Model and Underground Studies of the Influence of Stress, Temperature, and Radiation on Flow and Stability in Rock Salt," *Proc. 1st Cong. Int. Soc. Rock Mechanics*, Lisbon (1966).

16-10. Branyan, S. G., "Operation and Maintenance of Underground Storage," Bersticker, A. C. (Editor), *Symposium on Salt,* Northern Ohio Geological Society, Inc., Cleveland, Ohio (1963) p. 609.

16-11. Brown, L. W., "Abandoned Coal Mine Stores Gas for Colorado Peak-Day Demands," *Pipeline Industry*, September (1978).

16-12. CER Corporation *Survey of Salt Cavern Storage of Natural Gas in U.S. and Canada,* (1980).

16-13. Chao, R., "Long Term Creep Closure of Solution Cavity System," *4th Salt Symposium*, Vol. 2, p. 119, Northern Ohio Geological Society (1974).

16-14. Christensen, D. M., "The Determination of the In-Situ Elastic Properties of Rock Salt with a Three-Dimensional Velocity Log," Rau, J. L. (Editor), *Second Symposium on Salt*, 2 volumes, Northern Ohio Geological Society, Cleveland, Ohio (1966) p. 104.
16-15. Crow, R. D., "Salt Cavern Storage of LPG at Lowell, Michigan, and Hutchinson, Kansas," Bersticker, A. C. (Editor), *Symposium on Salt*, Northern Ohio Geological Society, Inc., Cleveland, Ohio (1963) p. 616.
16-16. Dreyer, W. E., "Results of Recent Studies on the Stability of Crude Oil and Gas Storage in Salt Caverns," *4th Salt Symposium*, Vol. 2, p. 65, Northern Ohio Geological Society (1974).
16-17. Dubois, D., and V. Maury, "Underground Storage of Hydrocarbons at Manosque, France," *4th Salt Symposium*, Vol. 2, p. 313, Northern Ohio Geological Society (1974).
16-18. Duchassin, M., M. Dussaud, and B. Hugout, "Natural Gas Underground Storage in Salt Cavities," *Pipeline Industry*, p. 25, June 7 (1984).
16-19. Gill, D., "The Belle River Mills Gas Field; Productive Niagaran Reefs Encased by Sabkha Deposits, Michigan Basin," Michigan Basin Geol. Soc. Spec., paper 2 (1977).
16-20. Gill, D., "Stratigraphy, Facies, Evolution, and Diagenesis of Productive Niagaran Guelph Reefs and Cayugan Sabkha Deposits, The Belle River Mills Gas Field, Michigan Basin," Ph.D. Dissertation, The University of Michigan (1973).
16-21. Gnirk, P., and R. Johnson, "The Deformation Behavior of a Circular Mine Shaft Situated in a Viscoelastic Medium under Hydrostatic Stress," *6th Symp. Rock Mechanics*, University of Missouri, Rolla p. 231 (1964).
16-22. Goldman, M. I., "Deformation, Metamorphism, and Mineralization in Gypsum-Anhydrite Cap Rock, Sulphur Salt Dome, Louisiana," Geol. Soc. America, Mem. 50 (1952).
16-23. Haun, R. R., "Worldwide LP-gas Outlook," *Proceedings 62nd GPA Annual Meeting*, 118–123 (1983).
16-24. Istvan, J., PB-KBB Inc., private communication (1987).
16-25. Kaufmann, D. W., *Sodium Chloride*, American Chemical Society Monograph Series, No. 145, Reinhold Publishing Corp., New York (1960).
16-26. King, M. S., and K. Z. Acar, "Creep Properties of Saskatchewan Potash as a Function of Changes in Temperature and Stresses," *3rd Symp. Salt*, Northern Ohio Geological Society, Vol. 2, p. 226 (1968).
16-27. Landes, K. K., "Origin of Salt Deposits," Bersticker, A. C. (Editor), *Symposium on Salt*, Northern Ohio Geological Society, Inc., Cleveland, Ohio (1963) p. 3.
16-28. Le Comte, P., "Creep in Rock Salt," *J. Geology*, Vol. 73, No. 3, 69 (1965).
16-29. Matheny, F., "Underground Storage of Liquefied Petroleum Gases," *Proceedings, NGPA*, Vol. 15 (1951).
16-30. McMonagle, C. A., and D. S. Rowe, *Analytical Modeling of a Hydraulically Compensated Compressed Air Storage System*, Pacific Northwest Energy Laboratory, Battelle, PN L3374 (1982).
16-31. Molinard, J. E., Gaz De France, private communication (1987).
16-32. Myers, A. J., "Sonar Measurements of Brine Cavity Shapes," Bersticker, A. C. (Editor), *Symposium on Salt*, Northern Ohio Geological Society, Inc., Cleveland, Ohio (1963) p. 546.
16-33. Nair, K., and D. N. Deere, "Creep Behavior of Salt in Triaxial Extension Test," *3rd Symp. Salt*, Northern Ohio Geol. Soc., Vol. 2, p. 208 (1968).
16-34. Nair, K., R. S. Sandhu, and E. L. Wilson, "Time Dependent Analysis of Underground Cavities under Arbitrary Initial Stress Field," *10th Symp. Rock Mechanics*, University of Texas, Austin (1968).
16-35. Obert, L., "Deformation Behavior of Model Pillars Made From Salt, Trona, and Potash Ore," *Proc. 6th Symp. Rock Mechanics*, University of Missouri, Rolla (1964).
16-36. Pattinson, R. L., "Method of Storing Gases or Liquids," Reissue 24,318, U.S. Patent; Original patent 2,590,066, March 18 (1952).
16-37. *Pipeline Industry*, "Transco Pioneers Salt Cavern Storage of High Pressure Gas," p. 59, March (1972).
16-38. Querio, C. W., and R. R. Hultin, "Ethylene Storage Near Midland, Michigan," Bersticker, A. C. (Editor), *Symposium on Salt*, Northern Ohio Geological Society, Inc., Cleveland, Ohio (1963) p. 579.

16-39. Scisson, S. E., "Planning for Mined Underground Storage," *Proceeding 39th Annual NGPA Convention*, 36–38 (1960).
16-40. Section on geology and geochemistry including paper on salt deposits at Heilbronn, Germany, and Bresse, Valence, France, Rau, J. L. (Editor), *Second Symposium on Salt*, 2 volumes, Northern Ohio Geological Society, Cleveland, Ohio (1966) p. 104.
16-41. Serata, S., "Continuum Theory and Model of Rock Salt Structures," 2nd Symp. Salt, Northern Ohio Geological Society, Vol. 2, p. 1 (1965).
16-42. Sevenker, L., "The Development of Energy—Strategic Petroleum Reserve," Presented to Solution Mining Research Institute, Mexico City, Mexico, Jan. 17–18 (1979).
16-43. Thoms, R. L., "Long-term Stability of Compressed Air Energy Storage Cavities in Salt Domes," AIME Preprint 7925 (1979).
16-44. Van Fossan, N. E., "Proving the Mechanical Integrity of Solution Mined Caverns," *Proceedings 61st GPA Annual Convention*, 206–220 (1982).
16-45. Vance, T. B., "Southeastern Michigan Gas Company's High Pressure Gas Holder in a Salt Stratum, Bersticker, A. C. (Editor), *Symposium on Salt*, Northern Ohio Geological Society, Inc., Cleveland, Ohio (1963) p. 597.
16-46. Witherspoon, P. A., U. Lindbolm, and I. Janelid, "Gas Storage in Mined Caverns," *Proceedings, AGA Gas Transmission Conference*, T155 (1974).

CHAPTER 17

MISCELLANEOUS TOPICS

17.1 COMPRESSED AIR ENERGY STORAGE (CAES) FOR ELECTRIC POWER PEAKING SERVICE

Just as the AGA underground storage committee sponsors gas storage projects, the Electric Power Research Institute (EPRI) has assumed responsibility for gathering information and making design proposals for maintaining continuity of electrical power on a second-to-second basis. Also, electric power personnel find underground storage technology a new discipline to encompass.

Just as the natural gas industry has a peak supply problem in cold weather, the electric power industry has a daily load fluctuation, in good part due to the summer air conditioning load. Figure 17-1 indicates a typical weekly demand. Currently, electrical systems have gas turbine generators to provide peak power. A limited number of pumped hydro units use excess or cheap power at night to lift water to a substantial level; during the daytime the water reverses flow and generates peak power, obtaining some 70 percent efficiency. The saving in power cost underwrites the cost of the hydro facility.

The components of a gas turbine/compressed air storage generating plant are shown in Fig. 17-2. With gas turbine–powered generators, two thirds of the power generated is required to compress the turbine air. For CAES, the turbine air is compressed at night with low-cost power and withdrawn to support combustion for daytime peak power generation. Again, the saving in low-cost power for two thirds of the peak load should underwrite the cost of the air storage facilities. In addition, the air compression and power generation units can be smaller in size for the same load. Figure 17-3 shows one possible weekly schedule for air storage and withdrawal.

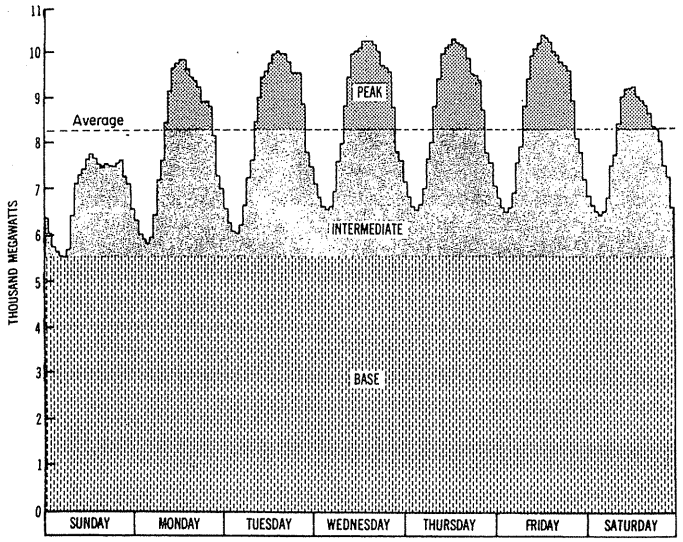

FIGURE 17-1
Typical weekly load curve for electric utility [Lady & Katz, 17-60, courtesy SPE-AIME].

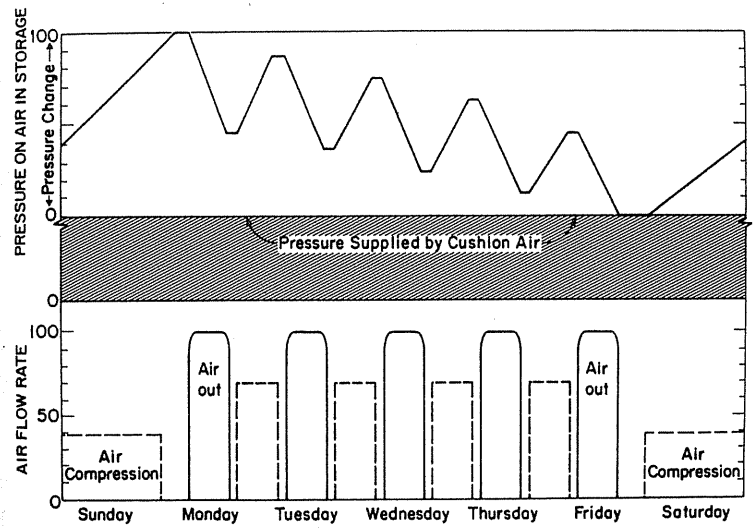

FIGURE 17-2
Schematic flowsheet of a compressed air storage system [Lady & Katz, 17-60, courtesy SPE-AIME].

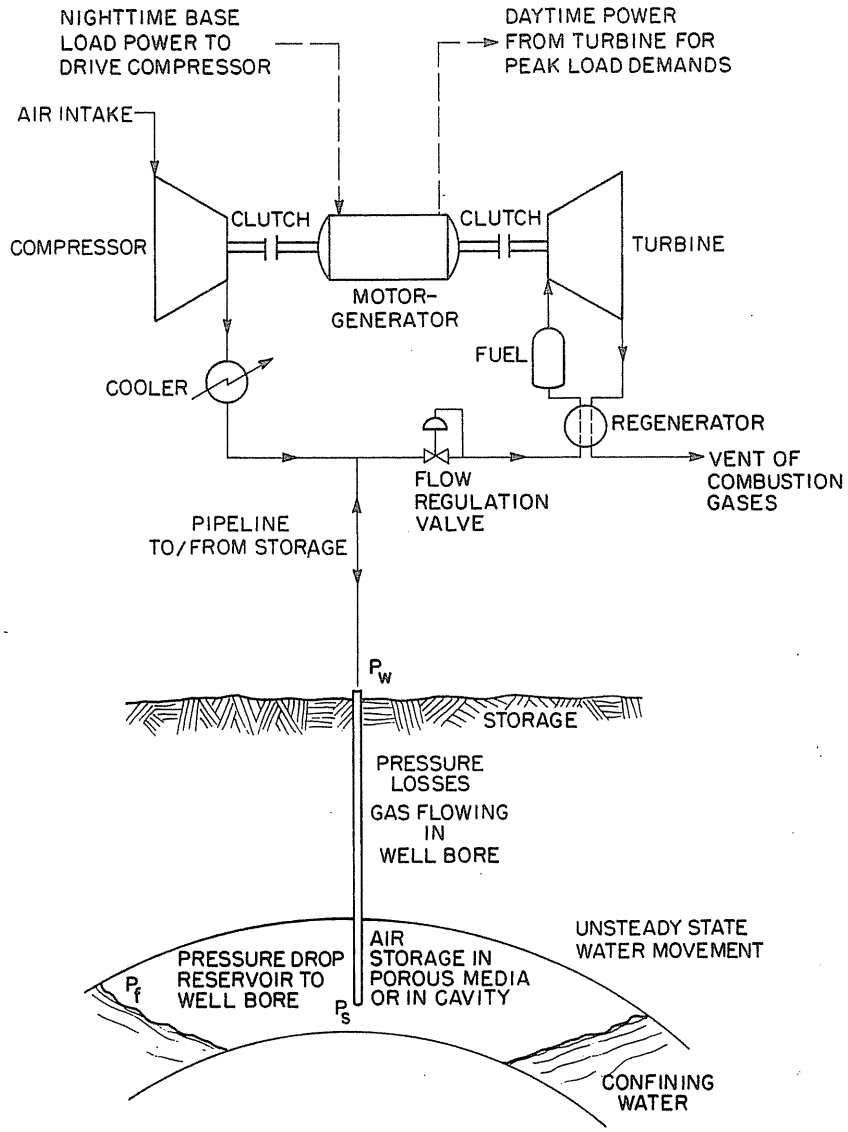

FIGURE 17-3
Air flow rates and storage pressure changes during the weekly cycle [Lady & Katz, 17-60, courtesy SPE-AIME].

TABLE 17.1
Information about Huntorf, Germany [17-67]

Where: Huntorf in Bremen/Oldenburg area	
Rated electrical capacity: 290 megawatt	
Compression power: 58 megawatt	Air flow: 900 lb/s, 42 MMcf/hr
Storage reservoir: Two salt cavities	Power hours/day: 2
Depth: Top 1800 ft, bottom 2400 ft	Compression hours/day: 8
Volume: Two-5,000,000-ft^3 cavities	Power turbine inlet pressure: 650 psi
Injection temperature of air: 120°F	Temperature after firing: 1000°F
Air pressure cycle in cavity: Maximum range 650–1000 psi; 2-hr normal day ΔP 140 psi	Reheat to 1500°F for low-pressure turbine
For power generation	Exhaust at 700°F

Huntorf Plant, Germany

An early compressed air peak load unit operates in Huntorf, West Germany, using air storage in salt cavities. Some pertinent information is given in Table 17.1. This system was commissioned in 1978. Although it is the first, the Huntorf turbine-generator is rated at 290 MW, a size believed to be adequate for even the larger utility systems. Multiple units of this size are preferred for 600 MW peaking capacity, rather than large single units. Because of the possible startup issues, EPRI is advocating mini-CAES, 25- or 50-MW units.

Success in Aquifer Natural Gas Storage—A Model [1-1,1-2] to Stimulate Studies for CAES

Over one trillion standard cubic feet of natural gas is stored in aquifers in the United States and Canada. This successful experience with the use of aquifers for natural gas storage pointed to their potential use for CAES by the electric utilities as part of handling peak electrical loads. A large commitment has been made to studies and research of CAES for electric utility operations.

In 1976, Katz and Lady published their research in a book on compressed air storage [17-50]. Since 1975, the Battelle-Pacific Northwest Laboratories have carried on an extensive research program, annual reports and interim studies have been made available and presented at DOE meetings [17-7,17-89], and a consortium in Indiana has made a full design study of nine volumes, supported by EPRI [17-18].

The DOE Pacific Northwest Laboratories planned a pilot test at Pittsfield, Illinois [17-95]. Before going on to the Pittsfield study, a presentation of the natural gas experiences is in order.

Criteria for Aquifer Storage

One does not simply pick an aquifer reservoir; one searches for it and examines its qualifications step by step. The schematic cross section of an aquifer storage

reservoir in Fig. 1-5 helps to illustrate the criteria for storing air or gas in a blanket water-bearing zone.

The *first* prerequisite for an aquifer storage reservoir is the existence of a suitable geostructure—often like an inverted saucer. The total air storage volume is obtained from the porosity of the porous media and the acre-feet of rock between the caprock and the minimum water level, somewhat above the spill point. The mean pressure of air should be at the initial discovery aquifer pressure.

The *second* criterion is a continuous impermeable caprock such as a shale or low-permeability carbonate. Its ability to confine air depends on the permeability being so low that the air pressure in the reservoir will not displace water from the pores of the caprock. The threshold displacement pressure is measured on caprock cores [1-38].

The *third* criterion is sufficient depth of the structure. Depth is normally related to the hydraulic pressure of the water. A hydraulic column of water to the reservoir depth represents the mean operating pressure of the air bubble. A depth of 1000 ft (305 m) represents an aquifer pressure of 433 psi (2.99 MPa) and for natural gas is considered the minimum desirable depth. For CAES, the depth should exceed 600–800 ft (183–244 m) and have the full hydraulic column pressure. The pressure level influences both the air content of a given pore volume of the aquifer and the flow rate of air from wells.

The *fourth* criterion is the permeability of the storage zone, not only in the reservoir containing air but also for the aquifer surrounding the structure. Air under pressure displaces water from the structure to create the storage reservoir. High permeability of the porous medium is needed (> 500 md desired) to give a reasonable time for growth of the reservoir. Another reason for desiring high permeability is that the air flow rate from injection/withdrawal (I/W) wells is proportional to the permeability at a given pressure level.

A *fifth* criterion is such items as the porosity and capillary pressure, which indicate what fraction of the pore space contains air and how much water is retained in the interstices of the porous medium.

A *sixth* criterion is the chemical composition of the rock; will it react with oxygen and remove it from the air, as found at Pittsfield?

A *seventh* criterion is the environment of the surface. One project known to the authors for developing an aquifer on farm land not far from a city was stopped by unexpected development of a shopping center there.

Before going through the procedure for discovering, developing, and using an aquifer for air storage, the properties of rocks as described in Chapter 2 should be reviewed.

Choice of Reservoir

Aquifers are unique in that the average storage pressure of air must be close to the discovery pressure if the size of the gas bubble is to stabilize. To increase the size of the air bubble, pressures above discovery are used; to allow water to return and shrink the bubble, air pressures below the discovery are required. Normally,

a reservoir at a depth of 2500 feet (762 m) would be near 1100 psi (2500 × 0.443 psi/ft), or 7.58 MPa. The amount of water movement during a weekly cycle is small, and the above statement applies during months of development.

A majority of natural gas storage reservoirs are depleted gas or oil reservoirs. They have a proven caprock, and their size should have been determined in the production of hydrocarbons. Although there has been a reluctance to consider these depleted reservoirs for CAES until recently, it will be assumed here that a choice between aquifers or depleted gas reservoir is possible.

Reservoirs with little or no pore volume change with pressure presumably come from depleted gas reservoirs. In many areas there are choices of size and rock properties, and many such reservoirs have been converted to gas storage. The pressure level can be chosen, with a volumetric capacity proportional to the chosen pressure. Added precautions are needed to make sure no premature combustion takes place, as discussed elsewhere. In establishing the best reservoir available for a given area, the problems for air storage are similar to those for gas storage.

The reservoir rock in situ permeability is a prime criterion for several reasons. The number of wells needed for a given CAES rating is essentially inversely proportional to the permeability and hence exerts a large influence on cost.

Feasibility Design Example to Give Understanding of Functioning of CAES Plant

The design problem given in references [17-50,17-60] is presented here. Belle River Mills is a fixed volume depleted gas reservoir used for air storage. Here the reservoir pressure is little disturbed in a weekly cycle. Design construction companies would have little difficulty in preparing for construction from such information.

17.2 DESIGN OF A STORAGE FACILITY TO MATCH POWER GENERATION NEEDS

General background has been given on the overall use of compressed air storage, the nature of the earth as it applies to storing fluids, equations governing flow and compression, and the functioning of the compression-generation plant. Next the design of an underground storage facility will be used to illustrate a suggested design process. This design will use a fixed volume storage reservoir and will achieve 600 MW output and 40 atm air delivery pressure.

The Design Process

Figure 17-4 shows schematically an underground storage system. It is composed of the air compression plant, the field lines between compression and wellheads, the wells, and the storage reservoir. This study is concerned with air leaving a

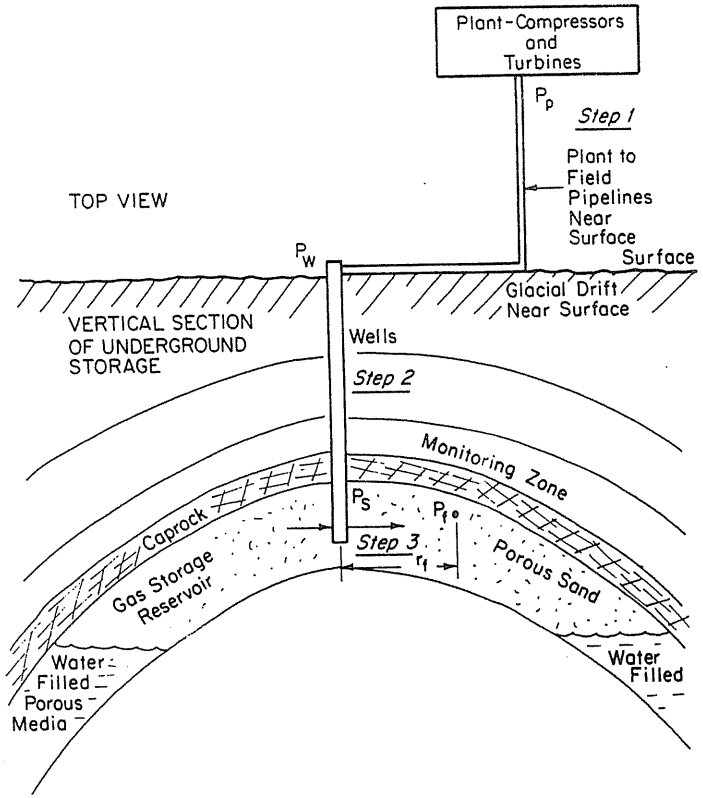

FIGURE 17-4
Components of underground air storage flow system with nomenclature [Katz & Lady, 17-50].

compression plant at the generation stations at pressure P_p, flowing through field lines to well heads at P_w, and flowing down the wells into the storage container. Shortly after this injection, the field operates in production mode, with flow from the reservoir to the plant. The size of the field lines, the diameter and number of wells, and the nature of the storage container are considered to obtain a balanced design. From the design quantities, the cost of the project can be estimated.

The design involves first the location of the structure and the determination of its size and storage content. The hourly and weekly air requirements and the specified air injection rates give the top storage quantity needed for a weekly cycle. From this top storage quantity, the pressure range of a weekly operating cycle is determined by the pressure level and quantity of pore space in the underground reservoir.

Design involves determining the sizes of the conduits to carry the gas from the generation station to the wells, as well as the number and diameter of the wells to be drilled. These determinations depend upon the pressure drop required

to convey the desired quantity of air to and from the storage reservoir, the cost of the facilities, and the comparative cost of compression.

Feasibility and Economic Questions

The designed facility's physical ability to serve the peak load must be examined. Is the pressure range for the reservoir within the limits of the reservoir under study? Is the reservoir permeability high enough to give individual well flows high enough that the well spacing is reasonable and the number low enough to be economical? For aquifer reservoirs, the ability of the caprock to contain the air and the time of development are important items. Will the reservoir remain stable over a period of time? What type of temperatures can be used in the reservoir?

The primary objective of feasibility and economic study is to discern the construction cost of the storage facility and the compression pressure level for storing the air compared to the delivery pressure of the returned air. Considerations include choices in size of surface lines, size of well casings, and number of wells to serve the plant. The total reservoir storage volume and the formation permeability are the prime parameters controlling the outcome of the design.

Design of Belle River Mills Reservoir

Belle River Mills will be taken as the fixed volume reservoir to be used for a 600-MW, 40-atm turbine plant 50 hr/week, 10 hr/day. The injection rate is fixed at 5/7 of the production rate, and injection proceeds 10 hours per night Monday through Thursday and 30 hours on the weekend. From Table 17.2, the hourly air production rate is

$$\text{Air production rate} = 2132\frac{\text{lb}}{\text{s}} \times 3600\frac{\text{s}}{\text{hr}} \times \frac{1}{29}\frac{\text{lb mol}}{\text{lb}} \times 379\frac{\text{ft}^3}{\text{lb mol}}$$

$$= 1.003 \times 10^8 \text{ ft}^3/\text{hr} = 100.3 \text{ MMcf/hr}$$

In 50 hours, the weekly production is 5015 MMcf (142×10^6 m^3). The air injection rate is $5/7 \times 100.3$ MMcf/hr = 71.6 MMcf/hr (2.03×10^6 m^3/hr). With 70 hours of injection, the weekly quantity stored matches the production.

The Belle River Mills reservoir is used for gas storage, yielding much information about its performance. The Belle River Mills discovery conditions and natural gas storage facts are given in reference [17-50]. Table 17.3 sets forth pertinent information for the air storage design.

The design calculations are carried out in steps:

1. Pressure drop in field lines that bring air to the generation plant
2. Pressure change in wellbore for proposed flow rates and size of wells
3. Pressure drop from reservoir to bottom of well for selected number of wells
4. The pressure rise in the reservoir from Friday P.M. until Monday A.M. when the total stored air is in the reservoir

TABLE 17.2
Design guidelines [Lady & Katz, 17-60]

1. Development in increments of 150 MW.
2. Turbine inlet pressures to be held constant 10 or 40 atmospheres.
3. Operating cycles use air 6–10 hours for 5 weekdays, compress air at night at no more than 5/7 of the rate it is used in daytime, rest on weekends.
4. Air requirements, in pounds per second, are as follows:

Plant size	10 atm	40 atm
300 MW	1432	1066
600 MW	2864	2132

5. Compression energy requirement for various final pressures are:

Final pressure, atm	kW · hr/lb
10	0.0412
20	0.0553
30	0.0659
40	0.0727
50	0.0790
60	0.0843

6. Cost of energy to be applied for compression is \$8.0/kW · hr.
7. The maximum allowable temperature for air leaving the compressor is 650°F.

TABLE 17.3
Pertinent data for Belle River Mills serving a 600-MW, 40-atm plant [Katz & Lady, 17-50]

The generation plant
- Peak power 10 hr per day, 5 days per week: 600 MW
- Pressure of delivered air: 40 atm, 599 psia
- Air rate: 100.3 MMcf delivered per hour
- Reinjection rate: 71.6 MMcf/hr, 10 hr, Monday–Thursday, rest on weekend
- Maximum working storage volume: 2151 MMcf (by Monday morning)

Belle River Mills reservoir
- Reservoir volume: 556 × 10^6 ft^3 space
- Depth of wells: 2150 ft
- Initial temperature: 60°F
- Suggested operating temperature: 150°F
- Acres, on crest: 400
- Total area: 1400 acres

5. Items 3, 2, and 1 in this order for gas injection at the maximum reservoir pressure
6. Review of pressure drops at intermediate time conditions like the injection period at minimum storage content
7. The construction and acquisition costs of the storage system

For those items that involve frictional pressure drop, a balance will be made between the cost of the extra facilities and the cost of the extra compression to overcome friction.

Process design is somewhat different for a fixed volume reservoir than for an aquifer. The Belle River Mills reservoir has a fixed volume of 556 million ft^3 (15.7 × 10^6 m^3) of pore space. The range of weekly fluctuation in stored air is the quantity stored during the weekend, or 30 hr × 71.6 MMcf = 2151 MMcf (60.91 × 10^6 m^3). This is equal to the air requirement minus the air injected during the week (50 × 100.3 − 40 × 71.6).

The size of the underground storage reservoir and the weekly fluctuation set the range of pressure in the reservoir during the week. It is assumed that air may be stored at 150°F (66°C) in the reservoir, and this value is used for calculations. The reservoir volume of 556 million ft^3 (15.7 m^3) of space will require a certain pressure rise (ΔP) from Friday evening to Monday morning, which is calculated as follows, using the ideal gas law:

$$2151 \text{ MMcf} \times \frac{14.7}{\Delta P} \times \frac{610}{520} = 556 \times 10^6 \text{ ft}^3$$

$$\Delta P = \frac{2151}{556} \times 14.7 \times \frac{610}{520} = 66.7 \text{ psi}$$

The step-by-step approach using a fixed turbine inlet pressure (P_p, Figure 17-4) uses the turbine inlet as the starting point. The inlet pressure is marked on Fig. 17-5 and identified in Table 17.4. The first calculation is the pressure drop in the surface lines to the wellhead.

Economic Balance for Surface Lines

The weekly capital cost of alternate sized lines is balanced against the total extra cost of compression for the frictional pressure loss during outflow and during injection. The costs of two parallel lines with each of three sizes, 48, 42, and 36 in. (1.22, 1.07, 0.91 m), are compared along with the cost of one 48-in. (1.22-m) line. The length is four miles from the compression-generation plant. The friction is computed using Eq. (6.13) with the friction factor read from a chart. The delivery pressure for the air is 40 atm, or 588 psia (4.05 MPa), with a flowing temperature of 150°F (65.6°C). The cost of laying pipeline is taken from Table 17.5.

The results in Table 17.6 indicate that two 42-in. (1.67-m) pipelines give a minimum cost. However, one should appreciate that nonoperating costs do

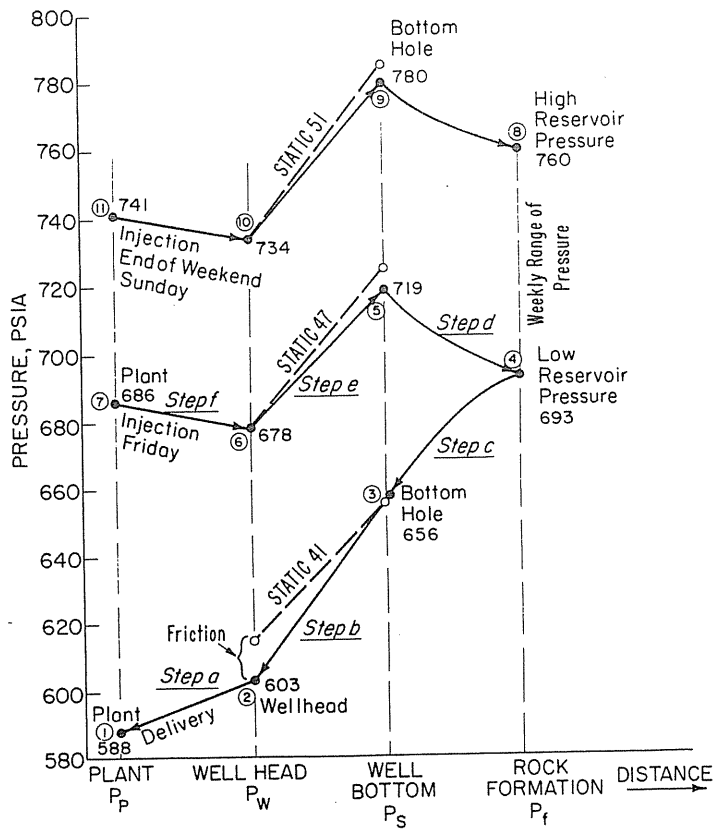

FIGURE 17-5
Pressure changes in three steps in injection or production of air (refer to Figure 17-4, Table 17.5) [Katz & Lady, 17-50].

not inflate with time and that the reservoir could serve a larger air need in the future. So two 48-in. (1.22-m) lines are selected at a slightly more than calculated minimum cost. These lines require a 603-psia (4.16-MPa) flowing wellhead pressure to deliver the air to the plant at 40 atm (4.05 MPa). This value is added to Table 17.4 and Fig. 17-5.

Economic Balance for Size and Number of Wells

Finding the number and size of wells involves two relationships:

1. The cost of compression for well friction and the cost of various diameter wells
2. The cost of compression to overcome flow resistance within the porous medium and the cost of the total number of wells

TABLE 17.4
Description of storage cycle corresponding to Figures 17-4 and 17-5 [Katz & Lady, 17-50]

	Point	Pressure, psia
Air pressure (P_p) on return to plant (40 atm) at end of weekly storage cycle	1	588
Production pressure at well heads (P_w)	2	603
Flowing pressure at bottom of well (P_w), 41 psi static, 11.8 psi friction gradients	3	655.9
Pressure in reservoir (P_f) on Friday at end of weekly withdrawal cycle	4	693
Bottom hole (P_s) injection pressure, first injection on Friday night, start of new cycle	5	719
Wellhead pressure (P_w) for 5	6	678
Plant pressure (P_p) for 6	7	686
Reservoir pressure (P_f) at termination of weekend injection	8	760
Injection bottom hole pressure	9	780
Injection wellhead pressure (P_w) for 9	10	734
Plant pressure at maximum compression pressure (P_p)	11	741

Based on 600 MW, 40 atm, 10-hr cycle, 22,334 MMcf of air in reservoir as cushion air:

Daily rate of production	1003 MMcf
Daily rate of injection	716.4 MMcf

TABLE 17.5
Cost of laying pipeline (estimated in 1976) [Katz & Lady, 17-50]

Nominal diameter, in.	Total cost, $ per mile	
	800 psia	300 psia
48	670,000 (est.)	560,000 (est.)
42	540,000	459,000
36	420,000	361,000
30	318,000	280,000
24	242,000	215,000
20	195,000	166,000
16	148,000	130,000
12	120,000	103,000
10	100,000 (est.)	86,000 (est.)

Source: N. Richardson, Michigan Wisconsin Pipeline Co.

TABLE 17.6
Computation of minimum cost of surface pipelines, Case I frictional pressure drop, production and injection [Katz & Lady, 17-50]

No. of lines	Pipe size, in.	MMcf	Re	e/d	f	P_1, psia	Pressure drop $(\Delta P_1)_p$,* psi	Pressure drop $(\Delta P)_{in}$,† psi	Pressure drop $(\Delta P)_{total}$, psi
2	48	50.15	2.475×10^7	0.000015	0.00865	602.98	14.98	7.494	22.47
2	42	50.15	2.830×10^7	0.000017	0.00865	616.95	28.95	14.47	43.42
2	36	50.15	3.30×10^7	0.000020	0.0088	650.25	62.25	31.13	93.38
1	48	100.30	4.95×10^7	0.000015	0.0085	644.89	56.89	28.44	85.33

Total weekly cost of lines plus compression

No. of lines	Pipe size, in.	Cost of lines 4 miles each, $/week	Total ΔP, psi	Compression cost: Equip. cost, $/week	Compression cost: Fuel cost, $/week	Total, $/week	Line & compression total, $/week
2	48	21,440	22.47	2272.9	1375.6	3,648	25,088
2	42	17,280	43.42	4392.1	2658.1	7,077	24,357
2	36	13,440	93.38	9445.8	5716.6	15,162	28,602
1	48	10,720	85.33	8631.5	5223.8	13,855	24,575

* During production 100.3 MMcf/hr

† During injection 71.6 MMcf/hr

The cost of wells is given in reference [17-50]. For wells of the depth of Belle River Mills, 2150 ft (655 m), the costs are given for various pipe diameters. The friction pressure drop in wells can be calculated [17-50] for various well sizes, flow rates, and pressure levels. Using the 600-psi (4.14-MPa) pressure level, an economic balance will be made between compression and well cost.

The economic number of wells to be used depends upon the well flow rate for a given pressure drop between the reservoir and wellbore. Figure 17-6 is an average well performance curve. Since the viscosity of air is higher, a correction is made in the flow rate to give a curve for the average well performance when flowing air is at 150°F (65.6°C).

To determine the economic number of wells and their size, the compression costs for extra pressure drops in the wellbore (in and out) as well as in the reservoir (in and out) become factors. The total number of wells required and their cost

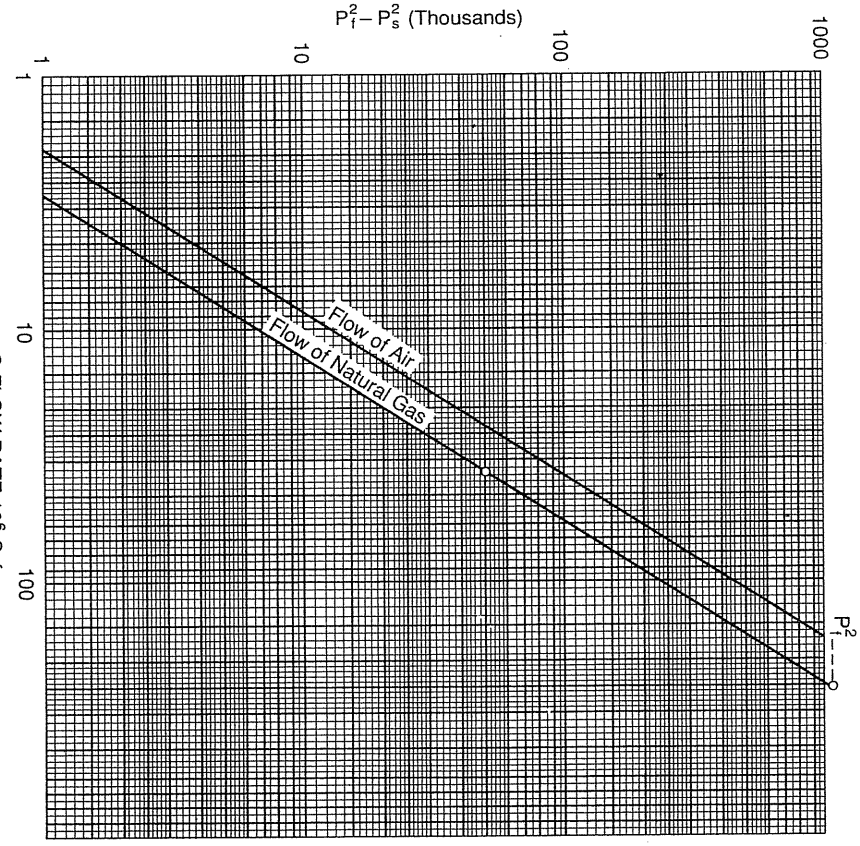

FIGURE 17-6
Well performance curve for Belle River Mills reef [Katz & Lady, 17-50].

must be coupled with the size of wellbores chosen and their costs. First, the friction loss and pressure change in the wells are determined for various well sizes and flow rates. Then, various numbers of wells are chosen for the Belle River Mills reservoir: 50, 100, and 125 [17-50]. The injection pressure drop is taken as 50 percent of the outflowing frictional pressure drop. The frictional pressure drop in the reservoir is calculated using the back pressure curve, well flow rate, and the flowing bottom hole pressure (P_s).

Enlarging the Concept for More Flexibility

Since Belle River Mills stores gas at pressures above 1200 psia (8.27 MPa), the use of such a constant volume reservoir would not be limited to the 760 psia (5.24 MPa) used here. But the schedule of air requirements used thus far is highly idealized, and surely the air needs and power availability for compression will vary during the year.

One strategy is to consider a higher pressure level for use during periods of the year when possible extraordinary demands are forecast. The extra horsepower of compression is not large because of a relatively low compression ratio. Using a 1200 psia (8.27 MPa) top pressure as compared to 760 psia (5.24 MPa), an additional 440 psia $\times$ 2151/67 = 14,126 MMcf (400×10^6 m^3) is stored. Since 100.3 MMcf (2.84×10^6 m^3) generates 600 MW $\cdot$ hr at 40 atm, the additional stored air could generate $14{,}126 \times 600/100.3 = 84{,}500$ MW $\cdot$ hr.

A good sequence of turbines operating at 1200 psia (8.27 MPa) from air storage should make possible the use of this stored energy and still operate at a lower pressure for some time before returning to the higher pressure level. Just maintaining the reservoir at 800 psi (5.52 MPa) and knowing that the turbine could operate at less than 588 psia (4.05 MPa), a reserve energy of 7700 MW $\cdot$ hr, or 12.8 hr of 600-MW generation, could be achieved.

Pittsfield Pilot Unit

A shallow aquifer structure was selected as a pilot study for air injection and withdrawal to give some hands-on experience for CAES development. Support shifted from DOE to EPRI with PB-KBB Inc. as the operator. ANR Storage Co. was commissioned to study the data and to give a report on the analysis of the findings [17-44]. An unexpected event was the loss of oxygen from air stored in the bubble.

Effect of Oxygen in Air—Corrosion and Depletion

It is well known that oxygen corrodes the steel tubular goods in wells. Corrosion rates depend in good part upon the presence of water. Partly for this reason, it has been argued that the sandface should be kept free of liquid water during air injection. During air withdrawal the sand should be liquid free at the wellbore to give the highest permeability.

The oxygen disappearance at Pittsfield was a new phenomenon. The reason for the loss could have been the oxidation of organic material, but no CO_2 was observed in the gas phase. Studies indicate that oxidation of metal sulfides, primary pyrite, and other reactive species in the St. Peter zones is most likely to be responsible. The ANR report also concluded that native water within the rock pores or water introduced with the injected air plays an important role in accelerating the oxidation of sulfide minerals.

Krapac et al. [17-58] made a detailed study of the oxygen disappearance at Pittsfield. They concluded: "Proposed mechanisms that may be involved with the oxygen depletion process are: (1) the oxidation of pyrite or other sulfide minerals with the subsequent release of sulfuric acid, (2) the oxidation of ferrous iron in minerals such as glauconite, and (3) the dissolution of ferrous iron from substituted illite minerals with subsequent oxidation of the ferrous iron."

Further studies are needed on technology for evaluating oxygen demand in cores of prospective air storage reservoirs. To date (1987), the loss of oxygen is likely to be tolerable for the one-week cycles discussed above. When reservoirs are treated on an annual basis, the oxygen demand may be a significant item.

17.3 CALCULATIONS FOR TRANSCONTINENTAL PIPELINES

The Weymouth equation (Eq. 6.11) is derived theoretically; in practice, it may need to be modified to accurately predict pressure drops or flow rates for pipeline operations. This section briefly discusses the AGA formula, corrections due to different elevations, Panhandle equations, and the Rhodes equation used by the ANR Pipeline Co.

Modified Weymouth Equations for Varying Elevations and AGA Formula

For considerable change in elevation of pipelines, the Weymouth equation should be modified to

$$Q(\text{measured at } T_0,\ P_0) = C\frac{T_0}{P_0}\left(\frac{1}{f}\right)^{0.5}\left(\frac{1}{GT_aZ_a}\right)^{0.5}\left(\frac{P_1^2 - e^sP_2^2}{L_e}\right)^{0.5} D^{2.5} \quad (17.1)$$

$$s = 2\left(\frac{29Gh}{T_aZ_aR}\right) \quad (17.2)$$

$$L_e = \left(\frac{e^s - 1}{s}\right) \cdot L = J \cdot L \quad (17.3)$$

where e^s is the correction term for elevation, L_e is the equivalent length, and the constant C is as listed in Table 17.7 for various units used. Equation (17.3) is

TABLE 17.7
Conversion constants C in Eq. (17.1) for various units.

C	P	T	D	L	Q
77.54	psia	°R	inches	miles	ft³/day
3.22	psia	°R	inches	miles	ft³/hour
5634.0	psia	°R	inches	feet	ft³/day
234.8	psia	°R	inches	feet	ft³/hour
1.1494×10^6	kPa	K	meters	meters	m³/day
4.788×10^4	kPa	K	meters	meters	m³/hour

valid only when the pipeline slopes are uniform; otherwise, it should be replaced by

$$L_e = L_1 J_1 + L_2 e^{s_1} J_2 + L_3 e^{s_2} J_3 + \cdots + L_n e^{s_{n-1}} J_n \tag{17.4}$$

The Moody friction factor f can be obtained by using AGA formulas:

Transition region:
$$\frac{1}{\sqrt{f}} = 2 \log (\sqrt{f}\mathrm{Re}) - 0.8 \tag{17.5}$$

Turbulent region:
$$\frac{1}{\sqrt{f}} = 2 \log \left(3.7 \frac{D}{e}\right) \tag{17.6}$$

Rhodes Equations

One widely used friction factor correlation is the Rhodes friction factor [17-27]:

$$f = 0.00592\mathrm{Re}^{-0.1505} = 0.00592\left(\frac{Du\rho}{\mu}\right)^{-0.1505} \tag{17.7}$$

Substituting Eq. (17.7) into Eq. (6.11), the flow equation in field units becomes

$$Q\ (\mathrm{ft^3/day}) = 211.35 \frac{T_0}{P_0}\left(\frac{1}{G}\right)^{0.46}\left(\frac{1}{\mu_a}\right)^{0.081}\left(\frac{P_1^2 - P_2^2}{T_a Z_a L}\right)^{0.541} \cdot E \cdot D^{2.624} \tag{17.8}$$

where μ_a(lb$_f$/ft · s) is the average viscosity, and E is the line efficiency based on empirical data gathered from a particular transmission pipeline; for example, $E = 0.9$ for the 30-in. Crystal Falls-Kewaskum line of ANR Pipeline Co. [17-27] and $E = 0.88$ for other lines.

Panhandle Equations

Another friction factor equation is the "Panhandle" formula:

$$\frac{1}{f} = 52\left(\frac{GQ}{D}\right)^{0.1461} \tag{17.9}$$

Combined with Eq. (6.11), this gives

$$Q = 435.87 \cdot E \cdot \left(\frac{T_0}{P_0}\right)^{1.07881}\left(\frac{P_1^2 - P_2^2}{G^{0.8539} T_a Z_a L}\right)^{0.5394} \cdot D^{2.6182} \tag{17.10a}$$

where E is the pipeline efficiency factor (0.92 average). Equation (17.10a) works well for flow in the transition region; for the turbulent region, it should be modified to

$$Q = 737 \cdot E \cdot \left(\frac{T_0}{P_0}\right)^{1.02}\left(\frac{P_1^2 - P_2^2}{G^{0.961} T_a Z_a L}\right)^{0.51} \cdot D^{2.53} \tag{17.10b}$$

17.4 GEOCHEMICAL IDENTIFICATION OF NATURAL GAS [Coleman, 17-14]

Most commercial deposits of natural gas were formed by thermal decomposition of buried organic material. The composition of natural gas is a function of the type of organic material from which it was formed, the pressure and temperature conditions that existed at the time of formation, and any changes that have occurred as a result of migration or mixing with gas from other sources. Because of the many variables involved in the formation of natural gas, it is highly unlikely that gas from two different sources will have identical compositions. The "geochemical fingerprint" of the gas can, therefore, be used for its identification.

Natural gases from different sources may sometimes be distinguished using standard chemical analyses of the gas. This method is complicated, however, by the fact that because of differences in the size, mass, and solubility of the different chemical constituents, the chemical composition of natural gas can change as it migrates. A more definitive method for distinguishing between natural gases that were derived from different sources is *isotopic analysis* [17-14,17-15,17-32, 17-81,17-85].

Isotopes are different forms of the same element, differing only in the number of neutrons within their nuclei and, thus, their mass. Carbon, for example, has three naturally occurring isotopes, carbon-12, carbon-13, and carbon-14. Carbon-14 is a radioactive isotope formed in the upper atmosphere by cosmic rays and has a natural abundance in atmospheric carbon dioxide of about 1×10^{-10} percent. Carbon-14 is the basis for the radiocarbon dating method but is not present in petroleum or petroleum gases and is, therefore, of no relevance to this study. Hydrogen also has three natural isotopes, protium (hydrogen-1), deuterium (hydrogen-2), and tritium (hydrogen-3). Protium and deuterium are stable isotopes and tritium is a cosmogenic isotope. Most of the tritium present in the atmosphere today is the result of nuclear weapons testing. Tritium is not present in natural gas.

The two stable isotopes of carbon, carbon-12 (^{12}C) and carbon-13 (^{13}C), are present in all organic materials and have average abundances of 98.9 and 1.1 percent, respectively. They undergo the same chemical reactions, but because of the small difference in mass, the reaction rates are sometimes slightly different.

As a result, the relative proportions of carbon-12 and carbon-13 may not be exactly the same in the reaction products as they were in the source materials. For example, the formation of methane by the thermocatalytic decomposition of organic material results in methane that is depleted in carbon-13 (or enriched in carbon-12) relative to the original organic material. Once methane is formed, however, its carbon isotopic composition, or $^{13}C/^{12}C$ ratio, is relatively unaffected by most natural processes.

The carbon isotopic composition of methane in natural gas depends on the nature of its source material and the conditions under which it was formed. Unlike the chemical composition of natural gas, the isotopic composition is relatively unaffected by migration [17-16,17-31,17-77,17-80,17-82,17-86]. Consequently, the isotopic composition of methane provides a reliable fingerprint for distinguishing natural gases from different sources.

The isotopic composition of carbon, or the isotope ratio ($^{13}C/^{12}C$), is normally expressed as the per mil (parts per thousand) difference from a given standard, where the difference is called delta C-13 (sometimes written $\delta^{13}C$ or Del 13C). The delta C-13 values are related to $^{13}C/^{12}C$ ratios by the following equation:

$$\text{Del } 13C_{sa} = \frac{(^{13}C/^{12}C)_{sa} - (^{13}C/^{12}C)_{st}}{(^{13}C/^{12}C)_{st}} \times 1000 \text{ per mil} \qquad (17.11)$$

where sa refers to the sample and st refers to the standard. Carbon isotopic compositions are most commonly reported relative to the Peedee Beleminite (PSB) standard used by Craig [17-19]. This material had a $^{13}C/^{12}C$ ratio similar to that of average marine limestone. Figure 17-7 shows variations in the carbon isotopic compositions of some organic materials [17-14].

Earlier works [17-16] demonstrated that carbon isotope analyses could be used to distinguish between storage gas and shallow biogenic methane when, due to migrational changes, chemical analyses could not distinguish between the two. In a later study [17-15], isotopic analyses were effectively used to identify storage gas that had migrated to nearby oil wells. In recent unpublished studies, it has been shown that the carbon isotopic composition of ethane and the hydrogen isotopic composition of methane can also be used to distinguish between storage gas and native gas.

In distinguishing gases from different sources, the first step is to determine the compositional range of gases of known sources (for example, storage gases and native gases). Gases from unknown sources may then be classified as one type or the other, or as a mixture of two, based on their chemical and isotopic compositions.

17.5 SUPERHEAT LIMIT VAPOR EXPLOSION

Should a liquid be heated above the boiling point at the prevailing pressure, the nucleation of bubbles of vapor depends upon the heating interface. When another

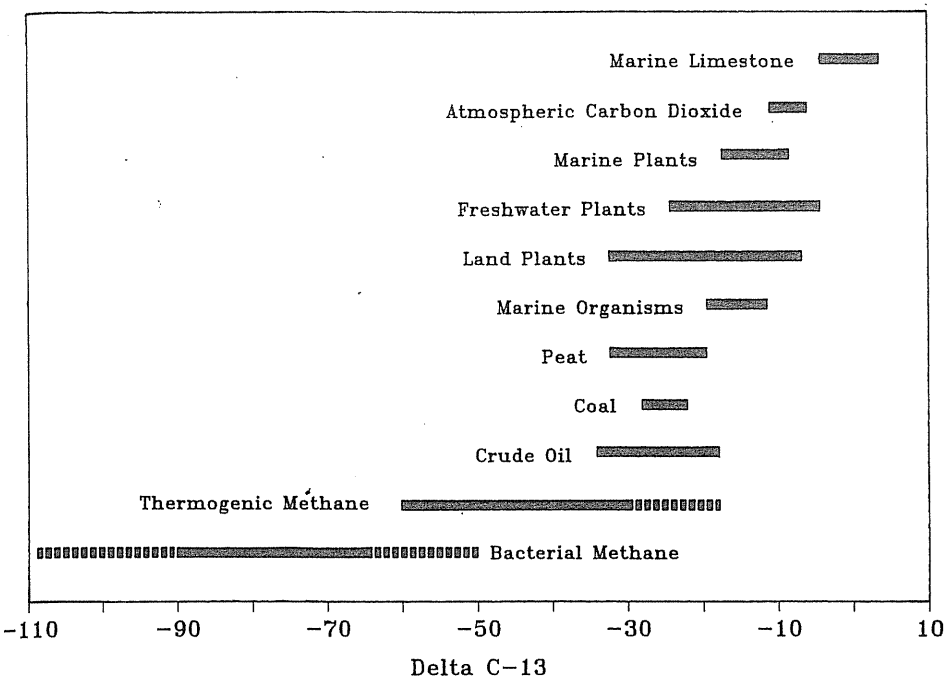

FIGURE 17-7
Variations in the carbon isotopic compositions of some organic materials [Coleman, 17-14].

liquid is used as the heating medium, there is no mechanism for initiation of bubble formation and the liquid superheats. If a liquid is being superheated, what happens when the temperature approaches the critical temperature of the liquid? The internal energy of the liquid reaches a limit at which homogeneous nucleation of vapor takes place.

The Bureau of Mines study of dumping liquefied natural gas (LNG) on water [17-9], which on occasion resulted in an explosion, led to intense study of the phenomenon [17-17,17-29,17-51]. Two aspects of the event were important: (1) the heat transfer mechanism by which the LNG was heated and (2) the physical behavior of a liquid being superheated. The phase behavior aspects are discussed first. The superheat limit event may be created by lowering the pressure on the system rather than raising the temperature, as in cavitation [17-5].

Phase Behavior

Normal phase behavior of fluids is expressed as a pressure-volume graph, Fig. 17-8, and a vapor pressure curve terminating at the critical point, Fig. 17-9. Lowering the pressure at a given temperature or raising the temperature at a given

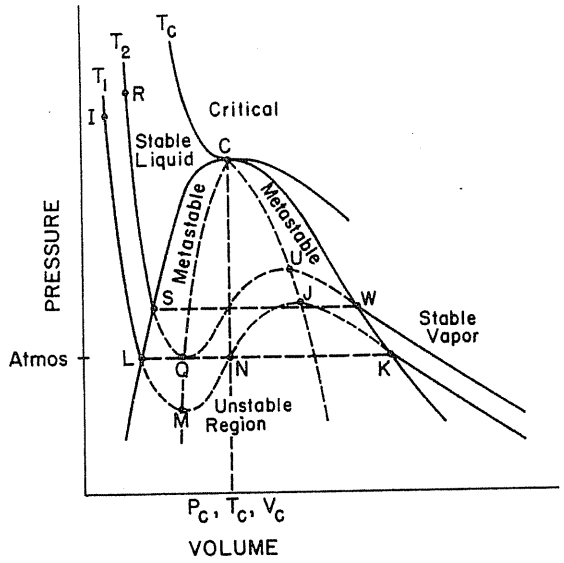

FIGURE 17-8
Schematic of pressure-volume curves (metastable and unstable behavior) [Katz & Sliepcevich, 17-51, courtesy *Hydrocarbon Processing*].

pressure causes the fluid to reach the boiling point. A liquid heated by another liquid may superheat at one atmosphere from L to Q on Fig. 17-8, and explode as it reaches the unstable region. The explosion is free of chemical reaction (flameless) except for the vapor formation, from K to D on Fig. 17-9, which takes place in nanoseconds. The energy is inherent in the molecules involved.

A simple experiment illustrates what happens when LNG (−250°F, −157°C) is dumped on *n*-pentane in a paint can at atmospheric conditions; see Fig. 17-10. The pouring of one gallon of LNG onto the pentane is followed by an explosive event likened to a shotgun report; the bottom of the paint can is blown off, but the cylindrical part of the can is not ruptured. This is a very rapid flameless event, but not too great a force is created since the energy released is the superheat of the LNG at some temperature K, (Fig. 17-9) short of the critical. This temperature K is called *superheat limit*. Wakeshima and Takata [17-91] measured the temperature

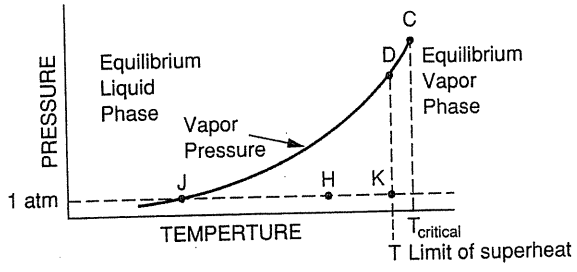

FIGURE 17-9
Pressure-temperature relationship and location of superheated limit [Katz, 17-49, courtesy *Chem. Eng. Prog.*].

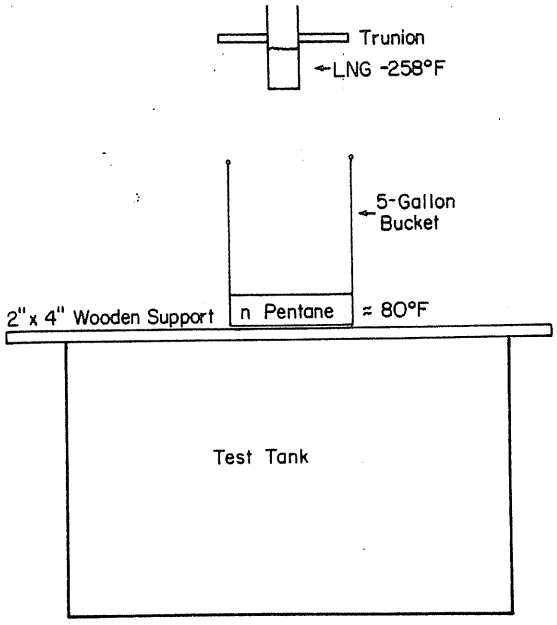

FIGURE 17-10
Arrangements for experiment giving an LNG-pentane explosion [Katz & Sliepcevich, 17-51, courtesy *Hydrocarbon Processing*].

at which small droplets of liquids would decompose explosively as they rise in a liquid column, as shown in Fig. 17-11. These superheat limit measurements were reported for seven liquids including *n*-pentane. They also referred to the calculated molecular behavior of *embryo bubbles*, which occur at temperatures near the superheat limit for pentane. Table 17.8 shows the effect of temperature on bubble formation, in terms of an increase in the J value of the gas from 6.37×10^{-25} at 140°C (284°F) to 5.89×10^{7} at 150°C (302°F). The J value is the probability of embryo bubble formation; a J value of unity coincides with the measured explosive temperature. The superheat temperature limit generally ranges from reduced temperature T_r 0.8 to 0.9. Any liquid at atmospheric pressure that is brought to this reduced temperature will explode spontaneously, or a homogeneous nucleation event will take place. This is called a *superheat limit explosion*.

Mechanism for Liquid Heating to Reach Superheat Limit

Returning to the Bureau of Mines LNG experiments, *why did they occur only on some of the last experiments?* Shell Pipeline studied the conditions at which explosions occur with LNG of different compositions in contact with water. They found that LNG with more than 50 percent methane did not explode when dropping on water. For LNG with the addition of ethane, propane, and so on,

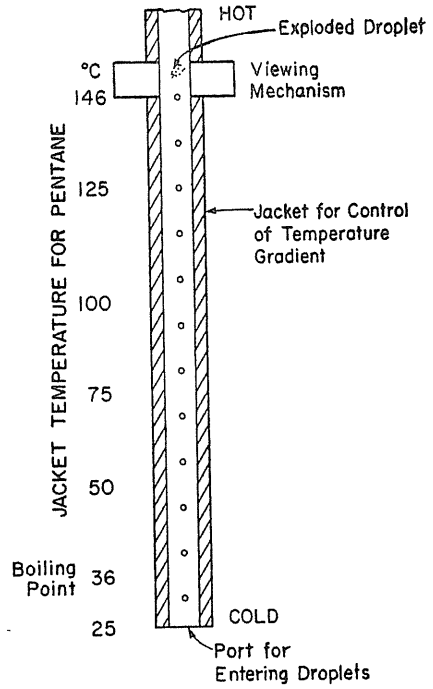

FIGURE 17-11
Schematic method of determining limit of superheat [Katz & Sliepcevich, 17-51, courtesy *Hydrocarbon Processing*].

explosive conditions could be related to LNG composition. Examination of the Bureau of Mines source of LNG showed that the explosive cases occurred when the specimen for the test was near the end of the truck load, possibly because the C_{2+} enriched liquid wet the water more effectively.

From the total information, it was postulated that the LNG-water systems in which the hydrocarbon wets the water permitted rapid heat transfer. Figure 17-12 shows the usual film-boiling curve when LNG is placed on water. If the water does not wet LNG, film boiling occurs. Shell experiments showed that an LNG

TABLE 17.8
Rapid change in number of embryo bubbles with temperature rise (*n*-pentane) [17-91]

Temperature	*J* value
140°C	6.37×10^{-25}
145°C	2.39×10^{-4}
150°C	5.89×10^{7}

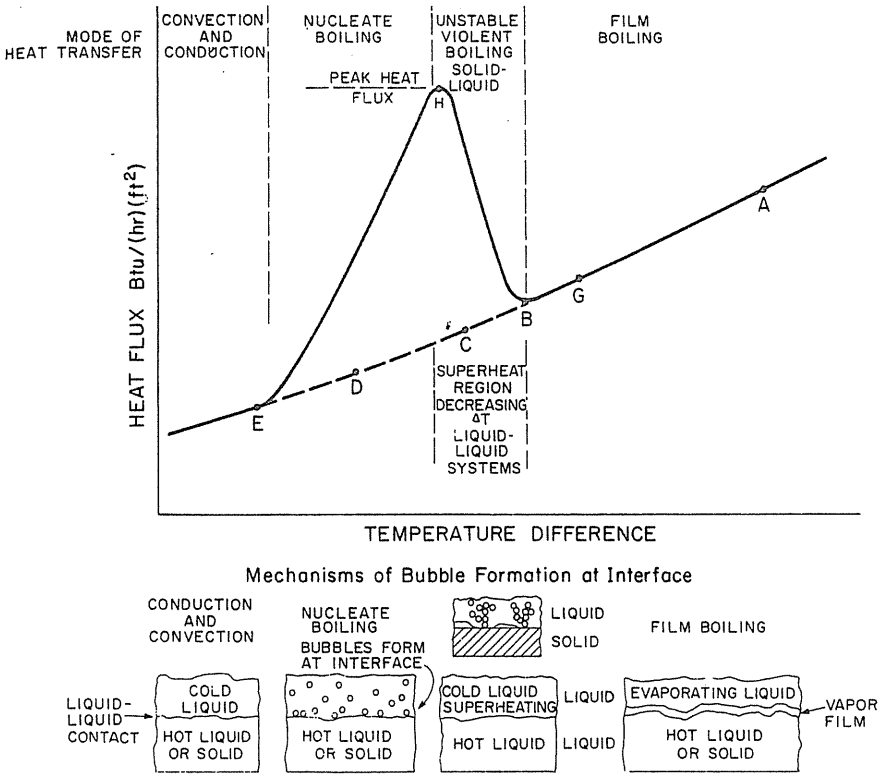

FIGURE 17-12
Boiling heat transfer mechanisms [Katz & Sliepcevich, 17-51, courtesy *Hydrocarbon Processing*].

with 50 percent methane did not explode in contact with water. After boil-down, enriching the liquid hydrocarbon content, it wet the water and exploded. The LNG pentane case has immediate wetting and explodes on contact. Reid [17-76] demonstrated that oil films on water could alter the wettability and hence change the point at which explosions occur.

It should be noted that many other systems encounter the superheat limit and explode as with water Kraft Smelt [17-51].

17.6 MIXING: GAS-GAS DISPLACEMENT IN POROUS MEDIA

In cycling processes [10-24,11-14] and in immiscible or miscible flooding [17-87], the *mixing* phenomena of displacing one fluid by another have been intensively studied. However, successful applications of displacing base gas by cheap gas in storage were not reported until the 1970s; the technology has not yet been

widely utilized in the United States. Although the commercially operated storages in the United States hesitated to carry out mixing projects, the Bureau of Mines supported studies of the use of inert gas cushions in gas storage [17-92].

In 1941, a potentiometric model was employed by Hurst and McCarty [17-42] to determine the pressure contours for flow between wells. Figure 17-13 shows one fluid displacing another at progressive times, and Fig. 17-14 gives the composition of the produced gas. The modern speedy computers make possible more thorough calculation for any proposed mixing schedule.

The following is a tentative mixing procedure:

1. Collect good data of pressure responses of various withdrawal/injection storage schedules.
2. History match the transmissibility (kh) contour of the storage reservoir based on the field data.

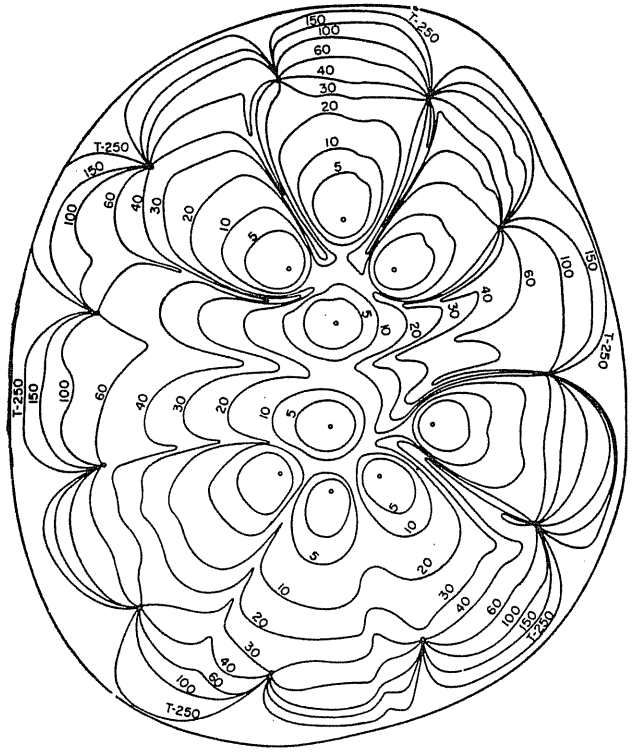

FIGURE 17-13
Area swept out at progressive times by dry gas [Hurst & McCarty, 17-42, courtesy *API Drill. Prod. Practice*].

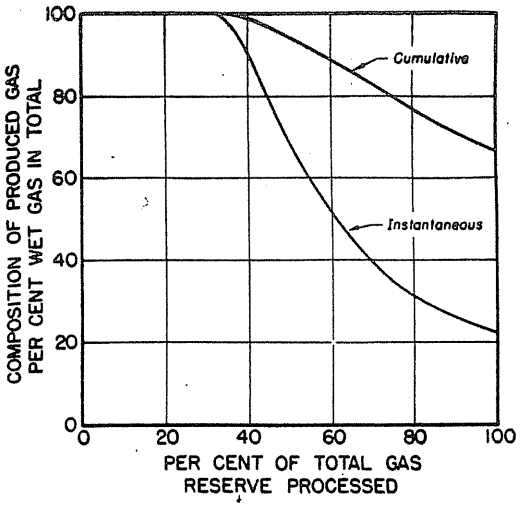

FIGURE 17-14
Variation of composition of produced gas [Hurst & McCarty, 17-42, courtesy *API Drill. Prod. Practice*].

3. Try to inject gas of different compositions in each well to verify (use the material balance calculation shown in Table 14.3; full-scale reservoir simulation is preferred) the reservoir transmissibility contour obtained by history match. If necessary, a tracer test should be conducted.
4. After economic evaluation, decide in what area the cheap gas would be injected via full-scale simulation.
5. Before injecting the cheap gas, a field experiment of injecting gas with different compositions or a tracer should be carried out.

A great opportunity now exists for studying gas mixing in gas storage operations. After a withdrawal season, with gas A in a depressured storage reservoir, gas B with different composition can be injected during the summer. Continuous gas analyses (weekly) and the use of the material balance, discussed in Table 14.3, permit calculation of mixing rates between sections of the reservoir. It is the authors' opinion that the most important element of a mixing project is field data collection. A small deviation of the collected field data may lead to a totally different kh contour, because the whole history-matching process of obtaining kh is an ill-posed problem in mathematical terms [17-13] (one may obtain multiple solutions).

What Is the Mixing Project in Storage Operation? [Fasanino, 17-30]

Storage operations often involve problems related to mixing of gases with different properties in the reservoir. Such problems mainly occur on two occasions:

1. *Total (or partial) conversion of the storage gas to another storage gas with a different heating value.* The Btu requirements of gas supplied to markets sometimes justify replacing part or all the resident inventory by a gas of a different heating value.
2. *Replacement of part of the cushion gas by an inert gas, either during the beginning of the storage development or at some later date during operation.* Whether used in aquifer or depleted field storage, the cushion gas represents a substantial component of the investment required to develop the storage. The economic advantage of an inert cushion, which can be produced at a lower cost (N_2, for example) than pipeline quality storage gas, has been recognized for some time.

   In both areas, successful full-scale field experiments have been carried out. Mixing phenomena are also encountered when produced reservoirs are converted to underground storage (when the pipeline gas is different from the native gas). The same kinds of studies are to be carried out to evaluate the feasibility of CAES (compressed air energy storage) in depleted gas fields.

What Are the Physical Phenomena Involved in Mixing?

The governing equations for two-phase flow with miscible ingredients inside the gas phase are to be discussed. There are three main mechanisms: (1) convective transport (one gas pushes out another gas), (2) diffusion-dispersion transport (two gases diffuse into each other), and (3) the effect of variable permeability, allowing one gas to move faster than another.

Convective transport results from the following physical phenomena (Fig. 17-15):

Gravity
Capillarity
Viscosity

These three phenomena may contribute to mixing between two different gases.

The difference of density between two gases may cause vertical movements that mix the two gases. On the other hand, one could take advantage of a vertical movement caused by gravity to introduce an inert (heavy gas) at the bottom of a thick gas storage.

The hysteresis of capillarity phenomena is responsible for a large part of the mixing problems with convective transport. Mainly, gas trapping/untrapping is involved. For instance, when a depleted field is converted to storage, most of the remaining gas may be trapped. When one develops storage in this field, the gas saturation will increase and the native gas will be mobile again and will mix with the storage gas. Gardner, Downie, and Wyllie [17-36] discuss how to recover the cushions from an aquifer.

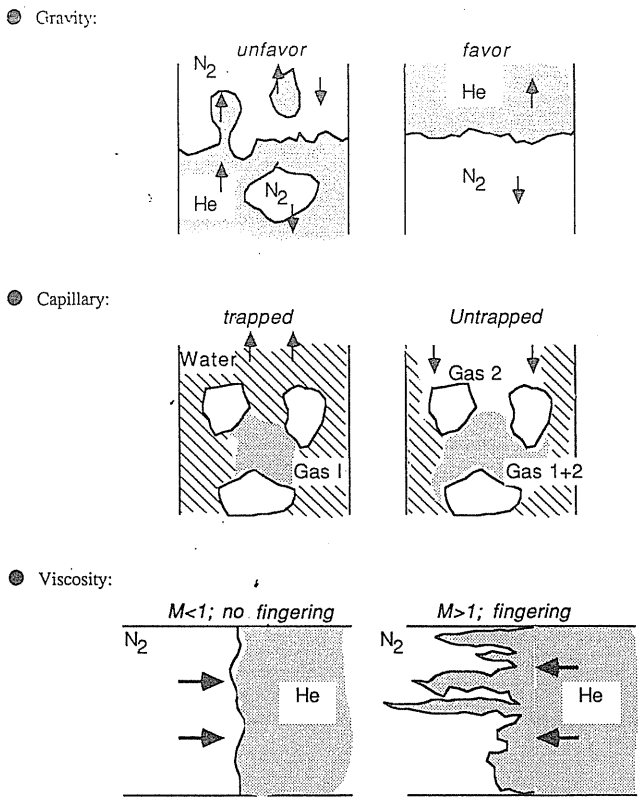

FIGURE 17-15
Convective mixing: (*a*) gravity, (*b*) capillarity, (*c*) viscosity.

The viscosity effect on mixing is the most well known. The mobility ratio M is defined as

$$M = \frac{\text{displacing fluid mobility}}{\text{displaced fluid mobility}} = \frac{k/\mu \text{ of displacing fluid}}{k/\mu \text{ of displaced fluid}} \qquad (17.17)$$

It has been demonstrated (by numerical simulation) that an unfavorable viscosity ratio ($M > 1$) in enhanced oil recovery (EOR) by gas sweeping sometimes causes poor efficiency because of too much mixing (by fingering). One has to take care of this problem when sweeping an inert gas (higher viscosity) by natural gas (lower viscosity, ratio = 1.6). A high-viscosity cheap gas (e.g. N_2) is preferred for displacing natural gas during mixing.

Both density and viscosity differences affect stability. If helium displaces a denser gas such as nitrogen in a downward direction, for example, a stable

displacement is likely to result, because buoyancy effects will work to damp out fingers as they are formed. On the other hand, if helium is being displaced in a downward direction, buoyancy effects will tend to increase fingering. Similarly, a less viscous fluid will tend to finger into a more viscous fluid during a displacement in any direction. For gases, a decrease in density corresponds to an increase in viscosity. For the example of helium displacing nitrogen in a downward direction in a homogeneous medium, one is ensured of stability, since both viscous effects and density effects will act to promote it.

Diffusion-dispersion transport results from several causes. *Molecular diffusion* is a physical phenomenon related to molecular agitation. "Brownian movement" creates particle displacement in all directions. This results in a transport of particles from the higher concentration zones to the lower ones. Molecular diffusion is isotropic and occurs even without any fluid displacement. Its action is very limited in porous media. It acts only inside the fluid gas phase. The magnitude of the diffusion depends on the formation factor of the reservoir, the porosity, and the gas saturation. The mass flux caused by molecular diffusion is proportional to the gradient of concentration: $\dot{m} = D_0 \, \partial C/\partial x$. The law of mass conservation, then, is (for a one-phase problem): $\partial C/\partial t = D_0(\partial^2 C/\partial x^2)$. For a field example, Fig. 17-16 [17-92] shows the calculated concentration profile using pure molecular diffusion and the field measurements; clearly, molecular diffusion must be coupled with convective diffusion to reflect the true field performance.

Kinematic dispersion is a mixing phenomenon created by the different velocities of fluids in pores and the heterogeneities in the porous medium, on any scale:

At the pore's scale: The velocity profile is not constant but parabolic for laminar conditions, Fig. 17-17*a*. This leads to a quicker transport in the middle of the pores, and then to mixing and dispersion of the transported fluid on both sides of the mean convective front.

Between the pores: Because of differences of paths the velocities are heterogeneous (Fig. 17-17*b*). These different paths also create a *transversal dispersion* because some elements go away from the main fluid flow direction.

At the reservoir's scale: Layering effects, clay lenses, fractures—any kind of "macro" geological heterogeneity—create various velocities, and consequently are responsible for mixing.

Kinematic dispersion results from the fact that the actual velocity field is very complex and unknown. When one simulates the convective flow, one only assumes a fictitious mean velocity field following Darcy's law. The decomposition of known heterogeneities included in the calculation of the convective flow and unknown heterogeneities represented by dispersion is one of the main tasks in the mixing calculation. The equivalent dispersion must be determined by proper methodology. It is believed that dispersive characteristics must be measured in situ rather than in the laboratory to be useful in predicting the real world behavior. An efficient tracer test technique has been described in references [17-10, 17-62].

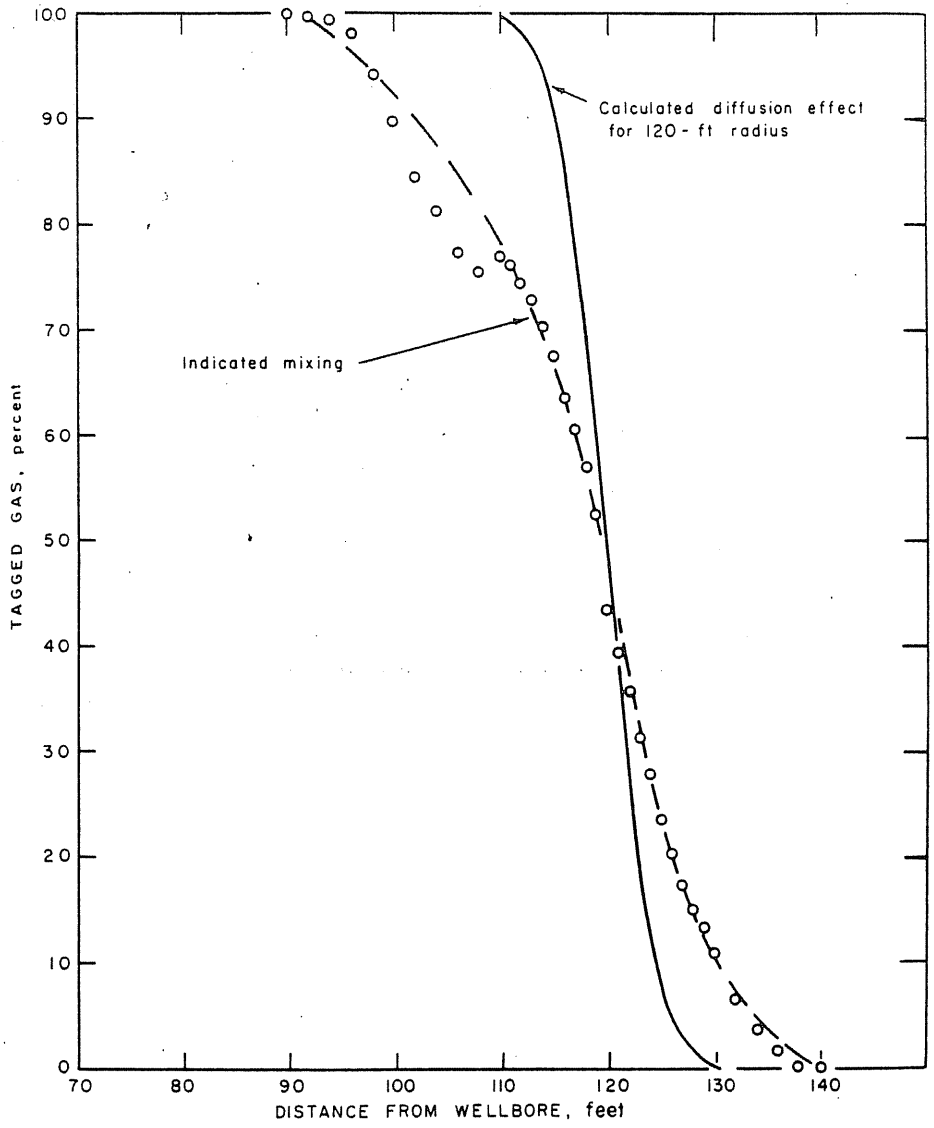

FIGURE 17-16
Concentration profiles of tagged gas in the interfacial zone for the field test [Walker & Huff, 17-92].

Now, which mathematical form should one use to describe the dispersion? The following equation is used to calculate the dispersive flux:

$$m = [D] \nabla C \tag{17.18}$$

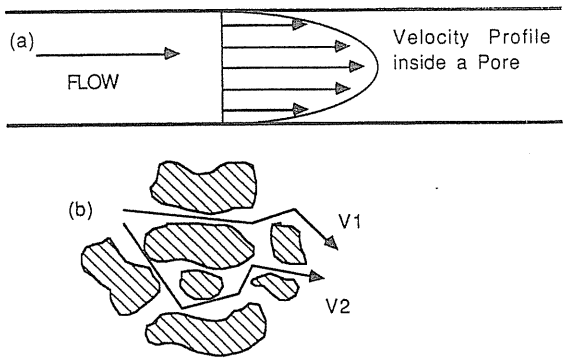

FIGURE 17-17
(*a*) Laminar velocity profile, (*b*) fluid flowing path.

where the in situ dispersion coefficient $[D]$ is

$$[D] = \begin{bmatrix} D_L & 0 & 0 \\ 0 & D_T & 0 \\ 0 & 0 & D_T \end{bmatrix} \tag{17.19}$$

D_L is the longitudinal dispersion (parallel to the flow lines), and D_T is the transversal dispersion.

When Peclet number, Pe, defined as the ratio of the dispersion strength to the convection strength,

$$\text{Pe} = \frac{U_g l}{\phi D_0} = \frac{U_g d_p \sigma}{\phi D_0} \tag{17.20}$$

is greater than one, D_L and D_T are simply proportional to the velocity, as shown in Fig. 17-18 where $\log (D/D_0)$ and $\log$ (Pe) have a straight line relationship if Pe is large:

$$D_L = \alpha_L |U_g|, \quad D_T = \alpha_T |U_g| \tag{17.21}$$

The value $l = d_p \sigma$ is the characteristic dimension of the pore for a particular rock; more discussion can be found in references [2-45,17-61].

Some known characteristics of kinematic dispersion are as follows:

1. Kinematic dispersion is anisotropic: α_T/α_L may vary between 0.5 and 0.01 (perhaps less in the vertical direction in sedimentary beds).
2. Kinematic dispersion depending on the velocity magnitude has also been demonstrated theoretically, considering dispersive flows through a network of parallel tubes.
3. Kinematic dispersion also depends on the distance traveled.

Experiences of tracer tests, and conversion operations conducted at GDF (Gaz de France) storages confirmed these statements.

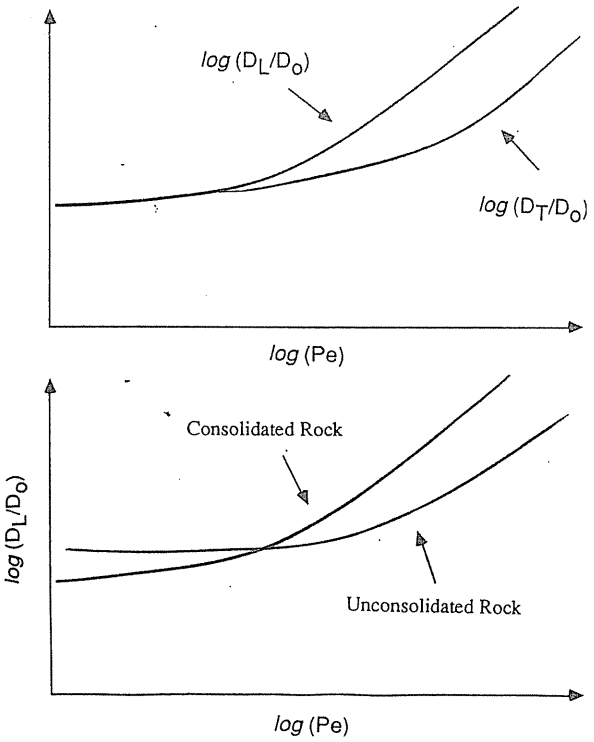

FIGURE 17-18
Sketch of corresponding D_L and D_T for Peclet number, and for consolidated or unconsolidated rocks.

A dimensional analysis shows that α is equivalent to a length. Typical values of the length are 1 to 100 m (3.28–328 ft) in gas reservoirs or aquifers. Measurements in the lab can only identify α's of a few millimeters or centimeters. These lab values are obviously inadequate to describe the phenomenon that takes place inside the reservoir.

Numerical Modeling in Mixing

The purpose of properly modeling mixing phenomena is to enable good decisions in the areas of inert gas substitution or inventory conversion. In the first case, the simulations permit determination of the optimum quantity to be injected, location of wells, and injection schedule, as well as estimates of time and space evaluation of compositions. In the case of a conversion of inventory, results from simulations provide the basis for the optimum mode (sweeping process, quantities, flow rates, schedule) and also enhance the understanding of long-term mixing effects between the gases involved.

Proper simulation of the behavior of several different gases in a gas field (or storage) involves a two-phase flow model when the gas phase itself is composed of several miscible ingredients. A summary of equations describing the flow of

miscible fluids in porous media has been given in Table 17.9. The complexity of a reservoir matrix obliges one to use 3-D representations.

The complexities involved in simulating miscible fluids in several dimensions (2-D or 3-D) and in a multiphase environment have caused certain mathematical difficulties often referred to as numerical dispersion and orientation effect

TABLE 17.9
Equations for mixing [Fasanino, 17-30]

Gas governing equation:*

Convection + dispersion = accumulation

$$\nabla \cdot (\rho_{gi} C_{gi} \vec{U}_g - \rho_{gi}[D] \nabla C_{gi}) = -\frac{\partial}{\partial t}(\phi \rho_{gi} C_{gi} S_g) \tag{17.12}$$

Water governing equation:

Convection = accumulation

$$\nabla(\rho_w \vec{U}_w) = -\frac{\partial}{\partial t}(\phi \rho_w S_w) \tag{17.13}$$

Diffusion equation:

Dispersion coefficient = molecular diffusion coefficient + mixing length × velocity magnitude

$$[D] = [D_0] + [\alpha]|\vec{U}_g| \tag{17.14}$$

General Darcy equations:

$$\vec{U}_g = -\frac{[k\,k_{rg}]}{\mu_g}(\nabla P_g + \rho_g \vec{g}), \qquad \vec{U}_w = -\frac{[k\,k_{rw}]}{\mu_w}(\nabla P_w + \rho_w \vec{g}) \tag{17.15}$$

Additional relationships:

$$\sum_i C_{gi} = 1, \qquad S_w + S_g = 1, \qquad P_g - P_w = P_c \tag{17.16}$$

Nomenclature (for details see Chapter 2):

C_i	gas i concentration	$\vec{U}_g$	gas velocity vector
$[D]$	dispersion tensor	$\vec{U}_w$	water velocity vector
$[D_0]$	molecular dispersion tensor	$[\alpha]$	mixing length
$\vec{g}$	gravitational vector	μ_g	gas viscosity
k	permeability	μ_w	water viscosity
k_{rw}	relative permeability to water	ϕ	porosity
k_{rg}	relative permeability to gas	ρ_g	gas density
P_g	gas pressure	ρ_w	water density
P_w	water pressure	∇ =	$\left(\frac{\partial}{\partial x}, \frac{\partial}{\partial y}, \frac{\partial}{\partial z}\right)$
P_c	capillary pressure		
S_g	gas saturation	$\nabla \cdot$ =	$\left(\frac{\partial}{\partial x} + \frac{\partial}{\partial y} + \frac{\partial}{\partial z}\right)$
S_w	water saturation		
t	time		

* $\vec{x}$ and [ ] denote vector and matrix.

(discussed in Chapter 11). Several methods have been proposed to reduce (not completely correct) the numerical dispersion. Recent work at GDF has resulted in the development of flexible grid models. This method enables one to use a very fine grid in areas where it is necessary (for numerical or physical reasons), and a normal grid where the simulation can afford to be less accurate. The sizes of grid blocks are proportional to the magnitudes of the mixing length α, so that the numerical results by ignoring the dispersion term of Eq. (17.12) have a numerical dispersion of the same magnitude as the physical dispersion. In other words, by controlling grid size, one can use numerical dispersion to represent physical dispersion.

Figure 17-19 depicts the results of calculations using the simulator of GDF to evaluate schematically in a constructed case the effects of substituting an inert gas for part of the cushion gas in a storage reservoir. The concentration of inert gas is plotted against the distance from the center of the storage reservoir for various cycles corresponding to withdrawal and injection operations. The effect of the dispersion has been increased to make it clearer by choosing a large, nonrealistic dispersion factor. The curves labeled $S_1, S_2, \ldots, S_5$ describe the concentration profiles of a previously introduced cushion gas in consecutive withdrawal seasons.

The curves labeled $I_1, I_2, \ldots, I_5$ represent the inert gas concentration profiles computed for consecutive injection seasons. It is interesting to note that over a period of five years, at the end of each withdrawal cycle, S_i curves remain

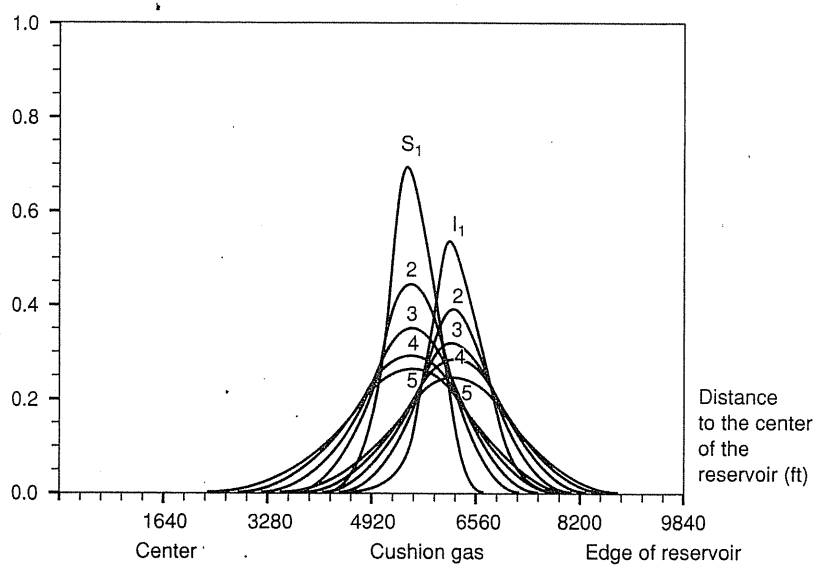

FIGURE 17-19
Evolution of inert gas concentration during I/W cycles of storage [Carriere et al., 17-10, courtesy SPE-AIME].

symmetrical about a fixed distance from the center of the reservoir while continually diffusing to a more attenuated shape. Similarly, the profiles computed at the end of each storage gas injection cycle remain symmetrical and also attenuate to distribution curves with lower maxima. While the main part of each curve appears symmetrical, the left-hand (central) leg becomes more and more skewed as one would expect in areas subject to higher flow rates. The computed results indicate continuing diffusion/mixing; however, the central area of the reservoir appears unaffected, at least by the end of five full withdrawal/injection cycles.

Field Experiences on Mixing

Several mixing projects, full-scale operations, have been carried out by GDF. These are:

Beynes storage conversion from town gas to natural gas in 1973 [17-10]
Gournay storage conversion from high-Btu gas to Groningen gas (low Btu) in 1986
Cerville storage conversion from low-Btu gas to high-Btu gas in 1986 [17-62]
Inert gas injection in St. Clain-Sur-Epte storage in 1979-80 [17-10]
Inert gas injection in Germigny storage in 1987 [17-10]

Ongoing GDF projects (1987) with inert gas injection and mixing studies are:

Substituting 20 percent of the cushion gas of the St. Illiers storage (already in operation for 15 years) in 1990
Substituting an optimum part of cushion gas of all nine GDF aquifer storages already developed
Performing with IGT and one U.S. company the first inert gas substitution in an American storage, 1988–90
Studying with ANR the feasibility of developing CAES in depleted gas fields

Other countries (such as the USSR) have been studying the feasibility of using inert gas as cushion gas; however, little information is available, and the results of the application in the USSR are not published.

The Amarillo helium storage (50% He and 50% N_2), operated by the Bureau of Mines [17-6] in a depleted gas field, is also a very good example of a multigas storage. Mixing problems occurred during the early time of operation.

Figure 17-20 is the isopach map of the Cerville-Velaine storage reservoir in France, and Fig. 17-21 shows the inert gas location at the end of injection [17-62].

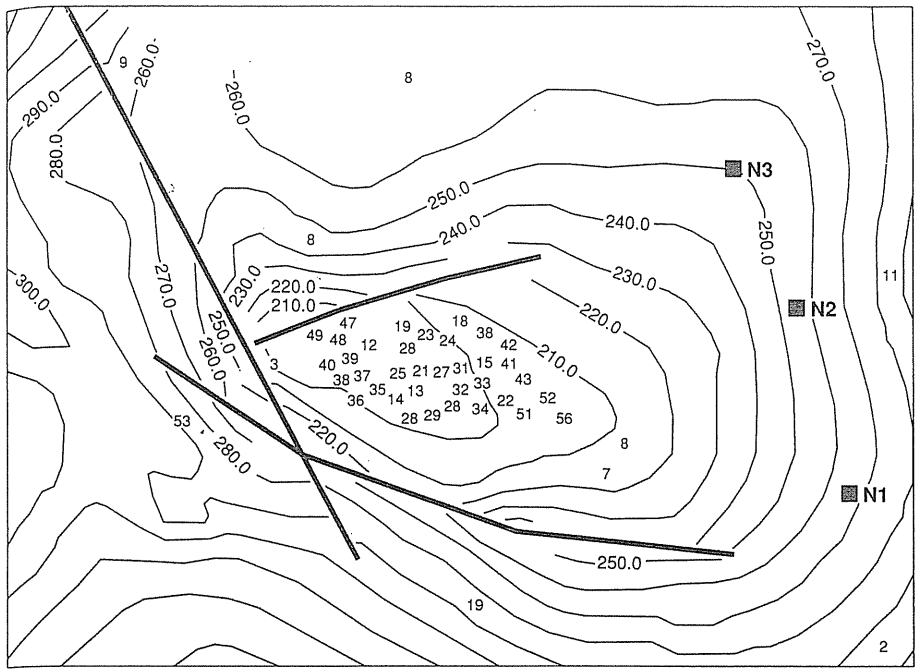

FIGURE 17-20
Location of wells on the Cerville-Velaine reservoir [Laille & Coulomb, 17-62, courtesy SPE-AIME].

17.7 PRODUCTION OF COAL BED METHANE

The presence of methane in coal seams in the earth has been known for many years, particularly because of the hazard of a methane-air mixture igniting. The Bureau of Mines has studied methane in coal beds and learned how it is retained

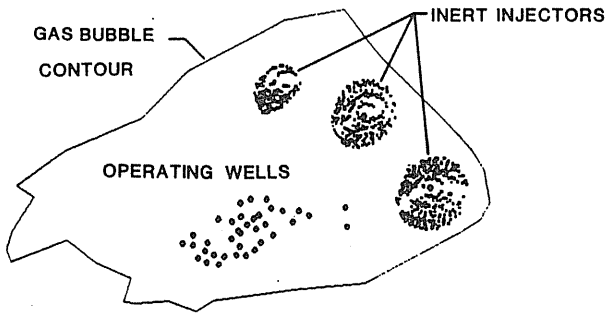

FIGURE 17-21
Frontal displacement at the end of inert injection [Laille & Coulomb, 17-62, courtesy SPE-AIME].

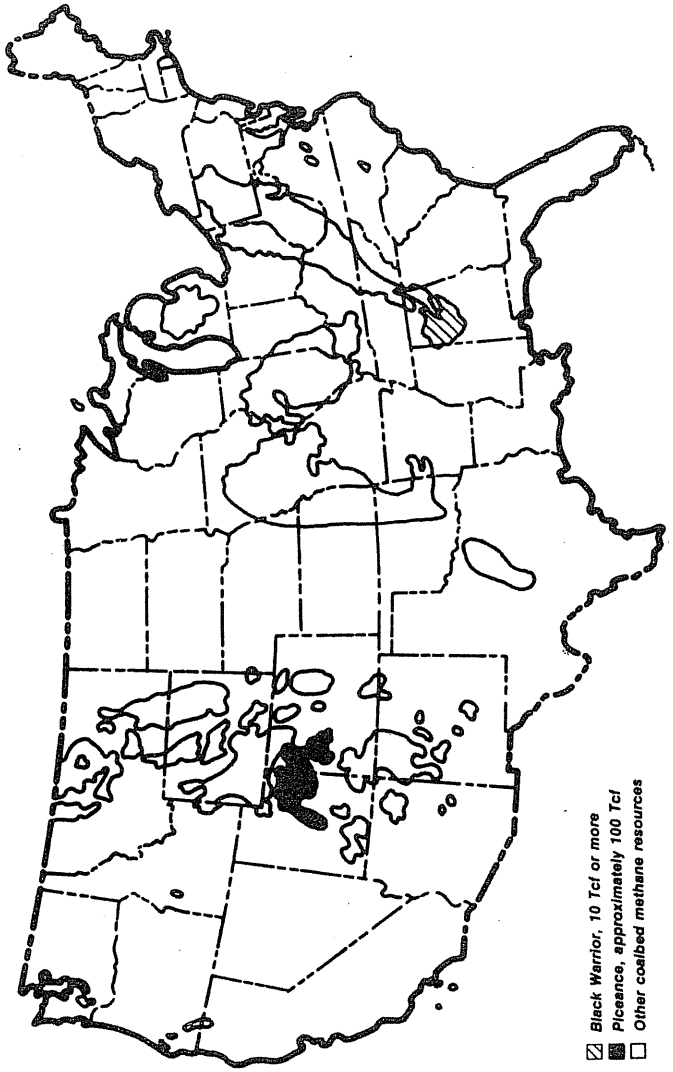

FIGURE 17-22
The coal basins in the United States containing natural gas [17-38, courtesy Gas Research Institute].

in the coal and how to release it. Some 25 years ago, a recovery process for methane, because of its fuel value, was teamed up with the contribution to safety in the mines. With the fuel crisis of the 1970s, extra government projects were sponsored for understanding the development of available methane as an energy resource. Rising prices for methane were part of the driving force, and this factor has produced a lull in the 1980s. The efforts of the Gas Research Institute of Chicago were added to the long ongoing efforts of the Bureau of Mines of DOE.

The coalbeds in the United States (Fig. 17-22) have been estimated to contain natural gas resources of about 450–500 Tcf ($12.7 - 14.2 \times 10^{12}$ m^3). This gas is mainly adsorbed on coal solids under a head of water corresponding in good part to depth. Methane from coal is an alternative to natural gas, generally free from high amounts of contaminants like hydrogen sulfide. With continued research and development on harvesting methane from coal prior to mining, the added value of better safety and better mining rates for degassed coal, coalbed gas production will be a viable economic endeavor.

The gas content of coal varies from near 0 at the surface of the earth for weathered coal to some 600 Scf (17.0 m^3) of methane per ton at depths of 2500 ft (762 m). Table 17.10 [17-25] gives some example data. Figure 17-23 [17-43] gives general estimates of gas content by rank and depth of coalbeds (1 cm^3/gm = 32 Scf/ton).

A small fraction of the gas resides within the fractures or pores of water-filled coal seams, but most of it is adsorbed on the walls of the fine pores of chunks of coal. It is generally held in a monolayer by pressure exerted by a head of water. There are standard methods of desorbing methane from cores as a gas phase, often presented as adsorption isotherms.

Comparison with Natural Gas Production

One might compare the initial state of methane in coal seams with that in gas reservoirs. Methane in coal is in an adsorbed state. The pressure on the adsorbent

TABLE 17.10
Gas potentials from Mary Lee group of coal beds at Jefferson, Walker, and Tuscaloosa Counties, Alabama [Diamond et al., 17-25]

	Average methane content		Methane potential, ft^3	
Overburden, ft	cm^3/g	ft^3/ton	Mary Lee	Mary Lee group
0–500	0.25	7.5	0.09×10^{11}	0.13×10^{11}
500–1000	2.00	64.0	0.90×10^{11}	1.15×10^{11}
1000–1500	7.50	240.0	2.65×10^{11}	3.76×10^{11}
1500–2000	13.10	419.0	2.30×10^{11}	3.54×10^{11}
2000–2500	18.60	595.2	1.23×10^{11}	1.96×10^{11}
Total	—	—	7.17×10^{11}	10.54×10^{11}

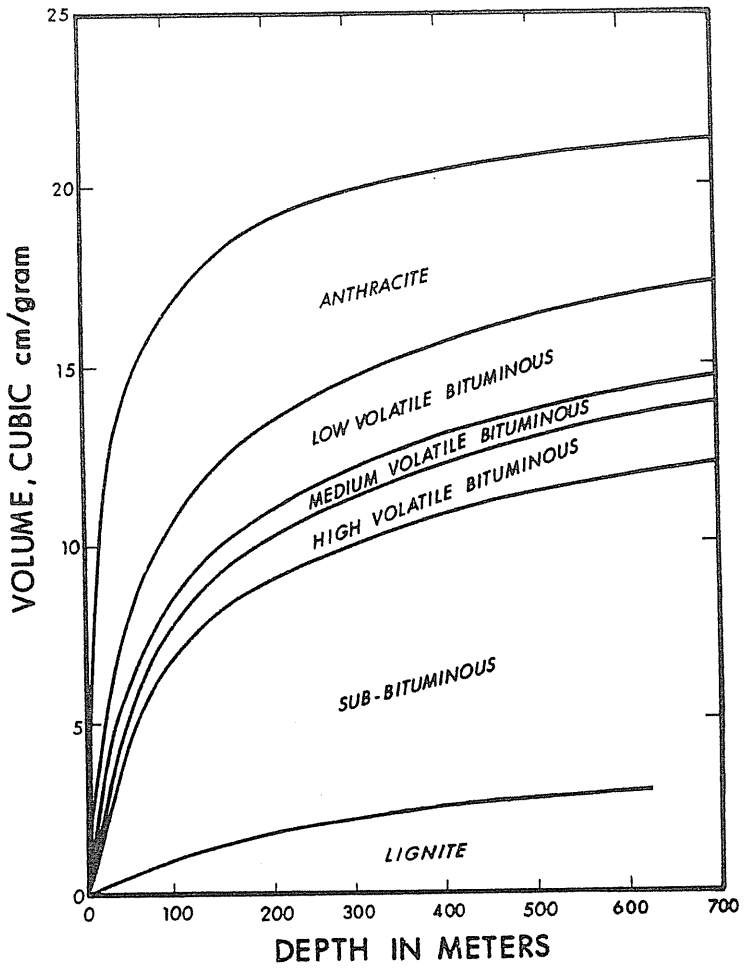

FIGURE 17-23
The estimates of methane content [17-43, courtesy Intercomp.].

is from water. Harvesting coalbed gas starts by water removal, followed by a period of time for adsorbed methane to detach itself from the solid and become gas phase methane. In a bed being drained with capillary water retention, some time is needed for methane to increase its gas phase saturation enough to become mobile under a pressure gradient, following principles of relative permeability. The possible three stages of coalbed methane flow are shown by Fig. 17-24 [17-57].

Natural gas contained in sands also containing connate water is free to move toward a well down the pressure gradient caused by production of gas from the

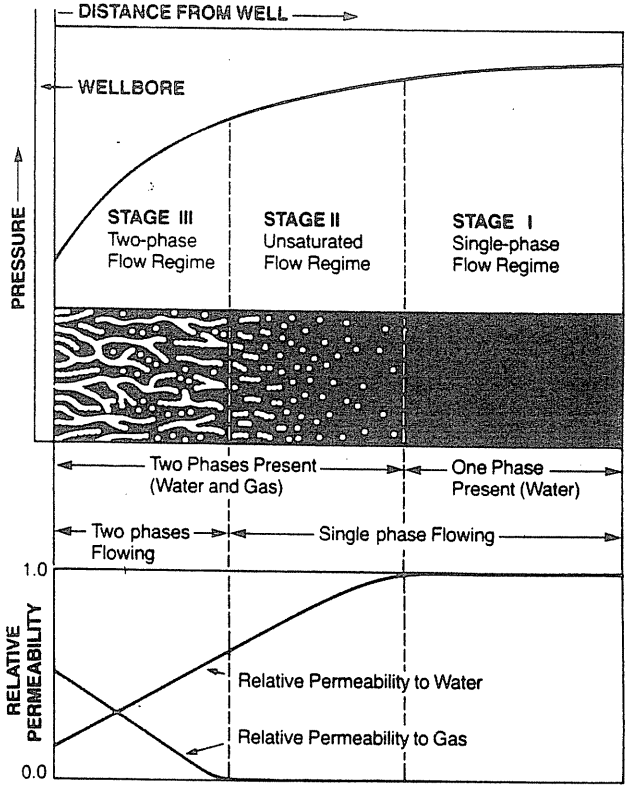

FIGURE 17-24
Schematic diagram of the three stages of harvesting coal seam methane [Koenig & Bell, 17-57, courtesy Gas Research Institute].

well. The permeability may be low, and hence the flow rates to wells could be slow. Gas production from tight shales bearing gas may merge to some degree with coal seam gas. Long wall mining and degasification work well together.

The longtime practice of making rooms and pillars leaves some 40 percent of the coal in the ground. To degas the coal in situ means that essentially all the coal to be mined will be degassed, including the pillars. In the *long wall process*, large blocks of coal are prepared for mining and degassed before the cutting line reaches that point in the block of coal. The roof is allowed to drop down after the cutter removes the bulk of the coal. The gas is released from the gob (the coal layers above the vein being mined) falling into the mine and thereby increasing the gas supply.

In the last decade, the processes of degassing coal beds and recovering methane have been simulated, going through the steps of data gathering, dewatering, desorption of gas, and flow to wells for recovery [17-2,17-3,

17-4,17-28,17-75]. Many investigators have been solving pieces of the total process.

Development of a degasification process includes simulation. Intercomp made a major effort to utilize their experience in simulation for the oil and gas industry by creating a viable degasification process. Selected literature from 1966 to 1986 on the degasification of coal beds is listed in references [17-1, 17-8,17-11,17-12,17-20 to 17-24,17-26,17-34,17-35,17-37,17-40,17-41, 17-46, 17-47,17-52 to 17-56,17-59,17-63,17-64,17-66,17-68 to 17-74,17-78, 17-79, 17-83,17-84,17-88,17-90,17-93].

REFERENCES

17-1. Ahrin, D. C., F. du Briel, and R. D. Saltsman, "Survey of Coal Industry Programs for Utilization of Methane from Coal Seams," Gas Research Inst., Bituminous Coal Research, Inc., Feb. (1980).

17-2. Ancell, K., et al., *The Feasibility of Methane Production from Coal Beds: Theory and Application of Coal Bed Degasification*, Intercomp Resources Dev. and Engr., Inc.,(1977).

17-3. Ancell, K. L., and J. W. Stevenson, "Degasification Parameters and Well Completion Procedures for Mary Lee Blue Creek Coalbeds," *Proc. 1st Sym. Unconventional Gas*, p. 67–81 (1979).

17-4. Ancell, K. L., S. Lambert, and F. S. Johnson, "Analysis of the Coalbed Degasification Process at a 17 Well Pattern in the Warrior Basin of Alabama," SPE/DOE preprint 8971 (1980).

17-5. Apfel, R. E., "Vapor Cavity Formation in Liquids," NR384-903 Tech. Memorandum No. 62, Acoustic Res. Lab., Harvard University (1970).

17-6. Bartlesville Petroleum Research Center, "Movement of Gas-Gas Interface under Gradients Due to Injection of Raw Helium and to Difference in Densities and Viscosities," a progress report to DOE (1969).

17-7. Battelle-Pacific Northwest Laboratory, *Underground Energy Storage Program*, 1982 Annual Report, PNL 4735, Report PNL 5127, June (1983).

17-8. Bielicki, R. J., et al., "Methane Diffusion Parameters for Sized Coal Particles," U.S. Bureau of Mines, RI7697 (1972).

17-9. Burgess, D. S., J. N. Murphy, and M. G. Zabetakis, "Hazards of LNG Spillage in Marine Transporation," U.S. Bureau of Mines, Report to U.S. Coast Guard, Feb. (1970).

17-10. Carriere, J. F., G. Fasanino, and M. R. Tek, "Mixing in Underground Storage Reservoir," *SPE preprint 14202* (1985).

17-11. Cervick, J., H. H. Fields, and S. N. Aul, "Rotary Drilling Holes in Coalbeds for Degasification (Horizontal Holes)," U.S. Bureau of Mines, RI8097 (1975).

17-12. Chen, L. L., D. L. Katz, and M. R. Tek, "Binary Gas Diffusion of Methane-Nitrogen through Porous Solids," *AIChE J.*, Vol. 23, No. 3, 336 (1977).

17-13. Chung, C. B., and C. Kravaris, "Identification of Spatially Discontinuous Parameters in Second-Order Parabolic Systems by Piecewise Regularization," *Inverse Problems*, in press (1987).

17-14. Coleman, D. D., private communication, Isotech Laboratories, Inc. (1986).

17-15. Coleman, D. D., "The Use of Isotope Ratios to Determine the Source of Natural Gas above Gas Storage Reservoirs," AGA conference, New Orleans (1979).

17-16. Coleman, D. D., W. H. Meents, C. L. Liu, and R. A. Keogh, "Isotopic Identification of Leakage Gas from Underground Storage Reservoirs—A Progress Report," Illinois State Geological Survey (1977).

17-17. *Committee on Hazardous Materials Conference Proceedings on LNG Separation and Terminal Safety*, U.S. Coast Guard Contract No. TEG 15559, June 13–14, (1972).

17-18. *Compressed-Air Energy Storage Preliminary Design and Site Development Program in an Aquifer*, Volumes 1-9, EPRI EM 2351, Palo Alto, Calif. (1982).

17-19. Craig, H., "The Geochemistry of the Stable Carbon Isotopes," *Geochimica et Cosmochimica Acta*, Vol. 3, 53–92 (1953).

17-20. Deul, M., "Coal Beds—A Source of Natural Gas," *Oil and Gas J.*, Vol. 73, No. 24, June 16 (1975).

17-21. Deul, M., "Gas Production from Coal Beds," *AGA Oper. Sect. Proc.*, P.T227 (1975).

17-22. Deul, M., and C. H. Elder, "Degasification of the Mary Lee Coalbed Near Oak Grove, Jefferson Co. Ala. by Vertical Borehole Advance of Mining," U.S. Bureau of Mines, RI7968 (1974).

17-23. Deul, M., and C. H. Elder, "Hydraulic Stimulation Increases Degasification Rate of Coalbeds," U.S. Bureau of Mines, RI8047 (1975).

17-24. Deul, M., and P. W. Jeron, "Cleat in Bituminous Coalbeds," U.S. Bureau of Mines, RI7910 (1974).

17-25. Diamond, W. R., G. W. Murrie, and C. M. McCulloch, "Methane Gas Content of the Mary Lee Group of Coal Beds: Jefferson, Tuscaloosa, and Walker Co., Ala.," Bureau of Mines, RI8117 (1976).

17-26. Doffous, M. K., et al., "The Permeability of Coal to Gas and Water," *Soc. Pet. Eng. J.*, Vol. 14, No. 6, 563, Dec. (1974).

17-27. Dowhan, D. J., private communication, ANR Pipeline Co. (1987).

17-28. Dunn, B. W., "Coal as a Conventional Source of Methane," *J. Pet. Tech.*, Vol. 31, No. 1, 157, Jan. (1985).

17-29. Enger, T., and D. E. Hartman, "LNG Spillage on Water I," A report to participants by Shell Pipeline Research and Development Laboratories, TP1-71 (1971).

17-30. Fasanino, G., and J. E. Molinard, private communication, Gaz de France (1987).

17-31. Fuex, A. N., "Experimental Evidence Against an Appreciable Isotopic Fractionation of Methane during Migration," *Physics and Chemistry of the Earth*, Vol. 12, 725–732 (1980).

17-32. Fuex, A. N., "The Use of Stable Carbon Isotopes in Hydrocarbon Exploration," *J. of Geochemical Exploration*, Vol. 7, 155–188 (1977).

17-33. Fields, H. H., et al., "Degasification and Production of Natural Gas from an Airshaft in the Pittsburgh Coalbed," U.S. Bureau of Mines, RI8173 (1976).

17-34. Fields, H. H., et al., "Degasification of Virgin Pittsburgh Coalbed through a Large Bore Hole," U.S. Bureau of Mines, RI7800 (1973).

17-35. Fields, H. H., J. H. Perry, and M. Deul, "Commercial Quality Gas from a Multi-Purposed Borehole Located in the Pittsburgh Coalbed," U.S. Bureau of Mines, RI8025 (1975).

17-36. Gardner, G. H. F., J. Downie, and M. R. J. Wyllie, "Problems in the Recovery of Gas from Aquifer Used for Gas Storage," *J. of the Ins. of Petro.*, Vol. 48, 457 (1962).

17-37. Gas Research Institute, "Coalbed Methane," *GRID*, Jan.–Feb. (1985).

17-38. Gas Research Institute, *GRID*, Jan.–Feb., Vol. 8, 1 (1986).

17-39. Gas Research Institute, *Methane from Coal Seams Technology*, June (1985).

17-40. Hagood, J. W., et al., "Methane Control in an Advancing Section of an Underground Coal Mine," Contract U.S. Bureau of Mines, Jim Walter Resources, Inc., Aug. (1982).

17-41. Hofer, L. J. E., et al., "Rates of Adsorption of Methane on Pocohontas and Pittsburg Seam Coals," U.S. Bureau of Mines, RI6750 (1966).

17-42. Hurst, W., and G. M. McCarty, "The Application of Electrical Models to the Study of Recycling Operations in Gas Distillate Fields," *API Drill. Prod. Practice*, 228 (1941).

17-43. Intercomp, Inc., private communication (1977).

17-44. Istvan J. A., C. V. Crow, J. C. Pereira, and H. Bakhtiari, "Compressed Air Energy Storage (CAES) in an Aquifer—A Case History," SPE preprint 12080 (1983).

17-45. Jeran, P. W., et al., "Methane Emissions from an Advancing Coal Mine Section in the Pittsburgh Coalbed," U.S. Bureau of Mines, RI8132 (1976).

17-46. Jeran, P. W., et al., "Methane Emissions from Four Working Places in the Beckley Mine," U.S. Bureau of Mines, RI8212 (1977).

17-47. Joubert, J. J., C. T. Grein, and D. Bienstock, "Effect of Moisture on the Methane Capacity of American Coals," *Fuel*, Vol. 52, 181 (1973).
17-48. Katz, D. L., "Compressed Air Storage Comparison with Natural Gas Storage," *Proceedings, AGA Conference*, T255–T258 (1977).
17-49. Katz, D. L., "Superheat Limit Explosions," *Chem. Eng. Progress*, Vol. 68, No. 5, May (1972).
17-50. Katz, D. L., and E. R. Lady, *Compressed Air Storage for Electric Power Generation*, Ulrich's Books, Inc., Ann Arbor (1976).
17-51. Katz, D. L., and C. M. Sliepcevich, "LNG/Water Explosion Cause and Effect," *Hydrocarbon Processing*, Vol. 50, No. 11, 240–244, Nov. (1971).
17-52. Kim, A. G., "Methane in the Pittsburgh Coalbed," U.S. Bureau of Mines, RI8026 (1975).
17-53. Kim, A. G., and L. J. Douglas, "Gases Desorbed from 5 Coals of Low Gas Content," U.S. Bureau of Mines, RI7768 (1973).
17-54. Kissell, F. N., and R. J. Bielicki, "Insitu Diffusion Parameters for Sized Coal Particles," U.S. Bureau of Mines, RI7668 (1972).
17-55. Kissell, F. N., and J. C. Edwards, "Two Phase Flow in Coalbeds," U.S. Bureau of Mines, RI8066 (1975).
17-56. Kissel, F. N., et al., "The Direct Method of Determining Methane Content of Coalbeds for Ventilation Design," U.S. Bureau of Mines, RI7767 (1973).
17-57. Koenig, R. A., and G. J. Bell, "Design of Single-Phase Flow Tests for Water-Saturated Coalbed Methane Reservoirs," GRI Quarterly Review of Methane from Coal Seams Technology, Vol. 3, 1 (1985).
17-58. Krapac, I. G., R. A. Griffin, and D. R. Dickerson, "Assessment of Oxygen Depletion by Inorganic Constituents at the Pittsfield, Illinois, Compressed Air Energy Storage Site," Final Report for EPRI, RP 2488-10 (1986).
17-59. Krickoiric, S., and C. Findlay, "Rate Studies in a Central Pennsylvania Mine," U. S. Bureau of Mines, RI7591 (1971).
17-60. Lady, E. R. and D. L. Katz, "Underground Compressed Air Storage for Electric Utility Load Leveling," *J. Pet. Tech.*, Vol. 30, No. 11, 1656–1660, Nov. (1978).
17-61. Lagaski, M. W., "Dispersion Coefficients for Gases in Consolidated Porous Media," Ph.D. dissertation, Univ. of Michigan (1966).
17-62. Laille, J. P., and C. Coulomb, "Underground Storage in Cerville-Velaine, France: A Case History in Conversion and Inert Gas Injection as Cushion Substitute," SPE preprint 15588 (1986).
17-63. Lambert, S. W., and M. A. Trevits, "Effective Placement of Coalbed Gas Drainage Wells," DOE: RLPMOC-2, Sept. (1978).
17-64. Lambert, S. W., M. A. Trevits, "Methane Drainage Ahead of Mining Using Foam Stimulation, Mary Lee Coalbed, Alabama," DOE: R1-PMTC-3, Jan. (1979).
17-65. Levykin, E. V., "The Application of Air in the Underground Storage of Gas," *The Gas Industry*, 32–35 (1977).
17-66. Maksimouic, S. D., C. H. Elder, and F. N. Kissell, "Hydraulic Stimulation of a Surface Borehole for Gas Degasification," U.S. Bureau of Mines, RI8228 (1977).
17-67. Mattick, W., H. Hadedenhorst, O. Weber, and Z. S. Stys, "Huntorf—The World's First 290 MW Gas Turbine Air Storage Peaking Plant," *Proc. American Power Conference*, Vol. 37, 322 (1975).
17-68. McCulloch, C. M., and M. Deul, "Geologic Factors Causing Pool Instability and Methane Emission Problems," U.S. Bureau of Mines, RI7769 (1973).
17-69. McCulloch, C. M., et al., "Measuring the Methane Content of Bituminous Coalbeds," U.S. Bureau of Mines, RI8043 (1975).
17-70. McKee, C. R., and A. C. Bumb, "Flow Testing Coalbed Methane Production Wells in the Presence of Water and Gas," SPE preprint 14447 (1985).
17-71. "Methane Emission Rate Study in a Deep Pocohontas No. 3 Coalbed Mine in Conjunction with Drilling Degasification Holes Horizontal in Coalbed," U.S. Bureau of Mines, RI7703 (1972).

17-72. Moore, T. D., Jr., et al., "Longwall Gas Degasification with Surface Ventilation Boreholes above the Lower Kittanning Coalbed," U.S. Bureau of Mines, RI8195 (1976).
17-73. Murrie, G. W., W. P. Diamond, and S. W. Lambert, "Geology of the Mary Lee Group of Coalbeds Black Warrior Coal Basin, Ala.," U.S. Bureau of Mines, RI8189 (1976).
17-74. Pandey, G. N., M. R. Tek, and D. L. Katz, "Diffusion of Fluids through Porous Media," *Bull. AAPG*, Vol. 58, No. 2, Feb. (1974).
17-75. Price, H. S., and A. A. Abdalla, "A Mathematical Model Simulating Flow of Methane and Water in Coal BA Mines," OFR, 10-72, NTIS PB209-273 (1972).
17-76. Reid, R. C., "Superheated Liquids," *American Scientist*, Vol. 64, No. 2, 146 (1976).
17-77. Reitsema, R. H., A. J. Kaltenbach, and F. A. Lindberg, "Source and Migration of Light Hydrocarbons Indicated by Carbon Isotopic Ratios," *AAPG Bull.*, Vol. 65, 1536–1542 (1981).
17-78. Reznik, A. A., et al., "Air-Water Relative Permeability Studies of Pittsburgh and Pocohantas," *Soc. of Pet. Eng. J.*, Vol. 14, No. 6, 556, Dec. (1974).
17-79. Ruppel, T. E., et al., "Adsorption of Moisture on Dry Coal," *Fuel*, Vol. 53, 155 (1974).
17-80. Sackett, W. M., "Carbon Isotope Composition of Natural Methane Occurrence," *AAPG Bull.*, Vol. 52, 853–857 (1968).
17-81. Schoell, M., "The Hydrogen and Carbon Isotopic Composition of Methane from Natural Gases of Various Origins," *Geochimica et Cosmochimica Acta*, Vol. 44, 649–661 (1980).
17-82. Schoell, M., "Isotope Techniques for Tracing Migration of Gases in Sedimentary Basins," *J. of the Geological Society*, Vol. 140, 415–422 (1983).
17-83. Smith, D. M., "Methane Diffusion and Desorption in Coal," Ph.D. Thesis, University of New Mexico, Aug. (1982).
17-84. Smith, D. M., and F. L. Williams, "Diffusional Effects in the Recovery of Methane from Coalbeds," *Soc. Pet. Eng. J.*, Vol. 24, No. 5, 529, Oct. (1984).
17-85. Stahl, W., "Carbon and Nitrogen Isotopes in Hydrocarbon Research and Exploration," *Chemical Geology*, Vol. 20, 121–149 (1977).
17-86. Stahl, W., and B. D. Carey, "Source Rock Identification by Isotope Analyses of Natural Gases from Fields in the Valerde and Delaware Basins, West Texas," *Chemical Geology*, Vol. 16, 257–267 (1975).
17-87. Stalkup, F. I., Jr., *Miscible Displacement*, SPE Monograph Vol. 8 (1983).
17-88. Stevenson, J. W., "Methane Control in the Warrior Coal Fields of Alabama," JWR, Birmingham, Alabama, American Mining Congress, May (1980).
17-89. Stottlemyre, J. A., D. L. Katz, and G. E. Smith, "Stability Criteria for Compressed Air Energy Storage in a Porous Rock Reservoir," *Proc. Pacific Grove Asilomar Conference on CAES*, May 16 (1978).
17-90. Thimons, E. D., and F. H. Kissell, "Diffusion of Methane through Coal," *Fuel*, Vol. 52, 275 (1973).
17-91. Wakeshima, H., and K. Takata, "On the Limit of Superheat," *J. Phy. Soc., Japan*, Vol. 13, 1398 (1958).
17-92. Walker, C. J., and R. V. Huff, "Feasibility of Inert-Gas Cushions in Gas Storages," Report of investigation 6534, U.S. Bureau of Mines (1964).
17-93. Warner, A. J., Sr., *Methane in Coal*, Report of U.S. Bureau of Mines to Federal Power Comm., Nov. (1976).
17-94. Whim, M. J., director, *Compressed Air Energy Storage in Porous Media*, EPRI, RP 2488-10, Prepared by ANR Storage Co. (1985).
17-95. Wiles, L. E. and R. A. McCann, "Reservoir Characteristics and Final Pre-Test Analysis—Pittsfield Aquifer Field Test," Pacific Northwest Laboratories, PNL 4743, June (1983).

APPENDIX A

PHYSICAL PROPERTIES OF NATURAL GASES AND CONVERSION FACTORS

TABLE A.1
Physical constants of hydrocarbon [GPSA, 1-28]

No.	See Note No.→		1.	2.	2.	3.	3.	Critical constants			
	Compound	Formula	Molecular mass	Boiling point, °C 101.3250 kPa (abs)	Boiling point, °F., 14.696 psia	Freezing point, °F., 14.696 psia	Freezing point, °C 101.3250 kPa (abs)	Pressure, kPa (abs)	Pressure, psia	Temperature, °F	Temperature, K
1	Methane	CH_4	16.043	−161.52	−258.69	−296.46[d]	−182.47[d]	4604.	667.8	−116.63	190.55
2	Ethane	C_2H_6	30.070	−88.58	−127.48	−297.89[d]	−182.80[d]	4880.	707.8	90.09	305.43
3	Propane	C_3H_8	44.097	−42.07	−43.67	−305.84[d]	−187.68[d]	4249.	616.3	206.01	369.82
4	*n*-Butane	C_4H_{10}	58.124	−0.49	31.10	−217.05	−138.36	3797.	550.7	305.65	425.16
5	Isobutane	C_4H_{10}	58.124	−11.81	10.90	−255.29	−159.60	3648.	529.1	274.98	408.13
6	*n*-Pentane	C_5H_{12}	72.151	36.06	96.92	−201.51	−129.73	3369.	488.6	385.7	469.6
7	Isopentane	C_5H_{12}	72.151	27.84	82.12	−255.83	−159.90	3381.	490.4	369.10	460.39
8	*n*-Hexane	C_6H_{14}	86.178	68.74	155.72	−139.58	−95.32	3012.	436.9	453.7	507.4
9	2-Methylpentane	C_6H_{14}	86.178	60.26	140.47	−244.63	−153.66	3010.	436.6	435.83	497.45
10	3-Methylpentane	C_6H_{14}	86.178	63.27	145.89	—	—	3124.	453.1	448.3	504.4
11	2,3-Dimethylbutane	C_6H_{14}	86.178	57.98	136.36	−199.38	−128.54	3127.	453.5	440.29	499.93
12	*n*-Heptane	C_7H_{16}	100.205	98.42	209.17	−131.05	−90.582	2736.	396.8	512.8	540.2
13	2-Methylhexane	C_7H_{16}	100.205	90.05	194.09	−180.89	−118.27	2734.	396.5	495.00	530.31
14	3-Methylhexane	C_7H_{16}	100.205	91.85	197.32	—	—	2814.	408.1	503.78	535.19
15	3-Ethylpentane	C_7H_{16}	100.205	93.48	200.25	−181.48	−118.60	2891.	419.3	513.48	540.57
16	2,2-Dimethylpentane	C_7H_{16}	100.205	79.19	174.54	−190.86	−123.81	2773.	402.2	477.23	520.44
17	2,4-Dimethylpentane	C_7H_{16}	100.205	80.49	176.89	−182.63	−119.24	2737.	396.9	475.95	519.73
18	3,3-Dimethylpentane	C_7H_{16}	100.205	86.06	186.91	−210.01	−134.46	2945.	427.2	505.85	536.34
19	*n*-Octane	C_8H_{18}	114.232	125.67	258.22	−70.18	−56.76	2486.	360.6	564.22	568.76
20	Diisobutyl	C_8H_{18}	114.232	109.11	228.39	−132.07	−91.200	2486.	360.6	530.44	549.99
21	Isooctane	C_8H_{18}	114.232	99.24	210.63	−161.27	−107.38	2568.	372.4	519.46	543.89
22	*n*-Nonane	C_9H_{20}	128.259	150.82	303.47	−64.28	−53.49	2288.	332.	610.68	594.56
23	*n*-Decane	$C_{10}H_{22}$	142.286	174.16	345.48	−21.36	−29.64	2099.	304.	652.1	617.4
24	Cyclopentane	C_5H_{10}	70.135	49.25	120.65	−136.91	−93.866	4502.	653.8	461.5	511.6
25	Methylcyclopentane	C_6H_{12}	84.162	71.81	161.25	−224.44	−142.46	3785.	548.9	499.35	532.73
26	Cyclohexane	C_6H_{12}	84.162	80.73	177.29	43.77	6.554	4074.	591.	536.7	553.5
27	Methylcyclohexane	C_7H_{14}	98.189	100.93	213.68	−195.87	−126.59	3472.	503.5	570.27	572.12
28	Ethene (Ethylene)	C_2H_4	28.054	−103.77	−154.62	−272.45[d]	−169.15[d]	5041.	729.8	48.58	282.35
29	Propene (Propylene)	C_3H_6	42.081	−47.72	−53.90	−301.45[d]	−185.25[d]	4600.	669.	196.9	364.85
30	Acetylene	C_2H_2	26.038	−84.88[e]	−119.[e]	−114.[d]	−80.8[d]	6139.	890.4	95.31	308.33
31	Benzene	C_6H_6	78.114	80.09	176.17	41.96	5.533	4898.	710.4	552.22	562.16
32	Toluene	C_7H_8	92.141	110.63	231.13	−138.94	−94.991	4106.	595.9	605.55	591.80
33	Ethylbenzene	C_8H_{10}	106.168	136.20	277.16	−138.91	−94.975	3609.	523.5	651.24	617.20
34	*o*-Xylene	C_8H_{10}	106.168	144.43	291.97	−13.30	−25.18	3734.	541.4	675.0	630.33
35	*m*-Xylene	C_8H_{10}	106.168	139.12	282.41	−54.12	−47.87	3536.	513.6	651.02	617.05
36	*p*-Xylene	C_8H_{10}	106.168	138.36	281.05	55.86	13.26	3511.	509.2	649.6	616.23
37	Styrene	C_8H_8	104.152	145.14	293.29	−23.10	−30.61	3999.	580.	706.0	647.6
38	Isopropylbenzene	C_9H_{12}	120.195	152.41	306.34	−140.82	−96.035	3209.	465.4	676.4	631.1
39	Methyl alcohol	CH_4O	32.042	64.54	148.1	−143.82	−97.68	8096.	1174.2	462.97	512.64
40	Ethyl alcohol	C_2H_6O	46.069	78.29	172.92	−173.4	−114.1	6383.	925.3	469.58	513.92
41	Carbon monoxide	CO	28.010	−191.49	−313.6	−340.6	−205.0[d]	3499.	507.	−220.	132.92
42	Carbon dioxide	CO_2	44.010	−78.51[e]	−109.3	—	−56.57[d]	7382.	1071.	87.9	304.19
43	Hydrogen sulfide	H_2S	34.076	−60.31	−76.6	−117.2	−85.53[d]	9005.	1306.	212.7	373.5
44	Air	N_2+O_2	28.964	−194.2	−317.6	—	—	3771.	547.	−221.3	132.4
45	Hydrogen	H_2	2.016	−252.87[v]	−423.0	−434.8	−259.2[d]	1297.	188.1	−399.8	33.2
46	Oxygen	O_2	31.999	−182.962[v]	−297.4	−361.8	−218.8[d]	5081.	736.9	−181.1	154.7
47	Nitrogen	N_2	28.013	−195.80	−320.4	−346.0	−210.0[d]	3399.	493.0	−232.4	126.1
48	Water	H_2O	18.015	100.00[v]	−212.0	32.0	0.00	22118.	3208.	705.6	647.3
49	Helium	He	4.003	−268.93	—	—	—	227.5	—	—	5.2

TABLE A.1
Physical constants of hydrocarbon [GPSA, 1-28] (*continued*)

4. Density of liquid 101.3250 kPa (abs), 15°C				4. Density of liquid 14.696 psia, 60°F			5. Density of ideal gas* 101.325 kPa (abs), 15°C			5. Density of ideal gas* 14.696 psia, 60°F			No.
Relative density 15° C/15° C[a,h]	kg/m³ *[a] (mass in vacuum)	kg/m³ *[a,c] (Apparent mass in air)	m³/kmol	lb/gal*[a] (Wt in vacuum)	lb/gal*[a,c] (Wt in air)	Gal/lb Mole*	Relative density Air = 1	Specific volume m³/kg	Volume ratio gas/ (liquid in vacuum)	Specific gravity Air = 1*	cu ft gas/lb*	cu ft gas/gal liquid*	
(0.3)[i]	(300.)[i]	(300.)[i]	(0.05)[i]	2.5[i]	2.5[i]	6.4[i]	0.5539	1.474	(442.)[i]	0.5539	23.65	59.[i]	1
0.3581[h]	357.8[h,x]	356.6[h]	0.08404[h]	2.971[h]	2.962[h]	10.12[h]	1.0382	0.7863	281.3[h]	1.0382	12.62	37.5[h]	2
0.5083[h]	507.8[h,x]	506.7[h]	0.08684[h]	4.233[h]	4.223[h]	10.42[h]	1.5225	0.5362	272.3[h]	1.5225	8.606	36.43[h]	3
0.5847[h]	584.2[h]	583.1[h]	0.09949[h]	4.872[h]	4.865[h]	11.93[h]	2.0068	0.4068	237.6[h]	2.0068	6.529	31.81[h]	4
0.5637[h]	563.2[h]	562.1[h]	0.1032[h]	4.695[h]	4.686[h]	12.38[h]	2.0068	0.4068	229.1[h]	2.0068	6.529	30.65[h]	5
0.6316	631.0	629.9	0.1143	5.261	5.251	13.71	2.4911	0.3277	206.8	2.4911	5.260	27.67	6
0.6250	624.4	623.3	0.1156	5.208	5.199	13.85	2.4911	0.3277	204.6	2.4911	5.260	27.39	7
0.6644	663.8	662.7	0.1298	5.536	5.526	15.57	2.9753	0.2744	182.1	2.9753	4.404	24.38	8
0.6583	657.7	656.6	0.1310	5.485	5.475	15.71	2.9753	0.2744	180.5	2.9753	4.404	24.15	9
0.6694	668.8	667.7	0.1289	5.577	5.568	15.45	2.9753	0.2744	183.5	2.9753	4.404	24.56	10
0.6668	666.2	665.1	0.1294	5.556	5.546	15.51	2.9753	0.2744	182.8	2.9753	4.404	24.27	11
0.6886	688.0	686.9	0.1456	5.738	5.728	17.46	3.4596	0.2360	162.4	3.4596	3.787	21.73	12
0.6835	682.8	681.7	0.1468	5.694	5.685	17.60	3.4596	0.2360	161.1	3.4596	3.787	21.57	13
0.6921	691.5	690.4	0.1449	5.767	5.757	17.38	3.4596	0.2360	163.2	3.4596	3.787	21.84	14
0.7032	702.6	701.5	0.1426	5.859	5.850	17.10	3.4596	0.2360	165.8	3.4596	3.787	22.19	15
0.6787	678.0	676.9	0.1478	5.654	5.645	17.72	3.4596	0.2360	160.0	3.4596	3.787	21.41	16
0.6777	677.1	676.0	0.1480	5.647	5.637	17.75	3.4596	0.2360	159.8	3.4596	3.787	21.39	17
0.6980	697.4	696.3	0.1437	5.816	5.807	17.23	3.4596	0.2360	164.6	3.4596	3.787	22.03	18
0.7073	706.7	705.6	0.1616	5.893	5.883	19.39	3.9439	0.2070	146.3	3.9439	3.322	19.58	19
0.6984	697.7	696.6	0.1637	5.819	5.810	19.63	3.9439	0.2070	144.4	3.9439	3.322	19.33	20
0.6966	696.0	694.9	0.1641	5.804	5.795	19.68	3.9439	0.2070	144.1	3.9439	3.322	19.28	21
0.7224	721.7	720.6	0.1777	6.017	6.008	21.32	4.4282	0.1843	133.0	4.4282	2.959	17.80	22
0.7346	733.9	732.8	0.1939	6.121	6.112	23.24	4.9125	0.1662	122.0	4.9125	2.667	16.33	23
0.7508	750.2	749.1	0.09349	6.256	6.247	11.21	2.4215	0.3371	252.9	2.4215	5.411	33.85	24
0.7541	753.4	752.3	0.1117	6.283	6.274	13.40	2.9057	0.2809	211.7	2.9057	4.509	28.33	25
0.7838	783.1	782.0	0.1075	6.531	6.522	12.89	2.9057	0.2809	220.0	2.9057	4.509	29.45	26
0.7744	773.7	772.6	0.1269	6.453	6.444	15.22	3.3900	0.2408	186.3	3.3900	3.865	24.94	27
—	—	—	—	—	—	—	0.9686	0.8428	—	0.9686	13.53	—	28
0.5231[h]	522.6[h,x]	521.5[h]	0.08069[h]	4.352[h]	4.343[h]	9.67[h]	1.4529	0.5619	293.6[h]	1.4529	9.018	39.25[h]	29
0.615[k]	—	—	—	—	—	—	0.8990	0.9081	—	0.8990	14.57	—	30
0.8850	884.2	883.1	0.08834	7.373	7.365	10.59	2.6969	0.3027	267.6	2.6969	4.858	35.82	31
0.8723	871.6	870.5	0.1057	7.268	7.260	12.68	3.1812	0.2566	223.7	3.1812	4.119	29.94	32
0.8721	871.3	870.5	0.1219	7.268	7.259	14.61	3.6655	0.2227	194.0	3.6655	3.574	25.98	33
0.8850	884.2	883.1	0.1201	7.377	7.367	14.39	3.6655	0.2227	196.9	3.6655	3.574	26.37	34
0.8691	868.3	867.2	0.1223	7.243	7.234	14.66	3.6655	0.2227	193.4	3.6655	3.574	25.89	35
0.8661	865.3	864.2	0.1227	7.218	7.209	14.71	3.6655	0.2227	192.7	3.6655	3.574	25.80	36
0.9115	910.6	909.5	0.1144	7.595	7.586	13.71	3.5959	0.2270	206.7	3.5959	3.644	27.67	37
0.8667	866.0	864.9	0.1390	7.223	7.214	16.64	4.1498	0.1967	170.4	4.1498	3.157	22.80	38
0.7967	796.0	794.9	0.04025	6.64	6.63	4.83	1.1063	0.7379	587.4	1.1063	11.84	78.6	39
0.7922	791.5	790.4	0.05820	6.62	6.61	6.96	1.5906	0.5132	406.2	1.5906	8.237	54.5	40
0.7893[m]	788.6[m]	—	0.03552[m]	6.68[m]	6.67[m]	4.19[m]	0.9671	0.8441	—	0.9671	13.55	—	41
0.8226[h]	821.9[h]	820.8[h]	0.05355[h]	6.89[h]	6.88[h]	6.38[h]	1.5195	0.5373	441.6[h]	1.5195	8.623	59.5[h]	42
0.7897[h]	789.0[h,x]	787.9[h]	0.04319[h]	6.59[h]	6.58[h]	5.17[h]	1.1765	0.6939	547.5[h]	1.1765	11.14	73.3[h]	43
0.856[m]	855.[m]	—	0.0339[m]	7.14[m]	7.13[m]	4.06[m]	1.0000	0.8163	—	1.0000	13.10	—	44
0.07106[m]	71.00[m]	—	0.02839[m]	—	—	—	0.0696	11.73	—	0.0696	188.2	—	45
1.1420[m]	1141.[m]	—	0.02804[m]	9.50[m]	9.49[m]	3.37[m]	1.1048	0.7389	—	1.1048	11.86	—	46
0.8093[m]	808.6[m]	—	0.03464[m]	6.74[m]	6.73[m]	4.16[m]	0.9672	0.8441	—	0.9672	13.55	—	47
1.000	999.1	998.0	0.01803	8.337	8.328	2.16	0.6220	1.312	1311	0.6220	21.06	175.6	48

TABLE A.1
(*continued*)

See Note No.→		6. Heating value, 15°C*			6. Heating value, 60°F*			7.	8.
		Net	Gross		Net		Gross		
No.	Compound	MJ/m³ Ideal gas, 101.3250 kPa (abs)	MJ/m³ Ideal gas, 101.3250 kPa (abs)	MJ/kg Liquid (Mass in vacuum)	Btu/cu ft, Ideal gas, 14.696 psia*,[f]	Btu/cu ft, Ideal gas, 14.696 psia*,[f]	Btu/lb liquid (wt in vacuum)	Heat of vaporization, 14.696 psia at boiling point, Btu/lb	Heat of vaporization, 101.3250 kPa (abs) at boiling point, kJ/kg	Refractive index[a], n_D 15°C
1	Methane	33.936	37.694	—	909.1	1009.7	—	219.22	509.86	—
2	Ethane	60.395	66.032	51.586[h]	1617.8	1768.8	—	210.41	489.36	1.21404[h]
3	Propane	86.456	93.972	50.008[h]	2316.1	2517.4	21513	183.05	425.73	1.21905[h]
4	*n*-Butane	112.384	121.779	49.158[h]	3010.4	3262.1	21139	165.65	385.26	1.33292[h]
5	Isobutane	112.031	121.426	49.044[h]	3001.1	3252.7	21091	157.53	366.40	—
6	*n*-Pentane	138.380	149.654	48.667	3707.5	4009.5	20928	153.59	357.22	1.36024
7	Isopentane	138.044	149.319	48.579	3698.3	4000.3	20889	147.13	342.20	1.35658
8	*n*-Hexane	164.402	177.556	48.344	4403.7	4756.1	20784	143.95	334.81	1.37746
9	2-Methylpentane	164.075	177.229	48.273	4395.8	4748.1	20757	138.67	322.52	1.37417
10	3-Methylpentane	164.188	177.341	48.300	4398.7	4751.0	20768	140.09	325.82	1.37918
11	2,3-Dimethylbutane	164.025	177.179	48.269	4391.7	4744.0	20742	136.08	316.50	1.37759
12	*n*-Heptane	190.398	205.431	48.104	5100.2	5502.9	20681	136.01	316.33	1.39017
13	2-Methylhexane	190.099	205.132	48.051	5092.1	5494.8	20658	131.59	306.06	1.38743
14	3-Methylhexane	190.243	205.276	48.082	5095.2	5497.8	20668	132.11	307.27	1.39119
15	3-Ethylpentane	190.327	205.359	48.101	5098.2	5500.9	20679	132.83	308.94	1.39594
16	2,2-Dimethylpentane	189.630	204.662	47.964	5079.4	5482.1	20620	125.13	291.03	1.38475
17	2,4-Dimethylpentane	189.803	204.836	48.000	5084.3	5487.0	20636	126.58	294.41	1.38408
18	3,3-Dimethylpentane	189.885	204.918	48.019	5085.0	5487.6	20638	127.21	295.87	1.39342
19	*n*-Octane	216.374	233.286	47.919	5796.7	6249.7	20604	129.53	301.26	1.39981
20	Diisobutyl	215.797	232.709	47.832	5781.3	6234.3	20564	122.8	285.69	1.39488
21	Isooctane	215.732	232.644	47.843	5779.8	6232.8	20570	116.71	271.44	1.39392
22	*n*-Nonane	242.398	261.189	47.783	6493.3	6996.6	20544	123.76	288.82	1.40773
23	*n*-Decane	268.396	289.066	47.670	7188.6	7742.3	20494	118.68	276.06	1.41411
24	Cyclopentane	131.114	140.509	46.955	3512.0	3763.7	20188	167.34	389.20	1.40927
25	Methylcyclopentane	156.757	168.032	46.825	4198.4	4500.4	20130	147.83	345.51	1.41240
26	Cyclohexane	156.034	167.308	46.606	4178.8	4480.8	20035	153.0	355.95	1.42892
27	Methylcyclohexane	181.567	194.720	46.525	4862.8	5215.2	20001	136.3	317.03	1.42566
28	Ethene (Ethylene)	55.942	59.700	—	1499.0	1599.7	—	207.57	482.77	—
29	Propene (Propylene)	81.482	87.119	—	2182.7	2333.7	—	188.18	437.68	—
30	Acetylene	53.098	54.978	—	1422.4	1472.8	—	—	—	—
31	Benzene	134.055	139.692	41.843	3590.7	3741.7	17992	169.31	393.32	1.50432
32	Toluene	159.534	167.050	42.450	4273.3	4474.7	18252	154.84	360.14	1.49973
33	Ethylbenzene	185.555	194.950	43.014	4970.0	5221.7	18494	144.0	334.98	1.49856
34	*o*-Xylene	185.092	194.487	42.900	4958.3	5210.0	18445	149.1	346.80	1.50795
35	*m*-Xylene	185.020	194.415	42.891	4956.8	5208.5	18441	147.2	342.47	1.49980
36	*p*-Xylene	185.050	194.445	42.901	4956.9	5208.5	18445	144.52	338.92	1.49839
37	Styrene	180.290	187.806	42.213	4828.7	5030.0	18150	(151.)	(351.23)	1.54969
38	Isopropylbenzene	211.328	222.603	43.410	5661.4	5963.4	18665	134.3	312.25	1.49400
39	Methyl alcohol	28.601	32.360	22.685	—	—	9760	473.	1075.97	1.33028
40	Ethyl alcohol	54.062	59.699	29.707	—	—	12780	367.	840.54	1.36345
41	Carbon monoxide	11.959	11.959	—	—	321.	—	92.7	215.70	1.00036
42	Carbon dioxide	0	0	—	—	—	—	238.2[n]	573.27[n]	1.00049
43	Hydrogen sulfide	21.912	23.791	—	588.	637.	—	235.6	548.01	1.00061
44	Air	—	—	—	—	—	—	92.	214.	—
45	Hydrogen	10.230	12.091	—	274.	324.	—	193.9	450.4	1.00013
46	Oxygen	—	—	—	—	—	—	91.6	213.	1.00027
47	Nitrogen	—	—	—	—	—	—	87.8	204.	1.00028
48	Water	0	1.879	0	—	—	—	970.3	2257.	1.33347
49	Helium	—	—	—	—	—	—	—	—	1.00003

TABLE A.1
Physical constants of hydrocarbon [GPSA, 1-28] (*continued*)

9.	10.	11.	Flammability limits, vol % in air mixture		ASTM octane number		12. Specific heat capacity 14.696 psia 60°F C_P Btu/(lb°F)		12. Specific heat capacity 101.3250 kPa(abs), 15°C C_P kJ/(kg°C)		
Temperature coefficient of density, at 15°C[a] −1/°C	Pitzer acentric factor, ω	Compressibility factor of real gas, Z 101.3250 kPa (abs), 15°C	Lower	Higher	Motor method D-357	Research method D-908	Ideal gas	Liquid	Ideal gas	Liquid	No.
—	0.0126	0.9981	5.0	15.0	—	—	0.5266	—	2.204	—	1
—	0.0978	0.9915	2.9	13.0	+.05[f]	+1.6[j,f]	0.4097	0.9256	1.706	3.807	2
0.00274[h]	0.1541	0.9810	2.1	9.5	97.1	+1.8[j,f]	0.3881	0.5920	1.625	2.476	3
0.00211[h]	0.2015	0.9641	1.8	8.4	89.6[j]	93.8[j]	0.3867	0.5636	1.652	2.366	4
0.00214[h]	0.1840	0.9665	1.8	8.4	97.6	+0.10[j,f]	0.3872	0.5695	1.616	2.366	5
0.00157	0.2524	0.942†	1.4	8.3	62.6[j]	61.7[j]	0.3883	0.5441	1.622	2.292	6
0.00162	0.2286	0.948†	1.4	(8.3)	90.3	92.3	0.3827	0.5353	1.600	2.239	7
0.00135	0.2998	0.910†	1.2	7.7	26.0	24.8	0.3864	0.5332	1.613	2.231	8
0.00140	0.2784	—	1.2	(7.7)	73.5	73.4	0.3872	0.5264	1.602	2.205	9
0.00135	0.2741	—	(1.2)	(7.7)	74.3	74.5	0.3815	0.507	1.578	2.170	10
0.00135	0.2475	—	(1.2)	(7.7)	94.3	+0.3[f]	0.378	0.5127	1.566	2.146	11
0.00124	0.3494	0.852†	1.0	7.0	0.0	0.0	0.3875	0.5283	1.606	2.209	12
0.00122	0.3303	—	(1.0)	(7.0)	46.4	42.4	(0.390)	0.5223	1.595	2.183	13
0.00124	0.3239	—	(1.0)	(7.0)	55.8	52.0	(0.390)	0.511	1.584	2.137	14
0.00126	0.3107	—	(1.0)	(7.0)	69.3	65.0	(0.390)	0.5145	1.613	2.150	15
0.00130	0.2876	—	(1.0)	(7.0)	95.6	92.8	(0.395)	0.5171	1.613	2.161	16
0.00130	0.3031	—	(1.0)	(7.0)	83.8	83.1	0.3906	0.5247	1.651	2.193	17
0.00117	0.2681	—	(1.0)	(7.0)	86.6	80.8	(0.395)	0.502	1.603	2.099	18
0.00112	0.3981	0.783†	0.96	—	—	—	(0.3876)	0.5239	1.601	2.191	19
0.00117	0.3564	—	(0.98)	—	55.7	55.2	(0.373)	0.5114	1.573	2.138	20
0.00117	0.3041	—	1.0	—	100.	100.	0.3758	0.4892	1.599	2.049	21
0.00113	0.4452	—	0.87[s]	2.9	—	—	0.3840	0.5228	1.598	2.184	22
0.00099	0.4904	—	0.78[s]	2.6	—	—	0.3835	0.5208	1.595	2.179	23
0.00126	0.1945	0.949†	(1.4)	—	84.9[j]	+0.1[f]	0.2712	0.4216	1.133	1.763	24
0.00128	0.2308	—	(1.2)	8.35	80.0	91.3	0.3010	0.4407	1.258	1.843	25
0.00122	0.2098	—	1.3	7.8	77.2	83.0	0.2900	0.4332	1.211	1.811	26
0.00113	0.2364	—	1.2	—	71.1	74.8	0.3170	0.4397	1.324	1.839	27
—	0.0869	0.9938	2.7	34.0	75.6	+0.03[f]	0.3622	—	1.514	—	28
0.00340[h]	0.1443	0.9844	2.0	10.0	84.9	+0.2[f]	0.3541	0.585	1.480	2.443	29
—	0.1893	0.9925	2.5	80.	—	—	0.3966	—	1.659	—	30
0.00119	0.2095	0.929†	1.3[g]	7.9[g]	+2.8[f]	—	0.2429	0.4098	1.014	1.715	31
0.00108	0.2633	0.903†	1.2[g]	7.1[g]	+0.3[f]	+5.8[f]	0.2598	0.4012	1.085	1.677	32
0.00097	0.3031	—	0.99[g]	6.7[g]	97.9	+0.8[f]	0.2795	0.4114	1.168	1.721	33
0.00099	0.3113	—	1.1[g]	6.4[g]	100.	—	0.2914	0.4418	1.218	1.741	34
0.00097	0.3257	—	1.1[g]	6.4[g]	+2.8[f]	+4.0[f]	0.2782	0.4045	1.163[i]	1.696	35
0.00097	0.3214	—	1.1[g]	6.6[g]	+1.2[f]	+3.4[f]	0.2769	0.4083	1.157	1.708	36
0.00103	0.1997	—	1.1	6.1	+0.2[f]	> +3.[f]	0.2711	0.4122	1.133	1.724	37
0.00097	0.3260	—	0.88[g]	6.5[g]	99.3	+2.1[f]	0.2917	(0.414)	1.219	1.732	38
0.00117	0.5648	—	6.72	36.50	—	—	0.3231[v]	0.594	1.352	2.484	39
0.00107	0.6608	—	3.28	18.95	—	—	0.3323[v]	0.562	1.389	2.348	40
—	0.0442	0.9995	12.50	74.20	—	—	0.2484	—	1.040	—	41
—	0.2667	0.9943	—	—	—	—	0.1991	—	0.8330	—	42
—	0.0920	0.9903	4.30	45.50	—	—	0.238	—	0.9960	2.08	43
—	—	0.9996	—	—	—	—	0.2400	—	1.005	—	44
—	−0.219[w]	1.0006	4.00	74.20	—	—	3.408	—	14.24	—	45
—	0.0200	0.9993	—	—	—	—	0.2188	—	0.9166	—	46
—	0.0372	0.9997	—	—	—	—	0.2482	—	1.040	—	47
0.00014	0.3434	—	—	—	—	—	0.4446	1.0009	1.862	4.191	48
—	0	1.0005	—	—	—	—	—	—	5.192	—	49

NOTES

a Air saturated liquid.
b Absolute values from weights in vacuum.
c The apparent values from weight in air are shown for users' convenience and compliance with ASTM-IP Petroleum Measurement Tables. In the United States and Great Britain, all commercial weights are required by law to be weights in air. All other mass data are on an absolute mass (weight in vacuum) basis.
d At saturation pressure (triple point).
e Sublimation point.
f The + sign and number following signify the ASTM octane number corresponding to that of 2,2,4-trimethylpentane with the indicated number of cm^3 of TEL added per gal.
g Determined at 100°C.
h Saturation pressure and 15°C.
i Apparent value at 15°C.
j Average value from octane numbers of more than one sample.
k Relative density (specific gravity), 48.3°C/15°C (sublimation point; solid C_2H_4/liquid H_2O).
m Densities of liquid at the boiling point.
n Heat of sublimation.
s Extrapolated to room temperature from higher temperature.
t Gross calorific values shown for ideal gas volumes are not direct conversions of each other using only the gas volume per liquid volume value shown herein. The values differ by the heat of vaporization to ideal gas at 288.15 K.
v Fixed points on the 1968 International Practical Temperature Scale (IPTS-68).
w Value for normal hydrogen (25% para, 75% ortho). The value for equilibrium mixture of para and ortho is −0.218; however in most correlations, 0 is used.
x Densities at the boiling point in kg/m^3 for: Ethane, 546.4; propane, 581.0; propene, 608.8; hydrogen sulfide, 960.; sulfur dioxide, 1462.; ammonia, 681.6; hydrogen chloride, 1192.
* Calculated values.
() Estimated values.
† Values are estimated using 2nd virial coefficients.

1. Molecular mass (M) is based on the following atomic weights: C = 12.011; H = 1.008; O = 15.9995; N = 14.0067; S = 32.06; Cl = 35.453.
2. Boiling point—the temperature at equilibrium between the liquid and vapor phases at 101.3250 kPa (abs).
3. Freezing point—the temperature at equilibrium between the crystalline phase and the air saturated liquid at 101.3250 kPa (abs).

4. All values for the density and molar volume of liquids refer to the air saturated liquid at 101.3250 kPa (abs), except when the boiling point is less than 15°C. In such cases, the density and molar volume are given for the liquid in equilibrium with its vapor at 15°C.

The relative density 15°C is defined as

$$\frac{\rho \text{ (liquid, 15°C)}}{\rho \text{ (water, 15°C)}}$$

The density of water at 15°C is taken as 999.10 kg/m^3.

The apparent density in air, ρ (mass in air), is related to the density in vacuum, ρ (mass in vacuum) by

$$\rho \text{ (mass in air)} = [\rho \text{ (mass in vacuum)} - \rho \text{ (air)}]\frac{\rho \text{ (brass)}}{\rho \text{ (brass)} - \rho \text{ (air)}}$$

"Mass in air" is the ratio of gravitational force on the object to the force of a standard brass weight, with both objects immersed in air.

The density of air at 15°C and 101.3250 kPa (abs) is taken as 1.22 kg/m^3, and the density of brass as 8700 kg/m^3.

The molar volume is related to density by

$$V \text{ (m}^3\text{/kmol)} = \frac{M}{\rho \text{ (kg/m}^3\text{)}}$$

5. The density of an ideal gas relative to air is M(gas)/M(air).

The molecular mass of air is taken as 28.964.

The specific volume of an ideal gas is

$$V = \frac{RT}{MP}$$

The volume ratio is V (ideal gas)/V (liquid in vacuum).

6. The heating value is the negative of the enthalpy of combustion ($-\Delta H_c^o$) of a gas or liquid in its standard state at 15°C to give combustion products in their standard states, all at 101.3250 kPa (abs). For a compound where the formula is $C_nH_mO_hS_jN_k$, the combustion reaction is

$$C_nH_mO_hS_jN_k \text{ (s, l, or g)} + \left(n + \frac{m}{4} - \frac{h}{2} + j\right) O_{2(g)} - nCO_2 \text{ (g)}$$
$$+ \frac{m}{2}H_2O \text{ (g or l)} + \frac{k}{2}N_2 \text{ (g)} + jSO_2 \text{ (g)}$$

For the gross heating value, the water produced by the combustion is in the liquid form, and for the net heating value, the water is in the gas state.

The enthalpies of combustion at 15°C were calculated from those at 25°C, as reported in the references cited, by

$$\Delta H_c^o \text{ (15°C)} = \Delta H_c^o \text{ (25°C)} - 10\Delta C_p^o,$$

where

$$\Delta C_p^o = nC_p^o \text{ (CO}_2\text{,g)} + \frac{m}{2}C_p^o \text{ (H}_2\text{O, g or l)} + \frac{k}{2}C_p^o \text{ (N}_2\text{, g)}$$
$$+ jC_p^o \text{ (SO}_2\text{, g)} - C_p^o \text{ (}C_nH_mO_hS_jN_k\text{, s, l, or g)}$$
$$- \left(n + \frac{m}{4} - \frac{h}{2} + j\right) C_p^o \text{ (O}_2\text{, g) at 25°C}$$

$$\Delta H_c^o \text{ (MJ/m}^3\text{)} = \Delta H_c^o \text{ (MJ/kg)}/\rho \text{ (kg/m}^3\text{, vacuum)}.$$

The above equations apply to the combustion of an (initially) "bone-dry" gas. The heat of combustion of 1 m^3 of an ideal gas, saturated with water vapor, is

$$\Delta H_c^o \text{ (g, sat)(MJ/m}^3\text{)} = 0.98322\ \Delta H_c^o \text{ (g)(MJ/m}^3\text{)}$$

The vapor pressure of water at 15°C is 1.70 kPa (abs). The gross heat of combustion of 1 m^3 of gas, saturated with water vapor for which all of the water is condensed to liquid in the final products, is

$$\Delta H_c^o \text{ (g, sat)(MJ/m}^3\text{)} = 0.98322\ \Delta H_c^o \text{ (g)(MJ/m}^3\text{)} - 0.0315$$

The heat of vaporization of water to an ideal gas at 15°C is 44.43 kJ/mol.

7. The heat of vaporization is the enthalpy of the saturated vapor at the boiling point at 101.3250 kPa (abs) minus the enthalpy of the liquid at the same condition.

8. The refractive index reported refers to the liquid or gas and is measured for light of wavelength corresponding to the sodium D-line (589.26 nm).

9. The temperature coefficient of density is related to the expansion coefficient by

$$\frac{1}{\rho}\left(\frac{\partial \rho}{\partial T}\right)_P = -\frac{1}{V}\left(\frac{\partial V}{\partial T}\right)_P \qquad \text{in units of } -1/°C$$

10. Pitzer acentric factor ω

$$\omega = -\log_{10}\left(\frac{P}{P_c}\right) - 1 \text{ at } T_r = \frac{T}{T_c} = 0.7$$

11. The compressibility factor of the real gas, Z, is

$$Z = \frac{PV}{RT}$$

12. The specific heat capacity of the ideal gas was calculated from the constant pressure molar heat capacity reported in the references cited. These were cal-

culated from the molecular partition functions. This quantity is independent of pressure. The specific heat capacities of liquids are derived from experimental measurements. For liquids boiling below 15°C, the values given are C_s/M, where C_s is the molar heat capacity of the liquid under saturated vapor pressure conditions.

TABLE A.2
Conversion factors, symbols, and prefixes

Area (L^2): A

1 ft^2	$=9.2903 \times 10^{-2}$ m^2	$=9.2903 \times 10^{2}$ cm^2	$=1.44 \times 10^{2}$ in^2
	$=2.2957 \times 10^{-5}$ acres	$=3.5870 \times 10^{-8}$ $miles^2$	

Density (M/L^3): $\rho = (PM)/(ZnRT)$

1 lb/ft^3	$=1.6018 \times 10$ kg/m^3	$=5.7870 \times 10^{-4}$ lb/in^3	$=1.3368 \times 10^{-1}$ lb/gal
	$=1.6018 \times 10^{-2}$ g/cm^3		$=5.6146$ lb/bbl

Distance (L):

1 ft	$=3.048 \times 10^{-1}$ m	$=3.048 \times 10$ cm	$=1.2 \times 10$ in.
	$=1.8939 \times 10^{-4}$ miles	$=3.048 \times 10^{-4}$ km	$=3.048 \times 10^{9}$ Å

Force (ML/T^2): $F = ma/g_c$

1 lb_f	$=4.4482$ N (newton)	$=3.2174 \times 10$ poundal	$=4.4482 \times 10^{5}$ dyn

$$\text{Newton} = \frac{kg \cdot m}{s^2}$$

$a = g = 9.80665\ m/s^2 = 32.17\ ft^2/s$ at sea level

$$g_c = 1\frac{kg \cdot m}{s^2 \cdot N} = 1\frac{g \cdot cm}{s^2 \cdot dyn} = 9.81\frac{m}{s^2}$$

$$= 32.17\frac{lb_m ft}{s^2 \cdot lb_f} = 1\frac{lb_m ft}{s^2 \cdot poundal} = 1\frac{slug \cdot ft}{s^2 \cdot lb_f}$$

Flow rate (L^3/T): Q

1 ft^3/s	$=2.8317 \times 10^{-2}$ m^3/s	$=2.8317 \times 10^{4}$ cm^3/s
	$=8.64 \times 10^{4}$ ft^3/day	$=8.64 \times 10^{-2}$ MMcf/day
	$=8.64 \times 10$ Mcf/day	$=1.5388 \times 10^{4}$ bbl/day
	$=6.4632 \times 10^{5}$ gal/day	$=448.9$ gal/min

Gas constant: R

$$R = 10.73\frac{psi \cdot ft^3}{lb\ mol \cdot °R} \quad = 8.314\frac{m^3 \cdot kPa}{kg \cdot mol \cdot K} \quad = 1545\frac{ft \cdot lb_f}{lb\ mol \cdot °R} \quad = 82.06\frac{atm \cdot cm^3}{mol \cdot K}$$

$$= 0.08206\frac{liter \cdot atm}{mol \cdot K} \quad = 1.987\frac{cal}{mol \cdot K} \quad = 1.987\frac{Btu}{lb\ mol \cdot °R} \quad = 0.729\frac{ft^3 \cdot atm}{lb\ mol \cdot °R}$$

TABLE A.2
(continued)

Mass (M):

1 lb_m	$=4.5359 \times 10^{-1}$ kg	$=4.5359 \times 10^{2}$ g	$=3.1081 \times 10^{-2}$ slug
	$=7 \times 10^{3}$ grain	$=1.6 \times 10$ ounce	$=5.0 \times 10^{-4}$ short ton
	$=4.536 \times 10^{-4}$ metric ton		$=4.4643 \times 10^{-4}$ long ton

Permeability (L^2): k

1 md	$=0.9869$ mD	$=1.0 \times 10^{-3}$ darcy	$=1.0623 \times 10^{-14}$ ft^2
	$=9.8692 \times 10^{-12}$ cm^2	$=9.8692 \times 10^{-16}$ m^2	

Power (ML^2/T^3):

1 hp (horsepower)	$=0.7457$ kW	$=745.7$ J/s	$=1.7823 \times 10^{2}$ cal/s
	$=5.5 \times 10^{2}\frac{ft \cdot lb_f}{s}$	$=3.3 \times 10^{4}\frac{ft \cdot lb_f}{min}$	$=2.5436 \times 10^{3}$ Btu/hr

Pressure (M/LT^2): $P = F/A$ (pascal = N/m^2)

1 psi (lb_f/in^2)	$=6.8948$ kPa	$=6.8948 \times 10^{3}$ pascal	$=6.8948 \times 10^{4}$ dyn/cm^2
	$=6.8046 \times 10^{-2}$ atm	$=2.306$ in Hg (32°F)	$=2.2523$ ft water (39.1°F)
	$=144$ psf (lb_f/ft^2)	$=6.893 \times 10^{-2}$ bar	$=5.172 \times 10$ torr (mm Hg)

Specific heat ($ML^2/T^2 \cdot$ deg): C_P or C_V

$$1\frac{Btu}{lb \cdot °F} \quad = 4.184\frac{kJ}{kg \cdot K} \quad = 1\frac{cal}{g \cdot °C}$$

Thermal conductivity ($ML/T^3 \cdot$ deg): k

$$1\frac{Btu}{hr \cdot ft^2 \cdot (°F/ft)} \quad = 1.730\frac{W}{m^2 \cdot (K/m)} \quad = 4.135 \times 10^{-3}\frac{cal}{s \cdot cm^2 \cdot (°C/cm)}$$

Time (T): t

1 hr	$=3600$ s	$=60$ min	$=4.1667 \times 10^{-2}$ day
	$=1.3699 \times 10^{-3}$ month		$=1.1416 \times 10^{-4}$ year

Viscosity (M/LT): $\mu = \tau g_c / (du/dy)$

1 cp	$=1 \times 10^{-3}$ Pa · s	$=1.0 \times 10^{-2}$ poise $\left(\frac{g}{cm \cdot s}\right)$	
	$=1.0 \times 10^{-3}$ Poiseuille $\left(\frac{kg}{m \cdot s}\right)$		$=1.0 \times 10^{3}\mu$Pa · s
	$=6.7197 \times 10^{-4}\frac{lb_m}{ft \cdot s}$	$=2.0885 \times 10^{-5}\frac{slug}{ft \cdot s}$	

Work, Energy, Heat:

1 Btu	$=1.055$ kJ	$=1.055 \times 10^{3}$ J	$=7.78 \times 10^{2}$ ft · lb_f
	$=2.52 \times 10^{2}$ cal	$=1.0759 \times 10^{2}$ kg · m	$=1.04125 \times 10$ liter · atm
	$=3.909 \times 10^{-4}$ hp · hr	$=2.9308 \times 10^{-4}$ kW · hr	

TABLE A.2
Conversion factors, symbols, and prefixes (*continued*)

Volume (L^3):

1 ft^3 = 2.832×10^{-2} m^3 = 7.481 U.S. gal = 6.23 British gal
= 28.316 liter = 0.1781 bbl

1 U.S. gal = 8.34 lb H_2O = 3.785 liter

1 British gal = 10 lb H_2O

Greek alphabet:

Alpha	A	α	Nu	N	ν
Beta	B	β	Xi	Ξ	ξ
Gamma	Γ	γ	Omicron	O	o
Delta	Δ	δ	Pi	Π	π
Epsilon	E	ϵ	Rho	P	ρ
Zeta	Z	ζ	Sigma	Σ	σ
Eta	H	η	Tau	T	τ
Theta	Θ	θ	Upsilon	Υ	υ
Iota	I	ι	Phi	Φ	ϕ
Kappa	K	κ	Chi	X	χ
Lambda	Λ	λ	Psi	Ψ	ψ
Mu	M	μ	Omega	Ω	ω

SI prefixes:

Factor	Prefix name	Symbol
10^{12}	tera	T
10^{9}	giga	G
10^{6}	mega	M
10^{3}	kilo	k
10^{-3}	milli	m
10^{-6}	micro	μ
10^{-9}	nano	n
10^{-12}	pico	p

APPENDIX B

COMPUTER PROGRAMS FOR CALCULATING STATIC AND FLOWING BOTTOMHOLE PRESSURES

```
1.C  THIS PROGRAM DETERMINES THE STATIC OR FLOWING BOTTOM HOLE
2.C  PRESSURE OF A WELL BY A SUCCESSIVE SUBSTITUTION METHOD. A
3.C  SUBROUTINE CALCULATES THE COMPRESSIBILITY FACTOR BY THE
4.C  METHOD OF YARBOROUGH & HALL (ref 4-19).
5.C
6.C  VARIABLES USED IN PROGRAM:
7.C       D      =  diameter of well, inch.
8.C       DH     =  section of well, ft.
9.C       DTDH   =  temperature gradient, R/ft.
10.C      ERR    =  tolerance.
11.C      FLOW   =  0.000667*(Q*Tav*Zav)**2/(d**5)*(EXP(s)-1)*f.
12.C      FM     =  Moody friction factor.
13.C      G      =  gas gravity.
14.C      FLAG   =  0: calculate gas gravity from given composition,
```

```
C                 1: given gas gravity.
C       H       =  depth of well, ft.
C       INJCT   =  0: for gas production,
C                  1: for gas injection.
C       IH      =  number of sections.
C       MW(I)   =  molecular weight of component i, lb/lb mole.
C       P(I)    =  pressure, psia.
C       PAV     =  average pressure, psia.
C       PIP1    =  iterating value of pressure, psia
C       PSEUPC  =  pseudo-critical pressure, psia.
C       PW      =  wellhead pressure, psia.
C       Q       =  flow rate, Mcf/D.
C       S       =  0.03754*G*H/(TAV*ZAV).
C       T(I)    =  temperature, R.
C       TAV     =  average temperature, R.
C       TB      =  bottom hole temperature, R.
C       TSEUTC  =  pseudo-critical temperature, R.
C       TW      =  wellhead temperature, R.
C       X(I)    =  mole fraction of component i.
C       Z(I)    =  z-factor.
C       ZAV     =  average z-factor.
C
C  COMPONENT NUMBERS:
C       1 = HYDROGEN SULFIDE, H2S
C       2 = CARBON DIOXIDE,   CO2
C       3 = NITROGEN,          N2
C       4 = METHANE,           C1
C       5 = ETHENE,            C2
C       6 = PROPANE,           C3
C       7 = I-BUTANE,         i-C4
C       8 = N-BUTANE,         n-C4
C       9 = I-PENTANE,        i-C5
C      10 = N-PENTANE,        n-C5
C      11 = HEXANE,           C6
C      12 = HEPTANE PLUS,     C7+
C
       PROGRAM BHP
       IMPLICIT REAL*8 (A-H, O-Z)
       DIMENSION H(100), T(100), P(100), Z(100)
       INTEGER FLAG
C
       COMMON/C1/FLAG, IH, INJCT, G, HIGH, PW, TW, TB, Q, D, ERR
       COMMON/C2/X(12)
C
C .... READ IN DATA
C
       CALL DATAIN
C
C .... CALCULATE PSEUDO CRITICAL VALUES
C
```



```
       IF (FLAG.EQ.0) THEN
           CALL GASGRA (G,PSEUPC,PSEUTC)
       ELSE
          CALL PSEUDO(G,X(1),X(2),X(3),PSEUPC,PSEUTC)
       ENDIF
       DTDH = (TB-TW)/HIGH
       DH   = HIGH/IH
C
C .... CALCULATE MOODY FRICTION FACTOR ASSUMING TURBULENCE
C
       IF(D.LE.4.277) FM = 0.0175/(D**0.224)
       IF(D.GT.4.277) FM = 0.01603/(D**0.164)
C
         H(1) = 0.0
         T(1) = TW
         P(1) = PW
C
C .... START ITERATION FOR EVERY SECTIONS FROM WELLHEAD
C
       DO 10 I = 1, IH
         H(I+1) = H(I) + DH
         T(I+1) = T(I) + DH*DTDH
         P(I+1) = P(I)
         TAV    = (T(I)+T(I+1))/2.0
 11      PAV    = (P(I)+P(I+1))/2.0
         CALL ZFAC(PAV, TAV, PSEUPC, PSEUTC, ZAV)
         S      = 0.03754*G*DH/(TAV*ZAV)
         FLOW   = 6.67E-4*(Q*TAV*ZAV)**2/(D**5)*(DEXP(S)-1.0)*FM
         IF(INJCT.EQ.1) FLOW = - FLOW
         PIP1   = DSQRT(P(I)*P(I)*DEXP(S) + FLOW)
         IF(DABS((PIP1-P(I+1))/PIP1).LE.ERR) THEN
           P(I+1) = PIP1
           GOTO 10
         ELSE
           P(I+1) = PIP1
           GOTO 11
         ENDIF
 10    CONTINUE
C
       OPEN(60,FILE='OUT.DAT')
       WRITE( *,*)
      & ' No.    DEPTH(ft)     Temp(R)     Pres(psia)     Z-factor'
       WRITE(60,*)
      & ' No .   DEPTH(ft)     Temp(R)     Pres(psia)     Z-factor'
       DO 20 I = 1, IH+1
         CALL ZFAC(P(I), T(I), PSEUPC, PSEUTC, Z(I))
         WRITE( *,601) I, H(I), T(I), P(I), Z(I)
         WRITE(60,601) I, H(I), T(I), P(I), Z(I)
 601   FORMAT(I3, 3(3X,F10.2), 5X, F8.5)
 20    CONTINUE
```

```
115.C
116.       END
117.C
118.C .... SUBROUTINE DATAIN READ IN DATA
119.C
120.       SUBROUTINE DATAIN
121.         DIMENSION ITEM (3),TERM(4:11)
122.       DIMENSION TERM2(12)
123.         CHARACTER*57 TITLE (11),AAA*72,BBB*72
124.       CHARACTER*57 TITLE2(12)
125.         IMPLICIT REAL*8(A-H,O-Z)
126.C
127.       COMMON/C1/ ITEM, TERM
128.       COMMON/C2/ TERM2
129.C
130. 1     OPEN(20,FILE='INPUT.DAT')
131.         READ(20,'(A72)') AAA
132.         READ(20,'(A72)') BBB
133.         READ(20,'(A57,I15)')     (TITLE(K),ITEM(K),K=1,3)
134.         READ(20,'(A57,D15.6)')   (TITLE(K),TERM(K),K=4,11)
135.         CLOSE(20)
136.         OPEN(20,FILE='INPUT.DAT')
137.C
138.         M=6
139.10       WRITE(*,'(//)')
140.         WRITE(M,'(A72)') AAA
141.         WRITE(M,'(A72)') BBB
142.         WRITE(M,'(A57,I15)')     (TITLE(K),ITEM(K),K=1,3)
143.         WRITE(M,'(A57,D15.6)')   (TITLE(K),TERM(K),K=4,11)
144.         WRITE(M,'(A72)') BBB
145.         IF(M.EQ.20) GOTO 11
146.         WRITE(*,'(/,''          Enter the number of an item to change'',
147.     &   ''it or [ 0 ] to continue'',//)')
148.         WRITE(*,'(38X)')
149.         READ(*,*) IASR
150.C
151.         IF(IASR.EQ.0) THEN
152.             M=20
153.               GOTO 10
154.       ELSE
155.         IF(IASR.LT.0 .OR. IASR.GT.11) THEN
156.          WRITE(*,'(/,'' WRONG INPUT ! '',//)')
157.          GOTO 1
158.           ENDIF
159.       ENDIF
160.C
161.         WRITE(*,'(A57,3X)') TITLE(IASR)
162.         IF(IASR.LE.3) READ(*,*) ITEM(IASR)
163.         IF(IASR.GE.4) READ(*,*) TERM(IASR)
164.         GOTO 10
```



```
165.C
166. 11    IF(ITEM(1).EQ.1) GOTO 999
167.C
168.C .... READ IN COMPOSITIONAL DATA
169.C
170. 2     OPEN(30,FILE='COMP.DAT')
171.         READ(30,'(A72)') AAA
172.         READ(30,'(A72)') BBB
173.         READ(30,'(A57,D15.6)') (TITLE2(K),TERM2(K),K=1,12)
174.         CLOSE(30)
175.         OPEN(30,FILE='COMP.DAT')
176.C
177.         M=6
178. 12    WRITE(*,'(//)')
179.         WRITE(M,'(A72)') AAA
180.         WRITE(M,'(A72)') BBB
181.         WRITE(M,'(A57,D15.6)') (TITLE2(K),TERM2 (K),K=1,12)
182.         WRITE(M,'(A72)') BBB
183.         IF(M.EQ.30) GOTO 13
184.         WRITE(*,'(/,''          Enter the number of an item to change '',
185.      *  ''it or [ 0 ] to continue'',//)')
186.         WRITE(*,'(38X)')
187.         READ(*,*) IASR
188.C
189.         IF(IASR.EQ.0) THEN
190.               M=30
191.               GOTO 12
192.       ELSE
193.         IF(IASR.LT.0 .OR. IASR.GT.12) THEN
194.          WRITE(*,'(/,'' WRONG COMPOSITION INPUT ! '',//)')
195.          GOTO 2
196.           ENDIF
197.       ENDIF
198.C
199.         WRITE(*,'(A57,3X)') TITLE2(IASR)
200.       READ(*,*) TERM2(IASR)
201.         GOTO 12
202.C
203. 13    SUM = 0.0
204.       DO 100 I = 1, 12
205. 100       SUM = SUM + TERM2(I)
206.       WRITE(*,*) ' TOTAL COMPOSITIONS IS ',   SUM
207.       WRITE(*,*) ' ----------  ENTER 0/1 FOR CONTINUE/STOP ----------  '
208.       WRITE(*,'(38X)')
209.       READ(*,'(I1)') INDEX
210.C
211.       IF(INDEX.EQ.1) THEN
212.         STOP
213.       ELSE
214.         DO 101  I = 1, 12
```

```
      TERM2(I) = TERM2(I)/SUM
      WRITE(*,*) ' -------- Compositions have been normalized ------'
    ENDIF
C
999 RETURN
    END
C
C .... SUBROUTINE GASGRA CALCULATE GAS GRAVITY AND PSEUDO-CRITICAL
C      PROPERTIES FROM GIVEN COMPOSITIONAL DATA
C
C .... VARIABLES:
C      AWA     = X(H2S) + X(CO2).
C      CWA     = Wichert & Aziz correlation factor.
C      PC(I)   = critical pressure of component i, psia.
C      PCMA    = molar average critical pressure, psia.
C      TC(I)   = critical temperature of component i, R.
C      TCMA    = molar average critical temperature, R.
C
      SUBROUTINE GASGRA (G,PSEUTC, PSEUTC)
C
      IMPLICIT REAL*8 (A-H,O-Z)
      REAL*8 MW
      COMMON/C2/X(12)
      DIMENSION MW(12), PC(12), TC(12)
C
      DATA MW /   34.08,   44.01,   28.01,   16.04,   30.07,   44.10,
     &            58.12,   58.12,   72.15,   72.15,   86.18,  128.02 /
      DATA PC / 1306.00, 1073.00,  492.00,  673.10,  708.30,  617.40,
     &           529.10,  550.70,  483.00,  489.50,  431.60,  396.90 /
      DATA TC /  672.40,  547.70,  226.90,  343.30,  549.80,  666.00,
     &           734.70,  765.30,  829.80,  845.60,  913.60,  975.80 /
C
C .... Calculate: Gas Gravity (G),
C                 Molar Average Critical Properties: TCMA & PCMA
C
        G    = 0.0
        TCMA = 0.0
        PCMA = 0.0
      DO 10 I = 1, 12
        G    = G + MW (I)*X(I)/28.966
        TCMA = TCMA + TC(I)*X(I)
        PCMA = PCMA + PC(I)*X(I)
10    CONTINUE
C
C .... Calculate Wichert & Aziz Correlation Factor of Sour Gases
C
      AWA    = X(1) + X(2)
      CWA    = 120.0*(AWA**0.9-AWA**1.6) + 15.0*(DSQRT(X(1))-X(1)**4)
      PSEUTC = TCMA - CWA
      PSEUPC = PCMA*PSEUTC/(TCMA + X(1)*(1.0-X(1))*CWA)
```



```
C
      RETURN
      END
C
C .... SUBROUTINE PSEUDO CALCULATES PSEUDO-CRITICAL VALUES FROM
C      GIVEN GAS GRAVITY WITH CORRECTION OF X(H2S), X(CO2), X(N2)
C
C .... VARIABLES:
C        XH2S =  X(H2S)
C        XCO2 =  X(CO2)
C        XN2  =  X(N2)
C
      SUBROUTINE PSEUDO(G, XH2S, XCO2, XN2, PSEUPC, PSEUTC)
C
      IMPLICIT REAL*8 (A-H,O-Z)
C
      PSEUPC = 678.0 - 50.0*(G-0.5) - 206.7*XN2 + 440.0*XCO2
     &       + 606.7*XH2S
      PSEUTC = 326.0 + 315.7*(G-0,5) - 240.0*XN2 - 83.3*XCO2
     &       + 133.3*XH2S
C
      RETURN
      END
C
C .... SUBROUTINE ZFAC CALCULATES Z-FACTOR FOR GIVEN PRESSURE AND
C      TEMPERATURE
C
C .... VARIABLES:
C       A,B,C,D = Temperature-Dependent functions.
C       PR      = reduced pressure.
C       RTR     = reciprocal reduced temperature.
C       Y       = reduced density.
C
      SUBROUTINE ZFAC(P,T,PSEUPC,PSEUTC,Z)
C
      IMPLICIT REAL*8 (A-H,O-Z)
C
      PR    = P/PSEUPC
      RTR   = PSEUTC/T
C
      A     = 0.06125 * RTR * DEXP (-1.2*(1.0-RTR)*(1.0-RTR))
      B     = RTR * (14.76 - 9.76*RTR + 4.58*RTR*RTR)
      C     = RTR * (90.7 - 242.2*RTR + 42.4*RTR*RTR)
      D     = 2.18 + 2.82*RTR
      Y     = 0.001
C
C .... Yarborough & Hall Procedure
C
      DO 10  I = 1, 30
        F     = - A*PR + (Y+Y*Y+Y**3-Y**4)/(1.0-Y)**3 - B*Y*Y
```

```
315.     &            + C*Y**D
316.          IF(DABS(F)-1.0E-5) 2,2,1
317. 1        DFDY   = + (1.0+4.0*Y+4.0*Y*Y-4.0*Y**3+Y**4)/(1.0-Y)**4
318.     &            - 2.0*B*Y + D*C*Y**(D-1.0)
319.          Y      = Y - (F/DFDY)
320. 10       CONTINUE
321.C
322. 2        Z = A*PR/Y
323.C
324.          RETURN
325.          END
326.
327.
328.
```

```
 1.      Input Data for Program on Appendix B of Katz & Lee, November 1987
 2.      ================================================================
 3.       1. Flag (0/1 - Calculating G/ Given G ) .....              1
 4.       2. Section of Well, ..............................        10
 5.       3. Index(0/1 - Production/Injection) .............         0
 6.       4. Gas Gravity, G ................................  0.600000D+00
 7.       5. Total Length of Well ..................... (ft)  0.245000D+04
 8.       6. Wellhead Pressure ........................ (psia) 0.108700D+04
 9.       7. Wellhead Temperature ..................... (R)   0.520000D+03
10.       8. Bottom Hole Temperature .................. (R)   0.580000D+03
11.       9. Flowrate, Q ............................ (Mcf/D)  0.342000D+04
12.      10. Wellbore Inside Diameter ............... (in)    0.244100D+01
13.      11. Error Bound (Convergence Tolerance) ..........   0.100000D-04
14.      ================================================================
```

```
 1.      Composition Data for Program BHP of Katz & Lee, November 1987
 2.      ================================================================
 3.       1. Hydrogen Sulfide,    H2S ....................   0.000000D+00
 4.       2. Carbon Dioxide,      CO2 ....................   0.000000D+00
 5.       3. Nitrogen,             N2 ....................   0.000000D+00
 6.       4. Methane,              C1 ....................   0.900000D+00
 7.       5. Ethane,               C2 ....................   0.100000D+00
 8.       6. Propane,              C3 ....................   0.000000D+00
 9.       7. i-Butane,           i-C4 ....................   0.000000D+00
10.       8. n-Butane,           n-C4 ....................   0.000000D+00
11.       9. i-Pentane,          i-C5 ....................   0.000000D+00
12.      10. n-Pentane,          n-C5 ....................   0.000000D+00
13.      11. Hexane,              C6 ....................   0.000000D+00
14.      12. Heptane Plus,        c7+....................   0.000000D+00
15.      ================================================================
```


No.	Depth(ft)	Temp(R)	Pres(psia)	Z-factor
1	0.00	520.00	1087.00	0.82963
2	245.00	526.00	1095.33	0.83597
3	490.00	532.00	1103.60	0.84202
4	735.00	538.00	1111.82	0.84782
5	980.00	544.00	1119.98	0.85337
6	1225.00	550.00	1128.08	0.85869
7	1470.00	556.00	1136.14	0.86380
8	1715.00	562.00	1144.15	0.86870
9	1960.00	568.00	1152.11	0.87341
10	2205.00	574.00	1160.03	0.87793
11	2450.00	580.00	1167.90	0.88229

APPENDIX C

DERIVATIONS OF GAS FLOW EQUATIONS AND LINE SOURCE SOLUTION

C.1 GAS FLOW EQUATIONS

For gas flow including a sink or a source term q (mass per unit volume per unit time), the continuity equation may be written

$$\nabla\ (\rho\bar{u}) = -\frac{\partial\phi\rho}{\partial t} - q \tag{C.1}$$

Substituting Eq. (8.5) ($\delta = 1$, Darcy equation) and Eq. (8.7) (equation of state) into Eq. (C.1), one obtains

$$\nabla \cdot \left[k\frac{P}{\mu Z}\nabla P\right] = \phi\frac{\partial}{\partial t}\left[\frac{P}{Z}\right] + \frac{RT}{M}q \tag{C.2}$$

The first term of the right-hand side can be expanded to

$$\phi\frac{\partial}{\partial t}\left[\frac{P}{Z}\right] = \phi\left[\frac{1}{Z}\frac{\partial P}{\partial t} + P\frac{\partial}{\partial t}\left(\frac{1}{Z}\right)\right]$$

$$= \phi\left[\frac{P}{Z}\frac{\partial P}{\partial t}\left(\frac{1}{P} - \frac{1}{Z}\frac{dZ}{dP}\right)\right]$$

$$= \frac{\phi cP}{Z}\frac{\partial P}{\partial t} \tag{C.3}$$

with

$$c \equiv \frac{1}{\rho}\frac{d\rho}{dP}\Big|_T = \frac{1}{P} - \frac{1}{Z}\frac{dZ}{dP} \tag{C.4}$$

In Terms of Pressure, P

The left-hand side of Eq. (C.2) can be written out as

$$\nabla \cdot \left[k\frac{P}{\mu Z}\nabla P\right] = \frac{P}{\mu Z}\nabla \cdot (k\nabla P) + (k\nabla P)\cdot\nabla\left(\frac{P}{\mu Z}\right)$$

$$= \frac{P}{\mu Z}\left[\nabla \cdot (k\nabla P) + \frac{d\ \ln(P/\mu Z)}{dP}k(\nabla P)^2\right] \tag{C.5}$$

Combining Eqs. (C.2), (C.3), and (C.5), one obtains

$$\nabla \cdot (k\nabla P) + \frac{d\ \ln(P/\mu Z)}{dP}k(\nabla P)^2 = \phi c\mu\frac{\partial P}{\partial t} + \frac{RT\mu Z}{MP}q \tag{C.6}$$

For $P/(\mu Z)$ near constant or small pressure gradient $(\nabla P)^2$, Eq. (C.6) can be simplified to

$$\nabla \cdot (k\nabla P) = \phi c\mu\frac{\partial P}{\partial t} + \frac{RT\mu Z}{MP}q \tag{C.7}$$

In Terms of Pressure Squared, P^2

In this case, the left-hand side of Eq. (C.2) can be rearranged and expanded as follows:

$$\nabla \cdot \left[k\frac{P}{\mu Z}\nabla P\right] = \frac{1}{2}\nabla \cdot \left[\frac{1}{\mu Z}k\nabla P^2\right] = \frac{1}{2}\left[\frac{1}{\mu Z}\nabla \cdot (k\nabla P^2) + (k\nabla P^2)\cdot\nabla\left(\frac{1}{\mu Z}\right)\right]$$

$$= \frac{1}{2\mu Z}\left[\nabla \cdot (k\nabla P^2) + \frac{d\ \ln(1/\mu Z)}{dP^2}k(\nabla P^2)^2\right] \tag{C.8}$$

Equation (C.3) can be rearranged as

$$\phi\frac{\partial}{\partial t}\left[\frac{P}{Z}\right] = \frac{\phi cP}{Z}\frac{\partial P}{\partial t} = \frac{\phi c}{2Z}\frac{\partial P^2}{\partial t} \tag{C.9}$$

Combining Eqs. (C.2), (C.8), and (C.9), one obtains

$$\nabla \cdot (k\nabla P^2) + \frac{d\ \ln(1/\mu Z)}{dP^2} k(\nabla P^2)^2 = \phi c \mu \frac{\partial P^2}{\partial t} + \frac{2RT\mu Z}{M} q \tag{C.10}$$

By assuming μZ near constant or small $(\nabla P^2)^2$, Eq. (C.10) can be simplified to

$$\nabla \cdot (k\nabla P^2) = \phi c \mu \frac{\partial P^2}{\partial t} + \frac{2RT\mu Z}{M} q \tag{C.11}$$

In Terms of Pseudopressure, $m(P)$

Since

$$\nabla m = \frac{dm}{dP} \nabla P = \frac{2P}{\mu Z} \nabla P \tag{C.11}$$

and

$$\frac{\partial m}{\partial t} = \frac{dm}{dP} \frac{\partial P}{\partial t} = \frac{2P}{\mu Z} \frac{\partial P}{\partial t} \tag{C.13}$$

Eq. (C.2) can be rewritten as

$$\nabla \cdot (k\nabla m) = \phi c \mu \frac{\partial m}{\partial t} + \frac{2RT}{M} q \tag{C.14}$$

by combining with Eq. (C.3), and no extra assumptions needed.

For convenience of numerical simulation, Eq. (C.2) can be expressed as

$$\nabla \cdot (k\nabla m) = 2\phi \frac{\partial}{\partial t}\left[\frac{P}{Z}\right] + \frac{2RT}{M} q \tag{C.15}$$

Since

$$\frac{\partial}{\partial t}\left[\frac{P}{Z}\right] = \left[\frac{d(P/Z)}{dm}\right] \frac{\partial m}{\partial t} \tag{C.16}$$

Eq. (C.15) is transformed into

$$\nabla \cdot (k\nabla m) = 2\phi \left[\frac{d(P/Z)}{dm}\right] \frac{\partial m}{\partial t} + \frac{2RT}{M} q \tag{C.17}$$

where $d(P/Z)/dm$ can be calculated and tabulated if the P-μ-Z relationships of the reservoir fluid are known.

Usually, the flow rate, Q_{sc}, is in standard conditions (14.7 psia, 60°F) and can be converted to mass flow rate q for use in Eq. (C.17):

$$q = \frac{Q_{sc} P_{sc} M}{RT_{sc}} \frac{1}{V} \tag{C.18}$$

TABLE C.1
Conversion factors

Units	C_1	C_2	C_3
Darcy	1	$2\phi \frac{d(P/Z)}{dm}$	$2\frac{TP_{sc}}{T_{sc}V}$
Field	1	$(3.7935 \times 10^3)2\phi \frac{d(P/Z)}{dm}$	$(1.5806 \times 10^8)2\frac{TP_{sc}}{T_{sc}V}$
Metric	1	$(2.7780 \times 10^2)2\phi \frac{d(P/Z)}{dm}$	$(11.5746)2\frac{TP_{sc}}{T_{sc}V}$

where V is the volume of the reservoir block from which gas is withdrawn or injected. Equations (C.17) and (C.18) can be combined to give

$$\nabla \cdot (k\nabla m) = 2\phi \left[\frac{d(P/Z)}{dm}\right] \frac{\partial m}{\partial t} + 2\frac{T}{T_{sc}} P_{sc} \frac{Q_{sc}}{V} \tag{C.19}$$

Equation (C.19) is only valid when Darcy units are used. If field or metric units are used, the conversion factors should be included. In general form, Eq. (C.19) can be expressed as

$$C_1 \nabla \cdot (k\nabla m) = C_2 \frac{\partial m}{\partial t} + C_3 Q_{sc} \tag{C.20}$$

where the conversion factors C_1, C_2, and C_3 are as shown in Table C.1 for different units used.

C.2 LINE SOURCE SOLUTION DERIVATION

The following derivation of the *line source* solution via the use of Boltzmann and Laplace transformations is based on the classic paper by van Everdingen and Hurst [8-18].

Solution Using the Boltzmann Transformation

The fundamental partial differential equations relating dimensionless pressure, radius, and time for flow in a permeable medium with infinite-acting boundary conditions are

$$\frac{1}{r_D} \frac{\partial}{\partial r_D}\left(r_D \frac{\partial P_D}{\partial r_D}\right) = \frac{\partial P_D}{\partial t_D} \tag{C.21}$$

$$P_D(r_D, t_D = 0) = 0 \tag{C.22}$$

$$P_D(r_D \to \infty, t_D) = 0 \tag{C.23}$$

$$\lim_{r_D \to 1} r_D \frac{\partial P_D}{\partial r_D} = -1 \tag{C.24}$$

where the dimensionless groups are defined as Table 8.1 except that t_D is based on any given radius r, not only the wellbore radius r_w. These equations are only true assuming no wellbore storage, no skin, and no high-velocity effects.

The Boltzmann transformation $s = r_D^2/4t_D$ can be introduced into Eq. (C.21). Then,

$$\frac{1}{r_D}\frac{d}{ds}\left(r_D \frac{dP_D(s)}{ds}\frac{\partial s}{\partial r_D}\right)\frac{\partial s}{\partial r_D} = \frac{dP_D(s)}{ds}\frac{\partial s}{\partial t_D} \tag{C.25}$$

where the partial derivatives can be obtained by

$$\frac{\partial s}{\partial r_D} = \frac{r_D}{2t_D} = \frac{2s}{r_D} \tag{C.26}$$

$$\frac{\partial s}{\partial t_D} = -\frac{r_D^2}{4t_D^2} = -\frac{s}{t_D} \tag{C.27}$$

After making these substitutions, Eq. (C.25) can be reduced to the following form:

$$\frac{d}{ds}\left(s\frac{dP_D}{ds}\right) = -s\frac{dP_D}{ds} \tag{C.28}$$

The boundary conditions should also be transformed to the s variable:

$$P_D(r_D, t_D = 0) = 0; \qquad P_D(s \to \infty) = 0 \tag{C.29}$$

$$P_D(r_D \to \infty, t_D) = 0; \qquad P_D(s \to \infty) = 0 \tag{C.30}$$

$$\lim_{r_D \to 1} r_D \frac{\partial P_D}{\partial r_D} = -1; \qquad \lim_{s \to 1/4t_D} s\frac{dP_D}{ds} = -\frac{1}{2} \tag{C.31}$$

Equation (C.28) can be expanded by differentiating the left-hand side:

$$s\frac{d}{ds}\left(\frac{dP_D}{ds}\right) + \frac{dP_D}{ds} = -s\frac{dP_D}{ds} \tag{C.32}$$

Introduction of $\bar{P} = dP_D/ds$ reduces Eq. (C.32) to the following form:

$$s\frac{d\bar{P}}{ds} + \bar{P} = -s\bar{P} \tag{C.33}$$

which can be rearranged and then integrated:

$$-\int \frac{1}{\bar{P}} d\bar{P} = \int \left(1 + \frac{1}{s}\right) ds + C' \tag{C.34}$$

$$-\ln \bar{P} = s + \ln s + \ln C \tag{C.35}$$

$$s\bar{P} = Ce^{-s} \tag{C.36}$$

Applying the inner boundary line source condition expressed by Eq. (C.31) to Eq. (C.36), allows determination of the constant of integration C:

$$\lim_{s \to 1/4t_D} s\bar{P} = \lim_{s \to 1/4t_D} Ce^{-s} = -\frac{1}{2} \tag{C.37}$$

$$C = -\frac{1}{2}e^{1/4t_D} \tag{C.38}$$

Substituting this value of C into Eq. (C.36) results in the last integral relationship:

$$\bar{P} = \frac{dP_D}{ds} = -\frac{1}{2}e^{1/4t_D}\frac{1}{s}e^{-s} \tag{C.39}$$

This can be integrated as follows using the boundary condition given by Eq. (C.30):

$$\int_0^{P_D} dP_D = -\frac{1}{2}e^{1/4t_D}\int_\infty^{r_D^2/4t_D} \frac{e^{-s}}{s} ds \tag{C.40}$$

The term $e^{1/4t_D}$ is approximately 1 for values of t_D greater than 25 and can be neglected. Making this assumption, and reversing the limits of integration, one obtains the familiar line source exponential integral solution to the radial flow equation:

$$P_D = \frac{1}{2}\int_{r_D^2/4t_D}^{\infty} \left(\frac{e^{-s}}{s}\right) ds = -\frac{1}{2}\,\mathrm{Ei}\left(-\frac{r_D^2}{4t_D}\right) \tag{C.41}$$

The function $\mathrm{Ei}(-X)$ can be expanded in a series:

$$\mathrm{Ei}(-X) = \int_\infty^X \frac{e^{-s}}{s} ds = \int_X^\infty \left(\frac{1}{s} - 1 + \frac{s}{2!} - \frac{s^2}{3!} + \frac{s^3}{4!} + \cdots\right) ds \tag{C.42}$$

which can be integrated. After performing the integration, the following form is obtained:

$$\mathrm{Ei}(-X) = 0.57722 + \ln X + \sum_{i=1}^{\infty} \frac{(-1)^i X^i}{(i)(i!)} \tag{C.43}$$

The last term can be neglected if $X < 0.01$. Hence, for $t_D/r_D^2 > 25$,

$$P_D = -\frac{1}{2}\mathrm{Ei}\left(-\frac{r_D^2}{4t_D}\right) \approx \frac{1}{2}\ln\frac{4t_D}{\gamma r_D^2} = \frac{1}{2}\left[\ln\left(\frac{t_D}{r_D^2}\right) + 0.80907\right] \tag{C.44}$$

where γ is Euler's constant, $e^{-0.57722}$.

Solution Using the Laplace Transformation

Letting $\bar{P}(s)$ represent the transformed variable and defining s to be the operator, then

$$\bar{P}(s) = \int_0^\infty e^{-st_D} P_D \, dt_D \tag{C.45}$$

is the Laplace transform of P_D. Using this definition, the transform of Eq. (C.21) can be shown to be

$$\frac{d^2\bar{P}(s)}{dr_D^2} + \frac{1}{r_D}\frac{d\bar{P}(s)}{dr_D} = s\bar{P}(s) + P_D(r_D, t_D = 0) = s\bar{P}(s) \tag{C.46}$$

by applying the boundary condition Eq. (C.29). The solution of Eq. (C.46) is a Bessel equation:

$$\bar{P}(r_D, s) = A\, I_0(r_D\sqrt{s}) + B\, K_0(r_D\sqrt{s}) \tag{C.47}$$

where I_0 and K_0 are the zero order modified Bessel functions of the first and second kinds, and A and B are constants that satisfy Eq. (C.46).

The functions I_0 and K_0 are respectively directly and inversely proportional to $r_D s$. As t_D approaches zero, s increases. To satisfy the initial and outer boundary conditions, Eqs. (C.22) and (C.23), the constant A must equal zero; thus,

$$\bar{P}(r_D, s) = BK_0(r_D\sqrt{s}) \tag{C.48}$$

To fulfill the second boundary condition, the derivative of Eq. (C.48) is taken with respect to r_D:

$$\frac{d\bar{P}(r_D, s)}{dr_D} = -B\sqrt{s}\, K_1(r_D\sqrt{s}) \tag{C.49}$$

The Laplace transformation of Eq. (C.24) is

$$\lim_{r_D \to 1} r_D \frac{d\bar{P}(r_D, s)}{dr_D} = -\frac{1}{s} \tag{C.50}$$

from which the constant B can be obtained. The result is substituted into Eq. (C.48) to give the following equation:

$$\bar{P}(r_D, s) = \frac{K_0(r_D\sqrt{s})}{s^{3/2}K_1(\sqrt{s})} \tag{C.51}$$

The inversion of Eq. (C.51) for any time is

$$P_D = \frac{2}{\pi}\int_0^\infty \frac{(1 - e^{-u^2 t_D})[J_1(u)Y_0(ur_D) - Y_1(u)J_0(ur_D)]}{u^2[J_1^2(u) + Y_1^2(u)]}\,du \tag{C.52}$$

where J and Y are the regular Bessel functions. Of more interest is the long-term

approximation to Eq. (C.52); that is,

$$P_D \approx \frac{1}{2}\ln\frac{4t_D}{\gamma r_D^2} = \frac{1}{2}\left[\ln\frac{t_D}{r_D^2} + 0.80907\right] \tag{C.53}$$

which is identical to Eq. (C.44), the line source solution.

Comparison of the Boltzmann and Laplace Transform Solutions

The Laplace transform solution, Eq. (C.52), should be considered as the exact solution to a constant flow rate radial flow system. Both solutions are listed in Table C.2 for various r_D and t_D. It is apparent that the approximate Boltzmann transform solution, Eq. (C.41) will produce sufficiently accurate results, especially for the pressure drop at the wellbore ($r_D = 1$).

Solutions for Finite Reservoir

For a bounded reservoir, the infinite-acting behavior for a constant withdrawal rate case will end as soon as the outer boundary r_e feels the transient pressure drop (the investigation radius r_i reaches r_e). The boundary behaves in two ways: (*a*) no flow boundary (natural fault) and (*b*) constant pressure boundary (100 percent water drive):

$$\text{No flow boundary:} \quad \frac{\partial P_D}{\partial r_D}(r_{eD}, t_D) = 0 \tag{C.54a}$$

$$\text{Constant pressure boundary:} \quad P_D(r_{eD}, t_D) = 0 \tag{C.54b}$$

where $r_{eD} = r_e/r_D$ is the dimensionless outer boundary radius.

TABLE C.2
Comparison of the P_D's computed using Eqs. (C.41) and (C.52) [Schafer-Perini, C-1]

r_D	t_D	Eq. (C.41)	Eq. (C.52)	|% error|
1	100	2.70837	2.71653	0.30
1	1,000	3.85854	3.85423	0.11
1	10,000	5.00972	5.00363	0.12
1	50,000	5.81443	5.80836	0.10
100	100	0.00000	0.00000	—
100	1,000	0.01246	0.01252	0.50
100	10,000	0.52214	0.52226	0.02
100	50,000	0.12340	1.23401	—
500	100	0.00000	0.00000	—
500	1,000	0.00000	0.00001	—
500	10,000	0.00014	0.00018	25.0
500	50,000	0.73207	0.07500	2.40

NO FLOW BOUNDARY CASE. With Eq. (C.54*a*) as a boundary condition, Eq. (C.21) can be solved by using the Laplace transform [1-22]:

$$P_D = \frac{2}{r_{eD}^2 - 1}\left(\frac{r_D^2}{4} + t_D\right) - \frac{r_{eD}^2 \ln r_D}{r_{eD}^2 - 1} - \frac{3r_{eD}^4 - 4r_{eD}^4 \ln r_{eD} - 2r_{eD}^2 - 1}{4(r_{eD}^2 - 1)^2}$$
$$+ \pi \sum_{n=1}^{\infty} \frac{e^{\alpha_n^2 t_D} J_1^2(\alpha_n r_{eD})[J_1(\alpha_n)Y_0(\alpha_n r_D) - Y_1(\alpha_n)J_0(\alpha_n r_D)]}{\alpha_n[J_1^2(\alpha_n r_{eD}) - J_1^2(\alpha_n)]} \qquad \text{(C.55)}$$

where t_{eD} is the dimensionless time at r_e, J_i and Y_i are the Bessel functions of the first and second kind of order i, and α_n are the roots of

$$J_1(\alpha_n r_{eD})Y_1(\alpha_n) - J_1(\alpha_n)Y_1(\alpha_n r_{eD}) = 0 \qquad \text{(C.56)}$$

For solution at wellbore ($r_D = 1$) and for practical purposes, Eq. (C.55) can be simplified to

$$P_{DW} = \frac{2t_D}{r_{eD}^2} + \ln r_{eD} - \frac{3}{4} \quad \text{for} \quad \frac{t_D}{r_{eD}^2} > 0.25 \quad \text{and} \quad r_{eD} >> 1 \qquad \text{(C.57)}$$

CONSTANT PRESSURE BOUNDARY CASE. Similarly, using the Laplace transform with Eq. (C.54*b*) as a boundary condition, Eq. (C.21) can be solved to give [8-17]:

$$P_D = \ln\left(\frac{r_{eD}}{r_D}\right) + \pi \sum_{n=1}^{\infty} \frac{e^{-\beta_n^2 t_D} J_0^2(r_{eD}\beta_n)[J_0(r_D\beta_n)Y_1(\beta_n) - Y_0(r_D\beta_n)J_1(\beta_n)]}{\beta_n[J_1^2(\beta_n) - J_0(r_{eD}\beta_n)]} \qquad \text{(C.58)}$$

Again, for all practical purposes, Eq. (C.58) is further reduced to

$$P_{DW} = \ln r_{eD} \quad \text{for} \quad t_D > 1.0\, r_{eD}^2 \qquad \text{(C.59)}$$

It is interesting to note that Eq. (C.59) is same as the steady state equation, Eq. (8.40), which was derived just by integrating Darcy's equation from r_w to r_e. Hence, for a constant pressure boundary finite reservoir, the pressure drop profile will eventually reach steady state; however, it will never achieve steady state for a no flow boundary finite reservoir.

REFERENCE

C-1 Schafer-Perini, A. L., "Estimation of Reservoir Parameters under Impending Blowout Conditions—Radial Liquid Flow," M.S. thesis, New Mexico Institute of Mining and Technology, Socorro, New Mexico (1986).

APPENDIX D

THE PENG-ROBINSON EQUATION OF STATE

A two-constant equation of state proposed by Peng and Robinson [D-1] gives better predictions than the Redlich-Kwong [D-2] or Soave [D-4] equations of vapor pressure, liquid densities, and phase equilibria, particularly near the critical point. The equation is

$$P = \frac{RT}{V - b} - \frac{a(T)}{V(V + b) + b(V - b)} \qquad \text{(D.1)}$$

which can be rewritten in terms of the compressibility factor as

$$Z^3 - (1 - B)Z^2 + (A - 3B^2 - 2B)Z - (AB - B^2 - B^3) = 0 \qquad \text{(D.2)}$$

where

$$A = \frac{a(T)}{R^2T^2}, \quad B = \frac{bP}{RT}, \quad \text{and} \quad Z = \frac{PV}{RT} \qquad \text{(D.3)}$$

Equation (D.2) yields one or three roots, depending upon the number of phases in the system. In the two-phase region, the largest root is for the compressibility factor of the vapor while the smallest positive root corresponds to that of the liquid.

Applying Eq. (D.1) at the critical point results in

$$a(T_c) = 0.45724\frac{R^2T_c^2}{P_c}, \qquad b(T_c) = 0.0778\frac{RT_c}{P_c}, \qquad \text{and} \qquad Z = 0.307 \tag{D.4}$$

For any temperature other than the critical, one could use

$$a(T) = a(T_c)\cdot\alpha(T) \qquad \text{and} \qquad b(T) = b(T_c) \tag{D.5}$$

where

$$\alpha\,(T)^{0.5} = 1 + \kappa(1 - T_r^{0.5}), \qquad \kappa = 0.37464 + 1.54226\,\omega - 0.26992\,\omega^2 \tag{D.6}$$

The acentric factor ω is defined as

$$\omega = -\left[1 + \log_{10} P_r(v)\right]_{T_r=0.7} \tag{D.7}$$

where $P_r(v)$ is the reduced pressure of saturated vapor at $T_r = 0.7$. The acentric factor ω are tabulated in Reid, Prausnitz, and Sherwood: *The Properties of Gases and Liquids* [D-3] for numerous fluids. If the acentric factor is not available, it can be approximated by the Edmister equation:

$$\omega = \frac{3}{7}\left(\frac{T_{br}}{1 - T_{br}}\right)\log_{10} P_c - 1 \tag{D.8}$$

where T_{br} is the reduced normal boiling point and P_c is the critical pressure in atm.

Mixture

For a mixture, the coefficients a and b in the Peng-Robinson equation could be extended by applying the mixing rule:

$$a_m = \sum_i \sum_j y_i y_j a_{ij}, \qquad b_m = \sum_i b_i y_i \tag{D.9}$$

where

$$a_{ij} = \sqrt{a_i a_j}(1 - k_{ij}) \tag{D.10}$$

In Eq. (D.10), k_{ij} is an empirically determined binary interaction coefficient for components i and j. The accuracy of the Peng-Robinson equation of state for mixtures depends on the use of the correct value of the interaction coefficient k_{ij}.

Fugacity

The thermodynamics relationship of fugacity f or fugacity coefficient ϕ is as follows:

$$\ln\phi = \ln\frac{f}{P} = \int_0^P \left(\frac{V}{RT} - \frac{1}{P}\right)dP = \int_1^Z dZ + \int_\infty^V -\frac{P}{RT}dV + \int_0^P -\frac{1}{P}dP \tag{D.11}$$

which is expanded by differentiating the Z factor in Eq. (D.3). Substituting with Eq. (D.1), the last two terms of Eq. (D.11) can be worked out as follows:

$$\begin{aligned}
&\int_\infty^V -\frac{P}{RT}dV + \int_0^P -\frac{1}{P}dP \\
&= \int_\infty^V \left(-\frac{1}{V-b} + \frac{a}{RT}\frac{1}{V^2 + 2bV - b^2}\right)dV + \int_0^P -\frac{1}{P}dP \\
&= \int_\infty^V \left[-\frac{1}{V-b} + \frac{a}{RT}\frac{-1}{2\sqrt{2}\,b}\left(\frac{1}{V + 2.4141b} - \frac{1}{V - 0.414b}\right)\right]dV + \int_0^P -\frac{1}{P}dP \\
&= -\ln\,(V-b) + \ln\,(V-b)\Big|_{V\to\infty} - \ln P + \ln P\Big|_{P\to 0} \\
&\quad - \frac{a}{RT}\frac{1}{2\sqrt{2}\,b}\left[\ln\frac{V + 2.414b}{V - 0.414b} - \ln\frac{V + 2.414b}{V - 0.414b}\Big|_{V\to\infty}\right] \\
&= -\ln\frac{P(V-b)}{RT} + \ln\frac{P(V-b)}{RT}\Big|_{V\to\infty} - \frac{1}{2\sqrt{2}}\frac{aP}{(RT)^2}\frac{RT}{Pb}\ln\frac{(P/RT)(V + 2.414b)}{(P/RT)(V - 0.414b)}
\end{aligned} \tag{D.12}$$

The key of deriving Eq. (D.12) is the breaking of the second term of Eq. (D.1) into two terms and combining all the low-limit ($V\to\infty$, $P\to 0$, $Z\to 1$) terms.

Finally, using the definitions of Eq. (D.3), the fugacity expression based on the Peng-Robinson equation is:

$$\ln\frac{f}{P} = (Z-1) - \ln\,(Z-B) - \frac{A}{2\sqrt{2}\,B}\ln\left(\frac{Z + 2.414B}{Z - 0.414B}\right) \tag{D.13}$$

which is only valid for pure components.

For a mixture, the following thermodynamics expression should be used:

$$\ln\,\phi_i = \ln\frac{f_i}{x_i P} = -\int_\infty^V \left(\frac{\partial(P/RT)}{\partial n_i}\right)_{V,T,n_j} dV + \int_\infty^V \frac{1}{V}dV - \ln Z \tag{D.14}$$

The Peng-Robinson equation of state expressed in terms of total volume would be

$$P = \frac{NRT}{V - b_m} - \frac{a_m}{V(V + b_m) + b_m(V - b_m)} \tag{D.15}$$

in which N, a_m, and b_m are functions of the composition.

Substituting Eq. (D.15) into Eq. (D.14) and carrying out the differentiation as well as integration, the final result can be rearranged as

$$\ln\frac{f_i}{x_i P} = \frac{b_i}{b_m}(Z-1) - \ln\,(Z - B_m) - \frac{A_m}{2\sqrt{2}\,B_m}\left(\frac{2\sum_j x_i a_{ij}}{a_m} - \frac{b_i}{b_m}\right)\ln\frac{Z + 2.414B_m}{Z - 0.414B_m} \tag{D.16}$$

Enthalpy

The enthalpy departure function is expressed as

$$(H - H^o) = (A - A^o) + T(S - S^o) + RT(Z - 1) \tag{D.17}$$

where $(A - A^o)$ is the Helmholtz energy departure function and $(S - S^o)$ is the entropy departure function:

$$A - A^o = -\int_{\infty}^{V}\left(P - \frac{RT}{V}\right)dV - RT \ln\frac{V}{V^o} \tag{D.18}$$

$$S - S^o = \int_{\infty}^{V}\left[\left(\frac{\partial P}{\partial T}\right)_V - \frac{R}{V}\right]dV + R \ln\frac{V}{V^o} \tag{D.19}$$

where superscript o denotes a reference state ($P = 0$) at the same temperature.

Combining the Peng-Robinson equation with Eqs. (D.17) through (D.19), the enthalpy departure function can be rearranged as

$$(H - H^o) = RT(Z - 1) - \frac{T(da/dT) - a}{2\sqrt{2}\,b}\ln\frac{Z + 2.414B}{Z - 0.414B} \tag{D.20}$$

HOME PROBLEMS

D-1. The Redlich-Kwong (R-K) EOS is given by

$$P = \frac{RT}{V - b} - \frac{a}{T^{0.5}V(V + b)}$$

where $a = 0.42748R^2T_c^{2.5}/P_c$ and $b = 0.08664RT_c/P_c$. Prove that, for reduced pressure up to 0.8, the compressibility factor Z can be obtained by

$$Z^3 - Z^2 - Z(B^2 + B - A) - AB$$

where

$$A = \frac{aP}{R^2T^{2.5}} = \frac{0.42748P_r}{T_r^{2.5}} \quad \text{and} \quad B = \frac{bP}{RT} = \frac{0.08664P_r}{T_r}$$

The R-K EOS, developed at the Shell Development Co., was modified by Soave assuming a variable $a(T)$ to replace a in the R-K EOS. The new equation is usually called the R-K-S EOS, and it uses

$$a(T) = 0.42748\frac{R^2T_c^2}{P_c}\alpha(T)$$

and

$$\alpha^{1/2} = 1 + m(1 - T_r^{1/2})$$

where $m = 0.48 + 1.574\omega - 0.172\omega^2$ and ω is the acentric factor, defined as $\omega = -(1 + \log P_{vr})_{T_r=0.7}$. $P_{vr}|_{T_r=0.7}$ is the reduced pressure of saturated vapor at a reduced temperature of 0.7. Acentric factors for fluids can be found in reference [D-3].

D-2. Prove that the fugacity for pure gases can be expressed by the R-K-S EOS as

$$\ln\phi = Z - 1 - \ln(Z - B) - (A/B)\ln\left(1 + \frac{B}{Z}\right)$$

where

$$A = \frac{a(T)P}{T^2R^2} = \frac{0.42748P_r\alpha}{T_r^2} \quad \text{and} \quad B = \frac{bP}{RT} = \frac{0.08664P_r}{T_r}$$

D-3. Prove that, for the R-K-S EOS, the fugacity coefficient of a component i in a gas mixture is

$$\ln\phi_i = (Z_m - 1)\frac{B_i}{B_m} - \ln(Z_m - B_m) - \frac{A_m}{B_m}\cdot\left[2\left(\frac{A_i}{A_m}\right)^{1/2} - \frac{B_i}{B_m}\right]\ln\left(1 + \frac{B_m}{Z_m}\right)$$

D-4. Prove that, for the R-K-S EOS, the Helmholtz function $A - A^o$ and the entropy departure function $S - S^o$ of a gas mixture are

$$A - A^o = -RT\left[\ln\left(1 - \frac{B_m}{Z_m}\right) + \frac{A_m}{B_m}\ln\left(1 + \frac{B_m}{Z_m}\right)\right]$$

$$S - S^o = R\ln(Z_m - B_m) - RT^{1/2}\frac{A_m}{B_m}\ln\left(1 + \frac{B_m}{Z_m}\right)$$

REFERENCES

D-1. Peng, D. Y., and D. B. Robinson, "A New Two-Constant Equation of State," *Ind. Eng. Chem. Fund.*, Vol. 15, No. 1, 59–64 (1976).

D-2. Redlich, O., and J. N. S. Kwong, "On the Thermodynamics of Solutions. V. An Equation of State. Fugacities of Gaseous Solutions," *Chem. Rev.*, Vol. 44, 233 (1949).

D-3. Reid, R. C., J. M. Prausnitz, and T. K. Sherwood, *The Properties of Gases and Liquids*, 3rd Ed., McGraw-Hill Publishing Co. (1977).

D-4. Soave, G., "Equilibrium Constants from a Modified Redlich-Kwong Equation of State," *Chem. Eng. Sci.*, Vol. 27, 1197–1203 (1972).

APPENDIX E

EQUILIBRIUM CONSTANTS FOR NATURAL GAS–CONDENSATE SYSTEM

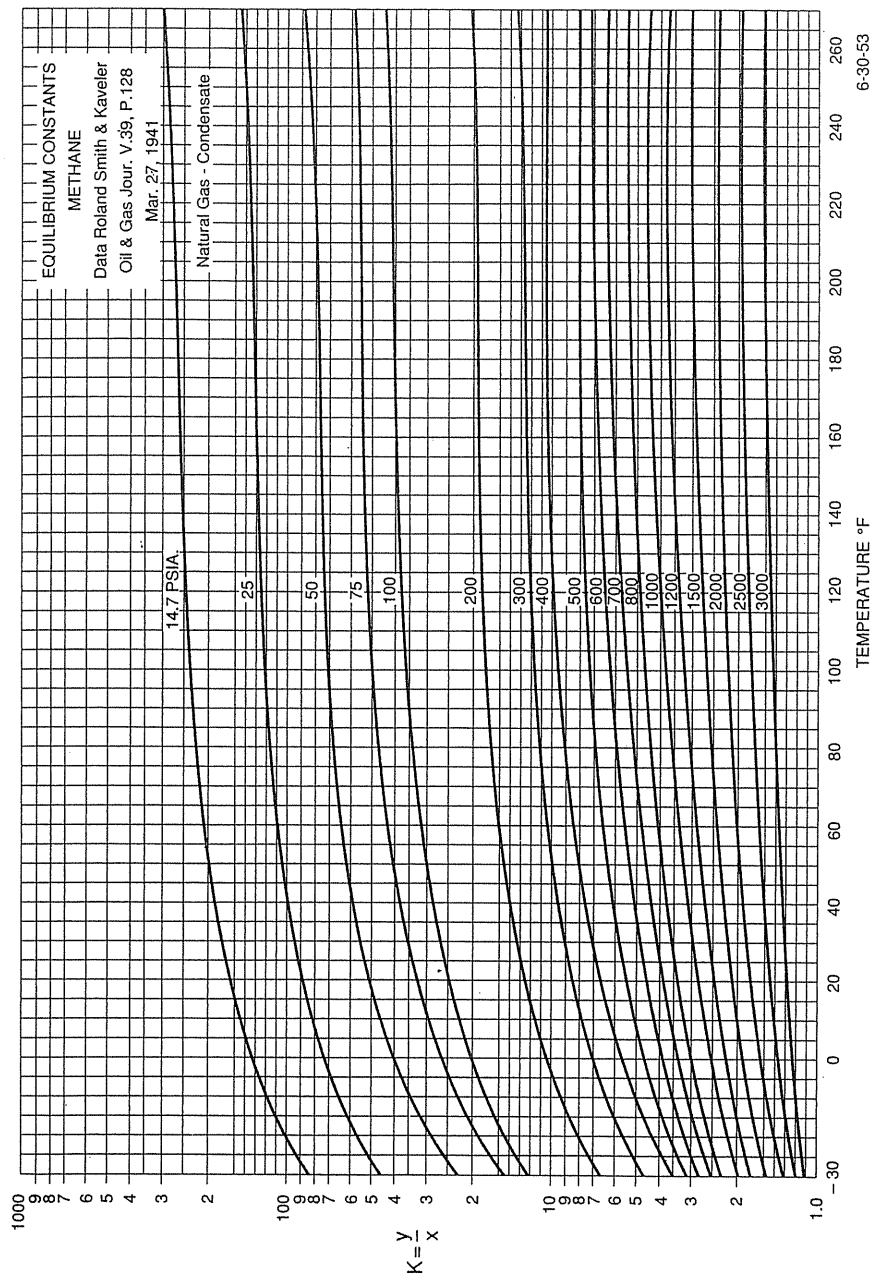

FIGURE E-1
Equilibrium constant $k = y/x$ for methane.

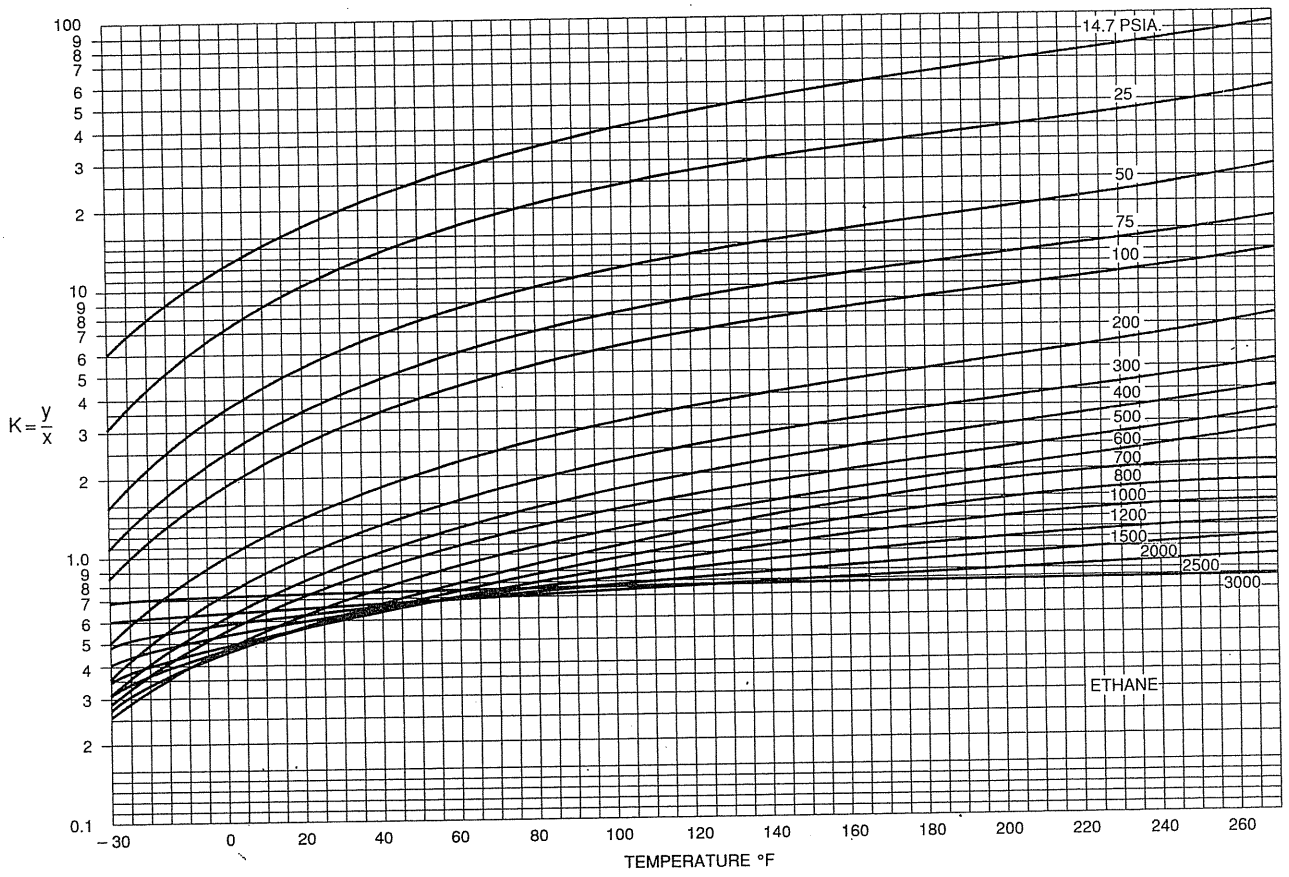

FIGURE E-2
Equilibrium constant $k = y/x$ for ethane.

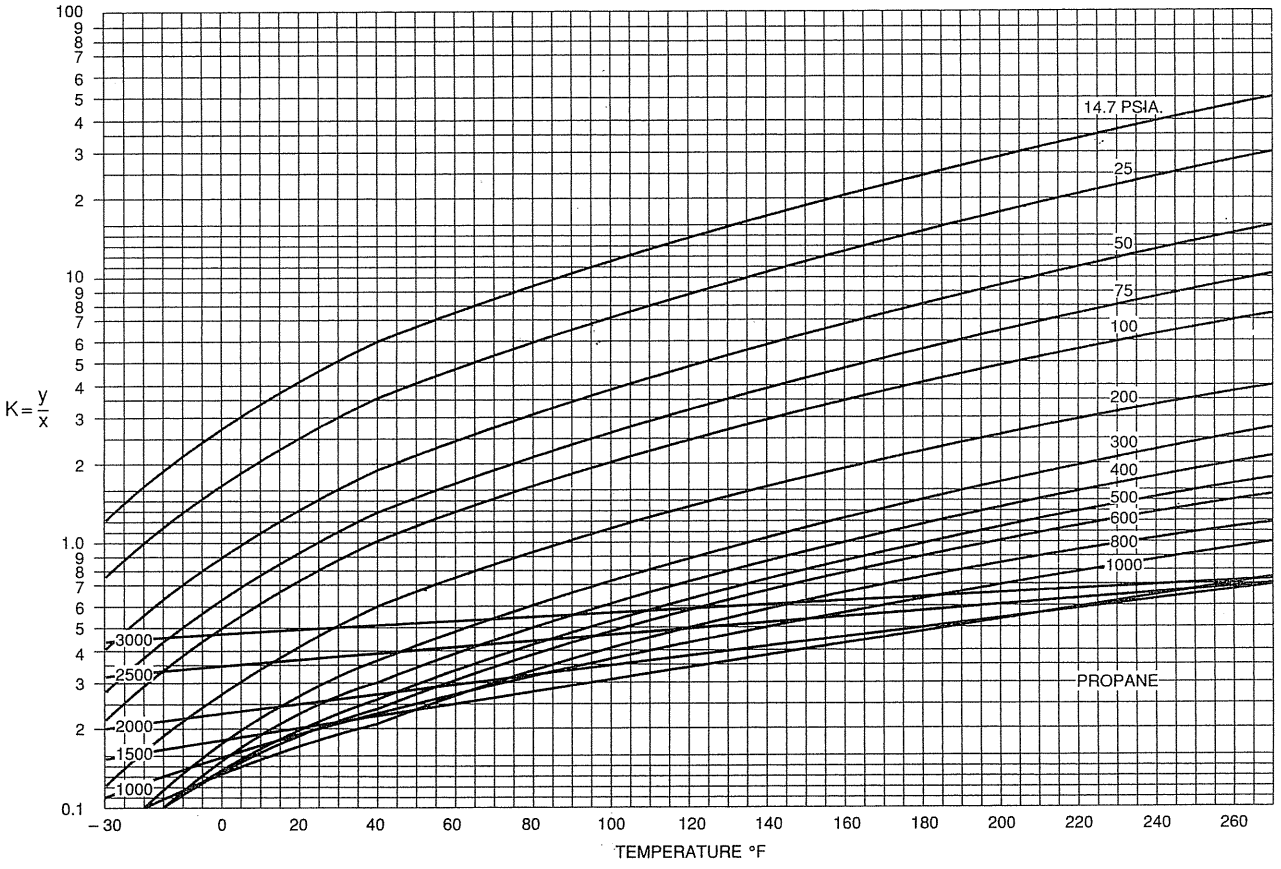

FIGURE E-3
Equilibrium constant $k = y/x$ for propane.

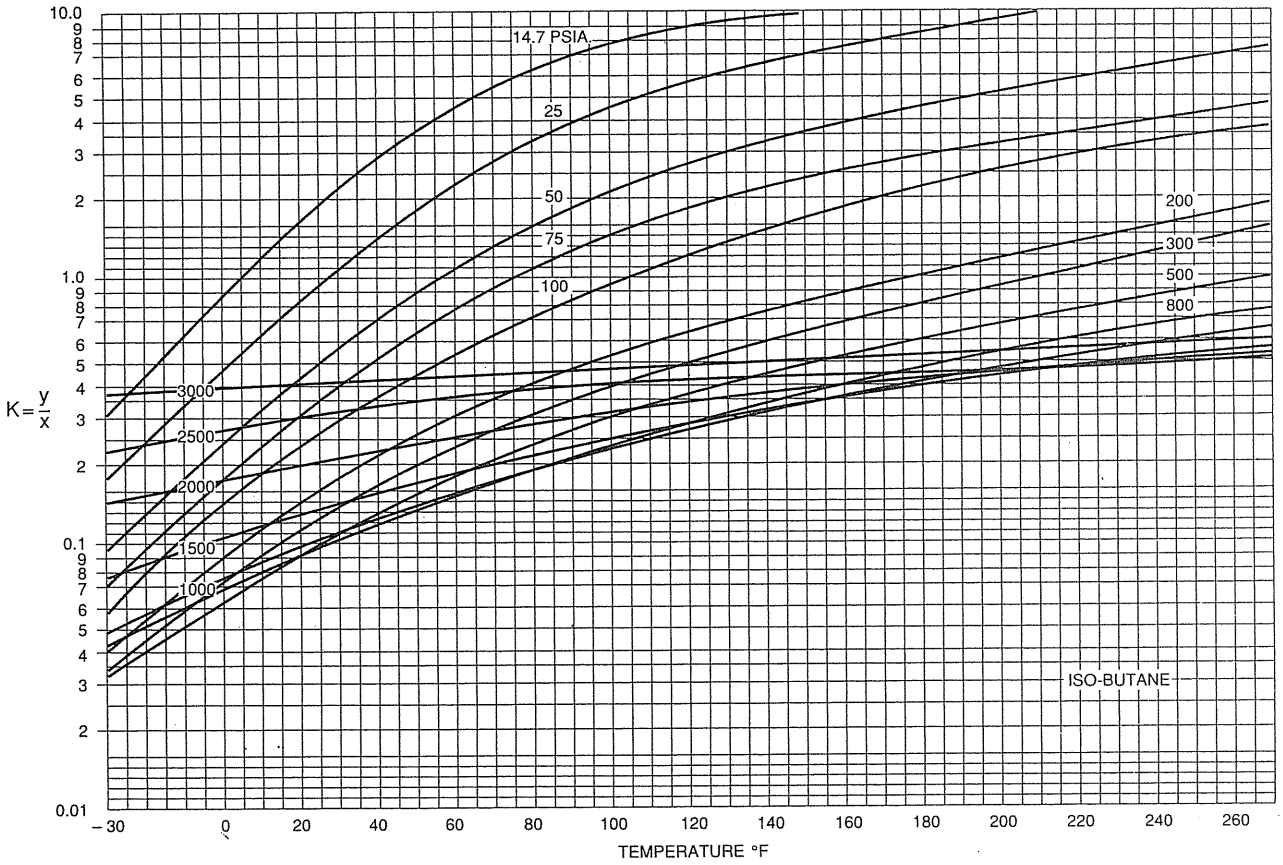

FIGURE E-4
Equilibrium constant $k = y/x$ for iso-butane.

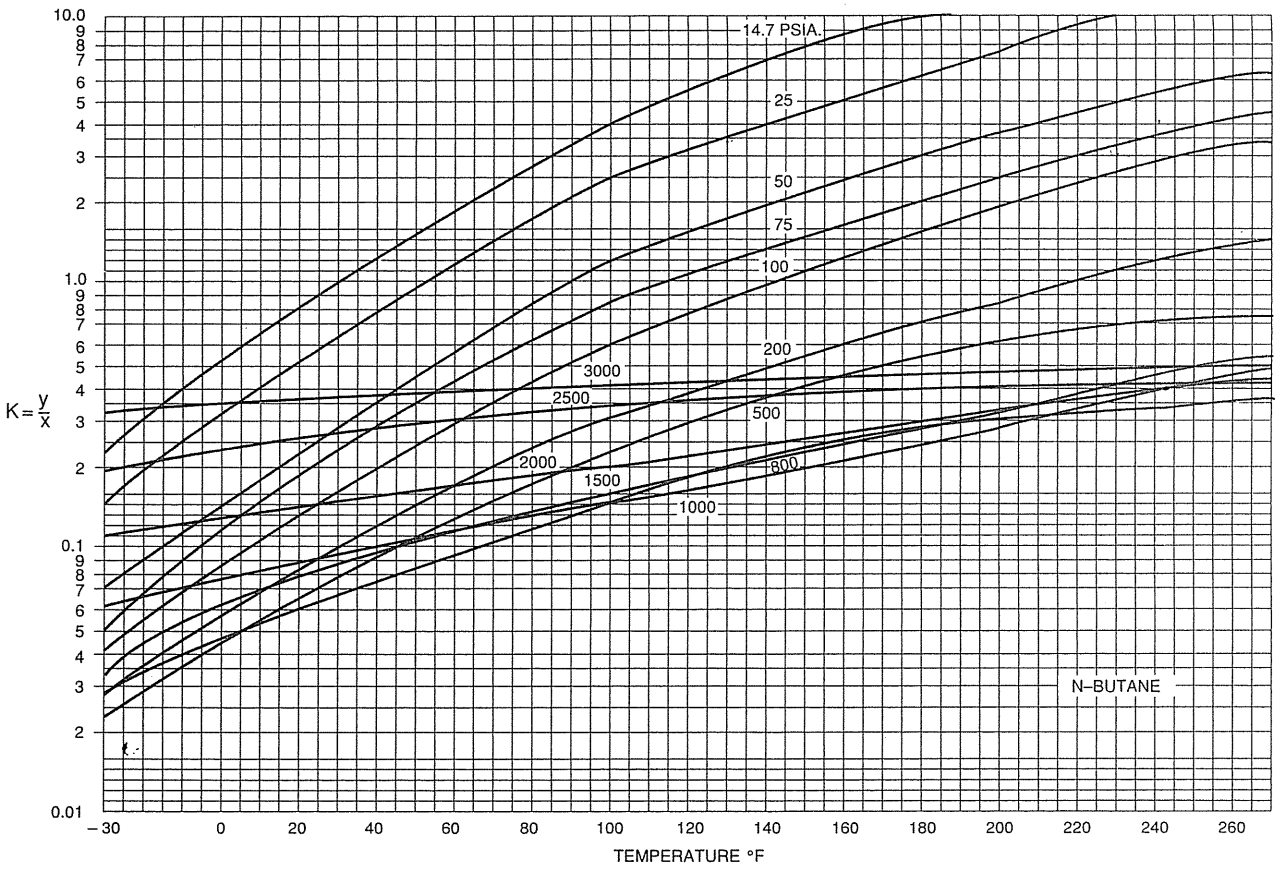

FIGURE E-5
Equilibrium constant $k = y/x$ for n-butane.

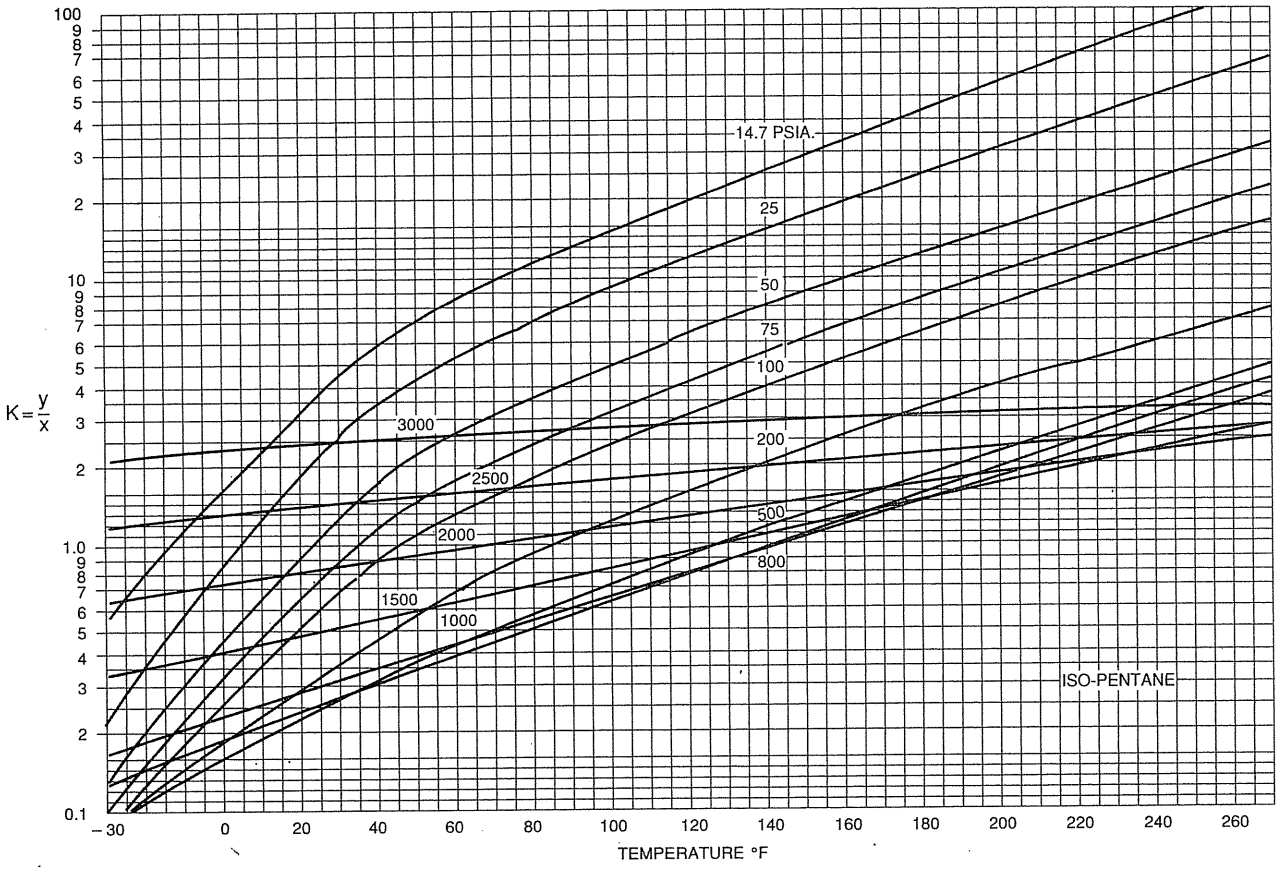

FIGURE E-6
Equilibrium constant $k = y/x$ for iso-pentane.

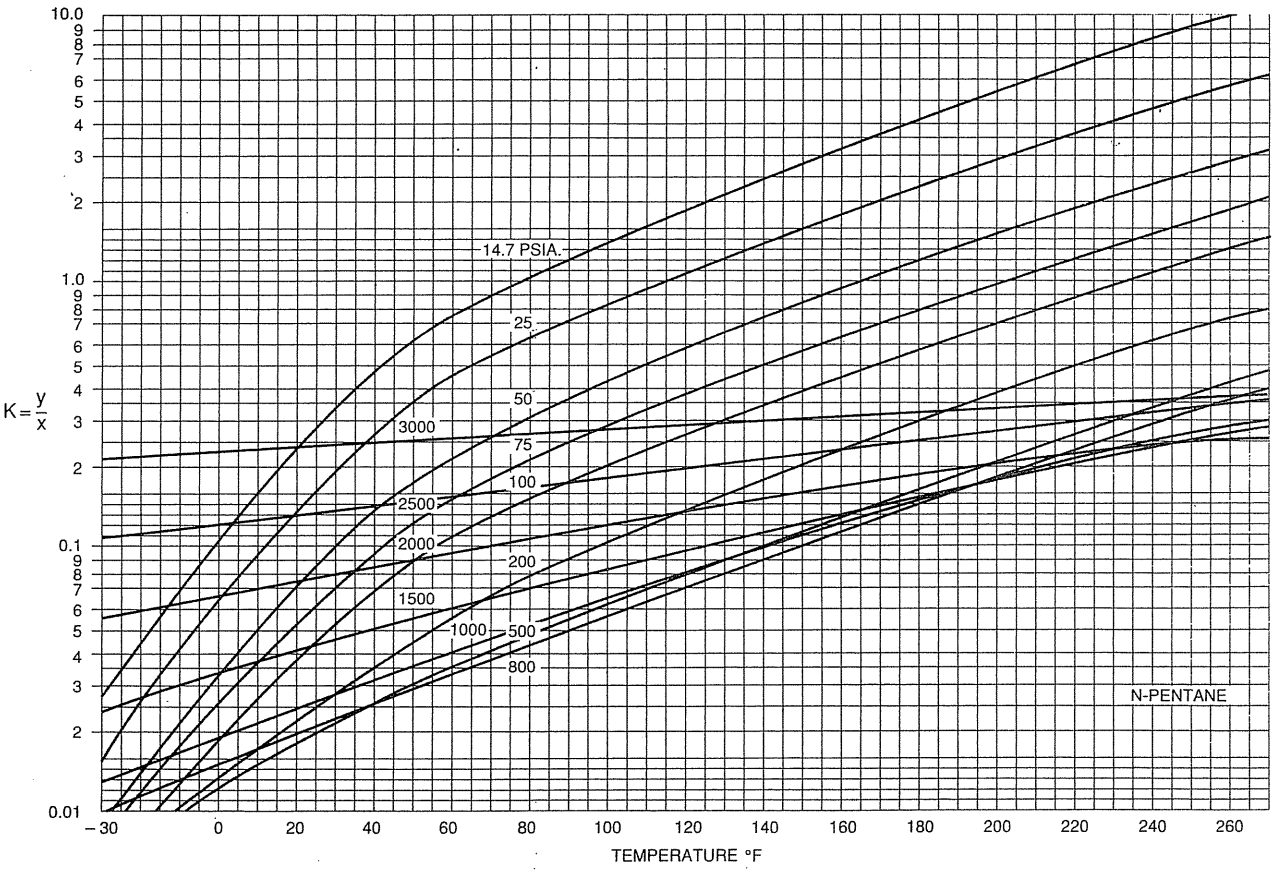

FIGURE E-7
Equilibrium constant $k = y/x$ for n-pentane.

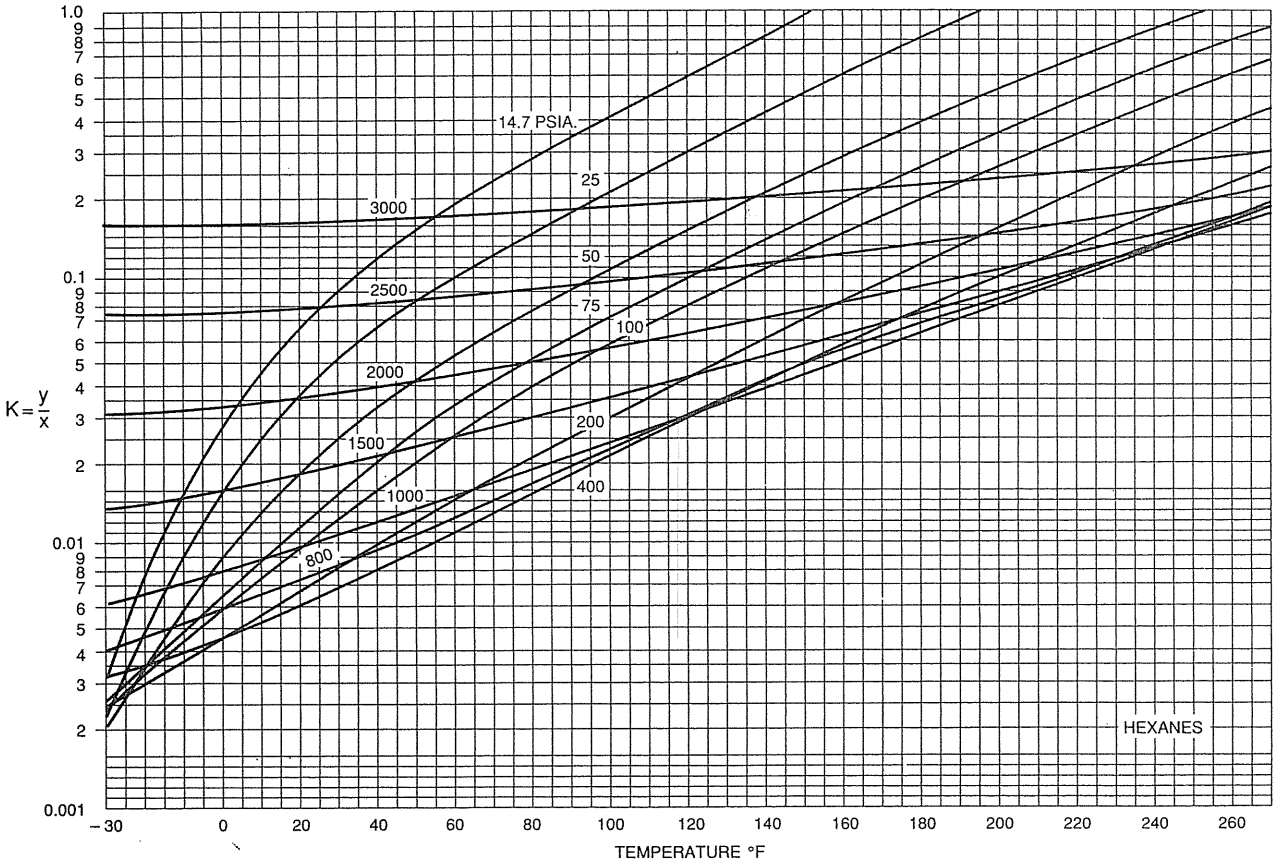

FIGURE E-8
Equilibrium constant $k = y/x$ for hexane.

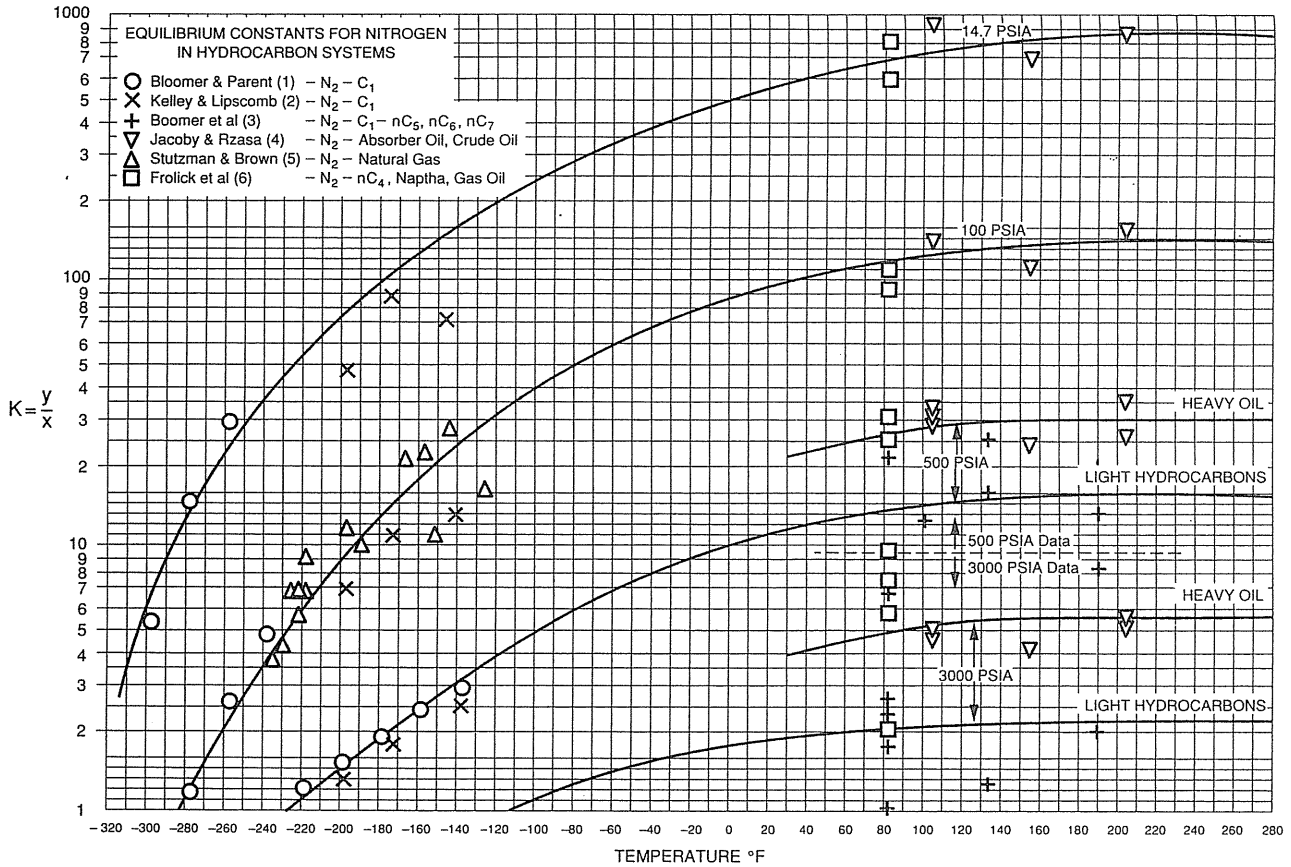

FIGURE E-9
Equilibrium constant $k = y/x$ for nitrogen.

APPENDIX F

NOMENCLATURE

A	area, ft^2 (L^2)
	group given by Eq. (D.3)
A	Absorption factor, dimensionless
$a(t)$	parameter in Appendix D
$a(t_c)$	parameter $a(t)$ at the critical point in Appendix D
B	formation factor
	group given by Eq. (D.3)
B_g	Formation factor, (L^3/L^3)
b	porous solid constant in Eq. (2.7), psi ($M/L \cdot T^2$)
	penetration ratio in Eq. (8.54)
$b(t)$	parameter in Appendix D
$b(t_c)$	parameter $b(t)$ at the critical point in Appendix D
C	compressibility, 1/psi ($L \cdot T/M$)
	coefficient for given-sized orifice in Eq. (6.21)
	performance coefficient in Eq. (9.1)
C'	orifice flow constant
C_A	shape function in Eq. (14.4)
C_D	wellbore storage constant, dimensionless
C_i	gas i concentration
C_n	number of independent components
C_P	heat capacity at constant pressure, ($M \cdot L^2/T^2 \cdot$ deg $\cdot$ mol)

C_t	total compressibility, 1/psi ($L \cdot T/M$)
C_V	heat capacity at constant volume ($M \cdot L^2/T^2 \cdot$ deg $\cdot$ mol)
C_w	wellbore compressibility, 1/psi ($L \cdot T/M$)
CR	compression ratio
D	"high-velocity" factor in Eq. (8.44) (T/L^3)
D_L	longitudinal dispersion coefficient, ft^2/s (L^2/T)
D_T	transverse dispersion coefficient, ft^2/s (L^2/T)
D_l	effective longitudinal dispersion coefficient, ft^2/s (L^2/T)
D_o	molecular diffusion coefficient, ft^2/s (L^2/T)
	molecular dispersion tensor in Chapter 17
d	diameter, ft (L)
d_p	particle diameter, ft (L)
$\dot{E}_w$	constant volume "rate" in Eq. (8.60)
F	electrical resistivity factor in Eq. (2.20)
	formation factor in Eq. (13.10), ft^3/MMcf (L^3/L^3)
	moles of feed
F_a	thermal expansion factor
F_b	basic orifice factor
F_{gr}	gas gravity factor
F_l	gauge location factor
F_m	manometer factor
F_n	number of degree of freedom
F_{pb}	pressure base factor
F_{pv}	supercompressibility factor
F_r	Renolds number factor
F_{sw}	sweep factor
F_{tb}	temperature base factor
F_{tf}	flowing temperature factor
F_w	fraction of water-flooded space containing gas
FT	flow rate–time factor
f	friction factor, dimensionless
	fugacity ($M/L \cdot T$)
f_{CK}	Cornell-Katz friction factor, dimensionless
f_L	fugacity of constituent in liquid
f_V	fugacity of constituent in vapor
f_m	mixture friction factor, dimensionless
G	gas specific gravity, dimensionless
G_0	initial gas-in-place, ft^3 (L^3)
G_p	accumulative production of gas, ft^3 (L^3)

GIP	gas in place, ft^3 (L^3)
GOR	gas oil ratio, bbl/ft^3 (L^3/L^3)
g	gravity acceleration, ft/s^2 (L/T^2)
	original content of reservoir in gas phase in Chapter 10, Scf (L^3)
$\vec{g}$	gravitation vector
g_c	conversion factor, 32.2 $lb_m \cdot ft/lb_f \cdot sec^2$
H	enthalpy, $ft \cdot lb_f$ $(M \cdot L^2/T^2)$
H_L	liquid volume fraction, dimensionless
ΔH_c	heat of combustion, ft·lb $(M \cdot L^2/T^2)$
ΔH_v	latent heat, ft·lb $(M \cdot L^2/T^2)$
h	enthalpy, $ft \cdot lb_f$ per unit mass (L^2/T^2)
h	height, ft (L)
h_v	impact head of water, in (L)
h_w	orifice differential of water, in (L)
IPI_N	normalized inverse productivity index, 1/MMcf/day (T/L^3)
J	productivity index, bbl/day·psi $(L^4 \cdot T/M)$
K	equilibrium constant, dimensionless
K_{vs}	vapor-solid equilibrium constant
k	permeability, darcy (L^2)
	thermal conductivity in Eq. (4.9), $Btu/hr \cdot ft^2$ $(M \cdot L/T^3 \cdot deg)$
	ratio of heat capacity at constant pressure to that at constant volume, dimensionless
	reaction coefficient, 1/s $(1/T)$
k_e	equivalent permeability, darcy (L^2)
k_g	measured gas permeability, darcy (L^2)
k_{ij}	empirically determined binary interaction coefficient
k_l	liquid permeability, darcy (L^2)
k_o	oil permeability, darcy (L^2)
k_p	shape function, ft^3/psi $(L^4 \cdot T^2/M)$
k_r	shape function, psi/ft^3 $(M/L^4 \cdot T^2)$
k_{rg}	relative permeability of gas
k_{rw}	relative permeability of water
k_w	water permeability, darcy (L^2)
L	length, ft (L)
	moles of liquid
L_w	lost work, $ft \cdot lb_f$ $(M \cdot L^2/T^2)$
l	characteristics length, ft (L)
l_w	lost work, $ft \cdot lb_f$ per unit mass (L^2/T^2)
M	mass, lb_m (M)

M_L	molecular weight of liquid
M_V	molecular weight of vapor
m	ratio of initial gas cap pore volume to initial oil phase pore volume
	mass, lb_m (M)
$\dot{m}$	dispersive flux, $lb_m/ft \cdot s$ $(M/L \cdot T)$
$m(P)$	pseudopressure, psi^2/cp $(M/L \cdot T^3)$
N	initial oil content of reservoir, stock-tank barrels (L^3)
N_d	diameter number, dimensionless
N_G	gas velocity number, dimensionless
N_L	liquid velocity number, dimensionless
N_T	high-velocity intensity, dimensionless
ΔN	accumulative oil production at given time, stock-tank barrels (L^3)
n	number of moles
n_H	moles of hydrate
n_0	initial moles
P	pressure, psi $(M/L \cdot T^2)$
P_{ab}	pressure to nonflooded gas reservoir at abandonment, psi $(M/L \cdot T^2)$
$\overline{P}$	average pressure, psi $(M/L \cdot T^2)$
P_{ac}	parachor for surface tension
P_b	base pressure, psi $(M/L \cdot T^2)$
P_c	critical/pseudocritical pressure, psi $(M/L \cdot T^2)$
	capillary pressure, psi $(M/L \cdot T^2)$
P'_c	adjusted critical/pseudocritical pressure, psi $(M/L \cdot T^2)$
P_D	dimensionless pressure
	dimensionless pressure drop
P_{DW}	dimensionless pressure drop at wellbore
P_g	gas pressure, psi $(M/L \cdot T^2)$
$P_g - P_f$	pressure difference of gas bubble and aquifer, psi $(M/L \cdot T^2)$
P_m	mean pressure, psi $(M/L \cdot T^2)$
P_{max}	maximum reservoir pressure used with V_{max}, psi $(M/L \cdot T^2)$
P_n	number of phases
P_r	reduced pressure, dimensionless
P_s	flowing sandface pressure, psi $(M/L \cdot T^2)$
P_t	influence pressure function, dimensionless
P_w	water pressure, psi $(M/L \cdot T^2)$
P_w	flowing wellhead pressure in Eq. (6.15), psi $(M/L \cdot T^2)$
P_0	base pressure, psi $(M/L \cdot T^2)$
P_1	upstream pressure, psi $(M/L \cdot T^2)$
P_2	downstream pressure, psi $(M/L \cdot T^2)$

Pe	Peclet number, dimensionless
PI	productivity index, bbl/psi $(L^4 \cdot T^2/M)$
Q	gas flow rate, ft^3/s (L^3/T) heat, ft·lb $(M \cdot L^2/T^2)$
Q_b	flow rate at base condition, ft^3/s (L^3/T)
Q_D	dimensionless flow rate
Q_{Df}	dimensionless sandface flow rate
Q_G	gas flow rate, ft^3/s (L^3/T)
Q_L	liquid flow rate, ft_m^3/s (L^3/T)
Q_h	flow rate at base condition, ft^3/s (L^3/T)
Q_{nr}	nonrecoverable gas, ft^3 (L^3)
Q_s	gas dissolved in water, ft^3 (L^3)
Q_{sc}	volume of gas in standard condition, ft^3 (L^3)
Q_{sf}	sandface flow rate in standard conditions, MMcf/day (L^3/T)
Q_t	influence flow rate function, dimensionless
q	flow rate, ft^3/s (L^3/T) heat, $ft \cdot lb_f$ per unit mass (L^2/T^2) mass per unit volume per unit time in Chapter 8 and Appendix C accumulative water movement in Chapter 12, ft^3 (L^3)
q_f	gas volume in reservoir condition, ft^3 (L^3)
q_{sf}	sandface flow rate in reservoir conditions, MMcf/day (L^3/T)
R	radius, ft (L) gas constant, $(M \cdot L^2/T^2 \cdot \text{deg} \cdot \text{mol})$ gas-oil ratio in Chapter 10, Scf/bbl (L^3/L^3)
Re	Reynolds number
Re_{CK}	porous media Reynolds number
R_s	gas-oil ratio for saturated crude oil, std ft^3/bbl (L^3/L^3)
r	radius, ft (L)
r_D	dimensionless radius
r_b	gas bubble radius, ft (L)
r_d	drainage radius, ft (L)
r_w	wellbore radius, ft (L)
S	interfacial tension in Eq. (2.11) entropy $(M \cdot L^2/T^2 \cdot \text{deg})$ solubility of gas at any pressure in Chapter 10, Scf/bbl (L^3/L^3) stripping factor, dimensionless
S_g	gas saturation gas solubility in Eq. (14.6)
S_o	oil saturation

	solubility of gas at initial pressure and reservoir temperature in Chapter 10, Scf/bbl (L^3/L^3)
S_w	water saturation fraction of connate water in Eq. (14.5)
s	skin factor entropy per unit mass $(L^2/T^2 \cdot \text{deg})$
s'	apparent skin factor
T	temperature (deg)
T_c	critical/pseudocritical temperature (deg)
T_c'	adjusted critical/pseudocritical temperature (deg)
T_r	reduced temperature, dimensionless
T_0	base temperature (deg)
t	time (T)
t_D	dimensionless time
t_{DA}	dimensionless time
U	internal energy, $ft \cdot lb_f$ $(M \cdot L^2/T^2)$
$\vec{U}_g$	gas velocity vector
$\vec{U}_w$	water velocity vector
u	interstitial velocity, ft/s (L/T) internal energy, ft · lb per unit mass (L^2/T^2)
V	volume, ft^3 (L^3) moles of vapor
V_{ab}	volume of gas reservoir space not flooded at abandonment, billion ft^3 (L^3)
V_{max}	maximum volume of reservoir space ever containing gas, billion ft^3 (L^3)
V_{SG}	superficial velocity of gas, ft/s (L/T)
V_{SL}	superficial velocity of liquid, ft/s (L/T)
V_w	wellbore volume, ft^3 (L^3)
$\bar{v}$	specific volume, ft^3/lb_m (L^3/M) velocity vector, ft/s (L/T)
v	velocity, ft/s (L/T) formation volume of 1 Scf gas in Chapter 10, ft^3/Scf (L^3/L^3)
v_m	mixture velocity, ft/s (L/T)
v_o	formation volume of 1 Scf gas at initial condition in Chapter 10, ft^3/Scf (L^3/L^3)
W	work, ft·lb $(M \cdot L^2/T^2)$ accumulative water influx into reservoir in Chapter 10, ft^3 (L^3)
W_T	mass flow rate, lb_m/s (M/T)

W_e water influx, ft^3 (L^3)
w work, $ft \cdot lb_f$ per unit mass (L^2/T^2)
accumulative water production in Chapter 10, ft^3 (L^3)
w_s adiabatic horsepower, $ft \cdot lb_f/s$, $(M \cdot L^2/T^3)$
X elevation, ft (L)
x mole fraction of constituent in equilibrium liquid phase
Y expansion factor
y mole fraction of constituent in vapor phase
Z compressibility factor, dimensionless
$\alpha(T)$ temperature correction factor
α_L longitudinal dispersivity coefficient, ft (L)
α_T transverse dispersivity coefficient, ft (L)
β high velocity coefficient in Eq. (2.9), ft^{-1} (L^{-1})
γ coefficient in Eq. (2.10) $(L \cdot T/M)$
conversion factor
δ flow correction factor in Eq. (8.5)
ϵ_3 adjustment factor to pseudocritical temperature
η conversion coefficient
θ contact angle in Eq. (2.11)
weighting factor in Eq. (11.11)
intercept angle in Eq. (11.23)
κ coefficient in Appendix D
λ conversion coefficient
μ viscosity, cp $(M/L \cdot T)$
chemical potential in Eq. (3.1)
μ_H chemical potential of water in the hydrate phase, $ft \cdot lb$ per unit mass (L^2/T^2)
μ_W chemical potential of water, $ft \cdot lb$ per unit mass (L^2/T^2)
μ_g gas viscosity, cp $(M/L \cdot T)$
μ_o oil viscosity, cp $(M/L \cdot T)$
μ_w water viscosity, cp $(M/L \cdot T)$
μ_β chemical potential of an unoccupied hydrate lattice, $ft \cdot lb$ per unit mass (L^2/T^2)
μ' Joule-Thomson coefficient
ρ density, lb_m/ft^3 (M/L^3)
ρ_V density of vapor, lb_m/ft^3 (M/L^3)
ρ_g gas density, lb_m/ft^3 (M/L^3)
ρ_l liquid density, lb_m/ft^3 (M/L^3)
ρ_m mixture density, lb_m/ft^3 (M/L^3)

ρ_w water density, lb_m/ft^3 (M/L^3)
σ surface tension in Eq. (2.12), dyn/cm (M/T^2)
packing factor in Eq. (2.20)
τ shear stress, g/cm^2 $(M/L \cdot T^2)$
ϕ porosity, dimensionless
Eucken coefficient
ψ arbitrary function in Chapter 11
ω acentric factor
∇ Hamilton operator

INDEX